14TH INTERNATIONAL SYMPOSIUM ON LANDSLIDES

Book of abstracts

8th → 12th July 2024
Chambéry ◆ France

ISBN 978-2-9585706-1-3

14TH

INTERNATIONAL SYMPOSIUM ON LANDSLIDES

After Kyoto 1972, Tokyo 1977, New Delhi 1980, Toronto 1984, Lausanne 1988, Christchurch 1993, Trondheim 1996, Cardiff 2000, Rio de Janeiro 2004, Xi'an 2008, Banff 2012, Napoli 2016, Cartagena 2021, The XIVth International Symposium on Landslides, ISL 2024 has been held in Chambéry (France) which draws a bridge between geosciences and alpine space.

This Symposium was organized in close partnership with a network strongly involved in geosciences and geomechanics applied to slope instabilities, bringing together the following institutions, all being representative of the French community involved in slope engineering:

The CFMR
French Society for Rock Mechanics
Visit the website :
https://www.cfmr-roches.org/

The CFMS
French Society for Soil Mechanics
Visit the website :
https://www.cfms-sols.org/

The CFGI
French Society for Engineering Geology
Visit the website :
http://www.cfgi-geologie.fr/

Focused on "Landslides across the scales: from the fundamentals to engineering applications", the Symposium, with 328 participants, 150 oral presentations and 100 posters, has addressed the following items:

- Multiscale constitutive modeling for soils and rocks
- Weathering effects on soils and rocks destabilization
- Permafrost and ground stability
- Survey techniques
- Modeling of soil and rock hazards
- Recent progress in numerical tools for landslide modeling
- Risk analysis and mitigation
- Modeling and design of protective structures
- Artificial intelligence and machine learning techniques applied to slope engineering
- Case studies

This book of abstracts constitutes an up-to-date synthesis of the latest scientific and technical productions which all contribute to a better understanding and mitigation of slope instabilities.
On behalf of the Scientific Committee, the Advisory Committee, and the Organizing Board as well, we would like to gratefully acknowledge all the contributors, and hope that this scientific material will constitute a fruitful literature resource.

Prof. Véronique Merrien
Prof. François Nicot
Chairs of ISL 2024

AGENDA

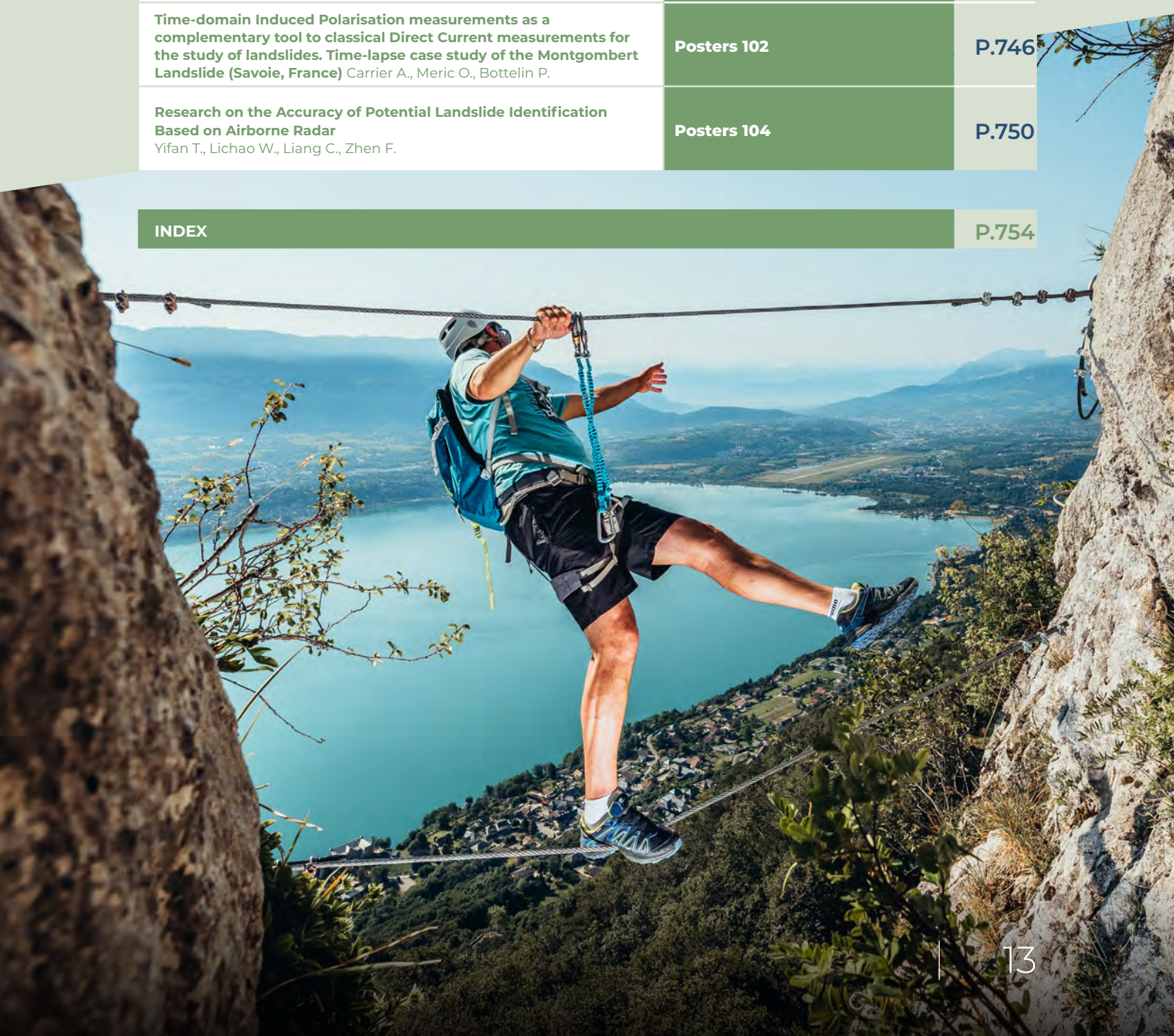

Assessment and management of landslide risk along roads: the potential of incident records for ex-post evaluation

Jordi Corominas[1]

[1] Department of Civil and Environmental Engineering, Universitat Politècnica de Catalunya-BarcelonaTech, Barcelona, Spain

SUMMARY: Landslide inventories have multiple uses. The main objective of this paper is to show the potential of the landslide inventories in risk management. In particular, the verification of the predictions made, the quantification of the consequences, the assessment of the performance of risk mitigation measures and ex-post cost-benefit analysis. The paper presents a brief summary of the procedures used and an example of application, the results of which are expected to contribute to decision-making.

Keywords: landslide inventories, quantitative risk analysis, cost-benefit analysis, roads, Gipuzkoa

Introduction

Landslide inventories (hereinafter LI) contain information on the spatial distribution, type, geometry and recurrence of slope failures and have multiple applications. They allow us to evaluate the extent and relevance of mass-wasting processes in mountainous regions, quantify the morphological changes of the slopes and, in this way, understand how landslides contribute to the evolution of the landscape (Hovius et al. 1997; Roering et al. 2005; Bishop, 2007; Korup et al. 2010; Parker and others 2011). Empirical relationships have been established between various features of the inventoried landslides to make estimates. Thus, it is possible to determine the volume of the landslide from its area for different types of landslides (Larsen et al. 2010; Jaboyedoff et al. 2020), predict the post-failure evolution of the landslide in terms of the expected runout and affected area (Hsü, 1975; Corominas 1996; Rickenmann, 1999; Legros, 2002; Copons and Vilaplana, 2008), or assess the survival of landslide dams from their volume and shape (Ermini and Casagli, 2003; Peng and Zhang, 2012; Fan et al. 2020).

The analysis of the LI may also reveal the role of both driving and conditioning factors of slope stability. Multitemporal LI are compiled to establish relationships between the occurrence of slope failures (e.g. number and size) and the magnitude of the triggering events such as heavy rain episodes (Guzzetti et al. 2008; Segoni et al. 2018; Emberson et al. 2022) and earthquakes. (Keefer, 1984, 2002). Although the relation between climate and landslides is complex and subject to limitations (Corominas, 2000), climatic inferences can be drawn from the presence of ancient landslide clusters, that were triggered under climatic scenarios different from the current ones (Trauth et al. 2003; Soldati et al., 2004). Likewise, historical and prehistoric earthquake series can be completed thanks to the inclusion of dated landslide clusters, improving seismic hazard assessment (Schuster et al. 1996; Bull, 1996; Yano et al. 2019).

On the other hand, LI serve to detect changes in the trend of landslide occurrence and the causes behind them. The analysis of multitemporal LI has evidenced the exhaustion of sediments and the consequent reduction in the number of landslides after major earthquakes (Liu et al. 2013; Marc et al. 2015; Zhang and Zhang 2017). Likewise, the systematic monitoring of the rate of

occurrence of debris flows, rock falls and rock avalanches and landslides in environments as diverse as high mountains and tropical regions has highlighted the relevance of climate change. (Kellerer-Pirklbauer et al. 2012; Coe at al. 2018; Frank et al. 2019). Thanks to their sensitivity to meteorological phenomena, multitemporal LI have become a consistent and reliable indicator to monitor the impact of climate change on slopes (Wood et al. 2015).

LI compilation is now a routine activity for landslide susceptibility and hazard analyses. One of the first applications of LI, more than 50 years ago, was the analysis of susceptibility. Pioneering work to evaluate landslide propensity was carried out by superimposing identified landslides on geological and slope angle maps (e.g. Brabb, 1984; Varnes, 1984). Subsequently, landslide susceptibility maps were prepared by performing more sophisticated data treatment, relating landslide occurrence to topographic and geoenvironmental variables (see reviews in Van Westen et al. 2008; Reichenbach et al. 2018). Considering that models must be verified and validated, one step forward in the use of LI is the evaluation of the performance of susceptibility and hazard assessment procedures. Multitemporal LI are used to train models with a given LI and validate them with a more recent one (Irigaray et al. 1999; Remondo et al. 2003; Chung and Fabbri 2003, Lee et al. 2008; Frattini et al. 2010). An output of the landslide hazard analysis is the definition of the potentially affected areas and their probability. To do this, it is required the knowledge of the magnitude and frequency of the slope failures, this being a relationship that can be obtained from complete LI (Guthrie and Evans, 2004; Malamud et al. 2004; Harp et al. 2011).

Quantitative Risk Analysis (QRA) has progressively gained ground because it provides quantitative estimates to make better informed decisions (Fell et al. 2005). The starting point for QRA, is the probability of landslide occurrence (or frequency) for a range of volumes. It can be estimated from LI. However, the lack of resolution of some of them may generate errors such as the underreporting of small events (Barlow et al. 2012; Marc and Hovius, 2015; Williams et al. 2019). This may underestimate risk in locations where loss of life is directly associated to the occurrence of frequent small-size events as it occurs in roads and railways.

LI have rarely been used to validate risk analyses and the subsequent prediction models. Neither have they been applied in the evaluation of the performance of the corrective measures and cost-benefit analyses. The objective of this contribution is to present additional applications of LI, in particular, the records of landslide incidents in roads. More specifically, we aim at showing the capability of the landslide incident records to test the predictive skill of the QRA (e.g. number of victims and impacted cars), the quantitative estimation of both direct and indirect losses, to assess the performance of the risk mitigation measures, and to carry out a preliminary cost-benefit analysis (CBA).

This contribution is organized as follows: first, we recall the basic concepts of QRA of roads of and cost-benefit analysis. Next, we present an application example in the coastal road of Gipuzkoa (N. Spain).

Quantitative Risk Analysis: estimating consequences and their associated probabilities

The objective of the quantitative risk analysis is to evaluate the consequences (e.g. damages, casualties) of potentially hazardous events and their associated probabilities. Several administrations have incorporated QRA into their decision-making process. The framework for the use of QRA for landslides and engineered slopes was reviewed by Fell et al. (2005) and recommendations for its implementation may be found at Corominas et al. (2014). In some contexts, the absolute value of risk is not as important as the relative risk. This may be the case of both excavated and natural slopes on road, in which the goal of the analysis is to prioritize the adoption of risk mitigation measures (Fell et al. 2005).

Risk can be estimated for different types of exposed elements such as buildings (Corominas et al. 2005; Agliardi et al. 2009; Ferlisi et al. 2016; De Biagi et al. 2017), roads and railways (Bunce et al. 1997; Hungr et al. 1999; Fell et al. 2005; Ferlisi et al. 2012; Macciotta et al. 2016; Lu et al. 2020) and people (Guzzetti et al. 2003; Corominas et al. 2019; Stock et al. 2014). Adjustments of each risk component are necessary with regard to the type of threatened element(s) as each display different exposure and vulnerability attributes. In practical terms, to quantify the risk on roads, it is necessary to break down the term hazard into its components, define the spatial-temporal characteristics of the threatened elements and specify the type of expected damage. The annual risk is determined as the product of the probability (or frequency) of a landslide of magnitude *m*, the probability that the landslide mass reach the road located at given distance *x*, and the spatial-temporal probability of the threatened elements (Dai et al. 2002; Fell et al. 2005; Agliardi et al. 2009):

$$R(A) = \sum_{m=1}^{M} f_m \,.\, P(X{:}\,R).P(T{:}\,X).V \quad [1]$$

Being:
R(A): Annual risk
f_m: annual frequency of landslides of magnitude *m* (between 1 and M).
P(X:R): probability that landslides of magnitude *m* reach the road located at a distance *x*, once the failure has occurred.
P(T:X): probability that any given element is in the trajectory of the landslide at the instant *t* of its occurrence (exposure)
V: vulnerability of the exposed element to a landslide event of magnitude *m*

Risk has to be calculated for all range of event magnitudes. In case of rapid landslides (e.g. debris flows, rockfalls, rock avalanches), large events are characterized by a lower frequency, larger runout and higher velocity (impact energy) than the small ones. Thus, the hazard components, f_m and *P(X:R)* have to be computed separately for every landslide source and range of landslide magnitudes (Corominas and Mavrouli, 2011). In case of roads, using Equation 1 requires knowing the probability of landslide occurrence in each of the slopes and cuts through which the road runs (Guzzetti et al. 2004). Since this information is not usually available, landslide frequency is typically obtained from the record of events that reach the roadway, without consideration of events retained on the slopes. Furthermore, the reported volume of fragmental rockfalls is usually that of the debris that reach the roadway, omitting the mass that remains in the slope. In this case, reach probability *P(X:R)* may be adapted to express whether the landslide debris occupies one or more lanes, or the entire width of the roadway. If the road is narrow, the reach probability is assumed equal to 1 (Bunce et al. 1997).

The elements threatened on a road are the infrastructure itself and moving vehicles and people. In the case of the road itself, since it is a static element, its exposure is 1. The procedure to quantify exposure *P(T:X)* of moving elements in roads and railways has been proposed by various authors (Roberds, 2005; Ferlisi et al. 2012; Macciotta et al. 2016). The probability of impact on any vehicle moving along a given section at the time of occurrence, is a function of the flow of vehicles and the width of the landslide debris, which is variable for each event size (Nicolet, et al. 2016):

$$P(T:X) = \frac{\frac{N_v}{24} \cdot \frac{L_v + W_r}{1000}}{V_v} \quad [2]$$

Being:
N_v: flow of vehicles (# vehicles/day)
L_v: vehicle length (m)
W_r: width of the front occupied by the landslide debris (m)
V_v: vehicle speed (km/h)

Consequences caused by landslides in roads generally include casualties (injuries and fatalities), property damage, clean-up and repair, loss of service (time) and environmental and social impacts (Roberds, 2005). The two later will not be addressed in this paper. Accordingly, equation [1] may be used to determine the annual risk of fatal accident by assigning a vulnerability value to people traveling in a vehicle. In this paper, vulnerability is used to refer the probability that a particular life will be lost, given that the person(s) is affected by the landslide (Li et al. 2010). The expected number of impacted vehicles *N(I)* per year (for a range of rockfall magnitudes) is calculated using equation [2], eliminating the vulnerability term. That is:

$$\mathrm{N}(I) = \sum_{m=1}^{M} f_m \,.\, P(X:R).P(T:X) \quad [3]$$

The return period T_i (years) of one vehicle being impacted is then obtained as follows:

$$T_i = \frac{1}{N(I)} \quad [4]$$

The economic consequences have two components. Direct costs, which are the damages to circulating vehicles as well as the debris removal, road cleaning, and replacement of the pavement if necessary, and the removal of remaining unstable mass from the slope and its stabilization. Direct damage on roads is often quantified based on the experience of the road managers and construction companies. A practical example is presented in the following section. In the cost estimate, slope reinforcement and protection work, such as the instalment of nets, construction of flexible protection barriers, walls or galleries, will not be considered repairs but rather as investments.

On the other hand, each incident produces indirect costs, which are difficult to estimate. The indirect losses refer to costs to the affected economic activity that follow the event, sometimes with a certain time lag. The most obvious are costs due to temporary traffic interruptions such as loss of working-time and detour costs. The latter include increased fuel costs in function of the additional distance, lost working-time for the commuters and motorway tolls. Other costs of the economic activity that can be monetized such as loss of productivity, isolation of population will not be addressed in this paper.

Consequently, the total costs are the sum of the direct cost and the indirect cost. It is a function of the severity of the damage and the number and value of elements affected. For this reason, no upper limit is set. The total risk (annualized losses) is obtained from the sum of the product of the annual frequency for each event magnitude class and its associated consequences. It is expressed as follows (Mavrouli et al. 2019):

$$R_T = \sum_{m=1}^{M} f_m . C \quad [5]$$

Being,
R_T, the total annualized risk (€/year)
f_m, the annual frequency of the slope failure of magnitude m
C: cost due to the occurrence of a landslide of magnitude m

The total annual surplus costs are (€/year):

$$C_a = \sum_{m=1}^{M} f_m . \left[r + (t.s + km.c_f + p)\right] \quad [6]$$

Where:
C_a: total annual excess cost (€/year)
f_m: annual frequency of each size range of landslides (1…M) (#/year)
r: cost of cleaning and repairing the road (€ for a m magnitude event)
t: excess travel time invested in diversions, for each size of landslide (in h)
s: hourly labour cost (€/h)
km: additional distance travelled on the detour (km)
c_f: cost of fuel (€/km)
p: tolls (€)

Cost-benefit analysis

One important task in risk management is the evaluation of benefits from preventive actions which can encourage authorities and population to invest money for preventing losses due to slope failures (Salbego et al. 2015). Cost-Benefit analysis (CBA) is an assessment method that quantifies in monetary terms the value of all consequences of a project or decision. The ultimate goal of CBA is to help decision-makers to make their decisions more rational and allocate resources more efficiently. This type of analysis has been introduced to evaluate the benefit of possible measures and projects designed to reduce the risk of snow avalanches and rockfalls (Fuchs et al. 2007; Moos and Dorren, 2021), debris flows (Narasimhan et al. 2016), large landslides (Crosta et al. 2005; Frattini and Crosta, 2006) or to quantify the savings in case they had been implemented (Salbego et al. 2015).

There are two major types of cost-benefit analysis (Broadman et al. 2011): *(i)* Ex-ante CBA, which is conducted before a project is started or implemented. It is most useful for deciding whether resources should be allocated to a particular project that is under consideration or to select possible alternatives; *(ii)* Ex-post CBA is conducted at the end of a project. The value of ex-post analysis is that it provides information on whether the investment was worthwhile, it provides guidance of the accuracy of earlier ex-ante CBA and it may help to understand the reasons for any divergence between predicted and actual benefits or costs.

Considering the flow of costs (*Ct*) and benefits (*Bt*), the real expense comparison (indicator of profitability) is expressed by the Net Present Value (*NPV*), defined as the difference between the benefits/savings and the costs throughout the years (Frattini and Crosta, 2006):

$$NPV = \sum_{t=0}^{T} \frac{B_t}{(1+r)^t} - \sum_{t=0}^{T} \frac{C_t}{(1+r)^t} \quad [7]$$

B_t are the savings at time t
C_t are the costs at time t
r is the interest rate

t can be set to a horizon time considering the minimum interest rate and the inflation. For C_t, r may be the interest rate for money; For B_t, r may be the inflation, that is the increase of savings (losses not produced) with time due to increase of repair and indirect costs.

Ex-ante analyses are a powerful tool for decision making. However, still are forecasts. It is therefore necessary to verify their accuracy and reliability. Various ex-post analyses show that the actual figures may show significant deviations, as has been observed in highway construction projects (CSIL, 2012).

Using incident records to support risk management: application example

The objective of the case study that we present here is to highlight the value of the compilation of incident records, in particular, their completeness and resolution. Preparing a good quality database is often a pending issue for road administrations and decision-makers, which have to combine their daily management duties and maintenance tasks with planning future actions.

Landslides affecting roads is a major problem because an accident induced in one place affects the entire length. One of the most difficult decisions faced by road managers is to allocate the correct proportion of resources to the treatment of potential threats so as to maximize the reduction of risks for a given level of expenditure (Hungr et al. 1999). To address this issue requires the availability of incident records with acceptable spatial resolution. Some quantitative risk assessments are carried out on very short stretches of road (e.g. Bunce et al. 1997; Macciotta et al. 2020). The analysis for long stretches of roads or railways is often addressed as a whole, considering several critical assumptions, such as the uniform spatial distribution of the landslide sources and of the observed incidents (Hungr et al. 1999; Ferlisi et al. 2012; Macciotta et al. 2016). The analysis can be somehow segregated by adding criteria for selecting potential landslides or rockfall sources (Guzzetti et al. 2004), by considering the frequency of outlying boulders (Stock et al. 2014), or by dividing the sources (Corominas et al. 2019). When the objective is to identify the most dangerous sections and prioritize preventive measures, risk analysis should be segregated into short sections.

<u>The coastal road of Gipuzkoa</u>

To illustrate the potential of landslide incident records in performance of the QRA, and in the ex-post CBA, we present the analysis of the road that connects Zarautz, Getaria and Zumaia by the sea (Gipuzkoa province, Basque Country, N. Spain). Risk in this road was analysed in a previous work (Corominas, 2022) using data from the newspaper library and the records of the road maintenance crews for the period 1994-2008. More recently, the record of the maintenance crews has been extended for the period 2009-2022. This additional information allows the

analysis of the risk trend and changes over the last 14 years and evaluate the performance of the reinforcement and protection works carried out on rock slopes. Risk on the coastal road will be calculated for the contexts selected, using equations [1] to [4].

Historically, the coastal road originates from the junction of various local connection roads that gave rise to the current N-634. Its construction was carried out on the initiative of several mayors of the area. The layout of the coastal road was configured by the addition of sections built separately: Zarautz- Getaria (1863-1865) and Getaria-Zumaia (1882-1886). The total length of the coastal road studied is 11 km although the length of the section that contains the slopes and rock cuts analysed is 8km (figure 1). Since its construction, the road has been very conflicting. The geologic materials that make up the cut slopes are alternations of sandstone and claystone (facies flysch). The incidents began shortly after its inauguration. As an example, in August 30th 1884, the newspaper La Vanguardia, mentioned that a rock detached from Mount Garatamendi fell rolling onto the road a short distance from the car in which Mr. Sagasta (Spanish President at that time) was traveling, fortunately without any damage. The largest event took place on December 29, 1960 at the current km 24+200 to 24+400. The plane of failure propagated more than 70m high, up to the top of the cliff that runs over the highway (figure 2). The affected rock mass exceeded 35.000 m^3 and a significant fraction of it (more than 20.000 m^3) remained on the slope itself (Macau, 1963). The repair works lasted for almost 6 months, the stretch was reopened on June 25, 1961.

Figure 1. Analysed section of the N-634 road between Zarautz-Getaria-Zumaia along the coast and location of the figures that are discussed in the text.


Figure 2. December 1960 slope failure at km 24+400 of the highway from Getaria to Zumaia (photo: Macau, 1963)

On December 1st 1998, a large translational landslide occurred at km 23+900 to 24+000 that completely displaced a 115m long section of the road platform. The mobilized volume exceeded 30,000 m^3. The repair works lasted 4 months and cost more than €1.1 million at the time. During all this time road was closed and the traffic diverted.

Materials and methods

The QRA of the coastal road of Gipuzkoa is based on the compiled incident records. This approach is widely used because its simplicity but it requires having a complete inventory of events, particularly the small ones. Missing small events may increase significantly risk in locations where loss of life is directly associated to the occurrence of frequent small-size events as it happens in roads and railways.

The inventory of rock falls was provided by Gipuzkoa road Department and consist of reports of the road maintenance crews and records of emergency calls (SOS-Deiak) for the period 1994-2022. The inventory has been completed with screening of the road incidents collected by the written press (mostly El Diario Vasco, Noticias de Gipuzkoa, and La Vanguardia). Sporadic references to incidents have been found in the written press since the road was built. However, only after the Spanish Civil War has there been continuity in the publication of the local daily press, more specifically since 1947. The digitized copies have been consulted using search criteria with keywords. The inventory includes 1176 records for the period between 1947 and 2022. As a precaution, the small events (< 500m^3) that occurred between 1947 and 1994 were removed from the inventory because the record is clearly incomplete. This gives a total of 1080 events available.

The description of the events is generally vague. The inventory includes rock falls, which are the predominant mechanism, debris flows that develop in the sectors of the clay-rich flysch outcrops, and a few large landslides (e.g. events of 1960, 1998, already mentioned). Based on the descriptions, it is not possible to separate the rockfalls from the debris flows and they will be analysed together. In the records of the written press, the kilometre point is rarely indicated with enough accuracy (errors of up to a few hundred meters have been detected) and references to the volume of the events are mostly qualitative. The incidents most frequently mentioned in the media are those involving road closures. The events that have had a significant impact on the traffic or have caused fatalities are documented in greater detail. However, records prior to 1994 are only a small sample of landslide occurrence before 1994. The records of the maintenance crews show the actual rate of slope failures is an order of magnitude higher than that reported by the written press. This shows the limitations of the information provided by the press for risk analysis.

The record of maintenance crews exists since 1994 and extends until 2022. We have verified and supplemented it, when required, with the record of calls to emergency telephones (SOS-Deiak). The record compiles landslide events (mostly rockfalls) and can be considered complete for rock blocks larger than 0.3m-length. The descriptions include the date, the location (kilometre point with a 100m resolution), time of occurrence and, often the time required for cleaning or closure time. Between 1994 and 2006, descriptions of the volume were ambiguous, using generic terms (see table 1). As of 2007, the maintenance teams systematically accompany the descriptions of the incidents with photographs. This has allowed obtaining a correspondence between the crew generic descriptions and the volumes estimated from the photos. Given the difficulty of estimating precise volumes, they are grouped into 6 magnitude classes ordered

according to a logarithmic scale (see table 1). Class F will likely represent the largest credible event because photographs of historical events (e.g. 1960, 1998) show that this failure-size involves the whole slope and not just the excavated part.

The maintenance crew descriptions may contain imprecisions that may affect the quality of the analysis. To verify the resolution of the LI, photographs and locations or geographical references of the compiled events (e.g. road intersections, local toponyms) were checked. It is found that there may be a hundred meters or more of error in some location, which is sufficient for the level of accuracy of the analysis we intend to perform.

Size class	Volume (m^3)	Descriptor	Traffic impact
A	≤0.5	"remove stones", "stones on the road"	No interruption; closure for cleaning <2h
B	0.5 to ≤5	"big stone", "rockfall", "obstructs circulation"	No interruption; alternate pass; closure 6-12h
C	5 to ≤50	"rockfall" "rockfall covering a lane"	1-2 days road closure
D	50 to ≤500	"rockfall occupying both lanes"	7-15 days road closure
E	500 to ≤5,000	"rockfall occupying both lanes"	30-45 days road closure
F	> 5,000	Large failure (e.g. 1963 and 1998) events	Road closure lasting for several months

Table 1. List of the maintenance crews' descriptors used to estimate the magnitude of the events and their impacts.

The observation period has extended by an additional 47 years with data provided by the written press only for size classes (D, E, F), resulting in a record of 76 years (table 2). Frequencies are obtained by counting the number of occurrences in a given volume bin. Note that the frequency of D, E, F events of the period 1947-1993 is lower than that of the period 1994-2008. This may be due to omissions from the newspaper's record, but it may also be due to natural variability itself. These events were incorporated in the inventory to verify the predictive capacity of the QRA for estimating accidents and fatalities. Despite all limitations mentioned, this inventory is one of the longest, most complete and accurate available in Spain.

class	Volume (m^3)	Events 1947-1993	events/yr	Events 1994-2008	events/yr	Events 2009-2022	events/yr
A	≤0.5			439	29,27	176	12,43
B	0.5 to ≤5			254	16,93	103	7,21
C	5 to ≤50			43	2,87	22	1,57
D	50 to ≤500	11	0,15	15	1,07	6	0,50
E	500 to ≤5,000	4	0,05	2	0,13	1	0,07
F	> 5,000	3	0,04	1	0,07	0	0,00
total		18		754		308	

Table 2 - Rockfall magnitude classes and their respective frequencies on the N-634 highway between Zarautz, Getaria and Zumaia

According to Hungr et al. (1999), censoring of data may occur because *(i)* data may be underreported or the record incomplete; *(ii)* the sample time interval may be too short to adequately represent low-frequency events; *(iii)* a systemic censoring may result from the presence of protective works in some parts of the routes, which are effective in intercepting some of the smaller events. As the 1994-2022 records come from two different overlapping and sources and were cross-checked, we consider the inventory complete. The compilation provided by the written press is assumed representative of the largest sizes, which are those that have caused closures and traffic detours. The events reported by the media since the inauguration of the road, in the period between 1865-1886 until 1947, were not incorporated due to lack of

continuity. It is important noticing, that in the latter, no reported event had exceeded the dimensions of the largest events included in the inventory. The records available for sizes A, B, C between 1994 and 2008 are assumed representative for the entire period 1947-2008. Finally, the censoring effect due to the presence of protection structures may exist. In the Gipuzkoa coastal road, slope reinforcement and protection work have been undertaken over time, but more intensively in the last 15 years. For this reason, although the volume distribution of 1947-2008 conforms to a power law, we have worked directly with the observed frequency.

In order to assess the predictive capacity of the risk analysis and evaluate the performance of the slope stabilization and protection works, the inventory will be divided into two parts of variable length based on the scenario analyzed.

Risk of loss of life (P_{LOL})

In this analysis, the inventory is first divided into two parts: 1974-2008 and 2009-2022. Each one contains a complete record of all event sizes of 15- and 14-years duration, respectively. Given that risk mitigation works have been carried out more or less continuously for the last 30 years, it does not make sense to test the predictive capacity of the risk model obtained with the 1947-2008 inventory with the observations from the period 2008-2022. Instead, we analyze the capacity of the model built with the 1947-2008 inventory to predict personal risk in the same period. Likewise, we also analyze the variation in risk between both periods, to assess the effect of the risk reduction measures implemented and the benefits obtained.

First, the predictive capacity of QRA (1947-2008) is tested for the entire length of the road (8 km). Several simplifying assumptions about the traffic and the rockfall occurrence are made: traffic is uniformly distributed in time and space, independent of rockfalls, and that each vehicle has an average length of 4.5m. The traffic flow in the road measured in two road sections is provided by the Gipuzkoako Foru Aldundia (DFG, 2023). The average flow of vehicles between Zarautz and Zumaia is 6340 vehicles per day (1995-2022 period). Of these, 3170 circulate in the inner lane (hillside) and 3170 in the outer lane (sea side). The risk has been calculated separately in each of the lanes because P(X:R) is different in each of them and also the flow of vehicles. An average speed of 60km/h is considered. Table 3 shows the values of the different risk components used to solve equations 1 to 3 while the results of the risk analysis are summarized in Table 4.

M_i (m^3)		**f_m**	**P(T:X) hill side**	**P(T:X) sea side**	**Wr front width (m)**	**V (people inside cars)**
≤0,5	A	29.27	0.40	0.05	1.5	0.01
0,5 a ≤5	B	16,93	0.80	0.40	3.5	0.10
5 a ≤50	C	2.87	1.00	0.85	10	0.30
50 a ≤500	D	0.42	1.00	1.00	20	0.75
500 a ≤5.000	E	0.10	1.00	1.00	50	0.90
> 5.000	F	0.06	1.00	1.00	100	1.00

Table 3. Values of the risk components used to calculate personal risk

Values of the probability components of equations 2 and 3 shown in Table 3 were empirically assigned. The frequency (*fm*) for each magnitude class is calculated from the inventory. The runout probability P(T:X) for the inside lane (hillside) or outside lane (seaside) is assigned separately based on the observations of the photos taken by the maintenance crews. In this case, the presence of ditches, shoulders and widenings next to the roadway was taken into account. The vulnerability of people inside vehicles was estimated from the analysis of various landslide

accidents. The size of the debris front width W_r (equation 3) includes the divergence of rock fragments' trajectories and the widening of the debris flow lobes observed in the photos.

The number of impacted vehicles per year is 0.80 that is, one impact every 1.25 years (Table 4). As expected, for small-size events, driving in the lane on the slope side carries a higher probability of impact than in the lane on the sea side (between eight and two times higher). This effect disappears as the size increases because the mass of debris covers the two lanes. The number of accidents caused by rockfalls reported by the newspapers during the period 1947-2008 (62 years) amounts to 24 accidents, which corresponds to a return period of 2.6 years. Although the frequency of the impacts reported is lower than the calculated, in our opinion real numbers are close to the value obtained with the QRA. The observations of the period 1947-1993 come exclusively from the written press. Impacts of small rock fragments, without causing significant damage to the vehicles, are not usually mentioned in the newspapers. Proof of this is the fact that in the period 1994-2008, only 2 of the 16 accidents reported by the SOS-Deiak emergency telephone number (1.14 impacts/year) were published in the written press.

Size	f_m	Hillside lane		Seaside lane		Total	
		P_{LOL}	Impacted vehicles/yr	P_{LOL}	Impacted vehicles/yr	P_{LOL}	Impacted vehicles/yr
A	29.27	0.0015	0.1546	0.0002	0.0193	0.0035	0.1740
B	16.93	0.0239	0.2386	0.0119	0.1193	0.0358	0.3579
C	2.87	0.0275	0.0915	0.0233	0,0778	0.0508	0.1693
D	0.42	0.0170	0.0226	0.0170	0.0226	0.0339	0.0452
E	0.10	0.0104	0.0116	0,0104	0.0116	0.0209	0.0232
F	0.06	0.0148	0.0148	0,0148	0.0148	0.0297	0.0297
total		0.0951	0.5338	0.0777	0.2655	0.1728	0.7992

Table 4. Probability of loss of life and number of expected vehicles impacted based on 1947-2008 observed frequency

The annual risk of loss of life is 0.173 that is, one fatal accident every 6 years. The press reports between 1947 and 2008 have recorded 5 accidents with victims, that is, one accident every 12.4 years, causing 2 deaths and 4 injuries. In light of these results, it looks like that QRA performs satisfactorily in estimating the number of impacts against vehicles but overestimates the number of fatalities. The calculation could be adjusted to the observations by reviewing the vulnerability criteria used, but it must be taken into account that it was carried out considering the current average daily traffic. At the beginning of the analyzed period, daily traffic was significantly lower and the personal risk with current traffic figures could be overestimated. A recurring question in risk analysis is whether the greatest risk is due to frequent small events or to large events with a low probability of occurrence. As regards the coast road, the highest risk of impact and death is associated with small to medium-size events. This finding make sense because the probability of impact increases proportionally with frequency.

First rockfall flexible barriers in the coastal road were installed in the early 1990s while in the mid-2000s the installation of meshes and the execution of bolting became widespread. These works should result in a reduction in risk. To check it, we may compare the personal risk of the period 1947-2008 with that of 2009-2022. The interpretation cannot be made directly because as mentioned, the construction of walls, barriers and other protection elements was successive over time. It is likely that the landslide activity of the period 2009-2022 reflects the performance of the protections made both in this period and in the previous one. Likewise, in the evaluation of the later period, it will not yet show the effect of some prevention works carried out in the last few years. Despite these limitations, the comparison is a first estimate of the ability of

protections to reduce risk. A more documented analysis can be carried out in a few years, when sufficient time has passed to evaluate its performance

Table 5 presents the calculated risk for the two lanes of the road, segregated by size. When comparing with table 4, it is observed that the annual risk has been reduced by almost half (from 0.17 to 0.094), which corresponds to one fatal accident each 10.6yr on average. The annual probability of impact has reduced to 0.386, that is, one impact every 2.6yr on average. The decrease is not distributed proportionally between the sizes as it is mainly concentrated in the medium and small sizes (classes A to C) due to the performance of the protection works and in the largest sizes (class F) due to the absence of events in this period.

Size	f_m	Hillside lane		Seaside lane		Total	
		P_{LOL}	Impacted vehicles/yr	P_{LOL}	Impacted vehicles/yr	P_{LOL}	Impacted vehicles/yr
A	12.57	0.0007	0.0664	0.0001	0.0083	0.0007	0.0747
B	7.36	0.0104	0.1037	0.0052	0.0052	0.0155	0.1555
C	1.57	0.0150	0.0502	0.0128	0,0128	0.0278	0.0928
D	0.43	0.0173	0.0231	0.0173	0.0231	0.0347	0.0462
E	0.07	0.0077	0.0086	0.0077	0.0086	0.0154	0.0171
F	0.00	0.0000	0.0000	0.0000	0.0000	0.0000	0.0000
total		0.0511	0.2519	0.0431	0.1344	0.0942	0.3864

Table 5 Annual probability of loss of life and number of vehicles impacted per year for the period 2009-2022. Calculations are segregated by landslide sizes and lanes (hillside and seaside)

The resolution of the inventory is enough to perform risk analysis by sections of 500 m of length. This level of detail is what allows the decision makers to identify the slopes that generate the greatest risk, in which prioritize mitigation actions. Figure 3 presents the risk of loss of life for vehicle occupants for the two time periods considered. The figure shows the risk in each of the road sections as well as the accumulated risk over the entire length analyzed.

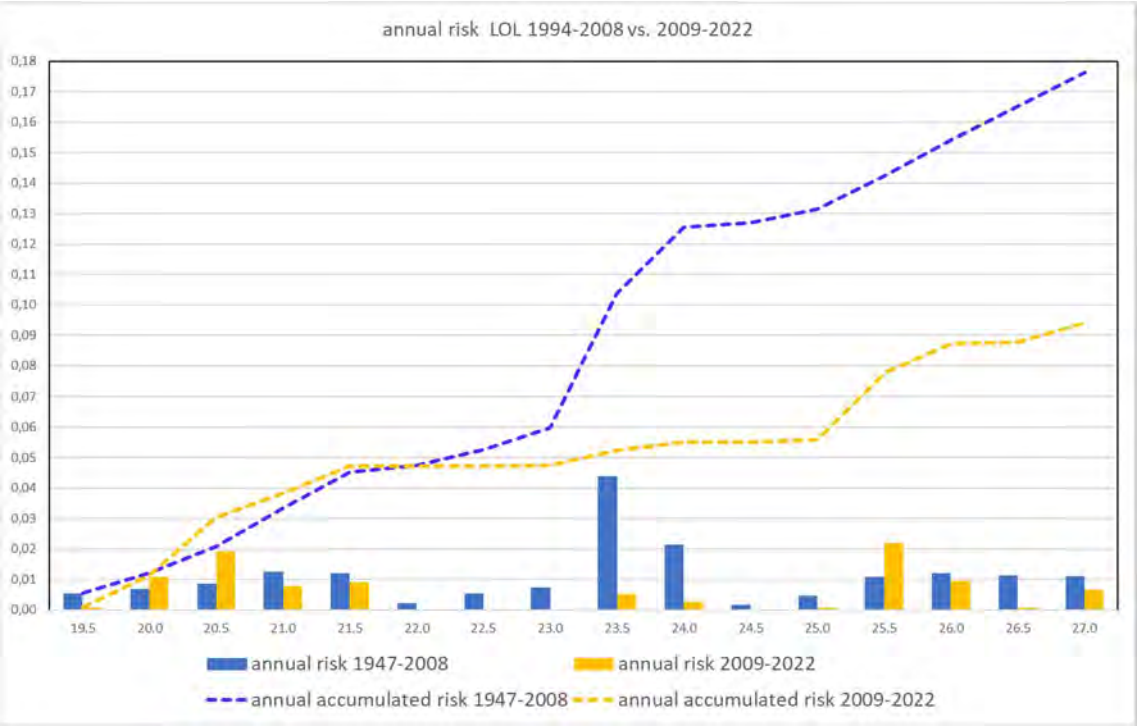

Figure 3. Annual risk of loss of life at each 500m-length stretch of the studied road and the accumulated risk for the entire length analyzed (from km point 19.5 to 27.5).

The first thing that stands out in Figure 3 is the reduction by half of the annual risk for the entire road length in the last 14 years (from 0.17 to 0.09), although it is still high. This value results from adding risk from each of the successive sections. This figure also shows how the risk has changed in each of the 16 sections into which the road has been divided. In 13 of the sections the risk level has been substantially reduced. In three of them, however, risk has increased. The risk reduction is mainly concentrated in the central stretches of the road with annual P_{LOL} less than 10^{-2} and 10^{-3}. In absolute terms, the greatest reduction has occurred in two sections: from km 23+500 to 23+990 and from km 24+000 to 24+490. In these two stretches major works were carried out during the years 2009 and 2004, respectively.

Protection structures are calculated for a design event of defined magnitude or intensity. Large events often cannot be fully retained resulting in residual risk. Different studies attempted to assess the performance of the protective works by numerical simulation of the rockfall trajectories and calculating the resultant risk (e.g. Guzzetti et al. 2004; Corominas et al. 2005). These studies found that a percentage of flexible rockfall barriers and protection walls can be either bypassed by high flying rock fragments, damaged or destroyed by fastmoving fragments and that a residual risk should be accounted for. In certain cases, other researchers have even observed that the annual risk of rockfalls with and without protective structures remains constant (Budetta et al. 2016). Among the reasons found by these authors are inadequate design and the occurrence of events greater than expected.

We present two examples of performance of protection structures with contrasting results. The first one refers to the mentioned road section from kilometer 24 to 24+490. This is the section that was affected by the big landslide event of December 1960 (figure 2), which is the largest observed on the entire highway since its inauguration. At that time, the repair work basically consisted of removing the head of the landslide, work that lasted for 6 months. Despite the repair, rockfalls have continued to occur. The current administration of the road decided to build two protection galleries and the construction of rockfall barriers founded on concreted walls. The works finished in 2004. Two quantitative risk analysis of this stretch compare the situation before (1994-2004) and after (2005-2022) the works. The results are presented in Table 6.

	1994-2004			**2005-2022**		
	events	f_m (#/yr)	P_{LOL}	events	f_m (#/yr)	P_{LOL}
A	20	1.818	$1.0 \cdot 10^{-4}$	7	0.412	$2.1 \cdot 10^{-5}$
B	14	1.273	$2.3 \cdot 10^{-3}$	2	0.118	$2.1 \cdot 10^{-4}$
C	5	0.455	$6.9 \cdot 10^{-3}$	3	0.176	$2.7 \cdot 10^{-3}$
D	1	0.091	$6.3 \cdot 10^{-3}$	0	0.000	0.000
E	1	0.091	$1.7 \cdot 10^{-2}$	0	0.000	0.000
F	0	0.000	0.000	0	0.000	0.000
total	41	3.727	$3.2 \cdot 10^{-2}$	12	0.706	$2.9 \cdot 10^{-3}$

Table 6. Annual risk of loss of life and number of vehicles impacted per year at km 24+000 to 24+490

The results show that risk has been reduced by an order of magnitude. However, it is surprising that the risk is generated mainly by small events considering that both rockfall barriers and galleries have sufficient capacity to intercept them. Viewing the available photographic documentation of some of the events sheds light on this apparent anomaly. Indeed, some recorded events are rockfalls retained on the barriers. Although in some cases the blocks did not reach the roadway, they did make it necessary to replace the damaged barriers and cut off traffic. In other occasions, some of the blocks passed over the fences or the intensity of the impact exceeded their capacity thus facilitating a fraction of the rock fragments to reach the pavement. In terms of personal risk, some of these events have not really posed a risk but in

terms of loss, as they have required repair work and road closure, so they remain included in the inventory. On the other hand, events retained by protective structures without causing apparent damage have generally gone unnoticed (Figure 4).

Figure 4. (a) unreported event, retained on top of the gallery, approximately in 2007; (b) reported event on 13/02/2007, without reaching the roadway; (c) event that destroyed the barrier on 02/02/2009; (d) event causing an accident that occurred on 16/11/2019, with much of the volume retained by the flexible barrier. Images b, c, and d, were provided by DFG and Ikerlur).

The second example is the analysis of the stretch of road between km point 20+000 to 20+490 for the periods 1947-2008 and 2009-2022. The results show that the risk has increased despite the protections made. Photographs taken from various events illustrate that, in some events, the impact of debris flows exceeded the capacity of rockfall barriers (figure 5). Likewise, the debris mass was able to cross the meshes and reach the road. Risk has increased for mid-size events (classes C to D) suggesting that remedial measures should be redesigned and resized to adjust to the prevailing mechanism in the stretch.

	1947-2008			**2009-2022**		
	events	f_m (#/yr)	P_{LOL}	events	f_m (#/yr)	P_{LOL}
A	28	1.867	$1.0 \cdot 10^{-4}$	10	0.714	$4.0 \cdot 10^{-5}$
B	13	0.867	$1.8 \cdot 10^{-3}$	15	1.071	$2.3 \cdot 10^{-3}$
C	3	0.200	$3.5 \cdot 10^{-3}$	2	0.143	$2.5 \cdot 10^{-3}$
D	1	0.016	$1.3 \cdot 10^{-3}$	1	0.071	$5.8 \cdot 10^{-3}$
E	0	0.000	0.0000	0	0.000	0.0000
F	0	0.000	0.0000	0	0.000	0.0000
total	45	2.950	$6.8 \cdot 10^{-3}$	28	2.000	$1.1 \cdot 10^{-2}$

Table 7. Annual probability of loss of life for and number of vehicles impacted per year at km 20+000 to 20+490

Figure 5. (a) event mostly retained by the barriers that occurred on 02/28/2006; (b) event reported on 05/01/2007, that although the barrier was destroyed, only a minor fraction of the debris reached the roadway; (c) event that occurred on 11/05/2011 in which the debris flow partially bypassed the wall. Images by DFG.

Economic losses: total annual cost

In the analysis of the Gipuzkoa coastal road, direct costs are estimated as a function of the size of the potential landslide event (Table 2). The criteria to estimate repair damages were set out in a previous work (Corominas et al. 2017), which has been updated with additional information of more recent repair costs mentioned in the written press and files of the road administration (table 9). A fixed repair cost is assigned to each event magnitude. The cost is an approximate estimate that may differ substantially for each specific case (for example, for the same volume, the repair costs of a rockfall are different from those of a debris flow).

	Consequences					
Class	A	B	C	D	E	F
Volume m^3	<0,5	0,5<V≤5	5<V≤50	50<V≤500	500<V≤ 5.000	> 5.000
Road closure	No, rarely	No, only partial	yes	yes	yes	yes
Actions	removal	Alternate pass + cleaning	Cleaning + slope scaling	Slope stabilization	Slope stabilization	Slope stabilization
Closure time	0.5h (*)	6h (*)	2d	10d	45d	4m
Repair Cost (€)	800	2.5k	60k	150k	500k	2M

Table 9. Estimated cost of the damage caused by rockfalls as function of the volume and actions required. The closure time is an intermediate value of the indicated in Table 1. (*) in case of small events, maintenance teams can cause sporadic traffic interruptions to proceed with the removal of debris and the cleaning of the road.

The indirect costs are basically the losses due to detours and the subsequent labor costs. We used equation 6 to calculate annualized total costs, considering the following parameters: (a) additional distances and travel times, calculated using the ViaMichelin routing application and checked with Google maps; (b) cost per additional kilometer is that indicated in the national allowances (€0.29/km) and that of heavy vehicles calculated by the Spanish Ministry of Transport (€1/km); (c) the average daily traffic (ADT) circulating along the N634 as well as the proportion between light (92%) and heavy (8%) vehicles obtained from the Getaria gauging station (DFG, 2023); (d) the cost of the tolls has been obtained from the rates in force in 2022 for the Zarautz toll station on the A8 motorway; (e) The cost per hour of work (€28/h), has been obtained from the National Institute of Statistics for the Basque Country. It has been considered that, on average, 1.5 people travel per vehicle. The range of landslide volumes and the annual frequencies are those indicated in Table 2.

Two scenarios are first considered. Scenario 1 assumes that all vehicle traffic is directed from Zarautz to Zumaia and vice versa, 6340 vehicles/day (traffic originating from or ending in Getaria is not considered). In this scenario, any closure of the road, be it between Zarautz and Getaria or Getaria and Zumaia implies a detour through any of the two possible alternatives: the Gi-2633 road through the Meaga Pass or the AP-1/AP-8 toll motorway (Figure 6).

Figure 6. Alternative routes (blue lines) in case of closure of the N-634 between Zarautz-Getaria-Zumaia along the coast: traffic between Zarautz and Zumaia is diverted through Meaga pass Gi-2633 or along the AP-1/AP-8 highway (scenarios 1, 1A and 1B); traffic between Zarautz-Getaria or Zumaia-Getaria diverted through Meaga pass, scenarios 2A and 2B, respectively (ViaMichelin image)

Scenario 2 assumes that a percentage of the traffic originates from and/or ends in Getaria (roundtrips). Therefore, if the landslide occurs between Zarautz and Getaria, only the traffic between these villages and between Zarautz and Zumaia is affected, but not the traffic between Zumaia and Getaria. Thus, scenario 2 quantifies the consequences of the road closure, considering whether it occurs within the Zarautz-Getaria section (scenario 2A) or in the Getaria-Zumaia section (scenario 2B). In both scenarios it is assumed that 3000 vehicles daily travel from Zarautz to Zumaia in either direction. In case of road closure due to a landslide, half choose the detour towards the Meaga pass and the remaining 50% towards the AP-8 (as in Scenario 1). The rest of the vehicles are supposed to have their origin or destination in Getaria from either Zarautz or Zumaia. In this case, all vehicles must travel through the Meaga pass. In

scenarios 2 A and B, the inventory of events from each of the sections is to calculate the closure time and the direct and indirect costs. Thus, in the period 1994-2008, 242 events occurred in the Zarautz-Getaria section and 514 cases in the Zumaia-Getaria section. The parameters used to estimate the extra cost of detours are shown in table 10.

	***d* (km)**	***Δd* (km)**	***v*$_m$ (km/h)**	***t* (h)**	***Δt* (h)**	**Scenario**
Zarautz-Getaria-Zumaia N-634 - Coastal road	11.1		60	0.19		1,2
Zarautz-Zumaia Gi-2633 via Meaga pass	12.7	1.6	50	0.28	0.09	1, 2A, 2B
Zarautz-Zumaia via AP-8 toll motorway	18.5	7.4	70	0.31	0.12	1, 2A, 2B
Zarautz-Getaria (return trip)	10		60	0.17		2A
Zarautz-Getaria Gi-2633 via Meaga (return trip)	18	8	50	0.30	0.13	2A
Zumaia-Getaria (return trip)	12			0.20		2B
Zumaia-Getaria Gi-2633 via Meaga (return trip)	24	12	50	0.40	0.20	2B

Table 10 Parameters used to calculate indirect costs, based on Via Michelin routing function. *d*: distance; *Δd*: additional travel distance; v_m: average speed; *t*: driving time; ; *Δd*: additional driving time

Table 11 shows the direct costs (for cleaning and repairing the road and slope reinforcement) and indirect costs (fuel and lost labor hours) calculated for scenario 1, considering that 50% of the traffic is diverted through the Gi- 2633 and the Meaga pass and 50% do it through the A8 toll road

Class	**Direct costs** (€/yr)	**Indirect costs** (€/yr)		**Total costs 1994-2008** (€/yr)
		Via Gi-2633	Via AP-8	
A	23,360	10,647	18,348	52,355
B	42,500	74.,385	128,183	245,068
C	172,000	100,347	172,922	445,268
D	160,000	186,691	321,715	668,406
E	66,667	105,014	180,965	352,645
F	133,333	140,018	241,286	514,638
total	597,860	617,102	1,063,419	2,278,381

Class	**Direct costs** (€/yr)	**Indirect costs** (€/yr)		**Total costs 2009-2022** (€/yr)
		Via Gi-2633	Via AP-8	
A	9,943	4,532	7,809	22,284
B	18,036	31,567	54,397	103,999
C	94,286	55,007	94,791	244,084
D	75,000	87,512	150,804	313,315
E	35,715	56,257	96,945	188,917
F	0	0	0	0
total	232,976	234,875	404,747	872,600

Table 11. Direct (D.C.) and indirect (I.D.) annualized costs of Scenario 1 for the period 1994-2008 (top) and 2009-2022 (bottom)

The results of table 11 show that although the repair costs are important for the road administration, the costs for the drivers due to detours and additional cost for fuel and hours lost is much higher, between 3 and 4 times. Contrary to what happens with the risk of loss of

life (tables 5 and 6), the economic costs are higher for large events. In the latter case, the users' losses due to traffic diversion is the key factor. In the period 2009-2022 direct economic costs (repair cost) have reduced to a 39%.

In scenario 2, the daily vehicle flow of 6,340 is distributed as follows: 3,000 vehicles make the complete trip between Zarautz and Zumaia (1,500 in each direction), 2,120 vehicles between Zarautz and Getaria (1,060 round trip) and 1,220 vehicles between Zumaia and Getaria (610 round trip). Table 12 shows the direct costs (for cleaning and repairing the road and slope stabilization) and indirect costs (fuel and lost labor costs) of scenarios 2A and 2B considering that 50% of the traffic diverts through the Gi- 2633 and the Meaga pass and 50% does it through the A1/AP8 toll motorway.

The results in Table 12 show the effect of performing the analysis in the two sections separately and the sensitivity to traffic hypotheses. Consideration of local traffic between the coastal villages without covering the entire length of the road makes the losses for the period 1994-2008 to differ substantially with those of table 11, by more than €700k. In this scenario, the indirect costs double the direct costs. The ratio has changed significantly with respect to scenario 1 because travelers not affected by the road closure are not disturbed in their daily activities nor are they subject to additional expenses. Furthermore, the breakdown into two sections shows that the risk is not homogeneously distributed. Both the direct and indirect costs of the road section between Zumaia and Getaria almost double those of the Getaria-Zarautz (table 12, above), which is something to consider when planning stabilization and protection works and their priorities. These values are the starting point for carrying out cost-benefit analyzes and quantifying the return on investments.

Class	**Road closure between Zarautz and Getaria (2A)**		**Road closure between Getaria and Zumaia (2B)**		**Total (€/yr)**
	D.C. (€/yr)	I.C. (€/yr)	D.C. (€/yr)	I.C. (€/yr)	
A	7,307	5,413	16,107	11,420	40,247
B	13,167	37,457	29,333	79,866	159,823
C	68,000	64,482	104,000	94,387	330,869
D	80,000	151,723	80,000	145,211	456,934
E	33,333	85,344	33,333	81,681	233,692
F	0	0	133,333	217,817	351,150
TOTAL	201,807	344.419	396,106	630,383	1,572,715

Class	**Road closure between Zarautz and Getaria (2A)**		**Road closure between Getaria and Zumaia (2B)**		**Total (€/yr)**
	C.D. (€/yr)	C.I. (€/yr)	C.D. (€/yr)	C.I. (€/yr)	
A	4,514	3,344	5,486	3,890	17,234
B	9,464	26,924	8,750	23,824	68,962
C	72,857	69,088	21,429	19,448	182,822
D	32,143	60,960	32,143	58,344	183,590
E	0	0	35,714	87,515	123,229
F	0	0	0	0	0
TOTAL	118,978	160,316	103,522	193,021	575,837

Table 12. Direct (D.C.) and indirect (I.C.) annualized costs of Scenarios 2A & 2B (top) calculated costs for the period 1994-2008; (bottom) calculated costs for the period 2008-2022.

Scenario 2 also shows that the landslide protection works carried out during the period 2009-2023 have benefited the Zumaia-Getaria section to a greater extent, whose losses have been reduced by 71%.

The exercise can be repeated to quantify the loss reduction obtained with the construction of specific protection structures. Economic comparison of the observed costs at km 24+000 to 24+490 before and after the construction of protection galleries in 2004.

	1994-2004			2005-2022		
	Repair (€/yr)	Detour (€/yr)	Total (€/yr)	Repair (€/yr)	Detour (€/yr)	Total (€/yr)
A	1,527	1,079	2,606	376	266	642
B	3,409	9,246	12,655	588	1,595	2,183
C	32,727	29,589	62,316	10,588	9,573	20,161
D	13,636	24,657	38,293	0	0	0
E	45,455	110,956	156,411	0	0	0
F	0	0	0	0	0	0
total	96,754	175,527	272,281	11,552	11,434	22,986

Table 13 Direct and indirect annual costs estimated at pk. 24+000 to 24+490 before the construction of protection galleries in 2004 and after the completion of works

This case is particularly interesting. Repair costs for the administration have been reduced by 88% but costs for users have been reduced by 93%. Cost savings are concentrated in large events (D, F). This is due, in part, to their absence during the observation period and also because the protections retain a substantial fraction of the rockfalls. In other sections, the protection measures have not been as effective as here.

Performance of remedial measures: cost-benefit analysis

Among the most obvious advantages of quantitative risk analysis is the possibility of comparing monetized risk between distant points and carrying out cost-benefit analyses (CBA) of the actions undertaken to mitigate it. In this section we present the analyses of the investments made in slope cut stabilization and protection works in the whole length and selected stretches of the coastal road. A number of ex-ante cost-benefit analyses are found in the literature that discuss different options for landslide management (Crosta et al. 2005; Frattini and Crosta, 2006; Moos and Dorren, 2021) and optimization of designs of protective works (Kanno et al 2023). It is less common the performance of ex-post analyses, in which the costs of the measures undertaken are compared with the estimated (real) benefits. This type of analysis has variants such as the comparison of the theoretical costs of prevention with those of remediation due to the occurrence of landslides (Salbego et al. 2015). The administration often performs this type of studies to set priorities and made allocation of resources to reduce risk (CSIL, 2012).

We present here an ex-post CBA adopting the incremental approach (EU, 2015) in which the scenario with-the-project is compared with a counterfactual baseline scenario without-the-project (or *do nothing* option). Ex-post CBA needs to be undertaken from today's viewpoint by considering an appropriate time horizon (usually 30 years for road and railway infrastructures). The year *zero* is the year where the investment was made. In the evaluation of projects in which investments occur over time, the analysis merge historical data and forecasts of future costs and benefits. In this case, a standard approach is to use constant prices (CSIL, 2012).

In CBA of roads, it is not easy to discriminate between repair costs (losses) and prevention costs (investments), this is also the case of the Gipuzkoa coast road. Some economic losses such as material damage to vehicles that have suffered an impact, the cost of cleaning and

repairing the road, slope scaling after the occurrence of the event, or the replacement of damaged protection elements are clearly defined. On the other hand, the construction of protection structures such as barriers against rockfalls and debris flows, and artificial galleries are included as risk reduction or prevention investments. However, other expenses are difficult to assign, such as some repair works undertaken after incidents of a certain magnitude, with the aim of ensuring the stability of the slope and avoiding their recurrence, at least in the short term. Within the latter group we can find the installation of meshes and rock bolts that should be considered preventive investments. In the case of the Gipuzkoa coastal road, it is not possible to separate the latter from the repair work. Thus, the work carried out in 1998 in the pk. 23 + 800, with a duration of 5 months, which consisted of the stabilization of the slope by means of an anchored wall and the reconstruction of the road that had been displaced, are computed as economic losses. On the other hand, protection works, such as the construction in 2004 of protection galleries for km 24+200 of the Getaria-Zumaia section, (at a cost of €2.8M), are computed as investments.

The design of the protection measures built in the coastal road faces several challenges, among them, the economic restrictions and the uncertainty of defining the design event. It is not then uncommon the occurrence of events that exceed the capacity of the protective structure. Under these circumstances, the cost-benefit analysis becomes a very helpful tool for those who make decisions and assess whether the investment is profitable or not. In this section we present a first attempt of analysis on the performance of both stabilization and protective measures undertaken and their benefit, if existing. We compare the economic benefits of landslide prevention measures versus *do nothing*. The prevention measures undertaken by the road authority is mainly justified by the expectation in the reductions on the number of incidents and their consequences (car accidents and losses). The savings may be estimated under the concept of *avoided losses* (Accastello et al. 2019), in which the protection service provided by the reinforcement and protection works carried out is valued in relation to the damages they prevent. The latter correspond to the average annual losses before the implementation of the protection works and are represented as the baseline in the plots. Non-monetized costs such as visual impacts and alteration of the natural environment are not considered.

We have computed all the investments made in the whole of the road length that connects Zarautz with Zumaia (including maintenance costs and replacement of the protection structures), the observed annual losses (both direct and indirect costs), and savings (figures 7 to 9). Savings result from subtracting the observed annual losses from the baseline (average annual losses before protection works). Benefits will be generated if savings exceed the cost of the investments. The list of investments made has been provided by the administration that manages the road, the Guizpukoa Provincial Council. It consists of the main contracts awarded to various engineering and construction companies from 1994 to the present. Direct and indirect costs are calculated using equation 5, according to the assumptions mentioned in the previous section. The baseline corresponds to the average annual losses for the period 1994-2008 (figure 7 and 9) and 1994-2004 (figure 8). Although the baseline represents losses that occur before the implementation of risk mitigation measures, this is a simplification. As mentioned, a few protection works were carried out in the period covered by the baseline. For this reason, the potential savings and benefits in relation to the option of doing nothing are greater than calculated.

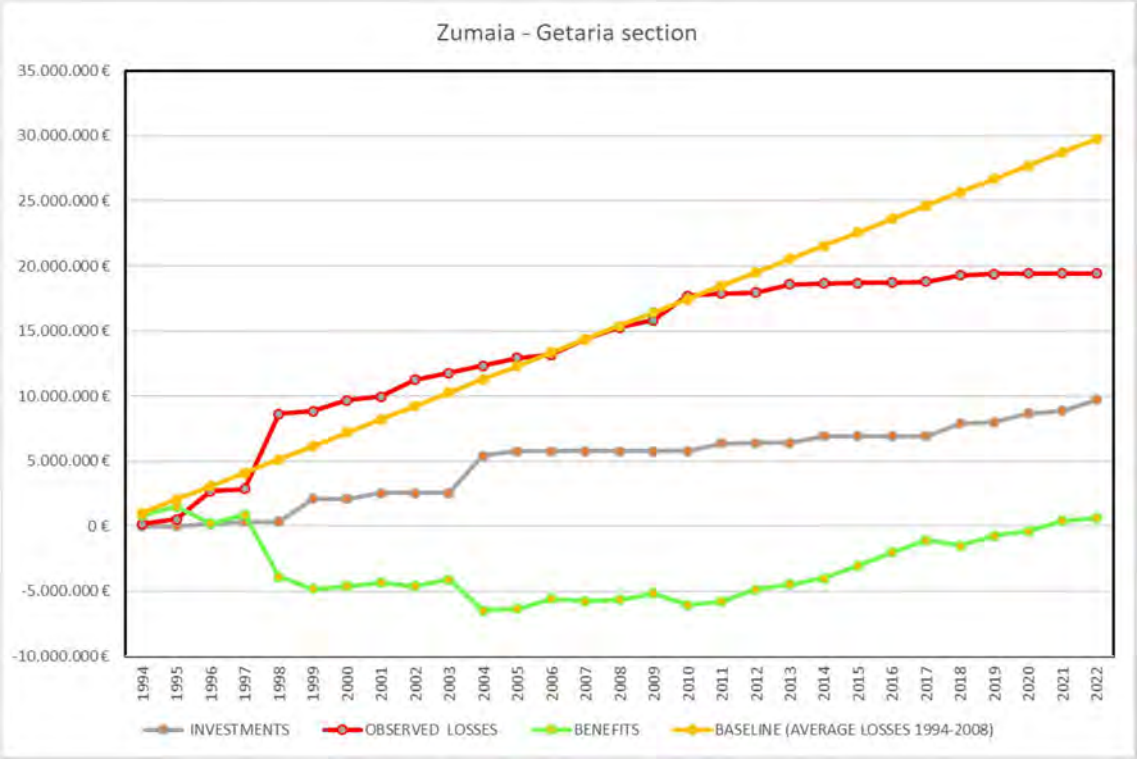

Figure 7. CBA analysis of the Zumaia – Getaria road section for the period 1994-2022. Accumulated observed losses, investments, baseline costs (average observed losses for the period 1994-2008), and benefits are plotted over time

In the first years with almost no investments (until 1998), losses observed increase significantly. After the first investments, losses moderated but continued to grow. Starting from the investments made in 1999 and later, the losses have been growing steadily at a low rate until, starting in 2010, a substantial reduction in the annual rate is observed. Savings (divergence of the observed losses and baseline) begin to generate from 2010 but benefits were still negative until 2020-2021, when the avoided losses accumulated exceeded the investments made. Figure 6 allows us to draw some conclusions about the effectiveness of the overall protections and risk reduction, but it is not sufficient to individually evaluate the interventions carried out in specific road stretches, which are of different nature and cost. Both the resolution of the incident record and the investments made allow the analysis to be carried out on a scale of road stretches of a few hundred meters in length. Consequently, it is possible to evaluate the performance of a specific protection and stabilization work, assessing its efficiency as well as the economic and social interest.

The results of the cost-benefit analysis of the road stretch between kilometer points 24+000 to 24+490 is shown in figure 8. As indicated, in 2004 two protection galleries against landslides and flexible barriers founded on concrete walls were built. The cost was €2.8M. The CBA compares the periods 1994-2004 (before the work was carried out) with that of 2005-2022. The presence of galleries has prevented the growth of annual losses. It is necessary to indicate that these protection works are not designed to prevent an event like the one that occurred in 1960, but they allow intercepting events of intermediate dimensions, which are those that historically generated the greatest number of road closures. As an additional preventive measure, the administration is currently monitoring the deformation of the entire slope in order to anticipate large events. The CBA shows that the structure satisfactorily fulfills its function and that the investment made is profitable for the administration and highly beneficial for the road user.

Immediately after the construction of the galleries, savings (avoided losses) have grown steadily, allowing the investment to be recovered in just 13 years (in 2017).

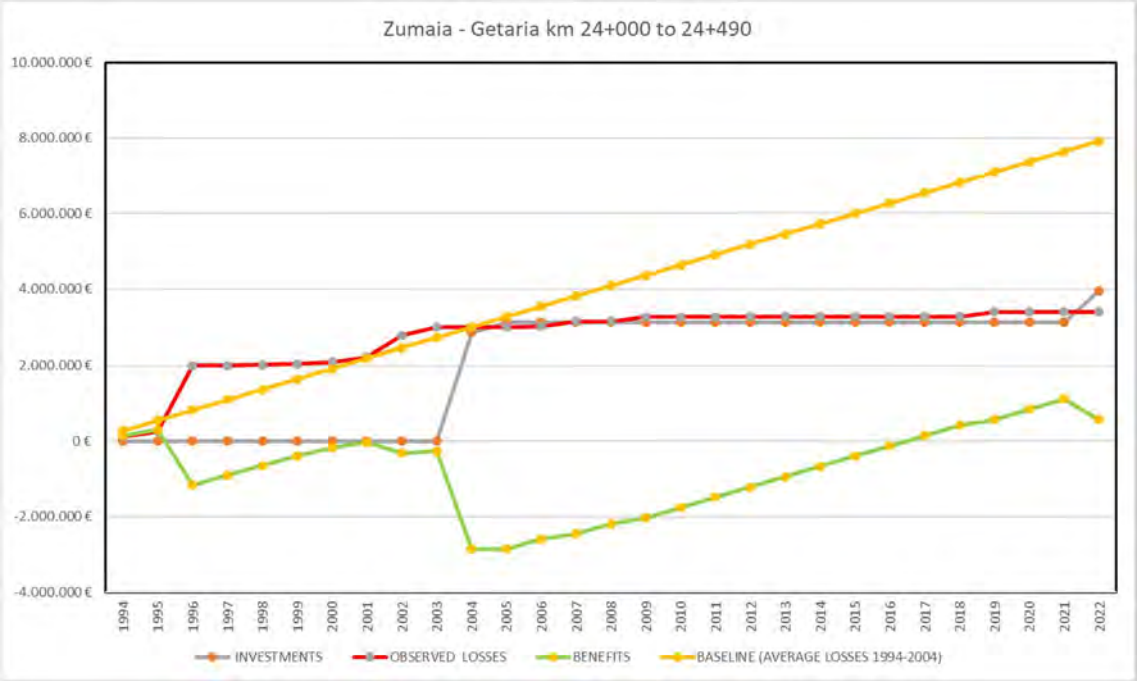

Figure 8. CBA analysis of the kilometer point 24+000 to 24+490 for the period 1994-2022. The accumulated losses, investments, baseline costs (period 1994-2004), and benefits are plotted over time.

The following example shows that, despite existing awareness of the hazard posed and the investment effort made, mitigation works do not always meet expectations. In this case, the coexistence of dangerous phenomena of different nature (rockfalls and debris flows) makes the appropriate selection of protective measures difficult.

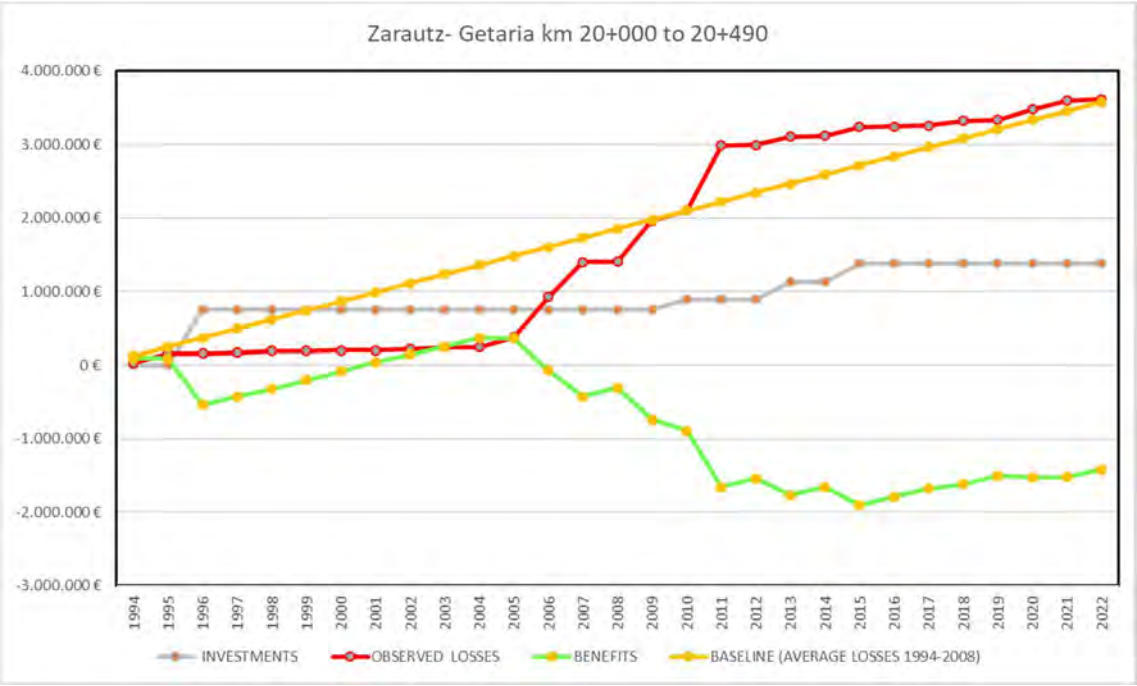

Figure 9. CBA analysis of the kilometer point 20+000 to 20+490 stretch for the period 1994-2022. Accumulated observed losses, investments, baseline costs (period 1994-2010), and savings are plotted over time.

The analyzed road stretch is located at km 20+000 to 20+490. At the beginning of the 90s, flexible rockfalls barriers were installed, founded on either concrete or masonry walls. Its goal was to intercept and retain the rockfall blocks detached from the slope and the debris flows. During the first years the behavior was reasonably satisfactory keeping losses lower than the 1994-2010 baseline (figure 9). However, in the middle of the first decade of this century, successive debris flow episodes destroyed the barriers several times, making it necessary to replace the barriers and requiring new investments. Although the latest actions carried out in 2010 have reduced the marked upward trend in losses, they continue to increase, which suggests that the design of the protections is not effective enough and should be reviewed. In fact, as Table 7 shows, the risk in the period 2009-2022 has even increased. For this reason, there are no benefits and the investment are far from being recovered. In any case, the performance of the protections cannot be evaluated from the current perspective. 30 years ago, construction solutions were not standardized and several designs that we have today were not available either. The retention capacity of meshes and barriers against rockfalls has improved over time.

Final remarks

Landslide inventories have been used to better understand the process of slope instability, the influence of conditioning and triggering factors, as well as to develop predictive models of susceptibility and hazard. In this communication we have sought to highlight the potential of high-resolution incident records (both in location and description) to support risk management It is not always possible to take advantage of the potential of the powerful tools available for risk analysis due to the insufficient resolution of the data that feed them. There exist new devices for the identification and detection of landslides, but their intensive use to capture daily incidents on lengthy linear infrastructures such as roads and railway lines is not yet ready. Successful experiences in detecting events on slopes, road cuts and rock outcrops have been described in the literature. Deploying it over long distances remains a challenge, especially capturing small events (e.g. $< 1m^3$). Meanwhile, the work of road maintenance teams and emergency services is an invaluable source of information that, with limited resources, can provide high-quality documentation for risk analysis and management.

The evaluation of risk of landslides on roads has more than 25 years of experience. Quantitative approaches are preferable because they facilitate monetization and establishing acceptability thresholds. Published QRA cases so far provide valuable criteria for decision-making and prioritization of available resources. However, the evaluation of the performance of risk predictions and of the implemented preventive measures has rarely been carried out. This was the objective of the work presented here. It consists in the quantitative analysis of the Gipuzkoa coastal highway, based on a comprehensive 29-year landslide record and completed with events reported by the local press for 76 years. The spatial and size resolution of the reported events is precise enough to perform overall analysis as well as short road sections (0.1 to 0.5 km in length) and perform comparative estimates.

The breakdown of the risk analysis into volume ranges has allowed us to address some statements that were consolidated by the qualitative risk analysis. One of them is the hazard matrix that results from the combination of the frequency of events and their magnitude. In applications for land use management and infrastructure planning, the hazard matrix is often transposed as a risk matrix although this might be debatable. The concept that numerous small events are equivalent in terms of risk to a few large events is not always true and it should be verified in each context. The analysis of the Gipuzkoa coastal road shows that the effect of the size of the landslides on personal risk differs from the economic risk. The highest probability

of impact and loss of life for road users is associated with medium to small events, since the probability of impact increases proportionally with frequency. Instead, material losses (both direct and indirect) are highly sensitive to the size of the landslide. Biggest losses are associated with medium to large-size events, despite their lesser frequency. The reason is in the lack of proportionality of the damages with size. Big landslides cause significant damage to the infrastructure and require major interventions on the affected slope to ensure its safety. These interventions require road closure that may last for weeks or months, which entails a significant socioeconomic cost.

In the case of the coastal road, the stabilization and protection work carried out by the administration last decades have reduced overall personal risk up to half. On specific road stretches, the reduction is more than an order of magnitude. The spatial resolution of the inventory also allows us to highlight those preventive actions that do not achieve the expected objective of risk reduction and that should be reconsidered.

Risk for the entire road is an aggregated function. The management of the Gipuzkoa coastal road raises the question of how safe is safe. Risk calculated for the entire road, gives clearly unacceptable personal risk values ($>10^{-2}$ annual P_{LOL}), even after the protection and stabilization works carried out. If road sections of 500m are considered, the risk has been reduced in most of sections below 10^{-2} and 10^{-3} annual P_{LOL}, the latter within the ALARP region (GEO, 1998). If the objective were to reduce the risk to acceptable levels, with values below 10^{-5} annual P_{LOL}, it would result that each of the 18 sections into which the study area has been divided should present risk values lower than $5.6 \cdot 10^{-7}$ annual P_{LOL} which does not look reasonable and it is unjustifiable economically. In this sense, it would be advisable to review the criterion of acceptability of risk on roads.

The breakdown of the economic cost of landslides between direct and indirect losses highlights some non-intuitive values. Although the detours on the Gipuzkoa Coast road are short, the costs they entail are up to four times higher than the repair costs for the administration and represent a heavy burden on the local economy and its productivity. The comparison of the economic costs caused by landslides between the periods 1994-2008 and 2009-2022 show that while repair costs have been reduced for the administration, savings for road users are bigger. This case provides strong arguments for decision makers to take decisive steps towards risk reduction policies.

Thus, the CBA allowed us to compare the preventive costs with the total remedial costs and indirect cost. In ex-ante CBA studies is often assumed that designs of protective works will be fully efficient. Reality shows that, in occasions, this assumption is optimistic. Events greater than the design event may occur and/or the design might not be the most appropriate. Then, risk reduction expectations are not met. Ex-post CBA analyses allow performance to be assessed with real data and quantify the economic balance and the efficacy of the solutions implemented. The case of the Guipuzkoa coastal road provides strong evidence that prevention is economically advantageous. Savings (avoided losses) of investing in disaster risk prevention outweigh the costs of not doing so on average. Furthermore, investment may be recovered (benefits) in the very short term as the CBA in some of the stretches have shown.

This study demonstrates the importance of recording road incidents and the need of improving their resolution. Current technology (e.g. geolocation and digital photography) facilitates incident documentation to be collected in a short period of time without interfering with the tasks of road maintenance crews. In road corridors where, continuous stabilization and

protection work is carried out, the observed frequency of events is disturbed and no longer conforms to a power law. To monitor risk in these conditions, evaluate the performance of the actions and the residual risk, it is necessary to have updated information on the frequency of incidents and this can only be obtained from inventories.

Acknowledgements

The author tis thankful to Susana Luzuriaga and José Antonio Navarro of the Gipuzkoako Foru Aldundia for providing the records of the coastal road maintenance crews, emergency calls and photographs of the incidents. He also thanks Iñaki Ibarbia and Joseba Jugo from the Ikerlur company for the photographic documents provided and data on the costs of the repair work.

The collaboration in various tasks of Olga Mavrouli from the University of West Attica, Nieves Lantada and Amparo Núñez from the Engeomodels group of the Universitat Politècnica de Catalunya is also appreciated.

This work is part of the activities of the GeoRisk project with reference PID2019-103974RB-I00 and which is funded by MCIN/AEI/10.13039/501100011033.

References

Accastello C, Bianchi E, Blanc S & Brun F (2019). ASFORESEE: A harmonized model for economic evaluation of forest protection against rockfall. *Forests*, 10(7), 578.

Agliardi, F, Crosta GB & Frattini P (2009) Integrating rockfall risk assessment and countermeasure design by 3D modelling techniques. *Nat. Hazards Earth System Sci.* 9,1059–1073.

Ardizzone F, Cardinali M, Carrara A, Guzzetti F & Reichenbach P (2002) Impact of mapping errors on the reliability of landslide hazard maps. *Natural Hazards and Earth System Sciences* 2, 3–14.

Barlow J, Lim M, Rosser N, Petley D, Brain M, Norman E & Geer M (2012) Modeling cliff erosion using negative power law scaling of rockfalls. *Geomorphology* 139, 416-424.

Bishop P (2007) Long-term landscape evolution: linking tectonics and surface processes. *Earth Surface Processes and Landforms* 32, 329-365.

Blahut J, Van Westen CJ & Sterlacchini S (2010) Analysis of landslide inventories for accurate prediction of debris-flow source areas. *Geomorphology* 119, 36-51.

Boardman AE, Greenberg DH, Vining AR & Weimer DL (2011) *Cost-benefit analysis. Concepts and practice.* Prentice Hall. 4th Edition. 560pp

Brabb EE, Pampeyan EH & Bonilla MG (1972) Landslide Susceptibility in San Mateo County, California. U.S. *Geol Surv Misc Field Studies Map*, MF-360.

Brabb EE (1984) Innovative approaches to landslide hazard and risk mapping. *IV International Symposium on Landslides*, Toronto, Canada. Vol 1: 307-323.

Brunetti MT, Guzzetti F & Rossi M (2009) Probability distributions of landslide volumes. *Nonlin. Processes Geophys* 16, 179–188.

Bull WB (1996) Prehistorical earthquakes on the Alpine fault, New Zealand. *J. Geophys. Res*., 101(B3): 6037-6050.

Bunce CM, Cruden DM, & Morgenstern NR (1997) Assessment of the hazard from rockfall on a highway: *Canadian Geotechnical Journal* 34, 344–356.

Cendrero A & Dramis F (1996. The contribution of landslides to landscape evolution in Europe. *Geomorphology* 15, 191-211.

Chung CJ & Fabbri AG (2003) Validation of spatial prediction models for landslide hazard mapping. *Nat. Hazards* 30, 451–472.

Coe JA, Bessette-Kirton EK & Geertsema M (2018. Increasing rock-avalanche size and mobility in Glacier Bay National Park and Preserve, Alaska detected from 1984 to 2016 Landsat imagery. *Landslides* 15, 393-407.

Copons R, Vilaplana JM & Linares R (2009) Rockfall travel distance analysis by using empirical models (Solà d'Andorra la Vella, Central Pyrenees). *Nat. Hazards Earth System Sci.* 9, 2107–2118.

Corominas J (1996) The angle of reach as a mobility index for small and large landslides. *Canadian Geotechnical Journal,,* 33, 260-271.

Corominas J (2000) Landslides and climate. In Bromhead E, Dixon N, Ibsen ML (eds).: *Proceedings 8th International Symposium on Landslides*, Cardiff, UK; A.A. Balkema, CD-ROM vol. 4: 1–33.
Corominas J, Copons R, Moya J, Vilaplana JM, Altimir J & Amigo J (2005) Quantitative assessment of the residual risk in a rockfall protected area. *Landslides* 2, 343–357.
Corominas J, Matas G & Ruiz-Carulla R (2019) Quantitative analysis of risk from fragmental rockfalls. *Landslides* 16. 5–21.
Corominas J & Mavrouli O (2011) Rockfall quantitative risk assessment. *Rockfall engineering*, Lambert, S., Nicot, F., Eds.; ISTE, London, UK, 255-301.
Corominas J & Moya J (2008) A review of assessing landslide frequency for hazard zoning purposes. *Engineering Geology* 102, 193-213.
Corominas J, van Westen C, Frattini P, Cascini L, Malet JP, Fotopoulou S, ... & Smith JT (2014) Recommendations for the quantitative analysis of landslide risk. Bulletin of engineering geology and the environment 73, 209-263.
Crosta GB, Frattini P, Fugazza F, Caluzzi L & Chen H (2005) Cost-Benefit analysis for debris avalanche risk management. In: Hungr O., Fell R., Couture R., Eberhart E. (eds.) *Landslide risk management*. Balkema, Rotterdam, 517-524.
Crosta GB, Hermanns RL, Dehls J, Lari S & Sepulveda S (2017) Rock avalanches clusters along the northern Chile coastal scarp. *Geomorphology* 289, 27–43.
CSIL – DKM Centre for Industrial Studies (2012) *Ten projects observed*. Ex-Post evaluation of investment projects co-financed by the European Regional Development Fund (ERDF) or Cohesion Fund (CF) in the period 1994-1999. European Commission Directorate-General Regional Policy. Final Report. 245 pp.
Dai FC, Lee CF & Ngai, YY (2002) Landslide risk assessment and management: an overview. *Engineering Geology* 64, 65-87.
De Biagi V, Napoli ML & Barbero M (2017) A quantitative approach for the evaluation of rockfall risk on buildings. *Natural hazards*, 88, 1059-1086.
Dussauge C, Grasso JR & Helmstetter A (2003) Statistical analysis of rockfall volume distributions—Implications for rockfall dynamics. *Journal of Geophysical Research*, 108, 2286, 11 p.
DFG – Diputación Foral de Gipuzkoa. (2023) *Información de aforos en las carreteras de Gipuzkoa*. Recopilación hasta 2022. 234 pp.
Dussauge-Peisser C, Helmstetter A, Grasso JR, Hantz D, Desvarreaux P, Jeannin M & Giraud A (2002) Probabilistic approach to rock fall hazard assessment—Potential of historical data analysis. *Natural Hazards and Earth System Sciences* 2, 15–26.
Emberson R, Kirschbaum DB, Amatya P, Tanyas H & Marc O (2022) Insights from the topographic characteristics of a large global catalog of rainfall-induced landslide event inventories. *Natural Hazards and Earth System Sciences,* 22(3), 1129-1149.
Ermini, L, & Casagli N (2003) Prediction of the behaviour of landslide dams using a geomorphological dimensionless index. *Earth Surface Processes and Landforms* 28(1), 31-47.
European Commission (2015) *Guide to Cost-Benefit Analysis of Investment Projects Economic appraisal tool for Cohesion Policy 2014-2020*. European Commission Directorate-General for Regional and Urban policy. 364 pp.
Evans SG & Hungr O (1993) The assessment of rockfall hazard at the base of talus slopes. *Canadian Geotechnical Journal*, 30, 620–636.
Fan X, Dufresne A, Subramanian SS, Strom A, Hermanns R. Stefanelli CT, ... & Xu Q (2020). The formation and impact of landslide dams–State of the art. Earth-Science Reviews, 203, 103116.
Fell R, Ho, KKS, Lacasse S & Leroi E (2005) A framework for landslide risk assessment and management. In O. Hungr, R. Fell, R. Couture and E. Eberthardt (editors) *Landslide Risk Management*. Taylor and Francis, London. pp. 3-25
Ferlisi S, Cascini L, Corominas J & Matano F (2012) Rockfall risk assessment to persons travelling in vehicles along a road: the case study of the Amalfi coastal road (southern Italy). *Nat. Hazards* 62(2), 691–721
Ferlisi S, De Chiara G, Cascini . (2016) Quantitative risk analysis for hyperconcentrated flows in Nocera Inferiore (southern Italy). *Nat. Hazards*, 81 (Suppl. 1), 89–115.
Frank F, Huggel C, McArdell BW & Vieli A (2019) Landslides and increased debris-flow activity: A systematic comparison of six catchments in Switzerland. *Earth Surface Processes and Landforms* 44, 699–712
Frattini P & Crosta G B (2006) Valutazione dell'accettabilità del rischio da frana e analisi costi-benefici, *Giornale di Geologia Applicata*,4, 49–56
Frattin, P, Crosta G, & Carrara A (2010) Techniques for evaluating the performance of landslide susceptibility models. *Engineering geology*, 111(1-4), 62-72.
Fuchs S, Thöni M, McAlpin MC, Gruber U & Bründl M (2007) Avalanche hazard mitigation strategies assessed by cost effectiveness analyses and cost benefit analyses—evidence from Davos, Switzerland. Natural Hazards 41, 113-129.

Gaidzik K & Ramírez-Herrera M T (2021). The importance of input data on landslide susceptibility mapping. *Scientific reports*, 11(1), 19334.
Galli M, Ardizzone F, Cardinali M, Guzzetti F & Reichenbach P (2008) Comparing landslide inventory maps. *Geomorphology* 94, 268–289..
GEO - Geotechnical Engineering Office (1998) *Landslides and Boulder Falls from Natural Terrain: Interim Risk Guidelines*. Government of the Hong Kong Special Administrative Region, Geotechnical Engineering Office, GEO Report No.75.
Guthrie R, & Evans S. (2004) Magnitude and frequency of landslides triggered by a storm event, Loughborough Inlet, British Columbia. *Natural Hazards and Earth System Sciences* 4, 475–483.
Guzzetti F, Mondini AC, Cardinali M, Fiorucci F, Santangelo M & Chang K T (2012) Landslide inventory maps: New tools for an old problem. *Earth-Science Reviews*, 112(1-2), 42-66
Guzzetti F, Peruccacci S, Rossi M, & Stark CP (2008) The rainfall intensity–duration control of shallow landslides and debris flows: an update. Landslides, 5, 3-17.
Guzzetti F, Reichenbach P & Ghigi S (2004) Rockfall hazard and risk assessment along a transportation corridor in the Nera Valley, central Italy. *Environmental Management* 34, 191–208.
Guzzetti F, Reichenbach, P., and Wieczorek, G.F., 2003, Rockfall hazard and risk assessment in the Yosemite Valley, California, USA: Natural Hazards and Earth System Sciences, v. 3, p. 491–503.
Harp EL & Jibson RL (1996) Landslides triggered by the 1994 Northridge, California earthquake. *Seismological Society of America Bulletin* 86, S319–S332
Harp EL, Keefer DK, Sato HP & Yagi H (2011) Landslide inventories: the essential part of seismic landslide hazard analyses. *Engineering Geology* 122(1-2), 9-21.
Hovius N, Stark CP & Allen PA (1997) Sediment flux from a mountain belt derived by landslide mapping. *Geology* 25, 231–234.
Hsu KJ (1975) Catastrophic debris streams (sturzstroms) generated by rockfalls. *Geological Society of America Bulletin* 86, 129–140.
Hungr O, Evans SG & Hazzard J (1999) Magnitude and frequency of rock falls along the main transportation corridors of southwestern British Columbia. *Canadian Geotechnical Journal* 36, 224–238
Irigaray C, Fernández T, El Hamdouni R & Chacón J (1999) Verification of landslide susceptibility mapping. A case study. *Earth Surface Processes and Landforms* 24, 537–544.
Jaboyedoff M, Dudt JP & Labiouse V (2005) An attempt to refine rockfall hazard zoning based on the kinetic energy, frequency and fragmentation degree. *Nat. Hazards Earth Syst. Sci.* 5, 621–632.
Jaboyedoff M & Labiouse V (2011) Preliminary estimation of rockfall runout zones. *Nat. Hazards Earth Syst. Sci.* 11, 819–828.
Jaboyedoff M, Carrea D, Derron MH, Oppikofer T, Penna IM & Rudaz B (2020) A review of methods used to estimate initial landslide failure surface depths and volumes. *Engineering Geology*, 267, 105478.
Jakob M, Bovis M & Oden M (2005). Estimating debris flow magnitude and frequency from channel recharge rates. *Earth Surface Processes and Landforms* 30, 755–766
Kanno H, Moriguchi S, Tsuda Y, Yoshida I, Iwanaga S & Terada K (2023) A method for rockfall risk quantification and optimal arrangement of protection structures along a road. Engineering Geology 314, 107004.
Keefer DK (1984) Landslides caused by earthquakes. *Geological Society of America Bulletin* 95, 406–421.
Keefer DK (2000) Statistical analysis of an earthquake-induced landslide distribution —the 1989 Loma Prieta, California event. *Engineering Geology* 58, 231–249.
Kellerer-Pirklbauer A, Lieb GK, Avian M & Carrivick J (2012) Climate change and rock fall events in high mountain areas: numerous and extensive rock falls in 2007 at Mittlerer Burgstall, Central Austria. *Geografiska Annaler*: Series A, Physical Geography 94, 59–78.
Korup O, Densmore AL & Schlunegger F (2010) The role of landslides in mountain range evolution. *Geomorphology* 120(1-2), 77-90.
Larsen IJ, Montgomery DR & Korup O (2010) Landslide erosion controlled by hillslope material. *Nature Geoscience* 3(4), 247-251.
Lee C T, Huang CC, Lee JF, Pan KL, Lin ML & Dong JJ (2008) Statistical approach to storm event-induced landslides susceptibility. *Natural hazards and earth system sciences* 8(4), 941-960.
Legros F (2002) The mobility of long-runout landslides. *Engineering geology* 63, 301–331
Li Z, Nadim F, Huang H, Uzielli M & Lacasse S (2010). Quantitative vulnerability estimation for scenario-based landslide hazards. Landslides, 7, 125-134.
Liu SH, Lin CW & Tseng CM (2013) A statistical model for the impact of the 1999 Chi-Chi earthquake on the subsequent rainfall-induced landslides. *Engineering geology* 156, 11-19.
Lu M, Zhang J, Zhang L & Zhang L (2020).Assessing the annual risk of vehicles being hit by a rainfall-induced landslide: a case study on Kennedy Road in Wan Chai, Hong Kong. Natural Hazards and Earth System Sciences 20(6), 1833-1846.

Macau F (1963) *Previsión de los movimientos del terreno*. Boletín de Informaciones y Estudios, 16. Servicio Geológico de Obras Públicas, Madrid.
Macciotta R, Martin CD, Morgenstern NR & Cruden DM (2016) Quantitative risk assessment of slope hazards along a section of railway in the Canadian Cordillera—a methodology considering the uncertainty in the results. *Landslides* 13(1), 115–127.
Macciotta R, Grapel C, Keegan T, Duxbury J & Skirrow R (2020) Quantitative risk assessment of rock slope instabilities that threaten a highway near Canmore, Alberta, Canada: managing risk calculation uncertainty in practice. *Canadian Geotechnical Journal* 57(3), 337–353
Malamud B.D, Turcotte DL, Guzzetti F & Reichenbach P (2004) Landslide inventories and their statistical properties. *Earth Surface Processes and Landforms* 29(6), 687-711.
Marc O & Hovius N (2015) Amalgamation in landslide maps: effects and automatic detection. *Nat. Hazards Earth Syst. Sci.* 15, 723-733,
Marc O, Hovius,N, Meunier P, Uchida T & Hayashi SI (2015) Transient changes of landslide rates after earthquakes. *Geology* 43(10), 883-886.
Mavrouli O, Corominas J, Ibarbia I, Alonso N, Jugo I, Ruiz J, Luzuriaga, S. & Navarro JA (2019) Integrated risk assessment due to slope instabilities in the roadway network of Gipuzkoa, Basque Country. *Natural hazards and earth system sciences* 19(2), 399-419
Moos C & Dorren, L (2021) Cost-Benefit Analysis as a Basis for Risk-Based Rockfall Protection Forest Management, IntechOpen, https://doi.org/10.5772/intechopen.99513, 2022.
Narasimhan H, Ferlisi S, Cascini L, De Chiara G. & Faber MH (2016) A cost–benefit analysis of mitigation options for optimal management of risks posed by flow-like phenomena. Natural Hazards, 81, 117-144.
Nicolet P, Jaboyedoff M, Cloutier C, Crosta GB & Lévy S (2016) Brief communication: On direct impact probability of landslides on vehicles. *Natural hazards and earth system sciences* 16(4), 995-1004.
Nilsen TH, Wright RH, Vlasic TC, Spangle W (1979) Relative Slope Stability and Land-use Planning in the San Francisco Bay Region, California. 96 pp. *U.S. Geol Surv Professional Paper* 944: 104pp
Parker, R. N., Densmore, A. L., Rosser, N. J., De Michele, M., Li, Y., Huang, R., ... & Petley, D. N. (2011). Mass wasting triggered by the 2008 Wenchuan earthquake is greater than orogenic growth. Nature Geoscience, 4(7), 449-452.
Peng, M., & Zhang, L. M. (2012). Breaching parameters of landslide dams. Landslides, 9, 13-31.
Pfurtscheller C & Genovese E(2018) The Felbertauern landslide of 2013: impact on transport networks, effects on regional economy and policy decisions. *SEEDS Working Paper* 02, 26 pp.
Ravanel L & Deline P (2010) Climate influence on rockfalls in high-Alpine steep rockwalls: the north side of the Aiguilles de Chamonix (Mont Blanc massif) since the end of the Little Ice Age. *The Holocene* 21: 357-365
Reichenbach P, Rossi M, Malamud, BD, Mihir M & Guzzetti F (2018) A review of statistically-based landslide susceptibility models. Earth-science reviews 180, 60-91.
Remondo J, Gonzalez A, Diaz De Teran JR, Cendrero A, Fabbr, A & Chung CF (2003) Validation of landslide susceptibility maps; examples and applications from a case study in Northern Spain. *Natural Hazards* 30, 437 – 449.
Rickenmann D (1999) Empirical relationships for debris flows. *Natural hazards*, 19, 47-77.
Roberds W (2005) Estimating temporal and spatial variability and vulnerability. In O. Hungr, R. Fell, R. Couture and E. Eberthardt (editors) *Landslide Risk Management*. Taylor and Francis, London. pp. 129-157
Roering JJ, Kirchner JW & Dietrich W E (2005) Characterizing structural and lithologic controls on deep-seated landsliding: Implications for topographic relief and landscape evolution in the Oregon Coast Range, USA. *Geological Society of America Bulletin* 117(5-6), 654-668.
Salbego G, Floris M, Busnardo E, Toaldo M & Genevois R (2015) Detailed and large-scale cost/benefit analyses of landslide prevention vs. post-event actions. *Natural Hazards and Earth System Science*, 15, 2461-2472.
Schuster RL, Logan RL &Pringle PT (1992) Prehistoric rock avalanches in the Olympic Mountains, Washington. *Science* 258, 1620-1621.
Segoni S, Piciullo L & Gariano SL (2018) A review of the recent literature on rainfall thresholds for landslide occurrence. *Landslides* 15(8), 1483-1501.
Soldati M, Corsini A & Pasuto A (2004). Landslides and climate change in the Italian Dolomites since the Late Glacial. *Catena* 55 (2), 141–161.
Steger S, Brenning A, Bell RS & Glade T (2016) The propagation of inventory-based positional errors into statistical landslide susceptibility models. *Natural Hazards and Earth System Science* 16, 2729–2745.
Stock GM, Luco N, Collins BD, Harp EL, Reichenbach P & Frankel KL (2014). Quantitative rock-fall hazard and risk assessment for Yosemite Valley, Yosemite National Park, California, US Geological Survey Scientific Investigations Report 2014-5129, 52 p. http://www.pubs.usgs.gov/sir/2014/5129/
Trauth MH, Bookhagen B, Marwan N & Strecker MR (2003) Multiple landslide clusters record Quaternary climate changes in the northwestern Argentine Andes. *Palaeogeography, Palaeoclimatology, Palaeoecology* 194(1-3), 109-121

Van Westen CJ, Castellanos E & Kuriakose SL (2008) Spatial data for landslide susceptibility, hazard, and vulnerability assessment: An overview. Engineering geology Reichenbach 102(3-4), 112-131
Varnes DJ (1984) *Landslide hazard zonation: a review of principles and practice*. Natural Hazard Series Vol 3 UNESCO, Paris. 60 pp.
Williams JG, Rosser NJ, Hardy RJ, Brain MJ (2019) The Importance of Monitoring Interval for Rockfall Magnitude-Frequency Estimation. *Journal of Geophysical Research: Earth Surface*, 124(12), 2841-2853.
Wood JL, Harrison S & Reinhardt L (2015) Landslide inventories for climate impacts research in the European Alps. *Geomorphology* 228, 398-408.
Xiao T & Zhang LM (2023) Data-driven landslide forecasting: Methods, data completeness, and real-time warning. *Engineering Geology*, 317, 107068.
Yano A, Shinohara Y, Tsunetaka H, Mizuno H & Kubota T. (2019) Distribution of landslides caused by heavy rainfall events and an earthquake in northern Aso Volcano, Japan from 1955 to 2016. Geomorphology 327, 533–541.
Zhang S & Zhang LM (2017) Impact of the 2008 Wenchuan earthquake in China on subsequent long-term debris flow activities in the epicentral area. *Geomorphology* 276, 86-103

Extracting debris flow model parameters from sparse observations: Significance of metric for calibration quality

Minu Treesa Abraham[1,2], V Mithlesh Kumar[1], Anil Yildiz[1] and Julia Kowalski[1]

[1] Methods for Model-based Development in Computational Engineering, RWTH Aachen University, Aachen, Germany
[2]Norwegian Geotechnical Institute, Oslo, Norway

SUMMARY: Numerical modelling of debris flows is a challenging task due to the challenges associated with precise data collection and the complex input parameters. Inverse analyses are often carried out based on historical data, to calibrate the otherwise difficult to measure rheological parameters. This study presents a case study from India, on calibrating the rheological parameters of Voellmy rheological model, using a Bayesian approach. The goal is to investigate to which extent sparse data can be inverted for quantitative information that guide further model-based predictions. The rheological parameters of the studied event were calibrated using a single observation only, namely information on the area inundated by the debris flow. Different performance metrics were used for the process, and it was found that the calibration result is highly sensitive to the metric that is used during the calibration process. A new metric was proposed in this study, the ratio of area of union to the intersection of observed and simulated shapes of debris flow, which showed better results for parametric calibration using coarse topographical data and sparse observations.

Keywords: debris flows, rheology, calibration, numerical modeling, sparse data

Introduction

Debris flows are flow-like landslides moving at rapid to very rapid speed (Hungr *et al.*, 2014). Owing to their high speeds and volumes, debris flows are often catastrophic, and possess severe threat to the human environments in mountainous regions. Numerical models aid in simulating these complex phenomena over real topographies and are widely used for understanding the dynamics of debris flows (Christen *et al.*, 2010). The most critical inputs required in modelling are the rheological parameters, which are difficult to be quantified based on field or laboratory investigations (Abraham et al., 2021). If the rheological parameters are known, numerical models have the potential to be used for forward modelling, and thereby disaster risk reduction. Estimation of these parameter are usually carried out by back analysis of historical debris flow events (Hussin *et al.*, 2012). The reliability of such inverse analyses depends upon the quality of data, and most case studies available in literature are carried out using volume, height and velocity information of the debris flow event. However, obtaining these data after debris flow events is challenging, and the most common and easily available information is inundated area. This information can be obtained from high resolution satellite images, or using field investigations, even after the occurrence of debris flows. This study evaluates in detail, the potential use of this single observation in calibrating the rheological parameters of debris flows, using a case study from Western Ghats, India.

Methodology

The methodology involves data collection, simulations, surrogate modelling and Bayesian calibration. The study area is located in the southwestern part of India, in Wayanad district of Kerala state, and the shape of debris flow is provided in Figure 1. The most critical data used in numerical modelling is the topographical information, obtained in this case from the Alos

Palsar Digital Elevation Model (DEM) (ASF DAAC, 2015), with 12.5 m resolution. The material properties were collected after field investigations, and the shape of the debris flow was delineated using high resolution satellite images from Google Earth. An open-source tool r.avaflow 3, release 20230411 (Mergili *et al.*, 2017; Mergili 2014-2020) was used for doing the simulations, with Voellmy turbulent friction model.

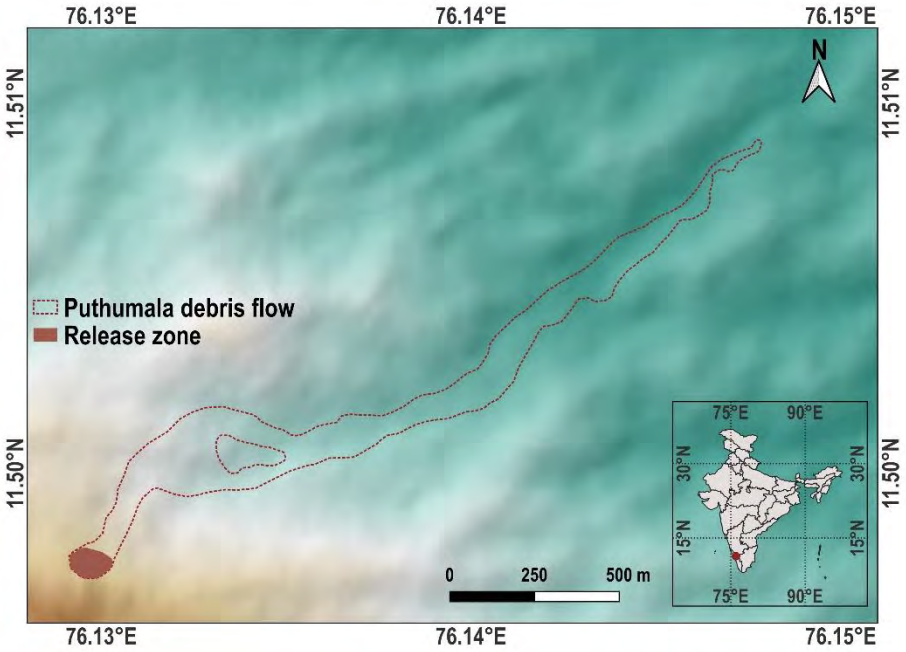

Figure 1. Location of Puthumala debris flow

The rheological parameters used for modelling are the dry-Coulomb friction (μ), and the viscous turbulent friction (ξ). A total of 100 simulations were carried out and different performance metrics were calculated using a confusion matrix comparing the observed and simulated shapes of the debris flow. The confusion matrix classifies the total grid space used for simulation into four categories: true positives (TP)s, where both observation and simulation agree on cells with a flow height more than 0.1 m, true negatives (TN)s where there is perfect agreement in cells without flow, false positives (FP)s on cells where the simulation yields a flow height above the threshold and no flow was actually observed in the field, and false negatives (FN)s where the simulation fails to predict the flow in a cell, but the cell is inundated in the field. Based on these four attributes, four different performance metrics for each simulation were calculated, three of them are already well established in literature, and one is proposed in this study (Eq. 1). The metrics calculated for each simulation were then compared with their true values, based on the observation, to find the residuals used for Bayesian calibration. The residuals can be directly used for random search calibration, where the minimum residual indicates best model. The true value of impact area (IA) is the scalar value of area covered by the rasterised polygon of the observation, which can be calculated as $TP + FN$. The trimline grid fitness (TGF) is a metric proposed by (Aaron *et al.*, 2019), which is a measure of mismatches between the observation and simulation. When the simulation and observation perfectly agree with each other, the value of TGF is zero. $F1\ score$ is a widely followed metric for quantitative comparison, and union to intensity ratio ($UI\ ratio$) is newly proposed in this study, which the ratio of the area covered by both debris flow in observation and simulation to the area intersected by debris flow in both observation and simulation. For both $F1\ score$ and $UI\ ratio$, the true value is 1, when both FPs and FNs are zero.

$$IA = TP + FP$$

$$TGF = FP + FN$$

$$F1\ score = \frac{2TP}{2TP + FP + FN} \qquad (1)$$

$$UI\ ratio = \frac{TP + FP + FN}{TP}$$

The residuals were then used to train a Gaussian Process (GP) based emulator, to emulate sufficient number of samples for Bayesian calibration (Zhao *et al.*, 2021; Zhao and Kowalski, 2022). Around 5000 samples generated using the emulator were used the find the conditional posterior distributions of the rheological parameters using different metrics. Such emulators can also aid in quantifying the uncertainties and sensitivity studies associated with numerical models (Yildiz *et al*., 2023).

Results and Discussion

The results indicate that both IA and TGF has limitations to be used for calibration purposes (Figure 2). The coarse resolution DEMs will result in increased lateral width of flow along the path, and this will lead to a very high number of FPs. Both IA and TGF will consider this increased FPs and ignore the longer runout simulations. This will result in unrealistic values of μ and ξ after calibration. However, both *F1 score*, and *UI ratio* overcomes this limitation and provide more realistic calibration results. It is also important to note that the calibrated values of both random search and Bayesian calibration are very close to each other. This clearly indicate that Bayesian calibration has no significant advantages in finding the calibrated values when the data is poor, but the insights from posterior distributions aided in choosing a better metric for calibration.

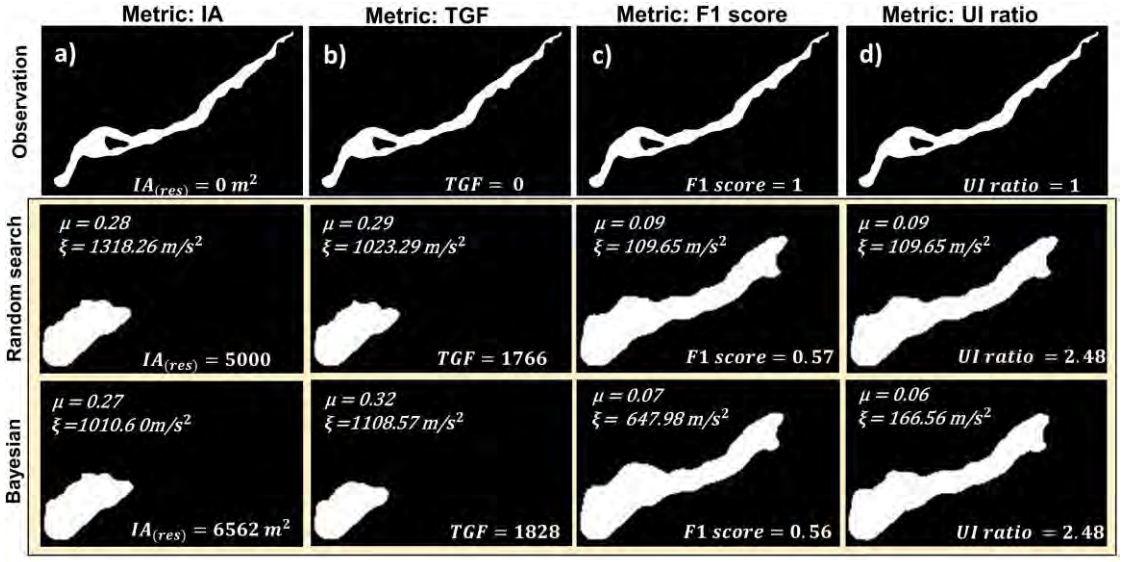

Figure 2. Observed and simulated shapes of the debris flow event, using calibrated parameters. The metrics used for calibration are: a) IA, b) TGF; c) $F1\ score$ and d) $UI\ ratio$

As observed from Figure 2, it is not possible to find any differences in the performance of $F1\ score$ and $UI\ ratio$ as a metric for calibration, from the results of random search calibration. However, the posterior distributions plotted in Figure 3 clearly indicates that $UI\ ratio$ provides more reliable predictions than $F1\ score$. The results indicate that the 95 % confidence interval for the calibrated value of μ and ξ using $UI\ ratio$ are 0.05-0.08 and 107.32 m/s^2 -245.54 m/s^2 respectively.

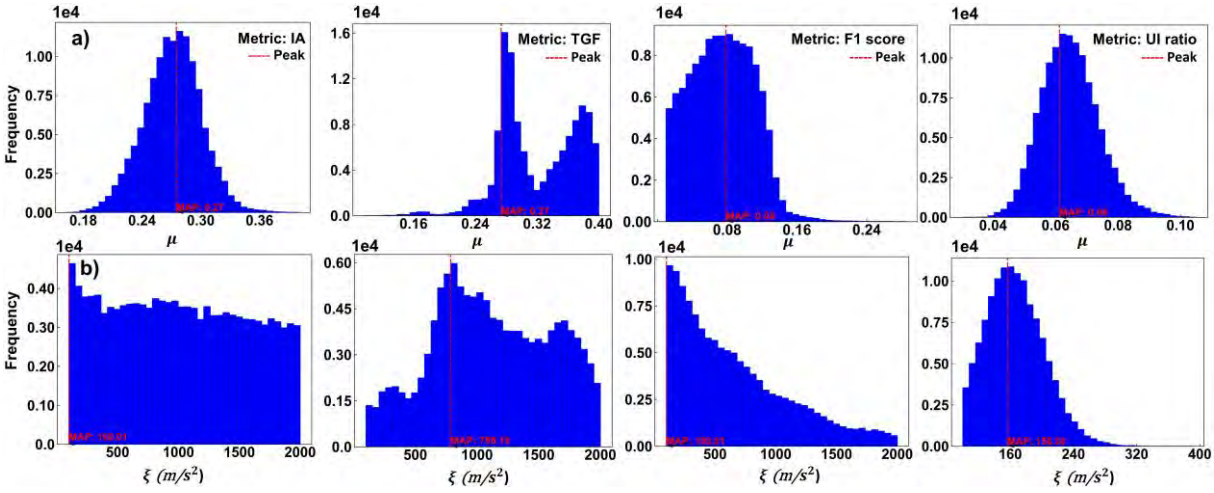

Figure 3. Posterior distributions of the rheological parameters, using different performance metrics. a) μ and b) ξ

Conclusions

The study demonstrates that even when the field observation is sparse, choice of a suitable metric can aid in making use of sparse data for calibration of rheological parameters. A new metric using the observed and simulated shapes of debris flow, called *UI ratio*, proposed in this study, can leverage the information provided by the scalar value of impact area itself, and can serve as a better metric for calibration. *UI ratio* can be used as a metric of evaluation for the similarity between observed and simulated shapes of debris flows and can be used for calibration of rheological parameters. It was also observed that a traditional random search calibration can also be used for approximating the rheological parameters. However, a Bayesian analysis considering the uncertainties can provide better insights by providing a probabilistic range of parameters, instead of a deterministic value. From the analysis conducted, the 95 % confidence interval for μ and ξ values of Puthumala debris flow were estimated to be between 0.05-0.08 and 107.32 m/s^2 -245.54 m/s^2 respectively.

References

Aaron J, McDougall S and Nolde N (2019) Two methodologies to calibrate landslide runout models, *Landslides*, 16(5), 907–920.

Abraham MT, Satyam N, Reddy SKP and Pradhan B (2021) Runout modeling and calibration of friction parameters of Kurichermala debris flow, India, *Landslides*, 18(2), 737–754.

ASF DAAC (2015) *Alaska Satellite Facility Distributed Active Archive Center (ASF DAAC) Dataset: ASF DAAC 2015, ALOS PALSAR_Radiometric_Terrain_Corrected_high_res; Includes Material © JAXA/METI 2007.* doi.org/10.5067/Z97HFCNKR6VA.

Christen M, Kowalski J and Bartelt P (2010) RAMMS: Numerical simulation of dense snow avalanches in three-dimensional terrain, *Cold Regions Science and Technology*, 63(1–2), 1–14.

Hungr O, Leroueil S and Picarelli L (2014) The Varnes classification of landslide types, an update, *Landslides*, 11(2), 167–194.

Hussin H Y, Quan Luna B, Van Westen C J, Christen M, Malet J P and Van Asch T W J (2012) Parameterization of a numerical 2-D debris flow model with entrainment: A case study of the Faucon catchment, Southern French Alps, *Natural Hazards and Earth System Science*, 12(10), 3075–3090.

Mergili M, Fischer J-T, Krenn J and Pudasaini S P (2017) r.avaflow v1, an advanced open-source computational framework for the propagation and interaction of two-phase mass flows, *Geoscientific Model Development*, 10(2), 553–569.

Mergili M, (2014-2020). r.avaflow - The mass flow simulation tool. r.avaflow 2.4 User manual. https://www.avaflow.org/manual.php

Yildiz A, Zhao H and Kowalski J (2023) Computationally-feasible uncertainty quantification in model-based landslide risk assessment, *Frontiers in Earth Science*,10, 1032438.

Zhao H, Amann F and Kowalski J (2021) Emulator-based global sensitivity analysis for flow-like landslide run-out models, *Landslides*, 18(10), 3299–3314.

Zhao H and Kowalski J (2022) Bayesian active learning for parameter calibration of landslide run-out models, *Landslides*, 19(8), 2033–2045.

Temperature- and rate-dependence of the residual shear strength of clays: a review

Gianvito Scaringi[1]

[1] Institute of Hydrogeology, Engineering Geology and Applied Geophysics, Charles University, Prague, Czechia

SUMMARY: The temperature of a landslide's shear zone can change in relation to endogenous processes, such as frictional heating and chemical reactions, but also as a consequence of changes in boundary conditions, through heat propagating from the bedrock or the ground surface. Various hydro-mechanical properties of soils (especially clay-rich soils) are temperature-dependent. Research suggests that the residual shear strength – a key parameter in reactivated landslides – may vary significantly in usual ranges of temperature in landslide shear zones. Literature also shows that the residual shear strength depends on the rate of shearing, with rate strengthening and weakening behaviours linked with the soil's mineral composition. In this contribution, we discuss the state of the art and present recent results of ring-shear experiments, suggesting that the temperature- and rate-dependence of the residual shear strength may exert a significant influence especially on shallow clay landslides, which may be exacerbated by climate change and should be accounted for in modelling explicitly.

Keywords: residual shear strength, rate effect, thermo-mechanical coupling, landslide, clay.

Introduction

The ongoing, rapid climate change is a complex and highly disruptive event. Understanding the physical processes underlying such disruption, which takes many forms including natural disasters, is essential for reducing the consequences of climatic changes from the local to the global scales. Landslides are often a key component of natural disasters and they are strongly affected by climate change (Gariano and Guzzetti, 2016). The stability of slopes is customarily described via equations of mechanical equilibrium and hydraulic flow. Models can conveniently account for disruptions caused by seismic shaking, earthworks, changes in moisture content and fluid pressure. Clay-rich soils are especially susceptible to slope instability owing to their low frictional resistance and enhanced interaction with water. Under compression and shearing, they easily deform and weaken, producing smooth surfaces of preferential sliding along which only a minimal resistance remains available. The concept of this "residual shear strength" originates from the experimental works of Tiedemann, Haefeli, and Hvorslev in the 1930s, and MacNeil Turnbull in the 1950s; however, it was Skempton who put the pieces together in his Rankine Lecture (Skempton, 1964).

Temperature-sensitivity in clay hydro-mechanics

Clay soils are sensitive to changes in temperature: most of their hydro-mechanical properties depend on temperature significantly (Scaringi and Loche, 2022). In addition to the consequences of phase changes of water in terms of volume change, stiffness, and hydraulic conductivity, this thermal sensitivity is important also within the range of temperatures of liquid water under atmospheric pressure. Research on thermo-hydro-mechanical coupling in clays can be traced back to the 1960s (e.g., Mitchell, 1969); however, this early research did not make an

impact in norms and engineering practice. Recently, the rise of energy geotechnics and research on engineered clay barriers (ECBs) for geological repositories of spent nuclear fuel have raised the attention on thermal effects in geomaterials. It is now established that changes in temperature may alter internal stresses and water pressures, triggering flows and strains via complex, coupled mechanisms. Water and clay minerals expand differently upon heating, resulting in changes in water pressure. As temperature rises, interparticle forces of physico-chemical interaction change as water becomes less viscous and more electrically conductive, and clay surfaces are less capable of withholding it. Heating-cooling cycles in soft soil can produce stiffening and, counterintuitively, net shrinkage (Tang et al., 2008), while the opposite holds true in overconsolidated soil. The dependence of the shear strength on temperature is not crucial in domains undergoing small strains, such as in the ECB problem. Consequently, little research has focused on this matter (Scaringi and Loche, 2022; Loche et al., 2021, 2022). Whether the shear strength increases or decreases with temperature depends on the soil nature and structure, which is the result of its stress-strain-thermal history. The residual shear strength (τ_r), typically available in landslide shear zones after large strains, does not depend on soil history. Therefore, evaluating the thermal sensitivity of τ_r should be more straightforward. Nonetheless, the literature is poor in such evaluations. In one notable study, the remobilisation of clay landslides was attributed to cooling-induced soil weakening (Shibasaki et al., 2017) which was confirmed by experiments that also highlighted the importance of the rate of shearing, suggesting different effects in slow and fast movements, to date largely unexplored.

Combined temperature and shear rate effects

The velocity-weakening phenomenon has especially been studied to explain large and long-runout landslides (Scaringi et al., 2018b), and many mechanisms have been suggested to explain it. Most of these mechanisms concern the frictional heat dissipation within the shear zone, where elevated temperatures can be attained. In slow-moving landslides, the contribution of frictional heating is negligible as heat conduction and convection efficiently prevent temperature from rising; therefore, temperature-dependent processes are typically not expected. However, other causes of variation in temperature exist – both endogenous and exogenous. The former can entail, for instance, endo- or exothermic chemical and biological processes. As for the latter, which are related to changing boundary conditions, a role of both direct and coupled flows in heat transfer can be identified: for instance, the flow of groundwater not only defines pore water pressures but also alters the thermal energy balance. Notably, although a variety of processes exist, which can potentially alter temperature patterns within the ground with consequences in terms of altered hydraulic and mechanical properties, little has been done to explicitly account for them in landslides and most geotechnical problems (Scaringi and Loche, 2022). With respect to the shearing behaviour, results of shear experiments in a wide range of confining pressures (typical of shallow to deep-seated landslides), shear rates (typical of extremely slow to rapid landslides), experimental devices, and soil compositions are often complex and, at times, difficult to interpret comprehensively (Scaringi et al., 2018a; Scaringi and Di Maio, 2016). Temperature adds a further layer of complexity to the interpretation of these experiments. In a recent review, we highlighted how a variegated literature exists on temperature effects in geomaterials which, however, lacks systematicity and clear field evidence (Scaringi and Loche, 2022).

Thermo-hydro-mechanical modelling

Current slope stability models typically only account for hydro-mechanical coupling. However, advanced model formulations exist – developed for other applications, such as for modeling

ECBs – that account for THM processes explicitly (Mašín, 2017). These models have not (yet) been adapted or developed further for application to landslides, and their applicability typically remains confined to small-scale domains, also owing, in part, to their computational burden. Without a modeling tool and solid knowledge on thermal sensitivity, it may seem that expected changes in slope stability in temperate regions under climate change should mainly be those caused by changing hydrological inputs. This perception could be justified in the light of the "dampening role" of soil heterogeneity and by temperature oscillations fading at large depths. A systematic study of the literature (Scaringi and Loche, 2022) reveals that even recent studies deem thermal effects negligible, dismissing the importance of investigating them. Qualitative conclusions of this kind can be found in various studies (e.g., Cekerevac and Laloui, 2004). A quantitative argument in favour of systematically incorporating or neglecting the temperature-shear strength dependence in general or in specific conditions, such as in clay-rich formations, pre-existing landslide bodies, or shallow movements, is lacking.

Recent evidence and perspective

Our recent research (Loche and Scaringi, 2023) aims to constrain the importance of temperature – changing according to boundary conditions, including global warming – in the remobilisation of shallow clay landslides. We performed ring-shear experiments (Fig. 1a-d) under controlled temperature and rate of shearing. These experiments indeed demonstrated changes in the residual shear strength by up to 1.5%/°C in pure clays, where the sign of the dependency relates to both the clay mineral composition (smectite vs. kaolinite) and the rate of shearing (slow vs. fast shearing).

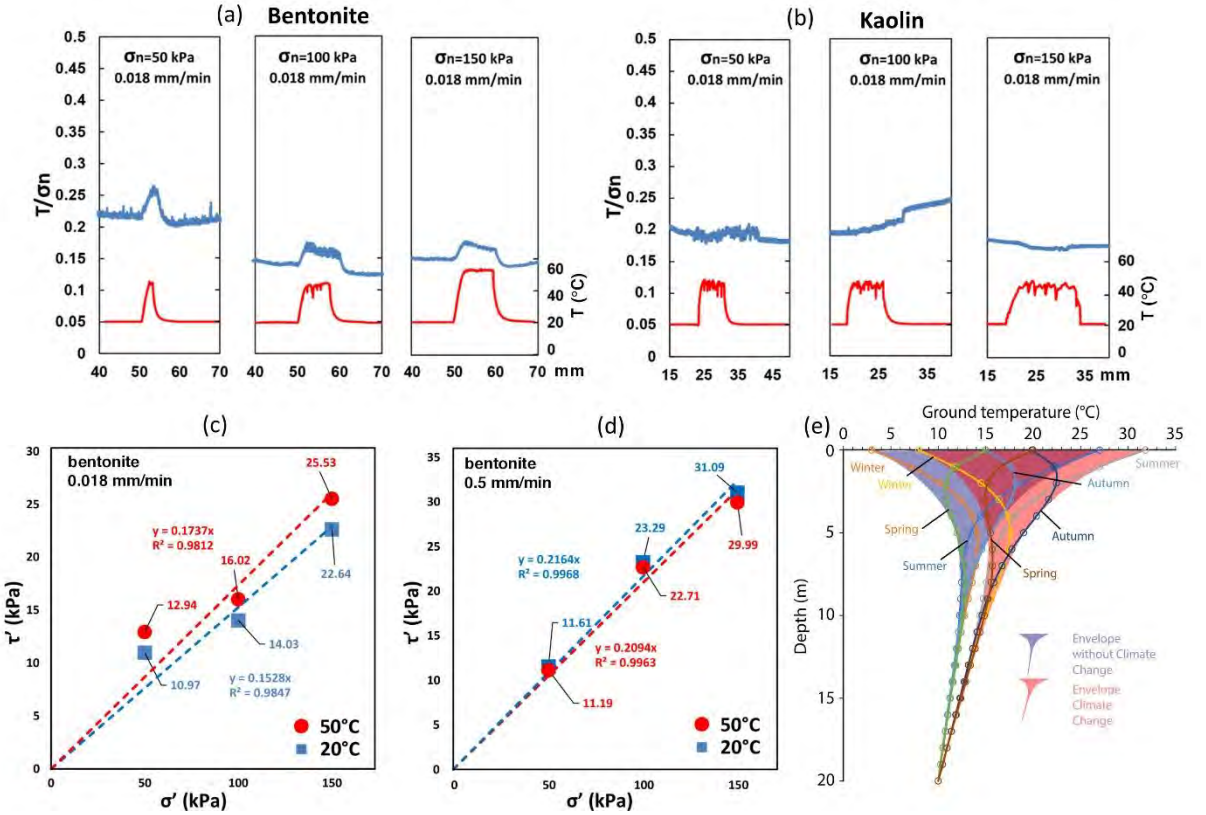

Figure 1. Results of ring-shear tests on (a) bentonite and (b) kaolin: the tests were performed under normal stresses (σ_n) of 50, 100, and 150 kPa and a shear rate of 0.018 mm/min. Residual shear strength envelope for bentonite at (c) 0.018 mm/min and (d) 0.5 mm/min: an increase in temperature from 20°C to 50°C caused an increase in friction coefficient from ~0.15 to ~0.17 (+13%) at 0.018 mm/min but a decrease from ~0.22 to ~0.21 (-3%) at 0.5 mm/min. (e) Depth profiles of ground temperature: seasonal variations in a hypothetical baseline case ("no climate change") and after 5°C of warming ("climate change"). Modified from Loche and Scaringi (2023).

We considered that shallow landslide bodies undergo seasonal variations in temperature, which propagate from the atmosphere to the shear zone (Fig. 1e). The amplitude of temperature variation decreases with depth but also depends on materials, moisture content, and groundwater flow. In a simplified situation, with fully saturated, homogeneous soil, we estimated to what extent the residual shear strength can vary solely because of its temperature dependency. As an example, in terms of the global factor of safety for a landslide body with a curvilinear slip surface reaching a depth of ~6 m, we evaluated seasonal changes in the order of ~20% if a clay-rich soil (e.g., smectite) is involved (Loche and Scaringi, 2023). Under global warming, values may increase/decrease with time, and we quantified this variation as an additional ~7% associated with a warming of 5°C. Although the numerical scenario was simplified (temperature does affect other hydro-mechanical parameters) and the evaluated thermal sensitivity should be intended as an upper bound, we argue that the magnitude of the effect should not be dismissed. A systematic evaluation of thermal sensitivity of natural soils is desirable, together with a modelling effort to better account for thermo-hydro-mechanical processes in slopes. By neglecting temperature sensitivity in any setting and scale, errors could emerge also in regional assessments of future landslide distributions and the associated risk.

Acknowledgements

The author acknowledges financial support from the Ministry of Education, Youth and Sport of the Czech Republic (MŠMT ERC CZ grant No. LL2316).

References

Cekerevac, C., Laloui, L., 2004. Experimental study of thermal effects on the mechanical behaviour of a clay. Int. J. Numer. Anal. Methods Geomech. 28, 209–228.

Gariano, S.L., Guzzetti, F., 2016. Landslides in a changing climate. Earth-Sci. Rev. 162, 227–252.

Loche, M., Scaringi, G., 2023. Temperature and shear-rate effects in two pure clays: Possible implications for clay landslides. Results in Engineering 20, 101647. https://doi.org/10.1016/j.rineng.2023.101647

Loche, M., Scaringi, G., Blahůt, J., Melis, M.T., Funedda, A., Da Pelo, S., Erbì, I., Deiana, G., Meloni, M.A., Cocco, F., 2021. An Infrared Thermography Approach to Evaluate the Strength of a Rock Cliff. Remote Sens. 13, 1265. https://doi.org/10.3390/rs13071265

Loche, M., Scaringi, G., Yunus, A.P., Catani, F., Tanyaş, H., Frodella, W., Fan, X., Lombardo, L., 2022. Surface temperature controls the pattern of post-earthquake landslide activity. Sci. Rep. 12, 988. https://doi.org/10.1038/s41598-022-04992-8

Mašín, D., 2017. Coupled thermohydromechanical double-structure model for expansive soils. J. Eng. Mech. 143, 04017067.

Mitchell, J.K., 1969. Temperature effects on the engineering properties and behavior of soil, in: Effects of Temperature and Heat on Engineering Behavior of Soils, Special Report 103, Highway Res. Board. Washington, D. C, pp. 9–27.

Scaringi, G., Di Maio, C., 2016. Influence of Displacement Rate on Residual Shear Strength of Clays. Procedia Earth Planet. Sci. 16, 137–145. https://doi.org/10.1016/j.proeps.2016.10.015

Scaringi, G., Hu, W., Xu, Q., 2018a. Discussion on: "Experimental study of residual strength and the index of shear strength characteristics of clay soil" [Eng.Geo.233:183–190]. Eng. Geol. 242, 218–221. https://doi.org/10.1016/j.enggeo.2018.06.021

Scaringi, G., Hu, W., Xu, Q., Huang, R., 2018b. Shear-Rate-Dependent Behavior of Clayey Bimaterial Interfaces at Landslide Stress Levels. Geophys. Res. Lett. 45, 766–777. https://doi.org/10.1002/2017GL076214

Scaringi, G., Loche, M., 2022. A thermo-hydro-mechanical approach to soil slope stability under climate change. Geomorphology 401, 108108. https://doi.org/10.1016/j.geomorph.2022.108108

Shibasaki, T., Matsuura, S., Hasegawa, Y., 2017. Temperature-dependent residual shear strength characteristics of smectite-bearing landslide soils: Temperature-Dependent Residual Strength. J. Geophys. Res. Solid Earth 122, 1449–1469.

Skempton, A.W., 1964. Long-term stability of clay slopes. Géotechnique 14(2), 77-102.

Tang, A.-M., Cui, Y.-J., Barnel, N., 2008. Thermo-mechanical behaviour of a compacted swelling clay. Géotechnique 58, 45–54.

The role of fabric on the operative strength of tectonized clay shales

M. Pirone[1], G. Urciuoli[1], L. Picarelli[2]

[1]Università di Napoli Federico II, Napoli, Italy
[2] Euro-MediterraneanCentre on Climate Change, CMCC, Lecce, Italy

SUMMARY: Tectonized clay shales, which widely outcrop all along the Apennines chain in Italy, display a highly fissured fabric, which strongly governs their mechanical behaviour making often unsuitable the basic principles of Soil Mechanics that looks at the material as a deformable continuum. On the other hand, the classical approaches of Rock Mechanics, which models the material as a rigid medium crossed by small sets of persistent and parallel discontinuities, generally cannot help.
This paper presents the results of some numerical experiments concerning a simple engineering problem, focusing on the complex role that is played by material fabric.

Keywords: tectonized clay shale, shear discontinuities, soil failure, operative shear strength.

Introduction

Highly fissured and sheared clay shales are widespread all along the Apennines chain in Italy, being a result of the tectonic events that led to formation of the chain. Experience shows that the mechanical response of these complex materials in boundary value problems is sometimes unpredictable, leading to unexpected results. In particular, the most severe problems concern excavations and tunneling; another major issue is about the instability of natural slopes, which often represents a threat to historic towns built on the top of hills, and, in general, to the network of roads and railways, which cross hilly and mountainous areas.
The difficulty in modeling the behaviour of these formations mostly depends on the problematic role that is played by material fabric. Its influence, in particular, concerns both the meso- and the macro-scale, i.e. the scale of laboratory specimens and of engineering problems respectively, making often unsuitable the methods of analysis based on the principles of Soil Mechanics. This issue is just the object of this paper.

2. The fabric of tectonized clay shales

The principal features of tectonized clay shales, which are often part of flysch formations and are usually referred to as “structurally complex formations”, are a highly fissured and sheared fabric, the frequent presence of a lapideous component in the form of deformed layers or of isolated blocks, and the high deteriorability of the clayey component. These materials are commonly described as “scaly” clay shales, since they consist of very small platy fragments (millimeters to centimeters in size), called “scales”, with polished faces (minor shears), which make the ensemble as sort of weak gravel. The single fragments, whose hardness is due to the high compressive components of stress induced by tectonics, can be subdivided into smaller and smaller pieces. The smallest ones are bonded (soil microstructure). Finally, this aggregate of “scales” is in turn crossed by major shear discontinuities (principal or major shears) that are often closely and irregularly spaced. The widespread presence of fissures and of major shears is the result of the deviatoric stresses induced by tectonics.

3. Role of fabric on material strength as from laboratory tests

In Italy, the hydraulic and mechanical properties of tectonized clay shales are being investigated since the Seventies (Bilotta et al. 1985) through the typical procedures of the Soil Mechanics. Of course, laboratory tests can mainly account for the role of microstructure and mesofabric (i.e., of the arrangement and properties of "scales" and fissures). However, sometimes, as in triaxial tests on specimens including principal major shears, the test results are also affected by macrofabric, i.e. by principal shears present in soil samples, and in some cases of lapideous fragments. Therefore, a major engineering problem concerns the reliability of the laboratory tests for the analysis of boundary value problems, which depend on material macrofabric (distribution of rock blocks and fragments, and density, persistence and orientation of principal shears and fractures), which, as mentioned above, is sometimes only randomly captured by triaxial tests. Figure 1, which presents the results of drained direct shear and triaxial tests performed on the "scaly" Laviano clay shale (Bilotta et al. 1985), gives an idea about the major role that is played by such factors; in particular, it shows that:

- the arrangement of "scales" can produce a highly anisotropic mesofabric (as shown by direct shear tests);
- due to some alignment of the shear lenses occurring during the triaxial tests, the results of these last may envelope the failure line obtained by direct shear tests carried out just in the direction of "scales";
- the shear strength measured in triaxial tests on specimens including principal shears may be very close to the residual strength measured in direct shear tests.

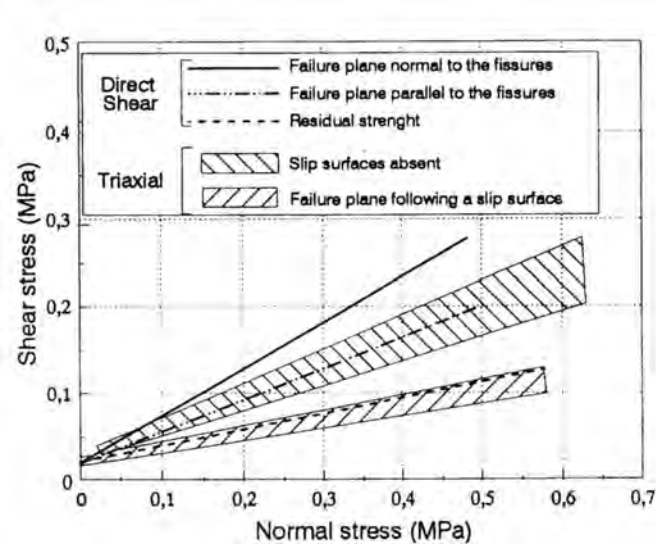

Figure. 1. Shear strength of the Laviano clay shale (Bilotta et al. 1985).

These data stress the inherent difficulty in the selection of the soil parameters to use in the geotechnical design. They however indicate that the material could be modeled as a "deformable discontinuum", whose properties at the mesofabric scale can be obtained from laboratory tests not including principal shears; a separate characterization of the principal shears is however always necessary.

4. The results of some numerical experiments

In order to focus on the role of the macrofabric on the mechanical response of tectonized clay shales with special reference to slope stability problems, some simple numerical experiments have been carried out. The analyses concern the stability conditions and the deformation

mechanisms of a sloping deposit of tectonized clay shales loaded by an embankment having a basal width of 20 m and infinite length (2D problem). In order to account for the influence of macrofabric, the material has been modelled as a deformable medium crossed by two sets of planar shear discontinuities. Due to the lack of reliable data about the distribution, spacing and orientation of principal shears in these formations have been assumed. The horizontal distance among them is 4 m and their inclination to the horizontal is variable. The four cases analysed in this paper, are presented in Figure 2 (cases b, c, d and e); the results have been compared with those which can be obtained in the absence of discontinuities (case a). The properties of the material comprised between principal shears and in the reference case a) are those that might be obtained by laboratory tests, thus implicitly accounting for the role of microstructure and mesofabric. Such a "continuum" is an elastic-perfectly plastic material. The major shears, which bring in the analysis the influence of macrofabric, have been modelled as very thin elements (0.01 m in thickness) having a Young modulus higher than the "continuum" and a shear strength equal to the residual value (Fig. 2). The geostatic state of stress has been calculated assuming k_0=1. Soil failure has been attained by the φ/c reduction method. The analysis has been carried out with the FEM Code Plaxis 2D, 2021.

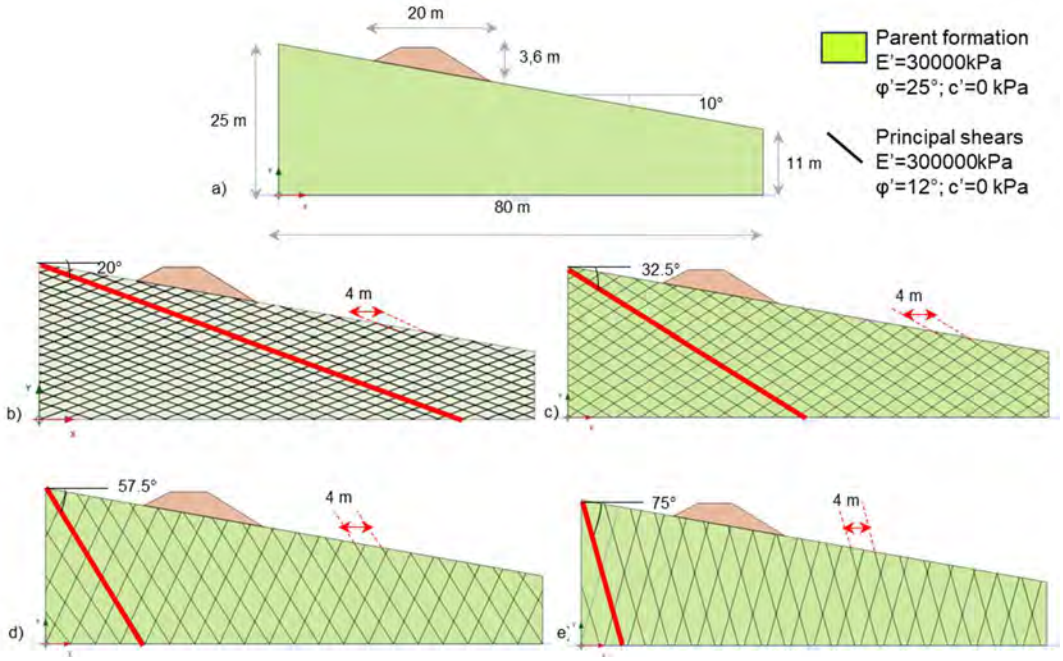

Figure 2. The investigated cases.

The results of the analysis are summarized in Figure 3: FS is the safety factor; the coloured areas indicate the induced horizontal displacements. The maximum safety factor (FS=1.9) has been obtained in case a), i.e. for a material free of major shears. However, a similar response as in case a) has been obtained in case d); this means that the discontinuities do not play any significant role. The minimum safety factor (FS=1.09) features the case c). As it is well evident, in this case the major displacements concentrate into a small soil volume. This is due to the unfavourable orientation of the major shears, which involves the part of subsoil that is located within such a volume in the failure mechanism. An intermediate response (FS=1.12) features case b), in which shear discontinuities play a key role as well. Of course, further situations might be found, which could provide even lower values of the safety factor, depending on orientation, spacing and properties of the shear discontinuities. A not negligible problem in the design of man-made works is thus recognizing them and correctly modelling the problem.

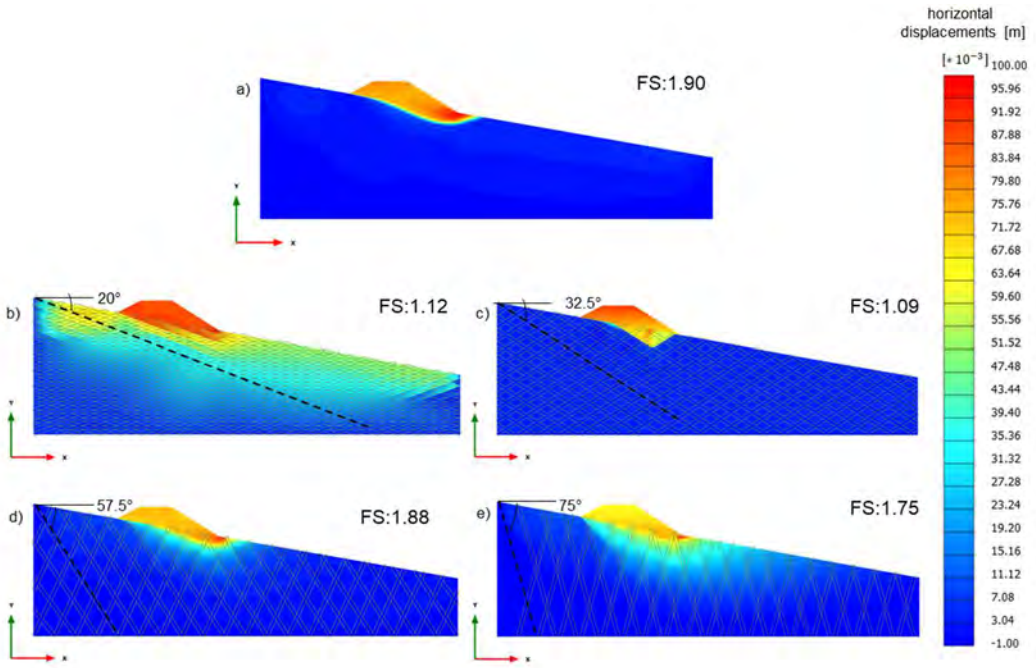

Figure 3. Safety factor and induced horizontal displacements for the case of Figure 2.

Further analyses show that the increase of both Young modulus and cohesion of the "continuum" leads in all cases to a strong increase of the safety factor and to more uniform displacements within a larger volume of the subsoil; an example is shown in Figure 4. The same analyses also suggest that, as higher are soil cohesion and Young modulus, as lower the influence of the orientation of the system of discontinuities on the safety factor. These results confirm the major role that is played by principal shears in the mechanisms of deformation and collapse of structurally complex formations.

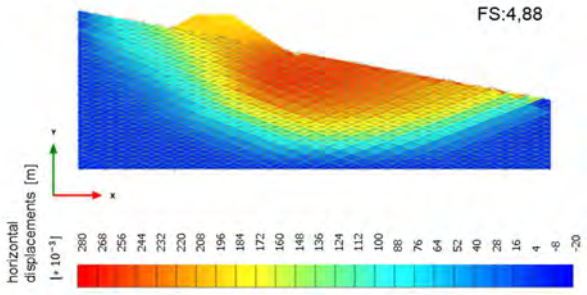

Figure 4. Safety factor and horizontal displacements assuming c'=500 kPa and E=300 MPa.

CONCLUSIONS

The analysis of geotechnical problems involving tectonized clay shales is a challenging issue. The simple examples considered in this paper focus on the kinematic constraints that are imposed by major discontinuities in failure problems. In these cases, in fact, the mechanical properties that are measured in laboratory tests can be useless for a correct analysis of the problem at hand. Further innovative criteria of investigation and analysis are then necessary.

References

Bilotta E, Pellegrino A & Picarelli L (1985) Geotechnical properties and slope stability in structurally complex clay soils. *Chapter 3: Physical and Mechanical Properties. Golden Jubilee Volume*, AGI, 195-214.

Plaxis 2D (2021) Reference Manual, CONNECT Edition V21.0, Bentley, pp 576

Forecasting landslide motion with machine learning models: the use case of Séchilienne landslide (French Alps) to identify the relevant predicting variables

Olivier Maillard[1], Catherine Bertrand[1], Jean-Philippe Malet[2, 3]

[1] Laboratoire Chrono-Environnement, CNRS UMR 6249, University of Franche-Comté, Besançon, France
[2] Institut Terre et Environnement de Strasbourg, CNRS UMR 7063, University of Strasbourg, Strasbourg, France
[3]Ecole et Observatoire des Sciences de la Terre, CNRS UAR 830, University of Strasbourg, Strasbourg, France

SUMMARY: The Séchilienne landslide is located in the Romanche valley, south-west of Belledonne massif and 20km south-east of Grenoble. The highly fractured nature of the landslide and the difference in hydraulic conductivity between fractured and micro-fissured rocks lead to the development of a perched aquifer located in the unstable zone. Pore water pressure variations of the perched aquifer led to a decrease in rock properties and are a key factor in landslide initiation. Thirty years of multi-parametric observations are available allowing to analyse the variation of terrain motion in relation to daily meteorological and hydrogeological conditions. These datasets are used to forecast landslide motion with supervised machine learning methods. The use of ensemble learning methods such as Random Forest and XGBoost allow to propose forecasting models while providing information about the most important predicting features. The features introduced in the model are described and discussed as well as the model calibration/validation strategy. We show that models combining meteorological and hydrogeological features obtained with a reservoir hydrological model have high predictive power.

Keywords: Landslide motion, Forecast, Machine Learning, Random Forest, Séchilienne landslide

Introduction

Recent works on landslide displacement forecasting using machine learning or deep learning models show relevant performance (Wang et al., 2022, Nava et al., 2023). However, these models 1) are mostly based on the use of past displacement information to forecast the futur displacement, 2) do not provide information on the most relevant predictive features in terms of meteorological and hydrogeological variables for the forecast, and thus the identification of possible precursory factors. Identifying these features is crucial as they could greatly improve the performance (reduction of false alarms) of early warning systems. In this context, the Séchilienne landslide is used as a use case to build a forecasting model based on Ranfom Forest and XGBoost supervised models and to identify possible precursory factors.

I. Geological and hydrogeological context of the Séchilienne landslide

The Séchilienne landslide is located in the Romanche glacial valley, in the Belledonne massif on the southern slope of Mont Sec, 20km south-east of Grenoble (Fig. 1a). The unstable slope is composed of micaschist with uncomformity Carboniferous to Lias sedimentary deposits as well as Würm glacial deposits. It extends from 450 to 1100m a.s.l. over an area of 1km^2 and involves a volume of 60 M m^3. The measured surface velocity is in the range of 10 cm.yr^{-1} for

most of the unstable slope to nearly 300 cm.yr^{-1} in the active part. The fracturation of the unstable slope leads to a dual-permeability behavior typical of fractured rock aquifers where conductive fractures play a major role in the drainage, while micro-fissured rocks ensure a slower flow (Vallet et al., 2015a, Nevers, 2021). The hydraulic conductivity gradient between fractured and micro-fissured rocks leads to a dual-aquifer layer system: the landslide-perched aquifer and the deep aquifer (Fig. 1c).

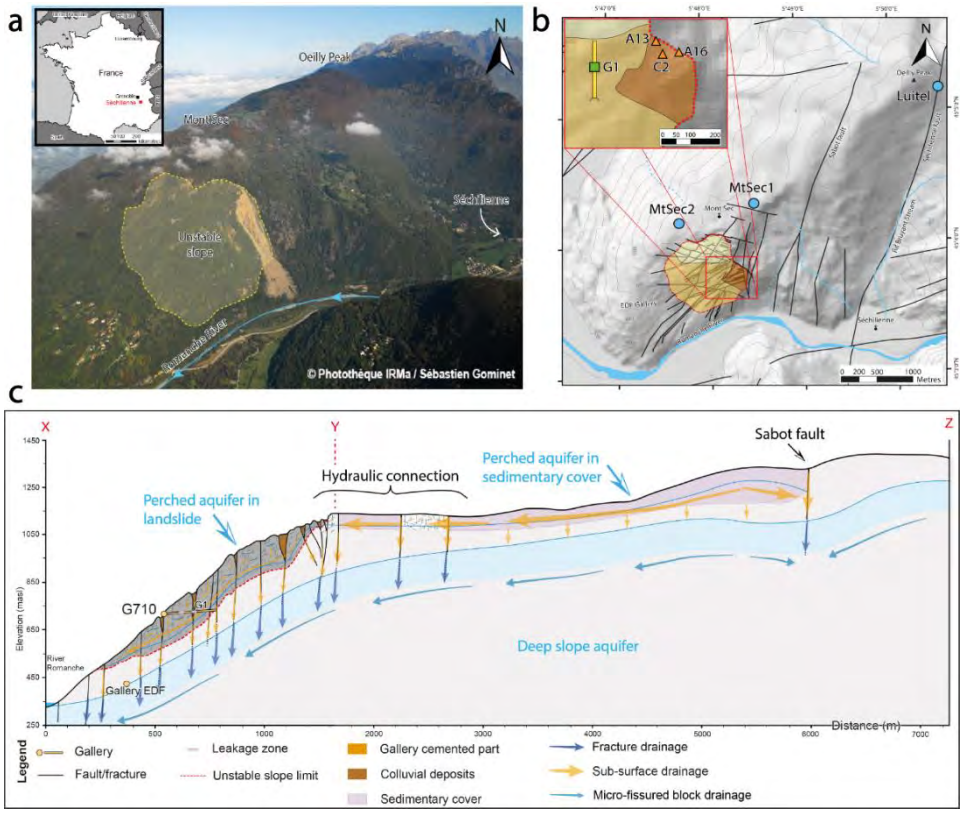

Figure 1. Aerial view of the Séchilienne landslide (a). Location of measurements stations (b). Hydrological cross-section of the instability (c) (modified from Nevers et al., 2021)

During low flow periods, the perched aquifer is structured as many saturated isolated zones which connect each other during high flow periods leading to an increase on the recharge area beyond the unstable slope limits (Vallet et al., 2015a, Nevers, 2021). Water levels fluctuation lead to pore pressure variations, resulting in a decrease in rock properties

II. Observation dataset

The Séchilienne landslide observation datasets consist in daily meteorological and displacement measurements over a period of thirty years (1992-2022). Temperature (°C) and rainfall data (mm) are acquired from three weather stations (MTSEC1, MTSEC2 and LUITEL) located around the unstable slope in order to obtain a continuous series of data (Fig. 1b). Evapotranspiration (ETP) is determined using the Oudin's method in order to calculate effective rainfall values, assuming a maximum available water storage capacity value of 10 mm (Vallet et al., 2015a).

The surface displacement data (mm) are acquired at three locations with extensometers devices (A13, A16, C2) in the most active part of the landslide and characterised by measurement errors of ± 0.5 mm. Raw displacement data are filtered with a moving average (5 days) window by defining a lower and upper threshold. Displacement time-series exhibit seasonal fluctuations characterized by intermittent periods of acceleration and deceleration. A persistent and ascending trend is observed until 2008, followed by a phase of accelerated displacements and an amplification of seasonal amplitudes extending until 2013. Subsequent to this acceleration period, a reversal trend is observed together with a progressive decrease in seasonal amplitudes, leading to low amplitude seasonal variations since 2017 (Fig. 2a).

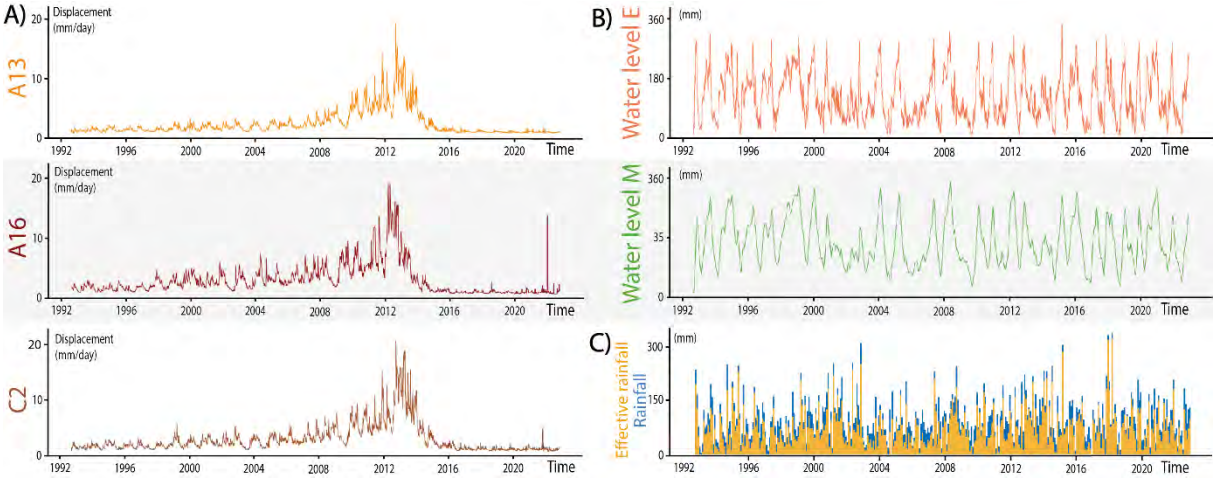

Figure 2 : Data from extensometers A13, A16 and C2 (a). Simulated water levels in reservoirs E and M (b). Monthly cumulated rainfall and effective rainfall data (c).

The dynamic of the perched aquifer is modelled using a reservoir model implemented in the Karstmod software (Mazzilli et al., 2019). This model consists of an upper reservoir (E), a matrix reservoir (M) and a hysteresis flow component, designed to represent slow and fast flow components of the fractured system. The input data for this model includes net rainfall, evapotranspiration (ETP) and groundwater flow measurements in gallery G710. The model simulates the water flow signal and water levels in the reservoirs E and M.
The water level time-series in reservoirs E and M do not show any significant trends but exhibit strong seasonality. Furthermore, they present strong responsiveness to precipitation for reservoir E, while reservoir M exhibits a long memory of precipitation with a more prolonged time response (Fig. 2b).

Net rainfall shows low seasonal variation, characterized by less rainy winters and summers compared to the rest of the year. Conversely, effective rainfall shows high seasonal contrast with dry summer and wet winters. The recharge signal is clearly influenced by air temperature variations through ETP processes. Both rainfall and effective rainfall time-series do not show any trend, and the amplitude of the seasonal variations remains constant over the whole period (Fig. 2c).

III. Methods

The surface displacement data were decomposed into three components (respectively trend, seasonality and random) using a multiplicative analysis over a 365-day period. In this study, the seasonal and random components are both assumed to be linked to the rainfall triggering

factors (Vallet et al., 2014). These two signals were aggregated into a single detrended displacement signal time-series.
We used supervised machine learning models (Random Forest / XGBoost) to simulate, in forecasting mode, landslide displacement for the three measurements points (A13, A16 and C2). We defined a list of 441 hydro-meteorological features derived from the observed net and effective rainfall and the simulated groundwater levels in the reservoirs E and M. The features consist of attributes derived from classical and advanced statistical descriptors (Tab. 1). The features are computed over moving temporal windows from 5 to 90 days in order to observe long-term forcing effects.

Table 1. Subset of predicting hydro-meteorological features (among 441 features)

Time series data	Features name	Features significiance
Rainfall	R_sd_5	5-day rainfall standard deviation
	R_max_10	10-day rainfall maximum value
	R_rainyday_30	30-day number of rainy days
	R_rainyday_10mm_90	90-day number of days with rainfall exceeding 10mm
Effective Rainfall	ER_min_15	15-day effective rainfall minimum value
	ER_cumul_20	20-day cumulated effective rainfall
	ER_3rainyday_30mm_60	60-day number of 3 consecutive days with effective rainfall exceeding 30mm
Water level E and M	hE_diff_20	20-day difference in water leve in reservoir E
	hM_diff_mean_30	30-day difference in the average water level of reservoir M compared to the overall average

Several strategies were employed to train and test the model performances, either on displacement time-series, either on detrended displacement time-series. For displacement data with trend, we selected three validation periods (1999, 2005 and 2012) that are representative of average displacement amplitudes. For each validation periods, we adjusted the length of the model training period from one to several years. Regarding the detrended displacement data, we also adjusted the duration of the training period. Moreover, due to the absence of trends in the signal, we were able to train and test the models over much longer periods.

IV. Results

For each extensometers and validation periods, the displacement predictions from the Random Forest and XGBoost models exhibit relatively close results. These observations are the same for detrended displacements forecasts. Therefore, we subsequently chose to present only the results of displacement forecast for extensometer A13 for the year 2005, as well as detrended displacement forecasts for the period 2005-2010 generated using the Random Forest model.

The variations and amplitudes of the predicted displacements show only partial with the measured data. These observations can be attributed to (1) a training period that is too short to establish significant relationships between the displacements and the features, and (2) the influence of the increasing trend of displacement associated with larger amplitudes, which can prevent the model's ability to identify lasting relationships.
Conversely, applying forecast model to the detrended displacement time-series yields results that are closer to the observed signal with a correlation coefficient of 0,45. This improvement in accuracy can be attributed to the ability to use longer training periods and the absence of trend, resulting in nearly constant displacement amplitudes over time.

In both cases, the principal used features by the models exhibit a consistent ranking of importance. The most significant features are hydrogeology features, particularly the variations and maximum water levels in reservoirs E and M over windows of 5 to 30 days, with importance ranging from 10 to 30%. Features related to effective rainfall are also prominent (with importance below 10%) and are mainly associated with the number of rainy days and/or the number of consecutive rainy days over windows 15 to 90 days.

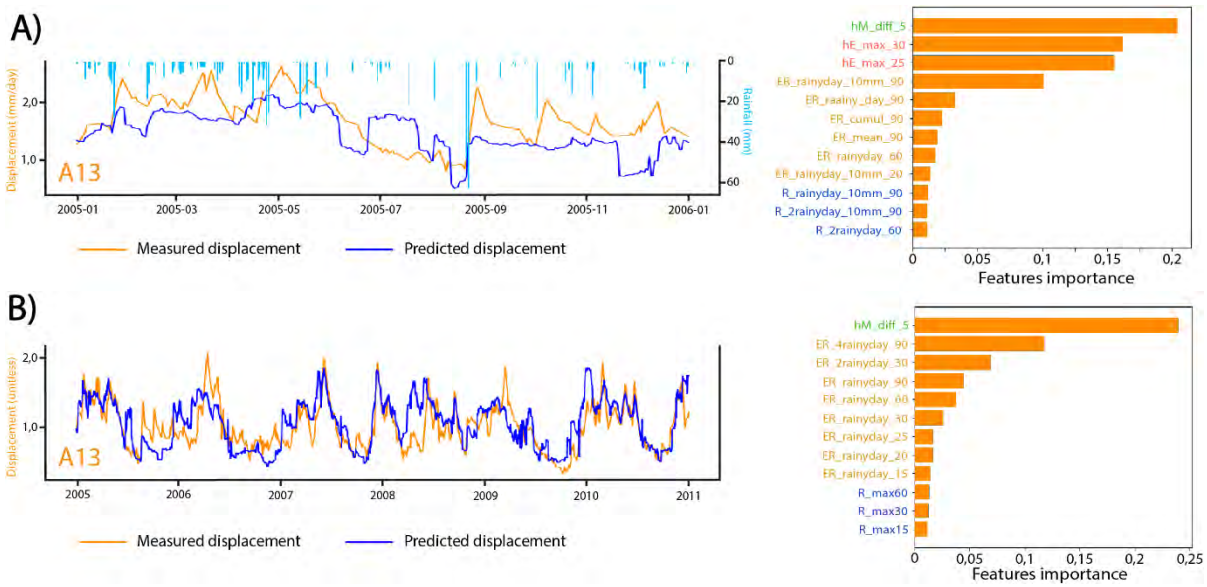

Figure 3. Forecasts and feature classifications of the Random Forest model on extensometer A13 for displacement time-series (a) and for detrended displacement time-series (b)

Conclusion

Random Forest and XGBoost algorithms are used to simulate terrain displacement at three locations for the Séchilienne landslide from a series of specifically calculated hydro-meteorological features. The results of predicted displacements is significantly closer to observed data on detrended displacements with an accuracy of 0,45 than on raw displacement signals. This can be attributed to (1) the potential to use larger training periods for the models and (2) constant displacement amplitudes over the time unaffected by the signal trend. The most predictive features are those derived from slope hydrogeological observations (eg. Variations of groundwater levels in the reservoirs) and from effective rainfall. Considering that the most promising results are associated with detrended displacements, it suggests the need to develop solutions to incorporate the prediction of displacement trends, in order to establish a comprehensive predictive model.

References

Mazzilli N, Guinot V, Jourde H, Lecoq N, Labat D, et al. (2019). KarstMod: A modelling platform for rainfall - discharge analysis and modelling dedicated to karst systems. Environmental Modelling & Software 122, 103927.

Nava L, Carraro E, Reyes-Carmona C, Puliero S, Bhuyan K, Rosi A, Monserrat O, Floris M, Meena SR, Galbe JP, Catani F (2023). Landslide displacement forecasting using deep learning and monitoring data across selected sites. Landslides 20, 2111-2129.

Nevers P (2021). Fonctionnement hydrogéologique et processus de transfert dans le massif fissuré de Séchilienne (Alpes Francaises), Apport du couplage de traceurs naturels et isotopiques. PhD thesis, University de Bourgogne Franche-Comté.

Vallet A, Bertrand C, Fabbri O, Mudry J (2014). A new method to compute the groundwater recharge for the study of rainfall-triggered deep-seated landslides. Application to the Séchilienne unstable slope (western Alps). Hydrology and Earth System Discussion 11, 6343-6403.

Vallet A, Charlier JB, Fabbri O, Bertrand C, Carry N, Mudry J (2015). Functioning and precipitation-displacement modelling of rainfall-induced deep-seated landslides subject to creep deformation. Landslides 13, 653-670.

Wang Y, Tang H, Huang J, Wen T, Ma J, Zhang J (2022). A comparative study of different machine learning methods for reservoir landslide displacement prediction. Engineering Geology 298, 106544.

Real time stability prediction of an unsaturated slope with IoT-based hydrological data monitoring

Luca Piciullo[12], Vittoria Capobianco[1], Håkon Heyerdahl[1]

[1] Norwegian Geotechnical Institute, Oslo, Norway
[2] Oslo Metropolitan University, Oslo, Norway

SUMMARY: Piciullo et al. (2022) proposed a framework for an Internet of Things (IoT)-based Local Landslide Early Warning System (Lo-LEWS), addressing monitoring, modelling, forecasting, and warning. Real-time monitoring captures the hydrological behaviour of the slope. To accurately assess real monitored conditions, a reliable hydrological model is essential. A trained machine learning (ML) model together with forecasted hydrological and meteorological variables proves effective for slope stability forecasting. This framework was applied to a natural unsaturated slope adjacent to a railway track in Eastern Norway. his case study serves as a fully operational example, showcasing the utilization of IoT and digital twinning. It also emphasizes collaborative efforts across diverse expertise areas, including geotechnical, hydrological, instrumental, and informatics.

Keywords: monitoring, modelling, calibration, validation, machine learning.

Framework for a IoT-based stability analysis as local landslide early warning system (Lo-LEWS)

The IoT-based real-time Local Landslide Early Warning System (Lo-LEWS, Piciullo et al., 2018), is structured around four main technical phases: monitoring, modelling, forecasting, and warning. The initial phase involves real-time monitoring of hydrological and climate variables. The modelling phase includes the collection of mechanicals, hydraulic and vegetation properties and the definition of a reliable hydrological model able of back-calculating the monitored data. ML algorithms can be used in this phase to train models based on the numerical modelling, identifying combinations of monitored variables that may lead to failure. In the forecasting phase, information on forecasted meteorological variables is gathered and utilized in trained ML algorithms to predict slope stability. If the FS is low, warning messages are sent to the system managers. In the event of a critical warning, an extra phase of response is activated with the application of emergency plans.

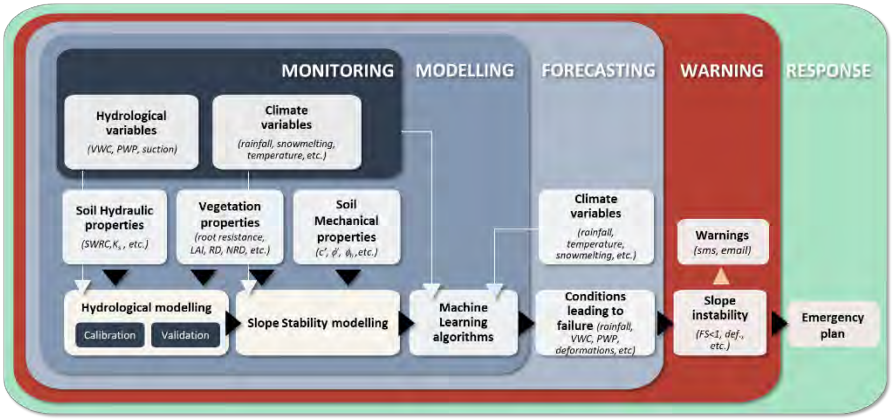

Figure 1. Framework for a IoT-based slope stability analysis and warning at a slope scale (revised from Piciullo et al., 2022).

Monitoring of the unsaturated slope

The study area is in Eidsvoll, Norway (60° 19' 23.376", 11° 14' 44.646"). The slope is 25-30 m high, with an inclination of about 45° in the upper part. The slope has not shown any deformations; however, it is a threat for the railway lines located at the toe. No structural mitigation measures were possible on the top of the slope since the zone is within a cultural heritage area. Volumetric water content (VWC) and pore-water pressure (PWP) sensors were installed in late spring/early summer of 2016 to monitor the hydrological conditions. Recently a weather station and extra soil water content and suction sensors have been installed (see Piciullo et al., 2022 for more details). The sensors and weather station regularly send data to NGIs IoT data platform (NGI Live), which stores and makes the data available in real-time through online dashboards and Application Programming Interface (API). Lab testing (granulometric curves, pressure plate tests, Atterberg limits) and in-situ CPTu have been carried out. The slope has been schematized with the following layering: a sand/silt layer of circa 6 meters, a smaller layer of clayey silt material (about 3 meters thick), a firm marine clay layer to large depths (Figure 2).

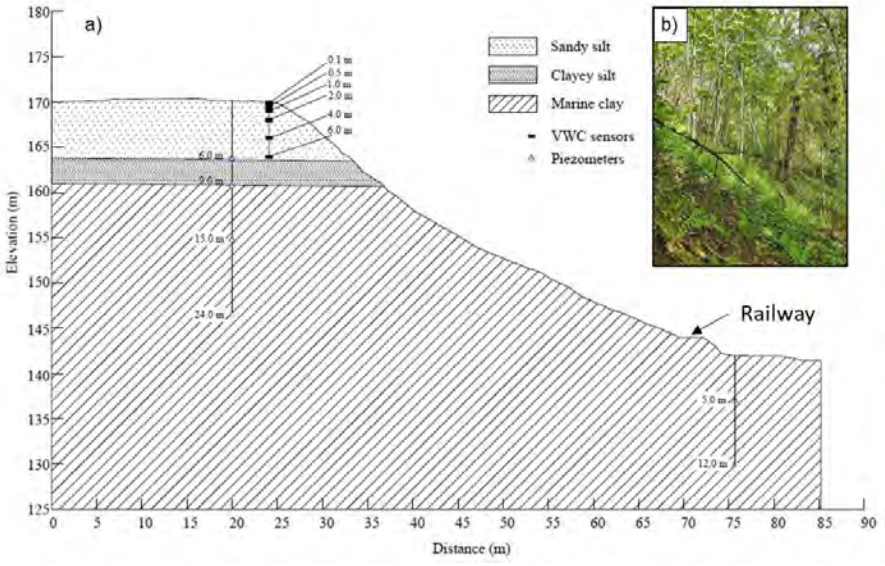

Figure 2. a) Cross section of the studied slope, with soil stratigraphy and location of the sensors and b) a picture of the vegetation cover along the slope.

Modelling and input data

The commercial software GeoStudio (GEO-SLOPE International, Ltd. 2012a,b) was used to create a digital twin of the slope, performing hydrological modelling and slope stability analysis. Two modules of the software were used: SEEP/W (analysis of unsaturated groundwater flow) and SLOPE/W (slope stability computation). The aim of the modelling is to back-calculate the in-situ monitored hydrological conditions and provide a reliable model for stability analysis to be used for training ML algorithms.

The 2D finite element module SEEP/W was used to analyses the transient seepage and obtain pore water pressure (PWP) and volumetric water content (VWC) variations in the soil. The governing equation in SEEP/W is Richards' equation (Richards, 1931), which describes two-dimensional flow in unsaturated soils. The extended Mohr-Coulomb failure envelope (Fredlund et al., 1978) was used to define the shear strength criteria as shown in equation (2):

$$\tau = c' + (\sigma - u_a)tan\phi' + (u_a - u_w)\, tan\phi^b \qquad (2)$$

Where τ is the shear stress on the failure plane at failure; c' the intercept of the "extended" Mohr-Coulomb failure envelope on the shear stress axis when the net normal stress and the

matric suction at failure are equal to zero, also referred as the "effective cohesion"; $(\sigma-u_a)$ the net normal stress at failure; ϕ' the angle of internal friction associated with the net normal stress state variable; (u_a-u_w) the matric suction at failure and ϕ^b the angle representing shear strength increase due to the matric suction.
Material properties were obtained: by triaxial tests for layer 1 (Heyerdahl et al, 2018) and layer 3 (NGI report 20160131-02-R); by literature (Statens Vegvesen, 2018; Melchiorre and Frattini, 2012) for layer 2. The material properties of the layers are summarized in Table 1.

Table 1. Soil properties for slope stability analysis in SLOPE/W.

Layer	Unit weight γ_{tot} (kN/m^3)	Cohesion c' (kPa)	Friction angle $\phi'= 2*\phi^b$ (°)	Failure envelope
1	18	8	36	Mohr-Coulomb
2	18	8	32	
3	20	10	32	

The experimental soil water retention curves (SWRCs) of the unsaturated layers of the slope were obtained through pressure plate testing (Lin and Cerato, 2012; Heyerdahl et al, 2018) performed at NGI labs. The van Genuchten (1980) SWRC equation was used to calculate the water content as a function of the matric suction and the hydraulic conductivity (for details refer to Piciullo et al., 2022). Initial total head values were assumed, respectively, on the left and on the right boundaries, of 163 meter and 142 meters. The total head values were defined considering the 4 piezometers installed on top of the slope and 2 other piezometers at the toe of the slope. Daily precipitation (rainfall and snowmelt) data were used to define the flux boundary conditions along the slope surface in the SEEP/W program.
A set of climate variables (i.e., air temperature, relative humidity, wind speed and solar radiation) were provided to feed the Penman-Monteith equation to determine the evaporation flux. The climate variables used for modelling were taken from the closest meteorological station, located about 11 km north from the slope. The precipitation (rainfall plus snowmelt) dataset was obtained from the daily gridded raster file on the Norwegian website senorge.no (http://www.senorge.no), evaluated combining weather stations and radar measurements. Furthermore, additional information related to the vegetation was also needed to determine the evapotranspiration flux: leaf area index; plant moisture limit; root depth; normalized root density; soil cover fraction, vegetation height.
To improve the performance of the model used for back-calculation a sensitivity analysis of the hydraulic conductivity has been performed. Specifically, the saturated hydraulic conductivity and the permeability anisotropy ratio (k'y/k'x) have been varied. A validation of the numerical modelling results has been carried out comparing the modelled and the measured hydrological variables values for 1 year period. The validated digital twin model has been used to evaluate the slope stability (i.e., factor of safety, FS) coupling SEEP and Slope analyses. Details are presented in Piciullo et al., 2022.

Forecasting of the factor of safety

A supervised, regression ML random forest model has been used to predict the FS from the modelled 1-year validation period. A baseline computing the train targets average has been evaluated (98.32%). It represents the reference value to compare the machine learning algorithm performance with. The prediction accuracy is calculated for different combination of features (i.e., monitored variables) used to predict the FS and it is compared with the baseline accuracy (Table 2). The highest accuracy (99.83%) is obtained considering VWC at different depths and PWP at 6-meter as well as precipitation and air temperature. This result highlights the possibility to predict the FS knowing VWC, PWP and climate variables. These variables, monitored in real-time, can be used as warning parameters in the IoT-based Lo-LEWS.

Table 2. Comparison between baseline and prediction accuracies for different considering features.

Id	Features	Baseline accuracy [%]	Prediction accuracy [%]	Increment [%]
#0	prec., air_t.	98.32	98.78	0.46
#1	prec., air_t., VWC_0.1		99.33	1.01
#2	prec., air_t., VWC_0.5		99.29	0.97
#3	prec., air_t., VWC_1.0		99.42	1.1
#4	prec., air_t., VWC_6.0		99.3	0.98
#5	prec., air_t., PWP_6.0		99.78	1.46
#6	Prec., air_t., VWC_0.1, 0.5, 1, 6		99.77	1.45
#7	Prec., air_t., VWC_0.1, 0.5, 1,6 PWP6		99.83	1.51

Then, the validated digital twin model has been used to evaluate the slope stability (i.e., factor of safety, FS) coupling SEEP and Slope analyses for 5 different 1-year datasets. Both past and future scenarios have been considered: 2019-2020, 2021-2022, 2022-2023, 2064-2065, 2095-2096. The inputs (i.e., hydrological and weather variables) and the FS results have been used to train a supervised random forest machine learning model. The feature considered were VWC, PWP, rainfall, temperature, LAI; the target was the FS.

To predict the FS for the upcoming three days, PASTAS model (Collenteur et al., 2019) and the Norwegian Meteorological Institute webpage have been used to respectively forecast the hydrological variables (i.e., VWC and PWP) and rainfall, air temperature and relative humidity data. We created a web service that once a day automatically (1) fetches measured data from NGI Live using the NGI Live API, (2) runs predictions for the next three days based on the measured data, and (3) sends the predicted values back to NGI Live, making them available for real-time visualization in online dashboards. If FS, VWC or PWP threshold values are exceeded, text messages and emails are sent to the system managers to take appropriate actions.

Concluding remarks

This contribution shows the application of a framework for a IoT-based early warning at a slope scale (i.e., Lo-LEWS) for an unsaturated slope in Norway. The monitoring, modelling and forecasting and warning phases have been described, with emphasis on the hydrological model, and ML analysis to predict the FS from the monitored variables.

The importance of using monitored data to back-calculate and validate a hydrological model has been highlighted. Moreover, the possibility to use real-time monitored hydrological variables to predict the FS has been shown.

This case study can be seen as a fully operational example of the use of IoT and digital twinning to provide a real-time stability assessment for a slope as well as a collaborative effort among different expertise: geotechnical, hydrological, instrumental and informatics.

References

Collenteur R. A., Bakker M., Caljé R., Klop S. A., Schaars F. (2019). Pastas: Open Source Software for the Analysis of Groundwater Time Series. Groundwater, 57(6):877–885, November 2019. location=USA, The Netherlands. URL: https://doi.org/10.1111/gwat.12925, doi:10.1111/gwat.12925.

Fredlund D G, Morgenstern N R, Widger R A (1978) The shear strength of unsaturated soils. Can Geotech J, 15(3), 313-321. https://doi.org/10.1139/t78-029

Heyerdahl H, Hoydal O A, Kvistedal Y, Gisnas K G, Carotenuto P (2018) Slope instrumentation and unsaturated stability evaluation for steep natural slope close to railway line. In UNSAT 2018.

Melchiorre C, Frattini P (2012) Modelling probability of rainfall-induced shallow landslides in a changing climate, Otta, Central Norway. Climatic change, 113:413-436. https://doi.org/10.1007/s10584-011-0325-0

Piciullo L, Calvello M, Cepeda J M (2018) Territorial early warning systems for rainfall-induced landslides. Earth-Science Reviews, 179, 228-247. https://doi.org/10.1016/j.earscirev.2018.02.013

Piciullo L, Capobianco V, Heyerdahl H (2022) A first step towards a IoT-based local early warning system for an unsaturated slope in Norway. Nat Hazards 114, 3377–3407. https://doi.org/10.1007/s11069-022-05524-3

Richards L A (1931) Capillary Conduction of Liquids Through Porous Mediums. Physics, Vol. 1. https://doi.org/10.1063/1.1745010

Deep-learning-based 3D surge-wave detection and tracking in debris flows using cameras and LiDARs

Jacob Hirschberg[1,2] and Jordan Aaron[1,2]

[1] Geological Institute, ETH Zurich, Zurich, Switzerland (jacob.hirschberg@erdw.ethz.ch)
[2] Swiss Federal Institute for Forest, Snow and Landscape Research (WSL), Birmensdorf, Switzerland

SUMMARY: Debris-flow movement is rapid and complex. Recently developed LiDAR sensors allow for monitoring debris-flow dynamics at high spatial (<2 cm) and temporal (10 Hz) resolution. We present a framework consisting of object detection in debris flows (surge waves) using deep learning algorithms on 2D camera images, which are fused with LiDAR data to obtain 3D information. This allows for tracking objects and determining their size and velocity. Continued monitoring and application of this method will help to improve our understanding of debris-flow dynamics.

Keywords: debris flow, LiDAR, deep learning, surge waves

Introduction

Debris flows are surging mixtures of water and sediments (Hungr et al., 2014). By transferring sediments from hillslopes downstream they are both a relevant geomorphic process and a destructive hazard, as they threaten people and infrastructure in mountain regions (Berger et al., 2011). Debris flows are further characterized by a surging behavior (Iverson, 1997). Surges are generated by a number of different mechanisms, including slope variation and temporary storage of sediments with subsequent release (e.g., Kean et al., 2016), longitudinal sorting (Iverson et al., 2010), and surge waves which are analogous to those present in open channel flow (e.g. Zanuttigh and Lamberti, 2007). Such surges may superimpose and magnify the peak discharge and impact pressures, which make them a practical challenge from and engineering perspective (Edwards and Gray, 2015).

Our understanding of debris-flow dynamics, including surge waves, and ability to develop better models is hampered by the limited availability of high-resolution field-scale observations. Apart from point-scale depth measurements, high-frequency field investigations of surges are rare but have been conducted with Doppler radars (e.g., Schöffel et al., 2023) or through imagery analysis (Theule et al., 2018). Aaron et al. (2023) present a monitoring setup that combines high-framerate LiDARs and cameras, which overcomes these important limitations. Specifically, it enables the study of individual features on the flow such as boulders and surge waves, and allows for the analysis of their behavior in 4D (time and space). Extracting feature-specific information from the imagery and LiDAR manually is very time consuming, however large amounts of this data is needed for a robust statistical analysis. Such monitoring frameworks can therefore benefit from recent advancements in deep-learning-based object detection techniques.

In this study, we present a method to automatically detect surge waves in camera imagery, and subsequently project the detections onto the LiDAR measurements to obtain 3D information (Aaron et al., 2023). The framework was applied in Illgraben, a debris-flow producing catchment in the Swiss Alps with 1-8 debris flows per year (Hirschberg et al., 2021). The

LiDAR sensor (Ouster) is mounted in the middle of the channel above a check dam and operates at a frequency of 10 Hz. The event analyzed here occurred on June 5, 2022, and was characterized by multiple surge waves, which were detected and tracked.

Methods

We manually labelled a dataset of rectangular bounding boxes that consists of 917 images of >50 surge waves using the open-source tool LabelImg (Tzatualin, 2015). We differentiated three surge wave classes as they may represent different states of wave evolution (Zanuttigh and Lamberti, 2007). We classified the waves as either breaking, diffuse or hybrid (a third class that represents a mixture of these two) (Figure 1). The data set was randomly split in 60% for training and 20% for validation and testing, respectively. To partially assess the generalizability of the network, entire surges were allocated to training, validation, and testing data sets by the same percentages, ensuring that entire waves were excluded from the training data set. We added a few unlabeled images of the front and the flow in the absence of surge waves for the detector to train on negatives as well. We report precision (P), recall (R), and mean average precision (mAP). P measures how well the detector can differentiate between objects and non-objects. R measures how well the detector identifies the objects. mAP, which is calculated from P and R, measures how well the model performs at a given or a range of confidence levels. These statistics can be computed over the entire dataset or for each class.

We used YOLO v5 (Redmon et al., 2016), a computer vision model for object detection, to detect surge waves in the camera images. Detections were tracked in a post-processing step by associating them in each frame with earlier detections (Bewley et al., 2016). We used a GPU-enabled virtual machine (NVIDIA Tesla V100) by Google Compute Engine for training and inference.

Figure 1. Example detections (blue box) of (a) a breaking, (b) a diffuse, and (c) a hybrid surge wave. The dots are the LiDAR measurements projected onto the image (colored within detection box).

Results and Discussion

The detector trained with the randomly split data set achieved high detection and classification scores (Table 1). It detected individual surge waves and consistently classified individual surges (Figure 2). This is evidence for that the detector can be trained on a few images of each wave and used to identify objects on the entire imagery data set. However, the high performance indicates overtraining resulting from the random splitting of the data set, because each wave is likely represented with some frames in the training. As expected, the performance metrics for the detector trained on individual surges has lower performance metrics, albeit only marginally (Table 2). Although this testing is limited to the very similar light conditions, camera scale, and debris-flow surface appearance, this is a promising result and indicates the potential for further generalization. In future, the detector will be further tested against data from other locations along the Illgraben channel and for other events.

The surge wave detection boxes on the 2D images can be projected onto the LiDAR point clouds (Figure 3). The front travels ~10 m in 1.5 s (Figure 3e-h), which corresponds to a surge

wave speed of 6.67 m/s. Although the boxes are quite long, this could be corrected relatively easily in a post-processing step, as the front is generally well captured (Figure 3a-d). Only close to the camera, it is slightly misplaced (Figure 3d), but may also be resolved with additional training close to camera.

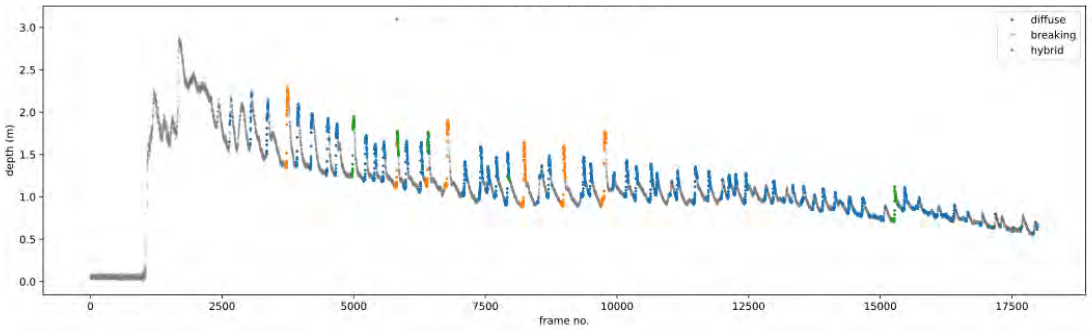

Figure 2. Average cross-sectional flow depth derived from LiDAR measurements (grey). The colors indicate the detections and their class (blue=diffuse, orange=breaking, green=hybrid).

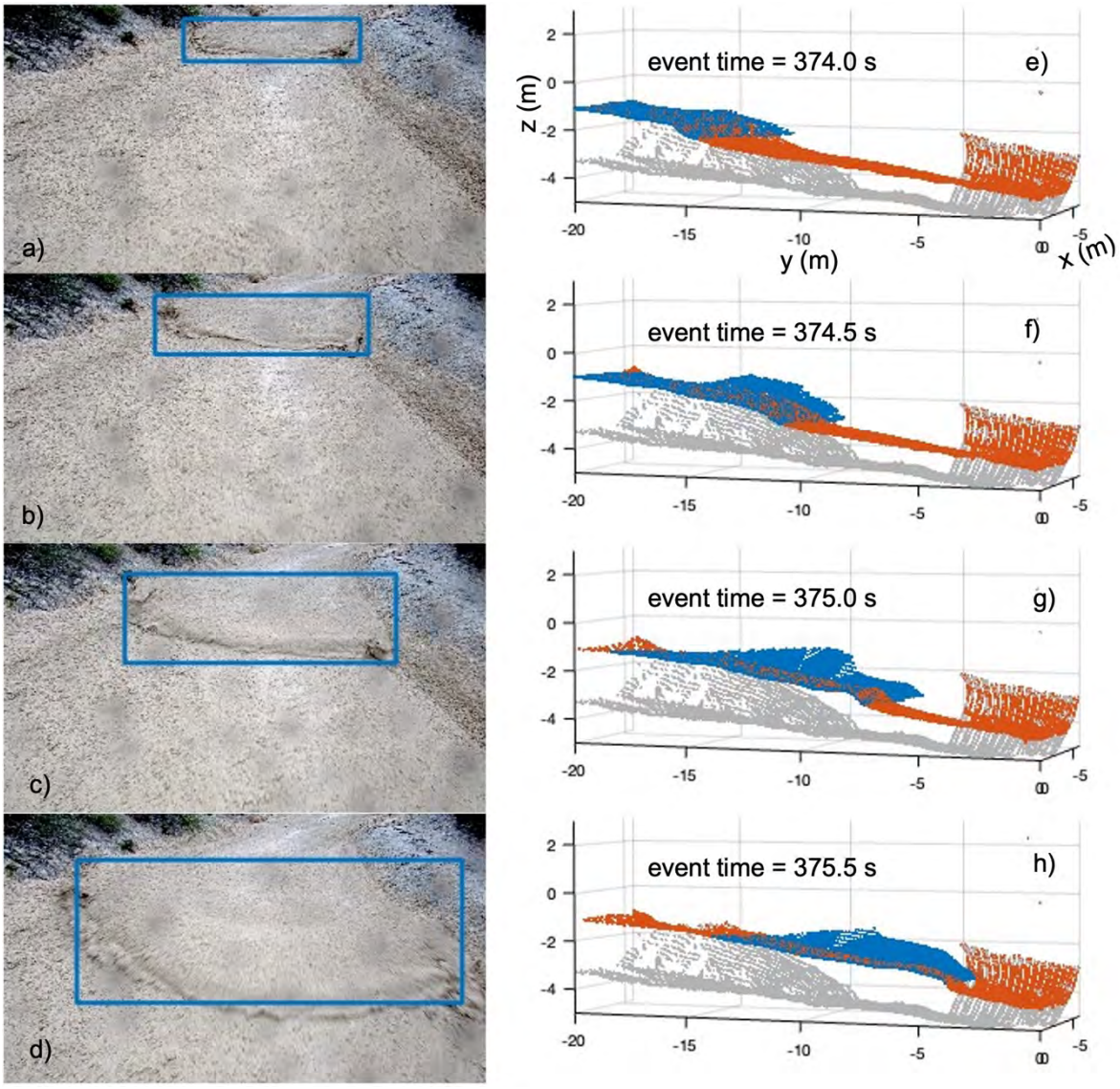

Figure 3. Detection boxes for a surge wave (a-d) and corresponding LiDAR point clouds (e-f), with the pre-event scan as an estimate for the channel bed (grey), and the scan (red) and the points within the detection box (blue) of the indicated event time.

Table 1. Performance metrics for the detection model based on the randomly split dataset.

Dataset	Class	Images	Instances	P	R	mAP@0.5	mAP@0.5:0.05:0.95
Training	all	677	553	0.998	1	0.995	0.901
Validation	all	225	178	0.98	0.951	0.99	0.711
Testing	all	226	185	0.965	0.964	0.961	0.666

Table 2. Performance metrics for the detection model based on the dataset split by surges.

Dataset	Class	Images	Instances	P	R	mAP@0.5	mAP@0.5:0.05:0.95
Training	all	572	548	0.992	0.999	0.995	0.823
Validation	all	202	202	0.872	0.964	0.961	0.707
Testing	all	151	151	0.893	0.884	0.930	0.621

Conclusions and Outlook

This study demonstrated the use of an off-the-shelf deep-learning-based object detector for debris-flow surge waves, which can be fused with LiDAR scans to derive 3D information of these objects. The good performance indicates that the method is feasibly for extracting the required information with orders of magnitude higher efficiency than a human. We showed that the detector was able to identify surge waves, which it had not been trained on. Further testing on other debris-flow events and other locations along the channel will be done in future works and will further elucidate about the generalizability. In combination with the LiDAR measurements, the detector will support addressing research questions related to surge wave dynamics. Possible extensions include a combination with a boulder detector (Aaron et al., 2023) to analyze how such surges interact with objects.

References

Aaron J, Spielmann R, McArdell BW & Graf C (2023) High-Frequency 3D LiDAR Measurements of a Debris Flow: A Novel Method to Investigate the Dynamics of Full-Scale Events in the Field. *Geophysical Research Letters*, *50*(5), e2022GL102373.

Berger C., McArdell BW & Schlunegger F (2011) Sediment transfer patterns at the Illgraben catchment, Switzerland: Implications for the time scales of debris flow activities. *Geomorphology*, *125*(3), 421–432.

Edwards AN & Gray JMNT (2015) Erosion–deposition waves in shallow granular free-surface flows. *Journal of Fluid Mechanics*, *762*, 35–67.

Hungr O., Leroueil S & Picarelli L (2014). The Varnes classification of landslide types, an update. *Landslides*, *11*(2), 167–194.

Iverson RM (1997) The Physics of Debris Flows. *Reviews of Geophysics*, *35*(3), 245–296.

Iverson RM, Logan M, Lahusen RG & Berti M (2010) The perfect debris flow? Aggregated results from 28 large-scale experiments. *Journal of Geophysical Research: Earth Surface*, *115*(F3), 3005.

Kean JW, McGuire LA, Rengers FK, Smith JB & Staley DM (2016) Amplification of postwildfire peak flow by debris. *Geophysical Research Letters*, *43*(16), 8545–8553.

Redmon, J, Divvala, S Girshick R & Farhadi A (2016) You only look once: Unified, real-time object detection. In 2016 IEEE Conference on Computer Vision and Pattern Recognition (CVPR), 779–788.

Schöffl T, Nagl G, Koschuch R, Schreiber H, Hübl J & Kaitna R (2023) A Perspective of Surge Dynamics in Natural Debris Flows Through Pulse-Doppler Radar Observations. *Journal of Geophysical Research: Earth Surface*, *128*(9), e2023JF007171.

Theule JI, Crema S, Marchi L, Cavalli M & Comiti F (2018) Exploiting LSPIV to assess debris-flow velocities in the field. *Hazards Earth Syst. Sci*, *18*, 1–13.

Tzutalin (2015). LabelImg. Retrieved from https://github.com/tzutalin/labelImg

Zanuttigh B & Lamberti A (2007) Instability and surge development in debris flows. *Rev. Geophys*, *45*, 3006.

Utilizing machine learning to forecast rockfall hazard in open pit mines

A. Giacomini, I.P. Senanayake, A. Watman, O. Buzzi, K. Thoeni

Centre for Geotechnical Science and Engineering, School of Engineering, The University of Newcastle, 2308 Callaghan, NSW, Australia

SUMMARY: The study investigates the applicability of machine learning (ML) models for fast rockfall hazard prediction based on automated extraction of geometrical features from 3D photogrammetric data. 2D profiles along highwall strikes were automatically extracted from 3D photogrammetric models of fifteen highwalls to identify and quantify significant geometrical features. Various ML models were tested to predict target parameters such as kinematic energy at the first impact, the first impact position, and the final run-out of blocks at the highwall base. A multi-linear regression model has proven the best predictions for kinematic energy while a multi-non-linear regression model with a quadratic term for the height performs best in predicting the first impact position and final rockfall run-out. The study shows that the proposed approach offers a practical and efficient way to predict rockfall hazards on different highwalls leveraging automated geometric feature extraction from 3D photogrammetric data.

Keywords: rockfall, predictive modelling, machine learning, run-out, highwall

Introduction

Rockfalls pose significant risks to human lives and infrastructure located at the toe of highwalls in open-pit mines, with the potential for considerable financial losses. Efficient mitigation can be provided when the energy at first impact at the bottom of the highwalls and the block run-out distance on the mine floor are appropriately predicted. A common approach is to employ computer-based simulations of rockfall trajectories and associated stochastic analyses to evaluate the associated risks. However, numerical analyses rely on site-specific input parameters that are extremely costly and time-consuming to routinely obtain via field-scale experiments, especially along hazardous, hard-to-access areas, requiring extensive back-analyses to assess the most suitable modelling parameters. Recent applications of AI techniques to rockfall hazards have shown that simple regression models trained on simulated rockfall trajectory data based on synthetic 2D slopes can reasonably estimate the expected ranges of energies and run-outs at the base of a sub-vertical rock cliff with the potential to replace conventional simulations (Ferrari et al. 2016, Fanos and Pradhan, 2019). However, limitations arise when using synthetic 2D slopes that do not account for the natural complexity of rock surfaces. The study investigates the application of current ML algorithms to extensive training and testing data sets of rockfall trajectories considering 2D slope profiles extracted from photogrammetric derived 3D models (i.e., with natural roughness and slope geometry) to obtain more reliable results.

Methodology

Probabilistic rockfall simulations were performed to generate trajectories using high-resolution 3D photogrammetric models of fifteen sub-vertical rock faces (highwalls) (i.e., slope angle >60°) (denoted “3D walls”) obtained from seven mine sites across New South Wales and

Queensland in Australia, with a combined length of approximately 3.4 km. An automated software solution using Python scripts was developed to extract 2D profiles as well as meaningful geometrical features from 3D photogrammetry data of the fifteen highwalls. The process (Figure 1) included i) rotating the rock faces to align the 3D walls with the same coordinate system, ii) conducting a geometric segmentation to account for the 3D local strike direction of the 3D mesh obtained for each highwall by extracting 3D wall segments of 10 m in length each and iii) extracting 2D profiles from the mesh of each wall segment. In total, 1,669 2D profiles capturing a wide range of slope geometries were extracted from the fifteen highwalls. A horizontal segment was added at the toe of each profile representing the mine floor.

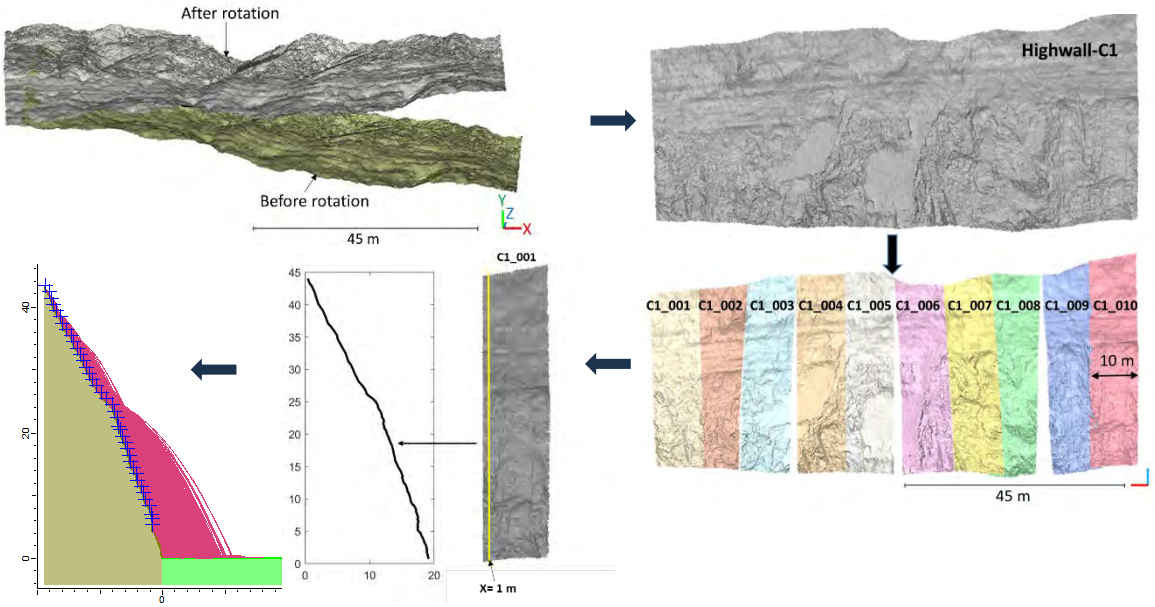

Figure 1. Process of extraction of 2D profile from a 3D highwall model. From wall rotation, to segmentation, extraction of a 2D profile, modification of the 2D profile by adding a floor; seeders, and material properties to perform 2D rockfall simulations.

A total of 4,550,500 rockfall trajectories were then automatically generated by a Python script using the module PyAutoGUI (PyAutoGUI, 2019). The simulations with respect to the natural slope profiles were conducted using RocFall2 lumped mass model (Rocscience). The initial block (unit mass of 1 kg and density of 1 kg/m^3) release positions on the slope profile, i.e., seeders, were defined at every 1 m along the height of the slope starting from a predefined height of 5 m from its toe for the bottom seeder. A vertical velocity corresponding to a 0.5 m vertical drop was added to simulate a fall from a ledge. The slope parameters, k_n, k_t and friction angle, φ, values were chosen based on Giacomini et al. (2012) (Table 1). The roughness of a slope, σ_r, defined as the standard deviation of the local slope angles, was defined as the standard deviation of the slope angle of a local line segment of the slope profile.

Table 1. Parameters assigned to slope and floor materials of the 2D profiles extracted from the 3D rock walls.

	Slope					Floor				
	Distribution	**Mean**	σ_r	**Min.**	**Max.**	**Distribution**	**Mean**	σ_r	**Min.**	**Max.**
k_n	normal	0.7	0.3	0.4	1.0	normal	0.5	0.2	0.3	0.8
k_t	normal	0.7	0.2	0.4	0.8	normal	0.8	0.2	0.5	1.0
φ	normal	30°	2°	24°	36°	normal	30°	2°	24°	36°

Each trajectory was automatically analysed to extract the energy at the first impact on the floor, E_1; horizontal distance from the toe of the wall to the first impact point, d_1; horizontal distance

from the toe of the wall to the final rock position, d_f; total height of the wall, H; height to the seeder, h (Figure 2). The 90th quantiles have been calculated for energy-related target values, i.e., $E_{90,x}$, ($E_{90,1}$) and 95th quantiles for distance-related target values, i.e. $d_{95,x}$, ($d_{95,1}$ and $d_{95,f}$) using the 100 trajectories at each seeder. Distance-related values were calculated as horizontal distance from the approximated toe position of the wall to the final rock position.

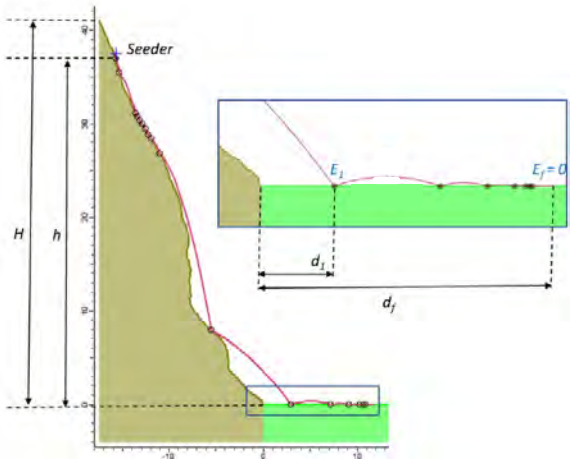

Figure 2. Illustration showing /quantities collected for each trajectory.

A meaningful split was performed on the stochastically evaluated simulation data to develop ML models for the target parameters (risk variables): kinematic energy at the first impact, the first impact position and the final run-out at the bottom of rock faces. Four representative highwalls were selected for model calibration capturing all possible ranges of wall geometric features. The remaining highwalls were used for model validation. The block release height, h, as well as the slope local roughness, σ_r, and average slope angle, α, were chosen as the principal features, i.e., ML input parameters. If each highwall, w, consists of a number, s, of 2D profiles and corresponding α and σ values are extracted from each 2D profile based on seeder heights, the features f can be defined as,

$$f^{w,s} = \{h^{w,s}, \sigma^{w,s,h}, \alpha^{w,s,h}\} \quad (1)$$

The application of simple and generalized multi-linear regression models was investigated for each individual target parameter and their performances were compared.

Results and Discussion

For each highwall, an initial Pearson correlation coefficient analysis was conducted to assess the correlations between features h, α, σ_r and target values, providing insights on the variables which should be used in a ML model. The study evidenced a stronger correlation of h with the target parameters, whereas no significant correlation was found with α and σ_r for most of the 3D highwall models. Data from the four representative highwalls have been merged and considered in the ML study. A multi-linear regression model has shown the best predictive behaviour for the kinematic energy at the first impact, $E_{90,1}$, and a multi-non-linear regression model with a quadratic term in the block release height has shown the best predictions for the first impact position, $d_{95,1}$, and the final run-out $d_{95,f}$. The proposed regressions were then used to predict $E_{90,1}$, $d_{95,1}$, and $d_{95,f}$ values for highwalls not considered in the calibration (labelled in Figure 3 as "Validation highwall") to validate the proposed approach (Figure 3).

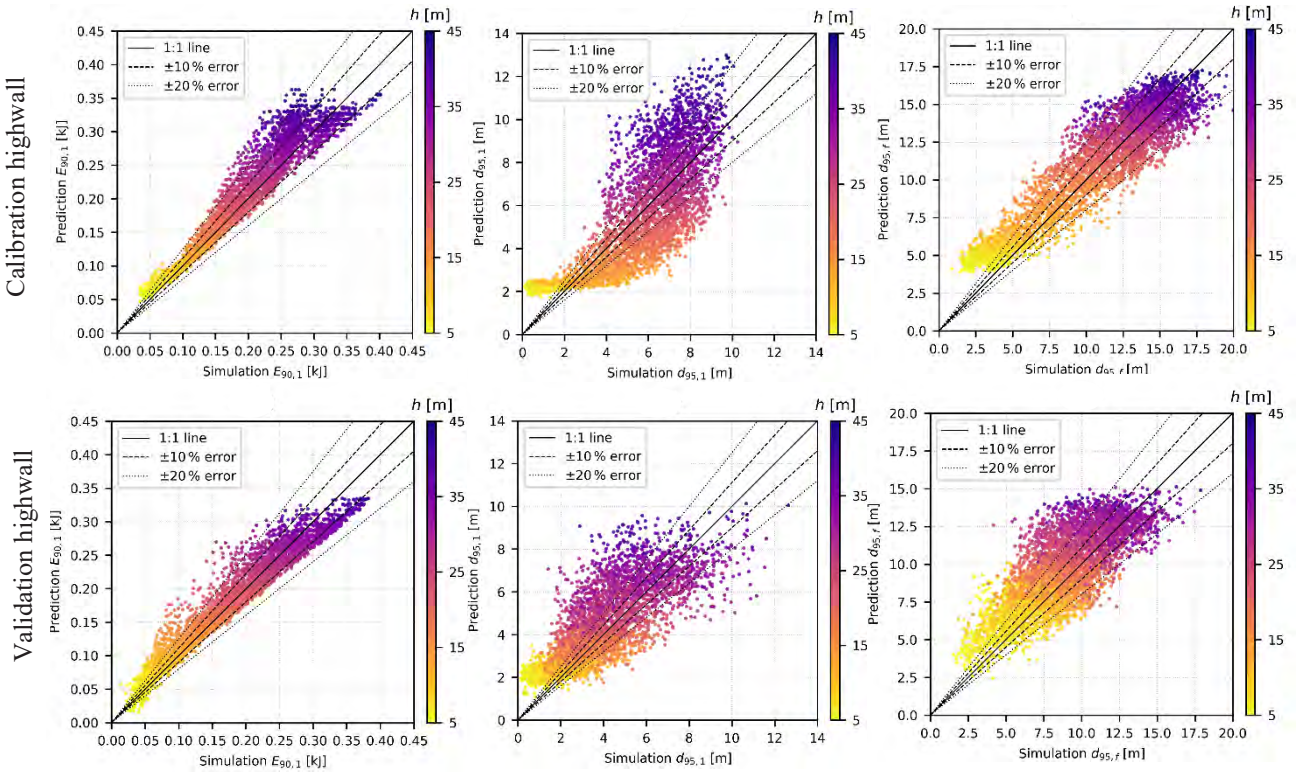

Figure 3. $E_{90,1}$ and, $d_{95,1}$, at first impact, and final run-out $d_{95,f}$, predictions vs simulations for a highwall which is part of the calibration data ("Calibration highwall") and a highwall which is not part of the calibration (labelled as "validation highwall").

Conclusions

This study has investigated the feasibility of applying ML models for fast and reliable predictions of rockfall hazard. An automated software solution was developed to extract 2D profiles along strikes of fifteen rock faces. Various ML models were tested between the main representative geometrical features (slope angle, slope roughness and seeder height - α, σ_r, h) and targets (energies at first impact at the bottom of the highwall, its location and run-out distances). A multi-linear regression model has shown the best predictions for kinematic energy and a multi-non-linear regression model with a quadratic term for the height performs best in predicting the first impact position and final rockfall run-out. The study shows that the proposed approach offers a practical and efficient way to predict rockfall hazards on different highwalls, leveraging automated geometric feature extraction from 3D photogrammetric data. Future work entails the validation of the approach with actual rockfall data collected at some of the mine sites considered in the current study.

References

Ferrari F, Thoeni K, Giacomini A & Lambert C (2016) A rapid approach to estimate the rockfall energies and distances at the base of rock cliffs. *Georisk,* 10, 179-199.

Fanos AM & Peadhan B (2019) A novel hybrid machine learning-based model for rockfall source identification in presence of other landslide types using LiDAR and GIS. *Earth Systems and Environment*, 3, 491-506.

Giacomini A, Thoeni K, Lambert C, Booth S. & Sloan S. (2012). Experimental study on rockfall drapery systems for open pit highwalls. *International Journal of Rock Mechanics and Mining Sciences*, 56, 171-181.

PYAUTOGUI. 2019. PyAutoGUI's documentation [Online]. https://pyautogui.readthedocs.io/en/latest

ROCSCIENCE. 2021. RocFall2 UserGuide [Online]. https://www.rocscience.com/help/rocfall/documentation

Towards The Italian Database Of Landslide In Situ Monitoring Systems: The Enhancement Of The IdroGEO Web Platform

Saverio Romeo[1], Carla Iadanza[1], Davide Romano[1], Alessandro Trigila[1]

[1] saverio.romeo@isprambiente.it - Geological Survey of Italy, Italian Institute for Environmental Protection and Research (ISPRA), Rome, Italy

Keywords: Landslide Monitoring Systems, IdroGEO, Italian Landslide Inventory, Database, GeoSciencesIR project

Summary

In the context of landslide risk management, data from monitoring systems is crucial to a better understanding and control of such processes. In fact, monitoring systems represent effective prevention measures that should be considered a mandatory stage both for the design of mitigation works and for the development of Early Warning Systems.
With reference to Italy, although the landslides surveyed in the Italian Landslide Inventory (IFFI) number more than 621,000, according to the National Register of Landslide Monitoring Systems, realized by ISPRA, at present only 1,222 landslides result monitored with in situ systems.
This work discusses the state of the art of monitored landslides in Italy with some preliminary results from such a Register and presents the experimental open-source National Database of Landslide in situ Monitoring Systems (NDLMS) that will be developed in the framework of Geosciences Research Infrastructure funded by Next Generation EU. In this context, the IdroGEO national web platform will be enhanced with new tools and services to support landslide mapping and will guarantee overtime data and interoperable mapping services, according to FAIR data principles and INSPIRE compliance.

Introduction

Landslides represent a major natural hazard that can threat human life, properties, and infrastructures worldwide. Recent data from the Centre for Research on Epidemiology of Disasters (CRED) indicate that landslides, among all natural hazards, cause more than 15% of deaths (Chae et al., 2017). With reference to the European continent, about 2/3 of landslides recorded in the databases from the European Geological Surveys are in Italy (Herrera et al., 2018). Taking this data as reference, it becomes clear that any rational action related to landslide risk management must include, besides conventional structural interventions (e.g., piles and retaining walls, etc.), the implementation and management of inventories, maps and associated information, and monitoring networks which represent effective prevention measures (Dei Cas et al., 2022). In this framework, data from monitoring systems is crucial to a better understanding of landslide processes. Thanks to recent technological developments, such as Remote Sensing technologies (Casagli et al., 2023), landslide detection and monitoring activities have become increasingly widespread and can be considered as a compulsory step in landslide risk assessment (Auflič et al., 2023) and for the development of Early Warning Systems (Hürlimann et al., 2019). However, monitoring data is often missing in landslide inventories, also due to restrictions on data dissemination.

The Italian Landslide Inventory (IFFI) and the IdroGEO web platform

The Italian Landslide Inventory (IFFI), realized by the Italian Institute for Environmental Protection and Research (ISPRA) together with Regions and Autonomous Provinces, nowadays contains over 621,000 landslides that occurred on the national territory and are recorded according to a standardized and shared methodology (Trigila et al., 2010). Each landslide is represented by a point located at the landslide crown, by a polygon when the surface of the landslide can be mapped at the adopted survey scale, or by a line when the width of the landslide can not be mapped (e.g., rapid debris flows). The Inventory covers the period 1116-2023, the dates of occurrence of the oldest and the most recent landslide contained in the database.
The IdroGEO Application (https://idrogeo.isprambiente.it/) was recently developed by ISPRA and allows the consultation, download and sharing of data, maps, reports, documents of the IFFI Inventory, the national landslide and flood hazard maps and risk indicators (Iadanza et al., 2021). IdroGEO is an interactive and collaborative web mapping application (Figure 1), accessible with different types of devices (smartphones, tablets, desktops) and based on REST API (Application Programming Interface) Services. In addition to the basic tools (zooming, panning, turning on/off layers), it provides tools for queries and production of reports, sharing content on social media, visualization of multimedia content on landslides, up to the possibility of multi-user online updating of the Inventory (e.g., editing of landslide geometries, collection of parameters into the landslide form, data validation by ISPRA and regional officers).

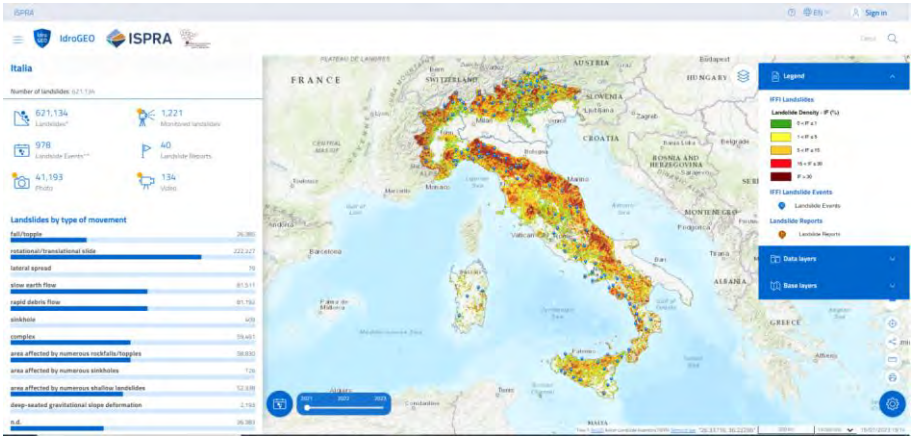

Figure 1. IdroGEO platform - IFFI section: Italian landslide density map and main statistics.

IdroGEO is a tool for communication and dissemination of information to support decisions in risk mitigation policies, land use planning, preliminary design of infrastructures, prioritization of mitigation measures, management of civil protection emergencies, and environmental impact assessment. The main categories of users are decision-makers, land use planners, rail and road companies, professionals, and citizens.

State of the art of monitored landslides in Italy

Although the landslides surveyed in the IFFI number more than 621,000, according to the National Register of Landslide Monitoring Systems, realized by ISPRA, about 1,222 landslides result monitored with in situ systems (Figure 2).
The National Register consists of the following key information: system code, location, managing entity, installation and dismantling dates, states of activity, typology (e.g., knowledge, early warning), acquisition type (e.g., manual, continuous, both), webpage link,

notes, instrumentation, associated landslide ID. At present, the Register contains data from 12 Regions, 2 Autonomous Provinces and from systems managed by ISPRA in 4 further Regions. Moreover, a census by 2 additional Regions is ongoing. Anyway, the Register will have to be completed and integrated especially for central and southern Italy. Overall, active monitoring systems are 487 (56%) while dismantled and under construction systems are 358 (42%) and 17 (2%) respectively. Most of the systems (678; 79%) have a knowledge purpose while 184 systems (21%) are or have been also used as Early Warning Systems (EWS). Data acquisition is performed manually (665), automatically (45) or in both ways (145). From an initial analysis of the recorded data, it can be stated that the most used instruments are inclinometers and piezometers, followed by topographic instrumentation, weather stations, crack meters, strain gauges, terrestrial interferometric radar, etc.

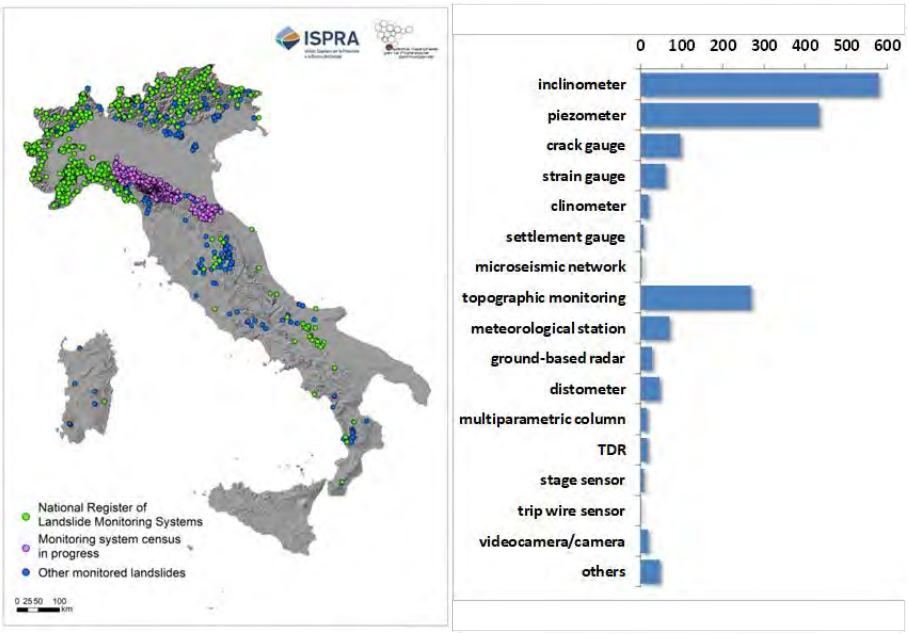

Figure 2. The location of monitoring systems (left) and the type of instrumentation used (right) in the National Register of Landslide Monitoring Systems.

The GeosciencesIR project

In the framework of Geosciences Research Infrastructure funded by Next Generation EU (https://geosciences-ir.it/en/), the IdroGEO web platform will be enhanced with new tools and services to support landslide mapping. An experimental open-source National Database of Landslide in situ Monitoring Systems (NDLMS) and the related User Interface UI will be developed. The platform will guarantee data and interoperable mapping services on landslides, according to FAIR data principles and INSPIRE compliance.

Structure of experimental database of in situ monitoring systems

The NDLMS and the User interface UI will be developed in a experimental way using open-source software and open and integrable technologies and standards in order to ensure extensibility and maintainability over time of all the components. The system will allow archiving of data from instruments with manual acquisition (data loading via User Interface), continuous acquisition (import of data downloaded from data logger) and remote acquisition (transfer protocol to the server).

The database will contain information about sensors, stations, instruments, and in situ monitoring data, such as data of surface geotechnical instrumentation, borehole geotechnical instrumentation, topographic instrumentation, doppler radar, cameras, soil-hydrological and meteorological stations, optical fiber sensors, etc. The database will also contain multimedia attachments (photos, videos, pdf documents). Input data to the NDLMS database will use open exchange formats (e.g., XML, TXT, etc.). The User Interface main functionalities will include, among others:

- search and selection of the monitoring sites;
- query and display of monitoring data;
- compilation of sensor information using ad hoc data entry forms;
- management, analysis, and export of monitoring data.

Conclusion

Considering the data collected to date in the National Register of Landslide Monitoring Systems, some considerations on the current state of monitoring systems in Italy can be made. Although the number of EWS is non-negligible (21%), there are still few monitoring systems having this purpose. Furthermore, continuous automatic data acquisition is still not widespread, and it should be improved to reduce monitoring costs and technician errors. Finally, conventional monitoring tools (inclinometers, piezometers) show significant use.
In the framework of GeoSciencesIR project funded by Next Generation EU and led by ISPRA, the IdroGEO web platform will be enhanced with new tools and services and an experimental open-source National Database of Landslide in situ Monitoring Systems will be developed. The main activities will concern implementation of database structure, minimum information needs, data quality requirements and access policies, following international standards on data and metadata (e.g., INSPIRE), according to FAIR principles.
The main purpose of the database will be to enable stakeholders to know new monitoring approaches and technologies as well as to possibly implement new systems based on well-tested methodologies with consistent data standards. Furthermore, a reliable and high-quality database provided to the scientific communities will represent a valuable resource to develop future data-driven studies for landslide assessment, modelling, monitoring, and prediction.

References

Chae BG, Park HJ, Catani F, Simoni A & Berti M (2017) Landslide prediction, monitoring and early warning: a concise review of state-of-the-art. *Geosci* J 21, 1033–1070. https://doi.org/10.1007/s12303-017-0034-4.

Herrera G, Mateos RM, García-Davalillo JC, Grandjean G, Poyiadji E, Maftei R, et al. (2018) Landslide databases in the Geological Surveys of Europe. *Landslides*, 15(2), 359-379. https://doi.org/10.1007/s10346-017-0902-z.

Trigila A, Iadanza C, Spizzichino D (2010) Quality assessment of the Italian Landslide Inventory using GIS processing. *Landslides*, 7, 4, 455-470. http://dx.doi.org/10.1007/s10346-010-0213-0.

Hürlimann M, Coviello V, Bel C, Guo X, Berti M, Graf C, Hübl J, Miyata S, Smith JB & Yin HY (2019) Debris-flow monitoring and warning: Review and examples. *Earth-Science Reviews*, Volume 199, 102981, ISSN 0012-8252. https://doi.org/10.1016/j.earscirev.2019.102981.

Dei Cas L, Pastore ML, Bonetti D & Ferrarini F (2022) Problems and solutions for the management of a unitary system of landslide monitoring networks: an experience in North Italy. *Italian Journal of Engineering Geology and Environment* (2), 41–57. https://doi.org/10.4408/IJEGE.2022-02.O-04.

Casagli N, Intrieri E, Tofani V, Gigli G & Raspini F (2023) Landslide detection, monitoring and prediction with remote-sensing techniques. *Nat Rev Earth Environ* 4, 51–64. https://doi.org/10.1038/s43017-022-00373-x.

Auflič MJ, Herrera G, Mateos RM et al. (2023) Landslide monitoring techniques in the Geological Surveys of Europe. *Landslides* 20, 951–965. https://doi.org/10.1007/s10346-022-02007-1.

Iadanza C, Trigila A, Starace P, Dragoni A, Roccisano M & Biondo T (2021) IdroGEO: A Collaborative Web Mapping Application Based on REST API Services and Open Data on Landslides and Floods in Italy. *ISPRS International Journal of Geo-Information*. 2021; 10(2):89. https://doi.org/10.3390/ijgi10020089.

Stability analysis of sea-cliffs coupling stress strain and hydrodynamic modelling: preliminary results from Punta Eolo case study (Ventotene, Italy)

F. Feliziani[1], G.M. Marmoni[1], D. Istrati[2], V. Gianni[1], F. Bozzano[1], S. Martino[1]

[1] Sapienza University of Rome, Rome, Italy
[2] National Technical University of Athens, Athens, Greece

Keywords: slope stability analysis, hydrodynamic modelling, computational fluid dynamics, stress-strain-modelling, climate stressors

Summary

This research represents a preliminary attempt to couple hydrodynamic modelling of sea-related actions with stability analysis managed through a limit-equilibrium and stress-strain approaches to account for the action of sea waves on a sea cliff. The quantitative analysis revealed the possibility that instability conditions will be reached for specific rock blocks if the hydrostatic backpressure due to the rock cracks filling is combined with a pseudo-static force, genetically related to the elastic rebound caused by the sea wave slams. This condition is the most recurrent action at studied cliff of Punta Eolo in Ventotene (Italy). Finally, the project of the ongoing installation of a tailor-designed monitoring system is presented. The system will be used to characterize the physical nature of the sea-related preparatory and triggering factors on the cliff, and to examine the deformative response of the cliff itself under the action of periodic thermal and hydrodynamic stressors.

Introduction

Cultural heritage (CH) sites are often located in coastal areas affected by landslide activity (Spizzichino et al., 2013) potentially influenced by the effects of climate (Sesana et al., 2021). An increasing number of researchers has begun to turn their attention to the study of mitigation strategies for CH sites affected by landslides (e.g., Beni et al., 2023). Numerous researches focused on the study of coastal retreat processes (e.g., Alberti et al., 2022), however, limited are quantitative studies focused on the comprehension of the relationships existing between coastal landslide activity and the climate-related factors. In particular, is not yet fully understood the extent to which both preparatory and triggering climate-related factors can contribute to the control of the systems predisposed to host slope instabilities. This is the case of waves and wind, whose action is much studied in coastal engineering applications. In these terms, several well established modelling techniques can now quantify the extent of wave hydrodynamic effect on coastal structures, such as, bridges (Xiang & Istrati, 2021), piers (Hasanpour et al, 2021) and buildings (Hasanpour & Istrati, 2022), but they do not have been yet diffusively applied to natural systems. The Punta Eolo sea-cliff (Ventotene island, Italy) is here analysed since it is frequently affected by rock-falls and topples that are threatening the vulnerable remnants of the roman archaeological site of Villa Giulia. This latter is one of the pilot sites selected in the framework of the H2020 TRIQUETRA European project, aimed to proposing a methodological framework for mitigating climate-related natural hazards affecting cultural heritage.

Study area: the Punta Eolo sea cliff (Ventotene, Italy)

Ventotene is a volcanic island belonging to the Pontine Archipelago located offshore the Tyrrhenian coast between Rome and Naples. This island is of particular interest both for a naturalistic and historical point of view since it belongs to a natural park and because of the presence of several archaeological sites such as the one of the Villa Giulia. By a geological point of view, Ventotene Island, together with the smaller Santo Stefano Island, represent the tip of a large stratovolcano built during the last 800,000 years (Perrotta et al., 1996). The whole island is formed by a tuff plateau slightly dipping towards NE and bounded by active cliffs ranging from 10 to 130 meters of height (Caso et al., 2015). Many landslides struck all the boundaries of the island undermining the conservation of many archeological sites, including the one of Villa Giulia. This latter is located in the northernmost sector of the island (i.e., Punta Eolo promontory), where the youngest volcanic deposits are represented by tuff rocks, namely the Parata Grande Tuff (PGT) (Perrotta et al., 1996).

Engineering-geological model conceptualization and preliminary analysis of climate related factors acting on landslide's control

Direct and remote analyses were carried out to conceptualize the engineering geological model of the Punta Eolo cliff. Firstly, a geomechanical characterization of the PGT was conducted according to the ISRM (2007) standard. A 3D model of the cliff slope was also reconstructed by drone photogrammetry technique. This product provided a useful tool to *i*) extract the orientation of the not-directly detectable joints, and *ii*) measure the isolated rock-block dimensions. N. 60 single-station seismic noise measurements were carried out and were processed according to the Nakamura (1989) method. In this way it was possible to characterize the vibrational nature of the geological layering and to constrain the geological unit contacts. Finally, bathymetric profiles were reconstructed to account for the underwater interaction of sea-waves front approaching the analyzed cliff. The performed conceptualization revealed the predisposition of the Punta Eolo sea cliff to host rock-falls and topples landslide mechanisms according to the Markland (1972) kinematic analysis.
A preliminary analysis of the most efficient climate-related factors which stress the Ventotene Island was conducted to characterize both nature and entity of the preparatory and triggering factors that may contribute to the activation and evolution of the Punta Eolo sea cliff failures. The Ponza Station was selected as reference station since it is the closest to the Ventotene Island. The site is located about 40 km away the Punta Eolo cliff and it is represented by an offshore monitoring buoy belonging to the Italian data buoy network (Bencivenga et al., 2012).

Numerical modelling of sea-waves impact

For the hydrodynamic modelling of this study a mesh-based computational fluid dynamics (CFD) method that had been validated previously for extreme wave impact on coastal structures both in 2D and 3D conditions (Istrati & Buckle 2021) was utilized. In the preliminary analysis phase, three cross-sections (AA', BB', CC') were selected as shown in Figure 1. Moreover, the recorded data from the Ponza Station were analyzed and was found that the wave periods were between 2sec and 11.5sec, and the wave heights between 0.25m up to 6.8m. Using this information and the available bathymetries, high-fidelity two-dimensional models were developed for the selected cross-sections, which solved the Navier-Stokes equations with a Large Eddy Simulation (LES) turbulence model. This type of CFD model can capture the transient wave propagation and the most complex physical phenomena that include the

nonlinear transformation of the waves as they approach the coast and interact with the bathymetry (shoaling process), the reflection phenomenon, the wave breaking process and the wave-cliff interaction. Although the investigation is ongoing and the sensitivity of the results is being analysed, preliminary results are shown in Figure 1. Interestingly, the wave impact process seems to present different trends, with the wave breaking in some cases and causing violent phenomena and slamming, and in other cases just propagating smoothly over the slope of the cliff generating different hydrodynamic effects. This can be observed also in the force histories, which consists of both high impulsive peaks and longer-duration components. It is expected that the ongoing CFD analyses and careful post-processing of the data will help decipher the hydrodynamic effects in relation to the incoming wave conditions and the geometry of the cliff (cross-section).

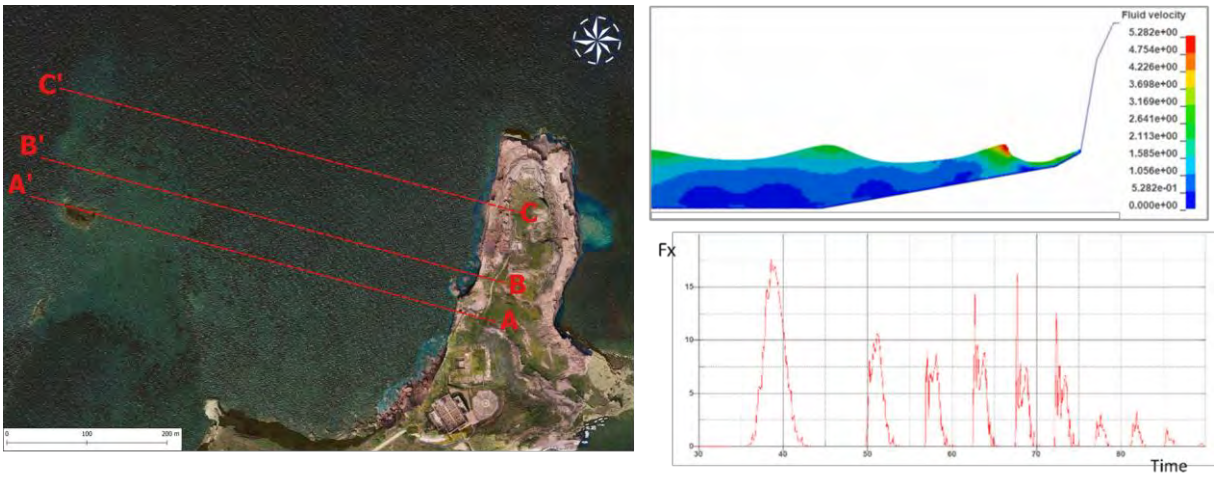

Figure 1 Orthophoto with three selected cross-section (left) and example of results from preliminary CFD models including fluid velocities and horizontal forces on the cliff

Stability analysis of the Ventotene sea cliff

The slope stability conditions of sea cliff at Punta Eolo were evaluated for a rock-toppling mechanism and the slope stability analyses were performed under static and pseudo-static conditions following the methodology proposed by Martino & Mazzanti (2014). Both the seismic action and the static water pressure within the joint sets were analysed; in a second time of analysis, also the sea-wave action was considered as a force responsible for an elastic rebound (*sensu* Hutchinson, 1988). Thanks to the hydrodynamic modelling, it was possible to convert the maximum computed value for the acting force against the cliff related to the sea waves into a pseudo-static coefficient. This latter served as input for the factor of safety (FOS) calculation. A sensitivity analysis was carried out by changing the values of the triggering pseudo-static action, and stability charts were derived by considering a concurrent contribution of different pseudo-static actions (i.e., seismic and hydrostatic) to the FOS evaluation. A Preliminary stress-strain numerical model has been developed reproducing the role of joint interfaces. The performed pseudo-static analysis indicates that the stability conditions can be achieved in most of the detected rock-blocks for realistic triggering scenarios.

Conclusions

The performed pseudo-static analysis indicates that the stability conditions can be achieved in most of the detected rock-blocks for realistic triggering scenarios. The quantitative analysis revealed the possibility that unstable conditions will be reached for specific rock blocks if the

seismic action is combined with a hydrostatic backpressure, as well as in case that hydrostatic backpressure is combined with an elastic rebound caused by the sea wave pushing action. This latter condition is the most likely occurring at Punta Eolo in Ventotene; very high sea wave can in fact impact on the sea cliff as to surmount it, inducing the instantaneously filling of the tension cracks present behind the edge of the cliff. An integrated geophysical and geotechnical monitoring system is going to be designed at the Punta Eolo. The installation will include several sensors that will be used to characterize the physical nature of the sea-related preparatory and triggering factors on the cliff, and to examine the deformative response of the cliff itself under the action of such stressors.

Acknowledgements
This study was carried out within the RETURN Extended Partnership and received funding from the European Union Next-GenerationEU (National Recovery and Resilience Plan – NRRP, Mission 4, Component 2, Investment 1.3 – D.D. 1243 2/8/2022, PE0000005).

References

Spizzichino, D., Cacace, C., Iadanza, C., & Trigila, A. (2013, April). Cultural Heritage exposed to landslide and flood risk in Italy. In EGU General Assembly Conference Abstracts (pp. EGU2013-11081).

Sesana, E., Gagnon, A. S., Ciantelli, C., Cassar, J., & Hughes, J. J. (2021). Climate change impacts on cultural heritage: A literature review. Wiley Interdisciplinary Reviews: Climate Change, 12(4), e710.

Beni, T., Nava, L., Gigli, G., Frodella, W., Catani, F., Casagli, N., ... & Spizzichino, D. (2023). Classification of rock slope cavernous weathering on UAV photogrammetric point clouds: The example of Hegra (UNESCO World Heritage Site, Kingdom of Saudi Arabia). Engineering Geology, 107286.

Alberti, S., Olsen, M. J., Allan, J., & Leshchinsky, B. (2022). Feedback thresholds between coastal retreat and landslide activity. Engineering Geology, 301, 106620.

Xiang, T., & Istrati, D. (2021). Assessment of extreme wave impact on coastal decks with different geometries via the arbitrary Lagrangian-Eulerian method. Journal of Marine Science and Engineering, 9(12), 1342.

Hasanpour, A., Istrati, D., & Buckle, I. (2021). Coupled SPH–FEM modeling of tsunami-borne large debris flow and impact on coastal structures. Journal of Marine Science and Engineering, 9(10), 1068.

Hasanpour A., Istrati, D. (2022): "Extreme Storm Wave Impact on Elevated Coastal Buildings", In Proceedings of the 3rd International Conference on Natural Hazards & Infrastructure, Athens, Greece

Perrotta, A., Scarpati, C., Giacomelli, L., & Capozzi, A. R. (1996). Proximal depositional facies from a caldera-forming eruption: the Parata Grande Tuff at Ventotene Island (Italy). Journal of volcanology and geothermal research, 71(2-4), 207-228.

Caso, I., D'Angelo, R., Palma, B., Parise, M., & Ruocco, A. (2015). Landslide susceptibility maps in the rock slopes of the Ventotene Island (Latium, Italy). In Engineering Geology for Society and Territory-Volume 2: Landslide Processes (pp. 941-945). Springer International Publishing.

ISRM (2007) The complete ISRM suggested methods for rock characterization, testing and monitoring: 1974–2006. In: Ulusay R, Hudson JA (eds) Suggested methods prepared by the commission on testing methods. International Society for Rock Mechanics (ISRM), Kozan Offset, Ankara

Nakamura, Y. (1989). A method for dynamic characteristics estimation of subsurface using microtremor on the ground surface. Railway Technical Research Institute, Quarterly Reports, 30(1).

Markland, J. T. (1972). A useful technique for estimating the stability of rock slopes when the rigid wedge slide type of failure is expected. Interdepartmental Rock Mechanics Project, Imperial College of Science and Technology.

Bencivenga, M., Nardone, G., Ruggiero, F., & Calore, D. (2012). The Italian data buoy network (RON). Adv. Fluid Mech. IX, 74(321), 305.

Istrati, D., Buckle, I.G. (2021): Tsunami Loads on Straight and Skewed Bridges–Part 2: Numerical Investigation and Design Recommendations (No. FHWA-OR-RD-21-13). Oregon. Dept. of Transportation. Research Section, https://rosap.ntl.bts.gov/view/dot/55947

Martino, S., & Mazzanti, P. (2014). Integrating geomechanical surveys and remote sensing for sea cliff slope stability analysis: the Mt. Pucci case study (Italy). Natural Hazards and Earth System Sciences, 14(4), 831-848.

Hutchinson, J. N. (1988). General report: morphological and geotechnical parameters of landslides in relation to geology and hydrogeology. In Proceedings of 5th International Symposium on Landslides, Balkema, Rotterdam, Netherlands, 1988 (pp. 3-35).

Núria M. Pinyol[1,2], Mateu Maglia[1,2], Gaia Di Carluccio[2], Eduardo E. Alonso[1,2]

[1] Universitat Politècnica de Catalunya (UPC), Barcelona, Spain
[2] Centre Internacional de Mètodes Numèrics a l'Enginyeria (CIMNE), Barcelona, Spain

SUMMARY: This paper revisits a well-documented 5 million m^3 landslide identified in 1985 in the East of Spain in a reservoir flank that was induced by a quarry excavation of the toe and later stabilized by transferring mass from upper to lower levels. The landslide is still active and shows an extremely slow motion. The construction of a new pumping station for power generation will change the range and time variation of the reservoir level which will affect the slope stability. This paper first presents a stability back-analysis based on the material point method. The computed displacements induced by the excavation confirm the observed failure. Then, the current stability is evaluated based on in-situ measurements of pore water pressure. Finally, the assessment of the stability, including coupled hydro-mechanical analysis of the pore water pressure, based on finite element method, is carried out to evaluate the future stability.

Keywords: landslide, case history, numerical modelling, material point method

Introduction

A 5 million m^3 landslide was identified in 1985 close to the left abutment of a 116 m high arch-gravity dam in construction at that time. The measured displacement rates alarmed the people in charge of the dam project due to a potential sudden accelerated movement into the reservoir. They had in mind the case of the rapid landslide with catastrophic consequences in Vajont (Italy, 1963). At that time the causes explaining the sudden acceleration were uncertain.
After the geological and geotechnical characterization of the landslide, its stability was analysed, the triggering causes were identified, and stabilization measures were proposed and applied (Alonso et al. 1993). Based on field measurements, the landslide was described as the reactivation of an old translational landslide constituted by broken and pervious limestone strata overlaying a 2 m thick low permeability marl layer, which dips towards the reservoir (Fig. 1). No indications of water levels were found in any of the drilled boreholes. The sliding surface was localized into this clayey layer according to the inclinometer's measurements.

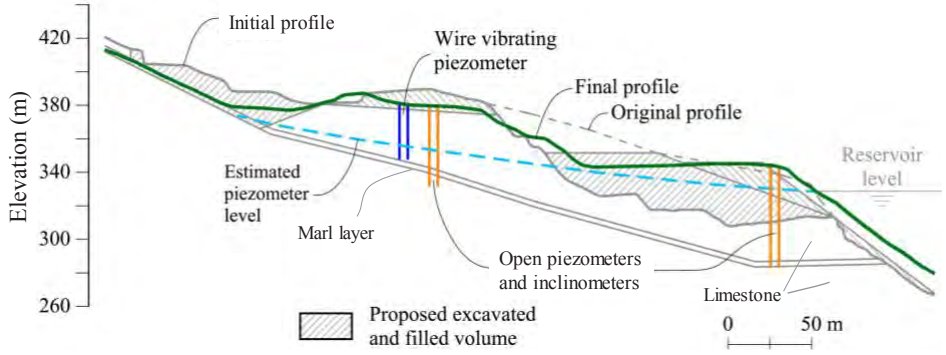

Figure 1. Representative section of the landslide

The quarry excavation of the landslide toe to provide granular aggregates for the concrete of the dam was identified as the triggering cause. Figure 1 shows the slope geometry before and after the quarry excavation. After evaluating several alternatives, the proposed measures to stabilize the slope consisted of excavating the upper part of the landslide and increasing the weight of the lower one. Figure 1 also includes the proposed geometry by Alonso et al. (1992) to stabilize the slope and the final geometry adopted.

The marl material was described as a low-plasticity clay ($w_L = 20 - 28\%$, $w_P = 13 - 14\%$) with high consistency ($w = 10 - 13.6\%$) and low porosity ($\phi = 0.25$). Block samples including the sliding surface were taken from the uncovered failure surface during the excavation works and tested in the direct shear apparatus. The sliding surface was aligned carefully with the middle plan of the shear box. The obtained frictional angle was 17-18º.

The back analysis and predictive stability analysis, after stabilization works, were carried out by Alonso et al. (1993) by means of a conventional limit equilibrium. They also presented a pioneering analysis of the internal distribution of stresses along the failure surface and the effect of loading and unloading sequences in the stabilization process through a finite element analysis with joint elements for the modelling of the failure surface. The stabilization works led to a decrease in the rate of movement, and the landslide was considered stabilized when the displacement rates remained non-relevant after the impoundment of the reservoir, which submerged the landslide toe, and two years of rainfall and reservoir level fluctuations.

The case is recovered in this paper and the landslide response is analysed with more recently developed numerical tools. The excavation process is simulated with a material point method-based analysis carried out with the open-source code Anura3D (Anura3D MPM Research Community, 2022). The accumulated displacement induced by the excavation is evaluated.

Almost 30 years later, the landslide, still instrumented with inclinometers and surface markers, as well as open and vibrating wire piezometers installed in the marl layer, remains active and exhibits an extremely slow motion (a few millimetres per year) (Fig. 2). The stability of the slope is analysed here under the established future variation of the water reservoir level due to the construction of a new pumping station for power generation.

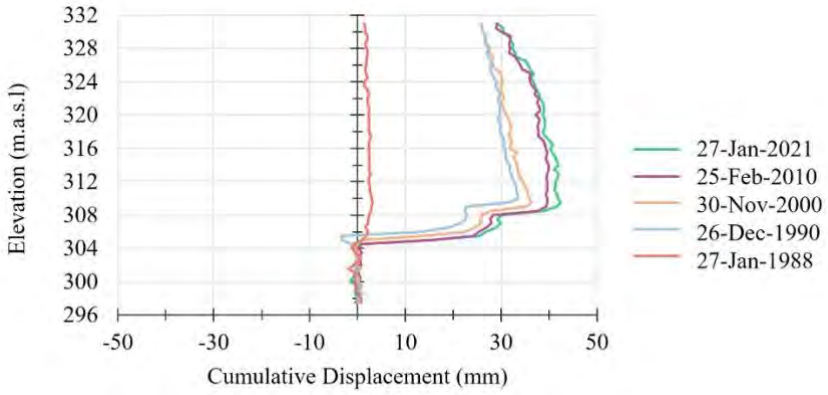

Figure 2. Inclinometer measurements

MPM modelling

The MPM (Sulsky et al., 1994) describes the continuum media with a set of Lagrangian material points that can move into a computational mesh that remains fixed through the calculation and covers the whole domain. A one-phase MPM analysis (Fern et al, 2019) is carried out to simulate the observed failure of the landslide induced by the excavation of part of the bank toe. No groundwater is included in the modelling according to Alonso et al. (1993).

Figure 3 shows the two materials considered and the domain discretization for the selected cross-section. Initially, four material points are defined per filled element.

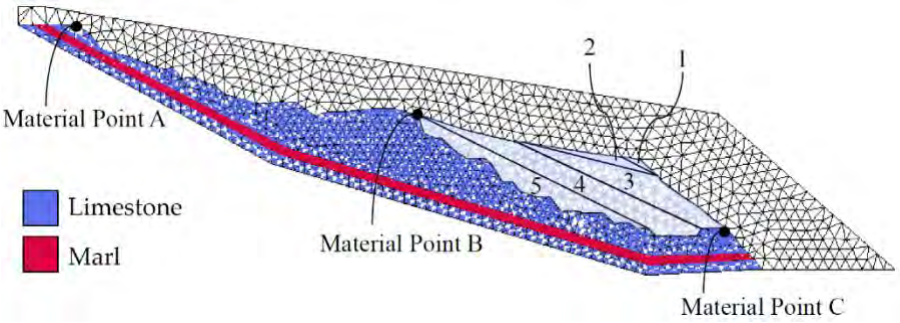

Figure 3. Materials, excavation volumes and computational mesh of 8,264 tetrahedral elements and 16,409 nodes.

The materials were characterized by a Mohr-Coulomb model with a linear elastic regime (Young's Modulus of 1000 and 200 MPa for limestone and marl, respectively, and Poisson's ratio of 0.33 for both). The limestone was defined as a brittle material with a strain-softening Mohr-Coulomb model in which the effective cohesion and effective friction angle drop from a peak to residual values as a function of the deviatoric plastic strain invariant, following an exponential law controlled by a "shape factor" parameter η:

$$c' = c'_r + (c'_p - c'_r)e^{-\eta\varepsilon_d^p}\ ;\ \varphi' = \varphi'_r + (\varphi'_p - \varphi'_r)e^{-\eta\varepsilon_d^p};\text{where}\ \varepsilon_d^p = \sqrt{\frac{2}{3}e_{ij}^p e_{ij}^p} \quad (1)$$

being e_{ij}^p the deviatoric component of the plastic strain tensor. Peak and residual values are indicated by the subindex p and r, respectively. Selected values are: c'_p=100 kPa, c'_r=20 kPa, φ'_p=35º, φ'_r=30º and η=500. Residual strength conditions (φ'_r=17.7º) were assigned to the marl layer.

The excavation of the volumes is simulated by instantaneously removing the material points of the volumes specified at the beginning of the calculation step. The total volume removed was divided into five subvolumes which are excavated subsequently (Fig. 3). Since no pore water pressure is included and the constitutive models are not time-dependent, the duration of the steps is not relevant. However, it is ensured that the slope is at rest before any subsequent excavation.

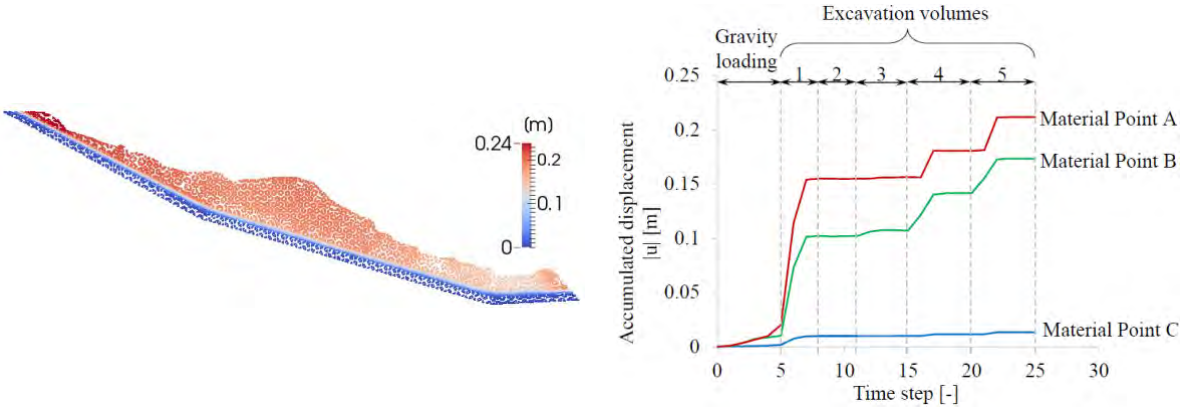

(a) (b)

Figure 4. (a) Total displacements at the end of calculation, after excavation. (b) Displacement versus time step of the three materials points indicated in Figure 3.

The calculation is divided into 7 stages. In the first stage, the initial stress distribution was estimated by a quasi-static stage in which the gravity loading is applied gradually and a local damping of 0.75 is applied. Afterwards, five stages were defined to simulate the excavation of the volumes (1 to 5) (Fig. 3). For these stages, the local damping is assigned equal to a low value of 0.05.

Figure 4 shows the computed displacements. The excavation process induces displacements of around 20 cm at the rock surface of the slope, resulting in a new equilibrium condition. The observed displacements are not homogeneous along the slope. A maximum accumulated displacement of 24 cm is computed in the upper part of the landslide, probably favoured by a local failure of the upper part due to the geometry of the cross-section. The minimum accumulated displacement calculated is located in the more stable portion of the slope's toe due to the shape of the marl layer. At each excavation stage, the accumulated displacement increases abruptly, and the motion is interrupted rapidly after a few centimetres once a new equilibrium is reached because of the evolution of geometry.

Analysis of actual state and future activities

The current stability of the landslide is evaluated taking into account the piezometric level estimated from operating open and wire vibrating piezometers (Fig. 1). The safety factor calculated is very close to 1, a fact that can explain the slow motion observed. The future stability is predicted by taking into account the pore water pressure distribution obtained from a numerical calculation carried out with the finite element method-based Code_Bright (Olivella et al., 2022) following the hydro-mechanical procedure presented in Pinyol et al. (2012). The evolution of the effective stress along the lower part of the sliding surface (Fig. 5) can be correlated with the variation of the safety factor. It is concluded that the slope will remain in very poor stability conditions with safety factors close to 1.

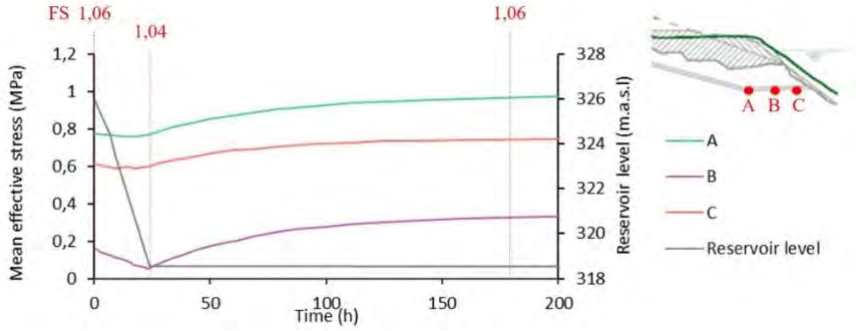

Figure 5. Effective stress in the three points plotted, reservoir level and the corresponding safety factor.

Conclusions

The stability of a well-documented landslide was reviewed by an MPM-based calculation procedure. The landslide reactivation may result in significant accumulated displacements but not in a catastrophic acceleration: the landslide moved downward in response to the excavation but it reached a new stable configuration at the expense of severe straining in the sliding surface and the rock cover. Analysing future stability requires the proper estimation of pore water pressure distribution induced by the established variation of the reservoir level.

References

Alonso EE, Gens A & Lloret A (1993). The landslide of Cortes de Pallas, Spain. *Géotechnique* 43(4), 507–521.

Anura3D MPM Research Community (2022) *Anura3D Version 2022 Source Code*. See http://www.anura3d.com

Fern EJ, Rohe A, Soga K, Alonso EE. (2019) *The Material Point Method for Geotechnical Engineering: A Practical Guide*. Editors, 271-286. CRC Press, 2019

Olivella S, Vaunat J & Rodríguez-Dono A. (2022). Code_Bright User's Guide. Version 9.

Pinyol NM, Alonso, EE, Corominas J & Moya J. (2012). Canelles landslide: modelling rapid drawdown and fast potential sliding. *Landslides* 9(1), 33–51.

Sulsky D, Chen Z & Schreyer HL (1994) A particle method for history-dependent materials. *Computer Methods in Applied Mechanics and Engineering*, 118(1–2), pp. 179–196.

Numerical modelling of a rainfall-induced landslide using hypoplastic model

Xuan Kang[1], Wei Wu[1], Shun Wang[2]

[1] Institute of Geotechnical Engineering, University of Natural Resources and Life Sciences, Vienna, Austria
[2] State Key Laboratory of Water Resources and Hydropower Engineering Science, Wuhan University, Wuhan, China

SUMMARY: This paper presents a numerical study on a rainfall-induced bedding landslide. The numerical simulation is carried out by adopting a novel hypoplastic model for overconsolidated clays. A catastrophic failure in the Three Gorges Reservoir area is chosen for the case study. In the numerical simulation, the deformation progress of basal shear zone within bedding landslide induced by intensive rainfall scenarios is reproduced. The simulation result is compared with the field observation to verify the reliability of the hypoplastic constitutive model.

Keywords: landslide initiation, FEM simulation, hypoplastic model, basal shear failure, rainfall-induced landslide

Introduction

Numerical simulation has been a useful tool for predicting the deformation of landslides. Some prevail approaches, such as finite element method (FEM), are widely adopted for analyzing the pre-failure deformation of landslides. FEM is widely implemented in many commercial software and further advanced for describing characteristics of geomaterials. These features make FEM technique suitable for analyzing landslide failure, especially reproducing the deformation progress under hydrological scenarios. Hypoplasticity is a prevailing constitutive theory and has gained a wide popularity in numerical computation in recent years (Wu et al., 2017; Wang et al., 2018). It employs tensor formula to represent the stress-strain relationship of materials, and has been enhanced for many versions for different types of soils. Additionally, it shows an outstanding performance in predicting the mechanical behaviour of overconsolidated clays, which is especially suitable for reproducing the failure of the shear-zone soils. These works already showed that the hypoplastic model is successfully implemented in the simulations of landslide materials and landslide failures.

In this work, the numerical investigation of a rainfall-induced landslide is carried out to uncover the deformation characteristics of the basal shear failure. The Shanshucao landslide featuring with an exposed basal shear zone after failure is selected as a case for the numerical study (Kang et al., 2022). A novel hypoplastic model proposed by Wang and Wu (2021a; 2021b) for overconsolidated (OC) clays is introduced and employed in the numerical simulations. Intensive rainfall scenarios and different boundary conditions are considered by referring to the real situation of landslide collapse. The simulation results are compared with field observations to verify the reliability of the constitutive model in simulating landslide materials.

Hypoplastic model for overconsolidated soils

The hypoplastic constitutive model manifests its superiority in describing nonlinear behaviours of soils. In 2021, the historic stress state is taken into account in the simple hypoplastic model

(Wang and Wu, 2021a; Wang and Wu, 2021b). The framework of the simple hypoplastic model is shown as follows:

$$\overset{\circ}{\sigma} = f_s[(\mathrm{tr}\,\breve{\sigma})\dot{\varepsilon} + f_v(\mathrm{tr}\,\dot{\varepsilon})\breve{\sigma} + a^2\frac{(\mathrm{tr}\,\breve{\sigma}\dot{\varepsilon})}{\mathrm{tr}\,\breve{\sigma}}\breve{\sigma} + a(\hat{\sigma} + \hat{\sigma}^*)\|\dot{\varepsilon}\|] \tag{1}$$

where $\overset{\circ}{\sigma}$ is the Jaumann stress rate tensor; $\dot{\varepsilon}$ is the Cauchy stress tensor; $\|\dot{\varepsilon}\|$ is the strain rate tensor. $\|\dot{\varepsilon}\|$ stands for the Euclidean norm of the stretching tensor. σ is the Cauchy stress rate tensor, whereas $\breve{\sigma} = \sigma + \mathrm{S}$ and $\hat{\sigma} = \sigma - \mathrm{S}$ are used to account for the history dependence with structure tensor S. The structure tensor is written as:

$$\mathrm{S} = \alpha\ln(\frac{1}{R})\sigma \tag{2}$$

in which α is a model parameter and R is the stress ratio representing the overconsolidation, which is defined as:

$$R = \frac{p_e^+}{p_e} \tag{3}$$

where p_e^+ and p_e are the preconsolidation pressure in the modified Cam Clay (MCC) model and the Hvorslev equivalent pressure, respectively. The stiffness factor f_s and the multiplier f_v are defined as:

$$f_s = -\frac{2}{3v_i\lambda^*}, f_v = \frac{3}{2}v_i - \frac{1}{3}(3 + a^2 - \sqrt{3}a) \tag{4}$$

where v_i is a modulus ratio and a is a material constant.

This simple model is capable of reflecting the history dependence of soil with only five parameters. Compared with the conventional models, this advanced hypoplastic constitutive model for OC clays possesses simpler formulations and better performance in modelling geomaterials. The details of the numerical implementation can be referred to Wang et al. 2018.

Numerical simulations of landslide initiation

The Shanshucao landslide was located in Zigui County, near the Three Gorges Dam in China (Figure 1). The landslide occurred on 2 September 2014 due to persistent rainfall and abrupt uprising of the water level of the Luogudong River, a tributary of the Yangtze River. The collapse of the landslide destroying all the infrastructure along the runway, including a hydropower station, a residential building and the G384 national road, as well as the agricultural land. Fortunately, no fatalities were caused owing to the successful emergency response.

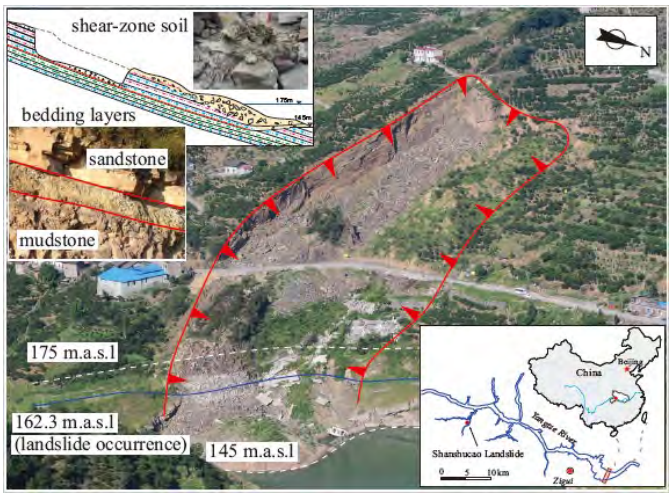

Figure 1. The characteristics of the Shanshucao landslide

In this simulation work, some simplifications are adopted to focus mainly on the failure initiation of the landslide. The entire landslide body without predefined shear surface is set to investigate how the basal shear zone develop within the slope. Moreover, the same material parameters are assigned to both the sliding mass and the shear-zone soil. The numerical model of the landslide is discretised using quadratic quadrangle elements with eight nodes. According to the numerical results of triaxial data and back analysis, the material parameters used for the numerical simulation are given in Table 1. Since there is no preset for elastic deformation, elastic parameters such as Young's modulus and Poisson's ratio are not considered in this simulation. According to the in-situ investigations in the nearby area, the permeability coefficient of the sliding mass is chosen as 2.7×10^{-5} m/s.

Table 1. Material parameters in FEM simulation

Mechanical parameters	γ	e_0	ϕ_c	λ^*	N	r_i	α
Landslide mass	20	0.6	18.1	0.016	0.54	1.3	0.1

γ: natural density (kN/m^3); e_0: initial void ratio; ϕ_c: critical friction angle (°); λ^*: compression index; N: specific volume; r_i: modulus ratio; α: OCR parameter

In the numerical model, both horizontal and vertical displacement is restrained at the bottom of the model. For the seepage condition, only a static reservoir water level of 163 m.a.s.l at the toe of the landslide is considered, which is the water level on the day of landslide failure. Based on the hydro-mechanical analysis, a continuous rainfall condition is adopted to facilitate the landslide initiation. According to the meteorological data, the magnitude of rainfall on the landslide day was 96.5 mm. Therefore, a rainfall intensity of 10 mm/h is adopted in the numerical simulation. Different boundary conditions are considered for simulating landslide initiation, as presented below.

As rainfall continues, water infiltration gives rise to a negative effect on landslide stability. As shown in Figure 2(a), local shear failure at the lower part of the landslide gradually forms. The shear strain distributions of numerical results show there is no obvious strain before 3-hour rainfall infiltration, then the shear strain generated quickly within one hour. At 3.5h, a local shear zone is found at the lower part of the landslide near the national highway G348. The multiple shear zones are formed after 4 hours of rainfall infiltration. It seems that the shear zones are more trend to generate at the thinnest part of the landslide body. At this time, the numerical iterations stop, which implies the initiation of the landslide failure caused by large strain at the shear zones.

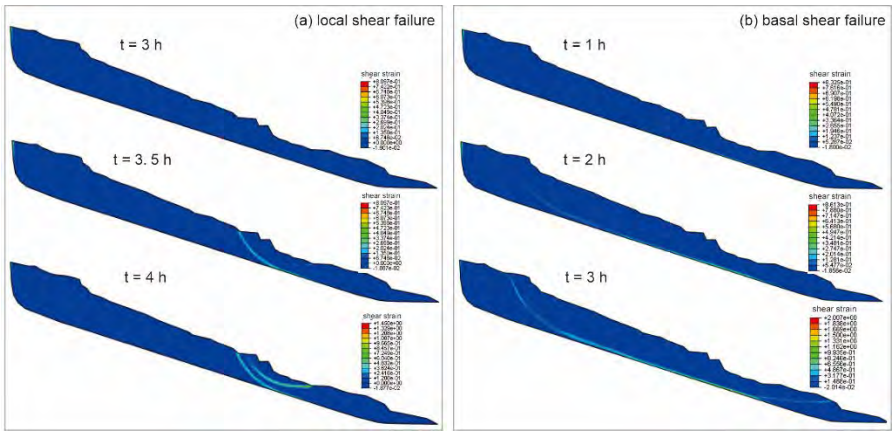

Figure 2. Numerical results: shear strain distribution with (a) local shear failure and (b) basal shear failure

For mimicking the rainfall infiltration within the uppermost crack of the Shanshucao landslide, a zero pore pressure zone is set at the upper part of the landslide model. As shown in Figure 2(b), after 1-hour rainfall infiltration, only slight shear strain is found at the bottom of the landslide body, namely the interface between landslide material and the bedrock. At 2 hours, the shear strain gradually extends to the backside of the crack. After 2.5h, a continuous shear strain develops from the upper part to the lower part of the landslide and clearly forms along the bedding-plane layer. At the lower part of the landslide, the shear zone extends to the location below the small hydropower station and is close to the reservoir water level.

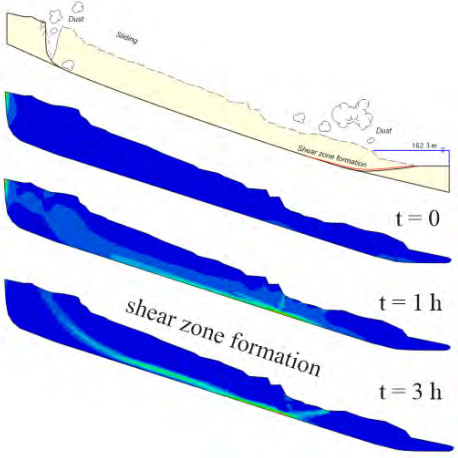

Figure 3. Numerical results compared with the geological profile of the Shanshucao landslide during initiation process

This result agrees well with the real situation of landslide failure that the unstable evidence of landslide activity is first observed near the road of the upper part, then the lower part of the landslide shows deformation signs. The key characteristic of the landslide is the bedding-plane shear zone along the intact bedrock, which is also predicted by the numerical simulation.

References

Kang X, Wang S, Wu W & Xu G (2022) Residual state rate effects of shear-zone soil regulating slow-to-fast transition of catastrophic landslides. *Engineering Geology* 304, p.106692.

Wang S, Wu W, Peng C, He X and Cui D (2018) Numerical integration and FE implementation of a hypoplastic constitutive model. *Acta Geotechnica*, 13, pp.1265-1281.

Wang S and Wu W (2021) A simple hypoplastic model for overconsolidated clays. *Acta Geotechnica* 16(1), pp.21-29.

Wang S. and Wu W (2021b) Validation of a simple hypoplastic constitutive model for overconsolidated clays. *Acta Geotechnica* 16, pp.31-41.
Wu W, Lin J. and Wang X (2017) A basic hypoplastic constitutive model for sand. *Acta Geotechnica* 12, pp.1373-1382.

Basal Layer of Granular Flow Down Smooth and Rough Inclines

Teng Wang[1, 2], Fiona Kwok[1], Lu Jing[2], Yuri Dumaresq Sobral[3]

[1] Department of Civil Engineering, The University of Hong Kong, Hong Kong, China
[2] Institute for Ocean Engineering, Shenzhen International Graduate School, Tsinghua University, Shenzhen, China
[3] Departamento de Matemática, Universidade de Brasília, Campus Universitário Darcy Ribeiro, DF, Brazil

Abstract

When granular materials flow down an incline, a thin layer near the base can occur if the base roughness is insufficient, leading to significant basal slip and strong agitation. In the present study, a series of discrete element method (DEM) simulations are carried out to systematically investigate the key factors (related to the nature of the base and various flow conditions) on the kinematic features of the basal layer. Two categories of bases are considered – flat frictional planes with varied friction coefficient and bumpy bases consisting of a layer of fixed particles with controlled size and spacing. The roughness of the former is controlled by the friction coefficient, whereas that of the latter is characterized by a dimensionless roughness parameter R_a. For $R_a \lesssim 0.55$, slip occurs and the basal velocity profile deviates from standard Bagnold's scaling. The velocity profile can be described by a semi-empirical function considering the granular temperature distribution in the basal layer. Results show an intriguing phenomenon that the presence and thickness of the basal layer is mainly controlled by the base roughness, but not the flow thickness or slope angle. Further investigation of the basal-layer kinematics can improve our understanding of the hyper-mobility of granular flows in geohazard assessment.

Keywords: velocity profile, granular temperature, base roughness, granular flow

Introduction

Gravity driven granular flow down inclines is frequently encountered in industry and fields, such as rock avalanches and long-runout landslides. Predicting the kinematics of the flowing mass is essential for geophysical flows as it is commonly employed to estimate the collisional stress on the protective structures (Song et al. 2018). In literature, extensive studies have been conducted to give empirical and analytical solutions with respect to velocity and shear rate, among which a solid work namely the three-halves velocity estimation was proposed by Bagnold (1954). However, this solution only suits the results for dense granular flows with packing density uniformly distributed throughout the height, which is not realistic in nature when the substrate is insufficiently rough. In addition, previous studies demonstrate that the slip velocity is significant at smooth to intermediate rough bases. An inverse packing (i.e., grain dilation) is typically observed for such boundary condition both physically and numerically (MiDi 2004, Delannay et al. 2007). All these evidences emphasize the crucial role that base roughness plays on characterizing the rich behaviour of granular assembly down inclines.

Besides the base roughness, the flow behaviour is remarkably influenced by the base morphology. As suggested by Delannay et al. (2007), the substrates are classified into three categories – flat frictional plane; rigid bumpy base; and the erodible substrate. In general, the flat frictional plane is created by imposing a constant friction coefficient μ along the chute,

whereas the bumpy base is formed by fixing a layer of grains or columns at the bottom. The latter introduces additional resistance to the overlying flow, which is termed as geometric roughness. Unlike the two aforementioned cases, the erodible scenario is commonly modeled by placing a layer of erodible material along the chute or in a rotating cylinder, or studied through the motion of a thick pile with wall effect considered (Zhang et al. 2019, Taberlet et al. 2003, Orpe and Khakhar 2007). For simplicity, here only the flat and bumpy bases are considered. Following Jing et al. (2016) pilot work, the degree of geometric roughness is quantified through a dimensionless indicator R_a, which involves the two parameters – grain size ratio (λ) and base particle spacing (ε) (Fig. 1). With appropriate combinations, a full range of R_a=0~1 is reached to simulate the base roughness condition from geometric smooth to sufficient rough.

In addition to the base condition, the flow kinematics are influenced by the geometry features comprising flow height (H) and slope angle (θ). For instance, a linear velocity profile is observed when a thin layer of granular media flowing down gentle slopes (MiDi 2004). However, enlarge the pile height and slightly increase the tilt angle will convex the profile, which is precisely described by the proportional scaling of $v \propto h^{3/2}$ (Pouliquen 1999). Further increase the chute inclination results in the presence of a unique basal layer with remarkable sliding. Ultimately, a plug flow of constant core velocity will be reached when the chute becomes vertical (MiDi 2004). All these numerical and experimental work highlights the crucial role that geometry plays on kinematics. Based on the experimental results associating H and θ, a phase diagram differentiating the no flow, steady fully developed (SFD) flow and unsteady flow regimes are given by Pouliquen (1999). For our numerical configurations, similar approach is adopted and appropriate combinations of H and θ are selected to ensure all the simulations can ultimately reach the steady state.

Though understanding of the base roughness, flow height and slope angle on basal layer thickness and velocity enhancement are fundamentally developed, a comprehensive study that quantitatively demonstrates such effects still remain deficit. Additionally, there is a lack of kinematics model that accurately and precisely describes the velocity distribution at basal layer in the presence of slip. In light of this, numerical simulations modelling steady state granular flows are carried out with systematically changed flow thickness (H/d_p=20~60, where d_p=5 mm is the mean particle diameter), slope angle (θ=23~27º) and geometric base roughness (R_a=0~1). Periodic boundaries are imposed in both longitudinal and transversal directions. The top surface is free of constraint whereas a particle fixed base is generated at the bottom. Hertzian contact model is adopted to simulate the particle interactions, with damping and restitution coefficient consistently specified. Other parameters such as particle density, Young's modulus and Poisson's ratio are constants, respectively given as 2,650 kg/m^3, 5×10^7 Pa and 0.5. After obtaining the discretized data at grain level, continuum kinematic properties with respect to velocity, shear rate and granular temperature are captured through binning strategy. All the simulations are conducted at least twice with changed seed number to ensure repeatability.

Summary

This study underscores the presence of slip velocity and the associated basal layer for granular materials propagating on insufficiently rough bases. The basal layer thickness is morphologically determined as the distance between the velocity separation to the ground surface (Fig. 1). Within the basal layer, the particles are strongly agitated due to rapid shear. Low packing density but high granular temperature (velocity fluctuations) is consistently observed. Numerical simulation results show that the base roughness is the dominant factor

controlling the basal layer thickness and velocity magnitude (Fig. 2). Increasing the base roughness will hinder the slipping behavior at the base, with a critical value of $R_a \approx 0.55$ distinguishing slip and no-slip regimes. By contrast, both flow height and slope angle are less pronounced with marginal influence on basal layer thickness. In addition, based on the strong association between the shear rate and granular temperature, a semi-empirical velocity reconstruction approach is proposed, which show good promises in generalizing Bagnold's scaling to incorporate smooth boundary effects.

Figures

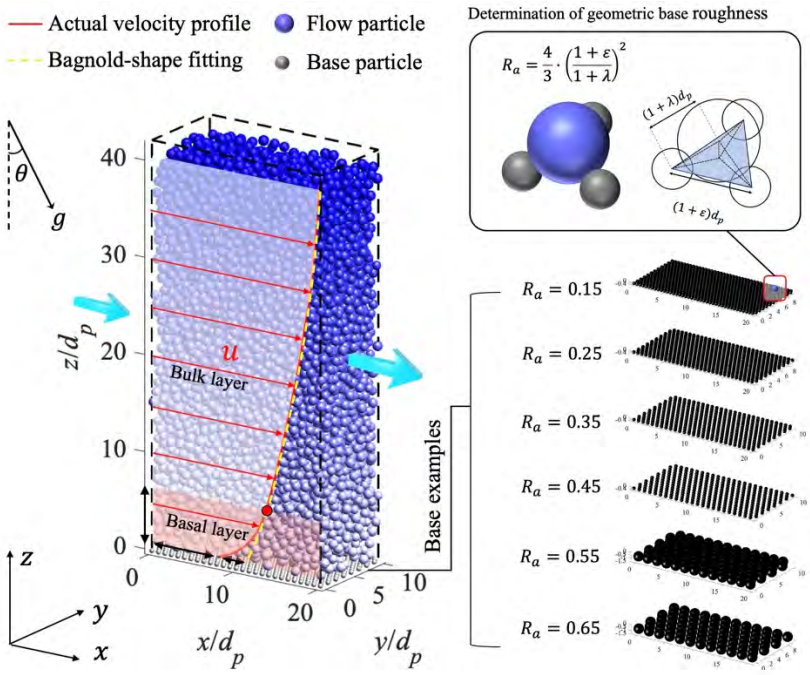

Figure 1. Snapshot of periodic granular flow down a relatively smooth base and determination of geometric base roughness (Note: u is the flow velocity, d_p is the mean particle diameter, λ is the flow-bed particle size ratio and ε is the bed particle spacing. The snapshot is captured from the case: H/d_p=40; θ=28°; R_a=0.35)

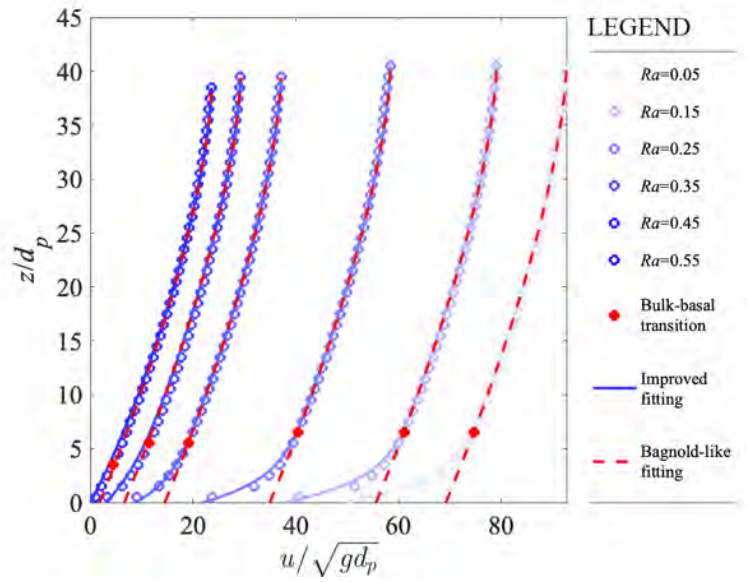

Figure 2. Comparison between slip and no-slip simulations with respect to the normalized velocity profile (Note: the degree of base roughness is indicated by the brightness of the symbols; the open circles denote the DEM

data; the red dash lines refer to the Bagnold-like fitting and the solid lines represent the improved fitting curve given by the proposed method)

References

Bagnold, R. A. (1954) 'Experiments on a Gravity-Free Dispersion of Large Solid Spheres in a Newtonian Fluid under Shear', *Proceedings of the Royal Society of London. Series A, Mathematical and Physical Sciences,* 225(1160), 49-63.

Delannay, R., Louge, M., Richard, P., Taberlet, N. and Valance, A. (2007) 'Towards a theoretical picture of dense granular flows down inclines', *Nature Materials,* 6(2), 99-108.

Jing, L., Kwok, C. Y., Leung, Y. F. and Sobral, Y. D. (2016) 'Characterization of base roughness for granular chute flows', *Phys Rev E,* 94(5-1), 052901.

Mangeney, A., Roche, O., Hungr, O., Mangold, N., Faccanoni, G. and Lucas, A. (2010) 'Erosion and mobility in granular collapse over sloping beds', *Journal of Geophysical Research,* 115(F3), n/a.

MiDi, G. D. R. (2004) 'On dense granular flows', *The European Physical Journal E,* 14(4), 341-365.

Orpe, A. V. and Khakhar, D. V. (2007) 'Rheology of surface granular flows', *Journal of Fluid Mechanics,* 571, 1-32.

Pouliquen, O. (1999) 'Scaling laws in granular flows down rough inclined planes', *Physics of Fluids,* 11(3), 542-548.

Silbert, L. E., Ertas, D., Grest, G. S., Halsey, T. C., Levine, D. and Plimpton, S. J. (2001) 'Granular flow down an inclined plane: Bagnold scaling and rheology', *Physical review. E, Statistical, nonlinear, and soft matter physics,* 64(5), 051302-051302.

Song, D., Choi, C. E., Ng, C. W. W. and Zhou, G. G. D. (2018) 'Geophysical flows impacting a flexible barrier: effects of solid-fluid interaction', *Landslides,* 15(1), 99-110.

Taberlet, N., Richard, P., Valance, A., Losert, W., Pasini, J. M., Jenkins, J. T. and Delannay, R. (2003) 'Superstable granular heap in a thin channel', *Phys Rev Lett,* 91(26 Pt 1), 264301.

Zhang, S., Yang, G., Lin, P., Chen, L. and Yang, L. (2019) 'Inclined granular flow in a narrow chute', *The European Physical Journal E,* 42(4), 40.

A novel hybrid method for modeling landslide dam overtopping failure

Zhengyang Su[1,2,3], Shun Wang[1], Wei Wu[2], Dianqing Li[1]

[1] State Key Laboratory of Water Resources Engineering and Management, Wuhan University, Wuhan, China
[2] University of Natural Resources and Life Science, Institute of Geotechnical Engineering, Vienna, Austria
[3] Nanjing Hydraulic Research Institute, Nanjing, China

SUMMARY: The overtopping failure of landslide dams is a complex process that involves strong soil-water coupling and structural failure. The aim of this study is to establish an SPH-DEM dam-break model that considers the combined effect of seepage and overflow. The key feature of the proposed high-fidelity dam-break model is that both solid and fluid phases are solved simultaneously in two different sets of Lagrangian particles using their own governing equations. In the numerical framework, the water phase is modeled as weakly-compressible Newtonian fluid using the SPH method, and the soil phase is modeled using the DEM method. The high-fidelity dam-break model is validated by two benchmarks. Furthermore, the high-fidelity dam-break model is able to reveal the failure mode of landslide dams and simulate many other soil-water coupling processes, such as reservoir water infiltration, dam slope erosion and collapse and breach development.
Keywords: landslide dam, overtopping modeling, SPH-DEM, soil-water coupling

1 Introduction

Overtopping failure of landslide dams is a complex process that involves strong interactions between soil and water. Currently, most of our knowledge on landslide dams overtopping failure comes from dam failure model tests. These dam break tests have improved our understanding of the failure mechanism and provided data for calibrating and validating dam failure models [1]. But those model tests involve considerable technical complexity and high cost. Mathematical models can be divided into empirical models and physically-based models [2,3]. Empirical models are based on historical dam break data but cannot consider the dam failure mechanism [4]. The physically based models can be further divided into simplified and detailed physically based models. Simplified physically based models, such as BRDAM, DAMBRK, BREACH, DB-IWHR models and others, only consider necessary physical process of dam breach. While the aforementioned models show well performance in predicting dam overtopping process with high computational efficiency, none of them can reflect the coupling effect of water and soil, nor predict the hydrodynamic process of dam breaching. Alternatively, detailed physically based models based on different numerical methods, such as particle-based method, grid-based method, or hybrid method, are suitable for simulating dam failure [5]. In recent years, particle-based methods, such as discrete element method (DEM), material point method (MPM), and smoothed particle hydrodynamics (SPH) method, have been widely adopted to simulate free-surface flows with large deformation. Among them, SPH method has gained much popularities to address fluid-solid coupling problems owing to its meshless and Lagrangian nature [6]. However, further investigation is still needed to refine the modeling of the dam breach process, considering the joint influence of external overflow and internal seepage, as well as the dynamic evolution of the dam section and flow erosion.

This work presents an SPH-DEM dam-break model that considers the combined effect of seepage and overflow in

the overtopping process of landslide dams. The proposed model is validated by simulating two benchmarks, including seepage through a landslide dam and a small-scale dam-break test. To gain a better understanding of the dam-break process, some typical physical processes, such as transient infiltration, overflow erosion, breach evolution and collapse of the breach slope, are characterized through our numerical simulations.

2 Methodology

2.1 SPH-DEM coupling framework

The dam-break process involves strong coupling of water and soil particles. Figure. 1 shows the coupling mechanism for each force. For the water-soil coupling forces, only the seepage force, buoyancy and adhesion, are considered in the proposed framework. The capillary force generated by the meniscus between two soil particles is calculated in the DEM framework.

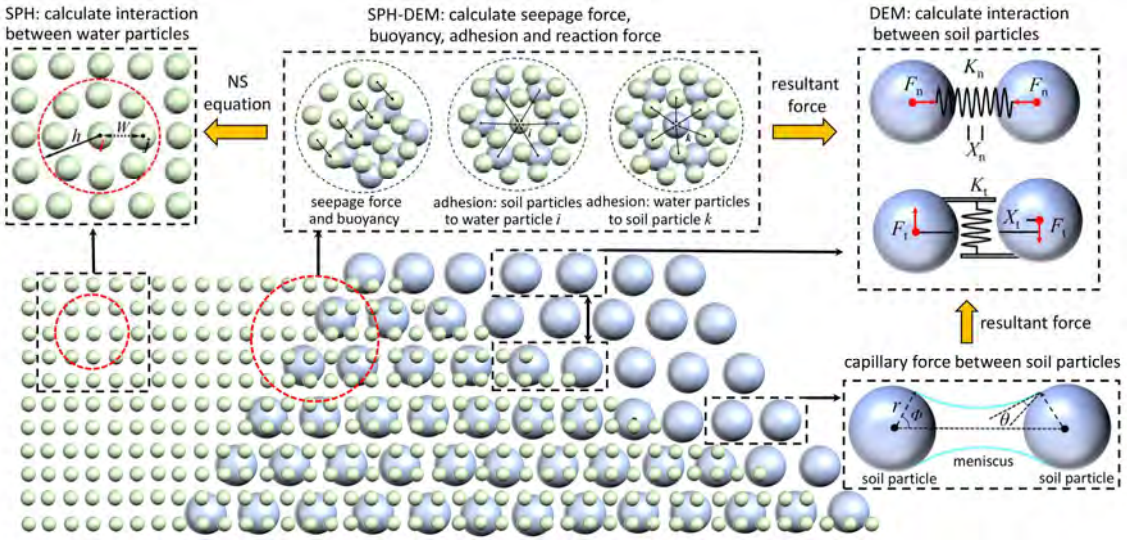

Figure. 1 Schematic diagram of the calculation of each force in the SPH-DEM framework

2.2 SPH fundamentals for water phase

For the water phase, the continuity equation can be written as:

$$\frac{d\bar{\rho}_i}{dt} = \sum_j m_j \left(\boldsymbol{v}_i - \boldsymbol{v}_j\right)\frac{\partial W_{ij}}{\partial \boldsymbol{x}_i} - 2\delta h c_0 \sum_j \left(\bar{\rho}_j - \bar{\rho}_i\right)\times\left(\boldsymbol{x}_i - \boldsymbol{x}_j\right)\frac{\partial W_{ij}}{\partial \boldsymbol{x}_i}\frac{1}{\boldsymbol{x}_{ij}^2}\frac{m_j}{\bar{\rho}_j} \quad (1)$$

The momentum equation in the SPH form is given by:

$$\frac{d\boldsymbol{v}_i^{\beta}}{dt} = -\sum_j m_j\left(\frac{p_i}{\bar{\rho}_i^2} + \frac{p_j}{\bar{\rho}_j^2} + \Pi_{ij}\right)\frac{\partial W_{ij}}{\partial \boldsymbol{x}_i} + \frac{\left(\boldsymbol{F}_{s\to w,i}^{drag} + \boldsymbol{F}_{s\to w,i}^{buoy} + \boldsymbol{F}_{s\to w,i}^{adhe}\right)}{m_i} + \boldsymbol{g} \quad (2)$$

where $\boldsymbol{v}$ is the velocity; ρ is the density; p is the pressure; Π_{ij} is the artificial viscous term; W is the kernel function; $\boldsymbol{x}_i$ and $\boldsymbol{x}_j$ denote the position vector of water particle i and j, respectively. δ is the diffusive coefficient; c_0 is the speed of sound at the reference density; subscript w and s denote the water and the soil, respectively. $\boldsymbol{F}_{s\to w,i}^{drag}$, $\boldsymbol{F}_{s\to w,i}^{buoy}$, $\boldsymbol{F}_{s\to w,i}^{adhe}$ are the drag force, buoyancy and adhesion exerted on the water particle i by the surrounding soil particles, respectively.

2.3 DEM fundamentals for soil phase

In the DEM framework, each particle k is regarded as a rigid body with position x_k and radius. The motion of soil particles is solved by Newtons second law. The translational and rotational equations of a single soil particle k are as follows:

$$m_k\frac{d\boldsymbol{v}_k}{dt} + \alpha m_k \boldsymbol{v}_k = \sum \boldsymbol{F}_k^{cont} + \boldsymbol{F}_{w\to s,k}^{drag} + \boldsymbol{F}_{w\to s,k}^{buoy} + \boldsymbol{F}_k^{capi} + \boldsymbol{F}_{w\to s,k}^{adhe} + m_k\boldsymbol{g} \quad (3)$$

$$I_k \frac{d\boldsymbol{\omega}_k}{dt} + \alpha I_k \boldsymbol{\omega}_k = \sum \boldsymbol{M}_k \qquad (4)$$

where α is the damping coefficient; $\boldsymbol{F}_k^{cont}$ is the contact force exerted by surrounding particles or boundaries; $\boldsymbol{F}_{w\to s,k}^{drag}$ and $\boldsymbol{F}_{w\to s,k}^{buoy}$ are the drag force and buoyancy exerted on the soil particle by the surrounding water particles, respectively; $\boldsymbol{F}_k^{capi}$ and $\boldsymbol{F}_{w\to s,k}^{adhe}$ are the capillary force and adhesion affected by the soil saturation degree; I is the moment of inertia; $\boldsymbol{\omega}_k$ is the solid particles rotational velocity and $\boldsymbol{M}$ is the torque of contact force.

3 Model validation

3.1 Seepage through porous media

More details about the dam model can be found in the literature [7]. Figure. 2 shows that the phreatic line of the dam obtained from the SPH-DEM simulation agrees well with FEM simulation.

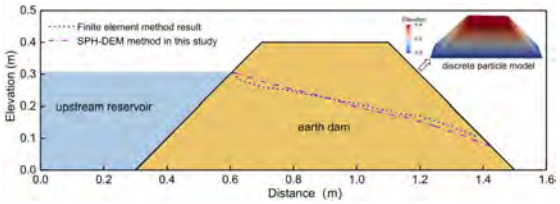

Figure. 2 Comparison of the phreatic line when the water level is static

In addition, the proposed SPH-DEM model also has good performance in calculating transient seepage process. Figure. 3 presents the comparison of transient evolution of phreatic line and saturation zone with FEM results when the upstream water level rises. And the calculation results of the phreatic line in Figure. 3 are in good agreement with the FEM results, indicating that the proposed model can reasonably capture the transient change of the dam's seepage field.

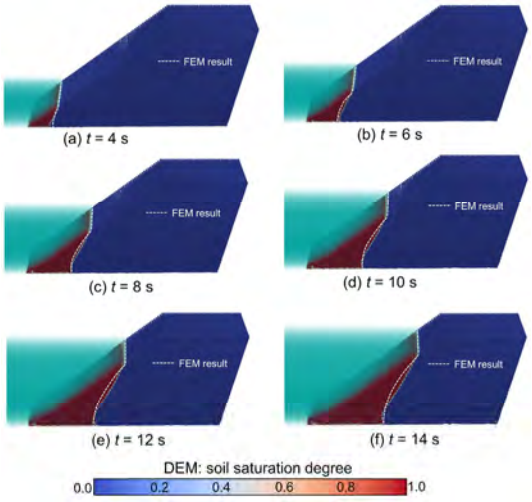

Figure. 3 Comparison of phreatic line and saturation zone with FEM results when the upstream water level rises

3.2 Simulation of a dam break flume test

The focus of the experiment is the progressive failure mechanism and the overtopping discharge of landslide dams. The experiment was carried out in a flume installation with a length of 8 m, a width of 0.2 m, and a depth of 0.3 m. Dam construction materials included dry sand with the median diameter of soil particles being 2 mm. Figure. 4 depicts the layout of the experiment and discrete particle model of the landslide dam.

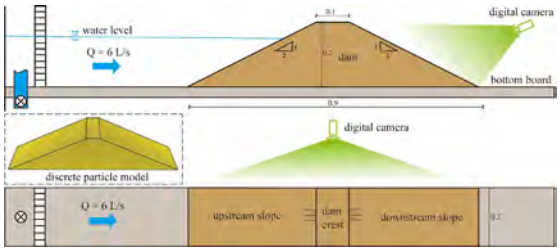

Figure. 4 Layout of the experiment and discrete particle model of the landslide dam

Figure. 5 shows the comparisons between the SPH-DEM model results and experimental results. A fan-shaped wet front is formed downstream the dam slope. Transitional flow occurs on the dam crest and the flow downstream dam slope is supercritical. Figure. 5 (c) and (d) show the entrainment-induced and seepage-induced erosion behavior between soil particles and water particles and the entrainment of the water front. These simulation results qualitatively compare well with the erosion process observed by Wang [8].

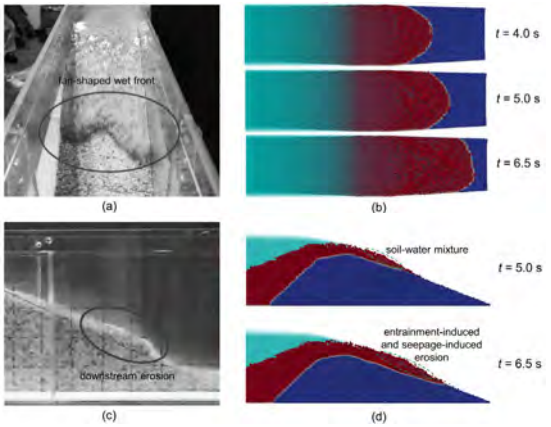

Figure. 5 Comparisons between the SPH-DEM results and experimental results [8], (a), (b): Process of water flow scouring downstream slope; (c), (d): Erosion downstream dam slope

The overtopping discharge flow is quantitatively compared in Figure. 6, demonstrating that the simulated maximum overtopping discharge flow and its emergence time are in good agreement with the experimental result. The maximum discharge flow in the dam-break test is 8.28 L/s, with an occurrence time of the 11th second. The SPH-DEM dam-break model calculates the maximum discharge flow to be 8.57 L/s with an occurrence time of the 16th second. In terms of the maximum discharge flow, our SPH-DEM dam-break model result has a margin of error of 3.5% when compared to the experimental result.

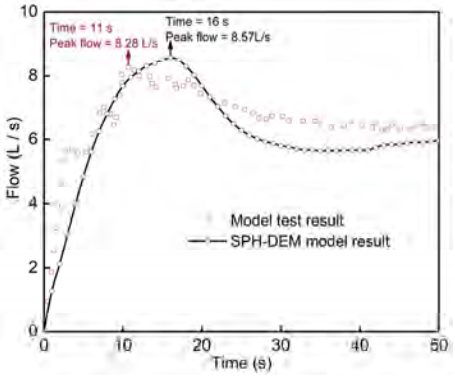

Figure. 6 Variation of discharge flow during the overtopping process

4 Conclusion

A fully-coupled SPH-DEM dam-break model that considers the combined effect of seepage and overflow is presented. The performance of the proposed dam-break model is demonstrated by two benchmark simulations. In a small-scale dam break test, the model showed a good performance with a calculation error of 3.5% for the overtopping peak flow.

The proposed SPH-DEM model is a refined framework for simulating the overtopping failure of landslide dams. Although this model can capture some significant features during a dam overtopping process, there are some inadequacies in considering turbulent effects, soil cohesion, and phase change. Our future development will focus on improving these issues and making breakthroughs in other areas.

References

[1] Zhang J Y, Li Y, Xuan G X, et al. (2009) Overtopping breaching of cohesive homogeneous earth dam with different cohesive strength. Science in China Series E: Technological Sciences, 52: 3024-3029.

[2] Zhong Q M, Chen S S, Deng Z. (2018) A simplified physically-based model for core dam overtopping breach. Engineering Failure Analysis, 90: 141-155.

[3] Zhou G G D, Li S, Lu X, et al. (2022) Large-scale landslide dam breach experiments: Overtopping and “overtopping and seepage” failures. Engineering geology, 304: 106680.

[4] Wang B, Chen Y, Wu C, et al. Empirical and semi-analytical models for predicting peak outflows caused by embankment dam failures. Journal of Hydrology, 2018, 562: 692-702.

[5] Jin Y F, Yin Z Y, Zhou X W, et al. (2021) A stable node-based smoothed PFEM for solving geotechnical large deformation 2D problems. Computer Methods in Applied Mechanics and Engineering, 387: 114179.

[6] Xu W J, Dong X Y. (2021) Simulation and verification of landslide tsunamis using a 3D SPH-DEM coupling method. Computers and Geotechnics, 129: 103803.

[7] Bui H H, Nguyen G D. (2017) A coupled fluid-solid SPH approach to modelling flow through deformable porous media. International Journal of Solids and Structures, 125: 244-264.

[8] Wang L J. (2020) Experimental research on overtopping breach flume of cohesionless earth rock dam. Low Temperature Architecture Technology (in Chinese), 42 (10), 118–120+124. https://doi.org/10.13905/j.cnki.dwjz.2020.10.028

Advanced and promising use of a rockfall protection structure numerical model

S. Lambert[1], G. Ritesh[1], F. Bourrier[1,2], V. Acary[2]

[1] IGE-INRAE, Grenoble, France
[2] INRIA, Montbonnot, France

SUMMARY: This article presents advanced applications of numerical models of rockfall protection structures exposed to impact. As an application case, a structure consisting in piled-up concrete blocks forming a wall with a zig-zag pattern is considered. A numerical model of this wall was developed based on real-scale experiments. The model is first used to investigate the wall response varying the impact conditions. Then, in an original manner, the model is used, first, for addressing and improving the wall response in terms of energy dissipation and, second, to conduct inverse analysis based on data pertaining to the wall exposed to real impact, on site. This latter application appears promising in view, for example, of retrieving information on the wall damage, upon impact and remotely, as well as on the rock block dynamics at impact.

Keywords: Rock fall protection, NSCD model, inverse analysis, structural monitoring, energy dissipation

Introduction

The number of numerical models of rockfall protection structures exposed to impact loading has considerably increased over the last decade. Models have in particular been developed for flexible barriers, embankments and walls based on data from real-scale impact experiments and appear to be accurate enough for having confidence in their predictive capacities. Most often, these models are used to investigate the structure impact response, in a design perspective for a given site or for design method improvement purpose. In this latter case, the model gives access to valuable information such as the loading experienced by the structure components.
This article investigates the potential of numerical models for further investigations of interest to both academics and end-users. In this purpose, a rockfall protection structure with a complex design was considered. A numerical model of this structure was developed based on real-scale impact experiments. This model was used to investigate the structure response against close to reality impact conditions, allowing highlighting its variability depending on the impact conditions. Then, the structure response was addressed focusing on energy dissipation within the structure computed thanks to the model. A criterion based on energy dissipation is proposed to help improving the structure design. Then, it is proposed to use simulation results to assist the inverse analysis of data measured on-site and relating to the structure response to real events. The proposed inverse analysis in particular aims at quantifying the structure damage, upon impact and remotely, and at retrieving information related to the rockfall dynamics.

Considered structure and numerical model

As an application case, a structure developed by Géolithe and consisting in piled-up concrete blocks forming a wall is considered. The 0.76*1.56*0.8 m in dimensions blocks are interconnected via metallic components passing through superimposed blocks, along the

vertical axis. This type of structure is versatile and allows building walls with different patterns, among which the zig-zag pattern (Figure 1). The structure thus forms an articulated wall that can deform during the impact, with a progressive increase of the number of blocks involved in the structure response. It is worth mentioning that the structure displacement is favoured by mechanical plays within the structure.

A non-smooth contact dynamics (NSCD) model of this wall was developed with the Siconos platform (Acary and Perignon, F., 2007). The structure was described a realistic way, paying a particular attention to the interaction between all the wall components (Gupta et al., 2023). The main noticeable advantage with this NSCD model is a reasonable computation time (typically 10 minutes for one impact simulation). The model accounts for five parameters to be calibrated. Two concerns the wall description and three concerns the interaction between the wall components in the normal and tangential directions. These parameters were calibrated from real-scale impact experiments at impact energies of 520 and 1020 kJ as described in Furet et al. (2022). The calibration was based on 24 measures describing the wall response with space and time and was conducted making use of the Bayesian interface statistical learning method, an artificial intelligence technique, resulting in a higher confidence in the model predictive capacities.

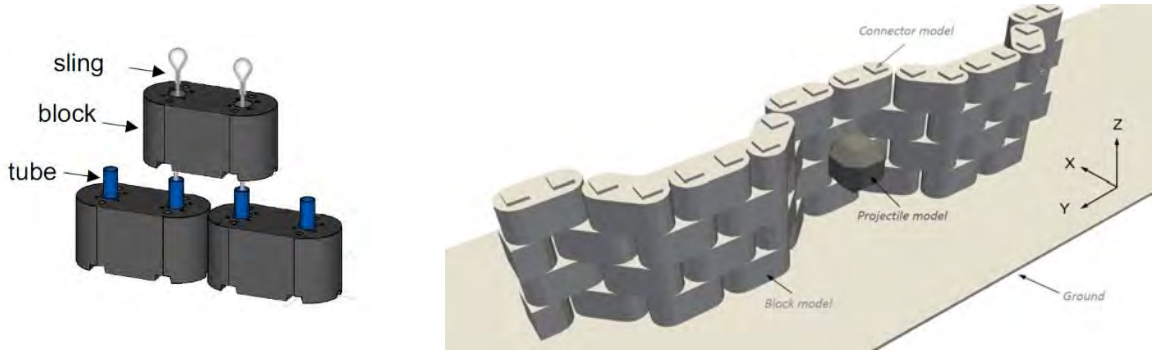

Figure 1. Schematic of the blocks and connecting components (left). Wall model (right).

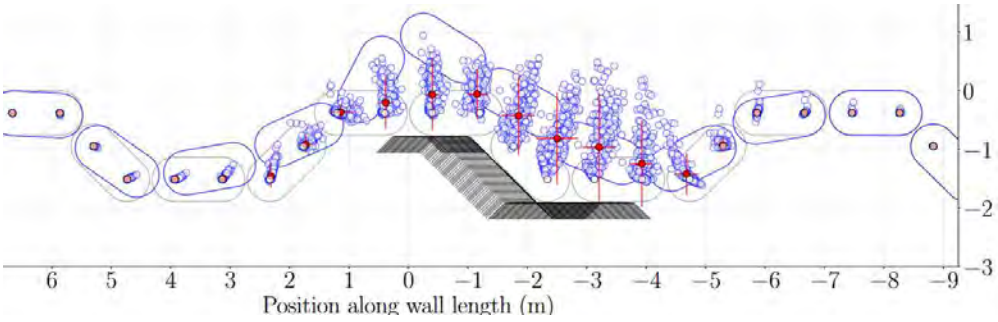

Figure 2. Displacement at the top of the wall obtained from 300 simulations of impact in varied impact conditions. The impact locations is varied along the dark zone, which is the wall pattern.

The model was used to investigate the response of a wall, 3.2m high and 25m long varying the impact conditions over realistic ranges, determined. 300 simulations were conducted varying the impact location, rock block velocity and trajectory at impact following the strategy proposed for flexible barriers by Toe et al. (2018). The wall response revealed complex and extremely dependant on the different parameters, and in particular on the impact location (Figure 2).

Wall energy dissipative capacities

The wall NSCD model accounted for energy dissipation by friction at the various interfaces and for energy dissipation due to plastic strain at the contacts (mimicking damage to the concrete in particular). A rigorous computation scheme guaranteed energy conservation in the system. The energy balance revealed that plasticisation was the dominating dissipative mechanism during impact. For example, for a 1020-kJ impact, dissipation by plasticization amounted about 750 kJ vs. 250kJ for dissipation by friction (*Ep* and *Ef, resp.* in Figure 3, left). The same trend was observed considering the results from the 300 simulations with different impact conditions. Indeed, the ratio of energy dissipation by friction to energy dissipation by plasticization was of about 0.7 on the average (Figure 3, right). Nevertheless, the probability density distribution of this ratio varied over a 0.2-2 typical range revealing that some impact conditions favour large damage to concrete blocks (low ratio value) while others favour large displacements resulting in larger dissipation by friction (large ratio value). This ratio thus relates to the whole structure response with time for a given impact. For this reason, it appears to be a relevant and novel criteria for optimizing the structure while considering realistic impact conditions. For a given site, the wall design optimisation could rely on different strategies depending on the context: reduce damage to the wall but favour large wall displacement (range below 1 is targeted), on the contrary reduce the wall displacement (range above 1 is targeted) or define the design such that both mechanisms equally dissipate energy.

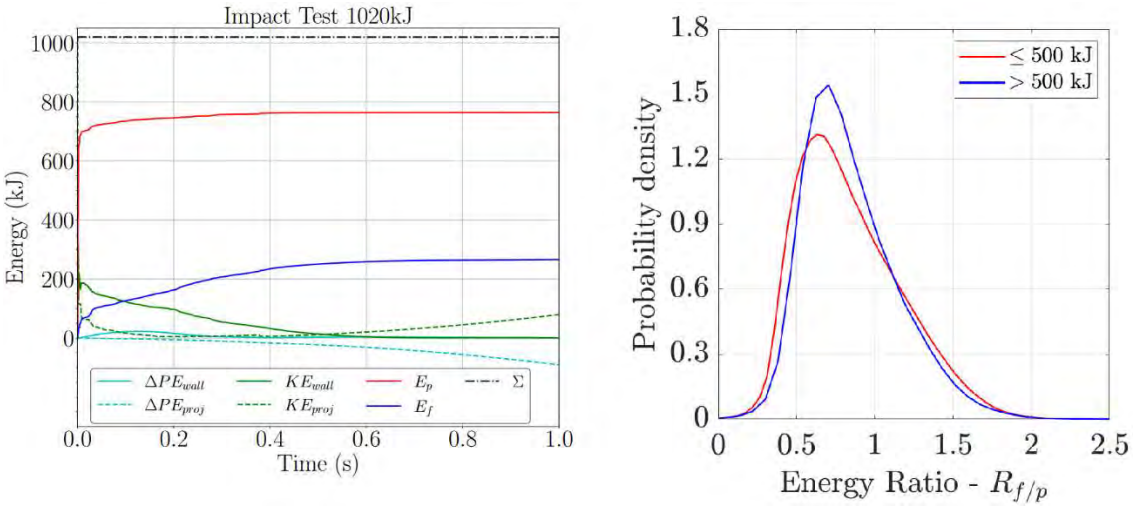

Figure 3. Energy balance in case of a 1020-kJ impact (left). Distribution of the ratio between energy dissipation by friction and energy dissipation by plastification (right).

Inverse analysis

Recent technological advancements allow collecting many data in relation with the on-site structure response to real rockfall. For example, scans made after impact may be used to measure the displacement experienced by the wall. Also, the wall response with time may be characterized from measurements made by sensors installed in various locations of the wall. In both cases, the interpretation of these data sets for serving some operational or more academic purposes is not straightforward. For this reason, the numerical model was used to help in the inverse analysis of data from the field. In the principle, the inverse analysis consists in comparing the data obtained from the field to the corresponding data predicted by the model.

This comparison allows defining the impact conditions which result in the best match between simulated response and real response. This comparison was achieved using metamodeling techniques and the Bayesian inverse analysis.
As an illustrative application, Figure 4 shows the predictions of the damage to the wall (dissipation by plasticization) over a large set of impact cases, versus the value obtained from the numerical model. The inverse analysis predictions are based on the maximum velocity recorded onsite during impact, at a few locations on the wall and results in a root mean square error of about 80kJ. This approach thus appears promising and rather reliable for estimating damage to the wall, remotely and just upon impact.

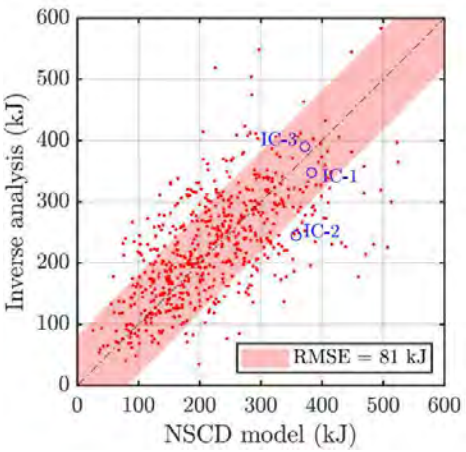

Figure 4. Comparison of the predictions by the inverse analysis approach of the damage to the wall with the value obtained from simulations.

Conclusion

This article has proposed using numerical models for describing and optimising the structure response based on the quantification of energy dissipation. In this purpose, a design optimization criterion was proposed. In addition, using simulation results for deriving data pertaining to real situation impacts from onsite measurements was shown to be feasible and rather precise.

Acknowledgements

This work was conducted in the frame of the SMART PROTECT research project, leaded by Géolithe with INRAe, INRIA and Myotis as partners and funded by the Auvergne-Rhône-Alpes region.

References

Acary, V. and Perignon, F. (2007). Siconos: A Software Platform for Modeling, Simulation, Analysis and Control of Non smooth Dynamical Systems, SIMULATION NEWS EUROPE, ArgeSIM/ASIM 17 (2007) 19–26.

Furet, A., Lambert, S., Villard, P., Jarrin, J. P (2022). Experimental and numerical impact responses of an innovative rockfall protection structure made of articulated concrete blocks. DOI 10.1007/s00603-022-02957-x. Rock Mechanics and Rock Engineering

Gupta, R., Bourrier, F., Acary, V. and Lambert, S. (Accepté) Bayesian interface based calibration of a novel rockfall protection structure modelled in the non-smooth contact dynamics framework. *Engineering structures*.

Toe, D., Mentani, A., Govoni, L., Bourrier, F, Gottardi, G., and S. Lambert (2018). Introducing Meta-models for a More Efficient Hazard Mitigation Strategy with Rockfall Protection Barriers. *Rock Mechanics and Rock Engineering*. DOI 10.1007/s00603-017-1394-9.

The impact of clips between the reinforced layers on the performance of rockfall protection embankment

Vigna Stefano[1], Marchelli Maddalena[2], De Biagi Valerio[2], Matteo Nadalini[3], Alberto Grimod[4]

[1] DIATI, Politecnico di Torino, Corso Duca Degli Abruzzi 20, 10129, Italy
[2] DISEG, Politecnico di Torino, Corso Duca Degli Abruzzi 20, 10129, Italy
[3] INCOFIL TECH SRL, Cirè (TN), Via degli Artigiani 52, 38057, Italy
[4]France Maccaferri, Valence, Via Rue Pierre Mechain 8, 26000, France

SUMMARY: Rockfall protection embankments (RPEs) represent valuable mitigation measures against rockfalls, however their behaviour during the impact is not yet fully investigated. In this study, several numerical models of RPEs reinforced with double twist wire mesh have been developed using Abaqus/Explicit FEM code. Specific focus is given to the impact of clips installed between adjacent reinforced layers. The study presents and discusses the macroscopic behaviour of these structures with and without clips.

Keywords: Rockfall, rockfall protection embankment, numerical methods, double twist wire mesh.

Introduction

Rockfall phenomena are significant hazards that affects mountain areas and, due to the climate change effects, they are increasing in frequency. Rockfall protection embankments (RPEs) represent valuable mitigation measures, widely adopted especially in case of events involving multiple impacting blocks or very high kinetic energies (Peila et al., 2007, Vigna et al., 2023). Currently, RPEs structural response when impacted has not been comprehensively investigated and real-scale impact tests were limited, primarily due to challenges in reproducibility and cost constraints.

The present study focuses on the influence of the clips between layers on the behavior of the RPE reinforced made with double twist wire mesh. Numerical models, developed in Abaqus/Explicit FEM code, accurately replicate the wrap-up layered geometry of the reinforcement, as well as the clips (Figure 1) installed in the wrap-up area, which are punctual connection elements recommended from the producers when this kind of reinforce is employed. However, the clips influence on the RPE behavior during the impact has not been yet investigated. The tests conducted by Peila et al. (2007), which have not incorporated clip elements, have been back analyzed to calibrate the numerical mechanical parameters of the soil. Subsequently, with the same test conditions a comparison is performed considering both cases with and without clip elements.

Methodology

The numerical models are developed using Abaqus/Explicit FEM. The reinforcing elements used in the model is the double twist wire mesh “Green Terramesh Light”, produced by Maccaferri, type 8x10 (EN 10223-3) and wire diameter of 2.20/3.2 mm. The mesh has, in accordance with ETA n. 16/0758 (version 06 of 30.08.2023), a tensile resistance of $F_{max} = 40 \pm 5\ kN/m$ and an ultimate strain $\varepsilon_{max} = 10\%$ as reported by the technical datasheet. The mesh producer recommends a clip spacings of 0.20 m, with an ultimate strength of $T_{max} = 2\ kN$ each one (EAD 200086-00-0602).

The compacted soil is modeled with three-dimensional elements (C3D8R) and the material constitutive law is linear elasto-plastic with modified Drucker–Prager yield criterion.

The impactor is spherical and modeled as perfectly rigid body.
The double twist wire mesh is modelled as shell element (S4RS) and the constitutive law is elasto-plastic associated with the "Ductile Damage" law. This choice allows to manage the large deformations to which the wire mesh is subjected in the impact zone. Moreover, when a mesh element reaches ε_{max} it is removed from the analysis in order to simulate a wire mesh local failure. The clips among the reinforced layers are modelled using Abaqus fasteners elements whit the failure criterion depending on T_{max}.
RPE foundation interaction is modelled with a base layer having the same mechanical property of the compacted soil and meshed with solid elements (CIN3D8) (Vigna et al., 2023).
Due to the three-dimensional geometry of the problem and the computational effort, the symmetry of the problem is considered and half of RPE and impactor are modelled.
Figure 1 shows the cross section of the RPE, the wrap-up geometry and the clips spacing (a). The impact is perpendicular to the upstream side bank with a velocity of 32 m/s located between the layer n°4-5 with an overall kinetic energy of about 4180 kJ (Peila et al., 2007).
After the calibration of the soil mechanical parameters, the results obtained with and without the clips are compared.

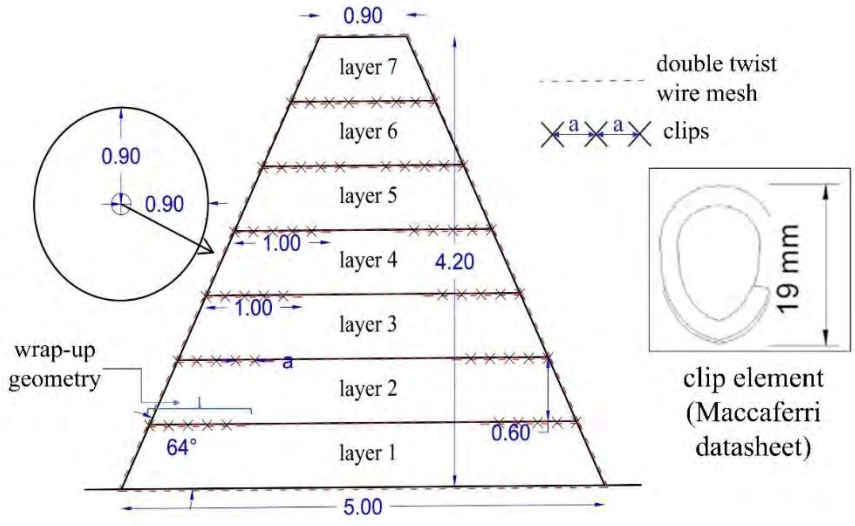

Figure 1: Cross section of the RPE tested by Peila et al., (2007) in which is shown the clips location used in the comparison models.

Soil mechanical parameters calibration

The soil mechanical parameters are calibrated by back analyzing the tests made by Peila et al. (2007). The tests have shown a behavior mainly involving the impacted layer and characterized by an upstream maximum depth of the crater (U_u) and a rigid downstream sliding (U_d) (more details are reported in Peila et al., 2007). The experimental values are $U_u \approx 1\ m$ and $U_d \approx 0.60\ m$ and are used as comparison values in the calibration process.
The soil calibrated parameters are shown in Table 1, in which ρ is the density, E is the Young modulus, υ is the Poisson ratio, φ is the friction angle, k is the flow stress ratio, ψ is the dilatancy and c is the cohesion. More details about the soil constitutive law are reported in Vigna et al., (2023). The back-analysis results are shown in Figure 3 and Figure 4 with reference to the curves with $a = NC$.

Table 1: Soil mechanical parameters back-analysed.

$\rho\ [kg/m^3]$	$E\ [MPa]$	$\upsilon\ [-]$	$\varphi\ [°]$	$k\ [-]$	$\psi\ [°]$	$c\ [kPa]$
2100	90	0.3	34	0.78	0	85

Results

The model results are presented in the following. The test is simulated with clips spaced apart of $a = 0.20\ m$ and $a = 0.30\ m$. Figure 2 shows a comparison of the final configuration of the RPE after the impact, respectively, without clips and with clips equally spaced of $a = 0.20\ m$.

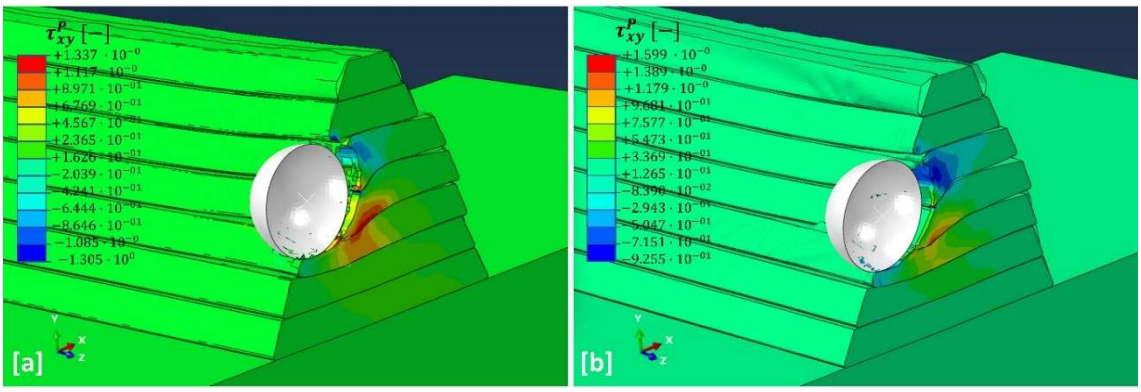

Figure 2: Final configuration of the RPE models in which it is shown the plastic shear strains (τ_{xy}^{P}): [a] without clips ($a = 0$), [b] with clips spaced of 20 cm ($a = 0.20\ m$).

Figure 3 and Figure 4 show the displacements curves of the most deformed layer along the RPE extrusion (layer names are referred to Figure 1). According to these models, the effect of clips appears to reduce the final maximum deformations of the RPE by a few centimetres: $U_u = 1.04\ m$ and $U_d = 0.48\ m$ without clips, $U_u \approx 1\ m$ and $U_d \approx 0.4\ m$ in both cases with clips. However, the presence of clips results in a more uniform deformation of the structure, engaging multiple layers in the resistance mechanism (Figure 2b).

Table 2 reports the number of clips broken during the impact upstream and downstream (respectively N_u and N_d), the maximum deceleration on the sphere a_{max}, the impact energy redistribution (plastic energy E_p, friction energy E_f and elastic energy E_{el}), the normal force F_n applied to the foundation in addition to the self-weight, and the tangential force F_t due to the impact. It is important to underline that few clips broke in the simulated impact condition. The clips tend to result a stiffer response of the RPE, leading to a higher a_{max} and lower displacement field. Regarding the effects on the foundation layer, the presence of clips tends to reduce the amplification of the self-weight, to the detriment of the increase in the tangential force; those values should be taken in to account in the overall stability of RPE-slope system. Based on the outputs of the analysis, the energy distribution remains largely unaffected by the clips density values investigated, confirming Peila et al. (2007) results.

Table 2: Numerical model results.

a $[m]$	N_u $[-]$	N_d $[-]$	a_{max} $[m/s^2]$	E_p [%]	E_f [%]	E_{el} [%]	F_n $[kN]$	F_t $[kN]$
NC	-	-	1412	86.6	8.9	4.5	3112	692
0.20	31	2	1679	88.8	5.6	5.6	2318	807
0.30	41	11	1595	88.8	5.7	5.5	2322	804

Conclusion

Numerical FEM models of a rockfall protection embankment reinforced with double twist wire mesh have been studied with special focus on the influence of clips between adjacent reinforced layers.

Based on the results, it appears that the presence of clips reduces the final deformation of the RPE (Figure 3 and Figure 4) improving, from a macroscopic point of view, the structural collaboration among the layers during the impact phase. Nevertheless, a deeper parametric

analysis is necessary to better understand the influence of clips on the dynamic response of the structure, as well as incorporate their structural contribution into current analytical design methods proposed by Marchelli & Deangeli (2022).

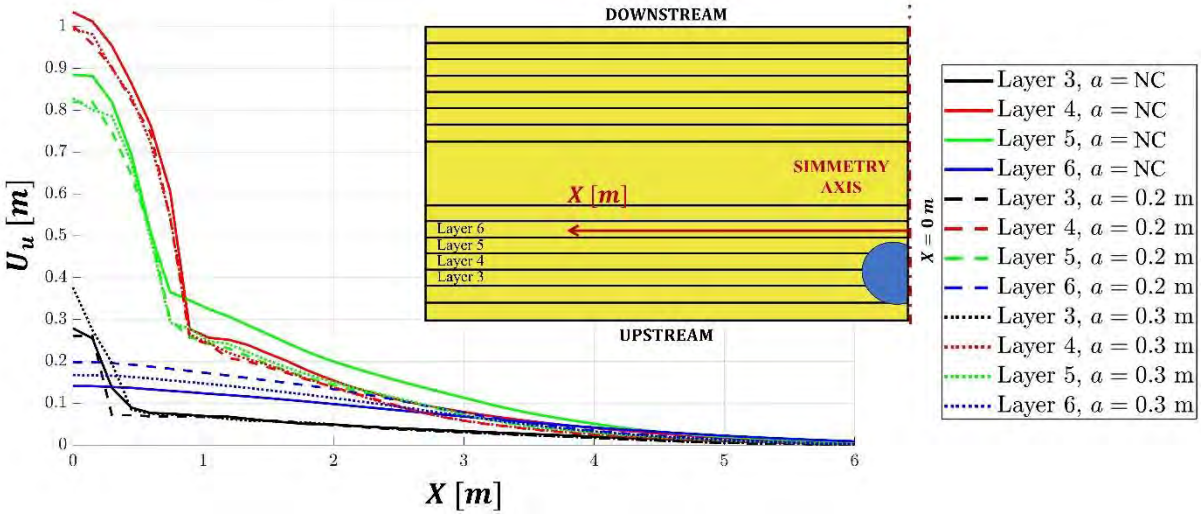

Figure 3: Downstream displacement at the impact n°2 tested by Peila et al., (2007) on different soil layers.

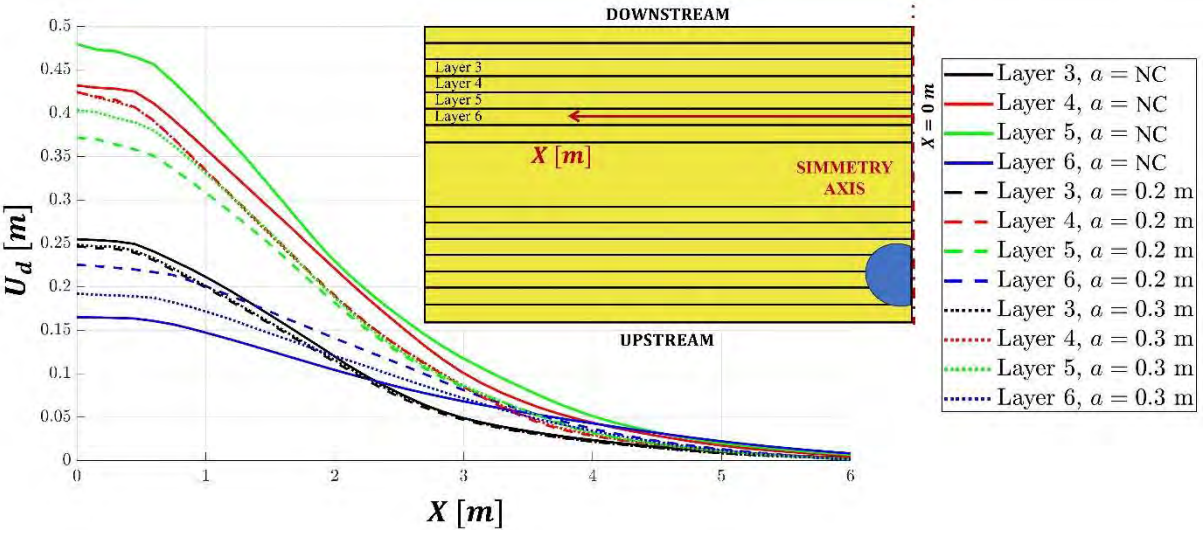

Figure 4: Upstream displacement at the impact n°2 tested by Peila et al., (2007) on different soil layers.

Acknowledge

This study was carried out within the project PERSEIDI funded by Provincia Autonoma di Trento (Provincial Law 6/99 " provincial law on business incentives" Article 5., Investment n° C39J21046780001).

References

Peila, D.; Oggeri, C.; Castiglia, C. (2007). Ground reinforced embankments for rockfall protection: design and evaluation of full-scale tests. *Landslides* 4, 255–265.

Vigna, S., Marchelli, M., De Biagi, V., & Peila, D. (2023). Numerical Simulation of Rockfall Protection Embankments in Natural Soil. *Geosciences*, 13(12), 368.

Marchelli, M., & Deangeli, C. (2022). Towards a codified design procedure for rockfall reinforced earth embankments. *GEAM. GEOINGEGNERIA AMBIENTALE E MINERARIA*, 165, 50-59.

Numerical back-analysis of impacted rockfall barriers steel posts: discussion on the effectiveness of the system

Francesco Pimpinella[1], Maddalena Marchelli[1], Andreas Lanter[2], Valerio De Biagi[1]

[1] Dipartimento di Ingegneria Strutturale, Edile e Geotecnica (DISEG), Politecnico di Torino, Torino, Italy
[2]Geobrugg AG, Romanshorn, Switzerland

SUMMARY: Flexible rockfall barriers are effective structures for rockfall risk mitigation, capable to withstand very high impact energies, up to 10000 kJ. The assessment of the barriers is demanded to the appropriate European Assessment Document EAD 340059-00-0106 (EOTA, 2018): it ties the performance to a standard test procedure, in which the net is the only impacted element. Despite this impacting case is representative of the majority of the cases, other impact positions are possible, e.g. on the supporting elements. Hence, the debate on the performance assessment for the rockfall barriers is still open.
The producing company Geobrugg AG has recently conducted experimental tests producing an impact at the midspan of an internal steel post on a 500 kJ rockfall barrier. In this paper, a numerical back-analysis of these tests is performed to analyze the failure mechanisms and to be able to extend the results for different impact positions on the structural element, evaluating the system effectiveness.

Keywords: rockfall barrier, impact, steel post, energy dissipation, numerical back-analysis

Introduction

Flexible rockfall barriers, also called net fences, are effective protection measures for mitigating rockfall risk, capable to withstand very energetic block impacts. For the limited encumbrance and environmental impact and the low weight of these systems, they are often the only option to protect elements at risk. Net fences are composed by an interception element (constituted by a steel net), sustaining elements (usually realised with structural steel commercial profiles), rope cables (which transmit the load to the anchor foundations) and energy dissipating devices. While traditional civil engineering structures are subjected to plastic deformations just in ultimate limit state conditions, an extensive damage of net fences can be produced even in impacts with low kinetic energy. These systems are thus realised so that a relevant portion of energy dissipation occurs in parts that can be easily substituted, like energy dissipating devices.

Even if rockfall protection structures performance assessment is still debated (De Biagi et al., 2020), today its evaluation is made through the procedure defined in EAD 340059-00-0106 (2018): through codified impact tests both a maximum and service energy absorption capacity are derived, named MEL and SEL, respectively. During the tests, block impacts are performed in a given position, i.e. in the centre of a three-modules structure: this might not be comprehensive of the wide variability of the possible impacting positions. Moreover, the impacting block is a quasi-spherical polyhedron realised in concrete which should impact the intercepting net with a velocity equal or higher to 25 m/s. Despite these limitations, the efficiency of systems designed and tested following the EAD 340059-00-0106 (2018) has been demonstrated for many other load cases (Yu et al., 2021). As an example, numerical simulations have demonstrated that a certified barrier can withstand to impacts due to areal loads such as small or large slabs (Koo et al., 2017). On the other hand, the standard test procedure has also

shown some lacks: experimental tests have shown that a decrease of the impactor size (keeping constant impacting energy) produces a decrease in failure energy (Spadari et al., 2011; Mentani et al., 2017).
All the works mentioned above considered the net as the impacted element. Nevertheless, the scientific literature has not adequately addressed the likelihood of block impact affecting the connecting elements or the support components, i.e. the posts. The steel posts main aim is to keep the interception structure, the steel ropes and the energy dissipating devices in their design positions: hence, sustaining components are not designed to bear the impact load. However, the possibility of an impact on these structural elements exists and it is not negligible. For this reason, producers have recently started to perform internal tests to evaluate their products response to this load case. In this context, the Swiss company Geobrugg AG performed an impact test directly on the post with an incoming energy equal to 180 kJ, that represents the product SEL value. The test performed in Walenstadt (CH) test site, has shown the rockfall barrier ability to stop the block for the first impact.
This paper aims to develop a feasible numerical model of the structure and the impact. The model is calibrated through the back-analysis on the impact that occurred in the test site. Failure mechanisms and energy dissipation at the impact are discussed. The simulation also allows to estimate how energy dissipation is allocated among the components of the system.

Methodology

The numerical simulation is tailored on the experimental test by comparing the steel post deformed shape after the impact. Then, the model is used to estimate how different impacting positions and different ropes layouts influence the system performance. In this section the realised experimental impact test is presented, together with the developed numerical model.

As can be seen from Fig. 1(a), in the experimental test the impact has been produced at the midspan of an internal steel post. This structural element is connected at one end with the ground anchor by means of a steel plate, and at the other one with the upslope rope cables and the rockfall barrier longitudinal rope: these ropes represent for the post an external restraint, being activated in the impact occurrence. The steel post is constituted by a HEA 120 profile realised in steel S355. The impacting block is realised in concrete, following the EAD 340059-00-0106 (2018) requirements for standardised tests. During the test, no ruptures have been observed in the impactor, while severe plastic deformations have occurred in the steel post, as can be seen in Fig. 1(b).

Figure 1(a). SEL impact on a 500 kJ flexible rockfall barrier steel

Figure 1(b). Deformed steel post

The realised numerical model is a FEM one (Abaqus CAE, 2024 release), shown in Fig. 2(a). The impactor is modelled as a discrete rigid element while the steel post is modelled using three tied shell elements, for computational time saving purposes. The impactor velocity field is imposed on a vertical axis (Y axis) which passes at the midspan of the impacted post. However, this does not necessarily imply an exact midspan impact occurrence, and possible imperfections in the impactor position on the X axis (Fig. 2(a)) are considered.
The steel post material is steel S355: due to the severe plastic deformation which occurs on the structural element, both hardening phase and damage phase are included in the finite element modelling. In particular, a Cowper-Symonds power low is introduced in the model for the former and a Johnson-Cook damage model for the latter. Appropriate parameters for these laws have been taken from specific studies on the material S355 (Forni et al., 2016; Ribeiro et al., 2016). Since the experimental deformed shape shows a significant portion of energy dissipation occurring in the connecting element between the ground anchor and the steel post, this connection is introduced in the model. It is realized through a shell element which is hinged at one end to reproduce the connection between the steel post and the base plate. At the other end the connecting plate is tied to the post profile web: this is believed to be a good approximation of the real behaviour because the actual connection is realized by means of both bolting and welding. The connection between the sustaining ropes and the steel post is realized by modelling the actual post head shape and inserting the steel ropes in their position inside the assembly. The interaction between materials during the dynamic phenomenon occurrence is considered by means of a general contact approach, considering a friction coefficient for tangential behaviour equal to 0.4.
Both upslope and longitudinal ropes are modelled using an indefinite elastic steel, since plasticity is not expected to occur in these structural elements. To consider that in the real conditions the ropes react with their stiffness after an initial displacement (Escallón et al., 2014), an extra rope loop is modelled on all the steel ropes. The extra rope loop length applied to each steel rope depends on its length. Mesh attributes are chosen after a mesh dependency analysis.

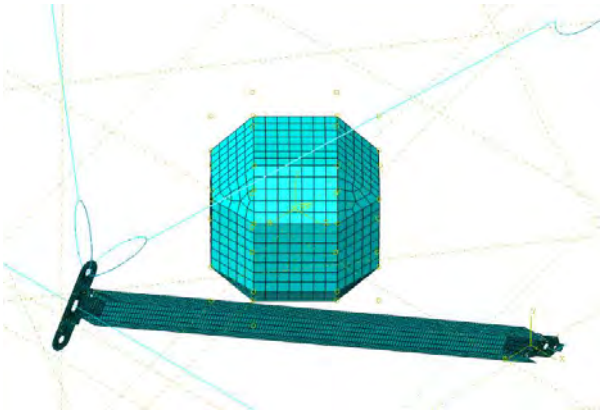

Figure 2(a). Numerical model of the impact

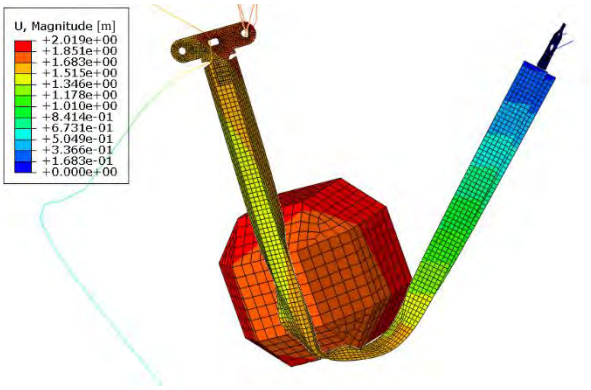

Figure 2(b). Deformed shape (t= 0.1 s)

Results

The impact numerical modelling confirms the suitability of the system to absorb at least one SEL event. The development of the plastic hinge shown in Fig. 1(b) is accurately reproduced in the model, as can be appreciated by the extraction of the deformed shape reported in Fig. 2(b). However, the rotation developed by this plastic hinge is strongly dependent on the introduction of X-axis imperfections in the impacting area (Fig. 3(a)) and on upslope and longitudinal ropes extra rope loop length (which is also dependent on the possible activation of energy dissipators). The experimental evidence of a significant energy dissipation occurrence in the base connecting plate and in the post head is confirmed by the model outcome (Fig. 3(b)).

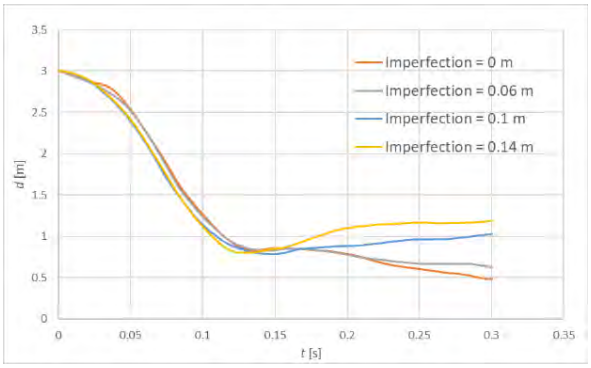

Figure 3(a). Distance between the post ends for various X-axis imperfections of the impact

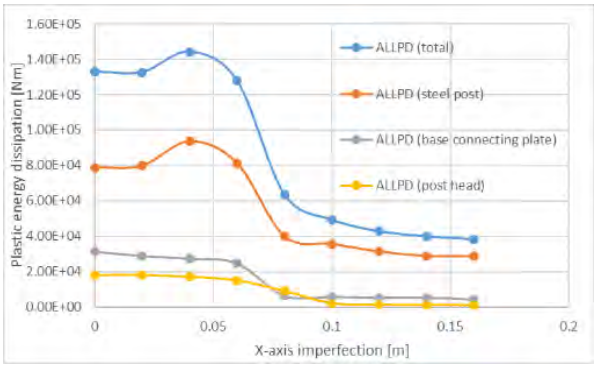

Figure 3(b). Plastic energy dissipation allocation: influence of the impact X-axis imperfection

Conclusion

The developed numerical model proved to be feasible to represent impact situations differing from the usual one, i.e. impacts directly on the posts of the system. The model can thus be used to evaluate the system efficiency in different loading conditions. In the modelled case, i.e. an impact with an energy equal to the SEL one, even if a large deformation of the post occurs, the barrier stops the block. It should be noted that the barrier ability to withstand impacts occurring on the posts is strictly related to the technology examined in this study. Thus, the result cannot be immediately extended to flexible rockfall barriers with different energy classes, and the model should be tailored for considering different technologies. Further refinements are currently under progress and include the detailed study of the effect that different impact positions and rope loose lengths have on the steel post energy absorption performance and the investigation on the contribution provided by the non-impacted steel posts.

References

European Assessment Document (EAD 340059-00-0106, 2018), Falling rock protection kits, EOTA.

De Biagi, Marchelli, Peila (2020) Reliability analysis and partial safety factors approach for rockfall protection structures. *Engineering Structures* 213, 110553

Yu, Luo, Liu, Guo, Qi, Zhao (2021) Dynamic response of flexible rockfall barriers with different block shapes. *Landslide* 18, 2621 - 2637.

Koo, Kwan. Ng, Yu, Choi, Ng, Ho, Pun (2017) Dynamic response of flexible rockfall barriers under different loading geometries, *Springer Link* 14, 905-916

Spadari, Giacomini, Buzzi, Hambleton (2011) Prediction of the Bullet Effect for Rockfall Barriers: a Scaling Approach. *Rock Mechanics and Rock Engineering* 45, 131 - 144.

Mentani, Giacomini, Buzzi, Govoni (2015) Numerical Modelling of a Low-Energy Rockfall Barrier: New Insight into the Bullet Effect. *Rock Mechanics and Rock Engineering* 49, 1247 – 1262.

Forni, Chiaia, Cadoni (2016) Strain rate behaviour in tension of S355 steel: Base for progressive collapse analysis. *Engineering Structures* 119, 164 - 173.

Ribeiro, Santiago, Rigueiro (2016) Damage model calibration and application for S355 steel. *Procedia structural integrity 2*, 656 - 663.

Escallón, Wendeler, Chatzi, Bartelt (2014) Parameter identification of rockfall protection barrier components through an inverse formulation. *Engineering Structures* 77, 1-16

Aknowledgements

This publication was produced while (F.P.) attending the PhD programme in Civil and Environmental Engineering at Politecnico di Torino, Cycle XXXVIII, with the support of a scholarship co-financed by the Ministerial Decree no. 352 of 9th April 2022, based on the NRRP - funded by the European Union - NextGenerationEU - Mission 4 "Education and Research", Component 2 "From Research to Business", Investment 3.3, and by Geobrugg AG.

Rockfall Canopies: next level bouncing for rocks

Helene Lanter[1], Franck Servant[2], Aron Vogel[1], Stu Mason[3]

[1] Geobrugg, Romanshorn, Switzerland
[2] Brugg France, Porte-lès-Valence, France
[3] Geobrugg NZ, Christchurch, New Zealand

Flexible steel canopies are an economical and environmentally friendly alternative to concrete galleries as rockfall protection for transport infrastructure neighbouring steep rock slopes. Based on full scale test experiences from the late 1990s first protoypes have been developed and finalized in standard solutions tested at MEL as per EAD 340059-00-0106-2018. Since then, no major projects have been undertaken with rockfall canopies. Since 2018 increasingly these solutions are gaining interest on global level.

Keywords: canopy, flexible protection systems, ring net, rockfall, mitigation

Introduction

Flexible rockfall galleries, termed here canopy, are an economical and environmentally friendly alternative to concrete galleries as a rockfall protection system for roadways in mountainous regions (see Figure 1). The rockfall canopy may act like a draping system, guiding the rocks in a maintenance-free manner to a place where they will stop without any danger to infrastructure, acting similarly to a trampoline. The system is designed to be self-cleaning for a design impact energy level and it will retain blocks above that energy, for a designated maximum impact energy.

Figure 1: Massive concrete gallery (left) versus flexible rockfall gallery- termed canopy (right).

Flexible rockfall canopies like rockfall barriers consist of steel posts anchored to the ground to which the wire ropes are connected. The intercepting structure consists of a steel ring net. The ropes are able to slide along the post heads and are anchored to the ground. The design concept, however, of rockfall canopies is different from standard rockfall barriers. Net and post inclinations are different, the rockfall canopies are designed to be less flexible to allow self-cleaning within a kinetic energy threshold. The higher structural overall stiffness is achieved by using additional ropes. Furthermore, the net forms an angle higher than 90 degrees with the slope, facilitating the impacting rocks to move horizontally. This design approach reduces the maintenance frequency of the system (Escallon & Wendeler 2014). This is possible with energies up to 500kJ, which were proven within 1:1 field testing. In case of higher energies, the canopy system is able to catch boulders up to 1’000kJ. The hazard potential underneath the

canopy must be inconsiderable or in better words the transfer of the blocks must take place under controlled conditions, for example into another rockfall barrier or more generally into the valley below featuring no infrastructure. Additional design load cases such as snow loads must be considered separately.

Real-scale testing and development of a finite element model

The first real-scale testing was done in Varnerfluh in 2000. The north-western connecting road betweeb Varen and Rumeling (near Leukerbad) in the canton of Valais, Switzerland, had to be closed for the winter 1999/2000 because of the danger of rockfall. The topography, with a vertical rock face up to 100 m high and a road passing below was ideal for field tests. The municipality and the civil engineering office gave their consent to place a 22 m long flexible system for testing. Different tests were setup with blocks ranging between 240 and 700 kg. The self-cleaning effect was observed with 700 kg block, taking with him even the smaller blocks out of the net. This was then used as a basis to apply in the year 2012 for an Innosuisse project in collaboration with the Swiss Federal Institute for Forest, Snow and Landscape Research (WSL). The primary goal of this project was to develop a new „self-cleaning“ rockfall barrier that could replace heavy (and expensive) concrete structures. The rockfall barrier was developed and optimized using advanced finite element modelling technology (Escallon, 2015). Real-scale tests were performed at the WSL rockfall test site at the time, enabling the validation of the simulation technology and the barrier design. These real-scale tests were done in a three-field system, with and without rotation, with energies between 500 and 1’000 kJ, testing the middle and the border fields.

First project dimensioned with the help of numerical simulation

Along the exposed cantonal road into the Val d’Anniviers in Valais/Switzerland, rockfalls occur regularly (Wendeler et al, 2013). At the exit and entrance of an existing old tunnel portal, which is adjoined by a very steep rock face (Fig. 2), serious hazards became apparent. Various studies in the pre-project phase showed that a flexible gallery at this location was the alternative to a tunnel extension with a concrete gallery or even a road relocation. The block size of 1 to 2.5 m^3 with a falling of > 100 m resulted in the design energy of E = 2’000kJ. The previously projected, flexible 1’000kJ canopy was adapted to the new protection target. The engineers quickly realized that 2’000kJ would be a new kind of challenge for a flexible canopy system, as the largest flexible galleries had previously only been designed for a quarter of this energy. Another complicating factor was the additional planned widening of the road, which gave the planners extra challenges. It was necessary to work with spans of up to 11 m of cantilevered posts which meant that considerable forces and stability problems were to be expected. As a standard, all flexible rockfall protection systems were designed in advance according to the Swiss Guideline and to the ETAG27 at the time by using 1:1 field tests. However, since this turned out to be a very special solution, it was not possible to carry out 1:1 tests during the short project timeline. The entire load-bearing system had to be appropriately dimensioned by numerical simulation, developed in the previously presented KTI Project (Volkwein, 2004, Escallon et al, 2014). Snow was also expected at 1000 m.a.s.l. and it was important to check whether the snow load in winter might activate the energy absorbers. After two months of intensive installation work and a total project duration of 3.5 months, the portal was completed, and the road could be reopened to traffic (Fig. 2). The canton presented the project as a new achievement, helping to save over 4 million francs. The entire construction, including the installation work, cost a total of 1.1 million Swiss francs, whereas the tunnel extension with a concrete gallery would have reached 5 million Swiss francs (Wendeler et al, 2013).

Multiplication of recent projects

As mentioned in the introduction, the project Tunnel des Pontis was completed in 2010. From 2018 onwards, an increasing demand for tested flexible rockfall canopies can be observed. In the following recent representative cases are presented. The planning and implementation period is 2018 to 2022.

2018 - Chalais-Vercorin road, Switzerland: In peak periods, over one thousand vehicles drive up the Chalais-Vercorin road, and the village of Vercorin is also served by the postal bus. Frequent low energy rockfalls permanently endanger the road traffic and the affected section between several tunnels. A self-cleaning rockfall canopy has been implemented for maximum energies of up to 500 kJ. Due to the extremely steep terrain up to the vertical, a 3D-field survey was undertaken (Figure 3, left). From this the precise measures for all single components of the system, such as ropes, posts, net area could be determined.

2022 – Kaikōura, New Zealand: High rockfall frequency from a vertical rock slope along the state Highway 1 (SH1) on the South Island of New Zealand led to the requirement of protection by means of a flexible self-cleaning rockfall canopy. A 104 m long canopy was installed. This system was selected due to its self-cleaning ability and being able to withstand multiple rockfall impacts up to 500 kJ prior to requiring maintenance (Figure 3, right).

Figure 3: left: Chalais-Vercorin canopy; right: Kaikoura canopy (www.geobrugg.com)

2022 - Mont Blanc, TramwaySaint Gervais les Bains, France: At the tunnel entrance, just before the Nid d'Aigle arrival station, the Mont Blanc Tramway passes the foot of a cliff subject to rock falls. The installation of a canopy system (again self-cleaning up to 500 kJ) on a 70-meter-long line, in addition to a wire mesh placed on the lower part of the rockface, allowed to secure the site (Figure 4).

Figure 4: Nid d'Aigle canopy (www.geobrugg.com)

2022: Gäsi, cycling and hiking trail along the Filzbach, Switzerland: On the southern shore of Lake Walen, the existing motorway gallery was extended with a rockfall canopy to protect the cycle and hiking path below (Figure 5, left).

2023 - Les Gorges du Chauderon, hiking trail Montreux, Switzerland; Various protection barriers, including a rockfall canopy system, were used to ensure the safety of the hikers (Figure 5, right).

Figure 5: left: Gäsi canopy; right: Montreux canopy

Conclusion

The self-cleaning canopy offers numerous benefits compared to conventional concrete galleries and represents a viable alternative solution, to the construction of a tunnel. It significantly shortens construction times and has a considerably reduced environmental impact, which is particularly noteworthy for minimising carbon footprints. The system's flexibility, thanks to the ring nets, allows it to absorb energies of up to 2000 kJ, making it suitable for various scenarios such as impacts in central areas, post impacts, and snow loads. These attributes were thoroughly investigated during the development of the standard rockfall canopy, expanding its applicability across a wide range of situations. The field tests and the numerical modelling will be explained in greater detail during the conference.

References

J. Escallon, C. Wendeler (2014) Rockfall protection canopies, *Proceedings of the Rocex Conference Lecco*, Italy

J. Escallon (2015) Simulation of a flexible steel wire-net rock-fall barriers via finite element model updating. *PhD. Diss. Swiss Federal Inst. of Technology Zurich*

C. Wendeler, A. Volkwein, B. Biedermann (2013) A Flexible Rockfall Gallery in the High-Energy Zone as an Alternative to Concrete Galleries or Tunnels - Design and Application, *Journal of Torrent, Avalanche, Landslide and Rock Fall Engineering* Nr. 171

A. Volkwein (2004). Numerische Simulation von flexiblen Steinschlagschutzsystemen, *PhD. Diss. Swiss Federal Inst. of Technology Zurich*, Switzerland

J. Escallon, C. Wendeler, E. Chatzi, P. Bartelt (2014) Parameter identification of rockfall protection barrier components through an inverse formulation, *Engineering Structures* 77, 1 – 16

Tunnel des Pontis (no date). https://www.geobrugg.com/de/Tunnel-des-Pontis-67193.html.

Route Chalais Vercorin (no date).https://www.geobrugg.com/en/Route-Chalais-Vercorin-Valais-103611.html

Kaikoura SH1-SR10 (no date). https://www.geobrugg.com/en/Kaikura-SH1-SR10-167077.html

Tramway du Mont Blanc – Nid d'Aigle (no date). https://www.geobrugg.com/en/Tramway-du-Mont-Blanc-Nid-dAigle-187145.html

Protecting Hydro-Power Generation from Massive Rockfall

William F. Kane[1], Joseph A. McElhany[1], Brian J. Forsthoff[1]

[1] KANE GeoTech, Inc., Stockton, California, USA

SUMMARY: Environmental concerns in the United States have created a renewed interest in small hydropower facilities. Many were constructed in the early part of the 20th Century. Large power companies found them too difficult to maintain economically for relatively small electricity production and sold them.

One such plant is in the rugged Kern River Canyon in Southern California. A 12-MW generator at the canyon mouth is powered by water which flows through a tunnel and penstock from a small check dam 1.2-km up the canyon.

Massive rockfall severely damaged the check dam and rendered it inoperable prior to sale. The new owner implemented measures to protect the workers and dam from rockfall. A protection system consisting of a rockfall attenuator, a debris flow/rockfall barrier, and a berm was constructed.

After construction, a rockfall event of an estimated 30,000-KJ struck the system. The dam and facility were protected but the system incurred damage. The most significant damage was to a support post on the attenuator which buckled under the load.

Repairs to the system included replacing the attenuator post with a 7.6-m high 1.8-m diameter steel pipe embedded 1.5-m into rock and increasing the berm height with the fresh rock debris.

Keywords: rockfall, attenuator, debris, barrier, berm

Introduction

In 1921, a 12-megawatt generator at the mouth of the canyon was constructed in Kern County, California, USA. It is downstream from a small intake diversion dam approximately 1-km up the canyon. The water flows through a tunnel and penstock to power the turbine in the plant.

The location of the intake dam has been subject to rockfall damage since it was first built, Figure 1. It was constructed at the bottom of a large rockfall chute along the Kern River. Between 1998 and 2011, there were several smaller, less than 2-m diameter, rockfall events. Bedrock in the canyon is granodiorite that is highly fractured due to the canyon's location on the Kern Canyon Fault (Brossy, et al., 2012). In 2017, a very large rockfall event occurred severely damaging the diversion dam and rendering it inoperative, Figure 2. The result was that the downstream generating plant could no longer function (Paulson, 2021).

Pacific Gas and Electric (PG&E) owned the facility until 2017 when it was determined that it was too difficult for a large utility to operate a small generating plant (12-MW). At that time, environmental concerns led to a renewed interest in small hydro power facilities and the facility was sold.

Rockfall Protection System

The priority of the new owner was to protect the workers during reconstruction and use the rockfall system to protect the dam in the future. Given the tremendous potential energy of the rock blocks, an innovative protection system consisting of a rockfall attenuator, a debris flow/rockfall barrier, and a berm to protect the facilities were implemented at the site (WSL, 2016; Kane, 2020).

The system was constructed in 2022. The attenuator was made of high-strength steel wire mesh, 60-m high and 55-m long. It was hung from 76-m long steel wire ropes that spanned the canyon and was supported on one side with a steel I-beam column. The rockfall barrier was 34-m long and 7.6-m high. It was held in place by 48 wire rope anchors grouted into rock. The berm was constructed of boulder material held together with steel wire mesh anchored into the subgrade. The berm was 46-m long, 6.1-m to 9.2-m wide, and 6.1-m high. Figures 3 and 4 are aerial views of the protection system.

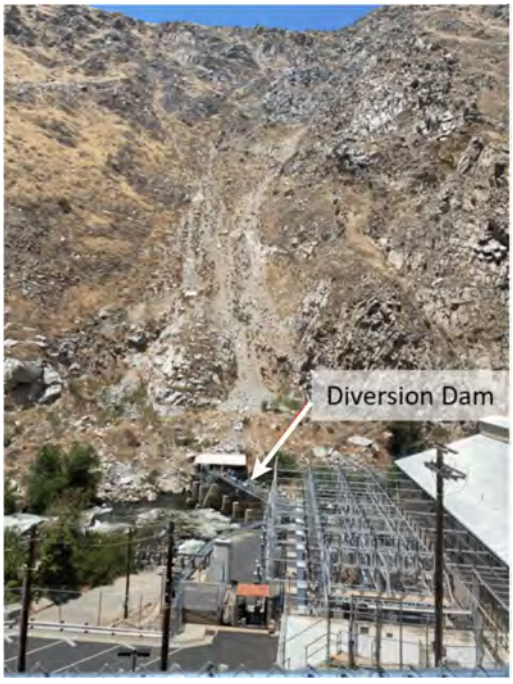

Figure 1. Diversion dam located at base of rockfall chute.

2022 Rockfall Event

In late 2022, the system was impacted by a tremendous rockfall event of extreme energy. It is likely that this rockfall/rockslide event contained even more damaging energy than the one which had destroyed the dam in 2017. The result, in this case, was reparable damage to the system but 100% protection of the dam and the intake.

Figure 2. Example of boulder from 2017 rockfall event.

Damage to the attenuator was caused by overloading the mesh resulting in buckling and collapse of the mid-canyon attenuator support post, Figure 5. The rockfall barrier subsequently was impacted and filled, Figure 6. Several brake rings were activated. Additional large blocks, unrestrained by the attenuator, were then able to bounce over the barrier and strike the berm with tremendous force, Figure 7.

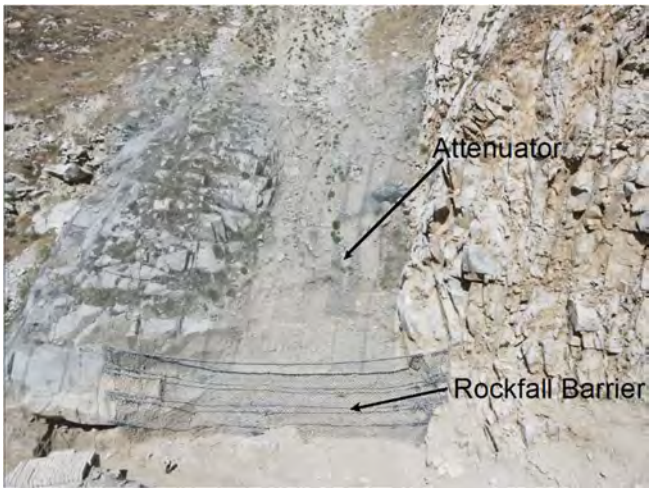

Figure 3. Aerial view of attenuator and rockfall protection barrier.

Despite the extreme magnitude of the rockfall/rockslide event the dam was fully protected and continued to supply uninterrupted flow to the downstream generating plant.

Repairs and Upgrades

Repairs/improvements to increase the resiliency of the system and prepare for future hydrologic conditions were made. These consisted of:

1. Repairing the attenuator and installing a robust steel reinforced, concrete support structure in place of the steel I-beam. The structure consisted of a 1.9-m diameter steel pipe embedded 1.8-m into rock and secured with two 6-m micropiles. A steel reinforcing cage was placed in the pipe and concrete poured into the pipe.
2. The height of the attenuator was increased by about 1-m.
3. The barrier was repaired by cleaning out the rock debris and replacing brake rings.
4. The berm heigh was increased and additional high-strength steel wire mesh was used to reinforce the structure.

Figure 4. Aerial view of entire rockfall protection system.

Figure 5. Attenuator mesh on ground after buckling of mid-canyon support post.

Conclusion

Extreme rockfall events may not always be contained but they can be mitigated, and infrastructure protected. Designed mitigation measures requires the ability to bring several rockfall protection tools into use. By combining systems to best suit the situation, protection and mitigation can be accomplished. However, it must be understood that systems may undergo damage even as they protect.

In Kern Canyon, the price of protection and subsequent repair was small compared to the ability to keep generating power.

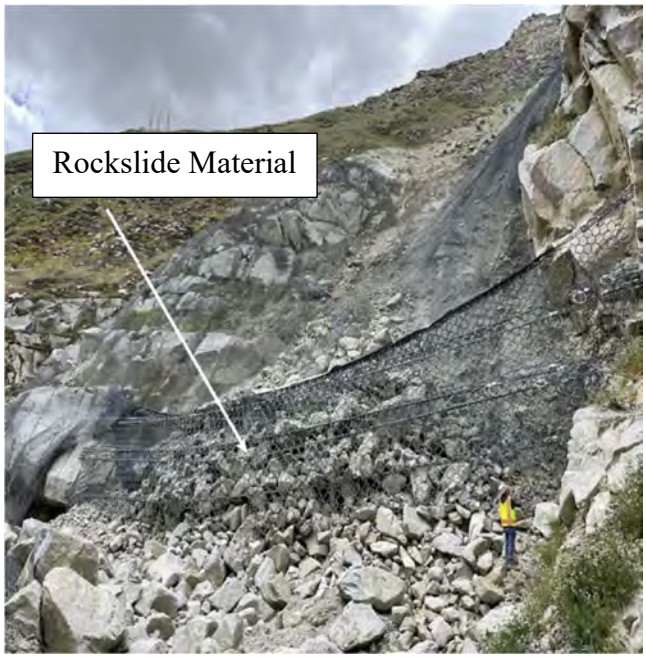

Figure 6. Barrier filled with rockfall and rockslide material.

Figure 7. Large 6-m boulder impacted on top of berm.

References

Brossy CC, Kelson KI, Amos CB, Baldwin JN, Kozlowicz B, Simpson D, Ticci MG, Lutz AT, Kozaci O, Streig A, Turner R, Rose R (2012) Map of the Quaternary active Kern Canyon and Breckenridge faults, southern Sierra Nevada, California. Geosphere 8, 3, pp. 581-591.

Kane WF (2020) Kern hydro rockfall mitigation, Kern County, California. *Report KGT20-17*, Sorenson Engineering, Inc.

Paulson LD (2021) Kern Canyon hydro sale finalized. *California Energy Markets* 1765.

WSL (2016) Debris flow protection systems for mountain torrents. *ISSN 2296-3456*. Swiss Federal Institute for Forest, Snow, and Landscape Research WSL. CH-8903 Birmensdorf, Switzerland.

Todstead landslide; investigation assessment and remediation

Fordham R [1], Daykin A[1].

[1] Atkins, Leeds, United Kingdom

Summary
Todstead landslide remediation is an example of an efficient design based on a reliable understanding of the ground conditions and with careful consideration of buildability and site constraints.

Keywords: artesian, Coquet Valley, remediation, pressure relief wells, steel sheet piles

Introduction

The section of the B6344 road which crosses the Todstead site has experienced continued failure of the slopes for over 30 years. The landslide is reported on the BGS Landside database (Landslide ID 19536) and recognised as an unstable site. This instability has resulted in cracking (Figure 1), deformation and settlement of the road which has required frequent resurfacing works to maintain serviceability of the B6344. This has been verified by intrusive investigations which have identified areas of bituminous road construction up to 6.0m thick.

Figure 1. Arcuate cracking within the B6344 following site works

The highway is owned by the local authority, Northumberland County Council (NCC), who initially commissioned Atkins in 2015 to undertake a geomorphological site walkover of the site and specify an intrusive ground investigation with an objective of monitoring slope failure. Following a number of years of monitoring and interpretation, NCC commissioned Atkins to undertake further ground investigation in 2021 to facilitate the design of a remediation scheme to stabilise the slope.

Site Constraints

The design and construction needed to account for site constraints. Firstly, the extents of the site are limited to the highway corridor which is only around 15m wide. As previously discussed, the site is prone to slope failure. Therefore plant movements, stockpiling and temporary works required diligent planning. To the south of the site is the River Coquet. The

river is classified as a Site of Special Scientific Interest (SSSI) owing to its species and habitat diversity. The design and construction had to satisfy environmental permitting requirements.

Ground Investigation

Three phases of ground investigation work were undertaken. The first phase was carried out in 2006 (prior to Atkins involvement) with the following two phases specified by Atkins in 2016 and 2021.

Phase 1 was a basic low-cost investigation comprising cable percussive boreholes and dynamic sampling, drilled from the highway. It provided a general indication of the ground conditions. However, it provided little information about the properties of the bedrock beneath the site, the groundwater and the position of the failure planes. This work was useful in supporting the design of the preliminary drainage improvements and for helping to design the second phase of investigation.

The aim of phase 2 was to determine the extent of movement (i.e., was it local to the road earthworks or was there a larger failure of the natural slope) and whether there was artesian water pressure. In total nine boreholes were formed using a combination of cable percussive methods followed by rotary coring into bedrock. Inclinometers and piezometers were installed. Inclinometers located within the road typically became unserviceable after 6-12 months due to excessive ground movement. This was acceptable, as proactive instrument monitoring commensurate to the rate of displacement had been undertaken to ensure adequate data about the depth of shear planes was obtained prior to becoming unserviceable. The instruments in the upper slope showed little movement. This indicated that the movement in the upper slope was limited to shallow movement associated with saturated near surface deposits.

In addition to slope displacement monitoring, understanding groundwater conditions across the site was crucial to understanding the slope failure mechanism. Especially due to the suspected artesian groundwater pressures (Figure 2). Vibrating wire piezometers (VWP) were selected to allow targeted monitoring of piezometric pressures within the slope.

Figure 2. An artesian groundwater strike during the 2016 GI

The phase 3 investigation was to address remaining unknowns about the ground conditions and thus facilitate an efficient and reliable remedial works design. This required investigation of the ground conditions between the road and the river. This had not been attempted previously due to the environmental constraints. However, when the decision had been made to use a piled retaining wall as a key component of the solution it became evident that a good knowledge of the ground conditions, in particular the depth of the slip plane, would be important factors in the design. To facilitate access to the floodplain area within the SSSI, drilling platforms were designed in collaboration with the GI contractor and environmental permitting organisations.

Drilling techniques were selected based on lessons learned during previous investigations. It had been difficult to recover in-tact specimens of the weak rock and the high artesian groundwater pressures had hindered progress and installation of instrumentation. Geobore S was selected as the preferred drilling method to recover high quality superficial and bedrock strata samples using the same rig. The vibrating wire piezometers were fully grouted using heavy grout weighted with barites. The heavy grout balanced artesian water pressures and simplified installation (Dunnicliffe, 1993). These were linked to data loggers to facilitate hourly monitoring. The instruments proved invaluable in quantifying the artesian water pressures as water levels observed during GI rose to such a height (+10m above ground level) that they could not be measured by conventional means. VWP installations were installed in arrays within boreholes to provide piezometric pressure profiles from the bedrock through the superficial deposits for later use in retaining wall design.

Ground modelling

Following completion of the 2016 ground investigation data was combined with observations from geomorphological mapping to produce a site wide ground model. The initial model shown as Figure 3 was refined as more monitoring data and the later third phase of GI was completed The question marks indicate where there were uncertainties, such as the depth of the slip planes in the ground between the highway and the river and whether or not the deep backscarp at the slope crest was associated with a current deep rotational failure, or if it was a remnant of historical movement. These questions were resolved following the third round of ground investigation and subsequent monitoring.

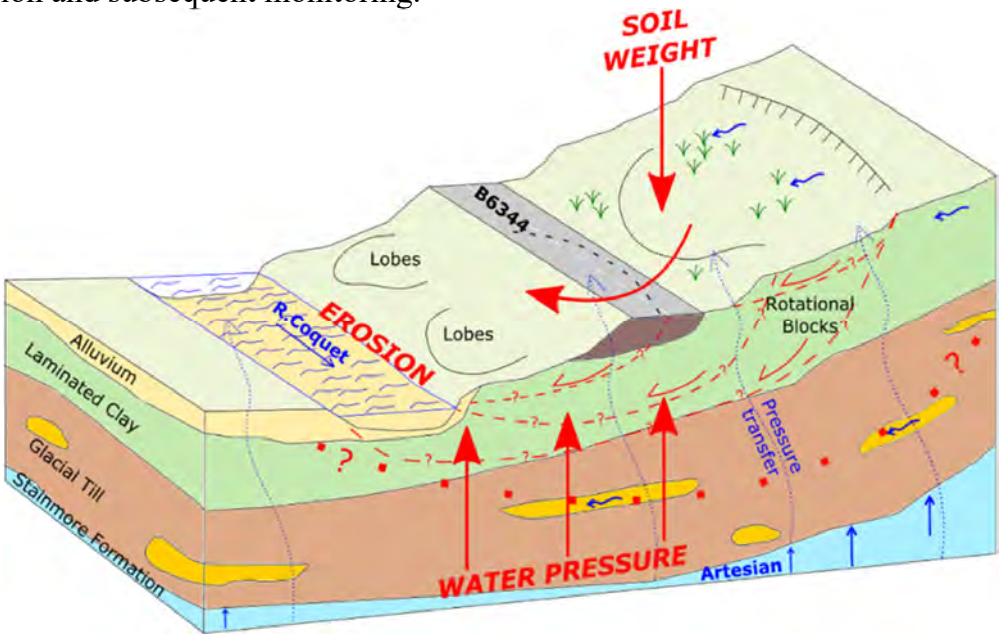

Figure 3. B6344 Todstead landslide ground model

General design approach

The main component of the design is the retaining wall which will provide lateral support to the highway. The wall was designed to comprise Z52 driven sheet piles (Figure 4), with lengths of up to 16.0m. The length was selected in order to provide sufficient lateral stability in the glacial till and the pile section was chosen to minimise deflection if the allowable ground-loss is realised in the future. The wall is reliant on the support of the adjacent downslope ground. As this ground has a history of instability the wall was designed to tolerate 2.5m of future ground loss on the downslope side. This value was derived based on and assessment of local geomorphology and slope analysis. Penetration of piles into the underlying sandstone was

Figure 4. Construction of the Z52 sheet pile wall with rigs advancing behind the wall as a temporary works measure

In addition to piling, pressure relief wells were installed to reduce the pore water pressure in the superficial deposits. These wells are located on upslope side of the road and have a response zone within the underlying Stainmore Formation bedrock. Our piezometer monitoring showed that the high artesian water pressure in the bedrock fed into the superficial deposits which formed the unstable slopes. Therefore, draining this pressure at its source is expected to improve the overall stability of the slope

Additional measures included shallow drainage in various locations around the site to reduce near surface pore water pressures and mitigate shallow slope failures. In addition, localised modification of the river bank was undertaken to improve slope stability by reducing the impact of localised erosion from the river. Brushwood is also included in the design as erosion mitigation along steepened areas of bank. For the river works, the design was a collaborative approach agreed with the Environment Agency which achieved the goal of improving slope stability whilst also improving the biodiversity value of the area.

Conclusion

Works undertaken at the Todstead site demonstrate the value of investing in thorough ground investigation and monitoring using carefully selected techniques. This approach resulted in cost effective and reliable slope remediation design. The project provides a case study for good practice when investigating landslides with valuable lessons learned during progressive phases of work.

References

British Standards, BS EN 1997-2:2007 Eurocode 7: Geotechnical design, 2007.

Dunnicliffe J (1993), Geotechnical instrumentation for monitoring field performance, *Whiley and Sons*, UK.

Gaba A, Hardy S, Doughty L, Powrie W, Selemetas D (2017), Guidance on embedded retaining wall design (C760), *CIRIA*, London.

Koe et al (2024). Natural slopes and landslides – condition, assessment, and mitigation (C810), *CIRIA*, London.

USACE (1992), Design, Construction, and Maintenance of Relief Wells, *US Army Corps of Engineers*, Washington D.C.

Rainfall induced slope failure prediction using finite element method: Evaluation based on physical model results

Fakher HAMROUNI[1], Mehrez JAMEI[1(*)]

[1] Tunis El Manar University, National Engineering School of Tunis, Civil Engineering Laboratory, Le Belvedere 1002 Tunis, Tunisia

(*) Corresponding author
Mehrez JAMEI
E-mail address: mehjamei@yahoo.fr

SUMMARY: The water infiltration in the soil is obviously governed by the unsaturated permeability and the water retention property. One of the practical common solutions used to avoid the negative effect of water infiltration on the slope stability is the coarse-soil drains. The drains govern the flow path and reduce the water pressure in the total volume of soil. This study provides understanding of the efficiency of drilled horizontal drains to stabilize the residual slope in a physical model. This has been conducted in relation to the water retention property of soil and coarse-soil drains. So, different types of soils characterized by their corresponding unsaturated permeability and water retention curve are considered. The unsaturated permeability and the water retention curves of the coarse grained soils, used as drains, are also introduced as parameters characterizing the local and overall response of the slope. A defined elastoplastic model as a function of the effective stress variables, was implemented in CODE-BRIGHT software. Results are presented in terms of displacement and analyzed considering the main parameters characterizing the water retention properties. The drain's efficiency is highlighted and optimized.

Keywords: Slope stability, drains, coarse grains soil, water retention, unsaturated permeability

Introduction

Climatic changes induce more and more rainfall intensity and temperature variations which lead to shallow and deep landslides (it was for example a case for the northwest of Tunisia). To avoid the shallow failure of slopes due to rainfall water infiltration, a network of coarse soil drains was implemented in the field. The network is formed by natural drains constituted by coarse granular material. In fact, initially the upper soil layers are in general unsaturated and the water-rainfall infiltration conducted to a transition between the unsaturated to saturated state leading to a dramatic decrease of suction (from the bottom to the upper layers). There are now some efficient unsaturated models which consider the suction as an independent variable (Jamei et al., 2015; Batali and Andreea, 2016; Qi and Vanapalli, 2018; Rahimi et al. 2010; Borja et al. 2012). So, the evolution of the suction as an independent variable or, for some other models, the evolution of degree of saturation, are considered as variables which are associated to the deformation of the unsaturated soil by elastoplastic flow-plastic rule. Since, the drains are classified as a hydraulic reinforcement technique and pointed out as an alternative to reduce the risk of the soil collapse, they are also defined as a warming solution from practical point of view and then for engineering design warming technique. Based on this fact, the proposed modeling of unsaturated slope was achieved based on data of physical slope models, designed

in two different laboratories, by using different identified soils. The two types of soils were characterized by the unsaturated permeability and the water retention. So, starting from the first stage of validation and calibration; the model was extended to investigate separately the role of the unsaturated properties of the fine soil and of the coarse granular soil or gravel used as lactated drains. A 2D finite element slope model with a blanket drain characterized by an equivalent permeability was considered in order to simulate a case of 3D geometry of drains used to dissipate the water pressure (characterized by the width and the depth). Based on the effective stress assumption (Laloui and Nuth, 2009), a simple formulation of a modified Mohr-Coulomb model which introduces the dependency of the cohesion on suction; is used in the modelling.

Modelling and results

1. Equivalent model of the coarse granular drains

Firstly, the relationship between the number of drains, the distance S between two successive drains and slope width B, is giving by the following equation:

$$S = \frac{B}{N-1} \tag{1}$$

where N is the number of horizontal drilled drains. Based on the previous condition, one finds a link between the blanket drain and the drilled drains characteristics:

$$Q_{blanket\ drain} = N \times Q_{drain} \tag{2}$$

Based on the Darcy's law, and by definition of length L, surface A and the hydraulic conductivity K, and under a difference of water pressure $\Delta u = \Delta u_w$, discharge through a coarse soil drain is giving by the following equation:

$$Q = \frac{K \times \Delta u \times A}{\rho_w \times g \times L} \tag{3}$$

where ρ_w(kg/m^3) is the water density ($\rho_w = 10^3$ kg/m^3) and g(m/s²) is the acceleration of gravity. Based on the Equations 1, 2 and 3, we obtain:

$$D = \frac{\pi d^2}{4} \frac{B+S}{B \times S} \frac{K_{drain}}{K_d} \tag{4}$$

where D is the blanket drain thickness in meter, d is the drilled drain thickness (m) in the case of square section, or the width of the equivalent blanket with the rectangular section. K_{drain} is drilled drain permeability (m/s) and K_d is the hydraulic conductivity of the blanket drain (m/s). According to the above equation, the characteristics of the blanket drain changes according to the drains number, drains square section thickness and slope width. Note that, the blanket drain permeability (equivalent parameter) was given when we select the coarse soil for drains (the gravel as an example).

2. Hydraulic unsaturated properties

We used the van Genuchten relation (van Genuchten 1980) represented by Equation 5 as follow:

$$S_e = \frac{S_r - S_{r\min}}{S_{r\max} - S_{r\min}} = \left(1 + \left(\frac{u_a - u_w}{P_0}\right)^{\frac{1}{1-\lambda}}\right)^{-\lambda} \tag{5}$$

where, P_0 represents the capillary pressure parameter, λ is a shape's parameter, S_{rmin} and S_{rmax} are the residual and the maximum degree of saturation, respectively. Table 1 summarizes the parameters of water retention of two tested soils. For the coarse granular drains, the same equation 5 was considered and the associated hydraulic properties are reported in Table 2.

Table 1. van Genuchten model parameters for both type of the considered soils

Soil type	λ	P (MPa)	S_{res}	S_{max}
Silty sand	0.40	4.0e-4	0.22	1.0
Ashes	0.60	9.0e-4	0.40	1.0

Table 2. The hydraulic parameters of the gravel blanket drain.

Parameter	van Genuchten parameters					Saturated permeability			
	λ	P (MPa)	n [-]	S_{rmax} [-]	S_{rmin} [-]	K_{sat} (m/s)	θ_s [-]	θ_s [-]	n [-]
Value	0.6	Variable	0.42	1.0	0.012	Variable	0.42	0.005	0.42

The chosen function to fit water relative permeability for all simulations for the silty sand was a generalized power function of a saturation degree (Y. Mualem, 1978), defined as follow:

$$k_{rw} = S_e^{\xi} \tag{6}$$

where S_e is the effective saturation and ξ is a material parameter ($\xi = 3$ is used for all simulations (Y. Mualem, 1978)). For the ashes soil, the variation of unsaturated permeability against suction was predicted using van Genuchten (1980)'s model, as given by Equation 7. Using associated water retention curve, van Genuchten equation was fitted based on experimental results. The water retention characteristic was obtained according the unsaturated laboratory tested (filter paper and osmotic methods (E. L. de almeida et al., 2015; Tiande Wen et al., 2020).

$$k_{rw} = \sqrt{S_e}\left(1-\left(1-S_e^{1/\lambda}\right)^{\lambda}\right)^2 \tag{7}$$

3. Mechanical shear properties

The mechanical Mohr-Coulomb failure criterion characteristic was modified as it is reported in Equation 8.

$$\tau = c' + (\sigma_n - u_a)\tan\phi' + (u_a - u_w)\tan\phi'\left(1+\left(\frac{u_a-u_w}{P_0}\right)^{\frac{1}{1-\lambda}}\right)^{-\lambda} \tag{8}$$

where σ_n is the total net stress, θ_w is the volumetric water content, θ_s is the maximum volumetric water content, θ_r is the residual volumetric water content, c' is the effective cohesion and ϕ' is the friction angle.

4. Main results

The results are presented here in terms of volumetric water flux during the time infiltration. Figures 1 and 2 give respectively the role of water retention property and the relative permeability (unsaturated permeability) of coarse granular drains.

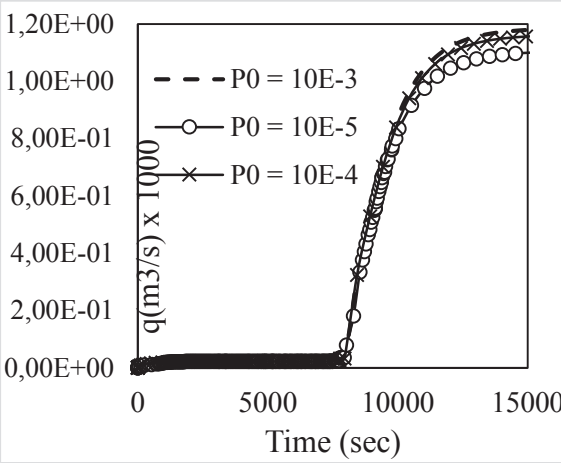

Figure 1: The role of the air entry suction of the coarse granular for drainage

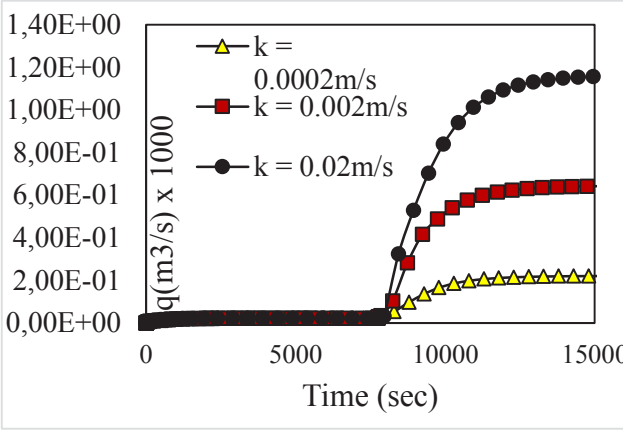

Figure 2: The role of permeability of the coarse granular for drainage

Conclusion

The elastoplastic model has been proposed and applied to simulate the role of the coarse granular soils to reinforce the slope and avoid the risk of failure. Previously the hydraulic properties of the soil have been taken into account. The proposed paper shows that the draining with coarse material is mainly governed by the permeability. However, the entry air suction, as one of main parameters of water retention property, has insignificant influence. Now, more results are expected from this study considering 3D geometry in order to consider the realistic disposition of the coarse-soil drains (gravel drains or ballast drains). The application of the proposed model for the case of geotextile and geocomposite drains is also expected.

References

Batali L, & Andreea C. (2016). Slope stability analysis using the unsaturated stress analysis: Case study. Procedia Engineering; 143: 284-291.

Borja R I, Liu X, & White J A (2012). Multiphysics hillslope processes triggering landslides. Acta Geotechnica; 7(4): 261-269.

Eurileny lucas de almeida, Adunias dos Santos Teixeira, Francisco Chagas da Silva Filho, raimundo Nonato de Assis Júnior and Raimundo Alípio de Oliveira Leão. (2015). R. Bras. Ci. Solo, 39 :1344-1352, 2015. DOI : 10.1590/01000683rbcs20140546.

Jamei M, Guiras H, Olivella S. (2015). Analysis of slope movement initiation induced by rainfall using the Elastoplastic Barcelona Basic Model. European journal of environmental and civil Engineering 2015. http://dx.doi.org/10.1080/19648189.2014.996670.

Laloui L, Nuth M. (2009) On the use of the Generalized effective stress in the constitutive Modeling of unsaturated soils. Computers and Geotechnics 2009; 36: 20-23, DOI: 10.1016/j.compgeo.2008.03.002.

Y. MUALEM (1978). Hydraulic Conductivity of Unsaturated Porous Media' Generalized Macroscopic Approach. Water Resources Research, vol. 14, No. 2; 1978. Paper number 7W 1118. 0043-1397/78/027W- 1118503.00.

Qi Shunchao, & Vanapalli Sai K (2018). Simulating hydraulic and mechanical responses of unsaturated expansive soil slope to rainfall: case study. International Journal of Geomechanical; 18.

Rahimi A, Rahardjo H, & Leong E C. (2010). Effect of hydraulic properties of soil on rainfall-induced slope failure. Engineering Geology; 114:135-143.

Tiande Wen, Longtan Shao, Xiaoxia Guo, Yanru Zhao. (2020). Experimental investigations of the soil water retention curve under multiple drying–wetting cycles. Acta Geotechnica (2020) 15:3321–3326. https://doi.org/10.1007/s11440-020-00964-2.

Modeling Progressive Slope Failure with the Rock Discrete Fracture Analysis Method

Bin Gong[1], Tao Zhao[1], Yongjun Zhang[2], Liwei Zhang[2]

[1] Brunel University London, London, UK
[2] Qingdao University of Technology, Qingdao, China

SUMMARY: Based on the continuum mechanics, statistical strength theory, and contact theory, the rock discrete fracture analysis (RDFA) method can model the continuous-discontinuous deformation of rock masses, including fracture and fragmentation. RDFA can effectively capture the initiation and propagation of zero-thickness cracks by dynamically adjusting nodes at crack tips while adhering to the Mohr-Coulomb criterion with a tensile cut-off. Meanwhile, RDFA can accommodate the inherent heterogeneity of rocks and therefore consider localized damage and fine crack propagation simultaneously. Then, it was applied to evaluate the failure characteristics of the rock slope at the Anshan Road station of the Qingdao metro in China. The results show that under the influence of the joints with orientation of 60° and spacing of 5m, the significant stress concentration first appears at the slope toe. Then, the local tensile damage occurs at the upper part, forming the sliding surface. During the mass movement, more blocks collide and compress with each other, leading to the continuous failure of the sliding body. Furthermore, the tunnel excavation can affect the fragmentation degree of the sliding masses. Additionally, when the intermittent joints exist, the progressive instability is mainly triggered by the local failure at the lower part of the slope.

Keywords: slope failure, rock fracture, continuous-discontinuous modeling, discrete element method, adaptive nodal updating

Introduction

Slope stability analysis presents a persistent challenge in the field of rock engineering, primarily due to the threat of slope slides characterized by the rapid mass movement. Rock masses inherently possess a discontinuous nature, featuring multiple joints and fractures (Hudson and Harrison, 1997). In terms of slope stability, the key discontinuities do not persist indefinitely in reality. Instead, slope failure necessitates the rupture of intact rock bridges (Terzaghi, 1962; Einstein *et al*., 1983). The rock failure process analysis (RFPA) (Tang, 1997) can effectively model the initiation, propagation, and coalescence of cracks in rocks. However, it is not well-suited for simulating the interactions of discrete blocks. The discrete element method (DEM) (Cundall, 1971) offers valuables insights in capturing the fracture geometry of rock masses. However, DEM is often constrained to single-scale analyses and is time-consuming, particularly when dealing with large-scale problems featuring complex fracture networks.

In this study, the rock discrete fracture analysis method (RDFA) was employed by integrating elements from both the RFPA and DEM methods, to assess the failure characteristics and instability patterns of the rock slope located at the Anshan Road station of the Qingdao metro construction in China. Furthermore, the effectiveness of RDFA in modeling slope sliding was discussed, including the key processes involving crack initiation, propagation, coalescence, and mass movement.

Methodology

The heterogeneity of rock masses can greatly affect their nonlinear deformation and progressive failure. To consider the influence of rock heterogeneity, the material parameters of elements are assumed to obey the Weibull distribution (Weibull, 1951) as follows:

$$f(x) = \frac{p}{x_0}\left(\frac{x}{x_0}\right)^{p-1} exp - \left(\frac{x}{x_0}\right)^{p} \quad (1)$$

where x is a specific mechanical property of elements; x_0 is the mean value of x; p (where $p > 1$) is the homogeneity coefficient that reflects the shape of the probability density function.

Besides, the Mohr-Coulomb failure criterion with a tensile cut-off is applied as follows:

$$\sigma_{c0} \leq \sigma_1 - \frac{1+\sin\varphi}{1-\sin\varphi}\sigma_3 \quad \text{and} \quad \sigma_3 \leq f_{t0} \quad (2)$$

where φ and σ_{c0} are the internal friction angle and uniaxial compressive strength. f_{t0} is the uniaxial tensile strength. σ_1 and σ_3 are the major and minor principal stresses, respectively.

Results

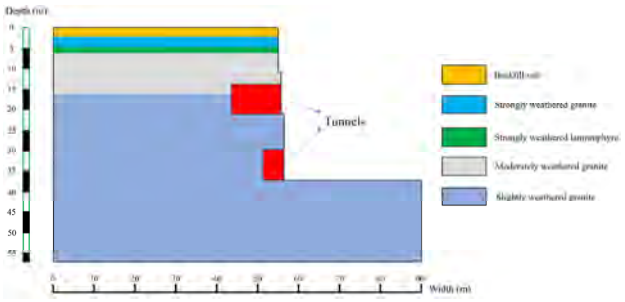

Figure 1. The slope size of the Anshan Road station of the Qingdao metro in Qingdao City, China

Based on the actual geological conditions (Figure 1), the numerical model was established. The model size was 90m×57.2m, with a slope whose height was 37.2m. After the slope excavation, two tunnels were excavated. The sizes of the upper and lower tunnels were 7.7m×10.7m and 8.5m×5m, respectively. The mechanical parameters of the rock masses are listed in Table 1.

Table 1. Mechanical parameters of different rock materials

Rock formation	Density (g/cm^3)	Elastic modulus (MPa)	Poisson's ratio	Cohesion (MPa)	Internal friction angle(°)	Uniaxial tensile strength (MPa)	Homogeneity coefficient
Backfill soil	1.8	35	0.22	3	28	0.8	3
Strongly weathered granite	2.4	45	0.23	5	28	1	3
Strongly weathered lamprophyre	2.4	50	0.23	10	35	2	3
Moderately weathered granite	2.6	10000	0.28	30	40	3	3
Slightly weathered granite	2.62	60000	0.12	50	45	5	6

The on-site monitoring data shows that the dip angle of the joints inner the slope changes from 60° to 80°. When a set of joints with the orientation of 60° and spacing of 5m exist, the sliding failure occurs after slope excavation, as shown in Figure 2 (a)-(c). Figure 2 (a) indicates that a

significant stress concentration first appears at the slope toe, and the local tensile damage also occurs at the upper part, forming a potential sliding surface. Then, the slope undergoes downward sliding, during which more elements collide and compress with each other, leading to the continuous failure of the sliding body. Finally, the whole slope is destroyed. Figure 2 (d) shows that after excavating the upper tunnel, crack initiation first appears at the upper rock layer. As the high stresses gradually accumulate, the local sliding failure occurs inside the slope, and the degree of rock fracture is greater than the previous scenario. Finally, the fractured rock masses cover a large area at the bottom of the slope (Figure 2 (f)). Figure 2 (g) shows that when the lower tunnel is excavated, the significant stress concentration first appears at the lower-left corner of the tunnel. As the sliding surface gradually forms, the slope undergoes the overall sliding failure, and the rock inside the sliding body is relatively intact. Besides, the volume of the sliding body is greater than the other two scenarios. In addition, Figure 2 indicates that the area of slope failure doesn't simply equal to the stress concentrated area. Meanwhile, under the influence of 60° joints, the slip failure can be caused by the small stress concentrations.

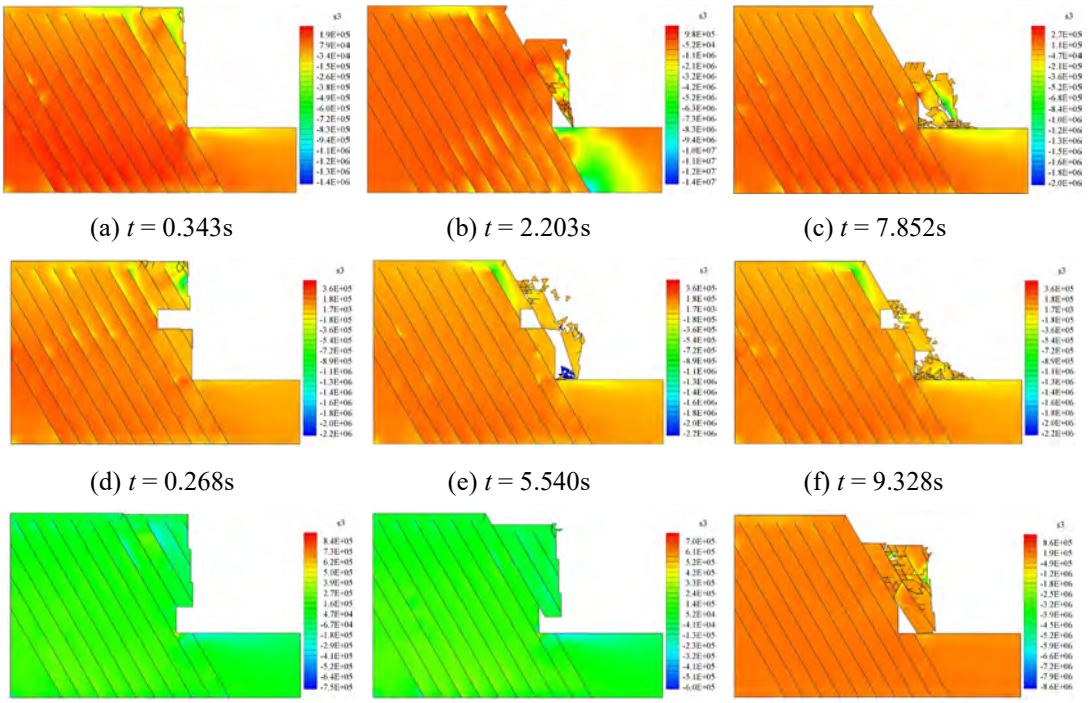

(a) t = 0.343s (b) t = 2.203s (c) t = 7.852s

(d) t = 0.268s (e) t = 5.540s (f) t = 9.328s

(g) t = 0.360s (h) t = 1.362s (i) t = 2.691s

Figure 2. The failure processes of the slopes containing joints with dip angle of 60°: (a)-(c) without tunnels; (d)-(f) with the upper tunnel; (g)-(i) with the lower tunnel indicated by the minor principal stress contours (Unit: Pa)

Figure 3 (a)-(b) shows the progressive slope failure caused by the gradual strength reduction when there are four parallel intermittent joints inside the slope body. Firstly, as the strength reduction proceeds, several micro-cracks occur at the lower part. Then, the lower cracks gradually develop upward and penetrate at the upper joints. Furthermore, the local instability at the bottom of the slope causes the rock mass to slide down along the joints. As the strength reduction proceeds, the cracks in the middle part gradually penetrate, resulting in the overall instability of the slope. Figure 3 (c)-(d) shows the progressive slope failure caused by the gradual strength reduction when there are four direction-changing intermittent joints inside the slope body. At the beginning of strength reduction, some cracks first appear at the end of the lower joints. As the strength reduction progresses, the cracks gradually develop, and more cracks appear at the upper jointed area. Then, the internal cracks in the rock mass further penetrated, which destroys the integrity of the rock masses and causes the local rock mass to

slide. During the sliding process, the rock masses are further broken into smaller pieces. Finally, the entire slope loses stability. Consequently, when there are the intermittent joints, the lower part of the slope is prone to firstly produce damage, leading to the final slope instability.

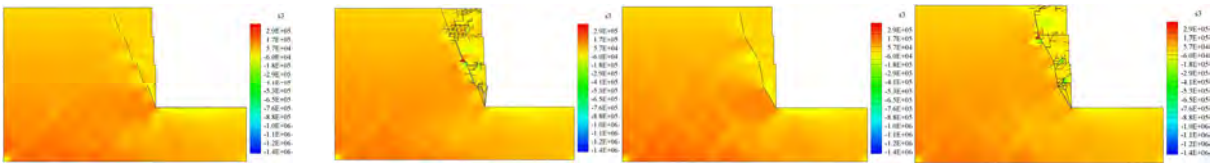

(a) t = 0.020s (b) t = 0.466s (c) t = 0.020s (d) t = 0.274s

Figure 3. The failure characteristics of the slopes containing: (a)-(b) parallel intermittent joints and (c)-(d) direction-changing intermittent joints indicated by the minor principal stress contours (Unit: Pa)

Conclusions

(1) Based on the continuum mechanics, statistical strength theory, and contact theory, the RDFA method offers a comprehensive approach to model the continuous-discontinuous deformation of rock masses. RDFA excels at simulating the initiation and propagation of zero-thickness cracks through its dynamic node adjustments at crack tips, adhering to the Mohr-Coulomb criterion with a tensile cut-off. Furthermore, RDFA possesses the flexibility to account for the inherent heterogeneity of rocks, allowing for the concurrent consideration of localized damage and the propagation of fine cracks.

(2) The failure characteristics and instability patterns of the rock slope at the Anshan Road station of the Qingdao metro in China was investigated by RDFA. Due to the presence of joints with an orientation of 60° and a 5-meter spacing, the significant stress concentration initially occurs at the slope toe. Subsequently, the tensile damage happens at the upper part of the slope, resulting in the formation of a sliding surface. As the mass movement continues, more blocks collide and compress with one another, leading to the progressive slope failure. The excavation of the tunnels has a notable impact on the fragmentation degree of the sliding masses. Furthermore, when the intermittent joints are present, the primary trigger for the progressive slope instability is identified as the localized failures occurring at the lower part of the slope.

Acknowledgements

This study was supported by the UK Engineering and Physical Sciences Research Council (Grant No. EP/V028723/1) and the UK Research and Innovation (Grant No. EP/Y02754X/1).

References

Cundall PA (1971) A computer model for simulating progressive large scale movements in blocky rock systems. *Proceedings of the symposium of the International Society for Rock Mechanics (ISRM)*. Nancy, France.

Einstein HH, Veneziano D, Baecher GB & O'Reilly KJ (1983) The effect of discontinuity persistence on rock slope stability. *International Journal of Rock Mechanics and Mining Sciences* 20(5), 227–236.

Hudson JA, & Harrison JP (1997) *Engineering rock mechanics: An introduction to the principles*. Pergamon, Oxford, U.K.

Tang CA (1997) Numerical simulation of progressive rock failure and associated seismicity. *International Journal of Rock Mechanics and Mining Sciences* 34(2), 249–61.

Terzaghi K (1962) Stability of steep slopes on hard unweathered rock. *Géotechnique* 12, 251–270.

Weibull W (1951) A statistical distribution function of wide applicability. *Journal of Applied Mechanics* 18, 293–297.

Development of a elasto-viscoplastic model to simulate the solid-fluid transition: application to mudflows on the Vaches Noires cliffs, Normandy, France

M. Kouah[1,5], H. Tran[2], F. Nicot[3], A. Wautier[4], Y. Thiery[1], O. Maquaire[5]

[1] Bureau de Recherches Géologiques et Minières (BRGM), Pessac, France
[2] Itasca Consultants, 29 Ave. Joannès Masset, 69009 Lyon, France
[3] Université Savoie Mont-Blanc, Laboratoire ISTerre - UMR CNRS 5275, Campus scientifique - Bat 8B, 73376 Le Bourget-du-Lac cedex, France
[4] INRAE, Université Aix-Marseille, UR RECOVER, 3275 Rte Cézanne, CS 40061, 13182, Aix-en-Provence Cedex 5, Marseille, France
[5] NORMANDIE UNIV, UNICAEN, CNRS, IDEES, 14000 Caen, France

SUMMARY: An elasto-viscoplastic model has been developed to simulate the solid-fluid transition by coupling two constitutive regimes: Modified Cam-Clay model (MCC) for the elasto-plastic behavior and Hershel-Bulkley rheological model (HB) for the viscous behavior. The second-order work criterion has been used to describe the solid-fluid transition. The model was applied to mudflows affecting the Vaches Noires cliffs (Normandy, France).

Keywords: elasto-viscoplastic modeling, mudflows, solid-fluid transition

Introduction

Numerical modelling of landslides evolving into mudflows (Cruden and Varnes 1996) requires to take into account the solid-fluid transition of geomaterials (Coussot and Ancey 1999; Prime 2012; Prime and Dufour 2013; Li *et al.* 2016) as these phenomena combine an initiation phase, transport and propagation, and a cessation phase (Fort *et al.* 2015). Each phase corresponds to a material state that can evolve from solid to fluid, and finally turns back to solid. For the movement initiation phase, the behavior of these materials is described by elasto-plastic behavior laws within the framework of soil mechanics (Magnan and Mestat 1997; Darve and Sibille 2016). However, these geomaterials may liquefy, leading to a viscoplastic flow. In such conditions, they are described by fluid rheology (a branch of mechanics concerned with non-elastic solids and complex non-Newtonian fluids) via viscoplastic behavior laws (Balmforth and Craster 2001; Prime and Dufour 2013; Li *et al*.2016; Han *et al*. 2019). These phase transformations are complex because they are non-linear over time. A slow-creep landslide may suddenly accelerate under the effect of precipitation, or remain unchanged after the same rainfall event.
Numerical modeling of these geomaterials requires a constitutive law that adapts to variations in material characteristics. It should be able to accurately describe the material in the different states, solid and fluid, as well as the transition between these two states. There are few models that consider both the elasto-plastic behavior of solid soils (quasistatic regime) and the viscous behavior of fluidized soils (flow regime), as well as the transition between the two regimes. A notable achievement was obtained with the work of Prime in 2012, who proposes a model combining these two behaviors, enriched with a transition criterion based on the second-order work computation (Hill 1958; Prime 2012; Prime and Dufour 2013).
During the initiation phase, the behavior of these materials is described by an elasto-plastic relation within the framework of soil mechanics. When these materials fluidize and give way

to mudflows, their behavior is determined by fluid rheology, through viscoplastic constitutive relations. These state transitions are intrinsically complex, as they evolve non-linearly over time.
Our aim was to develop an operational tool to model numerically the solid-fluid transition using the commercially available software package, *FLAC* 8.1. This tool integrates two constitutive models: Modified Cam-Clay (MCC) model for the elasto-plastic behavior and Hershel-Bulkley (HB) rheological model for the viscous behavior. The solid-fluid transition is detected by using the second-order work criterion. It should be noted that this numerical development is not designed to simulate propagation in the strict sense.

Modeling strategy

The FLAC 8.1 software, based on the finite-difference method, was selected. This method explicitly solves local problems step by step. It is popular for its ability to handle large-scale problems and for optimizing calculation time. In addition, FLAC software makes parametric studies easy thanks to its FISH scripting language. It also offers a wide range of elastoplastic behavior laws (e.g., Modified Cam Clay), and enables calculations with advanced hydromechanical coupling, adaptable to the user's needs (Cundall et al. 1993).
Since the behavior laws must manage instantaneous elasto-plastic deformations as well as viscous deformations, with a transition criterion between these two behaviors, the following numerical strategy was adopted (Fig. 1):

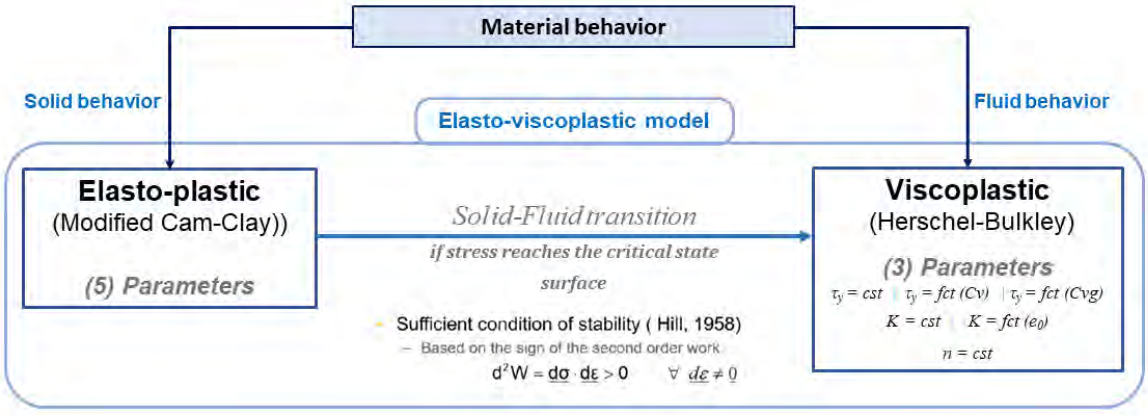

Figure 1. Diagram of the new constitutive model of elasto-viscoplastic behavior.

Elasto-plastic behavior law: Modified Cam-Clay model (MCC), with work-hardening adapted to the modeling of remolded clay materials (Mestat and Riou 2002);
Viscous behavior law: Hershel-Bulkley (HB) rheological model, which is the most widely used model for describing mudflows. It also offers the possibility of using evolving parameters, to cover the change in rheological parameters as a function of volume concentration and grain size distribution (Pellegrino and Schippa 2018);
Solid-fluid transition criterion: it was desirable to use the second-order work criterion as the phase transition criterion (Hill 1958). However, since the Cam-Clay model is an associated model, the second-order work criterion (W_2) coincides with the boundary plasticity criterion.

The constitutive model was implemented as an user-defined model in the *FLAC* software. Consolidated-drained triaxial tests were carried out on samples to calibrate the constitutive parameters.

Results

In order to simulate the landslide event, it is necessary to determine as accurately as possible the period of the event, and establish the relevant hydrogeological conditions. This requires information on the water table variation on the slope and within the flow, as well as on precipitation variation. In addition, the event was characterized by assessing displacements and initial flow velocities. The geometric model of the selected flow together with the hydraulic conditions are illustrated in Figure 2.A.

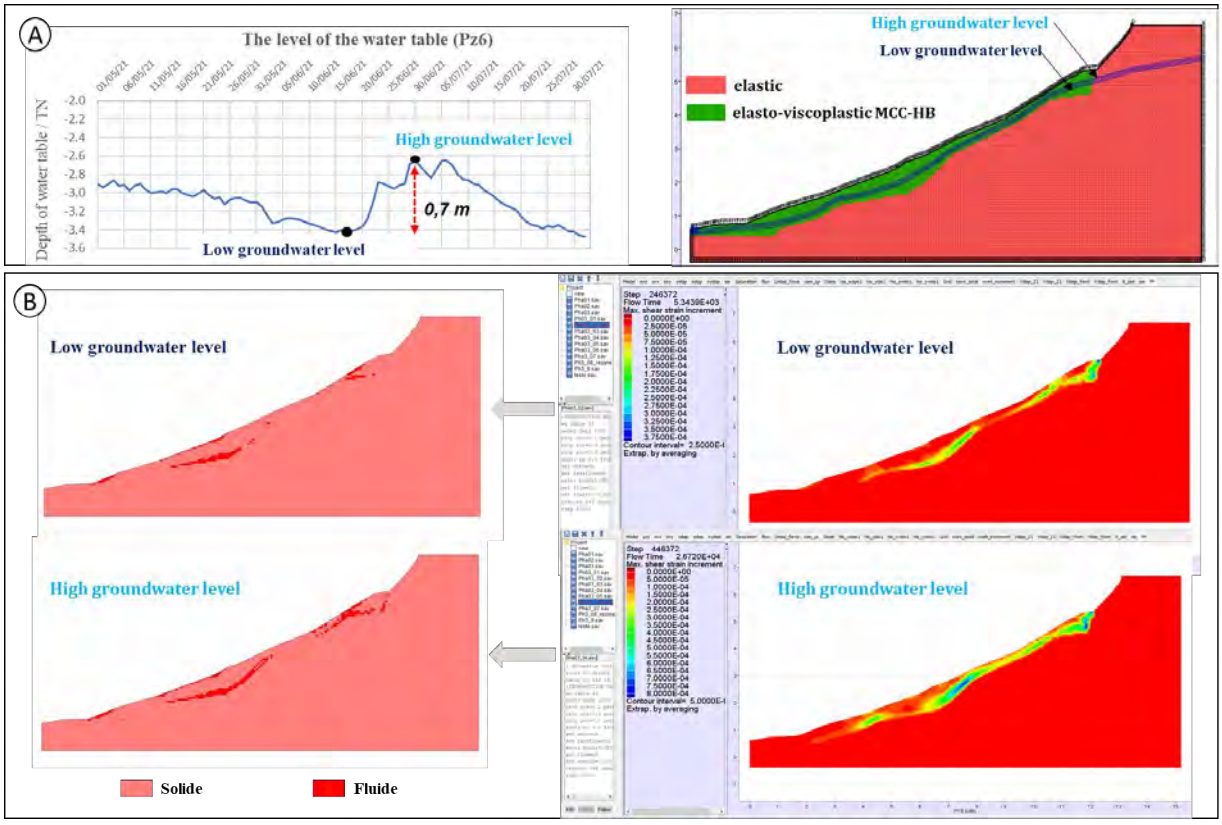

Figure 2. Application of solid-fluid transition modelling; A (left) Variation in water table level in the slope, represented by Pz6; A (right) Geometric model and introduction of hydraulic conditions; B (left) Solid-fluid transition in the flow with increasing water table level; B (right) Evolution of maximum shear strain in the flow with changing water table.

The initial stress state within the slope should be reproduced. Then, the hydraulic conditions were specified. Hydromechanical calculations were then performed, considering the evolution of the water table. The creep calculation was activated using the HB model.

Figure 2.B shows the transition between the solid and fluid regimes, under the control of the variations in hydraulic conditions. As the water table evolves, certain zones of the flow undergo a phase transition from solid to liquid. They transition from an elastoplastic regime, where the constitutive behavior is described with the MCC model, to a time-dependent viscous regime, where the constitutive behavior is described with the HB model. These transitions become increasingly pronounced with the evolution the groundwater inside the mudflow.

Discussion - conclusion

Numerical modeling of the solid-fluid transition using this new approach has overcome the limitations of viscous models, which present challenges in correctly representing solid behavior

(Prime et al. 2014). This approach adequately describes the solid behavior with instantaneous elastoplastic deformations, as well as the fluid behavior with time-dependent viscous deformations. This implementation has been successfully carried out on in the *FLAC* software (based on a Lagrangian approach), which is widely recognized within the geomechanics community. The aim is to ensure that these developments can be used in geotechnical engineering situations, providing an advanced modeling to better understand the behavior of geomaterials after the failure phase. However, in the context of this initiative, our model is incapable of detecting solid-fluid transitions that may occur before reaching the failure criterion, highlighting the need for a non-associated elastoplastic model with W_2 as the transition criterion. Moreover, the model is limited to only considering the initial phase of the solid-fluid transition, without the ability to handle the reverse transition fluid-solid. This limitation restricts our ability to track displacements and model the evolution of the mudflows. It should also be noted that this numerical tool is not designed to simulate the propagation *stricto sensu*, as this requires additional numerical methods based on hybrid approaches (Eulerian / Lagrangian) such as MPM (Material Point Method), FEMLIP (Finite Element Method with Lagrangian Integration Points), etc. (Sulsky and Schreyer 1996; Dufour 2005; Prime and Dufour 2013; Vicari *et al.* 2022).

References

Cruden DM, Varnes DJ (1996) Landslides: investigation and mitigation. *Chapter 3-Landslide types and processes*. Transp Res Board Spec Rep.

Coussot P, Ancey C (1999) Rheophysical classification of concentrated suspensions and granular pastes. Phys Rev E 59:4445-4457. https://doi.org/10.1103/PhysRevE.59.4445.

Prime N (2012) Modeling the solid-fluid transition in geomaterials: application to landslides. *Phd thesis*, University of Grenoble.

Prime N, Dufour F (2013) Unified Model for Geomaterial Solid/Fluid States and the Transition in Between. *J Eng Mech*. https://doi.org/10.1061/(ASCE)EM.1943-7889.0000742.

Li Z, Dufour F, Darve F (2016) Hydro-elasto-plastic modelling with a solid/fluid transition. *Comput Geotech* 75: 69-79. https://doi.org/10.1016/j.compgeo.2015.11.009.

Fort M, Bétard F, Arnaud-Fassetta G (2015) Chapter 4 - Ground movements. In: *Géomorphologie dynamique et environnement*. Armand Colin, Paris, pp 133-180.

Magnan J-P, Mestat P (1997) Lois de comportement et modélisation des sols. Ed. *Techniques Ingénieur.*

Darve F, Sibille L (2016) Models of elasto-visco-plastic behavior of geomaterials. *Mécanique Sols Géotechnique.* https://doi.org/10.51257/a-v2-c218.

Balmforth NJ, Craster RV (2001) Geophysical Aspects of Non-Newtonian Fluid Mechanics. In: Balmforth NJ, Provenzale A (eds) Geomorphological Fluid Mechanics. *Springer Berlin Heidelberg*, Heidelberg, pp 34-51.

Han Z, Su B, Li Y, et al (2019) Numerical simulation of debris-flow behavior based on the SPH method incorporating the Herschel-Bulkley-Papanastasiou rheology model. *Eng Geol* 255:26-36.

Hill R (1958) A general theory of uniqueness and stability in elastic-plastic solids. *J Mech Phys Solids* 6:236-249. https://doi.org/10.1016/0022-5096(58)90029-2.

Cundall P, Coetzee M, Hart R, Varona P (1993) FLAC user's manual. Itasca Consult Group USA.

Mestat P, Riou Y (2002) Modélisation des sols et des ouvrages avec le modèle Cam-Clay modifié. *Rev Fr Génie Civ* 6:801-815. https://doi.org/10.1080/12795119.2002.9692404.

Pellegrino AM, Schippa L (2018) A laboratory experiment on the effect of grains concentration and coarse sediment on the rheology of natural debris-flows. *Environ Earth Sci* 77:749. https://doi.org/10.1007/s12665-018-7934-0.

Prime N, Dufour F, Darve F (2014) Solid-fluid transition modelling in geomaterials and application to a mudflow interacting with an obstacle. *Int J Numer Anal Methods Geomech* 38:1341-1361. https://doi.org/10.1002/nag.2260.

Sulsky D, Schreyer HL (1996) Axisymmetric form of the material point method with applications to upsetting and Taylor impact problems. *Comput Methods Appl Mech Eng* 139:409-429.

Dufour F (2005) Finite element method with Lagrangian integration points-MEFPIL, Troyes.

Vicari H, Tran QA, Nordal S, Thakur V (2022) MPM modelling of debris flow entrainment and interaction with an upstream flexible barrier. *Landslides* 19:2101–2115. https://doi.org/10.1007/s10346-022-01886-8.

The Use Of Finite Element Analysis (FEA) To Assess The Efficiency Of Common Road Restraint Systems Impacted By Falling Boulders: A Case Study In Wallonia (Belgium) – XIVth ISL, Chambéry 2024

Jeffrey Himpe[1], Florian Duyckaerts[1], Joseph Marra[1], Simon Delvoie[2]

[1] GDTech Engineering, Liège, Belgium
[2] Direction de la Géotechnique, Service Public de Wallonie – Mobilité et Infrastructures, Liège, Belgium

SUMMARY: This study investigates different safety barriers made of steel and concrete as a mean to protect the road users from rockfalls. Different configurations and test conditions are assessed through Finite Element Analysis.

Keywords: rockfall, road safety barrier, LS-DYNA, simulation, Finite Element Analysis

Introduction

Rockfalls

Regional roads in Wallonia (Belgium) are frequently faced with rock instabilities. These are mainly located into river valleys. Common rockfall protection barriers are made of anchors, posts, interception nets, cables and possibly brakes. These systems allow to free up floor space but are usually expensive to install and maintain.
The majority of rockfalls reaching roads in Belgium consists of boulders or rock masses with a limited mass (< 500 kg) and a limited energy (< 50 kJ).
For these levels of energy, roads can properly be protected against these limited rockfalls with traditional road safety barriers. However, these barriers are not designed to specifically resist to rockfall impacts and intercept boulders. The main issue lies in that the impact is frontal and thus more localized, on the rear side of the barrier while vehicle impacts are assessed with an angle up to 20 degrees.

Road safety barriers

Road safety barriers are designed to save lives by safely retaining vehicles on the road in case of an accident. These barriers must be developed and tested in accordance with the EN 1317 for the European market and the MASH for the US market. The EN 1317 has established different containment levels determining the amount of impact energy it can sustain. Each containment level requires to conduct two tests, one with a heavy vehicle (bus, truck) to assess the resistance and deformation of the barrier, the other with a light vehicle (car) to assess the severity of the impact (decelerations). For all the tests, the barriers must redirect the vehicles smoothly (no rollover) on the road while passing into a so-called “Exit Box” ensuring that the angle of redirection remains small.
There are two main types of barriers: steel barriers and concrete barriers. Steel barriers are generally softer and allow a smoother redirection of the vehicle and smaller severity values. On the other hand, the deformations of steel barriers imply certain costs for the replacement of the damaged components. Concrete barriers are stiffer and cause the severity values to be higher but almost never have to be replaced.

Methodology

Knowing the threat of rockfalls and the purpose of safety barriers, it was decided to merge both worlds to assess how the safety barriers could help protect people also from rockfalls. The idea was to use the Finite Element Analysis using LS-DYNA to perform this assessment.
The use of FEA to assess safety barriers is quite commonplace. There is even a European Standard dedicated to this topic, the EN 16303. This Standard establishes criteria and recommendations to have a well-built numerical model as well as consistent, stable and robust results. This Standard is mainly used in the frame of numerical validations consisting in building a numerical model able to correctly reproduce a physical crash test. For a numerical model to be considered as validated, the global behavior of the simulation must match the real crash, the numerical results must lie within specific tolerances compared to the physical ones and the energy balance must be correct, i.e. the energy conservation laws must be respected.
The main purpose of the numerical validation is to use the validated model as a reference for a modification assessment. In a good number of European countries, it is accepted to obtain a certification for a modified product based on the simulation report only, given that it is coming from a validated model.

The rock is modelled with a shape and proportions in accordance with EAD 340059-00-0106 comparable to test equipment used for falling rock protection kits.
The following mechanical properties of common sedimentary rocks from Wallonia are used:

- Density: 2500 kg/m³;
- Young's modulus: 50000 MPa;
- Poisson coefficient: 0.3.

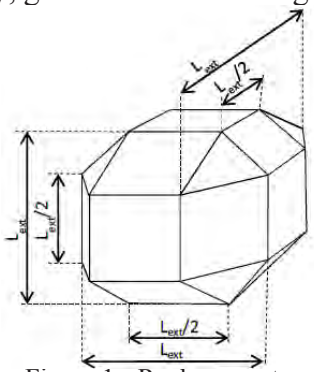

Figure 1 - Rock geometry

The external length (L_{ext} in the Figure 1) is chosen as a parameter to adjust the mass and, therefore, the kinetic energy of the impact.

In this study, one steel barrier and two concrete barriers are assessed as a protection system against rockfalls through a total of 20 simulations. The chosen investigated barriers correspond to commercialized and certified barriers on the regional market. The numerical models of these barriers have already been validated by GDTech. For steel barrier, most of the components are modelled using first order shell elements with a 15mm-characteristic length which have enough accuracy and are time efficient compared to solid elements. For concrete systems, first order hexahedron solid elements have been used with a 30mm-characteristic length.
The investigated barriers are considered as satisfying for boulders interception if the three following conditions are carried out. These conditions are defined arbitrary to have limited consequences for road user safety after boulder impact:

- They maintain the boulder behind the barrier;
- The permanent deflection of the barrier is lower than 500 mm;
- There is no toppling or tearing of main barrier elements.

Assessment of steel barriers

The steel barrier (barrier 1) used for the assessment is tested in three different configurations:

- Barrier 1 + Motocycliste Protection System (MPS);
- Barrier 1 + double-sided Motocycliste Protection System;
- Double-sided barrier 1 + double-sided Motorcyclist Protection System.

The total length modelled for the assessment is 48 m. The influence of several parameters are analyzed:

- Impact point (on the main rail, on the MPS, from the front and from the back);
- Boundary conditions (fixed or free extremities);
- Impact energy (ranging between 10 and 40 kJ).

Regarding the impact (kinetic) energy, the impact speed is always maintained to 14 m/s and the rock mass is progressively increased from 100 to 400 kg.
A summarizing picture of the simulations is given in Figure 2. The pictures are all taken when the rock is going away from the barrier. The Dynamic Deflection is the maximum dynamic displacement of any component of the barrier, the Permanent Deflection is the maximum static displacement of any component of the barrier. Figure 2 also indicates if the barrier has succeeded or failed to contain the block according to the three defined conditions.

The following conclusions can be drawn:

- Fixing the extremities of the barrier do not bring any improvement compared to the free ones (comparison test 1 / test 3 and test 4 /test 5).
- For an impact on the main rail, the rock could be contained with an impact energy up to 30 kJ when only one rail is used (test 1, test 3, test 6, test 8, test 9). The rock could be contained with an impact energy up to 40 kJ when a second rail is added on the other side (double-sided barrier) (comparison test 8 / test 10).
- For an impact on the MPS, a double-sided system is necessary, a single MPS with classical fixings cannot contain the rock when impacted from behind (test 2, test 4, test 5, test 7).

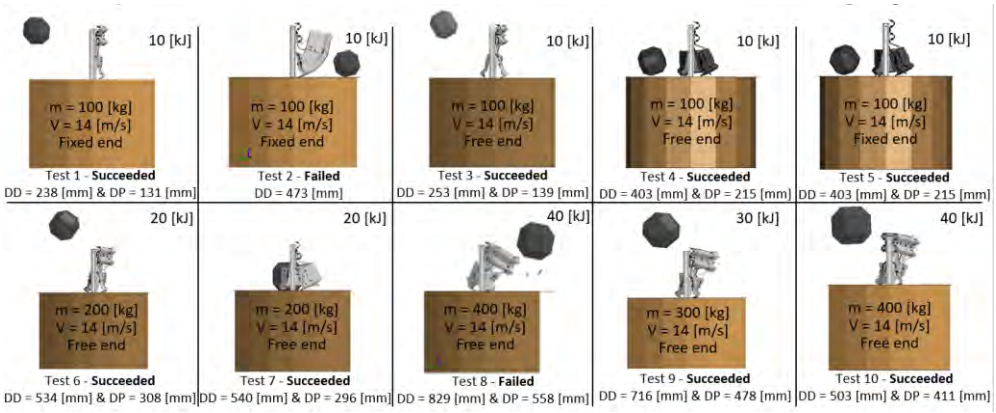

Figure 2 - Summary of the results for the steel barrier (DD = Dynamic Deflection, DP = Permanent Deflection)

Assessment of concrete barriers

Two concrete barriers are used for the assessment (called “barrier 2” and “barrier 3” hereunder). Two different lengths of blocks (3 m or 6 m) forming the barrier 2 are tested. The total length modelled for the assessment is 42 m. The influence of several parameters is analyzed:

- Impact point (on a coupling between two blocks, in the middle of a block, different heights);
- Boundary conditions (embedded in soil, placed on the ground);
- Impact energy (ranging between 30 and 60 kJ);
- Multiple impacts.

Regarding the impact (kinetic) energy, the impact speed varies between 14 and 20 m/s and the mass of the rock varies between 300 and 400 kg.
A summarizing picture of the simulations is given in Figure 3.

The following conclusions can be drawn:

- None of the configurations tested could contain the rock for an impact energy higher than 40 kJ;
- In most of the cases, the block bounces off the barrier and passes over it after being greatly slowed down (test 13, test 14, test 15, test 16, test 17, test 19, test 20);
- Damage is mainly limited to the impact area and does not involve a large quantity of material;
- The only two configurations that passed are the barrier 2 embedded in soil (impact on the coupling and in the middle of a block, almost at the top of the barrier – tests 11 and 12) and the barrier 3 placed on the ground (impact on the coupling, at the base of the barrier – test 18);
- When the barrier 3 from test 18 is impacted again with the same impact energy (40 kJ), the barrier fails to contain the rock (test 20).

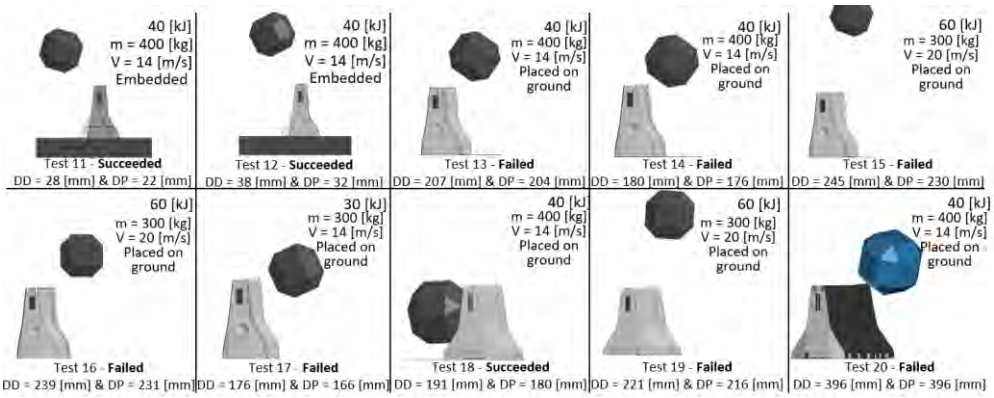

Figure 3 - Summary of the results for the concrete barriers (DD = Dynamic Deflection, DP = Permanent Deflection)

Conclusion

Different safety barriers made of steel and concrete are assessed through Finite Element Analysis as potential protection systems against rockfalls threat for the landscapes and thus energies often met in Belgium. It was highlighted that these barriers could indeed resist to an impact of boulder and contain it when installed according to the good configuration. The maximum accepted kinetic energy for steel barriers ranges between 30 and 40 kJ, depending on the barrier configuration. In all cases, the MPS must be double-sided. For concrete barriers, damage is limited, even for impact at 60 kJ. The main problem for concrete barriers simply installed on the ground is the trajectory of the boulder which bounces off the barrier and often passes over it. A vertical metal mesh extension attached to the concrete barrier should significantly increase the block retention rate. This configuration will be investigated in the next step of this approach.

References

EAD 340059-00-0106:2018, Falling rock protection kits, July 2018, 28 p.
EN 1317-1:2010, Road restraint systems - Part 1: Terminology and general criteria for test methods.
EN 1317-2:2010, Road restraint systems - Part 2: Performance classes, impact test acceptance criteria and test methods for safety barriers.
EN 16303:2020, Road restraint systems — Guidelines for Computational mechanics of crash testing against vehicle restraint system
Ihab HATIM (2020). Qualification de l'outil de Calcul scientifique LS-DYNA : Cas de test de Recette, de Vérification, et de Validation. Mémoire de fin d'étude, ESTP Paris.

Effect of multiple countermeasures on flow dynamics of debris flowby multi-scale experiment

Beom-Jun Kim[1], Chan-Young Yune[2]

[1] Gangneung-Wonju National University, Smart Infrastructure Research Institute, Gangneung, South Korea
[2] Gangneung-Wonju National University, Department of Civil and Environmental Engineering, Gangneung, South Korea

SUMMARY: In this study, we adopted a multi-scale approach to investigate the effect of multiple countermeasures on the flow characteristics of debris flow. Firstly, a series of small-scale experiments were conducted using a flume equipped with various sensors to confirm the flow interaction between multiple countermeasures and a debris flow. A real-scale experiment in a natural gully with cylindrical baffles and a flexible barrier was also conducted to examine the scale effect of a debris flow and to confirm the effect of multiple countermeasures on flow characteristics. The results showed that the installation of baffle arrays in front of a flexible barrier increased the energy dissipation of a debris flow. Moreover, increasing the baffle height produced a greater reduction effect on the energy dissipation in the debris flow.
Keywords: debris flow, multi-scale experiment, scale effect, multiple countermeasures, energy dissipation,

Introduction

Debris flows with entrained debris and boulders are extremely fast mountain hazards which can lead to disastrous consequences for urban areas and the infrastructure of societies (Hübl et al., 2009; Hungr et al., 1984). To prevent potential disasters by debris flows, various types of structural countermeasures have been widely utilized in mountainous areas. Recently, the installation of rigid baffles or a flexible barrier has been increased. The baffles can decelerate frontal velocity and reduce dynamic energy by impeding the mobility of a debris flow and can also be combined with other types of countermeasures. The flexible barrier has an advantage in filtering debris materials and inducing deposition by absorbing the dynamic energy of debris flows and has a lower environmental impact than a concrete check dam. If rigid baffles can be combined with a flexible barrier, they can work as effective countermeasures against debris flows. However, a design guideline for the specifications and arrangement of baffles has not yet been suggested. Moreover, the energy reduction due to frictional loss among grains in the design of flexible barrier has not been considered, which can accordingly lead to excessive design and increased cost. To understand the dynamic behavior of debris flows, dynamic interaction, and energy dissipation caused by debris flow countermeasures, there have been many experimental studies for modelling dry granular flows or debris flows. Most of researchers have conducted debris flow experiments using artificial and miniaturized flumes (Chae et al., 2006; Iverson et al., 2011; Scheidl et al., 2013; Zhou et al., 2018; Wang et al., 2017a, 2017b; Fei et al.,2020). However, debris flows are highly scale-dependent (Iverson, 2015). More specifically, small-scale experiments of debris flow may exhibit disproportionalities in terms of viscous shearing and pore pressures. The significance of these scale effects on debris flow-structure interaction has yet to be evaluated.
In this study, to investigate the effect of multiple countermeasures on the flow characteristics of a debris flow, a series of small-scale experiments were conducted using a flume equipped with sensors to investigate the dynamic behavior and the flow interaction of a debris flow with baffles and a flexible barrier. Furthermore, to verify the experimental results and the possible

scale effect of a debris flow and multiple countermeasures on flow characteristics, a real-scale experiment was performed in a natural gully with the installation of the multiple countermeasures in a similar configuration to the small-scale experiment. After the experiment, the velocity and flow depth were measured according to the configuration of the baffles. From the experiment data, the energy dissipation effect due to the multiple countermeasures was analyzed due to the scale effect of debris flow and the structure.

Small- and Real-Scale Debris Flow Experiment

Figure 1 shows images of the small- and real-scale experimental setup. As shown in Fig. 1(a), the rectangular flume for the small-scale test has an overall length of 4.0 m, a side height of 0.45 m, and a base width of 0.3 m. The width of the flume was determined as a similarity ratio (1/17) to the valley of a watershed as in a real-scale experiment site in Korea. The flume, which was made of 10-mm thick acrylic plate, was reinforced with a stainless-steel frame. The flume has a container for the storage of debris and water mixture at the upper end and a testing zone for the installation of cylindrical columns and a flexible barrier at the middle. The container has an automatic spring-loaded system for opening and closing the door, which is operated with an electromagnetic lock. To capture the flow velocity of the free surface of debris flows and the flow interaction with the baffle array, high-speed cameras were installed at the top and side of the flume. To measure the dynamic impact load of debris flow, load cells were installed at the top, middle, and bottom on both sides of the flexible barrier. Similar configurations of the multiple countermeasures were constructed in the real-scale experiment site as shown in Fig. 1(b). The real-scale experiment site was conducted at Jinbu, Gangwon province, South Korea (Yune et al., 2023). Because the experimental site was constructed at a natural gully, the channel bed contained various size of gravels and wound down to the end of the channel. Figures 1(c) and (d) show a schematic diagram and photographs of the debris flow initiation facility. The facility is 12.6 m in length and 12.0 m in width, consisted of a soil container at the front and a water container at the back. The height at the front and back of the facility were 6.5 m and 5.0 m, respectively. The maximum volume of soil and water container was 346 and 268 m^3, respectively.

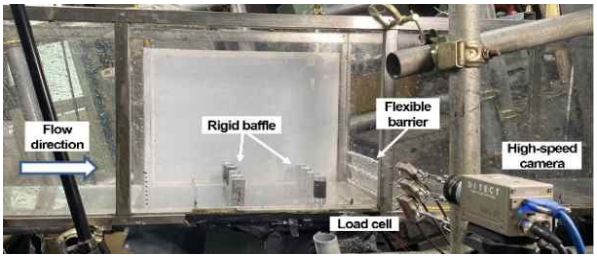

(a) Small-scale experiment setup

(b) Multiple countermeasures in real-scale experiment site

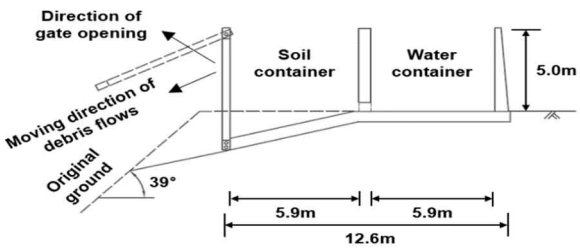

(c) Schematic diagram of debris flow initiation facility

(d) Debris flow initiation facility at top (left) and at front view (right)

Figure 1. Small- and real-scale experiment setup

As shown in Fig. 2, the multiple countermeasures consist of rigid hollow cylindrical baffles and a flexible barrier. The baffle arrays and a flexible barrier were installed at 188 (first row of baffles) and 212 m, respectively, from the debris flow initiation facility. The maximum allowable energy of the flexible barrier was 500 kJ. To measure the dynamic impact load of a debris flow, load cells were installed at the top, middle, and bottom of the front baffles. Shackle type-tension load cells were installed at the top, middle, and bottom on both sides of the flexible barrier as well. The detailed design and arrangement of multiple countermeasures for field experiment were determined based on the small-scale experiment. The experiment conditions are summarized in Table 1.

Table 1. Test conditions

Baffle condition		Flexible barrier (H_f)	Baffle height (H_b)/ Diameter (D_b)	Number of rows (R)	Spacing between successive rows (L)	Blockage ratio(B)	Channel inclination	Designation
Small-scale experiment	Without multiple countermeasures	120mm	-	-	-	-	15°	SH0
	With multiple countermeasures		60mm / 30mm	2	200mm	40%		SH60_R2
			120mm / 30mm					SH120_R2
Real-scale experiment	With multiple countermeasures	3m	2m / 0.5m	2	12m	40%	12°	R_R2

* Channel inclination of the real-scale experiment: inclination of the region where the multiple countermeasures were installed

Experiment Results

Figure 2 shows a comparison of downstream velocity change caused by multiple countermeasures for the small- and real-scale experiments. In Fig. 2(a), the velocity change ratio, defined as $((v_{upstream} - v_{downstream}) / v_{upstream})$, is compared in each test. Compared to the case without multiple countermeasures (SH0), the installation of multiple countermeasures significantly reduced the downstream velocity and caused the increase of the velocity change ratio. The velocity change ratio in small-scale experiment with multiple countermeasures (SH60_R2 and SH120_R2) was 1.43 times higher than that without multiple countermeasures (SH0). Moreover, taller baffles exhibited greater downstream velocity reduction. Increasing the baffle height from 60 to 120mm led to about 20% higher velocity reduction.

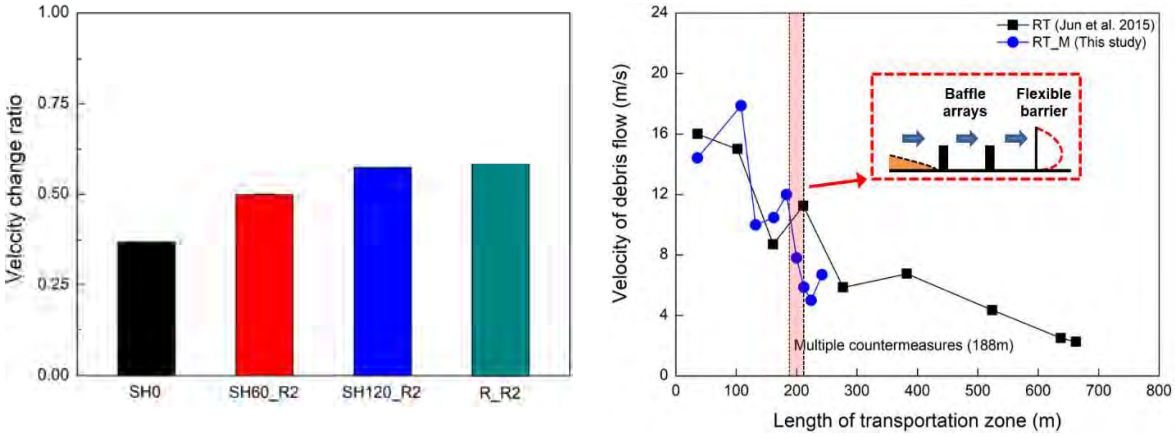

(a) Velocity change ratio in small- and real-scale experiments

(b) Debris flow velocity with transportation zone in real-scale experiment

Figure 2. Velocity reduction

Figure 2(b) shows the change in frontal velocity along the channel in the real-scale experiment. To figure out the effect of the multiple countermeasures on the frontal velocity of the debris flow, the results of the real-scale experiment conducted in 2012 without countermeasures were added to the figure. The frontal velocity of debris flow for the two experiments showed a peak

value after the release of debris from the initiation facility because of a steep inclination in the initial zone. However, there was a large difference in the frontal velocity depending on the presence of multiple countermeasures. Because of two rows of baffles and a flexible barrier, the downstream velocity decreased by 58%. Therefore, the use of the baffle arrays and the flexible barrier can effectively decrease the frontal velocity of a debris flow incorporating with the deposition of debris materials.

Conclusions

In this study, to investigate the effect of multiple countermeasures on the flow characteristics of debris flow, small-scale experiments were conducted according to various baffle configurations. Furthermore, to verify the experiment results for the scale effect of debris flow and multiple countermeasures on flow characteristics, the real-scale experiment was performed in a natural gully with the installation of cylindrical baffles and a flexible barrier. The test results showed that the use of multiple countermeasures significantly increased the energy dissipation of debris flow. Furthermore, increasing the baffle height produced a greater reduction effect on the energy dissipation in the debris flow.

Acknowledgment

This research was supported by the Basic Science Research Program through the National Research Foundation of Korea (NRF) funded by the Ministry of Education (RS-2023-00242141 and 2021R1A6A1A03044326) and by Institute for Smart Infrastructure of Gangneung-Wonju National University.

References

Chae BG, Song YS, Seo YS, Cho YC & Kim WY (2006) A test for characterization on landslides triggering and flow features of debris using a flume test equipment. *Journal of Engineering Geology* 16, 275-282. (In Korean)

Fei J, Jie Y, Sun X & Chen X. (2020) Experimental investigation on granular flow past baffle piles and numerical simulation using a (I)-rheology-based approach. *Powder Technology* 359, 36-46.

Hübl J, Suda J, Proske D, Kaitna R & Scheidl C (2009) Debris flow impact estimation steep slopes, *Proceedings of the 11th International Symposium on Water Management and Hydraulic Engineering*, WMHE, 1–5 September 2009, Ohrid, Macedonia.

Hungr O, Morgan GC & Kellerhals R (1984) Quantitative analysis of debris torrent hazards for design of remedial measures. *Canadian Geotechnical Journal* 21, 663-677.

Iverson RM, Reid ME, Logan M, LaHusen RG, Godt JW & Griswold JP (2011) Positive feedback and momentum growth during debris-flow entrainment of wet bed sediment. *Nature Geoscience* 4, 116-121.

Iverson, RM. (2015) Scaling and design of landslide and debris-flow experiments. *Geomorphology* 244, 9–20.

Jun KJ, Lee SD, Kim GH, Lee SW & Yune CY (2015) Verification of countermeasures by velocity estimation of real-scale debris flow test, *Proceedings of the 6th International Conference on Debris flow Hazard Mitigation: Mechanics, Prediction and Assessment,* DFHM6, 22–25 June 2015, Tsukuba, Japan.

Scheidl C, Chiari M, Kaitna R, Müllegger M, Krawtschuk A, Zimmermann T & Proske D (2013) Analysing debris-flow impact models, based on a small-scale modelling approach. *Surveys in Geophysics 34*, 121-140.

Wang F, Chen J & Chen X (2017a) Experimental study on the energy dissipation characteristics of debris flow deceleration baffles. *Journal of Mountain Science* 14, 1951-1960.

Wang F, Chen X, Chen J & You, Y. (2017b) Experimental study on a debris-flow drainage flume with different types of energy dissipation baffles. *Engineering Geology* 220, 43-51.

Yune CY, Kim BJ, Jun KJ, Park SD, Lee SW, Kim GH, Lee CW & Paik JC. (2023) Real-scale experiment of debris flow in a natural gulley: key findings and lessons learned. *Landslides* 248.

Zhou, GGD, Li S, Song D, Choi CE & Chen X (2018) Depositional mechanisms and morphology of debris flow: physical modelling. *Landslides* 16, 315-332.

On the relations between block volume and shape in rockfall analysis

Battista Taboni[1], Gessica Umili[1], Anna Maria Ferrero[1]

[1] Dept. of Earth Sciences, University of Turin, Turin, Italy

SUMMARY: The in-situ block size distribution (IBSD) is a reliable tool to describe the block volume variability within a rock mass. Research works are ongoing to spread it in the research and professional communities. Parallely, the block shape distribution should be assessed, too. In fact, the variability of block shape within the same IBSD was demonstrated, together with the effect of both volume and shape on block trajectories. The identification of a shape distribution grants the possibility to include this information in the rockfall analysis process, especially in numerical simulations performed with a rigid body approach. A case study where the shape and size of rock blocks manifest a correlation is presented.

Keywords: Rockfall, In-situ Block Size Distribution (IBSD), block volume, block shape

Introduction

A rigorous approach to rockfall phenomena involves the assessment of the volumes of potentially detachable blocks from a rock slope, owing to the fact that most countermeasures design methods depend on energy-based approaches. An approach based on the In-Situ Block Size Distribution (IBSD) has the potential to overcome the former concept of "characteristic block", namely a deterministic value of block volume (usually identified by averaging available measurements), which is unable to realistically represent the variability of such a parameter in a real rock mass (Umili et al., 2020).
A further step towards a more complete characterization of the block distribution should involve a combination of the IBSD and the associated block shape distribution. In fact, the variability of block shape within the same IBSD was demonstrated, together with the effect of both volume and shape on block trajectories (Umili et al., 2023). The recent development of rigid body methods for modeling block trajectories represents a great opportunity for researchers and designers, who, in parallel, must be provided with rigorous tools to quantify block shape distribution. This work presents an attempt to assess block shapes through a statistical approach and provide useful input parameters for rigid body simulations.

Case study

A case study in the Upper Varaita Valley, in the municipality of Bellino (Piedmont Region, Italy) was analyzed. It consists of a steep slope, including a large isolated rocky peak, above a small cluster of old buildings named Grangia Cruset. According to the Regional Landslide Inventory (SIFRAP), the buildings of Grangia Cruset were hit on the 22 of July 2017 by a large block detached from one of the rockfaces. In total, a volume of approximately 100 m^3 detached and fell towards the valley. Such a volume was most likely produced by different blocks detaching simultaneously; moreover, blocks fragmented into numerous smaller ones, with a dominant size ranging between 0.5 and 1.0 m^3. These blocks caused only marginal damages, mostly to the road running on the valley bottom. The largest block, though, measured to have a volume of approximately 6.0 m^3, rolled towards the buildings of Grangia Cruset, located on a

small rise and just above the main deposition area for rockfall. Climbing the small relief, the block hit the corner of one of the buildings before proceeding towards the nearby water stream, where it stopped.

The main rockface (Figure 1), more than 200 m high and almost vertically hanging over a slope whose steepness reaches 40°, has been the subject of a photogrammetric survey performed with a Parrot Anafi UAV. The image sequences obtained from the flights were aligned, and the DSM of the rockface was obtained. The overall rockface area covered by the DSM is about 60000 m^2, and its average resolution is 40 points/m. The non-contact survey of discontinuity orientation and spacing was performed on the DSM by means of the Rockscan code (Ferrero et al., 2009). To validate these results, a traditional survey was carried out. Three main discontinuity sets were identified (Table 1), which produce regular prismatic blocks, as the angles between them are always quite close to 90° (±20°). This fact allowed us to assume the length of block edges equal to the corresponding spacing.

Figure 1. Photo of the Bellino study area, focused on the rockface.

Table 1. Orientation and spacing of the three discontinuity sets.

Name	Dip	Dip Direction	Type	Spacing pdf	μ [m]	σ^2 [m^2]
K1	78	182	Joint	Log-Normal	2.21	7.69
K2	84	95	Joint	Weibull	1.91	2.48
K3	39	343	Foliation	Weibull	1.69	1.30

A Montecarlo simulation was run based on these spacing distributions, producing 1000 randomly generated values for each discontinuity set. The volume sample (1000 data) was obtained by multiplying each triplet of spacing values. By applying the methodology proposed by Umili et al. (2023) we quantified the cumulative frequency distribution of the possible block volumes within the rock mass, namely, its IBSD (Figure 2). The probability of not being exceeded that can be associated with the block involved in the event recorded on the 22 of July 2017 is 74%.

The spacing samples were processed, according to Palmstrom (2001), to calculate the ratios between the longest and shortest side of the block (Lo and Sh, respectively) and between the intermediate (In) and shortest sides. The obtained values were plotted on the shape diagram proposed by Palmstrom (2001) and classified. The distribution of the shapes is well balanced: the rod type is predominant (34.1%), while the equidimensional shape is the least represented (15.1%). The global shape diagram is visible in Figure 3. It is possible to appreciate that there exists a correlation between the size and shape of the blocks. To appreciate this even more, we presented in Figures 4 and 5 the four sectors of the shape classification diagram (Palmstrom, 2001).

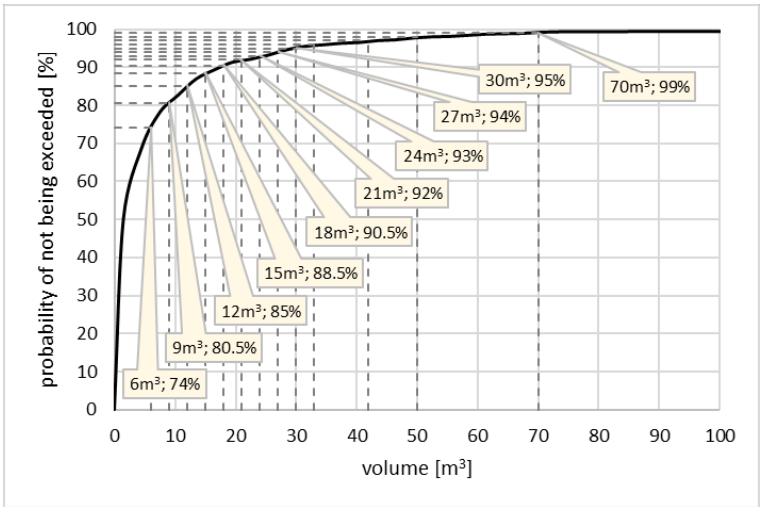

Figure 2. The IBSD for the Bellino case study.

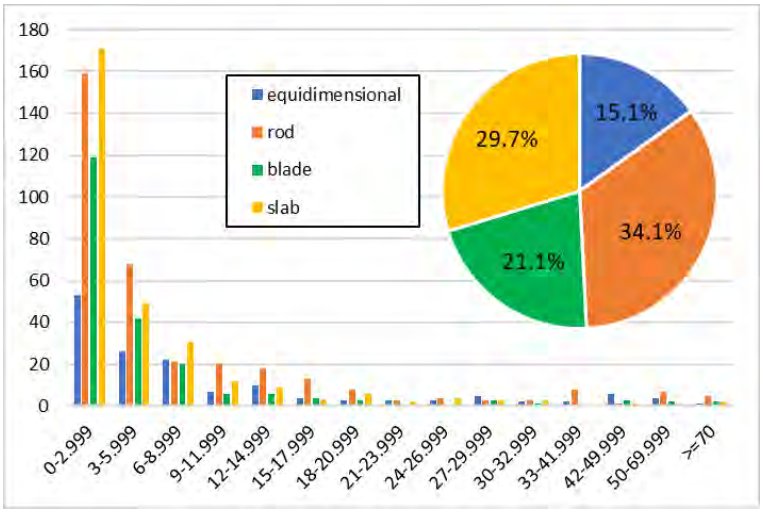

Figure 3. Shape distribution over volume classes and relative abundance of shape types

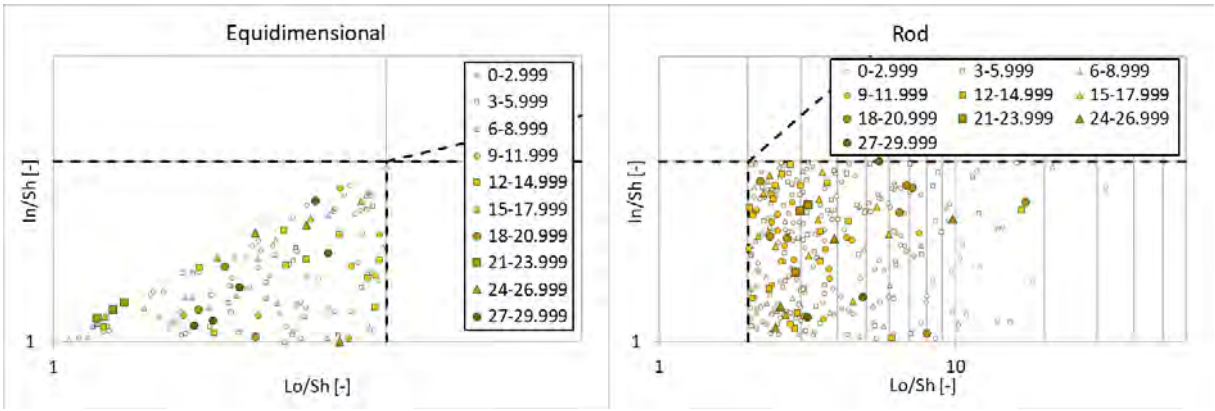

Figure 4. Shape distribution with respect to block size categories: a focus on (left) equidimensional and (right) rod type.

It can be seen how, in general, larger blocks manifest a more regular, equidimensional shape. In fact, the equidimensional sector is also that where the size-shape correlation is less visible.

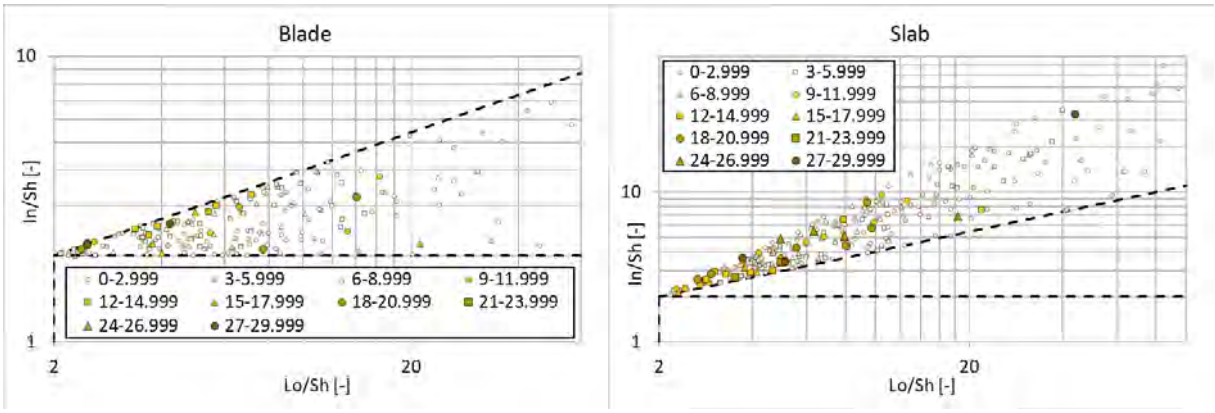

Figure 5. Shape distribution with respect to block size categories: a focus on (left) blade and (right) slab type.

The existence of such a correlation has been previously noted, for example, in Kalenchuk et al. (2006), where the authors highlighted the effects of different spacing CDFs, pointing out that the correlation is less and less visible the more the shape distribution is homogeneously associated to one shape.

Conclusions

The present work presents a case study where the shape and size of rock blocks manifest a correlation. Although we do not aim to provide an explanation for this fact, it's important to notice that to achieve high levels of accuracy in the description and assessment of rockfall phenomena, the size-shape correlation has to be accounted for. As an example, if employing the IBSD to identify multiple reference block sizes for running numerical simulations, it would be important to verify if the shape distribution pie chart changes, i.e., the relative frequencies of the four shapes change.
In general, the identification of a shape distribution grants the possibility to include this important information in the assessment process, especially in numerical simulations based on the rigid body method, as shown by Taboni et al. (2023). Employing a non-deterministic approach, such as that based on an IBSD, shape assessment as a function of block size becomes even more significant.

References

Umili G, Bonetto SMR, Mosca P, Vagnon F, Ferrero AM (2020) In situ block size distribution aimed at the choice of the design block for rockfall barriers design: a case study along gardesana road. *Geosciences* 10 (6), 223. DOI: 10.3390/geosciences10060223

Umili G, Taboni B, Ferrero AM (2023) Influence of uncertainties: A focus on block volume and shape assessment for rockfall analysis. *Journal of Rock Mechanichs and Geotechnical Engineering*, 15(9), 2250-2263. DOI: 10.1016/j.jrmge.2023.03.016

Sistema Informativo Fenomeni Franosi Piemonte (SIFRAP) - https://webgis.arpa.piemonte.it/geodissesto/sifrap/iilivelli.php

Palmstrom A (2001) Measurement and characterization of rock mass jointing. In: Sharma VM, Saxena KR (eds.). *In-situ characterization of rocks*, Rotterdam, Balkema, pp. 49-97.

Kalenchuck KS, Diederichs MS, McKinnon S (2006) Characterizing block geometry in jointed rock masses. *International Journal of Rock Mechanics and Mining Sciences*, 43, 1212-1225. DOI: 10.1016/j.ijrmms.2006.04.004

Ferrero AM, Forlani G, Roncella R. et al. (2009) Advanced Geostructural Survey Methods Applied to Rock Mass Characterization. *Rock. Mechanics and Rock. Engineering*, 42, 631–665. DOI: https://doi.org/10.1007/s00603-008-0010-4

Taboni B, Umili G, Ferrero AM (2023). A Design Scenario Approach for Choosing Protection Works against Rockfall Phenomena. *Remote Sensing*, 15(18), 4453. DOI: 10.3390/rs15184453

Instrumented rockfall on a backfilled slope covered with scattered rock debris and shallow vegetation

Bruma Souza[1,2], Marion Bost[2], Jean Benoît[1], Philippe Reiffsteck[3], Patrick Joffrin[2], Nicolas Vermorel[2], Christophe Pruvost[2]

[1] Department of Civil and Environmental Engineering, University of New Hampshire, Durham, NH, USA
[2] Rockfall Hazards and Design of Geotechnical Structures Laboratory, GERS, Gustave Eiffel University, Bron, France
[3] Soils, Rocks and Geotechnical Structures Laboratory, GERS, Gustave Eiffel University, Champs-sur-Marne, France

SUMMARY: Smart Rocks (SR) were used to instrument three rockfall experiments on a 14-m tall slope covered with vegetation and rock debris. SRs consist of small sensors equipped with two accelerometers, a gyroscope, and an altimeter. These sensors were embedded in the center of gravity of 13.5- and 107-kg compact concrete blocks, released from the top of the slope. The sensor measurements allowed for the characterization of rockfall movement along this type of slope.

Keywords: Rockfall, Falling Blocks, Smart Rocks.

Introduction

In slope locations where falling rocks may pose concern, effective hazard mapping, mitigation measures, and defense systems require reliable estimates of rockfall trajectories (Pfeiffer and Bowen, 1989; Turner and Duffy, 2012; Wylie, 2015). However, the unpredictability associated with rockfalls turns this task significantly more difficult, as the trajectories assumed by falling blocks are complex and still not well understood (Wyllie, 2015; Caviezel et al., 2021). After its initial detachment from a rock face or a soil slope, falling rocks can experience one or more modes of travel, including free fall, bouncing, rolling, and sliding (Ritchie, 1963). Better understanding of the interaction between the falling rock and impacted surfaces (e.g., rock, sand, gravel, vegetation, asphalt) is essential to predict energies and trajectories. Multiple studies demonstrated that the post-impact behavior of a falling block depends on a combination of factors such as the characteristics of the block itself, its kinematics before impact, and the impacted surface. The complexity of these trajectories is even higher, considering that block propagation occurs three-dimensionally, with a combination of translational and rotational motions.

This paper presents the methodology and preliminary results from in situ rockfall tests conducted on a 14-m tall soft ground slope randomly covered with rocks and boulders near Chambéry, France. Smart Rock sensors have been used to accurately characterize rockfall motion during the events and provide more information on the complex rock-ground interaction from three experiments.

Experimental rockfalls

The Smart Rock (Figure 1) sensors designed at the University of New Hampshire are small, fully autonomous devices suitable for a wide range of geotechnical applications where motion tracking is important (e.g., rockfalls, landslides, and debris flows). Each SR consists of a 3D

printed capsule equipped with ±400 g and ±16 g 3-axis accelerometers, a ±4000 dps (degrees per second) 3-axis high-rate gyroscope, and an altimeter. SRs are simple to operate, they process data in real-time, and can be prepared for testing in less than a minute. A Smart Rock records data at a maximum sampling frequency of 500 Hz if the altitude sensor is disabled. The altimeter was included in recent SR generations to track changes in altitude during field experiments, providing helpful information on the trajectory, especially when video recording is not available or possible because of obstructed views. The latest generation SRs have been extensively used to investigate rockfall events in field and laboratory experiments (Souza and Benoît, 2023; Souza et al., 2023).

Figure 1. Latest 5th generation Smart Rock sensor.

Three rockfall experiments were conducted on a 14-m tall on a backfilled slope covered with scattered rock debris and shallow vegetation, with an average inclination of 35°. Concrete blocks weighing 13.5 and 107 kg were released from the top of the slope while instrumented with two Smart Rock sensors each. The first SR was positioned at the center of gravity of the blocks and enabled at a sampling frequency of 400 Hz, while the altimeter was disabled. The second SR sampled data at 25 Hz with the altimeter enabled. A 400 Hz sampling frequency was selected to avoid eventual signal saturations on very vigorous block motion (e.g., very high acceleration upon impact against a rock face). This SR was used to track the vertical position of the falling rock from the altimeter measurements. The experiments were also recorded at 1000 fps from two lateral perspectives.

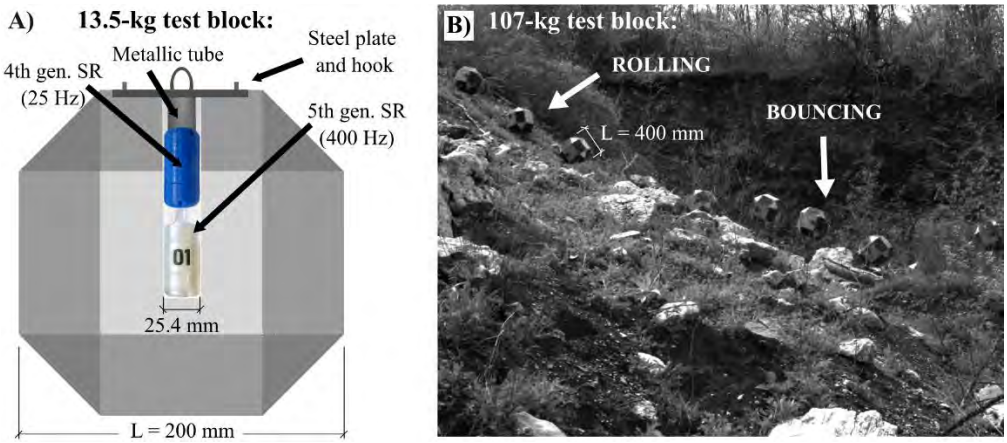

Figure 2. (a) Schematic of the 13.5-kg block, (b) 400-mm tall 107-kg block during rockfall.

A schematic of the 13.5 kg block is shown in Figure 2a, while the 107 kg block is presented in Figure 2b. All blocks were released from the same location with the least initial velocity possible (preferably zero). The three trajectories are shown in Figure 2c. Both lighter blocks stopped at the same location due to a change in slope cross-section (shown in Figure 3), while the heaviest block traveled the furthest distance downslope. The sensor outputs from all experiments are presented in Figure 3. Recent field experiments performed by Souza and Benoît (2023) demonstrated that the Smart Rock data can be used to determine impact forces (Eq. 1), and rotational kinetic energies (Eq. 2).

*Impact force = magnitude of resultant G-force * acceleration of gravity * block mass* (1)

*Rotational kinetic energy = 0.5 * (moment of inertia) * (resultant rotational velocity)²* (2)

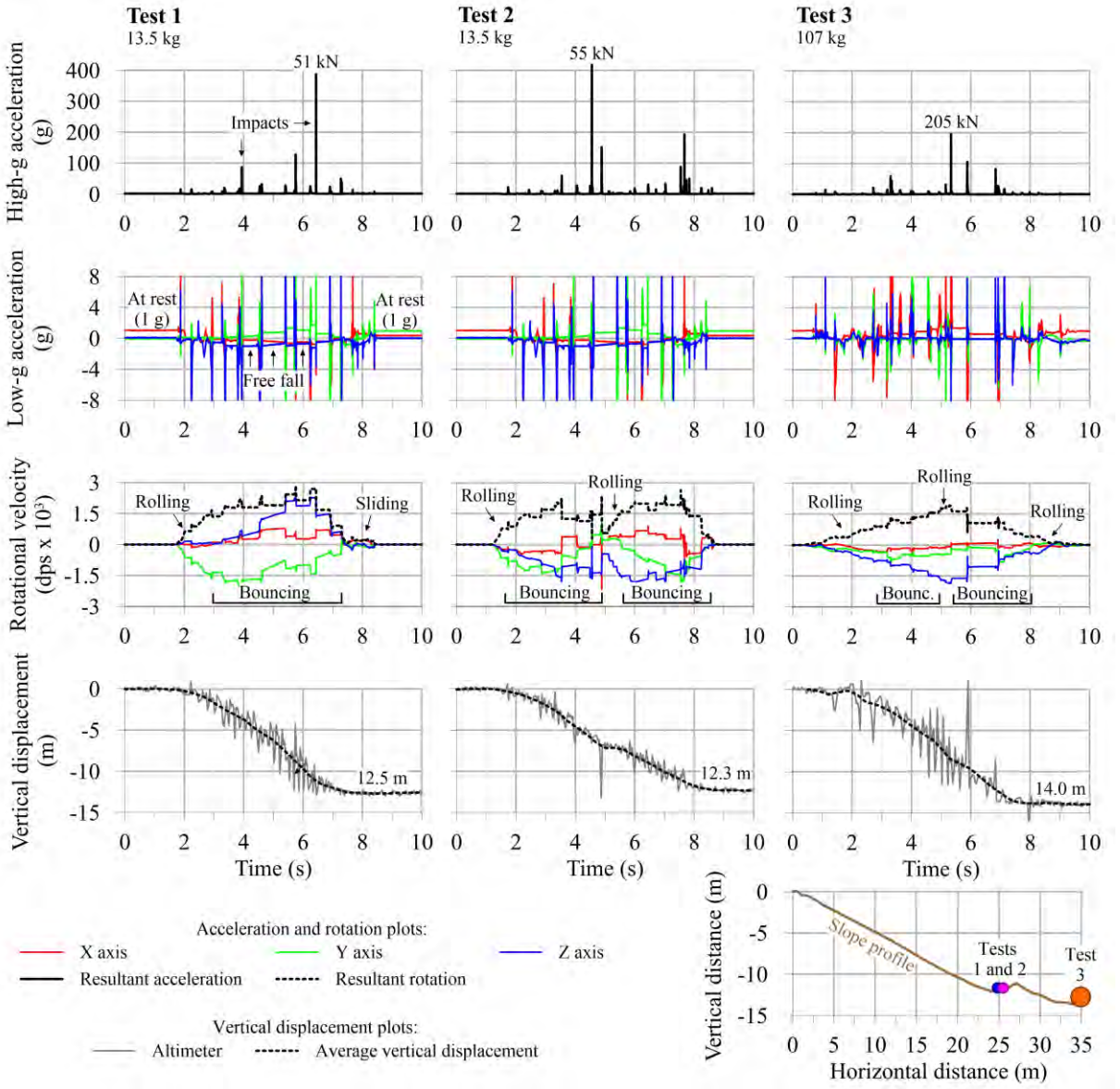

Figure 3. Smart Rock outputs from the three rockfall experiments.

First analysis

The 13.5-kg blocks experienced the highest resultant rotation rates (up to 3000 dps, corresponding to 0.07 kJ rotational energy) and accelerations (up to 400 g, or a 55 kN impact force). However, due to the higher mass and moments of inertia, the 107 kg block experienced higher peak impact forces (205 kN) and rotational kinetic energies (1 kJ). These behaviors have also been observed in previous research performed by Caviezel et al. (2021), Souza and Benoît (2023), and Souza et al. (2023).

The different modes of motion experienced by the falling blocks were identified based on sensor output patterns for different types of movement, identified by Souza and Benoît (2023). The flat acceleration (1 g) and rotational velocity (0 dps) at the beginning each test represent the rock at rest before the experiment. Impacts along the slope cross-section, especially during

block bouncing, can be identified through acceleration peaks, as indicated for a couple of impacts on test 1.

All three tests experienced a combination of rolling and bouncing, expected for slopes between 20° and 30° (Ritchie, 1963; Souza and Benoît, 2023). The 107-kg block recorded the highest ground contact time and revolved predominantly about a single axis. As the blocks bounce, free-fall intervals can be identified through 0 g resultant readings for the low-g accelerometers, and constant resultant rotational velocities between impacts. Rolling behavior can be readily identified though an increase or decrease in block resultant rotation, accompanied by small acceleration peaks that often do not exceed the low-g acceleration limit.

Although the altimeter does not capture horizontal movement, the moving averages of the altitude readings are useful to estimate block vertical displacements over time and especially to help identify rockfall endpoint locations considering the slope cross-section.

Conclusions and ongoing work

Smart Rock sensors present a high potential for expanding rockfall knowledge and quantifying relevant parameters that cannot be measured from conventional camera systems (e.g., rotational kinetic energy and impact forces). Direct measurements from the falling block perspective can be used to accurately identify rockfall motion and help improve existing models used in mitigation and protection design practices.

The results from this field experimental campaign will be further assessed regarding rockfall trajectories and kinetic energy quantification in a planned experiment in New Hampshire, USA. Total kinetic energy estimates will be examined along the rock paths to evaluate the contribution of block rotation and energy dissipation along the slope cross-section. Results will be compared to an extensive experimental campaign performed under controlled conditions by Souza et al. (2023), which evaluated kinetic and model input parameters under a wide range of test conditions. Finally, modeling assessments of the field trials will be conducted using existing rockfall modeling software. Ground characterization assessments through a PANDA dynamic penetrometer along the slope profile should help identify changes in material characteristics at different locations of interest, which should aid in precising boundary conditions in model simulations.

References

Pfeiffer, TJ & Bowen, TD (1989) Computer simulation of rockfalls. *Bulletin of the association of Engineering Geologists* 26(1), 135-146.

Turner, AK & Duffy, JD (2012) Evaluation of Rockfall Mechanics. In Turner, AK & Schuster, RL (Eds). *Rockfall Characterization and Control* (pp. 285-333). Washington, D.C.: Transportation Research Board.

Wyllie, DC (2015) *Rock Fall Engineering*. New York, NY: CRC Press, Taylor & Francis Group.

Caviezel, A, Ringenbach, A, Demmel, SE, Dinneen, CE, Krebs, N, Bühler, Y, ... & Bartelt, P (2021) The relevance of rock shape over mass—implications for rockfall hazard assessments. *Nature communications* 12(1), 1-9. https://doi.org/10.1038/s41467-021-25794-y

Ritchie, A (1963) Evaluation of Rockfall and its Control. *Highway Research Board* 17, 13-28.

Souza, B (2021) Use of Smart Rocks to improve rock slope design. Master's thesis, University of New Hampshire.

Souza, B and Benoît, J (2023) Rockfall motion using a Smart Rock sensor. *Canadian Geotechnical Journal.* https://doi.org/10.1139/cgj-2022-0599

Souza, B, Bost, M, Benoît, J, Reiffsteck, P, Joffrin, P, Pruvost, C, & Vermorel, N (2023) Small-and Medium-Scale Assessment of Rockfall Coefficients of Restitution. *Geo-Risk 2023 Proceedings* (pp. 121-130). https://doi.org/10.1061/9780784484982.013

Evaluating Deep Depressurization as a Means of Mitigating Risk from Active Landsliding Along the California Coast

Scott Anderson[1], Kenneth Johnson[2], Seamus Millett[1], Molly Winston[1]

[1] BGC Engineering, Inc., Golden, CO, USA
[2] WSP, San Francisco, CA, USA

SUMMARY: US Highway 101 is a critical route along the California coast, and it crosses landslides. In such situations, risk attributed to safety, mobility and operational cost can be related to landslide velocity. Here, the impact of deep depressurization is evaluated through calculated factors of safety and measured or anticipated velocity of the preexisting Last Chance Grade landslide. The landslide is too large and too constrained by valued natural resources to be stabilized in other ways. The method for evaluating impact of depressurization is practical and can be applied elsewhere, and the results suggest that slowing of movement can be achieved and risk reduced by depressurization that impacts the active slide surface.

Keywords: LiDAR, InSAR, risk, depressurization, velocity

Introduction

On the north coast of California, U.S. Highway 101 climbs the Last Chance Grade (LCG) from sea level at Wilson Creek to approximately 250 m elevation. The highway is critically important to California and the area has also been designated by UNESCO as a World Heritage Site, and there are no practical alternative routes. The highway crosses the Broken Formation, a Franciscan Complex unit that includes large (10s to 100s of m, or more) blocks of greywacke sandstone, and is host to a series of deep-seated trans-rotational slides moving on surfaces approaching 100 m deep. The department of transportation (Caltrans) has been working for years to keep it open, fixing one emergency after another, and is now interested in a more holistic solution. For this reason, and under their direction and support, a study was performed to evaluate the impact of deep depressurization with the hypothesis being that if deeper movement could be slowed or stopped, more conventional mitigation structures, such as walls, could hold the roadway prism stable for a reasonable lifespan, which is something not achievable now. For brevity, the work summarized here is with focus on the South Last Chance Grade (SLCG), which is one of the deep-seated trans-rotational slides.

Back Analysis

As shown in Figure 1, the slope is currently moving throughout the LCG and at the SLCG, specifically. To benchmark improvements to be gained by depressurizing, a limit equilibrium analysis was performed to calibrate an existing analytical factor of safety (FS) of approximately 1.0 when movement (and water pressure) was the lowest in this period of observation. Given the chaotic nature of the Broken Formation and the limited subsurface information (almost all along the existing highway), it was particularly helpful to be able to rely upon the geomorphology of the slope, LiDAR change detection, and interferometric synthetic aperture radar (InSAR) in addition to conventional slope monitoring instrumentation to estimate the deep surface attributable to the movement and for which the FS is near 1.0. LiDAR is an abbreviation for Light Detection and Ranging and it is a remote sensing method that uses a

pulsed laser to measure variable distances to the Earth to form a 3-dimensional (3D) model of the ground surface. LiDAR change detection (LCD) the process of comparing two 3D models of an area collected at different points in time and presenting the 3D differences in an easily understandable medium. Figure 2 is a demonstration of how LCD (colour of ground surface), InSAR (coloured dots on ground surface), inclinometers (flags on boring logs) and geologic descriptions were used to determine the approximate shape of the two-dimensional back analysis surface.

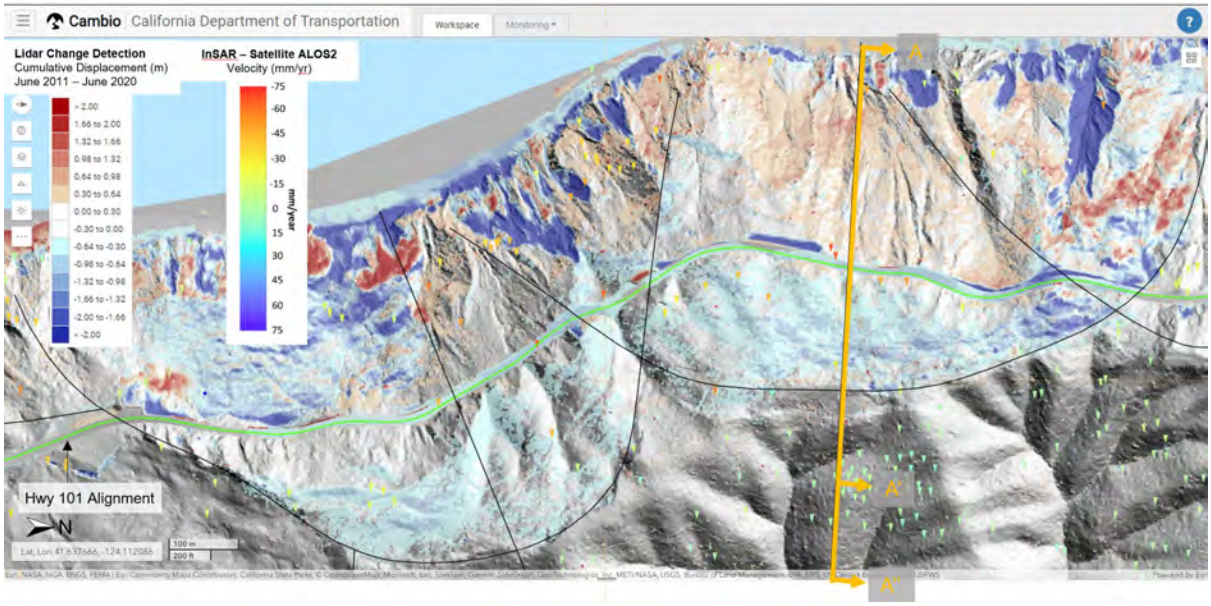

Figure 1. Image showing the SLCG portion, the analysis section presented herein (orange section line (Figure 2)), ALOS2 InSAR reflectors (triangles with colour bar scale shown) and LCD (blue is negative change and red is positive). Hillshade presented is from LiDAR collected on June 1, 2020.

Forward Analysis

Measurements of groundwater pressure and an understanding of the geology suggest a complex groundwater regime, but one that could also be approximated with a phreatic surface for this purpose. This is what we did to enable evaluating the impact of varying amounts of depressurization, as shown in Figure 3. The figure shows the concept of drainage through tunnels below the failure surface in a general concept described by Gillon et al. (1992) and at a site visited by the first author during the 6th ISL in Christchurch, NZ.

For each equivalent water table, a FS was calculated on the back-analysed surface and with back-analysed parameters. Of course, higher FS were calculated for the depressed water tables, and in diminishing amounts, as the water table dropped below the failure surface. To answer the question of whether the increase in FS is enough to justify the mitigation approach, a relationship between FS and velocity is used. This relationship was informed by calculating a FS using water pressures as high as have been measured on site, while recognizing that even higher water pressures are possible, in addition to the low water pressure condition used for the back analysis. The results of these calculations, using the two measured water pressure conditions are shown as the solid symbols in Figure 4 for the SLCG and for other portions of the LCG complex.

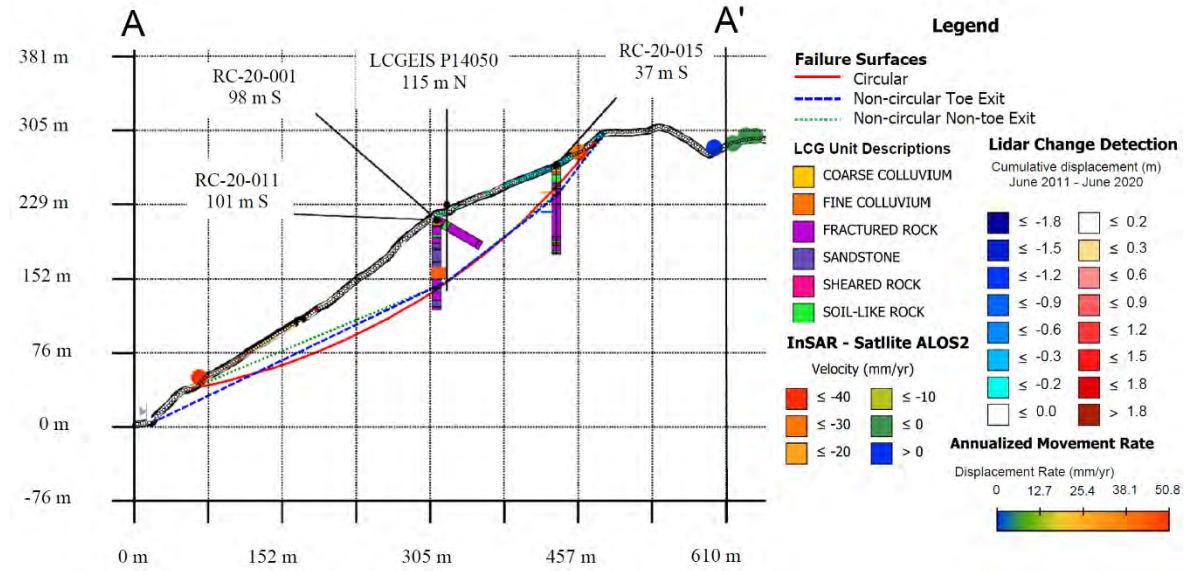

Figure 2. Back-analysis section for SLCG showing interpretations. Colours on the surface represent LiDAR change detection, dots on the surface are InSAR reflectors (negative change is downslope).

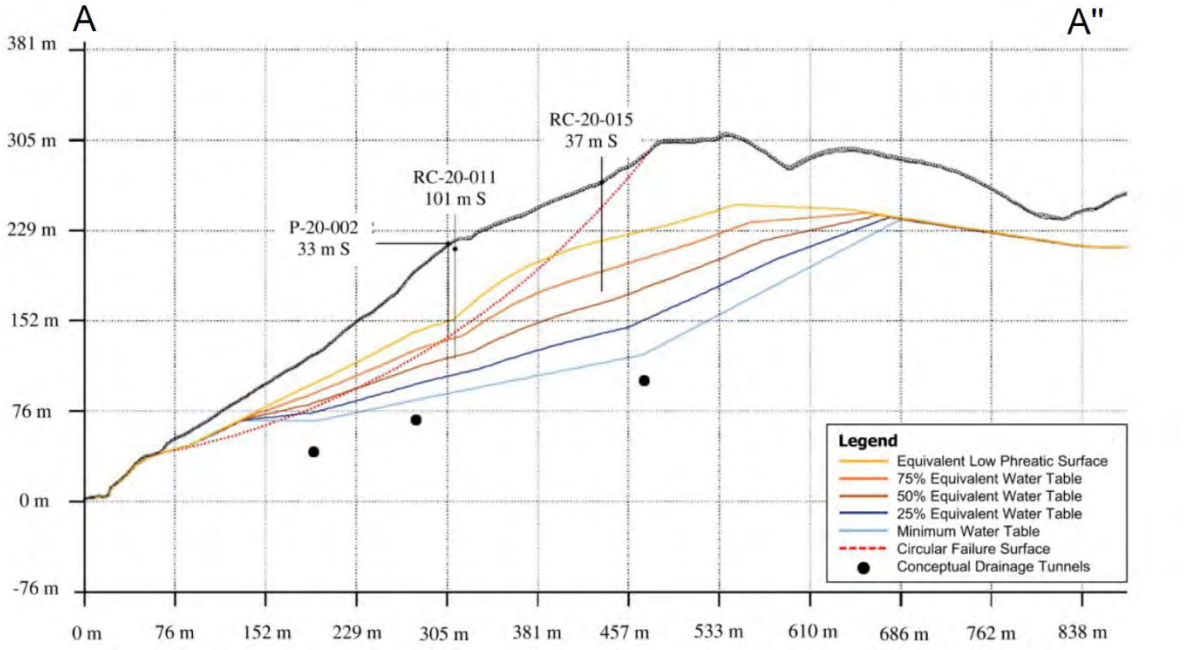

Figure 3. Representation of modelled water pressure and the back analysed failure surface (dotted red line). The upper, yellow, surface is from the back analysis.

Performance Expectations

The solid symbols in Figure 4 are cases where a velocity and a calculated FS coexist, one calculation being the back analysis condition, and the other being higher measured water pressure. The hollow circles are interpolations of theoretical water pressure conditions based on measured data and sitewide correlations. The curves assume an asymptotic approach to zero movement above the relative FS of 1.0. The FS is termed a relative FS in Figure 4 because it is used here as an indicator, and an absolute relationship should not be extracted from the plot. There is no physical meaning to a plot of limit equilibrium FS versus movement rate, but FS is a measure of the balance, or imbalance, of driving to resisting forces and moments, and it is a well understood term that is easily available, so it is useful. The highly non-linear curves are

similar to work by Porter et al. (2000) and the more linear curve is closer to that reported by Cornforth and Vessely (1992). They probably bound the actual curve that could be developed at these sections with further collection of pore pressure and movement data, which would be a logical next step to explore this further. Though there is no theoretical meaning to the relationship, only empirical, and the FS values are relative, the curves demonstrate that modest changes in the calculated FS can have a measurable impact on realized movement rates.

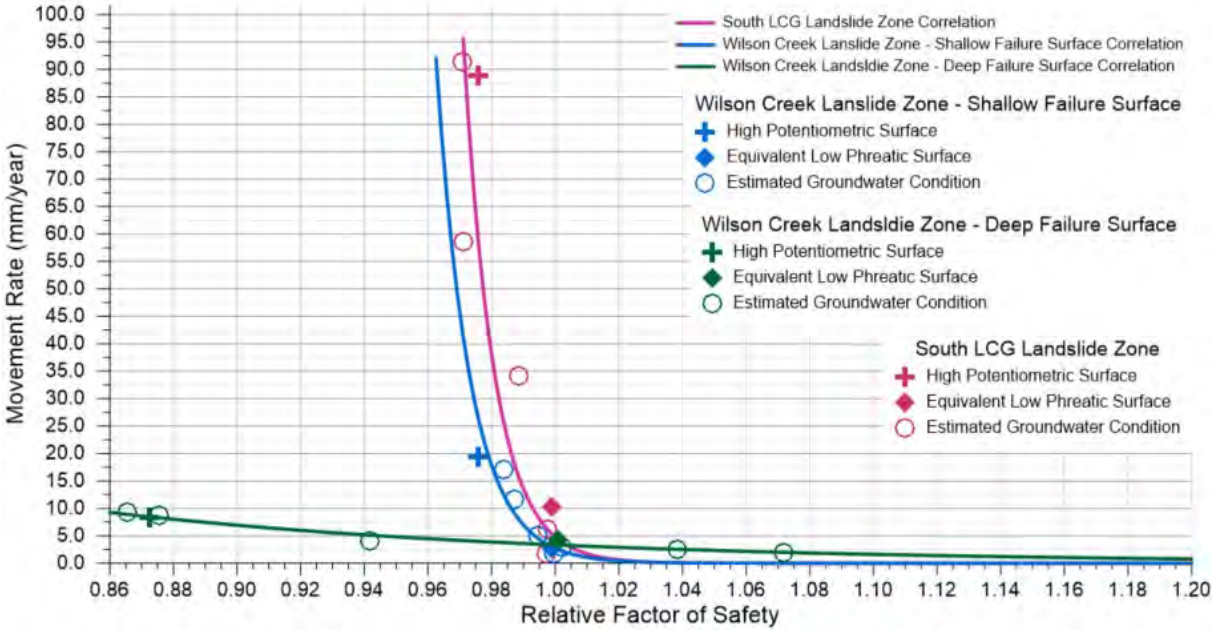

Figure 4. Calculated FS relative to the back-analysed case. Solid symbols are measured. Hollow circles are calculated based on interpolations of water pressure and velocity. Different parts of the LCG complex are shown.

Conclusions

Through observations of landslide movement and measured water pressure, it was demonstrated that depressurization increases the calculated relative FS on an existing LCG failure surface and that landslide velocity is inversely correlated with the FS. With additional data collected for this purpose, bounds on the relationship could be narrowed, but the current work is sufficient to show that depressurization can be expected to slow landslide velocity in potentially significant amounts, and may even stop deep movement. Slower velocity equates to longer highway life and reduction in safety, mobility and operational cost risks.

References

Cornforth DH and Vessely DA (1992) Factors of safety during landslide movements. *Proceedings of the Sixth International Symposium on Landslides, Christchurch, New Zealand*, Balkema, p. 367-372

Gillon MD, Graham CJ, & Grocott GG (1992) Low level drainage works at the Brewery Creek Slide. *Proceedings of the Sixth International Symposium on Landslides, Christchurch, New Zealand*, Balkema, p. 715–720

Porter MJ, Pritchard MA, Keegan TR & Cruden DM (2000) Investigation, analysis and stabilization of active parts of a pre-historic landslide affecting a railway in North Central British Columbia. In D. LeBoeuf (Ed.), *Proceedings of the 53rd Canadian Geotechnical Conference, Montreal, QC*, Canadian Geotechnical Society, p. 769-776

Numerical Study on Dynamic Behavior of Rock Avalanche and Its Disaster Reduction of Baffles Using Discontinuous Deformation Analysis

Changze Li[1], Gonghui Wang[2]

[1] Graduate School of Science, Kyoto University, Kyoto, Japan
[2] Disaster Prevention Research Institute, Kyoto University, Kyoto, Japan

SUMMARY: Rock avalanches with high mobility and kinetic energy pose a potential geological risk to surrounding buildings. However, the dynamic behaviors of rock avalanches and the interaction mechanisms between rock avalanches and baffles still require further investigation. Conducting real-scale experiments on rock avalanches is challenging due to the limitations and high cost of the experiments, hindering the exploration of these interaction mechanisms. Fortunately, with the rapid advancement of computing technology, numerical methods have become increasingly prominent in academic and engineering fields. This study employs discontinuous deformation analysis (DDA), a powerful numerical method, to unravel the dynamic behaviors of rock avalanches. Multi-block rockfall models, featuring a range of block sizes and varying friction angles, are under investigation. Additionally, the influences of baffle configuration on the affected area and the interaction between sliding mass and baffles are investigated through a series of numerical simulations. These simulations also enable us to draw conclusions and provide valuable suggestions for the mitigation and prevention of rock avalanches.

Keywords: numerical simulation, rock avalanche, disaster prevention, dynamic analysis

Introduction

Rock avalanches are high-velocity flows of fragmented rock that can dramatically alter landscapes and impact people and infrastructure, even when they are far from the source. For instance, the 2006 Leyte Island rock avalanche in the Philippines resulted in the tragic loss of more than 1100 lives and the complete devastation of the downstream village of Guinsaugon (Evans et al., 2007). The 2019 Shuicheng rock avalanche that struck Guizhou, China, affected over 1600 people, leaving 43 people dead and 9 people missing (Fan et al., 2020). As one of the most destructive geohazards, they are generally characterized by a large volume, high velocity, and an extremely long runout distance. Extensive research on catastrophic rock avalanches has been conducted for over a century.

Engineers have proposed various countermeasures to mitigate these hazards, including shed galleries, baffles, and retaining walls. Among them, baffles have gained popularity as a cost-effective and versatile disaster prevention structure, especially in steep mountainous areas. This design offers several advantages, prompting numerous researchers to embark on a series of investigations into the use of baffle arrays for protection against rock avalanches. For instance, Cosenza et al. (2006) installed baffles in a basin to reduce debris flow and showed the significant reduction in flow slippage the baffle system achieved. However, the dynamic behaviors of rock avalanche and the interaction mechanisms between rock avalanches and baffles still require further investigation. Conducting real-scale experiments on rock avalanches is challenging due to the limitations and high cost of the experiments, hindering the exploration of these interaction mechanisms.

This study employs discontinuous deformation analysis (DDA) to unravel the dynamic behaviors of rock avalanche, considering the interactions between the sliding masses and

baffles. Multi-block rockfall models with different block sizes and friction angles are investigated. Additionally, the influences of baffle configuration on the affected area and the interaction between sliding mass and baffles are also investigated through a series of numerical simulations. From the simulations, it is found that when the friction angle between the sliding blocks and the base is large, the blocks positioned closer to the front exhibit greater rotational displacements compared to those in the middle or rear. When the friction angle of the surface is low, the entire sliding mass tends to exhibit more translational movement. The model with less distance between adjacent piles exhibits greater effectiveness in reducing the velocities of sliding rocks. The closer the first row of baffles is to the sliding mass, the greater the reduction in impulse. These simulations also enable us to draw conclusions and provide valuable suggestions for the disaster mitigation and prevention of rock avalanche.

Brief Introduction of Discontinuous Deformation Analysis

DDA, originally developed by Shi (1988), represents a robust numerical method designed to investigate the kinematics of discontinuous systems. In the DDA method, blocks of arbitrary geometries constitute the fundamental elements, and each block features six (2D) or twelve degrees (3D) of freedom for displacements and deformations. DDA offers the capability to consider the translation, rotation, deformation, as well as extensive sliding and opening along block boundaries. The interaction between adjacent blocks is facilitated by contact penalty springs, and the conditions of non-penetration and non-tension are ensured through the iterative open-close process at each time step (Peng et al., 2022). DDA is a powerful technique for modelling the mechanical behaviors of rocks and structures. In 3-D problems, a block of any geometry is represented through a set of boundary points, edges, and polygons. The contact between adjacent blocks can only occur at these boundary elements (Peng et al., 2019). Thus, in 3-D problems, there are seven contact types, including vertex-to-vertex (V-V), vertex-to-edge (V-E), vertex-to-face (V-F), crossing edge-to-edge (E-E), parallel E-E, edge-to-face (E-F), and face-to-face (F-F). Figure 1 shows these seven contact modes and the schematic diagram of block contact springs. In a blocky system, the total potential energy comprises several components, including: The overall potential energy within a blocky system is a result of (1) elastic stresses, (2) initial constant stresses, (3) body forces, (4) point loadings, (5) point displacement constraints, (6) inertia forces, and (7) contact forces.

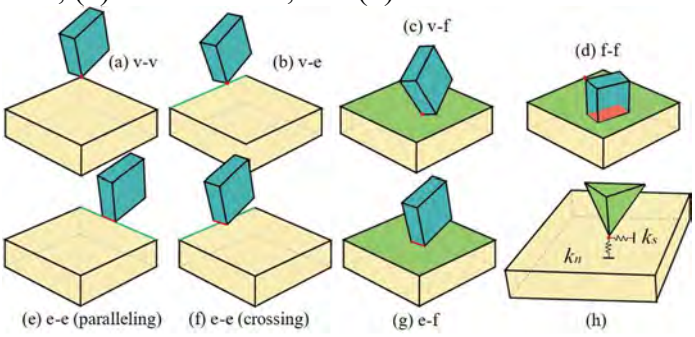

Figure 1. Block contact modes in 3D DDA and (h) schematic diagram of block contact spring

Model Setup for Rockfall Simulations

Figure 2 (a) shows the rockfall numerical model for studying the effect of rock size on the dynamic behavior of rock avalanche and its geometry parameters. These geometry parameters are determined by following the experiment conducted by Okura et al. (2000). To investigate the effect of block size, we control the volume as a constant value and then equally divide each side of the sliding mass into 2 pieces to 8 pieces. Each block has the identical size, density of

2500 kg/m^3, Poisson's ratio of 0.2 and Young's modulus of 10 GPa. The sliding blocks fall downslope due to the gravity. Figure 2 (b) shows the rockfall numerical model in 3D DDA with baffles and its geometry parameters. In this model, the parameters of the sliding mass are identical with those of the rockfall numerical model. The baffles are fixed to the base with the Young's modulus of 10 GPa.

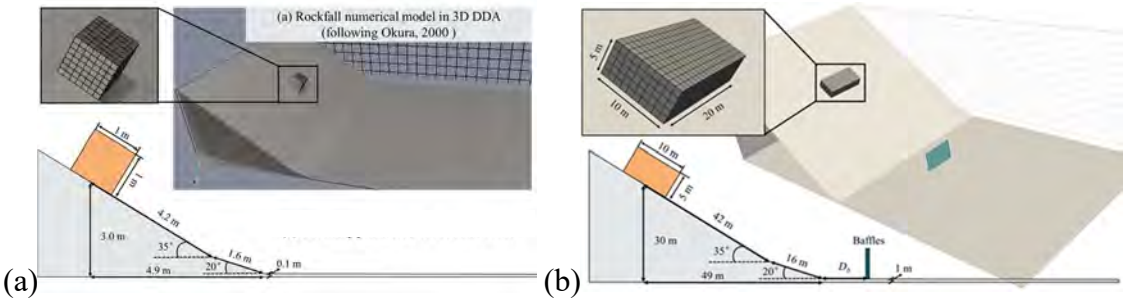

Figure 2 (a) Rockfall numerical model in 3D DDA following Okura et al. (2000) and (b) Rockfall numerical model in 3D DDA with baffles

Simulation Results and Discussions

Figure 3 (a) shows the relation between the equivalent coefficient of friction f, the equivalent coefficient of friction at gravity-center f_g and the number of the divided block in each side. It can be observed that with the increase of side number (that is decrease of block size), f decreases, which means a longer runout distance. It is also found that surface friction angle has great on the dynamic behavior of the rocks. As the surface friction angle increases, the average velocity decreases while the rotational movements increase. During the movement, the back-to-front relative positions among blocks are essentially consistent with the downflow direction. It is important to emphasize that the friction angle discussed in this context corresponds to the kinetic friction coefficient, while the rolling friction coefficient is determined automatically based on the stress and shape of the objects. The governing factor in the movement of the blocks will be the lower of these two coefficients.

We explore the impact of various baffle configurations on the effectiveness of blocking and the resultant impact forces of rock avalanches using a series of numerical simulations. These simulations enable us to draw conclusions and provide valuable suggestions. From the simulation of the rockfall model with baffles, as shown in Figure 4, it is observed that the positions of the first row of baffles significantly impact the velocities of sliding rocks through collisions. The model with less distance between adjacent piles exhibits greater effectiveness in reducing the velocities of sliding rocks. The impulse experienced by sliding rocks decreases upon colliding with the baffles. The closer the first row of baffles is to the sliding mass, the greater the reduction in impulse.

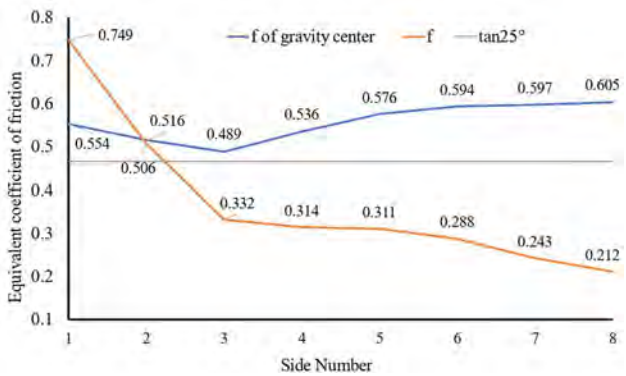

Figure 3 Equivalent coefficient of friction f and at gravity-center f_g.

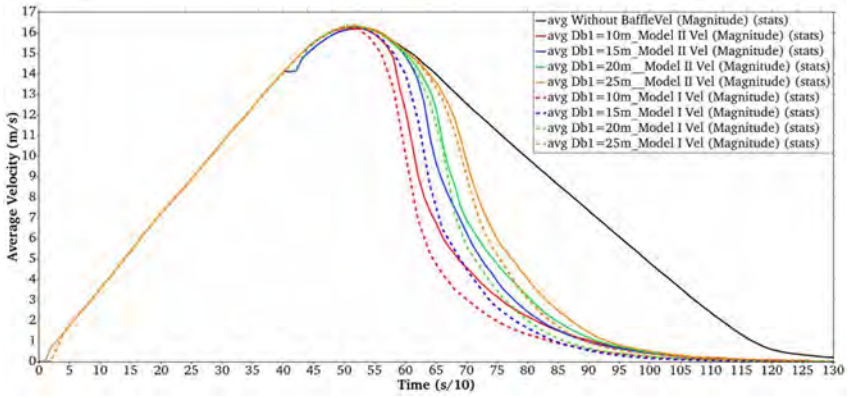

Figure 4 Average velocities of blocks in the models with baffles.

Conclusions

In this study, we present an approach for simulating rock avalanches considering the effect of block size, frictional and baffles as the preventive countermeasure. Through these numerical simulations, some conclusions and suggestions can be reached:

1. It is found that surface friction angle has great on the dynamic behavior of the rocks. As the surface friction angle increases, the average velocity decreases while the rotational movements increase.
2. It can be observed that with the increase of side number (that is decrease of block size), *f* decreases, which means a longer runout distance.
3. The model with less distance between adjacent piles exhibits greater effectiveness in reducing the velocities of sliding rocks. The closer the first row of baffles is to the sliding mass, the greater the reduction in impulse.

Acknowledgement

This work was supported JST SPRING (Grant Number JPMJSP2110).

References

Cosenza, E., Cozzolino, L., Pianese, D., Fabbrocino, G., & Acanfora, M. (2006). *Concrete structures for mitigation of debris-flow hazard in the Montoro Inferiore Area, Southern Italy.* 2nd International Congress, IFSC, Naples.

Evans, S. G., Guthrie, R. H., Roberts, N. J., & Bishop, N. F. (2007). The disastrous 17 February 2006 rockslide-debris avalanche on Leyte Island, Philippines: a catastrophic landslide in tropical mountain terrain. *Natural Hazards and Earth System Sciences*, *7*, 89–101.

Fan, X., Tang, J., Tian, S., & Jiang, Y. (2020). Rainfall-induced rapid and long-runout catastrophic landslide on July 23, 2019 in Shuicheng, Guizhou, China. *Landslides*, *17*(9), 2161-2171. https://doi.org/10.1007/s10346-020-01454-y

Okura, Y., Kitahara, H., Sammori, T., & Kawanami, A. (2000). The effects of rockfall volume on runout distance. *Engineering Geology 58* 109–124.

Peng, X., Chen, G., Yu, P., Zhang, Y., & Wang, J. (2019). Improvement of joint definition and determination in three-dimensional discontinuous deformation analysis. *Computers and Geotechnics*, *110*, 148-160. https://doi.org/10.1016/j.compgeo.2019.02.016

Peng, X., Yu, P., Cheng, X., Chen, G., Zhang, Y., Zhang, H., & Li, C. (2022). Dynamic simulation of the water inrush process in tunnel construction using a three-dimensional coupled discontinuous deformation analysis and smoothed particle hydrodynamics method. *Tunnelling and Underground Space Technology*, *127*. https://doi.org/10.1016/j.tust.2022.104612

Shi, G. H. (1988). *Discontinuous deformation analysis: a new numerical model for the statics and dynamics of block systems* [PhD thesis, Berkeley: University of California].

Modelling a rockfall field experiment using the stochastic RocPro3D software: effects of the DTM resolution

J.-D. Barnichon[1], C. Chautard[1]

[1] RocPro3D, Agreen Labo Village by CA, 4 rue Charles Sadron, 45100 Orléans, France

SUMMARY: In the context of individual rockfall simulations, the DTM is known to be a first-order factor influencing the trajectories of blocks. With available high resolution topographic surveys, the question arises as to what is the optimum DTM resolution required to perform such simulations. Based on an existing detailed field experiment and using the stochastic rockfall simulation software RocPro3D (v6.2.0), the influence of DTM resolution is investigated. The results indicate that the DTM mesh size should preferably be at least equal to the block size.

Keywords: rockfall, trajectory simulation, topography effect, RocPro3D

Introduction

Stochastic (Monte-Carlo) simulations have been used for several decades to simulate rockfall propagation (e.g. Crosta & Agliardi, 2003; Cottaz et al., 2010; Dorren et al., 2023). Most of them share a lumped-mass based formulation, in which the contact between blocks and the DTM is simplified as a unique point, and which allows the computation of very large numbers of blocks (millions and more) in a short amount of time (hours), taking into account many sources of uncertainty (Li & Lan, 2015). The effect of DTM resolution has already been studied at large scales in the past (e.g. Crosta & Agliardi, 2003). This effect is further investigated here using field experiments carried out in the Authume quarry, France (Bourrier et al., 2021).

Input data, soil mapping, and simulation

From the original raster data, a composite TIN-based mesh was generated from a Delaunay triangulation with the original raster resolution of 0.2 m. Three additional meshes were also generated to reduce this resolution (i.e., increase the size of the faces) by uniform resampling to 0.5 m, 1.0 m and 2.0 m, respectively. On these four DTM meshes, soils were mapped using a local slope criterion using the RocPro3D standard soil library parameter set (see Tab. 1 for the deterministic parameters). The resulting soil mapping is shown in Fig. 1 for the 0.5 m DTM.

Table 1. Soil mapping

Local slope [°]	Mapped soil	R_N [-]	R_T [-]	ΔR [-]	k [-]	Δk [-]
70-90	Sane rock	0.55	0.90	0.04	0.45	0.12
45-70	Altered rock	0.50	0.85	0.05	0.50	0.15
20-45	Compact debris	0.40	0.85	0.08	0.55	0.15
0-20	Loose debris	0.32	0.82	0.03	0.60	0.12

Consistent with experimental data and analysis (Bourrier et al., 2021), we introduced 2 release zones with constant block size (RZ-A and RZ-B) and 4 vertical evaluation screens (ES1-A, ES2-A, ES1-B, ES2-B), see Fig. 1. For each DTM, stochastic simulations were performed with the RocPro3D software (https://www.rocpro3d.com), using a hybrid **lumped-mass** formulation that accounts for block **rotation** (LM-R) and launching 1 million blocks per release zone, which resulted in a total CPU time between 11.8 min and 26.3 min on Intel core i5-12500H.

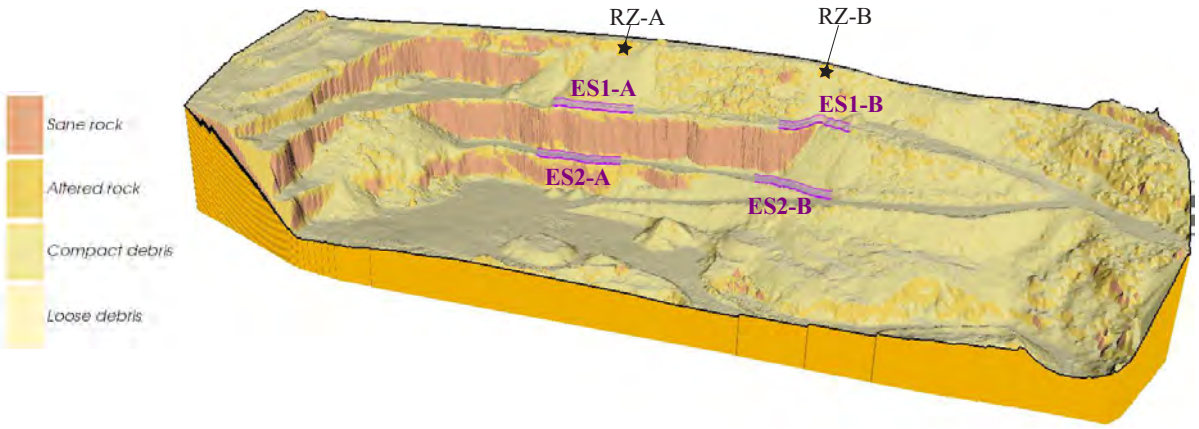

Figure 1. Full 3D view of the modelled zone and mapped soils (DTM resolution 0.5 m) - Black stars: release zones (RZ-A and RZ-B); Violet: evaluation screens ES1-A, ES2-A, ES1-B, ES2-B.

Stopping points

Observed block trajectory stopping points are shown in Fig. 2a, and computed maps (using a fixed analysis raster cell size of 1 m for all DTMs) of the number of stopping points per raster cell are shown on Figs. 2b-e. Visual analysis suggests that the computed stopping zones are broadly comparable to the field observations. However, a more detailed comparison of the medium and low-resolution maps (Figs. 2c-d-e) with the highest-resolution map (Fig. 2b) shows that the latter i) overpredicts the occurrence of stopping points in the slope immediately below RZ-A and in the access ramp below RZ-B (see solid red ellipses), and ii) underpredicts the occurrence of stopping points in the terminal slope below RZ-B (see dashed red ellipse).

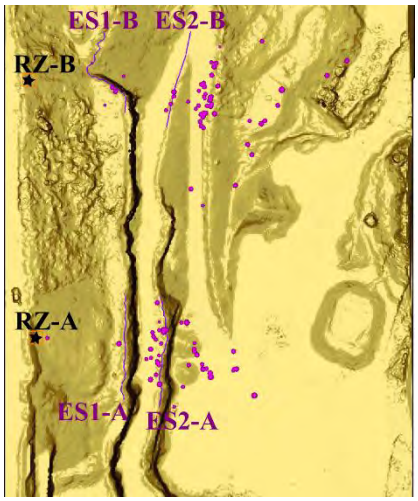

a) Position of evaluation screens (violet lines) and experimental blocks stopping position (fuchsia dots), for DTM resolution 0.5 m

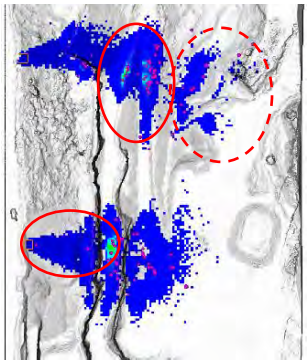

b) DTM resolution 0.2 m

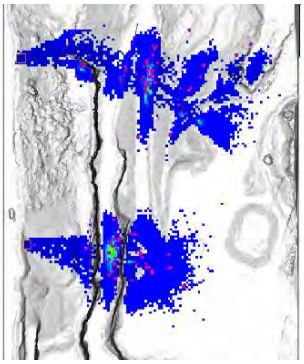

c) DTM resolution 0.5 m

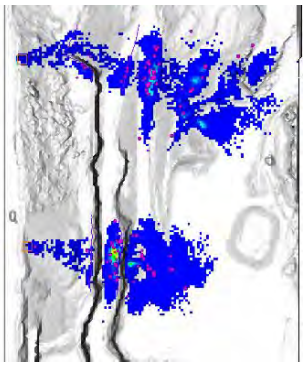

d) DTM resolution 1.0 m

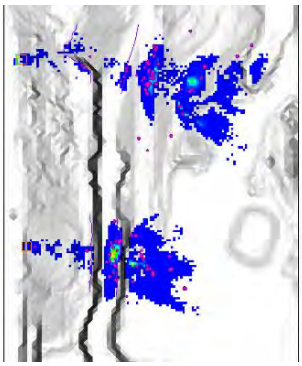

e) DTM resolution 2.0 m

Figure 2. X-Y plane view of: a) Experimental evaluation screens (violet lines) and blocks stopping position (fuschia dots), adapted from Bourrier et al. (2021); Maps of simulated number of stopping points for DTM resolution: b) 0.2 m, c) 0.5 m, d) 1.0 m, e) 2.0 m.

The highest resolution DTM (0.2 m) having a size smaller than the blocks, the perceived terrain orientation (Noël et al., 2021) could probably explain most the differences compared to lower resolution ones, as only a point contact between the blocks and the DTM is possible in the hybrid lumped-mass approach used here. With respect to the previous data, the calculation of the minimum distance (*MinDist*) between each observed block and all simulated stopping points allows to obtain quantile (Q) values (Tab. 2). As a result, the 0.5 m and 1.0 m resolutions roughly best fit observations up to Q90 (Qx: Q at x%) and are very close to minimum values for larger quantiles. This is interpreted as a result of the size of the blocks used in the field experiment (sphere equivalent diameter between 0.5 and 1.1 m), which are close to these DTM resolutions (0.5 m and 1.0 m).

Table 2. Computed *MinDist* quantile values (Qx: quantile at x%)

DTM resolution [m]	Q50 [m]	Q80 [m]	Q90 [m]	Q95 [m]	Q100 [m]
0.2	0.04	0.20	0.98	1.52	4.66
0.5	0.02	0.20	0.92	1.41	5.70
1.0	0.02	0.17	0.88	2.02	4.94
2.0	0.04	0.32	2.11	4.42	11.85

Reached distance

Cumulative Distribution Functions (CDFs) of the horizontal reached distance are shown in Fig. 3 for all DTM resolutions, together with experimental observations (Bourrier et al., 2021). The general shape of the observed CDFs compares quite well with the simulated ones, with the best fit being obtained for the 0.5 DTM at path B (orange curve in Fig. 3b). This reflects the consistent capture of the main zones of block deposition (flat zones, berms…) compared to the experimental data.

a)

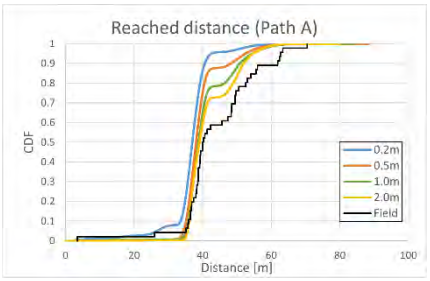

b)

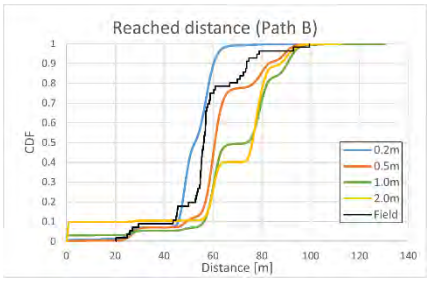

Figure 3. Reached distance CDFs (simulations and experiment) for: a) path A; b) path B.

Velocity at evaluation screens

The CDFs of translational velocities computed at ES1-A, ES2-A, ES1-B, ES2-B evaluation screens are compared with the corresponding observed CDFs in Fig. 4. For ES1-A, none of the computed CDFs reproduce the observed very low velocities (Fig. 4a), although the extreme values are well reproduced. This discrepancy could not be explained in the present simulations, as was also concluded from non-smooth dynamic simulations (Bourrier & Acary, 2022). For the other evaluation screens (ES2-A, ES1-B, ES2-B), the fit between computed and observed CDFs is well captured, especially the bimodal distribution at ES2-A (Fig. 4b) and the unimodal distribution at ES1-B (Fig. 4c). At ES2-B, the bimodal fit is not captured at intermediate velocities (Fig. 4d), although values close to extremes are well reproduced. It is noteworthy that the CDFs obtained in the present simulations, based on a hybrid lumped-mass approach that takes into account the rotational velocity (LM-R RocPro3D formulation), compare very well with CDFs obtained from non-smooth dynamic simulations (Bourrier & Acary, 2022).

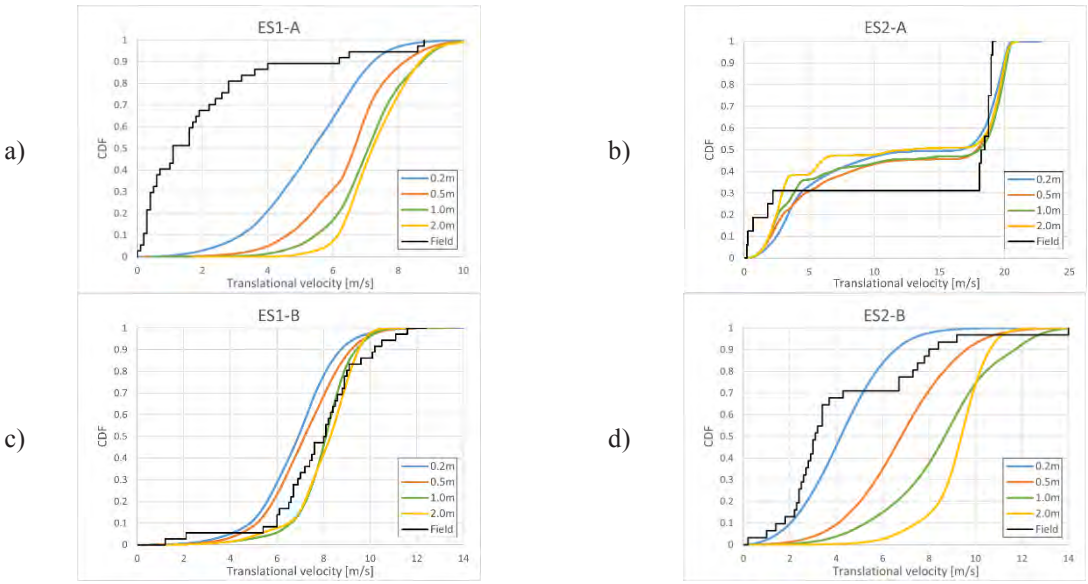

Figure 4. Translational velocities CDFs (simulations and field experiment) at each protection: a) ES1-A; b) ES2-A; c) ES1-B; d) ES2-B.

Conclusion

The Authume field experiment was used to investigate the effect of DTM resolution, considering values smaller and larger (0.2 m to 2.0 m) than the block size (equivalent diameter between 0.5 m and 1.1 m). Notably, all simulations were performed using the RocPro3D software without modification of the standard soil parameters, using a soil mapping procedure based on local slope criteria. Analysis of the results shows that the best agreement between our hybrid LM-R based simulations and the experimental observations is obtained at DTM resolutions of 0.5 m to 1.0 m, i.e. close to the experimental block size. This is consistent with the fact that DTM accuracy is recognised as a first-order factor in rockfall modelling (Bourrier & Accary, 2022).

With respect to block size, high resolution (i.e. small mesh size) DTMs do not necessarily improve the modelling quality, especially for oversampled DTMs. In fact, in lumped-mass based simulations, they may even introduce some bias in the propagation modelling due to an over-sensitivity to the DTM rugosity (if any). Where consistent with curvatures and slopes, the DTM mesh size should preferably be at least close to the block size.

References

Bourrier F & Acary V (2022) Predictive capabilities of 2D and 3D block propagation models integrating block shape assessed from field experiments. *Rock Mechanics and Rock Engineering* **55**-2, 591–609.

Bourrier F, Toe D, Garcia B, Baroth J & Lambert S (2021) Experimental investigations on complex block propagation for the assessment of propagation models quality. *Landslides* **18**-2, 639–654.

Cottaz Y, Barnichon JD, Badertscher N & Gainon F (2010) PiR3D, an effective and user-friendly 3D rockfall simulation software: formulation and case-study application. *In, Rock Slope Stability Symposium*, Paris.

Crosta G & Agliardi F (2003) A methodology for physically based rockfall hazard assessment. *Natural Hazards and Earth System Sciences* **3**-5, 407–422.

Dorren L, Schaller C, Erbach A & Moos C (2023) Automated Delimitation of Rockfall Hazard Indication Zones Using High-Resolution Trajectory Modelling at Regional Scale. *Geosciences* **13**-6, 182.

Li L & Lan H (2015) Probabilistic modeling of rockfall trajectories: a review. *Bulletin of Engineering Geology and the Environment* **74**, 1163–1176.

Noël F, Cloutier C, Jaboyedoff M & Locat J (2021) Impact-detection algorithm that uses point clouds as topographic inputs for 3D rockfall simulations. *Geosciences* **11**-5, 188.

Improved rockfall susceptibility map for Norway

Thierry Oppikofer[1], Clément Michoud[1], Pascal Horton[1], Martina Böhme[2]

[1] Terranum Sàrl, Bussigny, Switzerland
[2] Geological Survey of Norway (NGU), Trondheim, Norway

SUMMARY: The new rockfall susceptibility map for entire Norway uses the latest, high-resolution geodata (digital elevation model, geological and land-use maps) and modern, adapted modelling tools (Flow-R), which improves the spatial resolution of the map and its reliability and accuracy. Moreover, multiple large datasets with rockfall observations were used for the method calibration and validation. This calibration ensures that the map reflects the most realistic level of rockfall susceptibility. The improved rockfall susceptibility map introduces also different susceptibility levels distinguishing between extreme rockfalls (with the longest observed run-out distance) and more frequent, common events. More than 99% of rockfall observations are covered by the new rockfall susceptibility map for Norway; nonetheless, the total exposed population and infrastructure is significantly reduced compared to the current rockfall susceptibility map published in 2009.

Keywords: fragmental rockfall, susceptibility map, validation, land-use planning, exposure

Introduction

Landslide susceptibility is defined as a quantitative or qualitative assessment of areas where landslides, on a regional to national scale, may occur (Fell et al., 2008). Susceptibility maps are thus an important tool in land-use planning by highlighting exposed infrastructure, but also by showing areas without potential for landslides. Traditionally, susceptibility maps are binary (exposed or not exposed) and relatively coarse (scale of 1:50'000 or smaller), whereas novel maps combine high-resolution datasets and advanced computer models to define different susceptibility levels both for the failure and the runout modelling.

For fragmental rockfalls, susceptibility maps are largely based on terrain conditions (e.g., slope, geology, morphology), previous landslide events, and relatively simple approaches and modeling tools adapted for regional to national scales. Although fragmental rockfalls are expected to occur more frequently in the most exposed areas, the probability and intensity of rockfalls are explicitly not included in the susceptibility analysis.

In Norway, a first nationwide susceptibility map for fragmental rockfalls was published in 2009 based on a digital elevation model (DEM) with 25 m cell size (Derron et al., 2016) and is currently used by local and national authorities. The rockfall susceptibility map presented here will replace the current map and overcome some of its limitations by taking advantage of the new, high-resolution DEM from airborne laser scanning (HR-DEM) allowing to detect smaller cliffs coupled to more advanced propagation models leading to more realistic rockfall runout areas.

Methodology

The general methodology uses a similar approach as the current susceptibility map (Derron et al., 2016) with two main steps: 1) identification of source areas and 2) modeling of runout areas.

The present method relies, however, to a greater extent on past rockfall events and fieldwork in selected test areas for calibration and validation of the rockfall source areas and their runout areas. Furthermore, different susceptibility levels are introduced to distinguish between extreme, rare, and frequent rockfall events.

The rockfall source areas are mapped using critical slope angle thresholds for 34 different homogeneous geological units (HGUs) (Michoud et al., 2012). These HGUs are based on a combination of main lithology types and their tectonic setting in the recent 1:250'000 bedrock geological map published by the Geological Survey of Norway (NGU). For each HGU and using the slope angle computed from the HR-DEM (with a cell size reduced to 2 m), the slope angle thresholds for rockfall initiation are derived from the slope angle frequency distribution (Loye et al., 2009; Michoud et al., 2012). Based on this distribution, we distinguish three susceptibility classes for rockfall initiation (Fig. 1a):

- High: slopes steeper than the intersection of normal distributions *cliffs* and *steep cliffs* (54° in the example in Fig. 1a)
- Medium: slopes steeper than the intersection of the normal distributions *valley side* and *cliffs* (e.g., 46° in Fig. 1a)
- Low: slopes steeper than the 1st percentile of the cumulative distribution of *cliffs* & *steep cliffs*, clipped to the mean of the *valley side* normal distribution (e.g., 36° in Fig. 1a)

Medium and high susceptibility levels represent fragmental rockfall source areas from rock outcrops, while the low level represents the possible remobilization of blocks from scree deposits or other block-rich sediments (e.g., moraine). These potential remobilization sources are limited to certain land-use types (i.e., natural, non-built-up areas from 1:5'000 land-use maps) and unconsolidated sediment types (i.e., scree and avalanche deposits, moraine deposits and weathered surfaces (boulder fields) from NGU's 1:50'000 and 1:250'000 Quaternary maps). Moreover, source areas smaller than 25 m² are filtered (Fig. 1b).

Flow-R is a spatially distributed empirical model for the propagation modelling of mass movements at regional scale and used here for the runout modelling of rockfalls (Horton et al., 2013; Terranum, 2023). Flow-R combines a spreading algorithm controlling the path and the spreading of mass movements with a simplified friction-limited model determining the runout distance. The reliable and well-known reach angle approach (Jaboyedoff & Labiouse, 2011) is chosen as friction model (Fig. 2a), as it can easily be calibrated at regional scale using inventories of past rockfalls.

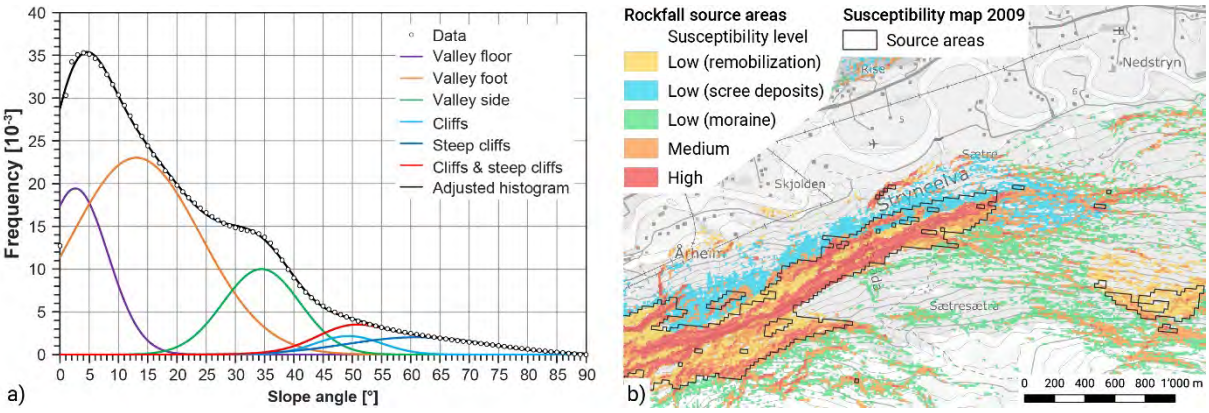

Figure 1. Slope angle thresholds for rockfall source areas: a) the slope angle frequency distribution for plutonic rocks is simulated with 5 normal distributions representing the valley floor, valley foot, valley side, cliffs, and steep cliffs; b) map of final rockfall source areas distinguishing several susceptibility levels.

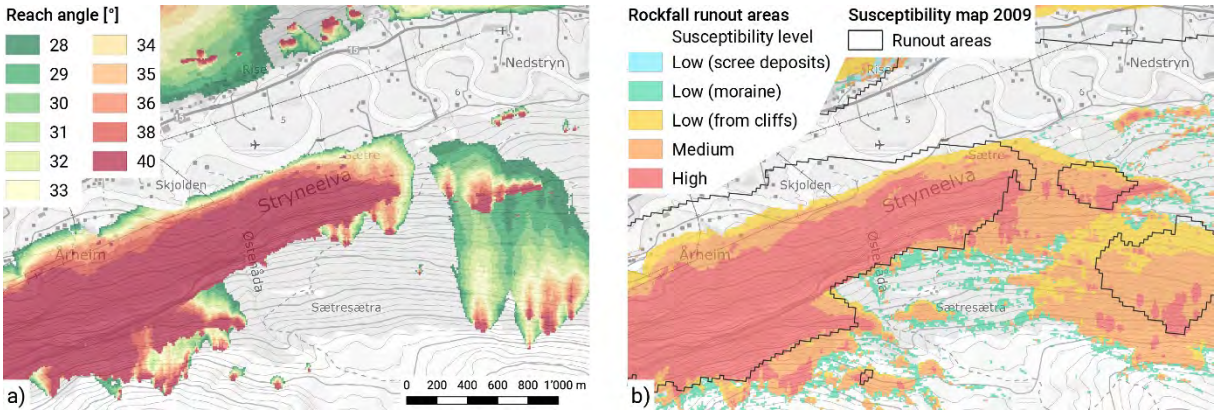

Figure 2. a) Effect of the reach angle parameter on the modelled rockfall runout areas; b) final rockfall susceptibility map combining the susceptibility levels for rockfall initiation (see Fig. 1b) with the three scenarios for rockfall propagation (extreme, rare, and current events); areas of possible remobilization of blocks are separated from the runout zones of fragmental rockfalls from cliffs.

A wide range of model parameters (176 parameter combinations with 4 different categories of source areas, 11 reach angles ranging from 28° to 40° and 4 velocity limits between 25 and 50 m/s) was used for the propagation modelling in Flow-R in different test regions during the calibration and validation phase of this study.

Validation of the new susceptibility map is crucial to find the best compromise between accurately mapping all relevant source areas and associated runout areas, without being too conservative. This validation uses thus different large datasets of rockfall observations: 1) historical rockfall events registered in the national landslide database (NVE, 2023), 2) mapped rockfall blocks and deposits in NGU's detailed Quaternary maps, and 3) field mapping carried out in selected test areas. For each dataset, we calculate the percentage of rockfall observations that lie within the modeled runout areas for the 176 parameter combinations.

Finally, the susceptibility levels are chosen such that percentages of historical rockfalls and mapped rockfall blocks covered by the susceptibility map are 66%, 95% and 99% for the high, medium, and low susceptibility levels, respectively.

Results

The methodology for the improved rockfall susceptibility map was applied to the entire land territory of Norway (ca. 308'000 km²). The slope angle frequency distribution for all 34 HGUs gives slope angle thresholds for the *steep cliffs* at 59° [54°; 62°] (average [min.; max.]), for *cliffs* at 44° [41°; 46°], and for the remobilization of blocks at 33° [31°; 37°]. These three classes of rockfall source areas cover 14.9% of the Norwegian land territory: 1.7% in the highest susceptibility class (from the *steep cliffs*), 4.6% in the medium susceptibility class (from the *cliffs*) and 8.5% in the low susceptibility class corresponding to the potential remobilization of blocks. These source areas are verified by the source areas of historic rockfall events, by field mapping in selected test areas and by visual inspection of the hillshade of the HR-DEM and orthophotos.

For the propagation modelling, the calibration and validation against different rockfall observation datasets leads to following parameter combinations for the three susceptibility levels (Fig. 2b):

- High: fragmental rockfalls from *steep cliffs* modelled with a reach angle of 37° and a velocity limit of 25 m/s are considered as common rockfall events (more than ⅔ of rockfall observations covered)
- Medium: fragmental rockfalls from *cliffs* & *steep cliffs* modelled with a reach angle of 33° and a velocity limit of 30 m/s are considered as rare rockfall events (>95% covered)
- Low: fragmental rockfalls from *cliffs* & *steep cliffs* and rockfalls from potential remobilization source areas modelled with a reach angle of 31° and a velocity limit of 35 m/s are considered as extreme rockfall events (99% covered)

The rockfall propagation modelling using these three scenarios is currently ongoing and will be completed by the end of 2023. For large representative test areas covering different geographical, geological and geomorphological settings in various parts of Norway (16% of the land territory), 18% of the surface are exposed to rockfalls: 7.7% are exposed to fragmental rockfalls with a high susceptibility level, 6.6% with a medium susceptibility level, and 3.8% with a low susceptibility level (including 1.9% that are exposed to rockfalls from possible remobilization of debris or boulders in block-rich sediments).

Conclusion & perspectives

The new rockfall susceptibility map for Norway uses the latest topographical and geological data, appropriate modeling tools (slope angle frequency distribution for HGUs, propagation modelling with Flow-R) along with extensive calibration and validation, to ensure that the susceptibility map reflects the rockfall hazard realistically. Compared to conventional binary susceptibility maps (yes/no), the improved rockfall susceptibility map introduces different susceptibility levels that distinguish between extreme rockfalls (with the longest runout distance), rare, and common events (with shorter runout). Although these susceptibility levels do not correspond to rockfall hazard zones, they are very useful for prioritizing efforts for hazard mapping and/or mitigation measures on the most rockfall-exposed infrastructure, but also for a quick validation of rockfall hazard zones (verification of mapping of relevant source areas, confirmation of realistic runout modelling, etc.).

References

Derron M-H, Stalsberg K & Sletten K (2016) Method for susceptibility mapping of rock falls in Norway. *Technical report NGU report 2016.033*. Geological Survey of Norway, Trondheim, Norway.

Fell R, Corominas J, Bonnard C, Cascini L, Leroi E & Savage WZ (2008) Guidelines for landslide susceptibility, hazard and risk zoning for land-use planning. *Eng. Geol.* 102, 85-98, doi:10.1016/j.enggeo.2008.03.022.

Horton P, Jaboyedoff M, Rudaz B & Zimmermann M (2013) Flow-R, a model for susceptibility mapping of debris flows and other gravitational hazards at a regional scale. *Natural Hazards and Earth System Sciences* 13, 869-885, doi:10.5194/nhess-13-869-2013.

Jaboyedoff M & Labiouse V (2011) Technical Note: Preliminary estimation of rockfall runout zones. *Natural Hazards and Earth System Sciences* 11, 819-828, doi:10.5194/nhess-11-819-2011.

Loye A, Jaboyedoff M & Pedrazzini A (2009) Identification of potential rockfall source areas at a regional scale using a DEM-based geomorphometric analysis. *Natural Hazards and Earth System Sciences* 9, 1643-1653, doi:10.5194/nhess-9-1643-2009.

Michoud C, Derron M-H, Horton P, Jaboyedoff M, Baillifard FJ, Loye A, Nicolet P, Pedrazzini A & Queyrel A (2012) Rockfall hazard and risk assessments along roads at a regional scale: example in Swiss Alps. *Natural Hazards and Earth System Sciences* 12, 615-629, doi:10.5194/nhess-12-615-2012.

NVE (2023) NVE Skredhendelser. Norwegian Water Resources and Energy Directorate (NVE), Oslo, Norway, https://temakart.nve.no/link/?link=skredhendelser.

Terranum (2023) Flow-R. Terranum Ltd., Bussigny, Switzerland, https://www.terranum.ch/en/products/flow-r/.

Early Warning and Collapse of the Insel Rockslide at Brienz/Brinzauls

Simon Loew[1], Andreas Huwiler[2], Stefan Schneider[3], Andri Largiader[2], Christoph Nänni[4], Daniel Figi[5], Reto Thöny[5], Michael Josuran[3]

[1]ETH Zurich, Department of Earth Sciences, Zuerich, Switzerland.
[2]Amt für Wald und Naturgefahren, Kanton Graubünden, Chur, Switzerland.
[3]CSD INGENIEURE AG., Thusis, Switzerland.
[4]Tiefbauamt, Chur, Switzerland.
[5]BTG Büro für Technische Geologie AG, Sargans, Switzerland.

SUMMARY: The village of Brienz/Brinzauls in the Swiss Alps was evacuated in May 2023 and the suspended rockslide above the village collapsed one month later. Due to the compound rupture surface in strong and weak rocks, the dynamic evolution of this landslide deviated from the expected behaviour and the classical time-to-failure laws. Based on in-depth geological investigations and continued process analyses the early warning system could handle successfully this geological complex situation.

Keywords: compound rockslide, landslide formation, collapse, early warning, velocity model

Introduction

The village of Brienz/Binzauls in the Swiss Alps (46°40'07.77''N/9°35'43.11''E) was evacuated between May 9 and 12, 2023 which triggered world-wide attention in most news channels and broad interest in the landslide causing this evacuation. The village of Brienz/Brinzauls is situated on an old deep-seated mountain slope deformation which is located in an Alpine stack of nappes and imbricates from the North Penninic and Austroalpine domain. The currently active compartments (moving at rates larger than 0.1 m/year) of this landslide complex have a total volume of about 170 million m^3. Detailed mapping of morpho-tectonic surface structures and 15 double and triple tube cored boreholes reveal a complex structure and multistage landslide history since at least the last 13'000 years, forming a series of stacked compound rock slides, dry debris flows and rock mass fall deposits. Since summer 2022 the most rapid compartment was identified in a steep convergent slope directly above the village of Brienz. This compartment was termed "Insel", is composed in the upper reaches of dip-slope dolomites (Vallatscha Fm.), and in the toe region of rauhwackes, dolostones (Raibler Fm.) and interbedded marly schists (Allgäu Fm.) dipping with low angles into the slope. This compartment is interpreted as a compound suspended rock slide, with a volume of about 1.5 million m^3 and a depth of about 70 m (Figure 1).

In September 2022 the future scenarios for the "Insel" compartment had been semi-quantitatively assessed using rock mechanical criteria expalined in Glastonburry and Fell (2008). The predicted scenarios were (i) accelerated sliding with increased rock (mass) fall activity (60%), (ii) transformation into a moderately rapid dry debris flow (30%), and (iii) transformation into a very rapid rock avalanche (10%). As such a rock avalanche would have completely destroyed the village of Brienz/Brinzauls and could have reached major traffic lines (railway and cantonal road) within 30 to 90 seconds, the early warning system (EWS) was mainly focused on this unlikely scenario. A comprehensive monitoring system was already in place since 2011, and a final detailed protocol for early warning parameter interpretation including alarm threshold values was established in March 2023. The most important

components of the monitoring system for the Insel compartment were: one Synthetic Aperture Georadar, one rockfall Doppler radar, one Robotic Total Station, several web cams and one Time-Lapse Cameras with automated Digital Image Correlation analysis. Many early warning parameters were periodically assessed, but the most critical parameters for the early alarm levels were velocity thresholds derived from Voight's tertiary creep model.

In this contribution we discuss the dynamic evolution and early warning of the Insel compartment, which is strongly related to the geological and kinematic complexity. We demonstrate the limitations of classical failure prediction models and explain why the Brienz rockslide collapse of June 2023 could be successfully predicted.

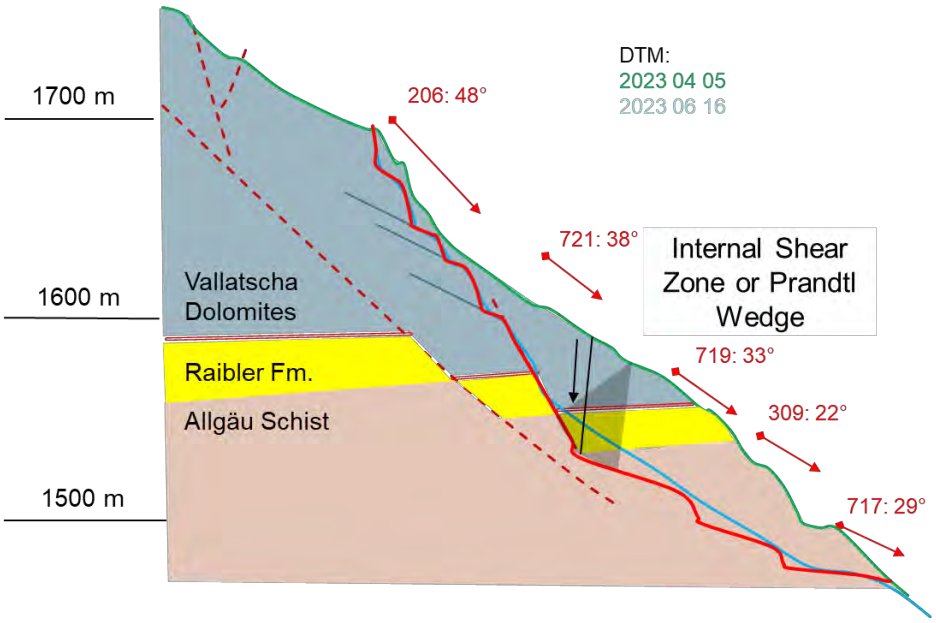

Figure 1: Simplified geological section and kinematic model of the Insel compartment in 2023, with topographic profiles as recorded before failure on April 5 (green) and after failure on June 16 2023 (blue line). A compound sliding plane (red line) and internal shear zone separates an active wedge in strong Vallatscha dolomites and a passive wedge in weak Allgäu schists. Red vectors indicate long-term TPS reflector displacements.

Compartment Formation and Landslide Dynamics

An acceleration of monitoring points located in the "Insel" compartment was observed since 2018. Elevated displacements were initially only observed at smaller hotspots in the Vallatscha Fm. and along the upper boundary at 1700 m elevation. In the years 2021-2023 the synthetic aperture Georadar showed a progressive downward extension of a zone with elevated displacements, and the formation of sharp compartment boundaries (head and lateral scarps) in 2022. Only in March 2023 the Insel compartment was fully developed as shown on Figure 1, and moved more or less coherently along structurally controlled lateral displacement boundaries. In addition, displacement vector orientations suggested that the basal rupture/sliding plane was fully developed at about the same time. Figure 2 shows the cumulative 3D displacement magnitudes (in mm, upper panels) and 24h-averaged velocities (in mm/day, lower panels) in the period between February and June 2023. Since the onset of acceleration in 2018, the velocities had been high compared to other brittle rockslides (>15 mm/day since 2020, and >100 mm/day since April 2023), reaching cumulative displacements of 30-60 m in April 2023. In the night of June 15th, 2023 the Insel compartment collapsed after a strong acceleration. The failure lasted several hours (mainly from 10 pm to 11.45 pm) and led to the formation of several, presumably very rapid, dry debris flows (mainly composed of layered Allgäu schists,

Raibler rauhwackes and dolomites), overlain by coarse rock mass fall deposits of Vallatscha dolomites.

As part of the EWS the Insel compartment velocity was modeled following Fukuzono (1985) and Voight (1988). They found that the increment of the velocity of surface displacement is proportional to the increment of acceleration of the surface displacement in the third stage of the slope creep motion before failure. That is:

$$d^2\Omega/dt^2 = A(d\Omega/dt)^{\alpha} \quad (1)$$

where Ω is displacement, and A and α are (strongly variable) material constants under time invariant external conditions (i.e., load, water pressure and temperature). For α>1 time integration leads to

$$v = [A(\alpha-1)(t_f-t)+v_f^{1-\alpha}]^{1/(1-\alpha)} \quad (2)$$

where v is displacement velocity, t_f time to failure, and v_f failure velocity (which can be assumed as infinite). For all individual TPS reflectors and Georadar observation points of the Insel compartment the velocity model (2) with parameters A, α and t_f have been determined periodically (weekly to daily) from non-linear regression fits to the observed past (90 and 180 day) velocities and displacements. Figure 3 (right) shows an example displacement/velocity model for reflector 725 (located between 719 and 721 on Figure 1), resulting from a fit to the observed (past 90 days) displacements. At longer time scales (90-360 days) the fitted models for all observation points always showed high correlations (similar to r^2=0.99878 in Figure 3). From these models, velocity thresholds (used as alarm levels of the EWS) have been determined for 30, 15, 7 and 2 days before the modeled collapse. The temporal variation of these thresholds is illustrated on Figure 3 (left) for reflector 725 and clearly shows that shorter velocity thresholds (few days before the collapse) become progressively more unstable (and unreliable). This is why the 7-day and 2-day alarms were finally issued based on other early warning parameters such as rockfall activity, run-out probability and short-term (24 hr) acceleration.

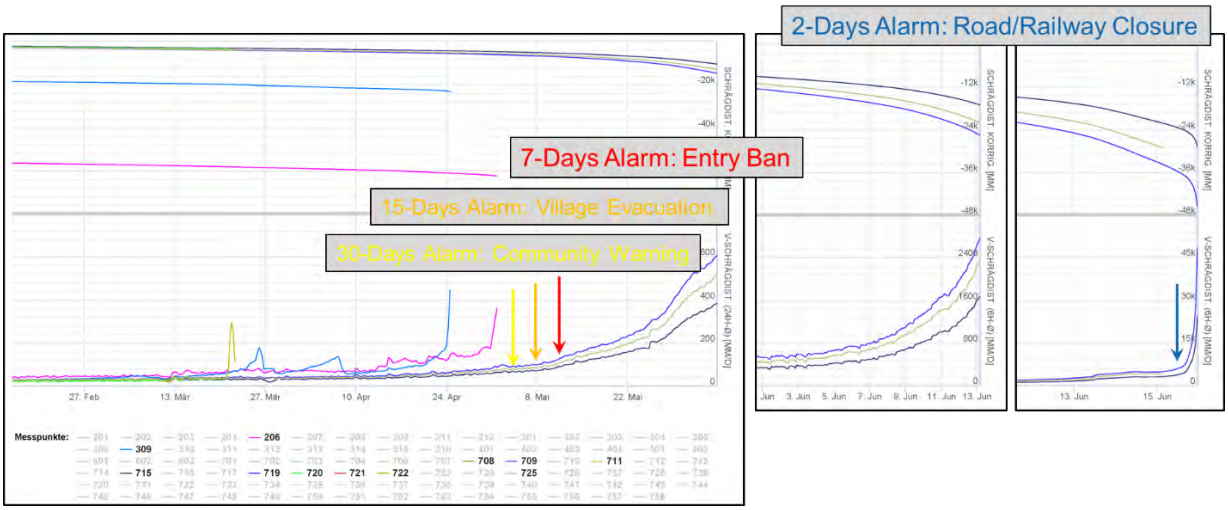

Figure 2: TPS displacements (in mm, upper panels) and 24-h velocities (in mm/day, lower panels) between February and June 2023. Many TPS reflectors were destroyed and had to be replaced periodically. Boxes highlight the timing of all implemented alarm levels.

A detailed analysis of the fitting parameters A and α showed significant variations through time (e.g. α of reflector 725 displacement varied between 2 and 5 in the period of February to June

2023), reflecting the non-uniform acceleration displayed on Figure 2. This acceleration variation most likely is related to the complex geology and kinematics of the suspended rockslide, composed of materials with strongly diverse mechanical properties forming the active and passive wedges. It is hypothesized that the Insel compartment dynamics since March 2023 was driven by a superposition of rate-strengthening plastic sliding along cataclastic breccia forming the basal sliding plane in the Allgäu schists, and damage and strength degradation of the Vallatscha dolomites in the Prandtl wedge or contact shear zone (Figure 1). Spring mapping, and nearby boreholes suggested that the water table lies below the basal rupture plane. This explains why only moderate reactions to rainfall events could be observed in 2023 and why hydro-mechanical coupling presumably played only a minor role for the recent rockslide dynamics and collapse.

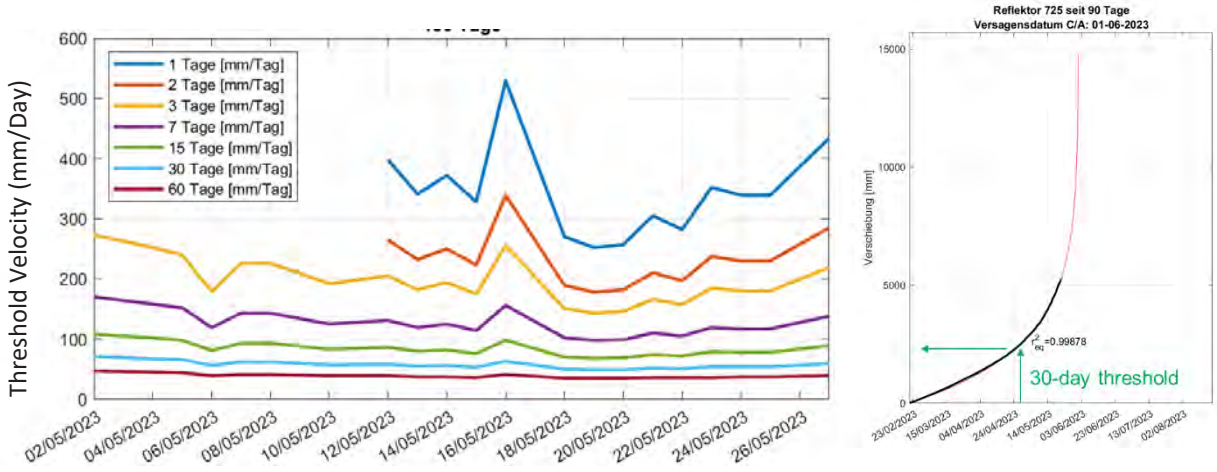

Figure 3: Left: Temporal variations of 1-60-day velocity thresholds for reflector 725 as determined from non-linear regression to Voight's velocity model (equation 2) between May 2nd and May 16th. Right: modelled (red line) and observed (black line) displacement evolution of reflector 725 between February and May 23rd 2023.

Conclusions

The Insel compartment developed from a minor instability to a 1.5 mio m^3 suspended rockslide within only 2-3 years. When the Insel compartment had developed a through-going basal shear zone (in March of 2023) the velocity reached 40 mm/day and accelerated further, leading to cumulative displacements of several tens of meters. This indicated significant control of the compartment dynamics by plastic displacements along a basal shear zone in Allgäu schists. The landslide long term dynamic behaviour could be approximated by Voight's law, but not the short-term velocity fluctuations in May and June. The compartment failed after an unexpected dramatic acceleration on June 15, 2023, which most likely was controlled by damage and strength loss of the active wedge in brittle Vallatscha/Raibler dolomites. The scenarios predicted in early 2023 were confirmed by the Insel compartment evolution.

References

Fukuzono, T. (1985). A new method for predicting the failure time of a slope. In Proceedings of the 4th International Conference and Field Workshop on Landslides, Tokyo, Tokyo Universit Press, p 145–150

Glastonbury and Fell (2008) A decision analysis framework for the assessment of likely post-failure velocity of translational and compound natural rock-slope landslides. Can. Geotech. J. 45: 329-350.

Voight, B. (1988) A method for prediction of volcanic eruption. Nature (London) 332:125–130

Leveraging Seismic Co-Detection for Early Warning

Jérome Faillettaz[1]

[1] GéoCod, Cerema, Bron, France.

SUMMARY: This study investigates the potential of seismic co-detection as a tool for early warning in gravity-driven instabilities like landslides and rockfalls. Leveraging the Fiber Bundle Model (FBM), we explore the relationship between seismic activity and impending catastrophic failure in heterogeneous materials. Our findings reveal that seismic co-detection offers early detection capabilities, insights into slope behavior, and the ability to characterize micro-seismic activity, making it a valuable addition to slope instability monitoring and early warning systems.

Keywords: Fiber Bundle Model, rupture prediction, co-detection, natural slope stability, early warning

Introduction

Gravity driven instabilities, such as landslides or rockfalls, pose significant risks to both human lives and infrastructure. These gravity-driven rupture phenomena occurring in natural heterogeneous media are rare, but have potential to cause major disasters, especially when they are at the origin of a chain of processes involving other materials such as snow (snow avalanche), water (flood) and/or debris (mudflow) (Gill and Malamud, 2014). Consequently, there is a critical need for reliable early warning systems that can detect and predict these events well in advance, offering an opportunity for timely evacuation and risk reduction.
In general, slope stability assessment (and prediction of slope failures) is based on the long-term monitoring and analysis of the temporal evolution of external parameters such as geometry and surface displacement (or surface velocity) as well as on the observation of external forcing such as meteorological/climatic conditions (e.g., rainfall duration and intensity, temperature, wind, snow accumulation).
Recently, Faillettaz et al. (2016) proposed a new method to investigate natural slope stability based on continuous monitoring and interpretation of seismic waves generated by the potential instability before the failure – i.e., an internal parameter. This method capitalizes on both heterogeneity and attenuation properties of natural media for developing a new strategy for early warning systems: as heterogeneous materials break gradually, with their weakest parts breaking first, they produce precursory "micro-cracks" with associated elastic waves traveling in the material. A new method - called **co-detection method** – was proposed (Faillettaz et al., 2016) to detect emergence of large events announcing impeding failure (precursors) based on a simple idea: As an elastic wave travels in the material, its amplitudes decays with distance from the source. An event (i.e., a crack formation in the material) may also be observed and recorded differently by an acoustic/seismic sensor depending on its location. Real-time processing of measured events that are detected concurrently on more than one sensor (co-detected) would then enable easy access to their initial magnitude as well as their approximate initial location. This simple method may provide a straightforward means to access characteristics and temporal evolution of surrogate variables linked to damage and mechanical state of the natural slope.

The aim of this work is to explore the co-detection strategy and its potential for early warning purposes. Specifically, we plan to characterize the behavior of the co-detection number as a function of the imminence of catastrophic failure and to assess slope stability for all types of ruptures, from brittle to ductile. Through this investigation, we hope to contribute to the development of more effective strategies for mitigating the risks associated with natural disasters caused by heterogeneous material failure.

Model and Method

We selected the Fiber Bundle Model for its simplicity and generality as a useful framework for systematically studying the progression of seismic activity preceding catastrophic failure in heterogeneous materials (Alava et al., 2006; Daniels, 1945; Faillettaz and Or, 2015; Kloster et al., 1997; Pierce, 1926; Pradhan et al., 2010). FBM offers simplicity, versatility, and a direct link between discrete failure events and acoustic emissions, making it an ideal candidate for monitoring progressive failures. Moreover, FBM can replicate various rupture behaviors, from brittle to ductile fracture, enabling the study of different types of rupture behavior observed in nature.

In essence, the model represents natural heterogeneous materials as a set of elasto-brittle fibers that are mechanically loaded in parallel; each fiber deforms in a linear elastic manner and breaks instantly at its prescribed rupture strength σ_{th} (whose values are drawn from a prescribed probability distribution). The load carried by the failed fiber is then redistributed according to specific rule ranging from global load sharing on all the surviving fibers (called DFBM) to local load sharing on their 4 neighboring fibers (called LFBM4), which could give rise to cascading failure events ("avalanches"). In each simulation, the fiber bundle is loaded in a quasi-static way towards catastrophic rupture. The FBM framework provides a simple and mechanically consistent means to study precursory signals preceding catastrophic rupture using recorded signals only. The application of 2-D spatially explicit FBM-based models has already provided new insights especially in terms of early warning perspectives.

To assess the effectiveness of the co-detection strategy, it's essential to evaluate the seismic wave amplitudes generated by avalanches at each sensor location. Note that the simulated avalanches in our model do not directly correspond to seismic wave amplitudes, as they omit the energy stored within the failed fibers. To address this, we follow a multi-step process within our Fiber Bundle Model (FBM). Firstly, we calculate the elastic energy released when the fibers comprising the avalanche fail. Next, we account for the attenuation of seismic waves as they propagate through natural media, considering the effects of geometric spreading. Ultimately, this enables us to express the signal amplitude measurable at any point within the FBM:

$$A_{att}(s) = \sum_{i \in S_j} \frac{\sigma_{th_i}}{|x_i - x_{sensor}|}, \quad (1)$$

Where Sj is the set of fiber composing the avalanche, x_i being the position of the failing fiber i with its associated strength σ_{th_i}.

To quantify seismic events and evaluate number of co-detections, we established a virtual network of sensors on the fiber bundle. We assessed the attenuated amplitude at each sensor location using equation (1). If the attenuated amplitude exceeded a predefined detection threshold (Thr), we considered the avalanche detected. We repeated this process for multiple virtual sensors, determining the number of simultaneous detections for each avalanche. For this study, we arbitrary deployed 49 virtual sensors in a grid-like pattern, ensuring comprehensive coverage of the bundle.

Results and Analysis

To assess the co-detection strategy, we arbitrary set a detection threshold (corresponding to the minimum amplitude of the elastic wave that can be detected by a virtual sensor), and evaluated simultaneous detections (co-detection number $\overline{N_{cod}}$) as macro-failure approached, i.e. $\delta = \frac{\sigma_c - \sigma}{\sigma_c} \rightarrow 0$ with σ_c representing the stress at the critical point (i.e., the failure of the bundle). This analysis involved evaluating $\overline{N_{cod}}$ (δ) for each avalanche in each simulation, followed by calculating the average $\overline{N_{cod}}$ for avalanches within predefined δ intervals across 1000 simulations.

We investigated the impact of sensor sensitivity on the co-detection number by varying detection thresholds. Figure 1 presents the mean co-detection number ($\overline{N_{cod}}$) for DFBM and LFBM4 models with different sensitivity settings, alongside the mean total radiated energy (<*E*>) as a reference. Notably, ductile-like rupture (DFBM) exhibited significantly higher total radiated energy and displayed increased seismic activity prior to global failure compared to brittle-like rupture (LFBM4), which had abrupt failure with fewer seismic precursors.

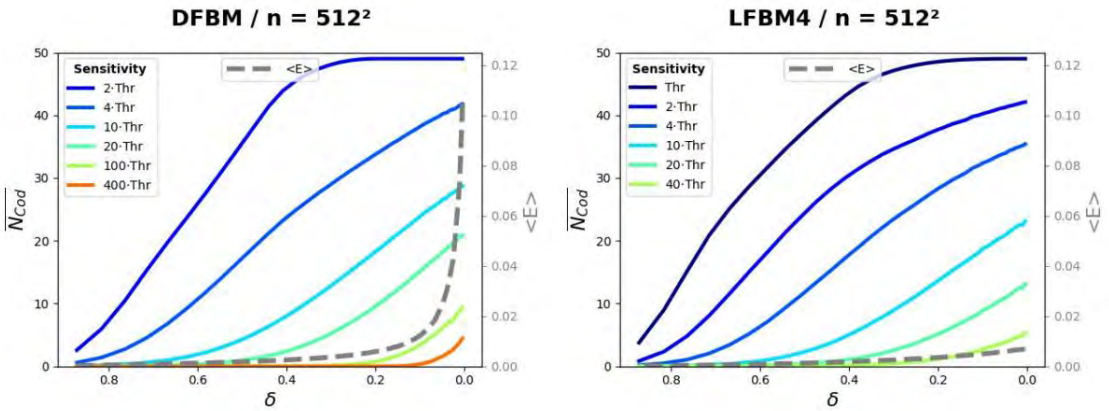

Figure 1: Evolution towards final catastrophic rupture of the mean number of codetection (averaged on 1000 simulations) for different sensor sensitivity (indicated as multiple of detection threshold *Thr* in legend) for DFBM and LFBM with 512² fibers, with δ (denoting the relative stress towards failure) $\delta = \frac{\sigma_c - \sigma}{\sigma_c}$ ranging from 1 to 0 (at rupture) and σ_c representing the stress at the critical point (i.e., the failure of the bundle). Dashed line indicates the evolution of mean radiated energy <*E*> as a function of δ. Note that to ensure comparison, *Thr* is the same in all cases.

As sensor sensitivity decreased (i.e. detection threshold increased), the co-detection number decreased, indicating that smaller avalanches, or those distant from sensors, went undetected due to attenuation. However, with sufficiently low detection thresholds, $\overline{N_{cod}}$ rapidly increased, reaching a plateau close to global failure, signifying saturation of detection. Conversely, higher detection thresholds led to lower co-detection numbers that increased near global failure. This trend was consistent across rupture types, including brittle-like rupture.

These findings suggest that sensitive sensor networks can detect the initiation of the failure maturation process but may not effectively gauge global failure imminence. In contrast, less sensitive networks can assess slope stability by detecting seismic activity in proximity to the rupture. If sensor sensitivity is excessively low, it may fail to detect signals before rupture, particularly in brittle cases with limited seismic activity.

Interestingly, for the same sensor sensitivity, $\overline{N_{cod}}$ (LFBM4) was only slightly lower than $\overline{N_{cod}}$ (DFBM), despite differences in statistical properties and avalanche sizes. This result can be attributed to the stress redistribution mechanisms; DFBM uses global load sharing rules,

resulting in diffuse ruptures, while LFBM promotes localized stress concentration and clustered avalanche patterns.
Due to attenuation effects, diffuse avalanches, even when large, may not yield significant co-detections, as some failed fibers may be distant from sensors. In contrast, clustered avalanches are more likely to be detected by nearby sensors. The co-detection method effectively identifies clustered activity, even with relatively weak seismic signals, making it suitable for capturing natural system ruptures where stress redistribution is not fully global.

Conclusion

In conclusion, seismic co-detection emerges as a powerful and sensitive tool for monitoring and predicting slope instability. Its ability to detect even minor seismic events makes it a valuable addition to existing early warning systems. This method offers several advantages:

- Early detection of precursory seismic events, providing crucial lead time for evacuation and mitigation.
- Effective characterization of micro-seismic activity, shedding light on the internal dynamics of the slope.
- Insights into the relationship between external conditions and seismic activity, enhancing our understanding of slope behavior.

While challenges such as sensor calibration and network deployment exist, they can be addressed with careful planning and calibration. The potential of seismic co-detection could transform our approach to monitoring slope instability, offering a flexible and adaptable complementary option for early warning systems.
To advance this field, future research should focus on experimental measurements in real-world scenarios. Combining seismic co-detection with other monitoring techniques, such as surface displacement measurements, can provide a holistic understanding of slope stability. With ongoing advancements in sensor technology and data analysis, seismic co-detection holds great promise for enhancing our ability to predict and mitigate natural hazards associated with slope instability.

References

Alava, M.J., Nukala, P.K.V.V., Zapperi, S., 2006. Statistical models of fracture. AP 55, 349–476. https://doi.org/10.1080/00018730300741518

Daniels, H.E., 1945. The Statistical Theory of the Strength of Bundles of Threads. I. Proceedings of the Royal Society of London A: Mathematical, Physical and Engineering Sciences 183, 405–435. https://doi.org/10.1098/rspa.1945.0011

Faillettaz, J., Or, D., 2015. Failure criterion for materials with spatially correlated mechanical properties. Phys. Rev. E 91, 032134. https://doi.org/10.1103/PhysRevE.91.032134

Faillettaz, J., Or, D., Reiweger, I., 2016. Codetection of acoustic emissions during failure of heterogeneous media: New perspectives for natural hazard early warning. GRL 43, 1075–1083. https://doi.org/10.1002/2015GL067435

Gill, J.C., Malamud, B.D., 2014. Reviewing and visualizing the interactions of natural hazards. RG 52, 680–722. https://doi.org/10.1002/2013RG000445

Kloster, M., Hansen, A., Hemmer, P.C., 1997. Burst avalanches in solvable models of fibrous materials. Phys. Rev. E 56, 2615–2625. https://doi.org/10.1103/PhysRevE.56.2615

Pierce, F.T., 1926. 32—X.—Tensile Tests for Cotton Yarns v.—"The Weakest Link" Theorems on the Strength of Long and of Composite Specimens. Journal of the Textile Institute Transactions 17, T355–T368. https://doi.org/10.1080/19447027.1926.10599953

Pradhan, S., Hansen, A., Chakrabarti, B.K., 2010. Failure processes in elastic fiber bundles. Rev. Mod. Phys. 82, 499–555. https://doi.org/10.1103/RevModPhys.82.499

Study on dynamic damage identification and failure mechanism of deep toppling slope under strong earthquake

Weihua Zhao, Xiang Lu, Fengjiao Wang

State Key Laboratory of Geohazard Prevention and Geoenvironment Protection, Chengdu University of Technology, Chengdu, Sichuan, China

SUMMARY: Deep-seated toppling slopes are widely distributed in Southwest China. Owing to the broken structure of the slope, it is easy to lose stability under strong earthquake disturbances, which poses a serious threat to the construction of the project. In this study, the model of typical deep-toppling slope was generalized. Through a large-scale shaking table test and vibration signal analysis, the damage evolution process and instability mechanism of a deep toppling slope under strong earthquake action considering complex discontinuous structural planes are revealed.

Keywords : deep toppling ; earthquake ; damage identification ; mechanism of instability

Introduction

Deep toppling is a typical slope deformation mode, which has the characteristics of a large development scale, deep toppling depth, developed structural plane, and cataclastic-discrete structure of the slope surface rock mass. Because there is no penetrating sliding surface like bedding, the fractured rock mass has locking section, so it has certain self-stabilization ability under natural conditions (O Yokoyama, 2020). The instability of such slopes is often triggered by seismic loads and is characterized by high speed, high energy, and serious disaster consequences (Zhang H et al., 2022). There are still many problems that need further research on how deep toppling is destroyed under strong earthquake action. In particular, it has not been clear how the slippery surface is formed. How do structural planes expand from one another? Where does the slip surface end up? Therefore, based on the shaking table experiment, we establish a deep topping slope model to simulate the response characteristics of the slope under seismic conditions, in order to reveal the evolution process of deep tipping into landslide.

Test and data processing

Based on the statistical analysis of typical toppling deformation slopes in Southwest China, phyllite (soft rock) and metamorphic sandstone (hard rock) developed in the study area were used as experimental prototype materials. Based on dimensional theory, the similarity ratios of other parameters were derived. Through the ratio and mechanical property parameter tests, the formula for similar materials was determined, and prefabricated blocks were prepared (Fig.1). According to the structural characteristics of the deep toppling deformation slope, soft rock and hard rock slope models with extremely strong toppling, strong toppling, weak toppling, and non-toppling zones are generalized. The model was built using prefabricated blocks to simulate the layers and discontinuities in the slope. Accelerometers and earth pressure gauges were arranged in different parts of the longitudinal section of the model to collect test data (Fig.2). In this experiment, the X-direction Wenchuan wave and 5 Hz sine wave were used as the input waves, and the duration was 18 s. White noise was applied to the model before each formal

loading.

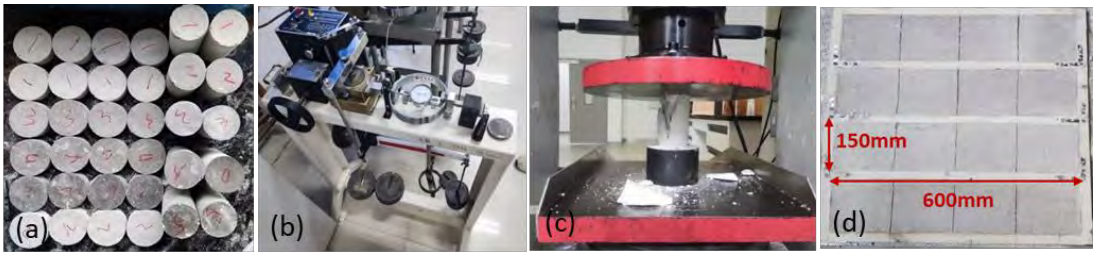

Figure. 1 Similar material proportioning experiment process. (a) specimen (b) direct shear test (c) uniaxial compression test (d) precast block

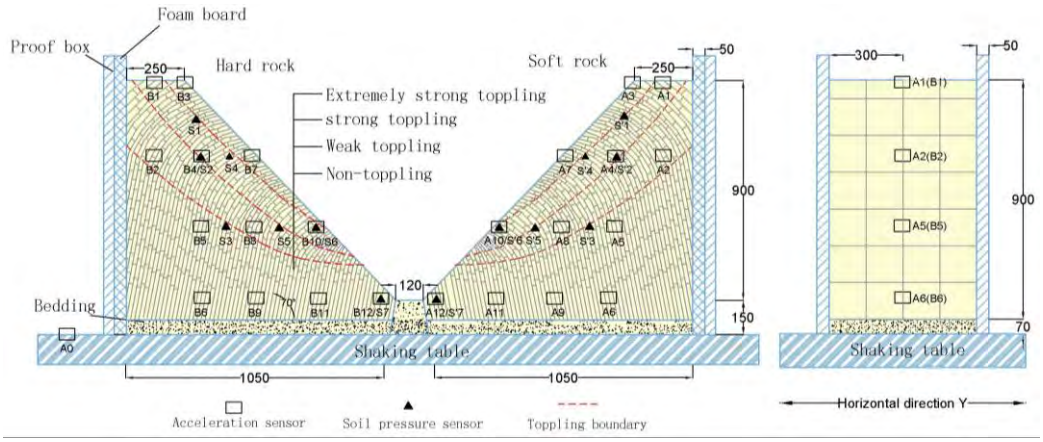

Figure.2 Model schematic and sensor layout

The transfer function method is used to process the measured white noise signal, and the change in the natural frequency and damping ratio of the slope under the action of seismic waves is analyzed to reflect the evolution trend of the internal damage of the model. The Hilbert marginal spectrum was obtained by processing the acceleration data of different parts of the slope surface using the Hilbert-Huang transform. The time and location of the damage inside the slope were analyzed based on the variation trend of the Hilbert marginal spectrum amplitude.

Experiment results

The soft rock slope model is loaded step by step with the seismic wave, and the natural frequency of the slope body decreases approximately linearly, from the initial 19.46 Hz to 14.92 Hz ; the damping ratio increased gradually from 0.152 to 0.334 (Fig.3a). Under the disturbance of seismic waves, the internal structure of the model is broken owing to the low mechanical strength of the soft rock, resulting in a significant change in the overall structural mode of the model.

The variation trend of the measured acceleration marginal spectrum amplitude at different elevation points on the slope surface is shown in Fig.3b. With the increase in seismic wave amplitude, the marginal spectrum amplitude at A3 changes abruptly at 0.2 g amplitude, indicating that structural damage occurs here, resulting in incomplete energy transmission. When the amplitudes of A7 and A10 are 0.3 g and 0.2 g respectively, the marginal spectrum amplitude changes abruptly. There was no mutation in the marginal spectrum amplitude at A12, indicating no structural damage at the foot of the slope. By comparing the time when the marginal spectrum amplitude of the monitoring points at different elevations of the slope table changes abruptly, it was found that the structural damage first occurred at the shoulder of the

slope and then gradually expanded to a low elevation.

Fig.4 shows the whole process of macroscopic instability evolution of soft rock slope. Under the action of an earthquake, tensile cracks were first generated at the shoulder of the slope (Fig.4b), and then the cracks gradually expanded to a low elevation along the extremely strong toppling zone (Fig.4c-d). Under the action of 0.8 g sine wave, the sliding zone was completely connected, and the sliding body was unstable along the sliding surface and accumulated at the foot of the slope (Fig.4e-f). The evolution process of the sliding body instability corresponds well with the evolution law of the slope natural frequency and marginal spectrum.

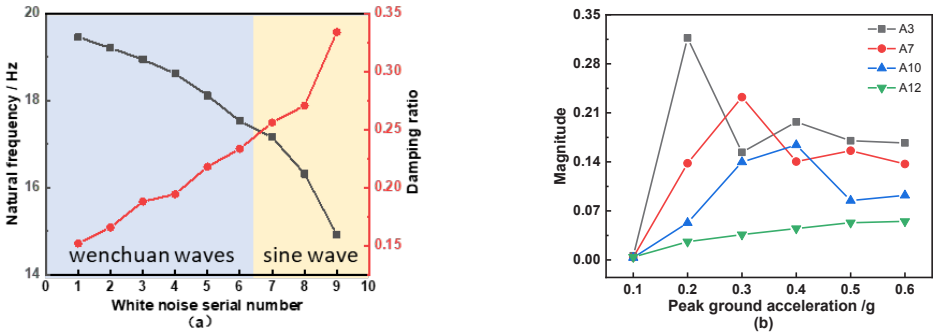

Figure. 3 Change of vibration parameters of soft rock model. (a) natural frequency and damping ratio (b) marginal spectrum amplitude of soft rock model

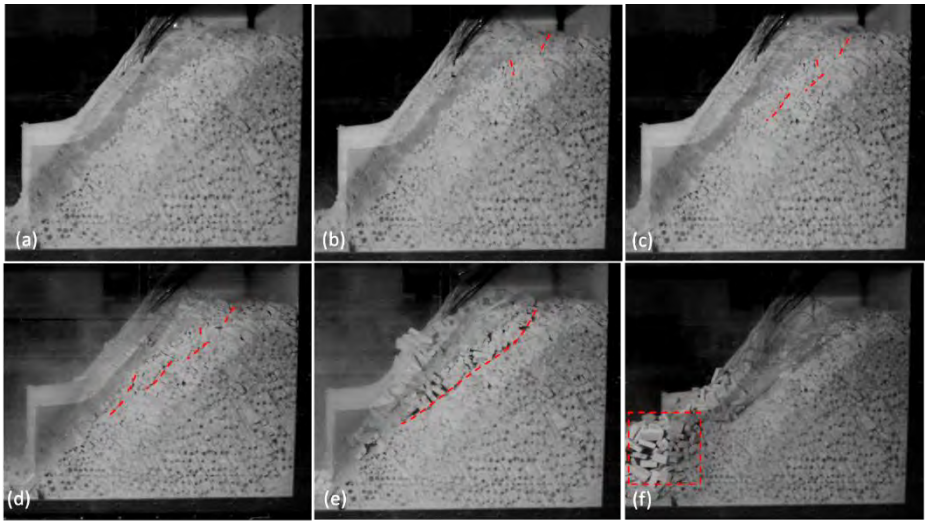

Figure.4 Damage evolution and instability process of soft rock model

The natural frequency of the hard rock slope model did not change significantly during the Wenchuan wave-loading stage. In the sine wave loading stage, the natural vibration frequency decreased sharply, and the damping ratio showed a sharp upward trend (Fig.5a). This is because the mechanical strength of hard rock is high and the energy of the Wenchuan wave is low, which has a weak influence on the slope structure. The energy of the sine wave was high, which caused the structural plane of the slope to expand sharply, and the structural damage increased sharply. The marginal spectrum amplitude of the hard rock slope model in the Wenchuan wave loading stage also did not produce a sudden change, which also shows that, at this stage, the internal structure of the hard rock slope model did not cause obvious structural damage (Fig 5b).

Fig.6 shows the process of instability evolution of the hard rock slope. During the loading stage of the Wenchuan wave, there is no obvious macroscopic deformation sign of the hard rock slope

(Fig.6a) ; when loading to 0.8 g sine wave, obvious tensile cracks are formed in the middle and upper parts of the slope along the extremely strong toppling zone (Fig.6b) ; and finally, under the action of 0.9 g sine wave, the overall instability of the slope occurs.

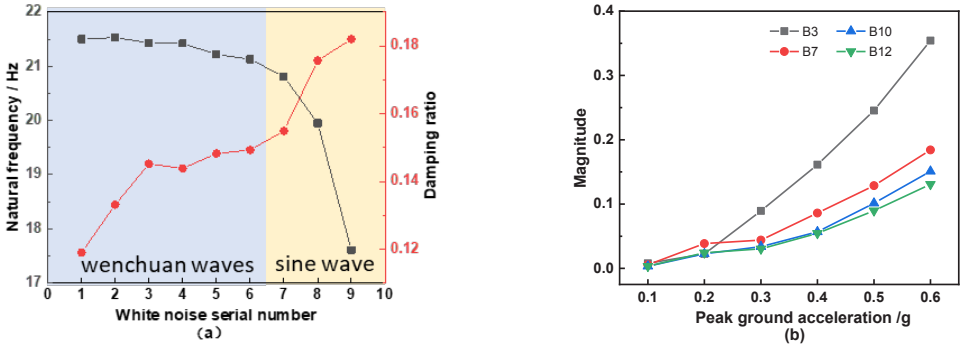

Figure. 5 Change of vibration parameters of soft rock model. (a) natural frequency and damping ratio (b) marginal spectrum amplitude of hard rock model

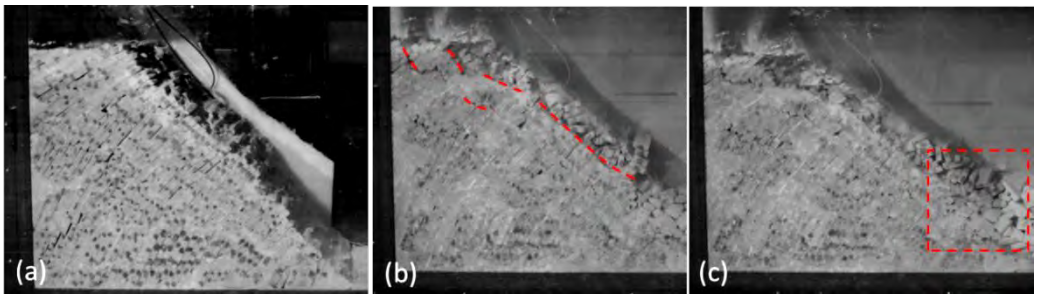

Figure.6 Damage evolution and instability process of hard rock model

Conclusion

Based on the characteristics of natural vibration frequency, damping ratio, and macroscopic deformation signs of soft rock and hard rock deep toppling deformation slope slopes under strong earthquakes, the corresponding slope instability mechanism is summarized.

Soft rock slopes show progressive failure, and the evolution process can be divided into four stages: internal structure adjustment, local fracture formation, crack propagation, and sliding surface penetration. The vibration parameters show that the natural frequency decreased approximately linearly, and the damping ratio increased approximately linearly. In the macroscopic deformation of the slope, tensile cracks are first generated at the slope shoulder, and then the cracks gradually expand to a low elevation along the extremely strong toppling zone. The slope was destroyed when the sliding surface was completely penetrated.

The failure of hard-rock slope was sudden. When the energy of the seismic wave reaches a certain degree, the formation, expansion, and penetration of the fracture surface occur in a short time. Under the action of the Wenchuan wave, the change in its natural frequency was not obvious ; under the action of a sine wave, the natural frequency decreased sharply and the damping ratio increased sharply.

References :

Yokoyama, O.(2020). Evolution of uphill-facing scarps by flexural toppling of slate with high-angle faults. Geomorphology, 352, 106977.

Zhang, H., Wu, Y., Huang, S., Zheng, L., & Miao, Y. (2022). Analysis of flexural toppling failure of anti-dip rock slopes due to earthquakes. Frontiers in Earth Science, 9, 831023.

Temperature distribution detected by electrical geophysics and rockfall monitoring in a permafrost-affected ridge

A field experiment under the Cosmiques refuge (Mont-Blanc, Chamonix)

[1]**P-A. Duvillard**, [2]L. Ravanel, [2]F. Magnin, [2]A. Revil, [2]J. Bock, [1]J. Richard,[1]P. Vaudelet and [1]A. Ghorbani

[1] NAGA Geophysics, pierre-allain.duvillard@naga-geophysics.com, Le Bourget-du-Lac, France,
[2] EDYTEM, ludovic.ravanel@univ-smb.fr, Univ. Savoie Mont Blanc, CNRS, Le Bourget-du-Lac, France
[2] EDYTEM, florence.magnin@univ-smb.fr, Univ. Savoie Mont Blanc, CNRS, Le Bourget-du-Lac, France,
[2] EDYTEM, andre.revil@univ-smb.fr, Univ. Savoie Mont Blanc, CNRS, Le Bourget-du-Lac, France
[2] EDYTEM, josue.bock@univ-smb.fr, Univ. Savoie Mont Blanc, CNRS, Le Bourget-du-Lac, France
[1] NAGA Geophysics, jessy.richard@naga-geophysics.com, Le Bourget-du-Lac, France,
[1] NAGA Geophysics, pierre.vaudelet@naga-geophysics.com, Le Bourget-du-Lac, France,
[1] NAGA Geophysics, ahmad.ghorbani@naga-geophysics.com, Le Bourget-du-Lac, France,

SUMMARY: Geoelectrical prospecting is a widely used method for detecting and studying permafrost. Electrical resistivity tomography, which has proven highly effective in permafrost contexts, is increasingly combined with induced polarization measurements on the field and in the laboratory. The use of recently developed petrophysical models allows the conversion of electrical conductivity into quantitative data, such as temperatures. This methodology has been validated and independent modelling and data are used to assess the validity of the approach and discuss application to monitor parameters leading to mass movement. We used this method to characterize high mountain infrastructure support ground (refuges and ski lifts), where measurements have been repeated over time to characterize permafrost degradation (warming).

Keywords: permafrost, electrical conductivity, temperature, rockfalls.

Introduction

Knowledge about the thermal state of steep alpine rock faces and of rock glaciers and the ice distribution is crucial to assess potential geohazards associated with the permafrost warming. Temperature measurements at the rock surface or in boreholes are however expensive, invasive, and provide spatially-limited information. Electrical conductivity tomography has been broadly used to detect and monitor mountain permafrost since 30 years on rock walls and rock glaciers (e.g. Magnin et al., 2015; Mollaret et al., 2019). Recent studies showed the interest of coupling, at several time and scales, methods of electrical conductivity tomography, induced polarization tomography in the field, in parallel with petrophysical characterization of core samples. The aim of the latter is to develop petrophysical transforms between geophysical observables and parameters of interest such as temperature. The advantages of these geophysical methods are their low cost and their non-invasive character. They provide 2D, 3D, and 4D tomograms/images of the subsurface.

In order to describe the degradation of permafrost during the 21st century, we used a methodology developed by Magnin et al. (2017) to simulate the long-term evolution of permafrost from the end of the Little Ice Age (around 1850) until 2100 to compare with a geophysical model.

Two high-resolution 3D topography methods are also used for monitoring rock face morphology (LiDAR and photogrammetry) since 2009 to monitor the NW and SE faces of the

lower Cosmiques ridge. Comparing the data allows us to assess morphological changes (rockfalls) and the lowering of the Glacier du Géant surface at the base of the SE face.
We used this methodology with the aim of characterizing the distribution and condition of permafrost below mountain infrastructures (refuges and ski lifts).

Study site

The Cosmiques Refuge (3613 m) is located on the lower Cosmiques ridge, SSW of the Aiguille du Midi (3842 m, **Figure 1**). The SE face underwent multiple rockfalls, notably a significant one the 22 August 1998 (Ravanel et al., 2013), destabilizing 600 m^3 near the foundations. Geologically, the Cosmiques ridge is mainly made of highly fractured granites.

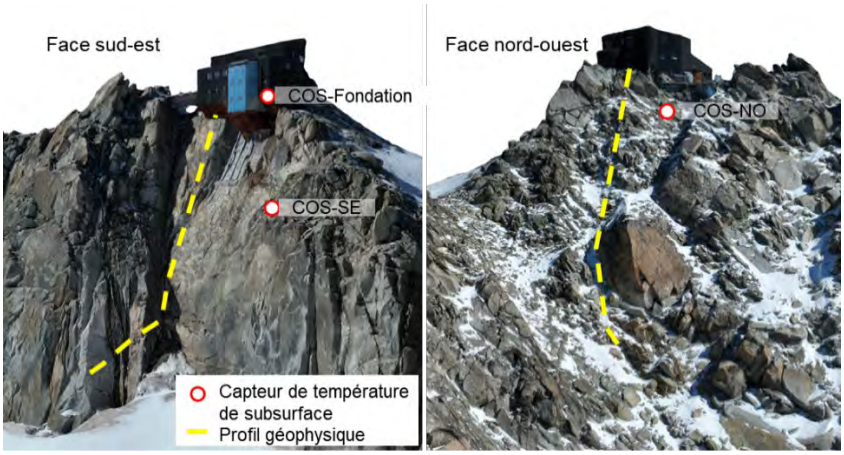

Figure 1. Location of geophysical profile and thermal instrumentation.

Methods

Geophysical datasets were repeated 3 times at the lower Cosmiques ridge (2016, 2019 and 2022) in conductivity and induced polarization tomography with ABEM SAS 4000, and ABEM LS2 instruments. Three rock surface temperature sensors were also installed at a depth of 10 cm in 2016 on different faces and near the refuge foundation (**Figure 1**).
After inversion of geophysical data sets, we converted electrical conductivity data into temperature using petrophysical models previously developed (Duvillard et al., 2021). Laboratory measurements were carried out on a rock sample in order to test the petrophysical model. After saturating the sample with melted snow water collected in the field, electrical conductivity measurements were performed between -15 °C and + 20 °C (Coperey et al., 2019). The simulation permafrost degradation in the 21st century used a methodology developed by Magnin et al. (2017) for simulating the long-term evolution of permafrost from sub-surface temperature between Little Ice Age (around 1850) up to the year 2100 using the IPCC scenarios.

Results of geophysical investigation

The 2D conductivity profiles acquired between 2016 and 2022 show a vertical distribution of conductivitiy, with relatively low conductivity values on the NW face and higher values on the SE face (**Figure 2**). This suggests that permafrost is limited to the NW face, with a vertical boundary of permafrost under the refuge and the absence of permafrost on the SE face. The repeated measurements indicate permafrost degradation in the NW face. Between 2016 and 2022, a vertical fracture filled with massive ice have been warmed, likely leading to the gradual disappearance of the ice joint.

The depth-estimated temperature profiles were obtained using a petrophysical model to convert electrical conductivity into temperature (Duvillard et al., 2021). In the NW face, permafrost in 2022 may have a temperature ranging between -1 and -3°C in the subsurface very close to the melting point. On the SE face, permafrost is now absent.

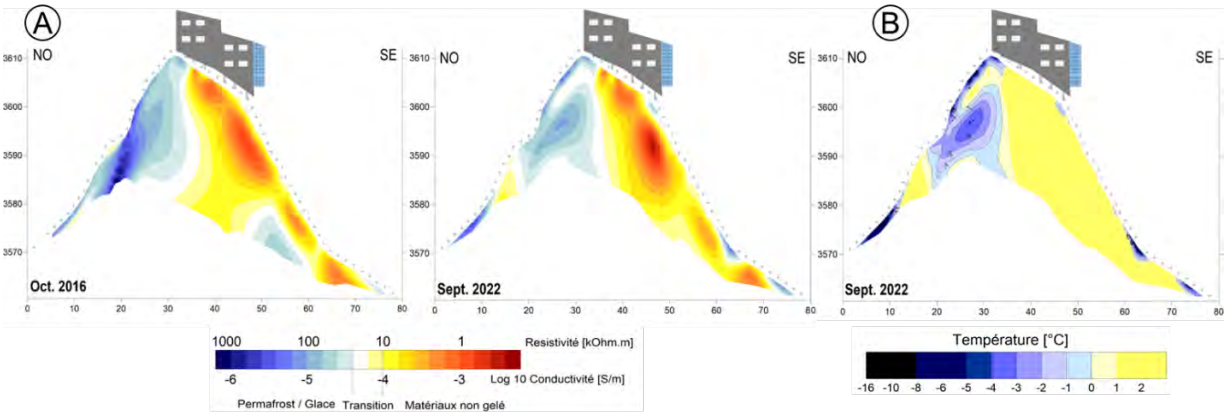

Figure 2. Cross-sections of conductivities in 2016 and 2022 and the temperature estimation in 2022 determined from the electrical conductivity.

Results of temperature modelling

The **Figure 3** illustrates permafrost evolution in the 21st century. The temperature distribution aligns closely with geoelectric measurements, showing persistent permafrost in the NW face. These independent methods validate the results. However, there is a ~2°C difference in temperatures between them, revealing inherent uncertainties. Simulations predict complete permafrost loss on the Cosmiques ridge in the next 2-3 decades due to climate warming, considering these uncertainties.

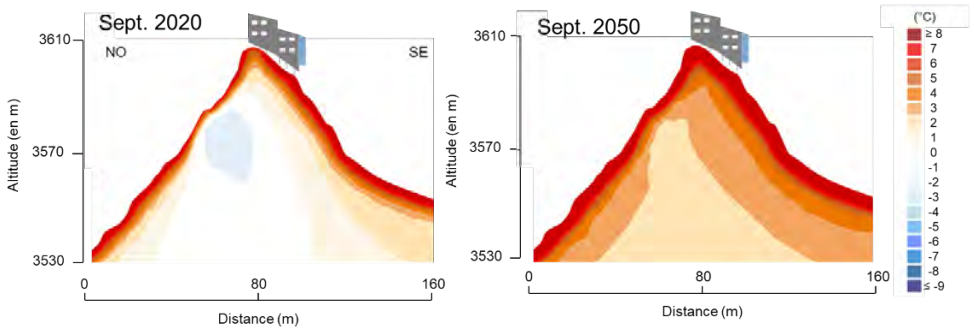

Figure 3. Simulation of permafrost evolution for the lower Cosmiques ridge over the 21st century.

Results of geomorphological monitoring

The topographic monitoring was conducted on the SE face, revealing 102 rock destabilizations (**Figure 4**). The NW face exhibited significant geomorphological activity with 32 events between 2019 and 2022. The accelerated degradation of permafrost in the coming decades is expected to intensify rock destabilizations, especially on the NW face. The majority of these instabilities occurred close to recently deglaciated areas, which characterizes a decadal paraglacial erosive crisis.

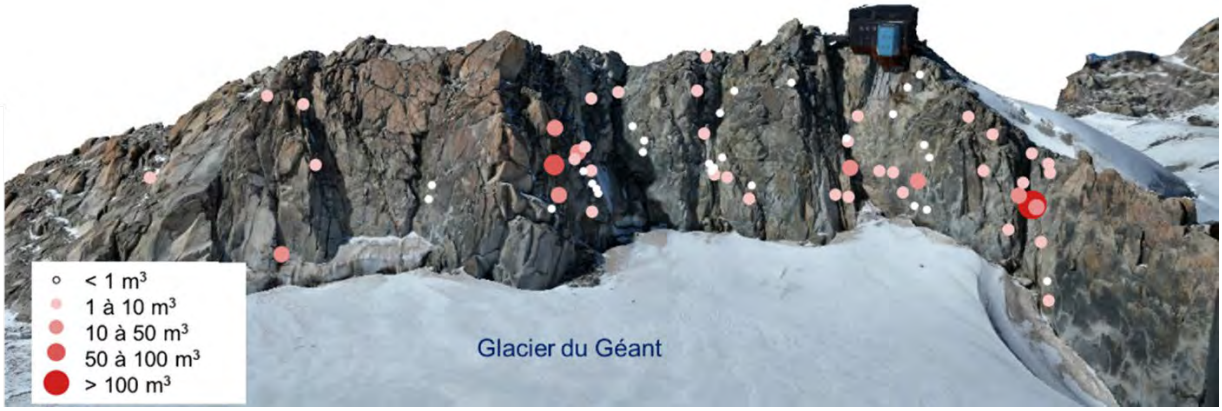

Figure 4. Location of the 70 identified rock destabilizations between 2010 and 2022 on the SE face.

Conclusion

These recent advances in geoelectrical methods for permafrost characterization show the great interest to combine geoelectrical and petrophysical models. In the short term, monitoring or repeating profiles with induced polarization masurement gives new perspectives to quantitatively characterize the ice / water phase changes. Monitoring of the rock face with 3D topographic surveys allows us to track morphological changes in the sub-surface as a result of permafrost degradation and glacier level decrease. This study demonstrates a strong interest in combining various methods to survey the surface and subsurface under mountain infrastructure in a permafrost context.

Acknowledgements

This study was funded by la Communauté de Communes de la Vallée de Chamonix-Mont-Blanc and the PrevRisk 1 project (2016-2018). The authors would like to thank the successive keepers of the Cosmiques refuge. We thank also all individuals who contributed to data acquisitions.

References

Coperey A., Revil A., Abdulsamad F., Stutz B., Duvillard P.A, Ravanel L. (2019). Low frequency induced polarization of porous media undergoing freezing: preliminary observations and modelling. Journal Geophys. Research, 124.

Duvillard P. A., Magnin F., Revil A., Legay A., Ravanel L., Abdulsamad F., & Coperey A., (2021). Temperature distribution in a permafrost-affected rock ridge from conductivity and induced polarization tomography. Geophysical Journal International.

Magnin F., Krautblatter M., Deline P., Ravanel L., Malet E. & Bevington, A. (2015). Determination of warm, sensitive permafrost areas in near-vertical rockwalls and evaluation of distributed models by electrical resistivity tomography, J. Geophys. Res., 120, 745–762.

Magnin F, Josnin J-Y, L. Ravanel, Pergaud J, Pohl B, Deline P (2017) Modelling rock wall permafrost degradation in the Mont Blanc massif from the LIA to the end of the 21st century. The Cryosphere 11(4):1813–1834. https://doi.org/10.5194/tc-11-1813-2017

Mollaret C., Hilbich C., Pellet C., Flores-Orozco A., Delaloye R., Hauck C. (2019). Mountain permafrost degradation documented through a network of permanent electrical resistivity tomography sites, The Cryosphere, 13, 2557–2578.

Ravanel L., Deline P., Lambiel C.,Vincent C. (2013) Instability of a high alpine rock ridge: the lower arête des cosmiques, mont blanc massif, france. Geografiska Annaler: Series A, Physical Geography 95(1):51–66.

Frozen Debris Lobes: A Glimpse into Landslides in Permafrost

Margaret M. Darrow[1], Ronald P. Daanen[2]

[1] University of Alaska Fairbanks, Fairbanks, Alaska, U.S.A.
[2] Alaska Division of Geological & Geophysical Surveys, Fairbanks, Alaska, U.S.A.

SUMMARY: Frozen debris lobes (FDLs) are landslide features in permafrost-affected terrain located in the Brooks Range of Alaska, U.S.A. We have investigated these features for over a decade, including: field observations; surface measurements; subsurface investigations; laboratory testing; and historic imagery, InSAR, and lidar analysis. Over this measurement period, rates of movement have increased, and the close proximity of one of these features (FDL-A) required a realignment of the Dalton Highway. In this overview of our research, we describe typical FDL composition and movement, and provide details of subsurface investigations, laboratory testing, and modeling of FDL-A.

Keywords: frozen debris lobe, landslide, permafrost, Alaska

Introduction

Frozen debris lobes (FDLs) are slow-moving landslides in permafrost-affected terrain, 43 of which are located on the slopes along the Dalton Highway and Trans Alaska Pipeline System (TAPS) corridor in the Brooks Range of Alaska, U.S.A. (Figure 1a). These features were first identified and mapped in the 1970's and 1980's with the construction of TAPS and the highway (e.g., Kreig and Reger 1982), but thought to be inactive at that time. In 2008, we recognized that several FDLs were actively moving (Daanen et al. 2012). By 2013, we conducted regular monitoring of selected FDLs (Figure 1b); of this group, FDL-A is the largest and closest to the Dalton Highway (Figure 1c). The Dalton Highway is the only roadway connecting the oil and gas fields of Alaska's North Slope to cities in the south, and therefore is an important road for the state's economy. Because of its proximity to the highway, FDL-A has received most of our attention, including several subsurface investigations. Here, we provide an overview of some of the FDL research conducted since 2012 with a focus on FDL-A, as well as a summary of ongoing research efforts.

FDL Composition and Movement

FDLs are composed of silt, sand, and gravel, as well as organic debris that they incorporate as they move downslope. Most of these features originate in catchments where the bedrock is heavily fractured, platy, and foliated (Darrow et al. 2016). FDLs move through a variety of mechanisms, including permafrost creep, basal sliding, debris flows, and retrogressive thaw slumps (RTS) (Daanen et al. 2012). Movement occurs throughout the year, leaving slickens in the FDL material in the fall and winter as frozen slabs override the original ground surface.

On an annual basis, we measure surface marker pins installed across each of the monitored FDLs with a real-time kinematic global positioning system (RTK-GPS) device; Figure 2a provides a summary of the annualized rates of movement for eight of the monitored FDLs. FDLs demonstrate negligible to minor lateral spreading, and most form levees that move more slowly than the adjacent lobe material, helping to direct their movement downslope. All of the

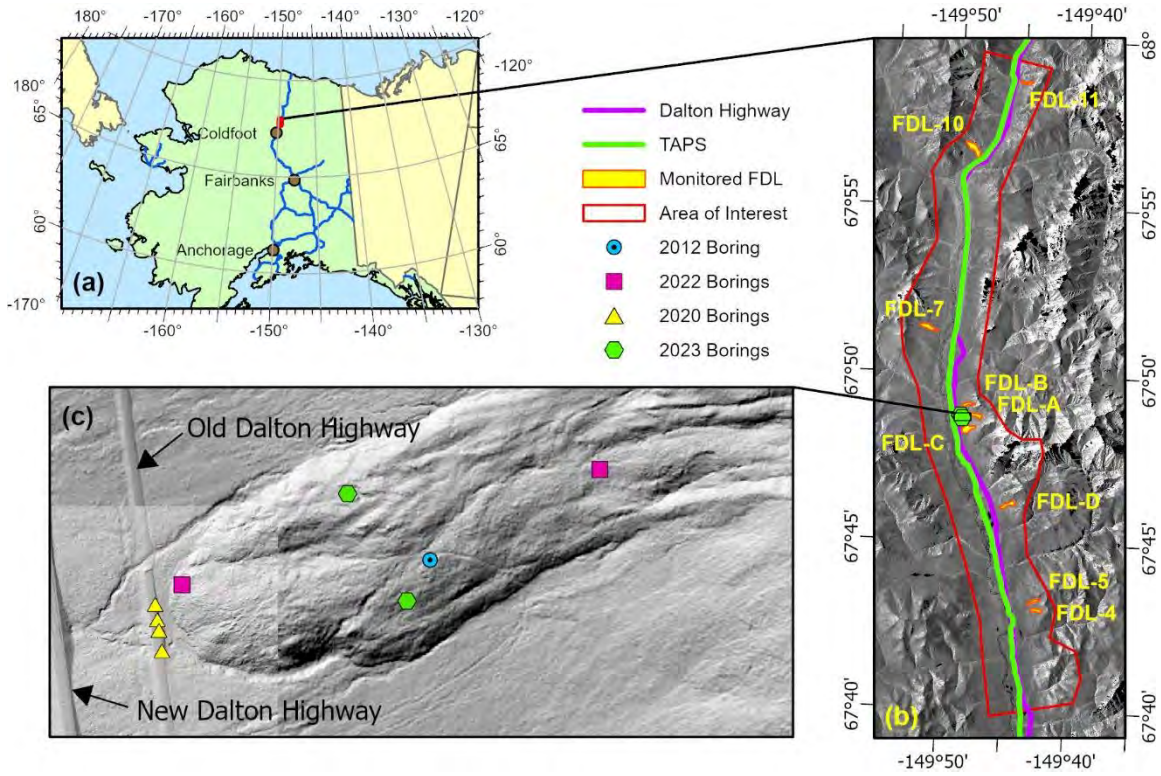

Figure 1. Study area location (a) within Alaska, showing proximity to road network; (b) nine monitored FDLs within area of interest; (c) FDL-A and location of referenced boreholes. Base map data from (a) SOA (2023), (b) GINA (2001), and (c) 2015 and 2020 unpublished lidar.

monitored FDLs demonstrate an increase in movement rate since 2013. Although we limit our yearly research to the features in Figure 1b, we have identified nearly 160 FDLs located throughout the Brooks Range (Darrow et al. 2016).

FDL-D, currently the fastest moving FDL, began to move rapidly downslope after an RTS formed in its catchment between 1993 and 2001. Field observations indicate that the RTS expose bodies of infiltration ice (i.e., ice formed in cracks open to the surface due to ongoing movement) to melting, which contributes to debris flows. The debris flows then provide more sediment and water to the FDL, increasing surface temperatures, which add to the movement and result in a feed-back loop of rate increase. Similar to FDL-D, FDL-A also has RTS in its catchment and along the left flank. We suggest that FDL-A is in the early stages of destabilization and rapid downslope movement that FDL-D is currently experiencing. This is also supported by changes in movement rates. Long-term movement rates from analysis of aerial and satellite imagery (Darrow et al. 2016) indicated a linear increase in the rate of motion for FDL-A. Current movement rates measured with the RTK-GPS, however, changed the long-term trend from a linear to an exponential function (Figure 2b).

FDL-A Subsurface Investigations and Analysis

We conducted the first subsurface investigation of FDL-A in 2012. Samples from a 30.5-m deep boring (Figure 1c) indicated that FDL-A consisted of 26.4 m of silty sand with gravel (SM) to silty gravel with sand (GM) with no excess ice, overlying white mica schist bedrock. We installed a MEMS-based in-place inclinometer (M-IPI), from which we identified a shear zone from 20.6 to 22.8 m below the ground surface (bgs). Temperatures in FDL-A were uniformly -0.85°C below the depth of zero annual amplitude, whereas temperatures measured in adjacent undisturbed permafrost were -2.1°C. We installed two vibrating wire piezometers

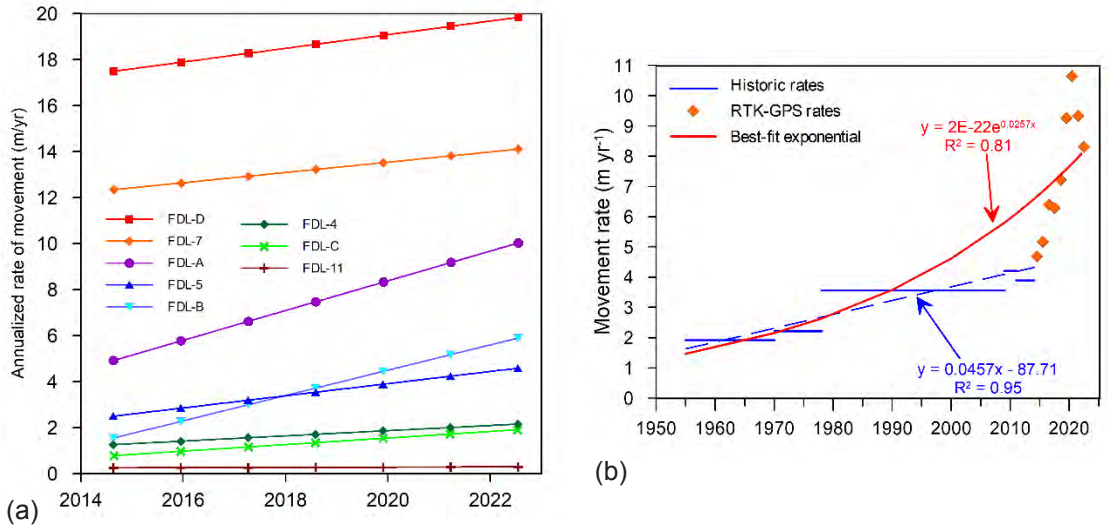

Figure 2. FDL movement rates: (a) annualized rate of movement for eight of the monitored FDLs; (b) FDL-A's rate of movement.

(VWPs), both of which indicated artesian conditions. The casing sheared within one month after installing. Fluid pressure within the lobe was high enough to cause fluid to enter into the sheared cables, travel up the boring, and into the data logger enclosure.

We conducted direct shear tests to determine the friction angle and cohesion of the frozen FDL soil, and incorporated these values in a slope stability analysis (Simpson et al. 2016). We conducted a back analysis to determine strength properties upon failure, varying the friction angle between 10° and 16°, cohesion between 33 and 63 kPa, and water pressure using the pore-water pressure ratio approach. The sensitivity analysis indicated that slope stability was most sensitive to changes in cohesion and pore water pressure (Simpson et al. 2016). This finding is significant, since we hypothesized that increased temperatures would result in melting ice within the lobe, contributing to an increased movement rate. As part of this study, we estimated that, given its rate at the time of 1.2 cm/day, 46,872 tons of material per year would impact the highway (Simpson et al. 2016).

Although the M-IPI sheared approximately one month after installation in 2012, the upper ~20 m continued to report data until the fall of 2015. Analysis of the subsurface data indicated that strain rates in deeper sections of the lobe demonstrated a cyclical pattern. Using that data, RTK-GPS measurements, and the results from an InSAR analysis, we developed a function to predict FDL-A's rate of movement (Darrow et al. 2017). The analyzed data suggested that FDL-A is sensitive to temperature and water. This was manifested in the predictive function by a phase lag, with peak shear (around October 1) occurring 140-150 days after snow melt. We hypothesized that cracks forming from ground movement remain open all winter and into early May as the ground has not yet thawed. Snowmelt readily infiltrates the cracks. Some of the water freezes to form infiltration ice, but some penetrates to the shear zone, where five months later, it has built enough pressure to lower the effective stress and cause a peak in shear movement and strain rate. Using the predictive function, we estimated that FDL-A would hit the Dalton Highway embankment in 2023.

Darrow et al. (2019) conducted thermal modeling of FDL-A to investigate the interaction between subsurface temperature and deterioration of the FDL vegetation cover. Ongoing movement causes cracks that damage the spruce forest and moss surface vegetation and expose mineral soil; we hypothesized that these changes result in warmer subsurface temperatures and increased movement. We modeled different scenarios with varying amounts of a bare mineral

surface. Results indicated that a through-talik formed under the exposed mineral surface within 50 years; when the entire surface was bare mineral soil, permafrost conditions were no longer sustainable beneath the FDL.

As a result of our research, in 2018 the Alaska Department of Transportation and Public Facilities (ADOT&PF) decided to realign the Dalton Highway downslope (Figure 1c), leaving a portion of the original embankment in place immediately downslope of FDL-A. Working with ADOT&PF in 2020, we drilled four borings, and installed M-IPI, VWP, temperature sensors, pressure plates, and tilt meters. Our goal is to measure the impact of FDL-A with the engineered embankment structure, including deformation of the embankment and the force with which FDL-A pushes on the structure. As soon as the instruments were in the ground, they recorded shearing between 6.0 and 8.7 m bgs when FDL-A was still 10 m away at the surface. In 2022, FDL-A reached the original Dalton Highway embankment, so we are currently monitoring its impact. Additionally, we conducted an electrical resistivity tomography investigation in 2021, and in 2022 and 2023 we drilled four more borings within FDL-A, installing M-IPI, VWP, and temperature sensors. We are testing frozen samples for their strength properties and unfrozen water content characteristics. We also continue to monitor annual movement rates of the nine FDLs through RTK-GPS measurements of surface marker pins.

Conclusions

Our research results indicate that the monitored FDLs are moving the fastest that they have in the last 70 years. As these features are sensitive to temperature and increased pore water pressure, climate strongly influences their stability. The accelerated movement of FDLs exposes bare mineral soil and causes debris flows that contribute to higher internal temperatures and increased movement rates. As part of our ongoing research, we will incorporate surface and subsurface measurements into thermo-hydro-mechanical models that can be used to determine mitigation strategies for the adjacent infrastructure.

References

Daanen RP, Grosse G, Darrow MM, Hamilton TD, Jones BM (2012) Rapid movement of frozen debris-lobes: implications for permafrost degradation and slope instability in the south-central Brooks Range, Alaska. *Natural Hazards and Earth System Sciences* 12, 1521-1537, doi:10.5194/nhess-12-1521-2012

Darrow MM, Daanen RP, Gong W (2017) Predicting movement using internal deformation dynamics of a landslide in permafrost. *Cold Regions Science and Technology* 143, 93-104, http://dx.doi.org/10.1016/j.coldregions.2017.09.002

Darrow MM, Freeman AE, Daanen RP (2019) Exploring subsurface temperature dynamics of frozen debris lobes through thermal modeling. *18th International Conference on Cold Regions Engineering and 8th Canadian Permafrost Conference*, August 18-22, 2019, Québec City, Québec, Canada.

Darrow MM, Gyswyt NL, Simpson JM, Daanen, RP, Hubbard TD (2016) Frozen debris lobe morphology and movement: an overview of eight dynamic features, southern Brooks Range, Alaska. *The Cryosphere* 10, 977-993, doi:10.5194/tc-10-977-2016.

Geographic Information Network of Alaska (GINA) (2001) *Interferometric Synthetic Aperture Radar (IfSAR):* http://www.gina.alaska.edu/data/ifsar

Kreig RA, Reger RD (1982) *Air-photo Analysis and Summary of Landform Soil Properties Along the Route of the Trans-Alaska Pipeline System.* Alaska Division of Geological & Geophysical Surveys, Anchorage, Alaska.

Simpson JM, Darrow MM, Huang SL, Daanen RP, Hubbard TD (2016) Investigating movement and characteristics of a frozen debris lobe, South-Central Brooks Range, Alaska. *Environmental and Engineering Geoscience* 22(3), 259-277.

State of Alaska (SOA) (2023) Open Data Geoportal. Available from: https://statewide-geoportal-1-soa-dnr.hub.arcgis.com/

Characterization of the Mechanism and Volume of the Sunnydale Slide (Yukon, Canada)

M. Sturzenegger[1], K. Séguin[2], L.U. Arenson[1], D. Cronmiller[3], J. Bond[3], C. Relf[3]

[1] BGC Engineering, Vancouver, Canada
[2] BGC Engineering, Kamloops, Canada
[3] Yukon Geological Survey, Whitehorse, Canada

SUMMARY: The Sunnydale Slide is a rock slope instability along the Yukon River in Dawson City (Yukon, Canada). A failure may generate an impact wave, which could propagate towards Dawson City and/or block a portion of the Yukon River. Following notifications about a potential increase in the landslide activity in 2020, the site was characterised and monitored. Near real-time monitoring data collected since April 2023 may help with the understanding of the failure mechanism and landslide volumes, as well as potential temporal control (e.g., weather, climate) on slope deformation, forming an essential part of a risk assessment.

Keywords: Sunnydale Slide, Landslide Activity, Failure Mechanism, Failure Volume

Introduction

In July 2020, the Yukon Geological Survey was informed by a citizen of Dawson City (Yukon, Canada) of a potential increase in activity at the so-called Sunnydale Slide, located across the Yukon River (Figure 1). A rock slope failure at the site could generate an impact wave propagating towards Dawson City and/or form a landslide deposit blocking a portion of the Yukon River. Monitoring of the site has been implemented and a range of studies are underway to understand the kinematics of the landslide and identify potential hazard scenarios (Bodtker et al., 2023; BGC, 2023). The current paper provides a summary of the site geomorphology, recent activity, potential failure mechanism and landslide volumes.

Site Geomorphology and Landslide Activity

The Sunnydale Slide is a 340 m wide and 450 m long, east-facing landslide (Figure 1). The upper part is on moderately steep (< 26°) slopes with a series of lineaments, including tension cracks, scarps and uphill-facing scarps (Figure 2). The main headscarp is 6 m high, in the upper southern part of the Slide; three distinct degrees of weathering and vegetation cover along the headscarp indicate episodic movement on a timescale of thousands to tens of thousands of years (Bodtker et al., 2023). The lower part of the Sunnydale Slide down to the Yukon River is steep (> 35°). Its upper limit is marked by a series of arcuate scarps and rock escarpments (Figures 1 and 2), which have retrogressed further upslope on the south side than on the north side. Shallow landslides are present in the lower part, in colluvium or in the upper bedrock layer.

The rock unit is a basalt and greenstone of the Campbell Range Formation (Yukon Geological Survey, 2019). Surficial materials consist of colluvium and loess (McKenna & Lipovsky, 2014). The area was unglaciated during the Pleistocene. Drainage reversal of the Yukon River occurred at the Plio-Pleistocene boundary due to paleo-drainage impoundment by advancing ice sheets, causing overtopping of a previous drainage divide nearby the Sunnydale Slide (Froese et al., 2011). This event caused downcutting of the modern Yukon River valley during the early Pleistocene. Permafrost modelling (Bonnaventure et al., 2012) indicates the

probability of permafrost at the site is medium to high, but no evidence of near-surface permafrost was observed during field work.

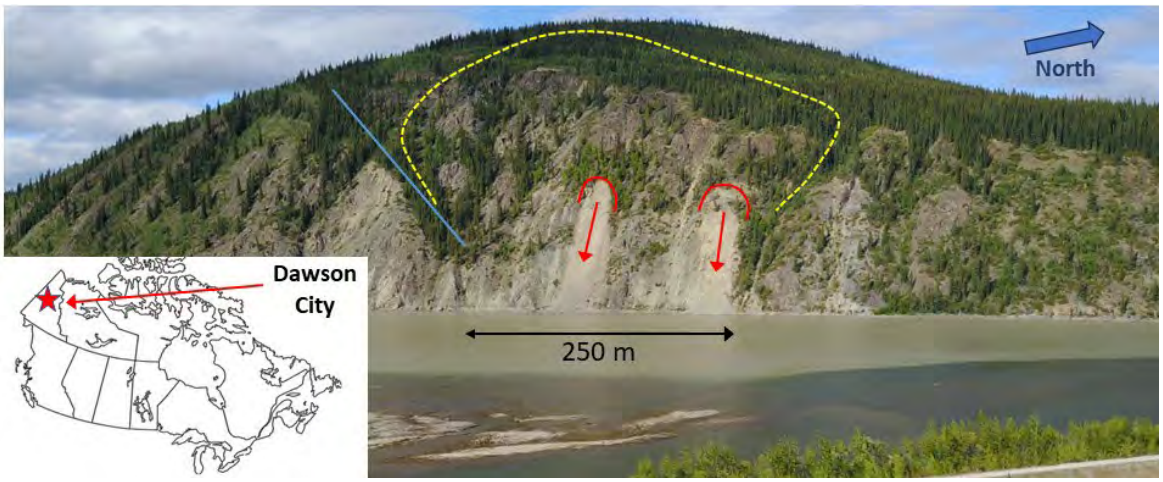

Figure 1. Sunnydale Slide (yellow outline) viewed from the south end of Dawson City, YT. The red outlines and arrows indicate the location of shallow landslides, and the blue line the location of a bench interpreted as a fault.

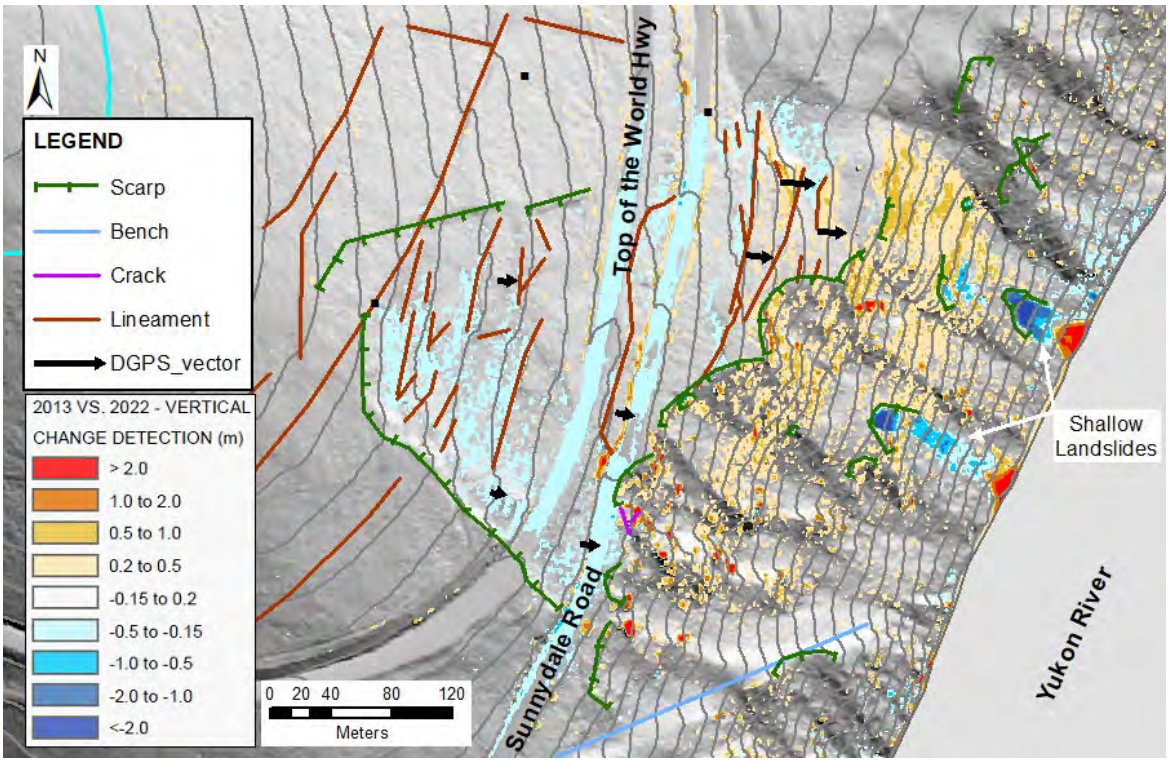

Figure 2. Site geomorphology, dGPS monitoring (vectors indicate relative average horizontal velocity between July 2021 and October 2022), and 2013-2022 vertical change detection analysis.

Surface evidence of recent landslide activity include tension cracks and grabens with freshly exposed/dilated bedrock, stretched roots and split trees; localized rockfall activity from rock escarpments; shallow debris slides on the lower part of the slope; and, deformation of the Top of the World Highway and Sunnydale Road. Landslide activity has been monitored since 2021 based on airborne lidar change detection (2013 to 2022 lidar data), surface monuments surveyed using a differential Global Positioning System (dGPS), tension crack monitoring stations and nails in split trees (Bodtker et al., 2023), and InSAR analysis (Stantec, January 10, 2023).

Preliminary results suggested that overall, the slide has been moving at a rate in the order of 10 to 15 cm/year since 2013. Five near real-time GNSS units have been installed in April 2023.

Failure Mechanism and Volumes

The rock mass at Sunnydale Slide is blocky to disturbed, with smooth and moderately weathered discontinuity surfaces. Deformation is expected to follow pre-existing discontinuities or disturbed zones within the rock mass. Three main discontinuity sets (J1, J2, J5), an infrequent set (J3) and foliation (S1) were defined based on field mapping and photogrammetry (Figure 3). J4 structures appears to be made of the combination of J2, S1 and failed intact rock bridges, forming very persistent and undulating or stepped surfaces.

Kinematic analyses suggest that simple failure mechanisms, such as planar or wedge sliding, are unlikely to control a large-scale instability (Figure 3). Preliminary monitoring data constrain the direction of sliding, while lidar change detection results constrain the potential extent of the unstable areas (Figure 2). The current understanding of the failure mechanism is sliding along a basal failure surface with dip direction towards the east-southeast (90° - 100°), lateral and upper release being provided by steep discontinuities, including J1, J2, J3 and J5. The nature of the basal surface is uncertain and is expected to consist of a combination of pre-existing discontinuities and rock mass bridges. A distinct bench present in the lower southern side (Figure 1) is interpreted as a fault and may also locally control the basal surface orientation.

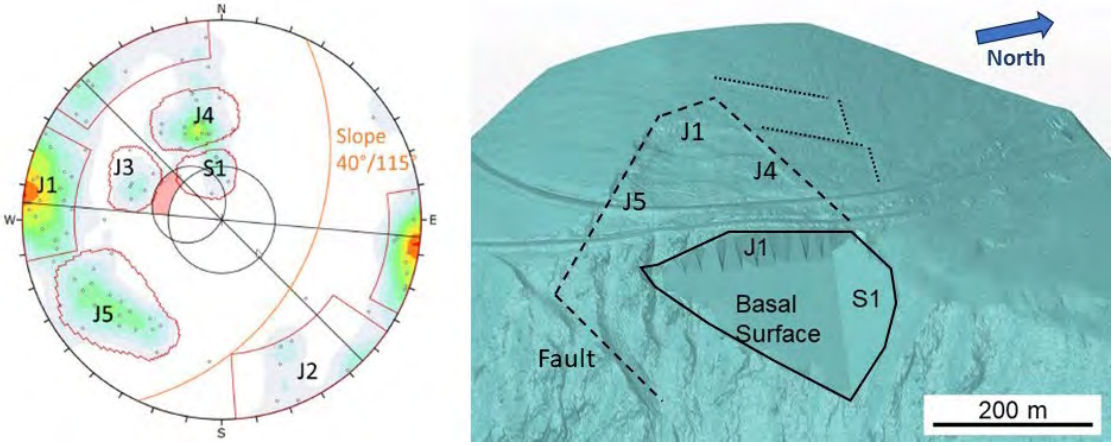

Figure 3. Kinematic analysis and re-constructed Source Volumes A (black line) and B (dashed line). The dotted line in the upper north correspond to lineaments defining the upper limit of Source Volume C.

Using the above structural constraints, several potential landslide scenarios (Source Volumes) were defined, considering that failure could either occur as a single large volume encompassing most of the slide area (e.g., Source Volumes B or C described below), or as smaller volumes corresponding to sections of the instability (e.g., Source Volumes A or D). The volumes were calculated using geometric constructions in the software Polyworks, using the discontinuity set orientations shown in Figure 3. The basal surface dip direction is constrained by the direction of movement (towards the east to east-southeast) measured at the dGPS locations. The dip angle of the basal surface is uncertain and was assumed to be 30°, constrained by the geometric construction and an angle considered realistic for sliding to occur assuming a partially pre-sheared basal surface, and that pore water pressure can at times reduce shear strength.

Source Volume A (0.7 Mm^3) consists of the north section of the Sunnydale Slide below Sunnydale Road (Figure 3). DGPS monitoring shows that this block is moving faster than the

rest of the slide and lidar change detection shows a greater density of positive change indicators (Figure 2). The block is defined by J1 lineaments at the top and foliation planes to the north.

Source Volume B (2.3 Mm^3) is a larger scenario supported by well-defined headscarps along J5, J1 and J4 structures, lidar change detection, and other observations, such as lineaments across the area and shallow landslides at the bottom (Figure 2). The basal surface of Source Volume B would be deeper than that of Source Volume A. Note that Source Volume B could fail in stages, following an initial failure of Source Volume A. The time between initial and retrogressive failures would depend on progressive fracturing processes that eventually define a continuous failure surface (Eberhardt, 2004; Gischig et al., 2016; Sartori et al., 2003).

Source Volume C (4.9 Mm^3) is an extension of Source Volume B to lineaments uphill of the main headscarp (Figure 3). Source Volume C is currently considered less likely because both dGPS and lidar change detection results show minimal displacement (Figure 2). The lineaments above the main headscarp are evidence that the slope has been subject to deep-seated gravitational slope deformation, but this type of deformation typically lacks a fully defined basal failure (Hungr et al., 2014; Bois et al., 2011) and consequently progressive fracturing is necessary for failure to happen.

Source Volume D (0.1 Mm^3, not shown on Figure 3) consists of a potential instability identified based on a secondary headscarp located between the Top of the World Highway and Sunnydale Road, a local concentration of positive indicators, and deep cracks in rock outcrops (Figure 2).

Conclusion

The Sunnydale Slide activity level and the consequences of a potential failure are concerning. Near real-time monitoring data may help with the understanding of the failure mechanism and volumes, as well as potential temporal control, such as weather, on slope deformation.

References

BGC Engineering Inc. (2023, June 15). Sunnydale Slide - Volume, Runout, Landslide-Generated Wave and Dyke Erosion Analysis, Revision 1. Technical report prepared for the Yukon Government.

Bodtker J, Cronmiller D, Bond J & Shugar D (2023) The Sunnydale landslide, current understanding and research, Dawson City, Yukon Territory, Canada (NTS 116B/3). In K.E. MacFarlane (Ed.), *Yukon Exploration and Geology 2022* (p. 19-33), Yukon Geological Survey.

Bois T, Bouissou S & Jaboyedoff M (2011) Influence of structural heterogeneities and large-scale topography on imbricate gravitational rock slope failure: New insights from 3-D physical modelling and geomorphological analysis. *Tectonophysics*, 526-529, 147-157.

Bonnaventure PP, Lewkowicz AG, Kremer M & Sawada M (2012) A regional permafrost probability model for the southern Yukon and northern British Columbia, Canada. *Permafrost & Periglacial Processes* 23, 52-68.

Eberhardt E, Stead D & Coggan JS (2004) Numerical analysis of initiation and progressive failure in natural rock slopes – the Randa rockslide. *International Journal of Rock Mechanics and Mining Sciences* 41, 69-87.

Froese D, Barendregt R, Enkin R and Baker J (2011). Paleomagnetic evidence for multiple Late Pliocene - Early Pleistocene glaciations in the Klondike area, Yukon Territory. *Canadian Journal of Earth Sciences* 37.

Gischig V, Preisig G & Eberhardt E (2016) Numerical investigation of seismically induced rock mass fatigue as a mechanism for progressive failure of deep-seated landslides. *Rock Mech. and Rock Eng. 49*, 2457-2478.

Hungr O, Leroueil S & Picarelli L (2014) Varnes classification of landslides, an update. *Landslides 11*, 167-194.

McKenna KM & Lipovsky PS (2014) Surficial geology, Dawson region; NTS 115O/14 & 15 and 116B/1, 2, 3 & 4. Yukon Geological Survey, Energy, Mines and Resources, Open File 2014-12, 1:25,000 scale.

Sartori M, Baillifard F, Jaboyedoff M & Rouiller J-D (2003) Kinematics of the 1991 Randa rockslides (Valais, Switzerland). *Natural Hazards and Earth System Sciences 3*, 423-433.

Stantec (2023, January 10) Sunnydale Slide Time of Failure Results. Report for the Yukon Geological Survey

Yukon Geological Survey (2019). Bedrock geology, Dawson (116B & 116C), Yukon. 250k maps.

The Varnes' classification of mass movement types to include the subaqueous environment and snow/ice materials

Jacques Locat[1], Roger Urgeles[2], Dieter Issler[3], Michel Jaboyedoff[4], Homa J. Lee[5], Serge Leroueil[6] and Thierry Mulder[7]

[1] jacques.locat@ggl.ulaval.ca, Laboratoire d'études sur les risques naturels (LERN), Université Laval, Québec, Canada
[2] urgeles@icm.csic.es, Institut de Ciències del Mar (CSIC), Barcelona, Spain
[3] dieter.issler@ngi.no, Norwegian Geotechnical Institute, Oslo, Norway
[4] michelk.jaboyedoff@unil.ch, Risk Group, Université de Lausanne, Lausanne, Switzerland
[5] hjlee@usgs.gov, US Geological Survey, Menlo Park, CA, USA
[6] serge.leroueil@gci.ulaval.ca, Serge Leroueil, LERN, Université Laval, Québec, Canada
[7] thierry.mulder@u-bordeaux.fr, Université de Bordeaux, Pessac, France

SUMMARY: In this article, it is proposed to expand the updated Varnes' classification of landslide types to cover the subaqueous environment as well as to include mass movements involving ice and snow materials. The classification considers fragmentation/disaggregation processes of the mass movements forming materials as well as the type of mechanics involved.

Keywords: mass movements, classification, soil, rock, snow/ice

Introduction

In practice, scientists and engineers are confronted with various types of mass movements that can involved not only soil and rock, but also ice and snow and evolve into various processes with turbidity currents as an end-member. This is particularly true in the case of the subaqueous environments where water replaces air within the flow allowing a substantially longer runout. e.g. (Jaedicke et al., 2009). Hungr et al. (2014) presented a revised version of Varnes' classification of landslide types (Varnes 1978, Cruden and Varnes, 1996) dealing mostly with the subaerial environment but not taking into account snow and ice (except for ice fall and ice avalanche). The revision by Hungr et al. (2014) consists primarily of adding a material component to the classification terminology (e.g., *rock* avalanche). The main objective of this article is to expand Varnes' classification to take into accounts snow and ice as well as sediments involved in subaqueous mass movements. Sediments are characterized by their size which is also considered for soils. In addition, soils are also defined by their physico-chemical properties. Here soils are considered to include sediments. The definition of a landslide could be modified as follows: a landslide is defined as the movement of a mass of rock, soil, snow, ice, or debris down a slope. Taking all these materials into account, the proposed classification is illustrated in Table 1 with numbers provided for references. This extended landslide classification is presented in three steps: (1) an overview, (2) considerations for the subaqueous environment, and (3) integration of snow/ice materials. An important consideration related to the presentation below is that the proposed expansion of Varnes' classification of landslide types does not introduce changes in the landslide types already considered by Hungr et al. (2014). Finally, this effort is not to replace other existing classifications (which often are more complex) but only to ensure practitioners that the Varnes' classification does contain all mass movements originating from a failure in soil, rock, ice and snow.

Overview of the proposed classification

The traditional terminology associate landslides with materials from the lithosphere while snow and ice are part of the cryosphere. On the other hand, snow and ice avalanches often entrain soil and rock material during the flow process, which will produce sedimentary deposits (Vasskog et al., 2011). To consider all materials involved in mass movements originating from an initial failure, the expanded Varnes' classification is presented in Table 1 with the new types in bold. It does contain all the elements of the updated version of Hungr et al. (2014) but also includes turbidity currents (for the subaqueous environment), and considers also ice and snow materials. The terminology uses the same approach as that of Hungr et al. (2014), i.e., a material and a type of movement. New with this presentation is the gradation of the mass movement types according to their degree of deformation and/or disaggregation and the mechanics involved (i.e. solid and/or fluid mechanics), in a way similar to what was considered by Meunier (1994). Landslides, or initial slope failures, are those where solid mechanics is involved. The ones below (involving fluid mechanics) are rather transformations of the initial slope failure as downslope movement proceeds. The only exception would perhaps be when soil/sediment fluidization occurs, so that onset of downslope mass movement is already in the form of a flow. As expected, the numbering of the various types of mass movements differs from the list proposed by Hungr et al. (2014). Table 1 also presents a column at the right showing some terminology used to describe landslide deposits in outcrops of sedimentary rocks, in a way similar to Stow and Smillie (2020). Its inclusion in Table 1 can help geologists to associate formation processes with specific types of deposit.

The subaqueous environment

As illustrated by Locat and Lee (2002), a unique characteristic of subaqueous landslides is that, for example, a slide can transform into a debris flow, which can, in turn, generate a turbidity current. This aspect is taken into consideration in a separate classification system for subaqueous landslides proposed by Mulder and Cochonat (1996), and to some extent by Hampton et al. (1996), which was developed using sedimentological considerations, while still being based on the types of mass movements included in Varnes' classification (Varnes, 1978). Although the classification proposed by Mulder and Cochonat (1996) is well adapted for the marine environment, we would like to extract, from that classification, elements that would be compatible with the approach used in Varnes' revised classification. Mulder and Cochonat (1996) also apply flow dynamics criteria in their classification, in a similar way as Leroueil et al. (2003) do, so that a portion of their classification is integrated in Table 1 as turbidity currents. Here, the term 'turbidity current' only applies to mass movements with sediment concentrations (c) less than 9% (Mulder and Cochonat, 1996). These mass movements are divided into low ($c \lesssim 1\%$, #39 in Table 1) and high ($\sim 1\% < c \lesssim 9\%$, #38) density turbidity currents. Not included here are turbidity currents generated by hyperpycnal flows from streams entering a water body. To that effect, the debris flood (#32), pyroclastic and lava flows would be limiting cases.

Snow and Ice mass movements

Snow and ice, when considering mass movements, do behave either like rock for ice or soil for snow as illustrated in their integration in Table 1. Snow avalanche classification can be quite complex (de Quervain et al. 1973). Before becoming an avalanche, a snow pack can fall (cornice fall, #11) or slide (snow-slab planar slide, #15 and snow gliding, #16) within the solid mechanics conditions. Snow avalanches include various types considering both dense and fluidized dry snow avalanches (#36 and 37) in addition to granular wet snow avalanches (#35)

and snow aerosol (#40). Contrary to snow avalanches, slushflows can initiate on gently inclined slopes less than 30° (Hestnes et al. 2000, Hétu et al. 2016), justifying a particular type. Snow avalanches have many properties in common with some types of rapid submarine mass movements (Norem et al. 1990). Like rock avalanches, dry snow avalanches exhibit granular behaviour and have a tendency to form a large suspension layer, which may travel beyond the dense core.

Table 1. Expanded Varnes' classification for mass movements, including the subaqueous environment in addition to ice and snow materials. New elements from the updated Varnes' classification are shown in boldface (Adapted from (Hungr et al., 2014)). See text for explanations.

TYPE OF MOVEMENT			ROCK/ICE	SOIL / SNOW	OUTGROP GEOLOGY
← Deformation / disaggregation	SOLID MECHANICS	SLOPE DEFOR-MATION	1. Mountain slope deformation	2. Soil slope deformation	
			3. Rock slope deformation	4. Soil / snow cover creep /	
				5. Solifluction / Gelifluction	Slump folds
		FALL	6. Rock / ice fall	*7. Boulder / debris / silt* fall	
	← Brittle / Plastic →	TOPPLE	8. Rock / **ice** block topple	*9. Gravel / sand / silt* topple	
			10. Rock flexural topple	11. **Snow cornice fall**	
		SLIDE	12. Rock rotational slide / slump	*13. Clay / silt* rotational slide / slump	Growth fault
			14. Rock / **ice** planar slide	*15. Clay / silt* / ***snow-slab*** planar slide *16.* ***Snow gliding***	
			17. Rock / **ice** wedge slide	*18. Gravel / sand / debris* slide	Olistostrome / sedimentary melange
			19. Rock compound slide	*20. Clay / silt* compound slide	
			21. Rock irregular slide		
		SPREAD	22. Rock slope spread	23. *Sand / silt* liquefaction spread	
				24. *Sensitive Clay* spread	
	FLUID MECHANICS (Sediment support mechanism)	COLLISIONAL/COHESIVE FLOW ← Cohesion / Grain dispersion →	25. Rock / ice avalanche	26. Debris avalanche	
				27. Sand / silt / debris flowslide	
				28 *Sensitive clay* flowslide	
				29. Debris flow	
				30. Earthflow	
				31. Mud flow	
				32. Debris flood	
				33. Peat flow	
				34. Slushflow	
				35. Granular wet snow avalanche	
				36. Dense dry-snow avalanche	
				37. Fluidized dry-snow avalanche	
		SUSPENSION FLOW Turbulence		***38. Sand / silt / clay* high density turbidity current**	
				39. *Sand / silt / clay* low density turbidity current	
				40. Snow aerosol	

Ice is a material which can deform and also break in various ways, like rocks. As shown in Table 1, any of the type of landslides which apply to rock material also apply for ice: ice fall (#6), topple (#8), slide (#14 and 17) and avalanche (#25). Ice fall and avalanche are already included in the updated version of Varnes' classification (Hungr et al. 2014).

Concluding remarks

We have presented a preliminary integration of new materials in Varnes' classification, which should be useful in practical applications. We believe that one of the main contributions is to provide a mass movement classification in a geomechanical perspective. By doing so, we may need to consider the proposed classification as Varnes' classification of *mass movement* types rather than landslide types alone. Due to space limitations, issues pertaining to some of the terminology not included in the work of Hungr et al. (2014) and the implications of this classification for related hazards such as tsunamis will be discussed in more details in a future publication.

Acknowledgements

R.U. was supported by MCIN/AEI, grant PID2020-114856RB-100, ICEFLAME.

References

Camerlenghi A & Pini GA (2009) Mud volcanoes, olistostromes and Argille scagliose in the Mediterranean region. *Sedimentology* 56, 319–365. doi:10.1111/j.1365-3091.2008.01016.x.

Cruden DM &Varnes DJ (1996) Landslides types and processes. *In: Landslides Investigation and Mitigation*, TRB Special Report 247, Chapter 3, pp. 36–75.

De Quervain M de Crecy L LaChapelle ER Losev K & Shoda M (1973) Proposal of the working group on avalanche classification of the International Commission on Snow and Ice. *Hydrological Sciences Bulletin*, 18: 391–402.

Hampton MA Lee HJ & Locat J (1996) Submarine landslides. Reviews of Geophysics 34, 33-59. doi:10.1029/95RG03287.

Hestnes E & Sandersen F (2000) The main principles of slushflow hazard mitigation. Proceedings of the *International Symposium Interpraevent 2020*, pp. : 267-280.

Hétu B Fortin G Dubé J Boucher D Buffin-Bélanger T & Gagnon JP (2016) Les conditions nivologiques et hydro-météorologiques propices au déclenchement des coulées de slush: L'exemple du Québec (Canada). *Climatologie, 13, 71-95.*

Hungr O Leroueil S & Picarelli L (2014) The Varnes classification of landslide types, an update. *Landslides*, 11: 167-194.

Jaedicke C Lied K & Kronholm K (2009) Integrated database for rapid mass movements in Norway. Nat. Hazards Earth Syst. Sci., 9, 469-479.

Leroueil S Locat J Levesque C & Lee HJ (2003) Towards an Approach for the Assessment of Risk Associated with Submarine Mass Movements. In: Locat, J., Mienert, J., Boisvert, L. (Eds.), Submarine Mass Movements and Their Consequences, *Advances in Natural and Technological Hazards Research*. Springer Netherlands, pp. 59–67. doi:10.1007/978-94-010-0093-2_7.

Locat J & Lee HJ (2002) Submarine landslides advances and challenges. *Canadian Geotechnical Journal*, 39, 193–212.

Lowe DR (1979) Sediment gravity flows: their classification and some problems of application to natural flows and deposits. In: Geology of Continental Slopes. *SEPM Special publication* Tulsa, pp. 75–82.

Meunier M (1994) Les progrès de la connaissance et les méthodes d'étude des phénomènes torrentiels, *La Houille Blanche*, 80:3, 25-31.

Mulder T & Cochonat P (1996) Classification of offshore mass movements. *Journal of Sedimentary Research* 66, 43–57.

Norem H Locat J & Schieldrop B (1990) An approach to the physics and the modelling of submarine landslides. *Marine Geotechnology* 9: 93–111.

Stow D & Smillie Z (2020) Distinguishing between deep-water sediment facies: turbidites, contourites and hemipelagites. *Geosciences* 10, doi:10.3390/geosciences10020068, 43 p.

Varnes DJ (1978) Slope movement types and processes. In: Schuster RL, Krizek RJ (eds) Landslides, analysis and control*, Special report 176*: Transportation research board, National Academy of Sciences, Washington, DC., pp. 11–33.

Vasskog K Nesje A Støren EN Waldmann N Chapron E & Ariztegui D (2011) A Holocene record of snow-avalanche and flood activity reconstructed from a lacustrine sedimentary sequence in Oldevatnet, western Norway, *The Holocene* 21, 597–614, doi:10.1177/0959683610391316.

Runout analysis of a reactivated landslide using MPM

Kun He, Xiewen Hu, Chuanjie Xi

Faculty of Geoscience and Environmental Engineering, Southwest Jiaotong University, Chengdu, China.

SUMMARY: Understanding the runout of hydraulic-related landslide reactivations is crucial for risk assessment, with complex interactions between the materials in solid and liquid phases. This paper reproduces the post-failure process of a reactivated landslide using Material Point Method (MPM). The kinematic characteristics show that the landslide has different moving features with different microtopography, which reveals retrogressive failure in front and middle part of slope initially and compound retro- and pro-gressive failures occur at the rear edge. The results of unsaturated two-phase MPM are in good agreement with the measured morphology. The antecedent rainfall and the pre-existing groundwater are the main contributing factors to the landslide runout.
Keywords: Landslide, Material point method, Pre-failure, Post-failure, Hydraulic-related

Introduction

Ancient landslide deposits (ALD) are ubiquitous in tectonically active regions and are prone to sliding repeatedly influenced by external triggering factors (Tang et al. 2019; Peranić et al. 2021). Due to the unconsolidated nature of ALD, hydraulic-related reactivated landslides have recently become more frequent. Landslides reactivated by rainwater infiltration and associated groundwater seepage are dangerous due to the long runout distance and flowing movement. Therefore, understanding the kinematic characteristics of the runout is crucial for assessing the risk of landslides related to hydraulic-related landslide.

The landslide runout process after slope failure occurred is crucial for risk management and the mechanics of the process is challenging because of its complexities. The post-failure behaviors are often associated with large deformations which differ from the pre-failure small deformations. The above traditional methods are not well suited for large-deformation analysis due to the resultant extreme mesh distortion. To this end, an appropriate numerical approach for large-deformation issues is indispensable. The MPM has been improved and successfully applied into various fields, particularly in solving multiphase interaction problem in geotechnical community (Yerro et al. 2015; Soga et al. 2016; Cuomo et al. 2021; Ceccato et al. 2021). MPM can simulate the hydro-mechanical coupled behaviors during a landslide. Previous MPM-derived studies examine the post-failure of saturated/unsaturated slope by imposing the critical phreatic surface instead of rainwater infiltration process (Soga et al. 2016;).

This paper uses MPM to analyze the runout behaviors of a given reactivated landslide. The specific objective is to investigate the post-failure process and kinematic characteristics changes during landslide movement. The results have potential to provide insights into the post-failure process for such hydraulic-related landslides.

Methodology

The MPM code employed in the study is from Anura3D MPM Community (Anura3D 2022), which is an efficient tool for solving large deformation problems in geotechnics. The predominant feature of MPM is that a continuum medium is schematized to a combination of material points (MPs) and background mesh. The discreted MPs can freely move through the problem domain based on the Lagrangian description of the media, and can carry all the physical information and stress-strain field values. The information of MPs are then transmitted

to the background mesh. Detailed basic mathematical formulations of MPM can be found in Ceccato et al. (2021).

The Boli reactivated landslide occurred in Yanyuan County of Sichuan China, after continuous rainfall of 5th to 18th July 2018 was selected as the study case (Fig. 1). A cumulative precipitation of 350.6 mm was recorded in this period. The landslide area had a length of about 1360 m and a maximum width of 810 m and a height difference of 310 m. The landslide covered 59.2× 10^4 m^2 and the deposition volume was estimated to be 1390.6 × 10^4 m^3 (He et al. 2021).

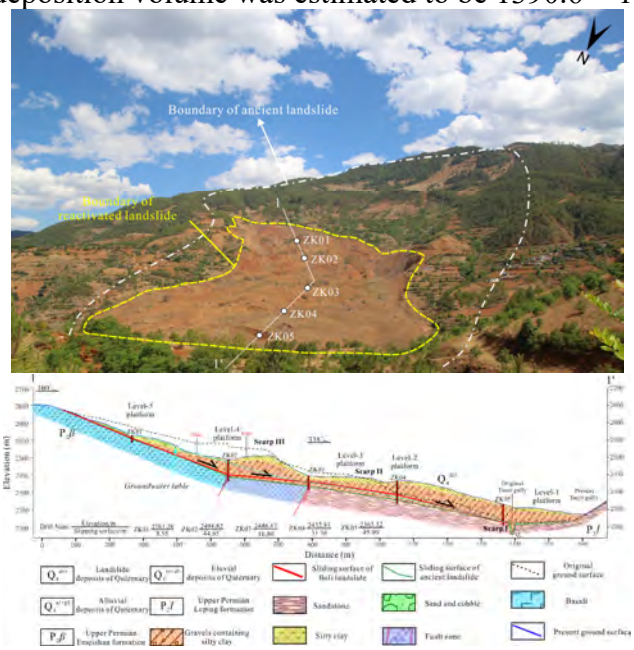

Figure. 1 Overview and Profile of the landslide

The numerical calculation model is established based on the geological profile in Fig. 5, with the X axis as the horizontal direction and the Y axis as the vertical direction. The calculation model is set at 1:1, with the horizontal length of 1700 m and the vertical height of 385 m. Figure 2 shows the MPM model and monitoring points of the slope. A three-node linear triangular element with 6 MPs was designed for the soil element. The size of the background mesh of the sliding mass was 2m×2m, and the size of the background mesh of other parts was 10m×10m. The bottom of the model background grid was fixed in the XY direction for solid phase and in the Y direction for liquid phase, the left boundary was fixed in the X direction for solid phase and the boundary above the groundwater table was fixed in the X direction for liquid phase, the right boundary was fixed in X direction for both the solid and liquid phases, and the upper part was fixed in Y direction for both the solid and liquid phases. Since the reactivated landslide was induced by the combination of rainfall and groundwater, the effects of groundwater and rainfall were considered in the modeling. The groundwater level was determined by the borehole drilling and set as the initial condition of the model. The rainfall was the hyetograph of the recording station and set as the hydraulic boundary of the model, which was applied to the upper surface of the model (Figure. 2). The time step was discretized in 5×10^{-3} s. The simulation was terminated until landslide motion stopped, which meant the velocity of the sliding mass was equal to zero.

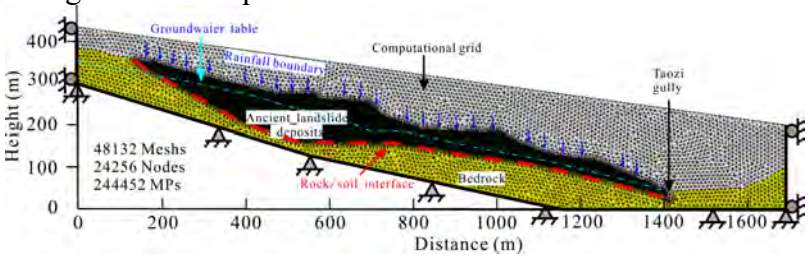

Figure. 2 Geometry and discretization of the MPM model

Table 1 Input material parameters for MPM simulation

Parmeter	Unit	Pore water	ALD	Bedrock
Material type		/	Saturated-unsaturated	Dry
Constitutive model		/	Mohr-Coulomb	Linear elastic
Porosity, n	/	/	0.225	/
Unit weight, γ	kN/m^3	10	23.5	27.8
Cohesion, c	kPa	/	25.4	/
Friction angle, φ	°	/	17.2	/
Poisson's ratio, v	/	/	0.30	0.23
Elastic modulus, E	MPa	/	45	30000
Bulk modulus, K	MPa	200	/	/
Saturated permeability, k	m/s	/	3.6×10^{-6}	/
Dilation angle, ψ	°	/	0	/

Results

Figure. 3 depicts the runout process after landslide initiation at eight different time steps, which lasted about 130s from the beginning to the stable accumulation after the 14-day antecedent rainfall. At the initial moment, the landslide began to slide as a result of gravity and seepage force, with the front edge of first failure. At t = 20 s, the sliding mass dammed the Taozi gully and then the soil masses in the middle and rear parts were retrogressed. At t = 60 s, the sliding masses in the middle part of slope moved downslope, resulting in overlap accumulation. At t = 80 s, the sliding masses in the rear part presented compound failure of retrogressive and progressive failure towards the front and middle part of the slope, forming platform-like accumulation landforms. At t = 130 s, the landslide movement terminated. The reactivated landslide reached the furthest elevation of 2338.3 m at the front edge. The final sliding distance was 227.6 m, which was similar to the farthest elevation of 2337.1 m and the maximum sliding distance of 225.4 m obtained in the field evidence. Thus, the simulation results of coupled hydro-mechanical two-phase unsaturated MPM were reasonable.

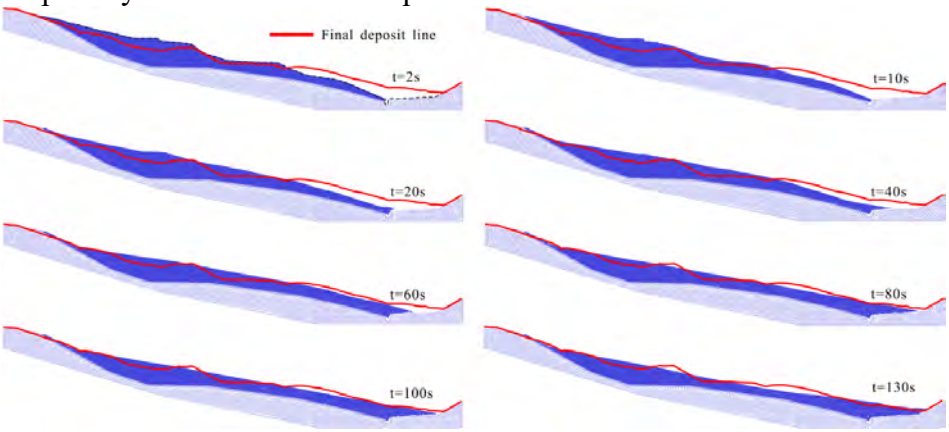

Figure. 3 The runout processes and final landslide deposits compared to field observation

Figure. 4 illustrates the velocity and displacement distribution at different times of the reactivated landslide. Initially, the soil masses in the front edge began to slide towards the free surface of the right bank of Taozi gully, the front sliding masses entered the gully channel with a velocity of 6 m/s and a displacement of 18 m at t = 5 s. The sliding masses at middle and upper slope began to move, and the velocity reached 5 m/s at the scarp II, and the maximum displacement reached 30 m at the scarp III. The displacement of about 14 m appeared at the backwall at the rear edge. The slope presented uncoordinated movement, and the velocity was concentrated at the micro-geomorphic mutations. Due to friction and collision, the MPs at the bottom of the gully bed had obvious deceleration and accumulation phenomenon, while the MPs at the top still maintained accelerating motion. Meanwhile, the middle and rear velocity concentrated on the MPs in the area with steep slope. At t = 40 s, the velocity of the front sliding masses decreased to 0 when it reached the opposite bank side for a certain distance, with a

displacement of 80 m. The middle sliding masses maintained accelerating movement with the velocity of 7.5 m/s and the maximum displacement reached 170m, while the rear sliding mass had the velocity of 5 m/s. After this, the movement of the front sliding masses showed stratified phenomenon. The velocity of the bottom MPs was close to 0 and that of the upper MPs was about 5 m/s, which was subjected to the overloading and shoveling of the following sliding masses. At t = 80 s, the middle sliding masses gradually moved to the leading edge accumulation with a velocity of 12.5 m/s and a maximum displacement of 400 m. The velocity of the rear sliding masses decreased to 0, and the displacement was about 120 m. Influenced by the terrain and the barrier of the anterior accumulation, the landslide was terminated until 130 s, when the overall velocity of the landslide reduced to 0, and the final displacement reached a maximum of 560 m, which belonged to the MPs below the scarp III in the middle of the slope. Thus, it could be inferred that the MPs with the maximum velocity and displacement of landslide were concentrated at scarps of the original slope, instead of the whole movement with the same velocity, and the different movement characteristics of the landslide were significant.

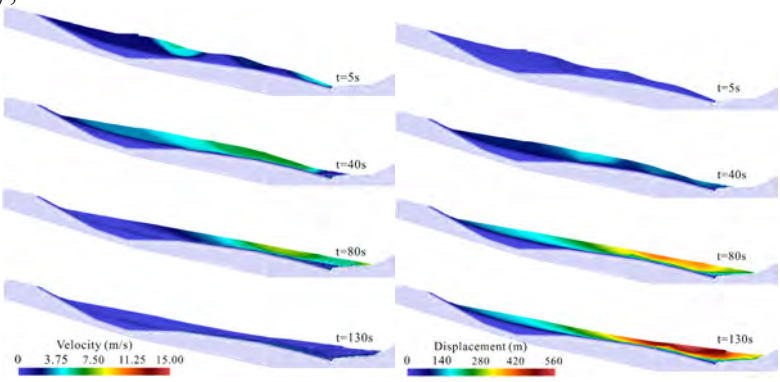

Figure. 4 The kinematic results of MPM: (a) velocity and (b) displacement

Conclusions

This paper explores the post-failure behaviors of a compound reactivated landslide induced by antecedent rainfall and groundwater seepage by using a single-point two-phase MPM. The duration of landslide movement is about 130 s, with a maximum velocity of 15 m/s, and the maximum displacement of 560 m. The kinematic characteristics (velocity and displacement) of the monitoring points show that the reactivated landslide presents different sliding features with different microtopography and depths. The simulation results of unsaturated two-phase MPM match well with the measured accumulation morphology, which indicates that the simulation of unsaturated two-phase MPM has a good performance on the simulation of landslide runout under the role of hydraulic seepage.

References

Anura3D MPM Research Community (2022). Anura3D Version 2022 Source Code, www.anura3d.com.

Ceccato F, Yerro A, Girardi V, Simonini P (2021) Two-phase dynamic MPM formulation for unsaturated soil. *Computers and Geotechnics* 129, 103876.

Cuomo S, Perna AD, Martinelli M (2021) Material point method (MPM) hydro-mechanical modelling of flows impacting rigid walls. *Canadian Geotechnical Journal* 58(11), 1730-1743.

He K, Ma G, Hu X, Liu B (2021) Failure mechanism and stability analysis of a reactivated landslide occurrence in Yanyuan City, China. *Landslides* 18(3), 1097-1114.

Peranić J, Mihalić Arbanas S, Arbanas Ž (2021) Importance of the unsaturated zone in landslide reactivation on flysch slopes: observations from Valići Landslide, Croatia. *Landslides* 18(12), 3737-3751.

Soga K, Alonso E, Yerro A, Kumar K, Bandara S (2016) Trends in large-deformation analysis of landslide mass movements with particular emphasis on the material point method. *Géotechnique* 66(3), 248-273.

Tang H, Wasowski J, Juang CH (2019) Geohazards in the three Gorges Reservoir Area, China–Lessons learned from decades of research. *Engineering Geology* 261, 105267.

Yerro A, Alonso EE, Pinyol NM (2015) The material point method for unsaturated soils. *Géotechnique* 65(3), 201-217.

A wireless sensor network for monitoring rockfall protective structures

Richard Koschuch[1], Tobias Schöffl[1,2], Johannes Hübl[2], Phillipp Jocham[3], Suzana Svetlicic[4]

[1]IBTP Koschuch, Langegg 31, Leutschach an der Weinstraße 8463, Austria
[2]University of Natural Resources and Life Sciences, Institute of Mountain Risk Engineering, Vienna, Austria
[3]IT Jocham Ungergasse 30, 8020 Graz, Austria
[3]DRI Investment Management Ltd, Kotnikova 40, 1000 Ljubljana, Slovenia

SUMMARY: In this study we present a wireless shock sensor (accelerometer) network that is integrated into an internet of things (IoT) architecture and supported by a user-friendly dashboard (Grafana). In case of an event, the system is designed to automatically trigger an alarm within one minute. We provide insight into the sensor design and data transmission, present two years of measurement experience gained at our test site in Slovenia, and discuss the results and limitations we encountered.

Keywords: wireless sensor network, rockfall net monitoring, IoT, decision support system

Introduction

Infrastructures such as roads and railroads are secured worldwide with rockfall protection nets. In the European Alps alone, approximately thousands of kilometres of nets extend along the mountain slopes. Ensuring maintenance through regular inspections by trained technicians is time-consuming and costly. In order to reduce the frequency of inspections and to enable safe and fast verification of the functionality of protective barriers, a growing number of electronic sensor-based monitoring systems have been developed recently (Barile et al., 2017; Yan et al., 2019; Scavia et al., 2020; Pellegrini et al., 2023; Segalini et al., 2023).
In addition to large impacts, gradual filling with small rocks also affects the functionality and durability of flexible barriers. Identifying these small events at sensor level and establishing a conclusive database would be of great benefit to operators. Besides a robust sensor system, it is particularly vital to create an architecture that displays the gathered data in a user-friendly and comprehensible manner (Ragnoli et al., 2023).
Here, we show a customized shock sensor-based architecture that can detect rockfall activity on flexible barriers (Figure 1), indicate the magnitude and frequency (Williams et al., 2019), and display the location of the event on a dashboard. We emphasize that the network can opt as a decision support system to optimize the maintenance procedure of the affected rockfall net sections.

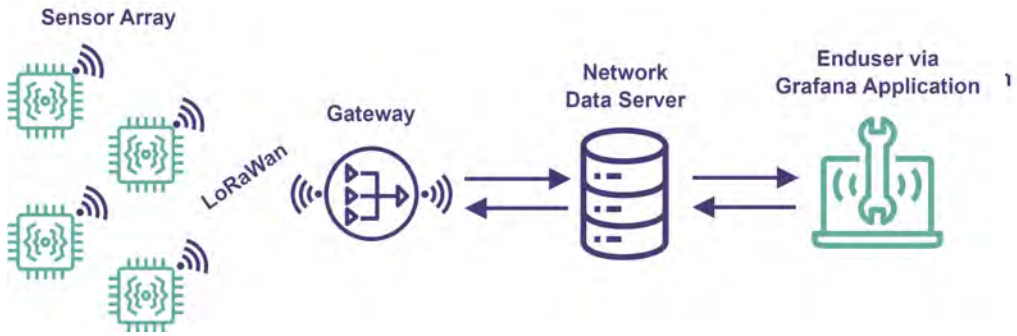

Figure 1. Schematic view of the rockfall detection system using LoRaWAN connection standard.

Test site

Due to the increasing frequency of rockfall events in the Slovenian state road network, the Slovenian Agency for Infrastructure, in cooperation with DRI Ltd, established a new project for preventive road protection measures against rockfall. Approximately 16,500 metres of flexible rockfall barriers and other mitigation measures were installed in recent years. As a result, many activities are now focused on establishing a regular maintenance schedule for these protective measures. This primarily aims to streamline on-site inspection time and reduce costs while determining the current condition of the barriers.
In October 2021, we installed 5 shock sensors on a 100-meter-long rockfall barrier (2000 kJ) located above the state road in the eastern part of Slovenia (Figure 2.) and a gateway station at a distance of 400 meters. Over the course of two years, data was collected on the number of rockfall events, their locations, and their intensities.

Figure 2. Test site in Slovenia and sensor installation.

Sensor description and data transmission

The sensor system is designed to detect and measure rockfall events directly at the pillar of flexible barriers. It consists of a digital output three-axis low g MEMS accelerometer in combination with a miniature-sized circuit board containing a Cortex processor, a long range (LoRa) connection module, and a crypto chip. The device power is supplied with a 6V-2W PV panel and a 4000 mAh supported battery, ensuring the device is energy self-sufficient. The accelerometer sensitivity is set to +/-16g in each of the three axes. The electronic components are fitted in a 200×80×50 mm³ waterproof and UV-resistant plastic housing suitable for convenient installation on any rockfall barrier. Thanks to the modular design, additional sensors can be efficiently connected to the system to measure other useful variables or to implement additional redundancy to the monitoring network.
As flexible barriers are designed to absorb the energy of an impact by transforming it into deformation energy, the pillars carry the lowest load of the total structure (Volkwein et al., 2009). Hence, we assume that the most stable measurable accelerations occur at the pillars

during an impact. To monitor an entire field, we mounted the sensor box on every second pillar.

The data is forwarded via Long Range Wide Area Network (LoRaWAN) connection to a mobile gateway. A single gateway supports several devices (up to 30), depending on the gateway model. The maximum distance at which communication between a device and the gateway is guaranteed is up to 2-3 kilometres. The sensor reports wakeup measurements every 12 hours (this can be adjusted before installation) as a sign of functionality or to assess the status of the network. In the event of an impact greater than the preset threshold, the sensor records a configurable number of measurements and transmits the data in real time.

Data visualisation and usability

At the gateway, the data is forwarded to a server and stored in a database. The data structure itself is specified by a three-dimensional acceleration vector (x, y, z) given by the unit of measurement g (acceleration due to gravity). To achieve a sensible reduction of the data volume, the sensor is programmed to transmit only the highest values from a 20-second interval.

Figure 3. Dashboard via Grafana. Besides the exact location (a) of each sensor, the data can be observed and qualitatively analysed in several plots (b).

The database is then visualized via Grafana (Figure 3), a multiplatform monitoring tool with web interface visualization. All locations and sensors are accessible here and anyone with authorization can view the data or make their own visualizations (Grafana dashboard). The data are used to determine the number of events or the location and intensity of an impact. In addition, Grafana generates automatic alarm SMS/Email for different thresholds using the database analysis. Herewith the user is informed immediately about significant events.

Discussion

The focus of this study was primarily on the development of a shock sensor network with a user-friendly dashboard tailored to it. Hence, the data is displayed in a purely qualitative evaluation. We emphasize that only minor rockfall events were detected during the two-year measurement period. Consequently, no data of a major impact could be collected, which would require a complete replacement of the safety net. In addition, disturbance signals with a strength of up to 2g could be attributed to strong storms and corresponding winds or hail. To filter these interfering signals, a comparison with data from another sensor would be essential. However, this is foreseen in a follow-up project in cooperation with Trumer Schutzbauten GmBh, Almosys and ÖBB for the next two years. The core of the upcoming project is to develop and test a novel structure-borne sound sensor and to compare it with the shock sensor presented here.

Conclusion

We anticipate that as our monitoring network expands, the data provided will enable the development of algorithms that yield information on the frequency and magnitude of rockfall events and support predictive maintenance. This advancement will facilitate the establishment of a consistent, long-term preventive maintenance plan. This marks the initial step towards optimizing future maintenance efforts and reducing associated costs.

References

Barile G, Ferri G, Leoni A, Muttillo M, Pantoli L, Stornelli V & Vettori D (2017) Automatic Wireless Monitoring System for Real-Time Rock Fall Events. *Proceedings* 1(4), p. 569.

Pellegrini S, Rizzelli G, Barla M & Gaudino R (2023) Algorithm Optimization for Rockfalls Alarm System Based on Fiber Polarization Sensing. *IEEE Photonics Journal* 15(3), pp. 1–9.

Ragnoli M, Scarsella, M Leoni, A, Ferri G & Stornelli V (2023) Wireless Sensor Network-Based Rockfall and Landslide Monitoring Systems: A Review. *Sensors* 23(16) p. 7278.

Scavia C, Barbero M, Castelli M, Marchelli M, Peila D, Torsello G & Vallero G (2020) Evaluating Rockfall Risk: Some Critical Aspects. *Geosciences* 10, p. 98.

Segalini A, Valletta A, Carri A & Savi R (2023) Impact identification on flexible rockfall barriers: on site test of a wireless monitoring system. *IOP Conference Series: Earth and Environmental Science* 1124(1), p. 012125.

Volkwein A, Roth A, Gerber W & Vogel A (2009) Flexible Rockfall Barriers Subjected to Extreme Loads. *Structural Engineering International*. 19(3), pp. 327–332.

Williams JG, Rosser NJ, Hardy RJ & Brain MJ (2019) The Importance of Monitoring Interval for Rockfall Magnitude-Frequency Estimation. *Journal of Geophysical Research: Earth Surface*. 124(12), pp. 2841–2853.

Yan Y, Li T, Liu J, Wang W & Su Q (2019) Monitoring and early warning method for a rockfall along railways based on vibration signal characteristics. *Scientific Reports* 9(1), p. 6606.

Rockfall Hazard Assessment Along the Newcastle Coastline (Australia)

A. Watman[1], P. Greaves[1], D. E. Guccione[1], K. Thoeni[1], A. Giacomini[1]

[1] Priority Research Centre for Geotechnical Science and Engineering, The University of Newcastle, Callaghan, Australia

SUMMARY: The collection of rockfall monitoring data is essential to addressing the challenges of rockfall hazard assessment in the coastal environment. This investigation explored the application of change detection techniques to three-dimensional photogrammetric data for rockfall monitoring of two Newcastle (Australia) coastal cliffs. Examination of change detection data from four monthly periods identified 99 and 14 rockfall events, respectively. Rockfall volumes of 0.002 m^3 – 8 m^3 (Site 1) and 0.01 m^3 – 0.9 m^3 (Site 2) were observed, with at least 75% being smaller than 0.1 m^3 (Site 1). Analysis of source locations did not reveal any clear susceptibility patterns, other than the identification of more active strata at Site 2.

Keywords: rockfall hazard assessment, change detection, coastal cliffs (max 5 keywords)

Introduction

The coastal environment provides unique conditions for rockfall hazard assessment and mitigation design. Along coastal rock cliffs, increased rock material degradation from harsh environmental factors influences rockfall susceptibility whilst high seasonal pedestrian and vehicular activity increases exposure probabilities, contributing to rockfall risk. Additionally, scenic coastal cliffs are often subjected to management constraints, as space can be limited and the desire to minimise visually intrusive mitigation measures and preserve the natural amenity exists. Consequently, improving the certainty of quantitative hazard estimations via the collection of rockfall monitoring data is particularly important for coastal areas.

The rock cliffs along the Newcastle (Australia) coastline present an opportunity to study rockfall hazard, considering the impact of harsh coastal environmental conditions on sedimentary strata. This investigation focusses on the application of change detection techniques to three-dimensional photogrammetric data for better rockfall hazard assessment of two coastal cliffs in the Newcastle area (Figure 1).

Figure 1 - Locations of two coastal cliff sites in the Newcastle area (annotated aerial view from MinView).

Geological Setting

To the south of Newcastle Harbour, the coastline consists of four main sandy beaches, separated by a series of rock cliffs comprising sedimentary strata from the late Permian Newcastle Coal Measures. Situated adjacent to Newcastle's popular beaches, and forming part of the Bathers Way coastal walk path, these cliffs receive significant pedestrian traffic year-round. Along the coastline, maximum cliff heights vary (20 – 60 m), with overall slope angles of 45 – 80°. The rock faces are mostly ungroomed, with only some localised areas of vegetation, leaving the strata directly exposed to the coastal environment. Figure 2 provides a visual overview of the geological and environmental conditions at both sites.

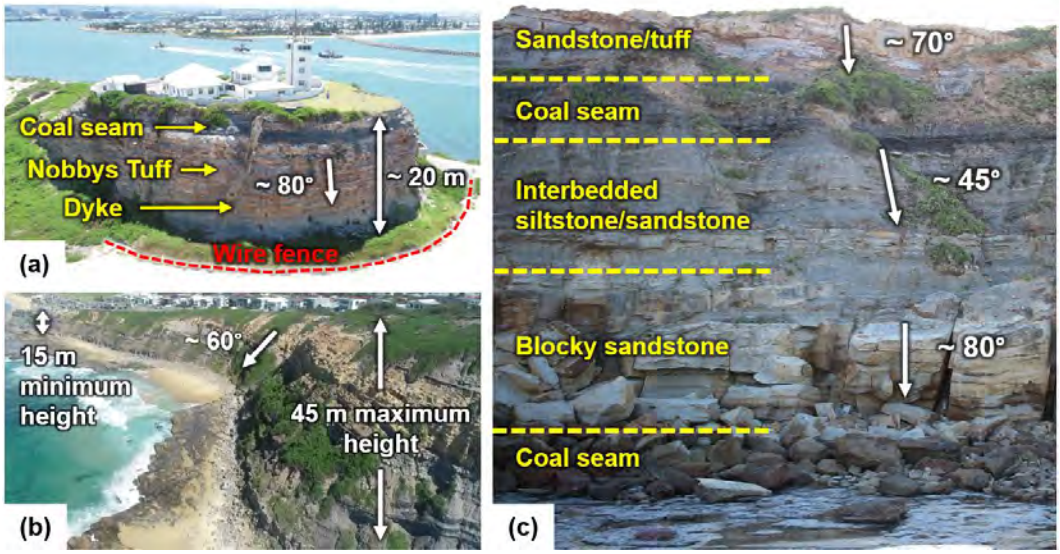

Figure 2 - (a) Westerly view of Site 1, showing key site features and stratigraphy. (b) Westerly view of Site 2, showing key site features. (c) Partial sequence from the Newcastle Coal Measures, as seen outcropping at Site 2.

Newcastle coastal cliffs have a history of instability, evident in the blocks along the toe of most slopes. Significant events, such as a 10 m^3 rockfall that destroyed a beach access staircase at Site 2 during a heavy rainfall event in 2001, have been well documented by authors such as Delaney (2005). As shown in Figure 2c, the Newcastle Coal Measures consist of interbedded layers of materials that are more resistant (sandstones, conglomerates, tuffs) and less resistant (siltstones, shales, coal seams) to weathering. Along the coastline, harsh environmental conditions (e.g. wind, waves) interact with this interbedded structure to cause instabilities. Preferential erosion of the less-resistant strata, seen via fretting and sloughing, leads to undercutting of the more resistant layers. These latter strata have a noticeably blocky structure, defined by two main sets of orthogonal near-vertical joints and a set of near-horizontal bedding planes, leading to toppling failures and rockfalls. As these instabilities have a history of impacting walkways, rockfall monitoring continues to be a priority for local authorities.

Methodology

The source location and size of rockfall events were observed via change detection performed on three-dimensional meshes and point clouds constructed from photogrammetric data collected over a four-month monitoring period. At both sites, five approximately monthly photogrammetric surveys were conducted using a DJI Phantom 4 RTK drone. Automatic angled flight routes (three for Site 1 and five for Site 2) about 20 m from each cliff, with additional manual flight strips, were followed to collect a series of overlapping 20-megapixel images. No

control points were used; images were aligned using GPS coordinates. Agisoft Metashape (2023) software was used to post-process the images, generating a three-dimensional point cloud and a mesh model for each survey. The quality of each point cloud was assessed via the surface density (with r = 0.5 m) in CloudCompare (Girardeau-Montaut, 2022) (see Table 1).

Table 1 - Quality (mean surface density) of point clouds produced over four monthly monitoring periods.

Site 1		**Site 2**	
Survey date	**Mean surface density *(points/m²)***	**Survey date**	**Mean surface density *(points/m²)***
16/11/2022	12000	17/11/2022	1300
13/12/2022	13000	16/12/2022	13000
24/01/2023	16000	23/01/2023	13000
20/02/2023	9000	21/02/2023	12000
03/03/2023	4000	03/03/2023	800

Further processing and change detection were performed in CloudCompare. Due to the curvature and length of the cliff lines, the models from both sites were cut into several sections for analysis: three for Site 1 and five for Site 2. For each section, any irrelevant areas (e.g. footpath, beach, vegetation) were trimmed away before they were aligned. For each monitoring period, the point cloud from the end of the period was aligned and compared to the mesh model from the beginning of the period. Once a satisfactory alignment was achieved, the cloud to mesh (C2M) distances were computed, generating a scalar field of distances. By checking the before and after photographs for each area of significant negative C2M distance, rockfall event source locations were identified and validated. For each validated rockfall event, the block was carefully cut from the two models (a point cloud with the same surface density as the mesh model was created for this process), defining a separate point cloud for each. A custom python script with functions from the *scipy* and *meshio* libraries was used to subsample (at 0.05 m) and merge the block surfaces, create closed meshes and estimate their volumes (via convex hull).

Results and Discussion

Change detection identified a number of rockfall events across both sites throughout the four-month monitoring period. Site 1 was more active, with a total of 99 rockfall events, compared to the 14 events observed at Site 2. Whilst 12/2022-01/2023 was the most active period for Site 1 (31 blocks), the greatest total rockfall volume (11.4 m^3) was observed for 02/2023-03/2023. This latter period was the most active (7 blocks) and had the greatest total rockfall volume (1.8 m^3) for Site 2. Block volumes for Site 1 ranged between 0.002 m^3 and 8 m^3, with at least 75% of blocks having volumes of less than 0.1 m^3 across all four monitoring periods. These blocks came from various source locations (all in Nobbys Tuff), with no clear pattern of rockfall susceptibility visible in the spatial distribution map (see Figure 3a). Site 2 had a narrower block volume range with estimations between 0.01 m^3 and 0.9 m^3, mean volume of 0.19 m^3 and median volume of 0.08 m^3. A direct comparison of the rockfall activity at Sites 1 and 2 has been provided in Figure 3b-d, in the form of volume-frequency plots.

With such a small number of rockfall events occurring at Site 2, it was not possible to directly investigate the spatial variability of source locations. Instead, the lithology of each block was investigated. As seen in Figure 3d, other than blocky sandstone, the interbedded siltstone-sandstone layer was the least active, with only two blocks of 0.1 – 1 m^3. As expected, the most erodible layer (coal) was the most active, with seven blocks mostly within 0.01 – 0.1 m^3. Interestingly, the sandstone/tuff layer, situated furthest from the ocean, was much more active than the other coarse-grained layer (blocky sandstone), with five blocks of 0.01 – 1 m^3.

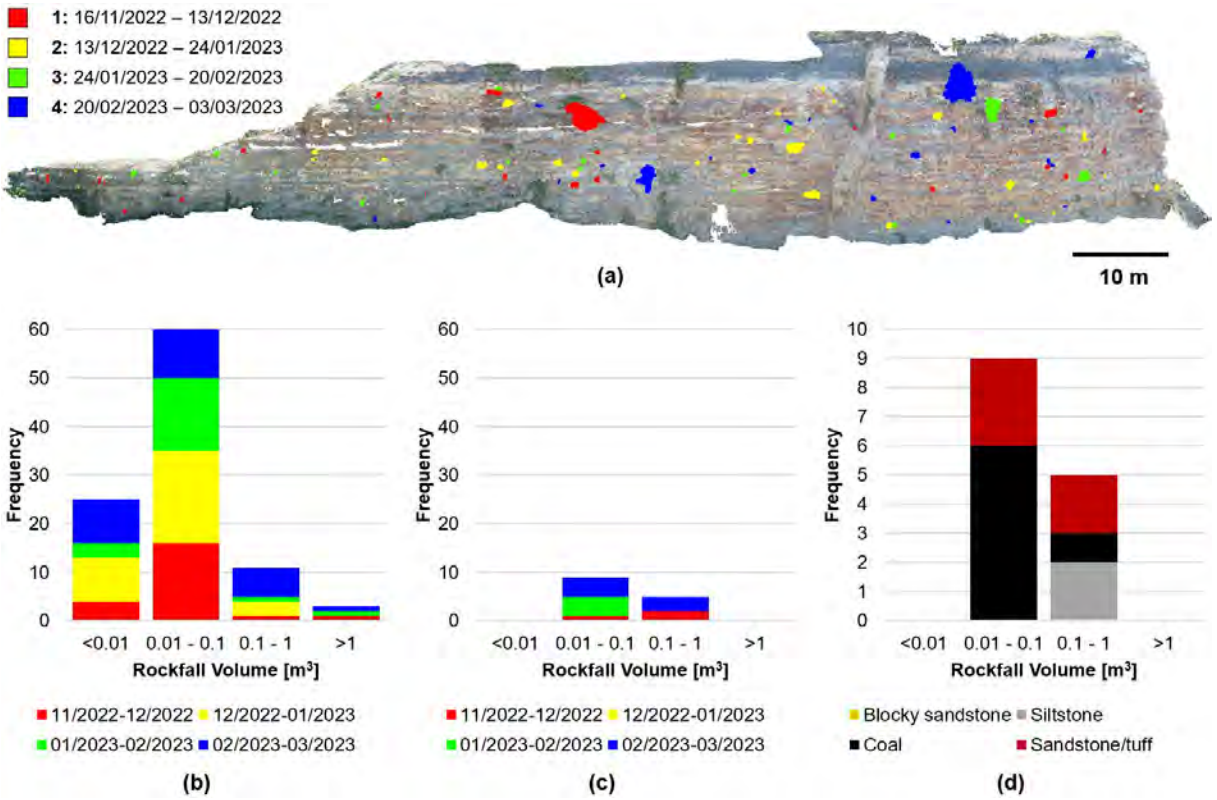

Figure 3 - (a) Spatial distribution of rockfalls occurring at Site 1 (11/2022 – 03/2023). (b) Volume-frequency by period for Site 1. (c) Volume-frequency by period for Site 2. (d) Volume-frequency by stratum for Site 2.

Conclusions

Change detection was performed across four monthly monitoring periods for two Newcastle coastal cliffs, identifying a total of 99 and 14 rockfall events at Sites 1 and 2, respectively. As expected, more frequent rockfall activity was observed at Site 1, as the lack of vegetation cover, steep slope angles and geology are more conducive to rockfall. Analysis of rockfall source locations did not give clear indications of susceptibility. Volume-frequency distributions of both sites showed that small volume events (< 0.1 m^3) occurred more regularly, however, more than four monitoring periods are needed to better understand the rockfall activity of Site 2. Whilst the findings of this study can already be used by practitioners to quantify part of the rockfall hazard, the authors continue to monitor these (and other) sites monthly, to increase the amount and reliability of data available, enabling the estimation of other hazard components.

Acknowledgements

This study was conducted with funding provided by Australian Research Council (grant number DP210101122) and an Australian Government Research Training Program (RTP) Scholarship. The authors would like to acknowledge the work conducted by L. Muxlow.

References

'MinView', [online], available: https://minview.geoscience.nsw.gov.au [Accessed 09/10/2023].
Delaney, M. G. (2005) 'Coastal Cliff Line Stability and Regression in the Newcastle Region', *Australian Geomechanics,* 40(1), 29–38.
Agisoft (2023) Metashape (2.0), [Software].
Girardeau-Montaut, D. (2022) CloudCompare (2.12.4), [Software].

Gypsum induced Landsides in Ollon, Switzerland

Prina Howald Erika[1], Torche Jérémy[1], Cujean Sébastien[1]

[1] School of Management and Engineering Vaud, Yverdon-les-Bains, Switzerland

This abstract presents a comprehensive case study of landslides in Ollon, Switzerland, emphasizing the complex geological and topographic factors contributing to these geotechnical hazards. Through historical analysis, geotechnical investigations, and geological assessments, the study aims to uncover the underlying causes and mechanisms of the landslides. The study area, situated in the "Bois de la Glaive" region of Ollon, features a challenging terrain characterized by karstified gypsum rock cover, which hinders surface runoff. Steep slopes, coupled with a dense root system, further complicate the stability of the area. Landslides in Ollon involve a debris mass consisting of soil and gypsum blocks, resulting from a complex interplay of geological and environmental factors. Geotechnical analysis involves evaluating slope stability, soil properties, and groundwater conditions. Field investigations and laboratory tests provide crucial insights into shear strength, permeability, and deformation behavior. Geological analysis explores the lithological composition, geological structure, and tectonic history of the region, aiming to understand how geological processes interact with external forces like weathering and erosion. The study also highlights the role of water content in destabilizing the terrain. Rainwater infiltration, especially in the context of gypsum's impermeability, plays a significant role in slope instability.

Keywords: Landslide, Gypsum, Geotechnics, Switzerland, Rainfall

Introduction

Landslides are prominent geotechnical hazards in Switzerland, primarily due to its complex geological and topographic characteristics. Understanding the mechanisms and factors contributing to landslides is essential for mitigating their impact on infrastructure and ensuring human safety. This paper presents a comprehensive case study focused on landslides in the village of Ollon, situated in the Canton of Vaud, Switzerland.

The study employs a multidisciplinary approach, including historical analysis, geotechnical investigations, geological assessments, and consideration of environmental factors. The objective is to uncover the underlying causes and mechanisms of landslides in Ollon, with a specific focus on its geological, geotechnical, and environmental aspects.

Ollon's geological features play a significant role in slope instability. It is characterized by karstified gypsum rock cover, which hinders surface runoff. Steep slopes and a dense root system further complicate stability. Landslides in Ollon involve a debris mass consisting of soil and gypsum blocks, resulting from complex geological and environmental interactions.

The geotechnical analysis involves assessing slope stability, soil properties, and groundwater conditions. Field investigations and laboratory tests provide critical insights into shear strength, permeability, and deformation behavior, contributing to a comprehensive understanding of the terrain's stability.

Additionally, the study considers the environmental factors, such as the impermeable nature of gypsum rock and the role of vegetation, including the dense root system, in slope stability.

Historical analysis utilizes aerial photographs to track landslide events over time, revealing patterns and trends in past occurrences. Pluviometry data is analyzed to examine the relationship between precipitation patterns and landslide events.
The laboratory results provide further insights into the composition and properties of the soil and rock in Ollon, enhancing our understanding of the terrain's behavior.
This paper aims to shed light on the complex interactions between geological, geotechnical, environmental, and climatic factors that contribute to landslides in Ollon. The findings have practical implications for predicting and mitigating future slope failures in the region.

Methodology

The investigation into landslides in Ollon employed a multidisciplinary approach, encompassing geological, geotechnical, environmental, historical, and climatic considerations. For this study, only the 30 January, 2021's one has been sampled.
The study area's geological features were thoroughly characterized, with geological mapping, rock sampling, and mineral identification forming the foundation. An exploration of the region's tectonic history provided insights into the geological processes that have shaped the area.
Environmental elements were integral to the analysis. The presence of karstified gypsum rock cover, impeding surface runoff, was examined, along with the impermeable nature of gypsum and its impact on water infiltration. Additionally, the role of vegetation, specifically the dense root system, was observed and assessed concerning slope stability.
A historical investigation was conducted using aerial photographs dating from 1938 to the present day. These images were analyzed to track the evolution of slope displacements and past landslide occurrences, identifying patterns and trends in historical events.
Precipitation data from nearby observation stations, including MétéoSuisse (Swiss Federal Office of Meteorology) and the Canton of Vaud, underwent analysis. This examination focused on understanding the relationship between precipitation patterns and landslide events, with particular attention to the duration and intensity of rainfall leading up to landslides.
Detailed investigations were conducted to assess slope stability. This included comprehensive slope stability analyses, taking into account factors such as slope angle, soil properties, and groundwater conditions. Soil samples collected from key locations underwent laboratory testing to determine their properties, including Unified Soil Classification System (USCS) classification, bulk density, granulometry, and Atterberg limits. Additionally, experiments were conducted to ascertain gypsum dissolution times.
This comprehensive and integrated methodology facilitated a holistic understanding of the complex interactions and contributing factors influencing landslides in the area.

Results

A historical study was conducted using aerial photographs sourced from the Swiss Confederation's database (map.geo.admin).
Since 1938 (Photo A, Figure 1), photography has enabled the observation of slope movements and various associated landslide events. Already, a landslide (highlighted in red) occurred a few meters away from the one in 2021. Further to the west, another larger unstable area is noticeable (highlighted in yellow), providing evidence that the region has been subjected to these events for nearly a century, at the very least.
In 2004 (Photo B, Figure 1), it is clearly evident that a detachment niche is forming on the upper part of the slope. Rockfall events appear to have increased in intensity, nearly reaching the road below during one of the events (highlighted in yellow). The landslide from 1938 (highlighted in red) has been completely absorbed by vegetation.

The 2010 photograph (Photo C, Figure 1) depicts the upper part of the slope completely devoid of vegetation due to a significant number of rockfall events since 2007.
On January 22, 2018 (Photo D, Figure 1), a new landslide (highlighted in red) occurs at the same location as in 1938, precisely 80 years later and likely under similar conditions. Vegetation is starting to reclaim its territory in the vicinity of the rockfall zone (highlighted in yellow).

Figure 1. Aerial photographs. A: 1938; B: 2004; C: 2010; D:2018 (modified after map.geo.admin)

The precipitation data related to the two most recent events in the region were collected from public meteorological authorities and have been compiled in Figure 2.

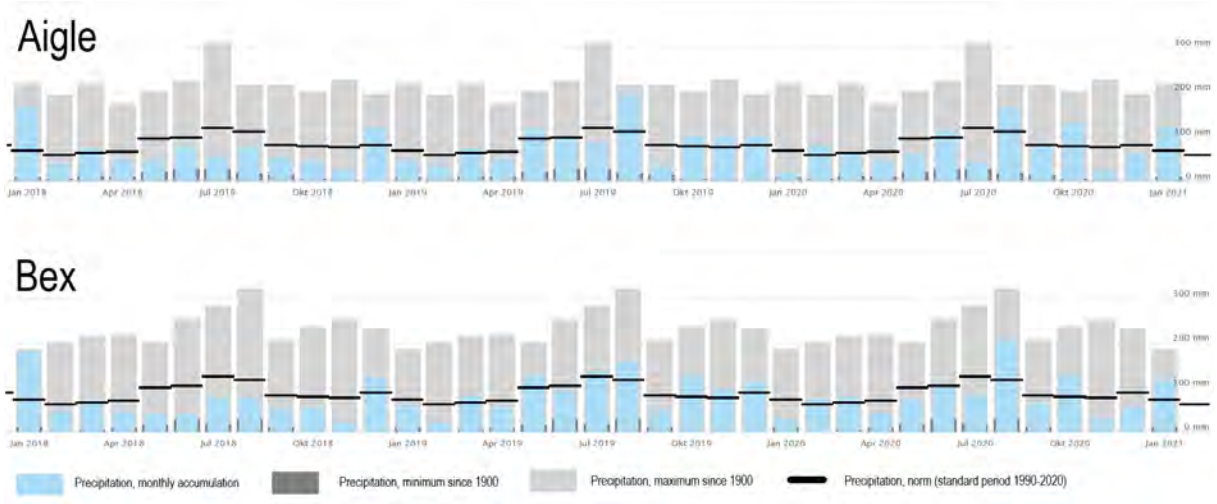

Figure 2 Precipitation data according to two nearby stations (modified after MétéoSuisse)

The laboratory analyses presented here were conducted on three samples collected from various key locations on the last landslide. The following table summarize the results of particle size analysis and Atterberg limits obtained according to the Unified Soil Classification System (USCS).

Table 1. Unified Soil Classification System for three samples

Sample	Fines %	Gravel %	Sand %	Liquid Limit %	Plastic Limit %	USCS
1	46.9	24.3	28.8	47.5	8.0	SM
2	45.6	25.4	29.0	48.0	3.3	SM
3	50.3	26.7	23.0	44.0	4.0	ML

Discussion

Gypsum's impermeable nature is a fundamental factor contributing to slope instability. This mineral inhibits surface runoff and hampers effective water infiltration, thereby disrupting the normal hydrological processes of the terrain. This disruption, in conjunction with the steep slopes commonly found in the area, sets the stage for instability. As water infiltrates the surface layer, it encounters the impermeable gypsum stratum, creating a saturation boundary. This boundary leads to an increase in pore pressure within the soil, ultimately compromising the soil's shear strength.

Moreover, gypsum's susceptibility to dissolution near the surface is another critical aspect to consider. When gypsum is exposed to water, it can undergo rapid dissolution, which alters its volume and properties. This dissolution process introduces variations in specific volumes, causing expansions and contractions within the rock. These volume changes, coupled with gypsum's tendency to deform under stress, contribute significantly to the overall instability of the slopes.

Analytical results from soil samples collected in the area reveal that the predominant soil type is Silty-Medium. Silty soils have moderate water retention capabilities and tend to compact easily when saturated, leading to reduced permeability. This reduction in permeability can result in poor drainage, particularly problematic in this area because of the particularly steep slope (around 43°).

Silty soils also typically exhibit low shear strength, which means they have a reduced ability to resist shearing forces. In slope stability analysis, this reduced shear strength can significantly elevate the risk of landslides or slope failures, particularly in regions with steep terrain.

While silty soils possess cohesion due to their fine particles, their friction angle is low. Cohesion provides some strength to the soil, but the lower friction angle makes silty soils more susceptible to sliding along failure planes. Altogether, these soil characteristics underscore the heightened vulnerability of the terrain to landslides, particularly when combined with the geological influence of gypsum, as observed in the area.

Conclusion

The comprehensive investigation into landslides in Ollon, Switzerland, has revealed the intricate web of factors contributing to these geotechnical hazards. The geological composition, characterized by gypsum-rich karst formations, plays a fundamental role in slope instability. Water, with its capacity to increase soil weight and generate shear forces, is a significant driver of landslides. Collectively, these findings underscore the vulnerability of the region to landslides and emphasize the need for an interdisciplinary approach to address these complex geotechnical challenges. This study highlights the critical importance of holistic geotechnical hazard analysis in safeguarding the region's infrastructure and enhancing the safety of its inhabitants. Hence, new investigations must be conducted with the aim of precisely determining the return periods of these events in the context of an acceleration of intense climatic phenomena.

Risk-informed decision-making for quick clay landslides in Norway

Zhongqiang Liu[1], Jean-Sébastien L'Heureux[1], Ørjan Nerland[1], Peter Løken Nilsson[2], Magnus Rømoen[1], Suzanne Lacasse[1]

[1] Norwegian Geotechnical Institute, Oslo, Norway
[2] Bane NOR, Oslo, Norway

SUMMARY: Society and standards require "risk-informed" decision-making as well as sustainable, holistic solutions. In this paper, the risk was assessed for two landslides in quick clay and for a standing slope with computed safety factor of 1.0. Measures to reduce risk and the added insight provided by risk assessment are discussed. A framework for improved landslide risk assessment and management is proposed.

Keywords: landslide, quick clay, hazard, consequence, risk assessment, event tree analysis

Approaches to assess the safety of a slope

Two approaches can assess the safety of a slope: (1) the conventional, standard-based approach with a global factor of safety (FS); and (2) the "risk-informed decision-making" (RIDM) approach (ISO 2394:2015). FS is not a sufficient indicator of safety because it does not account for the uncertainties in an analysis and can represent different failure probabilities (Lacasse *et al*., 2022). RIDM encourages a proactive mindset in identifying uncertainties and potential problems and requires justified reasoning for the choices made in the analysis. It recognizes that human judgment plays a role in decision-making, and that technical information is not the only basis for decision-making. Two simple RIDM methods, a qualitative risk matrix and a quantitative event tree analysis, illustrate the change in risk with time for three slopes in Norway.

The 2020 Alta landslide

In June 2020, a 900,000 m^3 quick clay landslide in Alta swept eight buildings into the sea and caused substantial damage but, fortunately, no loss of life. The masses started moving slowly as a large flake. The landslide scarp was 956 m long and nearly 20 m. Before the slide, residents observed a 30-40 m long tension crack in the terrain, parallel to the shoreline. The geological, hydrogeological, meteorological and geomechanical conditions were investigated (NVE, 2020), revealing quick clay from a depth of 10 m. The 24-m thick clay layer had interbedded layers of silt and sand. No precipitation was registered the days before the landslide, but snowmelt from a snow-rich winter was at its peak. The snowmelt alone could not explain the initiation of the landslide. LiDAR data revealed a yet unknown 2-m thick fill over 600 m^2 linked to a new house built in 2015. The small fill reduced the FS by 7%, which alone could not initiate the landslide. However, the combination of the snowmelt and the 2015-fill exposed the "new" slope to its highest porewater pressure so far and caused the failure.

The likelihood of a landslide at Alta was always present due to the thick deposit of quick clay, the high slope, and a stratigraphy making the slope sensitive to porewater pressure changes. The fill placement, the new house with increase in exposed persons and the snowmelt each contributed to increase the landslide risk at Alta, as illustrated on the risk matrix in Figure 1, where the risk increased from medium to high in the period 2015 to 2020.

The 2020 Gjerdrum landslide

On 30 December 2020, the catastrophic landslide in Gjerdrum caused 11 fatalities, destroyed 31 houses, required the evacuation of 1600 residents and led to severe chaos in services, infrastructure and ecosystem. The 1.2 million m^3 landslide retrogressed 630 m, had a scar of 1250 m and the debris ran 2 km downstream. Witness observations combined with physical evidence and slope stability analyses of the thick deposits of marine clay confirmed that the landslide started outside the fatality area, where the 25-m high slopes had progressively been subjected to 3 m deep erosion since the 1990s. Agricultural plans in the 1980s laid parts of the creek at the bottom of the slope in pipes. The erosion was exacerbated by changes in land use in the catchment while urbanization and vegetation removal led to increased runoff. Since the 90s, several human influences in the Gjerdrum area acted in the same direction and contributed to increased erosion at the foot of the slope that initiated the fatal landslide in 2020 (NoU, 2022).

Before 1997, the entire area around Holmen was farmland. Even though it was "likely" that a landslide could occur (Fig. 2), the risk was interpreted as low as the landslide would have impacted only farmland. Urbanization in the early 2000s increased the likelihood of a landslide because of its impact on the runoff and subsequent erosion in the creek after 2007. Stabilization was done as part of the plans for new housing in 2007, but those measures did not improve the conditions at Holmen. As a large contingent of people moved into the new dwellings, the risk associated with a landslide increased significantly in the period 2007-2020.

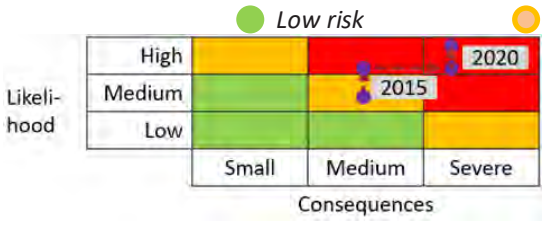

Figure 1. Change in risk with time at Alta

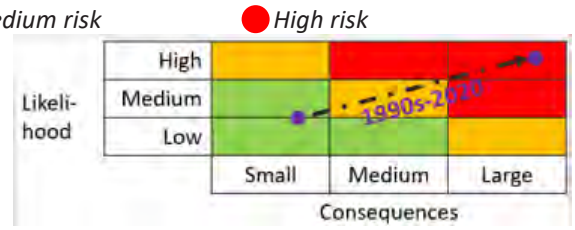

Figure 2. Change in risk with time at Gjerdrum

Standing slope in quick clay

In the centre of centre of Moss, just outside Oslo, a new intercity (IC) double track railway and a train station will be built on a quick clay area where about 2000 residents live. Several slopes were found to have a computed FS between 1.0 and 1.15 before the work started. The soil profile consists of varying thicknesses of sand over soft clay and quick clay. The slopes are standing today, even those computed to have a FS of 1.0 or less. There was concern that the slopes could fail under an external trigger or during construction. To ensure the safety of the people living in the area, mitigation measures, including jet grouting, retaining wall, toe erosion protection, installation of drains and soil improvement, were planned. Given the low FS, extreme care needed to ensure not worsening the stability before and during the stabilisation.

A risk assessment was carried out using the event tree analysis method. Figure 3 presents the results of the event tree analyses with rainfall as a trigger, with much surface water causing erosion. The event tree analysis is a "what if" type of analysis establishing the failure probability for each scenario that can lead to failure (Lacasse *et al.*, 2022). To set the probability values for each event in the tree, the approach seeks to achieve consensus among the opinions of experts and stakeholders based on the expertise and experience of the participants. Event trees were constructed for earthquake loading, human action (e.g., loading on top of slope, excavation near the toe, blasting, overloading of the harbour quay with containers) and erosion due to surface

water and/or underground leakage or pipe break(s). Figure 4 illustrates the total annual failure probability as a function of the level of risk mitigation (Phase 0: natural slope (no mitigation); Phase 1: natural slope, with live (24/7) instrumentation of the slope (inclinometers and piezometers) and increased awareness of the population; Phase 2: partial stabilisation of the area, and live instrumentation following all steps of the remediation work; and Phase 3: entire quick clay area stabilized. The figure on the right also illustrates that additional toe erosion protection over the entire area improves the situation. During execution of the mitigation measures between Phase 1 and 2, and possibly between Phase 2 and 3, the hazard (failure probability) could increase temporarily due to stabilisation work. This should be analysed explicitly for each mitigation measure to ensure the safety of the residents, workers and the existing railway.

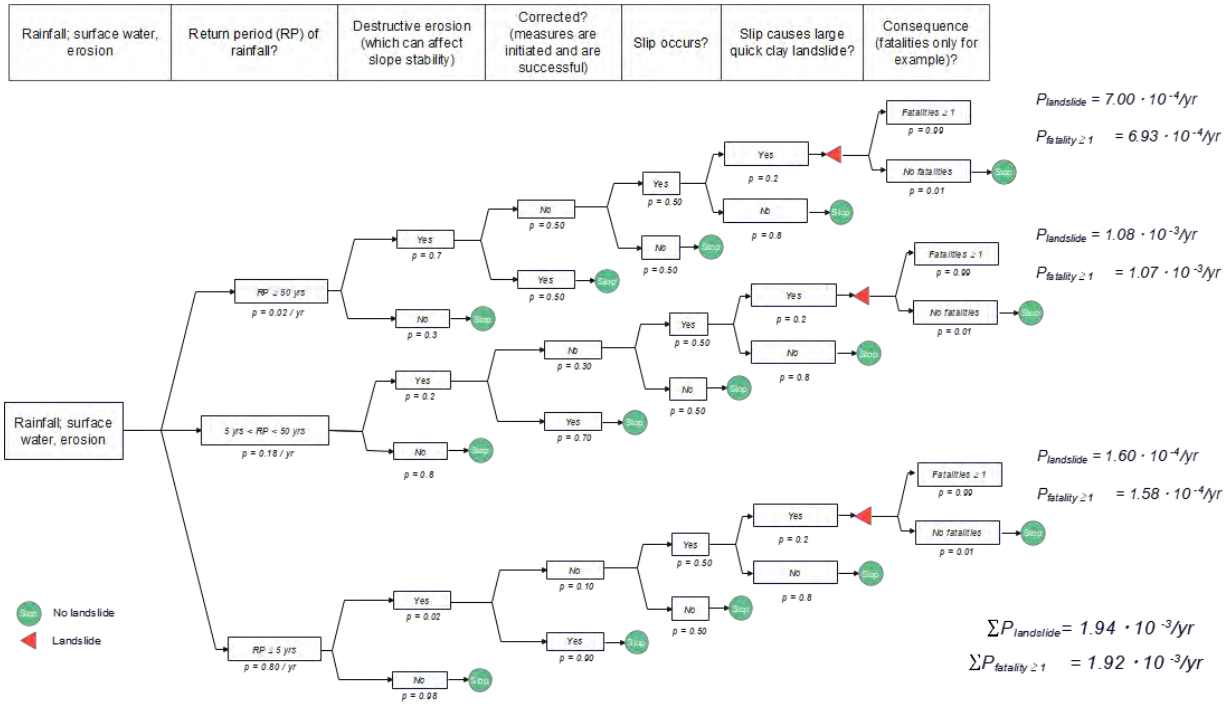

Figure 3. Event tree analysis under rainfall for IC Moss most critical slope

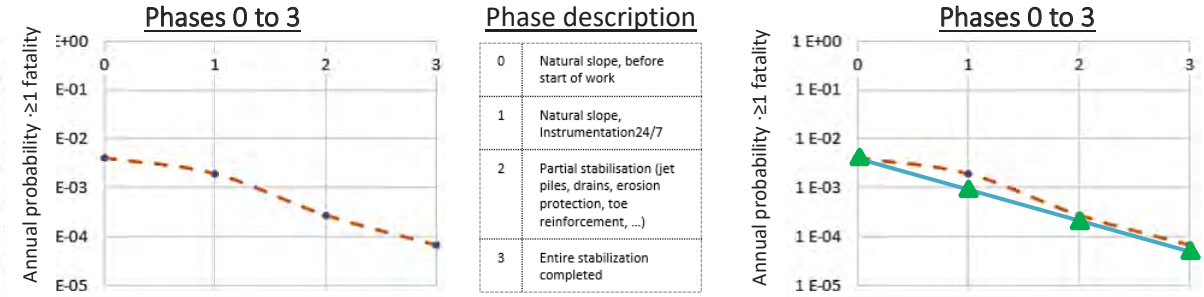

Figure 4. Risk reduction over entire IC Moss area vs time (left) and with more erosion protection (green, right)

Lessons learned from the two 2020 landslides and the IC Moss analyses

Key lessons learned from the two 2020 landslides and the IC Moss analyses include:

- Even small changes in "loads" or toe conditions can have disastrous consequences.
- To assess risk for slopes, one should consider changes in erosion, climate impact, changes in land-use and urbanisation, and the potential threat of surrounding areas.
- Landslides may occur following a long history of erosion and/or human activity.
- Strict control of construction activities, erosion and terrain changes is needed.

– One should use innovative and state-of-the-art remote sensing in landslide risk management.
– Risk assessments helps illustrate the benefit of risk mitigation measures.

Proposed risk management framework

Figure 5 proposes a management framework for risk-informed decision-making, integrating four parts: (1) assembling all available information and doing deterministic analyses of hazard and consequence (green zone); (2) risk assessment, qualitative or quantitative (yellow zone); (3) decision-making and risk reduction (blue zone); and (4) loop for reassessment of landslide risk (grey zone), as conditions change with time or if inspections reveal changed conditions.

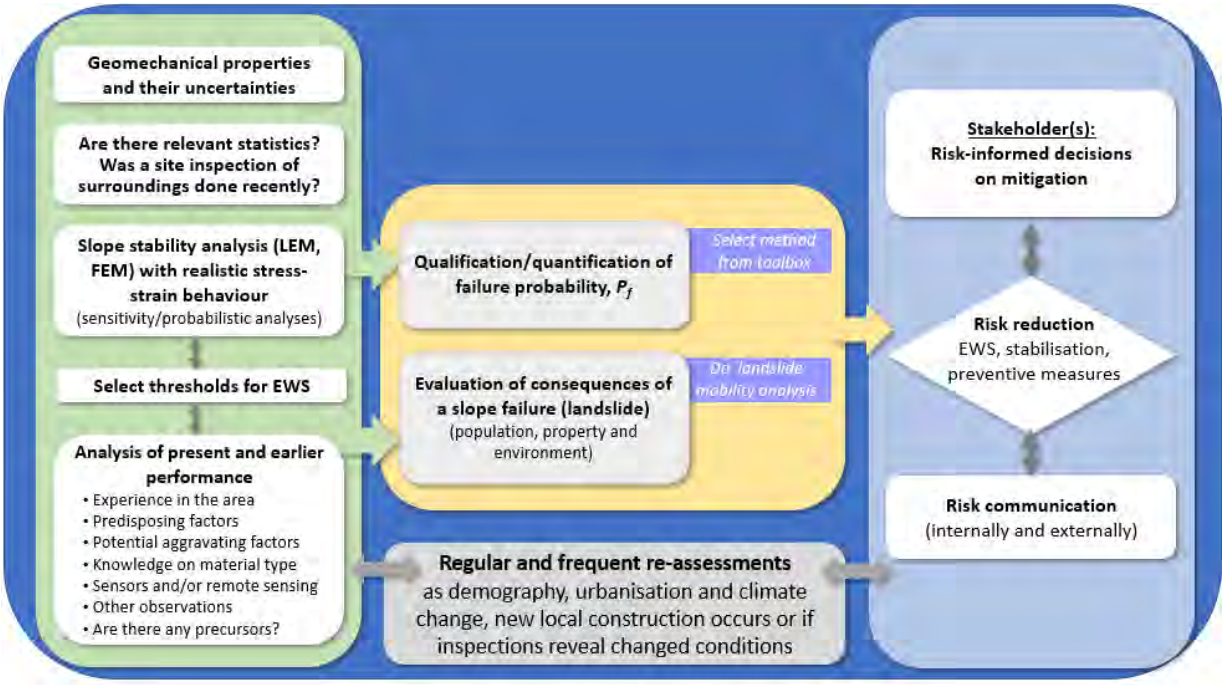

Figure 5. Proposed integrated framework for risk-informed management of landslides (Lacasse *et al.*, 2022) (LEM = Limiting Equilibrium Method, FEM = Finite Element method, EWS = Early Warning System)

Added insight with risk-informed approach

Data gathering and deterministic analyses are necessary. The probabilistic analyses provide enhanced insight into the aspects of the slope stability that can become critical under different natural and man-made triggers. The risk assessments are usually best made in a consensus format among experts and stakeholders (where also operative personal are involved). Even simple estimates, such as a qualitative or semi-quantitative risk matrix, are informative as they promote a discussion of what can happen, help identify the uncertainties affecting the outcome and map the effect of risk reducing measure options.

References

ISO 2394:2015. (International Standard Organization). ISO Standard: General principles on reliability for structures. ISO/TC 98/SC 2. 111 pp.

Lacasse, S., L'Heureux, and Liu, Z.Q. (2022). Reducing landslide risk - Emerging challenges and novel technologies. Keynote Lecture. Geohazards 8. Québec (June 2022).

NoU (2022). På trygg grunn. Bedre håndtering av kvikkleirerisiko. Norges offentlige utredning 2022:3. Olje og energidept. 29 March 2022. 207 pp. (*in Norwegian*)

NVE (2020). Årsaksvurdering–Kvikkleireskredet ved Kråknes i Alta 3. juni 2020. 10220443-RIG-RAP-001. NVE Ekst. Rap. 2021:4. https://publikasjoner.nve.no/eksternrapport/2021/eksternrapport2021_04.pdf *(in Norwegian).*

Challenges of characterizing an extremely slow-moving rockslide with minor total displacement: The case of Dutchman's Ridge rockslide in British Columbia, Canada

Camila Troncoso Klein[1], D. Jean Hutchinson[1], Thomas Stewart[2], Julia Marsh[2]

[1] Department of Geological Sciences and Geological Engineering, Queen's University, Kingston, ON, Canada
[2] Dam Safety, Reservoir Slopes-BC Hydro, Revelstoke, BC, Canada

SUMMARY: Extremely slow-moving rockslides move at velocities < 16 mm/year. Sometimes, cumulative displacements can be small enough that features such as scarps or tension cracks have not yet developed, which may hinder the ability of identifying these instabilities, especially in forested areas. Thus, it is crucial to utilize all available sources of data to define boundaries and recognize relevant features. Dutchman's Ridge rockslide is a good example of this kind of landslide, where information derived from surface and subsurface geological mapping, geotechnical instrumentation and LiDAR was used to redefine its boundaries and identify several zones. It is also challenging to determine an absolute factor of safety for these rockslides as the relationship between rate of displacement and this value is not well understood.

Keywords: rockslide, lidar, deep-seated, extremely-slow

Introduction

Rockslides are downslope movements of rock mass, occurring mostly on rupture surfaces or on relatively thin zones of intense shear strain (Cruden, 1996). According to Hungr et al. (2014), these events occur at velocities varying from Extremely rapid (~5 m/s) to Extremely slow (< 16 mm/yr) and present a wide range of sizes.

They are usually identified by the presence of typical features such as tension cracks, head and lateral scarps, linear troughs or a bulging toe. These features are easily recognizable on rockslides that have considerable total displacement, but their identification may become difficult on extremely slow-moving rockslides that have experienced small cumulative displacement, either because they are incipiently developing or have not yet developed.

Despite their apparently insignificant rate of movement, there are many cases where it is important to identify and characterize these instabilities, for instance, when critical infrastructure is compromised or when, due to their volume and location, a sudden failure could have catastrophic consequences. Thus, it is key to utilize all available sources of data to better understand their extent and behaviour. Typical available information originates from surficial geological mapping, drill core logging, geotechnical instrumentation and more recently, from remote sensing data. LiDAR (Light Detection and Ranging) is an excellent tool to identify incipiently developing features, especially in densely forested areas where newly generated instabilities are hardly identified.

In the Upper Columbia region, in British Columbia, these phenomena are common and have been studied, at least, since the 1950s, when investigations before the construction of two dams started. The most extensively studied is Downie slide (Brown & Psutka, 1980; Kalenchuk,

2010; Kalenchuk et al., 2012; Westin, 2017), located on the western bank of the Columbia River, with a volume of 1.5 billion m^3 and a displacement rate of <5 mm-30 mm/year. In Figure 1, differences in the morphology of Downie and Dutchman's Ridge rockslides can be noted. At Downie, both a clear lateral and head scarps are easily recognizable. Also, the river looks narrower due to the displacement towards the Revelstoke reservoir. In contrast, the presence of a rockslide at Dutchman's Ridge is not obvious and does not show a distinctive morphology at the toe.

In this paper, the results of a study reviewing the historical geological and instrumentation data of the Dutchman's Ridge rockslide, as well as a GIS analysis of LiDAR-derived data, will be briefly presented.

Figure 1. Top left: Location of the Upper Columbia River region in BC, Canada. Bottom left: view of Downie slide and Revelstoke reservoir from Google Earth satellite imagery. Note the clear head and lateral scarps, as well as the convex morphology towards the river. Right: Satellite imagery from Google Earth showing Mica Dam, Mica Reservoir and Dutchman's Ridge. Note how the extremely slow-moving rockslide cannot be easily identified.

Dutchman's Ridge rockslide

Dutchman's Ridge has an elevation of almost 2000 m a.s.l., with a slope angle of 30°, and is mainly composed of foliated metamorphic rocks. A potential rockslide, estimated to be 115 million m^3 (Hydro, 1993) in volume, was identified in the lower parts of the slope prior to the construction of Mica Dam (CASECO, 1969), only 1.5 km away. A Basal Shear Zone (BSZ), underlying the instability and dipping towards the reservoir, was recognized in boreholes.

No displacement was identified before the filling of the reservoir (CASECO, 1973), however, after a review of the instrumentation data (BC Hydro, 1984), small but consistent displacements of the rock mass overlying the BSZ were recognized to have occurred during Mica reservoir filling (1973-1976) at 5.1 to 18 mm/year, averaging 11.4 m/year. A drainage adit was built between 1986 and 1988, to reduce the rate of displacement. As of 2023, the slope remains marginally stable, with a displacement of 1 mm/year, according to an extensometer installed across the BSZ within the adit.

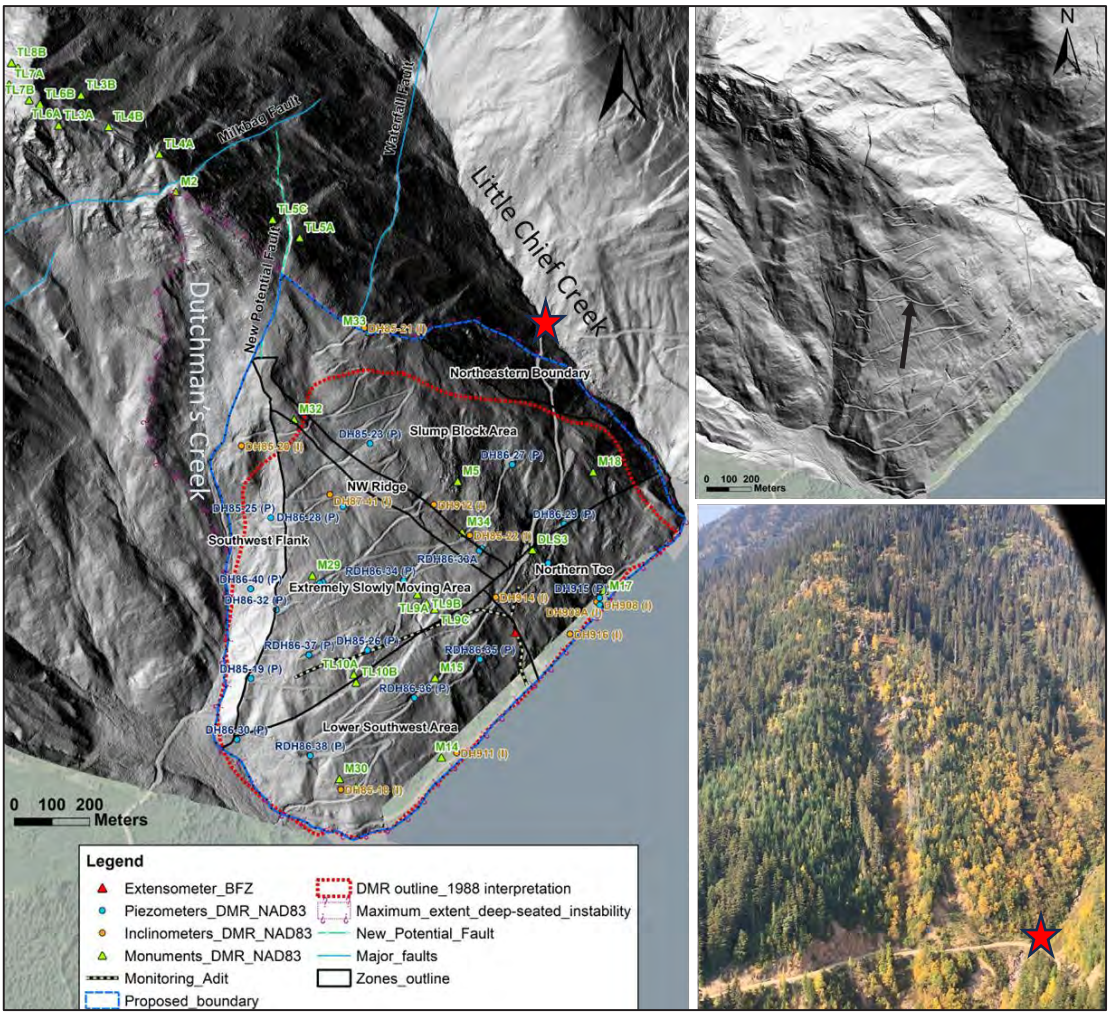

Figure 2. Left: LiDAR-derived hillshade (az. 270) showing the 1988 (red) and new proposed (blue) boundaries of Dutchman's Ridge rockslide. Black lines indicate the seven domains found on the rockslide. Top right: Hillshade image (az. 45). Note the NW Ridge-like feature in the middle of the slope. Bottom right: Proposed northeastern (NE) boundary next to the Main Road near Little Chief Creek (provided by Julia Marsh, BC Hydro).

Both the boundary of 1988 and the boundary and zonation proposed by Troncoso Klein et al. (2023) are shown in Figure 2. A 2014 LiDAR-derived DEM was very helpful to identify key features and define the limits of the extremely slow-moving mass, when analyzed together with available geological data. The proposed NE boundary can be seen in the bottom right photo.

A ridge-like feature trending NW (top right in Figure 2), fits well with the projection of Lavender Shear, a structure that truncates the base of the BSZ as observed in the adit. Steep foliation (up to 70°SW), that could be an expression of this shear, was found at its approximate position in the field (Figure 3).

A NNW shadowed feature crossing the Slump Block area and the Northern Toe (left in Figure 2), coincides with a deep postulated fault by BC Hydro (1989). In the field, it resembles a large and deep crack, near which the largest rock blocks are found (Figure 3). The interaction between this structure and foliation shears seems to be responsible for the morphology of this area.

Figure 3. Left: NNW large tension crack within the Slump Block area, possibly a fault at depth. Note the up to 12 m-high rock blocks. Right: Steep foliation found on some outcrops on the west of the Ridge-like feature.

What is the Factor of Safety of an extremely slow rockslide?

Assigning a Factor of Safety (FoS) value to an extremely slow rockslide can be difficult if not inaccurate. As stated by Hoek (2023), in cases like this one, a FoS may have no meaning, so, instead, the rate of change of this value is used to judge the impact of changes in slope conditions and the effectiveness of remedial actions. Narendranathan et al. (2013), based on case histories by other authors who presented FoS and rates of slope movement pairs from open pits in hard rocks, obtained an assumed FoS > 1.5 for a displacement rate lower than 1.5 mm/month. However, the relationship between the rate of displacement and this value remains not fully understood.

As an example, as an absolute FoS could not be determined for Dutchman's Ridge, it was assumed this value in the pre-drainage stage would be close to 1 on the northeastern side and higher on the southwestern side (Table 1). From this value, a Finite Element (FE) analysis was performed to assess the variation in FoS when increasing the piezometric level closest to the slide base.

Table 1. Results from an FE analysis showing the variation in FoS considering different piezometric levels on a cross section (MCS_4) just southwest of the Ridge-like feature on Dutchman's Ridge.

Case (MCS_4)	Critical SRF	% variation from RS	Reference Stage (RS)
Pre-drainage (SS 1986)	1.27		
Post-drainage (SS 2020)	1.32	3.9	Pre-drainage
Lost drainage capacity 1 (Back to 1986 PL + 10 m)	1.03	-22.0	Post-drainage
Lost drainage capacity 2 (Back to 1986 PL + 20 m)	1	-24.2	Post-drainage
Lost drainage capacity 3 (Back to 1986 PL + 30 m)	0.95	-28.0	Post-drainage

Conclusions

Defining boundaries on an extremely slow-moving rockslide with small total displacement is challenging as the typical features have not yet developed or are incipiently developing, therefore, a thorough critical examination of all possible available data sources is crucial. Besides, a better understanding of the use of the factor of safety for these rockslides is needed, in order to assess a potential failure.

References

Brown, R. L. & Psutka, J. F. (1980). Structural and stratigraphic setting of the Downie slide, Columbia River valley, British Columbia. *Canadian Journal of Earth Sciences,* 17**,** 698-709.

CASECO 1969. Mica Project - Supplementary Report on Stability of Reservoir Slopes.

CASECO 1973. Mica Project - Sixth Supplementary Report on Stability of Reservoir Slopes.

Cruden, D. M. & Varnes, D.J. (1996) Landslide Types and Processes. *Transportation Research Board, U.S. National Academy of Sciences, Special Report,* 247**,** 36-75.

Hoek, E. (2023) *Practical Rock Engineering*.

Hungr, O., Leroueil, S., Picarelli, L. (2014). The Varnes classification of landslide types, an update. *Landslides,* 11**,** 167-194.

BC Hydro (1984). Mica Project Reservoir Slopes Surveillance - Memorandum on Assessment of Movement of Dutchman's Ridge.

BC Hydro (1987). Dutchman's Ridge Remedial Works - Memorandum on 1985 and 1986 Investigation and Instrumentation Programs.

BC Hydro (1989). Dutchman's Ridge Remedial Works - Geological and Groundwater Information 1986-1988.

BC Hydro. (1993). Dutchman's Ridge Remedial Works - Summary Report

Kalenchuk, K. S. (2010). *Multi-Dimensional Analysis of Large, Complex Slope Instability*. Doctor of Philosophy, Queen's University

Kalenchuk, K. S. Hutchinson., D.J.; Diederichs, M.; Moore, D. (2012). Downie Slide, British Columbia, Canada *In:* Clague, J. S., D. (ed.) *Landslides: Types, Mechanisms and Modeling.* Cambridge University Press.

Narendranathan, S. Thomas, R.D.H.; Neilsen, J.M. (2013). The effect of slope curvature in rock mass shear strength derivations for stability modelling of foliated rock masses. *In:* DIGHT, P. M. (ed.) *Slope Stability 2013.* Perth, Australia: Australian Centre for Geomechanics.

Troncoso Klein, C., Hutchinson, D. J., Stewart, T., Marsh, J. (2023). Dutchman's Ridge: Results from the analysis of geologic, monitoring and LiDAR-derived data of an extremely slowly moving rockslide. *GeoSaskatoon 2023 Conference.* Saskatoon, SK, Canada.

Westin, A. M. (2017). *Downie Slide: An integrated remote sensing approach to characterization of a very slow moving landslide.* Master of Science. Simon Fraser University.

Distribution pattern and tectonic significance of landslides triggered by strike-slip faulting 2022 Ms 6.8 Luding earthquake

Siyuan Ma[1], Chong Xu[2], Renmao Yuan[1]

[1] Institute of Geology, China Earthquake Administration, Beijing, 100029, China;
[2] National Institute of Natural Hazards, Ministry of Emergency Management of China, Beijing 100085, China

SUMMARY: On September 5th, 2022, an Ms6.8 earthquake struck the Luding area of Gaze Tibetan Autonomous Prefecture, Sichuan Province, China. This earthquake with a focal depth of 16 km at 29.49°N, 102.22°E (hereinafter called the Luding earthquake) was generated by a strike-slip faulting and triggered at least 5000 landslides over an area of 5000 km2. Over 80% of landslides are distributed in areas with a seismic intensity of IX, which mainly consist of massive shallow landslides with a few topples, rockfalls, and debris flows. Statistically, coseismic landslides are prone to occur in areas with low elevations, steep hillslope gradient, and high ground motion.

Keywords: 2022 Luding earthquake; Coseismic landslides; Distribution pattern; Strike-slip fault

1 Introduction

Strong earthquakes frequently result in numerous seismic landslides in mountainous areas. The casualties and property losses brought by these catastrophes are significant factors that increase the risk of earthquakes \. Earthquake-induced landslides, as an important secondary geological disaster, typically occur during or shortly after an earthquake and have the characteristics of large quantity and scale, wide distribution, complex mechanism, serious casualties and economic losses, and long-duration post-earthquake effect\.

A good understanding of the principles governing the occurrence of coseismic landslides, their distribution patterns, and the corresponding influencing factors, can offer valuable insights into disaster prevention and mitigation of the earthquakes. Furthermore, it aids in understanding the progression of disaster chains and the evolution of regional landscapes \ On September 5, 2022, at 12:52, an earthquake with a magnitude of MS6.8 struck Luding County, located in Ganzi Prefecture, Sichuan Province, China. The earthquake had a focal depth of 16 km and reached a maximum intensity of IX. The epicenter was situated at coordinates 29.25°N and 102.08°E. The earthquake inflicted extensive damage upon transportation, communication, power supply, and various other forms of infrastructure. The results showed that the earthquake triggered at least 5,000 coseismic landslides, encompassing shallow landslides, rockfalls, topples, and debris flows (Fan et al., 2022; Huang et al., 2023; Zhao et al., 2022). The earthquake resulted in 93 deaths, 25 missing persons, and at least 400 injuries. Among these, 20% of the recorded casualties directly resulted from house collapses. Alarmingly, more than 80% of the deaths and missing persons were linked to landslides induced by the earthquake.

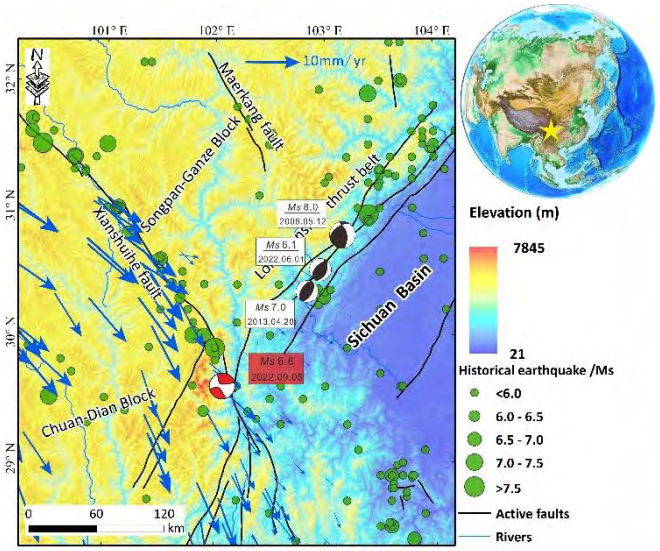

Fig.1 Map showing the active faults, historical earthquakes and topography distribution near the Xianshuihe fault. The active fault lines are from Xu et al. (2016c). The distribution of GPS velocity before the Luding earthquake is from the Second Monitoring Center of the China Earthquake Administration (https://data.earthquake.cn/20220905xbsj/info/2022/334669387.html)

2 Spatial distribution of coseismic landslides

The 2022 Luding earthquake triggered at least 5000 landslides over an area of 5000 km2, and more than 80% of landslides are distributed in areas with a seismic intensity of IX (Huang et al., 2023). The coseismic landslides covered an area of 17.4 km2, with a total volume of about 0.15 km3 using a power-law landslide area-volume scaling relationship (Xu et al., 2016a). The largest landslide area is 120,000 m2, the smallest area is 65m2, and the average is 3,500 m2 (Fig.2). Notably, a substantial portion of landslides clusters within the 1,000 to 10,000 m² range, constituting 60% of the total occurrences. t more than 85% of these landslides occur within a 5 km range on both sides of the seismogenic fault, and can be divided into four densely developed areas, namely Moxi area (Sub-1), Wandong area (Sub-2), Wanggangping area (Sub-3), and Xingfu area(Sub-4) (Fig.2).

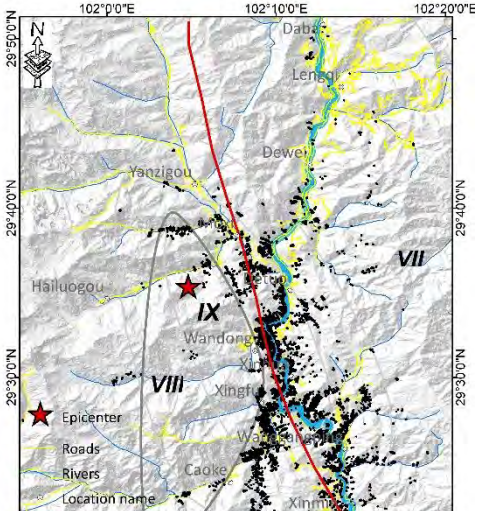

Fig.2 Spatial distribution of coseismic landslides caused by the Luding earthquake; The area with unavailable images comes from (Huang et al., 2023)

Fig.3 shows the frequency density distribution of landslide and landscape (non-landslide) areas under different influencing factors. Overall, landslides are mostly distributed in lower-elevation areas. In terms of hillslope gradient, most landslide areas are concentrated in the 30-45° range, while landscape areas are concentrated in the 18-38° range. For relief, landslides tend to concentrate within areas characterized by low relief. As for ground motion, most landslide areas are concentrated in the range of 0.49-0.51g, while non-landslide areas are distributed in the range of 0.47-0.49g. The average PGA of landslide areas is 0.49g, while that of non-landslide areas is 0.44g, which indicated that landslides are mostly distributed in areas with higher seismic motion.

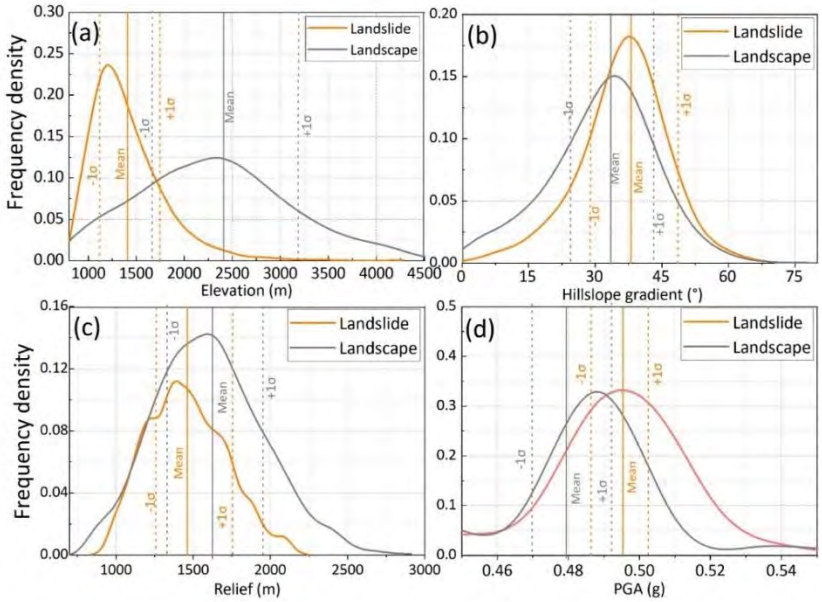

Fig. 3 Frequency density estimates of landsliding and non-landsliding areas for various influencing factors; (a) Elevation; (b) Hillslope gradient; (c) Topographic relief; (d) PGA

Finite-fault inversion analyses reveal a distinct rupture pattern during this event, characterized by a unilateral rupture extending from the northwest to the southeast, originating at the epicenter location. The region proximal to the epicenter exhibits a maximum slip displacement of approximately 1.4 m. Furthermore, a significant near-surface rupture measuring about 0.4 m is evident in the Wandong area. Field investigations further indicate that the most probable location for the coseismic surface rupture of the earthquake is the Wandong and Xingfu areas. These results suggest a significant influence of the seismogenic fault on the near-surface conditions in the western side of the seismogenic fault, particularly in the Wandong and Xingfu areas. In summary, the west side of the seismogenic fault exhibits elevated seismic energy, coupled with substantial surface deformation. This observation is corroborated by the fault's slight westward dip, as inferred from the source mechanism solution and the actual distribution of landslides (Fig.4).

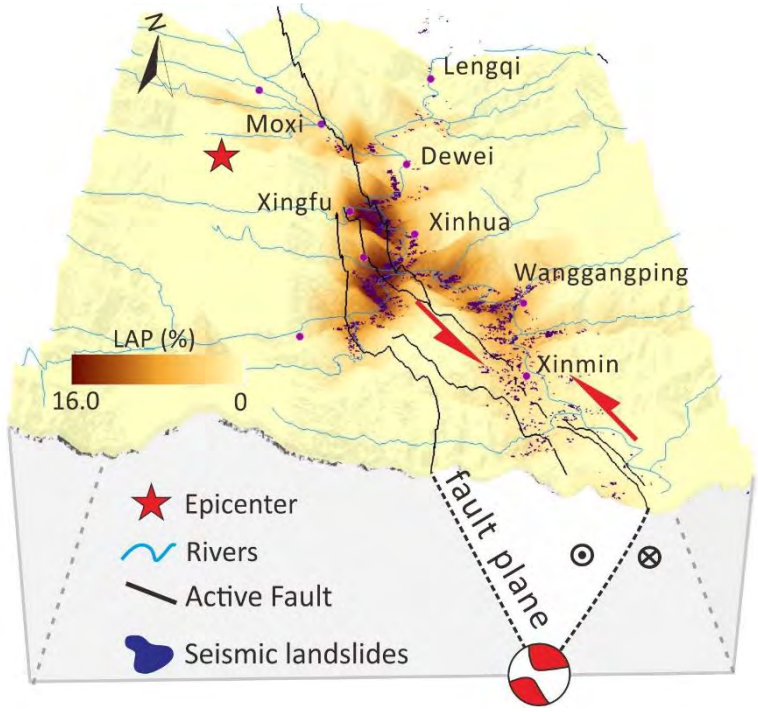

Fig.4 Map showing the three-dimensional (3D) seismogenic structure for the 2022 Luding earthquake and the relationship between the coseismic landslides and the seismogenic fault

References

Fan, X. et al., 2022. Characteristics and spatial distribution pattern of Ms 6.8 Luding earthquake occurred on September 5, 2022. Journal of Engineering Geology (In Chinese).

Huang, Y. et al., 2023. An open-accessed inventory of landslides triggered by the Ms 6.8 Luding earthquake, China on 5 September 2022. Earthquake Research Advances, 3, 100181.

Zhang, J., Su, F., Fan, J., 2013. Distribution of landslides and collapses induced by 2013 "4.20" Lushan earthquake and hazards assessment: a case study of S210 highway. Journal of Mountain Science, 31, 616-623.

Zhao, B. et al., 2022. Geomorphic and tectonic controls of landslides induced by the 2022 Luding earthquake. Journal of Mountain Science, 19.

Experimental study on the role of halloysite on the initiation and movement of landslides occurring on slopes of pyroclastic fall deposits triggered by earthquakes

Gonghui Wang[1], Baichuan Liu[2]

[1] Disaster Prevention Research Institute, Kyoto University, Kyoto, Japan
[2] Former student at Graduate School of Science, Kyoto University, Kyoto, Japan

SUMMARY: To unravel the role of halloysite on the initiation and movement of landslides occurring on slopes of pyroclastic fall deposits, we conducted field survey on some coseismic landslides and examined the existence and involvement of halloysite on the landslide materials. We observed the shapes of those halloysites in different landslide areas, and examined the shear behavior of those landslide materials and mixtures of sand/pumice with different contents of halloysites in drained and undrained conditions. Our results show that introduction of halloysite in the tephra can elevate the water retention capacity and then enable the tephra to have high-water content in natural condition. The introduction of halloysite does not greatly affect the undrained peak shear strength of tephra materials, but can elevate the liquefaction potential, increasing the slope instability potential and the mobility of displaced landslide materials.

Keywords: landslides, halloysite, water retention capacity, shear behavior, liquefaction

Introduction

Landslides occurring on tephra slopes during earthquakes are normally characterized by their high mobility with long runouts, presenting great threats to human safety and the built environment. This kind of landslides could be well exampled by those triggered by the 2016 Kumamoto earthquake in Minami Aso area, Kumamoto, and by those triggered by the 2018 Hokkaido Eastern Iburi Earthquake in the hillslopes near the epicenter. Field study on those landslides revealed that most of the landslides occurring on tephra slopes are shallow but destructive, the displaced landslide materials mainly consist of tephra, and their sliding surfaces are mostly developed within the weathered tephra layer, where the water content is very high and a clay mineral of halloysite resulting from the weathering of volcanic glass is normally presented (i.e., Chigira et al, 2019, among others). Similar phenomena have also been reported in the landslides occurring on tephra slopes in other countries (i.e., Moon, 2016 among others). Therefore, it is believed that the presence of halloysite has played a bad role in the initiation of slope instability and the movement of the displaced landslide materials for these coseismic landslides occurring on tephra slopes. Nevertheless, the role of halloysite in the initiation and the movement of landslide remains unclear, although some case studies have been conducted with the achievement of some preliminary pieces of knowledge. Hence, this study aims at clarifying the role of halloysite on the initiation and movement of landslides occurring on tephra slopes, through field investigation of some landslides triggered by recent earthquakes in Japan, and the conduction of a series of experimental works.

Methods

To clarify the role of halloysite on the initiation and movement of landslides occurring on slopes of pyroclastic fall deposits, this study employed three different approaches. The first approach

is to examine the possible formation and shape of halloysite in the soil layers along the sliding surface. To achieve these, we conducted field trips of those landslides occurring on pyroclastic fall deposits triggered by the 2016 Kumamoto Earthquake and 2018 Hokkaido Eastern Iburi Earthquake, respectively. We examined the soil layer profiles on the source areas of the landslides and took samples from the soil layers near the sliding surfaces, and then examined the clay minerals through XRD test, and conducted TEM observation on the minerals. The second approach aims to examine the effects of the introduction of halloysite on the water retention of tephra materials through pF tests. The samples were prepared by adding 0%, 10%, 15% and 30% of tubular halloysite by weight to the tephra materials taken from the Minami Aso area, Kumamoto (termed as P_0, P_{10}, P_{15} and P_{30}, respectively), or 10% and 30% of silica nanomaterial (20~30 nm in size) (termed as P_{s10} and P_{s30}, respectively). The third approach involves examining the effect of halloysite on the shear behavior of tephra material, which includes: 1) using an in situ direct shear box to perform shear tests on samples in disturbed or undisturbed states with natural water content on the landslide field; 2) conducting undrained ring shear tests on above-mentioned mixtures.

Results and Discussions

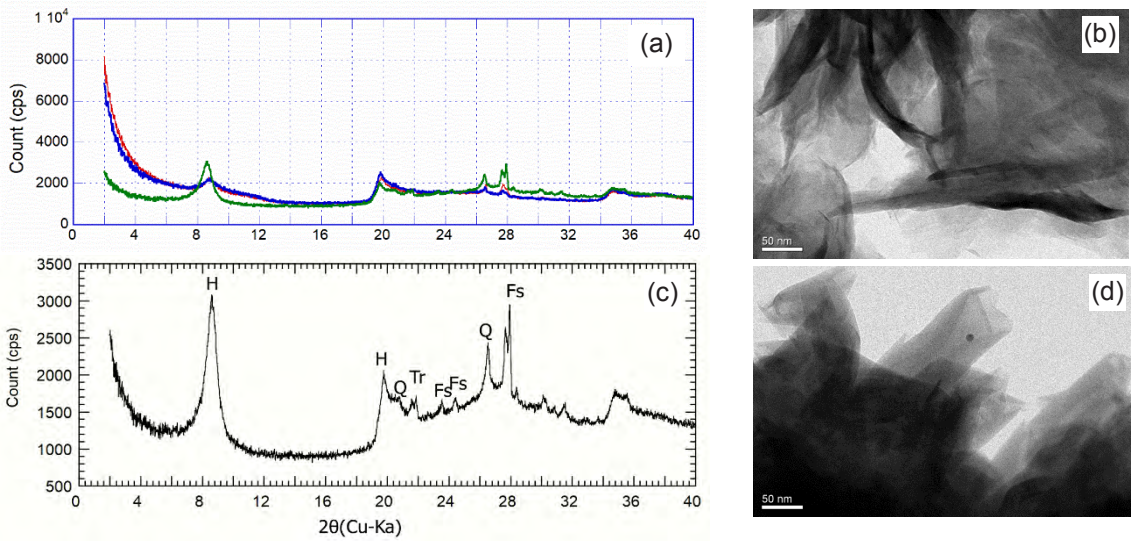

Figure 1. XRD analysis results and TEM images for samples taken from the weathered pumice layers in Yoshino area, Atsuma Town, Hokkaido (a, b), and for samples from the whitish thin layer of weather pumice, Takanodai area, Minamiaso, Kumamoto (c, d).

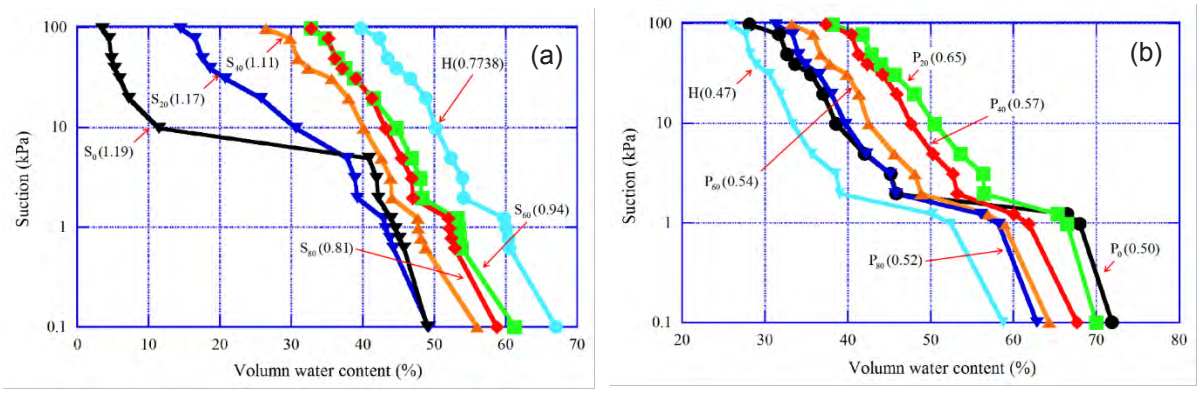

Figure 2. The results of the water retention experiment of the mixture of No. 8 silica sand and halloysite (a), and mixture of pumice and halloysite. All are in drainage process. S_{20}(1.19): Mixture of silica sand No. 8 with 20% of halloysite at the dry density of 1.19 g/cm^3. H (0.77): Pure halloysite at the density of 0.77 g/cm^3.

The results obtained from the first approach revealed that: 1) halloysite (Figs. 1a, c) has been formed and confirmed on the soil layers along the sliding surfaces of those landslides occurring on the hillslopes of pyroclastic fall deposits in Minami Aso and Atsuma areas; 2) the halloysite in the sample taken from the Minami Aso area presents the shape of a tubular one, while that from Atsuma area, Hokkaido shows the shape of a platy or crumpled lamellar (Figs. 1b, d)

Field examination on the weathered tephra layer with the formation of halloysite and the results of pF tests indicate that: 1) the weathered tephra layer with the formation of halloysite normally maintains high water content under natural conditions; 2) The sample containing halloysite showed higher water retention capacity than the mixture of tephra with fine silica sand (Fig. 2). Namely, besides the small particle size, the special structure of the halloysite may be capable of elevating the potential of water retention capacity.

Field moisture measurement and direct shear box tests on the intact samples showed that the strongly weathered pumice layer with the formation of halloysite has very high water content (around 198%) and presents very small values in both the peak and residual shear strengths (Fig. 3). Undrained ring shear tests on these above-mentioned mixtures show that adding halloysite to tephra material changes the peak shear resistance of the sample. As the halloysite content increases, the peak shear resistance decreases, given their initial densities being the same (Fig. 4). However, if evaluated by relative density, the peak and residual shear strengths present a reverse tendency with the increase of halloysite in the mixture (Figs. 5a, b). Concerning these tendencies, further analyses will be needed by adopting different concepts, such as equivalent intergranular/interfine void ratio or density.

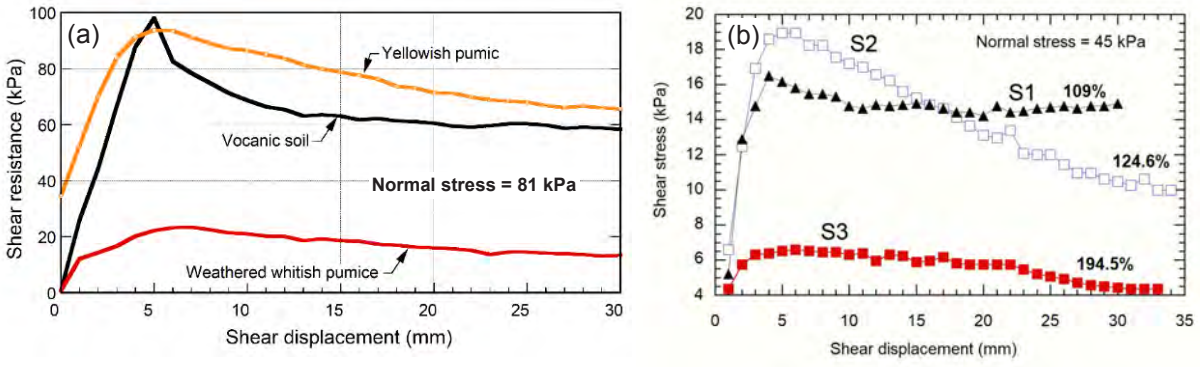

Figure 3. Results of in-situ direct shear box tests. (a) Takanodai area, Kumamoto. The water contents: 178%, 167%, and 198% for samples from the yellowish pumice, volcanic soil, and weathered whitish pumice layers, respectively. (b) Yoshino area, Hokkaido. S1, S2: reddish pumices; S3: strong weathered whitish pumice. 109%: water content.

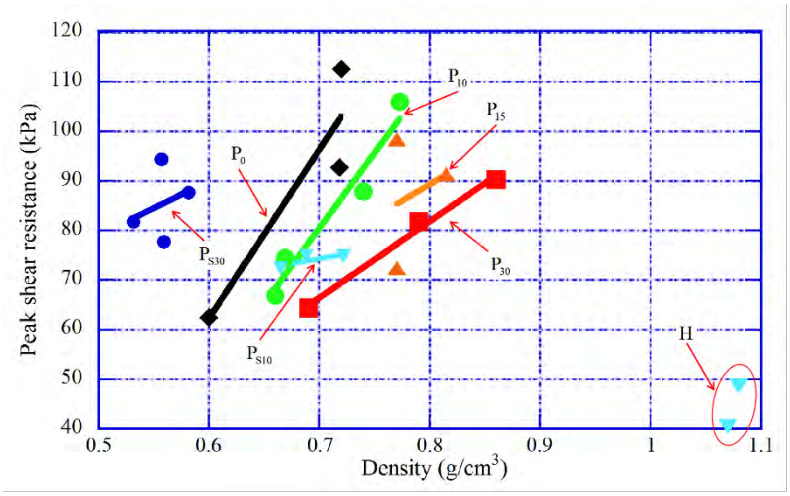

Figure 4. Undrained peak shear strengths against sample initial dry density..

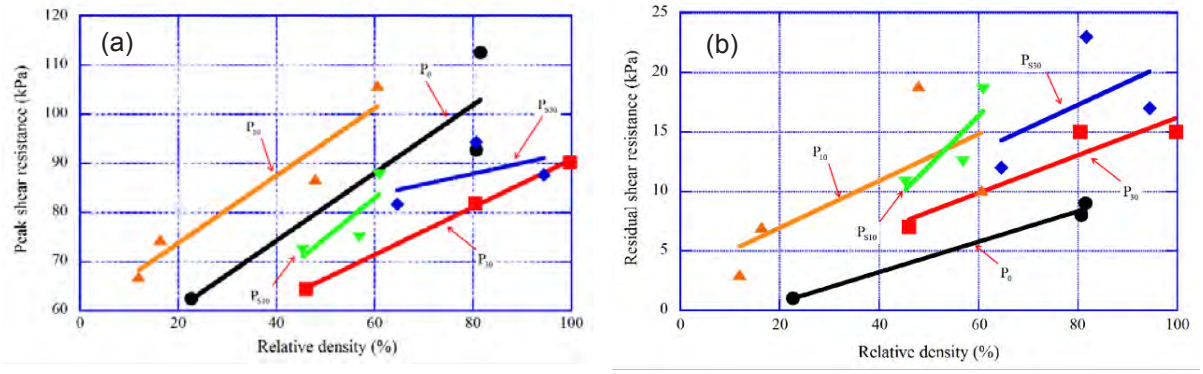

Figure 5. (a), (b): undrained peak and residual shear strengths against relative density, respectively.

Conclusions

Some conclusions could be drawn as follows.

- Halloysite was detected in the materials from the tephra layers forming the sliding surfaces for the landslides in Takanodai area, Minamiaso, Kumamoto, and the landslides in Atsuma, Hokkaido. The halloysite from Minamiaso was confirmed to be tubular by TEM images, while the halloysite from Atsuma shows the shape of platy and crumpled lamellar. The different shapes may result from different geological and hydrological environments.
- Introduction of halloysite to silica sand No. 8 elevate the water retention ability. Although the experimental data for the water retention capacity for the mixture of pumice with differing contents of halloysite are preliminary, it can be concluded that introduction of halloysite can affect the water retention capacity. This is supported by the water content of halloysite-rich tephra layers on the landslide areas.
- Adding halloysite to tephra material changes the peak shear resistance of the sample. Given the initial density being the same, it is found that as the halloysite content increases, the peak shear resistance decreases.
- Saturated tephra materials can suffer from liquefaction failure with very small residual shear resistance. This may be due to the fact that tephra materials have large void spaces and then pose high potential of negative dilatancy when subject to shearing. Adding fine materials of halloysite or silica powder may not greatly affect the final state where the residual shear strength was measured.

Finally, it is noted that the results presented in this abstract are mainly from the master thesis of Mr. Baichuan Liu (Liu BC, 2020). More references relating to this study can be found from this thesis. Great support from the authors' colleagues are sincerely appreciated.

References

Liu BC (2020) *Role of halloysite on the initiation and movement of coseismic landslides occurring on tephra slopes*. Master thesis, Graduate School of Science, Kyoto University, 80p.

Chigira M, Tajika J, Ishimaru S (2019) Landslides of pyroclastic fall deposits induced by the 2018 Eastern Iburi Earthquake with special reference to the weathering of pyroclastics. *DPRI Annuals* No. 62(B), 348- 356.

Moon V (2016) Halloysite behaving badly: geomechanics and slope behavior of halloysite-rich soils. *Clay Minerals* 51, 517-528.

Landslide Activity and Rock Mass Weathering in the High Himalaya of Bhutan

Larissa de Palézieux[1], Simon Loew[1,] Kerry Leith[2]

[1] Geological Institute, ETH Zurich, Switzerland, [2]GNS, Lower Hutt, New Zealand

SUMMARY: Landslide activity is controlled by predisposing factors, the rate of progressive rock strength reduction through time, modification of hillslope topography and triggering factors. While the exact nature of the interplay between episodes of landscape ageing or rejuvenation, progressive strength degradation and landslide formation can rarely be fully explained, the relative sequence between the different events can be constrained more reliably. We have reconstructed the sequence of geomorphic events in two large catchments in NW Bhutan and combined it with three landslide inventories and mapped outcrops classified with respect to the degree of rock mass weathering. We find the following chronology of events: 1) the most intensive Pleistocene weathering period created more than 10 m thick layers of regolith and saprolite on top of mafic gneisses, 2) these residual soils are incorporated into deposits of large rock slope failures covered by Holocene alluvial terrasses, 3) ongoing slow creep of large mountain or rock slope deformations frequently displacing river channels, and 4) shallow slope failures triggered by monsoonal rainstorms.
Keywords: landslide morphology, rock mass weathering, landscape evolution, landslide activity, Himalaya

Introduction

Bhutan is a landlocked country straddling the eastern Himalayas at altitudes ranging from 170 to 7600 m a.s.l.. Our study area in the NW of the country encompasses two large drainage basins (the Wang Valley in the East and the Punatshang Valley in the West) and can be further subdivided into three main geomorphic domains (Norbu et al., 2003; Fig. 1): The Inner Valleys (IV), situated in the South of the study area, are characterized by broad alluvial plains surrounded by a low relief landscape. At its upstream boundary this domain transitions into the Northern Valleys (NV), which are dominated by deeply incised, detachment-limited fluvial valleys. Topographic relief diminishes further North, where the landscape gives way to the glacially overprinted u-shaped valleys of the High Himalayan Plateau (HHP).

Despite being located in the tectonically active Himalayan arc, the tectonic and geologic setting of NW Bhutan are relatively homogeneous over large areas at the longitudes of our study (Long et al., 2011). In both drainage basins, the largest part of the topography is dominated by the predominantly metasedimentary units of Greater Himalayan Zone and the Paro formation (Neoproterozoic-Ordovician) and are composed of mafic gneisses and schists, which are intruded by deformed granitic orthogneisses in some locations. Much of the NV and the HHP in the Wang basin and two smaller regions in the HHP and the NV of the Punatshang basin are dominated by (meta-)sedimentary and paragneiss units of the Tethyan Himalayan Zone (Paleozoic-Eocene).

Throughout the study area but particularly within the mafic gneiss and schist units of the IV, weathering horizons of several tens of meters can be observed in the field, composed of mainly clay (kaolinite and illite) and silt. While the higher elevations have been glacially overprinted during the last glacial maximum, the topography below ca 3200 m a.s.l. shows no evidence of recent glacial erosion (Gansser, 1983). This absence of landscape rejuvenation allows for in-situ rock mass weathering to occur over long periods of time, with enhanced soil development

particularly occurring after the end of the Younger Dryas (Dorji et al., 2009), when with the end of the LGM, rates of precipitation and temperature increased to average values of 1000-1400 mm/yr and 10-15°C respectively (Fick and Hijmans, 2017).
With respect to landslide types, location, sizes, and activity, we use three landslide inventories, which were produced based on optical satellite images (907 landslides ranging from 5500 m^2 to 15 km^2; Dini et al., 2020), radar interferometry (639 features of a few thousand m^2 to 6 km^2; Dini et al., 2019b), and on time series analyses using SBAS (165 landslides ranging from 1500 m^2 to 0.2 km^2; Dini et al., 2019a).

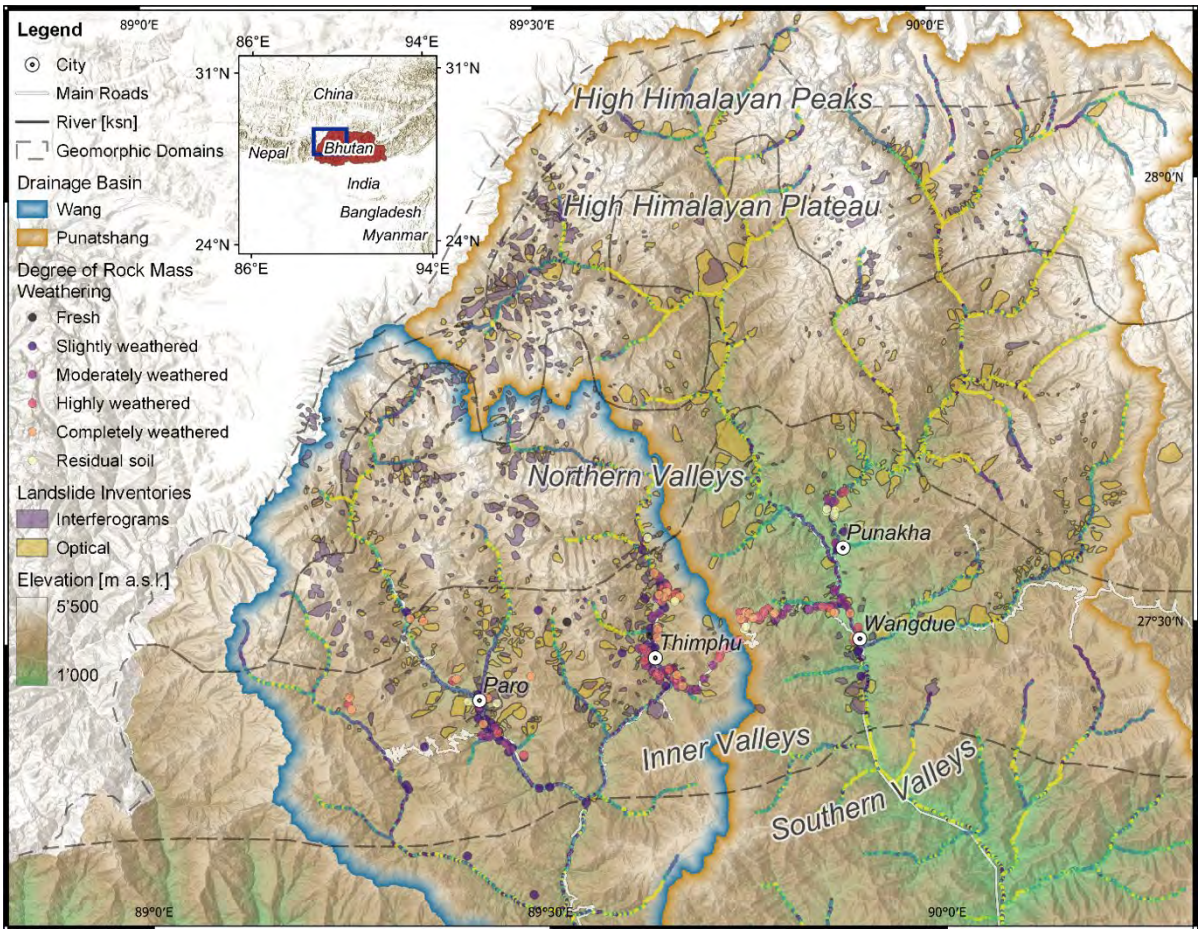

Figure 1 - Overview map of NW Bhutan with the two major drainage basins Wang Chhu and Punatshang Chhu, the geomorphic domains (Norbu et al., 2003), the inventory of mapped rock outcrops coloured by the degree of rock mass weathering, two landslide inventories based on optical and InSAR data respectively (Dini et al., 2020), and the river network coloured by steepness (k_{sn}).

Methods

As a result of recent road construction activity in these valleys - which can be constrained to the years 2013-2016 based on historical Google Earth images - many fresh rock and soil outcrops were easily accessible during three field campaigns between 2016 and 2019, allowing us to record 341 rock and 226 soil outcrops according to engineering geological standards. For 306 of the recorded rock outcrops, we determined the degree of rock mass weathering according to EN ISO 14689:2017 (2018). All rock outcrops for which a degree of weathering was recorded are located in the mafic gneiss-schists of the Paro Formation and the Greater Himalayan Zone (Long et al., 2011a). In addition to the rock and soil outcrops, we mapped morphological markers related to valley evolution (knickpoints, fluvial terraces, and moraine ridges) and slope instabilities (landslide phenomena and deposits) throughout the study area.

Results and Discussion

In both basins we observe deep weathering horizons reaching several tens of meters depth in numerous locations. The largest number of outcrops were classified as 'slightly weathered' (103 outcrops) or 'moderately weathered' (93 outcrops). 59 were classified as 'highly weathered', 34 as 'completely weathered', 12 as 'residual soil', and 5 outcrops were classified as 'fresh'. Comparing the recorded degree of rock mass weathering for outcrops situated within vs. outside of mapped landslides, we observe on average higher weathering grades in the outcrops within landslides. The largest difference in the two distributions is found in lower weathering grade classes, with 38% of all outcrops outside of landslides classified as 'slightly weathered' (with 22% within), while 46% of all outcrops mapped within landslides are classified as 'moderately weathered' (vs. 23% outside). At higher weathering grades ('highly weathered', 'completely weathered', and 'residual soil') the distribution is strikingly similar between outcrops within and outside of landslides and ranges from 17-20%, 9-11%, and 3-4% respectively.

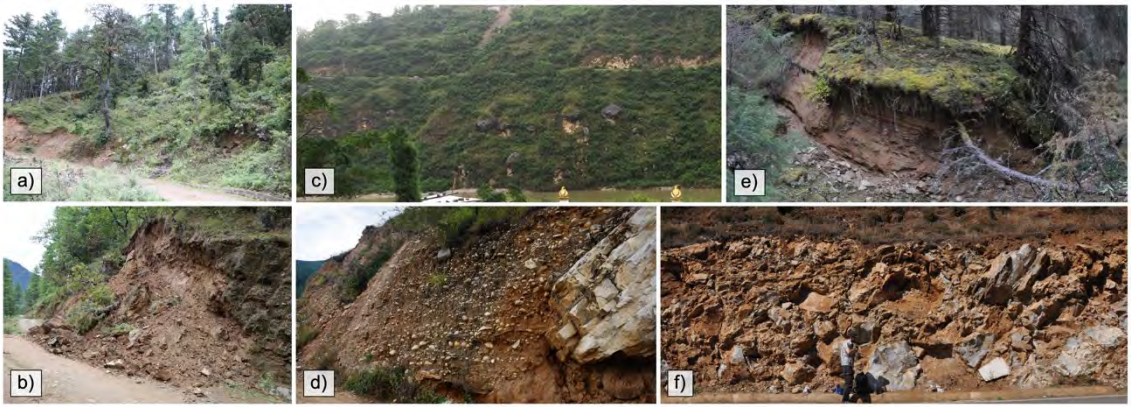

Figure 2 - Examples of degree of disintegration in landslides: a) Shallow, slow-moving landslide in (residual) soil; b) catastrophic failure of small landslide in (residual) soil; c) Fluvial deposits discordantly overlying a gravitationally displaced block; d) Large, sub-rounded boulders forming a discrete layer ca 15 m below ground surface. e) Non-catastrophic failure of a marble rock slope with soil lodged between the rotated blocks. f) Moderately weathered rock discontinuity surface exposed in a non-catastrophic, creeping landslide.

Throughout the study area, but particularly along newly constructed or widened road segments, we observe a large number of small (100-1000 m3) active landslides, which tend to form in highly weathered rock mass (Fig. 2a), residual soil (Fig. 2b), or reactivate preexisting colluvial deposits. They are typically triggered by a combination of anthropogenic activity (e.g., road cutting) and climatic events (i.e., heavy rainfall). It is rare to find traces of bigger landslides, which have failed catastrophically in recent times, i.e., since the main valleys have been infilled with alluvial sediments. Within the alluvial sediments, however, we find a small number of remnants of rock avalanche deposits of which typically only large, subrounded to rounded blocks and boulders are preserved, while the smaller grainsize fraction likely has been transported away post failure (Fig 2c). In addition to the catastrophically failed landslides, we find landslide bodies which have not failed catastrophically but which have been displaced (Fig. 2e) and distorted (Fig. 2f) close to their release area and in some locations are discordantly overlain by fluvial deposits of the main IV terrace (Fig. 2d). While the overall landslide composite is preserved, the sliding mass has often been strongly dissected into discrete blocks of slightly to moderately weathered rock, between which fine grained material previously located at ground surface (e.g., residual soil) has become entrapped forming the matrix of the landslide deposit. On top of the landslide mass, these deposits have only a shallow weathering layer of a few decimeters thickness. Present-day landslide activity of large landslides is most frequently observed for very slow moving (mm-cm/yr) mountain slope deformations, that can be detected using remote sensing techniques (Dini et al., 2020) or by river network analysis (de Palézieux, 2020).

Based on the observed degrees of rock mass weathering in the different landslide types in combination with their observed relative age relationships with morphological markers, we can outline a potential sequence of three major events between episodes of landscape evolution and landslide formation and activity: 1) The present-day rock surface beneath the alluvial infill represents a time of increased erosional efficiency, which can be due to increased runoff or lack of sediment to deposit or a combination of the two. Such a setting likely occurs during interglacial warm periods, where precipitation and temperature and consequently erosion rates typically reach relative highs driving bedrock incision. Hillslope topography can respond to the newly heightened relief with landsliding partially equilibrating the modified stress and strength distributions within the mountain slope. Where the rock mass strength resists this initial phase of re-equilibration, it can accumulate damage and fail progressively over long timescales forming large mountain or rock slope deformations. 2) During a following cold phase (e.g., LGM), temperatures and total precipitation will be reduced, leading to a reduction in erosion rates, while at the same time large amounts of sediment can be produced by paraglacial processes. During this phase, the low transport capacity of the river network can lead to an accumulation of river sediment in large alluvial terraces, potentially covering pre-existing landslide deposits or displaced landslides close to the river network. 3) These large alluvial infills will absorb much of the newly increased erosion rates of the following warm phase, leaving little erosional power for new bedrock incision. This effectively buffers the existing topography from additional drivers for new catastrophic landslide failures at pre-LGM scales. Nonetheless, with hillslopes having been in contact with climatic factors since their initial exposure prior to the LGM and no landscape rejuvenation occurring due to glacial erosion, the front of rock mass weathering had ample time to propagate into the rock mass, producing deep layers of weathered rock and regolith. While monsoonal precipitation and anthropogenic road cuts regularly trigger shallow slope failures in these strongly weathered bedrock and residual soils (Fig. 2b), catastrophic failure of large and deep slope failures would require massive triggers such as strong earthquakes or rare typhoons, neither of which have occurred in the study area since the 19th century.

References

Dini, B., Aaron, J., Manconi, A., De Palezieux, L., Leith, K., & Loew, S. (2020). Regional-scale investigation of preconditioning factors of rock slope instabilities in NW Bhutan. Journal of Geophysical Research: Earth Surface, 125(9), e2019JF005404.

Dini, B., Daout, S., Manconi, A., & Loew, S. (2019a). Classification of slope processes based on multitemporal DInSAR analyses in the Himalaya of NW Bhutan. Remote Sensing of Environment, 233(May), 111408. https://doi.org/10.1016/j.rse.2019.111408

Dini, B., Manconi, A., & Loew, S. (2019b). Investigation of slope instabilities in NW Bhutan as derived from systematic DInSAR analyses. Engineering Geology, 259(April), 105111. https://doi.org/10.1016/j.enggeo.2019.04.008

Dorji, T., Caspari, T., Bäumler, R., Veldkamp, A., Jongmans, A., Tshering, K., Dorji, T., & Baillie, I. C. (2009). Soil development on Late Quaternary river terraces in a high montane valley in Bhutan, Eastern Himalayas. Catena, 78(1), 48–59. https://doi.org/10.1016/j.catena.2009.02.018

Fick, S. E., & Hijmans, R. J. (2017). Worldclim 2: New 1-km spatial resolution climate surfaces for global land areas. International Journal of Climatology.

Gansser, A. (1983). Geology of the Bhutan Himalaya. Endeavour, 8(2), 106. https://doi.org/10.1016/0160-9327(84)90075-9

Hungr, O., Leroueil, S., & Picarelli, L. (2014). The Varnes classification of landslide types, an update. Landslides, 11(2), 167–194. https://doi.org/10.1007/s10346-013-0436-y

EN ISO 14689:2018. (2018). Geotechnical investigation and testing Identification, description and classification of rock (ISO 14689:2017); English version EN ISO 14689:2018. DIN Deutsches Institut für Normung e. V.

Long, S., McQuarrie, N., Tobgay, T., Grujic, D., & Hollister, L. (2011). Geologic Map of Bhutan. Journal of Maps, 7(1), 184–192. https://doi.org/10.4113/jom.2011.1159

Norbu, C., Baillie, I. C., Dorji, T., Dorj, T., Tamang, H. B., Tshering, K., & Hutcheon, A. A. (2003). A provisional physiographic zonation of Bhutan. Journal of Bhutan Studies, 54–87.

An update of the slow Gascons rockslide kinematics

Catherine Cloutier[1], Jacques Locat[2], François Bossé[1]

[1] Ministère des Transports et de la Mobilité durable, Québec, Canada
[2] Université Laval, Québec, Canada

SUMMARY: The Gascons rockslide is a slow active rockslide of 410,000 m³ in Québec, Canada. The first known engineering document describing the rockslide dates back from 1980. In 2009, an extensive study, including the installation of a sophisticated monitoring system, characterized the geometry and displacement of the rockslide, revealing its complexity. Automatic instruments stopped working in 2016, but monitoring of displacements with manual reading instruments was continued, and since 2021, GNSS and in inclinometers were installed. A sector, that was recognised as being more prone to rapid failure is accelerating.

Keywords: active, slow, rockslide, monitoring

Introduction

From displacement monitoring carried from 2009 to 2013 (Cloutier 2014, and Cloutier et al. 2015 and 2016), the Gascons rockslide was characterized as a very slow active rockslide (Cruden and Varnes, 1996). It was shown that the rockslide accelerates in late Fall and slows down in May; summer being its slowest season. Even though there was intra and inter-annual variations in displacement rates, prior to 2013 the slide was considered in a phase of constant displacement, in opposition to accelerating or slowing down (Crosta and Aligardin 2003).

A railroad runs across the rockslide over a 200 m distance. Traffic on the railroad stopped in 2012 for economic reasons. Afterwards, the monitoring of the rockslide was continued but the system was not maintained, and instruments ceased working gradually. The automatic monitoring system stopped working completely in 2016 and was not repaired. Only manual instruments (one inclinometer and rods measured with a Convex Ealy tape) remained functional, and measurements were taken about once a year. In 2021, four new traditional inclinometers and a GNSS network comprised of 8 antennas located inside the rockslide and two base stations located outside the rockslide were put in place. In 2023, an automatic inclinometer (SAA, Measurand) was installed.

We briefly present an update of the Gascons rockslide kinematics, which was described by Cloutier et al. (2015). Firstly, the geometric model of the rockslide is recalled, and new data are used to refine and confirm some of the previous hypotheses. Secondly, the potential evolution scenarios developed by Cloutier (2014) to conduct a risk analysis are discussed based on additional data collected between 2013 and 2023.

Geometry of the rockslide

The slide is an asymmetrical wedge failure of 410,000 m³ (Fig.1), in rocks consisting of centimetre scale beds of nodular calcilutite alternating with sandstone and limestone. The displacement analysis revealed the complex blocky geometry of the slide, with displacement rates and directions varying over the slide area and through time. Four specific kinematic

sectors were recognized: the main slide, the Petit-Massif, the East-Centre and Block-E (Fig. 1). The last three are part of the main slide. Failure surfaces follow the bedding.

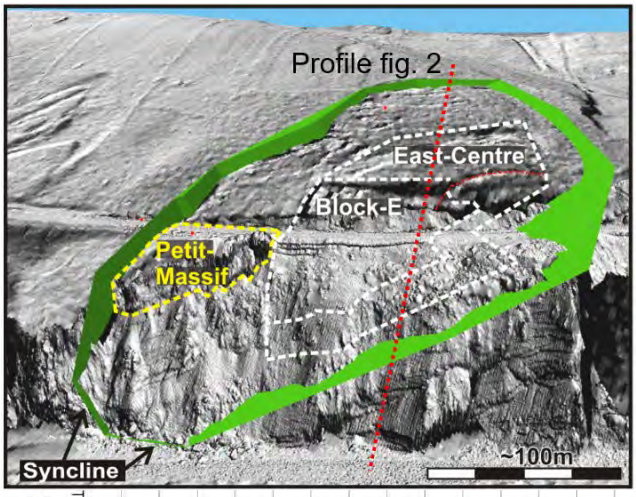

The deepest failure surface delimits the main slide and was confirmed in 2011 at two points by inclinometers. New inclinometers installed in 2021 and 2023 confirmed its location at two other points which validates the 2011 interpretation of the failure surface. It is represented by the green failure surface shown in Figure 1, and the deepest failure surface in Figure 2.

Figure 1. Main slide's failure surface (green) and locations of sectors (from Cloutier et al. 2015)

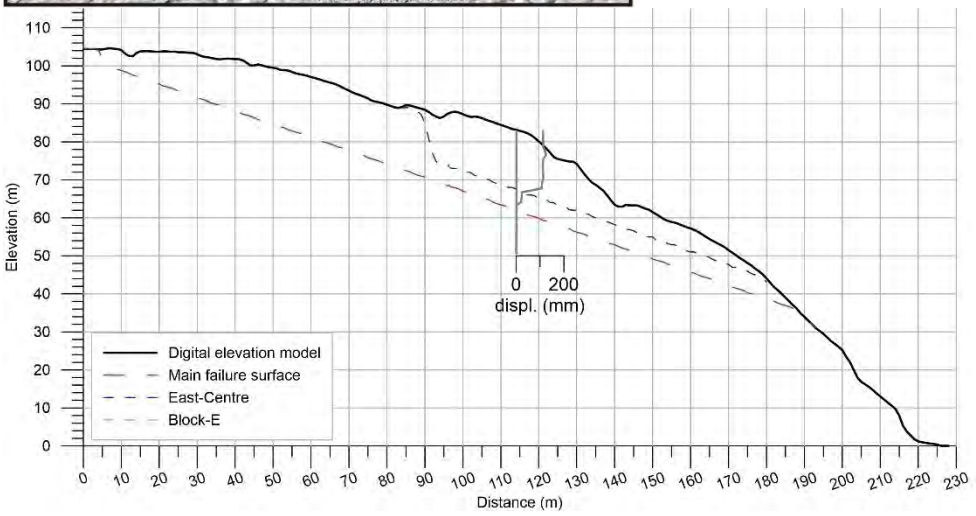

Figure 2. Failure surfaces interpreted by Cloutier et al. (2015) and 2023 SAA-inclinometer data (approximate location of the profile is shown in Fig. 1)

The western limit of the rockslide has always been clearly defined because it consists of a near-vertical fracture of one to two meters wide. The eastern limit was based on less evidence. Since 2014, that the railroad alignment is not corrected, and its deformation helps to locate the eastern end of the failure (Fig. 3B). The decommissioned railroad and the retaining walls show large deformation (Fig. 3A and C). No sign of retrogression (enlargement) of the rockslide were observed during recent years.

The depths of the Block-E and East-Centre failure surfaces were not previously confirmed by inclinometer data. In 2023, the East-Centre failure surface depth was characterized by a new inclinometer (SAA, Measurand), which fits very well with the hypothesis (Fig. 2).

Potential Evolution Scenarios

Evolution scenarios of the rockslide were developed to evaluate the risk and probability of failure. The most probable scenario is an acceleration and failure of part of the Petit-Massif, as a similar failure at this location in 1998. Displacement was quantified in 1993 by measuring the distance between rods installed on each side of fissures delineating a bloc. These measurements represent the opening rate of the tension crack four years prior to its failure in 1998, which is 86 mm/yr (Fig. 4). The data are extrapolated to the day of the failure (Fig. 4), considering a constant rate of opening.

The other curves on Figure 4 are displacement computed from distances measured between rods, and thus representing the opening of tension cracks from 2009 to 2023. These measurements are equivalent to the 1993 ones and can be compared directly. In the Petit-Massif, the opening of a fracture is accelerating since 2017 (Fig. 4). From 2009 to 2014, the mean displacement rate was 15 mm/yr and from 2020 to 2023 it was 65 mm/yr. In 2023, it increased to 91 mm/yr.

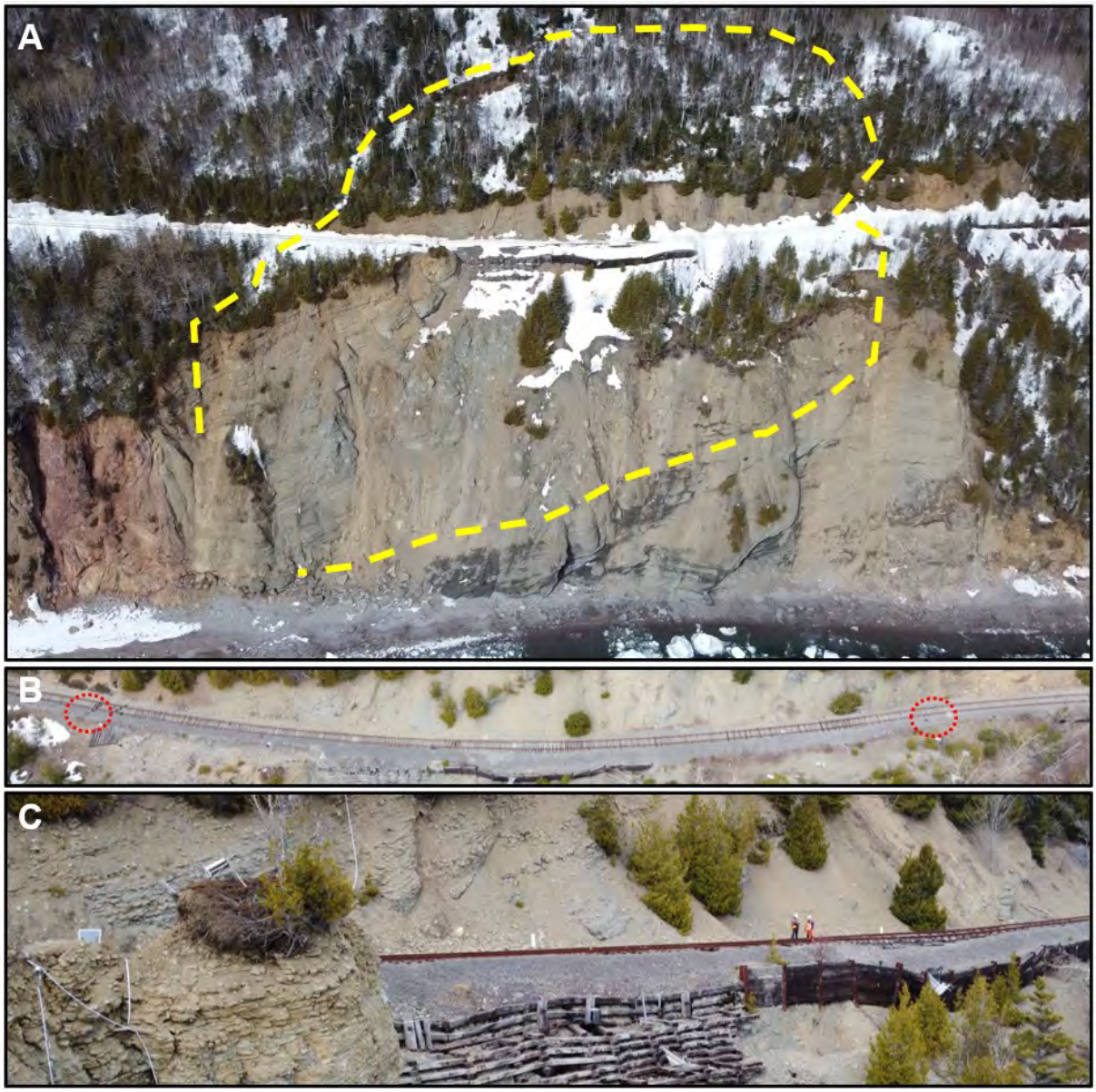

Figure 3. A) Yellow dashed line shows the extent of the rockslide B) Red circles show features on the track that identify the boudaries of the rockslide C) Deformation of the track and retaining walls.

We do not have data to know how the displacement rate evolved from 1994 to the 1998 failure, but it probably accelerated, and the final rate was faster than 86 mm/yr. The actual rate measured is now similar than it was 1993. It will probably keep accelerating, with some periods of constant speed until it reaches its final acceleration and failure. The plot of the inverse velocity versus time (Rose and Hungr 2007) is not a straight line (Fig. 4), but different extrapolations indicate that failure could occurred in about two years. Other signs in the field, such as new fractures opening, suggest that this scenario is the most probable.

PTA-InSAR monitoring indicated that the Block-E and East-Center were moving at an average rate of 110 mm/yr from 2010 to 2013. Inclinometers and GNSS installed recently measured rates from 97 to 176 mm/yr, which might indicate a tendency to acceleration, but could also be interannual variations.

Based on measured displacements, an acceleration of the main slide, leading to a catastrophic failure is very unlikely. However, some measurements are showing a slight increase in yearly cumulated displacements, since 2017. For example, the displacement rates at the back tension crack were 13 mm/yr and 7 mm/yr from 2010 to 2014 and are 18 and 12 mm/yr from 2022 to 2023 (Fig. 4). However, an inclinometer located near the back tension crack measures rates very similar to the 50mm/yr measured from 2009 to 2011. The main slide is still considered to be moving constantly.

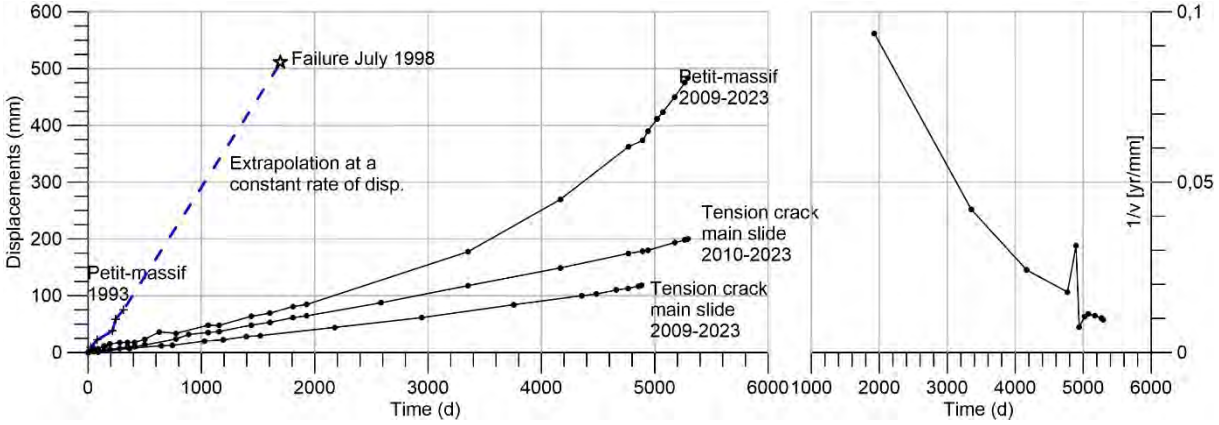

Figure 4. Displacement and inverse velocity versus time of selected measurements.

Conclusion

The monitoring using simple technology and manual readings allowed to keep track of the rockslide kinematics without important investments, as all electronic and real time instruments stop working through the years. New inclinometers installed in 2021 and 2023 were useful to validate the location of an intermediate failure surface. In the next years, it will allow to increase the understanding of the kinematic of the sector named the East-Centre.

References

Cloutier C (2014) *Évaluation du comportement cinétique et du risque associé aux glissements de terrain rocheux actifs à l'aide de mesures de surveillance : le cas du glissement de Gascons, Gaspésie, Canada*, Thèse de doctorat, Université Laval, 325p.

Cloutier C, Locat J, Charbonneau F & Couture R (2015) Understanding the kinematic behavior of the active Gascons rockslide from in-situ and satellite monitoring data. *Engineering Geology* 195, 1-15.

Cloutier C, Locat J, Couture R & Jaboyedoff M (2016) The anatomy of an active slide: the Gascons rockslide, Québec, Canada. *Landslides* 13, 241–258.

Crosta GB & Agliardi F (2003) Failure forecast for large rock slides by surface displacement measurements. *Canadian Geotechnical Journal*. 40(1), 176-191.

Cruden DM & Varnes DJ (1996) Landslide types and processes, in A. K. Turner et R. L. Schuster, (eds.), *Landslides : Investigation and mitigation Transportation Research Board Special Report 247*. Washington, D.C.: National Academy Press, pp. 36-71.

Rose ND, Hungr O (2007) *Forecasting potential rock slope failure in open pit mines using the inverse-velocity method*. Int. J. Rock Mech. Min. Sci. 44(2), 308–320.

Large Deformation Finite Element Modeling of Strain Softening Clay Slopes

Cletus C. Blum[1], J. DiBiagio[1], Hans Petter Jostad[1], Håkon Heyerdahl[1], Olivier Galland[2]

[1] Norwegian Geotechnical Institute, Oslo, Norway
[2] University of Oslo, Oslo, Norway

SUMMARY: Large scale landslides in quick and sensitive clays often exhibit retrogressive failure, sometimes with catastrophic consequences, such as in the Norwegian 2020 Gjerdrum landslide. Modeling retrogressive slope failure using traditional modeling techniques presents challenges due to problems arising with large deformation and the strain softening nature of sensitive and quick clays. The coupled Eulerian-Lagrangian (CEL) finite element (FE) modeling technique addresses many of these shortcomings. Simulation results of the Gjerdrum landslide show failure patterns recognized in quick and sensitive clay landslides.

Keywords: finite element analysis, retrogressive landslides, quick clay, Abaqus

Introduction

Sensitive and quick clays are known for their complex behavior such as strain-softening and retrogressive failure patterns, complicating traditional modeling methods. Due to the strain softening properties of quick clay, traditional methods for assessing slope stability have significant shortcomings when analyzing slopes where retrogressive failure occurs. Finite element (FE) methods using a purely Lagrangian framework can be quite good at modeling the initiation but struggle to handle large deformation as a landslide mobilizes. Recent studies have explored many applications of the coupled Eulerian-Lagrangian (CEL) finite element approach to large deformation problems involving sensitive soils. With CEL simulations allowing material to flow through the finite element mesh, large mesh deformation is avoided. Studies investigating sensitive clay landslides (Dey et al., 2014, 2015; Saha et al., 2022; Wang & Hawlader, 2017; Wang et al., 2016; Wang et al., 2022; Wang et al., 2015) using the CEL FE approach provide a foundation for implementation in the commercially available finite element software Abaqus.

The Gjerdrum 2020 quick clay landslide occurred on December 30, 2020, in the village of Ask in Gjerdrum, Norway. Ask is approximately 25 km northeast of Oslo, with a population of under 7000 people. The landslide occurred in multiple phases with erosion from a stream assumed to have caused the initial failure (Ekspertutvalg, 2021).

Abaqus Implementation

The following method uses Abaqus/Explicit commercial finite element program for all analyses without the need for coding additional subroutines. The main challenge relates to implementing the variation of undrained shear strength, S_u, with depth and accumulated plastic shear strain. For CEL simulations the slope must be modeled as one part, portioned into multiple sections. Each section can be assigned a material or void space. This allows material to move within the model. In Abaqus/Explicit, the Eulerian approach is only available for three-dimensional elements. The simulations performed here are therefore only one element length in the out-of-

plane direction to simulate 2-dimensional plane strain conditions. Following previous studies (Dey et al., 2015; Saha et al., 2022; Wang et al., 2016), an 0.5 meter element thickness is used in all simulations.

All soil layers (materials) are assigned a density, elastic parameter, and plastic parameters. material behaviors assigned to all layers give a density of 1900 $^{kg}/_{m^2}$, Youngs modulus of $5e6\ Pa$ and Poisons ratio of 0.495. The Mohr-Coulomb plasticity criterion is used for all simulations presented here. The crust is given a friction angle of 30° and a dilation angle of 0.1°, with no cohesion. For clay and quick clay materials, plasticity is modeled with zero angle of friction and 0.1° dilation, varying cohesion as the primary parameter. The Tresca criterion can be implemented by using the Morh-Columb model with no friction angle. The variation of yield strength ($= 2s_2$ in Abaqus FE analysis) is defined as a function of plastic strain, calculated assuming the shear band thickness is equal to the element thickness. The strain softening curves implemented for clay and quick clay materials are based on triaxial tests from borehole samples. An average of active, direct and passive shear strength is used as the isotropic shear strength of each element (isotropic shear strength = 0.66 active).

If the gravitational load is applied instantaneously to the model, the elastic material parameters produce an artificial bouncing effect in the model. This effect can be minimized by adding the gravitational load over a period of 100 seconds. The relative stability of the slope is indicated if plastic strains occur before 100% of the gravitational load has been applied. After gravity has been applied (over a step time of 100 seconds), a runout step (200 seconds) allows retrogressive failures to occur. The soil is modeled as Eulerian material using EC3D8R elements, which are 8-noded linear brick, reduced integration elements with hourglass control. A finer mesh 0.5 m mesh is used where the slip surface is expected to occur, increasing to a maximum of 5 x 5 m.

Profile Geometry

Slope geometry, Figure 1, is estimated from geotechnical reports (Multiconsult, 2021; NGI, 2021) with uncertainties, as limited data is available from before the landslide. A quick clay layer lies between two clay layers with a thin 2 meter crust layer on top. A portion of the crust at the base of the slope is removed to simulate the initial erosion of the toe failure.

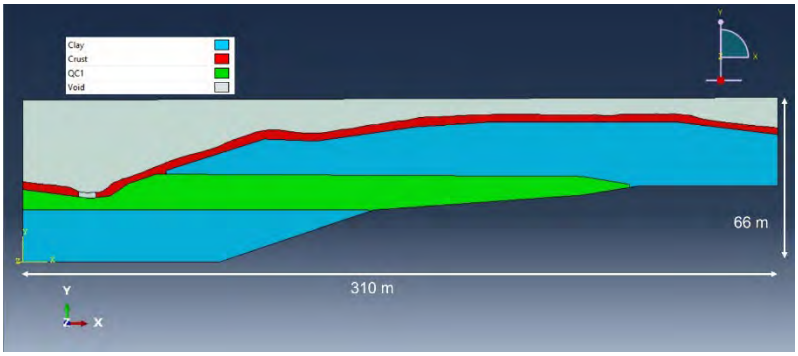

Figure 1: Profile geometry, with a quick clay layer between clay layers.

Results

Plastic strain is shown in Abaqus using the output variable PEVAVG: Plastic strain components arecomputed as a volume fraction weighted average of all materials in the element. The first failure plane in the Profile_1_CPTU simulation can be seen clearly 62 seconds into the add gravity step Figure 2(a), with the first retrogressive failure plane seen 90 seconds into the add gravity step Figure 2(b). The second retrogressive failure plane occurs 6 seconds into the runout step, Figure 2(c). The shear band in the first retrogressive failure primarily propagates along

the boundary between the clay and quick clay interface dipping into the bottom clay layer briefly. The second retrogressive failure propagates along the top boundary of the quick clay boundary before transitioning into a circular slope failure. A compound slip failure can be seen from the elemental velocities of the initial failure in Figure 3.

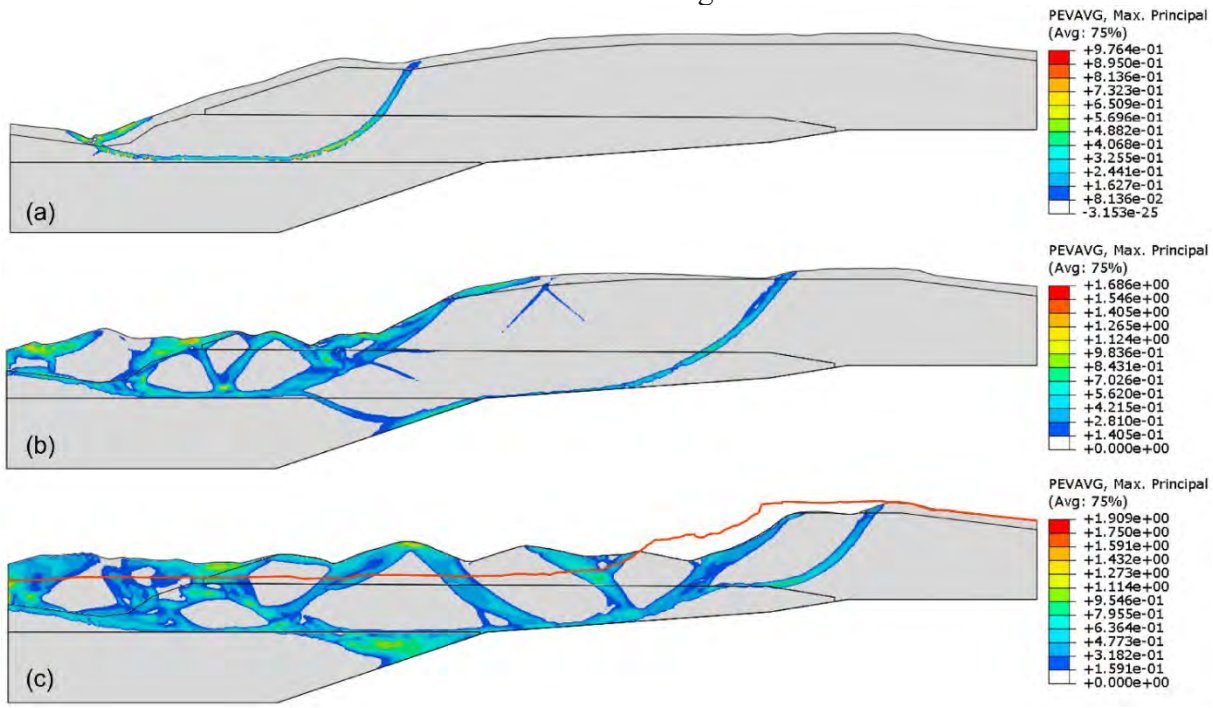

Figure 2: Failure surfaces shown using elemental strain component (PEVAVG). The initial failure plane (a) can be seen at 62 seconds into the add gravity step, the first retrogressive failure (b) can be seen at 90 seconds into the add gravity step and the second retrogressive failure (c) can be 6 seconds into the runout step. The post slide surface elevation is shown in red in (c)

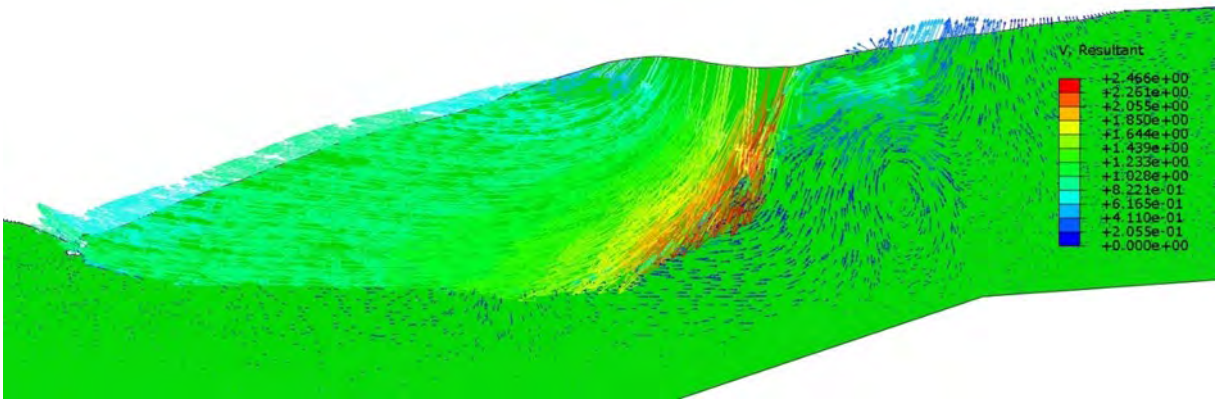

Figure 3: Velocity vectors showing resultant element velocity ($^{m}/_{s}$) during the initial failure, 62 seconds into the add gravity step.

Failure is observed 62 seconds into the add gravity step, suggesting the factor of safety is much less than 1. Although the shear band propagates through where the crust is removed at the base of the slope, this local instability is not seen to cause the larger initial failure. It is also worth noting the erosion material from the initial failure had stopped flowing before the first retrogressive failure. The first retrogressive failure, observed at 90 seconds can be attributed to an increase in gravity, in a slope with a new geometry. The failure progression shown in Figure 2 could be seen as a combination of a flowslide and a spread, with the intact blocks sliding along a horizontal shear band with successive curved failure surfaces. Elemental velocities shown in Figure 3 of the initial failure support a combination of a flowslide and spread, showing

a non-circular movement not necessarily as angular as would be expected in a spread. Since much of the shear band is on the bottom boundary of the model or on a layer contact, an outsized influence from the boundary conditions is suspected.

Conclusions

The simulation shows an unstable slope, failing before 62 percent of gravity has been applied. This is likely due to variations of shear strength with depth in the layer and brittleness of the clay. With the failure not being triggered by the removal of a section of soil at the toe of the slope, more calibrating of the soil parameters is necessary to ensure the slope stable before any erosion should be introduced. Simulations of the Gjerdrum landslide showed failure mechanics consistent with sensitive and quick clay landslides, although correlation to post slide investigations is relatively poor. Further calibration should be undertaken before the stability can be clearly evaluated and for simulations to more accurately represent failure conditions.

References

Dey, R., Hawlader, B., Phillips, R. and Soga, K., 2014. Stability analysis of a river bank slope with an existing shear band. In *6th Canadian GeoHazards Conf* .

Dey, R., Hawlader, B., Phillips, R., & Soga, K. (2015). Large deformation finite-element modelling of progressive failure leading to spread in sensitive clay slopes. *Géotechnique*, *65*(8), 657-668.

Ekspertutvalg. (2021). *Årsakene til kvikkleireskredet.*

Multiconsult. (2021). Datarapport – *Geotekniske grunnundersøkelser.*

NGI. (2021). *Grunnundersøkelser - Datarapport*.

Saha, P., Karmaker, R. and Hawlader, B., 2023. *Effects of undrained shear strength profile on retrogressive landslides in sensitive clays* (Doctoral dissertation, Memorial University of Newfoundland).

Wang, C., Saha, B., & Hawlader, B. (2015). Some factors affecting retrogressive failure of sensitive clay slopes using large deformation finite element modeling. Proceedings of the 68th *Canadian Geotechnical Conference and the 7th Canadian Permafrost Conference*, Quebec City, Canada,

Wang, C., Hawlader, B. and Perret, D., 2016. Finite element simulation of the 2010 Saint-Jude landslide in Quebec. In *Proceedings of the 69th Canadian Geotechnical Conference* .

Wang, C., & Hawlader, B. (2017). Numerical modeling of three types of sensitive clay slope failures. *Proceedings of the 19th International Conference on Soil Mechanics and Geotechnical Engineering*, ICSMGE, Soeul,

Wang, C., Hawlader, B., Perret, D., & Soga, K. (2022). Effects of geometry and soil properties on type and retrogression of landslides in sensitive clays. *Géotechnique*, 72(4), 322-336. https://doi.org/10.1680/jgeot.20.P.046

Using 3D lidar data to assess risks from rock cuts on transport infrastructure : geometric indicators proposal

Azemard Pierre[1], Chanut Marie-Aurélie[2], Fargier Yannick [3]

[1] Cerema, Team Géocod, Aix-en-Provence, France
[2] Cerema, Team GéoCoD, Bron, France
[3]Université Gustave Eiffel, Campus de Bron, France

SUMMARY: Recent developments in mobile laser scanner (MLS) technology provide access to high-resolution 3D point clouds of the environment. For the implementation of methods for assessing the risk of rockfall on infrastructure, these data provide access, on a virtual medium, to numerous parameters required to characterize the potentiality (probability) of a fall, its intensity (volume), but also the potential for damage to the pavement. Because of the high resolution and wide spatial coverage, methodological adaptations are required to go beyond the usual approach, based on the selection of a representative sample per homogeneous zone, and exploit the data available on the entire slope surface. Given the objective of prioritizing large linear systems, global approaches are preferred, which should make it possible to limit calculation times.

Keywords: Rockfall Hazard Assessment, Mobile Laser Scanner, transportation corridor, 3D point cloud, geometric indicators

Introduction

Linear transport infrastructures are crucial to the modern economy. Particularly in mountainous regions, they are subject to natural hazards that affect:

- their functional capacity (level of service / availability / interruption),
- their physical structure (damage to the infrastructure itself),
- or directly to users (damage to vehicles / injuries / deaths).

Among natural phenomena, rockfalls have the particularity of propagating at very high speeds, resulting in a much greater potential for damage, injury or death than other types of ground movement, even those of greater extent (Hoek, Evert, 2023; Pantelidis, 2009)
Methods for prioritizing the risk of rockfall along transport infrastructures were developed from the 1970s-80s, with the LPC n°80 guide in France (Méneroud and Olivier, 1978) and the studies leading to the Rockfall Hazard Rating System (RHRS) in the United States (Pierson, 1991). RHRS and its derivatives are proactive tools for rationally assessing the rockfall hazard along road rather than simply reacting to rockfall accidents (Pierson, 1991).
These methods and their many derivatives are essentially based on the segmentation of the road into homogeneous zones, followed by the selection of a representative site on which a generally qualitative assessment (descriptive classes) and scoring is carried out. The parameters determining stability can be grouped into topography, discontinuities, vegetation, hydrology, morphological indices, existence of protection. Parameters relating to user exposure are linked to traffic intensity, visibility distance, etc. The combination of these scores gives an overall indicator, generally quantified, of the exposure to risk of vehicles using the roads.
In parallel, mobile laser scanner technology has made remarkable progress, giving us access to extremely detailed 3D point clouds. In order to implement rockfall risk assessment methods for infrastructure based on these 3D point clouds, these data can provide essential information,

encompassing not only the probability of a rockfall event but also its potential volume and the anticipated damage it could inflict on the road. Some authors (Reich, 2021) have recently proposed that the measurements used in RHRS should be performed mainly on the digital model (3D point cloud).
But the 3D cloud holds a greater wealth of information than that used in the RHRS because of the high resolution and wide spatial coverage of these 3D data. We can hope to go beyond the usual approach, based on the selection of a representative sample per homogeneous zone, and exploit the data available on the entire surface of the rock slope. Methodological developments are then required to identify relevant indicators that can be calculated, and to combine them in the best possible way.
In the first section of this document, we will introduce the material and the data used for evaluating our methodology. Subsequently, new geometrical indicators will be presented and evaluated. Finally, we will discuss and draw conclusions from this research work.

Available data and point cloud construction

The Trimble MX9 mobile scanner used in this project consists of a positioning system (GNSS and IMU), a 360° camera (ladybug), three fixed cameras and two rotating lasers arranged in a butterfly pattern on the back of a vehicle. Technical data is provided in the manufacturer's technical documentation (Trimble, 2022). These lasers enable multi-echo measurement of range, measurement angle, return intensity, target reflectance and return deviation, as well as time stamping (GPS time) and device attitude (IMU). GNSS and IMU data, acquired at a frequency of 10 Hz, combined with filters for return intensity, divergence, range and intensity, are used by Trimble Business Center software to generate the 3D point cloud, colored according to the 360° camera images. This type of measurement produces very dense 3D points cloud of 362 million points for a campaign 5.2 km long. Each laser produces a series of lines of dots, the spacing between which depends on vehicle speed and laser rotation speed; the distance between dots also depends on the laser acquisition frequency and distance. In the example shown in Figure 1 (slope 25 m from scanner), the line spacing is 16 cm, with 326 mm between 10 points on the line. The uncertainty in the coordinates of each point is mainly due to the uncertainty of the IMU and GNSS; approximately 2 cm in the example in figure 1.

Figure 1. Left 3D point cloud of A75 motorway (France); Right measurements frame on a slope at 25 m (32,6 mm between points)

Proposal of geometric indicators

In this paper, we propose to develop a method for processing point clouds, enabling the calculation of useful indicators in a RHRS-type approach.

The 3D point clouds need to be pre-processed before the geometric indicators can be computed. The first step is to semantically classify the cloud (vegetation, buildings, pavement, road signs, etc.) to remove non slope points. The remaining points are then grouped into elementary units so that we can quickly work on the smaller clouds for each slope zone.

Then, indicators related to potential instabilities, as defined by Dunham et al.(2017) or Reich (2021) for example, can be calculated on the 3D model at various spatial scales. Among these indicators, the following should be considered in particular:

- Geometric irregularity of the slope is indicative of ancient falls, which can be assimilated to roughness at various scales up to the dimension of the slope. Roughness value is equal to the distance between the point and the best fitting plane computed on its nearest neighbors. An example of the results is shown in figure 2-a, with a calculation based on a radius of 50 cm.
- The presence of overhangs, which are particularly fragile areas, is characterized by normal pointing downward. The normal orientation is calculated as the normal of the best fit plane in the neighborhood. The calculations of the figure 2b are carried with a neighborhood defined by a 50 cm radius.
- Identification of faces and edges, which characterize the fracturing of the rock mass and for which numerous calculation methods have been proposed (Daghigh et al., 2022). They are often based on local curvature analyses followed by clustering procedures. However, indicators that are simpler to calculate are also being considered. Figure 2c shows a curvature calculation (on the basis of a best quadric fit in a neighborhood) on a 30 cm radius, which locates the edges quite correctly.

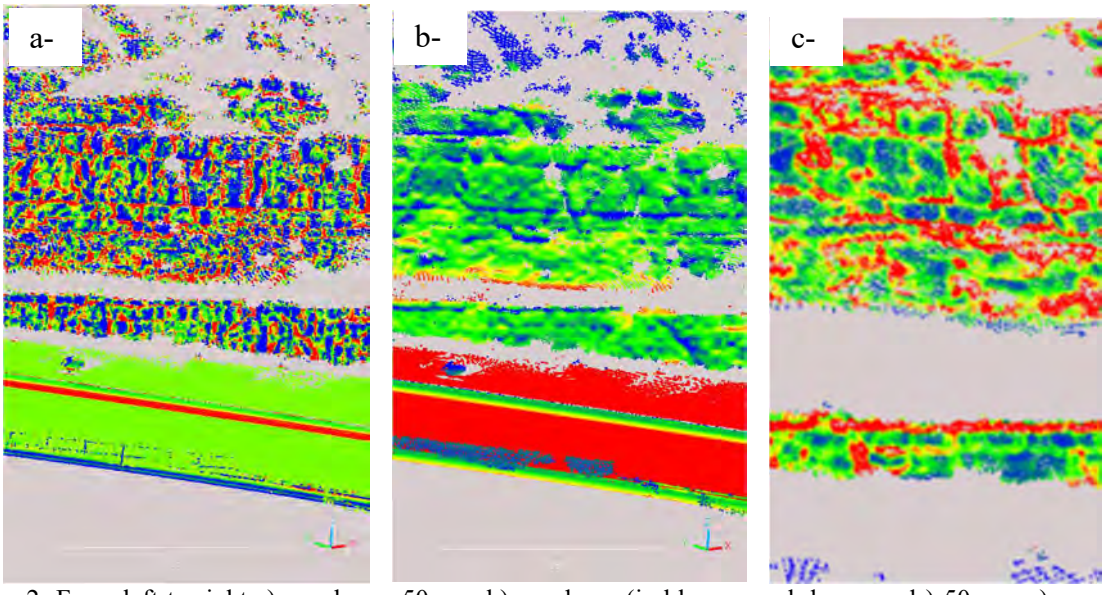

Figure 2: From left to right a) roughness 50 cm; b) overhang (in blue normal downwards) 50 cm, c) curvature 30 cm

Discussion and conclusion

3D point clouds acquired by mobile laser scanners potentially offer a richer processing capability than current analysis, with a more objective and repeatable approach and greater repeatability of results and objectivity. The use of a terrestrial laser scanner (TLS) provides better resolution and precision of the points coordinates in the cloud than MLS but does not have the advantage of the high acquisition speed of a mobile scanner, which is useful for corridor analysis. Several indicators have been proposed but could be developed further.
Regarding the indicators finally selected, the choice should be made in favor of a global approach rather than a more detailed analysis that would take longer to calculate in an automated process. For example, for faces and edges, a multi-scale approach based on the cloud's eigenvalues (linearity/planarity) should be tested, without trying to locate the edges as done by Zhang et al. (2020).
For all the proposed indicators, the dependence on the spatial scale of calculation is significant. One of our objectives will therefore be to determine the optimum scales for MLS data which can be different of the best settings for the terrestrial laser scanner data.

Finally, various calculation strategies are envisaged: either working at the scale of a slope as a whole to define the indicator by characteristics values or calculating the value of the indicator on the scale of a slice a few meters large and then aggregating on the scale of the slope, possibly segmenting it into homogeneous sub-zones.

References

Daghigh, H., Tannant, D.D., Daghigh, V., Lichti, D.D., Lindenbergh, R., 2022. A critical review of discontinuity plane extraction from 3D point cloud data of rock mass surfaces. Computers & Geosciences 169, 105241. https://doi.org/10.1016/j.cageo.2022.105241

Dunham, L., Wartman, J., Olsen, M.J., O'Banion, M., Cunningham, K., 2017. Rockfall Activity Index (RAI): A lidar-derived, morphology-based method for hazard assessment. Engineering Geology 221, 184–192. https://doi.org/10.1016/j.enggeo.2017.03.009

Hoek, Evert, 2023. Chapter-20-Analysis-of-Rockfall-Hazards, in: Practical-Rock-Engineering, Hoek's Corner. Rocscience.

Méneroud, J., Olivier, G., 1978. Eboulements et chutes de pierres sur les routes. Méthode de cartographie. (No. LPC n°80), Rapport de recherche LPC. Laboratoire Central des Ponts et Chaussées.

Pantelidis, L., 2009. Rock slope stability assessment through rock mass classification systems. International Journal of Rock Mechanics and Mining Sciences 46, 315–325. https://doi.org/10.1016/j.ijrmms.2008.06.003

Pierson, L.A., 1991. The Rockfall Hazard Rating Sytem (No. FHWA-OR-GT-92-05). Federal Highway Administration.

Reich, K.R., 2021. The Application of Structure from Motion Photogrammetry to the Ontario Rockfall Hazard Rating System (RHRON). Queen's University Kingston, Ontario, Canada.

Trimble, 2022. Trimble MX9 Mobile mapping solution Datasheet. https://trl.trimble.com/docushare/dsweb/Get/Document-868984

Zhang, K., Wu, W., Zhu, H., Zhang, L., Li, X., Zhang, H., 2020. A modified method of discontinuity trace mapping using three-dimensional point clouds of rock mass surfaces. Journal of Rock Mechanics and Geotechnical Engineering 12, 571–586. https://doi.org/10.1016/j.jrmge.2019.10.006

Fluid-Like Behaviour of Crushed Rock Flows

Wei Hu[1], Qiang Xu[1], Mauri McSaveney[1,2]

[1] State Key Laboratory of Geo-Hazard Prevention and Geo-Environment Protection, Chengdu University of Technology, Chengdu, China
[2] GNS Science, Lower Hutt, New Zealand

SUMMARY: In 1881, the Swiss village of Elm was devastated by a rock avalanche that had originated two kilometers away. Geologist Albert Heim reported on the impressive event, prompting over a century of research on the extraordinary long runout of giant landslides. However, after one century of research, the answer to the question of why a dry mass can behave similar to a fluid and cover long distances remains somewhat of a mystery. We used a series of high-speed rotary shear experiments to explore the high mobility flow-like behavior of crushable dense granular flow. We found that under high normal stress and high shear speed, granular particles behave similar to liquids. Moreover, the viscosity of this special "liquid" is as low as 500 Pa·s, which is similar to the viscosity of peanut butter. We might imagine the catastrophic outcome from millions of tons of peanut butter pouring down a mountain slope. This finding can help us explain the hypermobility of many large geophysical processes, such as rock avalanche motion, natural faults and crater collapse.

Keywords: Rock avalanche, Fluid-like behavior, high-velocity rotary tests

Introduction

Geophysical phenomena such as rock avalanches, fault ruptures, pyroclastic flows, and impact crater evolution involve the rapid motion of granular masses subjected to internal stresses that are high enough to crush some of the grains. They belong to the category of dense and dry granular flows, which are extensively studied to assess natural hazards but also for a multitude of industrial applications. Footage of large rock avalanches reveals a striking characteristic: a sudden transition from solid to fluid-like motion upon disintegration of the mass. If the event was not triggered by an earthquake or explosion, the rock block had most likely been undergoing slow and imperceptible deformation for months or years, with cracks forming and propagating along its boundary cracks that likely went undetected unless a sensitive monitoring system had been in place. Then, the transition is dramatic and nearly instantaneous; the whole mass disintegrates and rushes downslope in a matter of seconds, with enough momentum to travel for several kilometers, even on gentle slopes. Treating the deformation behavior of geophysical grain flows as frictional material is customary (Scaringi et al., 2018; Wang et al., 2017), which provides little insight into their fluid-like behavior. This is why we explain our shear experiments on dry granular assemblies with viscosity instead of friction, even though their apparent viscous resistance is largely derived from intergranular friction. In this study, we found that the flow behavior was more explicable when the shear resistance was considered as a viscous resistance rather than as a frictional resistance.

Although the rheology of dense granular flows has been the focus of much research at the frontier between physics and mechanics, it appears that the frontier is still open for further advances. In particular, the rheology of grain flows at comparatively higher stresses

(approximately 1 MPa) that cause widespread brittle grain damage is largely unexplored. Some constitutive equations for dry dense granular flow have been proposed (Jop et al., 2006; Pouliquen & Forterre, 2002), yet nearly all constitutive models are based on experiments conducted under normal stresses of a few kilopascals. The stress conditions in these experiments are far below the several megapascals encountered in large geophysical flows, such as rock avalanches, fault ruptures, pyroclastic flows and post impact evolutions of impact craters. The extensive dynamic crushing of brittle grains is an important aspect of deformation in many geophysical processes (McSaveney & Davies, 2006), yet grain crushing is largely ignored in many grain-flow studies (Jop et al., 2006; Savage, 1984). Until now, it has been mostly studied in theory, with little experimental basis.

In our study, we employed a rotary shear apparatus that has been extensively used in the study of faulting to focus on the fluid-like behaviors of dry dense granular flows under normal stresses that are high enough to cause extensive grain breakage. We compared the apparent shear resistances of a variety of largely brittle materials and found that the flow behavior was more explicable in terms of viscous resistance than frictional resistance. We observed that extensive weakening (a decrease in the shear resistance) was typical of flows under normal stresses >0.3 MPa and shear-strain rates >10 s^{-1}.

Results

We show the fluidity characteristics of the granular flows in terms of their shear resistance versus the shear-strain rate (Figure 1). All the crushing materials exhibited two different phases of shear-resistance behaviors. The red circle on each curve in Figure 1 separates the crushing phase from the weakening phase. For fluorspar and corundum (Figures 1b and 1c), the initial flow behavior of the crushing phase was either Newtonian-like fluid or Bingham-like plastic. The initial fluid behaviors of dolomite, quarts, and rock salt were less simple (Figures 1a, 1d and 1e), as they all showed some shear-thickening; such flow behavior is comparable to that of ketchup and mayonnaise. All crushable materials then exhibited abrupt weakening; the shear resistance decreased quickly with little change in the shear-strain rate, and the mass became much more fluid (much lower viscosity). The shear resistance eventually tended to a steady state (blue circle in Figure 1). Except for the steel balls and glass beads (uncrushable material), all the materials had extensive crushing during the rapid shearing. Crushing transformed the originally uniform grain size distributions into a widely graded, fractal distribution and few grains of the original size range.

The constitutive equations of the crushed dense granular flow were raised based on the experimental results shown in Figure 1. In fact, there are two phases of the flow behavior, separated at a weakening point in the accumulating strain for crushable materials. The first phase was a simple Newtonian or non-Newtonian-like flow. The second phase was more complex, in which the flow viscosity decreased profoundly and reached a constant viscous resistance at a considerable strain. The constitutive equations are as follows:

$$\tau = \tau_0 + K_0 \dot{\gamma}^n \left(\dot{\gamma} \le \dot{\gamma}_p\right) \text{ in the first phase} \quad (1)$$

$$\tau = \tau_p + K_0 \left(\dot{\gamma} - \dot{\gamma}_p\right) \left(\dot{\gamma} > \dot{\gamma}_p\right) \text{ in the second phase} \quad (2)$$

where τ is the shear resistance (kPa); τ_0 is the yield resistance (kPa); K_0 is the consistency index (Pa.s^n); $\dot{\gamma}$ is the shear rate; and n is the flow index. If $\tau < \tau_0$, the granular behaves as a rigid solid; otherwise, it behaves as a fluid. For $n < 1$, the granular flow is a shear thinning-like fluid, whereas for $n > 1$, it is a shear thickening-like fluid. If $n = 1$, it is a Newtonian fluid-like

behavior. $\dot{\gamma}_p$, and τ_p are the shear rate and the shear resistance at the weakening point, respectively.

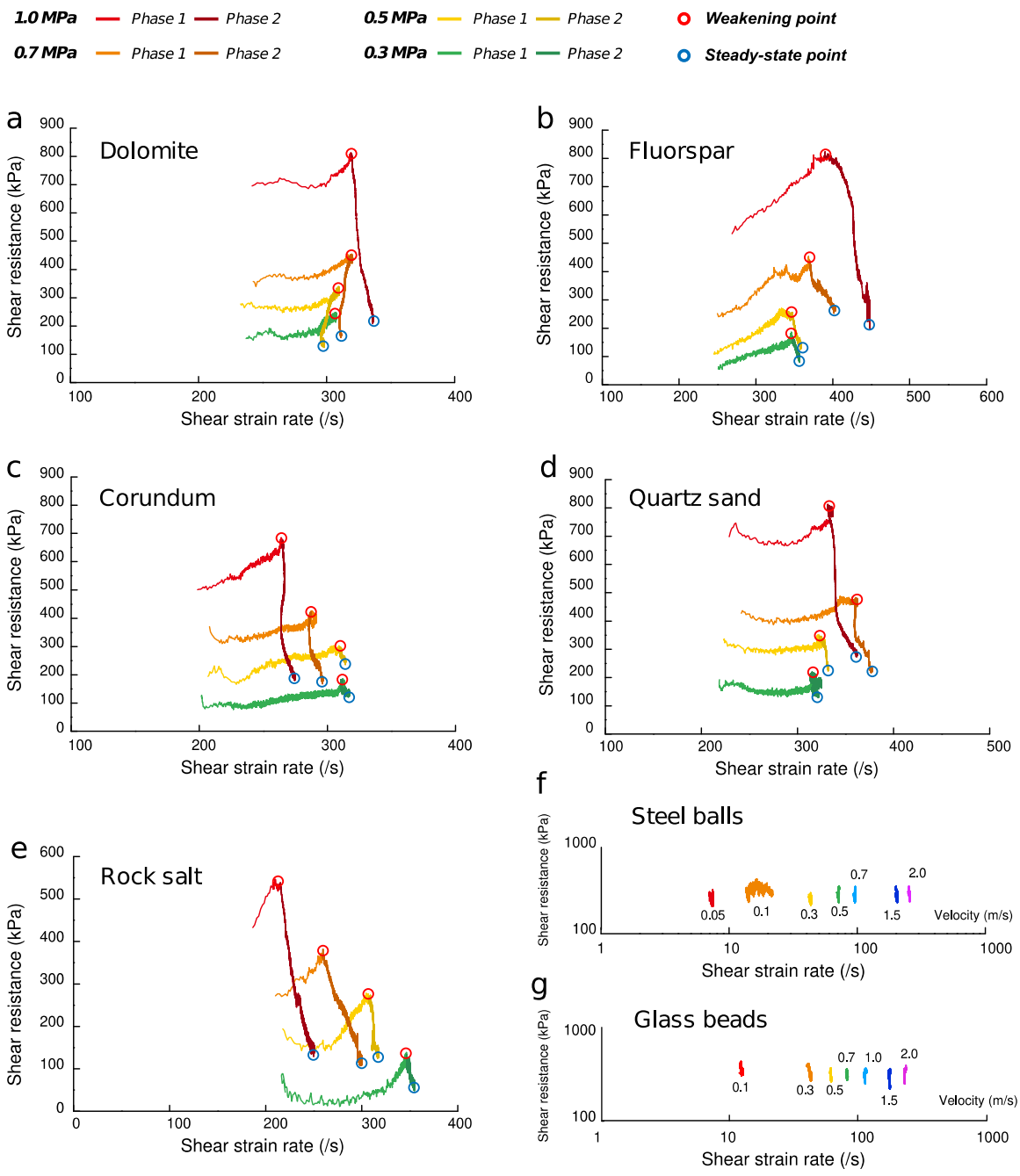

Figure 1. Fluidity characteristics of the experimental dense granular flows. Shear resistance versus shear-strain rate for the (a-e) crushing materials of different grain compositions and (f) uncrushable steel balls under different normal stresses (0.3-1.0 MPa). All crushable materials had an abrupt transition from the crushing phase to the weakening phase.

Conclusion

We found that it was much simpler to characterize dry dense flows of crushable grains in terms of their apparent viscosity. Thus, we found little complexity in the flow; the viscosity decreased with strain to become largely independent of the material hardness and normal stress but

strongly dependent on the strain rate over the range of materials, stresses, and strain rates present in our experiments. The viscosity tended to a seemingly unique quasi-steady-state value (~500 Pa-s at a shear strain rate of ~400 s-1). Most of the grain crushing occurred in an initial crushing phase, accompanied by an important volume reduction. The transformation of the size grading altered the internal grain structure, which appears to be connected in some manner to the ensuing strain weakening. The onset of weakening was marked by an abrupt transition in the fluid-like behavior in our dense grain flows. During an initial phase, crushing materials showed somewhat varied flow-like behaviors. However, from the weakening point, they all became soft thixotropic fluids and weakened to the same range of low shear resistances, independent of the material composition and normal stress in the investigated range. This finding can help us to explain the hypermobility of many large geophysical processes, such as rock avalanche motions, natural faults and crater collapses, and to improve the accuracy and reliability of the numerical simulation of rock avalanches by using the viscous model obtained from the experiments.

References

Scaring G, Hu W, Xu Q, & Huang, R (2018) Shear-rate-dependent behavior of clayey bimaterial interfaces at landslide stress levels. *Geophysical Research Letters*, 45(2), 766-777.

Wang YF, Dong JJ, & Cheng QG (2017) Velocity-dependent frictional weakening of large rock avalanche basal facies: Implications forrock avalanche hypermobility? *Journal of Geophysical Research: Solid Earth*, 122(3), 1648-1676.

Jop P, Forterre Y, & Pouliquen O (2006) A constitutive law for dense granular flows. *Nature*, 441(7094), 727-730.

Pouliquen O, & Forterre Y (2002) Friction law for dense granular flows: Application to the motion of a mass down a rough inclined plane. *Journal of Fluid Mechanics*. 453. 133-151.

McSaveney MJ, & Davies, TRH (2006) Rapid rock-mass flow with dynamic fragmentation: Inferences from the morphology and internalstructure of rockslides and rock avalanches. *In S. G. Evans, G. S. Mugnozza, A. Strom, & R. L. Hermanns (Eds.), Landslides from massive rock slope failure* (pp 285-304) Springer

Savage, SB (1984) The mechanics of rapid granular flows. *Advances in Applied Mechanics*, 24(28), 289-366.

The Role of Brittle Fracture and Damage in Multi-Block and Multi-StageLandslides

Davide Donati [1], Doug Stead [2], Nicola Fullin [3], Monica Ghirotti [3], Lisa Borgatti [1]

[1] Alma Mater Studiorum – University of Bologna, Bologna, Italy
[2] Simon Fraser University, Vancouver, Canada
[3] University of Ferrara, Ferrara, Italy

SUMMARY: The importance of block shape in the stability of rock masses has long been recognised, however the application of block theory to major landslides and rock slopes has received limited attention. In this paper the authors review the combined role of brittle fracture and block theory in the progressive three-dimensional failure of slopes with reference to observations from both state-of-the-art numerical modelling and remote sensing, Suggestions to allow an improved understanding of complex landslides and rock slope failures and thereby a more realistic assessment of slope hazards and risk are provided.

Keywords: Brittle fracture, landslides, numerical modelling, remote sensing.

Introduction

The stability of rock slopes is largely controlled by lithological and structural discontinuities, such as bedding planes, faults, joints, and foliation, which can intersect and form separate blocks within the slope. The size and shape of such blocks, the scale of the slope, as well as the damage that develops internally or along the block boundaries can play a key role in controlling both the stability and geomorphic evolution of the slope.

Single-block and multi-block landslides

Single-block landslides (SBLs) are controlled by the structural configuration of the rock slope, as the intersection of discontinuities must define a “removable” block that is kinematically free to displace and detach from the slope. Damage can play a role in the displacement of SBLs either a) by decreasing the shear and/or tensile strength of bounding discontinuities, allowing the block to displace without internal deformation or b) by increasing kinematic freedom through internal fracturing or deformation. The shape of the block also plays a crucial role in controlling the removability. As its complexity (i.e., number of faces) increases, the interlocking potential becomes more important for the stability of the slope, by decreasing its kinematic freedom. In such cases, brittle damage within the blocks ultimately controls rock slope stability. Indeed, where internal fracturing is kinematically required for the landslide displacement, damage accumulation can lead to the evolution into a multi-block failure, through the creation of new internal rupture surface or weak damage zones.
At all scales, multi-block landslides (MBLs) are constituted by discrete, independent blocks that are separated by discontinuities and can interact with each other. Published research on MBLs suggests that the number of blocks is independent of the size of the landslide (table 1). However, as the size of the blocks controls the strength and the deformability of the rock mass, larger blocks will be characterized by a markedly more ductile/plastic behavior, whereas smaller blocks are generally characterized by a more brittle behavior.

Table 1. Summary of the characteristics of selected multi-block landslides

Landslide	Volume	N. of blocks	Multi-stage	Migration
Downie Slide (BC, Canada) (Piteau et al. 1978; Westin 2017)	1 billion m^3	5-12	No	-
Hope Slide (BC, Canada) (Donati et al. 2021)	47 million m^3	5	Yes	Oblique
Joffre Peak (BC, Canada) (Friele et al. 2020)	5.3 million m^3	2	Yes	Lateral
Vajont Slide (Italy) (Semenza and Ghirotti 2000; Wolter et al. 2014)	250 million m^3	1-2	No	-
Randa landslide (Switzerland) (Willenberg et al. 2008)	30 million m^3	2	Yes	Vertical
San Leo (Italy) (Borgatti et al. 2015; Donati et al. 2019)	300,000 m^3	5	No	Lateral

Block theory considerations in landslide mechanisms

The orientation of major discontinuities controls the shape of the blocks forming the landslide, and their relative position with respect to the slope face can define the location and the removability of the block within the unstable slope. From a kinematic perspective, key blocks (Goodman 1995) are of paramount importance in controlling the stability and evolution of rock slopes. The removal of a key block leads to an increase in kinematic freedom in the landslide, resulting in the propagation of the instability to the blocks directly upslope of the key block (retrogression or vertical migration of the instability), or even laterally (lateral migration) or obliquely (oblique migration).

Landslide retrogression is commonly associated with roto-translational failures in weak rock masses, due to the shear stress concentrations that affect steepened slopes. Stress concentration along the incipient basal release surface, as well as rear and/or lateral release surfaces can also control vertical/up-slope instability migration within blocky rock masses. An example of a vertical/up-slope migration of an instability is the Randa slope failure, which affected a sub-vertical rock slope near the village of Randa (Switzerland) and caused the detachment of two time-separated landslides in 1991. Lateral/along-slope and oblique migration of landslide block instability is commonly controlled by the structural and kinematic configuration of the slope, as the landslide blocks often share a common rear release surface (i.e., lateral migration), or a basal and/or lateral release surface (i.e., oblique migration). The 2021 Joffre Peak landslide involved the detachment of two adjacent and similar sized blocks that shared a common rear release surface and also part of the basal rupture surface. The 1965 Hope Slide involved the detachment of five independent landslide blocks, which progressively detached in an oblique direction across the slope controlled by the orientation of the geological structures that also separated the different landslide blocks and shared a common (possibly stepped) basal rupture surface.

The increase in kinematic freedom of a MBL may also be the result of a progressive and long-term removal of material (as opposed to the sudden detachment of a key block), causing an oversteepening of the rock slope. The erosive action of glaciers and rivers are a common cause of slope toe oversteepening and are widely recognized as important factors controlling the long-term stability of rock slopes (Leith et al. 2014). In particular, landslides in alpine environment can potentially be exacerbated by ongoing global warming, due to the thinning and retreat of alpine glaciers, which are instrumental in preventing the rapid displacement of landslides (Kos et al. 2016; Sepúlveda et al. 2023). Progressive erosion in a resistant-over-recessive (ROR, Jackson 2002) lithological context can also lead to undermining of competent rock masses, and

an increase in kinematic freedom related to toe release can potentially lead to the detachment of landslide through rockfall or toppling. The detachment of the 2014 San Leo landslide was related to the erosion of clayshales within a lithologically controlled morphology (i.e., ROR setting, Borgatti et al. 2015).

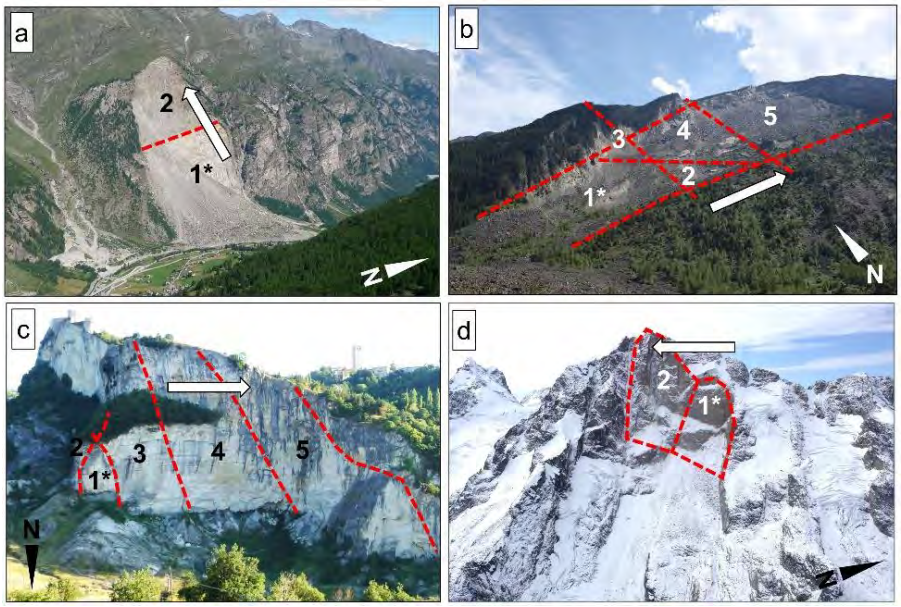

Figure 1. Examples of MBLs. a) Randa rockslide (photo by Wandervogel, via wikimedia commons, CC BY SA 3.0, modified); b) Hope Slide; c) San Leo landslide; d) Joffre Peak landslide. For each site, the block numbers are shown. Red, dashed lines mark the geological structures bounding the blocks. The white arrows show the direction of migration of the landslide instability.

The role of damage in multi-block, multi-stage landslides

Key blocks are often found in MBLs and can control their evolution in the short-term (hours/days/months), as well as in the long-term (tens/hundreds of years and beyond). Indeed, the detachment of MBLs can occur as a single event or in multiple, sequential stages (multi-stage landslides). Changes in slope kinematics and stress redistribution are among the principal factors in the occurrence of multi-stage landslides. The removal of a key block causes a local modification of the slope orientation that can modify the slope kinematics and hence the type of failure mechanisms that can affect the slope. The 2020 Joffre Peak landslide occurred in two stages, with the second block detaching three days after the first, toppling into the void left by the initial failure. Such a time gap probably allowed damage (e.g., fracture propagation, shearing of asperities, preparatory rock falls) to develop and accumulate along the release surfaces, ultimately allowing the movement of the block. The Hope Slide can also be considered a multi-stage landslide at over both the long- and short-term time scales. The 1965 failure was promoted by a landslide that occurred about 7900 years ago. The prehistoric event caused the initiation of an extremely slow deformation process within the slope, due to a redistribution of stresses within the remaining slope and resulting in the progressive development of a fully persistent basal rupture surface. The 1965 event itself was a multi-stage event, as the initial failure (involving three of the four blocks that remained in the slope after the prehistorical event) was followed, a few hours later, by the detachment of the last block, which caused four fatalities. The Randa rockslide was strongly controlled by brittle damage accumulation both during and between the two stages that formed the failure. Indeed, both the April 18 and May 9, 1991 events involved a progressive detachment of numerous blocks that progressively accumulated over a period of hours at the base of the slope. Each event was caused by a stress redistribution process (due to the continuous detachment of blocks) that resulted in the

accumulation of brittle damage within a high-quality rock mass. The progressive and gradual accumulation of damage prevented the simultaneous detachment of a large volume of rock mass, limiting the landslide mobility (farhboschung) and, in turn, the social and environmental impacts of the landslide.

Conclusions

MBLs are a critical geohazard in mountainous regions. Their characterization is of paramount importance to understanding their behavior, stability, and, in turn, to limit their impacts on surrounding communities and infrastructure. The mechanism and factors controlling the formation and accumulation of slope damage should be considered, as it can play a primary role in controlling the evolution of multi-block and multi-stage landslides. A combination of field analyses, remote sensing techniques for slope characterization and monitoring, as well as numerical modelling analyses can be critical in evaluating the stability and potential evolution of landslides, as well as the effects and factors that control the progressive accumulation of damage.

References

Borgatti L, Guerra C, Nesci O, et al (2015) The 27 February 2014 San Leo landslide (northern Italy). Landslides 387–394. https://doi.org/10.1007/s10346-015-0559-4

Donati D, Stead D, Brideau MA, Ghirotti M (2021) Using pre-failure and post-failure remote sensing data to constrain the three-dimensional numerical model of a large rock slope failure. Landslides 18:827–847. https://doi.org/10.1007/s10346-020-01552-x

Donati D, Stead D, Elmo D, Borgatti L (2019) A Preliminary Investigation on the Role of Brittle Fracture in the Kinematics of the 2014 San Leo Landslide. Geosciences 9:256. https://doi.org/10.3390/geosciences9060256

Friele P, Millard TH, Mitchell A, et al (2020) Observations on the May 2019 Joffre Peak landslides, British Columbia. Landslides 17:913–930. https://doi.org/10.1007/s10346-019-01332-2

Goodman RE (1995) Block theory and its application. Géotechnique 45:383–423. https://doi.org/10.1680/geot.1995.45.3.383

Jackson LE Jr (2002) Landslides and landscape evolution in the Rocky Mountains and adjacent Foothills area, southwestern Alberta, Canada. In: Evans SG, Degraff JV (eds.) Catastrophic Landslides. Geological Society of America. https://doi.org/10.1130/REG15-p325

Kos A, Amann F, Strozzi T, et al (2016) Contemporary glacier retreat triggers a rapid landslide response, Great Aletsch Glacier, Switzerland. Geophysical Research Letters 43:12, 412–466, 474. https://doi.org/10.1002/2016GL071708

Leith K, Moore JR, Amann F, Loew S (2014) Subglacial extensional fracture development and implications for Alpine Valley evolution. Journal of Geophysical Research: Earth Surface 119:62–81. https://doi.org/10.1002/2012JF002691

Piteau DR, Mylrea FH, Blown IG (1978) Chapter 10 - Downie Slide, Columbia River, British Columbia, Canada. In: Voight B (ed.), Developments in Geotechnical Engineering, Volume 14, Part A:365-392. https://doi.org/10.1016/B978-0-444-41507-3.50018-0.

Semenza E, Ghirotti M (2000) History of the 1963 Vaiont slide: the importance of geological factors. Bulletin of Engineering Geology and the Environment 59:87–97. https://doi.org/10.1007/s100640000067

Sepúlveda SA, Tobar C, Rosales V, et al (2023) Megalandslides and deglaciation: modelling of two case studies in the Central Andes. Nat Hazards 118:1561–1572. https://doi.org/10.1007/s11069-023-06067-x

Westin AM (2017) Downie Slide : An integrated remote sensing approach to characterization of a very slow moving landslide. M.Sc. Thesis. Simon Fraser University.

Willenberg H, Loew S, Eberhardt E, et al (2008) Internal structure and deformation of an unstable crystalline rock mass above Randa (Switzerland): Part I - Internal structure from integrated geological and geophysical investigations. Engineering Geology 101:1–14. https://doi.org/10.1016/j.enggeo.2008.01.015

Wolter A, Stead D, Clague JJ (2014) A morphologic characterisation of the 1963 Vajont Slide, Italy, using long-range terrestrial photogrammetry. Geomorphology 206:147–164. https://doi.org/10.1016/j.geomorph.2013.10.006

Rockfalls Run-out Distances
A low cost Data Base of trials realized on reduced models

Frédérique Leblanc[2] , Dominique Daudon[1]

[1] University Grenoble Alpes, 3SR, Grenoble, France
[2] University Grenoble Alpes, LJK-DATA, Grenoble, France

SUMMARY: Rockfalls have a significant risk of occurring in mountain areas and can cause heavy human and material damages. Hence, estimating the maximal propagation distance of a rockslide is essential, depends on various factors and codes used (Bourrier, 2020, Cuervo 2014, Garcia 2020). We present a database containing all the test results obtained with low-cost experimental devices acquired on two reduced models (Piras 2019). The factors at scales 1 and 3 are controlled by the experimenter, and 50 different configurations (called setups) are tested. Some statistical results over the run-outs in the single direction of the slope are given and highlight the more determinant factors for the propagation distances (Daudon 2021).Since some of the data are censored, statistical survival analysis tools are used (Mahfoud 2020).

Keywords: SQLite Data Base, experimental run-out , survival analysis, Weibull model.

Main Objectives and Results

1. Experimental devices for reduced models in two different sizes
2. Data acquisition : N launches ($50 \leq N \leq 100$) of n identical objects ($n \in \{1, 4, 7, 14, 28, 40, 42\}$) in various sets of known conditions under experimenter control (called setups)
3. Image processing for extracting information of interest of each image of the deposition surface after each trial
4. Organization of the already done trials in an SQLite Data Base
5. Statistical exploration of the data and modeling with Weibull distribution
6. Estimations with censored data of the parameters of the Weibull model fitted over observation of the deposition surface
7. Extrapolation of extreme quantile and of probabilities to overpass some given threshold
8. Identification of most determining factors for quantile assessment

Experimental Devices

The first reduced model P1 (presented in Figure 2) was designed by D. Daudon to mimic everyday situations of slope topography near mountain roads, infrastructures, or in similarity with a more scaled topography of Millau's rockfall. It is briefly described in the following images (extracted from Cuervo's thesis 2015):

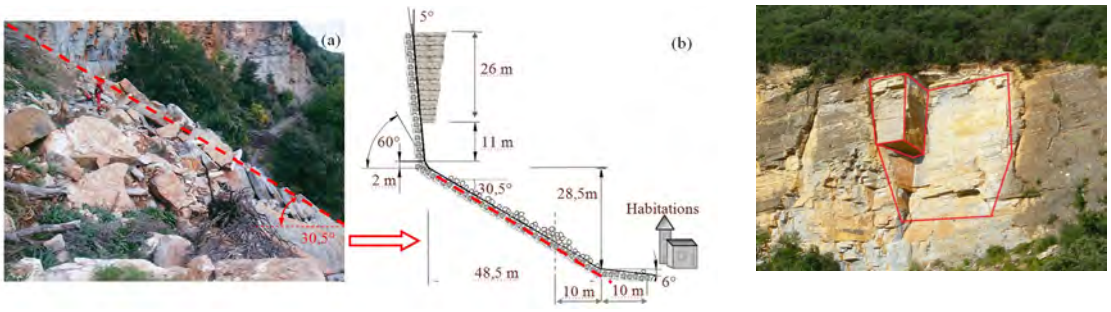

Figure 1: trial with P1 and arrival on sand and its corresponding data

The horizontal tray of the first reduced model P1 was too short (see Figure 3). When making trials for the main of the setups (except for the one presented in Figure 3), an essential part of the launched objects was ejected from the photographed deposition area. Hence, the proportion of censored data could be more than 50%, leading to a rather bad assessment of the maximum propagation distance. So a second reduced model was designed with a horizontal tray twice longer than in model P1. Next, to study scale effects over the results, a well-known challenged task in mechanics, a third reduced model was designed as a three-scaled size of the model P2. (figure 2)

Figure 2: scale 1 small tray P1 long tray P2 and scale 3 long tray P3

Data Acquisition and organization in a database

1. Image Processing

Homography and extraction of the n positions on the horizon-tal area of the n launched objects (possibly censored or non available)

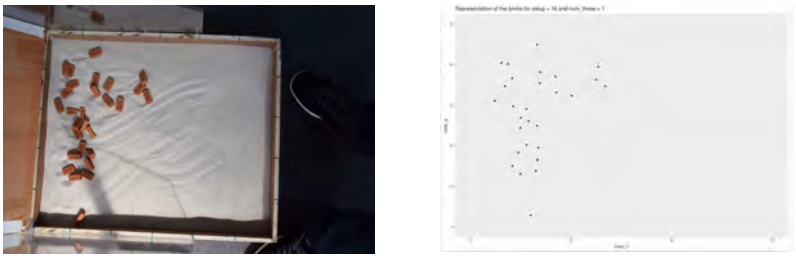

Figure 3: trial with P1 and arrival on sand and its corresponding data

2. Data Base

The tests are stored in an SQLite Database of 22 columns and approximately 50000 rows (50 setups). For each trial (among N in the same conditions given by a setup) of n launched objects, a set of n lines is included in the database where each line describes the position (x, y) of each object (x is the horizontal distance between the bottom of slope and object on the deposit surface and y the lateral distance with origin at the top left pixel of the homographied image). Each setup (numbered from 1 to 50) is characterized by the following variables that describe the conditions of trials. Remark that arrival and slope materials were chosen among the set :

AMLab= {wood,black,grey,teflon,wgrid,sand} (except sand for the slope) and that the different kind of objects belongs to *NOLab*= {brickFull, brickHalf, dice4, dice6, dice8, sdice4, brickHalfI, brickHalfW, brickFullM, brickHalfM, basalt, sbasalt}.

nb obj : nb. of thrown obj.
name obj: ∈ NOLab
angle : of the slope
height : fall height
sorted: loose or neat
slope mat : ∈ SMLab
arr mat : ∈ AMLab
length : of horiz. tray
width : of horiz. Tray
type plateau : P1,P2 or P3

Next, several variables describe the properties of thrown objects, where, in some cases, the value is set to −1 when the variable was not measured, which was the case of non-identical objects called basalt (a more realistic block geometry than identical regular polyhedra).

weight : in gr (-1 for NA) *nb vertices* : -1 when NA
volume : in cm3 (-1 for NA) *symmetry* : 1 if sym. polyh.
nb faces : -1 when NA

To end the variables that describe the positions of the n objects for each trial (caught by an image after each launch):

setup : in {1, ..., 50} *nb ejectas* : nb of cens. *values brick id* : in {1, ..., n}
nb throw : in {1, ..., 100} *coord x* : in cm coord y in cm

In order to appreciate the effect of n over the maximum runout in the last experimental trials (half of the setups), one of the n objects was marked. A supplementary variable named mistigri has been added and takes the value 1 when the marked object is concerned (0 otherwise). Moreover, when an object is ejected at the end of the board coord x takes the value 999 and coord y is missing (treated as NA in statistical analysis) and when it is ejected laterally (which could not be the case with tray P1), coord y = 998 and coord x is missing. To summarize, each database line gives all the available information of an object (positions and other characteristics) launched among n objects with all conditions defining a setup.

Statistical Results

Herein, we model the distance X, which is random by a Weibull distribution that depends on two parameters λ (localization) and α (shape). In each setup i (i = 1, ..., 50) and for each trial j (j = 1, ...N) we have n observations of X used to estimate the unknown couple ($\alpha_{i,j}$, $\lambda_{i,j}$).
The aim is here to estimate the survival function S(x) = P (X >x) = 1 − F (x) in any x or the quintile of order u given by F −1(u) for rather large u (for example u = 80% or u = 95%).
However, the main problem is that some of the x values are more often censored (when an object is ejected from the deposit area). Hence, statistical survival analysis tools are required to solve the problem. With no assumption over the law of X (non-parametric framework), one can use the Kaplan-Meyer estimator, which is adapted to censored data and gives a guide to extrapolate a convenient parametric model to fit the data. Once the model is chosen, here the Weibull one, whose survival function is defined as S(x) = exp[−(x/λ)α], its parameters are estimated by maximization of the log-likelihood that takes into account the censored data. The package flexsurv of R is used to fit the data. For example, in setup 12 with the first trial, which had more than 45% of censored data, the probability of over-passing 60cm cannot be reached with non-parametric Kaplan-Meyer estimator but can be obtained by extrapolation with a parametric model.

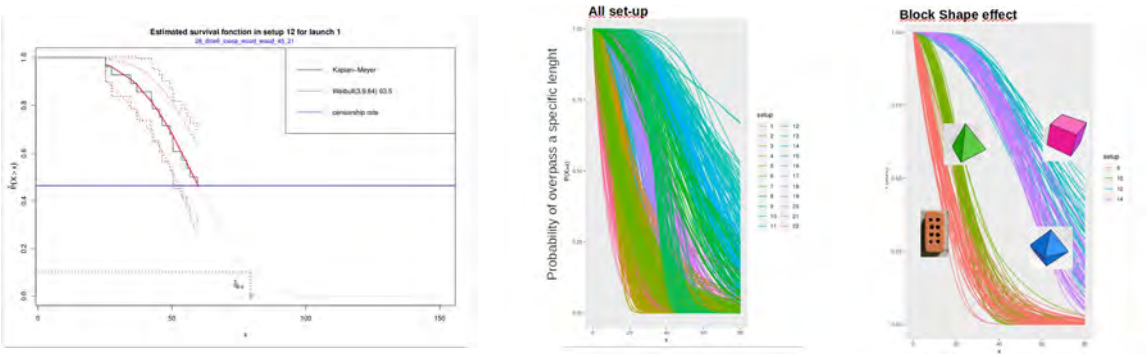

Figure 4: survival function set-up 12(left) and shape effect (s6,s10,s14,s12) (right)

As highlighted in the figure 4, the shape of objects is a significant factor for run-outs, particularly their sphericity and symmetry, but terrain characteristics also have some impact. In figure 5, the box-plots of the estimated probability of over-passing a given distance with trials realized over the tray P1 (setups 1 to 22) suggest that the arrival material and number of objects n launched from the box have some effect over the results

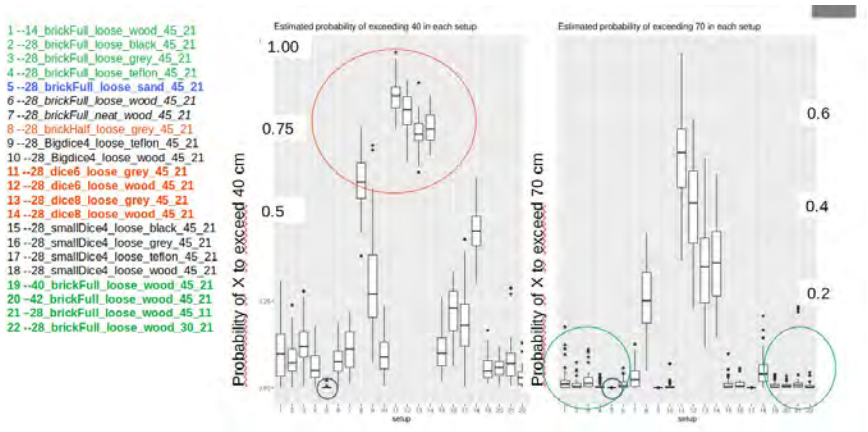

Figure 5: in setup5, arrival material is sand

Conclusions and Forthcoming Research

• Exploration of data acquired over P2 and P3 is still in course, and the effect of the number of neighbors over the mistigri's trajectory has to be studied.
• Comparison between results over the size 1 reduced model and the size 3 one should contribute to state the scale law.
• Quintile regression with some covariates under the experimenter's control can be reached.
• The results could be next compared to those obtained with numerical simulation.

Acknowledgment

The authors would like to acknowledge the university through URGA's project, and excellence founding and also the involuted student who implemented the database : B. Batail, W. Ardati, T. Piras, Nayib Hazim, A. Mafhoud, Y. Benlhabib, C. Wang, L. Tiamiou, C. Chenevas-Paule C., A. Audibert, D. Senshina, R. Kozhevnykov, E.&C. Touron.

References

Bourrier F; Toe, D.; Garcia, B.; Baroth, J.; Lambert,S. (2020). Experimental investigations on complex block propagation for the assessment of propagation models quality. *Landslides*.10.1007/s10346-020-01469-5.

Cuervo S; Daudon, D.; Richefeu, V. ; Villard, P. ; Lorentz, J. (2014). Discrete Element Modeling of a Rockfall in the South of the "Massif Central", France. *IAEG XII Congress - Torino*, September 15-19, 2014; 10.1007/978-3-319-09057-3_294.

Daudon D. Couailler V., Leblanc, F. (2021) Small scale rock fall experiments and statistical laws for run-out, *RSS 2021*, 17-18 nov 2021, Chambery, France.

Garcia B ; Richefeu, V.; Baroth, J.; Daudon, D. ;Villard, P. (2020). Collision of Shaped Boulders With Sand Substrate Investigated by Experimental, Stochastic, and Discrete Approaches. *Journal of Geophysical Research: Earth Surface*. 125. 10.1029/2019JF005500.

Piras T.(2019). O*rganisation de données acquises sur modèle réduit* . Internship report.

Mahfoud (2020). *Boulder rockfalls run-outs : statistical analysis of data collected on a scale model* Master's thesis.

Direct measurements of debris-flow feature velocities using high-frequency 3D LiDAR scanners

Raffaele Spielmann[1,2], Samuel Huber[1], Jordan Aaron[1,2]

[1] Chair for Engineering Geology, ETH Zürich, Zurich, Switzerland
[2] Swiss Federal Institute for Forest, Snow and Landscape Research (WSL), Birmensdorf, Switzerland

SUMMARY: Accurate measurements of debris-flow velocity are crucial for assessing their destructive potential and designing mitigation strategies. While previous monitoring methods have provided valuable insights, they often lack the spatial and temporal resolution needed to capture velocities of individual features, such as boulders and surge waves. This study employs high-resolution, high-frequency 3D LiDAR (light detection and ranging) scanners to conduct detailed field measurements of debris-flow velocities at the Illgraben, an active debris-flow catchment in the Swiss Alps. Three monitoring stations on the fan were equipped with LiDAR scanners and recorded an event on 5 June, 2022. The collected 3D timelapse point clouds were analyzed using manual and automated methods to measure the velocity of *i*) the flow front, *ii*) large boulders, *iii*) pieces of woody debris, and *iv*) surge waves. The results reveal a substantial decrease of the front velocity along the fan (by ~50%). They also demonstrate that objects immediately behind the front moved 1.4–1.8× faster than the front and that surge waves were approximately 1.5–2.7× faster than the front velocity. These findings, in combination with further analysis of data collected over the next years, promise to enhance our understanding of debris-flow motion and dynamics.

Keywords: debris flows, monitoring, LiDAR, velocity, surge waves

Introduction

Debris flows are very rapid to extremely rapid surging flows, composed of fine and coarse-grained material, boulders, woody debris and water (Hungr et al., 2014). They occur repeatedly in the same catchment and represent one of the most hazardous landslide types in mountainous regions (Badoux et al., 2009). This high hazard is mainly related to the high velocities, large impact forces and long runout distances of debris flows (Hürlimann et al., 2019). In the past, many researchers have measured debris-flow velocity in the field, as it is the most important parameter defining impact pressures and thus the destructiveness of this landslide type (Zheng et al., 2022). These measurements were conducted using time-distance methods (e.g. Comiti et al., 2014), video sequence analysis (e.g. Theule et al., 2018) or high-frequency radar measurements (e.g. Schöffl et al., 2023). Furthermore, only a few researchers were able to make direct measurements of the internal velocity distribution of a debris flow (Nagl et al., 2020).

Despite all these efforts, most of the abovementioned techniques have a limited spatial and/or temporal resolution and are unable to capture a debris flow in three dimensions. None of these methods is able to resolve the velocities of a debris flow at the "feature scale" (e.g. boulders, woody debris) as they rather focus on event scale (front velocity) or surge scale (surge or mean surface velocity) measurements. Moreover, most monitoring setups are limited to a single station per catchment, which inhibits us from making any statement regarding the spatial evolution of a debris flow (e.g. Hürlimann et al., 2019). However, knowing the velocities of individual features such as large boulders, at multiple locations along the channel, is not only

crucial for the design of mitigation measures (e.g. Berger et al., 2021), but also to improve our general understanding of the mechanisms governing front propagation (e.g. Johnson et al., 2012) as well as to infer the velocity profile of a debris flow (Aaron et al., 2023). In the present work, we leverage 3D laser scanners, originally developed for autonomous driving, to measure debris-flow velocities at high spatial and temporal resolutions. In particular, the velocity of *i*) the flow front, *ii*) large boulders, *iii*) pieces of woody debris, and *iv*) surge waves were measured using data recorded from a debris flow at the Illgraben, one of the most active debris-flow catchments in the Alps (McArdell & Sartori, 2021).

Site Description and Methods

In this project, high-resolution, high frequency, multi-beam LiDAR (light detection and ranging) scanners (*Ouster OS0* and *OS1*) were used to make detailed field measurements of debris flows. These laser scanners have the distinct advantage – especially over the abovementioned, conventional monitoring techniques – of capturing an undistorted, truly 3D representation of the surroundings, even in the absence of light or during rainfall. The LiDAR scanners record a 3D point cloud 10 times per second (i.e. at 10 Hz) and cover a channel segment of roughly 60 m – 80 m at each monitoring station. Three such monitoring stations (Figure 1), each of which is instrumented with one or two LiDAR scanners, have been installed at the Illgraben. In the present work, we analyze an event that occurred on 5 June 2022 and that was recorded by all three monitoring stations on the fan.

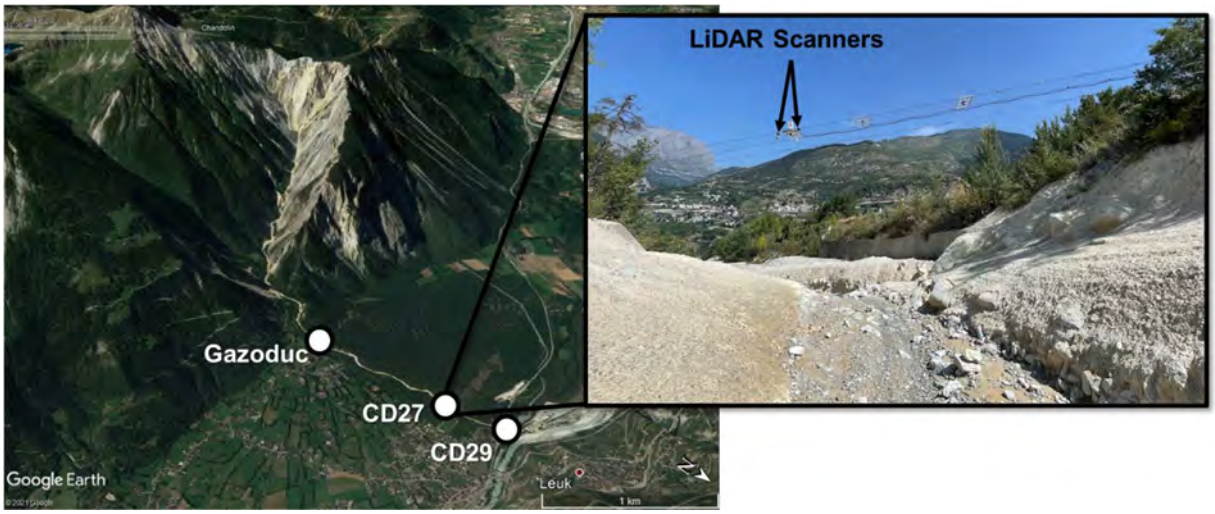

Figure 1: Overview of the Illgraben debris-flow catchment with the three monitoring stations *Gazoduc* (ca. 0.5 km downstream of the fan apex), *CD27* (ca. 1.7 km) and *CD29* (ca. 2.2 km). The monitoring stations are equipped with video cameras and LiDAR scanners.

The debris-flow data from the 5 June 2022 event collected by the LiDAR scanners consists of 3D timelapse point clouds. In a first step, these point clouds were rasterized and used to create hillshade projections with a 5-cm resolution (Aaron et al., 2023). We then tracked the flow front, individual boulders, pieces of woody debris and surge waves in every second frame of these hillshades by manually labelling these features. Based on these labels, we then derived the "instantaneous" velocities (i.e. at a rate of 5 Hz) as well as the mean feature velocities. Furthermore, a method to automatically derive debris-flow velocities was used. This method is based on particle image velocimetry (PIV), which was applied to the hillshade projections, and provides a velocity vector field throughout the channel segment around each monitoring station. We analyzed the velocities in the middle of the channel to obtain velocity timeseries of the mean debris-flow velocity at each station (Figure 2). Further details about the sensor and the methods can be found in Aaron et al. (2023) and Spielmann & Aaron (2023).

Results and Discussion

The velocities of the different features at the three monitoring stations are shown in Figure 2. For this event, the front velocities varied substantially along the channel: at the station Gazoduc (see Figure 1), the front moved at 5.5 m/s, at CD27 at 3.4 m/s and at CD29 only at 2.8 m/s.

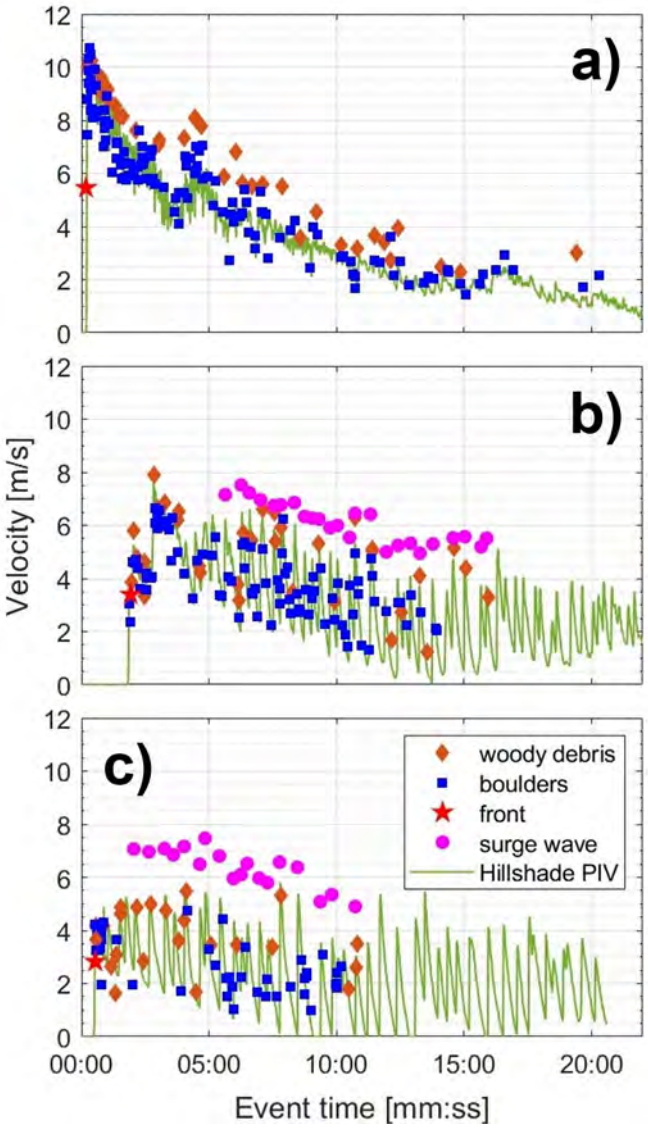

Figure 2: Mean feature and object velocities from manual measurements as well as PIV-based velocities for the 5 June, 2022, debris flow at the Illgraben; measured at the monitoring stations a) *Gazoduc*, b) *CD27*, c) *CD29* (see Figure 1; cf. also Åberg et al., 2024).

We tracked features such as boulders and woody debris directly behind the front (i.e. max. 30 s after the front had passed). These features moved at ~10 m/s (i.e. 1.8× faster than the front), ~5 m/s (1.5× faster) and ~4 m/s (1.4× faster) at Gazoduc, CD27 and CD29, respectively. The results are in good agreement with measurements from other researchers, including large-scale laboratory experiments (~1.5× faster than the front; Johnson et al., 2012) and field measurements from another event at the Illgraben (1.5–2× faster; Aaron et al., 2023).

As shown in Figure 2, a number of surge waves was identified in the event, but only at the two downstream stations CD27 and CD29, as they did not occur at Gazoduc. The waves moved at velocities between 5 m/s and 8 m/s at CD27 and CD29. This is 1.5× to 2.2× (CD27) and 1.8× to 2.7× (CD29) faster than the front velocity at these stations.

Finally, we provide the results from our automated PIV-based method, which are in good agreement with the feature velocities. The PIV-based velocities also show that the surge waves define the temporal evolution of debris-flow velocity and that substantial differences are apparent at the three monitoring stations.

Conclusion

In this study, we analyzed a debris flow at the Illgraben at the "feature scale" using high-resolution, high-frequency 3D LiDAR scanners. In particular, we measured the velocities of different flow features, including the front, large boulders, pieces of woody debris as well as surge waves, at three different monitoring stations on the fan along the Illgraben channel. Furthermore, we applied an automated PIV-based algorithm to hillshade projections of the

LiDAR data in order to derive continuous velocity timeseries of the mean debris-flow velocity at the three monitoring stations. In our measurements, we documented the following:

I) The front velocity decreased along the channel (over 1.7 km) by roughly 50% (from 5.5 m/s to 2.8 m/s).
II) Objects, such as large boulders or woody debris, directly behind the front moved at velocities 1.4–1.8× faster than the front itself.
III) The velocities of surge waves exceeded the front velocity by factors of 1.5 to 2.7.

The results presented herein have substantial implications for understanding the mechanisms governing debris-flow motion, as well as the design of protective measures. In particular, they demonstrate the highly unsteady and non-uniform velocity exhibited by these flows and show that surge waves can define hazard potential. In the future, data from at least ten more events, collected over the last three years, will be analyzed. Combining these results will further demonstrate the potential of using autonomous vehicle technology for natural hazard monitoring, as it enables velocity measurements at unprecedented spatial and temporal resolutions.

References

Aaron, J., Spielmann, R., McArdell, B. W., & Graf, C. (2023). High-frequency 3D LiDAR Measurements of a Debris Flow: A Novel Method to investigate the Dynamics of Full-Scale Events in the Field. *Geophysical Research Letters*, *50*(5). https://doi.org/10.1029/2022GL102373

Badoux, A., Graf, C., Rhyner, J., Kuntner, R., & McArdell, B. W. (2009). A debris-flow alarm system for the Alpine Illgraben catchment: design and performance. *Natural Hazards*, *49*(3), 517–539. https://doi.org/10.1007/s11069-008-9303-x

Berger, C., Denk, M., Graf, C., Stieglitz, L., & Wendeler, C. (2021). *Practical guide for debris flow and hillslope debris flow protection nets* (WSL Berichte). Swiss Federal Institute for Forest, Snow and Landscape Research WSL. Retrieved from https://www.dora.lib4ri.ch/wsl/islandora/object/wsl%3A28911/

Comiti, F., Marchi, L., Macconi, P., Arattano, M., Bertoldi, G., Borga, M., et al. (2014). A new monitoring station for debris flows in the European Alps: first observations in the Gadria basin. *Natural Hazards*, *73*(3), 1175–1198. https://doi.org/10.1007/s11069-014-1088-5

Hungr, O., Leroueil, S., & Picarelli, L. (2014). The Varnes classification of landslide types, an update. *Landslides*, *11*(2), 167–194. https://doi.org/10.1007/s10346-013-0436-y

Hürlimann, M., Coviello, V., Bel, C., Guo, X., Berti, M., Graf, C., et al. (2019). Debris-flow monitoring and warning: Review and examples. *Earth-Science Reviews*, *199*. https://doi.org/10.1016/j.earscirev.2019.102981

Johnson, C. G., Kokelaar, B. P., Iverson, R. M., Logan, M., LaHusen, R. G., & Gray, J. M. (2012). Grain-size segregation and levee formation in geophysical mass flows. *Journal of Geophysical Research: Earth Surface*, *117*(F1). https://doi.org/10.1029/2011JF002185

McArdell, B. W., & Sartori, M. (2021). The Illgraben Torrent System. In E. Reynard (Ed.), *Landscapes and Landforms of Switzerland* (pp. 367–378). Cham: Springer International Publishing. https://doi.org/10.1007/978-3-030-43203-4_25

Nagl, G., Hübl, J., & Kaitna, R. (2020). Velocity profiles and basal stresses in natural debris flows. *Earth Surface Processes and Landforms*, *45*(8), 1764–1776. https://doi.org/10.1002/esp.4844

Schöffl, T., Nagl, G., Koschuch, R., Schreiber, H., Hübl, J., & Kaitna, R. (2023). A Perspective of Surge Dynamics in Natural Debris Flows Through Pulse-Doppler Radar Observations. *Journal of Geophysical Research: Earth Surface*, *128*(9), e2023JF007171. https://doi.org/10.1029/2023JF007171

Spielmann, R., & Aaron, J. (2023). A new method for detailed discharge and volume measurements of debris flows based on high-frequency 3D LiDAR point clouds; Illgraben, Switzerland. *Engineering Geology*. https://doi.org/10.1016/j.enggeo.2023.107386

Theule, J. I., Crema, S., Marchi, L., Cavalli, M., & Comiti, F. (2018). Exploiting LSPIV to assess debris-flow velocities in the field. *Natural Hazards and Earth System Sciences*, *18*(1), 1–13. https://doi.org/10.5194/nhess-18-1-2018

Zheng, H., Shi, Z., de Haas, T., Shen, D., Hanley, K. J., & Li, B. (2022). Characteristics of the Impact Pressure of Debris Flows. *Journal of Geophysical Research: Earth Surface*, *127*(3), e2021JF006488. https://doi.org/10.1029/2021JF006488

Monitoring volcano landslides in an unresting caldera: the case of the Askja caldera, Iceland

Nicolas Oestreicher[1], Joël Ruch[1], Elisabetta Panza[1], Þorsteinn Sæmundsson[2], Halldór Geirsson[2], Jón Kristinn Helgason[3], Xingjun Luo[1], Jasmin Maissen[4], Nicolas Serrano[1], Patricia Leva[5], Jordan Aaron[5], Yohann Chatelain[1], Frédéric Arlaud[1]

[1] University of Geneva, Geneva, Switzerland
[2] University of Iceland, Reykjavik, Iceland
[3] Icelandic Meteorological Office, Reykjavik, Iceland
[4] Berner Fachhochschule, Bern, Switzerland
[5] ETH Zürich, Zürich, Switzerland

SUMMARY: Calderas are volcanic edifices able to trigger massive eruptions and often engendering flank collapses. A large landslide occurred within the Askja caldera in the summer of 2014, triggering a tsunami within the 4 km diameter Öskjuvatn Lake, affecting a touristic site. The volcanic edifice has started a new phase of unrest since 2021 with a cumulative uplift of 0.6 m until August 2023, in the centre of the caldera. Monitoring the caldera flanks is a critical task for increasing the safety of visitors, in addition to its scientific values. The rough weather conditions, remoteness, and difficult-to-inaccessible terrain make the monitoring challenging. We describe here a monitoring system which was installed in August 2023, composed of three time-lapse cameras, three corner reflectors, two extensometers, a GNSS station and three drone surveys acquired in 2020, 2021 and 2023 around the caldera rim. We present preliminary results of surface deformation between 2020 and 2023. We identified several deforming zones using DInSAR and high-resolution photogrammetric DEM differencing. Our monitoring system will allow multi-instrumental slope deformation analysis and must resist extreme Icelandic weather conditions. Its open-source nature and robustness should serve as an example for equipping other landslides in harsh environments around the world.

Keywords: volcano, landslide monitoring, remote sensing, Iceland

Introduction

The Askja caldera is one of the largest volcanoes in Iceland. Despite its remote location (Figure 1A), its explosive and destructive potential combined with the presence of tourists in the area during the summer period makes it essential to continuously monitor the volcanic system for a better understanding of the ongoing processes and hazards it causes (e.g., Figure 1B). The Askja caldera experienced a period of slow subsidence during the last 40 years that was best modelled by a Mogi source contraction at approximately 2.8 km depth in the middle of the caldera (Sturkell and Sigmundsson, 2000; Sturkell *et al.*, 2006). Continuous Global Navigation Satellite System (cGNSS) stations recorded a rapid uplift starting in the summer of 2021. In August 2023 the cumulative uplift, which started in August 2021, has reached ~0.65 m. Figure 1C and 1D shows the ground displacement recorded with the Differential Interferometric Synthetic Aperture Radar (DInSAR) method between August 2021 and August 2023 in the ascending and descending orbits of the Sentinel-1 satellites and concurrent seismic activity. The interferograms of Figure 1 show that the entire caldera was deforming upwards, with a maximum recorded uplift close to the shore of Lake Öskjuvatn. The strong unrest at the Askja

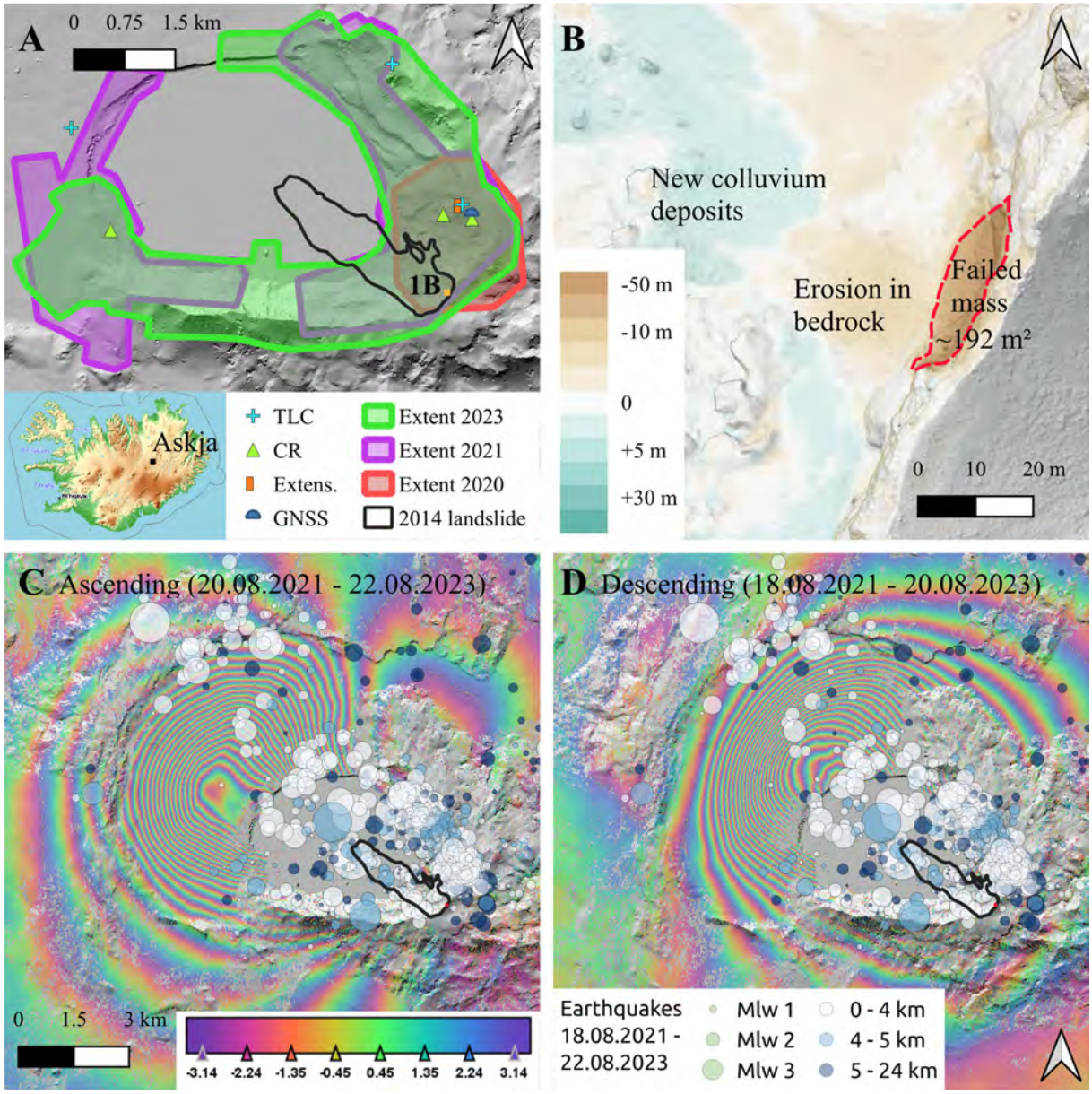

Figure 1: **(A)** New monitoring stations installed in 2023 (TLC: Time-Lapse Camera, CR: Corner Reflector, Extens.: Extensometers, GNSS: Global Navigation Satellite System) and extent of photogrammetric data coverage. The location of (B) is in orange. The location of the Askja caldera in Iceland is shown in the inset map. **(B)** Example of post-2021 slope collapse from the SE caldera edge with DEM differencing map overlaid on the 2023 DEM at a resolution of 0.1 m. **(C)** ESA Sentinel-1 wrapped interferograms for ascending orbit between 20 August 2021 and 22 August 2023. **(D)** ESA Sentinel-1 wrapped interferograms for descending orbit between 18 August 2021 and 20 August 2023. The 2014 landslide extent taken from Gylfadóttir *et al.*, (2017) is shown in black in (A), (C) and (D). The seismicity during radar acquisitions is shown in (C) and (D) with local moment magnitude (Mlw) taken from https://skjalftalisa.vedur.is/#/page/map.

caldera could be caused by magma intrusion at a shallow depth of around 2 km (Nobile *et al.*, 2022).

In 2014, a large rockslide with an estimated volume of 20 million m^3 occurred in the slopes SE from Lake Öskjuvatn (Suðurbotnar). It started at the caldera rim at night, when no tourists were present at the lake shore (Gylfadóttir *et al.*, 2017). Shortly after the collapse into Lake Öskjuvatn, a tsunami inundated the shores (Gylfadóttir *et al.*, 2017; Rauter *et al.*, 2022). There were signs of deformation in the Suðurbotnar area years prior to the failure in 2014, detected through back-analysis of photographs of the area (Saemundsson *et al.*, 2015). Some of the material from which the 2014 landslide originated is still present at the caldera rim, and cliffs

in the North of the landslide area are in a zone of enhanced microseismic activity. The elevated rate of ground displacement caused by the caldera unrest and the seismicity could potentially trigger another catastrophic event. The long-term deformation prior to failures gives us a chance to monitor and hopefully give out warnings prior to other failures in the Askja caldera.
In August 2023, we improved and complemented the current monitoring setup. While cGNSS stations offer only punctual information of the deformation, the DInSAR time series are consistently interrupted by snow covering the ground, allowing monitoring only during the short summer months (Nobile *et al.*, 2022; Cao, Jónsson and Hreinsdóttir, 2023). We installed a range of equipment enabling a better spatial and temporal monitoring of the slope and caldera floor deformation, and a better estimate of processes occurring in the subsurface in the Askja caldera, including time-lapse cameras, corner reflectors and extensometers. We further mapped the landslide phenomena in the east of lake Öskjuvatn, and pursue our effort of surface photogrammetric analysis from drone, as already started in 2020 and 2021 (Figure 1A).

Methodology

We installed surface displacement monitoring stations in the Askja caldera, at various locations with two focuses: the 2014 landslide and nearby slopes where potential new instabilities could form, and the SW shores of lake Öskjuvatn, that deformed over half a meter in the past two years and where the geothermal activity is very important.
We installed 3 solar powered and telemetered time-lapse cameras (TLC), that take between 1 and 4 pictures per day (depending on the network coverage and battery status). Two of the TLC are oriented towards the SE of Lake Öskjuvatn, in the area of the 2014 landslide. One is in the centre of the caldera (frontal view) and one is at the caldera rim (oblique view). The third TLC is oriented towards the SW of Lake Öskjuvatn and the geothermal area. There, large degassing and bubbling was observed in the middle of the lake, the lake shore locally have temperatures up to 36°C at a depth of 0.1-0.2 m and the shore uplifted by up to 0.6 m since 2021. The cameras have Ground Sampling Distances (GSD) of around 0.2 to 0.3 m/pixel. The images of the cameras are then correlated with Digital Image Correlation (DIC) techniques, allowing the identification and quantification of moving parts of the slopes.
In the N of the 2014 landslide, we installed a corner reflector (CR) on a large (63000 m^2) block that slid approximately 20 m vertically from the caldera rim and then stopped (Figure 1B). The base of the corner reflector is at 1.5 m above ground and orients the 3 aluminium plates and 1 plexiglass cover towards the descending orbit 111 from the ESA Sentinel-1 satellite. The data from Sentinel-1 are freely available online in the Copernicus open access Hub and the CR is therefore an open access system too. In winter, the snow should slide on the CR, and the coherence at this point should be maintained, allowing us to follow the deformation of the slope throughout the year with InSAR. Another CR is located lower in the slope, next to an actively deforming landslide, and a third CR is in the SW of Lake Öskjuvatn (Figure 1A).
Next to the first corner reflector, on the displaced block, we installed a cGNSS station. The cGNSS station is anchored in the bedrock with 4 inclined feet and powered by a car battery and a solar panel. On the same block, we also installed two extensometers in important fractures that dissect the block. They are anchored on both sides of the fractures and have a metallic roof to protect the cable from the snow.
To characterise the surface displacement at a higher spatial resolution than with the time-lapse cameras or satellites, we performed several surveying campaigns (2020, 2021, 2023) with a WingtraOne drone. The drone is equipped with an onboard precise GNSS antenna, and with a base station at the landing site, so that we can recalculate the accurate (at ~0.03 m) position of all pictures with the Post Processed Kinematic (PPK) method. The extent covered in the 3

campaigns are shown in Figure 1A. We post-process the images with Metashape and obtain DEM and orthophotos at ~0.06 m resolution and higher.

Results and Discussion

The first results of the 2023 fieldwork campaign show moving parts of the slopes around the lake, and some collapses of the unstable head scarp of the 2014 landslide. An example of such a collapse is displayed in Figure 1B, where a 50 m high block fell and deposited at the bottom of the cliff between the 2021 and 2023 drone surveys. During fieldwork in the area, numerous rockfall events could be heard and witnessed. The satellite surface displacement maps (Figure 1C, D) show the spatial extent and amplitude of the current uplift between August 2021 and August 2023. Each color cycle in the Figure represents ~27.7 mm displacement in the line of sight. Most of the surface displacement happens in the caldera and the centre of deformation is situated in the vicinity of Lake Öskjuvatn.
The slope deformation recorded from time-lapse cameras and the drone photogrammetric surveys serve beyond the assessment of unstable rock masses around the lake. They are an important tool to understand the evolution of the current unrest of the caldera, as they exhibit the slopes reaction before and during the period of unrest. In particular, the link between magmatic uplift of the caldera centre, associated tilt of the surface, and potential increase of the hydrothermal, seismic and landslide activities can be assessed.

Conclusion

The 2023 fieldwork campaign lasted the entire month of August in the Askja caldera. There, we could successfully install a range of instruments to monitor the surface displacement with high-resolution and all year-round. It is a challenge because of the harsh weather conditions, and we had to upscale batteries and solar panels for the low-light, cold winters in the Icelandic highlands. We installed three time-lapse cameras, three corner reflectors, one continuous Global Navigation Satellite System station, and flew the drone over a large part of the West, South and East caldera rims, repeating and extending previous campaigns in 2020 and 2021. Our installation offers the potential for surface displacement monitoring at high spatial and temporal resolution from now on, in a critical time as the ongoing unrest of the magmatic system might trigger further surface displacement, landslide activity or even an eruption.

References

Cao, Y., Jónsson, S. and Hreinsdóttir, S. (2023) 'Iceland Kinematics From InSAR', *Journal of Geophysical Research: Solid Earth*. John Wiley & Sons, Ltd, 128(3). doi: 10.1029/2022JB025546.
Gylfadóttir, S. S. *et al.* (2017) 'The 2014 Lake Askja rockslide-induced tsunami: Optimization of numerical tsunami model using observed data', *Journal of Geophysical Research: Oceans*, 122(5), pp. 4110–4122. doi: 10.1002/2016JC012496.
Nobile, A. *et al.* (2022) 'Likely ring-fault activation at Askja caldera (Iceland) during the 2021 unrest', in *EGU22*. Vienna: Copernicus Meetings. doi: 10.5194/EGUSPHERE-EGU22-9059.
Rauter, M. *et al.* (2022) 'Granular porous landslide tsunami modelling – the 2014 Lake Askja flank collapse', *Nature Communications*. Springer US, 13(1). doi: 10.1038/s41467-022-28296-7.
Saemundsson, T. *et al.* (2015) 'The rockslide in the Askja caldera on the 21st of July 2014', in *EGU General Assembly Conference Abstracts*. Vienna (EGU General Assembly Conference Abstracts).
Sturkell, E. *et al.* (2006) 'Volcano geodesy and magma dynamics in Iceland', *Journal of Volcanology and Geothermal Research*, 150(1–3), pp. 14–34. doi: 10.1016/j.jvolgeores.2005.07.010.
Sturkell, E. and Sigmundsson, F. (2000) 'Continuous deflation of the Askja caldera, Iceland, during the 1983-1998 noneruptive period', *Journal of Geophysical Research: Solid Earth*. Blackwell Publishing Ltd, pp. 25671–25684. doi: 10.1029/2000jb900178.

Use of geophysical methods to investigate quick clay landslide area in Gjerdrum Norway

Thi Minh Hue Le[1], Kristian Grønvold[2], Saman Tavakoli[1], Christos Boufidis[3]

[1] Norwegian Geotechnical Institute - Oslo, Norway
[2] Multiconsult - Formerly Norwegian University of Science and Technology, Trondheim, Norway
[3]TEMcompany, Aarhus, Denmark

SUMMARY: This study compares the use of Electrical Resistivity Tomography (ERT) with towed Transient Electromagnetics (tTEM) along one profile in the quick clay landslide area in Gjerdrum, Norway. The results show that the two methods show generally similar pattern of variations in resistivity in the areas which has been less disturbed by the landslide. The overall agreement between the two methods deteriorates in the upper layer and close to the sliding area where more disturbances by the landslide mass and new materials have been introduced after the landslide. ERT seems to be able to resolve the resistivity more correctly in the upper layer and to a greater depth than tTEM, while tTEM survey has advantage of being fast to perform. Both geophysical methods can be useful together with borehole data to investigate soil laying with good exercise of caution particularly for areas where there have been disturbances.

Keywords: ERT, tTEM, geophysics, landslide, quick clay

Introduction

Quick clay landslides occur in many cases in retrogressive mechanism and can become extremely mobile which poses a significant risk to human lives and infrastructure. On Dec. 30th 2020, the catastrophic landslide in Ask centre, Gjerdrum, Norway caused 10 fatalities and the destruction of 31 houses, and the evacuation of over 1000 residents (Fig. 1). The costs associated to the destruction of houses and infrastructure following the Gjerdrum landslide is estimated at £90 mill according to Finans Norge (Hovland, 2021).

Gjerdrum landslide stimulates the research need for more effective methods for detecting quick clay. This study investigates and compares the use of two geophysical survey methods: Electrical Resistivity Tomography (ERT) and towed Transient Electromagnetics (tTEM) to map soil layering and detect quick clay. The surveys were conducted in the landslide area in Gjerdrum. The resultant resistivities measured by these two methods are compared for as an example for one profile in this abstract.

Site conditions

The QCL occurred in Ask, the administrative centre of Gjerdrum municipality in southern Norway. After the landslide, intensive soil investigation campaigns were performed in the area to investigate the cause of the landslide, to prepare evacuation plans and to design stabilisation measures. The results from soil investigation indicate that the site is dominated by original marine clay under the landslide mass down to at least 30-40 m depth. There exists a continuous layer of quick clay within the marine clay with variable thickness over the area.

The geophysical surveys were conducted over the whole area, but the result along one profile (profile D) is presented as an example in this abstract (Fig. 1a). Along profile D, there are 15

boreholes within a distance 10 m from the profile. Most of them have a rotary pressure sounding, but some have total soundings, samples and CPTU (Fig. 1a).

Figure 1. (a) Site condition in Ask, Gjerdrum and the location of profile D in relation to geotechnical boreholes available at the site. Discrete symbols show location of the boreholes. (b) Destruction in the quick clay area in Gjerdrum Norway seen after 30.12.2020 (Photo credit: Norwegian Geotechnical Institute).

Geophysical surveys

Two geophysical survey methods were performed along a 400-meter profile (D) in order to compare their performance and investigate their applicability for mapping soil layers and detecting quick clay. The profile spans from the destabilised area in the northeast (NE) to the runout area in the southwest (SW). The initial terrain (shown in dashed line) indicates that almost 15 m slope slided down from the northeast area (between 0 and 150 m), ran out and deposited almost 5 m thick debris mass between 150 and 410 m along the profile.

Electrical Resistivity Tomography - ERT

ERT is a near surface geophysical method that uses direct current to measure the earth's electrical resistivity. The current is injected into the subsurface through steel electrodes installed manually 10-20 cm into the ground to measure the apparent resistivity distribution. Using data processing and inverse modelling a 1D, 2D or 3D resistivity model of the subsurface can be derived. For data acquisition in Gjerdrum, an ABEM LS 2 Terrameter was used with a spread of n x 21 electrodes, where "n" is the number of cables used. The chosen cable layout was with four cables of 21 take-outs. By implementing this procedure, high near surface resolution was acquired as well as high resolution towards the end of the measured section. The chosen cable layout resulted in an electrode spacing of 5 meters. This setup gives an approximate vertical resolution of approximately 2.5 meters. Accordingly, the ERT should have the capability of distinguishing soil layers with thickness of at least 2.5 meters. The measured apparent resistivity values are processed using inversion algorithms AarhusINV.

Towed Transient Electromagnetics - tTEM

The tTEM induces alternating currents to measure apparent resistivity. The alternating currents are induced through the transmitter coil, also known as the TX-coil, and creates a static primary magnetic field in the ground. The current is then abruptly shut off to generate eddy currents that circulates in the subsurface. From these currents, a secondary magnetic field is created. This field is continuously decaying as the resistance in the ground weakens the eddy currents. The

receiver coil, also known as the RX-coil, measures the attenuation of these currents and provides information about the resistivity of the ground (Auken et al., 2019).

The tTEM ground-based system was used in Gjerdrum (Fig. 2a). This system provides high-resolution data and operated at 15-20 km/h driving speed, thus much faster to carry out than the ERT survey. The TX-coil is located inside a frame with dimensions 3x3m. The TX- and RX-coils are placed on movable platforms and the coils' center were positioned 9 meters apart from each other, corresponding to approximately 4.5 meters vertical resolution. A GPS was located on the TX platform which was towed by an ATV (Fig. 2b).

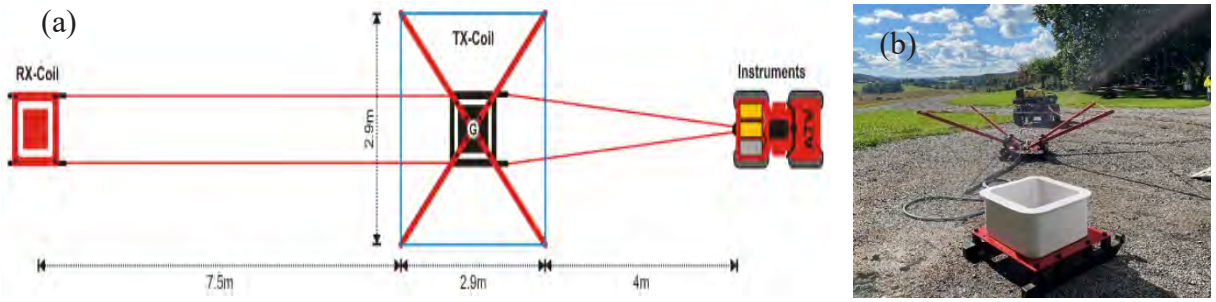

Figure 2. (a) Schematic illustration of the tTEM 3x3 system (Aarhus GeoInstruments, 2022) (b) Photo of the tTEM-equipment used in Gjerdrum. Photo credit: Christos Boufidis and Søren Bjørn (Aarhus GeoInstruments)

The measurements in Gjerdrum were conducted using two transmitter moments. A low (3A) and a high (30A) transmitter moment were applied sequentially, typically taking about 0.5 seconds per sequence. The lower moment is useful to receive shallow data, while the higher moment is able to reach greater depth. During one sequence, several hundred transient measurements were recorded. The position of the TX-platform was also recorded through the GPS, as well as instrument parameters such as temperature, current and voltage levels for quality control of data.

Results

The results for profile D is shown in Fig. 3 with the resistivity from tTEM imposed on the field of resistivity measured by ERT. Soil layering interpreted from borehole data are also presented in shorter columns. The agreement in between resistivity values obtained by ERT and by tTEM depends on location and depths (Fig. 3). The two methods display comparable resistivity patterns with one another in less disturbed areas in the southwest and under 5-7 m depth. Between approximately 7 and 40 m depth, the resistivity varies typically between 10 to 100 Ωm indicating dominantly clay and fine-grained materials. Some small areas in the middle of the domain exhibit resistivity values below 10 Ωm. The agreement between the two methods deteriorates in the uppermost layer and closer to the landslide area. Within the upper 5-7 m depth, the ERT often recorded values reaching up to 500 Ωm, whereas the tTEM method never exceeded 100 Ωm. On northeast end of the profile, the two methods display poor consistency over the whole depth. The discrepancy between the two methods, particularly near landslide area and in the uppermost layer, can be attributed to the presence of crushed stones used as surcharge in combination with vertical drains to consolidate the landslide mass in the northeast.

Notably, the tTEM data consistently demonstrates a faster increase in resistivity with depth compared to the ERT data. The discrepancy in between the measured resistivity between the two methods can be up to 15 meters. The resolved depth of investigation tends to be a bit deeper for ERT than tTEM. The tTEM tend to indicate coarser material shallower than the ERT. This

observation can be attributed to the inherent limitations of the tTEM method in distinguishing resistivity values above 200 Ωm. Consequently, the tTEM data tends to exhibit a rapid increase in resistivity values after surpassing the threshold of approximately 150 Ωm.

The resistivity does not show distinct difference between different soil types. The landslide mass and dry crust in the uppermost layer correspond to higher resistivity (>100-150 Ωm) while the clay and quick clay in lower layers correspond to resistivity less than 100-150 Ωm. There is no clear distinction between resistivity ranges between not quick clay and quick clay observable in profile D.

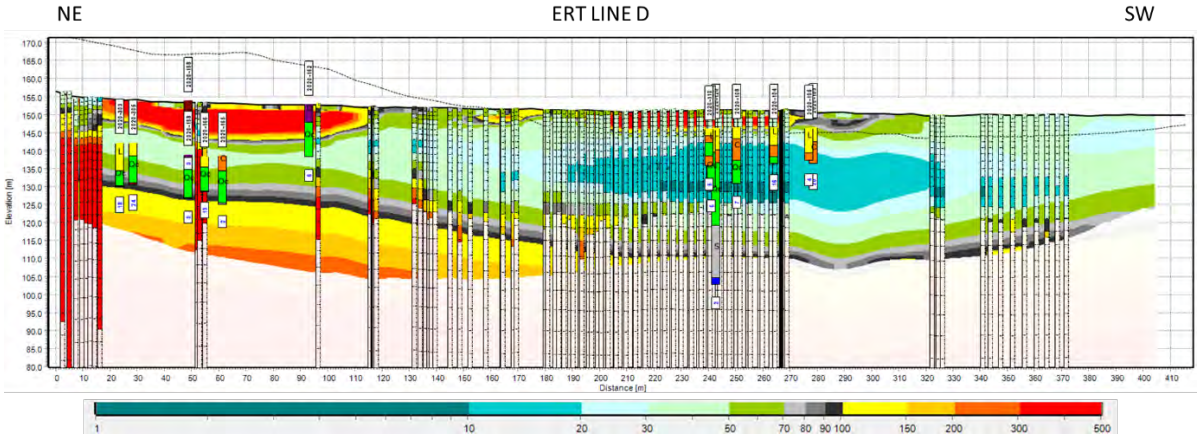

Figure 3. Comparison between resistivities obtained by ERT (continuous colour map) and tTEM (long columns with colour map). Discrete geotechnical boreholes are indicated as short columns with symbols (Qc = quick clay, L= landslide mass, D = dry crust, C = clay-not quick, S = Sand/silt, M = moraine). Dashed line indicate terrain before the Gjerdrum QCL.

Conclusions

The study shows that geophysical survey can be useful in indicating general soil layers, but caution must be exercised in interpreting detailed such as depth and thickness of the layers. In areas with complex geological history and conditions such as a landslide area, disturbance can significantly affect the results and should be carefully considered when interpreting measurements from geophysical survey. ERT can produce higher resolution and more accurate results in upper layers as well as larger resolved depth than tTEM. The tTEM method is however faster to perform. In less disturbed areas, the two methods show quite similar pattern of variation in resistivity and can be useful to be used in combination with borehole data.

Acknowledgement

The research is supported by the European Union's Horizon 2020 research and innovation program under Grant Agreement No. 101006512 (GEOLAB) in collaboration with project HIGELIG (project number 332792) - High-resolution Geophysical mapping of the quick clays in Gjerdrum financed by RFF-Viken.

References

Auken, E, Foged, N, Larsen, JJ, Lassen, KVT, Maurya, PK, Dath, SM & Eiskjær, TT (2019). tTEM — A towed transient electromagnetic system for detailed 3D imaging of the top 70 m of the subsurface. *Geophysics,* 84**,** E13-E22.

Hovland, KM. (2021). Har utredet kvikkleire for 46 mill. på fem år (Have investigated quick clay for 46 million in five years). *24*, 14.04.2021.

Drone-Based Geological Characterization of a Rockslide Site

Marte Gutierrez, Steven Benfield, Wendy Zhou

Colorado School of Mines, Golden, CO 80401, USA

SUMMARY: Drones are increasingly being used for remote geological characterization. They bring huge potential for pre- and post-landslide evaluation. This paper presents the use of an off-the-shelf drone and Structure from Motion (SfM) Digital Photogrammetry to characterize the geology of a site that has undergone a rockslide. The study site is composed of a heavily jointed interlayered gneiss rock mass with distinct planar discontinuities. The structural discontinuity orientations, which appeared to be homogenous across some sections of the rock mass, needed to be evaluated to understand the geologic factors that contributed to the slide. An improved contour-density methodology was used based on existing methods of structural domain identification to locally divide the rock mass into domains of similar structural orientation. The results of this study reveal that both blasting effects and tectonic features likely induced the historic wedge failure. This study also reveals that the remaining rock mass may have significant spatial differences in structural orientations, requiring appropriate domaining for rock mass characterization.

Keywords: geology, rock mass, discontinuities, rockslide, drone

Introduction

Rock masses are inherently discontinuous and may contain joints, bedding planes, faults, lamination planes, foliation planes, and lithological contact surfaces whose quantity and orientations govern the rock mass strength. Characterizing these discontinuities is time-consuming, expensive, and potentially hazardous. The engineering behavior of a rock mass is controlled by a variety of structural parameters including orientation, persistence, spacing, alteration, and roughness. However, rock masses are not completely random, and discontinuities come in "sets" or "domains." The engineering analysis and prediction of a slide in a rock mass requires the identification of similar areas or "domains" with similar discontinuity orientations (Mathis, 2016).

Drone technology is increasingly being used to characterize the discontinuities of slopes, particularly for steep and hard-to-access locations (Bar et al., 2021; Krajnovich et al., 2020). Furthermore, data acquired from remote digital photogrammetry can also be used in conjunction with existing semi-automatic discontinuity identification methods (Buyer et al., 2020; Krajnovich et al., 2020) to characterize the structural geology of a site. This paper presents the use of drone technology in tandem with Structure from Motion (SfM) Photogrammetry to identify failure surfaces of a historic wedge failure and identify the structural domains of the scarp of the rockslide.

Methodology

The study site is a rockfall located 0.25 miles west of Golden, Colorado, within the boundaries of Clear Creek Canyon Park, just north of the US-6 Roadway (Fig. 1). The slope consists of

interlayered gneiss lithology with a presumably large wedge failure bounded by a steep fault surface. The gneiss is reported as a plagioclase-quartz biotite gneiss containing thin dark-grey amphibolite layers.

The most striking feature of the abandoned quarry is a historical and large wedge failure feature. The wedge failure is bounded by a fault surface detailed in the Golden Quadrangle map and a secondary surface whose orientation is not documented. The fault is documented with a 74˚ dip, dipping southwest adjacent to a heavily jointed rock mass (Van Horn, 1972). The two wedge failure surfaces are noted in detail in Figure 1.

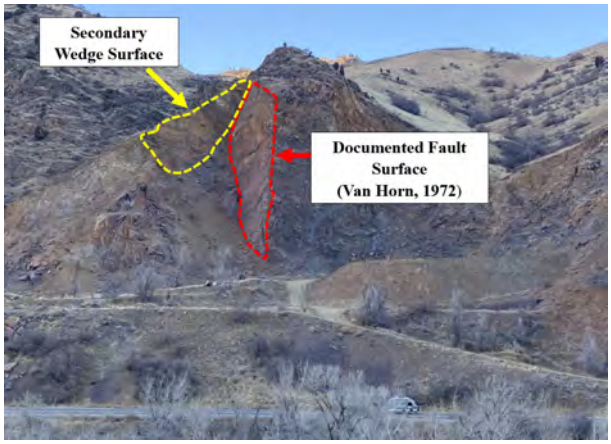

Figure 1. Location of the Wedge Failure Surfaces at the Clear Creek Canyon Rockslide The main fault surface was previously documented by Van Horn (1972).

An off-the-shelf DJI Mavic II drone was used to take photographs for photogrammetric reconstruction. In total, five separate flight plans were utilized, including four vertical flights and one nadir horizontal flight to ensure tie points for photogrammetry purposes. Vertical flights were flown ~15-24 m (50-80 ft) from the face, while the horizontal nadir flight was flown ~60 m (~200 ft) from ground level. software and utilized 80% and 75% front and side overlap, respectively. Eight ground control points were used to improve the accuracy of the final photogrammetric point cloud. Ground control points were placed at accessible locations and surveyed with an RTK DGPS Trimble using a base station and rover.

Following the drone flight, photogrammetric reconstruction was performed through DroneDeploy. Table 1 details the DroneDeploy processing specifications. The point cloud was then reduced to 10 million points to minimize computational time. In addition, the point cloud was manually segmented in CloudCompare to remove vegetation and surficial material while prioritizing locations of intact rock.

Table 1. DroneDeploy Point Cloud Processing Specifications for the Clear Creek Canyon Rockslide.

Processing Mode Quality	High Resolution
Total Points	37.5 million
Point density	181 points/ft^2
Mesh Triangles	1.4 million

The resulting point cloud consisted of 6.7 million points. Additional segmentation was performed to focus on areas of distinct planar discontinuities, forming a heavily jointed, blocky rock mass representing the main face of the excavation. An open-source MATLAB Discontinuity Set Extractor (DSE) Tool (Riquelme, 2023) was used to identify discontinuities and their structural orientations from point cloud data. Once a point cloud is loaded into the tool, the MATLAB code identifies the number of discontinuities and their orientation

(Riquelme et al., 2014). No universal guidelines exist for the classification of structural domains.

Miller (1983) developed a methodology to quantitatively identify structural domains or sets using orientation data. This methodology involved a chi-squared test between the frequency of orientation data falling in separate equal area gridded stereonets for comparisons. A correlation coefficient between the frequency of orientation data falling in each equal-area grid was calculated for discontinuities of each mine. This paper used a more robust approach using Kamb density contouring methods, which are related to binomial statistics (Kamb, 1959). In this approach, correlation coefficients are calculated using density values derived from the clustering of discontinuity density contours on a stereonet. Kamb proposed a model in which the expected value of a uniform distribution of data is equivalent to three times the standard deviation of random orientations during sampling from a particular area if those orientations are not clustered.

Results and Discussion

The failure surfaces of the historic wedge failure are identified to assess why and how the failure occurred. To estimate the orientations (dip/dip direction) of the failure surfaces belonging to the historic wedge failure, the CloudCompare plane fitting tool was used to fit a plane of best fit through each surface. Fig. 2 shows the MATLAB DSE identified two main wedge failure surfaces, consisting of a fault surface and a secondary surface, in the areas of intact rock adjacent to the wedge failure location. Based on the geometry of the scarp, it is reasonable to assume that the slide occurred by the re-activation of the fault followed by the shear failure of the shear surface. The main trigger for the slide is blasting in a rock quarry in the site.

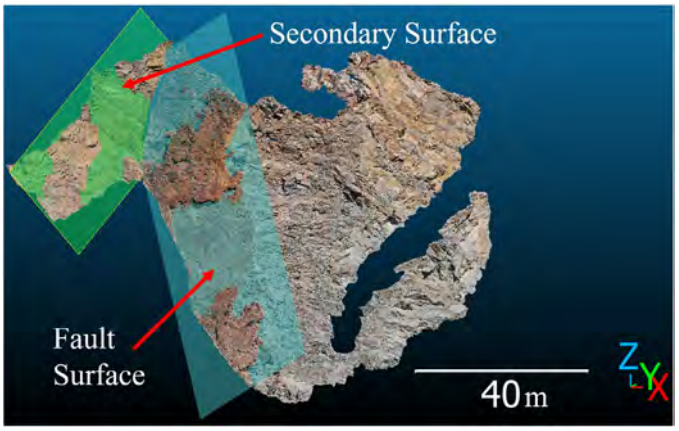

Figure 2. CloudCompare best-fit planes for wedge failure surfaces of previously unknown orientation (Green) and surface fault (Blue).

To investigate if these two main failure surfaces orientations are persistent and prevalent throughout the scarp, the MATLAB DSE was used to identify the orientations of the discontinuities in areas of heavily jointed rock mass adjacent to the historic wedge failure. Figure 3 shows the DSE-identified discontinuities domains in the areas of intact rock adjacent to the wedge failure location. A total of eight potential domains were identified. Domain 1 represents the bottom two-thirds of the rock mass and is comprised of point cloud elemental domains 2, 3, 4, and 8. The correlation coefficient between each of these elemental domains is no less than 0.555, indicating a “high” degree of similar structural characteristics. On the other hand, elemental domains 5, 6, and 7 have correlation coefficients amongst each other that are below the 0.5 cutoff. These remaining elemental domains 5, 6, and 7 do not display consistent “high” correlations amongst other elemental domains, providing justification to treat them all as separate structural domains.

Depending on the application, it may therefore be appropriate to consider elemental domains 2, 3, 4, and 8 as a single homogenous unit of similar discontinuity orientations. On the contrary, elemental domains 5, 6, and 7 may also be thought of as separate structural domains. Elemental domain 1 is consistent with the location of the wedge fault surface. Generally, elemental domain 1 is not well correlated with any other elemental domain. This again suggests there is a minimal continuation of the fault's orientation to nearby areas of rock mass.

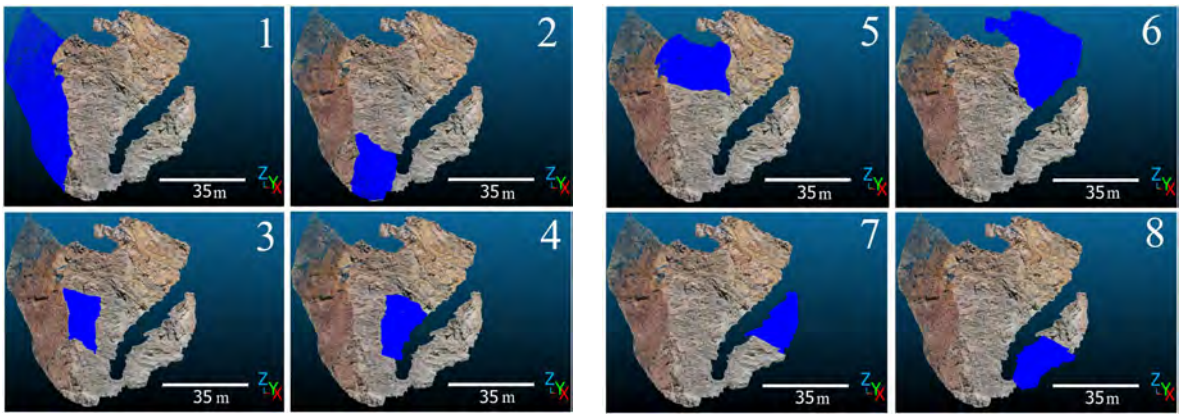

Figure 3. Selection of rock mass elemental domains (shaded in Blue) used for identification of structural domains for the Clear Creek Canyon Rockslide.

CONCLUSIONS

The paper developed techniques to identify the failure surfaces of scarp of rockslide, and the discontinuity sets or domains of the host rock mass via remote imaging utilizing an off-the-shelf DJI II Drone. The methodology used the DroneDeploy to plan the drone flights, CloudCompare to remove surficial material covering the outcropping rock, MATLAB DSE Tool to extract discontinuity locations and orientations, and Kamb methods to delineate the different discontinuity domains in the rock mass. The performance of the methodology was demonstrated using the Clear Creek Canyon Rockslide in Golden, Colorado, USA. Based on the geometry of the scarp, it is reasonable to assume that the slide occurred by the re-activation of the fault followed by the failure of the shear surface. The delineated geometry can be used as input to 3D Distinct Element Modeling (DEM) of the triggering of the slide and the subsequent debris follow following the procedure outlined in Gutierrez (2014).

References

Bar, N, Borgatti, L, Donati, D, Francioni, M, Salvini, R, & Ghirotti, M. (2021) Classification of natural and engineered rock slopes using UAV photogrammetry for assessing stability. *IOP Conference Series: Earth and Environmental Science*, *833*, 1–7.

Buyer, A, Aichinger, S, & Schubert, W (2020) Applying photogrammetry and semi-automated joint mapping for rock mass characterization. *Engineering Geology*, *264*(1), 1–9.

Gutierrez, M. (2014). "Distinct Element Modeling of the Massive February 17, 2006, Leyte, Philippines, Rockslide," Proc. Rock Slope Stability 2014, Marrakech, Morocco, April 2-4, 2014, pp. 565-574.

Krajnovic, A, Zhou, W & Gutierrez, M (2020) Uncertainty Assessment for 3D Geologic Modeling of Fault Zones Based on Geologic Inputs and Prior Knowledge. *Solid Earth,* 11, 1457–1474

Mathis, J (2016) Structural domain determination — practicality and pitfalls. APSSIM 2016*: Proceedings of the First Asia Pacific Slope Stability in Mining Conference*, 203–212.

Miller, SM (1983) A statistical method to evaluate homogeneity of structural populations. *Journal of the International Association for Mathematical Geology*, *15*, 317–328

Riquelme, A. (2023) Discontinuity Set Extractor (https://github.com/adririquelme/DSE), GitHub. 9/13/2023.

Van Horn, R (1972).Surficial and bedrock geologic map of the Golden Quadrangle, Jefferson County, Colorado. *USGS Numbered Series 761*. https://pubs.er.usgs.gov/publication/i761A

Dynamic Effect in the Mechanical Behavior of Friction Dissipator

Ali Osairan[1,2], Marie-Aurelie Chanut[1], Marion Bost[2]

[1] Cerema Centre-Est, GeoCod, 69674 Bron Cedex, France
[2] Universite Gustave Eiffel, GERS, RRO, 69675 Bron Cedex, France

SUMMARY: Rockfall is a natural event that causes damage to urban areas. To mitigate this danger, flexible barriers are installed as a protective measure. This structure has dissipators that absorb the impacting blocks' energy, thus reducing the stress in other barrier components. According to the flexible barrier certification standard (EOTA 2018), the dissipator's mechanical behavior is characterized by a quasi-static tensile test at a velocity 0.002 m/s. However, on site, the impacting blocks can reach velocities ranging between 5 and 30 m/s. Consequently, the dissipator is loaded at higher rates during rockfall events compared to the characterization test. Moreover, the non-activation of dissipators during rockfall events raises questions about the adequacy of the regulatory load used to assess the dissipator's performance. In this context, during the C2ROP national project, a friction dissipator was tested by 3 similar quasi-static and 3 similar dynamic tests. The results revealed notable variability in the dissipator's behavior during dynamic tests, while a slightly scattered behavior was observed during quasi-static tests. Furthermore, a significant increase in the dissipator's elastic rigidity and plastic displacement was recorded during the dynamic tests compared to quasi-static tests. Hence, a dynamic effect seems to exist in the dissipator's behavior during rockfall events.

Keywords: rockfalls, flexible barrier, friction dissipator, mechanical behavior, dynamic effect.

Introduction

Dissipators are components that are integrated into the flexible barrier system to absorb internal energy. In fact, dissipators absorb around 60 to 80% of the total impact energy experienced by the structure by undergoing large deformations (Zhao, 2020). Thus, accurate characterization of the mechanical behavior of the dissipator is crucial for two important reasons. The first reason is to model properly the dissipator in the numerical models of flexible barriers. The second reason is to determine the energy dissipation capacity of the dissipator for design purposes.

The characterization of dissipator's behavior can be done by either quasi-static tests (Xu, 2018) or dynamic tests (Dugelas, 2020). In this paper, the behavior of dissipators under quasi-static and dynamic loading is detailed. Then, based on the results obtained from the experiments conducted in the C2ROP national project, a comparison between the behavior of the friction dissipator under quasi-static and dynamic loads is carried out to highlight the existence of dynamic effects in the studied dissipator's mechanical behavior.

Behavior of Dissipator Under Quasi-Static (QS) Loading

According to the EOTA recommendation, the quasi-static test is usually performed by securing one end of the cable where the dissipator is connected to a fixed point and pulling on the other end using a horizontal traction machine with a velocity of 0.002 m/s, as shown in Figure 1. The load-displacement curves from quasi-static tests conducted on the different technological

devices exhibit the same pattern (Figure 2). First, there is an initial elastic phase with stiffness K_1 until the activation force of the dissipator is reached, denoted by F_A. Section A-B represents the plastic phase with a stiffness K_2 smaller than the elastic section OA. At the end of the test, the system behaves like a single cable, and follows the hardening branch BC (Castanon, 2017).

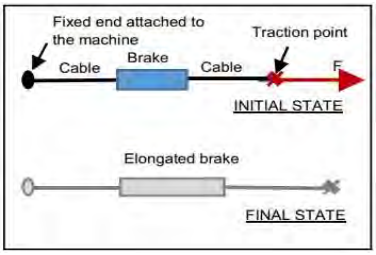

Figure 1. Quasi-static test on dissipator (Castanon, 2017)

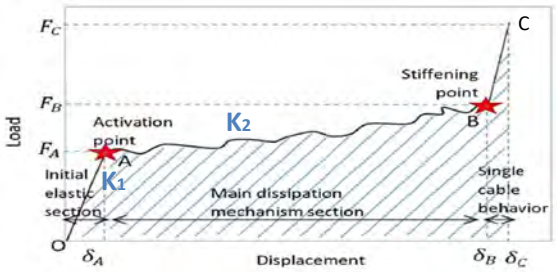

Figure 2. Typical behavior of dissipator under QS loading (Castanon, 2017)

In fact, the impact velocity during the real case of rockfalls (5-30 m/s) leads to a loading rate on the dissipator much higher than the loading rate during the quasi-static test (0.002 m/s). Hence, it is relevant to incorporate dynamic tests to assess the behavior of dissipators under loading closer to the real conditions. This was demonstrated through full barrier tests and on other site cases, which revealed unexpected results where dissipators may not activate as anticipated (Peila, 1998).

Behavior of Dissipator Under Dynamic Loading

The dynamic tests reported in the literature to analyze the mechanical behavior of dissipators can be divided into two types:
a) Type 1: Local test performed on the dissipator only by releasing a block from a certain height to load one end of the dissipator at a certain velocity (Figure 3) (C2ROP, 2019).
b) Type 2: Full scale test performed on the whole structure (Figure 4) (Fulde, 2013).

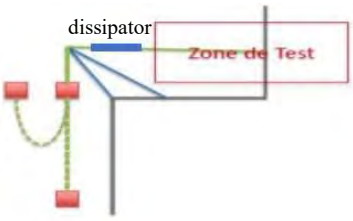

Figure 3. Local dynamic test on dissipator, type 1(C2ROP, 2019)

Figure 4. Full scale impact test, type 2 (Fulde, 2013)

The general behavior of a dissipator under dynamic testing is presented in figure 5.

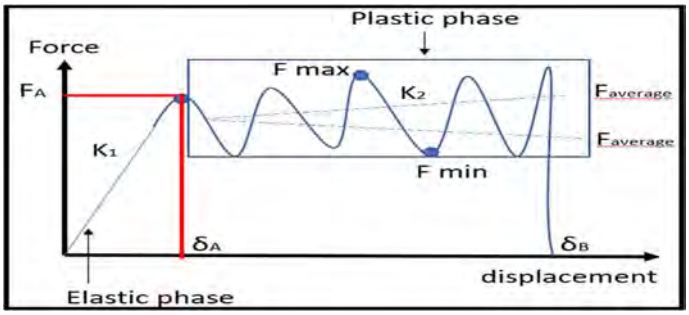

Figure 5. Typical response of dissipator under dynamic testing

The behavior of the dissipator in the initial phase is elastic (activation force F_A, elastic displacement δ_A and constant stiffness K_1). When the activation force is reached, the dissipator enters the plastic phase represented by fluctuations with minimum and maximum values (F_{min} and F_{max}), and average force value ($F_{average}$) increasing (Dugelas, 2020) or decreasing (Trad, 2013) depending on the dissipation mechanism.

Dynamic Effect

In the C2ROP national project, the friction dissipator represented in figure 6 (cross-section shown in figure 7) was studied. Three similar quasi-static tests were performed at a velocity of 0.002 m/s as shown in figure 1. Moreover, three similar dynamic tests were performed by releasing a 480 kg block from a height of 5 m to load the dissipator with a velocity of 10 m/s as shown in figure 3 (Olmedo 2019). The force-displacement curves of the dissipator under quasi-static and dynamic tests are shown in figures 8 and 9 respectively.

Figure 6. Friction dissipator (Dugelas, 2020)

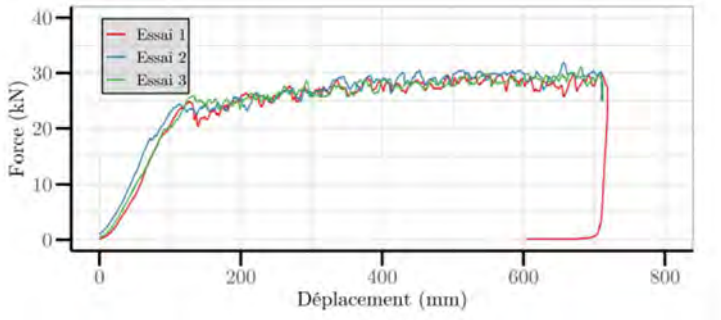

Figure 8. Response of friction dissipator to quasi-static tests (Dugelas, 2020)

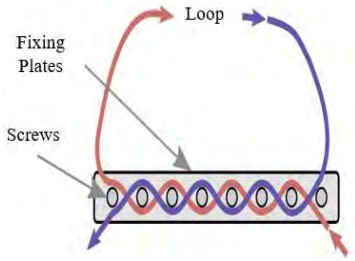

Figure 7. Friction dissipator section schema (Dugelas, 2020)

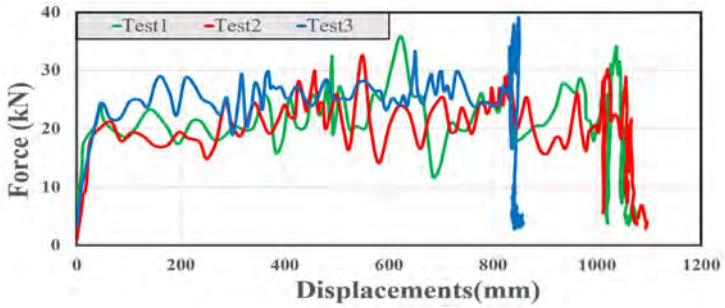

Figure 9. Response of friction dissipator to dynamic tests

Referring to figure 9, variability exists in the dynamic behavior of the dissipator. The parameters shown in figure 5 are compared between the three dynamic tests as shown in table 1. This comparison indicates that the dynamic behavior of dissipators could differ during similar impact events.

The dynamic effect is also detected when comparing the behavior of dissipator between quasi-static and dynamic tests as shown in table 2. The elastic displacement is 3 to 4 times smaller in the dynamic case; therefore, the behavior of the dissipator under dynamic loading is much more rigid. In addition, the activation force in the dynamic case is lower and the plastic displacement significantly increased in the dynamic case.

Table 1. Variability in response of friction dissipator

Parameter	Dynamic test 1	Dynamic test 2	Dynamic test 3	Mean	Relative. STD
F_A (N)	17620	18590	24360	20190	15 %
δ_A (m)	0.027	0.028	0.048	0.034	28 %
K_1 (N/m)	667000	597000	425000	563000	18 %
F_{min} (N)	12000	14000	19000	15000	20 %
F_{max} (N)	34000	30000	39000	34333	11 %
$\delta_A - \delta_B$ (m)	1.043	1.043	0.802	0.962	12 %
K_2 (N/m)	8400	12500	5630	8843	32 %

Table 2. Response of friction dissipator to QS vs dynamic tests

Parameter	QS test	Mean Dynamic	% variation
F_A (N)	25000	20000	-20 %
δ_A (m)	0.1	0.034	- 66 %
K_1 (N/m)	250000	563000	+125 %
F_{min} (N)	23000	15000	-35 %
F_{max} (N)	30000	34333	+14 %
$\delta_A - \delta_B$ (m)	0.6	0.962	+60 %
K_2 (N/m)	7450	8843	+19 %

Conclusion

A friction dissipator was tested from 3 similar quasi-static tests and 3 similar dynamic tests. The results show that variability exists in the dissipator's dynamic behavior in both elastic and plastic phases. Moreover, significant differences in the dissipator's behavior between quasi-static and dynamic tests is observed. The elastic rigidity is higher in the dynamic case and the plastic displacement is higher in the dynamic case too. This indicates that higher load rates affect the behavior of the friction dissipator due to the presence of the dynamic effect. Therefore, the quasi-static approach to assess the friction dissipator's behavior during rockfall events is inaccurate for numerical modelling and design purposes. To go further, it is proposed to perform a series dynamic test of type 1 with impact velocities ranging between 5 to 30 m/s to asses the dynamic behavior of the dissipator more accurately.

References

EOTA. (2018). Falling rock protection kits. EAD 340059-00-0106, 2018/C 417/07. *European organization for technical approavals*.

Zhao, L., Yu, Z. X., Liu, Y. P., He, J. W., Chan, S. L., & Zhao, S. C. (2020). Numerical simulation of responses of flexible rockfall barriers under impact loading at different positions. *Journal of Constructional Steel Research*, *167*, 105953.

Xu, H., Gentilini, C., Yu, Z., Qi, X., & Zhao, S. (2018). An energy allocation based design approach for flexible rockfall protection barriers. *Engineering Structures*, *173*, 831-852.

Dugelas, L. (2020). *Stratégies probabilistes appliquées à la modélisation numérique discrète: le cas des filets pare-pierres* (Doctoral dissertation, Université Grenoble Alpes).

Castanon-Jano, L., Blanco-Fernandez, E., Castro-Fresno, D., & Ballester-Muñoz, F. (2017). Energy dissipating devices in falling rock protection barriers. *Rock Mechanics and Rock Engineering*, *50*, 603-619.

Peila, D., Pelizza, S., & Sassudelli, F. (1998). Evaluation of behaviour of rockfall restraining nets by full scale tests. *Rock mechanics and rock engineering*, *31*, 1-24.

Fulde, M., & Müller, M. (2013). Development of a modular brake element for the use in modern rockfall catchment fences. In *64th Highway Geology SymposiumHighway Geology Symposium*.

Trad, A., Limam, A., Bertrand, D., & Robit, P. (2013). Multi-scale Analysis of an Innovative Flexible Rockfall Barrier. *Rockfall engineering*, 303-342.

Olmedo, I., Chanut, M. A., Douthe, C., Verdet, M., Galandrin, C., Dugelas, L., & Bertrand, D. (2020). Étude expérimentale multi-échelle sur les écrans pare-blocs: comportement des ouvrages hors cadre ETAG27. *Revue Française de Géotechnique*, (163), 8.

Dimensioning of flexible facings: the case of metal grids and nets

Thomas Naudin[1], Franck Servant[2]

[1] Geos Ingénieurs Conseils, Rueil-Malmaison, France
[2] GEOBRUGG, Portes-lès-Valence, France

SUMMARY: In order to develop new slope stabilization methods, Geos Ingénieurs Conseils and Geobrugg are working in partnership to integrate the Ruvolum methods into the GeoSpar and GeoStab design software for reinforced soil structures.
The aim of this partnership is to enable the design of flexible metal mesh facings to be integrated alongside reinforced shotcrete facings, opening up a wider range of design options for designers, builders and project managers.

Keywords: slope stability, flexible facings, metal mesh and netting, design software

State of the art: design of nailed walls

In France and more largely in Europe, the design and execution of reinforced soil structures of the nailed wall type almost systematically involves the installation of a reinforced shotcrete facing. This type of rigid facing offers a number of advantages, including protection of the surface soil against erosion, high mechanical strength and, in some cases, a degree of flexibility with regard to aesthetic constraints, particularly in the case of very steep nailed walls. In addition, these facings have become so commonplace in the design and construction of nailed walls that the calculation methodologies, design tools and construction methods have been mastered by most of those involved in such projects.

The result is the almost systematic use of reinforced shotcrete facings, which are regularly more expensive, more delicate and time-consuming to install, and less environmentally responsible than flexible facings.

However, for many years now, the European execution standard (NF EN 14490) has described the different types of facing that can be used on a nailed soil structure.
EAD 230025-00-0106, which is better known in the world of natural hazards, was explicitly published to set out the requirements for the use of flexible facings.

This led to a partnership between GEOS Ingénieurs Conseil (a geotechnical engineering consultancy) and GEOBRUGG (a manufacturer of high-strength steel nets) to develop tools for integrating flexible facings more consistently into the geotechnical and structural design of nailed walls.
The partnership involves integrating calculation methods from the Ruvolum design tool developed by GEOBRUGG into the GeoSpar software developed by GEOS.

[1]Thomas Naudin, Geos Ingénieurs Conseils, Rueil Malmaison (FRA)
[2]Franck Servant, GEOBRUGG, Portes-lès-Valence (FRA)

Ruvolum and GeoSpar/GeoStab methodology

The Ruvolum dimensioning tool provides internal justification of the facing. It provides an estimate of the behavior of the soils behind the facing, the forces on the head of the nails, on the fastening system to the facing and on the cladding between the nails in order to propose a suitable flexible cladding system.
This tool can be used independently in the event of skin failure or shallow surface instability (generally flat sliding), or as a complement to a general stability study to justify the facing.
The proposed design complies with EAD 230025-00-0106, and the free choice of safety and weighting coefficients allows compliance with the standards of the various countries (justification in accordance with the checks required by standard NF P 94-270).

GeoSpar is a software for dimensioning nailed wall facings. It can be used to design reinforced shotcrete facings (section of mesh, thickness of concrete, size of support plates, etc.). The software works in conjunction with GeoStab, which provides the tensile forces applied by the inclusions to the facing.
GeoSpar can be used for dimensioning in accordance with BAEL, NF EN 1992 or XP-NF 94-240.

Ruvolum works in the opposite way to GeoSpar. The former imposes a type of facing and determines the permissible stresses on it, while the latter imposes stresses on the facing for dimensioning purposes.

Case study: nailed wall in Francheville, France

Here we illustrate the advantages, in terms of both design and construction, of using a flexible facing as part of a project to build a soil nailed wall in Francheville, on behalf of the Métropole du Grand Lyon.

The project involves restoring an unstable slope by building a nailed wall. The wall varies in height from 1.5 m to 3 m and is 83 m long.
The head of the slope is made up of sandy-gravelly fill of very low mechanical strength, resting on more or less weathered gneiss.

The nailed wall requires the use of two beds of nails, spaced 2 m apart horizontally and vertically, inclined at 25° and 2 m long.
These nails apply a load to the facing of 15.5 kN for the first bed and 32.5 kN for the 2nd bed.

The design of the rigid facing, in shotcrete, was carried out using GeoSpar software. The wall is reinforced with two layers of ST15C mesh embedded in 200 mm of shotcrete. The nail support plates measure 200 mm x 200 mm x 15 mm.

[1]Thomas Naudin, Geos Ingénieurs Conseils, Rueil Malmaison (FRA)
[2]Franck Servant, GEOBRUGG, Portes-lès-Valence (FRA)

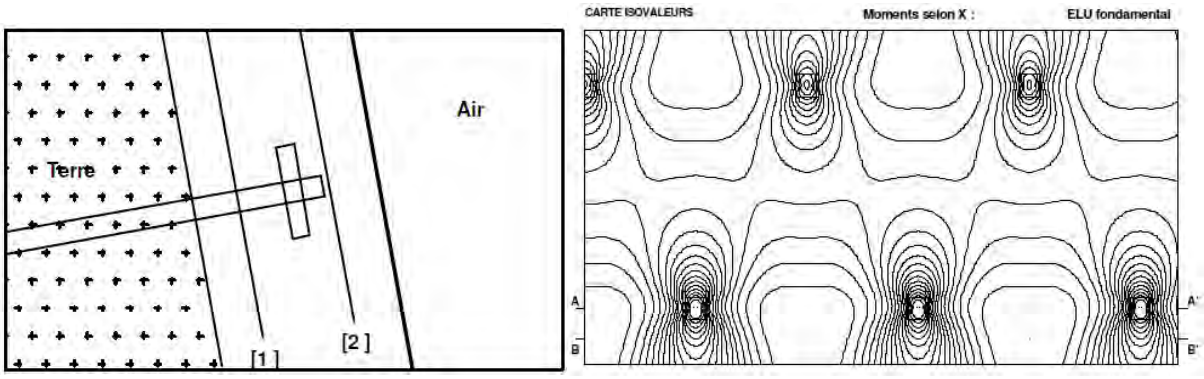

Figure 1. Scheme of the Geospar software (left) and bending moment isovalue result (right)

A redesign of the structure using the Ruvolum calculation module, taking into account the installation of a high-strength metal mesh of TECCO G45/2 type and support plates of P33 type, enables the structure to be verified.

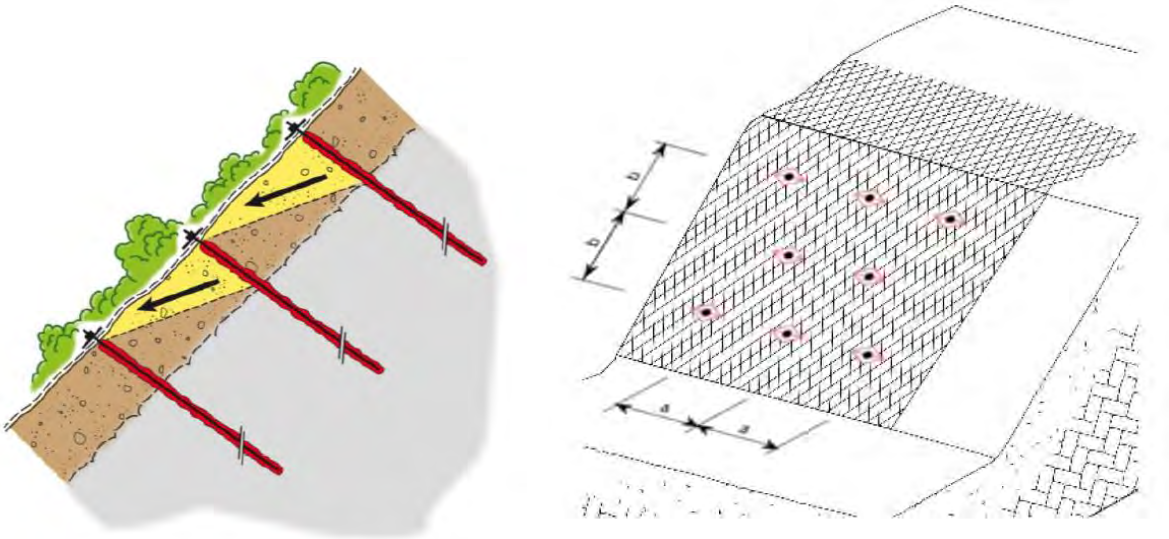

Figure 2. Scheme of the Ruvolum tool (left) and designed facing illustration (right)

To compare the quantities of materials, we take a 2.25m high facing in average and 1/2.25m² pattern of nails. For the facing, as the nail system has not been changed:

- A square plate 200mm x 200mm x 15mm is 4.65 kg weight, and a spike plate P33 is 2.2kg. Hence for 83 support plates, a benefit of 203.3 kg of steel with the flexible facing solution.
- The 2 layers of ST15C welded mesh weigh 4.4 kg/m² instead of 1.1 kg/m² for the layer of TECCO G45/2. Hence a benefit ratio of 4 for the flexible facing solution.
- Additionally for the rigid facing, the 200 mm thickness involve a volume of 37 m^3 of concrete.

Which represents a saving of 19 600 €, or 65% of the facing soil nailed wall price.

Concerning the work time for this part of the soil nailed wall, the concrete facing would take 5 working days instead of 1 day for the flexible facing installation.

[1]Thomas Naudin, Geos Ingénieurs Conseils, Rueil Malmaison (FRA)
[2]Franck Servant, GEOBRUGG, Portes-lès-Valence (FRA)

Conclusion

Although flexible facings cannot be used in all conditions because of their deformability (aesthetic or space criteria) and the need for a soil with short-term cohesion, it seems essential to incorporate them into the geotechnical design of nailed walls.
As we have seen, the use of this type of facing can make an effective contribution to optimizing a retaining wall project, both financially and in terms of time.
In addition, the use of flexible facings made entirely of steel helps to limit concrete consumption on a project. With current project issues moving more and more towards eco-responsible design, it is the responsibility of all those involved in a project (designers, builders and contractors) to identify and apply the measures most likely to limit the carbon footprint and material consumption of the works.

References

Eric Vermoote (2014) Manuel d'utilisation – GeoSpar 2014
GEOBRUGG (2023) Ruvolum Manual
NF EN 14490 (2010) Execution des travaux géotechniques spéciaux – Clouage
NF P 94-270 (2020) Calculs géotechnique – Ouvrages de soutènement – Remblais renforcés et massifs en sol cloué
EAD 230025-00-0106 (2016) Flexible facing systems for slope stabilization and rock protection

[1]Thomas Naudin, Geos Ingénieurs Conseils, Rueil Malmaison (FRA)
[2]Franck Servant, GEOBRUGG, Portes-lès-Valence (FRA)

Tracking the precursory movements of an unstable rock column within 3D point clouds to understand its deformation mechanism in the context of the Séchilienne landslide

Marie-Aurélie CHANUT[1], Laurent DUBOIS[2]

[1] Cerema, Team GéoCoD, 25 avenue François Mitterrand, Bron, France
[2] Cerema Centre-Est, Département Risques Infrastructures et Matériaux, 25 avenue François Mitterrand, Bron, France

SUMMARY: On the cliff above the Séchilienne landslide, an unstable rock column was detected with a slow rate of evolution. Monitoring using a terrestrial laser scanner and an innovative method for calculating low-amplitude 3D displacements of the same order of magnitude as the measurement noise are used to characterize the column's 3D movement. On the basis of these results, the deformation mechanisms of the column and the well-known landslide can be compared and the overall behaviour established**.**

Keywords: Séchilienne landslide, 3D point cloud, L-ICP method, cloud-cloud comparison, sliding mechanism

Introduction of the study site

The Séchilienne landslide is located in the French Alps, 20 km southeast of Grenoble in the Romanche valley. It covers an area of about 70 ha (Figure 1-a) and mobilizes a volume of several tens of millions of m^3. The southern mountainside of the Mont Sec, on the south-west edge of the Belledonne massif, forms the active part of the landslide, called "frontal zone" or "les Ruines" (Dubois et al., 2014; Kasperski et al., 2010). An unstable mass in a rocky cliff overhanging the Séchilienne landslide was recently identified (Figure 1-b). It consists of a 500 m^3 column. Its evolution is very slow and a monitoring with 3D point clouds has been set up to track the precursory movement prior to potential failure. The results obtained are thus put into perspective with current knowledge of the Séchilienne landslide, in order to understand the correlation between the two movements and to assess their consistency.

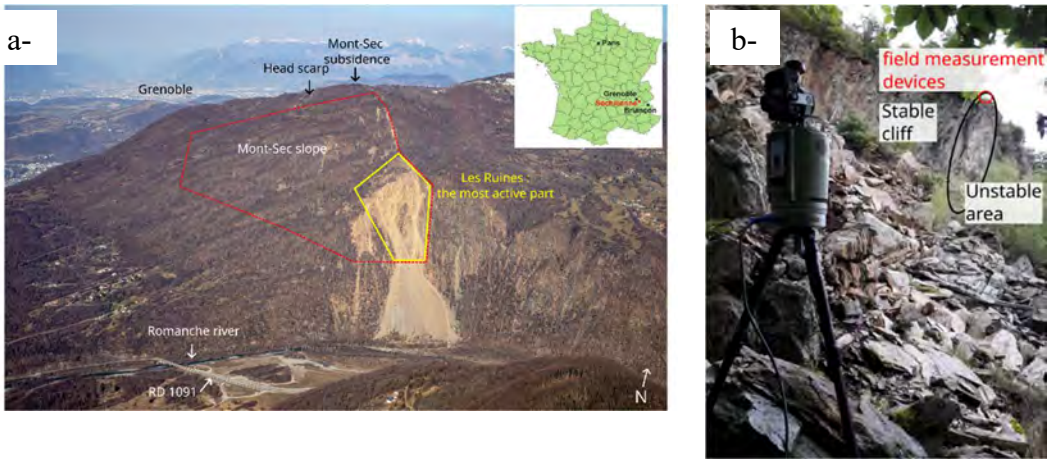

Figure 1. Location of the Séchilienne landslide and the unstable column

Current knowledge of Séchilienne landslide

The Mont-Sec slope is mainly composed of strong micaschists, alternating metamorphic sandstones and siltstones from ancient deposits of the beginning of the Paleozoic era. The schistosity is oriented N20°E (almost perpendicular to the slope direction) with a subvertical dip angle and weakens the mechanical strength of the rock mass. The steep slope (40° on average) and its morphology are inherited from glacial erosion, especially during the Last Glacial Period. The landslide area is crossed by several faults and fracture sets other than schistosity (Kasperski et al., 2010) and shows large-scale signs of deep-seated gravitational slope deformation (DSGSD) on the surface (open fractures, counterscarps, furrows, zones of depletion and accumulation).
Since 1994, the Séchilienne landslide has been studied in depth thanks to several geophysical investigations, boreholes, adits and monitoring (Alfonsi et al., 2004; Guglielmi et al., 2002; Kasperski et al., 2010; Le Roux et al., 2011; Meric et al., 2005). In particular, Kasperski et al. (2010) proposes a landslide failure mechanism of toppling of huge blocks separated by fractures almost parallel to the slope direction with a very high upstream dip and an average spacing equal to 25 m.

a-

b-

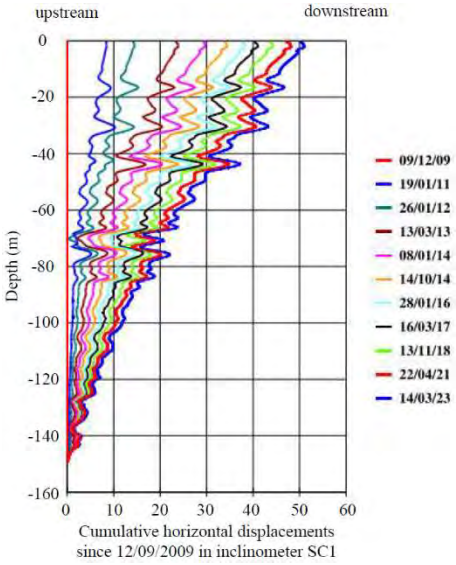

Figure 2. Inclinometer SC1: a- in situ measurements, b- cumulative horizontal displacements since 09/12/2009

Two 150 meter deep vertical boreholes called SC1 and SC2 were carried out in 2009 and 2010 immediately west of the most active part of the landslide (Figure 1). Inclinometer tubes were installed in this boreholes and regular measurements of cumulative horizontal displacements were made with the same inclinometer probe (Figure 2 a). The total displacements of the top of the inclinometers tubes were controlled in parallel by geodetic measurements. Fox example, the maximum horizontal displacement in the SC1 inclinometer tube reached 51 cm on March 2023 almost 14 years after the beginning of measurements, i.e. an average velocity equal to 4 cm per year (Figure 2 b). The lower part of this tube between 128 m depth and 150 m depth can be considered stable and the upper part between the surface and 128 m depth shows a complex toppling movement. The subsidence movement of the top of the SC1 inclinometer was equal to 17 cm between November 2010 and November 2023. These in-situ measurements reveal a deep block-flexural toppling deformation mechanism without basal failure plane, supporting the hypothesis of Kasperki et al. (2010).

Movement of the unstable column deduced from 3D point clouds analysis

More recently, ten terrestrial scanner laser acquisitions of an unstable column overhanging the Séchilienne landslide were carried out at various time intervals between December 2019 and March 2022 from approximately the same acquisition point. The resolution of the scans ranges between 1 and 3 cm. An innovative method developed to track the small displacements is used by comparing a series of 3D point clouds: the L-ICP method (Chanut et al., 2023) is based on a local ICP registration of nearby point clouds to determine the 3D displacement, i.e. both the value and direction of the movement. The aim of local registration is to locally follow the same geometric pattern from one point cloud to another. Using this method, significant displacements are observed, exceeding the level of detection (LoD). During the first period (December 2019-January 2020), the mean displacement of the unstable column is 2.1 mm (Figure 3 a et b) while the LoD is 1.4 mm. It should be noted that the displacement exhibits similar values with seasonal variations (acceleration during winter and spring, slowdown during the summer and autumn). Cumulative displacement over the first six months is equal to 7.4 mm (December 2019 - June 2020) and reachs 9.9 mm over the first year (December 2019 - December 2020). From the 3D components of the displacements, the dip and direction in relation to the x-axis of the computed displacements can be calculated (Figure 3 c). A preferential direction appears on the entire column with slight variations as a function of time for the dip (box length less than 16°) and a relative regularity for the direction (Figure 3 d). Dip values vary between -25° and -45 ° during the study period and the directions vary between -45° and -64°. The 3D displacements values and directions are constant along the column, with no gradient from bottom to top. We also observe a rigid translational movement, allowing us to identify a sliding mechanism rather than a toppling deformation mechanism (Figure 3 e).

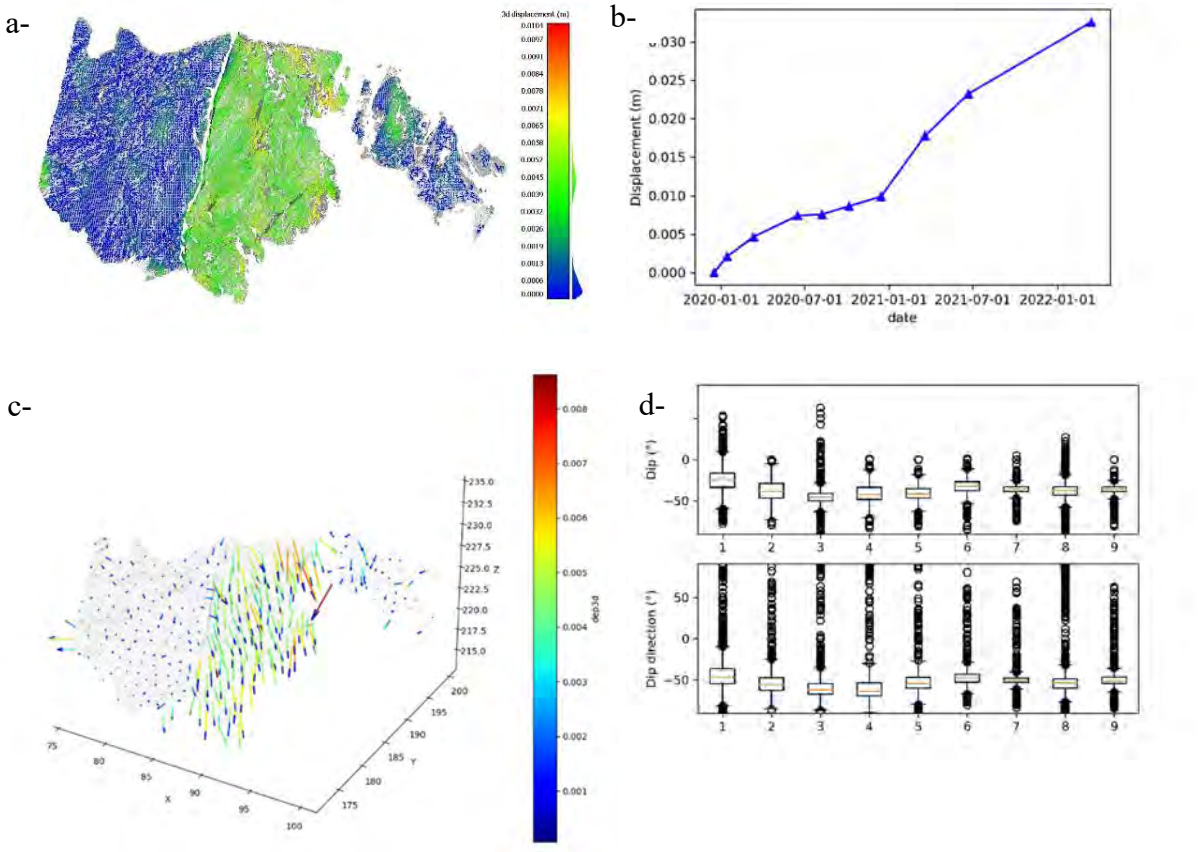

e-

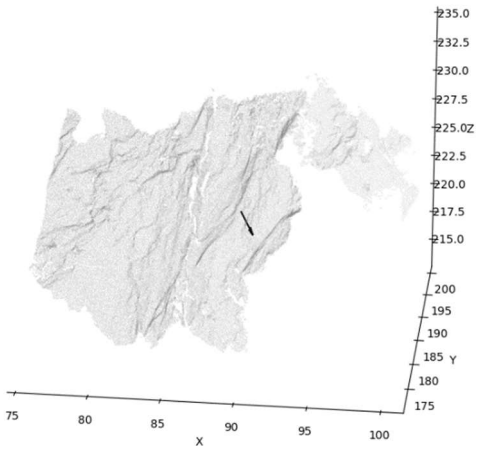

Figure 3. 3D displacements of the column derived by the L-ICP method : a- spatial results for the period 17/12/2019-12/03/2020, b- mean displacement value of the column during the time, c- 3D displacements for the period 17/12/2019-12/03/2020, d- dip and direction in relation to the x-axis during the time, e- sliding mechanism

Discussion and conclusion

At the top of the frontal zone, the most active part of the Séchilienne landslide, deep block-flexural toppling is responsible for large horizontal and vertical displacements. Between July 2011 and April 2023, the horizontal displacement of a differential GNSS receiver installed by Cerema was equal to 7.08 m, and its vertical displacement equal to 7.55 m. The subsidence movement of the top of the frontal zone weakens the earth stop at the base of the monitored column, allowing it to slide progressively downstream on a discontinuity surface (or on two discontinuity surfaces according to a wedge failure) that is still invisible. There is also a good temporal match between the seasonal variations in the movements of the frontal zone and the monitored column, confirming the existence of a close relationship between the two landslides.

References

Alfonsi, P., Durville, J.-L., Potherat, P., 2004. The morphology of deep-seated slope deformations: simple explanations or sophisticated interpretations ?, in: Proceedings of "Landslides: Evaluation and Stabilization." Presented at the IX International Symposium on Landslides, Lacerda, Ehrlich, pp. 1111–1117.

Chanut, M.-A., Peru, Y., Faillettaz, J., Dubois, L., Carotte, A., Azemard, P., 2023. Detecting rockfall precursory movements in 3D point clouds using a new method based on a local ICP registration, submitted.

Dubois, L., Chanut, M.-A., Duranthon, J.-P., 2014. Amélioration continue des dispositifs d'auscultation et de surveillance intégrés dans le suivi du versant instable des Ruines de Sechilienne. Géologues 182, 50–55.

Guglielmi, Y., Vengeon, J., Bertrand, C., Mudry, J., Follacci, J., Giraud, A., 2002. Hydrogeochemistry: an investigation tool to evaluate infiltration into large moving rock masses (case study of La Clapière and Séchilienne alpine landslides). Bull. Eng. Geol. Environ. 61, 311–324. https://doi.org/10.1007/s10064-001-0144-z

Kasperski, J., Delacourt, C., Allemand, P., Potherat, P., Jaud, M., Varrel, E., 2010. Application of a Terrestrial Laser Scanner (TLS) to the Study of the Séchilienne Landslide (Isère, France). Remote Sens. 2, 2785–2802. https://doi.org/10.3390/rs122785

Le Roux, O., Jongmans, D., Kasperski, J., Schwartz, S., Potherat, P., Lebrouc, V., Lagabrielle, R., Meric, O., 2011. Deep geophysical investigation of the large Séchilienne landslide (Western Alps, France) and calibration with geological data. Eng. Geol. 120, 18–31. https://doi.org/10.1016/j.enggeo.2011.03.004

Meric, O., Garambois, S., Jongmans, D., Wathelet, M., Chatelain, J.L., Vengeon, J.M., 2005. Application of geophysical methods for the investigation of the large gravitational mass movement of Séchilienne, France. Can. Geotech. J. 42, 1105–1115. https://doi.org/10.1139/t05-034

Main advances and perspectives in high mountain permafrost and steep rock slope failure research in the French Alps

Florence Magnin[1], Ludovic Ravanel[1], Matan Ben-Asher[1], Josué Bock[1], Maëva Cathala[1], Philip Deline[1], Jean-Yves Josnin[1], André Revil[1]

[1] EDYTEM, Université Savoie Mont-Blanc, CNRS, Chambéry, France

SUMMARY: Steep rock slope permafrost has started almost 2 decades ago in the French Alps, following pioneer studies in the Switzerland. Most investigations have been carried out in the Mont Blanc massif, notably with systematic rockfall inventories since 2007, permafrost monitoring with temperature boreholes and both statistical and physic-based model developments to map permafrost, to address its evolution through time and to assess its role in steep rock slope failures. This communication will sum up the main advances and perspectives of these first decades of research.

Keywords: rock wall, permafrost, high mountain, French Alps, rockfall

Introduction

Steep rock slope permafrost investigations have started right after the hot wave of summer 2003 that struck the European Alps and was marked by remarkably numerous rockfalls (Gruber et al., 2004). Swiss geomorphologists have inferred that these rockfalls were most likely triggered by permafrost degradation (*i.e.* the thawing of ground that remains permanently below 0°C). They thus started to investigate rock wall permafrost by installing temperature sensors and developing specific statistical and heat transfer models to address permafrost distribution and evolution at various time and space scales (*e.g.* Boeckli et al., 2012; Noetzli et al., 2007). In parallel, laboratory analyses have been developed to better assess the mechanical behaviour and properties of frozen bedrock and ice-filled discontinuities in rock (Krautblatter et al., 2013), renewing former engineering and periglacial geomorphology investigations from the 1970s and 1980s.

The most straightforward explanations to link rockfall occurrence and permafrost degradation considers that (i) the thickening of active layer (i.e. the thickening of the near-surface layer that stands above permafrost and that freezes and thaws every year) during hotter summers causes the melting of ice-filled fractures and the loss of bonding at the rock-ice interface in fractures in the one hand, and (ii) that the warming of the permafrost body below the active layer decreases the shear resistance of ice-filled joints in the other hand. A large part of the existing observations and models confirm the role of these two processes in rock wall destabilisation, but many observations also show more complex processes linking permafrost dynamics and rock slope failure (e.g. Fischer et al., 2010). In this communication, we will demonstrate that the increasing frequency of rockfalls in high mountain is clearly linked to permafrost degradation processes, but that a wealth of mechanisms can be involved, challenging hazard understanding and assessment.

Exploring statistical relationship between permafrost dynamics and rockfalls

Rockfalls have been inventoried in the Mont Blanc massif since 2007 thanks to a network of trained observers (mountain guides, hut keepers, etc.). Between 2007 and 2021, 1389 rockfalls have been recorded with precise coordinates, and for many of them, date of failure, scar depth

and surface areas have been determined. Preliminary analysis of this rockfall database reveals an evident link with the thawing season (96% of rockfalls occurred between June and September), as well as a strong relation between rock fall frequency and the intensity of summer heat, the hotter the summer the more frequent the rockfalls (Ravanel et al., 2017).
Magnin et al. (2015) mapped rock wall permafrost distribution in the Mont Blanc massif based on a statistical model using Alpine-wide rock wall surface temperature data. The comparison between modelled permafrost conditions and rockfalls distribution (Fig. 1) shows a clear link with permafrost conditions: most rockfalls occurred in negative Mean Annual Rock Surface Temperature (MARST, for the 1981-2010 period), with a peak in rockfall frequency close to 0°C. However, some rockfalls also occurred in positive MARST, which can reflect "sporadic permafrost" conditions (persisting ice-filled fractures in non-permafrost conditions), as well as in cold permafrost condition (MARST < -2°C) which is theoretically assumed as particularly stable.

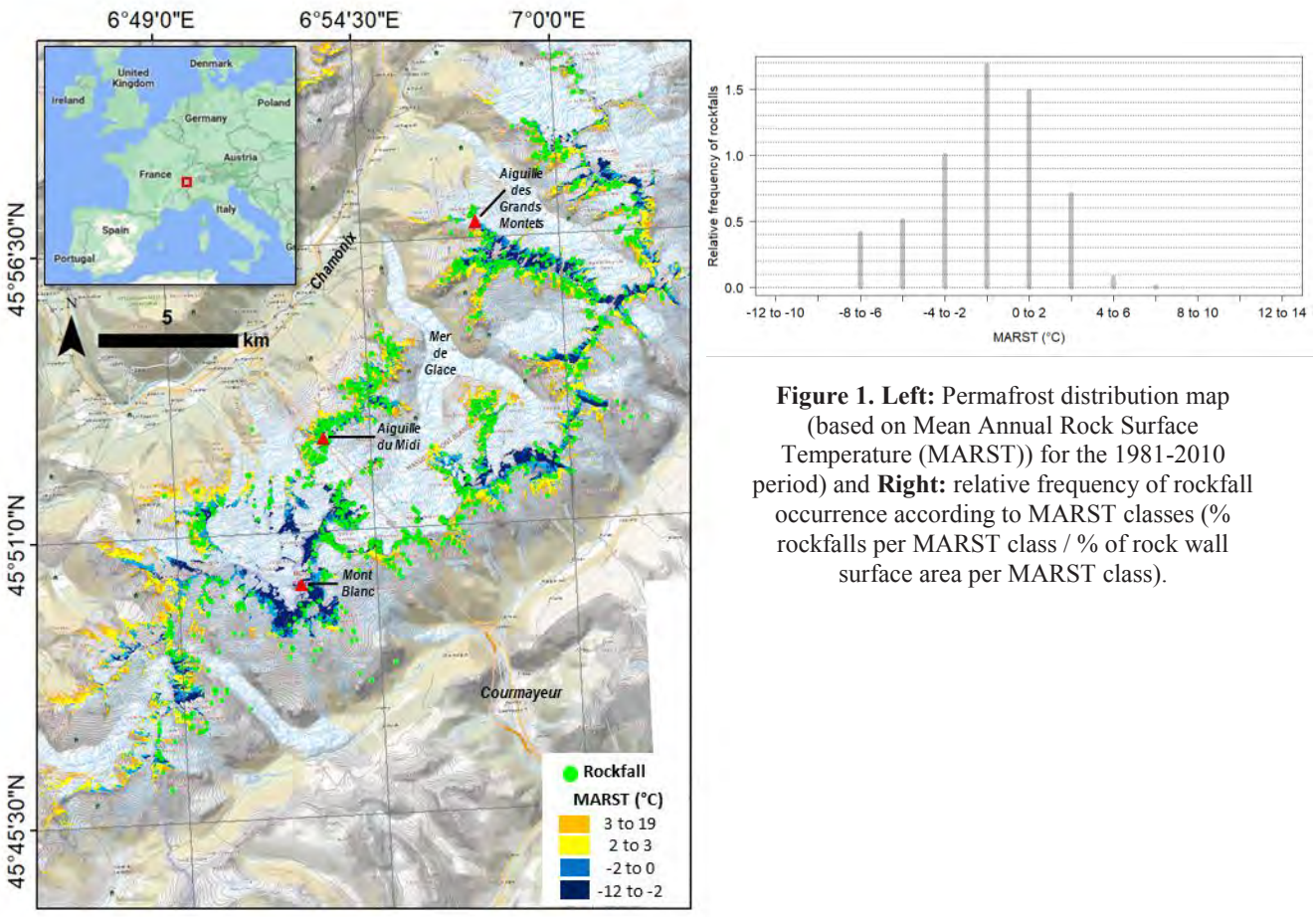

Figure 1. Left: Permafrost distribution map (based on Mean Annual Rock Surface Temperature (MARST)) for the 1981-2010 period) and **Right:** relative frequency of rockfall occurrence according to MARST classes (% rockfalls per MARST class / % of rock wall surface area per MARST class).

Heat transfer model at 209 rockfalls resulted in very promising perspectives to develop rockfall probability forecast that could help mountain practitioners in their risk mitigation strategy (Legay et al., 2021). Futhermore, the relationship between rockfall frequency and permafrost distribution has been recently used to map potential release areas from high mountain rockwall in the French Alps, while the rockfall inventory was further used to calibrate a simple propagation model to map hazardous areas that could be useful in a land-planning perspective (Cathala et al., 2023a).

Cases studies investigations with physic based approaches

To better assess permafrost dynamics that may lead to rock slope failure, several cases studies have been investigated recently in the French Alps using the most updated permafrost modelling approaches. *In-situ* temperature data (generally collected a few cm below the surface) were collected to calibrate or validate energy balance models that allow to reconstruct ground surface temperature (based on SM2-SAFRAN data from *Météo France*) and possible water input from rainfall and snowmelt. Figure 2 illustrates the investigation carried out on a recent rockfall (Fig. 2a) that occurred in the Vallon d'Etache (Maurienne Valley, France) in 2020. Simulated ground surface temperature time series are then used to force heat transfer models in order to assess permafrost conditions and evolution before failure occurred (Fig. 2b). In addition, electrical resistivity surveys can be conducted to better evidence the possible permafrost discontinuity and ice-richness (Fig. 2c).

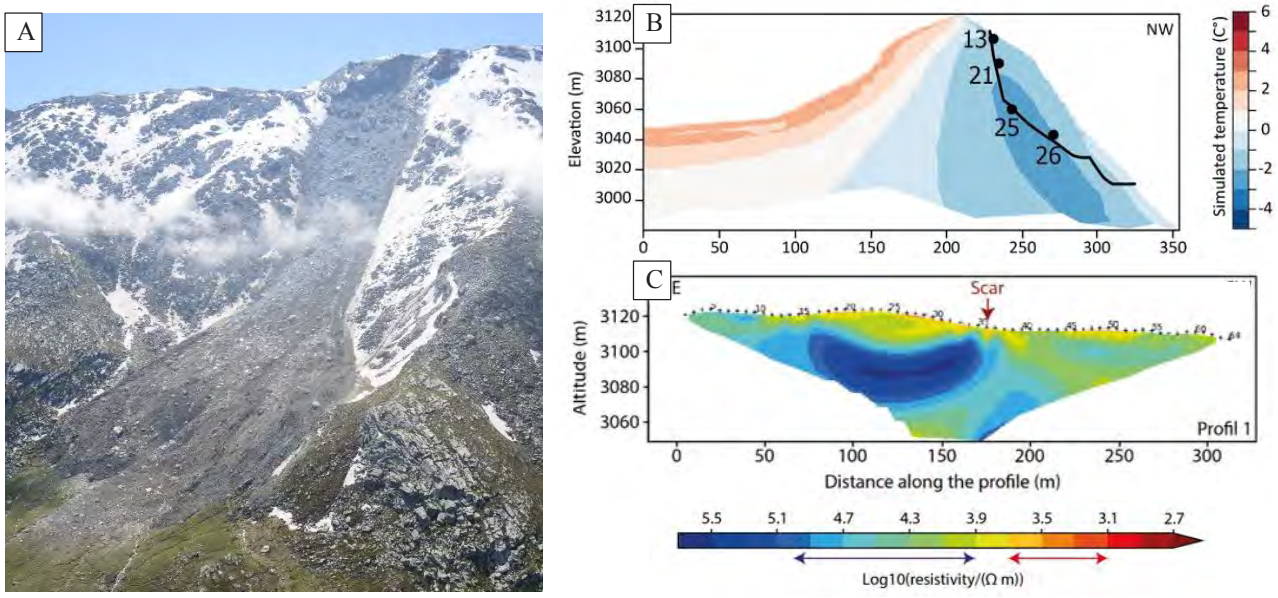

Figure 2. A. The 225,000 m^3 rockfall that occurred on June 18th, 2020 at the Vallon d'Etache (Maurienne Valley, France) from a summit culminating at 3126 m asl. and facing NW. **B**. Modelled ground temperature at the date of failure. The black line marks the scar and the dots are observation point from which temperature evolution has been extracted and will be presented during this communication. **C.** Electrical resistivity tomograms measured along the crest on the backside of the scar. The resistivity values have been fitted against laboratory measurements on local rock samples. The blue arrow represents the range of values covering negative temperature and the red arrow the range of values measured for positive temperature). Highest resistivity values go beyond values measured in the laboratory (down to -20°C) and rather reflect an ice-rich rock matrix rather than extremely cold permafrost conditions.

Analysis of this case study shows that the rockfall has occurred in cold but warming permafrost conditions since 2012, and notably after the warmest winter ever recorded, but also that water infiltration due to heavy precipitation on melting snow may have been a determinant factor in its triggering (Cathala et al., 2023b). Laboratory experiments have revealed that water infiltration in ice-filled cleft can locally accelerate the degradation of permafrost and cause ice-cleft erosion (Hasler et al., 2011). In addition, water infiltration could also cause high hydrostatic pressures that are favored by the ice-sealing (Fisher et al., 2011). However, deciphering the respective roles of these water related-processes remain challenging. To tackle these upcoming challenges, efforts are conducted to explicitly account for water infiltration in

realistic fracture networks to better assess its the thermal and mechanical implications (Magnin and Josnin, 2021) and to develop geophysical approaches that could allow to better assess the ground ice content..

Conclusion

Over the past 2 decades of high mountain steep rock slope permafrost investigations, a wealth of data has been collected and advance methods have been developed to better assess the role of permafrost in rock slope destabilization. There are clear evidences of the link between permafrost distribution and dynamics and rockfalls occurrence but various permafrost processes may be involved. Development of permafrost maps and rockfall inventory has allowed to evidence the link between close to 0°C permafrost and high rockfall frequency, leading to interesting perspective for risk assessment. Analysis of a rock avalanche cases-tudy in the Vallon d'Etache reveals the high complexity of possible triggering processes, that involves warming permafrost but also water infiltration. To better address the role of water infiltration in permafrost dynamics and rock slope destabilization, the recent development in physics-based approaches (modelling, geophysics) appears as the most promising perspective.

References

Gruber S, Hoelzle M & Haeberli W (2004) Permafrost thaw and destabilization of Alpine rock walls in the hot summer of 2003. Geophysical Research Letters 31. https://doi.org/10.1029/2004GL020051

Boeckli L, Brenning A, Gruber S. & Noetzli,J (2012) A statistical approach to modelling permafrost distribution in the European Alps or similar mountain ranges. The Cryosphere 6, 125–140. https://doi.org/10.5194/tc-6-125-2012

Noetzli J, Gruber S, Kohl T, Salzmann N & Haeberli W (2007) Three-dimensional distribution and evolution of permafrost temperatures in idealized high-mountain topography. Journal of Geophysical Research: Earth Surface 112. https://doi.org/10.1029/2006JF000545

Krautblatter M, Funk D & Günzel FK (2013) Why permafrost rocks become unstable: a rock–ice-mechanical model in time and space. Earth Surface Processes and Landforms 38, 876–887. https://doi.org/10.1002/esp.3374

Fischer L, Amann F, Moore JR & Huggel, C (2010) Assessment of periglacial slope stability for the 1988 Tschierva rock avalanche (Piz Morteratsch, Switzerland). Engineering Geology 116, 32–43. https://doi.org/10.1016/j.enggeo.2010.07.005

Ravanel L, Magnin F & Deline P (2017) Impacts of the 2003 and 2015 summer heatwaves on permafrost-affected rock-walls in the Mont Blanc massif. Science of The Total Environment 609, 132–143. https://doi.org/10.1016/j.scitotenv.2017.07.055

Magnin F, Brenning A., Bodin X, Deline P & Ravanel L (2015) Statistical modelling of rock wall permafrost distribution: application to the Mont Blanc massif. Géomorphologie : relief, processus, environnement 20.

Legay A, Magnin F & Ravanel L (2021) Rock temperature prior to failure: Analysis of 209 rockfall events in the Mont Blanc massif (Western European Alps). Permafrost and Periglacial Processes 32, 520–536. https://doi.org/10.1002/ppp.2110

Cathala M, Magnin F, Ravanel L, Dorren L & Zuanon N, Berger F, Bourrier F & Deline P (2023) Mapping release and propagation areas of permafrost-related slope failures in the French Alps. Geomorphology, *in press*

Cathala M, Bock J, Magnin F, Ravanel L, Ben-Asher M, Astrade L, Bodin X, Chambon G, Deline P, Faug, T, Genuite K, Josnin J-Y, Revil A & Richard J (2023b) Triggering and runout conditions at a permafrost-affetcte rock avalanche site in the French Alps (Etache, June 2020). Earth Surface Processes and Landforms, *In review*

Magnin F & Josnin J-Y (2021) Water Flows in Rock Wall Permafrost: A Numerical Approach Coupling Hydrological and Thermal Processes. Journal of Geophysical Research: Earth Surface 126, e2021JF006394. https://doi.org/10.1029/2021JF006394

Permafrost Monitoring Using Passive Seismology: Towards Predicting Rock Glacier Dynamics

Antoine Guillemot[1,2], Eric Larose[2], Laurent Baillet[2], Agnès Helmstetter[2], Alexandra Royer[1]

[1] Géolithe Alpes, Géolithe Innov, Crolles, France
[2] ISTerre, Université Grenoble Alpes, Université Savoie Mont-Blanc, CNRS, IRD, Université Gustave Eiffel, France

SUMMARY: A seismic instrumentation has been deployed for several years at Gugla, Tsarmine (Valais, Switzerland) and Laurichard (Hautes-Alpes, France) active rock glaciers. Seismic noise methods have been applied to compute daily relative change in velocity of seismic waves (called dV/V) which is directly linked to the elastic properties (stiffness or density) of the surveyed subsurface. For the three sites studied, seasonal variations of shear stiffness have been measured. We located these variations in depth by using a 1D inversion scheme. We correlated them to both thermal and hydrological forcings, highlighting the role of water content which induces rapid decrease in stiffness into the whole rock glacier body during melting periods.
Also, we developed a viscoelastic model to reproduce observed seasonal variations of the kinematics. By using observed shear stiffness as a parameter varying over time, this semi-empirical model reconstructs well the creep rates observed. In the long term, a pluriannual seismic monitoring allows to detect changes in ice content, by tracking changes in mechanics within a large volume. Such permanent instrumentation paves thus the way to predict rock glacier dynamics.

Keywords: permafrost, rock glacier, passive seismology, mechanics, viscoelasticity

Introduction

Among superficial mountain permafrost landforms, active rock glaciers can reach surface velocities of several m/yr. When connected to gullies, active and destabilized rock glaciers may generate debris flows as they supplied a significant volume of rock debris, causing emerging hazards (Kummert et al., 2021). Since decades, rock glaciers are then monitored to assess their kinematics, dynamics and potential destabilization. As a complement to active geophysical methods for investigating the subsurface, and to in-situ and remote sensing methods for tracking kinematics of these instabilities, passive seismic instrumentation offers the opportunity of a continuous monitoring in depth.
The influence of external forcings on rock glacier dynamics has then been investigated (Cicoira et al., 2021). Thermo-mechanical modelling is based on heat diffusion calibrated by borehole measurements, and temperature-dependent empirical laws. But a preponderant influence of water at the shear horizon depth is also suspected ((Cicoira et al., 2019). Moreover, a case study reveals an important seasonal variability of ice/water ratio in depth (Phillips et al., 2023).

A study site: the Gugla rock glacier

The Gugla rock glacier is located in the west-oriented side of the Mattertal valley in the south-western Swiss Alps. Its shape reaches approximately 350 m long and a width of about 100 m

separated in its terminal part into a northern part and a steeper southern sector. As its front directly overhangs a steep torrential gully dominating the main valley and the village of Herbriggen, this rock glacier regularly originates debris flows, which threaten railways, road and other human facilities.
Our seismological network monitors the lower part of the rock glacier, in the range from 2570 to 2720 m *asl*, since October 2015. It has been completely described in Guillemot et al. (2019). For this study, only four seismometers (C1 and C4 in the right stable side of the rock glacier, and C2 and C5 on the glacier's longitudinal axis) have been used, for the sake of data availability and data quality. We also performed seismic refraction campaigns, providing cross-section of elastic parameters at depth.
A weather station continuously records snow height, air surface temperature, and precipitation. Surface displacement rate has been derived from two available GNSS sensors.

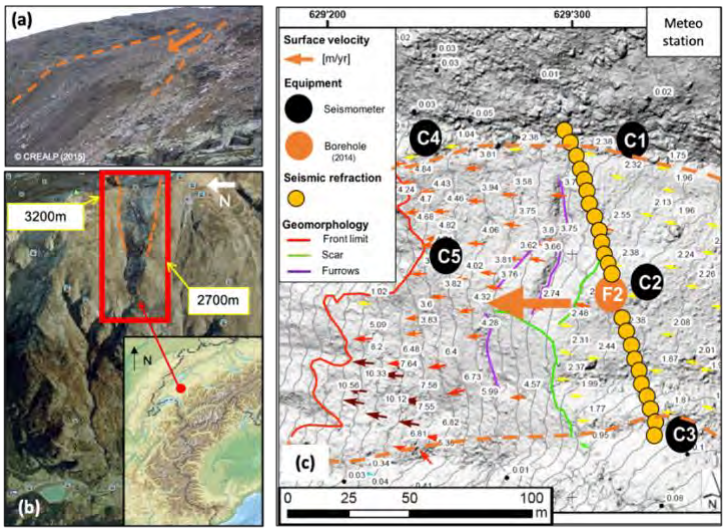

Figure 1: Overview of the Gugla rock glacier study site, adapted from Guillemot et al. (2019). (a) Terminal part of the rock glacier from a webcam image, with its edge limits depicted in orange dashed line. (b) Situation of the study site overhanging the Mattertal valley, with map location in Western Alps. (c) Instrumentation of the terminal part of the rock glacier. The main orange arrow indicates the general direction of the rock glacier displacement downwards.

Methods

First, we aim at computing the relative seismic velocity changes *dV/V* over time, by applying the interferometry method (Sens-Schönfelder & Wegler, 2006) to the coda part of ambient noise cross-correlations from pairs of sensors crossing the rock glacier.
Secondly, in a view of linking surface wave phase-velocity change to shear stiffness variations within the probed medium, we combined the measurements of averaged *dV/V* over frequency with shear-wave sensitivity kernels to reconstruct the shear stiffness variations over depth.
As outputs from our 1D coda wave inversion, we finally obtain depth-dependent *dV/V* over time. These values indicate changes in shear stiffness (quantified by the shear modulus), as changes in density of the medium is negligible over time.
We interpret these temporal shear stiffness fluctuations as a proxy integrating several physical processes acting in depth: freeze-thawing cycles of the active and permafrost layers, together with the infiltration of pressurized water from melting or rainfalls. To validate these interpretations, we analyzed the temporal correlation between seismologic proxies (*dV/V*, microseismic events (microquakes and rockfalls), seismic noise energy) and meteorological, thermal and kinematic data available for each site.

Results

Over years, seasonal variations of seismologic observables are visible, in correlation with freeze-thawing effects. When melting periods occur, bursts of microseismic events (mainly categorized as rockfalls) and drops of *dV/V* are significant.
In Gugla rock glacier, a continuous borehole provides valuable temperature profiles over time, that is correlated to changes in *dV/V* (Figure 2). Thermal diffusion through depth is highlighted, and roughly correlated to seasonal *dV/V* cycles at depth.

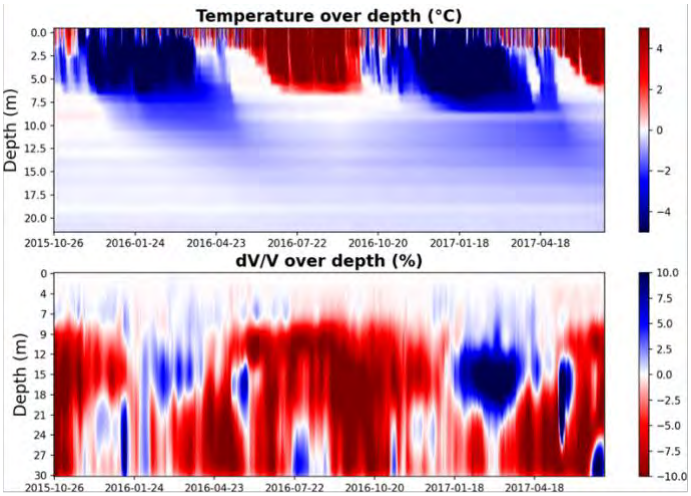

Figure 2: Temperature over depth from borehole measurements (upper panel), and results of dV/V inversion at depth during the same period (lower panel), at Gugla rock glacier.

Discussion

Through these results, the role of melting water is highlighted in rock glacier mechanics. Indeed, thermal diffusion only do not explain solely the diffusion of stiffness variations at depth (several tens of meters in few days) captured by *dV/V* measurements. The rapid fluctuations of the ice-to-water ratio through the highly permeable subsurface is probably the main process explaining the fast response of the elastic properties to environmental forcings. During melting periods, this decrease in shear stiffness occurs at large depth, probably in relation to the shear horizon layer that mostly contains the deformation of the rock glacier.
In a view of rock glacier dynamics modelling, we aim at relating continuous seismological observables (or the proxy of shear stiffness *dV/V*) to rock glacier kinematics measured at one point by GNSS sensors. We use a semi-empirical viscoelastic approach to model rock glacier creeping. As outputs, modelled creep rates evolve also with time, and reproduces well the seasonal variations of observed creep rates both in amplitude and delay (Figure 3). Thus, our approach reinforces the key role of liquid water in rock glacier mechanics.

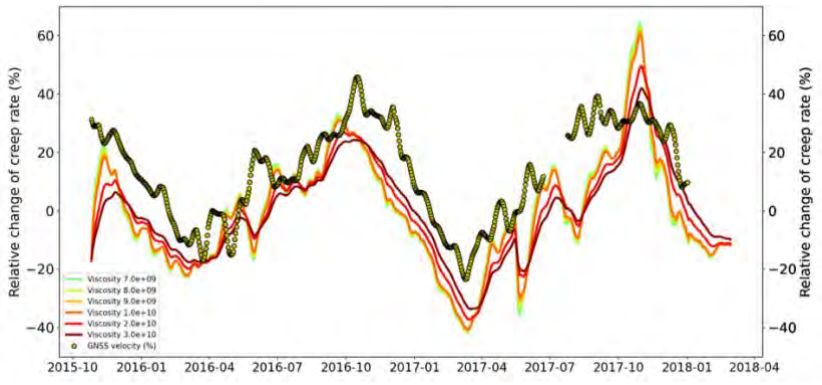

Figure 3: Results of the viscoelastic model for Gugla rock glacier, with observed (yellow dots) and modelled (green to brown curves, depending on the effective viscosity chosen) daily relative change in creep rates.

Based on these results, long-term passive seismic instrumentation can help to improve early warning systems, as a complement to other monitoring methods. While meteorological forecasting and melting models predict liquid water, results from dV/V at depth may quantify the mechanical response of the rock glacier to those water inputs, few days before a potential catastrophic failure. Abnormal rates of rockfalls and quakes can also be detected and used as precursors to debris flows, allowing an anticipative management of debris reservoirs and a preventive evacuation when necessary. Both data transmission and processing workflow should be implemented at the highest time resolution. To this end, a web portal named Evorisk (Figure 4) is already operating for risk managers, testing daily seismological proxies for future monitoring systems.

Figure 4 : Screenshot of the web portal Evorisk, visualizing the results of passive seismic monitoring at Gugla rock glacier.

Conclusion

This study highlights the key role of liquid water in rock glacier mechanics, thanks to a long-term continuous passive seismic instrumentation. We locate variations in shear stiffness over depth at a daily time step, allowing to better constrain the influence of environmental forcings on permafrost sites. We model the dynamics of frozen slopes by using these measurements. This model inverts some dynamic features (the depth and thickness of the layer that most represents the dynamic of the rock glacier, assumed to be the shear horizon), and it reproduces well the seasonality of the creep rates, both in amplitude and phase. A pluriannual seismic monitoring is required to accurately estimate those features about rock glacier creeping

References

Cicoira, A., Marcer, M., Gärtner-Roer, I., Bodin, X., Arenson, L. U., & Vieli, A. (2021). A general theory of rock glacier creep based on in-situ and remote sensing observations. *Permafrost and Periglacial Processes*, *32*(1), 139-153.

Cicoira, A., Beutel, J., Faillettaz, J., & Vieli, A. (2019). Water controls the seasonal rhythm of rock glacier flow. *Earth and Planetary Science Letters*, *528*, 115844.

Guillemot, A., Helmstetter, A., Larose, É., Baillet, L., Garambois, S., Mayoraz, R., & Delaloye, R. (2020). Seismic monitoring in the Gugla rock glacier (Switzerland): ambient noise correlation, microseismicity and modelling. *Geophysical Journal International*, *221*(3), 1719-1735.

Kummert, M., Bodin, X., Braillard, L., & Delaloye, R. (2021). Pluri-decadal evolution of rock glaciers surface velocity and its impact on sediment export rates towards high alpine torrents. *Earth Surface Processes and Landforms*, *46*(15), 3213-3227.

Phillips, M., Buchli, C., Weber, S., Boaga, J., Pavoni, M., & Bast, A. (2023). Brief communication: Combining borehole temperature, borehole piezometer and cross-borehole electrical resistivity tomography measurements to investigate seasonal changes in ice-rich mountain permafrost. *The Cryosphere*, *17*(2), 753-760.

Sens-Schönfelder, C., & Wegler, U. (2006). Passive image interferometry and seasonal variations of seismic velocities at Merapi Volcano, Indonesia. *Geophysical research letters*, *33*(21).

Numerical Terjectography Simulation for Breakable and Multiblock Rockfall

A. RAFIEE[1], F. RADJAI[2], JM. COME[3]

[1] R&D GINGER CEBTP, Grenoble, France
[2] CNRS, University of Montpellier, Montpellier, France
[3] R&D GINGER, Lyon, France

Abstract: Rockfalls are often natural events with potentially catastrophic consequences for human life and infrastructure. Therefore, predicting and correctly estimating their trajectories is essential for their mitigation. Perhaps the most crucial step in a rock instability hazard study is computing the trajectory by taking into account more realistic characteristics of the unstable mass, terrain topography, and the interaction of the slope surface with falling rock blocks. It should be remembered that a block of rock, as a naturally breakable material and in the presence of pre-existing fractures, often breaks into several blocks when it falls due to impact energy. Another scenario to consider is that, in many cases, instability results from a heavily fractured rock mass, causing several blocks to fall simultaneously at the start of the fall. Consequently, it is crucial to take into account the interaction between these fragments, as it can significantly modify the expected trajectories. In this paper, to address three-dimensional studies, we introduce the use of a physics engine integrated with home-made auxiliary codes in a gaming platform as a remarkably suitable alternative method to calculate multi-block rockfall trajectories. Furthermore, the calculation of the trajectory of falling rocks in two-dimensional sections is studied, taking into consideration the phenomenon of fragmentation during the fall. This is achieved through the utilization of a specially designed Discrete Element Method (DEM) code, which takes into account arbitrary particle shapes and their fragmentation by incorporating the concept of fracture energy.

Keywords: Multi-block trajectory, Discrete Element Method (DEM), Fragmentation, Rock fall simulation, Gaming platform

Introduction:

A rockfall is a rapid mass displacement resulting from the detachment of a rock mass from a slope, leading to its descent, rebound, and rolling as it progresses downward (Varnes, 1978). This type of event can involve significant destructive potential due to high speeds and, therefore, significant kinetic energy that rockfalls can generate (Hoek, 2000). During a rockfall, the initial unstable rock mass may be either a single massive block, a set of already detached blocks, or a breakable block due to pre-existing fractures (Matas et al., 2020). Each of these distinct scenarios has the potential to significantly affect the trajectory, speed, and kinetic energy of falling rock particles.

It is noteworthy to mention that a comprehensive and full trajectory analysis forms the main basis for the design of protective structures. Protective structures against rockfall hazards are placed along the potential path of the blocks or close to infrastructures potentially at risk. The design of this type of protective measures typically requires the quantitative prediction of the final travel distance of the rock masses and also a reliable estimate of the bounce height, speed and kinetic energy of the blocks falling along the path. Obtaining reliable estimates of these quantities are complicated by the interaction of the rocks and the surface of the slope which can affect the behavior of the blocks on impacts (Salciarini et al., 2009).

Another highly significant issue that can substantially impact the path of descending rock blocks is the occurrence of fragmentation during their descent or the interaction between individual fragments. Following fragmentation, smaller fragments may attain higher velocities compared to larger ones. The dispersion of energy after breakage remains uncertain, and in certain numerical investigations, there has been no established correlation between the fragment size and its kinetic energy at a specific impact velocity (Ye et al., 2020).

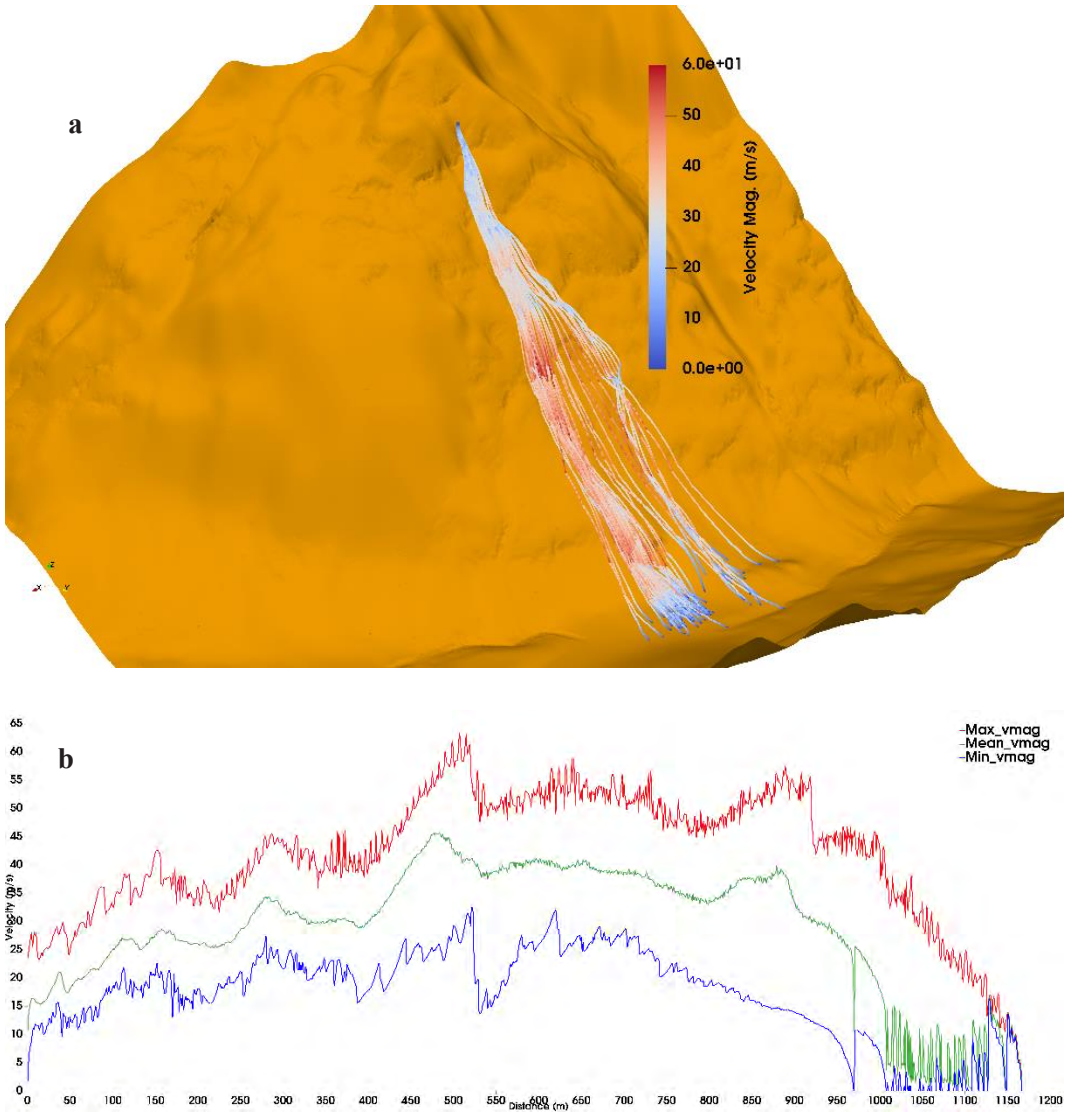

Figure 1. (a) 3D rockfall trajectories for a cube with 100 fragments, (b) the minimum, maximum and average velocity magnitude changes for all those hundred blocks along the falling path.

The present study proposes two approaches in two and three dimensions to obtain a more accurate analysis of rockfall trajectories. These approaches consider various scenarios, including a single rock block, multiple blocks and a breakable rock mass, as well as different analyses needed to get a comprehensive picture of the process.

Numerical simulations:
In this section, a two-phase approach for rockfall trajectory analysis is presented. First, we introduce the use of gaming platforms with real physics calculation to evaluate potential trajectories using real 3D topographic data acquired by photogrammetry or LiDAR scanning. Nowadays, gaming platforms find extensive applications in system simulation and virtual reality (Sala,2018; Hao et al., 2021; Harrap et al., 2019).

Figure 1 illustrates the results of the trajectory analysis on a real topographical surface, using a multi-block simulation in which 100 blocks of different volumes were released simultaneously. In Figure 1a, the calculated trajectories are presented for all these blocks, highlighting the changes in their speed during their descent. Achieving this level of detail and precision required the integration of auxiliary codes into the gaming platform. These codes were specifically designed to assign characteristics such as friction between blocks, blocks and topographic surface, as well as the rebound coefficients and other parameters. A set of auxiliary codes were developed to allow us to track the behavior of each block and record data including speed, kinetic energy, rotation speed, bounce height, etc. It is important to note that the possibility of generating a stochastic fractured rock mass taking into account a network of in-situ fractures is also added and this gives the possibility of simulating the trajectory of a multi-block rockfall as well as a landslide at large scale. Figure 1b shows the range of velocity amplitudes for all blocks within the model, displaying the minimum, average, and maximum values. In the extended presentation of this part of the study, the application of gaming platforms, their high-level possibilities and all developed auxiliary tools will be presented within the framework of some real case studies at different scales.

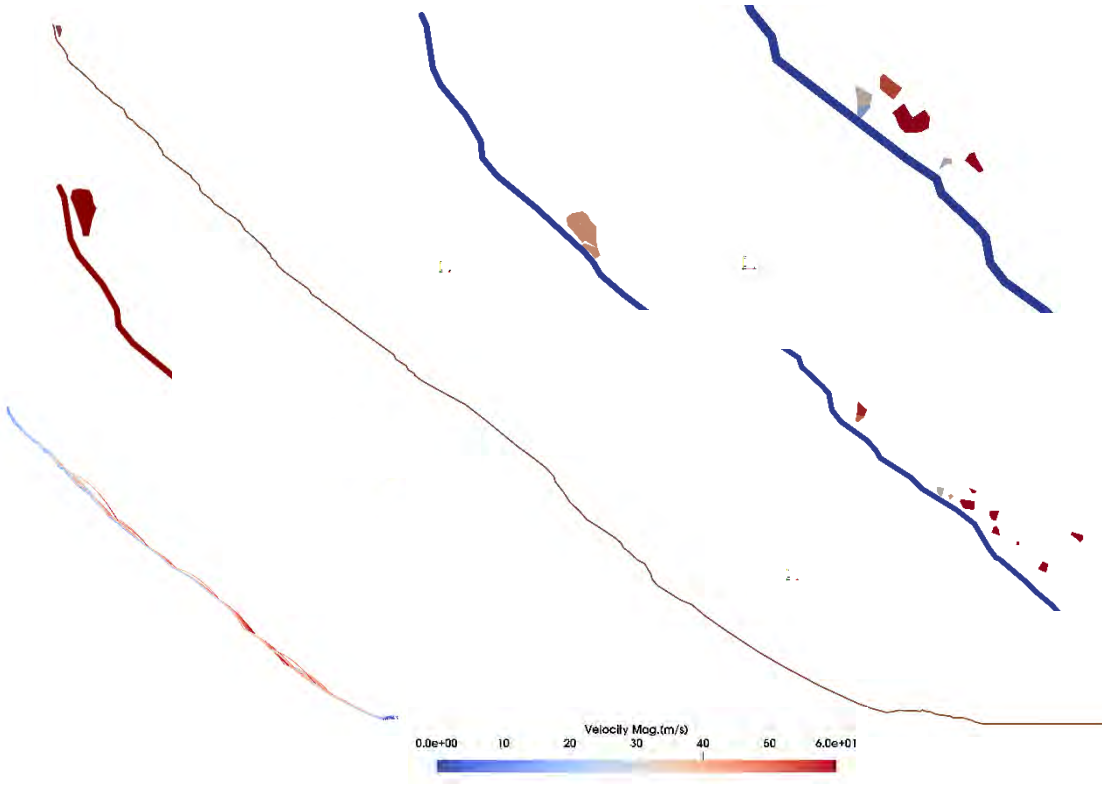

Figure 2 snapshots of a breakable block, 2D rock fall trajectory analysis.

The second section of the study focuses on the introduction of a homemade 2D code by discrete element method (G-DEM2D). The discrete element method can be defined as a method for calculating the dynamics (forces and displacements) of a set of rigid objects by taking into account their interactions. A key feature of the code presented here is its ability to consider diverse object shapes and the option to incorporate various contact laws. This versatility makes G-DEM2D applicable in a range of scenarios, including, but not limited to, rockfall, rock slope stability assessment, masonry structure analysis, and studies on fragmentation. In the extended version of the article, a comprehensive overview of this code will be provided. Here, an application case is presented, which concerns the analysis of rockfall trajectories with a particular emphasis on the behavior of breakable blocks. Figure 2 represents a set of snapshot images of fragmentation of a rock block during a rockfall on a real 2D topography section. This series illustrates how a block can gradually disintegrate during descent due to the impact energy exerted on the block. The trajectories observed for a breakable block are clearly different from those of the same block in the rigid state. In addition, the associated parameters, notably speed, energy and height of passage, present significant disparities and are not directly comparable between these two scenarios. This difference highlights the significant impact of breakage on the behavior of the block and the consequences that result during its descent. Several cases of comparison between different scarios will be presented for real case studies in the full version of the article.

Conclusion:

The initial and crucial step for carrying out a risk assessment arising from rockfall, particularly when determining the need for any type of protective structures, is the trajectory analysis phase, unfortunately often under-estimated. Our objective is to simplify and improve the understanding of the multifaceted nature of different aspects and potential events that could occur during a complex landslide or even during the fall of a single block. The complementary techniques used in this study aim to provide a holistic view of the subject, enabling a more in-depth analysis of the associated complexities. Special emphasis is placed on the complex dynamics of falling blocks, particularly in multi-block scenarios, and on the behavior of breakable blocks.

References:

Hao, W., Jian, H., Xiang, H., Jingqing, Y., Zicheng, H., & Ying, H. (2021, October). A New Rockfall Simulation Tool based on Unity 3D. In IOP Conference Series: Earth and Environmental Science (Vol. 861, No. 3, p. 032059). IOP Publishing.

Harrap, R., Hutchinson, J., Sala, Z., Ondercin, M., & Difrancesco, P. M. (2019). Our GIS is a Game Engine: Bringing Unity to Spatial Simulation of Rockfalls. GeoComputation 2019.

Hoek, E. (2000). Analysis of rockfall hazards. E. Hoek, Practical rock engineering, 117-136.

Matas, G., Lantada, N., Corominas, J., Gili, J., Ruiz-Carulla, R., & Prades, A. (2020). Simulation of full-scale rockfall tests with a fragmentation model. Geosciences, 10(5), 168.

Sala, Z. L. J. (2018). Game-Engine Based Rockfall Modelling: Testing and Application of a New Rockfall Simulation Tool (Doctoral dissertation, Queen's University (Canada)).

Salciarini, D., Tamagnini, C., & Conversini, P. (2009, July). Numerical approaches for rockfall analysis: a comparison. In Proceedings 18th World IMACS/MODSIM Congress, Cairns, Australia (Vol. 25, No. 12, pp. 1729-30).

Varnes, D. J. (1978). Slope movement types and processes. In 'Landslides, analysis and control'. Special Report 176.(Eds RL Schuster, RJ Krizek) pp. 11–33. Transportation Research Board, National Academy of Sciences: Washington, DC.

Ye, Y., Thoeni, K., Zeng, Y., Buzzi, O., & Giacomini, A. (2020). Numerical investigation of the fragmentation process in marble spheres upon dynamic impact. Rock Mechanics and Rock Engineering, 53, 1287-1304.

Numerical simulation of post-failure progress of a Large-scale Landslidein the Bailong River Basin, Western China

Zhen Feng[1], Yang You[2], Liang Chen[1]

[1] China Institute of Geo-Environmental Monitoring, Beijing, China
[2] Chongqing Institute of Geology and Mineral Resources, Chongqing, China

SUMMARY: The Beishan landslide is an ancient landslide situated on the northern bank of the Bailong River in Zhouqu. The landslide has a volume of 2.4 × 10^6 m^3 and the toe of the rupture surface is approximately 700m higher than the river surface. Since the 1970s, the landslide has exhibited continuous deformation. The engineering geological condition and characteristics of the Beishan landslide were identified through remote sensing interpretation and field investigation. Additionally, numerical simulation was conducted to predict the post-failure process, including run-out and hazard assessment. The results indicate that the Beishan landslide could turn into a rapid avalanche with a run-out distance of 1600m. The accumulation would cover half of the Lijie Town at the foot of the slope, potentially resulting in significant casualties and property loss.

Keywords: large-scale landslide, failure characteristics, run-out, kinematic process; numerical simulation

Introduction

The Bailong River Basin is situated at the northeastern edge of the Qinghai-Tibet Plateau. This area is known for its intricate geological structure, varied rock formations, deep-incised valleys, and significant differences in elevation, which make it highly susceptible to geo-hazards [1~5] (Fig.1). The Beishan landslide, due to its large scale, high position, and massive volume, poses a threat to the Bailong River and the town of Lijie (Fig. 2).

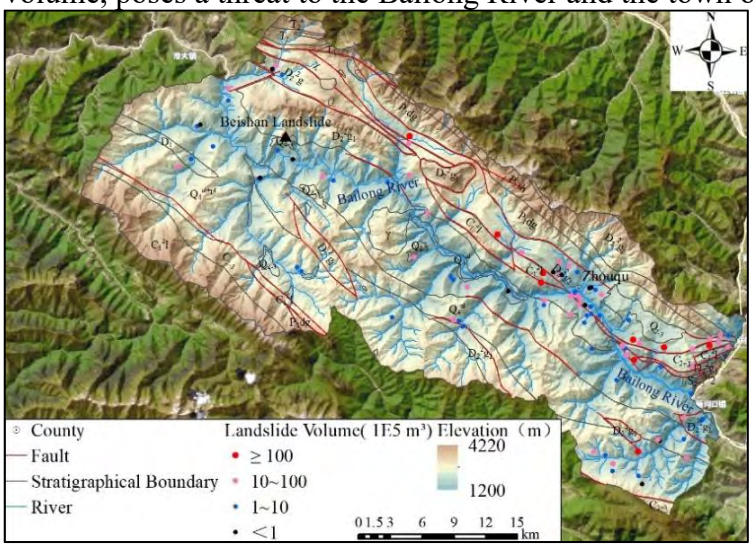

Figure 1. Landslides in Bailong River Basin

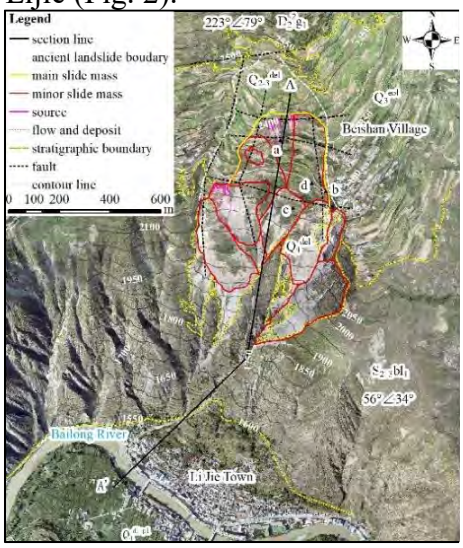

Figure 2. Topography and geology

Characteristics of the Beishan landslide

[1] No.20 Dahuisi Road, Haidian District, Beijing, PRC;
[2] No.111 Lanxin Road, Yubei District, Chongqing, PRC

The Beishan landslide displays a characteristic concave terrain morphology, featuring a circular planform and a horseshoe-shaped profile (Fig.3). The elevation of the rupture surface's tip is 2223 m, while the highest point reaches 2432 m. The sliding mass has a length of 391 m and an average width of 362 m, with an average thickness of 17 m, resulting in an overall volume of approximately 2.4×10^6 m^3.

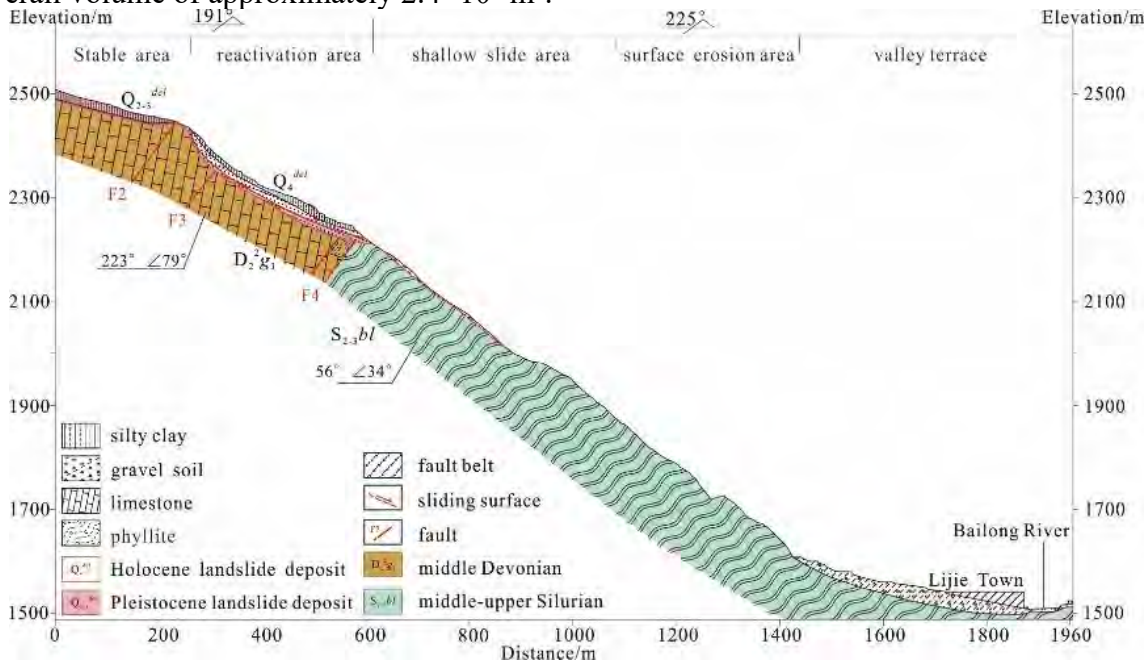

Figure 3. Engineering-geological profile of the

Thin-layered and slightly weathered limestone of the middle Devonian (D_2^2g1) is distributed in the main deforming area and above (Fig. 3). In the lower part of the slope, phyllite of the middle-upper Silurian ($S_{2+3}bl_1$) shows significant weathering and appears as clay-containing flakes on the surface. The average thickness of weathering is 5 to 30 meters. The phyllite has weak rock properties, with a uniaxial compressive strength of 22.45 MPa under natural moisture conditions. Its strength decreases significantly after saturation, with a softening coefficient ranging from 0.21 to 0.38. Surrounding the landslide area, there is Malan loess (Q_3^{eol}) with an average thickness of 18 m. The landslide area is mainly covered by silt containing small amounts of limestone gravel.

Figure 4. Rockfall and flow (Point a in Fig.2)

Figure 5. Road subsidence and exposed sliding surface (Point b in Fig.2)

The Beishan landslide has been experiencing long-term creeping since 1979. Shallow slides and rockfalls have been continuously occurring under the influence of heavy rainfall and

earthquakes [6]. In 1984 and 1998, heavy rainfall caused small-scale landslides at the front. The Wenchuan earthquake in 2008 and the Minzhang earthquake in 2013 caused an increase in shallow slides at the front. On August 17, 2020, heavy rainfall caused a significant landslide at the front, and the sliding mass of soil and rocks that slid transformed into a debris flow, rushing into the Bailong River. As a result, more than half of the river became blocked. On January 14, 2021, extensive ground cracks appeared throughout the main sliding mass. Rockfalls occur at the rear, while the roads at the front experienced severe deformation (Fig. 4, Fig. 5). On the eastern side, there are visible steep sliding surfaces exposed in the loess (Fig. 5)

In summary, the reactivation of the Beishan landslide is caused by erosion upstream of the front slope, leading to long-term creep and significant deformation (Fig. 6). Intense rainfall and strong earthquakes may trigger extensive sliding, resulting in rapid and long-distance avalanches, which pose a significant threat to Lijie town at the foot of the slope and the Bailong River.

Figure 6. Continuous crack extension indicating landslide creep (Point d in Figure 2)

Numerical simulation of post-failure progress

The DAN3D software was utilized to simulate the post-failure process of the Beishan landslide. It uses a meshless, Lagrangian numerical method to discretize and solve the depth-averaged equations of motion for an "equivalent fluid", a hypothetical material governed by simple internal and basal rheologies [7]. A variety of basal rheological model for basal resistance have been provided for different types of rapid landslides involving different geological materials. Previous research has shown that the Frictional and Voellmy models have produced good results for simulating the movement process of long-runout flow slides using DAN3D [8].

The frictional models is often exhibited by granular materials subjected to frictional basal resistance τ_f, which is proportional to the effective bed-normal stress at the base.

$$\tau_f = (\sigma - \sigma_u)\tan\varphi$$

where σ is total bed-normal stress and σ_u is pore pressure at the base, φ is the dynamic basal friction angle.

The Voellmy model combines frictional and turbulent behaviour.

$$\tau_v = \tau_f + \gamma \cdot g \cdot v^2 / \xi$$

where ξ is turbulence parameter and v is velocity.

Usually, a flow slide could be divided into source area, flow area, and accumulation area, and rheology changes along. Frictional model is used in source area and switched to Voellmy

model in flow area and accumulation area by simply changing the parameters. The parameters are listed in Table 1.

Table 1 Parameters and model for simulation

Parameters	Source	Flow	accumulation
Rheological model	Frictional	Voellmy	Voellmy
weight/(kN/m$^{3)}$	20	20	20
Friction angle/(°)	20		
coefficient of friction	-	0.1	0.15
turbulence coefficient /(m/s^2)	-	400	200
Internal friction angle/(°)	35	35	35
Maximum entrainment depth/m	0	5	0

The simulation results demonstrate that the Beishan landslide undergoes a complete transformation into a debris flow, sliding at high speed until a complete stop in the accumulation area（Fig.7）.

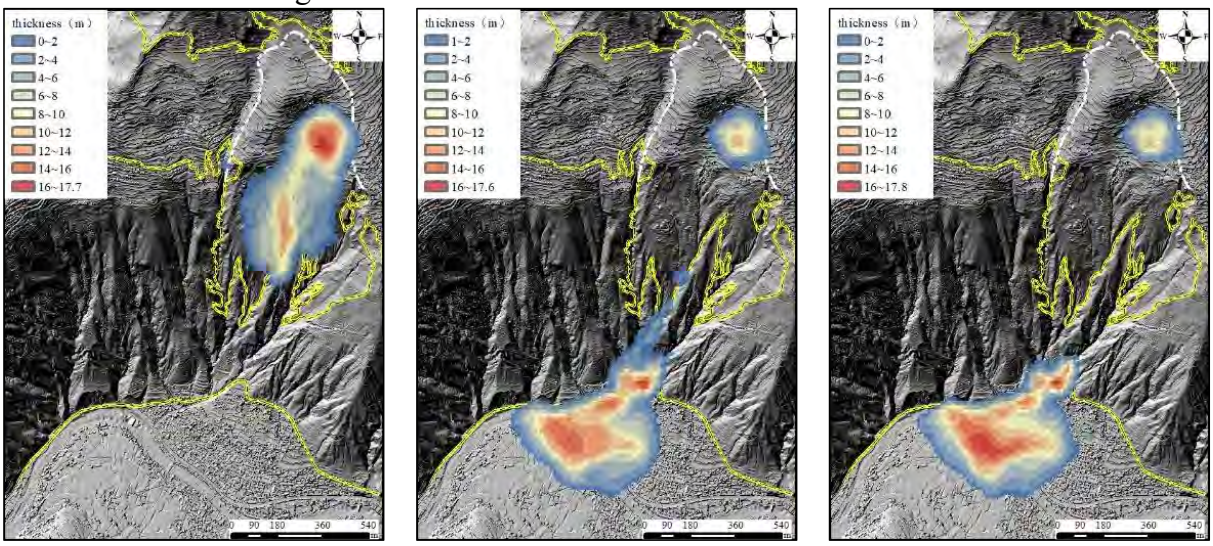

(a) t=20 s (b) t=100 s (c) t=200 s

Figure 7. Thickness of sliding mass varying during post-failure progress

（1）The initiation stage lasts about 20 s (Fig.7). The sliding mass starts moving, shearing at 2250 m. Due to the gentle slope of the sliding surface, the initiation speed is relatively small (0-15 m/s) (Fig.8).

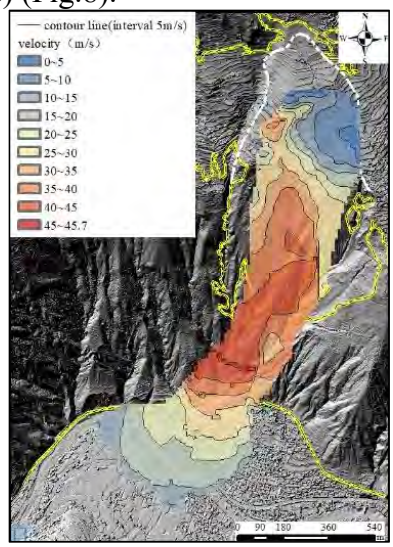

Figure 8 Maximum velocity during post-failure progress

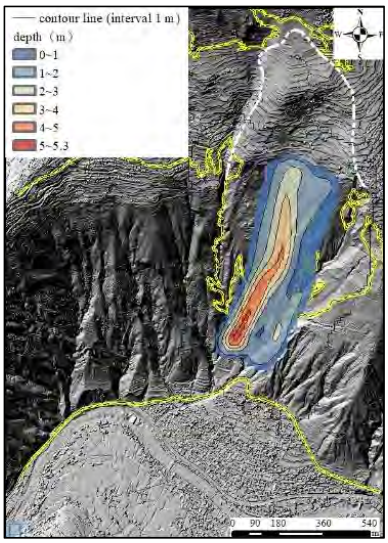

Figure 9. Coutor of Entrainment depth

（2）The flow stage starts from 20 s to 100 s (Fig.7). After detachment from the source area, the sliding mass moves downslope, transforming into a high-speed flow (Fig.8). The sliding mass scours and entrains shallow and loose materials along the way, rapidly increasing its volume. The average entrainment thickness is approximately 3 m (Fig. 9). Due to the high height and steep slope, the sliding mass keeps accelerating with velocities ranging from 24 to 52 m/s (Fig. 13).

（3）The accumulation stage starts at 100 s (Fig. 7). The flow reaches the foot of the slope, where the terrain becomes flat and open. The velocity starts to decrease and the sliding mass spreads out in the shape of a fan. The flow eventually reached the south bank of the Bailong River, and the maximum run-out distance was about 1600 m (Fig. 8). The accumulation covers an area of 0.22 km2, with a volume of approximately 3.177×106 m³ and a maximum thickness of 17.8 m.

Conclusion

Landslides with a velocity exceeding 5 m/s are generally classified as rapid. Those with an equivalent friction coefficient (vertical displacement to horizontal displacement) of less than 0.6 are referred to as long-run-out avalanches [9]. From the above, it is clear that a rapid and long run-out avalanche may result from the failure of the Beishan landslide. The maximum velocity of the avalanche is 45.7 m/s, and the equivalent friction coefficient is approximately 0.49. The accumulation would cover approximately 50% of the area of Lijie town, resulting in casualties and property damage.

References

[1] Zhang M S, Li Z H, Wang G L, et al (2011) The Geological Hazard Characteristics and Exploration Ideas of the Bailong River Basin. *Northwestern Geology* 44(03),1–9.

[2] Guo F Y, Meng X M, Chen G, et al (2016) Geomorphology evolution of Bailong River Basin and its impact on Geo－hazard. *Yangtze River* 47(07):37-43+49.

[3] Liu D F, Ma J Z, Tian L, et al.(2014) Dynamic characteristics of the Xieliupo landslide in Zhouqu County based on DAN-W. *Journal of Lanzhou University* (*Natural Sciences*) 50(05):733–738.

[4] Jiang S, Wen B P, Li Z H, et al. (2016) An analysis of the activity features of the Suoertou landslide in Zhouqu County of Gansu. *Hydrogeology & Engineering geology* 43(02):69-74+92

[5] Zhang W X, Yao X H, Ding Ba Y, et al. (2020) Causative analysis and comprehensive treatment of the Jiangdingya Landslide in Zhouqu County of Gansu Province. *The Chinese Journal of Geological Hazard and Control* 31(05):7-14

[6] Cong K, Cui X L, Chen Y. (2021) Geological Environment Monitoring Institute of Gansu Province, 2021. Survey of Beishan Landslide in Lijie Town, Zhouqu County, Gannan Prefecture, Gansu Province. *Technical Report*. Gansu Institute of Geo-environment Monitoring, Lanzhou, Gansu.

[7] Mcdougall S. 1998. A New Continuous Dynamic Model for The Analysis of Extremely Rapid Landslide Motion Across Complex 3d Terrain. Ottawa: University of Toront.

[8] Wang G Z, Li B, Feng Z, et al. (2014) Simulation of Rock collapse-clastic Flow in Jiguanling, Wulong, Chongqing. *Hydrogeology & Engineering Geology* 41(5): 101-106

[9] Zhang M, Yin Y P, Wu S R, et al. (2010) Development Status And Prospects Of Studies On Kinematics Of Long Runout Rock Avalanches. *Journal of Engineering Geology* 18(6): 805–817.

COMMENTS:
In particular, the constitutive models should be presented with more details (Frictional model and Voellmy model). In particular, what is a "frictional model"? How is the transition from frictional model to Voellmy model managed? What criterion is used?

RESPONSE:
Principle of DAN3D software, equations of two basal rheology model have been presented in Line 51-66. Frictional model is used in source area and switched to Voellmy model in flow area and accumulation area by simply changing the parameters.

Muon tomography, seismic noise survey and multi-scale topographic monitoring to assess rockfall hazard at the Maido Rampart (La Réunion Island)

Benoit Le Moigne[2], Catherine Truffert[1], Simon Bouteille[1], Clara Levy[2], Jacques Marteau[3], Nicole Hueber[2]

[1] IRIS Instruments, France
[2] BRGM, French geological survey, France
[3] IP2I, Lyon, France

SUMMARY: Instable rock compartments at the 1000 m high Maïdo rampart threaten the few dozen inhabitants of the islet of Roche Plate in Mafate located downslope, as well as the cliff top which is the second most popular touristic site of La Réunion Island (>500 000 tourists/year). These rock compartments of a few tens of m3 to several hundred thousand m3 are pre-cut by fractures subparallel to the cliff as far as hundred meters from the cliff edge. In November 2020, reports of crack openings after an important bush fire raised fears of the imminent collapse of several hundred m3. The stability of other rock compartments was also considered worrying. In order to assess the stability of these compartments, a permanent multi-scale and partly automated system was installed to survey crack openings and surface deformations. This set up was completed by a seismic noise survey designed to qualify the degree of individualization of rock compartments. Finally, a muon tomography survey of the upper part of the rampart was deployed to image the extension of crack roots. The acquired data should make it possible to better understand rupture processes and kinetics, helping in characterizing and managing rockfall hazard at this site.

Keywords: Rockfall, Muongraphy, Seismic noise, Rampart, La Réunion

Introduction

At the Maïdo rampart (figure 1), the fracture network was mapped on the surface using orthophoto and LIDAR data, revealing an extension of cracks over tens of meters, with openings up to several meters. The complexity of the fracture network and its large extent (50,000m²) make difficult the assessment of rockfall hazard. In order to prevent possible rock collapses at this very exposed site, it is therefore necessary to better understand the geometry of instabilities (particularly at depth) and the kinematics leading to rupture.

Hereafter, we present three complementary experiments designed to gather information on the geometry of instabilities, qualitatively assess their degree of stability and survey signs of evolutions toward collapse. The extent and complexity of the site required adapting state of the art methods such topographic monitoring and ambient noise survey. In addition, BRGM with Iris Instrument chose to test an innovative method, a muography to remotely monitor the rampart, passively, with the hope to evaluate the depth of decompression cracks.

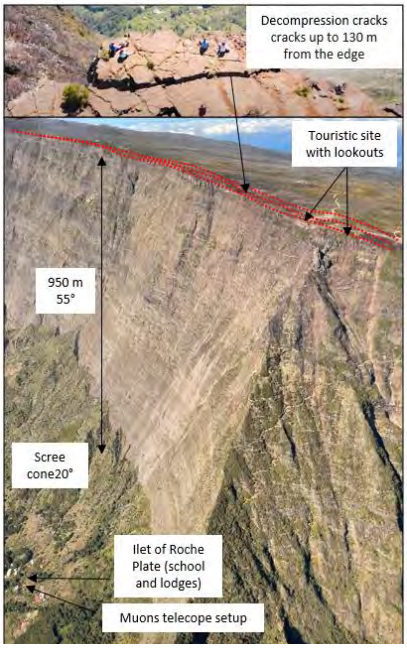

Figure 1: Maïdo rampart configuration

Topographic monitoring

The surface to be monitored is particularly large (50,000 m²) and makes it complex to detect topographic changes, knowing that stable sectors can be very far from measurement points. Devices such as extensometers might only measure the local component of the deformation. In order to overcome this problem, these instabilities are carefully monitored on behalf of the local authorities using multi-scale and partly automated topographic monitoring. The monitoring system was deployed in February and March 2022 and consists of :

- A geodetic reference system covering an area of 50,000 m², with semi-annual measurements of 22 control points using a total station, achieving sub-centimeter precision.
- Continuous monitoring equipment, including 12 extensometers (figure 2a) and an inclinometer with measurements taken every 4h, along with 40 displacement gauges. Additionally, an inclinometer was placed on the fissures delineating unstable compartments at the cliff's edge.
- 4 photogrammetric surveys conducted on the upper cliff near the tourist area to track erosion in rocky compartments at the cliff's edge, potentially linked to collapse triggers. The diachronic analysis of these data, only evidenced very smalls scattered rockfalls, with a maximum volume of 20 m^3, located outside of the area of interest.

During the initial two years of monitoring, precision assessment and the study of daily and seasonal variations were conducted. These variations were attributed to material expansion and contraction, including rock, measurement instruments, and fastenings, due to temperature fluctuations. Importantly, only reversible movement with a maximum amplitude of 2 mm displacement signaling an ongoing destabilization process was recorded during the first year of monitoring, extending until September 2023.

Seismic noise survey

A seismic noise survey was carried out to assess the degree of individualization of rock compartments. Over the past ten years, such method proved efficient for unstable volumes of a few thousand to hundreds of thousands of cubic meters and in different contexts (volcanic or sedimentary rocks, various compartment geometries, etc.; Lévy, 2011; Burjànek et al. , 2012; Bottelin, 2014; Burjànek et al., 2017; Colombero et al., 2018; Valentin, 2018). The principle is as follows: unstable rock compartments vibrate preferentially at certain frequencies which are characteristic of their geometry, their mass, the rigidity of the rock, but also the degree of attachment to the stable massif.

At the Maïdo, the survey consisted of seismic noise records at locations distributed according to a dense spatial grid for several hours (2 to 4 hours) between 08/04/2021 and 08/06/2021. In total, 40 measurement points were carried out spread over 30,000m². The seismometers are CMG6-TD with recording velocities along 3 directions for frequencies between 0.33 Hz and 40 Hz. The sampling frequency was set at 200 Hz. For the duration of the experiment, a reference sensor located in the stable area, 150 m from the edge of the rampart, also recorded data.

13 sensors, located near the edge of the rampart, have an average amplification ratio relative to the reference station greater than 5 in the horizontal direction perpendicular to the rampart on the frequency band [0.5 24] Hz (figure 2b). These observations are also consistent with those of Burjanek et al. (2012) which showed that the relative amplification between the reference

stations located on the stable massif and the stations located on the unstable structures always presents a preferential direction, with a maximum amplification generally observed in a direction perpendicular to the cracks found at the surface.

For a small group of compartments (6) considered to be the most unstable on the site, the amplification ratio relative to the reference station is greater than 20 at certain frequencies, with an observed maximum of 30 for one sensor. Thus, measurements confirmed the presence of unstable rock compartments and allowed to qualitatively compare their degree of instability. However, we do not have any information providing an estimate of the probability or time of rupture.

The performed analysis was relatively easy to set up and allowed to process and compare a large volume of data. This method is therefore operational for future studies of the rampart stability. It will be interesting to perform again this type of measurement in the future decade, in order to detect changes in the vibrations which might be linked to ongoing destabilization.

Muon tomography

In this scientific study, muography, a passive technique using natural cosmic muons, was employed to create a 3D map of the average density of the Maïdo rampart. Similar to radiography, the technique measures the attenuation of muon radiation as it passes through different materials (Procureur, 2018). The muon telescope used for this experiment utilized scintillator technology and featured three planes with high spatial resolution.

The primary goal was to establish a comprehensive 3D density map of the rampart and to study temporal variations in muon flux, which could provide insights into potential instabilities. The telescope was strategically positioned in Roche-Plate, 1,000 meters below the Maïdo rampart, and data collection occurred from November 2021 to August 2022.

Preliminary results indicate observable lithological differences, particularly the presence of thick basaltic flows (figure 3c). Nonlinear density variations with depth hold promise for estimating the depths of

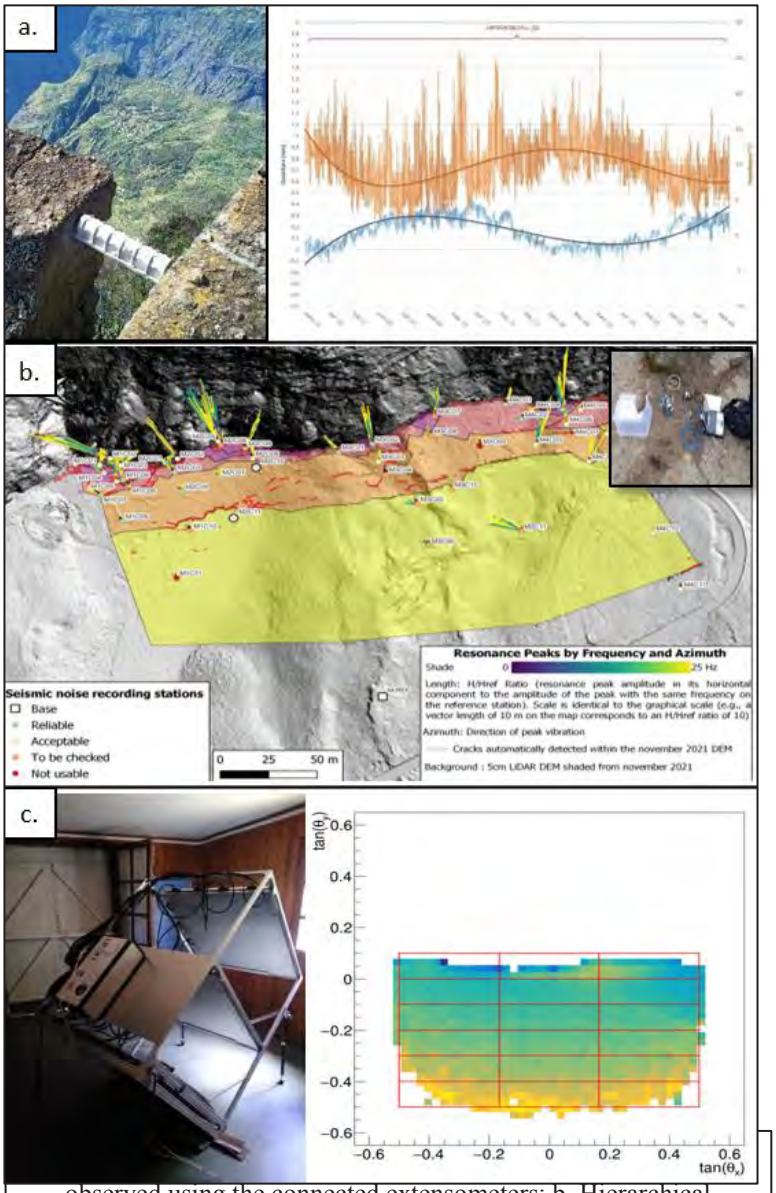

observed using the connected extensometers; b. Hierarchical Assessment of the instability degree of rock compartment based on seismic noise survey results; c. The first results of the muography scan show density variations in line with geological observations.

fissure networks. However, limitations related to depth and rock traversed should be considered, as uncertainties increase with depth.
Additionally, the study noted the challenge of assessing the distance of fissures from the wall using the frontal view and suggested potential improvements using a telescope configuration with an upper wall incidence. It's worth mentioning that the monitoring period was affected by Cyclone Batsirai in February 2022, although this meteorological event did not significantly impact the recorded muon flux.

Conclusion

Beyond its immediate significance in alerting systems, topographic monitoring provides insights into the thermo-mechanical behavior of rocks and rupture processes. The proposed analysis of passive seismic data allows for the characterization of rock compartment disintegration levels qualitatively. This approach may potentially improve from systematic estimation of the first resonance frequency and associated damping.
The first global monitoring of high rock walls through muography yields promising initial results in characterizing the depth of root fissures in decompression zones. However, data collected by the muon telescope is already on exploration.
The data collected through diverse monitoring methods have enabled qualitative assessments of detachment levels and the identification of unstable compartments at various scales.
Overall, the combination of both conventional and innovative monitoring techniques holds significant promise for advancing our understanding of Maïdo edge rampart stability and guides the authorities in the management of geological risk at this high-stakes site

References

Bottelin P., Jongmans, D., Baillet, L., Lebourg, T., Hantz, D., Lévy, C. & Turpin, J. (2013). Spectral analysis of prone-to-fall rock compartments using ambient vibrations. *Journal of Environmental and Engineering Geophysics*, 18(4), 205-217.

Burjánek, J., Gischig, V., Moore, J. and Fäh, D. (2017). Ambient vibration characterization and monitoring of a rock slope close to collapse. *Geophysical Journal International*. 212(1), 297-310.

Burjánek, J., Moore, J., Yugsi Molina, F. and Fäh, D. (2012). Instrumental evidence of normal mode rock slope vibration. *Geophysical Journal International,* 188(2), 559-569.

Colombero, C., Baillet, L., Comina, C., Jongmans, D., Larose, E., Valentin, J., & Vinciguerra, S. (2018). Integration of ambient seismic noise monitoring, displacement and meteorological measurements to infer the temperature-controlled long-term evolution of a complex prone-to-fall cliff. *Geophysical Journal International*, 213(3), 1876-1897.

Lévy, C., Baillet, L., Jongmans, D., Mourot, P., & Hantz, D. (2010). Dynamic response of the Chamousset rock column (Western Alps, France). *Journal of Geophysical Research: Earth Surface*, 115(F4).

Procureur, S. (2018). Muon Imaging : Principles, Technologies and applications. *Nuclear instruments and methods in Physics Research* Section A : Accelerators, spectrometers, detectors, and associated equipment. 2018, pp. 169-179.

Valentin, J., Capron, A., Jongmans, D., Baillet, L., Bottelin, P., Donze, F., Larose E. and A. Mangeney (2017). The dynamic response of prone-to-fall columns to ambient vibrations: comparison between measurements and numerical modelling. *Geophysical Journal International*, 208(2), 1058-1076.

Truffert, C, Bouteille, S, Bitri, A, Dietz, M (2021) The Muography — A passive technique among state-of-the-art geophysical methods DO - 10.3997/2214-4609.202120223.

Failure frequency in some types of rock walls

Didier Hantz[1], Michel Jaboyedoff[2], Christine Moos[3], Luuk Dorren[3]

[1] Univ. Grenoble Alpes, Univ. Savoie Mont Blanc, CNRS, IRD, Univ. Gustave Eiffel, ISTerre, 38000 Grenoble, France
[2] Risk Group, University of Lausanne, Lausanne, Switzerland
[3] Bern University of Applied Sciences – HAFL, Zollikofen, Switzerland

SUMMARY: Quantitative information on the failure frequency of rockfall is crucial for an effective hazard and risk management, but often lacking in reality. We here estimated the spatial-temporal failure frequency of rockfall events bigger than 1 m^3 based on data compiled from scientific studies analysing 18 natural mountain rock walls using terrestrial laser scanner, photogrammetry or historical inventories. The rock walls are located in temperate climate zone and under the permafrost area. The derived frequencies varied by at least three orders of magnitude from 0.006 to 19.1 $yr^{-1}.hm^{-2}$, depending mainly on the spacing of the discontinuities and the geomorphological context of the cliff. A primary classification is proposed, which allows for estimating the spatial-temporal failure frequency for some types of rock walls.

Keywords: rockfall, failure, frequency, rock wall, cliff

Introduction

A quantitative assessment of the failure frequency of diffuse rockfall hazards or the failure probability of localized hazards is indispensable for realistic hazard and risk analyses (Fell *et al.*, 2008a; Hantz *et al.*, 2020, 2021). This article deals with the assessment of the failure frequency in different geological and geomorphological contexts. Using published analyses of rockfall inventories, we estimated the release frequency of rockfall events bigger than 1 m^3 assuming a Poisson distribution of the rockfall events. We then analysed the factors influencing this frequency.

Method

As the number of rockfall failures is not constant over time, the temporal failure frequency F_t can be defined as the mean number of failures that occur per unit of time. The number of failures expected in a period of length T is a random variable whose mean is F_tT. Following Rat (2006), one can assume in a first approach that in a homogenous area where a lot of independent rock compartments are at different evolutionary stages, the occurrence of failures is stationary at a yearly scale and is described by a Poisson law. Note that at a daily scale, the dates of the rockfalls are not independent because several rockfalls can be triggered by the same meteorological episode. If μ $(=F_tT)$ is the mean number of rockfall events in a given duration, the probability that N failures occur is:

$$P(\mu, N) = e^{-\mu}(\mu)^N/N! \quad (1)$$

It appears that the number of failures (N_{obs}) detected in an observation period of length T is usually not equal to $\mu = F_tT$. and that the observation period is often too short for a precise estimation of the frequency. We propose a method to estimate a range of values for μ, given the observed number of failures (N_{obs}). A 95 % confidence interval for N can be defined for each

value of μ. If N_{obs} is not included in this interval, the value of μ is not considered as plausible. Thus, a range of plausible values of μ can be obtained for each value of N_{obs}. For $N_{obs} = 0$, the lower limit is $\mu_{min} = 0$ and the upper limit is the value of μ for which $P(\mu,0) = 5\%$. For $N_{obs} \neq 0$, the lower limit is the value of μ for which $P(\mu, N \geq N_{obs}) = 2.5\%$, and the upper limit is the value of μ for which $P(\mu, N \leq N_{obs}) = 2.5\%$.
Table 1 gives the minimal and maximal estimations of the mean number of events μ for $N = 0$ to $N = 10$. Since the frequency is usually represented by its logarithm, the geometric mean and the uncertainty factor are given. Note that for purpose of hazard assessment, the hazard level is usually qualified according to the decimal logarithm of the rockfall frequency (Fell *et al.*, 2008b). In this case, an uncertainty factor of 10 corresponds to an uncertainty of one hazard level.

Table 1. Minimal and maximal estimations of the mean number of failures for a given duration, as a function of the observed number (using the Poisson's law), geometric mean and uncertainty factor.

Observed number	0	1	2	3	4	5	6	7	8	9	10
μ_{min}	0	0.025	0.24	0.62	1.1	1.6	2.2	2.8	3.4	4.1	4.8
μ_{max}	3	5.6	7.2	8.8	10.3	11.7	13.1	14.4	15.8	17.1	18.4
Geometric mean (μ_{gm})		0.37	1.31	2.34	3.37	4.33	5.37	6.35	7.33	8.37	9.40
Uncertainty factor (μ_{max}/ μ_{gm})		15.0	5.5	3.8	3.1	2.7	2.4	2.3	2.2	2.0	2.0

Data

We used studies that analysed the frequency of failures or rockfall events in continental natural rock walls located under the permafrost limit and at latitudes from 40 to 50° North. We have excluded failures in rock cuts and inventories of deposited individual blocks, because most failures release several blocks. We selected studies that give explicitly the number of failures bigger than 1 m^3 and the corresponding cliff area, or that give enough data so that they can be estimated. Most inventories are derived from instrumental monitoring (terrestrial laser scanner or photogrammetry), but some of them are historical inventories with approximate estimation of the volume.
For each study site, we calculated the mean spatio-temporal failure frequency (representing the yearly frequency per area) and its confidence interval. When the confidence intervals of the frequencies observed in different cliffs belonging to the same massif were compatible, we considered these cliffs as a homogeneous group (French Tithonian cliffs, French Urgonian cliffs, Montserrat). This allowed for a higher number of failures and, thus, a smaller confidence interval. The characteristics of the study sites are given in Table 2.

Results

Results are summarized in Figure 1.

Discussion

Three groups of frequencies can be defined in Figure 1. The first group, with frequencies lower than 0.1 $yr^{-1}.hm^{-2}$, includes all the cliffs made up of massive hard rock (joint spacing > 2 m, high compressive strength) with the exception of the Mont Granier that has a frequency slightly

Table 2. Characteristics of the studied sites. Acronyms refer to the lithology or the stratigraphy and the location of the cliff. The letter h at the end refers to historical inventories.

Location	Acronym	Reference	Stratigraphy, zone	Lithology	Cliff area (hm^2)	Duration (yr)
Middle Brother	GRA-MB	Guerin et al., 2020		granitic rock	90	40
El Capitan	GRA-EC	Guerin et al., 2020		granitic rock	47	41
Venosc	GNE-VEN	Hantz, Levy, 2019		gneiss	38	7
Lauterbrunnen	MALM-LAU	Mohadjer et al. 2020	Malm (Quinten), Helvetic	limestone	520	5.2
French Urgonian cliffs (<1100 m)	URG (<1100)	Epinat, 2016; Guillemot, 2017; this study	Barremian (Urgonian), Dauphinoise	limestone	51.2	
French Tithonian cliffs (<1400 m)	TIT (<1400)	Hantz, Levy, 2019; this study	Malm, Tithonian, Dauphinoise	limestone	22.85	
French Urgonian cliffs (1500-2000 m)	URG (1500-2000)	Alber, 2016; this study	Barremian (Urgonian), Dauphinoise	limestone	39	
Mont Granier	URG-GRA	Alber, 2016; Hantz, Levy, 2019	Barremian (Urgonian), Dauphinoise	limestone	15	16
Montserrat	CON-MON	Janeras et al., 2023	Eocene	conglomerate	9.05	
Montserrat (historical)	CON-MONh	Janeras et al., 2023	Eocene	conglomerate	9.4	21
Gorgette gully	VAL-GOR	Hantz, Levy, 2019	Valanginian, Dauphinoise	limestone	5.1	6.9
Mont Saint-Eynard South	SEQ-SE	Hantz, Levy, 2019; this study	Sequanian, Dauphinoise	limestone	12.3	5.7
Mont Saint-Eynard Aiguille	SEQ-AI	Hantz, Levy, 2019	Sequanian, Dauphinoise	limestone	9.9	3.7
Bourg d'Oisans, Bassey	LIA-BO	Hantz, Levy, 2019	Lias, Dauphinoise	limestone	82.7	3.1
Castellfollit	BAS-CAS	Janeras, 2021		columnar basalt	2.64	12.65
Castellfollit (historical)	BAS-CASh	Janeras, 2021		columnar basalt	4.14	16
La Cornalle	MIO-COR	Carrea et al., 2021	Miocene, Molasse	sandstone-marl	0.22	5
Puigcercós	EOC-PUI	Abellan et al., 2010	Eocene	marl-sandstone-clay	0.375	0.8
Exhaustive only from a volume bigger than 1 m^3						
Andorra	GRA-AND	Corominas et al., 2018; Santana et al., 2012		granodiorie, hornfels	4.2	20
Illgraben	QUA-ILL	Bennett et al., 2012	Trias, Pennic	quartzite	70	19
French Tithonian cliffs (<1400 m)	TITh (<1400)	Hantz, Levy, 2019; this study	Malm, Tithonian, Dauphinoise	limestone	365	22
French Urgonian cliffs (<2000 m)	URGh (<2000)	Alber, 2016; this study	Barremian (Urgonian), Dauphinoise	limestone	2451	17

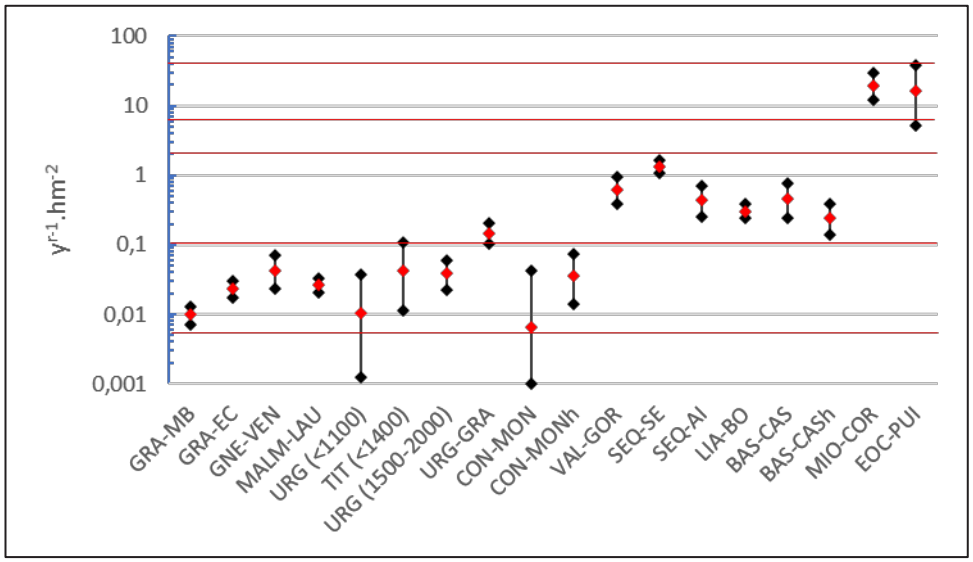

Figure 1. Spatio-temporal frequency of failures bigger than 1 m^3 expressed in $yr^{-1}.hm^{-2}$ (red points). Vertical bars: 95% confidence interval.

above 0.1 $yr^{-1}.hm^{-2}$. This exception can be explained by the fact that the cliff is a part of the scar of a huge rock avalanche (500 hm^3) occurred in 1248, which is the biggest one observed in the European Alps in the last millennium. The cliffs of this group consist of rocks that can constitute very high and steep cliffs. In rock engineering, those are qualified as very good in the RMR

classification (Bieniawski, 1989), which means that tunnelling in these rocks usually does not require support.
The second group, with frequencies between 0.1 and 2 $yr^{-1}.hm^{-2}$, includes cliffs made up of more jointed hard rock (joint spacing 0.2-2 m, moderate to high compressive strength). The cliffs of this group consist of rocks that can also constitute very high and steep cliffs, but they can't be qualified as very good rock in the RMR classification (tunnelling would require at least bolting).
The third group, with frequencies between 5 and 40 $yr^{-1}.hm^{-2}$, includes cliffs made up of heterogeneous rocks and located above an active landslide, which contrast with the other cliffs that are above globally stable slopes. Table 3 proposes a primary classification to estimate the spatial-temporal failure frequency for some types of rock walls.

Table 3. Spatial-temporal frequency of failures bigger than 1 m^3 depending on the joint spacing and the geomorphological context

Joint spacing (m)	Cliff above a stable slope	Cliff above an active landslide
>2	< 0.1 $yr^{-1}.hm^{-2}$	> 0.1 $yr^{-1}.hm^{-2}$
0.6-2		0.1 to 2 $yr^{-1}.hm^{-2}$
0.2-0.6	0.1 to 2 $yr^{-1}.hm^{-2}$	5 to 40 yr-1.hm-2

Conclusion

The proposed method allows for the estimation of the order of magnitude for the frequency of failures bigger than any volume of interest, even if few rockfalls have been observed in the past. This can serve as an important basis for the derivation and validation of rockfall release scenarios for diffuse hazards with limited data on past events. It further allows for the estimation of the rockfall onset frequency over larger scales based on a simple classification of the structure and the geomorphological context of rock cliffs.
More inventories are needed to enhance the proposed classification. Additionally, other geomorphological contexts could be included in the analysis, including rock walls in the permafrost zone, coastal and river bank cliffs or man-made cut slopes. Generally, the current literature indicates that failure frequencies in those cliffs are higher than in the natural cliffs considered in this study (for example, Hantz *et al.*, 2020).

References

Fell, Robin, Jordi Corominas, Christophe Bonnard, Leonardo Cascini, Eric Leroi, et William Z. Savage. « Guidelines for Landslide Susceptibility, Hazard and Risk Zoning for Land Use Planning ». *Engineering Geology* 102, nº 3-4 (décembre 2008): 85-98. https://doi.org/10.1016/j.enggeo.2008.03.022.

Hantz, Didier, Bastien Colas, Thomas Dewez, Clara Lévy, Jean-Pierre Rossetti, Antoine Guerin, et Michel Jaboyedoff. « Caractérisation quantitative des aléas rocheux de départ diffus (Quantitative assessment of rockfall release frequency) ». *Revue Française de Géotechnique*, nº 163 (2020): 2. https://doi.org/10.1051/geotech/2020011.

Hantz, Didier, Jordi Corominas, Giovanni B. Crosta, et Michel Jaboyedoff. « Definitions and Concepts for Quantitative Rockfall Hazard and Risk Analysis ». *Geosciences* 11, nº 4 (1 avril 2021): 158. https://doi.org/10.3390/geosciences11040158.

Rat, M. « Optimisation de la gestion de la route du littoral à la Réunion vis-à-vis du risque de chutes de blocs ». *BLPC*, nº 263-264 (2006): 43-52.

Bieniawski, Z. T. *Engineering rock mass classifications: a complete manual for engineers and geologists in mining, civil, and petroleum engineering*. New York: Wiley, 1989.

Strain Monitoring Using Distributed Fiber Optics during Rainfall Induced landslides

Umar Zada[1], Shu-Fan Wu[2], Chih-Chung Chung[1*], Fu-Chen Teng[2]

[1] Department of Civil Engineering, National Central University, No. 300, Zhongda Rd, Zhongli District, Taoyuan City, 320, Taiwan (Email: ccchung@ncu.edu.tw)
[2]Department of Civil and Construction Engineering, National Taiwan University of Science and Technology, Taipei, Taiwan

SUMMARY:
Landslides, a significant cause of annual financial and human losses, underscore the critical need for monitoring slope stability to prevent disasters. Employing distributed fiber optic systems, laboratory experiments, as well as physical model tests were carried out to monitor strain in a rainfall-induced slope model, using Brillouin Optical Time Domain Reflectometry as a data analyzer. Maximum strain values were observed near the toe and at the vicinity of the surface, which shows a shallow landslide with retrogressive failure. The results affirm the technology's efficacy in monitoring strain, showcasing its potential to mitigate landslide risks.
Keywords: Landslide modelling, Strain Monitoring, DFOS, BOTDR.

Introduction

Landslides, as surface phenomena of the Earth, consistently pose substantial risks to human safety and global infrastructures (Wang et al. 2023). The phase of failure is often linked to rainfall directly seeping into the slope surface and emerging from the bedrock beneath (Cascini et al. 2010). Hence, a thorough examination of the impact of rainfall is critical. Accordingly, observing the strain induced by rainfall and its distribution can offer a more comprehensive understanding of landslides.

Remote sensing and ground-based observation methods, like the global navigation satellite system (GNSS), total station, and synthetic aperture radar (SAR), monitor landslide deformation within specific spatial resolutions. However, these techniques are limited to providing measurements solely of the ground surface (Cenni et al. 2021, Mantovani et al. 2022, Donati et al. 2023). Conversely, geotechnical instrumentation based on boreholes, such as inclinometers, TDR, extensometers, and settlement plates, enables the measurement of subsurface displacements and the identification of potential sliding surfaces (Stark et al. 2008, Ruza et al. 2020, Xie et al. 2019). Nevertheless, despite their widespread use, comprehending the evolution of critical interface deformation in landslides using these conventional techniques remains challenging. This challenge primarily arises from the limited spatiotemporal resolutions of the sensors (Zhu et al. 2015).

The fiber-optic system offers a dependable and accurate solution for characterizing the deformation of sliding surfaces. It achieves this by enabling a continuous spatial measurement of the strain applied to a fiber-optic strain sensing cable over a considerable distance (Ma et al. 2022). Advancements in Brillouin optical frequency domain reflectometry (BOTDR) now allow for strain recording with spatial resolution on the scale of cm and strain accuracy at the micro strain level (Zhang et al. 2023).

The current study presents the development of a distributed fiber optic system based on a BOTDR interrogator. The system's prime objective was to assess and monitor the strain

distribution induced by the rainfall infiltration. This technique enables more effective preventive measures and informed decision-making in high-risk areas.

Calibration

Experiments were conducted in the laboratory and on a physical model. Fig. 1(a) and (b) illustrates that small-scale laboratory experiments were employed to calibrate the optical fiber cable for strain measurement. BOTDR measured the strains caused by extending the fiber optic cable at different strain levels. These measurements were then compared against the applied strain values to validate the system's accuracy.

The laboratory experiment results in Fig. 1(c) indicated applying strain values ranging from 1 to 8 mm as an extension on the cable. Simultaneously, the BOTDR recorded the strain values, and the monitored strain closely correlated with the applied strain values, showcasing a minimal variance. The slight difference observed might be attributed to the system's sensitivity. Overall, the results were highly satisfactory, indicating the system's capability for effective strain monitoring.

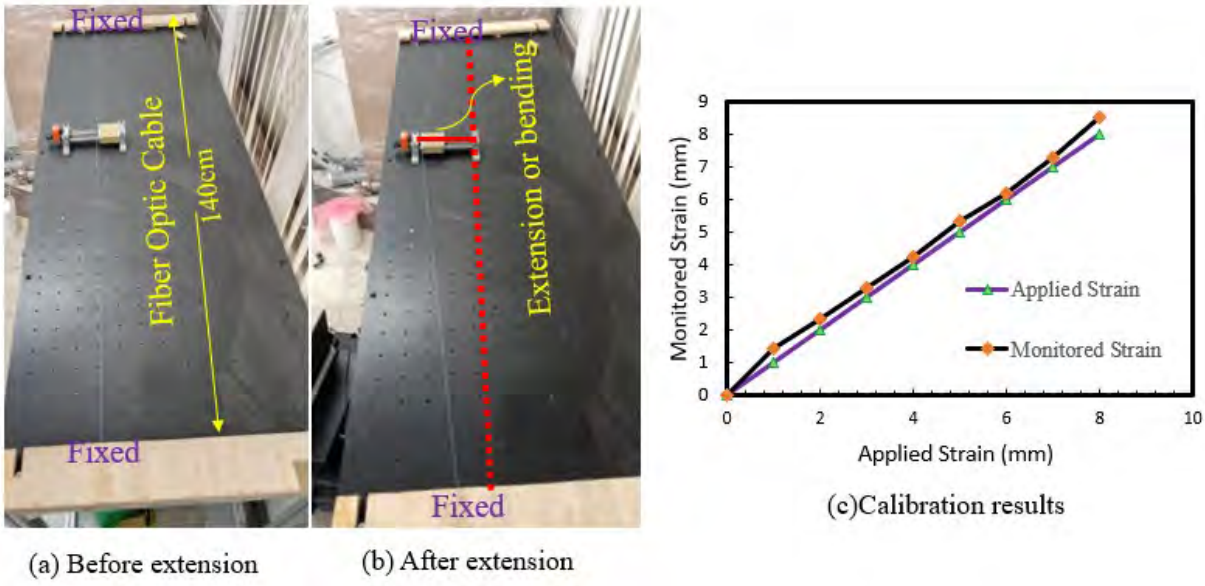

Fig. 1. Calibration set up and results

Physical model test

As shown in Fig. 2, the model slope was 1.3 m high, which included a slope height of 0.9 m and a base height of 0.4 m. The slope was constructed with a slope inclination of 42^0. During model construction, the test soil with an initial water content 10% was laid out in a series of horizontal layers with a thickness of 10 cm. Each layer was tamped equally with a tamping rod to obtain the prescribed height. The procedure was repeated until the full height of the model slope was obtained.

The slope was divided into three sections, each hosting a specific arrangement of optical fiber cables installed horizontally. These cables were strategically set in an S-shaped configuration within each section, a layout visualized in Fig. 2. The primary objective of this particular configuration was to gain insights into the slope and assess the distribution of strain under rainfall conditions. Primarily, baseline strain data was meticulously recorded before the commencement of the rainfall experiment. Following that, the strain data was recorded at regular intervals of 1 hour. Moreover, a rainfall of intensity 102.34 mm/h was applied and the slope was subjected to continuous rainfall for a total of 9 hours. The comprehensive BOTDR

collection method aimed to capture and analyze the evolving strain patterns induced by the rainfall, allowing for a detailed understanding of the slope's behaviour under rainfall conditions.

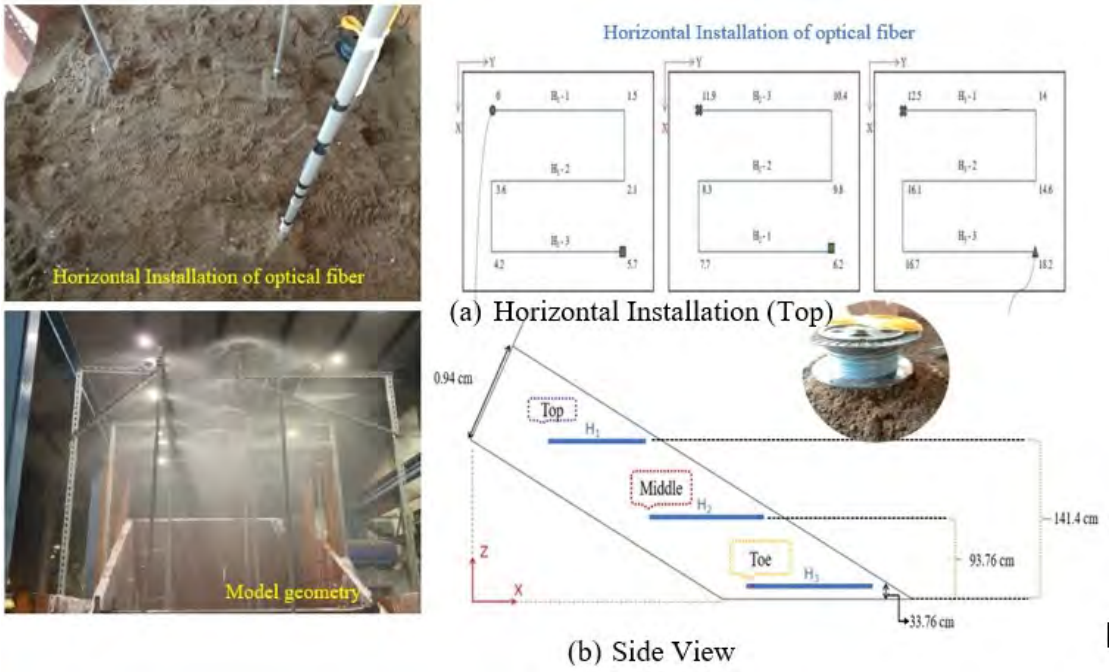

Fig. 2. Physical model test

Similarly, the system was used for physical model testing, and a rainfall experiment was conducted to generate strain in the soil slope, as illustrated in Fig. 3. The most significant strains were identified in Segment-3 (Toe) after 9 hours. In addition, the placement of fibers H3-3, H2-3, and H1-1 close to the surface indicates high strain values, highlighting the nature of shallow landslides where the initial movement originates from the surface soil. The failure exhibited a retrogressive pattern, in which the failure starts from the lower end or toe of the slope. Furthermore, the failure behaviour and the generation and distribution of strain can be supported by visuals captured before and after the test, as depicted in Fig. 4. It was evident that the failure initiated from the lower end, where the strain exhibited maximum values compared to other sections of the slope.

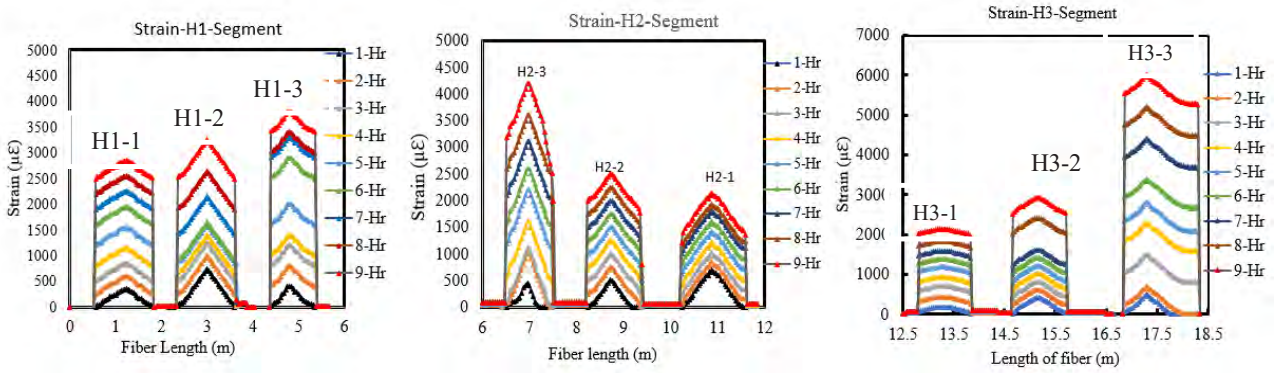

Fig. 3. Physical model results

(a) Before rainfall (b) After rainfall

Fig. 4. Visuales before and after the test

Conclusion

A Distributed Fiber Optic system was used for strain monitoring. The highest strain was detected in segment 3 and near the surface, indicating a shallow depth typical of a shallow landslide. Furthermore, the system has demonstrated its ability to monitor strain effectively.

References

Wang, D.-Y., et al., *Characterization of sliding surface deformation and stability evaluation of landslides with fiber–optic strain sensing nerves.* Engineering Geology, 2023. **314**: p. 107011.

Cascini, L., et al., *Modeling of rainfall-induced shallow landslides of the flow-type.* Journal of geotechnical and geoenvironmental engineering, 2010. **136**(1): p. 85-98.

Cenni, N., S. Fiaschi, and M. Fabris, *Integrated use of archival aerial photogrammetry, GNSS, and InSAR data for the monitoring of the Patigno landslide (Northern Apennines, Italy).* Landslides, 2021. **18**: p. 2247-2263.

Mantovani, M., et al., *Coupling long-term GNSS monitoring and numerical modelling of lateral spreading for hazard assessment purposes.* Engineering Geology, 2022. **296**: p. 106466.

Donati, D., D. Stead, and L. Borgatti, *The Importance of Rock Mass Damage in the Kinematics of Landslides.* Geosciences, 2023. **13**(2): p. 52.

Stark, T.D. and H. Choi, *Slope inclinometers for landslides.* Landslides, 2008. **5**: p. 339-350.

Ruzza, G., et al., *A multi-module fixed inclinometer for continuous monitoring of landslides: design, development, and laboratory testing.* Sensors, 2020. **20**(11): p. 3318.

Xie, J., et al., *A relationship between displacement and tilting angle of the slope surface in shallow landslides.* Landslides, 2019. **16**: p. 1243-1251.

Chung, C.-C., et al., A Comprehensive framework of TDR landslide monitoring and early warning substantiated by field examples, Engineering Geology, 262, 105330. Engineering Geology, 2019. **262**: 105330.

Zhu, H.-H., et al., *Investigation of the evolutionary process of a reinforced model slope using a fiber-optic monitoring network.* Engineering Geology, 2015. **186**: p. 34-43.

Ma, J., et al., *A review of previous studies on the applications of fiber optic sensing technologies in geotechnical monitoring.* Rock Mechanics Bulletin, 2022: p. 100021.

Zhang, L., et al., *Fiber optic monitoring of an anti-slide pile in a retrogressive landslide.* Journal of Rock Mechanics and Geotechnical Engineering, 2023.

Gravitational instabilities and earthquakes interactions at present and millennial time scales in Aiguilles Rouges massif (NW Alps)

Vassallo R.[1], Courtial-Manent L.[1,2], Mugnier J.L.[1], Zerathe S.[1], Metral L.[1], Carcaillet J.[1], Baron I.[3], Trcka T.[4], Comina C.[5], Vinciguerra S.C.[5], Bourrier F.[6]

[1] ISTerre, USMB, UGA, CNRS, IRD, UGE, Chambéry/Grenoble, France
[2] EDyTEM, USMB, Chambéry, France
[3] Institute of Rock Structure and Mechanics of the Czech Academy of Sciences, Prague, Czech Republic
[4] Brno Technical University, Czech Republic
[5] Università di Torino, Torino, Italy
[6] INRAE, Grenoble, France

SUMMARY: The Chamonix valley is subject to seismic and gravity hazards. More specifically, in the Aiguilles Rouges massif, these two aspects are closely linked. Our approach combines geological and geophysical/geodetic analysis to identify and characterize both long-term and present interactions between these processes. We focus particularly our study on a huge gravitational rupture that affect the eastern flank of the massif over several kilometres. At the northern tip of it, a rock column of at least ~1 million m^3 is hanging over Chamonix Valley with an 8 m scarp formed between 2000 and 600 years ago. Its downslope movement is still active nowadays and we started a monitoring at different spatial scales with satellite interferometry, seismic sensors, distancemeters and 3D differential topography. Numerical simulations based on geological and geo-mechanical data will be carried out to reproduce the fall of blocks and calculate their possible trajectory.

Keywords: rock instability, earthquakes, fault, scarp, Alps (max 5 keywords)

Introduction

Rock slope failures are large-scale gravitational instabilities that are set in motion or reactivated by a number of factors (earthquakes, precipitations, decompression when glaciers melt, etc.). We have highlighted such a kilometer-scale gravity rupture in the Aiguilles Rouges massif in the northwestern Alps. However, this geological hazard is not the only one in Chamonix. A major Alpine fault crosses the entire Aiguilles Rouges massif and shows morphologies compatible with past strong earthquakes. The seismic activity associated with this fault and with the Mont Blanc area is therefore another important local hazard and may also contribute to the enhancement of the gravitational processes.
A study of the geometry of the active tectonic fault of the Aiguilles Rouges and of the gravitational ruptures was carried out using a LiDAR DEM with metric resolution followed by helicopter survey (Figure 1).

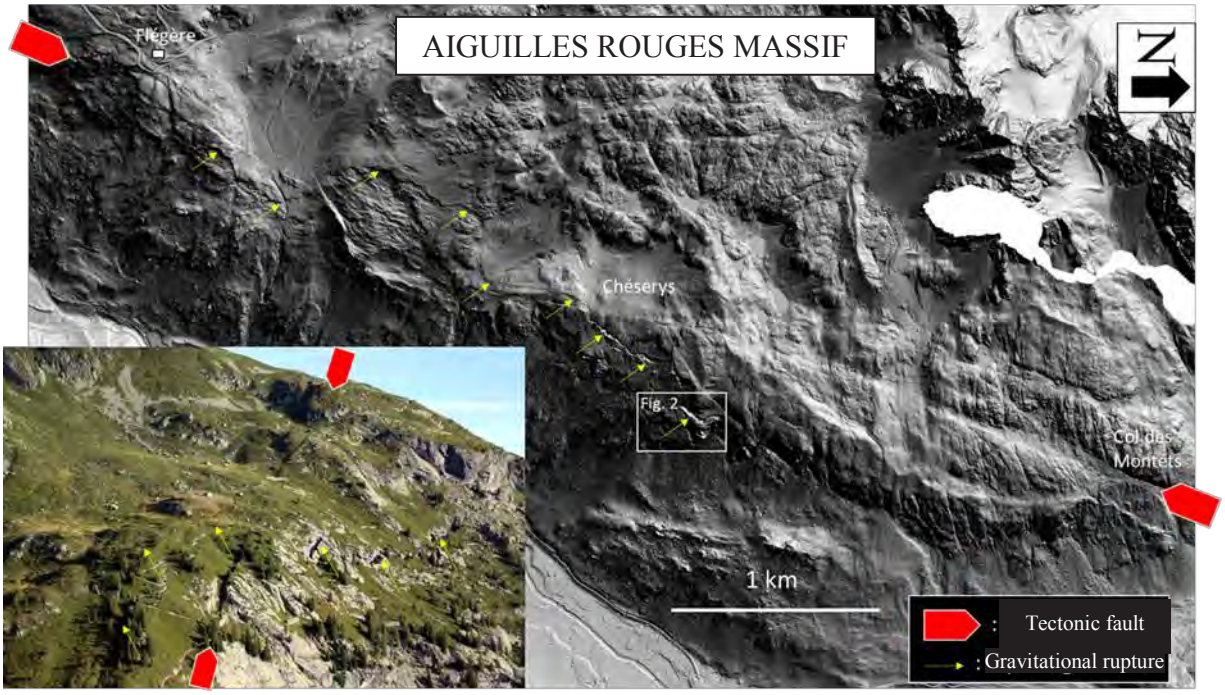

Figure 1: Aiguilles Rouges tectonic fault and gravitational ruptures revealed by LiDAR and aerial view.

Geological and geochronological analysis

These ruptures were mapped and measured in the field. In particular, a discrete rock column of at least ~1 million m^3 is separated from the rest of the mountain flank by a major opened rupture of 200 m long and up to 10 m wide. The movement along this rupture reaches ~8 meters in the dipping direction, with both an opening and a downslope sliding component (Figure 2).

Figure 2: Northern tip of the Aiguilles Rouges gravitational rupture and ~1 million m^3 rock column hanging over Chamonix valley. Note the 8 m scarp dated between 2000 and 600 years ago by ^{10}Be method.

.

To clarify the chronological elements - initiation, evolution of the movement over time - we sampled the gneiss rock-wall along the scarp created by the rupture in order to use the ^{10}Be cosmogenic isotope method. The ^{10}Be analysis shows a scarp initiation between ~2000 and 600 years ago (Courtial-Manent et al., 2022). This study demonstrates that the observed failure moved largely after the post-glacial decompression of the slope and that there is a genetic relationship with the tectonic fault.

Tectonics-gravity past interactions

The instability of the rock column could be accentuated by a major earthquake, of which the nearby seismic fault is a potential source. The geological study of this tectonic fault revealed that earthquakes of Mw ≥ 6 have occurred during the latest millennia (Ritz et al., 2021). Therefore, despite the strongest historical event is only Mw 5.3 in 1905, much bigger earthquakes on this structure are possible. The earthquake of 1905 provoked several rockfalls both in the Aiguilles Rouges and Mont Blanc massifs, one of which seriously affected the well-known Aiguillette d'Argentière (iconic climbing site in Chamonix Valley) located a few hundred meters far from our study site. We suppose that larger shakings could have reactivated the main gravitational structures on the flank of the massif in the past and that such a scenario may happen in the future. We will investigate and date Holocene morphologies and sediments, at surface and in surrounding lakes, to establish a calendar of both main seismic and gravitational local events and analyze their recurrence periods.

Monitoring and modelling of the present gravitational activity

The freshness of certain outcrops suggests very recent activity of the gravitational rupture, which agrees with the displacement fields estimated by InSAR interferograms produced in the western Alps from Sentinel-1 images. All these data suggest that the movement along the whole structure is still going on nowadays.
The large rock volume situated above the village of Argentière and SNCF railway deserves more detailed geo-mechanical characterization and continuous monitoring. To do this, we propose to instrument the rupture and the rock column using high-resolution distancemeters and seismic sensors (Colombero et al., 2018) for continuously monitoring movements and rock deformations. Part of this instrumentation was installed in 2023 and will be completed in 2024.
We also plan to realize a periodical fine 3D imagery of the topography of the rupture zone, especially in some caves formed along the main discontinuity. Finally, we will keep following the hillslope movements and possible accelerations at the massif scale by satellite interferometry. These techniques combined together allow detecting small rock displacements (mm to cm) at different spatial scales.
In parallel of these analyses, a numerical simulation based on geological and geo-mechanical data will be carried out to reproduce the fall of blocks and calculate their possible trajectory, their energy during the fall phase and the final position they will reach.

Conclusion

Our approach is based on long-term (millennia) and short-term (years, days) observation of the interactions between seismic and gravitational events. This allows identifying and characterizing both big past events, unknown in human memory but having a major impact in the landscape evolution, and small ongoing events or deformation phases, which are crucial data for the natural risk management.

References

Courtial-Manent L. J-L. Mugnier, S. Zerathe, J. Carcaillet, R. Vassallo, L. Ravanel, L. Tavernier, J-F. Buoncristiani (2022) Late Holocene initiation of a deep rock slope failure in an Alpine valley revealed by 10Be surface exposure dating (Chamonix, France). Quaternary International 652, 52-62.

Ritz et al. (2021). New perspectives in studying active faults in metropolitan France : the “Active faults France” (FACT/ATS) research axis from the Resif-Epos consortium. Comptes Rendus. Géoscience, Tome 353 (2021) no. S1, pp. 381-412. doi : 10.5802/crgeos.98. https://comptes-rendus.academie - sciences.fr/geoscience/articles/10.5802/crgeos.98/

Colombero C., Comina C., Vinciguerra S. and Benson P. (2018), Microseismicity of an unstable rock mass: from field monitoring to laboratory testing, Journal of Geophysical Research – Solid Earth, 123 (2), 1673-1693, doi: 10.1002/2017JB014612

RÉPUBLIQUE FRANÇAISE
Liberté
Égalité
Fraternité

MINISTÈRE DE LA TRANSITION ÉCOLOGIQUE ET DE LA COHÉSION DES TERRITOIRES
Liberté
Égalité
Fraternité

DIRECTION GENERALE DE LA PREVENTION DES RISQUES
Service des risques naturels et hydrauliques

Office National des Forêts
rtm

ISL Keynote 8

Public initiatives on landslides risk and mitigation

How Landslides risks are faced in France : PPR, PLU, PAC others « rules » …

An overview of French context


Les Eparres -1993


La Salle en Beaumont - 1994

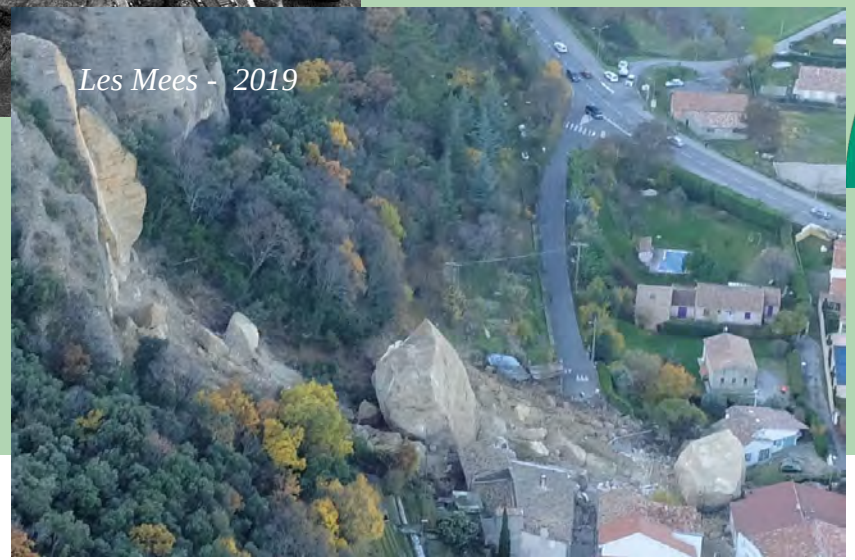
Les Mees - 2019

An overview of French context

Landslides risks in France

- The risk of landslides ***-Rockfall, landslide, cave collapse, swelling soil-***

is present on about 7000 municipalities.

- A high level of risk for the population exists for a third of the cases

- Public policy for the prevention of natural hazards, in particular risks of landslides, is essential in view of the preservation of people and property

Rockfall

Landslide

Cave collapse

Swelling soil

An overview of French context

History of significant landslides events

Mont Granier -2019

Sechilienne - @IRMa / Sébastien Gominet

En France			
1248	Mont Granier, Savoie	Éboulement en grande masse	Entre 300 et 500 millions de m³ recouvrent plusieurs villages, faisant 5 000 morts
1442	Claps de Luc-en-Diois, Drôme	Éboulement et glissement rocheux	1,1 million de m³ de matériaux. Création de deux lacs dont le plus grand couvrait plus de 300 ha
24 nov. **1926**	Roquebillière, Alpes-Maritimes	Glissement de terrain	28 victimes
13 nov. **1932**	Colline des Balmes, Lyon, Rhône	Glissement de terrain	40 victimes dans le quartier Saint-Jean
8 mai **1932**	Lyon, Rhône	Glissement de terrain	30 victimes sur le cours d'Herbouville
1 juin **1961**	Clamart, Hauts-de-Seine	Effondrement	8 ha surplombant une carrière de craie s'effondrent. 21 victimes
16 avril **1970**	Plateau d'Assy, Haute-Savoie	Coulées boueuses	71 victimes dans le sanatorium de Praz-Coutant
1980	Grand-Îlet, cirque de Salazie, la Réunion	Glissement de terrain et coulées boueuses	10 victimes
27 août **1987**	Modane, Savoie	Coulées boueuses	Environ 80 000 m³ de matériaux déversés dans la ville, entraînant 6 millions d'euros de dégâts
1989-1992	Ensemble du territoire métropolitain	Sécheresse géotechnique	Phénomène de retrait-gonflement dans les sols argileux sensibles causant 2 milliards d'euros de dommages
9 janvier **1994**	La Salle-en- Beaumont, Isère	Glissement de terrain	1,3 million de m³ de matériaux détruit 9 maisons et cause la mort de 4 personnes
Avril **2000**	Remire-Montjolly, Guyane	Glissement de terrain	10 victimes du glissement de la colline Cabassou
Été **2003**	Grande partie du territoire métropolitain	Retrait-gonflement des sols argileux	Plus de 100 000 bâtiments fissurés et 1,2 milliard d'euros d'indemnisation
24 mars **2006**	Route du littoral Réunion	Éboulement	Véhicules ensevelis, 2 morts, voie coupée pendant 5 semaines

An overview of French context

Costs for the repair of insured building

Since 1982 *(source CCR Les catastrophes naturelles en France Bilan 1982-2023) : 56,6 Md€*

Requests

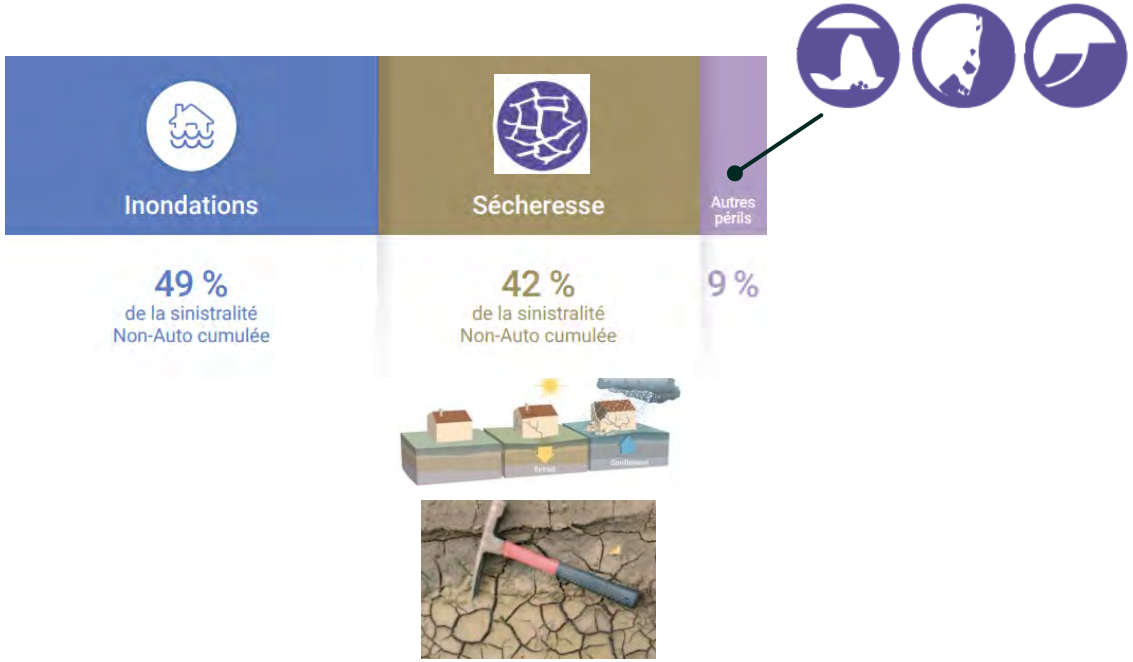

Amount of repairs

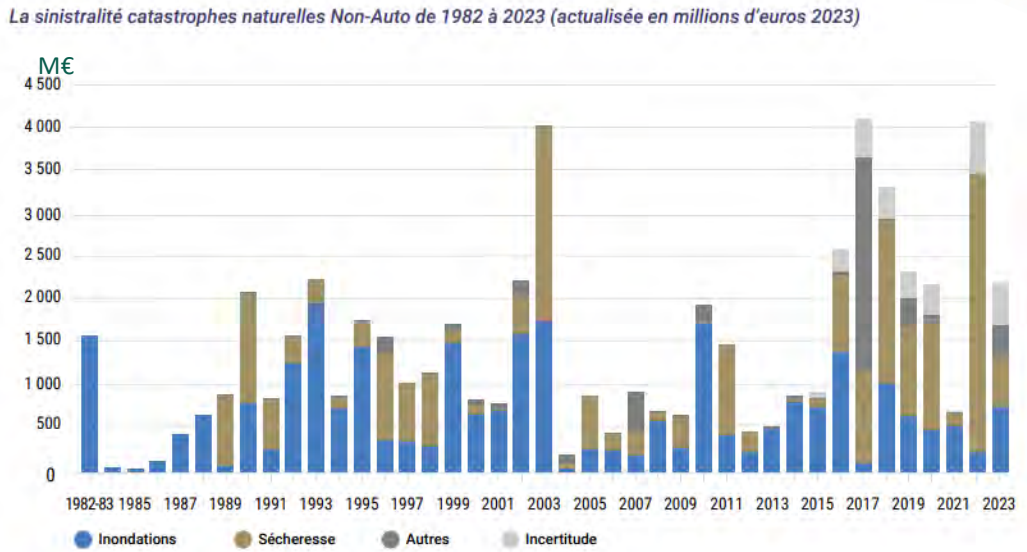

https://catastrophes-naturelles.ccr.fr/les-evenements

An overview of French context

Costs for the repair of insured building

Since 1982 *(source CCR Les catastrophes naturelles en France Bilan 1982-2023) : 56,6 M*

Requests

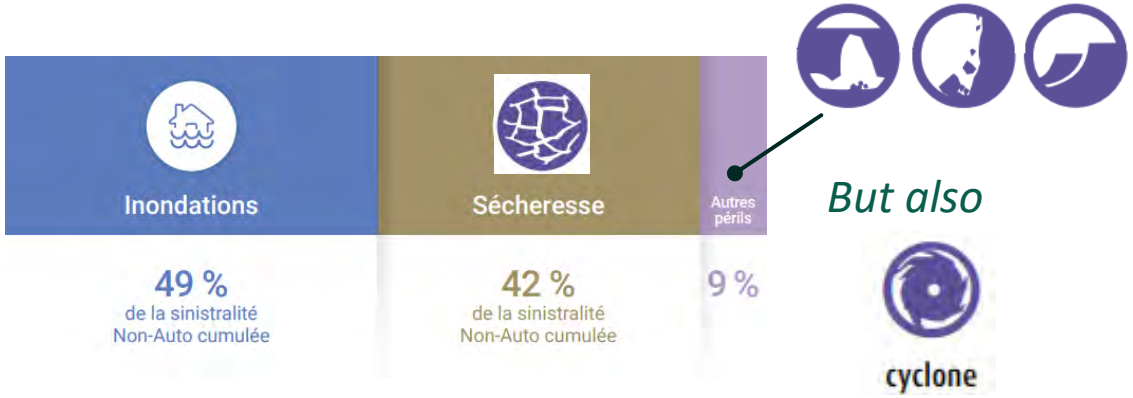

But also

cyclone

IRMA 2017

Amount of repairs

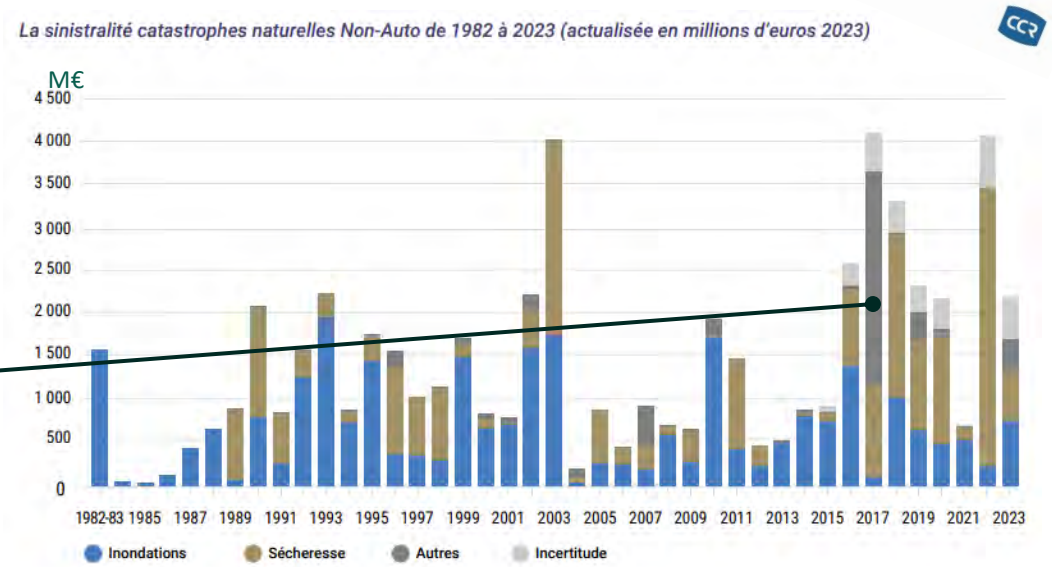

https://catastrophes-naturelles.ccr.fr/les-evenements

The cost of the repair of infrastructures and indirect costs are not included
They are more exposed to rockfalls and landslides

An overview of French context

Principles of public initiatives

Public policy for the prevention of natural hazards is based on a logic of actions :

- Improving knowledge of phenomena

- Reducing the vulnerability of territories

- Preparing for crisis management

- Developing the risk culture

Public actions on natural risks

Evolution of public action for the prevention of natural hazards

Public initiatives on landslides risk and mitigation : how landlisdes risks are faced in France : PPR, PLU, PAC, and others « rules »

Evolution of public action for the prevention of natural hazards

For more than a century, RTM policy

Evolution of public action for the prevention of natural hazards

For more than a century, RTM policy

1935, plan of submersible surfaces

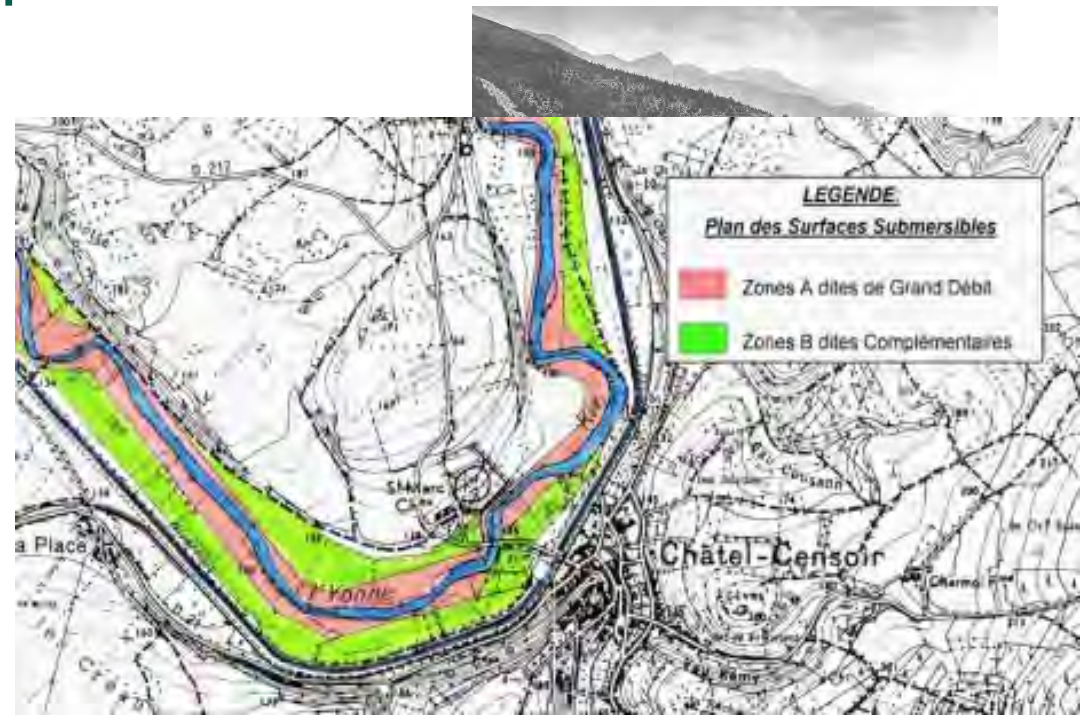

Evolution of public action for the prevention of natural hazards

For more than a century, RTM policy

1935, plan of submersible surfaces

1955, risk perimeter in building code


COMMUNES de Gruse et de Retuller

DELIMITATION D'UN PERIMETRE DE RISQUES

REGLEMENT

annexe à l'arrêté préfectoral du 28 OCT. 1982
pris pour l'application de l'article R 111.3 du code de l'urbanisme

Préambule

Article R 111.3 du code de l'urbanisme :

"La construction sur des terrains exposés à un risque tel que : inondation, érosion, affaissement, éboulement, avalanches, peut, si elle est autorisée, être soumise à des conditions spéciales."

"Ces terrains sont délimités par arrêté préfectoral pris après consultation des services intéressés et enquête dans les formes prévues par le code de l'expropriation pour cause d'utilité publique et avis du conseil municipal."

Règlement

Article 1er : en zone I, toute construction soumise au régime juridique des autorisations d'occupation du sol du code de l'urbanisme et visant à la création de nouvelles surfaces bâties, à l'augmentation de la

Evolution of public action for the prevention of natural hazards

For more than a century, RTM policy

1935, plan of submersible surfaces

1955, risk perimeter in building code

1982, risk exposure plan (PER)

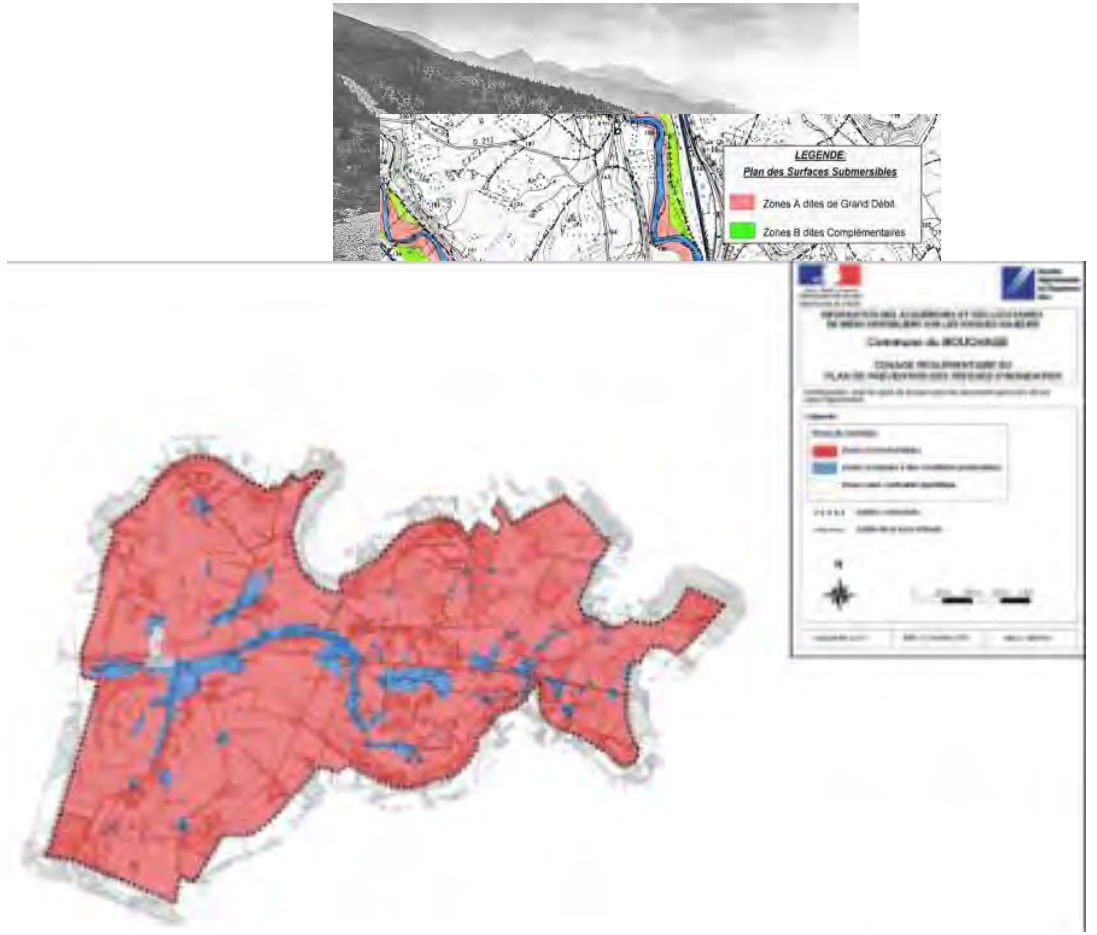

Evolution of public action for the prevention of natural hazards

For more than a century, RTM policy

1935, plan of submersible surfaces

1955, risk perimeter in building code

1982, risk exposure plan (PER)

1987, preventive information and forest fire risk mapping (PZSIF)

Evolution of public action for the prevention of natural hazards

For more than a century, RTM policy

1935, plan of submersible surfaces

1955, risk perimeter in building code

1982, risk exposure plan (PER)

1987, preventive information and forest fire risk mapping (PZSIF)

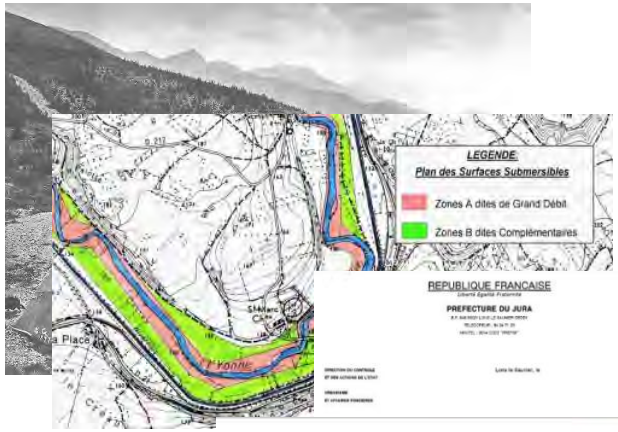

1995, natural hazard prevention plan

PPRN Plan de Prévention des Risques Naturels

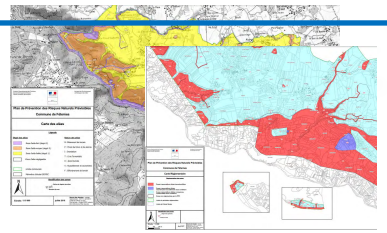

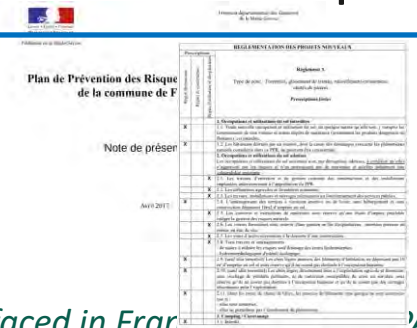

Evolution of public action for the prevention of natural hazards

1995, Plan de Prevention pour les Risques Naturels PPRN

Prevention Plan for natural hazards

- **More than half of the French municipalities are exposed** to natural hazard risk
- Risk is a combination of
  - **one or more hazards** (flooding, rockfall, landslides, cave collapse, earthquakes, avalanches, forest fires, hurricane, ...)
  - **existing local at–risks elements** (people, property, activities, resources, natural and urban heritage features that are likely to be affected by a natural phenomenon).

The Law on Strengthening Environmental Protection passed in 1995 provides the State with **a regulatory tool that is dedicated to the prevention of risks** : **PPRN** : the Natural Hazard Risk Prevention Plan.

Evolution of public action for the prevention of natural hazards

1995, PPRN

- **More than half of the French municipalities are exposed** to natural hazard risk
- Risk is a combination of
  - **one or more hazards** (flooding, rockfall, landslides, cave collapse, earthquakes, avalanches, forest fires, hurricane, ...)
  - **existing local elements at risk** (people, property, activities, resources, natural and urban heritage features that are likely to be affected by a natural phenomenon).

The Law on Strengthening Environmental Protection passed in 1995 provides the State with **a regulatory tool that is dedicated to the prevention of risks** : **PPRN** : the Natural Hazard Risk Prevention Plan.

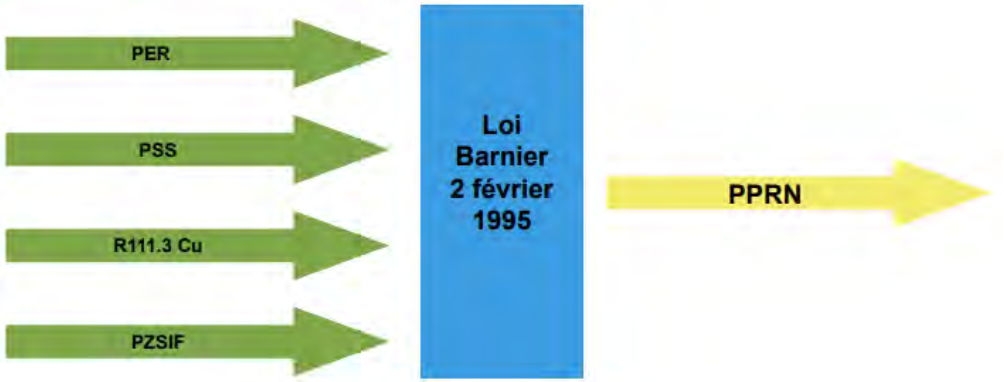

Evolution of public action for the prevention of natural hazards

Since 1995, PPRN has been one of the main tools for natural risks prevention

2024, more than 14 000 municipalities have a PPRN

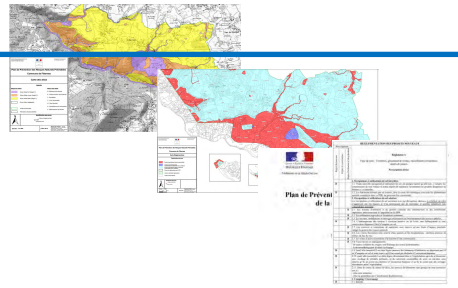

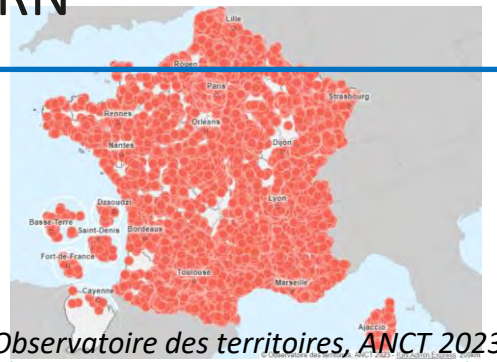

Observatoire des territoires, ANCT 2023

Evolution of public action for the prevention of natural hazards

Since 1995, PPRN has been one of the main tools for natural risks prevention

Legislative evolution

2003, risk law
2010,
2014,
2021, Climate resilience law
……..

2024, more than 14 000 municipalities have a PPRN

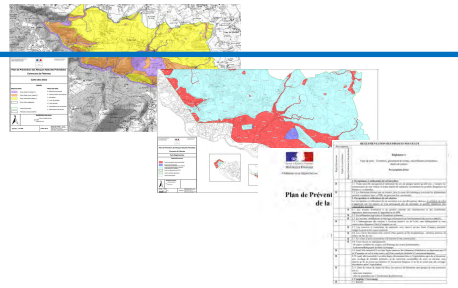

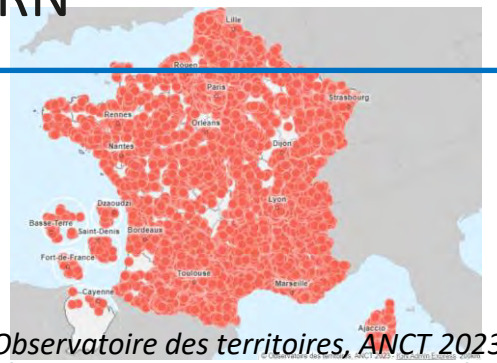

Observatoire des territoires, ANCT 2023

Evolution of public action for the prevention of natural hazards

Since 1995, PPRN has been one of the main tools for natural risks prevention

Legislative evolution

2003, risk law
2010,
2014,
2021, Climate resilience law
……..

Guide development

Hazard mapping
Framework
Consulting the public

2024, more than 14 000 municipalities have a PPRN

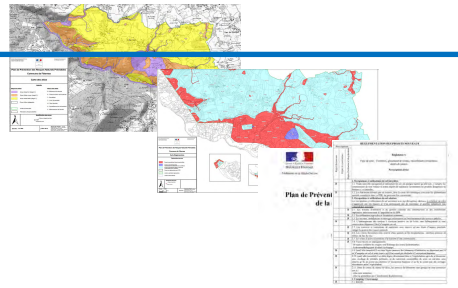

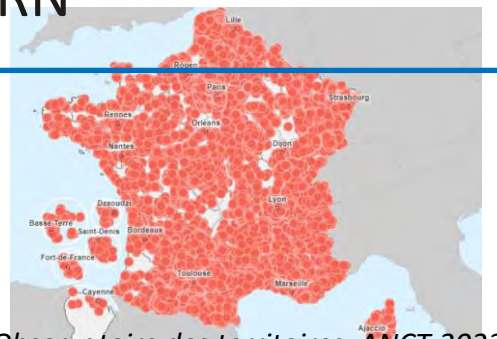

Observatoire des territoires, ANCT 2023

Evolution of public action for the prevention of natural hazards

Since 1995, PPRN has been one of the main tools for natural risks prevention

Legislative evolution

2003, risk law
2010, …
2014, ….
2021, Climate resilience law
……..

Feedback

2014, COTECH Montagne
……

Guide development

Hazard mapping
Framework
Consulting the public

2024, more than 14 000 municipalities have a PPRN

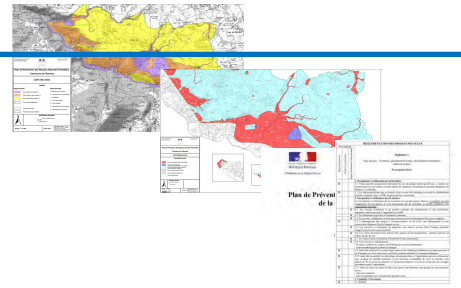

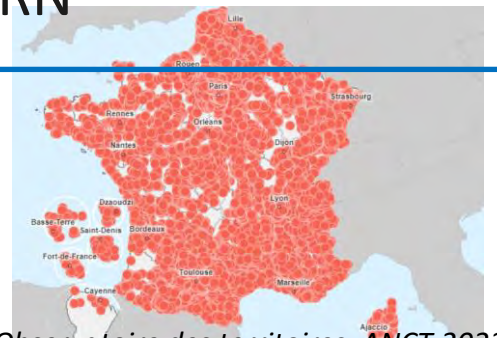

Observatoire des territoires, ANCT 2023

PPRN

A tool for the State's natural hazard risk prevention policy

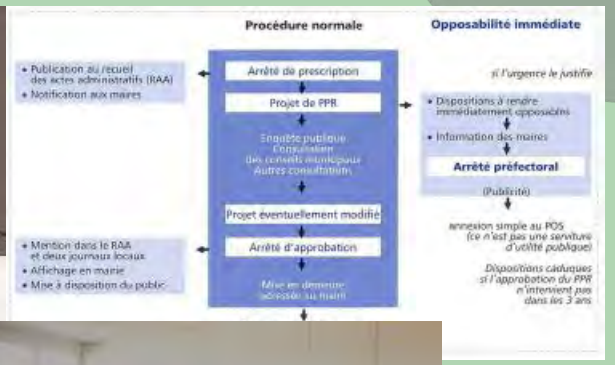

www.alpconv.org

www.alpconv.org/fileadmin/user_upload/Publications/RSA/RSA7_EN.pdf

A tool for the State's natural hazard risk prevention policy

The PPRN's aims :

- ✓ **Prevent** people and properties from being increasingly exposed to natural hazards risks;
- ✓ **Reduce the negative impact** of natural hazards on human lives, the environment, economic activity and cultural heritage;
- ✓ Always considering **sustainable development** of territories.

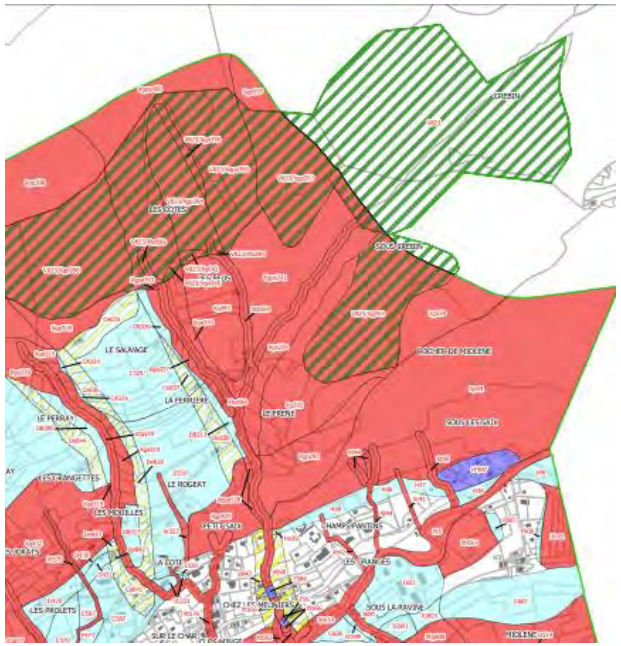

A tool for the State's natural hazard risk prevention policy

The PPRN's aims :

- ✓ **Prevent** people and properties from being increasingly exposed to natural hazard risks;
- ✓ **Reduce the negative impact** of natural hazards on human lives, the environment, economic activity and cultural heritage;
- ✓ Always considering **sustainable development** of territories.

The PPRN contributes to decreasing exposure to natural hazards :

- ✓ By **defining high risk zones** where buildings or other facilities are **prohibited**

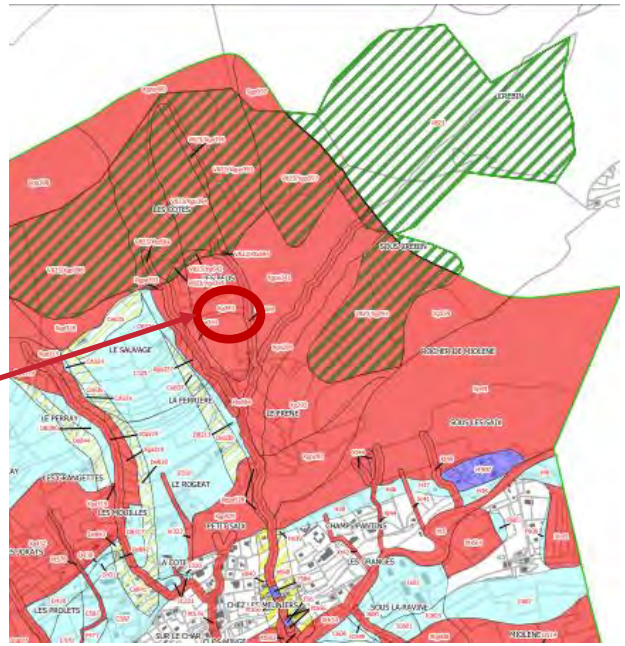

A tool for the State's natural hazard risk prevention policy

The PPRN's aims :

- ✓ **Prevent** people and properties from being increasingly exposed to natural hazard risks;
- ✓ **Reduce the negative impact** of natural hazards on human lives, the environment, economic activity and cultural heritage;
- ✓ Always considering **sustainable development** of territories.

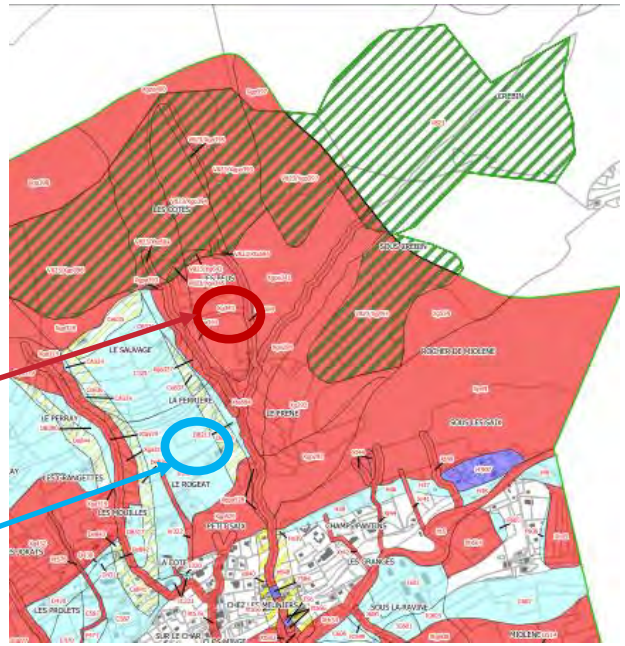

The PPRN contributes to decreasing exposure to natural hazards :

- ✓ By **defining high risk zones** where buildings or other facilities are **prohibited**
- ✓ By **allowing other zones to be developed** in a thought-out and safe manner complying **with certain requirements** in line with the potential hazard intensity (medium or low).

A tool for the State's natural hazard risk prevention policy

The PPRN contributes to the **reduction of potential damage** by defining prevention, protection and conservation measures, alongside measures relating to the development or use of buildings, civil engineering structures, and agricultural areas existing on the date of the plan's establishment.

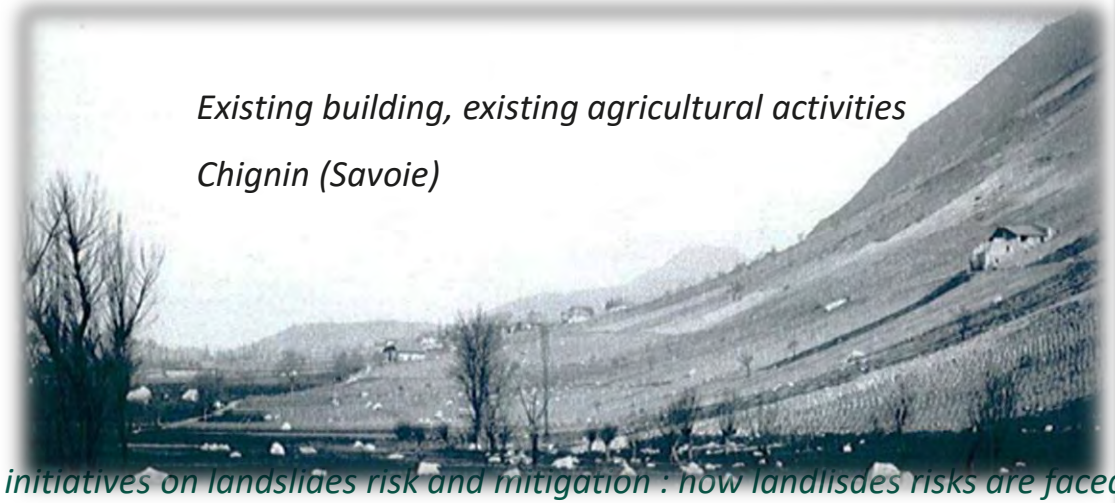

Existing building, existing agricultural activities

Chignin (Savoie)

A tool for the State's natural hazard risk prevention policy

The contents of a PPRN

A PPRN consists of three documents:

1) **A project outline** that indicates :
   - ✓ the geographical area concerned,
   - ✓ the nature of the natural phenomena in question
   - ✓ their possible consequences based on the current state of knowledge.


Liberté • Égalité • Fraternité
RÉPUBLIQUE FRANÇAISE
PRÉFECTURE DE LA HAUTE-SAVOIE
DIRECTION DÉPARTEMENTALE DES TERRITOIRES

P.P.R.

PLAN DE PRÉVENTION DES RISQUES NATURELS PRÉVISIBLES
DE LA COMMUNE DE
VEYRIER-DU-LAC

LIVRET I :

« RAPPORT DE PRESENTATION »

02 août 2010

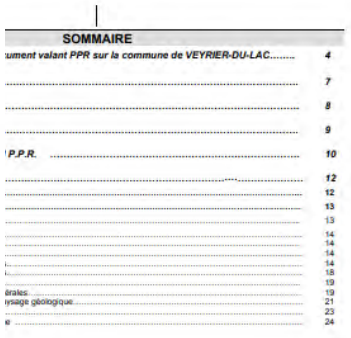
SOMMAIRE

02 août 2010


E CONTEXTE GENERAL

Extrait de la carte IGN au 1/100 000.

12

02 août 2010


Annecy, vue du synclinal de Leschaux (St-Eustache)
d'après B. DOUDOUX.

Articulation

le rocher des Grandes-Sulles et le Mont Baret forment un synclinal pincé
explique en partie la fracturation importante du massif... et les nombreuses

21

02 août 2010

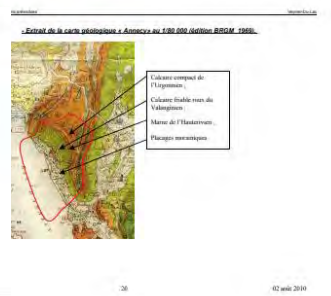
- Extrait de la carte géologique « Annecy » au 1/80 000 (édition BRGM, 1969).

Calcaire compact de l'Urgonien ;
Calcaire friable roux du Valanginien ;
Marne de l'Hauterivien ;
Placages morainiques ;

20

02 août 2010

It justifies preventive choices made, indicating the principles governing the PPRN's development and explaining the regulations in place.

A tool for the State's natural hazard risk prevention policy

2) **A regulatory zoning plan**:
   - ✓ Combines information from the hazard map and the at-risk elements' map to define the regulated areas by the PPRN
   - ✓ **Defines the current zones at risk**, but also zones where **development could aggravate the existing risks or cause new ones**
   - ✓ Hazard map characterizes the phenomena to which the risk area is exposed and determines a reference hazard
   - ✓ Allows to **locate** and **classify** the various hazard zones
   - ✓ At-risk elements are **assessed qualitatively** regarding land use and occupation patterns.

A tool for the State's natural hazard risk prevention policy

2) A regulatory zoning plan:

- ✓ Combines information from the hazard map and the at-risk elements' map to define the regulated areas by the PPRN
- ✓ **Defines the current zones at risk**, but also zones where **development could aggravate the existing risks or cause new ones**
- ✓ Hazard map characterizes the phenomena to which the risk area is exposed and determines a reference hazard
- ✓ Allows to **locate** and **classify** the various hazard zones
- ✓ Stakes are **assessed qualitatively** regarding land use and occupation patterns.

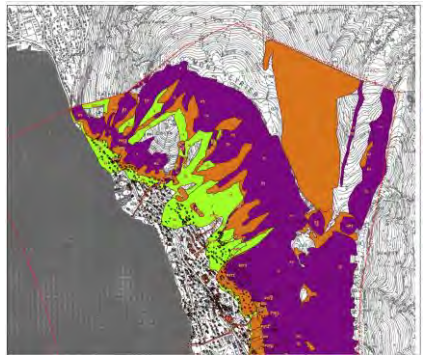

hazard map and at-risk elements map

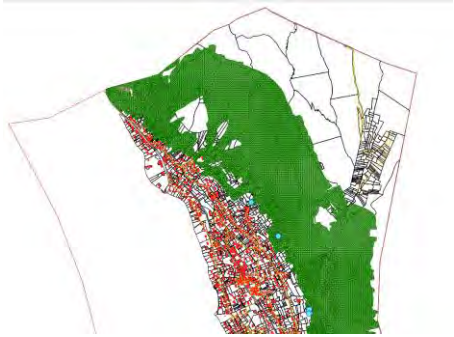

A tool for the State's natural hazard risk prevention policy

2) A regulatory zoning plan:

- ✓ Combines information from the hazard map and the stakes' map to define the regulated areas by the PPRN
- ✓ **Defines the current zones at risk**, but also zones where **development could aggravate the existing risks or cause new ones**
- ✓ Hazard map characterizes the phenomena to which the risk area is exposed and determines a reference hazard
- ✓ Allows to **locate** and **classify** the various hazard zones
- ✓ Stakes are **assessed qualitatively** regarding land use and occupation patterns.

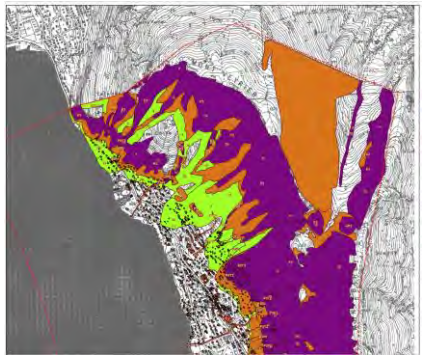

hazard map and elements at risk map

Zoning plan

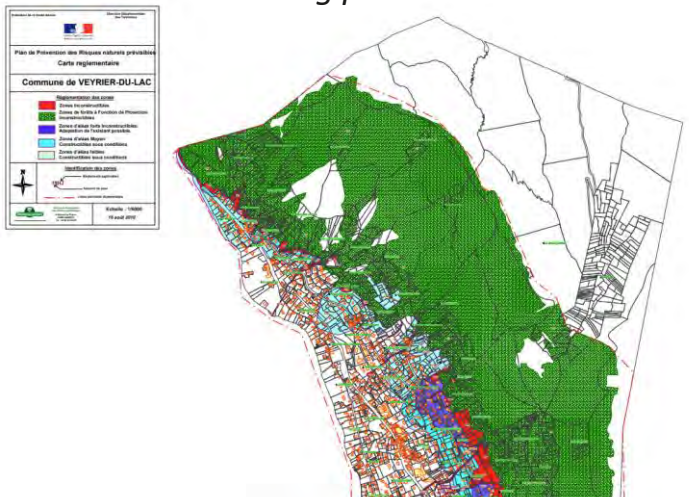

A tool for the State's natural hazard risk prevention policy

3) A regulatory document :

- ✓ **specifies the rules applicable** to each of the zones.
- ✓ **defines the conditions** in which any construction, civil engineering works, developments and agricultural, forestry, artisanal, commercial or industrial operations are to be carried out.
- ✓ **regulates the preventive, protective and conservation measures** for which individuals or local authorities are responsible, but also any mandatory measures applicable to existing property and activities.

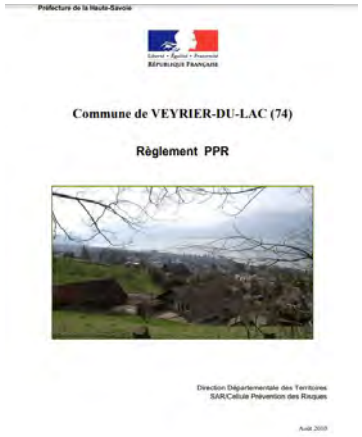
Préfecture de la Haute-Savoie

Commune de VEYRIER-DU-LAC (74)

Règlement PPR

Direction Départementale des Territoires
SAR/Cellule Prévention des Risques

Rules for new project

Rules for existing features

Preventive, protective measures

Public initiatives on landslides risk and [illegible] dlisdes risks are [illegible] PPR, PLU, PAC, and others « rules »

A tool for the State's natural hazard risk prevention policy

The role of a PPRN

The methodology regarding the development of risk prevention plans is described in a general guide and the specificities regarding the particular hazards dealt with are found in thematic guides. The PPRN can deal with a single type of risk or with several and may extend over one or more communes.

- The **PPRN** represents a **-PAC-** an official transmission of knowledge from state to local authorities
- As the PPRN represents a public utility easement, it is attached to any urban planning document **-PLU-**. It applies to everyone : individuals, businesses, local authorities and the State
- The PPRN is taken into account in the "Plan Communal de Sauvegarde" **-PCS-** established by the local authorities, this document specifies the organization of first emergency relief
- The PPRN enables **financial assistance** for protective measures

A tool for the State's natural hazard risk prevention policy

- Several General guides
- a guide for rockfalls and landslides
- Guides for other phenomena

A tool for the State's natural hazard risk prevention policy

MEZAP : national framework for rockfall hazard mapping

(Presentation of B. Colas Thursday 11th)

MEZAG : national framework for landslides – *in progress* –

MEZAR : national framework for rocky cliff top retreat– in progress -

Example: a landslide risk prevention plan

Hazar map

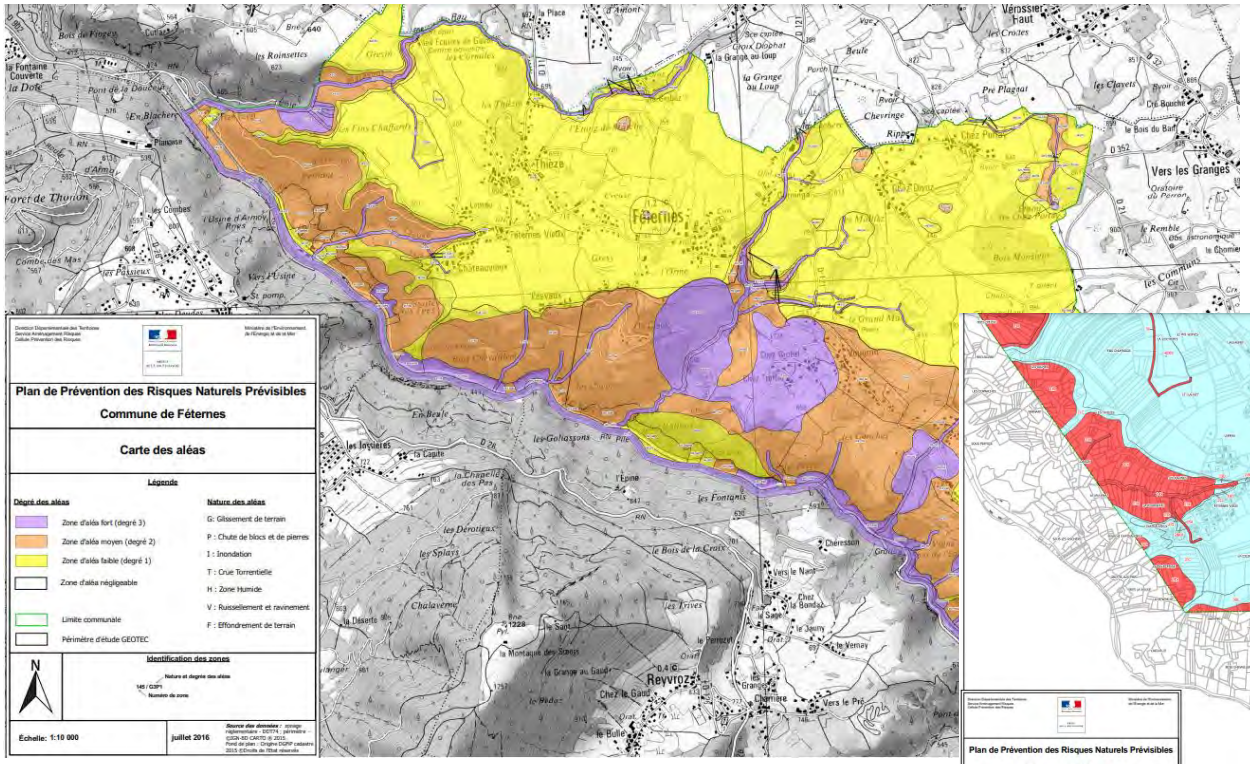

Regulatory zoning plan

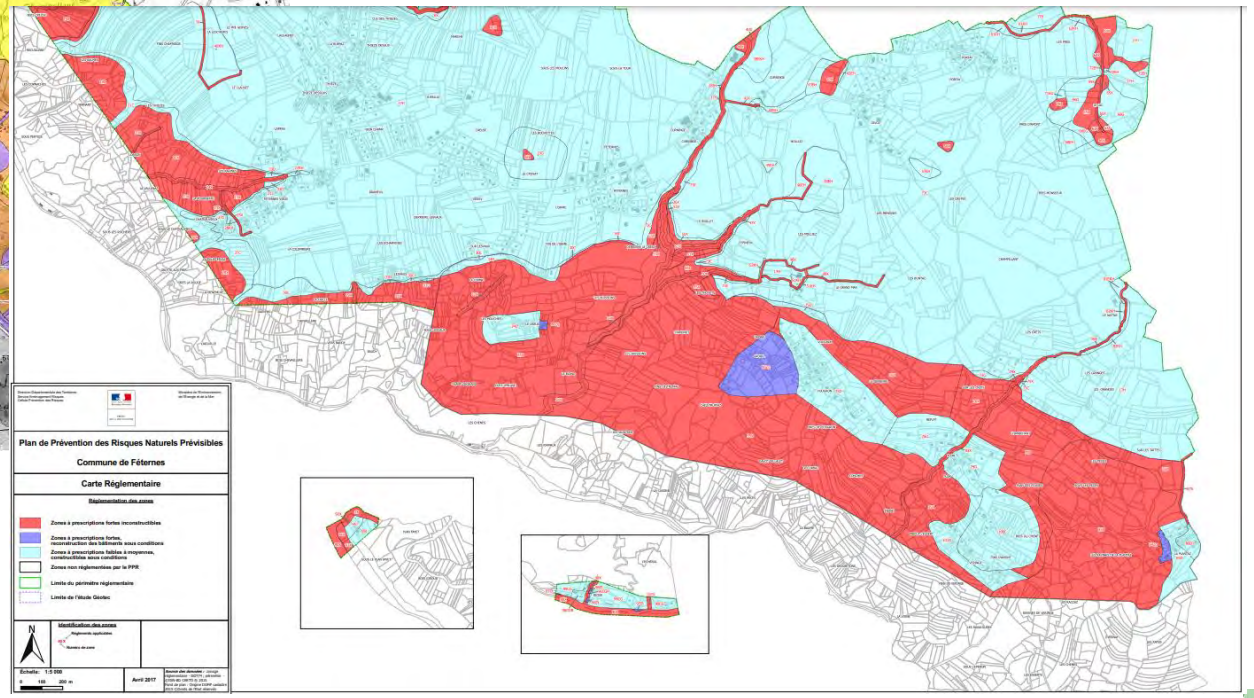

Example: a landslide risk prevention plan

PPRN specifies the rules applicable to each of the zones for the new project

REGLEMENTATION DES PROJETS NOUVEAUX			
Prescriptions			
Règles d'urbanisme	Règles de construction	Règles d'utilisation et d'exploitation	**Règlement X** Type de zone : Torrentiel, glissement de terrain, ruissellement-ravinement, chutes de pierres **Prescriptions fortes**
			1. Occupations et utilisations du sol interdites
X			1.1. Toute nouvelle occupation et utilisation du sol, de quelque nature qu'elle soit, y compris les terrassements de tout volume et autres dépôts de matériaux (notamment les produits dangereux ou flottants), est interdite.
X			1.2. Les bâtiments détruits par un sinistre, dont la cause des dommages concerne les phénomènes naturels considérés dans ce PPR, ne pourront être reconstruits.
			2. Occupations et utilisations du sol admises Les occupations et utilisations du sol suivantes sont, par dérogation, admises, à condition qu'elles n'aggravent pas les risques et n'en provoquent pas de nouveaux et qu'elles présentent une vulnérabilité restreinte :
		X	2.1. Les travaux d'entretien et de gestion courants des constructions et des installations implantées antérieurement à l'approbation du PPR.
		X	2.2. Les utilisations agricoles et forestières courantes.
		X	2.3. Les travaux, installations et ouvrages nécessaires au fonctionnement des services publics.
X			2.4. L'aménagement des terrains à vocation sportive ou de loisir, sans hébergement et sans construction dépassant 10m2 d'emprise au sol.
		X	2.5. Les carrières et extractions de matériaux sous réserve qu'une étude d'impact préalable intègre la gestion des risques naturels.
		X	2.6. Les voiries forestières sous réserve d'une gestion en fin d'exploitation : entretien pérenne ou remise en état du site.
		X	2.7. Les voies d'accès nécessaires à la desserte d'une construction.
		X	2.8. Tous travaux et aménagements : - de nature à réduire les risques sauf drainage des zones hydromorphes. - hydromorphologiques d'intérêt écologique
X			2.9. (sauf aléa torrentiel) Les abris légers annexes des bâtiments d'habitation ne dépassant pas 10 m² d'emprise au sol et sous réserve qu'il ne soient pas destinés à l'occupation humaine.
X			2.10. (sauf aléa torrentiel) Les abris légers directement liées à l'exploitation agricole et forestière, sans stockage de produits polluants, ni de matériaux susceptibles de créer un sur-aléa, sous réserve qu'ils ne soient pas destinés à l'occupation humaine et qu'ils ne soient pas des ouvrages structurants pour l'exploitation.
X			2.11. Dans les zones de chutes de blocs, les annexes de bâtiments type garages ne sont autorisées

REGLEMENTATION DES PROJETS NOUVEAUX			
Prescriptions			
Règles d'urbanisme	Règles de construction	Règles d'utilisation et d'exploitation	**Règlement D** Type de zone : Instabilité de terrain **Prescriptions moyennes**
			1. Tout projet
X			1.1. Adapter la construction à la nature du terrain par une étude géotechnique de sol obligatoire. Cette étude devra spécifier les modalités de terrassement, de soutènement de talus, de construction du bâti (notamment la résistance des façades) et du drainage des parcelles concernées par le projet. L'étude sera confiée à un bureau d'étude spécialisé (voir Partie I, paragraphe 2.3.).
X			1.2. Les eaux usées seront rejetées dans les réseaux existants ou après traitement dans un exutoire superficiel capable de recevoir un débit supplémentaire. Lorsqu'une étude d'assainissement le prévoit, les rejets pourront être infiltrés dans les conditions prévues. En l'absence d'une telle étude, les infiltrations sont interdites. Il conviendra, en outre, de s'assurer que la filière mise en oeuvre n'est pas de nature à aggraver le phénomène d'instabilité de terrain.
X			1.3. Les eaux pluviales et de drainage seront rejetées dans les réseaux existants ou dans un exutoire superficiel capable de recevoir un débit supplémentaire. Lorsqu'une étude de gestion des eaux pluviales le prévoit, les rejets pourront être infiltrés dans les conditions prévues. En l'absence d'une telle étude, les infiltrations sont interdites. Il conviendra, en outre, de s'assurer que la filière mise en oeuvre n'est pas de nature à aggraver le phénomène d'instabilité de terrain.
	X		1.4. Concevoir ou modifier les réseaux (eau, gaz, câbles) pour réduire leur sensibilité aux mouvements de terrain.
	X		1.5. Sous réserve de respecter les points 1.2 et 1.3 ci-dessus, les aires imperméabilisées seront limitées au stationnement et voies d'accès ainsi qu'aux aménagements nécessaires au respect de la réglementation agricole en vigueur.
X			1.6. Les abris légers annexes de bâtiments existants, ne dépassant pas 20 m² d'emprise au sol et non destinés à l'occupation humaine, sont autorisés et ne sont pas soumis aux prescriptions 1.1 à 1.3.
X			1.7. Les bâtiments, équipements et installations dont le fonctionnement est primordial pour la sécurité civile, pour la défense ou pour le maintien de l'ordre public ne sont pas autorisés.
X			1.8. L'implantation de terrains de camping/caravanage est interdite.
			2. Occupations et utilisations du sol
		X	2.1. Assurer la végétalisation des talus après terrassement.
X		X	2.2. Tous travaux de terrassement (remblai, déblais) de plus de 2 mètres de hauteur devront faire l'objet d'une étude de stabilité spécifiant les techniques de stabilisation du terrassement et de son environnement à mettre en œuvre. Un drainage devra être réalisé. Pour des terrassements de moins de deux mètres de hauteur, les pentes des talus devront être appropriées afin de ne pas

Example: a landslide risk prevention plan

PPRN specifies the rules applicable to each of the zones for the new project

For examples

High risk area : rules for new project

1- any new occupation and land use is prohibited

Buildings destroyed by a disaster cannot be rebuilt

…

2-By way of derogation, occupations and land uses may be permitted if they don't increase the risk :

Common agricultural and forestry uses

Works, facilities necessary for the operation of public services

…

For examples

Medium risk area : rules for new project

1- for all projects

Geotechnical study

Water control

Buildings, equipment and installations whose operation is essential for civil security, defence or the maintenance of public order are not allowed

…

2-For occupation and land use

Do a revegetation of slopes after earthwork

…

Example: a landslide risk prevention plan

PPRN specifies the rules applicable to each of the zones for existing features

MESURES SUR LES BIENS ET ACTIVITES EXISTANTS
Règlement Zg **Type de zone : Instabilité de terrain** **Zones à prescriptions fortes**
1.Constructions, occupations et utilisations du sol
Mesures obligatoires dans la limite de 10 % de la valeur vénale ou estimée des biens Mise en place de dispositifs de collecte des eaux avec rejet vers un exutoire naturel ou aménagé conformément aux normes en vigueur, si la parcelle est déjà desservie par de tels exutoires. Ces réseaux doivent être étanches et conçus pour réduire leur sensibilité aux mouvements de terrain. A l'occasion d'une réfection ou d'un entretien lourd, réduire la sensibilité des réseaux (eau, gaz, câbles).
2. Établissement recevant du public
Mesures obligatoires Dans un délai de 2 ans à compter de la date d'approbation du présent PPR : Pour les bâtiments, leurs abords et annexes, préexistants et recevant du public, une étude de risque définira les conditions de mise en sécurité des occupants et usagers, et, s'il s'agit d'un service public lié à la sécurité, les modalités pour assurer la continuité de celui-ci. Réalisation des protections définies par l'étude. Application des mesures définies par l'étude.
3. Camping / Caravanage
Pour chaque terrain aménagé, exposé à un risque naturel prévisible : respect des prescriptions d'alerte, d'information et d'évacuation prescrites par le maire ou, le cas échéant, par le préfet. (article L 443-2 du Code de l'Urbanisme.)

Example: a landslide risk prevention plan

PPRN specifies the rules applicable to each of the zones for existing features

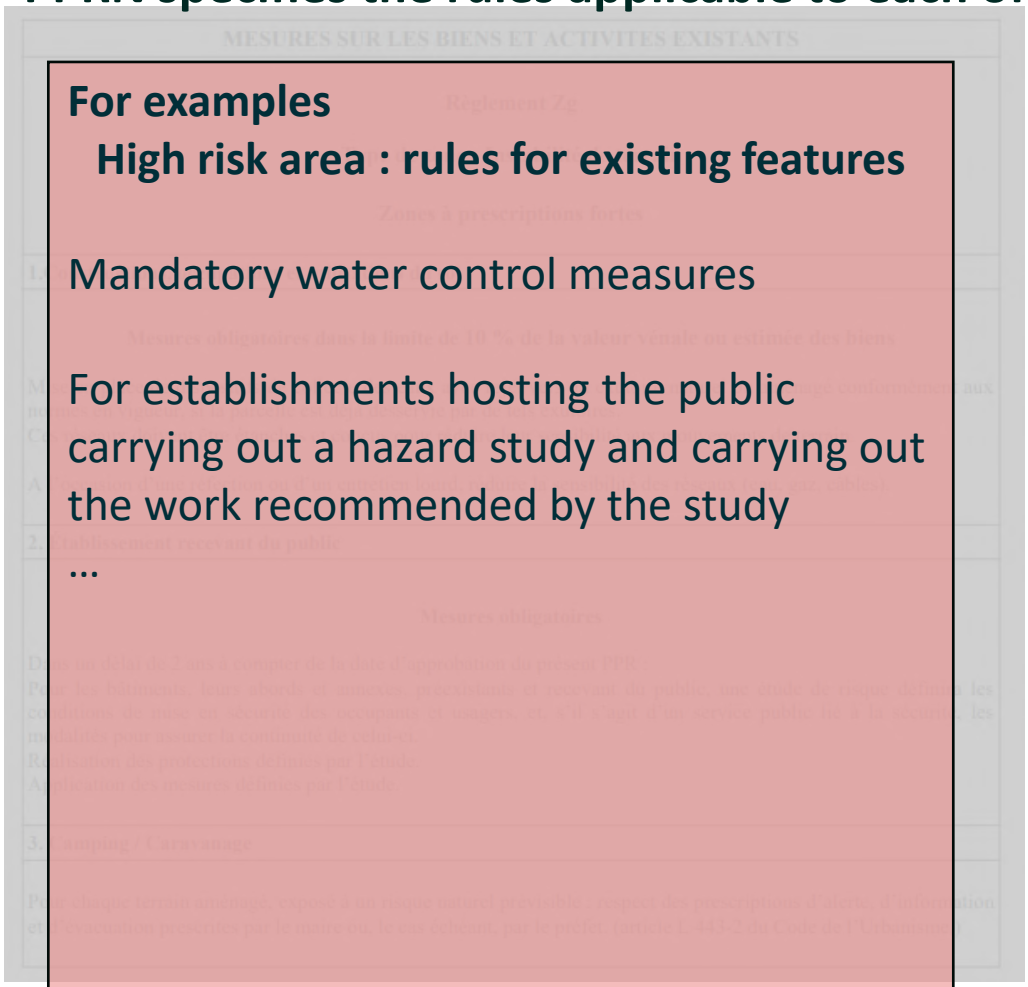

For examples

High risk area : rules for existing features

Mandatory water control measures

For establishments hosting the public carrying out a hazard study and carrying out the work recommended by the study

…

Example: a landslide risk prevention plan

PPRN specifies preventive, protective and conservation measures

Article1 : Les mesures de prévention

Elles permettent l'amélioration de la connaissance des aléas, l'information des personnes et la maîtrise des phénomènes.

Mesures de prévention	Mesures à la charge de	Délais de
Réaliser des campagnes d'information des particuliers et des professionnels sur les risques naturels concernant la commune ainsi que les règles à respecter en matière de construction et d'utilisation du sol. (article L. 125-2 du Code de l'Environnement)	Commune	Au moins tous les **deux** ans.
Le document d'information communal sur les risques majeurs (DICRIM) reprend les informations transmises par le préfet. Il indique les mesures de prévention, de protection et de sauvegarde répondant aux risques majeurs susceptibles d'affecter la commune. Ces mesures comprennent, en tant que de besoin, les consignes de sécurité devant être mises en oeuvre en cas de réalisation du risque. Le maire fait connaître au public l'existence du document d'information communal sur les risques majeurs par un avis affiché à la mairie pendant deux mois au moins. Le document d'information communal sur les risques majeurs est consultable sans frais à la mairie. (décret n° 2004-554 du 9 juin 2004)	Commune	Dès notification du porter à connaissance (préfet)
Les locataires ou les acquéreurs de biens immobiliers situés dans des zones couvertes par un PPR doivent être informés par le bailleur ou le vendeur de l'existence des risques visés par ce plan. (article 77 de la loi du 30 juillet 2003, décret 2005-134 du 15 février 2005)	Vendeur ou bailleur d'après un arrêté préfectoral transmis au maire et à la chambre départementale des notaires.	*Annexer à toute promesse de vente ou d'achat, à tout contrat constatant la vente ainsi qu'à tout contrat de location.*

Article 2 : Mesures de protection

Elles permettent de maîtriser l'aléa par l'entretien ou la réhabilitation des dispositifs de protection existants, ou de le réduire en créant des nouveaux dispositifs.

La maîtrise d'ouvrage des travaux de protection, s'ils sont d'intérêt collectif, revient aux communes dans la limite de leurs ressources.

- d'une part, en application des pouvoirs de police que détiennent les maires au titre du code général des collectivités territoriales (CGCT article L 2212.2.5°)
- d'autre part, en raison de leur caractère d'intérêt général ou d'urgence du point de vue agricole, forestier ou de l'aménagement des eaux (article L 151-31 du code rural).

Ces dispositions peuvent aussi s'appliquer à des gestionnaires d'infrastructures publiques et à des associations syndicales de propriétaires (article L 151-41 du code rural).

Mesures de protection	Mesures à la charge de	Délais de
Surveillance et entretien des ouvrages de protection (épis, enrochements, gabions, ouvrages paravalanches, merlons, digues, filets, ancrages…)	Maître d'ouvrage	Immédiat et régulier
Les coupes rases sur de grandes surfaces (> 2 ha) et sur des versants soumis à des phénomènes naturels sont en principe proscrites par arrêté préfectoral + règlement V	Commune ou propriétaire	
Entretien régulier du cours d'eau afin de maintenir son profil d'équilibre (article L 215-14 du Code de l'Environnement)	Propriétaire riverain **ou** commune ou EPCI compétent	Régulier
Entretien de la rive par élagage et recépage de la végétation arborée et enlèvement des embâcles et débris, flottants ou non, afin de maintenir l'écoulement naturel des eaux. (article L 215-14 du Code de l'Environnement)	Propriétaire riverain	Régulier et après chaque crue importante

Example: a landslide risk prevention plan

PPRN specifies preventive, protective and conservation measures

For examples

Preventive measures

Carry out information campaigns for individuals and professionals on natural hazards

Information for tenants and buyers

…

For examples

Protective measures

Monitoring and maintenance of protective structures

Prohibition of lear cutting of forest on large area

Regular maintenance of waterways

…

Governance and risk governance aspects

Governance and risk governance aspects

- PPRNs are **established for the most exposed areas** under the authority of the department prefect. Their development is **financed by the State** through the fund for the prevention of major natural hazards (fond Barnier). PPRNs are carried out within an involving and consultative framework together with the regional and local authorities in charge.

- **Involvement is essential** for public action to be effective. It creates the trusting climate necessary for accepting the analyses and decisions that form the basis of the PPRN project. The various stakeholders – particularly **regional and local authorities responsible for territorial planning – are therefore involved** from the very beginning of the process, mostly through meetings.

- **Consulting the public is a fundamental success factor** and should be done as comprehensively as possible. The objective is for the process to be shared by everyone concerned. It allows for an open debate and public discussion between the various stakeholders on a project that affects the area and the local population.

Consulting the general public

Consulting the general public

Consulting the general public is a fundamental success factor and should be done as comprehensively as possible. The objective is for the process to be shared by everyone concerned. It allows for an open debate and public discussion between the various players on a project that affects the area and the local population. Public consultation can take several forms (public meetings, websites, discussion forums, town hall registers …) and is particularly effective during the following stages :

- First discussions;
- Hazard, at-risk elements studies;
- Local preventive strategy and PPRN project.

Official authorization is given after conducting a public inquiry. Then, the PPRN must be approved (and authorised by the prefect).

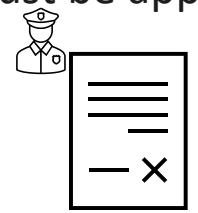

Conclusion

Conclusion

- ✓ The PPRN is ***an operational tool*** that has been available since 1995 with the aim of reconciling development and risk, while reducing the vulnerability of people and property.
- ✓ It requires a coherent approach ***involving all stakeholders*** (State, regional and local authorities, civil society etc.) and a consultative and instructive spirit.
- ✓ The ***involvement of the public*** is a fundamental factor to ensure that the plans are accepted by the local stakeholders and public.
- ✓ This approach should lead to a suitable formulation of the PPRN's regulatory requirements, so as not to hinder urbanisation unnecessarily. These requirements should also ensure suitable construction conditions in risk zones, ***taking into account the local heritage and architecture***.
- ✓ The existence of a PPRN also creates opportunities for ***financing and subsidies*** –especially for local authorities– to reduce vulnerability

Informations

https://www.ecologie.gouv.fr/politiques-publiques/prevention-risques-naturelsolution of public action for the prevention of natural hazards

https://www.georisques.gouv.fr/consulter-les-dossiers-thematiques/observatoire-national-des-risques-naturels

Thank you for your attention.

Towards a novel quantitative approach for rockfall hazard assessment

Arthur F. Rossignol[1], Rémy Martin[2], Franck Bourrier[3]

[1] École polytechnique, IP Paris, Palaiseau 91120, France
[2] French National Forests Office, RTM Service, Northern Alps Agency, Grenoble 38000, France
[3] University Grenoble-Alpes, INRAE, Grenoble 38000, France

SUMMARY: This study explores an approach based on a probabilistic modelling to quantify the rockfall reach probability. The method relies mainly on the combination of several intermediate probabilities. An operational application for diffuse hazard is provided to integrate results from rock propagation simulation, along with two examples and a discussion of the theoretical and practical issues involved.

Keywords: rockfalls / hazard quantification / reach probability / rock propagation simulation / propagation probability / diffuse hazard.

Introduction

Rockfall hazard assessment constitutes a major challenge for institutions in charge of security of human lives and material goods. Nowadays, it relies on diverse quantitative methods and several studies have dealt with this topic. Because of the increase of exposed at-risk elements, a precise quantification is required, which is enabled particularly thanks to recent progresses in rockfall simulations. Among the two classical approaches—*localized* and *diffuse hazard*—, the diffuse one is preferred when it comes to assessing hazard due to large homogeneous cliffs. Herein, we introduce a theoretical framework for the quantitative assessment of rockfall reach probability. More details are available in Rossignol et al. (2024).

Probabilistic model

Definitions and notations. A rockfall consists in the succession of two phenomena: release of a rock from a cliff (*departure*), then propagation of this rock until it stops or collides with an obstacle (*propagation*). In the case of one identified source of falling rocks, we define the *reach probability* of an at-risk element as the probability that this element be reached by a rock coming from the source. Because it takes into account both departure and propagation, the reach probability can be written as the probability of an intersection: $\mathbb{P}[\text{departure} \cap \text{propagation}]$. Then, the conditional probability formula gives:

$$\mathbb{P}[\text{departure} \cap \text{propagation}] = \mathbb{P}[\text{departure}] \times \mathbb{P}[\text{propagation}|\text{departure}] \quad (1)$$

where $\mathbb{P}[\text{departure}]$ is the *departure probability* and $\mathbb{P}[\text{propagation}|\text{departure}]$ is the *propagation probability* (conditional probability). In the case of multiple sources labeled $S_1, \dots, S_n$, we distinguish contributions of each source to the hazard threatening an at-risk element A. Indeed, contributions may vary from one source to another. The reach probability of element A considering contributions of all sources is called *global reach probability*, while it is called *partial reach probability* when it only considers contributions from one given source S_i. Henceforth, the following notations are adopted: $p_{d,i}$ is the departure probability (of source S_i), $p^A_{p,i}$ is the propagation probability (from source S_i to element A), $p^A_{r,i}$ is the partial reach probability (of element A by source S_i), and $\mathbb{P}^A_r$ is global reach probability (of element A).

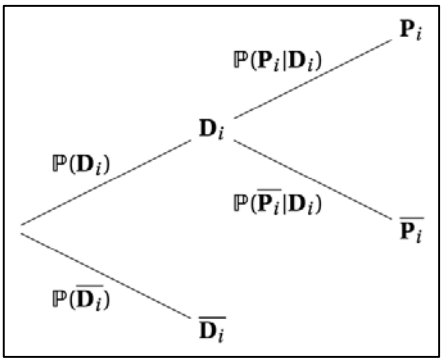

Figure 1. Probability tree

Partial reach probabilities. We now consider a source S_i and an at-risk element A. We define the two following probabilistic events: $\mathbf{D}_i =$ "departure of a rock from source S_i" and $\mathbf{P}_i =$ "propagation of a rock coming from source S_i towards at-risk element A". As propagation is conditioned by departure, we draw a probability tree for the random experiment associated to the rockfall (fig. 1). The three possible results of the random experiment are: departure and propagation ($\mathbf{D}_i \cap \mathbf{P}_i$), departure and non-propagation ($\mathbf{D}_i \cap \overline{\mathbf{P}_i}$), and non-departure ($\overline{\mathbf{D}_i}$). Only the first one leads to the effective reaching of element A. Thanks to the conditional probability formula, it comes:

$$\underbrace{\mathbb{P}[\mathbf{D}_i \cap \mathbf{P}_i]}_{\text{partial reach probability}} = \underbrace{\mathbb{P}[\mathbf{D}_i]}_{\text{departure probability}} \times \underbrace{\mathbb{P}[\mathbf{P}_i|\mathbf{D}_i]}_{\text{propagation probability}} \tag{2}$$

which is can also be written $p^A_{r,i} = p_{d,i} p^A_{p,i}$ with the notations we have introduced.

Global reach probability. The probability $\mathbb{P}^A_r$ can be expressed as a combination of all contributions from sources $S_1, \dots, S_n$ given that element A is *a priori* threatened by all the sources. The event "element A is not reached by any rock coming from the sources" is equal to $\bigcap_{i=1}^n (\overline{\mathbf{D}_i \cap \mathbf{P}_i})$ because, in order that element A be not reached by any rock, it is necessary that no source produce a rock that reaches element A. Here we introduce the following hypothesis: we assume that the n events $\mathbf{D}_1 \cap \mathbf{P}_1, \dots, \mathbf{D}_n \cap \mathbf{P}_n$ are mutually independent (so are events $\overline{\mathbf{D}_1 \cap \mathbf{P}_1}, \dots, \overline{\mathbf{D}_n \cap \mathbf{P}_n}$). Therefore:

$$\mathbb{P}\left[\bigcap_{i=1}^n (\overline{\mathbf{D}_i \cap \mathbf{P}_i})\right] = \prod_{i=1}^n \mathbb{P}[\overline{\mathbf{D}_i \cap \mathbf{P}_i}] = \prod_{i=1}^n (1 - \mathbb{P}[\mathbf{D}_i \cap \mathbf{P}_i]) \tag{3}$$

Since $\mathbb{P}^A_r$ corresponds to the probability of the event "element A is reached by at least one rock coming from the sources", which is the probability of the complementary of the event "element A is not reached by any rock coming from the sources" (eq. (3)), we thus obtain:

$$\mathbb{P}^A_r = \mathbb{P}\left[\overline{\bigcap_{i=1}^n (\overline{\mathbf{D}_i \cap \mathbf{P}_i})}\right] = 1 - \prod_{i=1}^n (1 - \mathbb{P}[\mathbf{D}_i \cap \mathbf{P}_i]) = 1 - \prod_{i=1}^n (1 - p^A_{r,i}) \tag{4}$$

Small probabilities' approximation. The inclusion-exclusion principle, applied to the De Morgan's relation $\bigcup_{i=1}^n (\mathbf{D}_i \cap \mathbf{P}_i) = \overline{\bigcap_{i=1}^n (\overline{\mathbf{D}_i \cap \mathbf{P}_i})}$, provides:

$$\mathbb{P}^A_r = \sum_{i=1}^n p^A_{r,i} + \sum_{k=2}^n (-1)^{k+1} \sum_{1 \le j_1 < \dots < j_k \le n} \mathbb{P}\left[\bigcap_{\ell=1}^k (\mathbf{D}_{j_\ell} \cap \mathbf{P}_{j_\ell})\right] \tag{5}$$

and, with the mutual independence of events $\mathbf{D}_1 \cap \mathbf{P}_1, \dots, \mathbf{D}_n \cap \mathbf{P}_n$, it follows:

$$\mathbb{P}^A_r = \sum_{i=1}^n p^A_{r,i} + \sum_{k=2}^n (-1)^{k+1} \sum_{1 \le j_1 < \dots < j_k \le n} \prod_{\ell=1}^k p^A_{r,j_\ell} \tag{6}$$

Notice that eq. (6) is the linear combination of n sums. Let $\bar{p}$ be the characteristic value of the $p^A_{r,i}$. Then, the characteristic value of the k^{th} sum of eq. (6) is $\binom{n}{k}\bar{p}^k$ where $\binom{n}{k}$ is a binomial coefficient. The $(k+1)^{\text{th}}$ sum is negligeable with respect to the k^{th} sum when $\binom{n}{k+1}\bar{p}^{k+1} \ll \binom{n}{k}\bar{p}^k$, i.e. $\bar{p} \ll \frac{k+1}{n-k}$. A brief study of the function $f : x \longmapsto \frac{x+1}{n-x}$ indicates that $\bar{p} \ll \frac{1}{n}$ is a sufficient condition for $\bar{p} \ll \frac{k+1}{n-k}$. Hence, if $\bar{p} \ll \frac{1}{n}$, then eq. (6) simply becomes:

$$\mathbb{P}^A_r \approx \sum_{i=1}^n p^A_{r,i} \tag{7}$$

Notably, eq. (7) corresponds exactly to the case where the events $\mathbf{D}_1 \cap \mathbf{P}_1, \dots, \mathbf{D}_n \cap \mathbf{P}_n$ are mutually exclusive (i.e., may not occur simultaneously). A limited development of eq. (4) can also lead to eq. (7).

Application in operational context

Estimation of probabilities. The effective quantification of $\mathbb{P}^A_r$ requires the assessment of every $p_{d,i}$ and $p^A_{p,i}$. On the first hand, depending on the hazard model (localized or diffuse), the departure probability is either *"expert-based"* or assessed with terrain surveys and historical studies. Classically, the second way leads to frequency-volume relationships ($\lambda(V) = \alpha V^{-\beta}$) which can be integrated in Poisson distributions. On the other hand, the propagation probability is generally quantified using 3D rock propagation simulations that has substantially developed for the last decades. Based on digital elevation models (DEM) with soil characteristics, propagation models are used to simulate plenty of potential rockfall trajectories starting from cell sources. Rock fragmentation is not yet modelled; we hence assume that fragmentation

occurs at initial release. Consequently, we set $p_{p,i}^{A} = \frac{N_{\mathrm{b},i}^{A}}{N_{\mathrm{sim},i}}$, where $N_{\mathrm{b},i}^{A}$ is the number of rocks coming from source S_i that reached element A and $N_{\mathrm{sim},i}$ is the total number of rocks simulated from source S_i.

Statistical problematic. The operational application of the probabilistic model requires the use of statistical estimations artificially generated with numerous simulations (to have estimations representative enough). Therefore, one must consider the temporal periodization of departure and the spatial discretization of propagation (thus, unit of $\mathbb{P}_r^A$ is year$^{-1}\cdot$m^{-2}). For instance, the spatial resolution of the DEM makes $\mathbb{P}_r^A$ a surface value which should be normalized to 1 m^2 in order to enable uniformized hazard mappings.

Case studies

Virtual example. We first illustrate our approach with a virtual example that we invented. The terrain was divided in 76 cells, 6 of which are source cells. We simulated 50 rockfall trajectories from each source cell (having a departure probability equal to 0.1), and we provided the distribution of crossings (fig. 2-A) for each of them. The global reach probability of each terrain cell was then computed with eq. (4) and eq. (7) (fig. 2-B). We see that eq. (7) overestimates the hazard. The absolute gap is particularly large when exposition is important. For the most reached cell, the relative gap is almost 2 %, which is not negligeable when one wants to precisely quantify rockfall hazard.

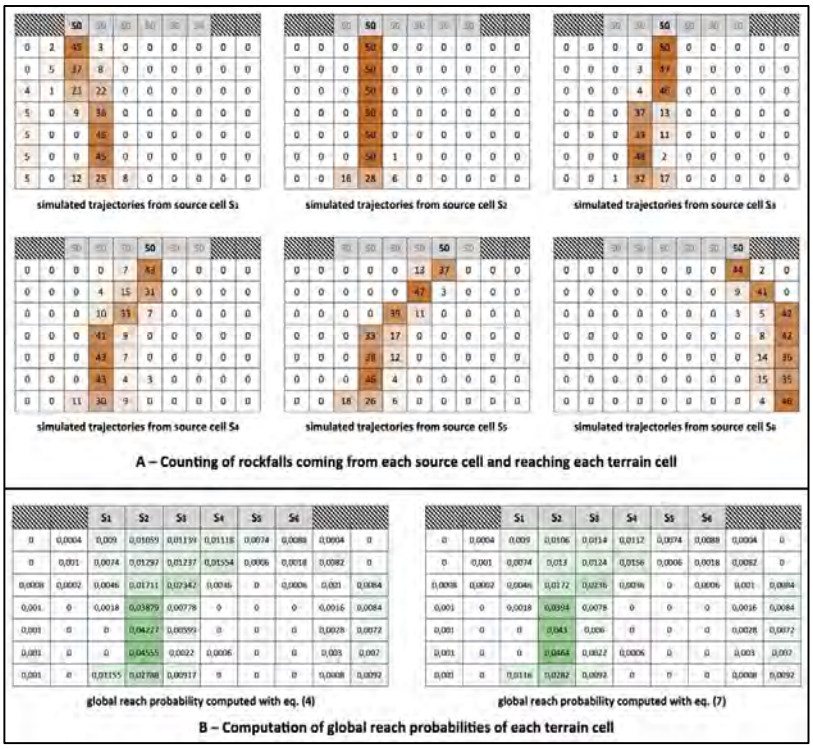

Figure 2. Numbers of crossings and reach probabilities of the virtual example

Example of Saint-Eynard. This example is based on a rock propagation simulation on a large rockfall-prone area (Saint-Eynard, French Alps). Using Rockyfor3D with a 1-meter DEM, we first generated rasters of propagation probability for each source cell which are then combined with departure probabilities to yield the raster of global reach probability (fig. 3-A). We tested both eq. (4) and eq. (7) to compare their precision of quantification in terms of absolute gap (fig. 3-B). Results show that gaps may be higher than 0.01 (year$^{-1}\cdot$m^{-2}) in very exposed areas. Nevertheless, a logarithmic zoning of the reach probability makes these absolute gaps negligeable with respect to log-probabilities intervals, which does not impact relative gaps too much. This example suggests that the approximated formula can be pertinent in real rockfall studies but requires attention when there are very exposed areas reached by many trajectories.

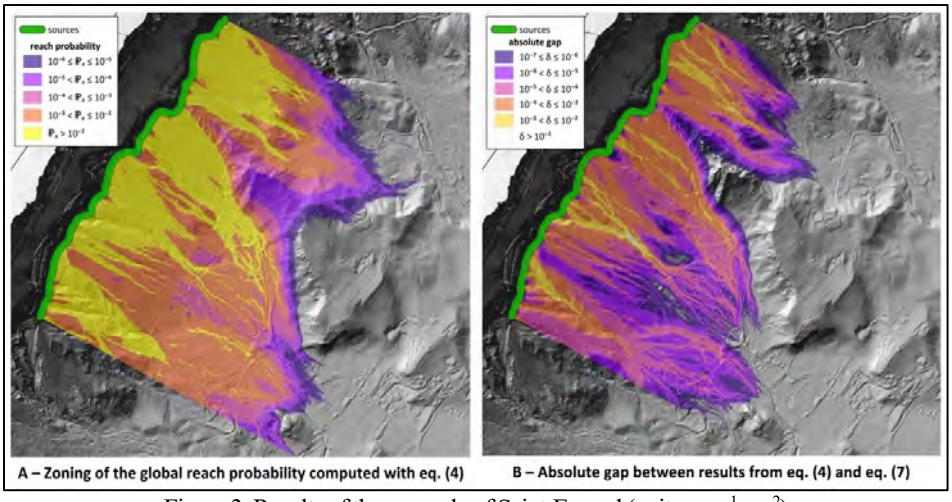

Figure 3. Results of the example of Saint-Eynard (unit: year$^{-1}\cdot$m^{-2})

Discussion and conclusion

Methods from literature. Most articles assessing rockfall hazard with simulations usually use the following expression for the reach probability: $P_r = P_d N_b / N_t$, with P_d the departure probability of the source zone, N_b the number of rocks reaching the cell, N_t the total number of simulated rocks (e.g., Moos et al., 2018). It is possible to easily obtain this expression starting from eq. (7):

$$\mathbb{P}_r^A \approx \sum_{i=1}^{n} \underbrace{p_{d,i}}_{p_d} \times \underbrace{p_{p,i}^A}_{N_{b,i}^A/N_{\text{sim}}} = p_d \sum_{i=1}^{n} \frac{N_{b,i}^A}{N_{\text{sim}}} = \frac{p_d}{N_{\text{sim}}} \underbrace{\sum_{i=1}^{n} N_{\text{b},i}^A}_{N_{\text{tot}}^A} = \underbrace{np_d}_{P_d} \times \underbrace{N_{\text{tot}}^A}_{N_b} \times \underbrace{\frac{1}{nN_{\text{sim}}}}_{1/N_t} = P_d \frac{N_b}{N_t} \quad (9)$$

This shows that the commonly used formula is basically derived from the small probabilities' approximation. However, authors usually do not verify the applicative condition of this formula, which can lead to a loss of precision.

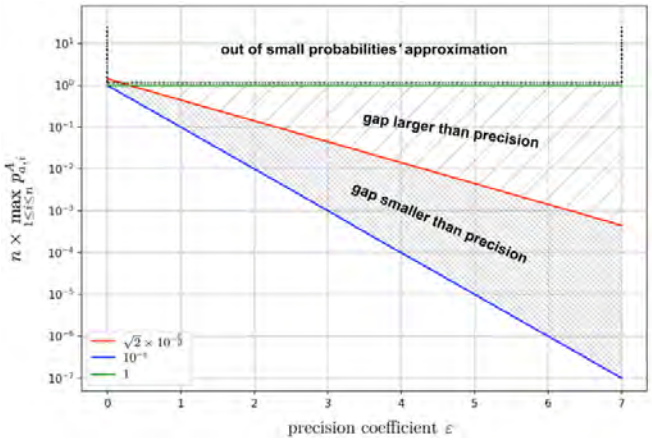

Figure 4. Graphical synthesis of the precision criterion

Precision criterion. Given that eq. (7) is easier to manipulate, we propose a criterion to control the error generated by the small probabilities' approximation. Indeed, applying this formula to unknown or uncontrolled values of probabilities may give reach probabilities higher than 1, which lead to erroneous hazard assessment. At order 2, the absolute gap between the exact and the approximated expressions is $G = \left|1 - \prod_{i=1}^{n}\left(1 - p_{r,i}^A\right) - \sum_{i=1}^{n} p_{r,i}^A\right| \approx \sum_{1\le i<j\le n} p_{r,i}^A p_{r,j}^A$. Therefore, we have $G \le \binom{n}{2} \max_{1\le i\le n}\{p_{r,i}^A\}^2 < \frac{n^2}{2} \max_{1\le i\le n}\{p_{r,i}^A\}^2$, hence, if we want $G \le 10^{-\varepsilon}$ where ε is called *precision coefficient*, then we require:

$$\frac{n^2}{2} \max_{1\le i\le n}\{p_{r,i}^A\}^2 < 10^{-\varepsilon} \iff n \max_{1\le i\le n}\{p_{r,i}^A\} < \sqrt{2} \times 10^{-\frac{\varepsilon}{2}} \quad (8)$$

which provides a useful precision criterion that can frame the approximation. Fig. 4 proposes a graphical synthesis of this criterion: there exists a zone in which the eq. (7) gives values precise enough (gap smaller than precision). That is why concentration or channelization effects on the terrain must be clearly considered while using rockfall simulations, because they sharply increase propagation probabilities.

Conclusion. The theoretical framework we presented here aimed to homogenize operational hazard quantification methods, often based on rock propagation simulations. We showed that strong hypotheses were required to deduce usable formulas, such as the mutual independence of events $\mathbf{D}_i \cap \mathbf{P}_i$ and the small probabilities' approximation, but they are often used implicitly by authors and without further verification although these hypotheses ought to call for precise discussions. Only a simple, reproducible, and consensual methodology will be able to ensure an equitable risk assessment.

References

Farvacque M, Eckert N, Bourrier F, Corona C, Lopez-Saez J, Toe D (2020) Évaluation quantitative du risque rocheux : de la formalisation à l'application à des zones urbanisées ou urbanisables, *Revue Française de Géotechnique*, 163, 7, 1-9.

Farvacque M, Lopez-Saez J, Corona C, Toe D, Bourrier F, Eckert N (2019) Quantitative risk assessment in a rockfall-prone area: the case study of the Crolles municipality. *Géomorphologie: relief, processus, environnement*, 25, 7, 7-19.

Fell R, Ho K, Lacasse S, Leroi E (2005) A framework for landslide risk assessment and management, *Landslides Risk Management*, CRC Press.

Hantz D, Corominas J, Crosta GB, Jaboyedoff M (2021) Definitions and concepts for quantitative rockfall hazard and risk analysis. *Geosciences*, 11, 158, 1-16.

Leroi E, Bonnard C, Fell R, McInnes R (2005) Risk assessment and management, *Landslides Risk Management*, CRC Press.

Moos C, Fehlmann M, Trappmann D, Stoffel M, Dorren L (2018) Integrating the mitigating effect of forests into quantitative rockfall risk analysis – Two case studies in Switzerland, *International Journal of Disaster Risk Reduction*, 32, 55-74.

Rossignol A, Martin R, Bourrier F (2024) Vers une nouvelle approche quantitative pour l'évaluation de l'aléa de chute de blocs, *Revue Française de Géotechnique*, 179, 2.

MEZAP: national method for rockfall hazard mapping in France

B. Colas[1], F. Berger[2], R. Martin[3]

[1] BRGM Montpellier, France
[2] INRAe Grenoble, France
[3] ONF-RTM Grenoble, France

SUMMARY: The MEZAP technical guide, known as the "Rockfall Hazard Mapping Method," is designed for state agencies responsible for conducting rock hazard assessments in the context of creating Public Awareness Campaigns (PAC) or Natural Risk Prevention Plans (PPRn). It is also relevant for operators such as design firms and public organizations involved in these assessments. In certain cases, local authorities may find it useful for issuing hazard maps of this kind.

The document represents the result of collective deliberations initiated in 2014. These discussions were carried out within a working group that brought together state agencies (INRAe, BRGM, Cerema, G. Eiffel University, ONF-RTM) and representatives from decentralized state services, all under the auspices of the Ministry of Ecological Transition.

MEZAP is a response to the state's objective of maintaining a proportional approach to meeting expectations and allocating resources for mapping rock hazards within PPRn or PAC frameworks. It is built on a shared foundation for characterizing rock hazards and a common terminology. MEZAP offers a practical approach to rock hazard mapping, encompassing a wide spectrum of phenomena, from isolated stones to large-scale events, ensuring consistency in production across different territories.

Keywords: rockfall, hazard, regulatory map, method, mapping

Introduction

The MEZAP (Rockfall Hazard Mapping Method) provides an approach aimed at ensuring consistency in hazard mapping across different regions in France. This approach relies on a shared foundation for characterizing rockfall hazards and a common vocabulary. Importantly, MEZAP does not mandate specific implementation resources but leaves them to the discretion of experts based on project specifications.

The guide offers clear definitions to enhance understanding and alignment of references. The method systematically outlines the process of defining rockfall scenarios, determining hazard intensity for mapping, mapping hazard failures, and the resulting run-out. Towards the end, matrices are introduced to combine i) failure and run-out to create a reaching map, and ii) intensity and reaching to generate a hazard map.

Definitions

As per the PPRn "Landslide" guide, to best predict potential phenomena and safeguard the affected populations and properties, it is essential to establish a reference hazard within a given homogeneous area. The reference hazard is defined as the natural phenomenon that serves as a

benchmark for shaping PPRn regulations. In the context of rock hazard mapping under MEZAP, this refers to a phenomenon of specified occurrence and intensity likely to run-out towards assets over the reference period. For rockfall hazard mapping within the framework of MEZAP, the reference period is set at one century.

Multiple reference scenarios can be proposed to construct the reference hazard, with each significant release area treated as a homogeneous unit.

MEZAP Method

The method is founded on the following principles: characterizing rockfall hazard within MEZAP involves an intersection of the intensity of a rock mass mobilization event and the probability of this mass reaching a specific point on the territory.

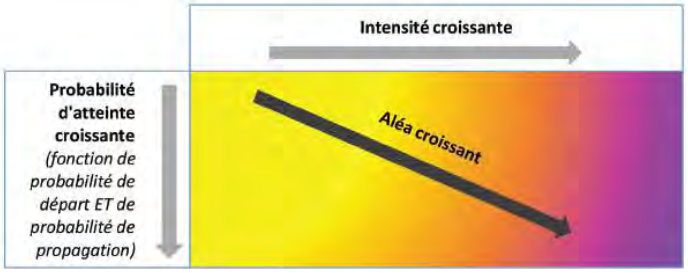

Figure 1. Définition of hazard in the MEZAP

The following steps are recommended for hazard mapping:

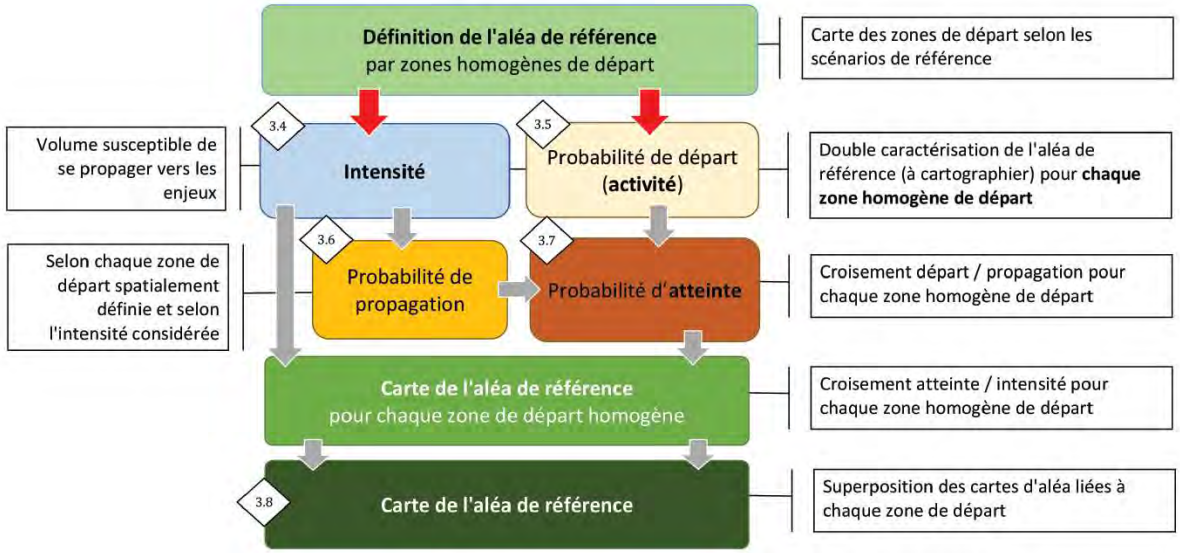

Figure 2. Simplified MEZAP flowchart for mapping rock hazard by reference scenario

The method proceeds by describing the following steps:

- Data collection for the creation of a geomorphological map tailored to rockfall hazards.
- Defining various scenarios that need to be taken into account.
- Establishing the boundaries and characterizing the sources of rockfall.
- Classifying the intensity.
- Restoring the run-out analyze.

Highlights of the MEZAP

MEZAP qualify hazard on every point of the study area following the matrix herebelow:

		Indice d'intensité				
		$V \leq 0.05\ m^3$	$0.05 < V \leq 0.25\ m^3$	$0.25 < V \leq 1\ m^3$	$1 < V \leq 10\ m^3$	$V > 10\ m^3$
		Très faible	Faible	Moyen	Fort	Très fort
Probabilité d'atteinte	Très faible	Nul à négligeable	Nul à négligeable	Nul à négligeable	Nul à négligeable	Nul à négligeable
	10^{-6} Faible	Faible	Faible	Moyen	Fort	Fort
	10^{-5} Moyenne	Faible	Faible	Moyen	Fort	Fort
	10^{-4} Elevée	Faible	Moyen	Fort	Fort	Très fort
	10^{-3} Très élevée	Moyen	Fort	Fort	Très fort	Très fort

Figure 3. Definition of the reference hazard level for each homogeneous zone (reference period of 100 years) (in red: annual reach probability)

As a reminder, it's important to note that the hazard qualification refers to potential damages to standard buildings. Therefore, MEZAP focuses on the safety of individuals within buildings, rather than those outside the buildings, considering that main damages to buildings involved systematically fatalities. Key highlights of the method include:

- The imperative need for a detailed informative map of phenomena, complemented by a geomorphological map specifically tailored for rockfall events.
- The decision to link the definition of intensity with the run-out mode, considering either the unit volume for individual boulders capable of reaching assets or the total volume of rockfall for certain specific scenarios.
- Distinguishing between 'diffuse hazard' (potential failure from any point within a delimited, homogeneous release area) and 'local hazard' (identifying a localized compartment).
- Quantitatively assessing the probability of initiation (failure) using an index based on scarp activity.
- The choice to represent the results of run-out analyses through the angle of the energy line in the final output.

Conclusion

The MEZAP technical guide serves as the standard approach for rockfall hazard mapping and risk zoning in France (PAC or PPRn). The method is comprehensively explained, with commentary provided at each step to assist users in conducting their analyses. MEZAP has made certain deliberate choices which, when taken out of context, might be subject to criticism. However, it is through these choices that a common, proportional approach aligning with state expectations has been established.

Ultimately, MEZAP offers a pragmatic method for rock hazard mapping, encompassing a wide spectrum of phenomena, from isolated stones to large-scale events, ensuring consistency in results across different regions.

References

Collectif (groupe de travail MEZAP). Guide technique MEZAP. Caractérisation de l'aléa rocheux dans le cadre d'un Plan de Prévention des Risques Naturels (PPRn) ou d'un Porter a connaissance (PAC). BRGM, 2021. Collection scientifique et technique. ISBN : 978-2-7159-2760-5

Besson, L., Durville, J-L., Garry, G., Graszk, E., Hubert, T., & Toulemont, M. (1999). Plans de prévention des risques naturels (PPR). Risques de mouvements de terrain. Guide méthodologique. La Documentation française. https://side.developpement-durable.gouv.fr/Default/doc/SYRACUSE/66935

C2ROP. (2020). Caractérisation de l'aléa éboulement rocheux - État de l'art. Cerema. https://www.cerema.fr/fr/centre-ressources/boutique/caracterisation-alea-eboulement-rocheux-etat-art

Cemagref & Arpa Piemonte. (2008). Projet n° 165 PROVIALP protection de la viabilité alpine. Rapport final. Alpes Latines Coopération Transfrontaliére France-Italie. https://www.arpa.piemonte.it/pubblicazioni-2/pubblicazioni-anno-2008/volumeprovialpbassa.pdf

Cherkaoui, A., & Herbaux, M. (2018). Aléa versant rocheux sous-cavé. Caractérisation et évaluation. INERIS - CEREMA. https://www.ineris.fr/sites/ineris.fr/files/contribution/Documents/Guide_VSC_A4_V15_web.pdf

Egli, T. (2005). Recommandations. Protection des objets contre les dangers naturels gravitationnels. Association des établissements cantonaux d'assurance incendie. https://www.vkg.ch/media/1578/wegleitung_objektschutz_gegen_gravitative_naturgefahren_f_v0-1.pdf

Cahora Bassa Dam South Bank protection design and execution – XIVth ISL, Chambéry 2024

AUDOYER B, Grenoble, France. BERGZOLL I, Clermont-Ferrand, France.

Keywords:
Rock stabilization, Cahora Bassa Dam, Geotechnical survey, Rockfall barriers, Trajectography

Introduction:
As part of an international tender, HYDROKARST & RAZEL-BEC were selected to secure a cliff in Mozambique. This work was carried out with the collaboration of HYDROGEOTECHNIQUE and SETEC geotechnical design offices.
The purpose of the study was to design a rockfall protection of the downstream slopes on the South Bank of Cahora Bassa Dam. This study was based on field investigations and 3D modelling using photogrammetry.
This work was performed in a challenging environment as often encountered in such remote international projects (logistics, security, climate, fauna, etc.).
The Cahora Bassa Dam is located on the Zambezi River, in the northwestern part of the country, in the province of Tete.

Figure 1. Project location

The area to be secured was located above the access road to the hydroelectric power plant.
The study area covered a length of 650m and was divided into two distinct zones, on either side of the access tunnel at the bottom of the dam.

- Sector 1: vertical cliff, 350m long, 250m high, located between the dam and tunnel head.
- Sector 2: sub-vertical slope, 150m long, 350m high, located between two tunnel heads, further downstream.

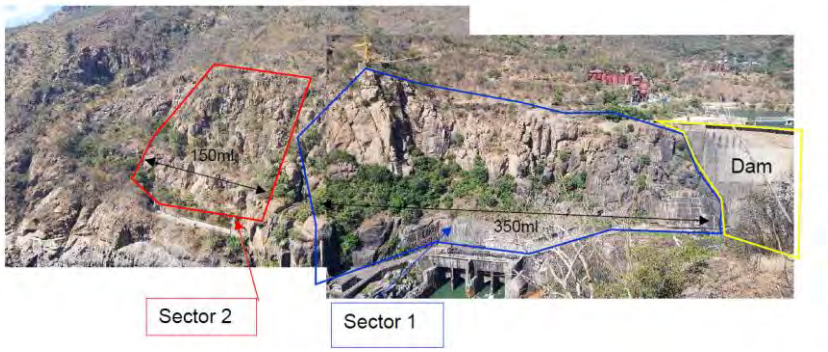

Figure 2. Zone definition

Survey techniques :

An important work of inspection using rope access was done to identify the type of materials and main rock instabilities. This task was led by one Geotechnical Engineer with the help of four Rope Access Technicians and a Civil Engineer specialized in rock reinforcement.

The site visit using alpine techniques allowed to perform fracture readings of unstable masses (dimensions, splitting possibilities, slip plane survey, type of cracks and supported orientations).

Visual and non-destructive reconnaissance were carried out with a geologist's hammer to test the weathering condition of the rocks, and a compass with clinometer to measure the orientations and inclinations of the fracture planes. Measurement of unstable zones was done with decameter and laser range finder.

Figure 3. Inspection paths used during the geotechnical survey

Evaluation of the trajectory of unstable elements and coverage of the terrain crossed. These trajectories were studied in the office on tracking software, but the observation and "feeling" in the field were also very important (presence of trees that can impact trajectories, small intermediate projections, etc.).

A preliminary positioning of protective structures foreseen on site was done on maps and photographs from aerial surveys.

Figure 4. 3D mode base on photogrammetry

Figure 5. Rock instability sheet.

Modeling and design of protective structures:

Using the data collected during the survey, the Geotechnical Engineer was able to model the cliff of zone 2 using the RocPro3D software.

The first step of the modeling was to define the theoretical implantation of the deflector to catch most of the rockfall according to the field topography.

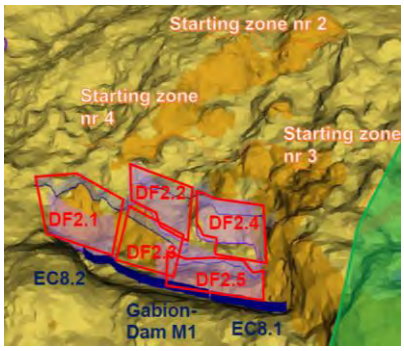

The second step was to define the necessary height and energy level required taking into consideration 90% of the rockfall.

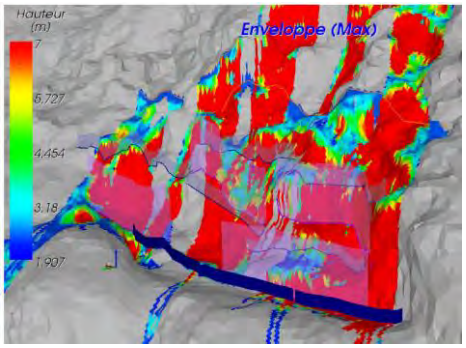

The third and last step was to check the percentage of catching rock and confirm the energy level according to the simulation and on site observations.

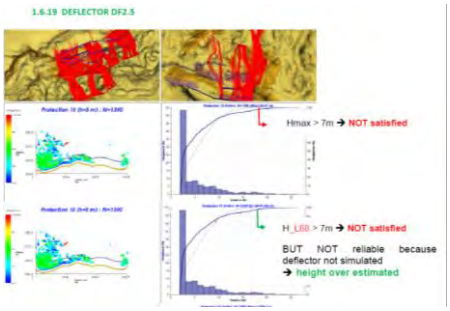

While the Contractor checked the feasibility of the structures with its Supplier, it appeared that the long span initially planned would be too complex to implement. It was therefore necessary to divide the structure into several elements.

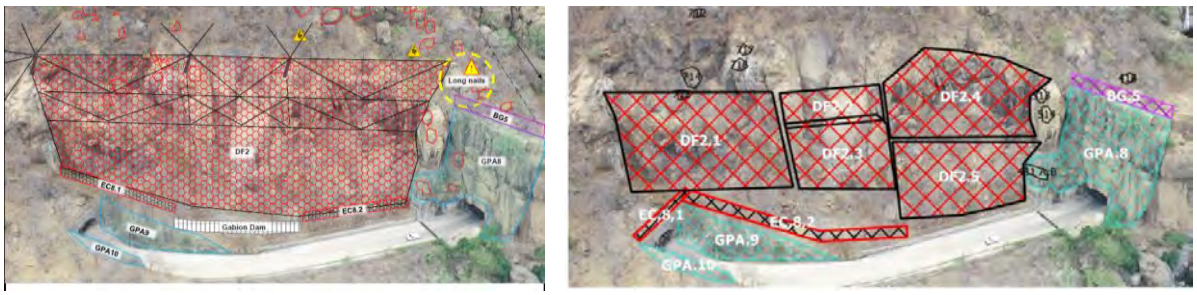

Figure 6. Structures's evolution

Figure 7. Structures completed

Conclusion:

Field survey is critical in the design of any rockfall protection project. This is even more important for large scale projects in remote locations with all the supply and logistics challenges. The information gathered from site by experienced Geotechnical professionals allow an optimized design of the structures by cross checking them with the outputs of software modelling. A close collaboration between the Geotechnical Engineers, the Contractors and Equipment Suppliers at an early stage of the design is also key in the success of a project.

References

VERGARA N & BERGZOLL I (2021) SBS-9001-A-TRGTO-REV0
VERGARA N & BERGZOLL I (2021) SBS-9014-A-GEOSTUDPART1-REV1

Related videos

https://www.youtube.com/watch?v=vecsHcEND0w
https://www.youtube.com/watch?v=x4okbvqau34&t=18s
https://www.youtube.com/watch?v=FRCf-3Z-HZU
https://www.youtube.com/watch?v=k5J9DldIGRg

Empirical quantification of rockfall reach probability: objective determination of appropriate topographic descriptor

M. Peruzzetto[1], B. Colas[2], C. Levy[1], J. Rohmer[1], F. Bourrier[3]

[1] BRGM, Orléans, France
[2] BRGM, Montpellier, France
[3] Université Grenoble Alpes, INRAE, ETNA, 38000, Grenoble, France

SUMMARY: For rockfall hazard assessment on areas more than several km² in size, the quantification of runout probability is usually done empirically. Classical methods use statistical distributions of reach or energy angles derived from rockfall databases. However, other topographic descriptors can be derived from the topographic profiles along the rockfall path. Using a database of more than 4,000 profiles of rockfall paths, we determine which topographic descriptors are most appropriate for reach probability estimation, by comparing their statistical distributions for rockfall stopping points, and for points the rocks overtook. We show that the curvilinear length of the propagation path, and the area under the propagation path can improve propagation estimations, especially when they are computed only along the final portion of the propagation path. This is illustrated by comparing an experimental distribution of rockfall stopping points to the estimated distributions.

Keywords: rockfall, database, propagation, probability

Introduction

The estimation of rockfall runout probability is a key step of rockfall hazard assessment for delimiting areas of low, moderate and high hazard levels below rocky cliffs. The most sophisticated tools used to analyse rockfall propagation are 3D trajectography numerical models. However they rely sometimes on many user-defined parameters that can be difficult to calibrate. They also require significant computing resources that are often incompatible with the size of the study area (e.g. several km² for regulatory hazard maps) and IT resources at disposal. Thus, practitioners commonly rely on empirical methods, with scalar topographic descriptors derived from 2D topographic profiles of rock propagation paths. A widely used indicator is the ratio $\mu = \tan(\delta)$ between the drop height H and the travel distance L, with δ the corresponding angle. δ is called the angle of reach when L is the curvilinear length of the real path, and the angle of energy when L is the horizontal distance between the starting and stopping points. By using empirical distributions of μ derived from rockfall databases, probabilistic runout maps can be easily derived (e.g. Jaboyedoff et al., 2003). It was also suggested that combining the energy angle with the area under the propagation path (normalized by the drop height) could also provide good results (MEZAP, 2021). This method is currently implemented by the BRGM to derive regulatory rockfall hazard maps (Levy et al., 2021).

The objective quantification of the precision of an empirical method for runout probabilistic prediction is difficult. How can we find a topographic descriptor that is best representative of rockfall stopping points, and not of the general shape of slopes the rocks propagate on? To the knowledge of the authors, this problem has never, or at least only scarcely, been addressed in the literature. We suggest that an appropriate criterion is the comparison between the statistical distributions of topographic descriptors computed for actual rockfall stopping points, and the distributions for other points, as explained in the next section.

Data and methods

We use a database of 4,015 topographic profiles $z = z(x)$ connecting with straight lines the initiation and stopping points of rockfalls, derived from 15 different catchments in Europe. For every point with coordinate x along a profile $z = z(x)$, we compute the distance $L(x)$ to the initiation point, the drop height $H(x) = z(0) - z(x)$, $A(x)$ the area under the profile and $C(x)$ the curvilinear length of the profile (both computed between 0 and x coordinates, on the vertically translated profile $z_x(r) = z(r) - z(x)$), and non-dimensional indicators given in Table 1.

Table 1. Non-dimensionnal topographic indicators

Topographic descriptor	μ	A_n	A_n^L	A_n^H	C_n	C_n^L	C_n^H
Definition	H/L	$A/(HL)$	A/L^2	A/H^2	$C/\sqrt{L^2+H^2}$	C/L	C/H

The indicators are also computed by considering only the last d meters before a given point. For instance, $\mu(x) = \frac{z(0)-z(x)}{x}$ and $\mu_{(d)}(x) = \frac{z(x-d)-z(x)}{d}$. As a result, for each indicator, we derive a sample of 4,015 points corresponding to rockfall stopping points (rockfall database), and a sample of almost 10^6 points corresponding to all $(x, z(x))$ couples from the 4,015 profiles that rockfalls have overtook (profiles database). The similarity between distributions is quantified by computing the Wasserstein (or Kantorovitch) distance D_W between bootstrapped samples of the normalized rockfalls and profiles distributions (taking the profiles distribution as a reference). The Wasserstein distance corresponds to the optimal value of the optimal transport problem: it is all the more important as distributions are different. Thus, topographic descriptors that allow to better discriminate between rockfall stopping points and points that they overtake are associated to higher values of W_d.

Then, to estimate reach probabilities on a new profile $z = z(x)$ with a given topographic indicator y, we first fit a non-parametric normal kernel density function f to the distribution of y for rockfall stopping points. Assuming that the rockfall is initiated at $x = 0$ and stops before $x = x_m$, the probability that the rockfall has a travel distance X larger than x is estimated as :

$$P(X > x) = 1 - \frac{1}{C}\int_0^x f\big(y(r)\big)dr \text{ with } C = \int_0^{x_m} f\big(y(r)\big)dr \qquad (1)$$

We compare estimated reach probabilities to observations from two experiments carried out in Dole (Jura, France) where 47 and 56 blocks with mass varying from 100 to 1,300 kg were released from two locations. This empriccaly derived probability distribution is termed as observed distribution in the following.

Results

As shown in Figure 1a, the topographic indicator that allows to best discriminate between rockfall stopping points and other points, when the full profile is considered, is A_n^L ($D_W = 0.36$). The difference between distributions is even more pronounced for $A_{n\,(30)}^H$ and $C_{n\,(30)}^H$ ($D_w = 1.5$ and $D_W = 4.3$ respectively).

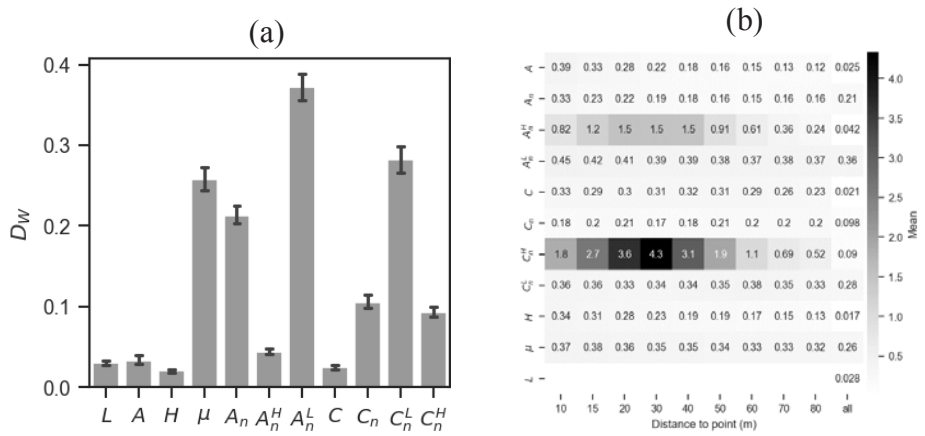

Figure 1 : Dissimilarity between distributions for rockfall stopping points, and other points, for different topographic indicators, measured with the mean of the bootstrapped Wasserstein distance D_W. Topographic indicators are computed using the whole profile in (a) and in the last column of (b), and using only the last 10 to 80 meters in (b).

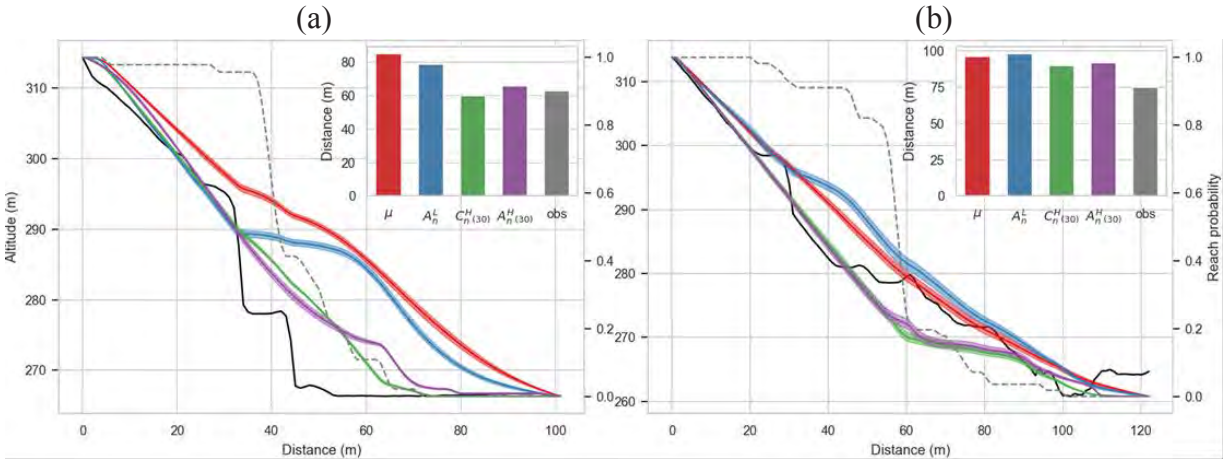

Figure 2 : Comparison between observed (grey dashed line) and estimated (coloured lines with 95% confidence intervals) travel distance exceedance probabilities, for two profiles (a and b) in Dole (Jura, France). The topographic profile is given in black. The insert gives the distance corresponding to an exceedance probability of 0.1. $C_{n(30)}^H$ and $A_{n(30)}^H$ (green and purple) are computed on the last 30 meters.

In Figure 2 a practical application is presented on two topographic profiles with several slope breaks, and an observed distribution of rockfall stopping points. The observed reach probability decreases sharply in response to slope breaks (see e.g. in Figure 2a between x=30m and x=40m). In comparison, the reach probability derived from μ and A_n^L decreases relatively regularly along the profile: it is under-estimated for the first 40 to 60 m, and then over-estimated. As a result, the travel distance associated to the 10% reach probability is over-estimated by 20 to 25 m (see inserts in Figure 2). On the contrary, the estimations deduced from $C_{n\,(30)}^H$ and $A_{n\,(30)}^H$ are in better agreement with observations (within 5 meters in Figure 2a). For these indicators, the reach probability is also under-estimated in the first 60 meters, but is then in good agreement with observations.

Discussion

Our results seem to validate the proposed methodology for determining topographic indicators that are characteristic of rockfall stopping points. However, the tested profiles are not representative of all rockfall propagation conditions. In particular, the drop height in the application in 50 m at maximum, which is not representative of high mountain cliffs. Testing

the methodology on such a cliff with a debris fan at its foot, and an associated database of observed rockfalls, would be interesting. In the meantime, other possible improvements include the analysis of the combined distribution of multiple topographic indicators. For instance, using the combined distribution of $C_{n\,(30)}^{H}$ and L allows a better match between the observed and estimated reach probability in the first 60 meters of the Dole profiles, but has limited influence on the results at further distances. Using the combined distribution of $C_{n\,(30)}^{H}$ and $A_{n\,(30)}^{H}$ does not significantly improve the results.

In the perspective of deriving the most realistic reach probabilities on a given profiles, some difficulties are yet to be overcome. First, it should be noted that the proposed estimation of the reach probability (which is classical in the literature) is only based on the probability to have a certain value of a topographic index, given a range of possible value. But this range of values does not define unequivocally the profile itself, neither does a topographic index corresponds necessarily to a single point along the profile. Besides, a descriptor may work well on average for various types of profiles (as indicated by high values of D_w), but another indicator could be more appropriate for a specific profile. This problem can be partly overcome by filtering the distribution used to compute the reach probability. For instance, using the distribution of $C_{n\,(30)}^{H}$ for rockfall stopping points with travel distance below 150 m allows to improve the estimation of the travel distance with 10% reach probability for the test profile in Figure 2b.

A significant methodological result of our work is that topographic indicators computed only on a portion of the profile are more effective to derive reach probabilities that indicators computed on the whole profile. This highlights the role of the local topography in rockfall propagation, and especially slope breaks. In practice, using partial topographic descriptors (such as $A_{n\,(30)}^{H}$) allows to estimate more realistic low reach probabilities than descriptors integrating the whole path.

Conclusion

This work contributes to improving rockfall propagation hazard assessment with empirical methods, in particular for extensive studies on large surfaces. By computing various topographic descriptors along profiles from a database of rockfall propagation paths, we show that the curvilinear profile length on the last 30 meters, normalized by the drop height, is a satisfying descriptor to estimate travel distances. It allows to improve low reach probability estimations in comparison to indicators integrating the whole profile, such as the energy angle. Future developments could explore four main directions : (i) using the combined distributions of multiple topographic descriptors from a subset of topographic profiles to improve reach probability description on a given profile, (ii) extending the current profile database and testing the methodology on new sites, (iii) conducting a formal analysis of reach probability estimation to estimate and reduce the bias associated to current estimation methods, and (iv) analyzing the influence of block volume on travel distance.

References

Jaboyedoff, M., & Labiouse, V.. 2003. 'Preliminary Assessment of Rockfall Hazard Based on GIS Data'. In 10th International Congresson Rock Mechanics ISRM 2003 – Technology Roadmap for Rockmechanics, 575–78. Johannesburgh, South Africa.

Lévy, C., Colas, B., Rohmer, J., & Berger, F. (2021). ELANA (Energy Line Angle Normalized Area): un outil d'aide à la cartographie de la propagation des chutes de blocs basée sur la méthode de la ligne d'énergie à différentes échelles. In 5th RSS Rock Slope Stability Symposium.

MEZAP. 2021. 'Guide Technique MEZAP'. Caractérisation de l'aléa rocheux dans le cadre d'un Plan de Prévention des Risques Naturels (PPRn) ou d'un Porter a connaissance (PAC). Collection Scientifique et Technique. Orléans: BRGM.

Monitoring evidence of slab creep under the effect of daily temperature cycles – The case study of Socoa coast (Bay of Biscay, France)

C. Lévy[1], T. Dewez[1], C. Garnier[2], L. Guillen[1], Y. Thiery[2]

[1] BRGM, Orléans, France
[2] BRGM, Pessac, France

SUMMARY: A supposedly active rock instability was instrumented at Socoa (municipality of Ciboure, France). The objective was on the one hand to diagnose the activity of the instability, and on the other hand, to understand the meteorological-marine phenomena and associated processes which could play a role in its destabilization. Analysis of in situ data (extensometers, temperature probes, weather data) shows that the instrumented slab moved by about 1.6 mm during the first year of measurement. The phenomenon which contributed the most to this small accumulation of deformation is the slab creep under the effect of daily temperature cycles. The amplitude of this yet undocumented phenomenon depends on the temperature conditions: the greater the amplitude of daily temperature, the greater the induced movements. The occurrence of rain reduces the amplitude of this phenomenon. The intensity of this phenomenon is highly likely to increase in connection with climate change, as this coastal zone is supposed to endure an increase of droughts and heat records.

Keywords: rockfall, extensometer, creep, temperature, Socoa

Introduction

Meteorological phenomena and associated processes known to contribute to the weathering and destabilization of cliffs are extremely varied and numerous: freezing of water in cracks and pores, increase in pore pressure, flexural movement of the cliff under the repeated action of waves inducing rupture by fatigue, temperature variations inducing stresses at the crack tips allowing crack expansions, haloclasty, etc. (among others authors, D'amato et al., 2016; Delonca et al., 2014; Collins et al., 2016; Brains et al., 2014). Depending on the geographical areas, the most contributing processes to cliffs destabilization and weathering can be different (Delonca et al., 2014). The identification of contributing processes remains complex because some processes induce phenomena of low intensity and/or are very rare to observe.

This study highlights a still undocumented process (the creep of a slab under the effect of daily temperature cycles) thanks to the implementation of instrumentation for a long observation period (1 year). We show that this phenomenon contributed the most to the accumulation of deformation during the observation period.

The study site at Socoa coast (France) and the monitoring set up

The study area is a coastal cliff composed of flysch, a stack of very different layers: massive limestone strata, marl strata and sometimes thin layers of clay. The instrumented volume is a thin limestone slab (<1 m), located in the upper third of the cliff which is nearly 40 m high at

this location (Figure 1). The supposed mechanism of this instability is a lateral rotation of the slab (Figure 1). The slab is pre-cut laterally by open vertical and horizontal joints connected in a continuous network. It is hypothesized that this rock instability accommodates deformation along its basal surface, this basal surface most certainly being a clay layer. As a result, the expected movement is a widening of the joints, as well as a downward movement of the rock mass. Located at the head of the cliff, this unstable volume is impacted by waves only during sea storms.

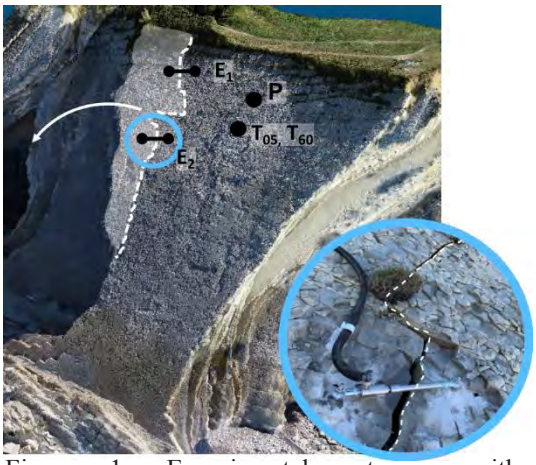

Figure 1: Experimental set up with extensometers (E), Pyranometer (P) and Temperature probes (T). The instable slab (white) is supposed to have a rotational movement. Inside the blue circle: photo of one extensometer across the joint (dashed line)

With the aim of following the expected rotation of the slab, 2 extensometers were installed across the joint network, **E1** and **E2**, in December 2021 (Figure 1). In order to record the largest possible movements, the extensometers were oriented perpendicular to the joints. They measure the deformation with an accuracy of ±0.10 mm according to manufacturer data. In order to understand the link between movements and environmental conditions, additional sensors were set up (Figure 1): a pyranometer **P** which allows quantifying direct sunlight; temperature probes at 5 and 60 cm depth, $\mathbf{T_{05}}$ and $\mathbf{T_{60}}$. These measurements are supplemented by rainfall data $\mathbf{P_u}$ and air temperature data $\mathbf{T_{air}}$ from the Fort de Socoa weather station located less than 100 m from the site.

Displacements analysis

Data between 16/12/2021 and 06/12/2022 show that the joint opened irreversibly by approximately 1.6 mm at **E1** and 1.2 mm at **E2** and that it opens and closes daily (daily cycles). These small variations (around 0.1 mm on average) are mostly reversible. They are due to the contraction and expansion of the rock with daily temperature cycles (Figure 2).

Figure 2: Air temperature and extensometer records during 1st year of experiment (16/12/2021-06/12/2022)

The opening at **E1** is almost perfectly proportional to **E2** with $E_1 = a \times E_2 + b$ (R^2=0.99, Figure 3), and a=1.45 with a 95% Confidence Interval (CI) of [1.448 1.454] and b=0.13with a 95% CI of [0.127 0.130]. This faster opening at the top of the joint compared to its bottom is consistent with the hypothesis of a rotation mechanism. At the time of installation, the joint was already open by about 5 cm at **E1** and 2 cm at **E2**. Thus, assuming a regular evolution of the joint opening, it began around 60 years ago. These observations confirm that the instability is active, with the recording of significant irreversible deformations long time before collapse.

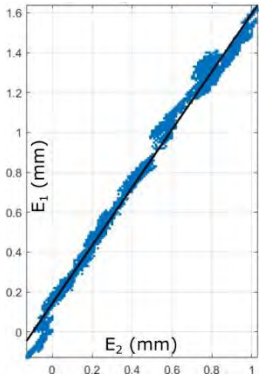

Figure 3: E_1 as a function of E_2 with linear fit (black line)

The ratio a between the movements at $\mathbf{E_1}$ and $\mathbf{E_2}$ imposes an assumed pivot point of the rotation about 18 m from $\mathbf{E_2}$ (Figure 4). This position is lower than the exit point of the joint around 12 m from $\mathbf{E_2}$, visible on topographical data. Despite the uncertainty of this estimate, it is very likely that the pivot point does not correspond to the exit point of the joint. It is therefore assumed that the physical phenomenon(s) at the origin of the observed activity is(are) the cause of the rotation movement.

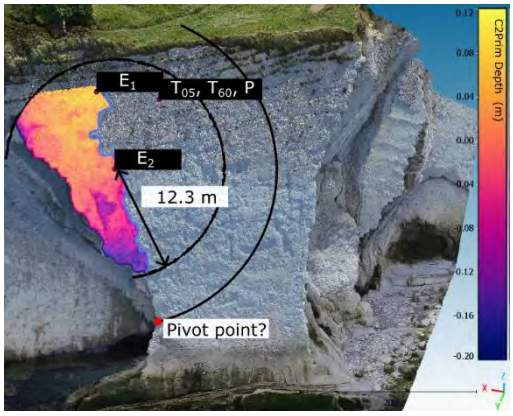

Figure 4: Circles of radius 12.3 and 18 m around E_2 (black). The colour scale indicates the estimated slab thickness for a basal surface assumed at 20 cm depth

Temperature measurements at 5 and 60 cm depth allowed resolving temperature variations at several depths using 1D simulation. Comparisons with the data at $\mathbf{E_1}$ show an optimal anti-correlation $\mathbf{C}$=-0.916 with the temperatures at 20 cm depth. The photogrammetry data show that there is indeed an interface at this depth, delimiting a volume of 27m3 to 39m3, estimated using the cloudcompare (Figure 4).

For the period 07/08/2022 to 07/14/2022, Figure 5 illustrates the joint opening when the temperature at 20 cm depth decreases (blue periods) and the rock contracts. Conversely, the joint closes when the temperature increases (red periods) and the rock expands. The movement does not appear entirely symmetrical between periods of contraction and expansion. Thus, expansion is systematically lower than contraction and each cycle contributes to the accumulation of irreversible deformation (Figure 5). A ΔT of approximately 2° at 20 cm depth over 24 hours (i.e. a ΔT of 8° at the surface) generates an irreversible accumulation of deformation ΔL of about 0.08 mm. This difference in behavior between the contraction and expansion phase seems less marked when it rains (Figure 5). Thus, as soon as it rains, the accumulation of irreversible deformation becomes negligible. On the scale of one year of measurement, it appears that temperature cycles are responsible for the majority of the observed irreversible deformation.

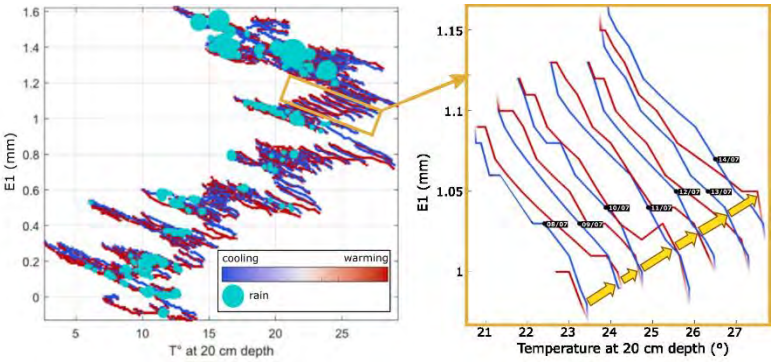

Figure 5: Left: E_1 as a function of the temperature estimated at 20 cm depth (01/2022 to 11/2022). Warming and cooling periods are indicated with alternating red and blue. Blue dots indicate hourly rain with size depending on rain intensity. Right: zoom on the period 07/08/2022 - 07/14/2022. Each daily cycle leads to the accumulation of a small irreversible deformation, shown by yellow arrows.

Conceptual model to explain the observed deformations

The deformation ΔL of a bar of isotropic material, placed horizontally, is proportional to the temperature variation ΔT with $\Delta L = -\alpha\, L_0 \Delta T$ and L_0 the initial length of the bar and α the coefficient of linear expansion of the material. This deformation is symmetrical with respect to a central axis. The forces acting on the basal surface during contraction are (Figure 6): the weight $\mathbf{P}$, the reaction to the ground $\mathbf{R_N}$, the traction force exerted by the contraction of the material $\mathbf{F_{cont}}$, and the friction force between the bar and floor $\mathbf{F_{fric}}$. During expansion, the force $\mathbf{F_{cont}}$ is replaced by the traction force exerted by the expansion of the material $\mathbf{F_{dil}}$, whose orientation is opposite to $\mathbf{F_{cont}}$. $\mathbf{F_{fric}}$ force also changes orientation between contraction and expansion.

For a bar placed on an inclined surface of slope β (Figure 7), the involved forces are the same, but the inclination has an impact on which forces facilitate or not the contraction or the expansion of the material. During contraction, the component of the weight tangent to the slope $\mathbf{P_T}$ helps contraction movements in the upper part of the bar. Conversely, during expansion phase, $\mathbf{P_T}$ opposes expansion movements in the upper part of the bar. As a consequence, the position of the fixed zone shifts downwards compared to the case of a horizontal bar. In the contraction phase, the length L_1 above this fixed zone is such that $L_1 > L_0$. Thus, for the same temperature variation ΔT, the deformation in the upper part of the bar is ΔL_1 with $\Delta L_1 > \Delta L_0$. Similarly, during expansion the length L_3 above the fixed zone is such that $L_1 > L_3 > L_0$. Thus, for the same absolute temperature variation ΔT, the deformation in the upper part of the bar is greater during the contraction phase than during the expansion phase: $\Delta L_1 > \Delta L_3$.

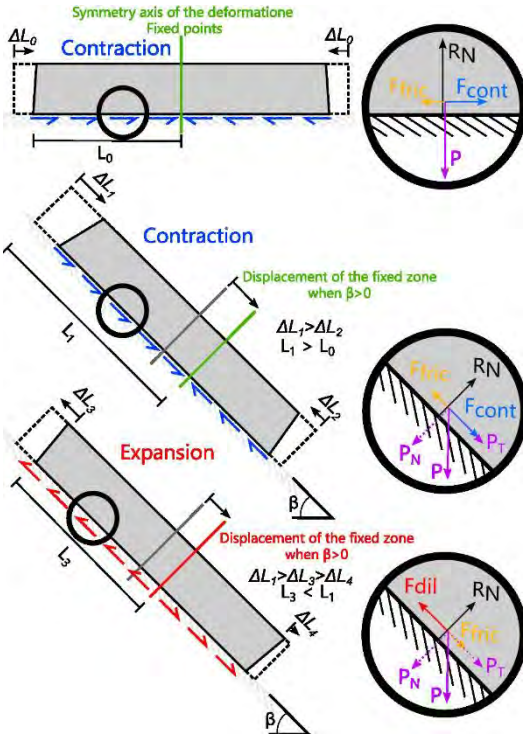

Figure 6: Conceptual model to explain the observed deformations. Forces applying locally on the basal surface are presented on the right

An accumulation of deformation is therefore possible step by step with the succession of thermal cycles leading to the contraction and expansion of the material. In particular, this conceptual model makes it possible to explain our observations of the slab creep during dry periods at Socoa site. We hypothesize that the force $\mathbf{F_{fric}}$ decreases with the lubrication of the basal surface when it rains, which would explain why the accumulation of deformation ΔL_1-ΔL_3 during rainy periods is negligible. This creep phenomenon can occur at our site thanks to its geometry: a slab placed on a very smooth and inclined surface, with free edges at its bottom and one side.

Conclusion

Analysis of in situ data shows that a small slab (27m3 to 39m3) accumulated irreversible deformation of about 1.6 during the first year of measurement. The phenomenon which contributed the most to this accumulation of deformation is the creep of the slab under the effect of daily temperature cycles. The amplitude of this yet undocumented phenomenon depends on the temperature conditions: the greater the amplitude of the daily temperature, the greater the induced movements. The occurrence of rain reduces the amplitude of this phenomenon. The intensity of this phenomenon is highly likely to increase in connection with climate change, as this coastal zone is supposed to endure an increase of droughts and heat records.

Acknowledgements

The EZPONDA project was granted by FEDER EU funds (grant FEDER FSE 2014-2020).

References

Delonca, A., Gunzburger, Y., & Verdel, T. (2014). *Statistical correlation between meteorological and rockfall databases*. Natural Hazards and Earth System Sciences, 14(8), 1953-1964.

D'Amato, J., Hantz, D., Guerin, A., Jaboyedoff, M., Baillet, L., & Mariscal, A. (2016). *Influence of meteorological factors on rockfall occurrence in a middle mountain limestone cliff*. NHESS, 16(3), 719-735.

Collins, B. D., & Stock, G. M. (2016). *Rockfall triggering by cyclic thermal stressing of exfoliation fractures*. Nature Geoscience, 9(5), 395-400.

Brain, M. J., Rosser, N. J., Norman, E. C., & Petley, D. N. (2014). *Are microseismic ground displacements a significant geomorphic agent?* Geomorphology, 207, 161-173.

Snowmelt, a major landslide triggering factor ?

Mathieu Le Breton[1], Yannick Thiery[2], Jérôme Faillettaz[3], Nicolas Villard[4], Muriel Gasc[3]

[1] Géolithe Innov, Crolles, France ;
[2] BRGM, Pessac, France
[3] CEREMA, GéoCOD, Bron, France
[4] NGE, Domène, France

SUMMARY: Snow plays a critical role on landslide stability. We emphasize it with four cases of landslide activation, in the French Alps during the winter 2021–2022, resulting from reheating and rain-on-snow. We then synthesize the available literature on the role of snow on landslide triggering. Three factors influence landslide stability: meltwater, soil temperature and mechanical loading. Yet, the governing factor may be different on each landslide. We then discuss the operational requirements from companies and risk managers, and the knowledge gaps and potential research directions. In particular, advances in snow sensing and modeling should be incorporated into early warning systems, and more landslides should be observed to better understand and classify their various mechanisms when covered by snow.

Keywords: landslide, snow, trigger, snowmelt, rain-on-snow

Introduction and motivation

Precipitations infiltrating into the ground are a major landslide trigger. The intensity of rainfall cumulated over a given period is a classical indicator used to estimate the probability of landslide activation, using statistical methods (Guzzetti et al., 2007) or physical methods (Iverson, 2000). This hydrologic approach, used in numerous regional early warning systems (Guzzetti et al., 2020), relies on rainfall as a primary input data. However, it faces challenges when there is snow cover. Snow cover modifies the quantity of infiltrated water, depending mostly on accumulated snow quantity and thermal energy. Depending on its state and on meteorologic events, the snowpack can influence the instant quantity of soil-infiltrated water in very different ways: (1) delay the infiltration of precipitations to later in the year, (2) increase the infiltrated water during rain-on-snow events (Brandt et al., 2022), (3) release water due to thermal snowmelt, and sometimes (4) modify local hydraulic conductivity due to frozen snow layers or soil (Osawa et al., 2017). Adding to the complexity, snowpack loading and thermal role can either stabilize or destabilize landslides (Matsuura et al., 2017). Finally, instrumentation is often more challenging in cold or snowy weather: displacement instruments may work poorly (Le Breton et al., 2019), and rain collectors get clogged by snow. As a result, few scientific studies investigate landslides triggered by snowmelt, and few early warning systems can anticipate landslides in the presence of a snow cover.

Landslides activated during early or mid-winter reheats in 2022: cases in Chartreuse

Figure 1 (a-d) presents typical small landslides often occurring now in the Alps after intense rainfall (~100 mm) in a global warm front, associated with massive and rapid melting of the snowpack (~ 50 cm). During 2021 and 2022 winters, they occurred during the Christmas break when road administrations were reducing the task force and thus, reactivity to warning and preventive tasks. In such situations it is difficult to engage emergency remediation works as a stability model should be retrofitted before designing soil reinforcement. Water table position and circulation are key parameters on which empirical hypotheses are done according to field observation and calculation tool limits (permeability, virtual level…).

Figure 1. Shallow landslides in the Alps: (a) St-Pierre de Chartreuse, (b) St-Pancrasse, (c) Châtel, (d) Sarcenas.

What we know from past landslide studies

Regional historical studies have highlighted the role of snowmelt on landslides in many areas. For instance, 40% of monitored landslide activations in Niigata (Japan) have occurred in the first two months of the snow season and 5% during spring snowmelt (Sato et al., 2004). In Umbria (Italy), intense snowmelt in 1997 triggered far more landslides in a few weeks (Cardinali et al., 2000) than in the rest of the year and previous decades (Guzzetti et al., 2003). The landslide activations correlated with cumulated temperature threshold in Colorado, USA (Chleborad, 1997), or with river runoff in Aconcagua (Argentina) and Ontonagon river valley (USA) (Moreiras et al., 2012; Weidner et al., 2019). Models for regional early warning systems have been proposed over large regions. Kawagoe et al. (2009) used a physical model over Japan, based on inputs of snow water equivalent, snowfall precipitations and temperature, and on parameters such as the type of soil and the slope. Martelloni et al. (2013) proposed to use a simple snowmelt model (taking precipitations and air temperature as input) in conjunction with existing landslide warning systems based on empirical rainfall thresholds.

Few landslide-scale studies have investigated specific stabilization/destabilization processes. In the Busuno area, Japan, a landslide (10 m depth) with deep snowpack (several meters) was highly monitored (Matsuura et al., 2003, 2017; Osawa et al., 2017; Shibasaki et al., 2016). It moved at the beginning of the summer, and stabilized during winter and spring, likely due to snow load. On the contrary, the deep-seated Slumgullion landslide (Colorado USA), with shallow snow cover (<60 cm), moved mostly during spring melt (Coe et al., 2003). The Roesgrenda shallow landslide in Norway, saw its pore water pressure dominated by snow load, with negligible snowmelt influence due to the low hydraulic conductivity of its quick clay (Okamoto et al., 2018). These three landslides had different activation periods (early winter or

spring) and different dominating influences (melt snow, soil temperature or snow loading). Therefore, predicting a landslide reaction to the snowpack is not straightforward, as every site could behave very differently.

Mechanisms that influence landslide stability

Three factors influencing the stability of a landslide covered by snow have been identified. (1) Snowpack can store precipitations and release it later. The resulting snowmelt runoff (DeWalle & Rango, 2008) is estimated for example to predict floods (Haeberli & Whiteman, 2021). It is modeled by cumulating precipitations and thermal fluxes over the season (Morin et al., 2020; Zhou et al., 2021). Rain-on-snow, in particular, can either reduce or augment the quantity of liquid water released depending on the snow conditions (Beniston & Stoffel, 2016; Brandt et al., 2022). (2) The thermal flux between soil and snow cover can influence landslide stability in several ways. In early winter, a hot soil and a wet shallow snowpack may accelerate snow melting (later in the season, soil heat influence becomes negligible (DeWalle & Rango, 2008)). Then, snowpack's thermal insulation may keep the soil at 0 °C and prevent its freezing. On one side, that favors destabilization due to higher soil hydraulic conductivity (Mohammed et al., 2018) and lower mechanical rigidity of unfrozen soils (Patton et al., 2019). On the other side, it may stabilize landslides made of materials which rigidity decrease with cold (Shibasaki et al., 2016) (3) Snowpack weight results in landslide loading, that both stabilize it mechanically (Matsuura et al., 2003) and destabilize it by increasing its pore water pressure (Okamoto et al., 2018). In conclusion, each landslide covered by snow can be governed by a different factor, depending on many parameters (e.g., geology, shallow/deep landslide, altitude, early/mid/late snow season) and no single indicator may predict the risk of failure.

Needs for risk management tools

The anticipation of landslide probability in the presence of snow cover is of paramount importance for risk mitigation. (1) Regional landslide early warning systems rarely account for the role of snowmelt (Guzzetti et al., 2020). (2) Local early warning systems can be required to react to fast activation of some shallow landslides. New tools are necessary to forecast risk of activation in order to close a road temporarily, halt a construction work, or support the decision to reopen the activity. (3) Geotechnical consultants would need to account for the role of snow when dimensioning protections works against landslide. In particular, extreme snowmelt events that activate many landslides within a few days (e.g., Cardinali et al., 2000) put high stress on risk managers, and require fast action based on little data. (4) Long-term risk prevention plans should account for the role of snowmelt in the context of climate change (Ding et al., 2021).

Thus, research on the role of snow on landslide triggers is needed. Numerous research was made on landslides triggered by groundwater (Davies & Rosser, 2021) or on snowmelt water (Haeberli & Whiteman, 2021), but few connections were made between them. The little research attention on snow-triggered landslides (Ding et al., 2021) might be due to a lack of snow data on monitored landslides and to the difficulty to monitor landslides in winter (Matsuura et al., 2017). Investigating further the role of snow on landslides will require (1) collaboration with snow hydrologists to better quantify snowmelt, and (2) investigating more landslides to understand and classify their different behaviors under snow cover.

Conclusion

This bibliographic study highlights the complex relationship between snow and landslide occurrence. Snow impact landslides by influencing liquid water dynamics, loading and soil temperature, with different governing mechanisms on each landslide. Understanding these interactions is essential for improving landslide prediction and risk mitigation strategies, ultimately safeguarding vulnerable communities in landslide-prone areas.

References

Beniston, M., & Stoffel, M. (2016). Rain-on-snow events, floods and climate change in the Alps : Events may increase with warming up to 4 °C and decrease thereafter. *Science of The Total Environment*, *571*, 228-236.

Brandt, W. T., Haleakala, K., Hatchett, B. J., & Pan, M. (2022). A Review of the Hydrologic Response Mechanisms During Mountain Rain-on-Snow. *Frontiers in Earth Science*, *10*.

Cardinali, M., Ardizzone, F., Galli, M., Guzzetti, F., & Reichenbach, P. (2000). *Landslides triggered by rapid snow melting : The December 1996-January 1997 event in Central Italy*. 10.

Chleborad, A. F. (1997). *Temperature, snowmelt, and the onset of spring season landslides in the central Rocky Mountains*. Citeseer.

Coe, J. A., Ellis, W. L., Godt, J. W., Savage, W. Z., Savage, J. E., Michael, J. A., Kibler, J. D., Powers, P. S., Lidke, D. J., & Debray, S. (2003). Seasonal movement of the Slumgullion landslide determined from Global Positioning System surveys and field instrumentation, July 1998–March 2002. *Engineering Geology*, *68*(1), 67-101.

Davies, T., & Rosser, N. (2021). *Landslide Hazards, Risks, and Disasters*. Elsevier.

DeWalle, D. R., & Rango, A. (2008). *Principles of Snow Hydrology* (1st edition). Cambridge University Press.

Ding, Y., Mu, C., Wu, T., Hu, G., Zou, D., Wang, D., Li, W., & Wu, X. (2021). Increasing cryospheric hazards in a warming climate. *Earth-Science Reviews*, *213*, 103500.

Guzzetti, F., Gariano, S. L., Peruccacci, S., Brunetti, M. T., Marchesini, I., Rossi, M., & Melillo, M. (2020). Geographical landslide early warning systems. *Earth-Science Reviews*, *200*, 102973.

Guzzetti, F., Peruccacci, S., Rossi, M., & Stark, C. P. (2007). Rainfall thresholds for the initiation of landslides in central and southern Europe. *Meteorology and Atmospheric Physics*, *98*(3), 239-267.

Guzzetti, F., Reichenbach, P., Cardinali, M., Ardizzone, F., & Galli, M. (2003). The impact of landslides in the Umbria region, central Italy. *Natural Hazards and Earth System Sciences*, *3*(5), 469-486.

Haeberli, W., & Whiteman, C. (2021). *Snow and Ice-Related Hazards, Risks, and Disasters*. Elsevier.

Iverson, R. M. (2000). Landslide triggering by rain infiltration. *Water Resources Research*, *36*(7), 1897-1910.

Kawagoe, S., Kazama, S., & Ranjan Sarukkalige, P. (2009). Assessment of snowmelt triggered landslide hazard and risk in Japan. *Cold Regions Science and Technology*, *58*(3), 120-129.

Le Breton, M., Baillet, L., Larose, E., Rey, E., Benech, P., Jongmans, D., Guyoton, F., & Jaboyedoff, M. (2019). Passive radio-frequency identification ranging, a dense and weather-robust technique for landslide displacement monitoring. *Engineering Geology*, *250*, 1-10.

Martelloni, G., Segoni, S., Lagomarsino, D., Fanti, R., & Catani, F. (2013). Snow accumulation/melting model (SAMM) for integrated use in regional scale landslide early warning systems. *Hydrology and Earth System Sciences*, *17*(3), 1229-1240.

Matsuura, S., Asano, S., Okamoto, T., & Takeuchi, Y. (2003). Characteristics of the displacement of a landslide with shallow sliding surface in a heavy snow district of Japan. *Engineering Geology*, *69*(1), 15-35.

Matsuura, S., Okamoto, T., Asano, S., Osawa, H., & Shibasaki, T. (2017). Influences of the snow cover on landslide displacement in winter period : A case study in a heavy snowfall area of Japan. *Environmental Earth Sciences*, *76*(10), 362.

Mohammed, A. A., Kurylyk, B. L., Cey, E. E., & Hayashi, M. (2018). Snowmelt Infiltration and Macropore Flow in Frozen Soils : Overview, Knowledge Gaps, and a Conceptual Framework. *Vadose Zone Journal*, *17*(1), 180084.

Moreiras, S., Lisboa, M. S., & Mastrantonio, L. (2012). The role of snow melting upon landslides in the central Argentinean Andes. *Earth Surface Processes and Landforms*, *37*(10), 1106-1119.

Morin, S., Horton, S., Techel, F., Bavay, M., Coléou, C., Fierz, C., Gobiet, A., Hagenmuller, P., Lafaysse, M., Ližar, M., Mitterer, C., Monti, F., Müller, K., Olefs, M., Snook, J. S., van Herwijnen, A., & Vionnet, V. (2020). Application of physical snowpack models in support of operational avalanche hazard forecasting : A status report on current implementations and prospects for the future. *Cold Regions Science and Technology*, *170*, 102910.

Okamoto, T., Matsuura, S., Larsen, J. O., Asano, S., & Abe, K. (2018). The response of pore water pressure to snow accumulation on a low-permeability clay landslide. *Engineering Geology*, *242*, 130-141.

Osawa, H., Matsuura, S., Matsushi, Y., & Okamoto, T. (2017). Seasonal change in permeability of surface soils on a slow-moving landslide in a heavy snow region. *Engineering Geology*, *221*, 1-9.

Patton, A. I., Rathburn, S. L., & Capps, D. M. (2019). Landslide response to climate change in permafrost regions. *Geomorphology*, *340*, 116-128.

Sato, H., Shiraishi, S., & Ito, T. (2004). The behavior of the Tertiary landslides through the snowy period in Niigata Prefecture, central Japan. *Landslides - Journal of the Japan Landslide Society*, *41*(1), 37-42.

Shibasaki, T., Matsuura, S., & Okamoto, T. (2016). Experimental evidence for shallow, slow-moving landslides activated by a decrease in ground temperature. *Geophysical Research Letters*, *43*(13), 6975-6984.

Weidner, L., DePrekel, K., Oommen, T., & Vitton, S. (2019). Investigating large landslides along a river valley using combined physical, statistical, and hydrologic modeling. *Engineering Geology*, *259*, 105169.

Zhou, G., Cui, M., Wan, J., & Zhang, S. (2021). A Review on Snowmelt Models : Progress and Prospect. *Sustainability*, *13*(20), Article 20.

Landslide risk assessment and mapping at national scale for France: toward reflections on the integration into the national prevention strategy

Y. Thiery[1]; B. Colas[2], O. Maquaire[3], M. Fressard[3], M. Premaillon[2]., M. Peruzzetto[4], S. Bernardie[4], G. Grandjean[4]

[1] BRGM, Pessac, France
[2] BRGM, Montpellier, France
[3] IDEES - UMR 6266 CNRS - Université de Caen Normandie, Caen, France
[4] BRGM, Orléans, France

ABSTRACT: Indicators and landslide risk maps for France at national scale are computed and presented. Two quantitative approaches are employed, and the results, including the landslide hazard map and landslide risk maps generated from composite indicators for built-up areas and roads, are examined. These documents are intended to be used in the national strategy for landslide risk prevention.

Keywords: landslides, hazard and risk, national scale, France, strategy for prevention

Introduction

Landslide risk is the spatial and temporal probability of a phenomenon of a certain intensity occurring over a defined period of time in a specific area, causing damage to people, buildings, infrastructure and services (Thiery et al., 2020). To assess this risk, both the hazard and the vulnerability of exposed elements must be considered. Assessing and anticipating landslide risk are generally conducted at the local, and regional scales, involving the production of cartographic documents using different methods (Thiery et al., 2020). Few countries, such as Cuba, Georgia, India, China, and Italy, have undertaken quantified assessments on a national scale involving different quality datasets and specific mapping strategies (Donini et al., 2022).

While France was a pioneer in the systematic assessment and mapping of landslide risk at the municipal level (PPR, Plan de Prévention des Risques, MATE/MATL, 1999), and some semi-quantitative National Landslide Susceptibility Maps (NLSM) have been produced (Malet et al., 2013), no indicative landslide risk assessments and maps have been undertaken at the national scale. It conveys that the French national strategy lacks a comprehensive and informative documents about the most vulnerable areas regarding landslides.

This work presents a quantified approach to producing a national landslide risk map (NLRM) in France at 1:500 000. The methodology was based on the principles the exposed elements and risk assessment part. These principles are as follows:

i. Use of a quantitative, data-based calculation method, reducing the subjectivity of weightings used previously (Malet et al., 2013);
ii. Introduction of new spatial variables to improve the identification of specific areas;
iii. Introduction of exposed elements (built-up areas, roads) to assess landslide risk.

The approach is designed to be straightforward and practical, minimizing the reliance on overly complex data. The documents generated serve as a preliminary step in identifying landslide risk areas. Furthermore, they can initiate a process of consideration regarding how to incorporate these documents into the national landslide risk assessment strategy, particularly in areas lacking hazard maps for regulatory purposes, which may warrant increased attention.

Materials and method

The spatial variables, principally derived from national databases, can be grouped into 6 groups (landslides, topography, geomorphology, geology, landuse, physio-geographic areas).

Landslides were derived from the BD-Mvt, the national incident database (Thiery et al., 2020). The phenomena are essentially shallow landslides causing damage to infrastructure; debris flows and mudflows are not included in the study. It lists the locations of events, trigger dates, activity, and sometimes the damage caused. Topography was represented by two DEMs selected from IGN databases; one at a 250 m resolution and the other at a 50 m resolution. They were used to generate maps as: slope, aspect, curvature, etc. Geomorphology was automatically derived from DEMs into 8 major classes (Iwahashi and Pike (2007). Soil parent materials was derived from a simplification of lithological surveys conducted at a one-millionth scale (https://infoterre.brgm.fr/page/cartes-geologiques). Two maps were used: one with 11 classes, and one more detailed with 27 classes. Additionally, a map depicting the state of regolith destructuration based on the density of faults, their types, and the different class of seismicity was created. The idea was to add a component on the state of the lithology as a function of tectonics. Landuse was derived from Corine Land Cover (CLC), THEIA database (https://www.theia-land.fr/product/carte-doccupation-des-sols-de-la-france-metropolitaine/) and road database from IGN (https://geoservices.ign.fr/route500). Physio-geographic units represented macro-geographic units based on climatic areas and relief.

Considering that a comprehensive landslide risk assessment, including the temporal aspect and propagation, is not feasible at this working scale and due to the lack of consistency about this information in the BD-MVT (Thiery et al., 2020), it was decided that the susceptibility map would replace the hazard map. The strategy was divided into four steps:

i. Selection of the best spatial variables (i.e. landslides, topography, geomorphology, geology, land use, physio-geographic area ...) according to their aptitude to build LSM. The computations were performed with a cell size of 250 m in order to optimize the processing time.
ii. After defining the optimal set of spatial variables, calculations were conducted using a 50 m cell size and dividing the country into 18 physio-geographic units;
iii. Each unit was subjected to a statistical validation procedure with four tests before reclassification into 6 classes following the limits given by the JTC-1. The limits are given for guidance purposes. The reclassified maps were merged to obtain a single NLSM.
iv. Finally, the new NSLM (Fig. 1) was compared to different local landslide databases not implemented in the national landslide database (BD-MVT) and to different national, regional, and local LSM for different areas.

Once validated, the NLSM served to generate indicative NLRM for the built-up areas and the roads for each municipality. Data used were THEIA landuse database and IGN road database (Route500©). Two indicators were computed for each municipality:

i. The first was the absolute risk index (ARI) representing the total of weighted surfaces for exposed elements to a specific hazard class. It quantitatively reflects the surface areas of exposed buildings or roads, assigning higher weights to areas with higher levels of hazard. The objective is to prioritize efficiency, operating on the premise that: "if we were to select a single municipality for our prevention efforts, with unlimited resources, which one would we select?"
ii. The second was the relative risk index (RRI). Its computation involved dividing the ARI by the total surface area assessed, whether it's a municipality or the entire stake's surface area. RRI aimed to identify municipalities most significantly impacted by the risk, based on the proportion of the area being considered.

Both indices were standardized and merged to form a composite municipal risk index (CMRI). This ranking system has allowed for the organization of municipalities in order of priority. Consequently, three maps can be presented for each exposed element.

Results

The results obtained for the NSLM were considered as excellent. (Fig. 1). For the entire territory, the relative error the success rate and the prediction rate were 0.27, 72.8%, and 73.7% respectively. The non-recognition rate was low with 9% (i.e. very few landslide occurrences were classified as negligible). Plateau edges, known to be prone to landslides, were accurately identified with recognition rates exceeding 80% (Fig. 1B & 1C). Recognition tests using landslides from local landslide databases not integrated into the NLSM computation process demonstrated the identification of between 80% and 97% of landslides within the very high, high, and moderate susceptibility classes. These results display strong similarities with LSM obtained at different scales with various techniques. Despite variations in the number of classes, NLSM aligned well with the high and moderate classes with the other maps.

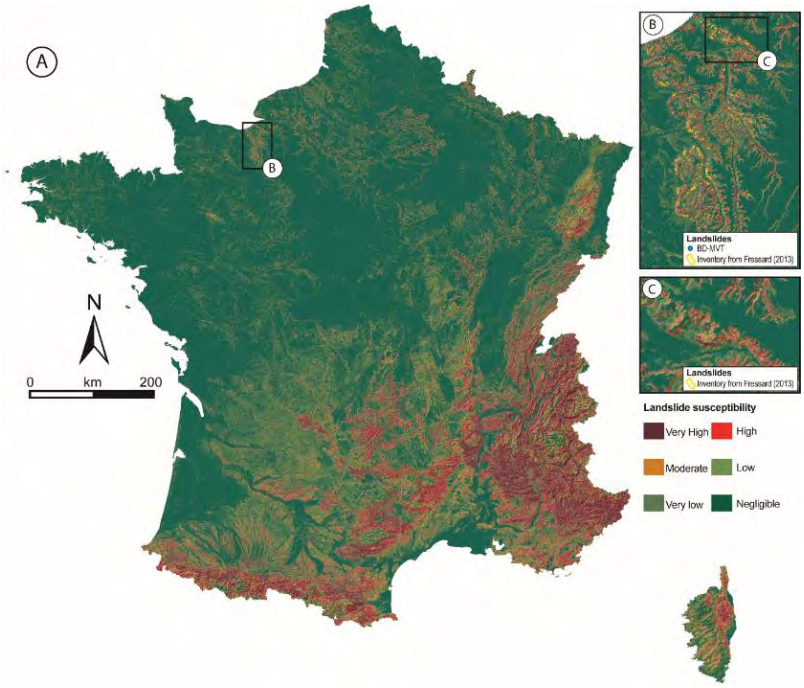

Figure 1. National landslide susceptibility map (NLSM; Thiery et al., 2022). A. LSM for metropolitan territory and Corsica. B Zoom of the NLSM for the Pays de Caux (with BD-Mvt and independent landslide inventory). C. Zoom for the Touques area.

The calculated risk indices for urbanized areas and roads in each municipality help to pinpoint priority municipality. For each index, a classification based on Jenks thresholds was attempted in order to prioritize the risk to built-up areas and roads for the various municipalities (Fig. 2).

For ARI, where prioritization is not constrained by funding limits, 238 municipalities were considered in very high risk or risk 1 (R1). These are highly urbanized municipalities located mainly on the Côte d'Azur and in the Northern Alps. For roads, 400 municipalities are identified as R1. The same areas stand out overall, with the addition of the Pyrenean foothills. This index also expresses the way in which the various municipalities have developed on morphological sectors prone to landslides.

For RRI, which takes into account the surface area of the municipality, 2056 and 1788 municipalities were identified as R1 for risk to buildings and risk to roads respectively. For both indexes, the municipalities located on major communication axes stand out, such as the Seine axis to Normandy, Champagne, the Rhone axis, the Garonne axis, and part of the Côte d'Azur.

Lastly, the CMRI (Fig.2) was used to prioritize the municipalities to be targeted, both in terms of the total surface area potentially impacted by landslides and the relative proportion of the territory affected. For built-up areas, 480 municipalities were classified as R1 (Fig. 2A). The municipalities of the Côte d'Azur, the northern Rhône axis, and Champagne axis stand out. For roads, 1376 municipalities were defined as R1 (Fig. 2B). The same areas been identified as for the built-up risk map, with the addition of the Pyrenean foothills, part of the Massif Central and the Causse hills and plateaus.

Discussion - conclusion

The results of the National Landslide Susceptibility Map (NLSM) are highly satisfactory, both from a statistical and expert perspective. The methodology, based on selecting the most

relevant variables and computation by physio-geographical units, has significantly improved the map's quality. Comparisons with other maps and inventories demonstrate the effectiveness of the strategy. However, it should be noted that some areas, particularly in the Alps and parts of the Pyrenees, appear to be underestimated due to a problem of transfer information in the BD-MVT (Thiery et al., 2020). Indeed, these areas are supplied with event data by the RTM services and not the BRGM. There remains a problem of interoperability of data which are located in the municipality centroids and not on the slopes. The calculations are thus biased and do not reflect reality. These regions must be cross-referenced with local inventories provided by local services.

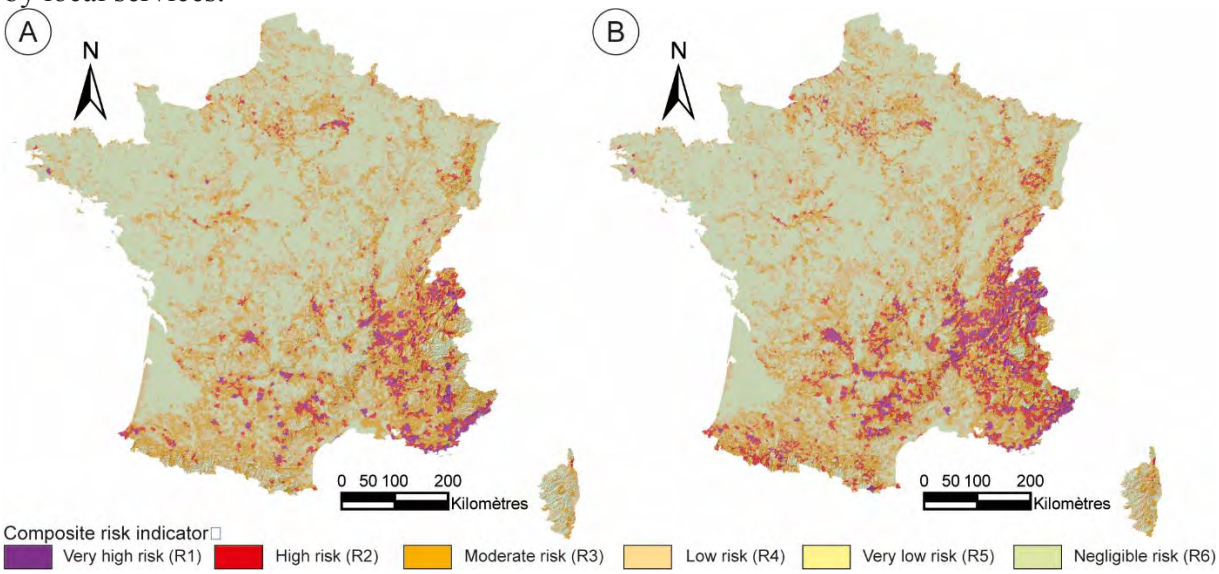

Figure 2. National landslide risk maps based on the CMRI. A. Landslide risk map for built-up areas. B. Landslide risk map for roads.

The results for the indicative risk maps are promising. The utilization of THEIA database has improved upon prior results, as mentioned in Thiery et al. (2022). While there are uncertainties regarding the quality of the BD Route (with missing sections in certain municipalities) and the subjectivity of classifications, these documents offer an overview of municipalities that could be prioritized within the Ministry of the Environment's risk mapping strategy. However, before finalizing these documents, a comparison with the GeoHazards database (http://www.georisques.gouv.fr/) and the prefecture policy in term of landslide hazard mapping is necessary. The cross-checking of information on planned, ongoing hazard and risk analyses and PPR approved is considered essential to successfully complete this study.

References

Donnini M, Esposito G, Pisano L et al. (2022). National and regional-scale landslide indicators and indexes: Applications in Italy. Open Geosciences, 14(1), 763-775.

Iwahashi, J, & Pike R J (2007). Automated classifications of topography from DEMs by an unsupervised nested-means algorithm and a three-part geometric signature. Geomorphology, 86(3-4), 409-440.

Malet J-P, Puissant A, Alexandre M, et al. (2013). Integrating spatial multi-criteria evaluation and expert knowledge for national-scale landslide susceptibility analysis: application to France. In: Margottini C, Canuti P, Sassa K (Eds.), Landslide Science and Practice (Proc. 2nd WLF, 3-7 October 2011, Rome), Springer, Heidelberg, Vol. 1, pp. 303-311.

MATE/MATL (1999). Plan de Prévention des Risques (PPR): Risques de Mouvements de terrain. Ministère de l'Aménagement du Territoire et de l'Environnement (MATE), Ministère de l'Equipement des Transports et du Logement (METL), La Documentation Française, Paris, 1999.

Thiery Y, Terrier M, Colas B, et al. (2020). Improvement of landslide hazard assessments for regulatory zoning in France: STATE–OF–THE-ART perspectives and considerations. Int. Jour. Dis. Ris. Red. 47, 101562.

Thiery Y, Grandjean G, Cottereau Y et al. (2022). From landslide susceptibility to risk mapping for France: improvement and application at 1:500,000 scale of work. Journées Aléas Gravitaires-2022, May 2022, Montpellier, France. hal-03653686.

Landslide risk mitigation: the experience of the MITIGO project in southern Italian Apennines

Caterina Di Maio, Roberto Vassallo

University of Basilicata, Potenza, Italy

SUMMARY: Herein we shortly illustrate the experience gained in a complex and very interdisciplinary research project co-funded by European Union. The project aims to the mitigation of landslide and seismic risks for road infrastructures and strategic structures of a large portion of a regional territory in the southern Italian Apennine chain. We develop the geotechnical part working together with sociologists, planners, physicists, geologists, and hydraulic, seismic, road, transport, mechanical and energy engineers. In particular, for landslide problems, the remedial measures are defined with a holistic vision of the problems and with sequences of bottom-up and top-down procedures.

Keywords: landslide, monitoring, mitigation, mobility, mountain areas

The MITIGO project: aims and strategies

The MITIGO project (Mitigation of landslide and seismic risks for road infrastructures and strategic structures in mountain areas) is 3.5 years *National Operative Project (Research and Development)* co-funded by European Union; it is aimed at the mitigation of natural risks for safety and mobility in mountain areas. In particular, the project pursues solutions to mitigate the risks related to transportation routes and strategic structures (e.g., hospitals, schools) of communities in Basilicata Region, in the southern Italian Apennines, in areas known to be historically affected by landslides, floods, earthquakes, shortage of public services, mobility problems and thus by depopulation phenomena.
The final goals are: providing a contribution to the improvement of the social and economic conditions of communities in mountain areas of southern Italy; reducing the migration of local populations; fostering development, transforming current criticalities into growth opportunities. So, the project works in an articulate manner on several main tasks: 1) safety and monitoring of territory and critical infrastructures; 2) prevention of critical events and risk reduction; 3) cyber safety and use of data; 4) smart mobility; 5) improvement of relationships administrations-populations, and 6) social participation.
The project proposes interdisciplinary investigation models and remedial measures at various scales, it is led by University of Basilicata and involves other universities, research institutions, companies and public administrations, with more than 150 participants, and many stakeholders: local authorities, transportation infrastructure managers, engineers and geologists active in hydrogeological risk reduction (www.mitigoinbasilicata.it).
The activities of all the project partners focus on a study area located between the cities of Potenza and Matera and between the Basento and Bradano river valleys (Fig. 1). Starting from this “natural laboratory”, the goal is to carry out risk analysis, and risk management and prevention models of general interest.
The project investigates systems for surveying, monitoring and securing the territory, infrastructures and strategic structures by solutions as sustainable and innovative as possible, also considering the need for CO_2 emission reduction. In fact, the project considers as well

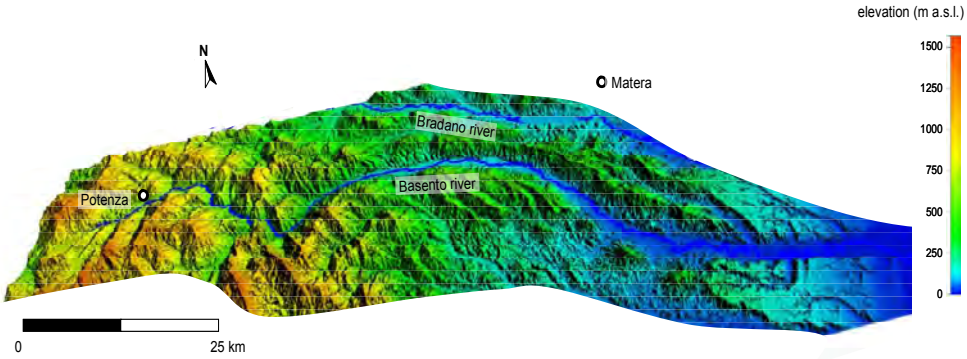

Figure 1. Digital Terrain Model of the Basento River valley

complementary and/or alternative transportation systems, such as solar powered cable ways, characterized by low risk levels and ensuring a drastic reduction of risk of isolation.

Remote sensing systems at different scales and resolutions (satellite, aircraft, helicopter, drones, UAVs) are integrated with terrestrial indirect geophysical and direct engineering systems for surveying and monitoring the territory and engineering works. Risk mitigation is also pursued through the formulation of models for social participation, as well as encouragement toward self-protection behaviors.

For the development of integrated monitoring systems, a widespread investigation of ground and infrastructure movements in the study area was possible thanks to LIDAR surveys and PSP-IFSAR analyses of COSMO-SkyMed satellite data acquired in the period 2011 - 2021 and Sentinel-1 data in the period 2015 - 2021. Drone monitoring was also successfully employed for studying the displacement evolution of both rock and soil instabilities.

Studies for lithological and geomorphological characterization took advantage of such data, and allowed to update the inventory maps of the entire study area. The climate framework of the area and its possible variations over the next 50 years were analysed. Studies were therefore carried out to evaluate the local effects of climate change on clayey earthflows of small and medium depth (Rianna et al., 2022). Procedures were developed at a municipal scale and a detailed scale for the analysis of damage induced by slow landslides along the road connecting some municipalities to the main regional highways (Nicodemo et al., 2023). Monitoring of suction regime in slopes was used to interpret weather effects and understand the influence of deep-rooted vegetation (Tagarelli & Cotecchia, 2022). Advances have thus been made in the field of modelling the hydro-mechanical behaviour of landslides, including the effects on slope stability of weathering, and specifically of pore fluid ion concentration decrease and swelling in clayey soils (e.g., Di Maio et al., 2021; Vassallo et al., 2021; Ghalamzan Esfahani et al., 2022).

Particular investigations were carried out on slopes affected by very/extremely slow landslides in structurally complex formations. Kinematic and hydro-chemo-mechanical characterization of the different instability phenomena occurring in the *Costa della Gaveta* slope were performed. Interaction between the landslides and the Basento river was also studied.

The study of slope stability plays a crucial role in the project. The most widespread types of landslide systems, problematic for populations, have been identified. Then, some of these systems have been studied in detail, in order to understand the fundamental characteristics that allow the definition of the most effective intervention strategies. In the following section, an example relative to the influence of rainfall on displacements is shown.

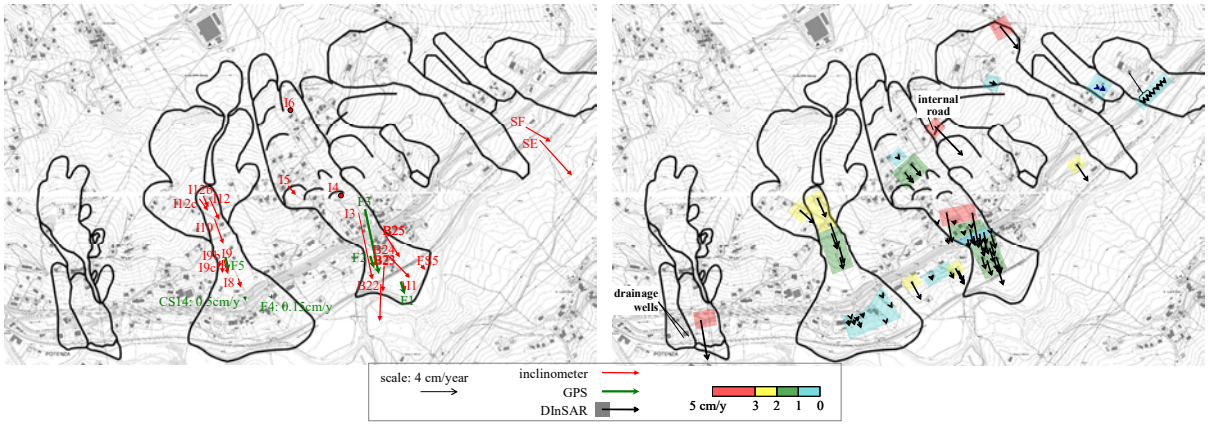

Figure 2. Displacement rate distribution in the *Costa della Gaveta* slope (Vassallo et al., 2021)

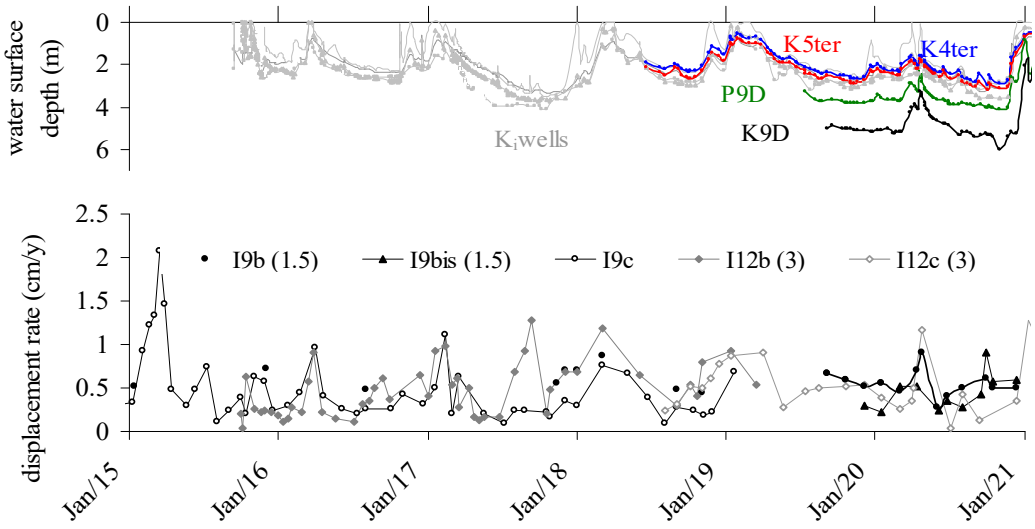

Figure 3. Piezometric levels and displacement rates in correspondence of the slip surface of *Costa della Gaveta* earthflow. Inclinometer data in I9b, I9bis, I12b, I12c are divided by the bracketed numbers (Di Maio et al., 2021)

Results relative to earthflow kinematics and relation between rain and displacements

We studied the kinematics of some landslide systems affecting *Costa della Gaveta*, a large slope in structurally complex clay formations close to Potenza city (Vassallo et al., 2021), where deep and superficial displacements are being monitored by inclinometers and GPS stations since 2005. However, inevitably, such measurements are discontinuous in time and space. Images acquired by the COSMO-SkyMed satellite system, supplemented by ERS and Envisat data, were used to reconstruct rather continuous displacement series which: i) filled the gaps of ground measurement series, ii) allowed to confidently exploit displacement field information in areas wider than those investigated by ground sensors.

The results obtained by the different systems thus allowed the evaluation the average (over about 30 years) displacement rate field (Fig. 2). As a matter of fact, the yearly displacement rates in each measurement location have been rather constant over the years, whereas seasonal variations linked to the hydrological regime, with prompt response to rain, have been clearly observed. Given the very high clay fraction of the considered soils, this phenomenon was considered to deserve a deeper study. In order to evaluate how rain influences pore water pressures and how these latter, in turn, can cause acceleration of the landslide movements, Di Maio et al. (2021) presented data of a long-term monitoring of pore water pressures, and the

results of many field permeability tests carried out with several procedures. The data were evaluated in three different zones of the subsoil: landslide body, parent formation and slip zone. The experimental data show that, in the shear zone, the permeability k varies in the range 10^{-8} m/s ÷ 10^{-5} m/s. On the other hand, in the landslide body, k varies in the range 10^{-10} m/s ÷ 10^{-8} m/s. In the stable formation, k exhibits even lower values, i.e. 10^{-10} m/s ÷ 10^{-11} m/s.
Consistently, the piezometric data obtained by many measuring devices installed in the parent formation and in the landslide body do not show significant variations due to rainfall, even at depths of a few metres. Conversely, as shown by Figure 3, pore water pressures measured in the slip zone vary sensibly and quickly with rainfall, inducing almost synchronous variations in the basal displacement rates registered by the inclinometers (Di Maio et al., 2021). This suggests that the effectiveness of a drainage system is linked to its ability in controlling pore water pressures directly in the slip zone.

Concluding remarks

The MITIGO Project uses a holistic approach to the resolution of hydrogeological and seismic risk problems relative to large areas of the southern Italian Apennines, based on sociological and territorial planning, and technical-scientific investigations. The project is receiving considerable attention from civil society from several points of view. From the technical point of view, this abstract briefly shows some results which can be useful in the design of one of the most diffused remedial measures, such as drainage systems.

Acknowledgements

This research was supported by MIUR PON R&I 2014-2020 Program (project MITIGO, ARS01_00964). Cosmo-SkyMed DInSAR data were provided by the Italian Space Agency (ASI).

References

Di Maio C, De Rosa J, Vassallo R (2021). Pore water pressures and hydraulic conductivity in the slip zone of a clayey earthflow: experimentation and modelling. *Engineering Geology* 292, 106263.

Ghalamzan Esfahani F, De Rosa J, Gajo A, Di Maio C (2022). Swelling and swelling pressure in a clayey landslide: experimental data and model simulations. *Engineering Geology* 297, 106512.

Nicodemo G, Pecoraro G, Rianna G, Reder A, Luongo D, Peduto D, Calvello M (2023). Remote sensing meteorological and DInSAR historical data to analyse the kinematic behaviour of slow-moving landslides at municipal scale. *Proceedings of the VIII Italian Conference of Researchers in Geotechnical Engineering (CNRIG 2023)*. A. Ferrari, M. Rosone, M. Ziccarelli, G. Gottardi (eds.). Springer Series in Geomechanics and Geoengineering, Springer.

Rianna G, Comegna L, Reder A, Urciuoli G, Picarelli L (2022). A simplified procedure to assess the effects of climate change on landslide hazard in a small area of the Southern Apennines in Italy. *Natural Hazards* 115, 2633–2654.

Tagarelli V & Cotecchia F (2022). Preliminary field data of selected deep-rooted vegetation effects on the slope-vegetation-atmosphere interaction: results from an in-situ test. *Rivista Italiana di Geotecnica* 1/2022, 62-83.

Vassallo R, De Rosa J, Di Maio C, Reale D, Verde S, Fornaro G (2021). In situ and satellite long-term monitoring of slow clayey landslides and of the structures built on them. *Rivista Italiana di Geotecnica* 55(4), 77-95.

Rock avalanche and debris flow runout prediction for suggested failure scenarios. Case study of Cima del Simano rockslide (Switzerland)

Charlotte Wolff[1], Michel Jaboyedoff[1], Andrea Pedrazzini[2], Marc-Henri Derron[1]

[1] ISTE – University of Lausanne, Lausanne, Switzerland
[2] Sezione forestale – Repubblica e Cantone Ticino, Bellinzona, Switzerland

SUMMARY: Rock avalanches and debris flow events are of major concerns in mountainous areas with deep and narrow valleys. Cima del Simano instability in the Swiss Alps is a rockslide which could trigger in the future such events. A previous work suggested scenarios for the rockslide failure defined by an area, a volume and a susceptibility to happen. Based on those conclusions, this work suggests predicting the runout distance L of the flow propagation in the case of a rupture of one of those instable volumes and their runout exceedance probability. During the propagation, some material deposits in the gullies and can trigger future debris flow.

Keywords: rock avalanche, debris flow, runout distance, exceedance probability.

Introduction

Most of the rock avalanche propagation simulations and runout distance estimation found in the literature are based on back-analysis of former events to find the best parameters to fit the propagation models. Here we suggest a method to estimate the runout distance of rock avalanches from a potential failure of an instable volume. The results are completed by a runout exceedance probability assessment.

Geological settings and failure scenarios

Cima del Simano instability in the Blenio Valley, near Acquarossa commune consists of orthogneiss with a schistosity averaging 20°/035°. The summit, at an altitude of 2500 meters, exhibits multiple fractures, including a significant 500-meter-long crack situated about 100 meters southeast of the crest. Preliminary satellite InSAR monitoring from 2015 to 2022 conducted by GAMMA AG highlighted slow but constant movements with an average speed of 7 mm/yr at the summit, which were confirmed by GB-InSAR acquisitions in 2021 and 2022. A previous work (Wolff *et al.*, 2023) suggests different rupture scenarios of important volumes based on monitoring results and on a structural analysis (Table 1).

Table 1. Two rupture scenarios, whose volume propagation is studied in this study.

Scenario	Type of instability	Deformation rate [%/yr]	Volume of rupture [m^3]	Susceptibility
SS1	Superficial planar rockslide	0.018	2.30×10^5	High
S1	Deep-seated rotational landslide	0.0023	4.30×10^6	Moderate to high

Methods

Rock avalanches

The fahrböschung angle f is defined as the angle between a horizontal plane and the line joining the top of the rupture source and the stopping point of the propagation of a landslide. It is linked to the propagation height H [m] and the maximum runout distance L [m] by the equation:

$$\tan f = \frac{H}{L}. \quad (1)$$

Several studies inventory the landslides propagation (Scheidegger, 1973; Corominas, 1996), giving a power-law relationship between the volume of rupture V [m^3] and f [deg]:

$$tan\, f = aV^{-b}, \quad (2)$$

with a [m^{3b}] and b [-] being two site type-dependent (Strom *et al.*, 2019) and hazard type-dependent (Corominas, 1996) empirical parameters to estimate. The angle f for each scenario is estimated here with various couples (a, b) found in the literature. The equivalent L is estimated with the software CONEFALL (Jaboyedoff and Labiouse, 2011).

A numerical simulation is conducted with Dan3D software, using the Voellmy rheology model where the parameters μ [-] and ξ [$m.s^{-2}$] must be selected. The propagation simulation is based on the principle of mass and momentum conservation (Hungr, 1995). Schraml et al. (2015) inventories the couples (μ, ξ) for different simulations found in the literature. To be sure encompassing all the propagation possibilities in terms of minimal/maximal lateral spreading and runout distances, four simulations are conducted corresponding to the four combinations assumed delimitating the possible domains of μ and ξ, denoted C1, C2, C3 and C4 (Figure 1). C2 and C4 correspond respectively to the minimal and maximal propagation envelope.

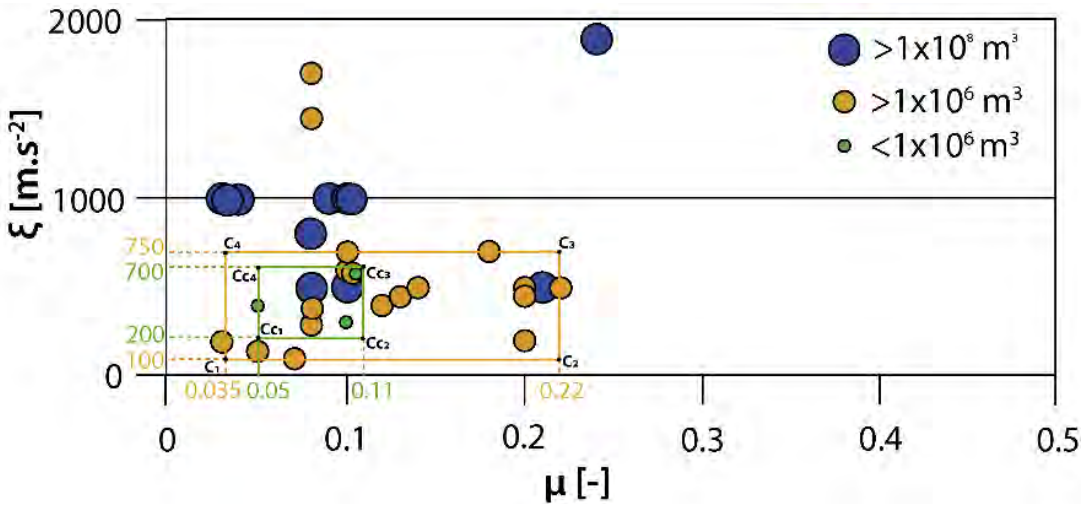

Figure 1: Couples of Voellmy parameters from back-analysis of different landslides events with Dan3D (Schraml et al., 2015)

The runout exceedance probability (Mitchell *et al.*, 2020) is estimated with the equation:

$$P(L \geq l \mid H = h, V = v) = 1 - \Phi\left(\frac{log_{10}l - \beta_0 - \beta_1 log_{10}v - \beta_2 log_{10}h}{\sigma}\right), \quad (3)$$

where β_0, β_1 and β_2 empirical regression values are determined from the landslides inventories of Pollet (2004) and Φ is the cumulative function for a normal standard distribution N(0, σ).

Results and discussion

After the different methods to estimate *f* (Figure 2a) and using CONEFALL to estimate the runout distances (Figure 2b), the rock avalanches propagation flow reaches the villages of Castro and Prugiasco. But these latter are not impacted after the numerical simulations, the flow being constraint by the topography. With scenario 'SS1' (Figure 2c), a part of the material remains in the gullies during the propagation and a part is retained by the main road with an average thickness of 5 m. Only 65% of the rupture volume reaches the runout distance. With scenario 'S1' (Figure 2d), 81% of the rupture volume propagates to the run out with a deposit thickness reaching 8 m along the river (Table 2).

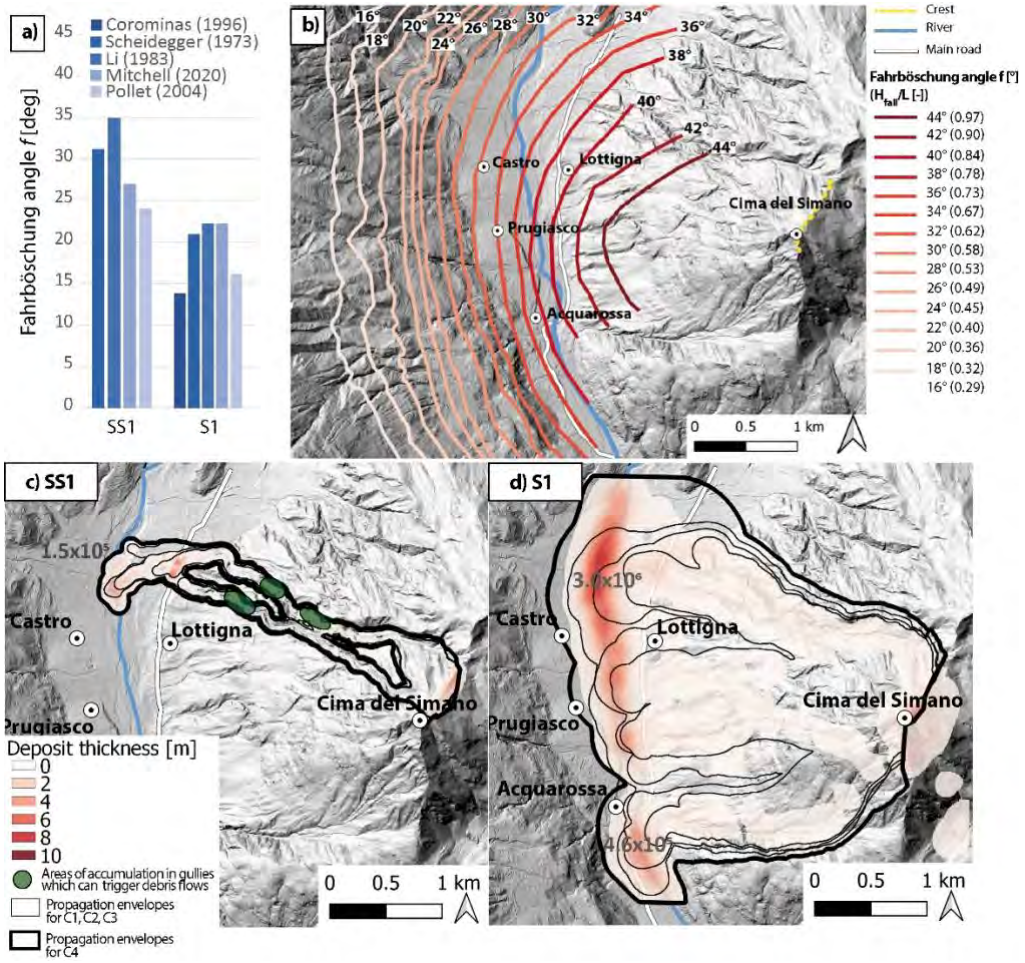

Figure 2: Rock avalanche runout estimation for scenarios SS1 and S1. A) Fahrböschung angle after different studies. B) Equivalent runout distance for different fahrböschung angles computed with CONEFALL. C) Dan3D simulation for SS1 and simulation C4. D) Dan3D simulation for S1 and simulation C4.

Table 2. Results of the propagation numerical simulations

Scenario	Deposit volume at the runout [m³]	% of the rupture volume reaching the runout	Maximum deposit thickness on the road [m]	Maximum deposit thickness at the runout [m]
SS1	$1.5x10^5$	65%	5	4
S1	$3.0x10^6$	81%	6	8

Conclusion

The chronological study first highlights the areas likely to be affected by the rock avalanche in the event of the rupture of one of the unstable volumes suggested at Cima del Simano. The flow distances estimated empirically with the Fahrböschung angle correspond to the maximum propagation distances. However, the actual propagation could be shorter due to the frontal confinement of the flow. The results obtained with the Corominas (1996) confinement assumption provide more reliable results for the extreme scenario, but with a low probability of realization. This is because the numerical simulations provide a range of potential propagation scenarios that are shorter and more likely to occur following recent calibrations of the Dan3D model. Materials deposited in gullies during propagation can then generate debris flows. These results are valuable for risk assessment and for making informed decisions, such as an evacuation plan based on an early warning system.

References

Corominas, J. (1996) 'The angle of reach as a mobility index for small and large landslides', *Canadian Geotechnical Journal,33, 260-271, doi: 10.1139/t96-005*.

Hungr, O. (1995) 'A model for the runout analysis of rapid flow slides, debris flows, and avalanches', *Canadian Geotechnical Journal*, 32, pp. 610–623. Available at: https://doi.org/10.1139/t04-052.

Jaboyedoff, M. and Labiouse, V. (2011) 'Technical Note: Preliminary estimation of rockfall runout zones', *Natural Hazards and Earth System Sciences*, 11(3), pp. 819–828. Available at: https://doi.org/10.5194/nhess-11-819-2011.

Mitchell, A. *et al.* (2020) 'Rock avalanche runout prediction using stochastic analysis of a regional dataset', *Landslides*, 17(4), pp. 777–792. Available at: https://doi.org/10.1007/s10346-019-01331-3.

Pollet, N. (2004) *Large high-speed gravity rock slope movements: Contributions of field observations in order to understand propagation and deposition processes. Application to three alpine cases: La Madeleine (Savoie, France), Flims (Graubunden, Switzerland) and Köfels (Tyrol, Austria)*. Ecole des Ponts ParisTech.

Scheidegger, A.E. (1973) 'On the prediction of the reach and velocity of catastrophic landslides', *5, 231-236, doi: 10.1007/BF01301796* [Preprint].

Schraml, K. *et al.* (2015) 'Modeling debris-flow runout patterns on two alpine fans with different dynamic simulation models', *Natural Hazards and Earth System Sciences*, 15(7), pp. 1483–1492. Available at: https://doi.org/10.5194/nhess-15-1483-2015.

Wolff, C. *et al.* (2023) 'Assessing the Hazard of Deep-Seated Rock Slope Instability through the Description of Potential Failure Scenarios, Cross-Validated Using Several Remote Sensing and Monitoring Techniques', *Remote Sensing*, 15(5396). Available at: https://doi.org/10.3390/rs15225396.

Bonifacio coastal cliff case study: what did the instrumental observation bring?

S. Coccia[1], E. Klein[1], C. Franck[1]

[1] Ineris, Verneuil en Halatte, France

SUMMARY: France is one of the most sensitive countries to coastal erosion. In some regions of France, the cliffs represent a major potential risk, due to the presence of high stakes and their appeal to tourists. Among these cliffs, there is the Citadel cliff at Bonifacio. Between September 2018 and December 2023, Ineris investigated its stability as part of a study commissioned by the French government and led by BRGM (French geological survey), with the aim of improving the knowledge of the "large-scale rockfall" hazard. Ineris performed several studies in this context, including the installation and management of a continuous multi-parameter observation system and periodic terrestrial LiDAR surveys. This paper presents the results of these two studies highlighting their contribution to the stability assessment of the Citadel cliff.

Keywords: rockfall, coastal cliff failure, survey instrumentation, terrestrial LiDAR, web-monitoring

Introduction

The prediction of “when and where” cliff failure will occur is tricky, but the stakes are high, in particular due to the increasing attractiveness of coastal areas leading to population growth (Balk et al., 2009), and climate change-related environmental changes. The latter may increment the vulnerability of coastal cliffs (IPCC, 2021, 2022).

The limestone coastal cliff of Bonifacio, located in Corsica (France), reaches heights of up to 100 m. It is characterized by the presence of two families of major fractures (oriented N20° and N110°) with one of the N110° fractures that can be seen on the wall at the bottom of Citadel area, which has a 20 m overhang. Since 2018 a large variety of investigations have been performed to improve the qualification and quantification of the “massive collapse” hazard and to assess the level of risk regarding public safety. One of the major challenges in achieving this objective was to gain a better understanding of the network and interaction of the fractures N20° and N110° involved, by acquiring multi-scale and multi-source data to build a 3D geomechanical model and thus provide information on the expected instability mechanism.

It is in this context that Ineris installed in April 2019 a real-time multi-parameter system to monitor the stability of the Citadel area and performed periodic terrestrial LiDAR surveys from 2018 to 2023. These two approaches and their contribution to hazard assessment are described below.

Description of the continuous multi-parameter survey

Cliff failure results from the interaction of both internal (e.g., rock strength, tectonics) and external factors. There is a knowledge gap about how much each triggering factor contributes to cliff failure (Letortu et al., 2022), and it is often assumed that the installation of local monitoring system can permit to reduce this gap. The Bonifacio continuous monitoring focused on a 220 m long cliff section located at the Citadel area and comprises nine sensors of two different types: cliff mechanical response (multi-point borehole extensometers, crack-meters, dual axis inclinometers and GPS-RTK stations) and subaerial forcing (weather station,

temperature probes). According to the previous studies (Cerema, 2013) Citadel was characterised by 2 different hazard levels (high and very high level of hazard), so two different Citadel sectors (Torrione and Marché) were instrumented (figure 1). These two sectors were delimited by the known surface position of the major facture oriented N110°. At this stage, it has also to be noted that the design of this system was strongly influenced by urban-planning constraints.

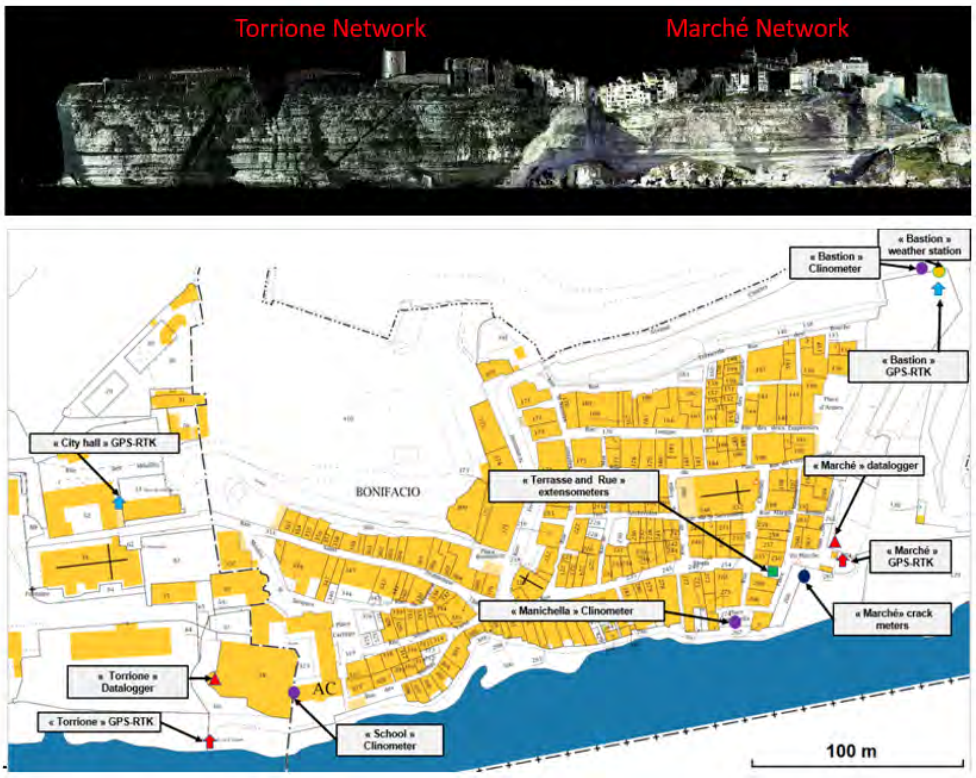

Figure 1. Location of the sensors on the cliff top and the cliff face.

Based on previous studies, it was obvious to concentrate the equipment close to the N110° fracture. The two crack-meters were therefore installed on the wall on either of the fracture and two boreholes were equipped with 4 points extensometers. One of them (Rue, figure 1) cuts this fracture at a depth of 10 m, which really enables to monitor the main fracture (N110°). Near this fracture is also installed one clinometer (Manichella, figure 1), which permits to monitor the evolution of a particular sector, marked “rock scale scenario” on figure 2 (see Vignerot et al., 2021 for details).

Each geotechnical sensor was coupled with a temperature sensor to correct the measurements from its effects. The dataset (collected from April 2019 to December 2023) shows no significant movement, but a good agreement with daily and seasonal temperature variations, in particular for the crack-meters. In fact, we noted that the opening of the fracture N110 is sensitive to meteorological situations combining a sudden drop in temperature and heavy precipitations.

All data are available in real time on the Ineris web-monitoring platform, called e.cenaris (https://cenaris.ineris.fr), with a secure access.

Description of the terrestrial LiDAR survey

In addition to the continuous instrumental observation, six topographic surveys were carried out by terrestrial LiDAR almost every year from 2018, except in 2018 when 2 acquisitions were done and in 2020 because of Covid situation.

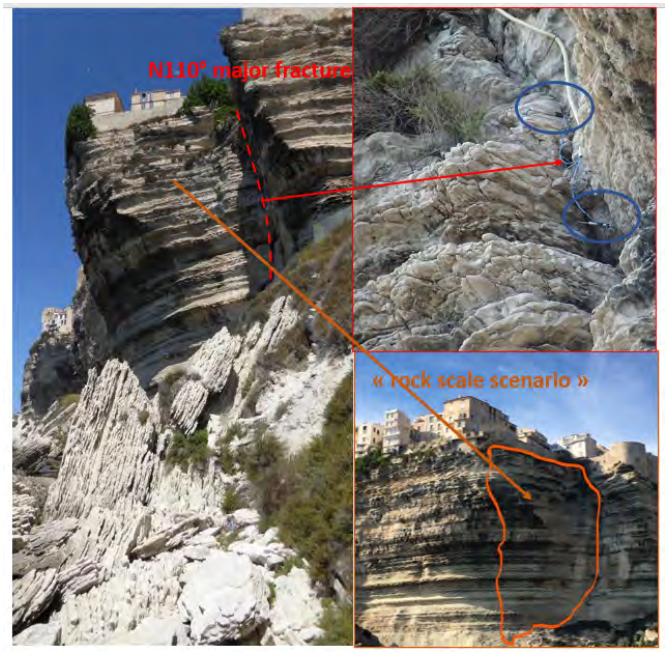

Figure 2. location of the two crack meters and “rock scale scenario”

The first survey is considered as the reference for the diachronic comparisons made to detect local deformations. These deformations are estimated in terms of the distances of common points between two clouds (reference one and another) acquired at different period. Repeated topographic surveys were carried out using short and long range scanners. Each campaign was performed according to the same acquisition protocol; it was based on 12 scanner stations positioned on the ground at a horizontal distance varying from 5 to 2000 m from the subvertical cliff face. The survey design allows to reduce occlusion and poor incident angles and enable large spatial coverage with a very high-resolution 3D data. In 2023 however, we introduced GPS control points to enable direct georeferencing and to better quantify measurement accuracy.

Figure 3. Cloud to cloud comparison (diachronic comparison 2018-2023). The main negative distances are due to coastal erosion and variations in vegetation.

The diachronic comparison between the reference survey (2018) and the last campaign in 2023 shows an accuracy of the recalibration and georeferencing between 5 and 10 cm, so displacements smaller than this cannot be validated as existing. For the Citadel sector, no instability (figure 3) was detected, including along the main N110° fracture. By displaying only

the points with a distance between -10 cm and -50 cm, some points stand out at the bottom of the cliff, that because there is mainly friable rock sensitive to sea erosion and wind. The other negative values are due to the difference in vegetation between the two periods (see red oval in the figure 3). When looking at the “Peninsula” scale, diachronic comparison (2018-2022) reveals 2 rockfalls (Campo Romanello and Trois Pointes beach) in the cliff undeveloped area (figure 4).

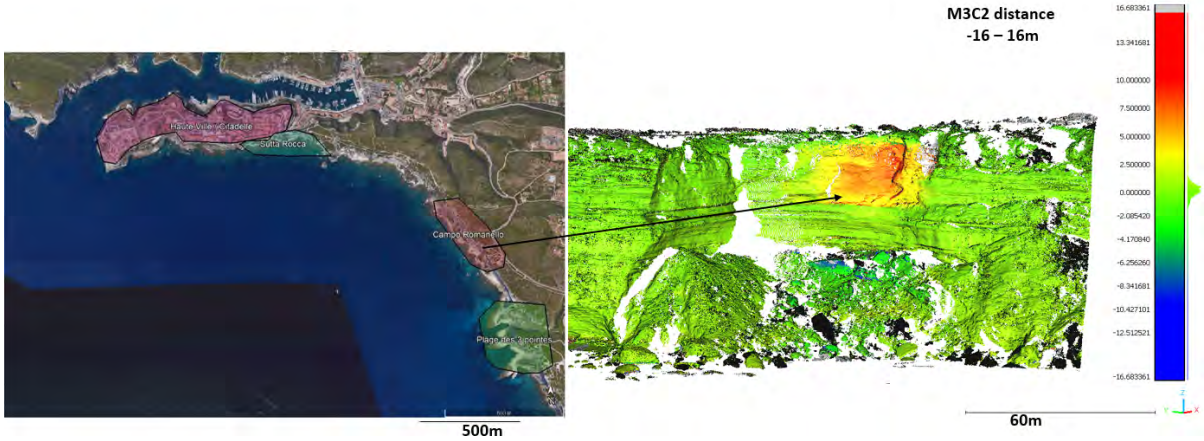

Figure 4. On the left the Campo Romanello rockfall location and on the right the diachronic comparisons 2018-2022 showing the presence of this rockfall.

Conclusion

In terms of observation techniques, these two investigations are complementary, as they provided useful information for assessing cliff evolution in the Citadelle area and on a larger scale. The multi-parameter monitoring provides in real time (sub-millimetric) very precise measurements on a very local scale. The periodic terrestrial LiDAR survey allows to study how the entire cliff is evolving with multi-centimetre precision. Both show that Citadel sector is stable. However, two rockfalls were detected by terrestrial LiDAR away from Citadel sector in a non-urbanised area.

More generally, the results of investigations have shown that a local sector affected by the "rock scale scenario" is at high risk, with a fairly brutal mechanism. It is therefore planned to extend and reinforce the multiparameter system in the vicinity of the N110° fracture.

References

Cerema (2013) Réalisation de la carte multi-aléas « mouvement de terrain » et « hydraulique » dans les secteurs à enjeux de la commune de Bonifacio. N° d’affaire 10R000046.

Balk, D., Montgomery, M.R., McGranahan, G., Kim, D., Mara, V., Todd, M., Buettner, T., Dorélien, A., 2009. Mapping urban settlements and the risks of climate change in Africa, Asia and South America. In: Population Dynamics and Climate Change, United Nations Population Fund, pp. 80–103.

IPCC, 2022. IPCC 2022: summary for policymakers. In: Climate Change 2022: Impacts, Adaptation and Vulnerability. Cambridge University Press, p. 35.

IPCC, 2021. IPCC, 2021: summary for policymakers. In: Climate Change 2021: The Physical Science Basis. Working Group I Contribution of Working Group I to the Sixth Assessment Report of the Intergovernmental Panel on Climate Change, p. 31.

Letortu P., Le Dantec N., Augereau E., Costa S., Maquaire O., et al., 2022. Experimental field study on the fatigue and failure mechanisms of coastal chalk cliffs: Implementation of a multi-parameter monitoring system (Sainte-Marguerite-sur-Mer, France). Geomorphology, 2022, 408, pp.108211. ⟨10.1016/j.geomorph.2022.108211⟩.

B. Vignerot, C. Franck, M. Malascrabes (2021) – Bloc 4 : Evaluation de l’aléa et proposition de mesures de gestion du risque - Secteur de la citadelle, falaise de Bonifacio, 79 p., 51 fig., 1 ann. Rapport Cerema ASA20_068 Ineris-175501-2397775 BRGM/RP-70230-FR

Regional scale identification and intensity-based ranking of landslide candidates based on A-DInSAR analysis for risk management purposes

Benedetta Antonielli[1], Gian Marco Marmoni[1], Patrizia Caprari[1], Maria Elena Di Renzo[1], Roberta Marini[2], Paolo Mazzanti[1,2], Francesca Bozzano[1]

[1] Earth Sciences Department of "Sapienza" University of Rome and CERI - Research Centre for Geological Risks, P.le Aldo Moro n.5, 00185 Rome, Italy
[2] NHAZCA S.R.L., Startup Company of "Sapienza" University of Rome, Via Vittorio Bachelet n.12, 00185 Rome, Italy

SUMMARY: European Ground Motion Service (EGMS) provide high-resolution ground motion maps of the European continent, providing large volumes of information, consisting of time series of displacement and related velocity maps, that generally cannot be quickly or easily analysed for studies that involve large areas. A semi-automatic identification of clusters of active deformation zones and their subsequent ranking has been developed. The proposed method consists of three main modules: (1) selection of landslide candidates, aimed at the detection of the Areas Of Interest (AOIs) basing on measurement points distribution resulting from Advanced Differential Interferometric Synthetic Aperture Radar (A-DInSAR) analysis; (2) ranking of the level of hazard and risk posed by each landslide candidate; (3) in-situ validation of the effectiveness of the methodology. The results of the presented methodology can properly guide the update of the landslide catalogues at the regional scale, both in terms of mapping of the landslide bodies and as regards the state of activity. The possibility to update the results of this procedure, based on the new release of EGMS products every year, represents an interesting opportunity for authorities that manage the landslide risk at regional scale.

Keywords: Mapping, Regional scale, Semi-Automatic selection; landslides; A-DInSAR.

Introduction

One of the main advantages of satellite SAR interferometry is the capability to investigate large areas and monitor the territory at regional scale (Thomas and Li., 2017; Raspini et al., 2018). Sentinel-1 data are today implemented in the Copernicus European Ground Motion Service (EGMS) into high-resolution ground motion maps of the European continent. These products were achieved by Advanced Differential SAR Interferometry (A-DInSAR) techniques, which exploited large data stacks of images to reconstruct the time series of displacement of the measurement points. The results are made publicly available and annually updated, representing the largest project of interferometric applications in the world (Costantini et al., 2021).
However, the outputs consist of a map of displacement at regional scale over millions of points, for each of which a displacement time series is obtained, providing large volumes of information that generally cannot be quickly or easily analyzed (Barra et al., 2017). This work aims to semi-automatically extract information from massive data over large areas that could be effectively used by stakeholders and professionals. The object of the study concerns mapping active landslides at the regional scale and retrieving the intensity of the process and the level of hazard. In recent years, several studies have gone in this direction, trying to automate part of the post-processing analysis process of interferometric data. Some procedures have been developed to automatically or semi-automatically identify, from A-DInSAR maps, deforming areas (Barra et al., 2017; Meisina et al., 2008; Bianchini et al., 2012), different kind of ground

instabilities (Zhao et al., 2012; Raspini et al., 2018; Solari et al., 2018), or infrastructure settlement or tilt (Herrera et al., 2013).
In this work, we develop a semi-automatic procedure for identifying landslide candidates and ranking in terms of their intensity (area and velocity), as a proxy of hazard in a test area located in the Lazio Region (Italy). In-situ geomorphological survey has been conducted to validate landslide identification and validate the effectiveness of the whole methodology. The presented approach has been implemented and supported in the frame of an institutional agreement between the Geological and Seismic Service of Lazio Region (Italy) and the Research Centre on Prediction, Prevention, and Mitigation of Geological Risks (CERI), focused on the monitoring of ground deformation process in the administrative territory through satellite interferometry. This study has proved to be effective in implementing an operational service suitable for landslide risk mitigation at the regional scale and supporting the land management authorities on the updating of landslide catalogues.

Materials and Methods

In this study, we used EGMS basic products that are spatially referred to a virtual reference point, which time series are derived through statistical analysis. Uncorrected Basic products have been selected to exclude the large-scale tectonic deformation that has been considered in the Calibrated products (harmonized on a continental scale by the use of GNSS data), in order to pinpoint local phenomena within the extensive study area, and to properly investigate areas undergoing deformation on slopes.
The method proposed here starts from the extraction of mean ground movement and articulates in subsequent steps: (i) spatialization of the punctual PS data; (ii) automatic identification of velocity anomalies; (iii) automatic spatial clustering and perimeter delimitation of active deformation areas (namely AOIs); (iv) semi-automatic ranking of the deformation intensity for every AOIs; (v) integration of the results obtained for ascending and descending orbital geometry into a unique ranking, iv) spatial overlay analysis with existing landslides catalogues, (v) validation procedure on a selected subset of AOIs, by in situ survey and local scale analysis and characterization of the detected ground deformation processes. This flow chart is represented in Figure 1.

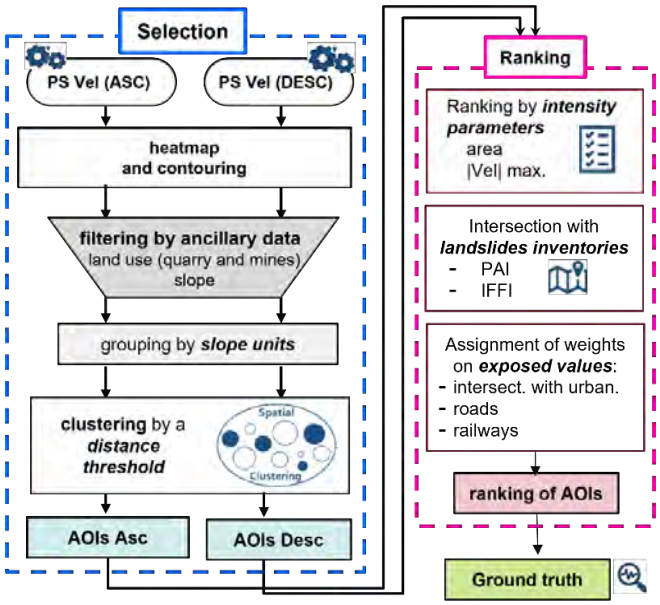

Figure 1. Conceptual flow chart of the developed method

The implemented methodology consists of algorithms for the semiautomatic detection and ranking of areas characterized by velocity anomalies. These steps lay on ancillary input datasets, like DEM and DEM-derived products, land use map and in particular the location of quarries, mines, landfills, basin scale and national landslide inventories, road and railway layers.
A post-processing product of the mean velocity maps, the so-called *heatmaps,* has been used to retrieves the landslide candidates (both in ascending and descending geometries) and to areally analyse the punctual A-DInSAR original data, by using an interpolation process, that involves thresholds and neighbourhood parameters iteratively selected. The velocity anomalies were identified with a threshold of ±2 mm/yr and were selected under the following conditions: location with average slope >5°, no intersection with quarry, mine, or landfill areas. Then the velocity anomalies located at a maximum distance of 200 m from each other have been clustered to form a single AOI.
The next step of the process, that is the semiautomatic ranking of the AOIs, consisted in order the AOIs according to a multi-level numerical code, representing the intensity of the process (hazard-oriented classification) and the potential risk, due to interaction of the deformation phenomenon with anthropic elements or infrastructures.
The validation phase concerned (i) a supervised check of the top-ranked areas of interest, guided by expert judgment and (ii) field surveys on a subset of 32 AOIs selected in the pilot area of Frosinone province, that consisted of a geomorphological analysis and the building damage inspection.

Results and validation

The result of the adopted procedure and aggregation of province subsets, led to the identification of the AOIs for the Provinces of Frosinone, Viterbo, Latina, and Rieti, for both ascending and descending dataset (number reported in Tab.1), excluding the area most affected by seismic deformation during the 2016-2017 seismic sequence.
For each AOIs, any overlap with the landslides inventoried in the Italian Landslide Inventory (IFFI) and in the basin authority (PAI) catalogues was verified and analysed.

Table 1. Number of AOIs retrieved for each analysed province.

Province of Lazio region	N° of AOIs			
	Ascending	Descending	Both geometries	Total
Frosinone	641	704	56	1289
Rieti	274	282	59	497
Viterbo	352	385	20	717
Latina	313	199	14	498

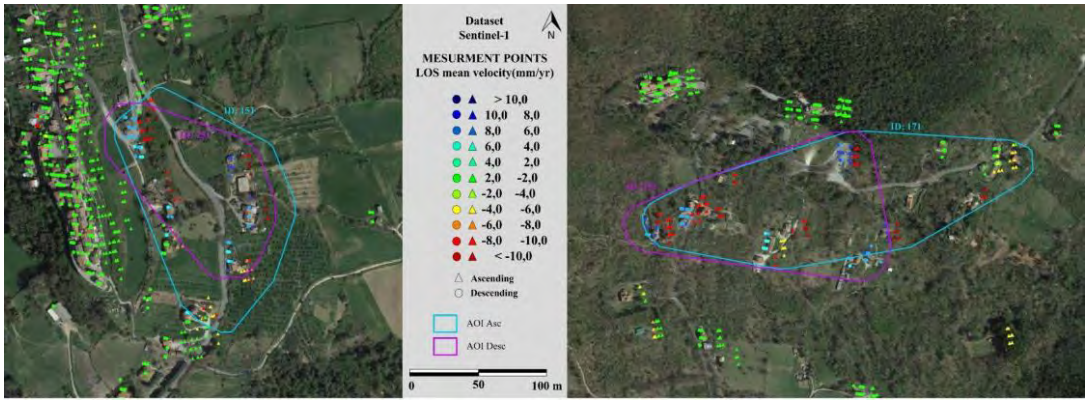

Figure 2. Example of AOIs in the municipalities of Greccio and Configni, Rieti province, obtained with the proposed method.

During the semi-automatic ranking of the deformation intensity, each AOI has been listed in order of danger and risk, using the multi-level code.
A subset of 32 AOIs selected in the province of Frosinone was used for the validation phase through field surveys. The results of the validation phase demonstrate that the procedure is effective to identify landslides: the 98% of the AOIs selected for the validation show geomorphological evidence of landslide; the 59% show damage to buildings and infrastructures related to landslides, and the 56% may require an update of landslide inventories, as the areas identified by the AOIs are not included (or only partially) in the catalogues.

Conclusion

The presented semi-automatic methodology drives the implementation of a database of active landslide candidates at regional scale, for which a score of hazard and risk is provided.
This tool proved to be reliable and effective for identification of slow-moving landslide mechanism. Thanks to the extensive in-situ validation process, carried out through geomorphological survey and building damage inspection on a selected subset of AOIs, the identification and ranking procedure results accurate. The method can be used to propose a list of areas affected by active landslides, whose update can suitably support the systematic updates of process inventories both in terms of mapping of the landslide bodies and as regards the state of activity. This update will also benefit of the availability of newly released EGMS products year by year, orienting mitigation strategies carried out by local municipal and regional controlling authorities.

Acknowledgments

This study was carried out within the Spoke VS2 Ground Instabilities of the RETURN Extended Partnership and received funding from the European Union Next-Generation EU (National Recovery and Resilience Plan – NRRP, Mission 4, Component 2, Investment 1.3 – D.D. 1243 2/8/2022, PE0000005).

References

Barra A, Solari L, Béjar-Pizarro M, Monserrat O, Bianchini S, Herrera G, Crosetto M, Sarro R, González-Alonso E, Mateos R, et al. (2017) A Methodology to Detect and Update Active Deformation Areas Based on Sentinel-1 SAR Images. *Remote Sens*., 9, 1002.

Bianchini S, Cigna F, Righini G, Proietti C, Casagli N Landslide HotSpot Mapping by means of Persistent Scatterer Interferometry (2012) *Environ Earth Sci.* 67 1155–1172.

Calò F, Ardizzone F, Castaldo R, Lollino P, Tizzani P, Guzzetti F, Lanari R, Angeli M-G, Pontoni F, Manunta M (2014) Enhanced landslide investigations through advanced DInSAR techniques: The Ivancich case study Assisi Italy. *Remote Sens Environ* 142, 69–82.

Costantini M, Minati F, Trillo F, Ferretti A, Novali F, Passera E, & Andersen HS, (2021 July) European ground motion service (EGMS) *In 2021 IEEE International Geoscience and Remote Sensing Symposium IGARSS* (pp 3293-3296) IEEE.

Herrera G, Gutiérrez F, García-Davalillo JC, Guerrero J, Notti D, Galve JP, Fernández-Merodo JA, Cooksley G (2013) Multi-sensor advanced DInSAR monitoring of very slow landslides: The Tena Valley case study (Central Spanish Pyrenees) *Remote Sens. Environ.* 128, 31–43.

Meisina C, Zucca F, Notti D, Colombo A, Cucchi A, Savio G, Giannico C, Bianchi M (2008) Geological Interpretation of PSInSAR Data at Regional Scale. *Sensors* 8, 7469–7492.

Raspini F, Bianchini S, Ciampalini A, Del Soldato M, Solari L, Novali F, Del Conte S, Rucci A, Ferretti A, Casagli N (2018) Continuous semi-automatic monitoring of ground deformation using Sentinel-1 satellites *Sci. Rep.* 8, 7253.

Solari L, Barra A, Herrera G, Bianchini S, Monserrat O, Béjar-Pizarro M, Crosetto M, Sarro R, Moretti S (2018) Fast detection of ground motions on vulnerable elements using Sentinel-1 InSAR data *Geomat Nat Hazards Risk* 9, 152–174.

Tomás R, Li Z Earth Observations for Geohazards: Present and Future Challenges (2017) *Remote Sens.* 9194.
Zhao C, Lu Z, Zhang Q, de la Fuente J Large-area landslide detection and monitoring with ALOS/PALSAR imagery data over Northern California and Southern Oregon USA (2012) *Remote Sens Environ* 124, pp 348–359.

Possible strategy for landslide prediction

Manchao He, Shulin Ren, Zhigang Tao

State Key Laboratory for Tunnel Engineering, China University of Mining and Technology (Beijing), China

SUMMARY: With the expansion of the scope of human activities and the increasing demand for resources, the frequency of landslides is becoming higher and higher, resulting in huge casualties and economic losses. Therefore, the research of precise monitoring and timely prediction technology of landslide is urgent. In this paper, a new monitoring and prediction method based on the academic idea of "the sufficient and necessary condition for landslide occurring is the change of Newton force" has been proposed. First, the Newton force change law of rock mechanics was proposed for the first time in the field of rock mechanics, and a double-block mechanics model based on Newton force change measurement was constructed, and a complete set of landslide Newton force measurement theory was formed. Then the monitoring and prediction system and the NPR anchor cable suitable for landslide monitoring with high constant resistance and large deformation were independently developed. The warning mode and warning level of landslide with Newton force was proposed and an integrated landslide control technology was formed. Finally, the system was implemented in 723 monitoring points in 26 demonstration areas in China. All 14 landslide disasters within the scope of the deployment were successfully predicted, more than 100 lives and hundreds of millions of equipment and property was saved. At present, based on the similarity of landslide and earthquake in the double-block disaster mechanical model, the research work of cross-fault Newton force measurement for earthquake prediction is also being carried out.

Keywords: Landslide, monitoring and prediction, Newton force measurement, NPR anchor cable

The law of Newton force in rock mechanics

In 1687, Newton's three laws of motion were summarized and put forward by Newton. Among them, Newton's second law describes that if an object with a mass of m wants to move and obtain acceleration a, it must be subjected to a force, which is the resultant force (Newton force), which satisfies the necessary and sufficient conditions for the movement of the object. According to the indoor Newton force monitoring and warning physical model experiment of landslide, the change curve of Newton force was obtained (Figure 1). From the formation to the occurrence of landslide disaster, the Newton force changes through three stages, which are the gradual deformation stage, the sudden drop stage and the destruction movement stage. The gradual deformation stage refers to the process of accumulation of deformation before the failure of the geological rock mass. This process follows Hooke's law without major deformation catastrophe. The destruction movement stage refers to the movement of geological rock mass and the catastrophe has already occurred. This stage follows Newton's law of motion. The sudden drop stage that connects Hooke's law and Newton's law is the essence and core of landslide catastrophe. However, due to the non-linear large deformation of rock mechanics from the deformation stage to the movement stage, and the lack of corresponding mechanical theory explanation basis, it is difficult to realize the accurate warning of landslide geological disasters. Based on this problem, the Newton force change law of rock mechanics was proposed, and the bridge of geological rock mass from Hooke's law to Newton's law was established. In essence,

the three major problems from the deformation stage to the movement stage are solved, which are the time of Newton force generation, the precursor of catastrophe, and the time of catastrophe.

The first law: Newton force generation

$$a \neq 0, t = 0^{-} \tag{1}$$

The second law: Catastrophic precursory

$$F = F_0 - \Delta F, t = 0 \tag{2}$$

The third law: Catastrophe time

$$t = \sqrt{2mu/F}, t > 0^{+} \tag{3}$$

Where a is the acceleration / ms^{-2}, t is the time / s, F is the Newtonian force / kN, ΔF is the Newton force increment / kN, m is the mass of the moving object / kg, u is the catastrophic displacement /m.

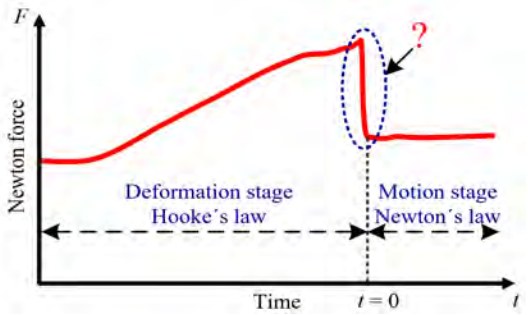

Figure 1. Diagram of Newton force change law of landslide

NPR anchor cable

In 2009, a constant resistance and large deformation anchor cable with negative Poisson's ratio effect was successfully developed, namely NPR anchor cable. The anchor cable is mainly composed of a constant resistance sleeve, a constant resistance body, a steel strand and other structures, and has extraordinary mechanical properties such as high constant resistance, large deformation, energy absorption, and impact resistance. During the large deformation of the rock mass, the constant resistance body slips in the constant resistance sleeve. Since the diameter of the large end of the constant resistance body is slightly larger than the inner diameter of the sleeve, the casing expands radially while being stretched, resulting in NPR effect. This is the reason why the NPR cable has an extraordinary deformability. According to the actual field application, two NPR models of anchor cables have been developed: NPR 350 and NPR 850. The constant resistance of the NPR 350 anchor cable is 350 kN, and the maximum deformation is 1000 mm. The NPR 850 anchor cable has a constant resistance of 850 kN and a maximum deformation of 2000 mm.

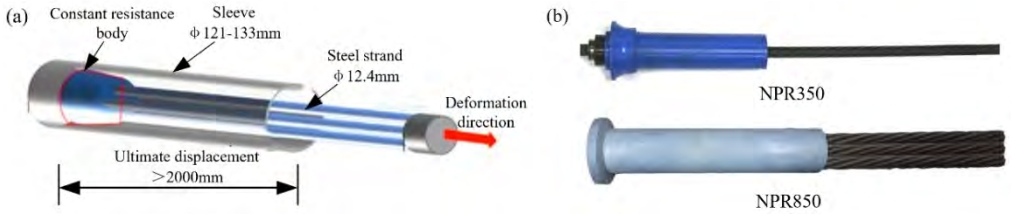

Figure 2. Structure and classification of NPR anchor cable

Newton force remote monitoring and early warning system

The real-time measurement of Newton force on the potential sliding surface of a landslide is directly related to the timeliness of the advance monitoring and warning of landslide disasters.

In addition, landslide is a complex mechanical system, and the Newton force monitoring data that meets the necessary and sufficient conditions for its catastrophic occurrence are very large, and manual calculations will be very cumbersome and time-ineffective. Based on the actual needs of the monitoring and early warning system, combined with modern communication and computer technology, a set of remote real-time monitoring and early warning equipment systems for landslide Newton force and big data analysis technology have been developed to improve the intelligence, information and networking of landslide monitoring and early warning level. The system consists of a data acquisition subsystem, a data transmission subsystem, a data processing subsystem and a data publishing subsystem.

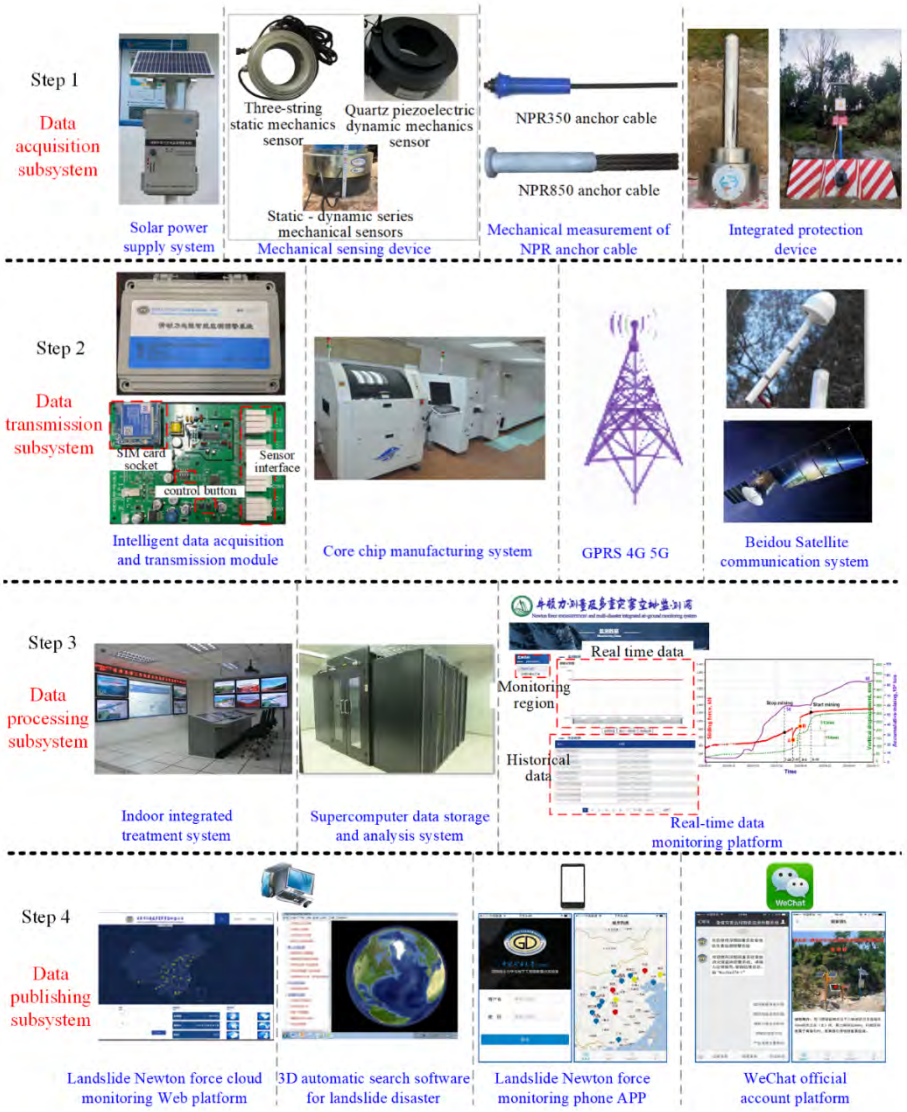

Figure 3. Remote monitoring and forecasting system structure composition

Summary of successful cases

As of April 2024, the Newton force remote monitoring and early warning system for landslide geological disasters has been promoted and used at 723 monitoring points in 26 demonstration areas in China. And the Newton force remote monitoring and early warning system for landslide geological disasters has successfully predicted 14 landslide disasters, with a 100% critical-sliding warning success rate. More than a hundred lives and hundreds of millions of equipment and property have been saved, and huge social and economic benefits have been achieved.

Figure 4 shows the information of successful critical-sliding warning cases and curves, which effectively verifies the scientific law of " Sudden drop in Newton force indicates a landslide will occur". The critical-sliding warning time of a landslide is within 3.5-20 hours and the warning time is positively correlated with the scale of the landslide.

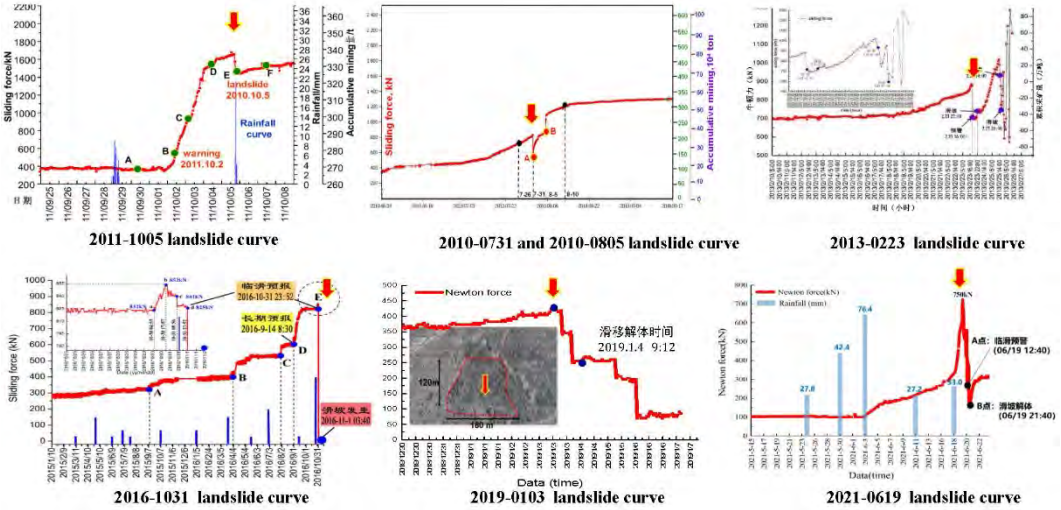

Figure 4. Newton force monitoring curves of successful cases

Conclusions

(1) The law of Newton force in rock mechanics is proposed, which essentially solves the problems of Newton force generation time, catastrophe precursor and catastrophe time during the transition from Hooke's deformation law to Newton's motion law.

(2) The thought of "the necessary and sufficient condition for the occurrence of landslides is the change of Newton force, which is the main parameter of landslide monitoring and early warning". Through the on-site Newton force monitoring curve, the scientific phenomenon is proved: "sudden drop in Newton force indicates that a landslide will occur".

(3) The NPR anchor cable suitable for landslide monitoring and the Newton force remote monitoring and early warning system for landslide geological disasters have been developed. Newton force warning model and warning criterion is proposed, and the goal of integrating ground disaster monitoring-early warning-control is achieved.

(4) As of April 2024, the Newton force remote monitoring and early warning system for landslide disasters has been promoted and used at 723 monitoring points in China. The 14 landslides within the scope of the deployment were all successfully warned 3.5-20 hours in advance, successfully solving the scientific problem of short-term landslide prediction.

References

He MC, Gong WL, Wang J, et al. (2014) Development of a novel energy-absorbing bolt with extraordinarily large elongation and constant resistance. *International Journal of Rock Mechanics & Mining Sciences*. 67: 29-42.

He MC (2016) Real-time remote monitoring and forecasting system for geological disasters of landslides and its engineering application[J]. *Chinese Journal of Rock Mechanics and Engineering*. 28(6): 1081–1090.

He MC (2016) Research on the double-block mechanics based on Newton force measurement. *Chinese Journal of Rock Mechanics and Engineering*. 35(011): 2161-2173.

Tao ZG, Li HP, Sun GL, et al. (2015) Development of monitoring and early warning system for landslides based on constant resistance and large deformation anchor cable and its application. *Rock and Soil Mechanics*. 36(10): 3032–3040.

Applying Induced Polarization to Characterize Landslides
XIVth ISL, Chambéry 2024

C. Casotti[1], A. Revil[2], T. Houtteville[3], G. Martin[3]

[1] Univ. Savoie Mont-Blanc – GINGER CEBTP, EDYTEM, 73370 Le Bourget du Lac, France
[2] Univ. Savoie Mont-Blanc, CNRS, UMR CNRS 5204, EDYTEM, 73370 Le Bourget du Lac, France
[3] GINGER-CEBTP, 38330 Montbonnot, France

Abstract

The development of clay-rich landslides is closely related to the change of their water content. Determining the hydraulic properties of a landslide makes it possible to better understand its dynamic rheological behavior. Induced polarization is a geophysical method that can be used to map water content, clay content and permeability. The Harmalière landslide in the Triève region (Isère, France) offer a natural laboratory to test the usefulness of induced polarization to gain a better understanding of such landslides. A field survey was undertaken conducted to acquire data along 2D profiles with an inter-electrode spacing of 20 meters, distributed across the entire landslide area. A 3D electrical conductivity and normalized chargeability distributions are determined and converted into 3D tomograms of the water content, clay content and permeability using a petrophysical model and clustering techniques. Induced polarization measurements enable to gain a better understanding of the landslide dynamics, as it let possible to know its structure and internal properties, as well as how it fits into the local geology.

Keywords: Induced polarization, Electrical tomography, Water content, Clay content, Landslide

Introduction:

The Harmalière landslide is located 30 km south of Grenoble, in the vast Triève depression. With a total length of 1450 m, and a vertical difference of 450 m, this landslide ends in the Monteynard artificial lake fed by the Drac river. Around 40,000 years ago, this river was blocked at Harmalière by the tongue of the Isère glacier, forming a periglacial lake where layers of lacustrine clay up to 200 m thick were deposited. Following the glacial retreat, the Drac was able to flow again, carving its bed in lacustrine clay and Toarcian marl-limestone bedrock.

The landslide is now embedded in this clay horizon, with rotational movements at the head, creating scarps up to 15 m high. Further downstream, the landslide transitions to mudflow behavior, with convex lobes and a smoother topography down to the lake. The study of the entire landslide and its surroundings represents a major challenge, given the exceptional size of this landslide.

Geophysical methods are particularly well-suited to this type of study, as they can be applied over large areas at high depths of investigation (200 m in the present case). The electrical resistivity tomography (ERT) method is being increasingly extended to include induced polarization measurements (Revil et al., 2020; Flores Orozco et al., 2022; Carrier et al., 2023). By measuring the ability of rocks to conduct an electrical current and the ability of porous materials to store reversibly electrical charges in an applied electrical field, it is possible to use

recently developed petro-physical models (Revil et al., 2017a, 2017c, 2017b; Soueid Ahmed et al., 2020) to quantitatively estimate crucial parameters such as soil water content, clay content and permeability .

Here, we have carried out a series of 2D Time Domain Induced Polarization (TDIP) acquisitions on the Harmalière landslide. This approach allows us to map its structural properties in 3D.

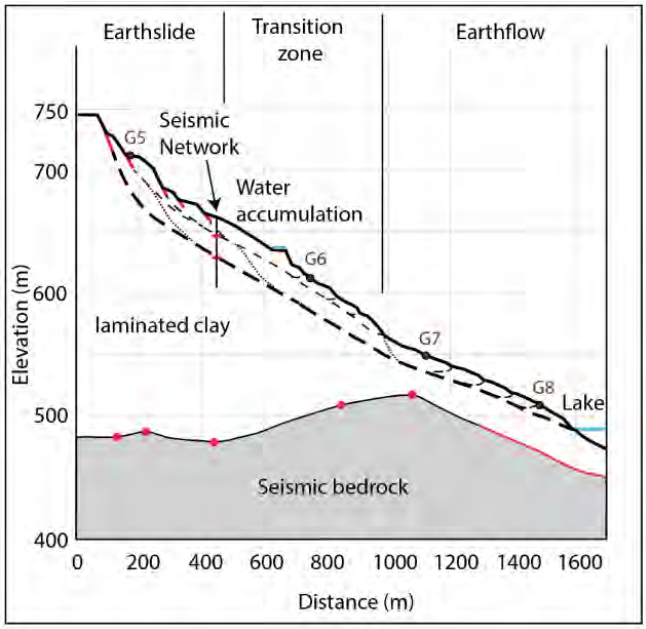

Figure. 1 From (Fiolleau, 2020).Interpretative cross-section of the Harmalière landslide from the topography extracted from the LIDAR DEM acquired in November 2019. Red dots: bedrock roof from H/V measurements refined from (Bièvre et al., 2011) results. Red part of the bedrock correspond to the 1950 topography. Red bars: constraints on the scarps and shear surface deduced from the seismic network. The shallow and deep slip surfaces are represented by fine and bold dotted lines, respectively. The connections between the two slip surfaces are schematic (dotted line).

Methods

TDIP acquisitions consist of injecting square wave current, often set at 1Hz, into the ground using two current electrodes A and B and measuring the electrical potential induced during and after the injection. The apparent chargeability data, which represents the phenomenon of ground polarization, depends on the temporal decrease in potential after the injection has stopped.

In the context of landslides, chargeability data alone may not provide significant insights. Its value becomes apparent when integrated with electrical conductivity to calculate normalized chargeability. Petro-physical models based on stern layer model enable the prediction of water content, cation exchange capacity (a proxy for clay content), and permeability from normalized chargeability data (Revil et al., 2020).

Height induced polarization profiles were carried out in the field with a length between 1260 m and 2860 m (see Fig. 2). The location of the 480 electrodes was measured using a dGPS. The DEM from the LIDAR survey, accurate to 1m, was used to set the topography of the electrodes and for the 3D inversion. For now, we collected 7775 TDIP measurements with an ABEM SAS400 and an ABEM LS2 by using Wenner-α and multigradient protocol.

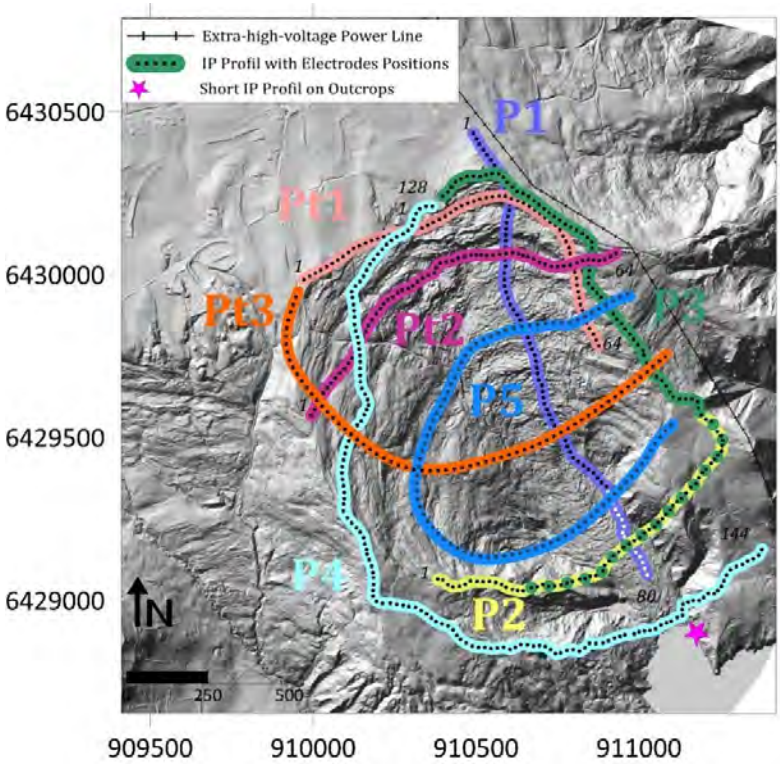

Figure.2 TDIP profiles superimposed on DEM Hillshade from ONF RTM

Results

In previous research on a shallow landslide (Revil et al., 2020), it has been shown that petrophysical models based on the stern layer model provide consistent results and make it possible to couple electrical data with water content, cation exchange capacity (CEC), and permeability. These findings were used to create tomograms that revealed a high-permeability channel within the study site, which probably played a role in triggering the landslide.

First results from Harmalière landslide reveal the ability of TDIP to distinguish the overall geology of the landslide, differentiating between clay-rich layers, the underlying Toarcian substrate, and the Drac alluvial deposits. The use of chargeability data, although complicated by noise introduced by high-tension lines, prompted us to employ full waveform acquisitions to mitigate the influence of the 50 Hz fundamental signal and its harmonics. Nonetheless, the results are already demonstrating the potential of chargeability in highlighting clay-rich horizons and likely offering enhanced the complicated differentiation between the Toarcian substrate and clay layers due to their similar conductivity characteristics.

Conclusion

By using a petrophysical model to interpret the conductivity and normalized chargeability as key parameters distribution like water content, clay content and permeability, TDIP method shows a significant potential in characterizing clay-rich landslides and unraveling their geological complexities. This valuable insight is promising as it can be coupled with point geotechnical surveys, by correlating the hydro-mechanical parameters obtained from the TDIP method with the results of pressuremeter tests or borehole permeability tests.

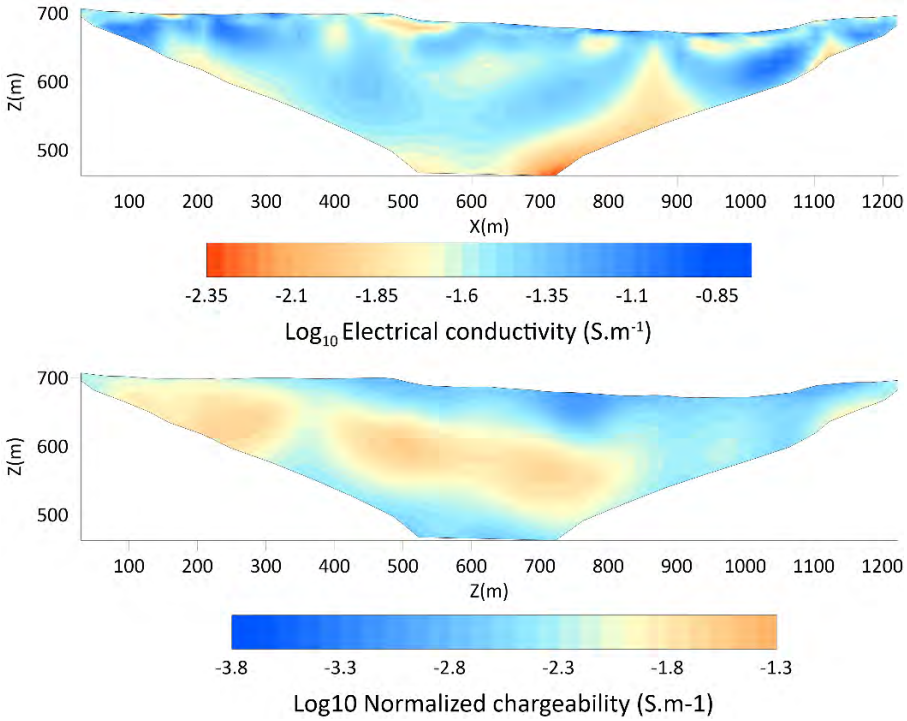

Figure. 3 TDIP tomogram from Pt2 profile a. Electrical resistivity distribution show mainly two structures. A shallow conductive material corresponding to clays (above 10-60 Ω.m) and a more resistive layer located beneath the clayey formation, which corresponds to the Toarcian geological formation, b. The normalized chargeability tomography clearly shows a particularly chargeable clay horizon (above 10^{-2} S/m). The formation below this horizon is probably the Toarcian.

Reference

Bièvre, G., U. Kniess, D. Jongmans, E. Pathier, S. Schwartz, T. Villemin, C. van Westen, and V. Zumbo, 2011, Paleotopographic control of landslides in lacustrine deposits (Trièves plateau, French western Alps): Geomorphology, **125**, 214.

Carrier, A., O. Meric, and P. Bottelin, 2023, Characterizing landslide dynamics from time-lapse time domain induced polarization and ground-based imaging: a case study of the MontGombert landslide (French, Alps): Landslides.

Fiolleau, S., 2020, Etude des mécanismes de déformation d'un glissement-coulée par une approche multi-méthodes.phdthesis, Université Grenoble Alpes [2020-....]p.

Flores Orozco, A., M. Steiner, T. Katona, N. Roser, C. Moser, M. J. Stumvoll, and T. Glade, 2022, Application of induced polarization imaging across different scales to understand surface and groundwater flow at the Hofermuehle landslide: CATENA, **219**, 106612.

Revil, A., M. Le Breton, Q. Niu, E. Wallin, E. Haskins, and D. M. Thomas, 2017a, Induced polarization of volcanic rocks – 1. Surface versus quadrature conductivity: Geophysical Journal International, **208**, 826–844.

Revil, A., M. L. Breton, Q. Niu, E. Wallin, E. Haskins, and D. M. Thomas, 2017b, Induced polarization of volcanic rocks. 2. Influence of pore size and permeability: Geophysical Journal International, **208**, 814–825.

Revil, A., A. Soueid Ahmed, A. Coperey, L. Ravanel, R. Sharma, and N. Panwar, 2020, Induced polarization as a tool to characterize shallow landslides: Journal of Hydrology, **589**, 125369.

Revil, A., A. Coperey, Z. Shao, N. Florsch, I. L. Fabricius, Y. Deng, J. R. Delsman, P. S. Pauw, M. Karaoulis, P. G. B. De Louw, E. S. Van Baaren, W. Dabekaussen, A. Menkovic, and J. L. Gunnink, 2017c, Complex conductivity of soils: Water Resources Research, **53**, 7121–7147.

Soueid Ahmed, A., A. Revil, F. Abdulsamad, B. Steck, C. Vergniault, and V. Guihard, 2020, Induced polarization as a tool to non-intrusively characterize embankment hydraulic properties: Engineering Geology, **271**, 105604.

Passive seismic characterization and monitoring of La Praz unstable slope until failure (Savoie, France)

P. Bottelin[1,2]; O. Méric[1,2]; L. Baillet[3]; D. Beniamine[4]; A. Lescurier[5]

[1] SAGE Ingénierie, Gières, France
[2] ADRGT, Gières, France
[3] Centre National de la Recherche Scientifique (CNRS), Institut des Sciences de la Terre (ISterre), Université Grenoble Alpes, 38000 Grenoble, France.
[4] Tétras Libre, 8 rue Mayencin, 38410 Saint Martin d'Hères, France.
[5] Conseil Départemental de la Savoie, Service Risques Naturels,

SUMMARY: We applied passive seismic technique in order to characterize and monitor La Praz unstable rock slope (Savoie, France) prior to August 2023 collapse. We first used Horizontal to Vertical Spectral Ratio (HVSR) to map the rockfall hazard. HVSR amplitude at fundamental resonance frequency (f_0) agreed very well with i) geological and geotechnical observations, ii) surface displacement rates and iii) the actual august 2023 collapse sequence. Significant and permanent drop in slope's fundamental resonance frequency f_0 was detected. It shows progressive reduction in bulk slope stiffness under the action of damaging processes. To our knowledge, this is only the second, worldwide, passive seismic case study conducted until rock slope failure.

Topics: Survey techniques; Case studies

Keywords: Passive seismic; Ambient vibrations; Natural frequency; Structural Health Monitoring; Rockfall;

Introduction

Degraded, fractured unstable rock slopes are frequent in mountainous areas. Determining the unstable volume, monitoring its destabilization and establishing failure scenarii is often challenging for risk mitigation authorities (Jaboyedoff et al., 2019). Ambient vibration technique has proved its ability to detect and to delineate rock instabilities (Häusler et al., 2019, 2018). However, only few passive seismic studies revealed clear mechanical changes affecting natural structures. To our knowledge, one single case study recorded ambient vibrations until rock failure (Lévy et al., 2010). A 30 % drop in fundamental resonance frequency (f_0) was detected a few weeks before the collapse of a 21,000 m^3 limestone rock column in the Vercors massif (France). In a reverse way, another case study reported up to +17 % increase in f_0 during the bolting of a 760 m^3 limestone column (Vercors massif, France) (Bottelin et al., 2017). Both cases studies dealt with monolithic limestone rock columns. The efficiency of ambient vibration surveys and monitoring in degraded, fractured unstable rock slopes remains to be proved.
In this work, we present a passive seismic study conducted on La Praz unstable slope (Savoie, French Alps). We first used ambient vibrations to map the amplitude of the f_0 peak across the site. Then, we tracked the changes in f_0 peak frequency until the slope collapse.

Methodology

Surface displacements of the unstable slope were monitored since 2006 with a set of extensometers, a Leica total station and successive GNSS campaigns. Passive seismic

measurements were carried out during successive surveys spanning between 2011 and 2023. Single-station, Horizontal to Vertical Spectral Ratios (HVSR) were acquired during 20 min at each location. 30 s long windows were smoothed with a b=90 Konno-Ohmachi filter. Air temperature and rainfall were recorded on a nearby weather station.

Site activity

La Praz unstable rock slope consists in about 15,000 m^3 of highly fractured and degraded sandstone and shale alternance (Figure 1). This unstable volume hangs ~250 m in elevation above the SNCF railway, the RD1006 road, the Arc river and then the A43 motorway. Surface displacements measured since 2006 (not shown here) showed seasonal trends, with an acceleration at the end of each winter and a slow down every summer. During late winter and spring 2023, slope displacement rate became sensitive to rainfall events. After a dry and warm month, a significant rainfall event occurred in late august 2023. A major ~10,000 m^3 rockfall occurred on the 2023-08-27: compartments cB-cB' collapsed first, then followed by cC. The RD1006 and the SNCF railway remain closed at the date of writing, while the A43 motorway reopened 2 weeks after the rockfall thanks to additional risk mitigation measures.

Results

We observe that Horizontal to Vertical Spectral Ratio (HVSR) amplitude is greater on the most unstable compartments cB' and cC, which also show the highest displacement rates (colored arrows, Figure 1). HVSR amplitude at peak ranges between 20 and more than 100 for these compartments. The southern and western areas within the unstable slope show smaller HVSR peak amplitudes, scaling generally between 3 to 10. They also exhibit smaller displacements rates. We observe HVSR in the range 10-40 immediately at south of compartment cC, suggesting strong rock weakening in this area. In contrast, no peak in HVSR is detected on nearby stable rock mass.

Figure 2 shows the changes in HVSR curves over time, for cB' and cC most unstable rock compartments. The curve color scales with time, since 2011 until 2023. The last survey before slope collapse was conducted in July 2023 and is shown in red. 2011-2021 surveys show comparable HVSR curves with clear and repeatable peak centered around 6.0 Hz, which is the fundamental resonance frequency of the site (Bottelin et al., 2013). In contrast, July 2023 survey shows a clear drop in resonance frequency f_0 of about -20 % and -15 % for cB' and cC, respectively. We believe that this drop in f_0 is related to rock damaging processes prior to failure. Interestingly, this remarkable drop in f_0 is spotted about 1 month prior to the 2023-08-27 slope collapse. In contrast, topographic measurements at the same date (i.e. July 2023) only showed a rapid but steady trend in surface displacement. The major, final slope acceleration was only spotted one day before the slope collapse, i.e; during the significant 2023-08-27 rainfall event.

Figure 1 (next page). Aerial view of the site (background). The main rear crack (MRC) separating the unstable slope (at north) and nearby stable slope (at south) is shown with thick black dashed line. Cracks withing the unstable rock mass are shown with thin black dashed lines. The two most unstable rock compartments cB' and cC are shaded with red. Mean annual surface displacement (in mm/year) between 2021 and 2023 is shown with colored arrows. The amplitude of Horizontal to Vertical Spectral Ratio (HVSR) at fundamental resonance f_0 is shown with colored dots. Both dot color and size scale with peak amplitude (see legend).

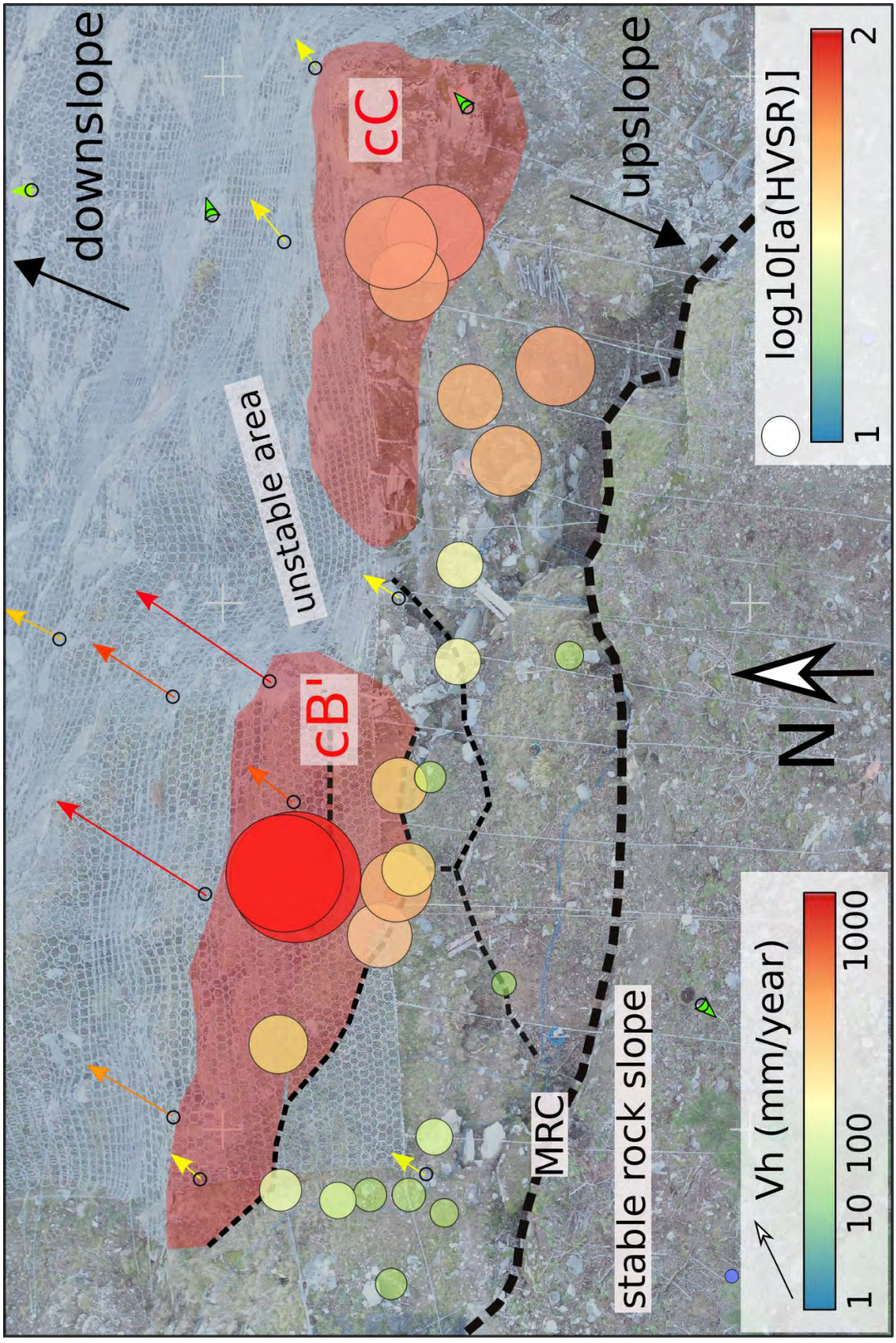
downslope
upslope
cC
cB'
unstable area
MRC
stable rock slope
N
log10[a(HVSR)]
2
1
Vh (mm/year)
1
10
100
1000

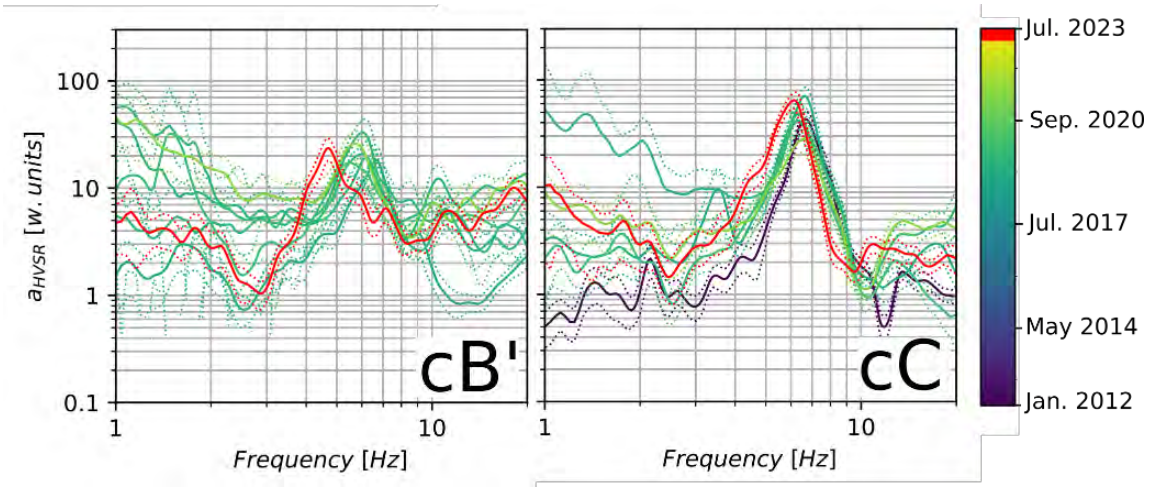

Figure 2. Changes in HVSR over time, for cB' and cC most unstable rock compartments. Curve color scales with time from 2011 until 2023 (see colorbar). Last survey (July 2023) is highlighted in red.

Conclusion

Clear and systematic HVSR peaks were spotted on La Praz unstable slope, in contrast to nearby stable rock mass. HVSR peak amplitude at fundamental resonance (f_0) varies greatly across the unstable body, ranging from [3-10] within the less degraded compartment up to [20 - >100] within the most prone-to-fall compartments. The ambient vibration map agrees very well with slope displacement rates and the succession of compartment collapse during the slope failure (2023-08-27). In addition, passive seismic monitoring based on successive surveys clearly pointed out changes in bulk slope mechanical stiffness prior to the collapse: significant -20 % and -15 % drops in f_0 were spotted in July 2023 for cB' and cC compartments, respectively. In order to obtain more details in slope dynamic response prior to collapse, we conducted a continuous passive seismic monitoring spanning from February 2023 until the rockfall. Results are currently under investigation, and suggest additional -10 % drop in f_0 in early August 2023, i.e. a few weeks before the collapse.
This suggests that ambient vibrations can yield a global insight into the rock slope behavior, which is complementary to detailed surface displacement measurements.

References

Bottelin, P., Baillet, L., Larose, E., Jongmans, D., Hantz, D., Brenguier, O., Cadet, H., Helmstetter, A., 2017. Monitoring rock reinforcement works with ambient vibrations: La Bourne case study (Vercors, France). Engineering Geology 226, 136–145. https://doi.org/10.1016/j.enggeo.2017.06.002

Bottelin, P., Jongmans, D., Baillet, L., Lebourg, T., Hantz, D., Lévy, C., Le Roux, O., Cadet, H., Lorier, L., Rouiller, J.-D., 2013. Spectral analysis of prone-to-fall rock compartments using ambient vibrations. Journal of Environmental and Engineering Geophysics 18, 205–217.

Häusler, M., Kleinbrod, U., Burjánek, J., Fäh, D., 2018. Characterization of an unstable mountain slope using ambient seismic noise: fundamental techniques and case study "Chilchenstock," in: Session 28: Applications and Developments in Ambient Noise Seismology. Presented at the European Seismological Comission, Valletta, Malta, p. 2.

Häusler, M., Michel, C., Burjánek, J., Fäh, D., 2019. Fracture Network Imaging on Rock Slope Instabilities Using Resonance Mode Analysis. Geophysical Research Letters 46, 6497–6506. https://doi.org/10.1029/2019GL083201

Jaboyedoff, M., Del Gaudio, V., Derron, M.-H., Grandjean, G., Jongmans, D., 2019. Characterizing and monitoring landslide processes using remote sensing and geophysics. Engineering Geology 259, 105167. https://doi.org/10.1016/j.enggeo.2019.105167

Lévy, C., Baillet, L., Jongmans, D., Mourot, P., Hantz, D., 2010. Dynamic response of the Chamousset rock column (Western Alps, France). Journal of Geophysical Research: Earth Surface 115.

Gravitational movements in the stiff clays of the Sinard plateau (western Alps): the case of the Harmalière landslide

Grégory Bièvre[1], Sylvain Fiolleau[2], Christophe Dano[3]

[1] Univ. Grenoble Alpes, Univ. Savoie Mont Blanc, CNRS, IRD, ISTerre, Grenoble, France
[2] Lawrence Berkeley National Laboratory, Earth and Environmental Sciences Area, Berkeley, USA
[3] CNRS, Grenoble-INP, Université Grenoble Alpes, 3SR, Grenoble, France

SUMMARY: The Harmalière landslide (French Western Alps) affects Quaternary lacustrine rigid clays in the Trièves region. This work presents the analysis of three reactivation events (1981, 2016 and 2017) with the aim to understand the landslide mechanisms.

Keywords: Clay, landslide, mechanism, fluidization

Introduction

The Harmalière landslide, which affects the Quaternary lacustrine rigid clays in the Trièves region (French Western Alps), is a compound landslide, transitioning from an earthslide at the upper section to an earthflow at the lower part. Over the past four decades, it has exhibited multiple surges, with two of them surpassing a volume of $1 \cdot 10^6$ m^3 and manifesting distinct flow-like characteristics (Fiolleau *et al.*, 2021). This study, utilizing a combination of field observations, aerial photographs, and geotechnical data (details of which are not included in this extended abstract), aims to unravel the variations in clay rheology both spatially and temporally, focusing on three specific events.

Location and geological context

The Harmalière landslide is located on the Trièves plateau in the French Western Alps (Fig. 1). This area is covered with Quaternary clays that were deposited in a glacially-dammed lake during the last glacial maximum, some 30 to 50 kyr ago. The lake was formed by the damming of the Drac River by the Romanche glacier spreading southward and the site is located at the edge of this glacier. More detailed descriptions on the geology and chronology can be found in Monjuvent (1973) and Bièvre & Crouzet (2021).
The clay deposit can reach a thickness of about 250 m and has been over-consolidated by the weight of the glacier, his further retreat, and the subsequent erosion of the topping morainci and clayey layers. During the last glaciation, the glacier advanced and retreated several times, causing the reworking of the deposited clay layer. At the time of its retreat, the glacier covered the clays with up to 50 m of moraines. At the top of the landslide, this layer of moraine results in a yellowish granular colluvium layer a few metres thick, containing pebbles. After the glacier retreated, the lacustrine sediments were quickly incised by the Drac River, causing the instability of the entire slope below the Sinard Plateau (Fig. 1), including the Harmalière landslide. Finally, a dam was built on the Drac, downstream of the Harmalière gully, creating an artificial lake in 1961, the level of which is at an elevation of about 480 m.
The landslide has been categorized into three zones (Fig. 2), delineated based on morphology inferred from a 2019 LiDAR image, field observations, and satellite image analysis (Fiolleau et al., 2021). The Source Zone is characterized by a predominant compound earthslide mechanism, imbricated rupture surfaces, and a concave upward slope of 13°. The Transportation Zone features a convex upward slope of 10° and involves material movement

through a mechanism of translational (planar) sliding. The Discharge Zone exhibits a gentle convex slope of 9° and smoother topography ; this zone displays a flow-like mechanism (presently an earthflow), with continuous erosion occurring at the base of the material.

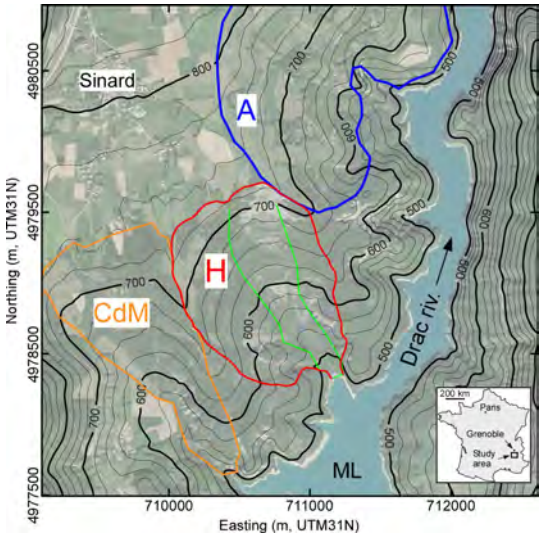

Figure 1: Location of the Harmalière landslide (H, delimited by the red line), south of village of Sinard. The most active zone is delineated with the green lines. The two adjacent landslides of Avignonet (A) and Champ du Mouton (CdM) are shown with blue and orange lines, respectively. ML: Monteynard Lake. Contour lines stand for topographic elevation in metres above sea level.

As shown in Fiolleau *et al.* (2021), this three-zone structure constitutes an effective and continuous mass transfer agent whose mechanism has contributed to a 700 m headscarp retrogression over the last 70 years, with the 30 m high headscarp being maintained in the most active area. During this period, the landslide has experienced several surges of very different sizes and under very different climatic conditions. Three particular and relatively well-documented events (March 1981, June 2016 and January 2017) that have occurred in the last 40 years will be briefly exposed to try to understand the mechanisms involved.

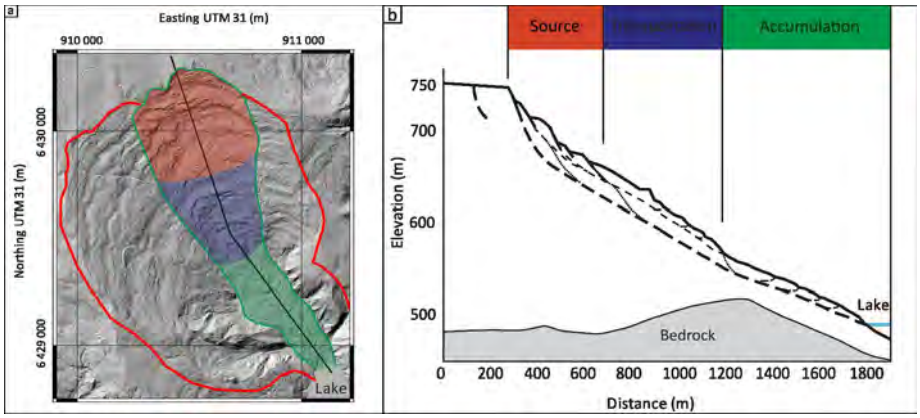

Figure 2: Harmalière landslide zoning. **a)** The three zones corresponding to the different gravitational mechanisms: source zone with compound slide in red, transition zone with translational slide in blue, discharge zone with flow-like mechanism and erosion at the toe in green. **b)** Cross-section along the black line drawn in Fig. 2a.

Analysis of 3 reactivation events in 1981, 2016 and 2017

After signs of activity from the 1960s, the landslide was triggered in March 1981 following heavy rains that melted a 0.4 m thick snow cover. The reactivation of 1981 created a 30 m high escarpment at an elevation of about 700 m and generated a mudflow of more than several hundred thousand m^3 at its base 24 h after the triggering. In 40 years, the headscarp has retrogressed discontinuously at an average annual rate of 4-5 m/y (Fiolleau *et al.*, 2021). At present, the Harmalière landslide, with total a volume of about $45 \cdot 10^6$ m^3, presents a very

active central zone of 150 to 400 m width (green lines in Fig. 1) and an average slope of 9°. A major reactivation involving $1 \cdot 10^6$ m^3 occurred in this zone in June 2016, followed by a smaller one ($0.1 \cdot 10^6$ m^3) in January 2017. During the 2016 event, the mass transfer was achieved in the course of 5 weeks, from a slide mechanism at the top to an earthflow at the toe (Lacroix *et al.*, 2018; Fiolleau *et al.*, 2021).

The two events of 1981 and 2017 took place in early spring or winter, at a time of sudden warming, after snowfall and a period of frost. On the other hand, the 27 June 2016 event occurred in summer during a dry period with only 2 mm of rainfall in the previous week. The main characteristics of these three main regression events are detailed in Table 1.

Table 1: Comparison between the three events of 1981, 2016 and 2017.

Landslide	1981	2016	2017
Weather conditions	Snow, rain and warming	Dry	Snow and warming
Retrogression distance (m)	500	60	20
Retrogression area (10^4 m^2)	28	2.5	< 1
Total runout (m)	1300	1525	400
Runout time	< 1 day	5 weeks	10 days
Volume displaced (10^3 m^3)	[1000-3500]	1000	112
Mechanism at the toe	mudflow	earthflow	No mechanism
Mean velocity	50 m/h	43 m/day	40 m/day

Assuming a linear relationship between displaced volume and regression distance, the volume displaced after 1981 can be estimated to be about 2.5 10^6 m^3, implying a maximum volume of about 3.5 10^6 m^3 for the 1981 event (Table 1). Based on the runout time and distance values, the mean slide velocity is about 40 m/day for the two events of 2016 and 2017 and more than 50 m/h for the mudflow of 1981. These figures, which are consistent with the ones given for such mechanisms (Hungr *et al.*, 2014), illustrate the different rheological behaviours of the same material when submitted to different weather conditions.

Mechanism(s) of the landslide

The main results of the new geologic observations, *in situ* (penetrometer) and laboratory (triaxial, rheological) tests, and analysis of events from 1981 to 2017 were used to construct a schematic interpretive section of the Harmalière landslide (Fig. 3). First, the material that are driven into the unstable zone by sliding includes three types of soils (morainic colluvium, laminated clays and unlaminated clays with pebbles; Fig. 3). Behind the headscarp, these layers are affected by sub-vertical micro-cracks on the surface that progressively develop in the colluvium and weathered clay layer (Fiolleau *et al.*, 2020). Drying-wetting cycles lead to the progressive localization of a listric fracture with a near vertical face in the colluvium layer and an inclined slope with slickensides in the underlying compact clays. The movement type in the source area is an earthslide with a slip surface of uneven curvature and generating significant internal distortion of the moving mass. Once in the landslide, the layers mix and are exposed to rapid weathering and mechanical degradation over time as they move downslope (Fiolleau *et al.*, 2022). It is also noticeable that the clayey material exhibits a yield-stress fluid behaviour for water contents close to the liquid limit, leading to fluidization (Carrière *et al.*, 2018; Fiolleau *et al.*, 2021). The drop in cohesion within the landslide favours the appearance of more and more sliding surfaces towards the lower part with an earthflow type mechanism (Fig. 3).

In the dry conditions of June 2016, a mass of $1 \cdot 10^6$ m^3 was displaced from the headscarp to the toe in 5 weeks, with a mechanism evolving from an earthslide to an earthflow. In case of heavy rainfall and/or snowmelt (1981 and 2017 events), the rapid increase in pore pressure along the failure surfaces can lead to a rapid triggering of a landslide in the upper part. When the displaced mass is sufficiently large, as was the case in the 1981 event, it generates an increase in shear stress, potentially resulting in the fluidization of saturated material leading to a mudflow-type movement.

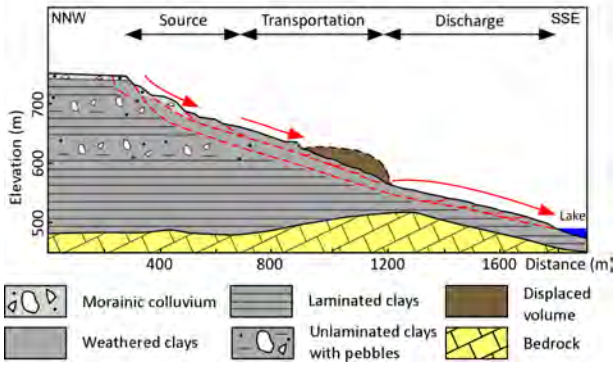

Figure 3: Interpretative scheme of the landslide.

Conclusions

The Harmalière landslide has shown a discontinuous retrogression over 40 years with two major surges in 1981 and 2016, and a minor one in 2017, that were analysed. These events displaced a volume of more than $1 \cdot 10^6$ m^3 with a different flow-like mechanism (mudflow and earthflow). A geotechnical campaign was carried out after 2017 to better characterize the material inside and outside the landslide and to understand the factors controlling the rheology of the clay. The first outcome is that, once the rigid clay blocks have slid into the source area, they undergo a rapid degradation under the effect of the weather conditions to a material mixing the different layers. This degradation favours the generation of multiple slide surfaces. The associated landslide mechanism is earthflow, which was observed during the 2016 event. The second finding is that the material has the behaviour of a yield stress fluid at high water content with a strong viscosity bifurcation. The critical stress measured is of the order of magnitude of the shear stress likely to have been generated by the 1981 event, which was triggered in very wet conditions and propagated as a mudflow. The results obtained are corroborated by previous data and the overall interpretation contributes to provide new insight into the solid-fluid transition in the Harmalière landslide.

References

Bièvre G & Crouzet C (2021) Multi-proxy analysis of boreholes in remolded Quaternary paraglacial deposits (Avignonet landslide, French Western Alps). *Engineering Geology* 286: 106073.

Carrière S, Jongmans D, Chambon G *et al*. (2018) Rheological properties of clayey soils originating from flow-like landslides. *Landslides* 15: 1615-1630.

Fiolleau S, Jongmans D, Bièvre G *et al*. (2020) Seismic characterization of a clay-block rupture in Harmalière landslide, French Western Alps. *Geophysical Journal International* 221: 1777-1788.

Fiolleau S, Jongmans D, Bièvre G *et al*. (2021) Multi-method investigation of mass transfer mechanisms in a retrogressive clayey landslide (Harmalière, French Alps). *Landslides* 18: 1981-2000.

Fiolleau S, Jongmans D, Bièvre G *et al*. (2022) Study of clay degradation in an earthslide combining OBIA and roughness analysis of UAV-based optical images. *Earth Surface Processes & Landforms* 47: 3465-3480.

Hungr O, Leroueil S & Picarelli L (2014) The Varnes classification of landslide types, an update. *Landslides* 11: 167-194.

Lacroix P, Bièvre G, Pathier E *et al*. (2018) Use of Sentinel-2 images for the detection of precursory motions before landslide ruptures. *Remote Sensing of Environment* 215: 507-516.

Monjuvent G (1973) La transfluence Durance-Isère. Essai de synthèse du Quaternaire du bassin du Drac (Alpes françaises). *Géologie Alpine* 49: 57-118.

Slope-scale deformation process interacting with karstic hydrostructure: insights from geotechnical - geophysical monitoring and remote sensing

Marmoni G.M.[1], Grechi G.[1], Hussain Y.[1], Rivellino S.[1], Battaglia S.[2], Mineo C.[2], Varriale A., Martino S.[1]

[1] Department of Earth Sciences of Sapienza University and CERI Research Centre, Rome, Italy
[2] ACEA Ato2 s.p.a, Rome, Italy

SUMMARY: Mass rock creep processes are responsible for slope-scale gravitational induced deformations driving to rock failures that can culminate in high severity geological hazard scenarios. In karst systems these deformations can also involve hypogeous conditions accelerating their evolution by collapses of caves. An accurate monitoring is a prime concern in geological hazard analysis. In the Peschiera Spring hydrostructure case study, data from a multiple-parametric monitoring system are evaluated in a comparative pattern for the stability conditions (i.e., destabilization and failure precursors) evaluation and establishing a linkage between the triggering factors over the landslide volume involved. Mechanical damaging is studied with an integrated geophysical-geotechnical monitoring network. The zonation of ongoing deformations on the slope can be performed by considering surface markers by change detection on Multitemporal LIDAR imagery and field surveying.

Keywords: slope deformation, monitoring, microseismicity, infrastructures, hydraulic stressor

Introduction

The recognition of pre-failure events of natural systems is an important focus to mitigate the geological risks posed by abrupt massive rock-mass failures. In the large-scale processes, such as the rock mass spreading or sliding, periodic or episodic hydraulic or seismic transient influence variations in stress wavefield which can impose rapid acceleration or impulse on the slow viscous deformations (Lacroix et al., 2020; Agliardi et al., 2020). Such slow-to-fast transitions can cause crack growth and instability phenomena like rock failure or hypogeous collapses that could anticipate more intense events or a generalized failure (Evans et al. 2006). For this reason, an integrated approach encompassing geotechnical and geophysical monitoring have to be adopted to study the temporal progression of the slope movements and evaluate signals precursors of instability or itself expression of an ongoing acceleration. In case of a karstic pervasively fractured rock mass context stressed by a complex hydraulic circulation, with high flow and seasonal peak discharge, complex scenarios must be depicted trying to account for future variation of the hydraulic stressor within the slope (Maffei et al., 2005). The here reported case study, exemplify this large-scale process, where the concurrent presence of a regional aquifer and a slope scale gravity-induce deformation that threaten a strategic infrastructure. The deformation mechanism has been characterized through the results of almost a decade of measurements, collected by a dedicated and tailor-made monitoring systems that continuously evolve in technology, resolution, and sensor redundancy.
The here presented study report the recent outcomes from the monitoring project of the Peschiera Springs slope, which hosts the main drainage plant of the Rome's aqueduct system

managed by the ACEA-ATO2 S.p.A. Italian company. Such case study exemplifies a virtuous example of synergic work among researchers and local companies for Geological risk mitigation and infrastructure management.

Case Study

The study area is represented by the Peschiera slope, located in the W flank of the M. Nuria (Rieti, Central Italy), represents the southern termination of one of the largest massif and hydrogeological structures in central Italy (Boni et al. 1986, 1995). The slope sector in the exam hosts the emergence of the Peschiera Spring and the drainage plant of Rome's aqueduct, which with a total discharge of about 16-18 m^3/s, represent the largest water feeding of the capital, supplying for ab. three million inhabitants. The structural setting of the slope is a monoclinal N-dipping structure, which is dissected by mayor fault lines and minor conjugated joint sets. Active karst process also involves the jointed rock mass, which expressed with large sinkholes and collapsed dolines on-slope and over the S. Vittorino Plain. This slope is affected by a gravitational slope deformation process consisting in a rock lateral spreading (Martino et al., 2004) associated to several landforms including sinkholes, subvertical scarps and trenches (Lenti et al., 2012). Major tension cracks indicative of slow, intense, and pervasive slope deformations related to a mass rock and time-dependent process were also retrieved from multi-temporal LIDAR remote surveys, which, for the last acquisition reach cm-resolution (Fig. 1).

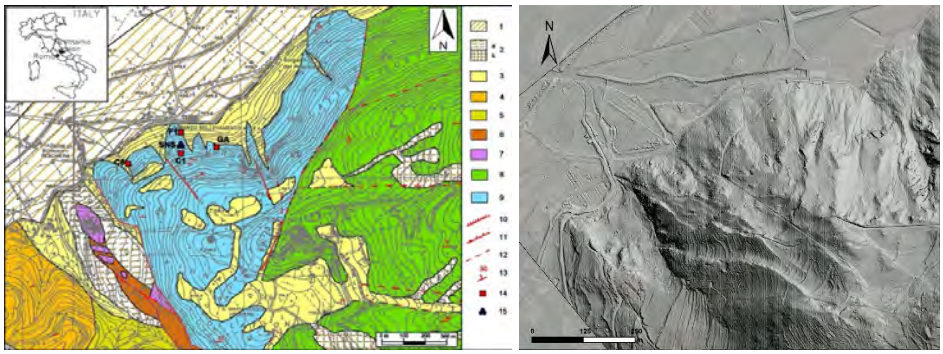

Fig. 1 left) Geological map of the Peschiera Springs slope (after Fiorucci et al., 2017). right) Hillshade view of the Peschiera slope derived from 1x1m DEM based on the 2022 LIDAR remote survey. Main scarp of the large deep-seated deformation is clearly visible (legend of geological units reported in Fiorucci et al., 2017).

The progression of slow creep deformation process over decades, caused the damage of different portions of the drainage plant, composed of longitudinal and transversal drainage tunnels and a main Drainage Collector Tunnel (DCT), featured by a length of 250 m and a section of 4 m, aligned parallel and 80m inside the slope. The most important effect was registered after the 1997 Umbria Marche earthquake (Mw = 6). The episode involved one of the deepest sinkholes on the slope and caused the partial roof collapse of a tunnel, demonstrating the spatial continuity between sinkholes and karst caves inside the slope. Other ruptures are cumulated over time in the DCT, causing spalling and intense fracturing that obliged the authorities to undertake consolidation interventions and an extraordinary maintenance. Concurrently, during the tunnel restoration, a redundant geotechnical monitoring system composed of circumferential (CIR) and radial (RAD) arrays, borehole extensometers, wire extensometers, load cells, and triaxial crack-meters was installed with the aim of monitoring the excavation stages and follow the deformation process over time. The collected results over the last years allow to better understand the kinematics of the deformation process, evaluate the mechanical response of the newly consolidated DCT and identify sectors of interest, where localisation of deformation occurred.

Materials and Methods

The Peschiera slope has been instrumented, in the last two decades, through multi-parametric monitoring system to support a safe management of the local geological risk. For monitoring purposes, passive seismic techniques were applied on the prone-to-fall compartment using two different approaches. Monitoring activities of the Peschiera Spring slope deformation have been conducted for several years through traditional geotechnical sensor deployed within the aqueduct plant across of structural elements relevant for the geotechnical construction. Such monitoring allows to preliminary focus the kinematics and deformation rates of the slope scale rock mass deformation. After the tunnel restoration, ended in 2018, a new dedicated monitoring system was installed with the twofold aim of verify the response of the consolidation intervention with respect to the expected behaviour and monitor the rock mass spreading over time. For this reason, 7 instrumented sections (E1-E7) made up of 10m-long linear array composed of 10 triaxial accelerometric sensors have been installed within the rock mass along radial boreholes on mount and valley side of the DCT. In addition to this sensor multipoint borehole extensometers at depth of 5, 8 and 10 m within the rock mass have been included to validate consistency of results. Triaxial crack-meters, wire extensometers, load cells have been also distributed along tunnel ribs and beams to verify the stress-strain response of the engineering structure. Additional pre-existing 3D crack-link inside the DCT of the former geotechnical system have been maintained to follow up evolution of strain rates over a decade. Geophysical monitoring is ongoing with the aim to record and detect with high sensitivity seismic events with Magnitude down to -2, generated by underground instabilities such as failures and collapses within the rock mass, thanks to different seismometric networks installed (starting from 2008) inside the whole drainage plant. At this aim a accelerometric networks (Kinemetrics and HBM-Bruel Kjaer) were deployed within the plant, inside the rock mass and on the slope, using for the HBM array a specific geometric array called Seismic Navigation System (SNS; Fig. 1) (Walter et al, 2012). Basing on Multitemporal LIDAR acquisitions carried out in 2009 and 2021, a quantification of morphological changes occurred on slope have been also performed through Change Detection (CD) and Digital Image Correlation (DIC) algorithm (Cosentino et al., 2023).

Results and Current Works

Continuous monitoring of the radial deformative array distributed in left and right side the gallery arch along the DCT (example in Fig. 2) allow to monitor the evolution of rock mass deformation above the tunnel, confirming the stationary trend of creep deformation that range in 1-2 mm/yr. The inter-section analyses for the RAD conducted at the farthest node of the linear array (N1) highlight a complex deformation dynamic characterized by horizontal movements towards the slope, with a vertical movement that, except of section E3, show a general downward movement tendency towards the decline of the upstream sector. As regards the valley side's array, this dynamic appears reversed (Fig. 2). The distribution of both horizontal and vertical displacements appears to be consistent with the downward back-tilting the slope block under gravitational deformation, with a sagging that involve internal part of the DCT between the two consolidated and reinforced structural sections (red sections in Fig. 3).
The use of multitemporal LIDAR DTM also support the inventory of several new generated sinkholes on slope surface and, through CD and DIC processing, the localisation of a mature deforming sector where counterslopes developed. This sector located in the left shoulder of the deep-seated deformation, at the terminal portion of the DCT, where water is transferred to distribution aqueduct. On the other side, the seismic monitoring, allowed to record regional and teleseismic (i.e. far field) earthquakes and local seismic events like underground collapses or

cracking. These events were characterized in two different typologies: underground collapses and cracks precursors of larger failures. Some of the seismic crises registered so far showed a significant sequence of precursors anticipating of tens of minutes before the strongest collapse (Fiorucci et al., 2017). The locations of these events are in good agreement with the evolutionary geological model of the ongoing gravitational slope deformation and reflect the spatial distribution of the main trenches and slope scarps reconstructed over the years by field surveys and LIDAR data.

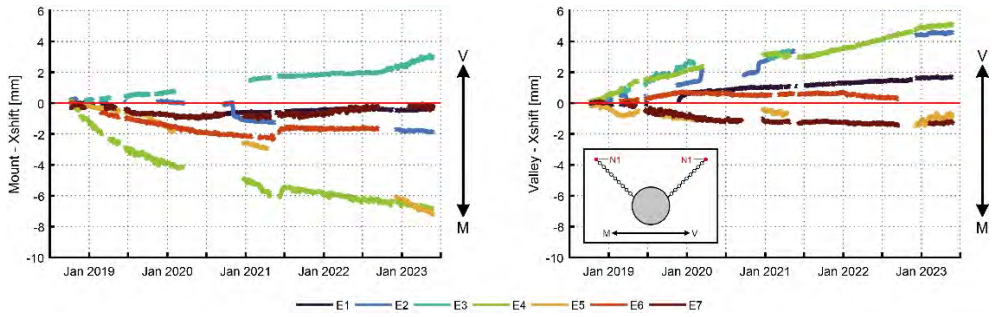

Fig.2 Trend of the Horizontal displacement series recorded at the first node of the 7 RAD sections located on the upslope (Mount) and downslope (Valley) side. XShift values indicate downstream (to the Valley) deformation. Sketch of the RAD instruments and monitored node of the array is reported.

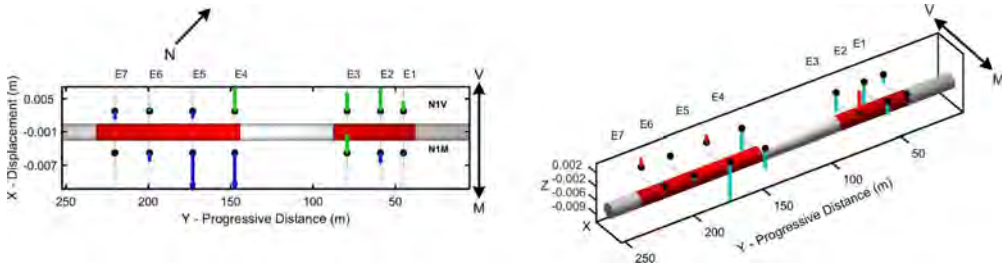

Fig. 3 Analysis of the displacements reconstructed through vector composition of the horizontal XShift (left) and vertical ZShift (right) displacement components recorded at Node 1 of the Radial Arrays distributed along the DCT. Left (N1M) and Right (N1V) chains are reported. The green displacement vectors are directed downstream, right the blue vectors are directed downwards.

High sensitivity seismic monitoring has been implemented within the Peschiera Spring hydrostructure to mitigate the geological risk through management strategies adopted by the owner of the aqueduct, which support the computation of control index functional for the definition of alert levels. Further research on displacement time series is ongoing to define and integrate alert levels suitable for the definition of an Early Warning System of the aqueduct.

References

Agliardi, F., Scuderi, M. M., Fusi, N., & Collettini, C. (2020). Slow-to-fast transition of giant creeping rockslides modulated by undrained loading in basal shear zones. Nature communications, 11(1), 1352.

Cosentino, A., Marmoni, G. M., Fiorucci, M., Mazzanti, P., Scarascia Mugnozza, G., & Esposito, C. (2023). Optical and Thermal Image Processing for Monitoring Rainfall Triggered Shallow Landslides: Insights from Analogue Laboratory Experiments. Remote Sensing, 15(23), 5577.

Evans S, Scarascia Mugnozza G, Strom A (2006) Landslides from massive rock slope failure. Nato Science Series, Springer, Netherlands. Series IV: Earth Environ Sci 49:662

Fiorucci, M., Iannucci, R., Lenti, L., Martino, S., Paciello, A., Prestininzi, A., & Rivellino, S. (2017). Nanoseismic monitoring of gravity-induced slope instabilities for the risk management of an aqueduct infrastructure in Central Apennines (Italy). *Natural Hazards*, 86, 345-362.

Lacroix, P., Handwerger, A.L. & Bièvre, G. Life and death of slow-moving landslides. *Nat Rev Earth Environ* **1**, 404–419 (2020). https://doi.org/10.1038/s43017-020-0072-8

Walter, M., Arnhardt, C., & Joswig, M. (2012). Seismic monitoring of rockfalls, slide quakes, and fissure development at the Super-Sauze mudslide, French Alps. *Engineering Geology*, 128, 12-22.

Monitoring vegetated, snowy or rapid landslides using RFID

M. Le Breton[1,2], E. Rey[1, 2], F. Guyoton[1], F. Muller[1]

[1] Geolithe Innov, Geolithe, Crolles, France
[2] ISTerre, Grenoble, France

SUMMARY:
Total station and recent RFID measurement systems can monitor a landslide with myriads of low-cost passive reflectors of optical or microwave waves. By comparing them on two French landslides (Châtel and Villa Itxas Gainas) we find that RFID is more robust to cold and vegetated environments and has a faster time sampling, while total station has better accuracy and read range. Therefore, we advise using RFID to detect fast movements in cold or vegetated areas, and total stations to monitor large and slow landslides.
Keywords: template, layout instruction, regulation, specification, references

Introduction

Landslide early warning systems often use surface displacements monitoring. Total station, that localize passive optical reflectors wirelessly with a robotized laser, is often the ideal technique, allowing tracking displacement of multiple targets in a rather robust way. Yet, the laser can be blocked by obstacles such as snowfall and vegetal cover, and the delay of measurement is too large to detect fast accelerations in real time (e.g., mudflows). The passive radiofrequency identification (RFID) technique was recently introduced to monitor landslides (Le Breton et al., 2019), improved (Charléty et al., 2023a, 2023b, 2022; Le Breton, 2023), and deployed on five landslides (Pont-Bourquin 2017-2023, Châtel 2023, Villa Itxas Gaïanas 2021-2022, Valloire 2020-2022, Harmalière 2020-2022). We compare its performance with a total station.

Setup on Two Landslides

This study uses measurements from two sites.
(1) Châtel landslide, in Savoie, France, occurred between a skiing ropeway and a road to access the skiing slope. 17 points of the landslide were monitored both with laser reflectors seen by a total station (model Trimble S9) and with RFID tags seen from an RFID station (Figure 1.a). The points were equipped with three medium-range RFID tags up at distance <60 m (Figure 1.b) or one long-range tag protected by a casing at 60–120 m from the station. One long-range tag and 3 medium-range tags were also installed behind a vegetal cover, to assess the ability to monitor without field of view across vegetation (Figure 1.c). The cover consisted of fir trees, with an opacity sufficient to block total station measurements or visual observation.
(2) The Villa Itxas Gaïnas landslide is situated on the Basque coast, France (Figure 2). It has been equipped with RFID for a year, including during a fast displacement on January 17th (up to 3 meters in 30 minutes). During this event, half of the tags felt on the ground or were taken down by the landslide; another half continued to monitor the displacement. Here, we present the fastest moving target observed, to evaluate the capacity of RFID to track fast displacements that are not measurable with total stations.

On both sites, we used an experimental acquisition setup that alternated between two bands (the classic 865-868 MHz band, and the recently-allowed 915-918 MHz band) for R&D purpose (Le Breton, 2023). That created regular gaps of 15min on tags not read by the secondary band.

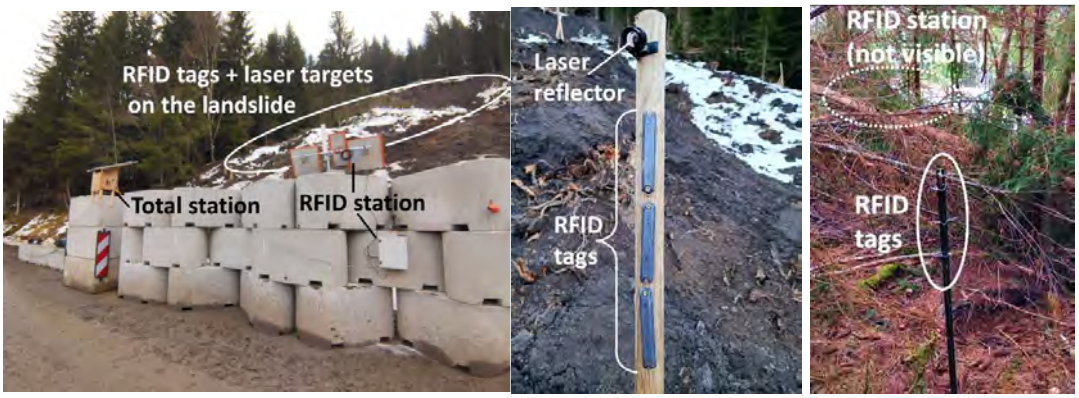

Figure 1: Chatel alpine landslide in winter. (left) the two stations; (center) the points equipped with laser reflectors and RFID tags; (right) RFID tags placed behind a vegetal cover (fir trees) without direct view.

Figure 2: Villa Itxas Gaïana landslide (left) on 15/12/2022 and (right) on 20/01/2023, highlighting the transformations caused by the exceptional acceleration of January 17th. The site was equipped with an RFID station (white cross), 30 tags deployed over the landslide (black circle, and black cross for the tag n° 8)

Measurement Accuracy and Availability

After its activation, Châtel landslide showed very heterogeneous displacement features across space: some area stayed almost immobile and other displayed strong displacement. Displacement of the fastest-moving target (Figure 3) is coherent between RFID and total station, with however a much higher accuracy of the total station. RFID accuracy was around ±2 cm in general, and ±6 cm with snow, confirming previous accuracy estimations (Le Breton et al., 2019; Charléty et al., 2022). On the other side, the total station suffered numerous data gaps, due to several issues related to snow, ice and ground motion (that required 5 maintenance operations in a month), while RFID had no data gap and required no maintenance.

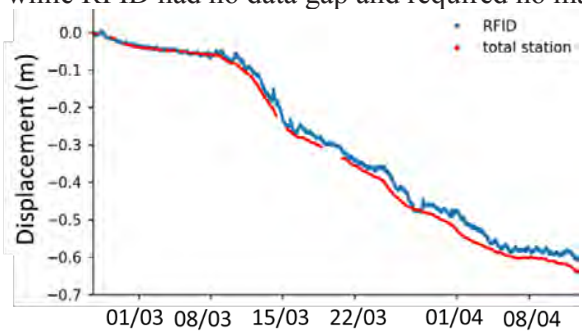

Figure 3: Displacement measured by RFID (single tag) and by a total station at Châtel on the point with most displacement, from 25/03/2023 to 15/04/2024.

Fast Displacements

Another potential advantage of RFID is its capacity to making from 30 (used here) to 800 measurement per second while switching rapidly reading between targets, opening the possibility to track displacement even during fast accelerations. It is illustrated on the acceleration that has occurred on January 17th on the Villa Itxas Gaïnas landslide (Figure 4), where a motion of up to 3 meters occurred in 30 minutes. Unfortunately, an ongoing test of R&D dual band acquisition (instead on a single band used in general) has led to regular 15-minute data gaps when using the secondary band. Nevertheless, interrogation on the primary band was sufficient to measure an instant velocity of up to 15 cm/minute. In theory, RFID could track instant velocity up to 1 m/s with one target, 0.1 m/s with 10 targets, etc. This opens the possibility for early warning systems with a few seconds reactivity only, and also precise motion data during fast movements.

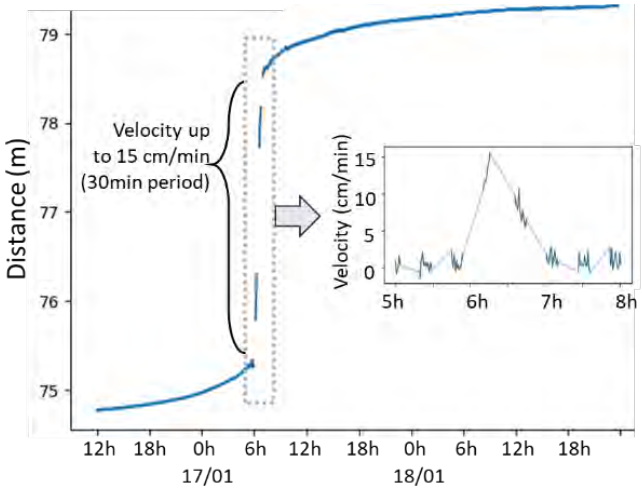

Figure 4: Displacement measured with RFID at Villa Itxas Gaïanas, 16/01/2023–18/01/2023. It highlights the acceleration of the 17th between 6:00 and 7:00. Short and regular measurement discontinuities occurred due to the test of a new experimental dual-band functionality when the acceleration occurred (Le Breton, 2023)

Measurement Through Vegetation (fir woods)

To confirm the performance of RFID through vegetation, we installed four tags on a stable ground at Châtel, behind fir trees (see Figure 1c). The results on Figure 5 show that, despite the vegetation, (1) the monitoring worked continuously (2) no displacement was measured, as expected, and (3) the noise is within ±2 cm in general, and ±6 cm during precipitations for unprotected tags. That is coherent with the bias measured a controlled experiment as 0.5% of the transmission distance across dense grass (Le Breton et al., 2023).

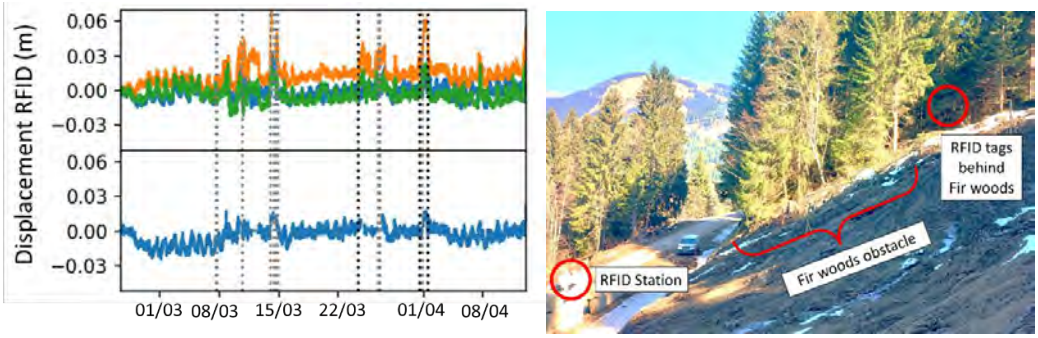

Figure 5: Displacement measured through vegetation with RFID at Châtel from 25/02/2022 to 15/04/2023, using (top-left) three unprotected commercial tags and (bottom-left) one enclosed long-range tag. Dash bars indicate (gray) snowfalls and (black) rainfalls deduced from a camera. (right) Side-view showing the vegetation (fir woods) between the RFID tag and the station.

Synthesis of Performance and Perspectives

Table 1 summarizes the performances of RFID motion tracking compared to total stations observed in this study.

Table 1: Synthesis of performances (*in case of snow cover)

	Accuracy at 100 m	Maximum distance	Lateral motion	Downtime dt=3h	Largest delay	Median delay	Through vegetation
RFID	±2 cm ±6 cm*	100 m	Inaccurate	0.03%	4.8 h	1.5 s	Yes
Total station	± 0.1 cm	1 000 m	Accurate	11.6%	47 h	514 s	No

Perspective of improvement

Radial displacement accuracy in RFID is intrinsically related to low bandwidth and multipath interferences. Yet, millimetric accuracy has been demonstrated with non-standard RFID readers that use higher bandwidth and could be available commercially (Ma et al., 2017). Similarly, read range has been constantly increasing in the last decades and is likely to continue increasing. Measuring accurate lateral motion would require multiple reader antennas around the landslide (Charléty et al., 2022).

Conclusions

In terms of performance, RFID was x38 more available (0.3% vs. 11.6% downtime) without maintenance (vs. 5 maintenance operation on the total station) in this setup. RFID can monitor tags 230x faster (0.068 v 16 seconds/point), which moves very rapidly, even through vegetation. Total station is x20 more accurate for radial measurements (0.1 v 2 cm), reads targets x10 times further (1 v 0.1 km) and tracks lateral motion accurately. Total stations are better on large slow landslides, and RFID on fast shallow landslides. In terms of usage, total station placement is more flexible due to their larger distance and the lateral measurements. RFID opens the capacity to measure across vegetated areas. In early warning systems (Intrieri et al., 2012), we think total station is better for forecasting hours to days in advance (Intrieri et al., 2019) and RFID for real-time warnings. Both are complementary in an operational early warning system.

Conflict of interest: Géolithe company sells a patented RFID monitoring system.

References

Charléty, A., Le Breton, M., Baillet, L., Larose, E., 2023a. RFID Landslide Monitoring: Long-Term Outdoor Signal Processing and Phase Unwrapping. IEEE J. Radio Freq. Identif. 7, 319–329.

Charléty, A., Le Breton, M., Larose, E., Baillet, L., 2022. 2D Phase-Based RFID Localization for On-Site Landslide Monitoring. Remote Sens. 14, 3577.

Charléty, A., Olivier J.J., M., Le Breton, M., 2023b. Kalman Smoothing for better RFID Landslide Monitoring, Presented at the European Signal Processing Conference (EUSIPCO 2023), Helsinki, Finland, p. 4.

Le Breton, M., 2023. Increased ranging accuracy of RFID tags in ETSI regions using 53MHz wide dual bands. Presented at the IEEE Int Conf RFID TA, Aveiro, Portugal.

Le Breton, M., Baillet, L., Larose, E., Rey, E., Benech, P., Jongmans, D., Guyoton, F., Jaboyedoff, M., 2019. Passive radio-frequency identification ranging, a dense and weather-robust technique for landslide displacement monitoring. Eng. Geol. 250, 1–10.

Le Breton, M., Baillet, L., Larose, E., 2023. Tomography of the quantity of grass using RFID propagation-based sensing. Presented at the IEEE Int Conf RFID TA, Aveiro, Portugal. http

Intrieri, E., Gigli, G., Mugnai, F., Fanti, R., Casagli, N., 2012. Design and implementation of a landslide early warning system. Eng. Geol. 147–148, 124–136.

Intrieri, E., Carlà, T., Gigli, G., 2019. Forecasting the time of failure of landslides at slope-scale: A literature review. Earth-Science Reviews.

The residual shear strength mobilised by slow active landslides

L. Picarelli[1], L. Comegna[1,2], G. Urciuoli[3]

[1] Euro-Mediterranean Centre on Climate Change, CMCC, Lecce, Italy
[2] Università della Campania Luigi Vanvitelli, Aversa, Italy
[3] Università di Napoli Federico II, Napoli, Italy

SUMMARY: Slow translational landslides are widespread phenomena in Italy, especially in stiff clay and clay shale deposits. After the triggering phase, which is generally characterized by moderate to rapid velocity, the landslide turns into a slow slope movement driven by fluctuations of the water table, which lead to consistent variations of the displacement rate. Such a behaviour is generally assumed to be governed by soil viscosity; in particular, the increase of the mobilized friction angle with the displacement rate is attributed to rate effects, which however in many cases seem to be overestimated. The paper focuses on some aspects of the problem that are often neglected.

Keywords: stiff clay, slow active landslide, stress field, mobilized shear strength.

Introduction

Slow translational slides in stiff fine-grained deposits are widespread in the world and in Italy in particular. The initial displacement rate is often moderate to rapid, then it gradually decreases to slow or extremely slow; in the long-term, it eventually drops to mms or tens of mms per year with peaks in the wet season and, sometimes, a temporary arrest in the dry season. Landslides starting in the form of earthflows display the same behaviour, gradually turning into slow slide-style movements; in the final stage of evolution, in fact, the typically high shear strains, which initially involve the entire landslide body, tend to concentrate into a thinner basal shear zone.
In the technical literature these long-lasting slow landslides are often referred to with the ambiguous term creep, highlighting in this way the role that is presumably played by soil viscosity. Moreover, the increase of the mobilized friction angle associated with the growth of the displacement rate due to the rising of the water table is generally explained to be just a rate effect. A correct interpretation of the landslide behaviour should however account for further factors that are sometimes disregarded.

Considerations about the mechanics of slow landslides in clay

Experience shows that the behaviour of slow landslides is characterized by a well-defined relationship between depth of the groundwater table and displacement rate, which increases as the groundwater table rises; this relationship appears to be non-linear (see for example Corominas et al., 2005). Some Authors (Bertini et al., 1986) have also recognized a hysteretic landslide behavior, characterized by higher velocity peaks, for the same depth of the water table, in the stage of water table rising than in the stage of water table lowering.
As mentioned above, the mechanical landslide response is usually thought to be governed by soil viscosity. Referring in particular to reactivated slides, creep should be already operative before full mobilization of the residual shear strength, φ'_r. Then, since the safety factor should

maintain a unit value as far as the movement remains slow, the decrease of the normal effective stress on the slip surface due to rising of the water table is assumed to be compensated by a parallel increase of viscous nature of the mobilized residual friction angle. Referring to the theoretical case of an infinite slope having an angle of 10.5° and a depth of 5 m, and assuming that the residual strength is mobilized when the water table is just at depth of 5 m, in the usual hypothesis of water flow parallel to the slope and γ_{sat} = 20 kN/m^3, it is easy to calculate a mobilized friction angle comprised between 10.5° and 20.3°, the highest value being operative when the groundwater table reaches the ground surface. In this respect, it is worth to mention that such an example is not unrealistic; in fact, it is based on data collected through the monitoring of the Masseria Marino earthflow (Picarelli et al., 2005), which presents a residual friction angle of 11.4°. What is important to outline is that the wide range of values of the mobilised friction angle, which can be calculated in many other similar cases, does not match any published laboratory data, which generally recognize a modest increase of φ'_r with the displacement rate, v, usually in the range of not more than 1°-2° per log increase of v (Kenney, 1967; Skempton, 1985; Mesri & Huvaj-Sarihan, 2012).
Certainly, the problem is more complicated than described above. First, pre-failure creep deformations should be clearly recognized in order to correctly calculate the initial mobilized residual friction angle, which might be higher than the virtual value corresponding to the start of movement; moreover, the dependence of the residual friction angle on the effective normal stress due to an often significant non-linearity of the residual failure envelope that entails a decrease of the residual friction angle with the increase of the effective stress, should be accounted for (Picarelli et al., 2022); finally, the actual variation of the effective stress on the slip surface due to rainwater infiltration and water table recharge should be carefully calculated for a correct assessment of the mobilized friction angle. The effect of rainwater infiltration on internal stress field and mobilized shear strength by a slow-moving landslide is just the object of this paper.

The investigated case

The considerations presented in the following are based on the analysis of the response to rainfall of an infinite slope, a model that is widely used to simulate the behaviour of translational landslides on gentle clayey hillslopes. In this case, however, it takes into account the presence of a basal shear zone, which incorporates the slip surface. The thickness of the shear zone is generally very thin (Skempton & Petley, 1967); earthflows, which may present much a thicker and highly remoulded shear zone (Guerriero, 1995), represent a special case.
As mentioned above, the mobilized residual friction angle is often calculated through a simplified approach, assuming water flow parallel to the ground surface, thus neglecting the effects of the actual hydraulic process that leads to the recharge of the aquifer. To focus on this aspect of the problem accounting for the presence of the shear zone, some numerical analyses have been carried out through the F.E. code SEEP/W considering a slope (Fig. 1) characterized by the same angle (10.5°), total depth (5 m) and unit weight (γ_{sat} = 20 kN/m^3) as the Masseria Marino earthflow. The effects of rainwater infiltration on the pore water pressure regime in the wet season have been investigated in a simplified way by imposing nil pore pressure, u, at the ground surface over 6 consecutive months (wet season), in this way assuming the constant presence of a water film on the ground surface. The hydraulic and mechanical soil properties adopted in the analysis (see Fig. 1) are those which were measured in the Masseria Marino earthflow body (Comegna & Picarelli, 2008): the average values, which are shown in Figure 1, highlight the high compressibility and anisotropy of the shear zone, due to remoulding and shearing respectively. In the analysis, three different values of the shear zone thickness, d, have been adopted, i.e.: 5 cm, a value that probably represents an

upper limit for many slides, 40 cm, which is the average value measured in some earthflows in the Basento valley (Guerriero, 1995), and 100 cm, which is the highest measured value in the same earthflows (Comegna, 2005). All results are compared with those concerning the case $d = 0$, i.e., in the absence of a shear zone.

Soil	K_n [m/s]	K_p [m/s]	m_v [kPa^{-1}]
earthflow body	2.2E-09	2.2E-09	3.7E-05
shear zone	8.6E-11	4.7E-10	8.0E-05
parent formation	1.5E-09	1.5E-09	2.3E-05

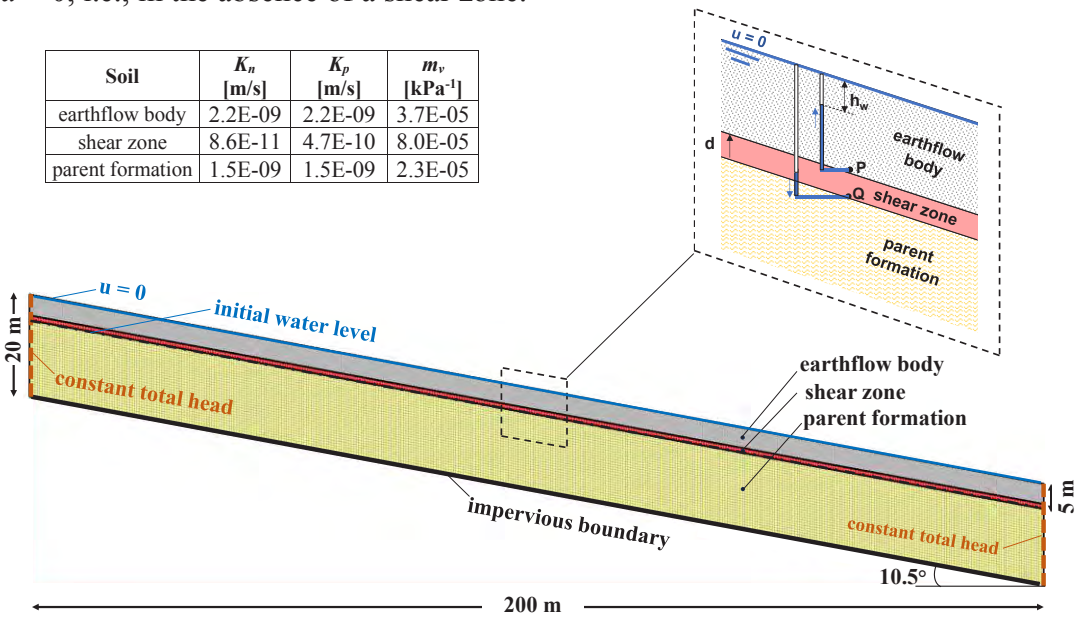

Figure 1. Slope section, hydraulic boundary conditions and soil properties adopted in the analysis (hydraulic conductivity normal to the slope direction, K_n; hydraulic conductivity parallel to the slope direction, K_p; volumetric compressibility, m_v).

The results of the analysis are presented in the Figure 2. Figure 2a, in particular, shows the evolution of the water level, $h_w = z–u/\gamma_w$, at points P and Q (Fig. 1) located just above the shear zone and the slip surface respectively, while Figure 2b presents the direction of the seepage vectors at the same points P and Q, through the angle β that they form with the horizontal. Finally, Figure 2c shows the mobilized friction angle (assuming nil cohesion) along the slip surface, i.e. at point Q; it of course depends on the actual normal effective stress. What clearly emerges from these results is the important role played by the shear zone, at least when it presents a not negligible thickness. As shown in Fig. 2a, the infinite slope model tends to overestimate the values of h_w in the shear zone, because of the combined effect of the lower permeability and of the lower stiffness of the soil, which govern the rate of water absorption. As a consequence, due to the quite high normal effective stress associated with the actual water flow conditions, the mobilized friction angle, φ'_{mob}, which ranges between about 12.5° and 14.5° as a function of d, compared to the measured value of 11.4°, is however lower than that provided by the simplified model (about 17.5°, for $d = 0$). In the case $d = 0.05$ m, which should represent the one of slides, the influence of the shear zone is lower, leading to higher values of the mobilized friction angle (a little less than 17°). Naturally, as previously mentioned, the non linearity of the residual failure envelope and the creep mechanisms that precedes actual landslide "reactivation", might have a significant influence on the mobilized friction angle, minimizing even more the influence of the rate effects.

Conclusions

The evolution of slow active landslides in clay is characterized by displacement rates that fluctuate according to the oscillations of the water table. Such a behaviour is often considered to be governed by soil viscosity; in particular, any increase of the velocity is thought to mobilize an increasing component of resistance due to the viscous nature of clay.

Simple analyses of the effects of rainwater infiltration in a schematic landslide model based on the results of in depth investigations on soil properties, show that actual hydro-mechanical processes governing the effective stress field, coupled with other neglected factors can, at least in some cases, significantly downgrade the role that is often attributed to soil viscosity.

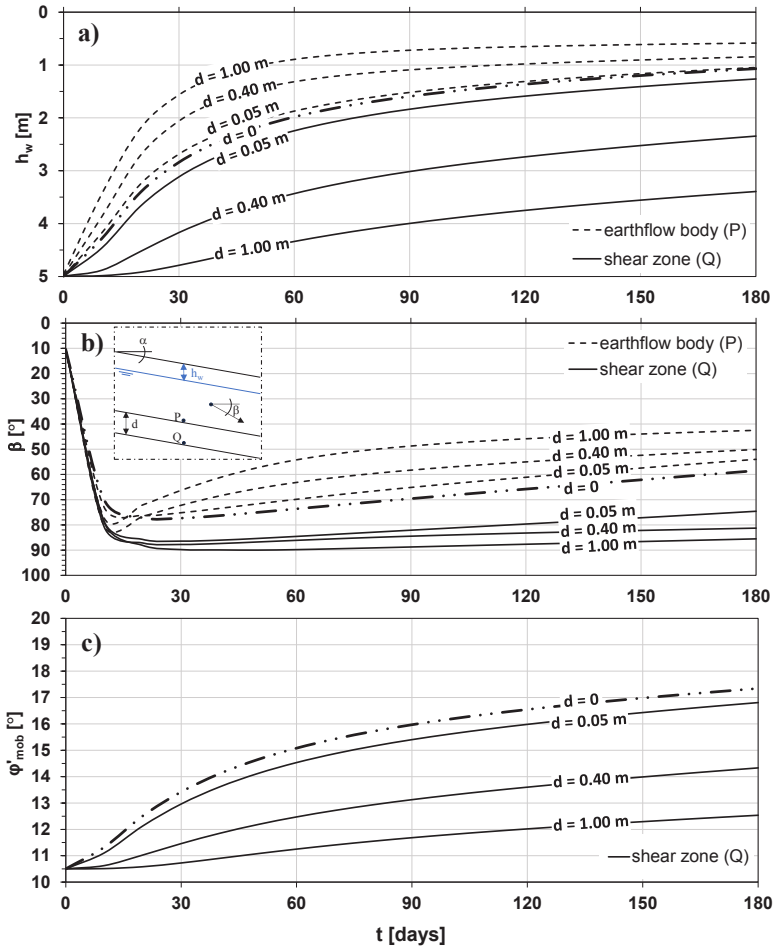

Figure 2. Results of the analysis: a) calculated water levels at points P and Q; b) inclination to the horizontal of the seepage vectors at the same points; c) mobilized friction angle along the slip surface.

References

Bertini T, Cugusi F, D'Elia B, & Rossi-Doria M (1986) Lenti movimenti di versante nell'Abruzzo adriatico: caratteri e criteri di stabilizzazione. *Proc. 16th Italian Geotechnical Conf., Bologna* 1, 91-100.

Comegna L (2005) Proprietà e comportamento delle colate in argilla. PhD Thesis, Seconda Università di Napoli.

Comegna L & Picarelli L (2008) Anisotropy of a shear zone. *Géotechnique* 58(9), 737-742.

Corominas J, Moya J, Ledesma A, Lloret A & Gili JA (2005) Prediction of ground displacements and velocities from groundwater level changes at the Vallcebre landslide. *Landslides* 2, 83-96.

Guerriero G (1995). Modellazione sperimentale del comportamento meccanico di terreni in colata. PhD Thesis Università di Napoli Federico II.

Kenney TC (1967) The influence of mineral composition on the residual strength of natural soils. *Proc. Geotech. Conf. on The Shear Strength of Natural Soils and Rocks*, Oslo 1: 123-129.

Mesri G & Huvaj-Sarihan N (2012) Residual shear strength measured by laboratory and mobilized in landslides. *J. of Geotechnical and Geoenvironmental Engineering*, 138(5): 585-593.

Picarelli L, Comegna L & Urciuoli G (2022) The friction angle mobilized by shallow earthflows in tectonized clay shales. *Italian Geotechnical Journal* 56(1), 5-16.

Picarelli L, Urciuoli G, Ramondini M & Comegna L (2005) Main features of mudslides in tectonized highly fissured clay shales. *Landslides* 2(1): 15-30.

Skempton AW (1985) Residual strength of clays in landslides, folded strata and the laboratory. *Géotechnique* 35(1): 77-101

High Fluidity in Flowslide Induced by Shear Thinning

Yan Li[1], Wei Hu[1], Qiang Xu[1], Mauri McSaveney[1,2] Gonghui Wang[3],

[1]State Key Laboratory of Geo-Hazard Prevention and Geo-Environment Protection, Chengdu University of Technology, Chengdu, China
[2]GNS Science, Lower Hutt, New Zealand
[3]Disaster Prevention Research Institute, Kyoto University, Japan.

SUMMARY: We performed flume experiments and ring shear tests with natural co-seismic landslide deposits to study the dynamics of flowslide, which are destructive due to their high fluidity. Our experiments showed that flowslide could exhibit high fluidity even in the absence of pore pressure. We conducted drained ring shear experiments with a transparent shear chamber. Thus, the granular velocity distribution profiles and the shear zone thickness can be directly observed, and the rheology of the saturated granular flow can be obtained. Ring-shear experiment results showed that the apparent viscosity of the granular flow decreased with the increase of shear rate, which was termed as "shear-thinning" behavior. The shear-thinning behavior can well explain the flowslide high fluidity in some conditions.

Keywords: Flowslide; High fluidity; Rheology of granular flow; Transparent ring shear tests; Acoustic emissions

Introduction

A flowslide can be simplified as a sliding mass moving on (or without) a thin liquefied basal layer (Hungr, 1995; Iverson, 2005). The slide mass above the basal shear layer is simplified as a slide mass (or a number of blocks contacting each other) with a depth-average velocity. A regulation of Coulomb friction by dilation or contraction of water-saturated basal shear zone was used to estimate the landslide mobility (Iverson, 2005). However, the slide mass in a real flowslide will exhibit evident flow-like behavior, which is an apparent fluid rather than a solid mass. A method that adequately describes the flowslide fluidity and a further explanation for the fluidization mechanism is still needed.

The flowslide fluidity can originate from intergranular physics as it does with dry granular flows (rock avalanches), or from the viscosity of the interstitial fluid. Bagnold (1954) introduced dispersive pressure caused by successions of granular collisions, and found that the pressure is related to the shear strain rate. The dispersive pressures can play a similar role as the excess pore pressure, reduce the effective grain-grain contacts, and increase the fluidity of granular mass flows (Iverson & Vallance, 2001). However, the fluidity caused by granular agitations is likely to be ignored due to the obvious excess pore pressure accompanying the motion stage. However, strict experimental evidence is still needed to take further insights into the intergranular mechanisms and rheology of saturated granular flow without the interference of excess pore pressure.

In this work, we use transparent ring shear experiments to provide direct observation of the variation in shear zone thickness and granular velocity distributions. This makes it possible to well determine the shear strain rate and thus the viscosity of the granular flow. The drained ring shear experiment is designed to simulate a mechanical element inside a real flowslide under (quasi-) real stress state over a wide range of shear speeds. We obtained rheology to better describe the real flowslide fluidity. We also conducted miniaturized flume experiments to reproduce flowslide dynamics, and the experimental data including velocity profiles, pore pressure evolutions, acoustic emissions, etc. are simultaneously recorded. The evolution of the velocity profiles in flume experiments demonstrates that the fluidity of slide mass increases significantly with the increase of shear velocity, which is consistent with the shear-thinning behavior obtained from the ring-shear experiments. By using acoustic emission measurements combined with dimensionless analysis, we took further insights into the mechanisms of the shear thinning behavior in saturated granular flows, which can induce flowslide high fluidity.

Results

In the flume experiment, the initial compactness was close to its critical state (Dr=0.57), so there was no evident shear-induced non-equilibrium pore pressure. The fluidity of flowslide independently of excess pore pressure can be well observed. The fluidity of the flowslide was recognized from the velocity distribution patterns (Fig. 1). In the low-velocity initiation and deposition state, the granular mass behaved as a quasi-solid and slid on a sliding surface or bedding plane with uncoordinated velocity distribution profiles. With increasing velocity, the granular mass gradually flowed in a more ordered manner as a viscous fluid as it entered the fluid phase, with a coordinated flow-like velocity distribution, i.e. the Bagnold profile. Such fluidized behavior is generally attributed to a shear-induced positive pore pressure. However, no fluctuation of pore pressure was evident in this physical experiment. It was inferred that the pore-pressure increase of about 1 kPa was mainly due to their changed positions rather than being shear-induced. This inference was made because the pore-pressure values remained at the same level after the motion had stopped. The solid-fluid phase transition and the fluidity of the granular flow were strongly correlated with velocity, as is visible in Fig. 1. The more flow-like velocity distributions corresponded to the higher velocity gradients with depth. Therefore, we make the hypothesis that the velocity-related fluidity originates mostly from the intrinsic rheology of saturated granular flow.

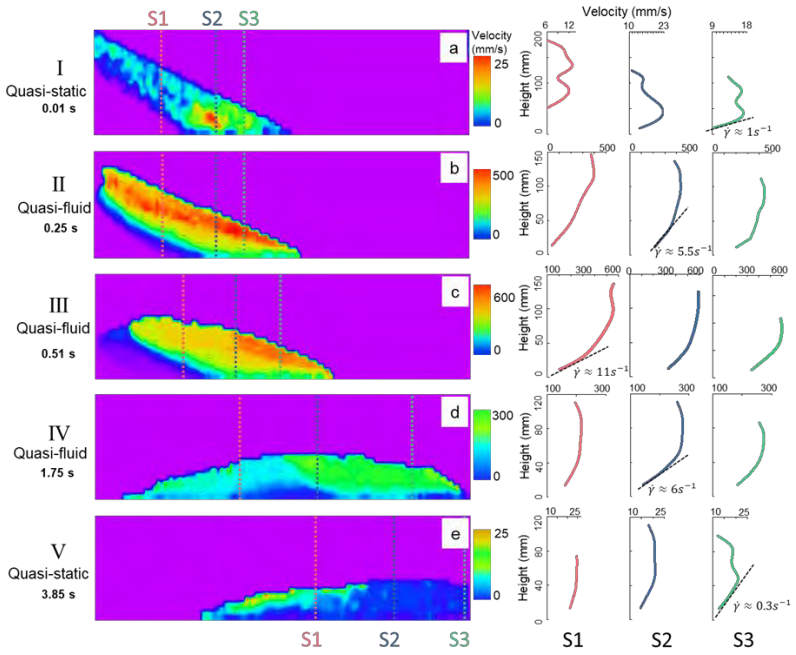

Figure 1. Evolution of the velocity field and velocity profiles in different sections (S1-S3). t = 0 s is the moment of initiation.

In order to further understand the fluidity of saturated granular material under natural conditions, a series of drained ring-shear experiments were conducted (Fig. 2). The shear speed varied from 1 mm/s to 500 mm/s, while the normal stress was kept constant at 30 kPa and 100 kPa (corresponding to burial depths of about 2 m and 6.7 m) respectively, which is frequently occurring stress conditions in natural shallow landslides and flowslide. An external torque was applied on the bottom plate to maintain the assigned shear speed, and the corresponding shear resistance was recorded. In the experiments, particularly at high shear speeds, grain segregation, abrasion, and crushing are inevitable. However, these phenomena also occur in natural flowslide. In the low-speed drained shear experiments (<50 mm/s), the pore pressures remained at 0 ± 1 kPa (a fully drained boundary condition). While for high-speed drained experiments (>50 mm/s), a slight rise in pore pressure (approximately 5 kPa) was observed due to limitations imposed by the valve-drainage rate, which was a partially drained condition. Furthermore, interactions between coarse soil particles may also cause data fluctuation under relatively low normal stress. Despite these inevitable influences, the experimental results showed two types of flow behavior for crushable natural materials. Under lower shear speed (shear speed $\leqslant$ 100 mm/s), results of the ring shear experiments exhibited strengthening of steady-state shear resistance with increasing shear speed, demonstrating that the system was in the dense inertial regime (Kuwano et al., 2013).

When the shear speed exceeded 100 mm/s, the steady-state shear resistance was slightly weakened, which was possibly associated with the granular crushing (Hu et al., 2020).

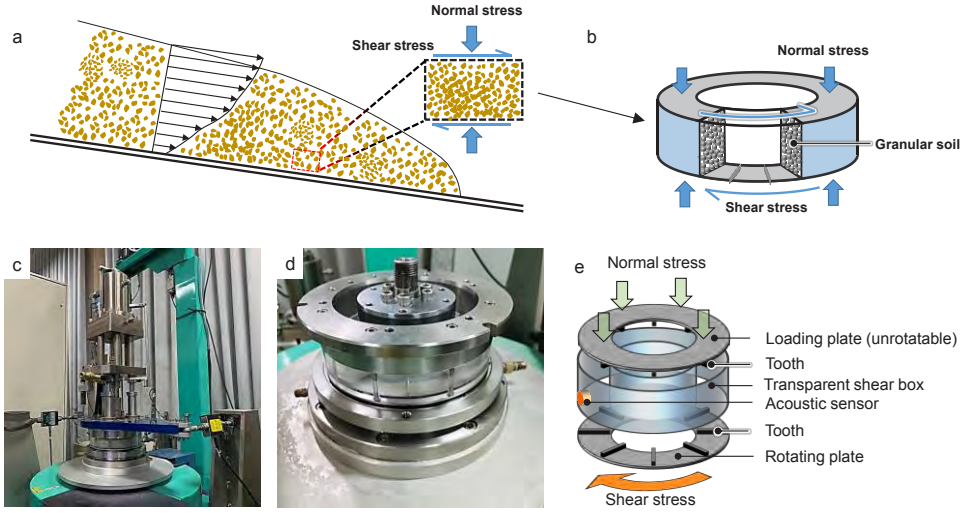

Figure 2. (a) Illustration of the concept of modeling a flowslide. Both basal friction and flow-like behavior of slide mass may exist in a flowslide. (b) The mechanical model of the "Bromhead" mode ring shear tests, which is convenient to simulate a long-distance shear of granular flow in the slide mass. (c) ICL-2 ring shear machine. (d) The photo and (e) the schematic diagram of the transparent shear chamber without a forced shear surface.

The soil particle motions were well captured by a high-speed camera in this work. A PIV system was used to process the high-speed images to measure the shear rate of the viscous shear zone and the particle velocity distribution within it. The particle shear velocity $u(y)$ was calculated by the average value over horizontal sections of the sample. The shear strain rate, e.g. the derivative of the velocity in the direction perpendicular to the rotating plate $(\partial u(y))/\partial y$, was almost constant; thus, we could define the mobilized shear zone as a plane shear flow, and its height was equal to the flow-like shear zone thickness. The hydrodynamic expressions below were used to determine the rheology of the granular flow (Coussot & Proust, 1996):

$$\tau = \tau_0 + K\dot{\gamma}^n \quad (1)$$

$$\dot{\gamma} = \frac{\partial u(y)}{\partial y} \quad (2)$$

where τ is the shear stress, τ_0 is the yield shear stress, the shear rate $\dot{\gamma}$ is the derivative of the fluid speed $u(y)$ in the direction perpendicular to the shear plates, K is a consistency index, and n is the flow index. For n< 1, the fluid is shear-thinning, whereas for n> 1 the fluid is shear-thickening.

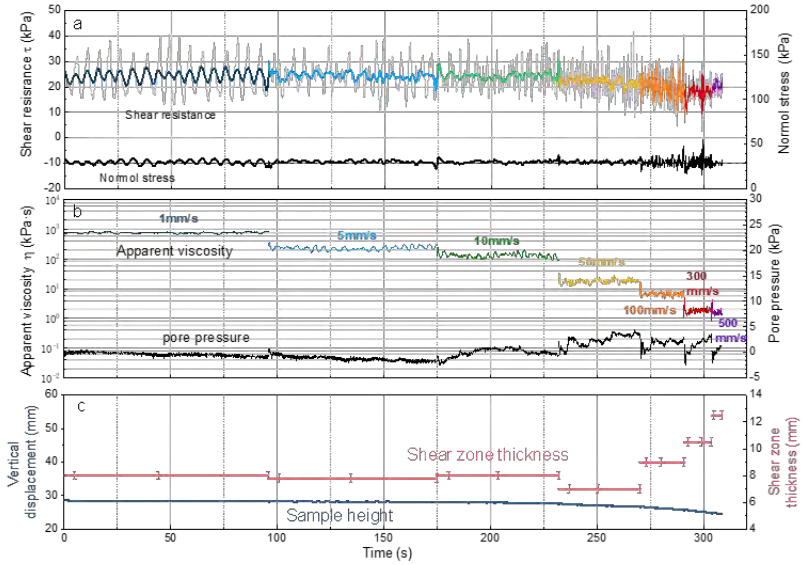

Figure 3. Experimental data of ring-shear tests under 30 kPa normal stress: (a) variation of the shear resistance and (b) viscosity with increase in shear speed, and (c) simultaneous variation of sample shear-zone thickness. The experimental data under 100 normal stress kPa was shown in the supplementary materials.

The variation in steady-state shear resistance with shear rate followed the rheological expression of Equation (1) (Fig. 3). The flow index n was ~0.13 from the experiment under 30 kPa normal stress, and $n \approx 0.22$ from 100 kPa normal stress experiment, indicating substantial shear thinning of the saturated granular soil in different confining pressure. The yield shear strength of the material could not be ignored. The granular soil exhibited Bingham pseudoplastic behavior and could be classified as a Herschel-Bulkley fluid (Coussot & Proust, 1996) during the drained shear experiments. The viscosity can be calculated as a generalized Newtonian fluid by Equation (3), and also can be expressed by Equation (4) with the same parameters in Equation (1).

$$\eta(\dot{\gamma}) = \frac{\tau}{\dot{\gamma}} \tag{3}$$

$$\eta(\dot{\gamma}) = \begin{cases} \eta_0 & |\dot{\gamma}| \le \dot{\gamma}_0 \\ K|\dot{\gamma}|^{n-1} + \tau_0|\dot{\gamma}|^{-1} & |\dot{\gamma}| \ge \dot{\gamma}_0 \end{cases} \tag{4}$$

It can be seen that the viscosity significantly decreased from nearly 103 kPa·s to several kPa·s as the shear speed increased from 1 mm/s to 500 mm/s. Fig.10b clearly showed shear-thinning behavior with the viscosity η of the saturated material significantly decreasing with increase in shear rate under different confining pressure. This shear-rate-dependent weakening in shear resistance (decrease in apparent viscosity) well described the high fluidity of the flowslide during high-speed motion.

Conclusion

We conducted flume experiments and transparent ring shear experiments to investigate the fluidized mechanisms and introduced a method to better describe the flowslide fluidity. The flume experiments were conducted to reproduce the miniaturized flowslide dynamics, while the ring-shear experiments are designed to simulate a mechanical element inside real flowslide. In the flume experiments, we observed shear-rate-dependent fluidity of slide mass through the evolution of velocity profiles. For further insights into this shear-rate-dependent behavior, we conducted transparent drained ring-shear experiments with the saturated granular material over a range of shear speeds (1–500 mm/s) under 30 and 100 kPa normal stresses. We obtained not only the shear resistance but also the apparent viscosity by direct measurements of the shear strain rate. Experimental results demonstrated that once the yield shear strength was overcome, the granular flow showed a substantial weakening in apparent viscosity with an increasing shear rate. This shear thinning well explained the ultra-high fluidity in flowslide.

References

Bagnold, R. A. (1954). Experiments on a gravity-free dispersion of large solid spheres in a Newtonian fluid under shear. Proceedings of the Royal Society of London. Mathematical and Physical Sciences, 225, 49–63.

Coussot, P., & Proust, S. (1996). Slow, unconfined spreading of a mudflow. Journal of Geophysical Research: Solid Earth, 101(B11), 25217–25229. https://doi.org/10.1029/96jb02486

Hungr, O. (1995). A model for the runout analysis of rapid flow slides, debris flows, and avalanches. Canadian Geotechnical Journal, 32(4), 610–623. https://doi.org/10.1139/t95-063

Iverson, R. M., & Vallance, J. W. (2001). New views of granular mass flows. Geology, 29(2), 115–118. https://doi.org/10.1130/0091-7613(2001)029<0115:NVOGMF>2.0.CO;2

Iverson, R. M. (2005). Regulation of landslide motion by dilatancy and pore pressure feedback. Journal of Geophysical Research, 110(2), 1–16. https://doi.org/10.1029/2004JF000268

Kuwano, O., Ando, R., & Hatano, T. (2013). Crossover from negative to positive shear rate dependence in granular friction. Geophysical Research Letters, 40(7), 1295–1299. https://doi.org/10.1002/grl.50311

Hu, Wei, Chang, C. S., McSaveney, M., Huang, R., Xu, Q., Zheng, Y., & Yu, J. (2020). A Weakening Rheology of Dry Granular Flows With Extensive Brittle Grain Damage in High-Speed Rotary Shear Experiments. Geophysical Research Letters, 47(11), 1–10. https://doi.org/10.1029/2020GL087763

Landslide Modelling using a High-Resolution Three-Dimensional Slope Stability and Multi-Phase Mass Flow Model

Avinash Sajwan[1], G.V. Ramana[2]

[1] Research scholar, Department of Civil Engineering, Indian Institute of Technology Delhi, India-110016
[2] Professor, Department of Civil Engineering, Indian Institute of Technology Delhi, India-110016

SUMMARY: Landslides present a significant hazard to humans and the built environment and require accurate prediction and modelling to develop a resilient infrastructure against landslides. Of late, the advances made in the numerical modelling of landslides can capture the complex landslide behaviour often overlooked by physical models and analytical approaches. This study analyses the landslide hazard at a hydropower structure using a high-resolution Digital Terrain Model (DTM), three-dimensional slope stability and subsequent mass flow from a slope failure using a multi-phase mass flow model. Initially, the location and depth of failure obtained using the traditional slope stability analysis are used as an input for the mass flow model. Finally, the kinematics of landslides, such as flow depth, velocity and runout distance, are analysed using the multi-phase mass flow model. In the slope stability assessment, the area near the hydropower structure was stable, and a vulnerable slope was identified 350 m uphill from the reservoir. Subsequently, mass flow analysis was carried out from i) the most critical zone and ii) the entire critical zone. The failed mass from these zones impacts the reservoir as well as can potentially damage the structure. Hence, this study highlights the importance of mass flow modelling in addition to the slope stability assessment for improved landslide hazard assessment.

Keywords: Landslide, multi-phase, runout distance, resilient infrastructure

Introduction

A resilient infrastructure against landslides needs to endure and recover from the impacts of landslides while reducing infrastructure vulnerability and ensuring functionality and serviceability (Hill & Kakenmaster, 2020). The pressing need for resilient infrastructure against landslides marks the importance of numerical tools in landslide modelling, as physical models are often expensive and do not fully capture the complex physics associated with landslides, and analytical methods oversimplify the interactions inherent in these flows (Booker et al. 1989; Schweiger et al. 2019). Numerical methods can address the complexities of landslides and play a vital role in predicting and mitigating landslide hazards. Traditionally, mesh-based methods such as Finite Element Method (FEM), Finite Difference Method (FDM) have been used widely to model several aspects of landslides due to lesser computational requirements and more straightforward interpretation (Augarde et al., 2021). The kinematic characteristics of mass flows, such as flow depth, velocity, and runout, are intricate and influenced by the composition and interactions of varied materials. Moreover, non-homogeneous soil, rock, ice, and water matrices within these mass flows further complicate the analysis, necessitating a multi-phase approach to simulate their behaviour accurately (Pudasaini and Mergili 2019). In this study, landslide hazard assessment near a slope close to a hydropower structure is carried out using a high-resolution DTM, three-dimensional slope stability and multi-phase mass flow model.

Study area

The study area is located in the Northeastern region of India (exact location cannot be disclosed due to agreement with the client). Figure 1 depicts the orthophoto, elevation and slope in the study area. A National Highway (NH) was proposed near a hydropower structure in this study area. The hydropower was constructed taking into consideration the slope instability in the region. However, the alignment and construction of the NH near the hydropower structure have increased the vulnerability to slope failure. The hydropower structure, which was safe earlier, may now come in the path of the mass flow in case of a slope failure.

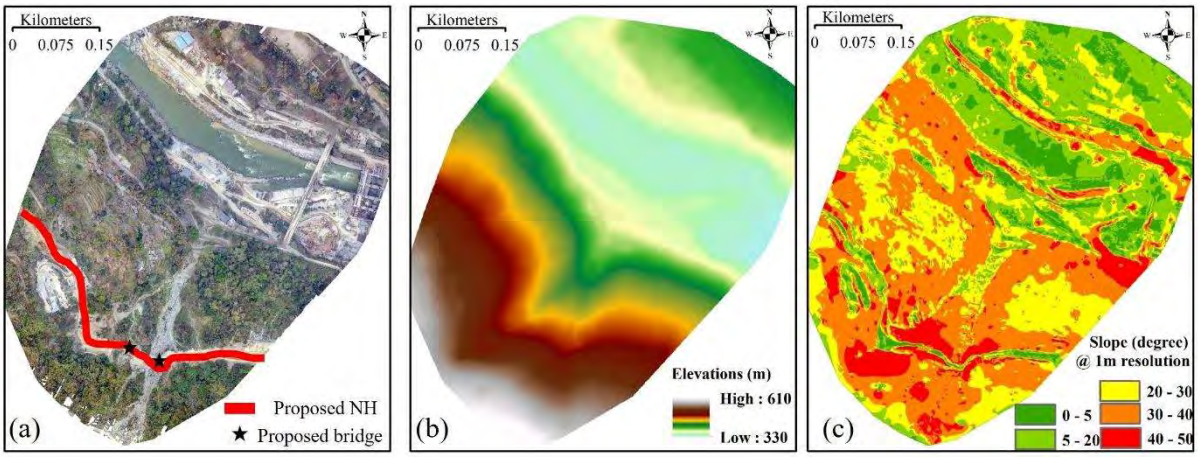

Figure 1. (a) Orthophoto, (b) Elevation map, and (c) Slope map of the study area.

Material and Methods

We used a DTM of 1m spatial resolution (resampled from 5 cm DTM) from an aerial survey to include the topography of the study area. The laboratory tests (Grain Size Distribution, Direct Shear Test, Relative density) were carried out in triplicates on disturbed representative soil samples (depth up to 5 m) collected from proposed bridge locations (Fig.1a). The soil was characterised as silty sand (SM) with 23%, 63.6% and 13.4% of gravel (> 4.75 mm), sand (0.074 – 4.75 mm) and fines content (< 0.074 mm) respectively. The DST was conducted under saturated conditions at normal stress of 50, 100, and 200 kPa for soil samples prepared in the laboratory at 85% relative density. The average results are summarised in Table 1. They are adopted as geotechnical parameters in the slope stability and mass flow model.

Table 1 Geotechnical parameters used in slope stability and mass flow model.

Parameter	Symbol	Unit	Value
Solid density	ρ_s	kgm^{-3}	2600
Fine solid density	ρ_{fs}	kgm^{-3}	1800
Fluid density	ρ_f	kgm^{-3}	1000
Angle of shearing resistance	ϕ	degree	40
Cohesion	c	kNm^{-2}	0
Phase fractions (solid: fine solid: fluid)	α	-	9:4:7

Numerical tools for slope stability analysis and multi-phase mass flow modelling

A Geographic Information System (GIS) supported, open-source, three-dimensional slope stability model, r.slope.stability (https://www.landslidemodels.org/r.slope.stability) is adopted to compute the Factor of Safety (FOS) based on the Hoveland method using ellipsoidal or truncated sliding surface, DTM, geotechnical parameters, and soil depth (Cordoba et al., 2020). A GIS-enabled open-source software, r.avaflow (www.landslidemodels.org/r.avaflow), is adopted to simulate multi-phase mass flows by considering the motion and interaction of distinct phases (coarse solid, fine-solid, and fluid) captured by best suitable rheology. The details of the numerical framework are outlined thoroughly in Pudasaini & Mergili (2019).

Methodology

A high-resolution DTM, saturated soil conditions, soil depth of 2.5m (based on site survey) and model parameters given in Table 1 are used to compute the FOS for the probable-case scenario (Fig. 3a) and worst-case scenario (Fig. 3b). Initially, the slope stability model is employed to identify the location and depth of all the unstable zones based on a computed FOS as the worst-case scenario. Thereafter, the most unstable zone was identified as the probable-case scenario using a refined search based on the most critical slip surface from the worst-case scenario. Subsequently, the mass flow model is employed to compute the kinematics of failed mass from these identified unstable slopes.

Results and Discussion

The slope instability and mass flow propagation from the most critical zones are illustrated in Figure 2 as a probable case. The unstable zones (Fig.2b) and depth of failure (Fig.2c) are determined based on computed FOS (Fig.2a) from the slope stability analysis. Figure 2 (d1-d3) shows the mass flow propagation from the most unstable zone located 350 m uphill from the reservoir. The failed mass travels downhill with a maximum flow depth and velocity of 7.80 m and 28.9 m/s, respectively. If not remediated, the mass flow reaches the reservoir site within 20 seconds, which can be disastrous for the existing infrastructure and onsite personnel.

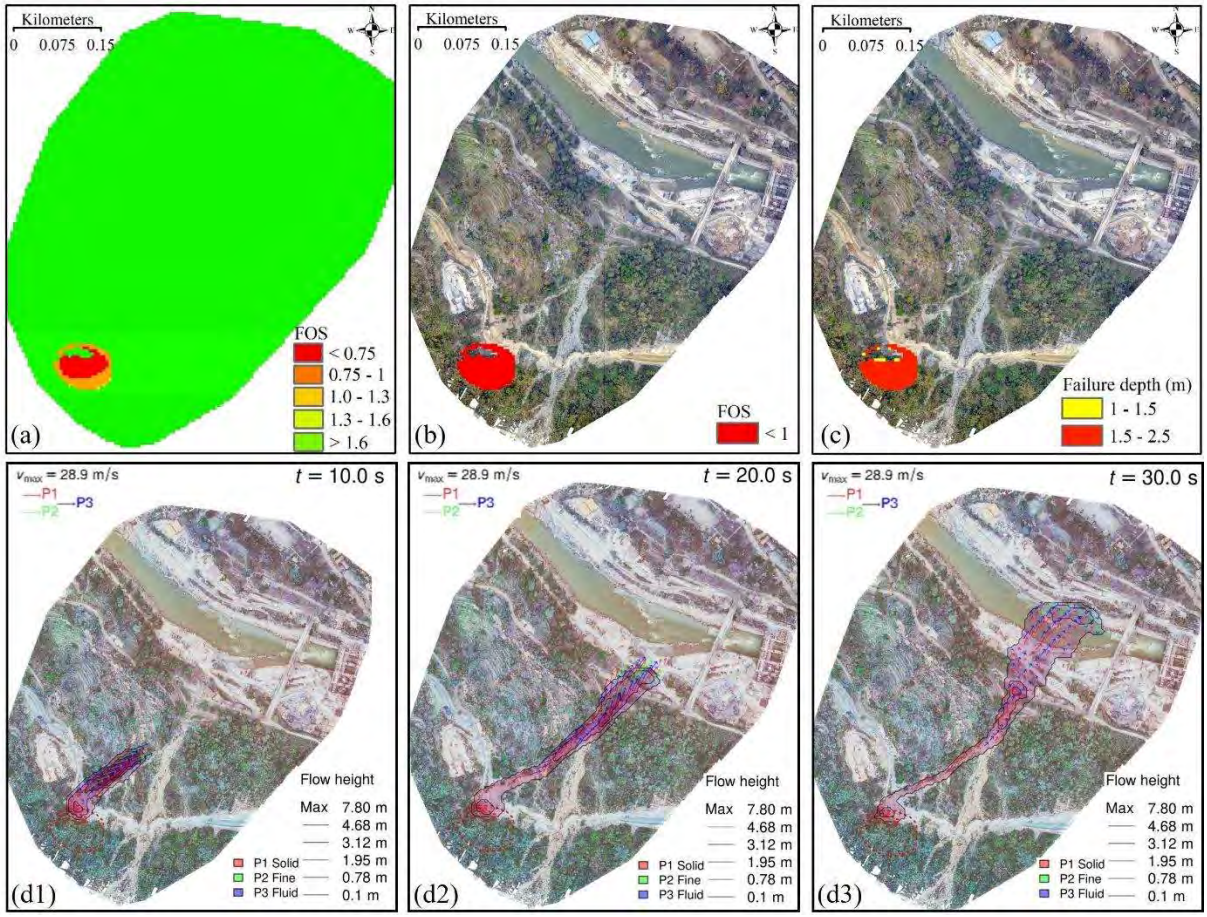

Figure 2. Results of slope stability (a) FOS, (b) Unstable zones, (c) failure depth and (d) propagation of multi-phase mass flow at time (t) (d1) 10 sec, (d2) 20 sec, and (d3) 30 sec after initiation.

Figure 3 illustrates a worst-case scenario considering the slope instability and mass flow propagation from the entire unstable zone. The vulnerable zones (Fig.3b) and associated failure depths (Fig.3c) are obtained based on a computed FOS (Fig.3a). The slope material from all the unstable zones travels downhill with a maximum flow depth and velocity of 11.6 m and 30.1

m/s respectively (Fig. 3(d1-d3)). The maximum flow depth and velocity increase by 48.72% and 4.15%, respectively, for the worst case compared to the probable case.

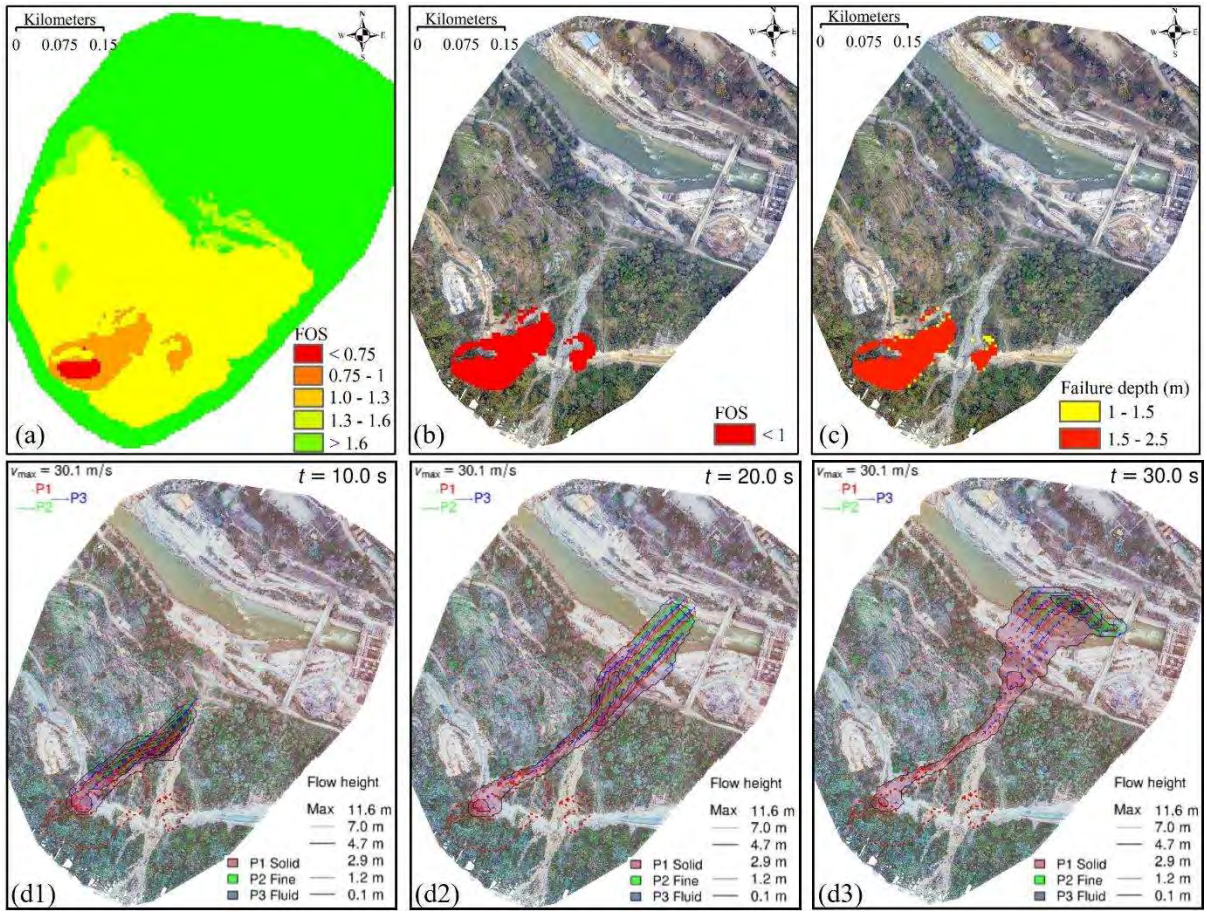

Figure 3. Results of slope stability (a) FOS, (b) Unstable zones, (c) failure depth and (d) propagation of multi-phase mass flow at time (t) (d1) 10 sec, (d2) 20 sec, and (d3) 30 sec after initiation.

Conclusions

The sequential process of triggering and propagation of landslides near a hydropower structure was modelled using slope instability and a multi-phase mass flow model considering a probable and a worst-case scenario. The reservoir area was safe in the slope stability assessment based on computed FOS using limit equilibrium methods but came under imminent threat from the mass flow studies. This study highlights the importance of conducting multi-phase mass flow modelling in addition to traditional slope stability assessment for improved landslide hazard assessment and constructing resilient infrastructure.

References

Augarde CE, Lee SJ, Loukidis D (2021) Numerical modelling of large deformation problems in geotechnical engineering: A state-of-the-art review. Soils and Foundations 61(6):1718–1735.

Booker JR, Carter JP, Small JC, Brown PT, Poulos HG (1989) Some recent applications of numerical methods to geotechnical analysis. Comput Struct 31(1):81–92.

Cordoba JP, Mergili M, Aristizábal E (2020) Probabilistic landslide susceptibility analysis in tropical mountainous terrain using the physically based r.slope.stability model. Natural Hazards and Earth System Sciences 20(3):815–829.

Hill AC, Kakenmaster W (2020) Resilient Infrastructure: Understanding Interconnectedness and Long-Term Risk. In: Optimising Community Infrastructure: Resilience in the Face of Shocks and Stresses. Elsevier, pp 5–21

Pudasaini SP, Mergili M (2019) A Multi-Phase Mass Flow Model. J Geophys Res Earth Surf 124(12):2920–2942.

Schweiger HF, Fabris C, Ausweger G, Hauser L (2019) Examples of successful numerical modelling of complex geotechnical problems. Innovative Infrastructure Solutions 4(1):2.

Stabilization of a Slow Landslide Affecting a Road Embankment by Rigid Inclusions – Analytical and Finite Element Design Methods

Jonas Verschuere[1],

[1] Hydrogéotechnique Sud Est, Sainte Hélène du Lac (74), France

SUMMARY: The following paper presents the design of the stabilization of a low-height road embankment in an area affected by a slow rotational landslide in clayey ground, in "Haute Savoie" region, France, close Switzerland boundary.

Due to the fact that this road cannot be fully closed, the reinforcement has to be limited to the downhill half of the road. A design with small diameter (250 mm) bored rigid inclusions, armed with steel tubes and capped with large-size concrete plates, has been proposed. The inclusions act both as shear reinforcement of the instable soil layers and load transfer of the road fill and traffic loads to deeper, stable soil layers.

Several methods, including traditional slope stability calculations and Finite Element Method modelling, have been used conjointly to perform a robust detailed design of these inclusions

Keywords: rigid inclusions, landslide, shear reinforcement, finite element method, settlement

Introduction

Road RD18 is located in Haute Savoie (74), close to the boundary between France and Switzerland. This road is heavily used by peopled travelling from France to Switzerland and viceversa. It is built as a low-height roadfill, no more than 2 m high, in a gently sloping area.

Close to the "Arbigny" hamlet of the town of Archamps, a circular landslide affects the road and creates cracks and settlement at the surface, as shown in Figure 1.

Figure 1. View of surface cracks of the road

Several geotechnical and geophysical investigations have been performed in this area, starting in 2011, to try to understand the instability processes occurring at this location and design a reinforcement solution. Cored boreholes used to obtain undisturbed samples for laboratory testing, destructive boreholes with pressuremeter testing, dynamic penetrometer testing, test pits and resistivity surveys have been conducted.

Below the granular roadfill layer, clayey glacial drift deposits are encountered down to at least 10 m deep. These deposits are highly plastic clays (A3 class of French GTR) of low consistency on the top 3 m to 8 m (layer C1a). Below, they become more consistent and less plastic layers (C1b and C1c).

Groundwater conditions are highly variable in the area. In dry season, no water has been encountered in the boreholes, while in wet conditions water levels rise significantly and are close to ground level. Infiltrations from the ditch located uphill is very likely. Geophysical survey has revealed low resistivities in the top C1a layer, associated with high water content and possible underground water flows.

The typical geological cross-section is presented in Figure 2.

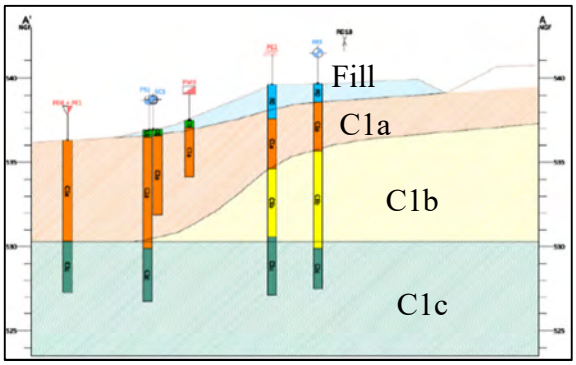

Figure 2. Geological cross-section

Reasons for the observed instability and back-analysis

The reasons for the observed instability are likely be linked with the high plasticity and low consistency of the upper C1a clay layer, together with seasonal variations of the groundwater table level.

A back analysis of the current limit equilibrium situation with a slope stability software, together with laboratory and in-situ testing, has allowed to obtain the geotechnical parameters of Table 1.

Table 1. Design soil parameters

Layer	Bulk weight kN/m³	Friction angle °	Drained cohesion kPa	Drained Young Modulus MPa
C1a	17	17	2	6
C1b	18	21	12	6
C1c	20	27	30	30

Note: As a usual assumption in France, the Drained Young modulus is defined as E_m/α, E_m being the soil modulus measured by the pressuremeter tests and α a rheological coefficient varying between 0.33 and 0.66 depending on type of soil.

Proposed reinforcement solution

The proposed reinforcement solution has to efficiently stop the current movements, which excludes slope drainage works which would lead to increase stability but likely cause additional settlements meanwhile. On the other side, the road has to be kept in operation, so only the downhill part of the road can be temporarily closed, which exclude large-scale reinforcement works such as large diameter bored piles.

These requirements lead us to consider an innovative reinforcement method consisting in small diameter (250 mm), 13 m long bored mini piles armed with steel tubes on a 2 m x 2 m mesh, acting as rigid inclusions. As the thickness of the road fill above the rigid inclusions is small (around 1 m), to avoid differential settlements of the surface of the road, these mini-piles are capped with 0.8 m x 0.8 square concrete caps. The proposed reinforcement is shown in Figure 3 below.

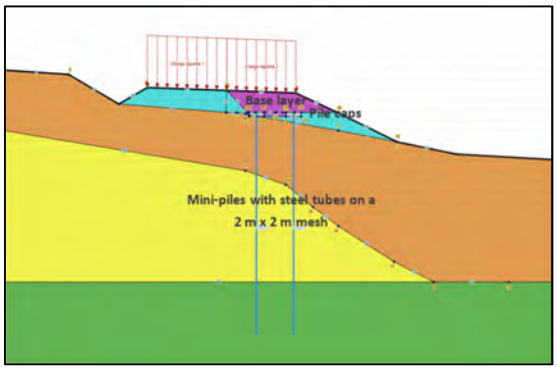

Figure 3. Proposed reinforcement

The works to be performed consist in the following sequence:

- Excavation of the downhill half on the road on 1 m thick,
- Installation of the rigid inclusions and caps
- Backfill of the downhill half of the road,
- Installation of a temporary paving for 4 months to allow for settlement to occur
- Installation of permanent paving

Rigid inclusions have two positive effects:

- Transfer of fill and traffic loads, initially applied to weak layer C1a, to deeper, more stable layers
- Shear reinforcement for layers C1a and C1b

Design calculations

In order to perform a robust design of this innovative solution, two different calculation methods were followed.

The first one uses different analytical tools for each reinforcement mechanism. First, the vertical load transfer effect of the rigid inclusions is evaluated by TASPIE+ module of FOXTA ® software which is based on French recommendations ASIRI (IREX, 2012), and uses transfer functions (elastoplastic "t-z" curves based on pressuremeter test results) to model vertical soil/inclusion interaction, assuming elastic behavior of the soil and an infinite mesh of inclusions. This calculation gives an estimate of the expected post construction settlements.

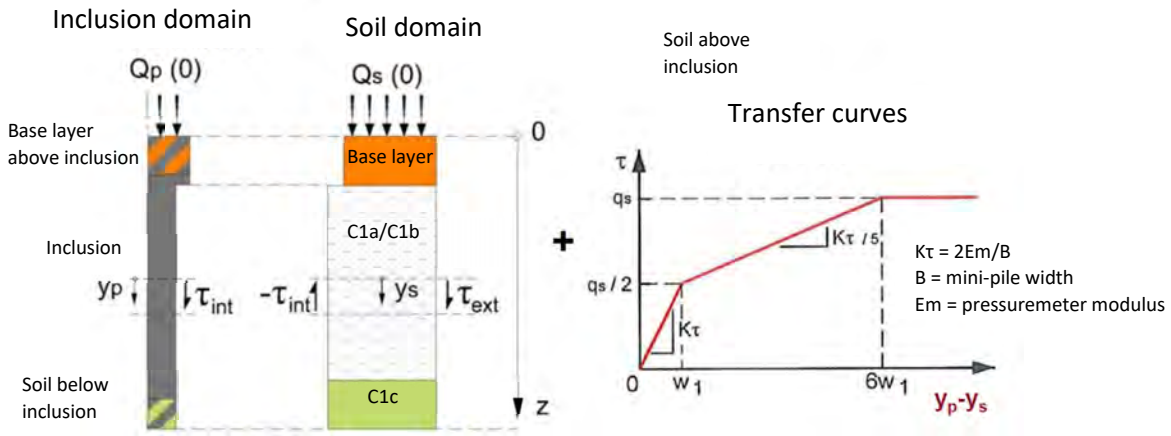

Figure 4. TASPIE+ ® soil/inclusion model

Then, this load transfer effect and the shear reinforcement effect of the inclusions are input in TALREN ® slope stability software to assess the slope stability safety factor after construction.

The second one is a full-scale 2D Finite Element Method (FEM) model using PLAXIS 2D ® software, which allows to encompass all expected effects in a single model. Some model details are presented here below:

- The inclusions are modelled as “embedded beam elements”, which are linear elements connected to the nodes of the 2D-model by transfer functions governing both vertical and lateral behaviors (as elastoplastic “p-y” and “t-z” curves). This feature of PLAXIS 2D ® software allows modelling of rows of “3D” elements such as piles and anchors in 2D models, which is usually a major issue of 2D models.

- An elastic model with Mohr Coulomb plasticity criterium has been defined for all soil layers, with the parameters defined above. The use of a more complex soil model, such as Hardening Soil Model, which would account for unloading/reloading effect, has been considered, but discounted as the current “consolidation status” of natural soil layers under fill weight is unknown, thus it is not possible to clearly define the current boundary between “first loading” behavior and “unloading/reloading” behavior for these soils.

- Due to the low permeability of the soil layers under water level, the groundwater level is considered “phreatic” without considering groundwater flow effect, as flows are likely very slow.

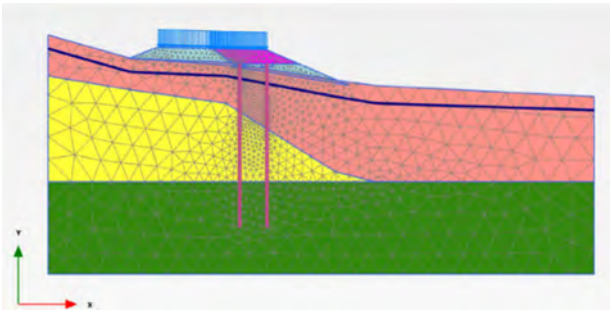

Figure 5. Finite element model mesh

The mesh is shown in Figure 5 on the side.

Both methods give similar results as shown in Table 2 below.

Table 2. Design calculation results summary (unitary coefficients)

Calculation results	Analytical	FEM
Slope stability safety factor	1.42	1.39
Post construction settlements with traffic loads (mm)	3 - 8	7 - 11

Conclusion

Traditional design methods for rigid inclusions works as slope reinforcement generally only consider them either as vertical load bearing elements, transferring surface loads to deeper, stronger layers, or as shear reinforcement elements, acting as a general reinforcement of the weak layers.

In this specific study for the reinforcement of a road affected by a circular landslide, both effects have been considered together in order to optimize the reinforcement as work options were limited due to the need of keeping half of the road open to traffic.

Both analytical and FEM design methods have been used to assess the efficiency of the proposed reinforcement in terms of safety and reduced settlements. Similar results were obtained by both calculations.

References

IREX (2012) ASIRI - Recommandations pour la conception, le calcul, l’exécution et le contrôle des ouvrages sur sols améliorés par inclusions rigides verticales

The operational Shallow Landslide Hazard Forecasting System of the Digital Twin Alps platform: method and applications in the French and Swiss Alps

Clément Michoud[1], Thierry Oppikofer[1], Jean-Philippe Malet[2,3], David Michéa[3], Aline Déprez[3], Pascal Horton[1], Maxim Lamare[4]

[1] Terranum Sàrl, Bussigny, Switzerland
[2] Institut Terre Environnement de Strasbourg (ITES), CNRS/Université de Strasbourg, France
[3] Ecole et Observatoire des Sciences de la Terre (EOST), CNRS/Université de Strasbourg, France
[4] Planet Labs Austria GmbH, Graz, Austria

SUMMARY: Shallow landslides and other natural hazards pose significant challenges in mountainous regions, with growing human activity, infrastructure, and population. To face these challenges, we introduce a prototype for an automated Shallow Landslide Hazard Forecasting System that combines a static landslide susceptibility map with hydro-meteorological triggering factors for the next 3 days. If water inputs from precipitation and snowmelt exceed predefined antecedent rainfall index thresholds, a warning for shallow landslide is triggered and the extent of the potentially affected area is computed. Implemented within the framework of ESA's Digital Twin Alps project, this innovative operative system has been applied and is currently running daily in the Entremont District, Swiss Alps, as well as the Alpes-de-Haute-Provence Department, south-eastern French Alps, contributing to enhance the landslide hazard and risk management in these exposed regions.

Keywords: shallow landslide, hazard forecasting, runout modelling, digital twin, Alps

Introduction

Shallow landslides are a significant natural hazard in many mountainous regions and pose significant challenges for hazard and risk management owing to growing human activity and exposed infrastructure and population. To support stakeholders in their operational mandate for landslide hazard and risk management, the Shallow Landslide Hazard Forecasting System has been developed to forecast areas at risk over a regional territory within the next three days. This system assists stakeholders in identifying areas at risk, allowing them to prioritise protective measures. The approach presented here is similar to well-established techniques, such as the LHASA model (Kirschbaum & Stanley, 2018), which we also applied in Morocco (Michoud et al., 2021). However, the key improvements are the focus on forecasting instead of nowcasting, the high-resolution susceptibility models and the inclusion of snow melting as a triggering factor in combination with the rainfall.

Implemented as a prototype in the Digital Twin Alps initiative sponsored by ESA (digitaltwinalps.com, ESA AO/1-11034/21/I-DT), the Shallow Landslide Hazard Forecasting System serves as a demonstration example of how the Digital Twin concept can act as decision support systems, enhancing our understanding of intricate physical processes useful for Disaster Risk Management (DRM). This innovative automated system has been applied in the Entremont District of Valais, Switzerland, as well as the Alpes-de-Haute-Provence Department in SE France, contributing to enhancing the landslide hazard and risk management in these exposed regions.

Methodology

The implemented processing chain is an automated service to forecast the triggering susceptibility of slopes that are already identified as inherently unstable and to dynamically model their runout extents (Fig. 1). To do so, the service works with a sequence of two models.

First, the Shallow Landslide Failure Forecast model assesses the probability of landslides triggering on slopes over the next three days. Indeed, it combines existing landslide susceptibility maps, which locate areas over a large territory that are inherently unstable and thus prone to fail (Fell et al., 2008), with dynamic triggering factors corresponding to water-related variables that act as the most critical triggering factors for Alpine shallow landslides (Tiranti et al., 2019). It therefore requires additional information on rainfall and snowmelt rates estimates over the next few days and rainfall thresholds must be fixed. As shallow landslides can be triggered by short, very intense rainfalls but also by long-lasting rainfall periods, most threshold approaches consider the duration of a rainfall event and its intensity or its daily rainfall amount. Here, we use the robust approach of the antecedent rainfall index (ARI), a weighted sum of precipitation over 7 days (D-3 to D+3) with a decreasing weight the longer in the past the rainfalls occurred (e.g., Crozier, 1999; Kirschbaum & Stanley, 2018).

Second, the Shallow Landslide Runout model assesses the maximum run-out areas of forecasted landslide sources detected by the failure forecasting model. The runout assessment is based on Flow-R, a software for rapid and robust propagation modelling of gravity-driven geohazards, optimised for regional susceptibility mapping (Horton et al., 2013; Terranum, 2023). Landslide propagation extents are controlled by two algorithms: the lateral spreading of a landslide is controlled by Holmgren's (1994) multiple flow direction algorithm modified by Horton et al. (2013). The maximum runout distance is assessed by the Simplified Friction-Limited Model (SFLM, Horton et al., 2013), which uses the landslide reach angle (Corominas, 1996) with a maximum velocity threshold.

Finally, maps of forecasted shallow landslide sources and runout areas are computed every day, forecasting the landslide hazard within the next three days. It therefore supports stakeholders in charge of landslide hazard and risk management to identify populations and or infrastructures that might be exposed to shallow landslides within the next few days and thus prioritise actions.

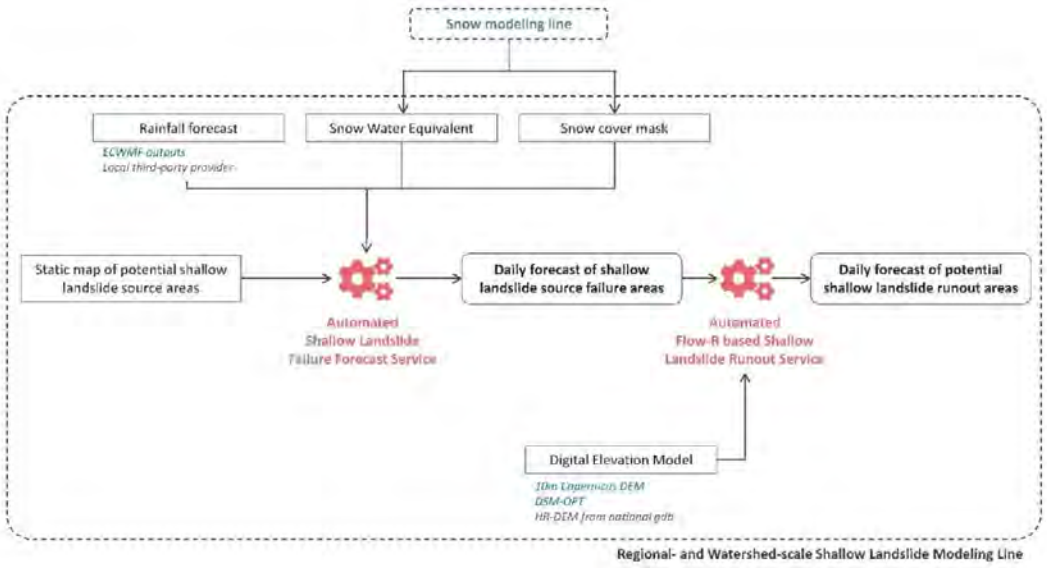

Figure 1. Illustration of the Shallow Landslide Hazard Forecasting processing chain.

The Shallow Landslide Hazard Forecasting System is running on the 1.5 Tier HPC/Datacenter of University of Strasbourg. The processing chain is based on Python modules and an in-house specific workflow management system (FireWorks) to distribute the calculation load on the processing cores. All input data sources are directly harvested from FAIR repositories, transformed, filtered, formatted, and stored. Outputs are stored on the HPC/Datacenter and are remotely accessed by the DTA web platform (digitaltwinalps.com) through APIs.

Results

The Shallow Landslide Hazard Forecasting Service has been implemented as a prototype within the DTA project for two areas of interests:

- The district of Entremont in the Swiss canton of Valais that covers 680 km² between 600 and 4,300 m altitude. This region faces major challenges since landslides threaten many settlements and infrastructure of national importance, such as the Grand Saint-Bernard alpine pass, the Mauvoisin power dam and the Verbier ski resort.
- The Alpes-de-Haute-Provence, a department in south-eastern France covering ~6,900 km², was chosen because of the regular occurrence of shallow landslides in different contexts (high mountains, low hills).

For both AOIs, the static shallow landslide sources susceptibility maps are based on local high-resolution DEMs (with 5 m cell size) and an infinite slope stability model approach (Pack et al. 1998) implemented in a SInMap-like inhouse GIS model. For each mapped loose sediment formation and land-use type, we defined a range of geotechnical soil characteristics to set the stochastic stability model computing safety factors. We iteratively derived the geotechnical characteristics from literature and past local experiences by comparison with available landslide inventories (914 reported events for the Alpes-de-Haute-Provence AOI and 45 in the Entremont AOI) to obtain several susceptibility levels for shallow landslides triggering (Fig. 2).

For this demonstrator, triggering thresholds are set on daily cumulated rainfalls from the ICON weather models of the German Weather service (DWD), harvested on open-meteo.com. The ARI, used as a proxy for the state of humidity and the drainage of the soil (Crozier, 1999), is based here on a 7-days moving window (D-3 to D-1 from rainfall measurements, D+0 to D+3 from rainfall forecasts) with a decay constant k of –1. We use two fixed ARI thresholds, which are based on historical meteorological data (from 1940 to 2022, harvested on open-meteo.com): a first ARI threshold of 15 mm triggers only the *unstable* to *very unstable* susceptibility levels (Fig. 2a), while the second ARI threshold of 20 mm triggers all landslide source areas (Fig. 2b).

The forecasted shallow landslide source areas are used in the Flow-R runout model to map their propagation extents. This Shallow Landslide Runout Service is calibrated for two scenarios: one for modelling mudflow-like propagations with a reach angle of 19° and maximum velocity of 8 m/s and one for simple roto-translation propagations with a reach angle of 27° and maximum velocity of 2 m/s.

The Shallow Landslide Hazard Forecasting System is operational on the DTA platform since end of June 2023 and two periods with intense rainfall exceeding the set ARI thresholds were observed: for parts of the Alpes-de-Haute-Provence AOI) on 19 September 2023 (Fig. 2a) and in the Entremont AOI from 25 to 27 August 2023 (Fig. 2b).

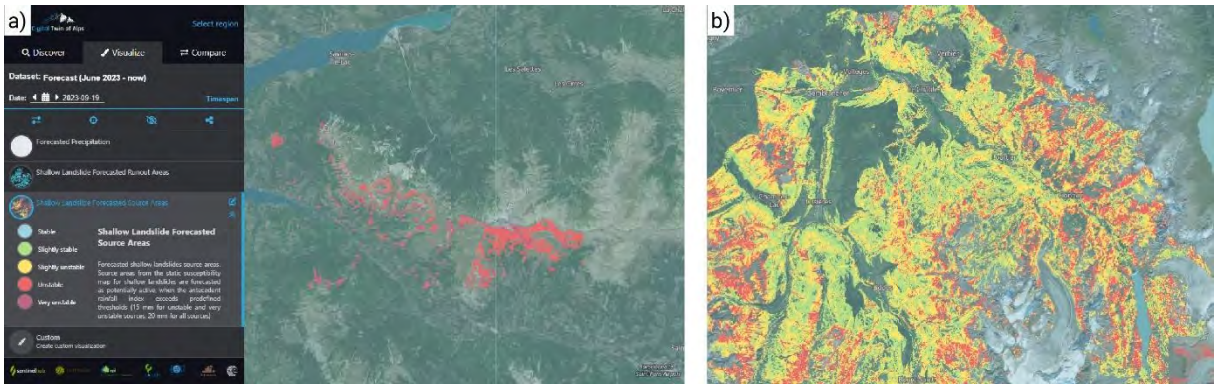

Figure 2. Shallow Landslide Failure Forecasts for a) the Ubaye Valley (Alpes-de-Haute-Provence AOI) on 19.09.2023, where only the first ARI threshold was exceeded, and b) the Entremont AOI on 25.08.2023, where the second ARI threshold was exceeded (screenshots of the DTA platform on digitaltwinalps.com).

Conclusion & perspectives

The demonstrator of the operational Shallow Landslide Hazard Forecasting System on the DTA platform showcases the potential of up-to-date landslide modelling tools coupled with dynamic hydro-meteorological triggering factors to support stakeholders in landslide hazard and risk management. Several promising perspectives in hazard forecasting include improved accuracy through high-resolution hourly temporal and spatial weather forecasts, particularly for regions with complex terrain. These advances are essential for forecasting accurate precipitation rates, even for localised and intense events such as summer thunderstorms. In addition, the integration of Quantitative Risk Assessment into the system, which combines the shallow landslide hazard forecasts with infrastructure and population data, means that warnings can be better targeted when risks are high. Finally, there are plans to generalise this prototype to cover the entire Alps as part of a larger Digital Twin, to provide comprehensive hazard forecasting and risk management across a wider region.

References

Corominas J (1996) The angle of reach as a mobility index for small and large landslides. *Can. Geotech. J.* 33, 260-271.

Crozier MJ (1999) Prediction of rainfall-triggered landslides: A test of the antecedent water status model. *Earth Surface Processes and Landforms* 24, 825-833.Fell R, Corominas J, Bonnard C, Cascini L, Leroi E & Savage WZ (2008) Guidelines for landslide susceptibility, hazard and risk zoning for land-use planning. *Eng. Geol.* 102, 85-98.

Holmgren P (1994) Multiple flow direction algorithms for runoff modelling in grid-based elevation models: an empirical evaluation. *Hydrol. Process.* 8, 327-334.

Horton P, Jaboyedoff M, Rudaz B & Zimmermann M (2013) Flow-R, a model for susceptibility mapping of debris flows and other gravitational hazards at a regional scale. Nat. Hazards Earth Syst. Sci. 13, 869–885.

Kirschbaum D & Stanley T (2018) Satellite-Based Assessment of Rainfall-Triggered Landslide Hazard for Situational Awareness. *Earth's Future* 6.

Michoud C, Malet JP, Oppikofer T, Emberson R, Kirschbaum D et al. (2021) Landslide Information System for Disaster Risk Financing: Earth Observation and Modelling Products for Near-Real-Time Assessment. IEEE International Geoscience and Remote Sensing Symposium IGARSS, Brussels, Belgium, pp. 1812-1814.

Landslide Hazard Information System for Landslide Disaster Risk Financing: Earth Observation and Modelling Products for Near-Real-Time Assessment, EGU General Assembly 2021.

Pack RT, Tarboton DG & Goodwin NC (1998) Terrain Stability Mapping with SINMAP, technical description and users guide for version 1.00, Report Number 4114-0, Terratech Consulting Ltd., Canada

Terranum (2023) Flow-R. Terranum Ltd., Bussigny, Switzerland, https://www.terranum.ch/en/products/flow-r/.

Tiranti D, Nicolò G & Gaeta AR (2019) Shallow landslides predisposing and triggering factors in developing a regional early warning system. *Landslides* 16, 235-251.

Revisiting Hazard Assessment for the Deep-Seated Gravitational Slope of Paterno (Central Italy)

Berardo Giorgia[1], Amato Gabriele[1], Cornacchia Irene[2], Fiorucci Matteo[3], Marmoni Gian Marco[1,4], Scarascia Mugnozza Gabriele[1,4].

[1] Sapienza University of Rome, Piazzale Aldo Moro 5, 00185, Rome, Italy
[2] Italian National Research Council-Institute of Environmental Geology and Geoengineering (CNR-IGAG), Piazzale Aldo Moro 5, 00185, Rome, Italy
[3] University of Cassino and Southern Lazio, Via G. Di Biasio 43, 03043, Cassino, Italy
[4] CERI Research Centre on Geological Risks, Sapienza University of Rome, Piazzale Aldo Moro 5, 00185, Rome, Italy

Summary

The study presented here proposes an approach, based on the combination of InSAR techniques and geological field observations, to assess and quantify the hazard of the Deep-Seated Gravitational Slope of Paterno (Rieti, Central Italy). The deformation process that affected the Paterno slope has already been identified and featured by high landslide hazard rank in the PAI catalogue, which designs territorial planning documents. Until nowadays, the Paterno slope movement has never been investigated in depth. The new data collected contribute to revisiting of landslide hazard level in the study area, where old settlements and other infrastructures are located. The lack of evidence of activity of this deformation process suggests a lower hazard rank concerning that assigned in the PAI and, therefore, needs reviewing.

Keywords: Deep-seated gravitational slope deformation, Central Apennines, Structural Control, Hazard, Satellite Interferometry

Introduction

Deep-seated gravitational slope deformations (DSGSDs) are geological time-dependent processes driven by gravity, affecting entire hillsides and involving volumes larger than several tens of millions of cubic meters (Zischinsky, 1969; Crosta, 1996). While the displacement rates may be relatively slow, returned as millimetres or centimetres per year, they may damage local infrastructure and trigger smaller-scale failures (Chigira, 1992; Panek & Klimes, 2016). In this work, we focused on the Paterno DSGSD, located in the central-eastern sector of the Apennine chain. The slope of interest is under the competence of the Basin Authority of the District of Central Apennines, connected with the Italian Government, which has started, in collaboration with the Structure of the Commissioner for the Reconstruction of the municipalities affected by the 2016-2017 Central Italy seismic sequence, an activity carried out to update the landslide hazard plan of the area (labelled PAI). These actions aimed to indicate a high hazard, namely P3, and very high hazard, namely P4, areas interacting with the post-earthquake reconstruction plan.

Paterno DSGSD

The Paterno rock-slope is located close to the San Vittorino Plain, in the province of Rieti (Lazio Region, Italy), NE-SW oriented and with a highest elevation of approximately 1010 m a.s.l (Fig 1a). The structural general framework, with regional faults and folds, imposed a

complex jointing system on the carbonate rocks, facilitating karst processes. This latter, which is a dissolution process, led to the emergence of various peculiar landforms such as sinkholes and dolines. These effects are prominently observed in the San Vittorino Plain by decametric-sized collapse dolines and diffused sinkholes, such as the Paterno Lake (Salvati & Sasowsky, 2002; Petitta, 2009), situated at the footslope within alluvial deposits. The Paterno DSGSD is characterised by two flat/low-angle surfaces which define the upper and lower parts of the slope. The morphological features associated with the upper part of the Paterno slope are double ridges, trenches, scarps, and counter-slope portion while bulging, scree slopes and buckling foldes characterize the slope toe (Radbruch-Hall et al., 1977; Varnes et al., 1989; Agliardi et al., 2001). The survey of these morphologies is crucial for their inventorying and accurately quantifying landslide hazard conditions, potentially posed by their tertiary paroxysmal evolution (Chang et al., 2015; Vick et al., 2020).

Materials and methods

A 1: 5.000 map was used as cartographic base during the field survey. A project on the Geographic Information System (GIS) was developed to store geological and geomorphological data derived from the surveys, data from geomechanical stations, and elaborating analyses. Photointerpretation and the geomorphological analysis were combined with satellite images (by Google Earth®) and a 5x5 m Digital Elevational Model (DEM). Morphometric dataset and satellite images allowed the preliminary identification and interpretation of geomorphological features (i.e., main scarps, secondary scarps, landslide, dolines), verified during the geological field survey. In addition, 20 geomechanical stations have been conducted to assess the degree of fracturing and evaluate the extent of the slope involved in the deformation process. Field survey was combined with two sets of Satellite Synthetic Aperture Radar (SAR) stacks of images for conducting an interferometric analysis. These analyses aim to derive displacement results by utilising Persistent Scatterers (PS). This technique allows the analyses of the spatial and temporal evolution of slope instabilities, in particular of DSGSD phenomena, characterised by low velocities (Cignetti et al., 2023; Antonielli et al., 2019). The SAR techniques detect the ground deformation velocity along the satellite's line of sight (LOS). A stable region where the velocities are included between -1.5 mm/yr and 1.5 mm/yr is recognised (Figure 1b). Otherwise, velocities greater than 1.5 mm/yr or less than -1.5 mm/yr represented displacements relative to the LOS. The application of the satellite interferometry technique in the case study of Paterno aims to assess the DSGSD activity and its associated hazard level.

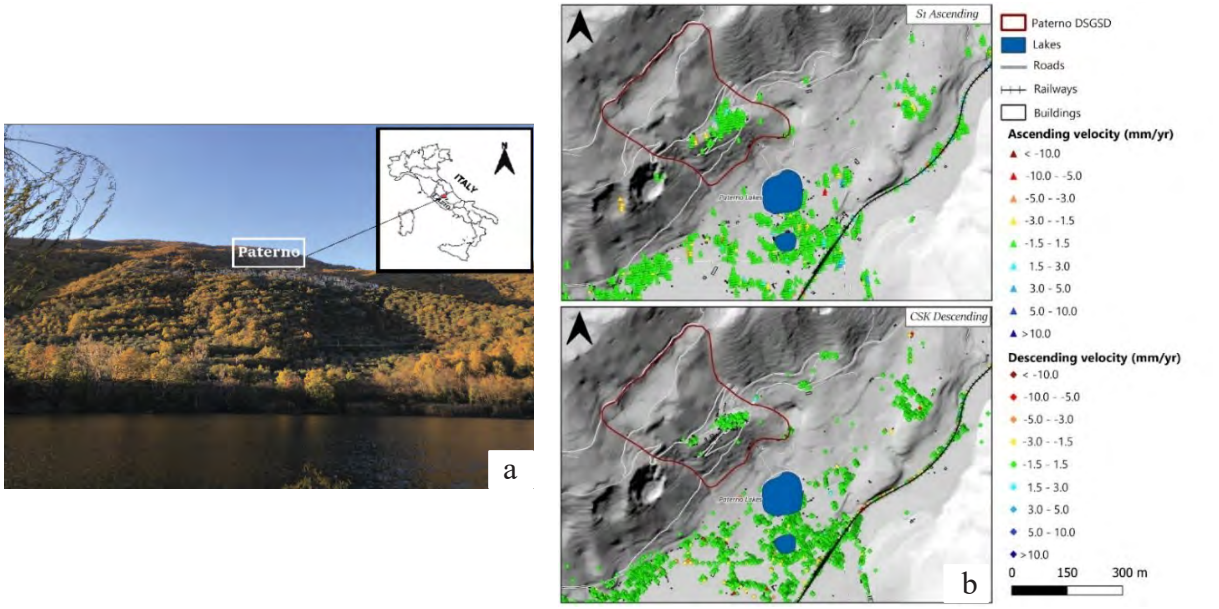

Figure 1: a) Geographic location of the study area; b) Mean displacement rate maps for Sentinel-1 (5-02-2017/21-06-2022) and Cosmo-SkyMed (7-02-2017/29-06-2022) datasets. The Paterno DSGSD is bordered by the red line.

Evidence of Paterno slope instability

The complex network of joints can be attributed to the interplay between tectonic and slope deformation processes, such as faults and shear zones. These features have driven the formation of weakness zones, facilitating the development of the Paterno DSGSD. The counterslope topographic surface, also affected by a regional fault, represents the most highly fractured area of the slope. This is highlighted by the validation of data collected from the geomechanical stations, which identified zones with heightened fracturing that define the deformation process. As a result, the main scarp has been indicated in that area. Geological surveys and morphometric analysis illustrate that the bedrock displacements derived from the combined influences of fault slip and gravitational process. Although the presence of gravitational processes and geomorphic features associated with the Paterno DSGSD are notable, there is no evidence of its current activity. Geological surveys do not show cracks on buildings or other signs of active deformation, which was confirmed also by the InSAR monitoring of ground movements. The analysed dataset, composed of Sentinel-1 and COSMO-SkyMed Persistent Scatterers (PS), reveals the absence of active displacements in the Paterno DSGSD. Otherwise, deformations in the San Vittorino Plain near sinkholes were detected during the observation period.

Assessing Hazard of Paterno DSGSD

Our results emphasise the dominant role of tectonic influence in driving the overall slope deformation. Several field surveys have been conducted, and no evidence has been found to attribute an active state to the DSGSD. Therefore, based on the field surveys, it can be affirmed that the landslide is currently in a quiescent or inactive state. Alluvial deposits cover the Paterno footslope, which does not appear deformed on field, and shows no signs of recent activity. The alluvial deposition occurred under non-deforming conditions, representing a minimum temporal limit of inactivity or quiescence state for the DSGSD. Differently, karst processes persisted and matured even after Paterno DSGSD activity. These landforms constitute, at present, the main geological hazard in the study area that can endanger buildings, infrastructure, and human lives, causing structural damage or even leading to accidents and fatalities. The geomechanical stations provided valuable insights into the spatial extent of the deformed area,

with direct observations and measurements on the ground, while the InSAR data measurements have contributed to defining the state of activity. The analyses performed in this study have enabled us to delineate the boundaries of the Paterno DSGSD, assess its evolutionary model, and evaluate its associated hazard. The confirmed perimeter of the DSGSD does not directly correspond to the hazard rank assigned to the process by PAI. The associated state of inactivity, resulting from our analysis on the slope, allows us to attribute a low degree of hazard to the Paterno DSGSD. However, we cannot exclude the possibility of reactivation due to potential near-field earthquakes.

Conclusion

This work contributes to assessing the hazard associated with a DSGSD process through a combination of field surveys and interferometric analysis. This multi-technique approach highlights no signs of recent deformation activity, indicating a state of inactivity or, at least, quiescence. Therefore, revisiting the high landslide risk of the Paterno DSGSD allows us to attribute a lower risk to this process. The results of this study can contribute to updating the landslide risk areas in the PAI catalogue.

Acknowledgement

The present study was conducted in the frame of the research project “The review of PAI landslides high P3 and very high P4 hazard areas interacting with the reconstruction in municipalities affected by the 2016-2017 Central Italy earthquake” funded by “ABDAC” (Autorità di Bacino Distrettuale Appennino Centrale), managed by the Research Center "CERI-Center for Research Prediction and Prevention of Geological Hazards" of Sapienza University of Rome, P.I. Prof. Gabriele Scarascia Mugnozza.

References

Agliardi F, Crosta G & Zanchi A (2001) Structural constraints on deep-seated slope deformation kinematics. *Engineering Geology* 59, 83–102.

Antonielli B., Mazzanti P., Rocca A., Bozzano F., & Dei Cas L. (2019) A-DInSAR performance for updating landslide inventory in mountain areas: An example from Lombardy region (Italy). *Geosciences* 9(9), 364.

Chang KT, Ge L & Lin HH. (2015) Slope creep behaviour: Observations and simulations. *Environ Earth Science* 73, 275–287.

Chigira M (1992) Long-term gravitational deformation of rocks by mass rock creep. *Eng. Geol* 32, 157–184.

Cignetti M, Godone D, Notti D, Zucca F, Meisina C, Bordoni M, ... & Giordan D (2023) Damage to anthropic elements estimation due to large slope instabilities through multi-temporal A-DInSAR analysis. *Natural Hazards* 115(3), 2603-2632.

Crosta (1996) Landslide, spreading, deep-seated gravitational deformation: analysis, examples, problems and proposals. *Geografia fisica e dinamica quaternaria* 19(2), 297-313.

Panek T & Klimeˇs J (2016) Temporal behaviour of deep-seated gravitational slope deformations: a review. *Earth Science Reviews* 156, 14–38.

Petitta M (2009) Idrogeologia della media Valle del fiume Velino e della Piana di S. Vittorino (Rieti, Italia Centrale). *Italian Journal of Engineering Geology and Environment* 1, 157-181.

Radbruch-Hall D, Varnes DJ, & Colton RB (1977) Gravitational spreading of steep-sided ridges (“Sackung”) in Colorado. *Journal of Research of the US Geological Survey* 5(3), 359-363.

Salvati R & Sasowsky ID (2002) Development of collapse sinkhole in areas of groundwater discharge. *Journal of Hydrology* 264, 1-4.

Varnes D.J. (1978) Slope movement types and processes. *Landslides, analysis and control, special report 176*, 11–33.

Vick LM, Böhme M, Rouyet L, Bergh SG, Corner GD & Lauknes TR (2020) Structurally controlled rock slope deformation in northern Norway. *Landslides* 17, 1745–1776.

Zischinsky U (1969) Uber Sackungen. *Rock Mech* 1, 30– 52.

LiDAR-based validation of the superelevation method used for debris flow velocity estimation

Amanda Åberg[1,2], Jacob Hirschberg[2,1], Tjalling de Haas[3], Brian McArdell[1], Jordan Aaron[2,1]

[1] Swiss Federal Institute for Forest, Snow and Landscape Research WSL, CH8903 Birmensdorf, Switzerland
[2] Department of Earth Sciences, ETH Zürich, 8092 Zürich, Switzerland
[3] Department of Physical Geography, Utrecht University, 3584 CS Utrecht, the Netherlands

SUMMARY: The inclination of the flow surface in a bend is sometimes used to estimate the velocity of a debris flow in a post-hoc analysis, using the mudlines left behind by the passing flow to measure the cross-channel tilt. Combined with a known radius of curvature of the bend, this surface tilt can be used in the forced vortex equation to calculate a flow velocity. The results are affected by uncertainties, such as how to appropriately define the radius of curvature, as well as whether a correction factor is needed to adapt this equation from water flows to debris flows. Here we present a first attempt at validating the traditional approach to superelevation velocity estimation using mudlines, by using new, high-resolution 3D LiDAR data to directly measure the inclination of the surface during the full duration of a debris flow. The results indicate that when the true inclination of the flow surface is known, the forced vortex equation can produce accurate velocity estimates without the need for a correction factor.

Keywords: debris flow, superelevation, velocity estimation, forced vortex equation

Introduction

Debris flow hazard assessment requires accurate velocity estimates, but direct measurements are seldom available. To overcome this limitation, researchers and practitioners collect field data after an event has occurred and use this to make post-hoc velocity estimates. The superelevation approach is one commonly applied method of this type. It entails measuring the elevation of the mudlines left behind by a debris flow in a bend and using this to calculate the corresponding cross-channel tilt of the flow surface, which has a relationship with the velocity of the flow as described by the forced vortex equation:

$$v_{df} = \left(\frac{R_c g^*}{Bk}\Delta h\right)^{0.5} \quad (1)$$

in which R_c represents the radius of curvature of the bend, g^* is gravitational acceleration, B is the width of the flow, Δh is the difference in flow surface elevation on the inside and outside of the bend, and k is a correction factor (Scheidl et al., 2015; Hungr et al., 1984).

This approach contains uncertainties, requiring accurate estimation of the radius of curvature of the bend (Prochaska et al., 2008) as well as accurate interpretation of mudlines to measure flow width and surface inclination (Pierson, 1986). Additionally, the forced vortex equation was based on water flows, with the correction factor k (Eq. 1) proposed to adapt it to debris flows (Hungr et al., 1984). The actual need for this correction factor and its appropriate value have not yet been established due to a lack of field data for validation, and the general approach has only been validated using limited field measurements. Here we present the use of high frame rate 3D LiDAR data of the surface of a debris flow to validate the traditional superelevation approach to velocity estimation.

Methods

Two high-resolution LiDAR-sensors were installed over top of a check dam located in a bend in the Illgraben torrent in southwestern Switzerland. These sensors collected 3D point clouds at 10 Hz throughout the duration of a debris flow event on June 5th, 2022, enabling interpolation of the flow surface in the bend at high temporal and spatial resolution, and the direct estimate of the surface inclination for each timestep ($\Delta h/B$). Additionally, 3D velocity vector fields were obtained (see Aaron et al., 2023) and streamlines were estimated from these velocity vectors. A circle was in turn fitted to a central streamline to achieve a mean radius of curvature (Fig. 1). The velocity vectors were, furthermore, interpolated along the cross-section to extract mean cross-channel surface velocities for each timestep. The cross-section presented here is located approximately 15 m upstream of the check dam.

To enable a validation of the traditional method, the superelevation was also measured using orthophotos and digital elevation models (DEM) (de Haas et al., 2021; 2022). Three plausible, alternative radii of curvature were defined topographically (Fig. 2), and the mudlines were digitised and imported into the 3D point clouds created by the LiDAR. These mudlines were then used to independently measure the surface inclination for the corresponding cross-section.

Results

The event had a front velocity of approximately 3.4 m s^{-1} (Spielmann et al., 2024), followed by a peak stage momentarily exhibiting surface velocities of close to 8 m s^{-1}, followed by a series of roll waves producing peaks and troughs in the velocity measurements (Fig. 3). The overall pattern of the surface velocities is well replicated by those obtained using the LiDAR-based surface inclination and the forced vortex equation (k = 1). The radii of curvature of the bend defined topographically from the orthophotos ranged from 29.9 to 49.1 m, whilst the radius of curvature of the flow obtained from the LiDAR-data had a mean of 46 m during the first 15 minutes of the event.

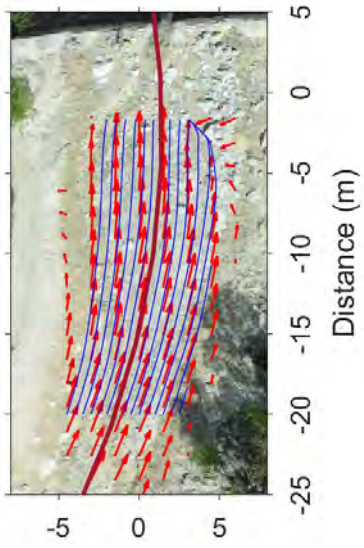

Figure 1. Example of the fitting of streamlines to the surface velocity vector fields (spacing and size exaggerated for clarity) and subsequent fitting of a radius of curvature to a central streamline.

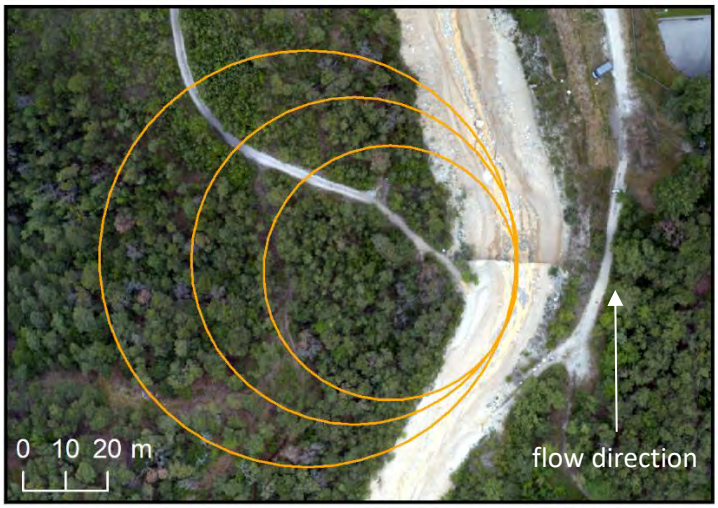

Orthophoto: Tjalling de Haas, 2019. Coordinate system WGS 1984 UTM 32N.

Figure 2. Overview photo of the studied bend and the radii and cross-sections used in the traditional mudline approach. Radii from small to large: 29.9 m, 38.5 m, 49.1 m.

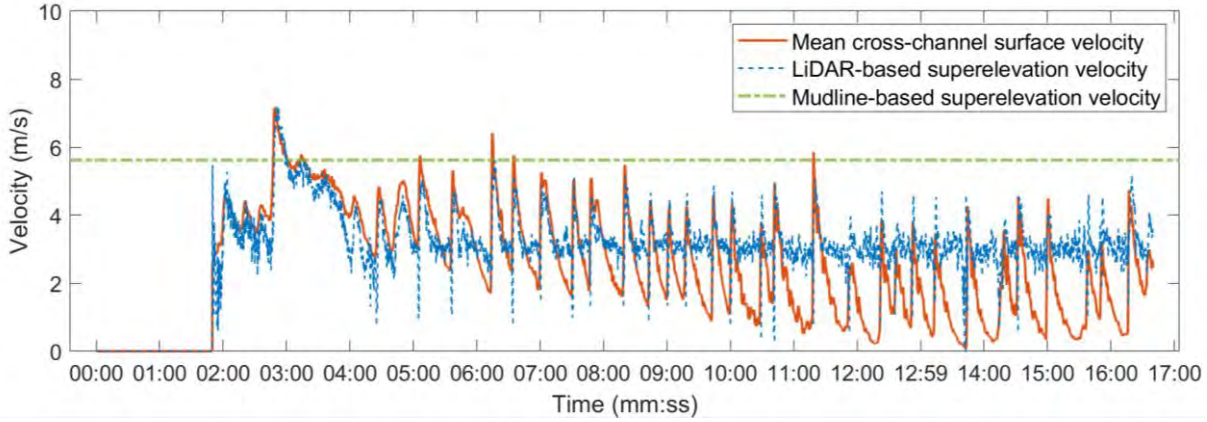

Figure 3. Time series of the flow velocities obtained using the LiDAR-data and the traditional mudline approach, as well as the LiDAR-based surface velocities.

A velocity of 5.6 m s^{-1} was obtained using the traditional mudline approach, which exceeds the velocity of the flow front but is lower than the peak surface velocity (Fig. 3). The peak velocity estimated using the LiDAR-data and the inclination of the flow surface does, however, correspond well to that obtained by averaging the surface velocity measured across the full width of the flow.

Discussion

For this June 5th, 2022, event it is clear that direct measurements of the surface inclination provide very accurate velocity estimates when used in the forced vortex equation. Whilst the traditional mudline approach provides a reasonable average velocity estimate, it does not replicate the peak flow velocities occurring approximately one minute after the flow front arrival. A cross-section from the moment of maximum surface inclination (Fig. 4) indicates that the maximum elevation on the inside and outside of the bend did not occur at the same moment, and that the surface of the flow may have exhibited some convexity toward the outside of the bend. The latter may have resulted in a mudline at a slightly lower elevation than indicated by the overall inclination of the flow surface as seen in the LiDAR-data.

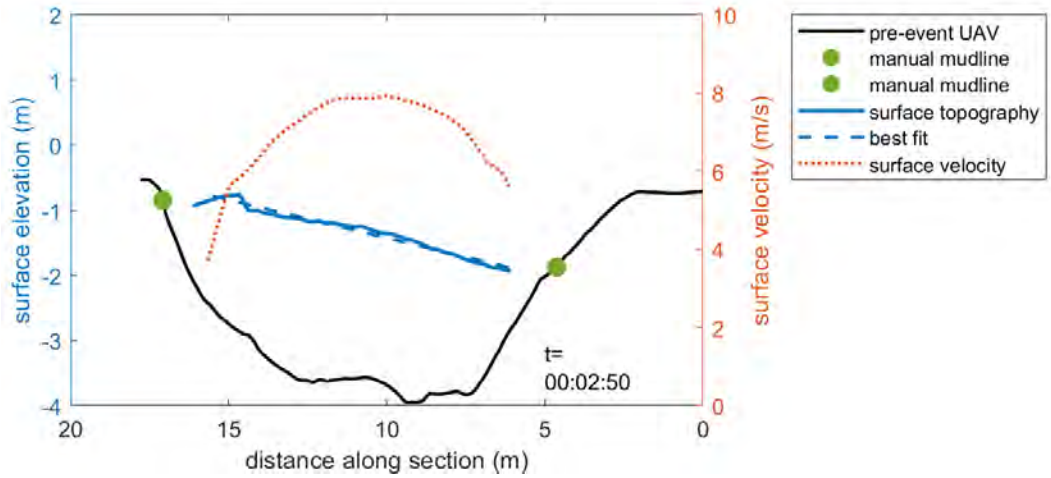

Figure 4. Cross-section of the channel during the moment of maximum surface inclination, showing both the surface topography, the corresponding best fit line, the surface velocity across the width of the channel, and the mudline elevations as identified in the orthophotos and DEM.

Additionally, we see that the topographically defined and the LiDAR-based radii of curvature are similar. Though it has been suggested previously that the subjectivity involved in defining a radius of curvature may be a considerable problem (Prochaska et al., 2008), it is proposed elsewhere by the authors that the radius of curvature has a limited influence on the superelevation velocity calculated with the forced vortex equation when compared with the influence of variability in superelevation measurements in the field and, possibly, the chosen value of k (Åberg et al., 2023, conference proceedings). However, the preliminary results presented here indicate that a correction factor may not be necessary to account for differences between pure water and a debris flow slurry. The challenge may rather lie in obtaining accurate measurements of mudlines, interpreting these correctly and accounting for potential surface convexity during peak flow stages, as well as the mismatch in timing between peak flow surface elevation on the inside and outside of a bend.

Conclusions

This preliminary validation of the traditional mudline approach to superelevation-based velocity estimates indicates that the forced vortex equation may not necessarily need a correction factor to adapt it from water flows to debris flows. When the inclination of the surface is measured directly, the forced vortex equation produces velocity estimates that align well with measured surface velocities for the front and peak of the flow, indicating that the challenge rather lies in accurately measuring the mudlines and accounting for the influence of a mismatch between the timing of maximum mudline elevation on the inside and outside of a bend. These conclusions are currently limited to the one event presented here but will be further investigated by applying the analysis to additional events from the 2022 and 2023 debris flow seasons in Illgraben.

References

Åberg, A., Aaron, J., de Haas, T., McArdell, B. and Hirschberg, J. (2023). Analysis of superelevation and debris flow velocities at Illgraben, Switzerland. In *E3S Web of Conferences* (Vol. 415, p. 01002). EDP Sciences. 8th International Conference on Debris Flow Hazard Mitigation, DFHM8, 26-29 June 2023, Torino, Italy.

Aaron, J., Spielmann, R., McArdell, B.W. and Graf, C. (2023). High-Frequency 3D LiDAR Measurements of a Debris Flow: A Novel Method to Investigate the Dynamics of Full-Scale Events in the Field. *Geophysical Research Letters*, 50(5), p.e2022GL102373.

de Haas, T., Nijland, W., McArdell, B.W. and Kalthof, M.W. (2021). Case report: Optimization of topographic change detection with UAV structure-from-motion photogrammetry through survey co-alignment. *Frontiers in Remote Sensing,* 2, p.5.

de Haas, T., McArdell, B.W., Nijland, W., Åberg, A.S., Hirschberg, J. and Huguenin, P. (2022). Flow and bed conditions jointly control debris-flow erosion and bulking. *Geophysical Research Letters*, 49(10), p.e2021GL097611.

Hungr, O., Morgan, G.C. and Kellerhals, R. (1984). Quantitative analysis of debris torrent hazards for design of remedial measures. *Canadian Geotechnical Journal*, 21(4), pp.663-677.

Pierson, T.C. (1985). Initiation and flow behavior of the 1980 Pine Creek and Muddy river lahars, Mount St. Helens, Washington. *Geological Society of America Bulletin*, 96(8), pp.1056-1069.

Prochaska, A.B., Santi, P.M., Higgins, J.D. and Cannon, S.H. (2008). A study of methods to estimate debris flow velocity. *Landslides*, 5, pp.431-444.

Scheidl, C., McArdell, B.W. and Rickenmann, D. (2015). Debris-flow velocities and superelevation in a curved laboratory channel. *Canadian Geotechnical Journal*, 52(3), pp.305-317.

Spielmann, R., Huber, S. and Aaron, J. (2024). Direct measurements of debris-flow feature velocities at sub-second intervals using high-frequency 3D LiDAR scanners. *14th International Symposium on Landslides*, ISL 2024, 8-12 July 2024, Chambéry, France (submitted).

Rockfall monitoring with a Doppler radar on an active rock slide complex in Brienz/Brinzauls (Switzerland)

Marius Schneider[1], Nicolas Oestreicher[1], Thomas Ehrat[2], Simon Loew[1]

[1] Department of Earth Sciences, ETH Zurich, Sonneggstrasse 5, 8092, Zurich, Switzerland
[2] Geopraevent AG, Räffelstrasse 28 8045 Zurich, Switzerland

SUMMARY: We present and analyze a rockfall catalog from an active landslide complex in Brienz/Brinzauls of the Swiss Alps, collected with a new Doppler radar system. This radar system provides a complete and continuous time-series of rockfall events with volumes of 1 m^3 and bigger since 2018. In the period between January 2018 and October 2022, 6743 events were detected, which is two orders of magnitude higher activity than in stable continental cliffs. We found that the background rockfall activity is controlled by seasonal climatic triggers. In winter, more rockfalls are observed during thawing periods, whereas in summer the rockfall activity increases with hourly rainfall intensity. We also found that due to the geological setting in an active landslide complex, increased rockfall activity occurs clustered in space and time, triggered by local displacement hotspots.

Keywords: Rockfall Monitoring, Doppler Radar, Trigger, Rockslide

Introduction

Rockfall is a common hazard in alpine environments, endangering people on roads and in railways due to its high speed and energy (e.g., Hungr et al. 1999). To improve the understanding of rockfall hazards at a certain site, inventories have to be obtained for the spatio-temporal distribution of past rockfall events. Blocks that have rolled or bounced beyond the base (apex) of talus slopes are of special importance for rockfall hazard analysis and risk mitigation. In this distal part of the deposition area, termed shadow, typically only a few boulders are sparsely distributed on the initial substrate (e.g., Evans & Hungr, 1993). Additionally, complete and accurate temporal data allow detailed analyses of site-specific rockfall triggers. General rockfall inven- tories are mostly based on systematic recordings of deposited blocks along transportation lines (e.g., Hungr et al., 1999). Similar methods are used by road authorities in the Swiss Alps. Since it is known that the rockfall reach angle highly depends on its volume (e.g.,Evans & Hungr, 1993), such catalogs include a bias towards large rockfall events and only a rough estimation of the event timing is possible. Other methods to collect rockfall data include tree-ring injury analysis (Stoffel and Bollschweiler 2008) rockfall volume estimations with traps (e.g., Krautblatter & Moser, 2009), time-lapse cameras (D'Amato et al. 2016), repeated laser scans of rock walls (Rabatel et al. 2008) or simple audience reports. All of these methods lack either temporal or spatial completeness and precision.
In this contribution we report about a study where we apply for the first time a Doppler radar rockfall monitoring system, developed by Geopraevent AG, providing detailed spatio-temporal information for each rockfall event in all weather conditions and darkness (Schneider et al. 2023). This contribution aims to analyze rockfall frequency in time and space on the active rock slide complex of Brienz/Brinzauls to understand drivers and event triggers in such environments, utilizing the novel Doppler radar data set with unprecedented temporal completeness. Drivers and triggers of rockfall events are assessed by combining the Doppler

radar catalog with robotic total station, ground-based differential interferometric radar (GBdInSAR) displacement measurements of the moving landslide and local meteorological signals. This study also provides new insights into statistical properties of rockfall blocks reaching the shadow area and the benefits of the advanced Doppler radar monitoring system with its potential and limitations are presented.

Methodology

Radar rockfall monitoring was used for the first time in Brienz/Brinzauls. The device uses the Doppler shift to detect fast moving objects of 0.1 m^3 and 1 m^3 within 100 m to 1 km line of sight respectively (Geopraevent 2022). Advanced algorithms, developed by Geopraevent AG further distinguish events between rockfall events or environmental noise (e.g. wildlife, weather). Since January 2018, the Doppler radar system has been monitoring the active rockfall slope at Brienz/Brinzauls continuously. For each event, an exact timestamp of start and end time is registered. Additionally, GBdInSAR data were compared with the long and short term rockfall activity to investigate the role of local rock mass acceleration on rockfall activity. The Doppler radar data also contain an intensity map for each rockfall event, enabling the determination of the release area. Wrong intensity maps (due to the radar sensitivity to abrupt incoming weather fronts such as intensive rain, hail or snow) were automatically detected and excluded with a machine learning algorithm.
To study potential correlations between rockfall activity and environmental signals, local weather data from nearby stations were used. To assess the influence of temperature on rockfall activity, positive degree hours (i.e. sum of hours per day with air temperature above 0 °C) and freezing potential (FP) with data from a local weather station were applied (Matsuoka 1994). The latter further allows to subdivide a freezing period into negative cooling when the temperature (T) is below 0°C and temperature decreases ($dT < 0$), negative warming when temperature is increasing ($dT > 0$) but still below 0 °C and thawing when temperature is above 0 °C. Consequently, this method allows to identify potential rockfall triggering factors during a freezing phase.
Furthermore, the number of blocks extending into the shadow area was quantitatively analyzed using aerial imagery from Swisstopo and own drone flights.

Results and Discussion

Time Series Analysis: Between January 2018 and October 2022, the Doppler radar detected a total of 6743 rockfall events (Fig. 1a). Consequently, the study area of about 100'000 m^2 has a high spatio-temporal rockfall frequency of 78 to 190 $y^{-1}hm^{-2}$, which is two orders of magnitude larger than in stable slopes (Hantz et al. 2020). The yearly total of rockfalls fluctuates, with values between 856 (2018) and 2088 (2020) events (Fig. 1a). It has been observed that increased rockfall activity (>10 events per day) predominantly occurs within short-term clusters, typically spanning only a few days (Fig. 1a). However, in February 2020 and July-August 2021, intense rockfall activity over several weeks was observed, with 108 and 78 events recorded on a single day respectively. The event cluster of February 2020 was comprehensively examined in the spatial domain. It was observed that a majority of the events originated within a spatially confined area (Fig. 1b). Spatially random origins were rarely encountered. While this specific cluster of rockfall events cannot be easily explained by weather or hydro- logic factors, none of the nearby reflectors or GNSS stations recorded a significant increase in the velocity of the corresponding landslide compartment. However, detailed inspection of the GBdInSAR data and optical images shows that a 600 m^2 patch of this compartment accelerated in January and reached its peak velocity of 1.5 md^{-1} in mid-February (Fig. 1c). The rockfall release zone closely resembled the area where the local acceleration took place (Fig. 1b & c). After, the

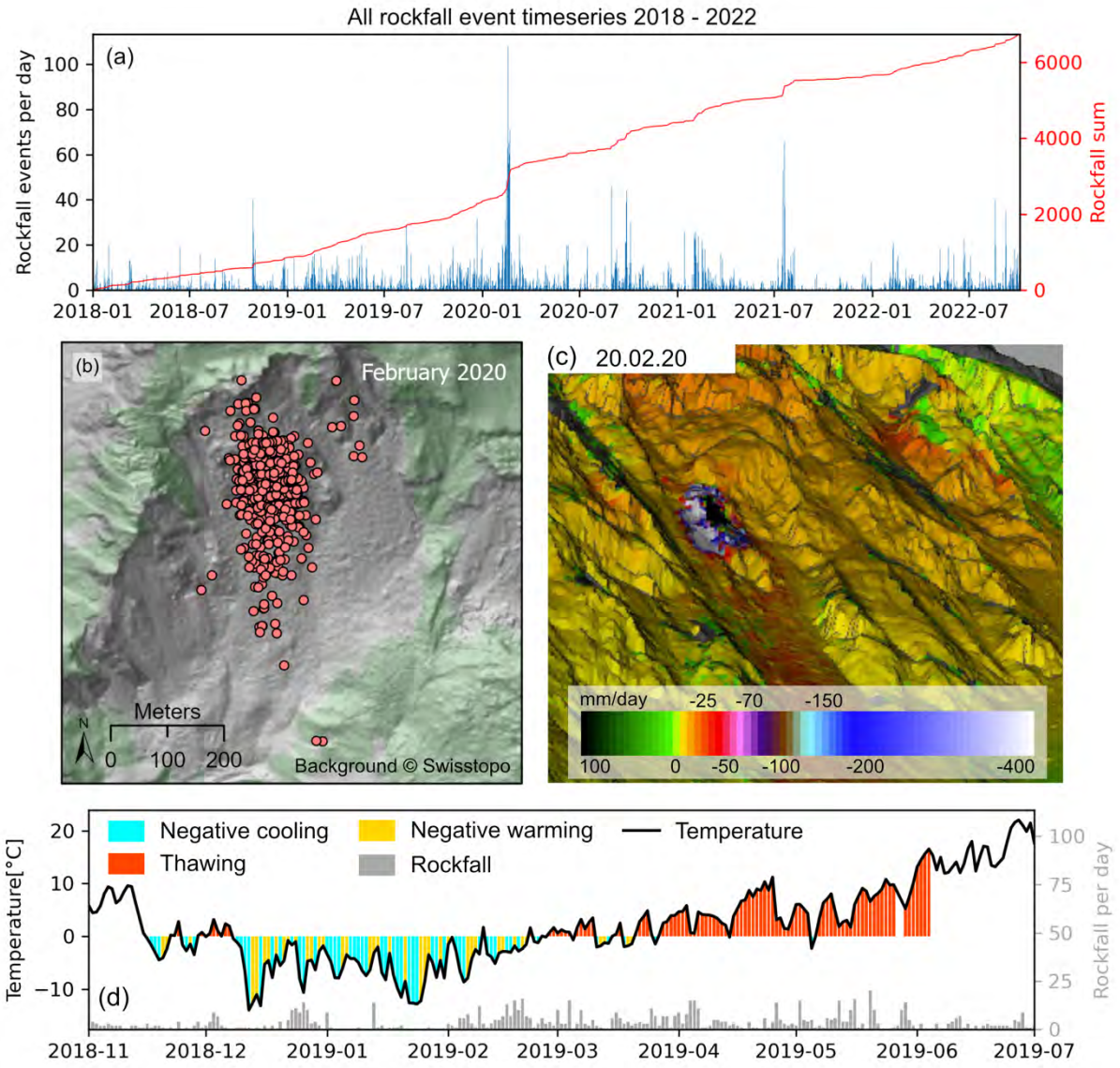

Figure 1. (a) Rockfall time-series from January 2018 to October 2022 (b) Spatial distribution of rockfall events during February 2020 event cluster (c) Local acceleration hotspot observed with ground based differential interferometric radar measurements (d) Rockfall activity during negative cooling, warming and thawing for winter 2018-19. Figure edited after Schneider et al. (2023).

velocity of this patch reduced again back to background velocity (5 to 50 mmd^{-1}) and the rockfall release area became scattered again.

Weather as a Rockfall Trigger: The rockfall data set was also investigated for potential climatic triggering factors, such as surface water input from rainfall and snowmelt, temperature, and freeze-thaw cycles. The analyses have revealed that across the entire data set, only a low correlation between daily rockfall activity and precipitation (0.23), as well as temperature (-0.05) is present. However, when differentiating the data set between summer and winter, a slightly higher correlation between daily rockfall activity and precipitation during summer (0.33) is observed. However, meteorological parameters can exert a significant short-term influence on rockfall activity. To further investigate this phenomenon, hourly mean precipitation and temperature values during the winter were computed for summer and winter respectively. These values were compared with the hourly cumulative rockfall activity for the respective seasons. During summer, only a weak correlation between hourly mean precipitation and rockfall activity was found. However, by inspecting the rainfall intensity, a tendency to an increased rockfall activity with increasing rainfall intensity was found. During winter, it was

observed that there exists a remarkable linear correlation of 0.94 between the mean hourly temperature and rockfall activity. Also, the highest rockfall activity was observed on days with 12 hours of positive temperature. Days with temperatures below 0 °C show no to very few rockfall events while days with only positive temperatures have a rockfall activity close to the overall daily mean of 3.8 events per day. The analysis using freezing potential as defined by Matsuoka (1994) revealed that rockfall activity during winter is increased during thawing phase, yielding a mean of 6 events per day. The increase occurs mainly during the early thawing phase (Fig. 1d).

Shadow Area: It was determined that the farthest-reaching block had a travel angle of about 27°. Overall, about 2.5% of all rockfall events detected by the Doppler radar reach into the shadow area. Aerial images further highlight an increase in frequency where rockfall events reach into the shadow area. From January 2022 to January 2023, about 6% of the events reached the shadow area.

Conclusion

The analyses have revealed that active geological mass movements fundamentally act as a driver for rockfalls. This background activity is, in turn, modulated by various local drivers, such as kinematic modes and topography. Such displacement hotspots can be reliably detected and monitored by continuous GBdInSAR and serve as a primary early-warning indicator. Seasonal meteorological factors act as secondary rockfall triggers in such environments. During the winter months, increased rockfall activity was observed during thaw periods. Additionally, it was discovered that during the summer months, rockfall activity is associated with precipitation intensity.

References

Hungr, O., Evans, S.G., and Hazzard, J. (1999) Magnitude and frequency of rock falls and rock slides along the main transportation corridors of southwestern British Columbia, *Canadian Geotechnical Journal*, 36 (2), pp. 224–238.

Evans, S.G. and Hungr, O. (1993) The assessment of rockfall hazard at the base of talus slopes, *Canadian geotechnical journal*, 30 (4), pp. 620–636.

Stoffel, M. and Bollschweiler, M. (2008) Tree-ring analysis in natural hazards research–an overview, *Natural hazards and earth system sciences*, 8(2), pp. 187–202.

Krautblatter, M. and Moser, M. (2009) A nonlinear model coupling rockfall and rainfall intensity based \\newline on a four year measurement in a high Alpine rock wall (Reintal, German Alps), *Natural Hazards and Earth System Sciences*, 9 (4), pp. 1425–1432.

D'Amato, J., Hantz, D., Guerin, A., Jaboyedoff, M., Baillet, L., and Mariscal, A. (2016) Influence of meteorological factors on rockfall occurrence in a middle mountain limestone cliff, *Natural Hazards and Earth System Sciences*, 16 (3), pp. 719–735.

Rabatel, A., Deline, P., Jaillet, S., and Ravanel, L. (2008) Rock falls in high-alpine rock walls quantified by terrestrial lidar measurements: A case study in the Mont Blanc area, *Geophysical Research Letters*, 35 (10).

Schneider, M., Oestreicher, N., and Loew, S. (2023) Rockfall monitoring with a Doppler radar on an active rock slide complex in Brienz/Brinzauls (Switzerland), *EGUsphere [preprint]*, 2023, 1–25.

Geopraevent (2022) Monitoring Systems for Gravitative Natural Hazards, *Technical Report*, Zürich, 42 p.

Matsuoka, N. (1994) Diurnal freeze–thaw depth in rockwalls: Field measurements and theoretical considerations, *Earth Surface Processes and Landforms*, 19 (5), pp. 423–435.

Hantz, D., Colas, B., Dewez, T., Lévy, C., Rossetti, J.-P., Guerin, A., and Jaboyedoff, M. (2020) Quantitative assessment of rockfall release frequency, *Revue Française de Géotechnique*, 163, 2.

Changing Landslide Potential Based on Ground Deformation Activity with Slope Unit in Taipei City, Taiwan

Kuo-Lung Wang[1], Jun-Tin Lin[1], Shih-Yuan Lin[2], Min-Hsi Hsieh[2], Chen-Kan Liao[2]

[1] National Chi Nan University, Nantou, Taiwan
[2] Taipei City Government, Taipei, Taiwan

SUMMARY: Approximately 70% of Taiwan is characterized by hilly terrain, and due to the rapid urbanization of Taipei City, ensuring the safety of structures and roads built on these slopes has become a top priority, particularly with the growing population density. This study seeks to employ remote sensing techniques to proactively identify potential slope deformations. Traditionally, this task relies on visual image analysis and physical site inspections, but Synthetic Aperture Radar (SAR) remote sensing technology offers an additional tool for monitoring surface deformations. In this research, DInSAR technology is harnessed for a comprehensive, multi-sequence investigation to scrutinize potential variations in slopes. By evaluating the quantity and extent of deformation in slope units, we undertake a comparative analysis between the in-situ survey method and observational data to classify slope conditions. Utilizing data from both ascending and descending orbits, we gain a holistic understanding of surface deformation possibilities in Taipei City. Furthermore, we delve into the discussion of shifting landslide potential, specifically in the context of the heavy rainfall event that occurred in 2022.

Keywords: ground deformation, landslide potential, DInSAR,

Introduction

In order to assess the potential risks associated with hillside slopes in Taipei City, annual surveys, observations, and patrols are conducted by the city to identify areas with possible hazards. This ongoing effort aims to gain a comprehensive understanding of whether these vulnerable slopes are at risk of sliding. In addition to current methods, the application of remote sensing detection techniques is a viable option for conducting advanced, multi-sequence investigations to proactively monitor and analyze potential variations in slope conditions, thereby obtaining a comprehensive overview of surface deformation trends. This proactive approach serves as an early warning system to mitigate potential losses. The use of remote sensing investigations is crucial for analyzing continuous changes in slope characteristics, geological attributes, and critical assets. This study employs a wide-area detection approach to inform disaster prevention and management strategies in Taipei City.

Monitoring slope sliding poses challenges due to factors such as rugged terrain, atmospheric disturbances, dense vegetation cover, and rapid slope movement. Traditional DInSAR analysis has its limitations in this context. Wang et al. (2021) conducted a study verifying DInSAR results against GNSS data. They highlighted the impact of incorrect orbit data on the outcomes, as well as the influence of rainfall on deformation rates.

Because of the favorable vegetation conditions in Taiwan, longer-wavelength SAR such ALOS/ALOS2 is more effective in terms of accuracy and analytical feasibility when conducting differential interferometric SAR analysis. Nevertheless, the use of Stripmap mode,

which provides high-resolution images of Taiwan, has been on the decline in Japan in recent years. For Stripmap (SM) mode, the ground swath is illuminated by a continuous sequence of pulses while the antenna beam is pointing to a fixed azimuth angle and an approximately fixed off-nadir angle. Stripmap images have continuous along-track image quality at an approximately constant incidence angle. In some regions, there is now only one Stripmap image available per year. Over an extended period, significant surface changes occur, leading to a degradation in coherence. This makes it challenging to utilize Stripmap data for long-term or event-based detection. As a solution, this research relies on data from the Sentinel-1 satellite, a program operated by the European Space Agency.

Analysis Data

The European Sentinel-1, part of the European Space Agency's Copernicus Program (GMES), comprises two satellites, Sentinel-1a and 1b, equipped with C-band Synthetic Aperture Radar (SAR) technology. The radar waves have a wavelength of 5.6 cm and offer various spatial resolutions, including 5 × 5 m, 5 × 20 m, 25 × 100 m, and 5 × 20 m, with image widths spanning from 80 to 400 km. Sentinel-1 delivers continuous imagery, regardless of day, night, or weather conditions, making it ideal for monitoring surface movements and surveying land features such as forests, water bodies, and soil.

One of its most notable features is the accessibility of data from the European Space Agency website. In Taiwan, the available polarization data includes VV and VH. Imaging coverage in Taiwan extends from the end of October 2014 to the present, with a revisit cycle ranging from 6 to 12 days. Figure 1 displays images from ascending orbit 69 and descending orbit 105 in the Taiwan region.

By employing the Small Baseline Subset (SBAS) method, utilizing differential interferometric synthetic aperture radar analysis and interferometric stacking technique, we can acquire a series of data on surface deformation. This data proves effective in identifying the extent and magnitude of sliding blocks. However, the comprehensive analysis of surface deformation encompasses phenomena like subsidence and uplift, necessitating a screening process to pinpoint the potential sliding block's location.

Initially, the subsidence area is earmarked as the likely sliding block. Once extensive data on surface deformation and subsidence is collected, we proceed to investigate the cause of the slippage. Given that hillside slippage in Taiwan is typically characterized by a gradual creep, the prediction of catastrophic events is challenging. Hence, this study utilizes the acceleration in deformation rates within the multi-series data to identify potential sliding events triggered by external factors, such as heavy rainfall or seismic activity, as depicted in Figure 2.

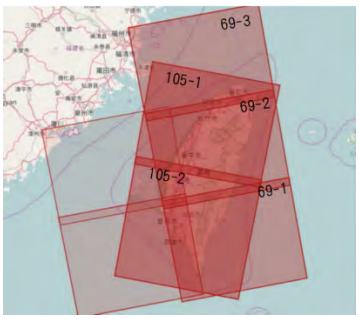

Figure 1. Schematic diagram of rate-of-change screening

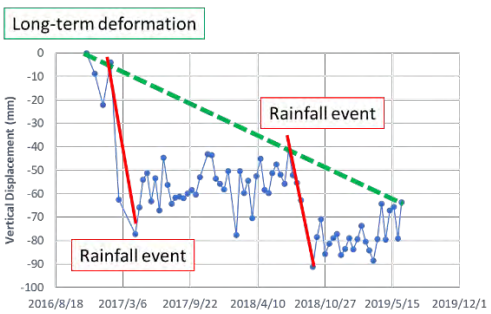

Figure 2. Schematic diagram of rate-of-change screening

In the analysis process, one of the crucial screening criteria involves establishing the ratio between the quarterly deformation rate and the long-term deformation rate. Let's take the ascending orbit as an example, and assess the terrain change rate over several seasons spanning 3 years. It is observed that the cumulative results of the ratio for each season relative to the long-term deformation rate remain consistent throughout. To address this accumulation, the double tangent method is applied to assess the bending situation.

The selectable range for the rate of change screening value varies from 0.5 to 1.35. To ensure a comprehensive consideration of each change event, a screening value of 1.1 is chosen. Additionally, the moving window method is employed, shifting every 8 scenes, to determine whether a sliding event has occurred or not. Given the abundance of screened points, the filtering threshold was set to the mean minus one standard deviation to retain the majority of significant event points. The calculation standard was established based on points within the slope unit. To facilitate early detection, the analysis focused solely on the numerical value of elevation reduction. The evaluation flowchart is shown in Figure 4.

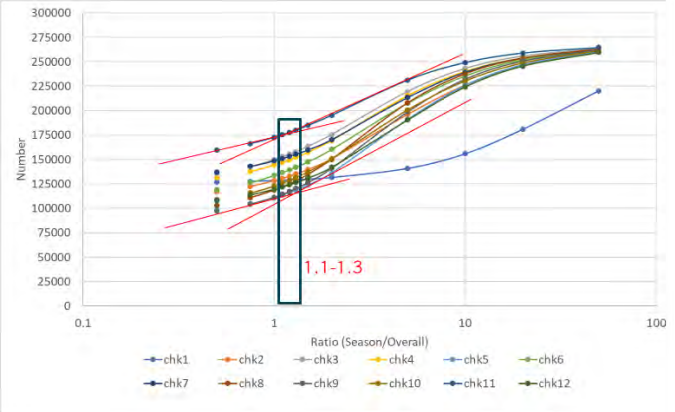

Figure 3 The threshold example of rate-of-change

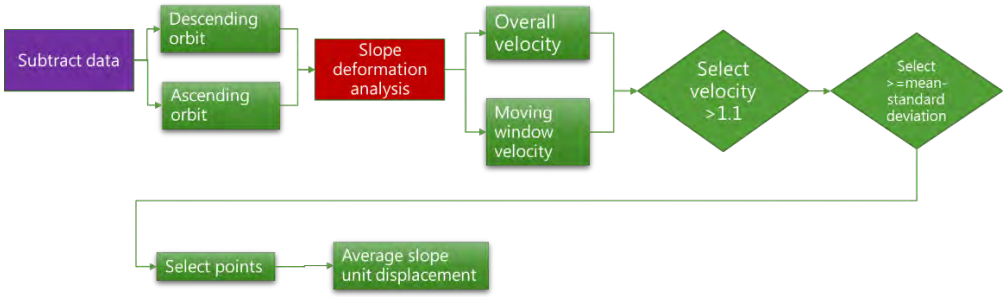

Figure 4 The flowchart to evaluate the deformation within slope unit

Results and Discussions

The study's analytical timeframe spans from March 2017 to May 2023. Employing the short baseline method, the gap between two consecutive images in the screening process should not exceed 72 days. This specific setup is particularly effective for shorter wavelengths, enhancing image correlation with Sentinel-1. The short baseline approach, employed in multipath analysis, allows for repeated validation.

Figure 5 illustrates the average total displacement of effective points within each slope unit to fulfill the primary analytical goal. The colored slope units on the figure denote the 4 mm/month

threshold for monthly vertical deformation attained during the analysis period. To streamline the consistent identification of Taipei City's displacement potential, a criterion of 4mm per month is applied to slopes undergoing continuous deformation. It's crucial to clarify that this condition doesn't imply the detection of a 4mm change each month; rather, it denotes an average change of 4mm per month throughout long-term alterations. The deformation classification is determined using the 4mm per month deformation amount. High displacement potential is defined as 288mm over 6 years; subsequently, half of this value is allocated for each classification.

In the latter part of 2022, Taiwan experienced typhoons and heavy rainfall, which led to landslides in northern regions, including Taipei city. Figure 6 presents the assessment of landslide potential during this brief period in 2022. Typhoon Nesat and the rainfall in 2022 surpassed levels observed in previous years. Most landslide occurrences are situated in areas with small collapses or rockfall events along roads, and some incidents are within slope units with medium-displacement potential. Given that most previous survey findings focus on small disaster areas, the method proposed in this study may not be suitable for small areas.

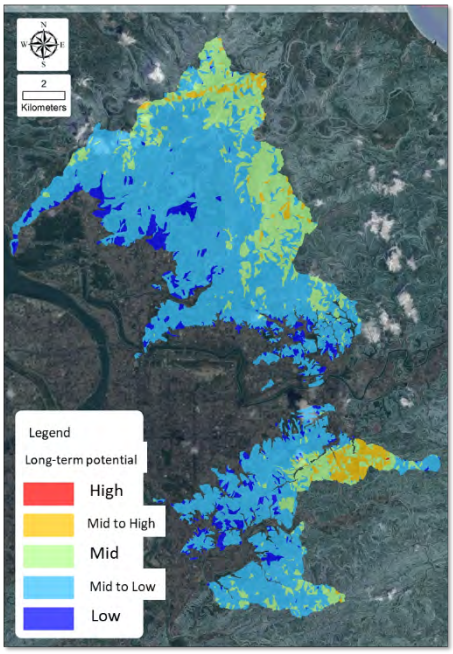

Figure 5. The long-term deformation-based landslide potential map of Taipei City

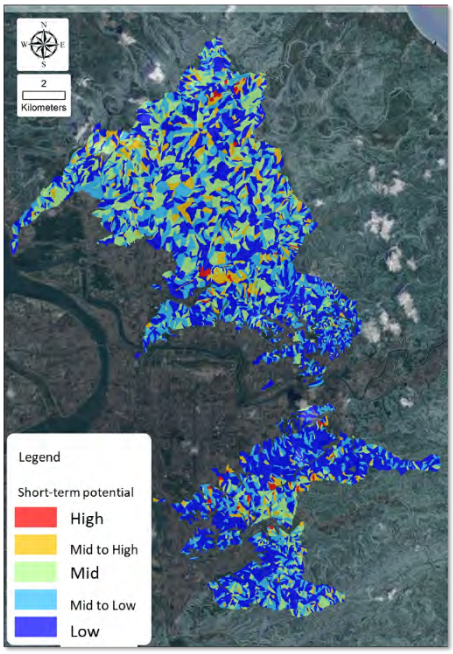

Figure 6. The short-term deformation-based landslide potential map of Taipei City

References

Wang, K.-L., Lin, J.-T., Chu, H.-K., Chen, C.-W., Lu, C.-H., Wang, J.-Y., Lin, S.-H., and Chi, C.-C. (2021) High-resolution LiDAR digital elevation model referenced landslide slide observation with differential interferometric radar, GNSS, and Underground measurements, Applied Sciences, 11(23), 11289

A probabilistic method to assess rockfall risk on mountaineering trail: the Couloir du Goûter study case

M. Marchelli[1], V. De Biagi[1], D. Peila[1]

[1] Politecnico di Torino, Turin, Italy

SUMMARY: Rockfall represents one of the most crucial hazards in mountain environment. Global warming and climate change increase the frequency and the altitude at which events occur, increasing the number of fatal accidents or injuries on mountaineering trail paths. To predispose effective actions, a quantification of the risk in terms of annual probability of death for hikers becomes an urgent issue. A quantitative risk assessment method based on event tree analysis, tailored for the specific case, is proposed and applied to the study case of the Couloir du Goûter, one of the most critical points of the ascent to Mont Blanc.

Keywords: rockfall risk, mountaineering trail, event tree analysis

Introduction

Climate trends indicate that natural hazards are expected to increase as a result of global warming, underlining the urgency for accurate risk assessment and management. Among all natural hazards, rockfall represent one of the most dangerous and its spatial and temporal frequencies are expected to increase due to permafrost and rock degradation and massive glaciers retreat (Knoflach et al., 2021; Mirhadi & Macciotta, 2023). The growing number of people in mountain regions, and thus of people doing mountaineering activities, increase the vulnerability of high-mountain areas and mountaineering trails, underlining the urgency for an accurate rockfall risk assessment to predispose effective mitigation strategies.
A quantification of the possible damages, particularly in terms of annual probability of death, is often required by Authorities to manage the risk and measure the effectiveness of the mitigation measures. This means that detailed information and accurate analyses on events occurrence probability and their propagation are required, together with the characteristics of the elements at risk. Being people movable elements at risk, their exposure represents one of the most important parameters, whose proper evaluation could be very difficult in mountaineering trail, where climbing could be in teams roped up together or alone and in which climbing time could vary significantly during the path.
A method tailored to hikers on mountaineering trail is herein presented. The proposed method accounts for all the possible scenarios leading to a fatal event or injury and is based on a mixed formulation of the Quantitative Risk Assessment and the Event Tree Analysis approaches, firstly developed for vehicular traffic road (Marchelli et al., 2021). The proposed method is applied to the study case of the Couloir du Goûter, one of the most critical points of the ascent to Mont Blanc on the French Normal Route, popularly known as the "Couloir of Death".

Methodology

Rockfall is generally considered as a Poisson point process phenomenon, in which the events are independent, with an average frequency of occurrence according to their magnitude (De Biagi, 2017). Assuming the exposed area consisting of q elements at risk and p different rock block volumes that can detach, the risk R is computed as (Corominas et al., 2005):

$$R = \sum_{l=1}^{p} \sum_{m=1}^{q} \left(P_T^l P_S^{l,m} E^m V^{l,m} W^m \right) \quad (1)$$

where P_T^l is the detachment probability, i.e. the frequency associated to the possible l released volume, $P_S^{l,m}$ is the spatial probability that this block reaches the m-th element at risk, and E^m, $V^{l,m}, W^m$ are the exposure, the vulnerability, and the value, respectively. The exposure represents the probability that the elements are exposed to potential loss, while vulnerability is the degree of loss, when a phenomenon of given intensity occurs. The detachment probability depends on several factors, i.e. lithology, orientation and structural configuration of the discontinuities sets on the rock face, degree of weathering, freeze-thaw cycles, other external factors, e.g. seismic actions or wildfires (Pérez-Rey et al., 2019). Nevertheless, due to the complexity and the uncertainties related to the data, the definition of P_T^l is often based on statistics of past events. In case of mountaineering trail, $P_S^{l,m}$ can be referred to the system on which the elements at risk (P_S^l), i.e. hikers, are moving, i.e. the path. As people are the element at risk, the vulnerability could be considered magnitude-independent, assuming that every block of any volume, can cause a fatality. Thus, the correlation between release volume and frequency can be neglected and P_T^l can be estimated as the mean annual frequency of event N_y with any volume. If $N_y \geq 0.5$, Eq. (1) returns in:

$$R = 1 - \left(1 - \sum_{m=1}^{q} (E^m V^{l,m} W^m) \right)^{N_y P_S^{l,m}} \quad (2)$$

In principle, different source areas can be individuated, as well as different hiking conditions, i.e. climbers roped together or alone. Subdividing the path into portions equal for number of source areas insisting on it and hiking conditions, it results:

$$R = \sum_{k=1}^{n} P_T^{l,k} P_S^{l,k} \left[\sum_{m=1}^{q} (E^{m,k} V^{l,m,k} W^{m,k}) \right] \quad (3)$$

in which as $P_S^{l,k}$ can vary along the k-th portion; thus, a homogenization process is required. To evaluate the term $\sum_{m=1}^{q} (E^{m,k} V^{l,m,k} W^{m,k})$, for each k-th portion a method based on event tree analysis approach (ETA) has been developed by the Authors (Marchelli et al., 2021). The ETA is a logical procedure in which, starting from a single initiating event, in this case the arrival of a block on the path, and defining all the possible mutually exclusive options which can occur, all the possible scenarios are individuated and their probabilities of occurrence are computed. Each possible outcome probability is given by the conditional probability along its own pathway, while the probability of more outcomes is given by the sum of the probabilities of each outcome. The monetary value associated to death is neglected in the analysis. Once obtained $\sum_{m=1}^{q} (E^{m,k} V^{l,m,k} W^{m,k})$ as the probability of having at least one fatality due to the certain occurrence of an event, this must be inserted into Eq. (3) to consider the temporal and spatial variabilities of the events. Figure 1 displays the procedure to compute the risk R for each k-th portion with the proposed event tree. Referring to this last, a probability is associated to each branch of the tree. Several hiking conditions are considered: (i) hikers alone or roped up, (ii) moving in the hazardous area or stationary (i.e. as climbing a vertical rock face just under the potential source zone or at rest). For the latter aspect the probability is computed knowing the expected total time for travelling the portion and the resting time. The probability that hikers are hit by the block is derived knowing their spatial and temporal probability that they are in

the investigated section. Trajectory analyses can be used both to evaluate $P_S^{l,k}$ and the expected kinetic energies to estimate whether the impact is fatal.

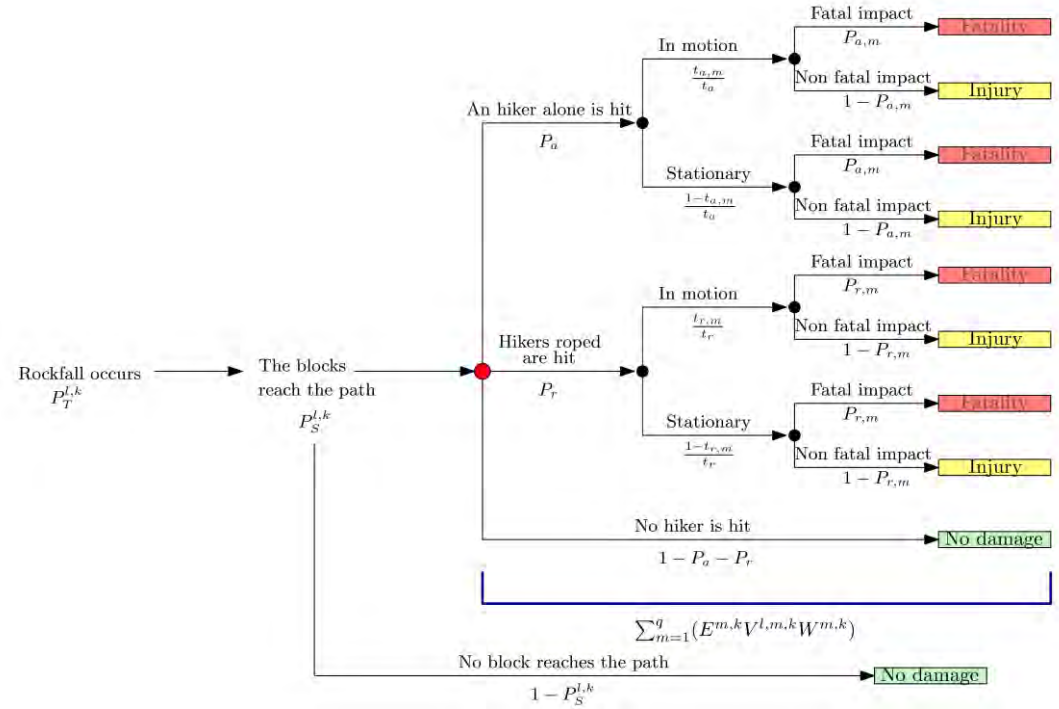

Figure 1: Event tree procedure for rockfall risk on mountaineering trail

Case study

The proposed procedure (refer to Figure 1 for the notation) is applied to the particular case of the Couloir du Goûter, one of the most beloved but dangerous mountaineering routes, climbed by about 17000 mountaineers per year (Figure 2). Due to its topographical and geological features, the Couloir du Goûter is particularly suitable for rock destabilization and consequent rockfall events: the intense degree of fracturation, enhanced by daily freeze-thaw cycling and meltwater refreezing, together with abundant water infiltration, due to increasing snow melt and liquid precipitations, result in frequent rockfall detachments (Mourey et al., 2021). Between 1990 and 2017, 387 incidents were recorded, of which 122 in the traverse across the couloir, and mainly due to rockfall (79%). Referring to those in the crossing, about 25% were fatal and the remaining with injuries (Mourey et al., 2022). Due to this, a huge monitoring campaign was conducted between 2018 (26 days) and 2019 (68 days) (Mourey et al., 2022) in which rockfall phenomena and associated energies were hourly recorded together with the numbers of climbers. A digital camera and a seismic network were used for detecting rockfalls and characterising their energy, while traffic sensors to record passages. Weather sensors were installed for finding correlations with events (Figure 2). The selected period was summer only, i.e. when the Couloir is generally climbed. In this period, a total of 747 events were recorded (28 events/day in 2018 and 39 events/day in 2019), mainly in the afternoon, with mean and maximum energies of 160 and 4000 kJ, respectively, i.e. much greater than the maximum energy absorbed by a helmet, i.e. 100 J. A total of 21 000 ascending-descending passages were recorded, mainly between 9.00 am and 3.00 pm and almost all not roped up, i.e. P_a equal to 1. This campaign allows calculating the mean number of passages and expected events, i.e. $P_T^{l,k}$, for each hour in a day. The risk is thus calculated hourly. The potential source areas insist on a 100 m horizontal mountain pass, generally hiked without stationary phase, i.e. $t_{a,m} = t_a$ of about 2 minutes. Due to the verticality of the rock face, $P_S^{l,k}$ can be considered equal to 1. To

compute the yearly risk, only the effective days of possible climbing are considered. Hence, the obtained annual risk is equal to $5.713 \cdot 10^{-3}$, while the daily risk is $1.566 \cdot 10^{-5}$.

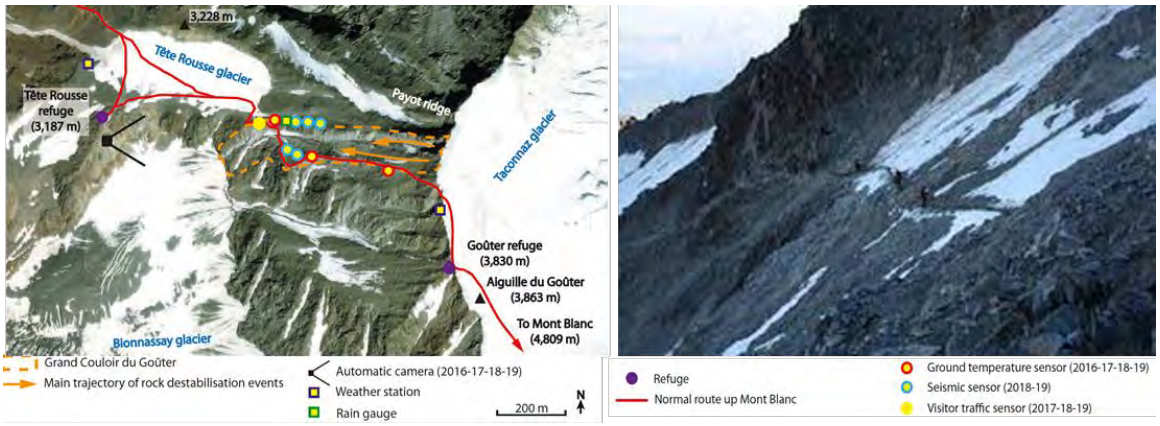

Figure 2: Study site and monitoring system (adapted by Mourey et al., 2021 and Matt Charland / Fondation Petzl)

Conclusion

The study proposes a method to address the risk due to rockfall on mountaineering routes, considering the possible hiking/climbing configurations that occur in such outdoor activity. The profitability of the method has been investigated applying it to the study case of the Couloir du Goûter. Thanks to a detailed monitoring campaign, all the required input data are derived and an annual risk in terms of probability of fatal accident is calculated. The method can be used by Authorities to evaluate the priority of intervention and predispose effective mitigation plans.

Acknowledgment

This study was carried out within the RETURN Extended Partnership and received funding from the European Union Next-GenerationEU (National Recovery and Resilience Plan – NRRP, Mission 4, Component 2, Investment 1.3 – D.D. 1243 2/8/2022, PE0000005).

References

Corominas, J., Copons, R., Moya, J., Vilaplana, J. M., Altimir, J., & Amigó, J. (2005). Quantitative assessment of the residual risk in a rockfall protected area. *Landslides*, 2, 343-357.

De Biagi, V. (2017). Brief communication: Accuracy of the fallen blocks volume-frequency law. *Natural Hazards and Earth System Sciences*, 17(9), 1487-1492.

Knoflach, B., Tussetschlaeger, H., Sailer, R., Meissl, G., & Stötter, J. (2021). High mountain rockfall dynamics: rockfall activity and runout assessment under the aspect of a changing cryosphere. *Geografiska Annaler: Series A, Physical Geography*, 103(1), 83-102.

Marchelli, M., De Biagi, V., Bertolo, D., Paganone, M., & Peila, D. (2022). A mixed quantitative approach to evaluate rockfall risk and the maximum allowable traffic on road infrastructure. *Georisk: Assessment and Management of Risk for Engineered Systems and Geohazards*, 16(3), 584-594.

Mirhadi, N., & Macciotta, R. (2023). Quantitative correlation between rock fall and weather seasonality to predict changes in rock fall hazard with climate change. *Landslides*, 1-15.

Mourey, J., Lacroix, P., Duvillard, P. A., Marsy, G., Marcer, M., Ravanel, L., & Malet, E. (2021). Rockfall and vulnerability of mountaineers on the west face of the Aiguille du Goûter (classic route up Mont Blanc, France), an interdisciplinary study. *Natural Hazards and Earth System Sciences Discussions*, 2021, 1-29.

Mourey, J., Lacroix, P., Duvillard, P. A., Marsy, G., Marcer, M., Malet, E., & Ravanel, L. (2022). Multi-method monitoring of rockfall activity along the classic route up Mont Blanc (4809 m asl) to encourage adaptation by mountaineers. *Natural Hazards and Earth System Sciences*, 22(2), 445-460.

Pérez-Rey, I., Riquelme, A., González-deSantos, L. M., Estévez-Ventosa, X., Tomás, R., & Alejano, L. R. (2019). A multi-approach rockfall hazard assessment on a weathered granite natural rock slope. *Landslides*, 16, 2005-2015

Landslide hazard mapping within a regulatory framework: which lessons can be learned from a quantitative approach in New-Caledonia?

Y. Thiery[1], B. Colas[1], M. Premaillon[2], M. Edet[2], M. Mengin[3], Y. Guyomard[3], O. Monge[3], V. Mardhel[4]

[1] BRGM, Pessac, France
[2] BRGM, Montpellier, France
[3] DIMENC, Nouméa, New-Caledonia
[4] BRGM, Nouméa, New-Caledonia

ABSTRACT: A project was engaged to create landslide hazard maps for multiple municipalities in New Caledonia within a regulatory framework. A quantitative method was selected, offering the benefits of both qualification and quantification of landslide hazards, including temporal and intensity factors. Although some bold choices were made in the project's implementation, feedback from experience confirms the suitability of the strategy for regulatory purposes.

Keywords: landslide hazard, quantitative method, regulatory framework, mapping

Introduction

Landslide hazard H_L expressed the spatial and temporal probabilities that an event with a particular intensity occurring within an area for a reference period (Corominas et al., 2014):

$$HL = P(SL) \times P(TL) \quad (1)$$

With L represents a specific type of landslide (with a certain magnitude); H_L corresponds to the landslide hazard; P is a probability; $P(S_L)$ denotes the spatial probability for the type of landslide; T represents a given period; and $P(T_L)$ depicts the temporal probability of landslide occurrence within the period. Two groups of methods can be used to assess H_L: qualitative (i.e. expert and multicriteria methods) and quantitative (i.e. statistical and physically based methods) methods. In France and its overseas territories, including New Caledonia, the preference has traditionally been for qualitative, expert-based methods (Thiery et al., 2020). However, the available heuristic landslide hazard maps in New Caledonia lack consistency and standardization, making practical applications for land-use planning challenging. The need for quantifying and mapping landslide hazards became evident after a significant event in Houailou in 2016, resulting in fatalities, injuries, and property damage. This challenge is exacerbated by the increasing number of events linked to climate change impacts (Colas et al., 2022).

In recent years, the multiplication of available spatial data and quantitative mapping tools under GIS, R and Python have simplified the process of assessing H_L. The advantage of this type of approach is that large areas can be assessed and mapped rapidly, and spatio-temporal probabilities can be obtained to better quantify the hazard. Given these requirements and observations, it is evident that this type of quantitative approach should be employed in New Caledonia. Nonetheless, it's essential to maintain a certain simplicity to ensure its applicability and comprehensibility by uninitiated (end-users, practitioners, etc., Thiery et al., 2020). Furthermore, it should enable the tracing of each stage to facilitate an understanding of the various choices made for regulatory implementation.

Thus, the objective of this article is to outline the different steps of quantitative H_L mapping applied in New Caledonia within a regulatory framework. After introducing the area and its characteristics, an explanation of the methodology and its underlying philosophy is described. Then, the outcomes of a calibration and validation step and systematic application to several

municipalities are presented. These results emphasize the challenges faced at different stages of the methodology and the insights gained from conducting quantitative H_L mapping within a regulatory framework. This allows for the evaluation of the complexities and difficulties related to the cartographic context of the study.

Site

New-Caledonia is located in the southwestern part of the South Pacific Ocean, and comprising five islands (Fig. 1). The main island, known as Grande Terre, stretches 400 km in length and 50 km in width. It is structured by a continuous line of medium-elevation maintains oriented northwest-southeast, incised by deep valleys. This mountainous relief divides the island into two distinct regions: the narrow, steep-sloped east coast and the broader west coast with a well-developed piedmont area extending between the peaks and the coastline (Colas et al., 2022). The island is characterized by three distinct morphological regions:

(i) The southern massif, primarily composed of peridotites, with mountains reaching approximately 1,600 meters (a.s.l.), deeply incised by valleys, and a metamorphic complex known for its steep slopes and a substantial regolith layer;

(ii) The central chain, featuring an ancient depressed zone marked by hills and flattening features, with altitudes ranging between 400 and 600 meters (a.s.l.);

(iii) The western piedmont, a vast system of glacis connecting the coast and alluvial plains to the western edge;

New-Caledonia experiences periodic tropical depressions and cyclones, with a recorded 55 such events in 141 years (source: www.meteo.nc). These events bring rainfall intensities exceeding 350 mm within 24 hours. The island's steep slopes, surficial formations, and heavy rainfall make it prone to numerous landslides and debris-flows.

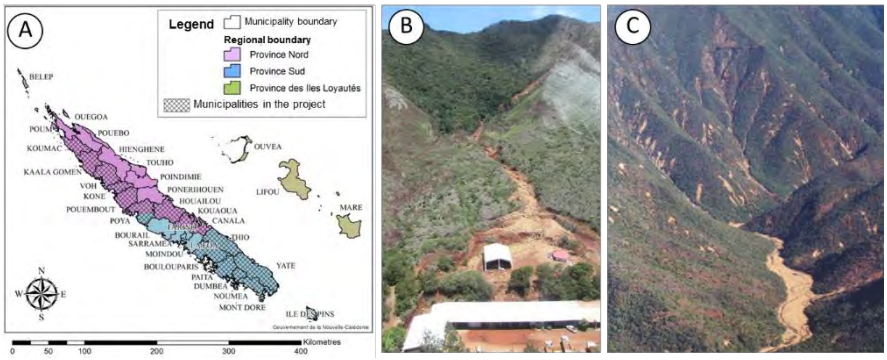

Figure 1. A. New-Caledonia and municipalities in the project. B. Debris-flow in Houailou (2016). C. Shallow landslide in coarse materials.

Methodology

The methodology relies on essential assumptions to account for each component of the hazard equation (1). It is designed to be understandable within a regulatory framework, especially for non-scientists. The field and observation component serves as the foundation of this project's logic. The use of numerical models aids in quantifying and tracking the various stages of the process. This rationale involves systematic inventories conducted in each municipality. For each one an associated database includes information on event type, the nature of materials involved, occurrence and reactivation dates, source documents, and morphometric parameters. Spatial probabilities of failure and propagation are computed based on morphometric attributes. A straightforward quantitative method (Weight of Evidence, Thiery et al., 2007) is employed to assess failure susceptibility. It allows for a quick analysis of the influence of each variable class and obtaining failure probabilities based on the density of phenomena per class. The strategy used for assessing susceptibility is based Thiery et al. (2007). Propagation is assessed using an empirical method that relies on the reach angle of the phenomena (Corominas et al., 2014). A cellular automaton computes propagation probabilities for each type of event (Flow-R, Horton et al., 2013). Temporality is determined for the next 100 years through probability calculations by period, assuming stationarity (the same number of phenomena will recur for the same period in the future). Finally, intensity is

based on velocity, translating the potential damage to a residence for each type of event. Before the systematic application of the methodology, a cross-calibration-validation technique (Chung and Fabbri, 2003) is used in the Mont-Dore to define the set of best predictive variables.

Results

The first step was to create an inventory for each municipality with a specific nomenclature based on the materials involved and mode of propagation (Fig. 2). 27372 landslides of different types have been inventoried for 12 municipalities (Fig. 1A & 1B) for a density of 3.25 event per km^2. From the cross-validation-calibration technique used in Mont-Dore 4 essential variables for each type of landslide emerged (i.e. slope classes, landforms, lithology and surficial formations). Other variables were tested, but without any improvement for the various statistical tests (success rate, prediction rate, relative error, certainty tests). Each susceptibility map was then reclassified into 5 classes according to JTC-1 recommendations with some adjustments (Fig. 2.A). For each failure susceptibility class, propagation envelopes were computed. The rules adopted were defined on the basis of the reach angle distributions for each event and for each susceptibility class (Fig. 2B). Annual probabilities for each class are then applied according to the number of events per year for each susceptibility class. Finally, these probabilities are updated by integrating the intensity (i.e. velocity classes) selected for each type of event. The Fig. 3 shows the final results for the Mont-Dore and Houailou.

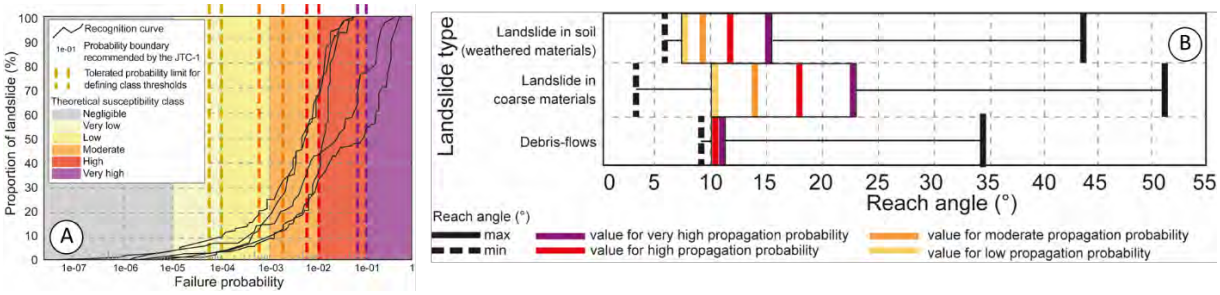

Figure 2. A. Recognition curve for landslide in coarse materials to identify failure susceptibility classes for several municipalities and tolerance admitted to establish the classes. B. Reach angle identified for different type of landslides and minimal values selected for each failure susceptibility classes for 6 municipalities.

Discussion: lessons learned from this operationally-oriented project

While the methodology may appear simple and easy to implement, in practice, several challenges were noticed. They provided valuable lessons that should be considered for the remainder of the project and for other hazard mapping projects applied in a regulatory context.

(i) Lesson 1: in France, typically, H_L maps are generated based on the prediction of the most probable and intense event expected over the next 100 years. However, this approach does not necessitate a breakdown by landslide type. In this study, a comprehensive inventory and a classification system for the observed events was performed. Furthermore, despite the inventory not being exhaustive (as some events may have been overlooked for various reasons), it appears to be representative. The hazard maps obtained have yielded positive feedback.

(ii) Lesson 2: the environment in New Caledonia is distinctive, encompassing formations prone to landslides, both natural and human-induced. To address this uniqueness, a specific map of surficial formations was carried out, considering such as weathering and mining formations prone to landslides and debris flows.

(iii) Lesson 3: despite calibrating and validating the methodology, it became evident that adjustments were required. They involved considering only the relevant areas or adopting a specific strategy that incorporated a simplified lithological map. In a regulatory context, as opposed to a research project, practicality and adhering to reasonable deadlines are essential. Thus, while not deviating from the underlying methodology's philosophy, some pragmatic adjustments were deemed necessary.

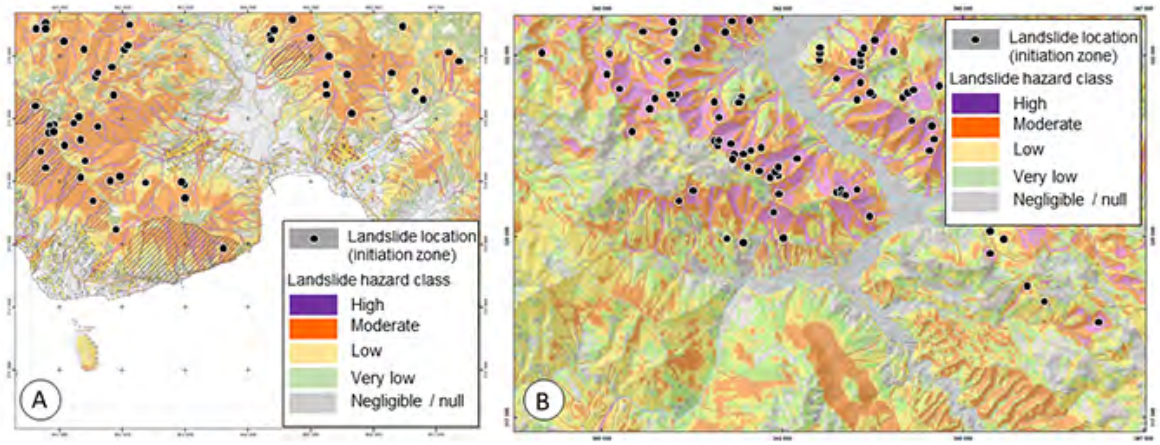

Figure 3. Extract of landslide hazard map (for all landslides). A. For Mont-Dore. B. For Houailou.

(iv) Lesson 4: the calculation of propagation envelopes is based on strong assumptions derived from reach angles and statistical calculations. This solution proved suitable for our mapping. However, two salient points have to be emphasized. The first concerns landslide reach angle classes. The approach is based on quantiles to be used per susceptibility class. While this choice is suitable for our purposes, it raises questions about its applicability elsewhere. The second point concerns the reach angles selected for debris-flows: some expert adjustments were performed with values sometimes quite far from the statistical results (probably due the quality of the DTM and the complexity of phenomena difficult to model with empirical method and cellular automaton). However, values remained within the ranges used generally.

(v) Lesson 5: to establish a framework for H_L assessment, intensity based on velocity has been incorporated. This intensity criterion relies on expert opinion rather than monitoring, which may raise concerns about its singularity. However, recent cyclonic events that triggered landslides in Mont-Dore have demonstrated that the hazard classes determined with this criterion align well with the observed events. This feedback underscores the suitability of the strategy adopted for a regulatory framework.

Conclusion

The H_L mapping project for the 15 municipalities of New Caledonia demonstrates the feasibility of creating quantified hazard maps using a representative inventory. Recent feedback from the commune of Mont-Dore affirms the suitability of the adopted strategy. However, it's important to note that current maps do not consider triggering factors, and despite their regulatory nature, they lack specific thresholds. Addressing these aspects is the next step, which will involve the development of a demonstrator.

References

Chung CF, Fabbri AG (2003) Validation of spatial prediction models for landslide hazard mapping. Nat Hazards 30, 3,451–472.

Colas B, Thiery Y, Guyomard Y, Mengin M, Vandromme R, Prémaillon M, Monge O, Edet M (2022) Cartographie de l'aléa mouvement de terrain. Méthode générale. (Nouvelle Calédonie). Echelle 1 :25 000ème. Rapport d'avancement 2022. BRGM/RP-72236-FR – DIMENC/SGNC-2022(20). 207 p.

Corominas J, van Westen C, Frattini P, et al. (2014) Recommendations for the quantitative analysis of landslide risk. Bull Eng Geol Environ, 73, 209–263.

Horton P, Jaboyedoff M, Rudaz B, and Zimmermann M (2013) Flow-R, a model for susceptibility mapping of debris flows and other gravitational hazards at a regional scale, Nat. Hazards Earth Syst. Sci., 13, 869–885.

Thiery Y, Malet J-P, Sterlacchini S, Puissant A, Maquaire, O (2007) Landslide susceptibility assessment by bivariate methods at large scales: Application to a complex mountainous environment, Geomorphology, 92, 1–2, 38-59.

Thiery Y, Terrier M, Colas B, Fressard M, Maquaire O, Grandjean G, Gourdier S (2020). Improvement of landslide hazard assessments for regulatory zoning in France: STATE–OF–THE-ART perspectives and considerations. International journal of disaster risk reduction, 47, 101562.

Radar and optical monitoring of the Brienz/Brinzauls landslide in its critical phase

Susanne Wahlen[1], Johannes Gassner[1], Maxence Carrel[1], Severin Stähly[1], Andreia Farrér[1],

[1] GEOPREVENT, Räffelstrasse 28, 8045 Zurich, Switzerland

SUMMARY: A 1.2 million m^3 landslide nearly reached the village of Brienz/Brinzauls in Southeastern Switzerland on June 15, 2023. GEOPREVENT solutions were key elements within the Early Warning System for monitoring the landslide and substantially helped to manage the risk to the village, road, and infrastructure at the valley floor. An interferometric radar has been applied since 2019 for continuous measurement of the slope displacement rate. A high-resolution camera system was added to monitor the landslide from the crest in 2023 for automated image analysis from a different viewing angle. The gathered data clearly show the landslide's acceleration prior to the failure. After the event, the movement of the landslide and the rockfall activity decreased abruptly. The Early Warning System is still in place to monitor further evolution of this site.

Keywords: Interferometric radar, image analysis, Early Warning System, landslide

Introduction

The population of the village of Brienz/Brinzauls in Southeastern Switzerland was evacuated on May 12, 2023, due to the imminence of an estimated 2 million m^3 landslide. The village is located on a slope that has been in motion for decades and since 2011, various technologies have been applied for monitoring. A compartment named the "Insel" (island in German) had accelerated since 2018, reaching velocities around 20 m per year at the end of 2022, whereas the village moved at a velocity of ca. 1-1.5 m per year (The Landslide Blog 2023). Several scenarios were considered for further evolution of the landslide and based on the most pessimistic ones a portion of the village would have been buried by the expected failure. On June 15, 2023, 7 weeks after the evacuation of the village, the landslide failed shortly before midnight. About 1.2 million m^3 of material were released and missed the village by a few meters (The Landslide Blog 2023). This event received a lot of interest from the scientific community and worldwide media coverage. To protect the inhabitants and infrastructure in the village and valley below, an early warning service including comprehensive Early Warning System (EWS) was set up and financed by of local authorities (the local municipality of Albula with funding from the municipality, the Canton of Grisons and the Swiss Confederation) and run by a consortium led by a private company in collaboration with further companies and research institutions. This EWS consisted of several components such as periodical Lidar measurements and satellite based InSAR analyses as well as continuous monitoring with piezometers, inclinometers, a total station, seismic sensors and GNSS systems (Gojic et al., 2021, Häusler et al., 2021, Jones et al. 2022). GEOPREVENT contributed to this EWS with two different technologies that provided insights to understand the processes and monitor the acceleration of the landslide over the last years and during the weeks before the collapse.

Ground-based interferometric radar (Gb-InSAR)

Caduff et al. (2015) showed that ground-based interferometric radars are powerful tools to measure the displacement of landslides as they are suitable to cover areas of several km^2, provide measurements 24/7, during all weather conditions, and the possibility to correct the impact of atmospheric perturbations on the data. GEOPREVENT installed a ground-based interferometric radar in Brienz/Brinzauls in April 2019 as part of the early warning service for permanent monitoring of the accelerating landslide. The instrument applied is an IBIS-FM produced by IDS Georadar, Pisa, Italy. After conducting visibility analyses, a location was chosen on the lower, opposite slope to ensure sufficient visibility of the area of interest. No mains connection was available for the site with the best view, located 3 km away from the landslide. Therefore, an energy self-sufficient system was installed in a small hut to protect the hardware from adverse weather conditions. Solar panels and a fuel cell were combined with batteries to ensure a redundant power supply able to overcome bad weather periods of several days. At this location, the mobile network coverage is sufficient to transfer the data measured on site to the cloud for further processing. The radar system and its location, with the landslide on the other side of the valley are displayed in Figure 1.

Figure 1. Left: location of the interferometric radar with the solar panels and the hut (under construction). Right: radar head moving on the system's rail with protection cases containing the batteries, the fuel cell and the transmission unit.

Measured velocities in the most active zones were of ca. 3 – 5 m / year in 2020, reaching 15 – 20 m / year at the end of 2022 up to more than 40 meters per day immediately before the collapse of the landslide (The Landslide Blog, 21st of June 2023). The maximal velocity the radar could reliably measure was ca. 4.5 m/day, phase wraps occurred for faster velocities making an interpretation difficult. This represented a major challenge given the magnitude of the landslide velocities immediately before the collapse. To cope with the atmospheric conditions of the site, an adaptative interferometry model was developed (Gassner et al., 2022). This model is based on the comparison of actual scans with recent ones obtained under similar conditions to obtain optimal results. Additional details concerning these analyses can be found in Gassner et al., 2022. An example of the resulting displacement data obtained with adaptative interferometry model for the 25th of April 2023, about a month two months before the collapse, is displayed on Figure 2.

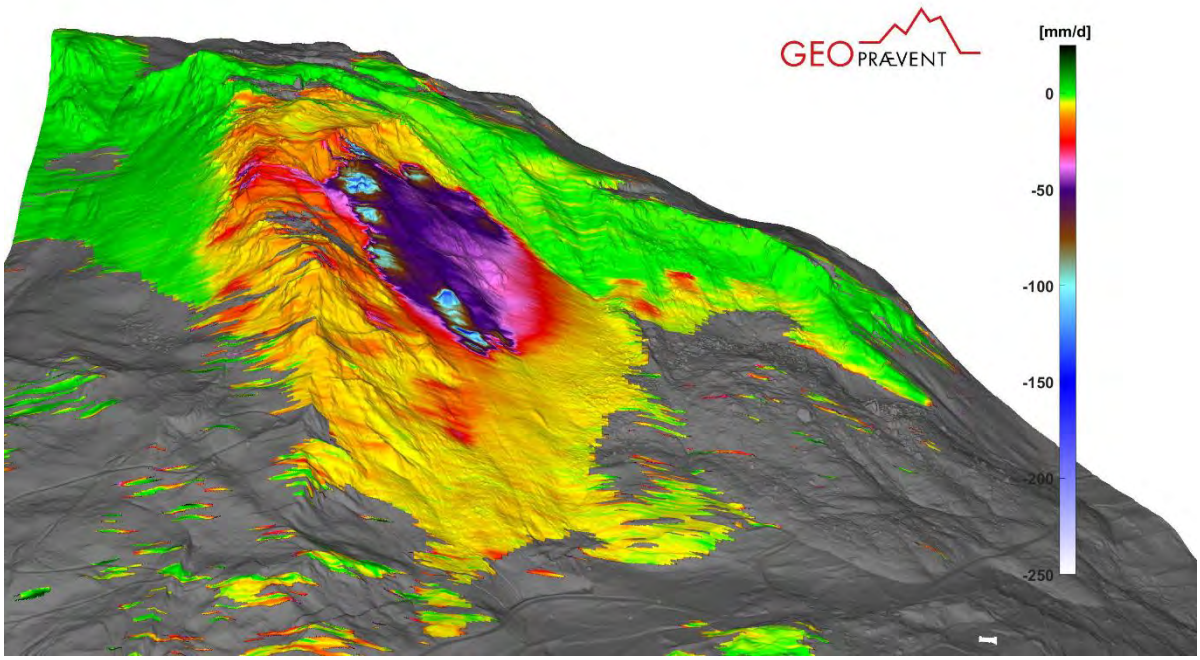

Figure 2. Interferometric radar measurements of the 25 April 2023, 2 months before the collapse, mapped on a digital elevation model with maximal measured velocities of more than 200 mm per day.

Deformation camera

In addition to the radar systems, GEOPREVENT also installed an energy self-sufficient camera on the crest on the East side of the landslide to generate displacement data from another point of view. Deformation measurements based on correlation analysis of optical images have shown a high potential for landslide monitoring (Travelletti et al. 2012). The camera system records 42 megapixels high dynamic range images every 15 minutes, and a deformation analysis is computed daily. Results of this image analysis obtained a few days before the collapse are displayed in Figure 3 with the most active zone of the landslide well recognizable. The average displacement rates in defined regions of interest (ROIs) were determined and the time series of these measurements shown in the inset of the Figure 3 illustrate the acceleration phase leading to the collapse of this landslide and the consecutive failure.

Conclusion

Various technologies were applied to monitor the landslide above Brienz/Brinzauls. Among others a ground-based interferometric radar system as well as a deformation camera were installed by GEOPREVENT to monitor the acceleration of this landslide that led to the collapse of June 15, 2023. These technologies provided insights to monitor the situation leading to the collapse. After the failure, the landslide movement and its activity decreased substantially. The data gathered with the interferometric and with the deformation camera substantially supported the early warning service and the authorities during the entire process, from taking the decision to evacuate the village to monitoring the collapse closely until the situation stabilized, and people were allowed to return to their homes.

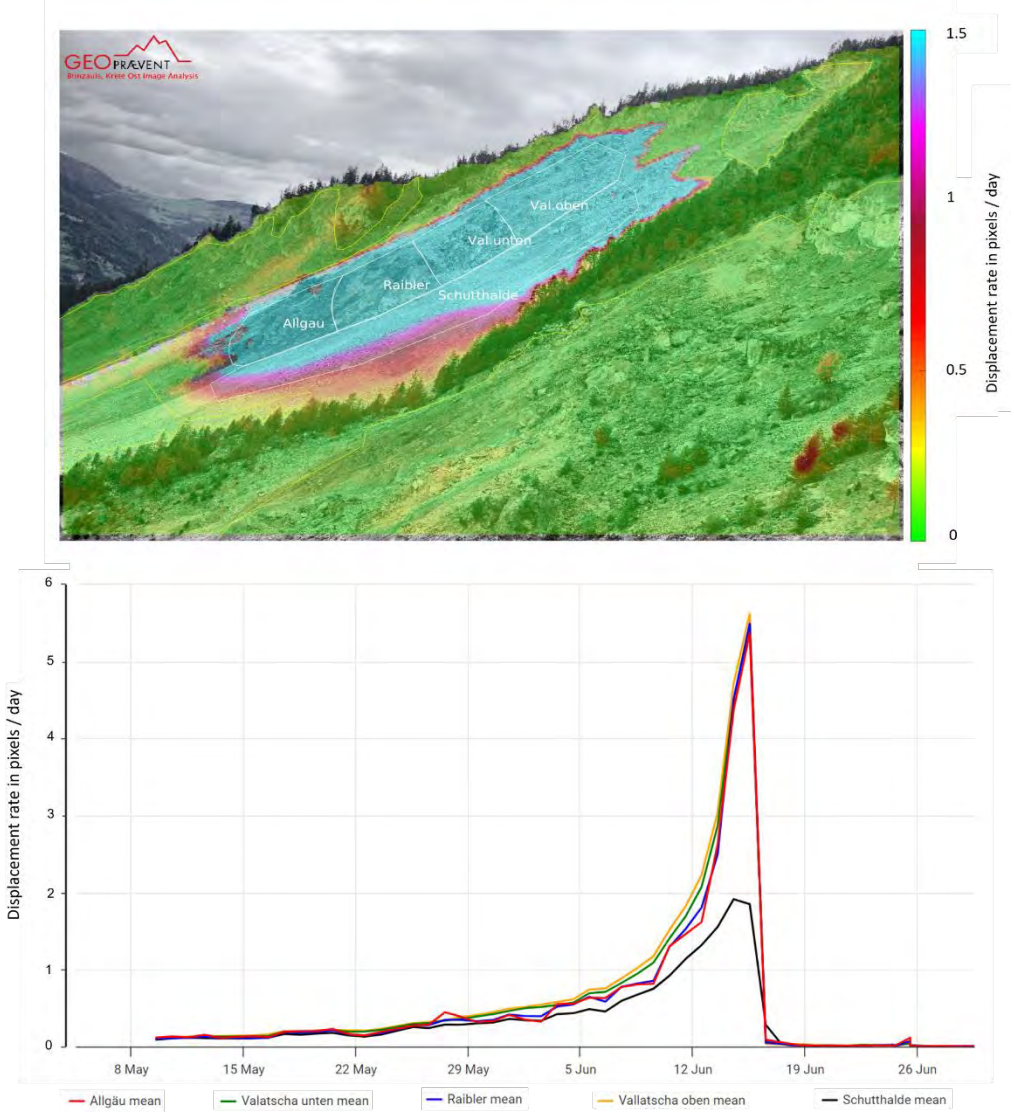

Figure 3. Displacement field a few days before the collapse, with different ROIs defined and delineated in white and the names of the ROIS displayed in the corresponding regions (top). Time series of 2 months of the averaged displacement measured in the different ROIs (bottom).

References

Caduff R, Schlunegger F, Kos A & Wiesmann A (2015) A review of terrestrial radar interferometry for measuring surface change in the geosciences, Earth Surf. Process. Landforms, 40, pages 208– 228.

Gassner J, Wahlen S & Meier L (2022) Radarüberwachung von Massenbewegungen. *Schweizerische Zeitschrift fur Forstwesen* 173 (3): 124–129.

Gojcic Z, Schmid L & Wieser A (2021) Dense 3D displacement vector fields for point cloud-based landslide monitoring. *Landslides* 18, 3821–3832.

Guardian (2023) Huge landslide misses Swiss mountain village of Brienz 'by a hair'. Available at: https://www.theguardian.com/world/2023/jun/16/huge-landslide-misses-swiss-mountain-village-of-brienz-by-a-hair (Accessed: 20 July 2023).

Jones N, Manconi A & Löw S (2022) Satellitenfernerkundung der räumlichen und zeitlichen Entwicklung der Oberflächendeformationen. *Schweizerische Zeitschrift fur Forstwesen* 173 (3): 118–123.

The Landslide Blog (2023) Summary of the 15 June 2023 Brienz/Brinzauls rockslide collapse in the Swiss Alps. Available at: https://blogs.agu.org/landslideblog/2023/06/21/brienz-brinzauls-rockslide/ (Accessed: 20 July 2023)

Travelletti J, Delacourt C, Allemand P, Malet JP, Schmittbuhl J, Toussaint R & Bastard M, 2012. Correlation of multi-temporal ground-based optical images for landslide monitoring: Application, potential and limitations. *ISPRS Journal of Photogrammetry and Remote Sensing* 70, pp.39-55.

Methodology for rockfall hazard and risk assessment

Patrick DIVOUX[1] , Romain JARLAN[2] , Francois VAYSSE[2] , Olivier GUILHEM[1]

[1] EDF Hydro, Chambéry, France
[2] EDF TEGG, Aix en Provence, France

SUMMARY: Rockfall hazard and risk assessment are the subject of various and heterogeneous approaches. Studies are generally conducted by geologists and based on in-house methodologies. They usually focus on the probability of reaching a sector or a target (the hazard) and are often less detailed in terms of knowledge of the issues (human, material, functional), their importance, their exposure, and the associated risks.

The context is sensitive (human risk management) and the scope of works may have no limits. It is usually complicated for the owner to adopt a coherent and rational approach, and to allow subjectivity only a fair and known part in the establishment of its risk management plan. This paper presents a new methodology for a homogeneous rockfall risk management policy at EDF-Hydro. The objective of this methodology is to clarify the role of the various stakeholders and to ensure the solutions chosen correspond to justified, relevant and reasonable choices. It has proven to be useful in solving complex safety issues. The next few years will have to be used to validate and enrich it.

Keywords: rockfall, risk management, hazard, safety issue, methodology

Introduction

This document presents a new methodology for a responsible rockfalls risk management policy developed by EDF and shared within the French national C2ROP project.

Stakeholders

Main stakeholders involved in the management of rockfall risks are :

	Players	At EDF
	The owner	EDF Hydro
	The engineer	EDF-CIH
	Geologist/Geotechnician	EDF-TEGG + Independent Geologist/Geotechnician
	Specialized contractor	Specialized contractor

Table 1: Main stakeholders involved in the management of rockfall risks

French regulations

In France, rockfall issues must be managed in compliance with :

- General principles of prevention: Employers have a duty of safety towards their employees.
- Standard NF P 94 500 - Geotechnical engineering

The main concepts

The main concepts are :

- Geographical perimeter: geographical area in which the study is being carried out.

- Issue: A person, property, activity, resource, asset, etc. likely to be affected directly or indirectly by a natural phenomenon. A distinction is made between human, functional and material issues.
- Target area: Area where the issue could be located.
- Resulting hazard: Uncertain phenomenon that can cause damage. It results from a failure hazard and a propagation hazard.
- Risk: Consequences of a hazard on a stake. A distinction is also made between human, functional and material risk.

Figure 1 illustrates the fundamental difference between risk and hazard. A hazard, even a significant one, does not necessarily generate risk.

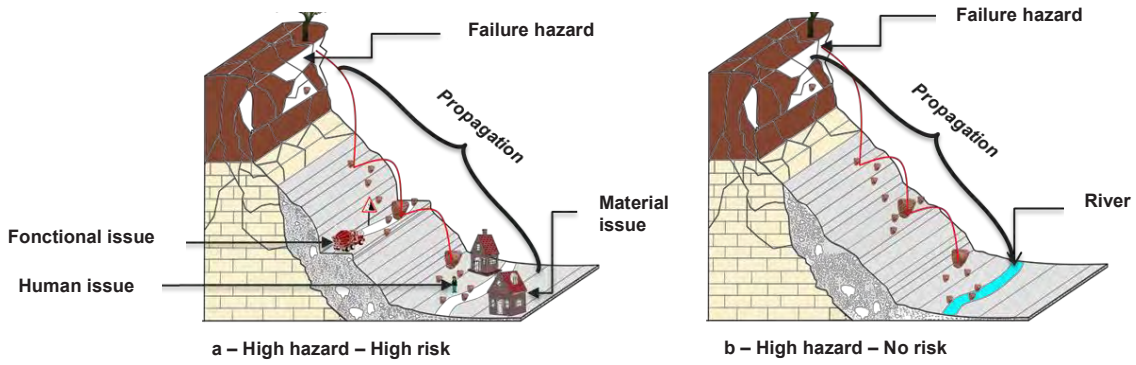

Figure 1 - Difference between a hazard scenario with risk (a), and without risk (b).

Main stages in rockfall risk management

There are 5 main stages in the process of managing a rockfall risk:

1. Defining the issues and the geographical perimeter of the study
2. Assessing the hazard and the risk
3. Study how to reduce the risk (if necessary)
4. Reducing risk
5. Monitoring and maintenance

Defining the issues and the geographical perimeter of the study

The information acquired during the initial site visit should help to define the geographical limits of the study.

The issues identified are classified according to their nature:

- Material issues (property at risk) ;
- Human issues (people under threat) ;
- Functional issues (functionality under threat).

For example:

- the cyclist ≠ the road structure ≠ the link between 2 places
- the operator ≠ the structure of the spillway ≠ the capacity to discharge floods.

Once the issues have been identified, we will consider whether they are permanent or temporary, fixed or mobile.

Assessing the hazard

The hazard assessment is based on a site visit by a geologist charged with assessing the instability of a rock mass and its propagation to the target.

Failure hazard:

The *break-up hazard level* assesses the potential for rock masses to fall within a 30-year reference period according to 4 levels ("Low", "Medium", "High" and "Very high"). As far as possible, the geologist assesses the risk of rock failure on site, based on a geological description of the *factors that determine rock failure*: slope, frostiness of the facies, structure of the rock mass, presence of water or vegetation, history of instabilities....

Propagation hazard:

The aim of the *propagation hazard* study is to characterize the trajectories of rock masses. The *propagation hazard level* assesses the potential for the target to be hit by the rock masses according to 3 levels ("Low", "Medium" and "High").

Resulting hazard:

The *resulting hazard* is the input data for the risk study. The *resulting hazard level* corresponds to the product of the *failure hazard* and the *propagation hazard*. It can be defined as follows:

Resulting hazard	Definition
Low	Low probability that the block will reach the target during the reference period (30 years or 5 years)
Medium	Approx 50% probability that the block will reach the target during the reference period
High	High probability that the block will reach the target during the reference period
Very high	Very high probability that the block will reach the target within a timeframe that is short comparing to the reference period

Table 2: Definition of resulting hazard levels

In the case of a point source hazard, the resulting hazard is given by the following matrix :

Resulting hazard		Failure hazard			
		Very high	**High**	**Medium**	**Low**
Propagation hazard	**High**	**Very high**	**Very high**	**High**	**Medium**
	Medium	**High**	**Medium**	**Medium or Low**	**Low**
	Low	**Medium**	**Medium or Low**	**Low**	**Low**

Table 3: Resulting hazard matrix

Assessing the risk

Considering an issue located in a the target area, its value decreases because of the risk of damage. The loss of value is the risk. It is a directly dependent on:

- the probability that an event occurs and damages the issue,
- the exposure ratio and resistance of the issue in the event of an impact.

The risk equation is:

$$\mathbf{Risk} = P_{Resukting} \cdot T_{Exp} \cdot T_{Damage} \cdot \mathbf{Issue}$$

With :

- **Issue:** Value of the issue
- $P_{Resukting}$ **:** Resulting hazard
- T_{Exp}: Exposure ratio (for a mobile issue)
- T_{Damage} **:** Damage rate in the event of an impact

There are 3 ways to limit the risk of rockfall issues:

1. Decreasing the hazard: Active or passive protection
2. Decreasing the exposure ratio: Decreasing the presence of the issue in the target area
3. Decreasing the damage rate: Improving resistance of the issue

However, not all the parameters in the risk equation can be quantified. Using a qualitative approach, the risk equation becomes:

Risk = Level of hazard x Level of exposure x Damage in the event of an impact

Risk levels are defined in the table below.

Risk	Definition
High to Very High risk (VH/H)	A High to Very High risk requires fast risk mitigation measures to be defined, while permanent solutions are studied and put in place. A Very High risk requires immediate risk mitigation measures.
Moderate risk (M)	A Moderate risk requires a fast study of risk mitigation measures.
Limited risk (L)	A Limited risk requires a high level of vigilance and an appropriate monitoring policy.

Table 4: Definition of risk levels

Assessing the risk for people

The risk analysis will conservatively assume that a person dies in the event of an impact. Thus, the damage rate is equal to 1.

Human life is the unit for measuring human risk. The risk equation becomes (qualitative approach) :

Life Risk = Resulting hazard level x Life exposure level x 1

The risk matrix is based on the knowledge of the resulting hazard level and the exposure level:

			Resulting Hazrad			
			VH	H	M	L
Exposure level	$T_{Exp} > 0.1$	VH	VH	VH	H	M
	$0.01 < T_{Exp} < 0.1$	H	VH	H	M	L
	$0.001 < T_{Exp} < 0.01$					
	$10^{-4} < T_{Exp} < 0.001$	M	H	M	L	L
	$10^{-5} < T_{Exp} < 10^{-4}$					
	$T_{Exp} < 10^{-5}$	L	M	L	L	L

Table 8: Risk assessment matrix for human issue

A similar approach is proposed for the analysis of functional and material risks. More details are given in the paper.

Conclusions

The proposed new methodology for rockfall risk assessment is to move towards more standardized, clear and objective practices. Its aim is to clarify the roles of the various players involved and to assist the owner to implement a risk management policy by adopting a coherent and rational approach. It will be tested and improved over the next few years.

References

CEREMA (2020) - C2ROP - Glossaire du risque rocheux – France - 2020
CEREMA (2020) - C2ROP - Caractérisation de l'aléa éboulement rocheux – état de l'art – France - 2020
CEREMA (2020) - C2ROP - Prise en compte du risque rocheux par les maîtres d'ouvrage gestionnaires d'infrastructures – France - 2020
Divoux P (2021) Rockfall risk assessment – Methodology – EDF CIH - H-30575704-2021-0000142 A
Jarlan R (2020) Rockfall hazard assessment – Methodology for geologists – EDF-TEGG - D309518021923C

Systematic computing for risk assessment of rock slope instability: a case study for Walloon regional roads (Belgium)

Simon DELVOIE[1], Luc FUNCKEN[2], Marc SALMON[3], Gérard SWINNEN[4], Éric HALLOT[4]

[1] Direction de la Géotechnique, SPW-MI, Liège, Belgium
[2] Retired, ex-Direction de la Géotechnique, SPW-MI, Liège, Belgium
[3] Service géologique de Wallonie, SPW-ARNE, Namur, Belgium
[4] Cellule Télédétection et Géodonnées, ISSeP, Liège, Belgium

SUMMARY: Regional roads in Wallonia (Belgium) are frequently faced with rock instabilities. To optimise investments in rockfall risk mitigation along regional roads, a decision-making tool has been developed at the regional scale. This tool consists of an automatic calculation of the rockfall hazard every 10 m on both sides of all regional roads and motorways. The calculation is based on six geometric criteria extracted from a 2D profile perpendicular to the road. A systematic computing approach has been developed to generate these profiles and to determine related geometric criteria. Calculated rockfall hazard values have been compared to well-known rockfall events and give promising results. Additional criteria (*e.g.*, geology, vegetation, water flows) will be included in this approach in a future development.

Keywords: rockfall, hazard, risk, road, Wallonia.

Introduction

Despite its low relief, Wallonia (Belgium) faces with rock instabilities along its roughly 8360 km of motorways and regional roads. These roads are managed by the Service public de Wallonie – Mobilité et Infrastructures (SPW-MI).

Rockfall hazard is not distributed equitably throughout the region. Indeed, most instabilities occur in river valleys and mainly involve limestones, sandstones and shales. In order to reduce the risks on people and regional infrastructures induced by rockfalls, the SPW-MI continuously invests in network security. To optimise investments in rockfall risk mitigation, the SPW-MI in the partnership of the Institut Scientifique de Service Public (ISSeP) are developing a decision-making tool at regional scale. This tool aims to classify road sections according to the risk of rockfalls causing damage. The ultimate goal is to focus the resources allocated for risk mitigation along the road sections characterised by the highest risk values.

Development of the rockfall hazard management tool from a systematic computing approach

Various types of data are utilised for this development. Two vector datasets (shapefiles) represent the road network structure considered in the study. The first corresponds to the road axis (Walloon Geoportal), and the second represents the roadbed (data from the Walous Project). The last data used is smoothed version of the Digital Elevation Model (DEM) of Wallonia with a one-meter resolution, derived from airborne LiDAR acquisitions carried out between 2012 and 2014. The resulting DEM has a horizontal precision less than 1 m and a vertical precision lower than 40 cm.

A Python script is employed to create two perpendicular profiles every 10 meters on either side of the axis of each considered road, capturing the positions and altitudes of 200 points spaced at 1-meter intervals. The "Extract raster values at point locations" function of the ArcGIS Pro software (ESRI) is invoked in the code for this step. The use of this proprietary software function is justified for reasons of efficiency and processing time.

Following the initial data collection, the script loads the 200-point profiles into a Pandas DataFrame. Within this DataFrame, a total of six geometric criteria (F1a, F1d, F2, F3, F4 and F5) are determined from the generated profiles to calculate the corresponding rockfall hazard values (Figure 1). The use of this type of Dataframe allows for matrix calculations. This presents several advantages. First, it enables vectorized operations, significantly speeding up calculations compared to basic Python nested loops. Additionally, maintaining data in a DataFrame ensures consistency and simplifies data manipulation. Finally, the use of Pandas' built-in statistical and analytical functions provides a direct way to apply complex calculations to DataFrame columns, saving time and reducing the risk of errors.

Geometric criteria used for the calculation of rockfall hazard (*R*) (Figure 1) are as follows:

- *F1a* and *F1d* are related to the presence of a maximum local slope. Both criteria bring information on the existence of a rock face that could generate block instabilities on the slope. *F1a* represents the angle of the maximum local slope (minimum 5 m high) while *F1d* is the horizontal distance between this escarpment and the slope foot. *R* and *F1a* are related by a sinusoidal trend starting from 30°. Concerning *F1d*, the closer the maximum local slope is, the higher rockfall hazard is.
- *F2* is the "mean" angle of the slope, starting from the slope foot and determined when the line intersects the profile. *F2* gives an idea of the mean slope on which blocks can move. *R* evolves according to a sinusoidal relationship with *F2*.
- *F3* corresponds to the total height of the slope. Slope height is the vertical distance between roadside and the point on the profile where the slope angle starts to be lower than 30°. Below this angle value, it is generally assumed that isolated blocks settled down the slope can only move slowly by creeping (Schyns et al., 2008). It is considered the higher the slope is, the higher rockfall hazard is.
- *F4* represents a security parameter as it corresponds to the horizontal space available to collect rockfalls between roadside and the slope foot. The latter is arbitrary defined as the point of the profile at which the slope angle starts to be higher than 15°. *R* value decreases according to an exponential equation with *F4*.
- *F5* is the energy line angle used to determine rockfall runout zones. In this study, the energy line connects roadside to the point on the profile used to calculate *F3*. Previous studies assessed the minimum energy line angle is 25° for boulder instabilities (*e.g.*, Guide technique MEZAP, 2021). As a result, *F5* acts on rockfall hazard as a global condition.

Finally, rockfall hazard (*R*) is calculated according to the equation (1):

$$R = \begin{cases} \frac{(F1a.F1d)/3+2.F2+F3}{F4}, & F5 \geq 25 \\ 0, & F5 < 25 \end{cases} \quad (1)$$

All data and calculated values are subsequently stored in a PostgreSQL database. Each record is indexed by the road number, the division relative to road kilometre markers, the road side (left or right), and the calculated hazard values. This offers the advantage of connecting this database to various representation systems or GIS software, as well as the ability to modify or update all or part of the data based on a new road network or changes in one or more criteria or weighting factors.

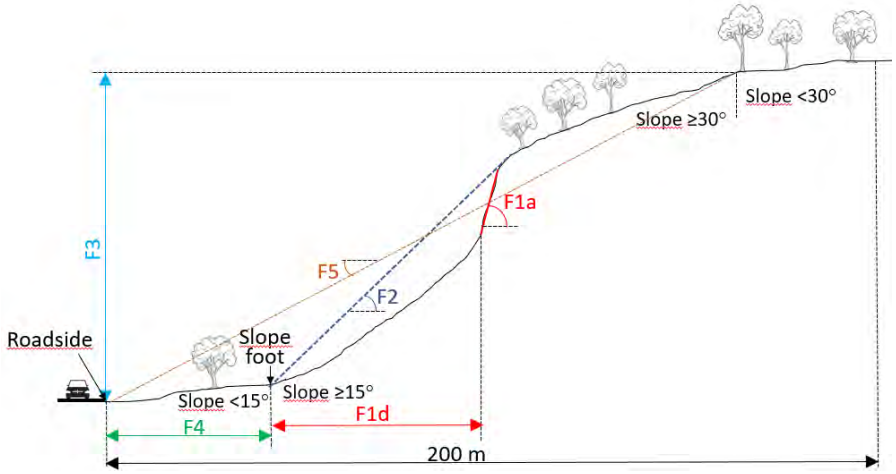

Figure 1. Diagram illustrating criteria used in the rockfall hazard calculation.

A second Python script queries the database to find profiles where the calculated rockfall hazard values exceed a specific minimal threshold below which the danger is considered non-existent. For segments where the hazard should be considered, the script generates an image (*.png format) of a standardised graph displaying the elevation profile, calculated criteria, and the positions of various thresholds necessary for calculating the rockfall hazard for that profile. This graph is then referenced and associated with the profile in the PostgreSQL database for future reference.

Results

The methodology was tested firstly on pilot sites in order to confirm calculated rockfall hazard values with field reality. Pilot sites were chosen with different topographies and configurations (cliff, inclined slope, distance from the road, total height). Once this step validated, calculation was extended to the entire regional road network.

Results are displayed on a GIS application (Figure 2) also accessible on the field using a tablet or smartphone application. It displays the position of road sections characterised by rockfall risks according to a defined scale. The application also offers the possibility to display various topographic maps, the hillshaded digital elevation model and graphs in image format for a comprehensive understanding of the situation.

Rockfall hazard is classified in three categories according to calculated values:

- $R \in [12; 30]$: low risk
- $R \in]30; 50]$: moderate risk
- $R \in]50; 74]$: high risk

Profiles with calculated values lower than 12 do not present enough rockfall risks to be considered further in the study. The distribution of profiles characterised by a rockfall risk higher than 12 is illustrated in Figure 3a. According to these results, the regional road network is composed of roughly 9500 cumulated meters having a high rockfall risk (R>50). Some of these roads are already secure.

Afterwards, rockfall hazard calculated values are compared to known rockfall events on roads. In total, 35 well-documented rockfall events are used, occurring between 1988 and 2023 all over the region (Figure 3b).

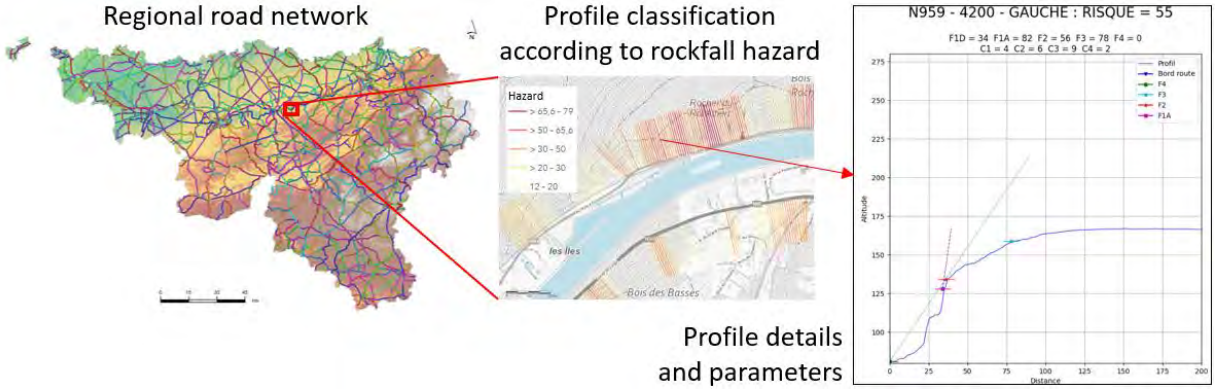

Figure 2. Illustration of the GIS application available to access rockfall hazard data.

Rockfall events should occur more frequently along roads characterised by a high degree of risk. Based on the well-documented rockfall events located throughout the region, Figure 3c confirms this assumption.

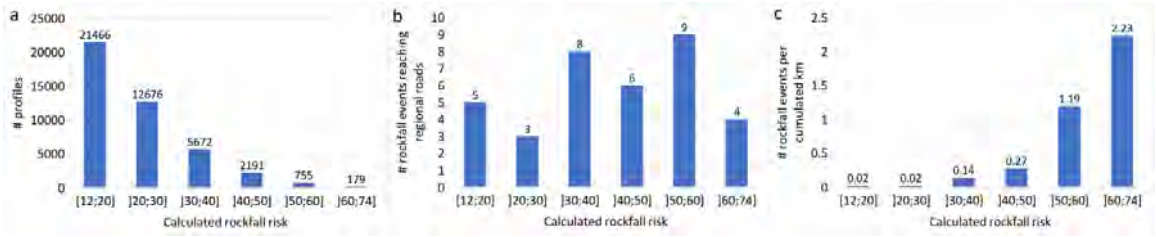

Figure 3. Results of the calculated rockfall risk values. (a) number of profiles; (b) number of well-documented rockfall events reaching regional roads; (c) number of rockfall events by cumulated km of regional roads.

The field application also offers a field survey form to describe the environment (wall structure, presence of blocks or landslides, vegetation type, water flow, etc.), allowing for validation or dismissal of the risk. Field photographs can also be associated with the data. All of this is saved and updated in real-time within the database.

Conclusions and perspectives

This study has developed a decision-making tool at regional scale (Wallonia) to prioritise road sections that require investments in rockfall risk mitigation. The calculated rockfall hazard is based on six geometric criteria determined from the 2D slope perpendicular to the road. At site scale, these six geometric criteria give a first idea of the mean rockfall hazard. However, at local scale, these criteria are not enough, and further investigations are needed to make more accurate and more reliable rockfall hazard.

Future developments of the tool will include data characterising rock mass (stratification, fracturing), water and vegetation. These additional parameters will be obtained in the field and from existing geological data.

References

Guide technique MEZAP (2021) Caractérisation de l'aléa rocheux dans le cadre d'un Plan de Prévention des Risques Naturels (PPRn) ou d'une Porter à connaissance (PAC). BRGM éditions. Collection scientifique et technique. Orléans, France, 70p.

Schyns J-C, Salmon M., Juvigné E & Ozer A (2008) Cartographie numérique des zones à risques d'éboulement de parois rocheuses en relation avec les zones urbanisables et les voies de communication. Synthèse finale des Conventions 1 (98/46065), 2 (03/42281) et 3 (05/47864). DGATLP, Région wallonne, 26p.

Analysis of Rainfall-induced Multiple-Occurrence Regional Landslide Events (MORLEs) in the Philippines

Malyn Tumonong[1], Jean-Philippe Malet[1,2], Catherine Bertrand[3]

[1] University of Strasbourg, CNRS UMR 7063, Institut Terre et Environnement de Strasbourg, Strasbourg, France
[2] University of Strasbourg, CNRS UAR 830, Ecole et Observatoire des Sciences de la Terre, Strasbourg, France
[3] University of Bourgogne Franche-Comté, CNRS UMR 6249, Laboratoire Chrono-Environnement, Besançon, France

SUMMARY: On average, around 20 typhoons hit the Philippines annually. Of these numbers, 1 or 2 per year have caused multiple-occurrence regional landslide events (MORLEs), yet it is a barely studied phenomena in the Philippines. This research focuses on the analysis of 11 typhoon events from 2015 to 2022 that caused MORLEs in several provinces all over the country. The research aims at constructing multiple landslide event inventories coincident with detailed rainfall events, analyse their statistical properties, together with the typhoon properties, not only to identify rainfall – landslide threshold values but also try to understand the quantity and properties of landslides that can be predicted to likely occur given a particular typhoon level or rainfall event and a particular landscape. This will help in establishing the basis for increased landslide disaster resilience for the communities through early-warning.

Keywords: multiple-occurrence regional landslide events (MORLEs), Philippines, landslides, tropical cyclones, typhoons

Introduction

The importance of landslide studies in the Philippines cannot be overemphasized as landslide disasters in the country is a fairly regular occurrence causing thousands of deaths and millions of pesos in infrastructures and agriculture damages. In the Global Fatal Landslide Database (GFLD), a landslide database that contains a total of 5490 landslides incidents for the period from 2004 to 2017, the Philippines ranks the third (3rd) worldwide with 480 landslides (Froude & Petley, 2018). Whereas in the Global Landslide Catalog (GLC), a database with 6784 landslides recorded between 2007 and 2015, the country ranks the fourth (4th) worldwide with 591 landslides (Gomez et al, 2023). Moreover, in Southeast Asia, Philippine data accounts for 46% of rainfall triggered landslides and 42 % of rainfall-triggered landslide events were caused by typhoons (Froude & Petley, 2018).

I. Hydrometeorological triggers and regional geology of incident sites

On average, around 20 tropical cyclones enter the Philippine Area of Responsibility (PAR) annually (PAGASA, n.d.) (Fig. 1a and 1b) more than any other location on earth (PAGASA, n.d., Carlowicz, 2021). Of these number, five (5) are considered destructive (ADRC, n.d.). Aside from the 2018 study of Froude & Petley that showed that in 2009, 67 % of rainfall-triggered landslide events in the Philippines were associated with tropical cyclones: 60 landslide events compared with an average 12 triggered by tropical cyclones, many triggered on the same day (8 October 2009) by Typhoon Parma, there are very few published articles that

establishes how many of the annual typhoons cause how much landslides in the country. In the same study, Froude & Petley mentioned that monsoons also cause rainfall-triggered landslides in the Philippines. This should be differentiated from the tropical cyclone rainfall-induced landslides. In this research, focus will be on rainfall-triggered landslide associated with tropical cyclones.

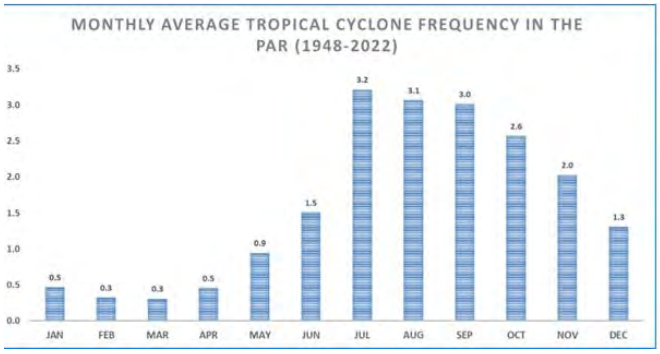

Figure 1a: The number of tropical cyclones in the Philippines per month from 1948 - 2022

Image source: PAGASA website (https://bagong.pagasa.dost.gov.ph/information/about-tropical-cyclone)

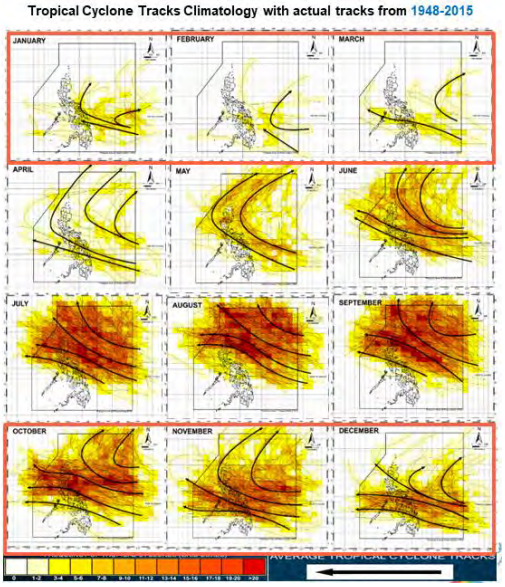

Figure 1b: Tropical cyclone tracks in the Philippines 1948 - 2015

Image source: PAGASA website (https://bagong.pagasa.dost.gov.ph/information/about-tropical-cyclone)

Of the tropical cyclones from 2015 to 2022, there have been several that have been identified to have caused multiple-occurrence regional landslide events (MORLEs, Crozier, 2005) in different parts of the Philippines. It should be noted that there could be more. However, for this research, 11 tropical cyclones from that period and 1 from 2009 (Fig. 2), from 11 different sites will be studied.

The region covered by the landslides varies in size up to more than 600 km^2. Aside from the varying intensities of these tropical cyclones, the affected sites also vary in terrain and geology. The regional geology of the study sites are summarized in Table 1. A more detailed geology will be utilized when available.

Table 1. Summary of Regional Geology of Incident Sites

Hydrometeorological Trigger	Year	Location	Regional Geology	Description
1) Tropical Storm Nalgae	October 2022	Datu Odin Sinsuat, Maguindanao	Sandstone,shales,reef limestone	Extensive mixed shelf marine deposits largely wackes, shales and reef limestone assoc with paralic coal
2) Tropical Storm Megi	April 2022	Abuyog, Leyte	Andesite and/or basalt flows	Mostly submarine andesite and/or basalt flows intercalated with pyroclastics and clastic sed'y rocks and/or reef limestone
3) Typhoon Rai	December 2021	Puerto Princessa, Palawan	Spilitic and basic flows	Essentially spilitic and basic flows; usually intercalated with graywackes. Transgressive on basement rocks

4) Tropical Cyclone Vamco	November 2020	General Nakar, Quezon	Undifferentiated	Largely graywacke and metamorphosed shale interbedded w/ spilitic,basic,intermediate flows and/or pyroclastics
5) Typhoon Kammuri	December 2019	Iligan, Isabela	Undifferentiated	Largely graywacke and metamorphosed shale interbedded w/ spilitic,basic,intermediate flows and/or pyroclastics
6) Typhoon Mangkhut	September 2018	Itogon, Benguet	Undifferentiated metavolcanics	Metamorphosed spilites and basalts, keratophyres and andesites
7) Tropical Storm Tembin	21-25 December 2017	Tubod, Lanao del Norte	Marine clastics, pyroclastics	Marine clastics overlain by pyroclastics and tuffaceous sedimentary rocks assoc with calcarenites
8) Tropical Storm Kai-Tak	16 -19 December 2017	Biliran, Biliran	Marl, reworked tuff, pyroclastic	Marine and terrestial sediments associated with limestone; with pyroclastics,gravel deposits
9) Super Typhoon Haima	October 2016	Boliney, Abra	Quartz Diorite	Largely intra-Miocene Quartz diorite, batholiths and stocks.
10) Typhoon Melor	December 2015	Baco, Oriental Mindoro	Gneiss, schist, phyllites-slates	Undifferentiated gneiss, quartzofeldspathic and mica schist, and phyllites-slates assoc with marble, limestone and arenite
11) Typhoon Koppu	October 2015	Gabaldon, Nueva Ecija	Spilitic and basic flows	Essentially spilitic and basic flows; usually intercalated with graywackes. Transgressive on basement rocks
12) Typhoon Parma	October 2009	Itogon, Benguet	Undifferentiated metavolcanics	Metamorphosed spilites and basalts, keratophyres and andesites

II. Objectives

Landslide research is thriving and a growing field of study in the Philippines (Gumiran & Daag, 2021; Lagmay 2017; Oh & Lee, 2011; Nolasco-Javier & Kumar, 2018). In spite of this there is no detailed landslide inventory maps aside from point-identified landslide maps (Jones et al, 2023). Consequently, existing landslide susceptibility maps are limited and inadequate to provide the necessary information to better equip the authorities in managing and mitigating landslide risks in the country.

Hence, this research aims to answer this primary resource gap and construct multiple landslide event inventories coincident with detailed rainfall events with more details that can define magnitude and define magnitude-frequency relationship (Guzzetti, 2021). Secondly, this research will analyse the landsides statistical properties, together with the typhoon properties, not only to identify rainfall – landslide threshold values but also try to understand the quantity and properties of landslides that can be predicted to likely occur given a particular typhoon level or rainfall event and a particular landscape.

Ultimately the goal will be the development of a landslide initiation and propagation model to better explain the phenomena. Finally, the recognition and definition of a link between rainfall properties and the spatial pattern of landslides will be applied in the establishment of early-warning systems and disaster resilience programs for the communities.

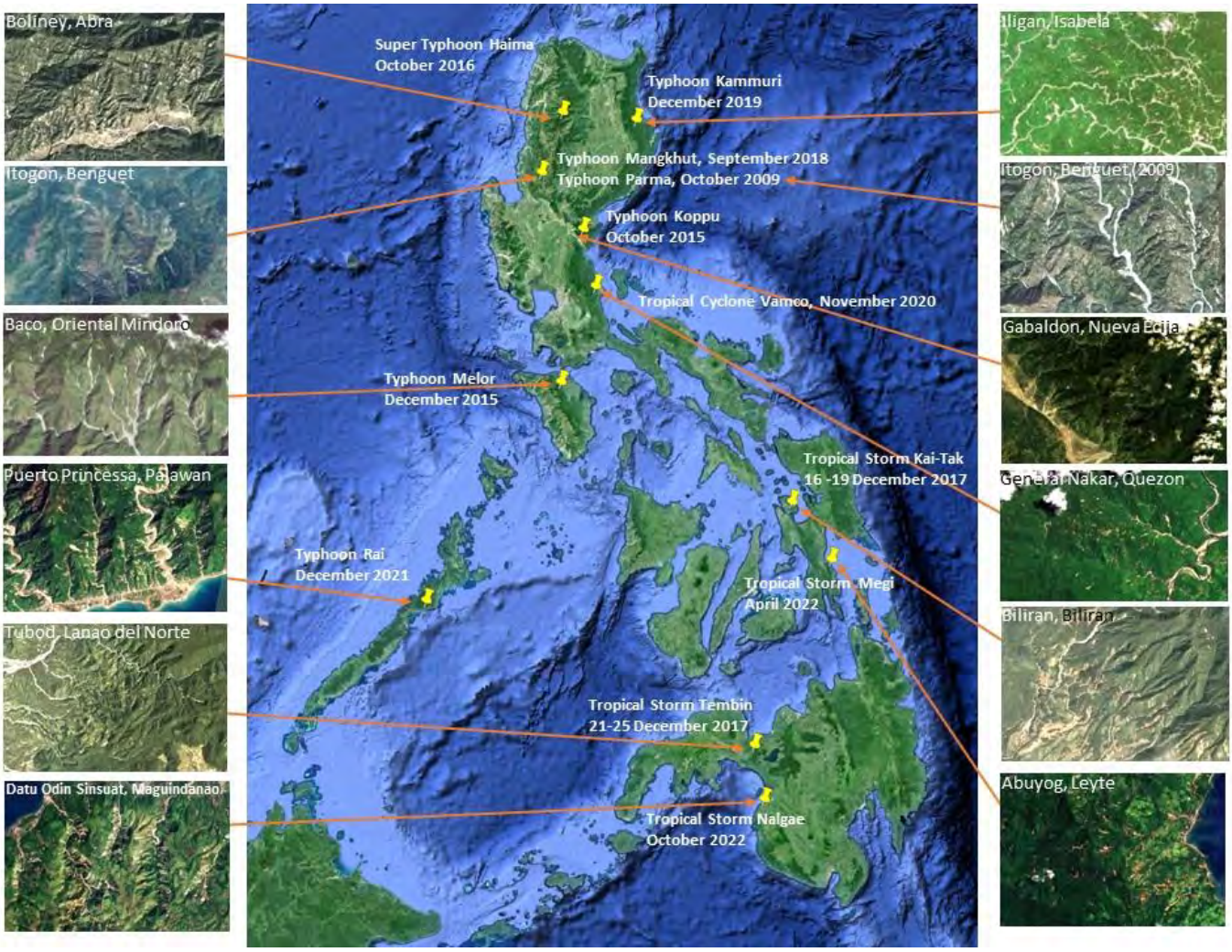

Figure 2: Location of the study sites and the different meteorological events that triggered them.

III. Methodology

In pursuit of these objectives the several methodologies will be applied. In the creation of a detailed landslide inventory, different satellite imageries will be used considering both pre and post typhoon images. These would be Planet Labs (3 m resolution), Sentinel 2 (10 m resolution) and Google Earth imagery. Upon identification and manually digitizing the landslides as polygons, these then will be synthesized with the relevant thematic layers of geology, soil type, land cover, including geomorphological parameters such as a DTM (Digital Terrain Model). All these will be analysed with the information of the hydrometeorological triggers.

To better define magnitude, a landslide polygon will be further delineated as to the source area, propagation zone and the depositional area where applicable (Fig. 3c). This is done to ascertain that landslide size statistics are not summed up from both landslide source area and run out or propagation zone to avoid overestimation of landslide volume (Marc et al, 2018). This will contribute to developing a better landslide initiation and propagation model.

For the hydrometeorological triggers, aside from the rainfall amount, the relationship between the landslide spatial patterns and spatiotemporal pattern of the tropical cyclone will be

particularly looked into as current data has shown a weak relationship between rainfall and landslides in Southeast Asia that is reflective of the complex weather systems active in the region (Froude & Petley, 2018). In the Philippines, in the study site of Itogon, Benguet, multiple landslides occurred during high-intensity rainfall coinciding with the highest soil moisture values. However, other rainfall events in the months leading up to Typhoon Mangkhut that had similar or higher rainfall intensities and also occurred when soils were saturated did not trigger widespread landsliding (Abanco et al, 2021). Moreover, the density of landslides was higher in areas of greater antecedent rainfall and not at the core of rainfall intensity cell (Nolasco-Javier & Kumar, 2018; Abanco et al, 2021). Thus, the use of rainfall anomaly will be applied (Marc et al, 2019) that might prove better relate the complex weather system and geographic setting of the country.

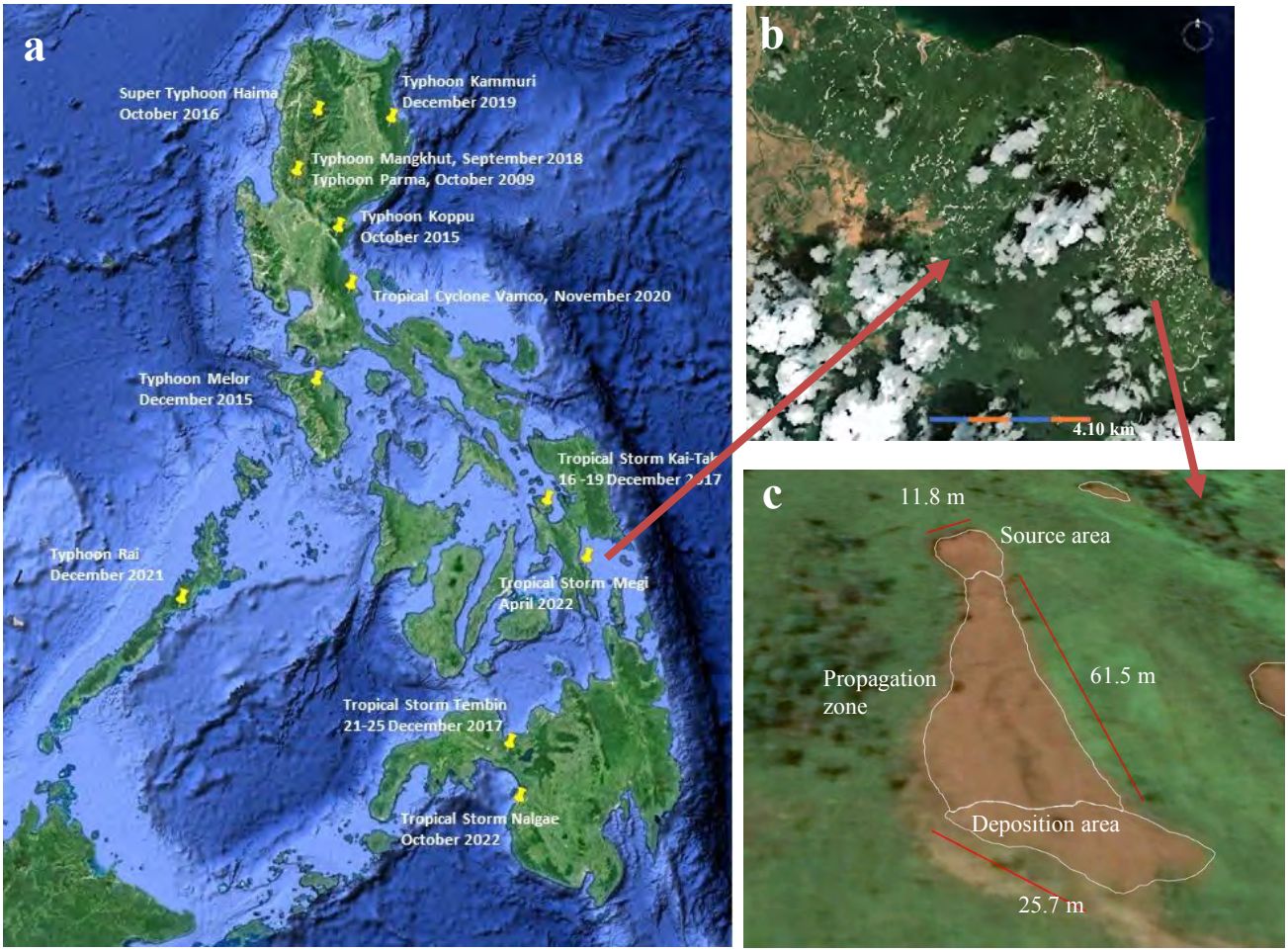

Figure 3: a) Map of the Philippines showing study sites and tropical cyclone triggers; b) Inventory map of landslides caused by Tropical Storm Megi on April 2022 in Abuyog, Leyte Province; c) a digitised landslide polygon

References

Asian Disaster Reduction Center (ADRC). Information on Disaster Risk Reduction of the Member Countries. Retrieved October 4, 2023 from https://www.adrc.asia/nationinformation.php?NationCode=608&Lang=en,

Carlowicz M (2021). Super Typhoon Rai https://earthobservatory.nasa.gov/images/149228/super-typhoon-rai.

Crozier, M.J. (2005). Multiple-occurrence regional landslide events in New Zealand: Hazard management issues. Landslides, 2, 247-256.

Froude M.J., Petley D.N. (2018) Global fatal landslide occurrence from 2004 to 2016. Nat Hazard 18(8):2161–2181.

Gómez, D., García, E.F. & Aristizábal, E. (2023) Spatial and temporal landslide distributions using global and open landslide databases. Nat Hazards 117, 25–55. https://doi.org/10.1007/s11069-023-05848-8
Gumiran, B. A., & Daag, A. (2021). Negotiated participatory action research for multi-stakeholder implementation of early warning systems for landslides. International Journal of Disaster Risk Reduction, 58, 102184.
Guzzetti, F. (2021). Invited perspectives: Landslide populations – can they be predicted?, Nat. Hazards Earth Syst. Sci., 21, 1467–1471, https://doi.org/10.5194/nhess-21-1467-2021.
Jones, J. N., Bennett, G. L., Abancó, C., Matera, M. A., & Tan, F. J. (2023). Multi-event assessment of typhoon-triggered landslide susceptibility in the Philippines. Natural Hazards and Earth System Sciences, 23(3), 1095-1115.
Lagmay, A. M. (2017). Nationwide Operational Assessment of Hazards (NOAH). A responsive program for disaster risk reduction in the Philippines. Humanit. Technol. Survey. Singap. RSIS Cent. NTS Stud, 16-19.
Marc, O., Stumpf, A., Malet, J.-P., Gosset, M., Uchida, T., and Chiang, S.-H. (2018). Initial insights from a global database of rainfall-induced landslide inventories: the weak influence of slope and strong influence of total storm rainfall, Earth Surf. Dynam., 6, 903–922, https://doi.org/10.5194/esurf-6-903-2018.
Marc, O., Gosset, M., Saito, H., Uchida, T., Malet, J-P. (2019). Spatial Patterns of Storm-Induced Landslides and Their Relation to Rainfall Anomaly Maps. Geophysical Research Letters, 46 (20), pp.11167-11177. 10.1029/2019GL083173 . hal-03517587
Nolasco-Javier, D. and Kumar, L. (2018). Deriving the rainfall threshold for shallow landslide early warning during tropical cyclones: a case study in northern Philippines, Nat. Hazards, 90, 921–941, https://doi.org/10.1007/s11069-017-3081-2, 2018.
Oh, H. J., & Lee, S. (2011). Landslide susceptibility mapping on Panaon Island, Philippines using a geographic information system. Environmental Earth Sciences, 62, 935-951.
Philippine Atmospheric, Geophysical and Astronomical Services Administration (PAGASA) (n.d.). Tropical Cyclone Information. Retrieved October 4, 2023 from https://www.pagasa.dost.gov.ph/climate/tropical-cyclone-information.
Petley, D. (2012). Global patterns of loss of life from landslides. Geology, 40(10), 927 930.

Management of a major landslide : feedback from Passy state forest (Haute-Savoie, France)

Rémy Martin[1], Jérôme Palisse[2], Guillaume Thirard[3]

[1] French National Forest Office, RTM Service – Northern Alps Agency, 38000 Grenoble, France
[2] French National Forest Office – Natural Hazards Department, 38000 Grenoble, France
[3] French National Forest Office, RTM Service – Southern Alps Agency, 04000 Digne-les-Bains, France

SUMMARY: This study shows an example of operational management of a landslide in a mountainous area by the "Restoration of Mountain Land" department of the French National Forest Office (ONF-RTM) on behalf of the Ministry of Agriculture. The aim is to share a concrete case of natural risk management, with feedback from several decades on a specific site. This study seeks to highlight the improvements made to the local risk management system, but also the difficulties and constraints associated with the management of complex phenomena by several stakeholders.

Keywords: landslide, mudflow, risk management, mountain hazard, land restoration.

Context and origin of the issue

In 1886, the municipality of Passy (Haute-Savoie) began discussions to limit the damage caused to the village of Passy by mudflows from a stream called “Nant des Pénys”, by asking the State to acquire lands under the RTM policy. However, the first mention of the creation of the state forest dates to 1940.

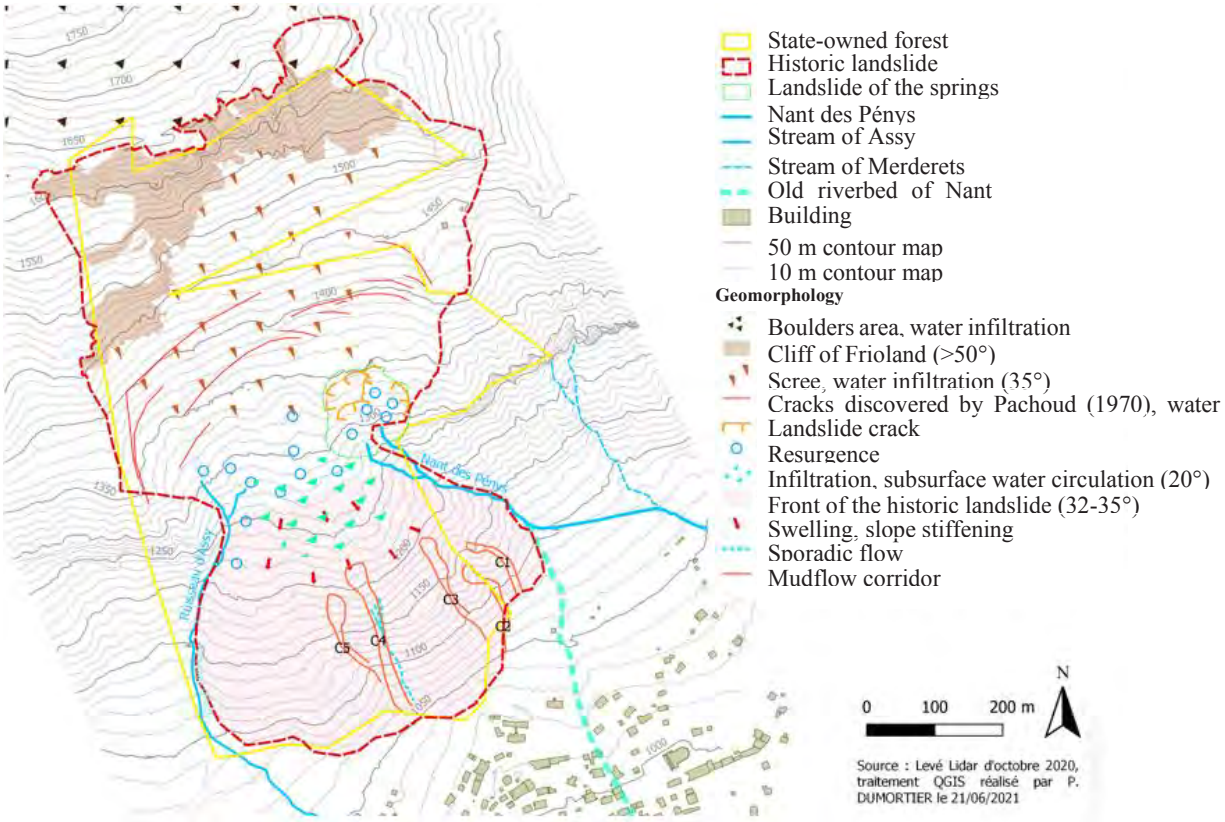

Figure 1 - Geomorphological sketch of the Pénys’ landslides (ONF-RTM, 2015)

In April 1970, the Plateau d'Assy disaster later occurred in this area (71 deaths in a sanatorium following a mudslide). That same year, on 15 May 1970, two mudslides flowed through the C2 and C4 corridors in the forest because of melting snow (Figure 1), stopping close to houses.

The phenomenon occurring here is related to two nested landslides (Figure 1): the historic Pénys landslide and a second one triggered at the springs of the Nant des Pénys. The former is the result of a large-scale slope movement, while the latter is a worsening of the former within the deposits in the accumulation zone.

Technical studies and landslide assessment

At the beginning, the statement is clear and observation-based: mudflows are occurring from an active landslide zone in the catchment area of the Nant des Pénys. The role of water has been established from the outset.

The geological studies conducted by BRGM (French geological survey) in the early 1970s laid the foundations for understanding the dynamics of the slope (Pachoud, 1970 and 1972). The problem was no longer just the landslide at the "springs of the Nant des Pénys" but the discovery of a potential movement of the whole slope. The investigations were based on core drilling, active tracing, the implementation of piezometers and measurements of drain flow.
This study revealed cracks upstream, identified as signs of retrogression. It also raised the question of the origin of the initial trigger: marly flow followed by a break in the tithonic bar at the centre of the slope, or an overall movement from the Urgonian limestones in the upstream.

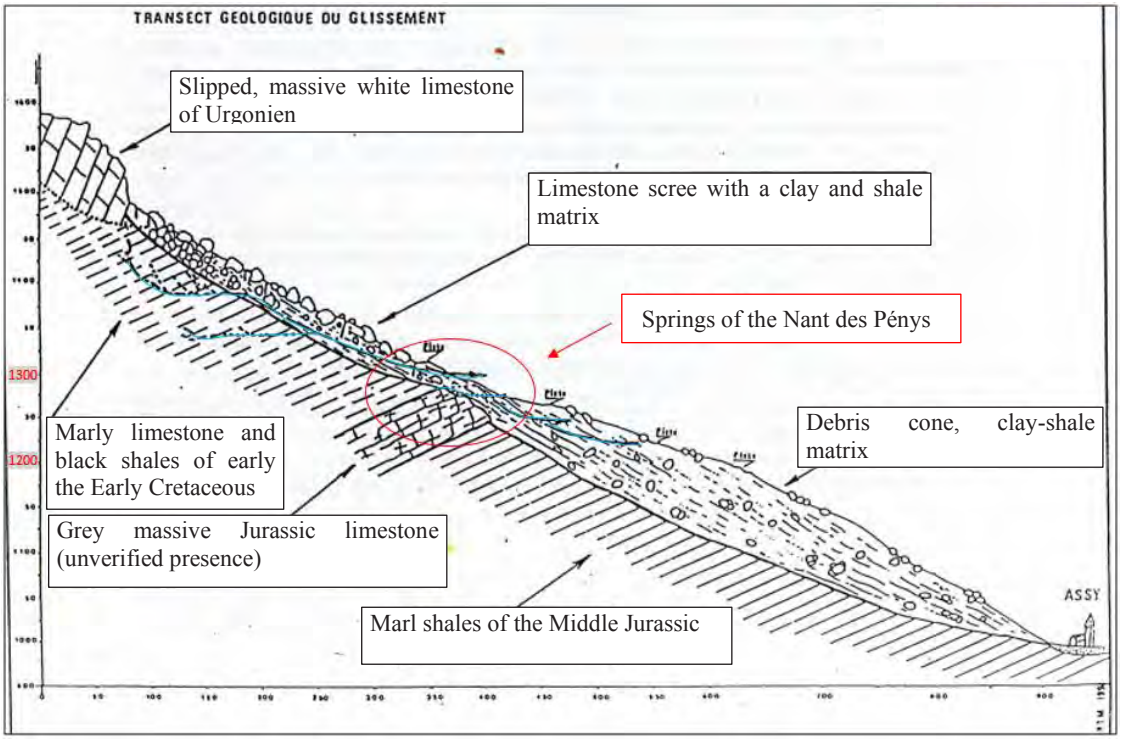

Figure 2 – Extract of the Geological diagnosis of the landslide (ADRGT & Cogoluenhes; 1989)

The investigations and instrumentation carried out in the following years led to the hypothesis of a 250 m failure in the Jurassic limestone (ADRGT, 1988; Cogoluenhes, 1989), without being able to establish a link between deformation and climatic forcing. From these observations, it is decided to focus on the most frequent downstream induced phenomenon: mudflows due to

the increase of the slope of the deposits on the front of the slide because of the slow advance of the debris cone. The origin of these mudflows was identified at around 1,220 m altitude. In addition, the minimum mudflow volume required to reach houses from the gullies have been specified (1,000 to 2,000 m^3), as well as the corresponding return period (30 to 50 years). Thus, material traps could be sized and built.

From a hydrogeological approach, the karstic functioning of the tithonic limestones has been confirmed, explaining the presence of the springs line. The weathering of the limestone wall, which is fractured and underlain by reworked deposits, makes it a permeable bedrock into which water from resurgences can seep at around 1,250 - 1,300 m. These shallow circulations would then be the origin of sporadic flows and mudflows at the historical landslide front lobe.

At the beginning of the 21st century, new investigations, in particular topographical ones by DGPS, revealed an average displacement of 3 cm/year, and the need to streamlining the monitoring. This streamlining will involve setting up a five-year lidar survey, recommended in the risk catchment study (EBR) carried out in 2015 (ONF-RTM, 2015). Subsequently, the landslide of the Nant des Pénys springs was reactivated in 2020, allowing more precise requirements for a reliable lidar survey to be defined. In 2021, an avalanche followed by an acceleration of the “springs landslide” also highlighted the relationship between these two natural hazards.

Corrective measures and operational management

Since the 1940s, the protective measures implemented have required constant adaptation, according to the "observation-correction" method implemented by the ONF-RTM service:

- 1941: creation of a 9.3 m high masonry dam and drainage system to manage the landslide of the springs. These structures were quickly destroyed.
- 1976-1977: rehabilitation operation with curtainwall and counter-dam downstream, to save time in the light of new landslide observations. It was severely damaged in 1978.
- 1978-1979, a system for channeling and storing mudflows has been set up in the Nant des Pénys, and deviation structures for avalanche and mudflows are made with gabions.
- 1982-1990: 24 precast concrete weirs are built in the Ruisseau d'Assy, to limit erosion. At the same time, the drainage network is extended to a total of 1,900 m, extending the water control strategy to the whole slope affected by landslides.
- 1984-1988: a passive mudflow trap solution is implemented and designed for a return period of 50 to 100 years, based on the ADRGT study (1988).
- 1990: set-up of an automatic monitoring system, then destroyed by a collapse in 2000.

Nowadays, drainage maintenance is ongoing and requires recurrent repair work, based on empirical knowledge, and constrained by the technical ability to build trenches on slopes. This system is complemented by the lidar monitoring recommended in the 2015 study. The reactivation of the “springs landslide” in 2020 served as a reminder of the overall management required by the mudflow deviation system, which needs frequent curating. Indeed, the drainages are in state-owned forest, while the deviation and storage structures are on municipal land.

Protection strategy against natural hazards

When the Passy state forest was created, the aim was not to stabilise the landslide but to reforest it and carry out the required facilities.

In 1976, a ZERMOS map (zones exposed to the risks of soil and subsoil movement) was produced for the municipalities of Passy and Servoz (Pachoud, 1976). This map is produced by expert method and aims to map at a scale of 1:25,000 the spatio-temporal probability of occurrence of ground movements (Humbert, 1977). This mapping classifies the area as a "declared, active hazard".
Since 2014, a natural risk prevention plan (PPR) has been approved, setting out measures to reduce vulnerability through regulatory preventive action. The hazard maps classify the exposed areas as follows:

- ***Historical landslide***: landslide hazard G2 (moderate) to G3 (high) with a reference scenario of 1,000 m^3 mudflow.
- ***Pénys "springs landslide"***: torrential hazard T3 (high), but for a scenario that does not consider the deviation structure. The PPR would therefore need to be updated, as current regulations consider the failure of sufficiently sized structures.
- ***Urgonian cliffs***: rockfall hazard P1 (low) resulting from a collapse of 500 to 1,000 m3.
- ***Avalanche corridors:*** avalanche hazard A2 (moderate) to A3 (strong), with a large extent that imposes regulations on the entire eastern part of the municipality.

It should be noted that the mudflow management facilities for the "springs landslide" are also identified as avalanche protection, as they are in the axis of the avalanche corridors.

Summary and conclusion

The assessment and operational management of the Pénys' landslides at the Passy state-owned forest is based on geological and geotechnical analyses, and several years of ground movement monitoring. The investigations were sufficiently conclusive to enable a protection strategy to be adopted for the historical landslide. Several issues remain in relation to the "springs landslide", in the lower part of the slope, regarding (1) the rockfall hazard initiated by scouring around the boulders on the slopes, and (2) the link between landslide activity and avalanches.
Although adjustments have been necessary since the creation of the state-owned forest (the so-called "observation-correction" principle), it has been possible to define a type of monitoring, the sizing of facilities and urban planning regulations.
In the end, all the studies carried out have merely confirmed Pachoud's initial findings. Another clear statement for effective and operational risk management is the requirement of a coordination between stakeholders, i.e., the municipality, the French government, and the ONF-RTM service.

References

ADRGT, AZIMI C., DESVARREUX P. (1988) Etude des risques de formation de coulées boueuses dans le versant du Nant des Pénys, Commune de Passy. Etude ADRGT

COGOLUENHES P. (1989) Périmètre de l'Arve, Série domaniale RTM de Passy, Secteur du glissement des Pénys, Travaux dans les périmètres. Etude ONF-RTM 74

HUMBERT M. (1977) La cartographie en France des zones exposées à des risques lies aux mouvements du sol—cartes ZERMOS. Bulletin de l'Association Internationale de Géologie de l'Ingénieur, Vol.16, N°1, 80-82.

ONF-RTM. (2021) Etude de bassin de risque, division domaniale des Pénys. Rapport ONF-RTM74

PACHOUD A. (1970) Etude des relations entre la circulation de l'eau et les glissements de terrains dans la région des Pénys à Assy, Commune de Passy (Haute-Savoie), *BRGM*

PACHOUD A. (1972) L'instabilité des terrains au-dessus d'Assy, Résultat des travaux de reconnaissance effectués en 1971, *réf. 72 SGN 036 JAL, BRGM*

Preliminary Landslide Risk Assessment and Monitoring along theWhitehorse Escarpment, Yukon, Canada

Marc-André Brideau[1], Lukas U. Arenson[1], Michael Porter[1], Adam Mickey[2], Taylor Eshpeter[2], Severin Staehly[3], Adam W. Wallace[4]

[1] BGC Engineering Inc., Canada
[2] City of Whitehorse, Canada
[3] Geoprevent, Switzerland
[4] Tetra Tech Canada Inc., Canada

SUMMARY: Downtown Whitehorse, Yukon (northwestern Canada) is located at the base of a 50 to 60 metre high glaciolacustrine terrace (the Escarpment). At least 22 landslides were recorded along the Escarpment between 2021 and 2023. These caused traffic disruptions and posed a risk to people and infrastructure. Starting in 2021, the City of Whitehorse and its geotechnical consultants developed a multi-faceted monitoring program. To understand the risk to life safety from landslide activity along the Robert Service Way (RSW) section of the Escarpment, a landslide risk assessment was commissioned by the City of Whitehorse. The risk assessment found that the un-mitigated risk to individual motorists along RSW was tolerable but that the group risk based on vehicle traffic volume was likely unacceptable when compared with tolerance criteria used in other western Canadian jurisdictions. Measures to reduce risk are in the process of being designed and implemented.

Keywords: glaciolacustrine, risk assessment, surface displacement monitoring

Introduction

Whitehorse, with a population of nearly 30,000, is the capital of the Yukon Territory in northwestern Canada. Downtown Whitehorse is located at the base of a 50 to 60 metre (m) high glaciolacustrine terrace (the Escarpment). The downtown is accessible through two main access routes – Two Mile Hill to the north and Robert Service Way (RSW) to the south. Approximately 500 m of RSW, directly downslope of the Erik Nielsen Whitehorse International Airport, is located within 10 m of the toe of the Escarpment, and on the left banks of Yukon River (Figure 1). The Escarpment has a long history of slope instability involving a wide range of mass movement types (e.g., Leggett and Johnson, 1959; Lipovsky, 2023). Between 2021 and 2023, at least 22 landslides were recorded along the entire length of the Escarpment and have caused traffic disruptions and posed a risk to people and infrastructure.

Most of the Escarpment consists of glaciolacustrine material deposited during the last deglaciation (Bond, 2004). As the glacial lake retreated deltaic sediment was deposited on top of glaciolacustrine sediments (Lipovsky, 2023). The deltaic sediment ranges in thickness from 1 to 9 m and is composed of fine- to medium-grained sand with little to no fines content. The texture of the glaciolacustrine sediment is variable but typically consists of horizontally laminated fine sand, silt and clay (Lipovsky, 2023). The deltaic sediments are well-drained with a relatively higher permeability compared to the underlying glaciolacustrine sediments. Landslide activity along the Escarpment is associated with spring snowmelt, resulting in horizontal groundwater flow along the contact between the sandy unit and underlying silty unit and creating instability where seepage daylights on the Escarpment slope. It is noteworthy that 2021 to 2023 had the thickest annual maximum snow depths on record since 2010.

Figure 1. View looking south at the high mobility April 30, 2022 landslide that blocked Robert Service Way.

Characterization of the Landslide Activity

In 2021 and 2022, three moderate size (1,000-3,000 m^3) and two small (<1,000 m^3) landslides occurred in the south end of the RSW project area along with one small landslide in the north end (Figure 2A). The April 30, 2022 landslide ran over the RSW and into the Yukon River (Figure 1). A sheet pile wall was installed following the event to provide protection to the workers removing the landslide debris and to reduce the risk to the public following re-opening of the road. The sheet pile wall was left in place and the area between it and the base of the slope had been cleared of debris forming a small catchment basin. In 2023, all five small landslides reported along RSW occurred at the northern end of the project area (Figure 2).

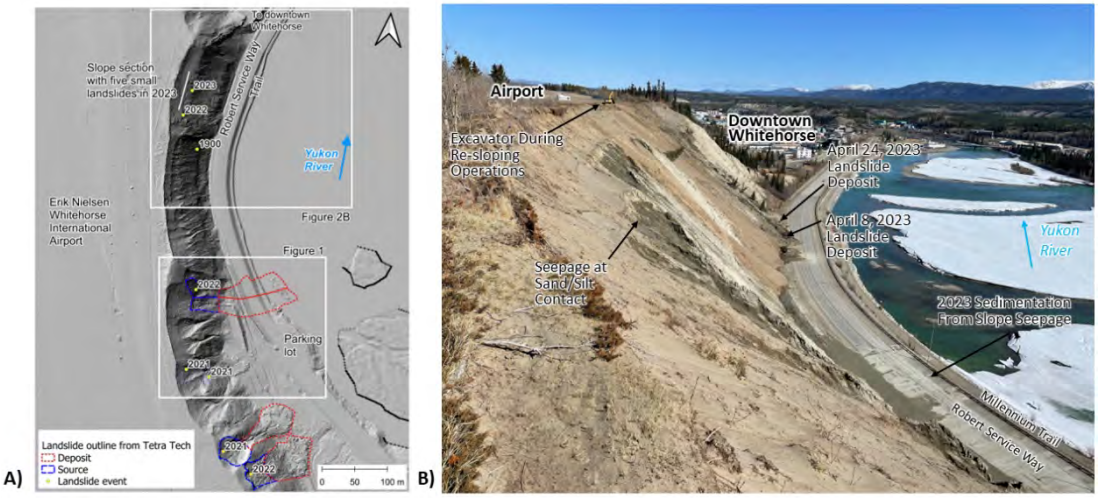

Figure 2) A) 2022 hillshade view of the project area and B) May 2023 view of the Escarpment looking north.

Monitoring Program

Starting in 2021, the City of Whitehorse (the City) and its geotechnical consultants developed a slope monitoring and risk management program. Surface displacement monitoring techniques

used in the project include regular visual ground inspection (weekly or daily inspections, based on the landslide activity), geodetic survey of prisms installed on the slope, GPS survey of monuments, and crack meters. Uncrewed aerial vehicle surveys were used to supplement the ground inspections and map tension cracks. The City made use of social media and a dedicated website to inform the public about the latest slope activity. In 2023, a ground-based interferometric radar system was installed across the Yukon River, approximately 800 m away, to monitor the Escarpment along RSW. Data from the radar was automatically recorded on site, uploaded to cloud servers, processed, and then provided to the City in near real-time using an online portal. The information provided included velocity time series (6-hour rates) for selected regions of interest (ROIs) and points of interest (POIs), radar movement maps, and images which informed the City's risk-based decision making based on current slope activity. This monitoring system provided the City with advanced warning of several small landslides (Figure 3).

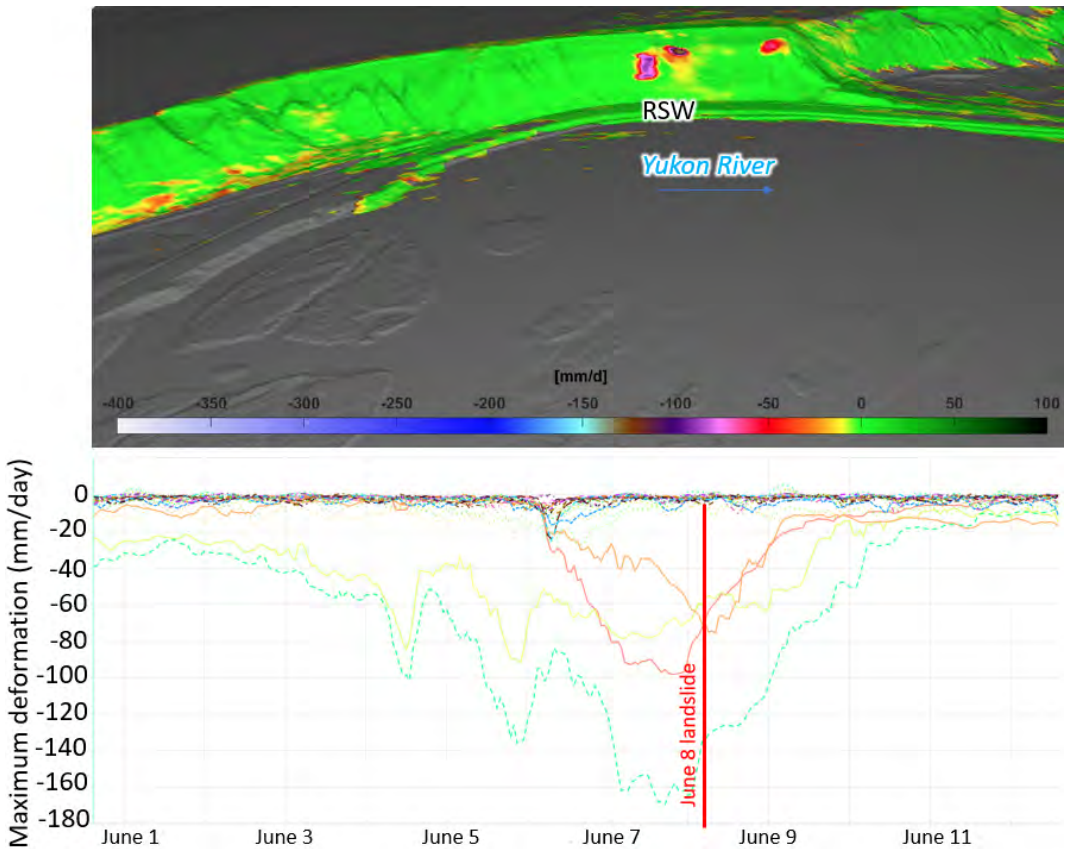

Figure 3. Ground-based InSAR surface displacement monitoring associated with the June 8, 2023 landslide. A) three-dimensional view of the 6-hour average rate, B) 6-hour maximum deformation rate time series for various user defined regions of interest (ROIs) with acceleration recorded leading up to the June 8 landslide.

Risk Assessment

The landslide activity along the RSW section of the Escarpment was seen as an expensive and disruptive hazard but the risk to life safety was not well understood. A preliminary risk assessment was commissioned by the City to fill that gap and to provide insights to the potential effectiveness of mitigation strategies to reduce risk via monitoring and warning systems and/or structural measures. The preliminary risk assessment focused on life safety with two types of risk estimated: the total group risk for all individuals potentially exposed to the landslide hazard; and the risk to an individual who might have the greatest exposure to the hazard.

The geohazards considered in this assessment are debris avalanches initiating from the Escarpment during spring melt with a volume between 500 and 5,000 m^3. The elements at risk include motorists travelling along RSW and pedestrians walking along the adjacent Millennium Trail. The five geohazard scenarios evaluated are a landslide impacting a car during the (1) day or (2) night, a car impacting landslide debris during the (3) day or (4) night, and (5) a landslide impacting a pedestrian during the day. Review of the Escarpment debris avalanche runout since 2021 indicates two categories of mobility (based on ratio of fall height to travel distance, H/L). The difference in mobility is assumed to be driven by the water content of the source material. The frequency for each landslide mobility was estimated based on events recorded since 2021, which appear to be considerably higher than the long-term average frequency that has been observed. The probability a landslide reaches the element at risk was based on compilation of runout distances of landslides from glaciolacustrine material in Yukon and British Columbia. The probability that the element at risk is present when the landslide occurs considered expected landslide dimensions, element at risk dimensions, vehicle and pedestrian traffic data, average speed of travel, and stopping distances. The vulnerability of motorists and pedestrians when struck by debris avalanches was estimated based on a review of published literature of representative case studies. Event tree analyses were used to capture the multiple conditions that could lead to fatalities for each of these geohazard scenarios.

The results suggest that the risk for the individual most at risk along RSW or the Millennium Trail is between 10^{-4} and 10^{-5}. The group risk for motorists along RSW is estimated to be about 10^{-2}. The risk is estimated to be greater during the day than at night because of the higher traffic count. The group risk for pedestrians along the Millennium Trail is around 10^{-2}. This is similar to that for motorists along RSW because pedestrians have a longer exposure time (from crossing the hazardous area at a slower speed) and higher vulnerability, even though there is much less pedestrian traffic than vehicle traffic. The study provides estimates of annualized risk, but from recent observations about the timing of landslides, much of this risk is likely to be concentrated during an approximately 60-day period beginning during the spring thaw. In the summer, fall, and winter, the probability and risk of landslides occurring along the Escarpment are expected to be substantially lower.

Conclusions

Based on the approach presented and available data, the estimated individual risk for a motorist or pedestrian along RSW or Millenium Trail ranged from 10^{-4} to 10^{-5}. When considering total group risk to motorists or pedestrians (i.e., traffic data) the estimated frequency of one or more fatalities was around 10^{-2}. The results suggest that the un-mitigated risk to individual motorists along RSW is tolerable but that the group risk is likely unacceptable when compared with tolerance criteria used in other western Canadian jurisdictions. Therefore, measures to reduce risk are in the process of being designed and implemented by the City.

References

Bond, J. (2004). Late Wisconsinan McConnel glaciation of the Whitehorse map area (105D), Yukon. In: Yukon Exploration and Geology 2003. [Journal] Yukon Geological Survey p. 73-88.

Legget, R.F., Johnston, G.H. (1959). The Whitehorse Escarpment. Prepared for the Advisory Committee on Northern Development, Department of Northern Affairs and National Resources. Report No. 136 of the Division of Building Research.

Lipovsky, P., (2023). Surficial geology and geohazards of the greater Whitehorse area. *Yukon Geological Survey, Open File* 2023-1.

Application of Millimeter Wave Radar in Slope Deformation Monitoring

Tianbin Li[1,2], Jianfeng Wang[1,2,3], Ken Chen[3]

[1] College of Environment and Civil Engineering, Chengdu University of Technology， Chengdu, China
[2] State Key Laboratory of Geohazard Prevention and Geo-environment Protection, Chengdu University of Technology, Chengdu, China
[3] Sichuan Digital Transportation Tech Co. Ltd, Chengdu, Chengdu, China

SUMMARY: Millimeter Wave Radar is a research hotspot and has been widely used in the field of in-vehicle due to its advantages of small size, low price, and high accuracy. However, in the field of deformation monitoring, there is less research. To compensate for this scenario, a photographic slide is used to perform deformation monitoring simulation tests as a deformation simulation device. And carry out engineering case studies in Ehan Expressway. Study shows that: 1) Millimeter Wave Radar can monitor deformation with an error of 5 mm or less and accurately reflects the slide rail's motion characteristics. 2) A single Millimeter Wave Radar can monitor a horizontal coverage of up to 200 m and obtain accurate deformation information, which can meet the monitoring needs of medium-sized landslides. 3) When two or more Millimeter Wave Radars are used to observe a Corner Reflector (CR, the same below) at the same time, the azimuth information can be better interpreted, and the interpretation of the azimuth angle tends to be consistent with the direction of the actual slide movement. 4) The case of Ehan Expressway shows that the monitor results have good stability and match the geological environment of the site, which has the promotion value.

Keywords: Landslide; Deformation monitoring; Landslide simulation; Millimeter wave radar

Introduction

The deformation of slopes often induces disasters, which may destroy property or deprive human lives. Since humanity has been engaged in engineering activities, it has been a cruel struggle with these disasters. In the mid-20th century, people could observe the deformation information of slopes and engineering structures regularly by total station, which was highly accurate and widely applicable but needed to be operated manually and had a large workload in the field. After the 1990s, with the development of science and technology, more and more automated monitoring products, such as GNSS (Dai et al., 2023), fiber-optic sensors (Zheng et al., 2019), InSAR (Amitrano et al., 2019), GBSAR (Bozzano et al., 2011), etc., were deeply applied in the deformation monitoring of slopes. Still, all of them have their advantages and disadvantages. For example, InSAR usually obtains a wide range of regional deformation, mainly applied to the early identification of disasters, and cannot accurately detect a single landslide. GBSAR requires robust reflection point information, usually applied to monitoring high-level deformation bodies with exposed rock. GNSS, the leading monitoring equipment in the market, is widely used to verify slopes because of its ability to obtain three-dimensional information. Still, its monitoring cost is expensive and easily interfered with by satellite, etc. It can be seen that the current automated monitoring technology has largely saved labor and enriched data. However, due to its own defects, it cannot be applied to all slope deformation monitoring scenarios.

Millimetre wave radar (Scherr et al., 2015) is currently a research hotspot, with small size, low price, high precision, intense penetration, and other advantages, and it has been

widely used in the field of vehicles. After the concept of "intelligent transport" was put forward in 2014, millimeter-wave radar has been commonly used in intelligent transport due to its accurate sensing ability, such as the currently hot "Radar-camera Fusion" technology.

Millimeter wave radar has yet to be a mature application in slope deformation monitoring. The advantages of millimeter wave radar, such as low price, high accuracy, and quiet time delay, make millimeter wave radar valuable for application in the field of slope deformation monitoring. Therefore, this study will take the deformation monitoring simulation test and Ehan high-speed engineering application as an entry point to explore the deformation monitoring capability of millimeter-wave radar and provide some reference for the subsequent application of meter-wave radar in slope disasters.

Millimetre Wave Radar Ranging Theory

Millimeter-wave radar calculates the distance from the millimeter-wave radar to an object by transmitting a signal and receiving an echo signal reflected from the object. The time τ used for the round trip is assumed to have a value equal to two times the radial distance d between the radar and the object divided by the speed of light c.

$$\tau = \frac{2d}{c} \tag{1}$$

FMCW millimeter-wave modulation sweep period T_c and sweep bandwidth B (Fig. 1), then the transmit slope k of the FMCW signal can be expressed as:

$$k = \frac{B}{T_c} \tag{2}$$

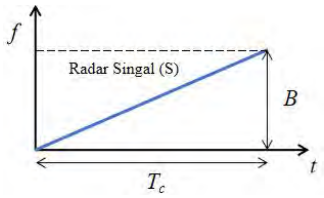

Figure 1. FMCW millimeter wave sweep period and sweep bandwidth

When an object exists in front of the radar, the mixer will generate an IF signal with a constant frequency. Its signal frequency is equal to time multiplied by the slope of the transmitted signal k. Combined with equation (2), the IF signal frequency (f_τ) can be expressed as:

$$f_\tau = \frac{2dk}{c} = \frac{2dB}{cT_c} \tag{3}$$

Then the radial distance (d) between the radar and the target can be expressed as:：

$$d = \frac{T_c c}{2B} f_\tau \tag{4}$$

Deformation Monitoring Simulation Tests

The deformation monitoring system mainly comprises millimeter wave radar (Fig. 2) and corner reflectors (Fig. 3). Whether the sliding device is selected reasonably is crucial in verifying the performance of deformation monitoring. The sliding device needs to have the following three characteristics:

1) The characteristics of slow motion can simulate the creep effect of the slope.

2) The characteristics of variable speed are because the deformation rate of natural landslides constantly changes.

3) Measure the length of the movement of the Corner reflectors, which is used to determine the reasonableness of the deformation monitoring results of the millimeter-wave radar.

Therefore, photographic slide was selected as the deformation simulation device (Fig. 4).

Figure 2. Millimeter wave radar

Figure 3. Octahedral corner reflector

Figure 4. Photography slide

The test plane layout is shown in Fig. 5a. The deformation monitored by the three radars is shown in Fig. 5b. Since the millimeter wave radar can only observe the radial deformation, the size of the deformation monitored by the three radars varies. However, the overall trend can be consistent, indicating that the monitoring results have high reliability. For engineering applications, obtaining the azimuth of deformation is also necessary. To achieve a balance between economy and efficiency. Three radars are used to establish the equations of three spheres, and then the azimuth is solved; two radar combinations are used to establish two plane circles, and then the azimuth is solved. The results are shown in Fig. 5c. It can be seen that the interpretation results of two radars and three radars are very close to each other, indicating that two radars can be deployed to solve the azimuth problem in the practical extension application.

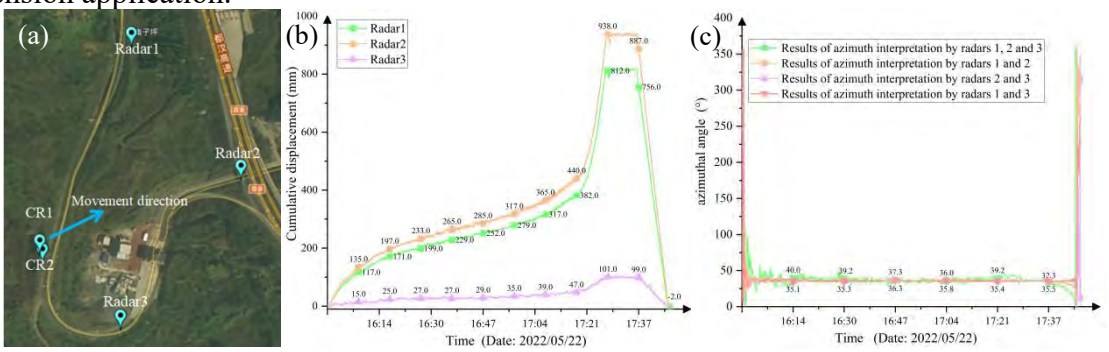

Figure 5. Layout and monitoring results of simulation test: a) Plan view of millimetre-wave radar layout; b) Cumulative displacement monitored by three separately millimetre-wave radars; c) Azimuth information decoded by millimetre-wave radar in different combinations

Engineering Applications

The sedimentation roadbed is at the junction of Taoyuan Village and Dingping Village in Longchi Township of Ehan Expressway. The terrain is a tectonic denudation of the middle-low mountain accumulation landform; the whole is relatively flat. There is a small river ditch on the left side of the road. The left side of the road (CR1) is an artificial slope with farmland, and the right side is close to the mountain (CR3). The overall stratigraphy is softer on the left than on the right (from top to bottom: artificial fill, silty clay, sandstone). One radar and nine corner reflectors were deployed on-site to observe the deformation trend. The overall terrain environment and the relationship between the millimeter-wave radar and the deployment of the corner reflectors are shown in Fig. 6a.

Taking CR1, CR2, and CR3 as case studies, the specific monitoring results are shown in Fig. 6b. As can be seen from the figure, the results of the millimeter wave radar monitoring are overall more stable. The deformation of CR1 reaches 130 mm, CR2 is about 50 mm, and

CR3 has the smallest deformation at about 10 mm. From the topographic environment in Fig. 6a, it can be seen that the area to the left of the CR1 is farmland, and the stratum is overall softer and has a free face, resulting in the largest deformation. CR3 is close to the mountain, and the point is more gentle, so it tends to be stable. The monitoring results, combined with the analysis of geological conditions, show that the deformation monitoring results of millimeter-wave radar are reasonable.

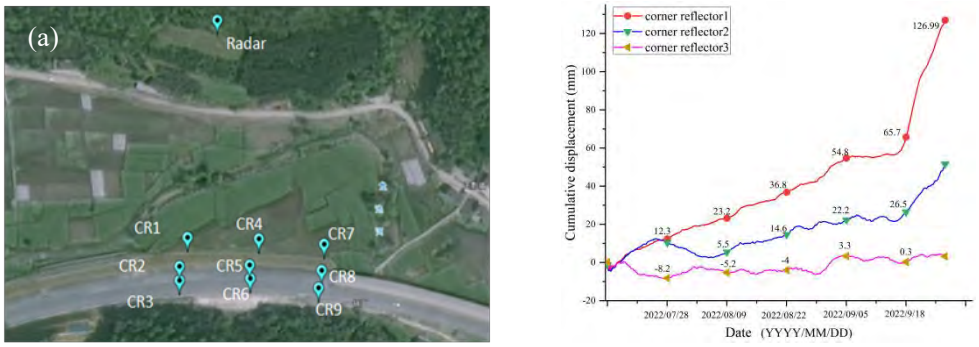

Figure 6. Monitoring layout map and monitoring results of Ehan Expressway: a) Layout of a millimetre-wave radar; b) Cumulative displacement

Conclusion

Through the millimeter wave radar to monitor the deformation process of the photographic slide, and combined with the specific engineering cases of Ehan Expressway, the deformation monitoring capability of millimeter wave radar is demonstrated, and the following conclusions can be drawn as a whole:

1）Millimetre wave radar can monitor deformation, and when the photographic slide is returned to its origin, the millimeter wave radar has an error of less than 5 mm and accurately reflects the deformation characteristics of the photographic slide (including the amount and rate of deformation, etc.).

2）A single millimeter-wave radar can monitor the horizontal coverage within 200 m of the corner reflector and can get better deformation information, which can meet the monitoring needs of medium-sized landslides.

3）When two or more Millimeter Wave Radars are used to observe a Corner Reflector at the same time, the azimuth information can be better interpreted, and the interpretation of the azimuth angle tends to be consistent with the direction of the actual slide movement.

4）The case of Ehan Expressway shows that the monitor results have good stability and match the geological environment of the site, which has the promotion value.

References

Scherr S, Ayhan S, Fischbach B, et al. (2015) An efficient frequency and phase estimation algorithm with CRB performance for FMCW Radar applications. *IEEE T INSTRUM MEAS* 64(7), 1868-1875.

Amitrano D, Guida R, Dell'Aglio D, el al. (2019) Long-term satellite monitoring of the slumgullion landslide using space-borne synthetic aperture radar sub-pixel offset tracking. *Remote Sens* 11(03), 369.

Dai WJ, Dai Y, Xie JW (2023) Back-Analysis of Slope GNSS Displacements Using Geographically Weighted Regression and Least Squares Algorithms. *Remote Sens* 15, 759.

Bozzano F, Ciprizani I, Mazzanti P, et al. (2011) Displacement Patterns of a Landslide Affected by Human Activities: Insights from Ground-Based InSAR Monitoring. *Nat Hazards* 59(3), 1377-1396.

Zheng Y, Zhu ZW, Li WL, et al. (2019) Experimental research on a novel optic sensor based on OTDR for landslide monitoring. *Measurement* 148, 106926.

Study on Effective Rainfall Model for Meteorological Early Warning of Geological Disasters in Fujian, Southeast of China

Chen Chunli, Fang Zhiwei

China Institute of Geo-Environment Monitoring

SUMMARY: An effective rainfall model of Fujian is established and verified by field monitoring. This model is applied to geological disasters early warning and the results shows that it can reduce the warning area by remaining the accuracy.

Keywords: group-occurring geological disaster; southeastern China; rainfall; effective rainfall model; geological disasters early warning

Introduction

Rainfall is one of the important cause for geological disasters. Taking rainfall as a trigger factor, regional meteorological early warning of geological disasters can predict the risk of geological disasters in advance, which is one of the most effective measures for disaster prevention and reduction. In the meteorological early warning of geological disasters, the trigger effect of early rainfall is calculated by effective rainfall model. The effective rainfall model is generally derived from the early effective rainfall model proposed by Crozier in 1980 (Crozier MJ, 1980,1986), which has been modified by many researchers and applied to the calculation of the early effective rainfall of geological disasters in different regions (Li Changjiang et al., 2011). However, empirical parameters are used in many regions due to the constraints of conditions, it is urgent to carry out the research of effective rainfall model.

Model Establishment

The typical rainfall processes that trigger geological disaster in Fujian are screened according to the collected rainfall data of historical geological disasters. The correlation analysis between 460 geological disasters and rainfall showed that the occurrence of geological disaster in Fujian is related to effective rainfall within 3 days, and the reduction coefficient is 0.79 (Table 1, Fig.1). Then the effective rainfall model in Fujian is established based on the general formula of early effective rainfall model proposed by Crozier.

$$P = \sum_{i=0}^{2} 0.79^{i} R_i \qquad (1)$$

Where, P is the effective rainfall (mm); R_i is the daily rainfall (mm) of the previous day.

Table 1 Correlation between geological disaster and daily rainfall

daily rainfall（mm）	intraday	previous day	2 days ago	3 days ago	4 days ago	5 days ago	6 days ago	7 days ago	8 days ago	9 days ago
coefficient of association	0.290**	0.463**	0.137*	-0.066	0.046	-0.057	-0.049	-0.051	-0.058	-0.085

**. significant association at 0.01 level (bilateral)

*. significant association at 0.05 level (bilateral)

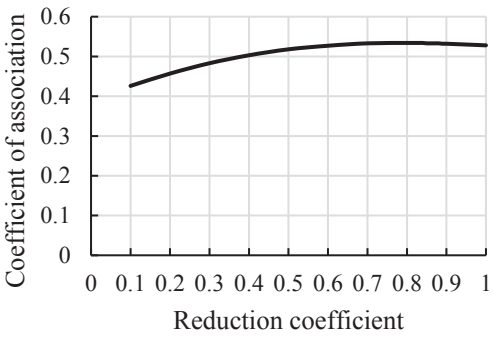

Fig.1 Effective rainfall coefficient - correlation coefficient change curve

Model Validation

For shallow landslides, the stability of landslides can be predicted according to the fluctuation of groundwater level (Xu Jiancong and Shang Yuquan et al., 2005; Wang Zhilei and Sun Hongyue et al., 2011). A landslide site monitoring was carried out in Ningde, northern Fujian Province (Fig 2). The effective rainfall model is verified by the response of the rise-ebb and rainfall sequence of the slope groundwater. After a single rainfall, the groundwater level rose rapidly and then fell back. On the third day after the rainfall, the measured groundwater level coincided with the trend water level (Fig. 3). Therefore, it was concluded that the influence period of a single rainfall was within 3 days, which was consistent with the effective rainfall influence period mentioned above. In the case of continuous rainfall, the effective rainfall can better reflect the subsidence of groundwater level in time (Fig. 4), indicating that the effective rainfall model proposed above can reflect the changing trend of slope stability in time.

Fig. 2 Site monitoring of rainfall infiltration

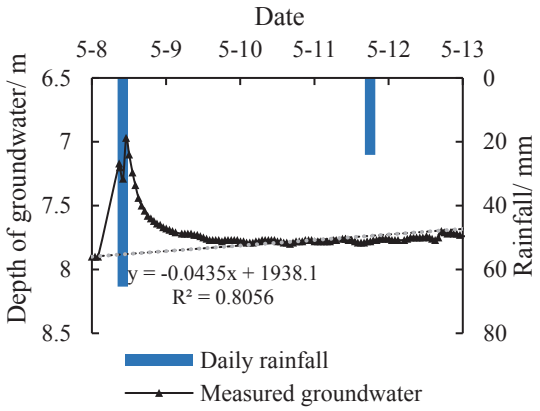

Fig. 3 Fluctuation curve of groundwater level

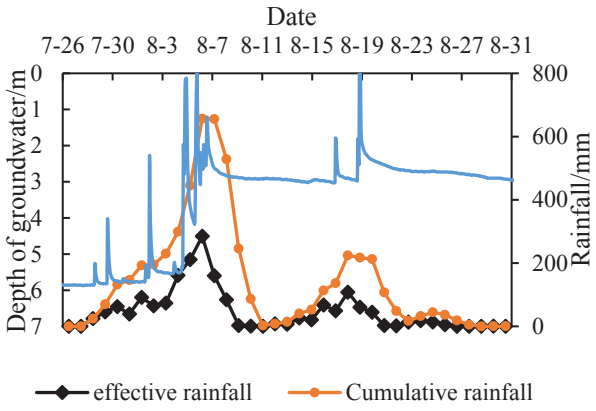

Fig. 4 Response of groundwater and rainfall

Application of the Model

The effective rainfall model is applied to the prediction of geological disaster in 2021. The rain-induced disaster process from June 28 to July 3, 2021 in Nanping, northern of Fujian Province is selected for verification. On the premise of ensuring the accuracy, the early warning area of effective rainfall evaluated by the new model is smaller and the warning level is more accurate (Fig 5). For example, the area of the early warning area adopted by the new model on July 1 is 56% of the original model (Fig 6). Therefore, the effective rainfall model proposed in this paper can effectively improve the accuracy of geological disaster meteorological warning.

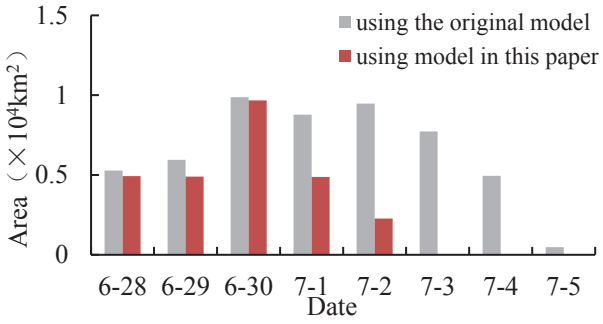

Fig.5 Comparison of area of warning area

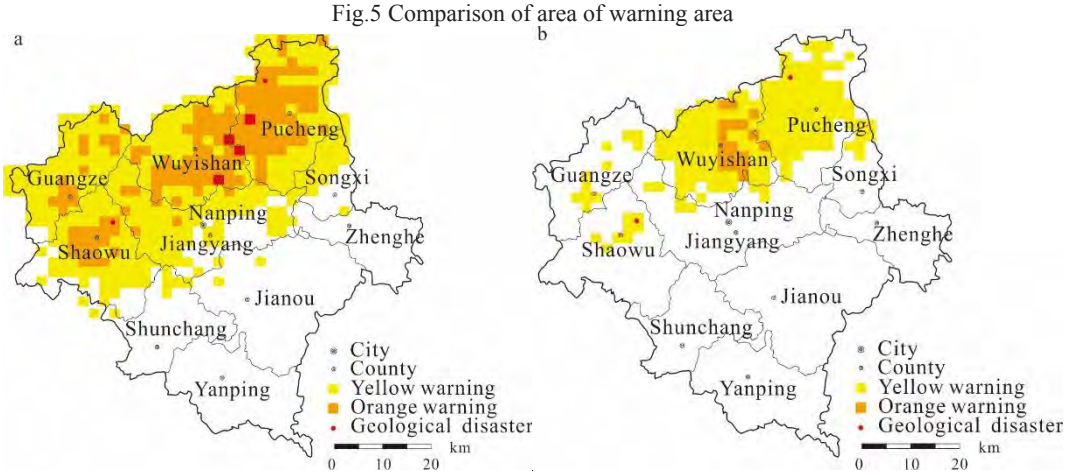

Fig.6 The meteorological early warning of geological disasters results on July 1, 2021
(a) using the original effective rainfall model (b)using the effective rainfall model in this paper

Conclusion

The effective rainfall model for meteorological early warning of geological disasters in Fujian, southeast of China is proposed in this paper. It is verified by site monitoring. The effective rainfall model can reflect the changing trend of slope stability in time. Then the effective rainfall model is applied to meteorological early warning of geological disasters. The result shows that The effective rainfall model in Fujian is applied to geological disasters early warning and the results shows that using the effective rainfall model proposed in this paper can reduce the warning area, the warning level and warning duration by remaining the accuracy.

References

Aleotti P (2004). A warning system for rainfall-induced shallow failures. *Journal of Engineering Geology* 73(3-4):247-265.

Baum R L, Godt J W（2010）. Early warning of rainfall-induced shallow landslides and debris flows in the USA. *Landslides* 7(3):259-272.

Crozier, M.J., Eyles, R.J（1980）. Assessing the probability of rapid mass movemen. *Proceedings of the Third Australia-New Zealand Conference on Geomechanics,* New Zealand Institute of Engineers, Proceedings of Technical Groups, 6, (1g):247 -253.
Crozier, M.J, 1986. Landslides: Causes, Consequences and Environment. London: CroomHelm:185 -189.
Crozier M J 1999. Prediction of rainfall-triggered landslides: a test of the Antecedent Water Status Model. *Earth Surface Processes and Landforms* ,24(9):825-833.
DI Jingyue，XU Fengwen，LI Yumei，et al.（2019）. Precipitation type and threshold analysis of geological disasters in southeast. *Journal of Catastrophology* 34 (1): 62- 67，93.
FANG Ranke, LIU Yanhui, SU Yongchao, HUANG Zhiquan（2021）. An early warning model of regional landslide in Qingchuan County, Sichuan Province based on logistic regression. *Hydrogeology & Engineering Geology* 48(1): 181-187.
Glade T, Crozier M, Smith P (2000). Applying Probability Determination to Refine Landslide-triggering Rainfall Thresholds Using an Empirical "Antecedent Daily Rainfall Model". *Pure and Applied Geophysics* 157(6):1059-1079.
HAN Shuai, LIU Mingjun, WU Jianbo, et al. (2022). Risk assessment of slope disasters induced by typhoon-rainfall in the southeast coastal area, China: A case study of the Shiyang north slope. *Journal of Geomechanics* 28 (4): 583-595.
HUANG Junbao. (2013). Preliminary studying of landslide critical rainfall in Dehua County. *Geology of Fujian* 32(01):65-69.
JIAN Wen-bin， XU Xu-tang， ZHENG Min-zhou， et al. (2013). On effective rainfall of slope instability. *Rock and Soil Mechanics* 34(Z2): 247-251.
LI Changjiang,MA Tuhua,SUN Leling,et al.(2011). A New Approach to Calibrate Antecedent Precipitation for Rainfall triggering Landslide Forecast. *Mountain Research* (01):81.
LI Tiefeng, CONG Weiqing (2006). A method for rainfall induced landslides prediction based on Logistic regression and effective antecedent rainfall. *The Chinese journal of geological hazard and control* 17(01):33-35.
LI Zhuang, GAO Yang, HE Kai, et al. (2020). Analysis of the fluidization process of the high-position and long-runout landslide in Shuicheng, Liupanshui, Guizhou Province. J*ournal of Geomechanics* 26(4): 520-532.
LIU Chuanzheng (2004). Study on the early warning methods of landslide-debris flows. *Hydrogeology & engineering geology* 31(03):1-6.
LIU Chuanzheng, LIU Yanhui, WEN Mingsheng, et al. (2009). Early warning theory for regional geohazards in China.Beijing: Geological Publishing House.
LIU Yanhui, LIU Chuanzheng，LIAN Jianfa, er al. (2008). Method of regional early warning of geohazards based on the explicit statistical theory. Statistical relations between geo-hazards and rain-type. *Geology in China* 02: 344-350.
Piciullo L, Calvello M, Cepeda J M (2018). Territorial early warning systems for rainfall-induced landslides. *Earth-Science Reviews* 179:228-247.
WANG Zhilei, SUN Hongyue, LIU Yongli, et al. (2011). Tim e series analysis about groundwater level in slope and rainfall. *Journal of Zhejiang University (Engineering Science)* 45(07): 1301-1307.
Wei Deguang, Jie Yujing, Huang Tinggan (1997). Regional geological structure of Fujian. *Regional geology of China* 16(2):9.
WEI Fangqiang, JIANG Yuhong, YANG Hongjuan, et al. (2010). Relationship between Debris flow activity and precipitation characteristics in Southeastern China. *Mountain Research* 28(05):616-622.
Wu Yiping, Zhang Qiuxia, Tang Huiming, et al. (2014). Landslide Hazard Warning Based on Effective Rainfall Intensity. *Earth Science* 23(7): 889-885. doi: 10.3799/dqkx.2014.083.
XU Jiancong, SHANG Yuequan, CHEN Kanfu, et al. (2005). Analysis of shallow landslide stability under intensive rainfall. *Chinese Journal of Rock Mechanics and Engineering* (18): 3246-3251.
China Institute of Geological Environment Monitoring (2019). Construction of 1:500,000 geological disasters early warning model.
China Geological Disaster Prevention Engineering Industry Association. T/CAGHP039-2018. Standard of early warning of geological hazards based on the meteorological factor. *Beijing: China University of Geosciences Press.*

Research on a Regional Landslide Early-Warning Model Based on Machine Learning— A Case Study of Fujian Province, China

Yanhui Liu[1], Junbao Huang[2], Ruihua Xiao[1], Shiwei Ma[3], Pinggen Zhou [1]

[1] China Institute of Geo-Environment Monitoring (Technical Guidance Center for Geo-Hazards Prevention of MNR), Beijing, China
[2] Fujian Monitoring Center of Geological Environment, Fuzhou, China
[3] Institute of Geology and Geophysics, Chinese Academy of Sciences, Beijing, China

Abstract: China's landslide disasters are serious, and regional landslide disaster early-warning is one of the important means of disaster prevention and mitigation. The traditional regional landslide disaster early-warning model, however, is limited by the complex landslide induction mechanism, limited data accumulation, and insufficient big data analysis methods, and has problems such as limited early-warning accuracy and insufficient refinement. In this paper, a machine learning method was introduced into the field of regional landslide disaster warning. From the model construction process of training sample-set construction, sample learning and training, model parameter optimization, model preservation, warning output, and so on, a method for constructing a regional landslide early-warning model based on machine learning was systematically proposed. In the sample learning and training, 80% of the training sample-set was used as the training set, and 20% was used as the test set for five-fold cross validation. The Bayesian Optimization algorithm was used to optimize the model parameters, and the accuracy, ROC curve, and AUC value were used to verify the model accuracy and model generalization ability. With China's Fujian province as an example, based on nine years of geological and meteorological data (2010–2018), geological environment factors, factors of hazard-affected bodies and historical disaster situations, and rainfall-induced factors in four categories, a total of 26 indicators were used as input characteristic parameters. Six machine learning algorithms were adopted to improve model training; the results showed that the Random Forest algorithm performed the best, giving an accuracy of 92.3%, and was the model with the best generalization ability (AUC was 0.955). The second best was the Artificial Neural Network model, with an accuracy of 0.937 and an AUC of 0.935. Next were the Nearest Neighbor model, the Logistic Regression model, and the Support Vector Machine; the poorest results were from the Decision Tree model. Finally, the typical rainfall-type landslide disaster process in Fujian Province was selected as an example to verify the Random Forest algorithm model. The results showed that compared with the early-warning results of the original explicit statistical model, the hit rate of the new model was 6 times, or equal to that of the original model, and the landslide density in the early-warning area of the new model was 1.6–1.7 times that of the original model. Preliminary verification showed that the new model based on the Random Forest method has obvious advantages, a higher hit rate and a smaller warning area, and can achieve more accurate warnings. The follow-up will continue to track the new landslide disaster situation in the study area and carry out model verification and correction.

Keywords: landslide; early-warning model; machine learning; Random Forest; model study

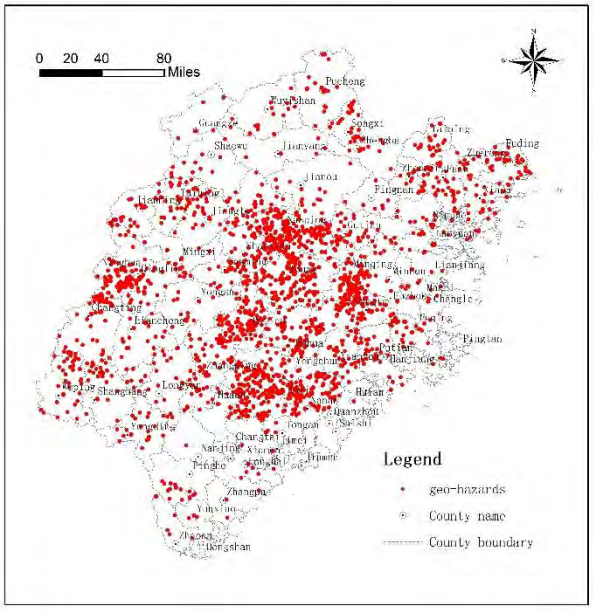

Figure 1. Distribution map of geological disaster points in Fujian Province

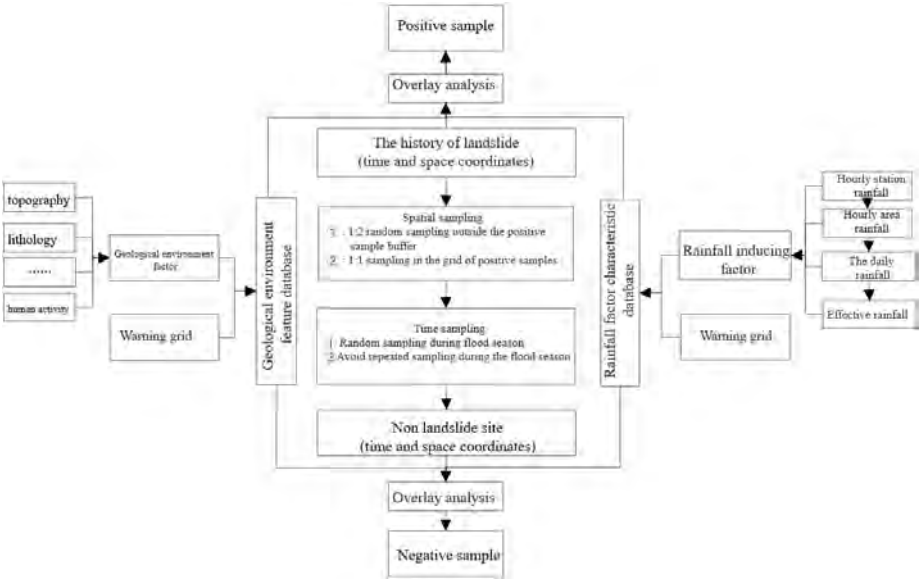

Figure 2. Distribution map of geological disaster points in Fujian Province

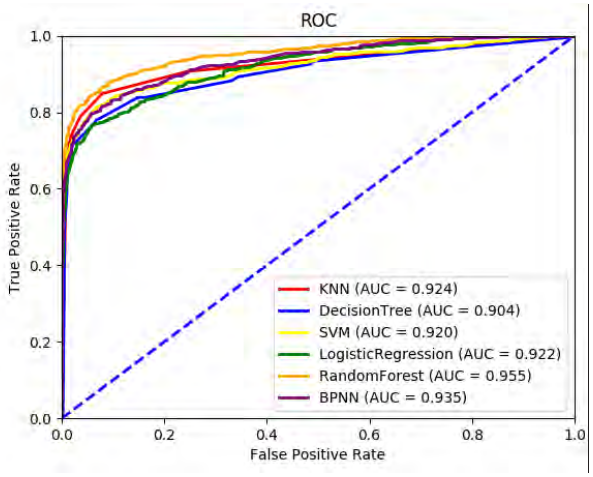

Figure 3. Comparison of ROC and AUC of six machine learning early-warning models.

Table 1. Comparison of partial hyperparameter optimization and model evaluation of six machine learning algorithms.

Machine Learning Model	Accuracy	Model Generalization Ability	Hyperparameter	Hyperparameter Value
Random Forest algorithm	0.923	0.955	n_estimators	118
			max_depths	10
			min_samples_split	3
Nearest Neighbor algorithm	0.932	0.924	n_neighbors	10
Decision Tree	0.937	0.904	max_depths	4
Support Vector Machine	0.932	0.920	C	3
			gamma	0.003
Logistic Regression	0.940	0.922	C	5
Artificial Neural Network	0.937	0.935	hidden_layer_sizes	(6,7)
			max_iter	1680

References

Guzzetti, F.; Gariano, S.L.; Peruccacci, S.; Brunetti, M.T.; Marchesini, I.; Rossi, M.; Melillo, M. Geographical landslide early warning systems. Earth Sci. Rev. 2020, 200, 102973.

Liu, C.-Z.; Liu, Y.-H. Early warning theory for regional geo-hazards and design of explicit statistical system. Hydrogeol. Eng. Geol. 2007, 34, 11–18.

Liu, C.-Z.; Liu, Y.-H.; Wen, M.-S.; Tang, C.; Xue, Q.-W. Method and Application of Regional Warning for Geo-Hazards in China; Geological Publishing: Beijing, China, 2009.

Liu, C.-Z.; Liu, Y.-H.; Wen, M.-S.; Tang, C.; Zhao, L.-Q.; Tian, H. Early warning for regional geo-hazards during 2003-2012, China. Chin. J. Geol. Hazard Control. 2015, 26, 1–8.

Liu, Y.-H.; Liu, C.-Z.; Lian, J.-F.; Wen, M.-S.; Tang, C. Preliminary study of geo-hazards regional early warning based on explicit statistical theory. Geol. China 2008, 35, 344–350.

Liu, Y.-H.; Liu, C.-Z.; Wen, M.-S.; Tang, C. Study of Early Warning Models for Regional Geo-Hazards in China. J. Eng. Geol. 2015, 23, 738–746.

Liu, Y.-H.; Zhang, Z.-X.; Su, Y.-C. Case study of vulnerability evaluation for geo-hazards bearing capacity of a region. J. Eng. Geol. 2018, 26, 1121–1130.

Liu, Y.-H.; Su, Y.-C. Early-warning model of regional geological disasters based on meteorological factor in Qingchuan County, Sichuan Province. J. Eng. Geol. 2019, 27, 134–143.

Li, S.-D.; Bai, Y.-H.; Jiang, Y.; Wang, Z.-H.; Wie, W.-H.; Li, X.;Liu, L.-N. Explicit Statistic Meteorological Early-warning Model of Geological Hazards in Xinjiang, China Based on the Genesis Theory of Endogenic and Exogenic Couping. J. Earth Sci. Environ. 2017, 39, 287–300.

Wei, P.-X.; Li, X.-J. The meteorologic early warning research of sudden geo-hazard in Guangdong province. Chin. J. Geol. Hazard Control. 2015, 26, 138–144.

Wen, M.-S.; Liu, Y.-H.; Su, Y.-C.; Fang, Z.-W.;Xiao, R.-H.; Chen, C.-L.; Xu, W.; Chen, Y.-C.. Geo-Hazards Investigation Report of Qingzhujiang River Region, Sichuan; China Institute of Geo-Environmental Monitoring: Beijing, China, 2016.

Hou, S.-S.; Li, A.; Han, B.; Zhou, P.-G.; Ye, H.-J.; Zhu, B.; Ma, W.-F. An approach of geo-hazard warning system in Ya'an, Sichuan and its analysis. Chin. J. Geol. Hazard Control. 2014, 25, 134–138.

Liu, C.-Z.; Wen M.-S.; Liu, Y.-H.; Liu, Q.-Q.; Gu, X.-X. Study of Geo-Hazards in Wenchuan Earthquake Zone; Geology Press: Beijing, China, 2017.

Cannon, S.H.; Ellen, S. Rainfall conditions for abundant debris avalanches, San Francisco Bay region, California. Calif. Geol. 1985, 38, 262–272.

Pietro, A. A warning system for rainfall-induced shallow failures. Eng. Geol. 2004, 73, 247–265.

Hong, H.; Pourghasemi, H.R.; Pourtaghi, Z.S. Landslide susceptibility assessment in Lianhua County (China): A comparison between a random forest data mining technique and bivariate and multivariate statistical models. Geomorphology 2016, 259, 105–118.

Peruccacci, S.; Brunetti, M.T.; Gariano, S.L.; Melillo, M.; Rossi, M.; Guzzetti, F. Rainfall thresholds for possible landslide oc-currence in Italy. Geomorphology 2017, 290, 39–57.

Wei, L.-W.; Huang, C.-M.; Chen, H.; Lee, C.-T.; Chi, C.-C.; Chiu, C.-L. Adopting the I3-R24 rainfall index and landslide sus-ceptibility for the establishment of an early warning model for rainfall-induced shallow landslides. Nat. Hazards Earth Syst. Sci. 2018, 18, 1717–1733.

Ding, G.-L.; Wang, Y.-H.; Mao, J.; Yao, K.; Liu, H.-H. A study of the rainfall threshold of debris flow forewarning in Beijing based on susceptibility analysis. Hydrogeol. Eng. Geol. 2017, 44, 136–142.
Keefer, D.K.; Wilson, R.C.; Mark, R.K.; Brabb, E.E.; Brown, W.M., III; Ellen, S.D.; Harp, E.L.; Wieczorek, G.F.; Alger, C.S.; Zatkin, R.S. Real-Time Landslide Warning during Heavy Rainfall. Science 1987, 238, 921–925.
Mulyana, A.R.; Sutanto, S.J.; Hidayat, R.; Ridwan, B.W. Capability of Indonesian Landslide Early Warning System to detect landslide occurrences few days in advance. In Proceedings of the 21st EGU General Assembly, EGU2019, Vienna, Austria, 7–12 April 2019.
Pennington, C.V.; Freeborough, K.; Dashwood, C.; Dijkstra, T.; Lawrie, K. The national landslide database of Great Britain: Acquisition, communication and the role of social media. Geomorphology 2015, 249, 44–51.
Ponziani, F.; Berni, N.; Stelluti, M.; Zauri, R.; Pandolfo, C.; Brocca, L.; Moramarco, T.; Salciarini, D.; Tamagnini, C. LAND-WARN: An Operative Early Warning System for Landslides Forecasting Based on Rainfall Thresholds and Soil Moisture. In Landslide Science and Practice; Margottini, C., Canuti, P., Sassa, K., Eds.; Springer: Berlin/Heidelberg, Germany, 2013; pp. 627–634.
Chen, W.; Pourghasemi, H.R.; Zhao, Z. A GIS-based comparative study of Dempster-Shafer, logistic regression and artificial neural network models for landslide susceptibility mapping. Geocarto Int. 2017, 32, 367–385.
Bui, D.T.; Tuan, T.A.; Klempe, H.; Pradhan, B.; Revhaug, I. Spatial prediction models for shallow landslide hazards: A com-parative assessment of the efficacy of support vector machines, artificial neural networks, kernel logistic regression, and logistic model tree. Landslides 2016, 13, 361–378.
Bui, D.T.; Tuan, T.A.; Hoang, N.-D.; Thanh, N.Q.; Nguyen, D.B.; Van Liem, N.; Pradhan, B. Spatial prediction of rain-fall-induced landslides for the Lao Cai area (Vietnam) using a hybrid intelligent approach of least squares support vector machines inference model and artificial bee colony optimization. Landslides 2017, 14, 447–458.
Liu, Y.-L.; Yin, K.-L.; Liu, B. Application of logistic regression and artificial neural networks in spatial assessment of landslide hazards. Hydrogeol. Eng. Geol. 2010, 37, 92–96.
Xu, C.; Xu, X.-W. Logistic regression model and its validation for hazard mapping of landslides triggered by Yushu earthquake. J. Eng. Geol. 2012, 20, 326–333.
Trigila, A.; Iadanza, C.; Esposito, C.; Scarascia-Mugnozza, G. Comparison of logistic regression and random forests techniques for shallow landslide susceptibility assessment in Giampilieri (NE Sicily, Italy). Geomorphology 2015, 249, 119–136.
Sun, D.; Gu, Q.; Wen, H.; Shi, S.; Mi, C.; Zhang, F. A Hybrid Landslide Warning Model Coupling Susceptibility Zoning and Precipitation. Forests 2022, 13, 827. https://doi.org/10.3390/f13060827.
Zhou, T.-Z.; Chen, G.; Zhao, X.-F.; Zhu, Y.-F. Study of distribution laws and genesis of landslides in Fujian province. J. Chongqing Univ. Sci. Technol. Nat. Sci. Ed. 2007, 9, 17–19.
Gao, S.; Liu, A.-M.; Huang, Z.-G.; Zheng, W.-W. The character analysis on heavy rainfall inducing geological hazards in Fujian province. Geol. Fujian 2010, 29, 64–71.
Ye, L.-Z.; Liu, K.; Huang, G.-P.; Zheng, M.-Z. The characteristics and influence factors of catastrophic geological disaster in Fujian province. Chin. J. Geol. Hazard Control. 2015, 26, 98–102.
T/CAGHP 039-2018; Standard of Geo-Hazards Early Warning Based on Meteorological Factor. China University of Geosciences Press: Wuhan, China, 2018.
Liu, Y.-H.; Fang, R.-K.; Su, Y.-C.; Xiao, R.-H. Machine learning-based model for warning of regional landslide disasters. J. Eng. Geol. 2021, 29, 116–124.
Miao, Y.-M. A New Approach to Generating Absence Samples for Landslide Susceptibility Assessment. Master's thesis, Nanjing Normal University, Nangjing, China, 2016.
Snoek, J.; Larochelle, H.; Adams, R.P. Practical Bayesian Optimization of Machine Learning Algorithms. In Proceedings of the 25th International Conference on Neural Information Processing Systems, Lake Tahoe, NV, USA, 3–6 December 2012.
Sun, D.; Wen, H.; Wang, D.; Xu, J. A random forest model of landslide susceptibility mapping based on hyperparameter op-timization using Bayes algorithm. Geomorphology 2020, 362, 107201.

Rockfall trajectography: 3D (three dimensional) models predictive capability assessment and coefficients calibration using optimization-based processes

Fantin Raibaut[1], Olivier Ivanez[2], Benjamin Barry[3], Cyril Douthe[4]

[1] IRS, Nice, France
[2] TERZATEC, Nice, France
[3] AEGIS GROUPE, Nice, France
[4] Laboratoire Navier, Champs-sur-Marne, France

SUMMARY: This paper presents a method for assessing the predictive capability of three-dimensional (3D) trajectographic simulation models by back-analysis of real rockfall events. The observed and simulated stop points clouds are seen as probability measures, and are compared with help of the Wasserstein distance, which assesses the average stop point forecast error. The method is illustrated through a case study where the most realistic set of soil restitution coefficients is sought by minimising the Wasserstein distance between the forecasted stop points cloud and the observed one, via a black-box optimisation algorithm.

Keywords: rockfall hazard, 3D trajectographic simulation, predictive capability, coefficients calibration, optimization, Wasserstein distance, Mesh Adaptive Direct Search

Introduction

Trajectographic (2D and 3D) methods, which allow to quantify stop points densities, rock velocities and passing heights at any point in space, are mostly used to assess rockfall hazard. Without prior calibration of the soil parameters, different trajectographic studies might lead to very variable results. The forecast uncertainty is therefore high (C2ROP, 2020). Rockfall models are usually calibrated and validated by comparative analysis with experimental results (laboratory / in situ tests), or with natural rockfall events. Assessing the predictive capability of models, i.e. the accuracy with which simulations approximate real rockfalls, is an issue addressed in various ways.
Unidimensional parameters are often used as model precision indicators: runout distances, energy of impact at the base of rock cliffs, translational and rotational velocities, passing height through virtual evaluation screens. These indicators do not assess the 3D model predictive ability regarding lateral dispersions. Hence, the distribution of stop points within predefined zones, or the dispersion angle of the trajectories can be used to characterize rockfall events. Two dimensional methods to compare the overall distribution of stop points have recently been developed, using goodness-of-fit indices (Žabota, 2020). These indices only depend on the coincidence between real and forecasted stop points, consequently they fail to account for the distance between the simulations and the observations (an observed and a forecasted stop point are treated the same as long they do not coincide, no matter how far apart they are).

The aim of the present paper is thus to propose a methodology to evaluate the predictive capability of trajectographic models and to calibrate their calculation coefficients by comparative analysis with real events. This methodology should be reproducible and easy to implement. It should not require costly trials, and should be based on simple and reliable calibration results, such as stop points clouds. The proposed methodology relies on the use of the Wasserstein distance to assess the predictive capability of the numerical model. This method

will be first presented and then used in a case study to calibrate the soil restitution coefficients by reverse analysis, minimising the Wasserstein distance with a black-box optimization algorithm called Mesh Adaptive Direct Search (Audet, 2006).

Theory of the Wasserstein distance applied to rockfalls

The Wasserstein distance is related to the Optimal Transport problem and was already used in many geosciences applications: seismology, sea ice dynamics, meteorology, etc. In the present case, the observed stop points cloud is treated as a probability measure R, and the simulated stop points cloud is seen as a probability measure S. The Wasserstein distance evaluates the similarity between the probability measures R and S:

$$W(R,S) = \inf_{\{\lambda_{i,j}\},i,j} \left\{ \sum_{i=1}^{n} \sum_{j=1}^{n'} \lambda_{i,j} \cdot c(\omega_i, \omega'_j) \,|\, \sum_{i=1}^{n} \lambda_{i,j} = s_j \wedge \sum_{j=1}^{n'} \lambda_{i,j} = r_i \wedge \lambda_{i,j} \geq 0 \right\} \quad (1)$$

Where R is a discrete probability measure on $(\Omega, \mathcal{F})$ and $\mathcal{F}$ is a σ-field on $\Omega = \{\omega_i\}_{i=1}^{n}$. S is a discrete probability measure on $(\Omega', \mathcal{F}')$ where $\mathcal{F}'$ is a σ-field on $\Omega' = \{\omega'_i\}_{i=1}^{n'}$. We write $R(\omega_i) = r_i$ and $S(\omega'_j) = s_j$. Let c be the cost function $c : \Omega \times \Omega' \mapsto \mathbb{R}_+$.
The Wasserstein distance is known in computer sciences as the Earth's Mover Distance. It gives the minimum cost of turning the distribution R into the distribution S. The analogy consists in seeing R as piles and S as holes. The goal is to determine the optimal transport plan $\lambda_{i,j}$ so that all the piles are moved, and all the holes are filled. The optimal transport plan depends on the chosen cost function c. In the presented methodology, piles are observed stop points and holes are forecasted stop points. The volume of each pile (resp. hole) is proportional to the number of observed (resp. simulated) stop points at a given location. The piles might be split up in order to be moved. The Wasserstein distance is the minimum average Euclidean distance (the chosen cost function) by which each observed stop point has to be moved in order to coincide with a simulated stop point area i.e. the average forecast error. The Wasserstein distance is computed with Python OT module (Flamary, 2021).

Case Study

The study site is located in Saint-Sauveur-sur-Tinée, (France, 06420), approximately 1 km South of the village. The fall of an unstable boulder overhanging the RM2265 was man triggered. The roadway had previously been covered with a 1 m-thick mattress of alluvial material (soil B) to protect the asphalt. The talus on either side of the road are rock screes (soil A) with little vegetation, with slopes ranging from 35° to 55°.
A Digital Terrain Model and an orthophotography of the study site were generated after the fall by drone images photogrammetry. A video of the rockfall was recorded. Several areas of vegetation had to be corrected. The stop points of the rocks bigger than a reference rock were identified on the orthophotography, with the help of the video. We chose to pinpoint the rocks in which a 150 mm radius disc could fit (Figure 1). The comparison is made in 2D (projection on a horizontal plane), but it could also be carried out in 3D.
Professional 3D stochastic trajectometric simulation software RocPro3D was used. Probabilistic modelling and hybrid mass options were selected. The starting zone, rocks volume, initial speed and soils positions were defined according to onsite inspections. 10^5 trajectories were simulated (Figure 1). Simulated stop points are then processed in a user-defined $2m \cdot 2m$ grid (Figure 1). The default soil coefficients for "compact scree" and "loose soil" were chosen from the RocPro3D soil bank (X_0 set of coefficients in the next chapter).

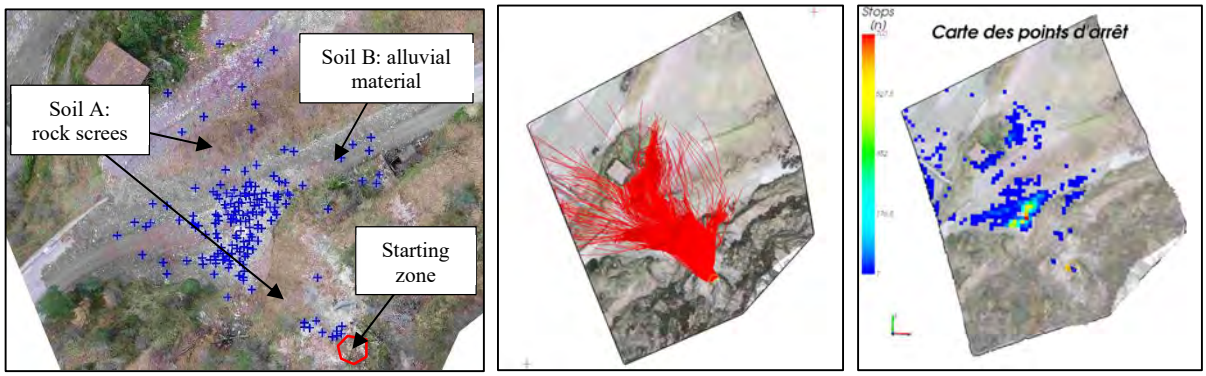

Figure 1. Left – study site: the observed stop points are marked with blue crosses.
Centre – RocPro3D: simulated trajectories – coefficients set sX_0.
Right – RocPro3D: simulated stop points map – coefficients set X_0.

We then processed the results with Python. Each blue cross (resp. red disc) is an observed (resp. simulated) stop point (Figure 2). The radius of each disc is proportional to the number of simulated stop points at a given location. The optimal transport plan $\lambda_{i,j}$ is plotted with Python Matplotlib: the blue lines thickness is proportional to the transported volume between a pile and a hole. Hence, the longer the blue lines, the higher the forecast error. The simulated stop points cloud convex hull was computed with Python Scipy (Figure 2).

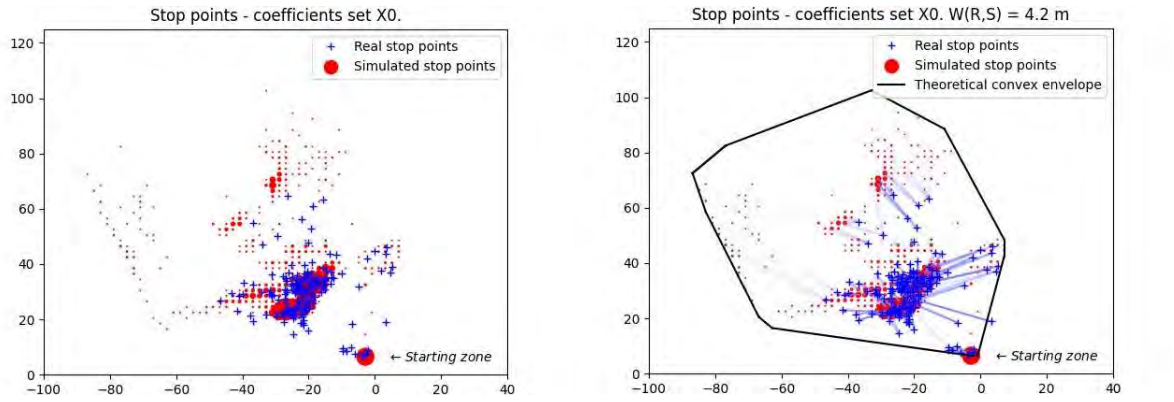

Figure 2. Left - Real and simulated stop points clouds – coefficients set X0.
Right – Optimal transport plan (blue lines) and theoretical convex envelope (black line) – coefficients set X0.

The average predicting error with coefficients set X_0 is $W(R,S) = 4.2m$. A significant proportion of real rocks stopping in the theoretical convex hull means that the simulation is not excessively optimistic.

Calibration of the parameters and conclusion

The calibration methodology consists in determining the coefficients set X* giving the lowest forecast error. We decided to optimize five parameters: the energy dissipation coefficient K – that we assumed to be the same for the two soils -, and the two restitution coefficients R_n and R_t of the soils. The best set of coefficients among the RocPro3D soils bank is X_0.
The RocPro3D simulations processed with Python OT can be seen as a Black Box function: the input is a set of coefficients, the output is a real number, there is no explicit expression nor information on the derivatives. The Black Box is optimized with the Mesh Adaptive Direct Search method implemented in Nomad program (Figure 3) (Audet, 2006). We chose to stop the optimization process after 100 steps. The variation ranges of the coefficients, that have a direct

influence on the speed convergence of the algorithm, are chosen from the literature (extreme soil coefficients: K being bound by 8m/s and 20 m/s, and R_n and R_t ranging respectively from 0.25 to 0.65 and from 0.5 to 1). The same variation ranges were chosen for both the compact soil A and the loose soil B. The optimization result is highly sensitive to the initial set of parameters. Thus, the process was initialized with the best set found by hand, with coefficients from the RocPro3D soils bank: X_0.

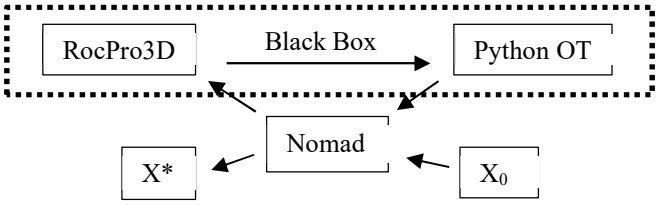

Figure 3. Coefficients calibration via the Black Box optimization process.

The best set of coefficients after 100 optimization steps is X* (average error of 3.1 m):

Table 1. Optimization of the trajectography coefficients with Nomad.

Set	K *(m/s)*	$R_{n,A}$	$R_{t,A}$	$R_{n,B}$	$R_{t,B}$	Wasserstein distance *(m)*
X_0	9	0.4	0.85	0.3	0.8	4.2
X*	9.80	0.59	0.73	0.38	0.71	3.1

The forecast error with coefficients set X* is more than 25% lower than the one of the best simulation with coefficients from the soil bank (X_0) (Table 1). Moreover, the optimal normal restitution coefficient is lower than the tangential one for both soils, which is what is commonly admitted in the literature, even though the variation ranges of R_n and R_t are overlapping. Finally, the algorithm automatically converges to higher coefficients for compact soil A than for loose soil B. Thus, without prior constraints on the coefficients (soil A and soil B coefficients have the same variation ranges), X* is physically relevant: the energy loss is lower on hard soils than on loose ones. The explanation is that an increase in soil B coefficients can balance a decrease in soil A ones regarding the average runout distances, but these sets of coefficients lead to irrelevant lateral dispersions, that are penalized by the Wasserstein distance.

Hence, this case study shows that the average forecast error of rock stop points can be assessed objectively with the Wasserstein distance by comparison with real rockfall events. The soil parameters can be calibrated by back analysis via the minimization of the Wasserstein distance with Mesh Adaptive Direct Search based methods (a large database is however crucial here to achieve robust calibrations). The repetition of such studies could help improving initial parameters for simulations in the future.

References

Collectif des participants à l'action A.3.1 du projet C2ROP (2020) Benchmark des approches d'analyse trajectographique par analyse comparative des simulations prédictives et d'essais de terrain. *Revue Française de Géotechnique* 163, 6.

Barbara Žabota & Milan Kobal (2020) A New Methodology for Mapping Past Rockfall Events: From Mobile Crowdsourcing to Rockfall Simulation Validation. *ISPRS International Journal of Geo-Information* 9, 514.

Charles Audet & J.E. Dennis (2006) Mesh Adaptive Direct Search Algorithms for Constrained Optimization. *SIAM Journal on Optimization* 17, 188-217.

Rémi Flamary & al. (2021) POT: Python Optimal Transport. *Journal of Machine Learning Research*. 22, 1-8.

Analysis Of The Impact Of Wildfire On Root Characteristics And Stability Of Shallow Landslides

Yu Zhang [1], Xiewen Hu[1], Kun He[1], Yonghao Zhou [1], Xueqiang Gong [1]

[1] Southwest Jiaotong University, Chengdu, Sichuan 610031, China

SUMMARY: The post-forest fire landscapes in burned areas are highly susceptible to shallow landslide disasters, and this susceptibility is closely associated with the deterioration of root-soil strength. In this study, the mechanical characteristics of soil root systems are explored in the burned areas of Muli County by conducting in-lab root tensile resistance tests and direct shear tests on the root-soil composites collected. This is purposed to understand how the characteristics of root systems change before and after a fire, along with their impact on the shear strength of root-soil composites. Additionally, the stability of shallow slopes is analyzed using the Wu-Waldron Model before and after the occurrence of wildfire. The results suggest a notable decrease in both the number and density of root systems in the shallow surface soil of burned areas compared to the unburned areas. Furthermore, there is a significant decline in the shear strength of the root-soil composite in the burned areas, which increases the instability of shallow landslides in these regions.
Keywords: Burned areas, Root characteristics, Shear strength, Factor of stability

Extended Abstracts

As one of the common forest hazards, wildfire affects the properties of hillslope materials in the burned area, such as soil and hydrologic. As the root system decays, the soil ceases to be protected by the hydrological and mechanical effects of the roots. This leads to an increase in the occurrence of shallow landslides, especially during rainfall.

According to the existing research, root decay can reduce the capability of soil reinforcement, which contributes significantly to the instability of post-fire shallow landslides. The roots play a crucial role in stabilizing shallow landslides through both hydraulic and mechanical effects. With soil moisture absorbed through transpiration, the hydraulic influence of roots alleviates pore-water pressure in the soil (Indraratna et al., 2006; Nyambayo et al., 2010) and improves soil shear strength (De Baets et al., 2007; Ng et al., 2014). However, the stability of shallow landslide is barely affected by hydraulic effects when rainfall occurs. To a large extent, this influence is attributed to the mechanical reinforcement induced by the root systems against shallow landslides (Zhu et al., 2017; Greenwood et al., 2004; Gehring et al., 2019). This results from the integration of root networks with the soil, with a root-soil composite generated to improve soil friction properties and enhance the apparent cohesion of the soil (Fan et al., 2008; Switala et al., 2019). When intense wildfire occurs, the properties of the root systems within 10 cm beneath the ground surface are affected, thus reducing root quantity and strength. This triggers the instability of shallow slopes due to a compromise on root reinforcement. Therefore, it is necessary to quantitatively analyze the contribution of root reinforcement to the stability of shallow landslides, which is essential for evaluating the impact of forest fires on the stability of shallow landslides.

To conduct this study, field sampling was performed in the burned areas of Muli County, revealing the complex influence of fire behaviors on the characteristics of root systems and the mechanical properties of root-soil composites. Besides, in-lab root tensile resistance and root-soil composite direct shear tests were conducted to thoroughly analyze the characteristics of root systems and shear strength of root-soil composites within the burned areas, for comparison

with those unaffected areas. The analytical results demonstrate the impact of fire behaviors on the aforementioned parameters. By applying the Wu-Waldron Model, the stability of shallow landslides within the burned areas was computed, which lays a foundation for analyzing the failure mechanism of shallow landslides in the burned areas.

1. Root characteristics

Root system counting and sampling were separately performed at different randomly chosen locations within the burned and unburned areas, with each characterized by similar topographies and identical root system types. Then, the typical root parameters were measured and statistically analyzed, including root weight, root distribution density, root diameter, and root length.

A comparative analysis was carried out to explore the significant impact of forest fires on the typical root parameters, revealing a notable post-fire downward trend in root weight, root distribution density, root diameter, and root length. Specifically, after the occurrence of fire, the average root quantity of soil per 0.001 m^3 decreased by approximately 35.96%. To a large extent, this is attributed to the large-scale destruction of surface vegetation by the fire, which causes partial root decay and death. After the fire, the average root diameter was observed to be 0.43 mm, down 46.91% relative to the pre-fire average diameter of 0.81 mm. Meanwhile, there was an observable reduction in root length and root weight by around 13.83% and 56.73%, respectively. These changes result mainly from the high-temperature root dehydration and shrinkage caused by the fire.

Table 1. Root characteristics in the burned and unburned area

Sampling area	**Sum of roots**	**Root weight** /g	**Root diameter** /mm	**root length** /mm
Unburned areas	317	23.18	0.18~1.72	9174
Burned areas	203	10.03	0.13~0.83	7905

2. Roots' tensile resistance and strength.

In this study, tensile pull test was performed on the root segments of 5-10 cm in length using the NK pointer-type push-pull dynamometer. Ten root samples were collected from the unburned areas and another ten were obtained from the burned areas. The experimental results show that the individual tensile resistance of roots generally increased with a rise in root diameter. However, the tensile strength of the roots declinsed in this case. Besides, the average individual tensile resistance of roots in the burned area was only about 33% that of the unburned soil roots. When the root diameter is constant, both the individual tensile resistance and tensile strength of roots in the burned areas were lower than in the unburned areas. This is attributed to the forest fire that increases soil temperature, which causes root dehydration and shrinkage, thus significantly reducing the tensile resistance and strength of the root.

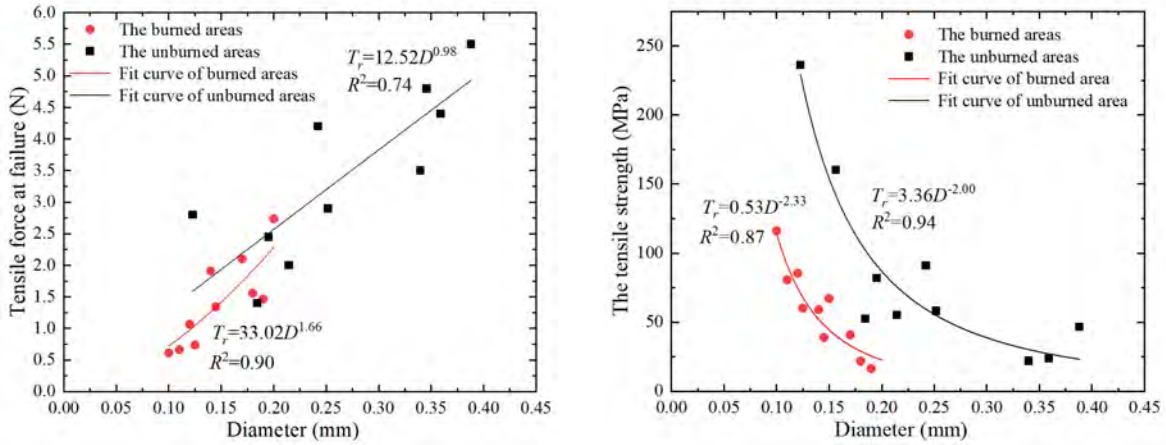

Fig 1. Relationship between the roots' ultimate tensile strength and the largest root anti-rally with diameter in the study area

3. The root-soil composite intensity

Direct shear tests were performed on the root-soil composite at a soil depth of 50 mm, revealing that the shear strength of the root-soil composite is lower in the burned areas than in the unburned areas. Notably, there is a significant change in the cohesion of the root-soil composite before and after the fire. Despite some relatively insignificant variations in the shear strength of the root-soil composite, the changes in root characteristics in the burned areas contribute mainly to the diminishing cohesion of the root-soil composite, with a lesser impact caused on the internal friction angle.

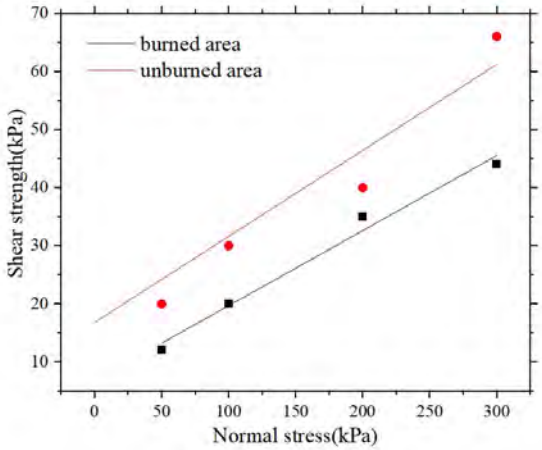

Fig 2. Relationship between normal stress and shear strength

4. Stability analysis of shallow landslides

The approach proposed in this paper relies on the infinite slope stability equation derived from the Mohr-Coulomb criterion. To factor root reinforcement into slope stability calculation, the addition of cohesion is considered. The factor of safety (F_s) is expressed as follows:

$$F_s = \frac{c_r + c_s + g\cos^2\theta[\rho_s(Z - Z_w) + (\rho_s - \rho_w)Z_w]\tan\varphi}{\rho_s g Z \sin\theta\cos\theta + \ _w g Z_w \sin\theta\cos\theta} \quad (1)$$

Where c_r and c_s represent root and soil cohesion respectively; θ indicates the slope angle of the ground; φ denotes soil internal friction angle; ρ_s and ρ_w refer to the saturated soil bulk density and water density; Z and Z_w represent the perpendicular depth of the failure surface and water table; and g denotes the acceleration induced by gravity.

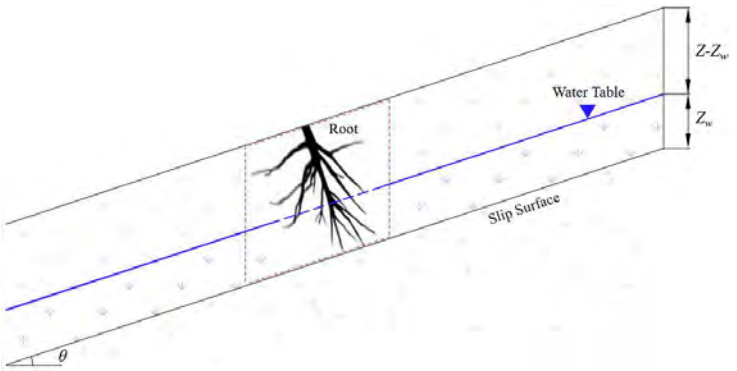

Fig 3. Model of the effect of root system on shallow landslides

This formula takes into account the actual parameters of shallow landslides and the root test results obtained from the burned areas. Based on field measurement and experiment, the stability of shallow surface landslides in the burned area was assessed by using Formula (1), the results of which are presented in Table 2.

Table 2. Root characteristics in the burned and unburned area

Area	**Root cohesion** (c_r / kPa)	**Soil cohesion** (c_s / kPa)	**Soil internal friction angle** (φ /°)	**Saturated soil bulk density** (ρ_s / kN/m^3)	**Water density** (ρ_w / kN/m^3)
Unburned areas	12.6	16.2	25.2	17.5	9.8
Burned areas	5.3	7.9	24.8		
Area	**The depth of failure surface** (**Z** / m)	**The depth of water table** (**Z_w** / m)	**Slope angle of the ground** (θ/°)	**The factor of safety**	
Unburned areas	1.6	0.3	19.0	1.37	
Burned areas				1.16	

According to the above results, the safety factor of the shallow landslides is 1.37 before the fire, down to 1.16 after the fire. This reduction in the safety factor indicates that burning reduces the strength of the root-soil composite, thereby affecting the mechanical reinforcement of the roots against shallow landslides. Consequently, shallow landslides are destabilized.

5. References

INDRARATNA B, FATAHI B, KHABBAZ H (2006) Numerical analysis of matric suction effects of tree roots. *Geotechnical Engineering* 159(2), 77–90.

NYAMBAYO V P, POTTS D M (2010) Numerical simulation of evapotranspiration using a root water uptake model. *Computers and Geotechnics* 37(1), 175–186.

DE BAETS S, POESEN J, KNAPEN A (2007) Impact of root architecture on the erosion-reducing potential of roots during concentrated flow. *Earth Surface Processes and Landforms* 32(9), 1323–1345.

NG C W W, LEUNG A K, KAMCHOOM V (2014). A novel root system for simulating transpiration-induced soil suction in centrifuge. *Geotechnical Testing Journal* 37(5), 1–15.

Zhu H, Zhang L M, Xiao T (2017). Enhancement of slope stability by vegetation considering uncertainties in root distribution. *Computers and Geotechnics* 85, 84－9.

Greenwood J R, Norris J E, Wint J (2004). Assessing the contribution of vegetation to slope stability. *Geotechnical Engineering* 157(4), 199－207.

Gehring E，Conedera M，Maringer J (2019). shallow landslide disposition in burnt European beech (Fagus sylvatica L.) forest. *Scientific Reports* 9(1), 8638.

Fan C C, Su C F(2008). Role of roots in the shear strength of rootreinforced soils with high moisture content. *Ecological Engineering* 33(2), 157－166.

Switala B M，Wu W，Wang S (2019)． Implementation of a coupled hydromechanical model for root-reinforced soils in finite element code. *Computers and Geotechnics* 112, 197－203.

Quantifying the effects of fire severity on soil aggregate stability under laboratory conditions and field measurements from the Pine forest burned areas in Sichuan Province, China

Yonghao Zhou [1], Xiewen Hu[1,*], Kun He[1], Yu Zhang [1], xueqiang Gong [1]

[1] Southwest Jiaotong University, Chengdu, Sichuan 610031, China

SUMMARY: Aggregate stability (AS) is the key factor influencing infiltration capacity and susceptibility to soil erosion. Since the fire has affected other related properties such as organic matter content, water repellency, and soil mineralogy, AS response to the forest fire is complex. To investigate the difference of soil AS in different burn severity, field soil samples were obtained within different fire intensities in the pine forest in Sichuan Province, China. And heated at various temperatures (100°C、200°C、300°C、400°C、500°C、600°C) for 5 min, 15 min, 30 min, 60 min, and 120 min, respectively. Both the heated samples and the field samples within different fire intensities were processed with the AS tests so as to compare the laboratory and field results. The results show that compared to unburned control samples, low-severity burning (heating below 100°C) increases the porosity and reduces the AS; Moderate burning (burning at 200) improves the soil water repellency and hence the AS; However, very-high burning (temperature greater than 300 °C) may entirely destroy the AS by consuming all the organic matter contained in its particles and damaging the soil structure.
Keywords: Aggregate stability, temperature threshold, fire severity

Introduction

Forest fires can alter soil properties that correspond closely to runoff and erosion in burned areas, as well as raise the possibility of subsequent natural disasters likely post-fire debris flows and flash floods (Wang et al., 2022). Aggregate stability (AS), as a significant indicator of soil quality in burned areas, is the key factor influencing infiltration capacity and susceptibility to soil erosion. Since the fire has affected other related properties such as organic matter content, water repellency, and soil mineralogy, AS response to the forest fire is complex (Thomaz, 2021). many scholars have conducted numerous experiments in the field to address the changes in soil properties introduced by fire (Zhang et al., 2018). However, too many influencing factors in the field lead to not facilitating quantitative comparative analysis. Therefore, laboratory-controlled experiments are necessary to accurately control the variables of interest and to differentiate the effects of fire directly on various properties (Gimeno-García et al., 2004).

In this study, to investigate the difference of soil AS in different burn severity, field soil samples were obtained within different fire intensities in the pine forest in Sichuan Province, China. The effects of fire severity on soil AS were quantitatively analyzed using the SVD (Shock and vibration damage) method. The relationships between combustion temperature, combustion duration, organic matter concentration, water repellency, and AS were explored.

Study area

A pine forest soil at the Township junction of Lawo and Jinlin, located in Mianning County, (Sichuan Province, Southwest China:28°09′N, 101°52′E) was selected for this study. The forested area, belonging to the subtropical monsoon climate, has an average temperature is about 16℃ and the average precipitation is about 1,014mm annually. The terrain was distributed with steep and high mountains, and the altitude is 2,100~2,800 m, which makes the environment complex and changeable.

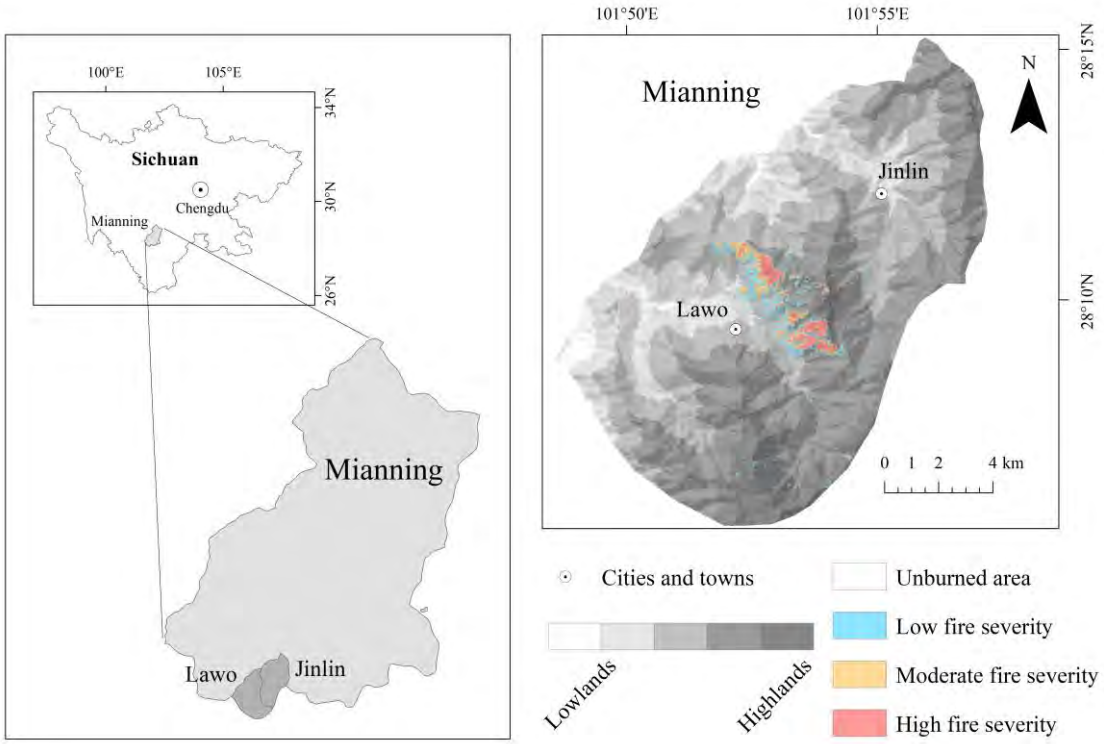

Figure 1 Location of the study area and the distribution of fire severity

Materials and methods

In the unburned area, undisturbed soil cores (with a diameter of 10 cm and a height of 4 cm) were collected for indoor fire simulation. When the samples were stratified and sieved (soil aggregate with a diameter of 4-5 mm was obtained in four levels: 0-1 cm, 1-2 cm, 2-3 cm, and 3–4 cm), they were heated at various temperatures (100°C、200°C、300°C、400°C、500°C、600°C) for 5 min, 15 min, 30 min, 60 min, and 120 min, respectively. Both the heated samples and the field samples within different fire intensities were processed with the AS tests so as to compare the laboratory and field results.

The shock and vibration damage (SVD) method is suitable for stability testing of soil aggregates in burned areas with high organic matter content and widely distributed stability levels. From each composite or individual soil sample, 20 agglomerates 4-5 mm in diameter were selected. For the test, the soil aggregates were first slowly moistened to saturated water content and their initial saturated mass M_a was measured. Secondly, the water-saturated soil aggregates were placed into the device shown in Fig. 2 for the test. Finally, the water and saturated agglomerates after impact shaking were passed through a sieve of 2.8 mm aperture (Imeson & Vis, 1984), and the mass M_b of saturated aggregates with a diameter > 2.8 mm was measured, and the mass loss rate (*MLR*) of the aggregates was calculated as shown in equation (1):

$$MLR = (M_a\text{-}M_b)/M_a \quad (1)$$

where *MLR* is the mass loss rate of soil aggregates, M_a and M_b are the weight of saturated soil aggregates before shock and vibration damage, and the weight of saturated soil aggregates after shock and vibration damage, respectively.

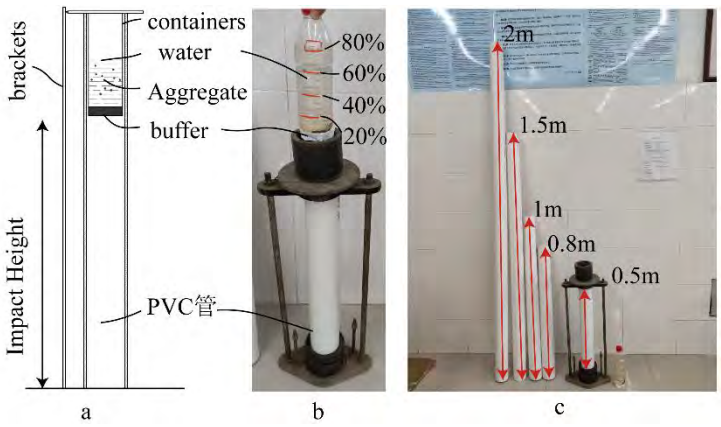

Figure 2. SVD method testing device

Conclusion

From Fig. 3, it can be seen that the most important factor determining the stability of the agglomerates is the temperature, and the agglomerate stability is only enhanced around 200°C. This may be caused by the change of hydrophobic compounds in the humus-clay matrix (Urbanek et al., 2007). When the temperature is low (around 100°C in this experiment), the organic carbon content in the soil does not change significantly. At this stage, the aggregates were affected by heating, and the weakly bound and unbound water on the surface of the soil particles was evaporated by heat, reducing the stability of the aggregates (Thomaz, 2021). Heating the soil with high temperatures (>300°C) decreases the organic matter content of the soil aggregates, and the weight of the aggregates decreases as the soil organic matter is depleted.

Compared to unburned control samples, low-severity burning (heating below 100°C, No matter how long heated) speeds up the evaporation of liquids and gases in the aggregate, increasing the porosity and reducing the AS; Moderate burning (burning at 200°C under 60 min) results in the chemical reaction of organic matter on the surface of aggregate particles, which improves the soil water repellency and hence the AS; However, very-high burning (temperature greater than 300 °C or 200 °C burning for more than 60 min) may entirely destroy the AS by consuming all the organic matter contained in its particles and damaging the soil structure. Additionally, laboratory results show that the AS has a temperature destruction threshold, the value varying from 200°C to 400°C. This temperature threshold continuously decreases with the duration increases; for example, for burns lasting 5 minutes, the temperature threshold for AS is around 400°C; for burns lasting 15 to 30 minutes, it changes to 300°C; and for burns lasting continuously for more than an hour, it reduces to 200°C. when comparing the laboratory results with the field results, AS has the same Phenomenon.

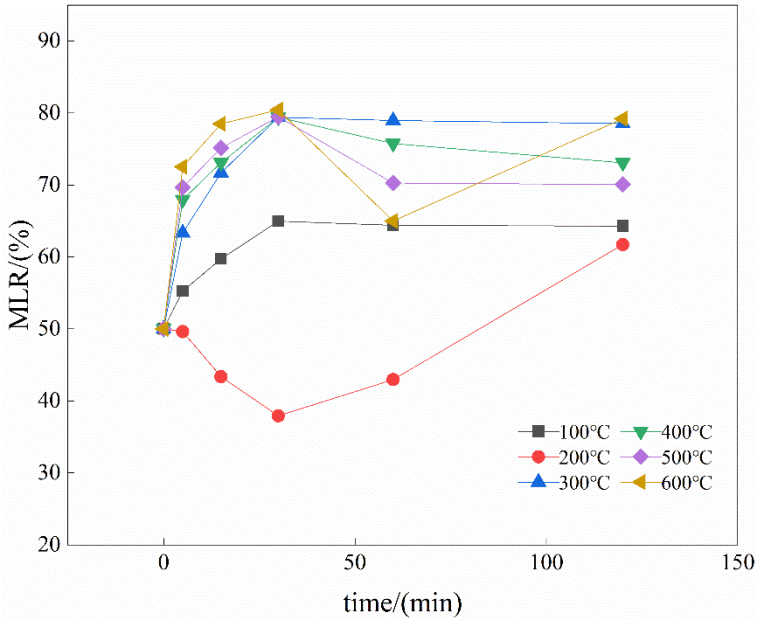

Figure 3. The results of laboratory-controlled experiments

References

Gimeno-García, E., Andreu, V., & Rubio, J. L. (2004). Spatial patterns of soil temperatures during experimental fires. Geoderma, 118(1–2).

Imeson, A. C., & Vis, M. (1984). Assessing soil aggregate stability by water-drop impact and ultrasonic dispersion. Geoderma, 34(3–4).

Thomaz, E. L. (2021). Effects of fire on the aggregate stability of clayey soils: A meta-analysis. In Earth-Science Reviews (Vol. 221).

Urbanek, E., Hallett, P., Feeney, D., & Horn, R. (2007). Water repellency and distribution of hydrophilic and hydrophobic compounds in soil aggregates from different tillage systems. Geoderma, 140(1–2).

Wang, Y., Hu, X., Wu, L., Ma, G., Yang, Y., & Jing, T. (2022). Evolutionary history of post-fire debris flows in Ren'e Yong valley in Sichuan Province of China. Landslides, 19(6).

Zhang, F., Kong, R., & Peng, J. (2018). Effects of heating on compositional, structural, and physicochemical properties of loess under laboratory conditions. Applied Clay Science, 152.

Revealing the deformation and mechanism of a reactivated landslide occurrence based on multi-source data, case study in Li County, China

Xiewen Hu, Kun He

Faculty of Geosciences and Environmental Engineering, Southwest Jiaotong University, Chengdu, China.

SUMMARY: Appropriately multi-source data can provide insights into deformation field and enhance understanding of landslide mechanisms. This paper reports a recent Tangjiawan reactivated landslide along the Wenchuan-Maerkang Highway in Li County, China. The outcomes including satellite InSAR, in situ real-time monitoring, and detailed ground and UAV investigation, conducted at this landslide are presented. Early deformation of the reactivated landslide began from 2019, with an InSAR-derived velocity of -11.7 mm/year, furthermore, a significant subsidence of about 21.2 mm occurred within a span of only 12 days from June 3, 2020 to June 15, 2020 was observed. The deformation characteristics derived from in situ monitoring during the remedial works were likely associated to the initial unreinforced slope condition and the heavy rainfall firstly. Subsequently, the displacement evolution transformed into deformation induced by time-dependent reduction in slope strength under rainfall conditions. The presence of unconsolidated ancient landslide deposits at the base of the slope, along with a fragile geo-structure consisting of rock blocks and gravels interlayered with breccias, exacerbated by large relief created a predisposition for landslide reactivation. Moreover, 13 days of antecedent cumulative rainfall of 224.5 mm directly triggered the landslide occurrence. The significance and implications of integrating multiple monitoring techniques are emphasized.

Keywords: Reactivated landslide; deformation; mechanism; integrated monitoring

Introduction

Landslides are a significant concern in the field of geomorphology for road planning, design, construction, and maintenance (Yan et al. 2022). Particularly in the areas that characterized by alpine-canyon terrain, active tectonism, intense seismic activities, and weak rock mass, landslides not only occur in the form of new landslide, but also exhibit as the reactivation of ancient landslide deposits (Massey et al. 2013). The construction of major roads and highways on mountain slopes necessitates attention to anthropogenic activities such as slope excavating, which can significantly increase the likelihood of reactivated landslide occurrences (Jaafari et al. 2015; Tanyaş et al. 2022). However, little emphasis has been placed on monitoring slope activity for landslides that do not reactivate due to excavation but fail sometime after the completion of construction.

Relevant to the absence of in situ monitoring data, remote sensing techniques present significant advantages for landslide analysis (Casagli et al. 2023). Particularly, it gives an excellent tool to reveal landslide deformation during the pre-event phase. For decades, among the various remote sensing techniques, increasingly contribution has been provided by Interferometric Synthetic Aperture Radar (InSAR), which is currently one of the foremost methods for landslide monitoring (He et al. 2023). For the post-reactivation phrase, especially when the remedial works are performed, it is of utmost importance to center on the continuous monitoring of the slope deformations (Nappo et al. 2019). In situ real-time monitoring strategies are often employed to analyze the landslide behaviors and to follow the remedial work performance, during and after its implementation (Tang et al. 2015; Lollino et al. 2020).

This paper aims to analyze the Tangjiawan reactivated landslide in Southwestern China by means of a joint analysis of InSAR-based and in situ real-time monitoring data. Coupled with geological and geomorphological observations from detailed and immediate field investigation, the integration of the monitoring datasets provided a comprehensive view of the deformation field of the landslide pre-reactivation, during and following the remedial works, and enable the unravelling of key features concerning its mechanism and behavior. The work highlights advantages and implications that multi-sources monitoring data can improve the understanding of reactivated landslides along the major road engineering.

Methodology

Ground and UAV investigations

The detailed field and UAV investigations were conducted from 22 June 2020 to 31 December 2020. To character the landslide, we identified the location and occurrence of all the cracks, the deformation signs of infrastructures, the boundaries of the reactivated landslide. Six boreholes were drilled and cored to explore geo-structures of the landslide (Fig. 1a).

InSAR technique

We collected 72 Sentinel-1 Single Look Complex (SLC) products (Track 62) in descending orbital direction spanning from 9 January 2018 to 15 June 2020 to generate a stack of 237 interferograms (Fig. 1a). The small baseline subset InSAR (SBAS-InSAR) analysis was performed to generate the deformation velocity and time-series displacement.

In situ real-time monitoring

The position of in situ monitoring points was selected within the landslide area by employing a remote application and delivered daily through an FTP server in real time. A monitor network of 12 permanent Differential Global Navigation Satellite System (GNSS) stations, 4 crack meters, 4 inclinometers, was deployed on the landslide in the aftermath of the June 2020 reactivation (Fig. 1b). The deadline for all data statistics presented in this study is 29 June, 2022.

Figure. 1 (a) Integrated monitoring dataset and temporal coverage from different sources. (b) In situ real-time monitoring network and the locations of different instruments

Results

Characteristics of the landslide

Based on the field investigation, borehole drilling and UAV photogrammetry, reactivated area and depth are identified. The reactivated landslide has a chair shape in the plane, with a length of 100 m, a maximum width of 100 m, an area of about 10×10^3 m^2, summit altitude of the area of approximately 1855 m a.s.l and minimum altitude near the toe of about 1685 m a.s.l. The toe of reactivated area falls into the K93+900~K94+200 section of the Wenchuan-Maerkang Highway. The gradient of front edge is about 20~30°, while the middle and rear parts have a slope gradient of 30~40°, and the main sliding direction is 300° (Fig. 2). The thickness of the sliding mass is obtained by borehole drilling, which is about 25.3~40.1 m, with an average thickness of 35.0 m, thus, the reactivated landslide has a volume of about 350×10^3 m^3 (Fig. 2).

Ground deformation

The ground surface tensile cracks involved three major cracks, mostly located along the boundary of the landslide. The crack L1 had developed at the rear edge, composing of several

small cracks (Fig. 2b). The crack L2 was located at the right part of the landslide, belonging to the extension of rear boundary of the local collapse (Figs. 2c). The crack L3 was near the front edge of the local collapse, mainly composed of cracks parallel and oblique to the road (Fig. 2d). The local collapse had occurred on 22 June, 2020, which was located in the right-lower part of the reactivated landslide (Fig. 2a). This local collapse had a length along the sliding direction of 30 m, and a width of 20 m, covering an area of 600 m^2. Based on the geometry measurement with the surrounding slope, the collapse had a thickness of about 2 m, corresponding to a shallow landslide. The volume of this area is approximately 1200 m^3. The slide direction of this local collapse was approximately 30°, and several tensile cracks and fissures formed in its rear part. Borehole drilling reveal that the sliding mass is mainly composed of rock blocks, gravels and breccias (Fig. 2e, f).

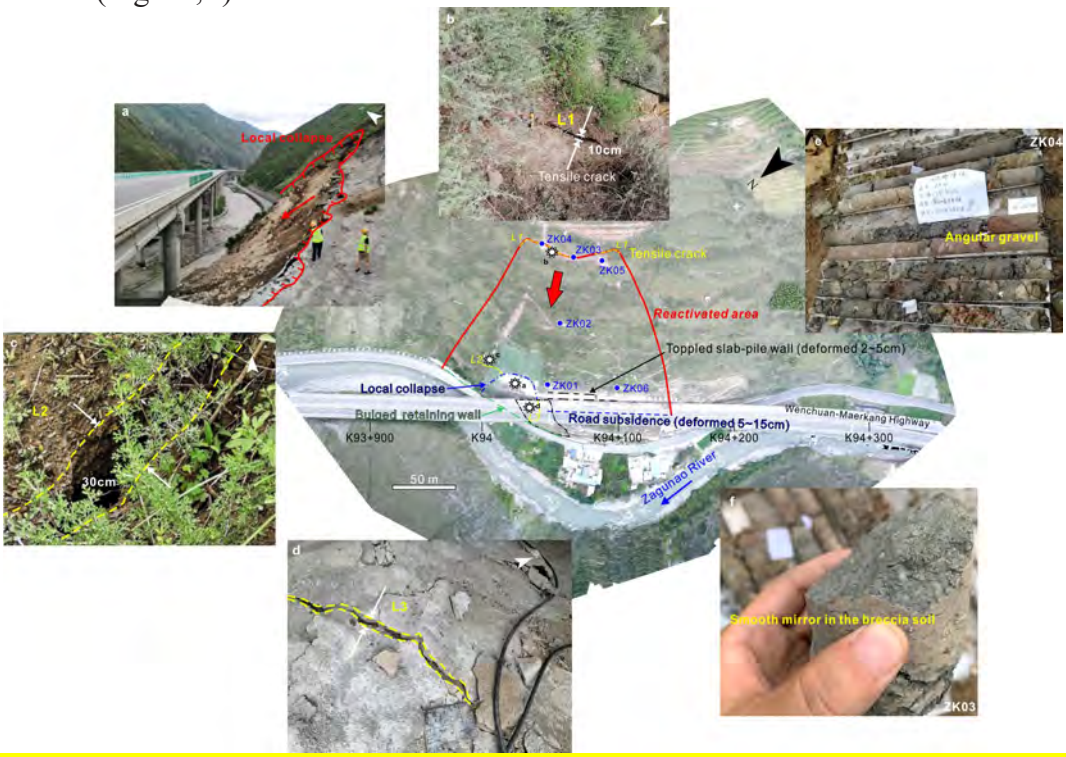

Figure. 2 Orthographic map and the field investigation images of the reactivated landslide and the distribution of in situ investigation points.

InSAR-derived history deformation

Based on the mean velocity of deformation in LOS direction of the study area between 9 January 2018 and 15 June 2020, the monitored time stack has a mean LOS velocity of -18.9~6.5 mm/yr. The subsidence area is mainly distributed along K94+000~K94+200. The landslide area suffered uneven subsidence, with the mean LOS velocity of -18 ~ -5 mm/year.

Post-event In situ real-time monitoring results

Figure 3 depicts the monitoring results of the surface deformation of the reactivated landslide after the failure obtained from the GNSS stations. For instance, GNSS01-03 stations are installed on the original anti-slide piles at the toe of the slope. From the aspect of deformation varying with time, a period rapid deformation is recorded in the three monitoring points from 17 July to 13 November 2020, with the horizontal displacement increments of 56.4 mm, 77.3 mm and 92.6 mm for GNSS01-03, respectively. Such deformation characteristics are likely attributed to the unreinforced slope condition and the heavy rainfall. Subsequently, the displacement evolution transforms into that of deformation induced by time-dependent slope strength reduction under rainfall and anthropogenic activities.

a b

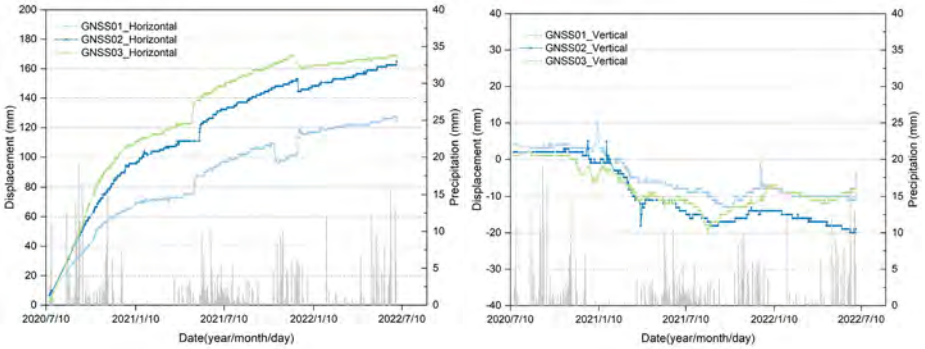

Figure. 3 (a) horizontal and (b) vertical displacement and rainfall versus time monitored by GNSS01-03.

Figure 4 depicts the deep displacement data measured by four inclinometers. For instance, it can be seen the cumulative displacements of inclinometers IN-01 and IN-03 have been increasing during the selected monitoring period, suggesting that the landslide deformation is still ongoing but with low deformation rates. In addition, Figure 4 illustrates that inclinometers IN-01, IN-03 show obvious shear displacement at different depths, which reveals that the depth of the sliding zone is 10~12 m and 28~30 m in borehole IN-01, 20~22 m in borehole IN-03.

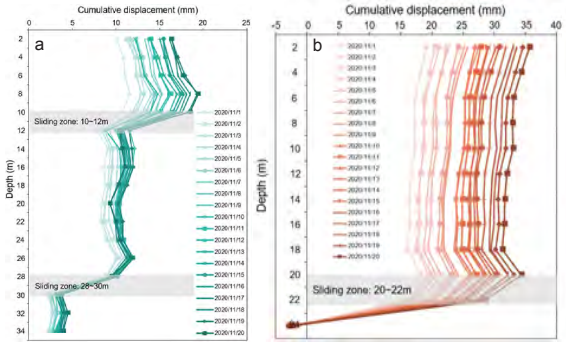

Figure. 4 Cumulative displacement of inclinmeters IN01 (a) and IN03 (b)

Factors contributing to the reactivated landslide

Unconsolidated ancient landslide deposits at the base of the slope

The surrounding mountainous landscape and the chair-like shape of the studied slope shows that an ancient landslide had occurred. Based on the materials indicated by the borehole drillings, the ancient landslide deposits overlie the alluvium deposits formed by the Zagunao River, indicating that a river-damming event had occurred by the ancient landslide. Moreover, the ancient landslide accumulation layer had the characteristics of high porosity, high water content and rich water medium. The sliding mass has a loose structure, mainly composed of rock blocks, gravels and breccias, with the content of coarse particles of 50%~60%.

Fragile geo-structure of rock blocks and gravels interlayered with breccias

The ancient landslide deposits consist of rock blocks, gravels interlayered with breccias, in which the breccias with poor permeability are located between the rock blocks, gravels with high permeability. A large amount of precipitation in this area is transferred to groundwater through the rock blocks, gravels and discharged along the interlayer of breccias and bedrock. However, due to the limited drainage points, part of the groundwater is retained in the breccias layer. Under the action of the high overlying sliding mass weight pressure, the water and the breccia are strongly hydrated, that is, the breccia is argillated, and the strength of the breccia is greatly reduced and becomes a potential slip zone.

Large relief of the original slope

The ancient landslide has an area of 2.96 km^2, with a height difference of 1620 m, an average slope of 36°, presenting a steep-gentle-steep terrain longitudinally. The rear edge of the reactivated landslide is located at the slope break zone, which belongs to the concentrated region of tension stress. The Zagunao river valley is characterized by deep incised, showing a "V" shape, with 80 m in width near the Tangjiawan ancient landslide at the valley bottom and

less than 20 m wide at the narrowest section. Due to the strong incising of the river, the landslide dam was eroded and the high-steep free slope surface formed in the toe of the ancient landslide deposits with a height of more than 130 m and an average slope of 40°, resulting in the re-distribution of stress and providing the potential energy of the deformation or even failure.

13 days of extreme rainfall preceding the reactivation

The deformation of the reactivated landslide began on 22 June, 2020, corresponding to 13 consecutive days of precipitation of 224.5 mm prior to the event. The cumulative rainfall from 10 May to 22 June, 2022 reached 546.8 mm, which exceeded 55% of the total annual rainfall. Thus, the long-term rainfall, particularly the last 13 days of antecedent rainfall period, was utmost triggering factor of this reactivated landslide.

The contribution of anthropogenic activity in changing the strength of the slope

National Road G317 and Wenchuan-Maerkang Highway pass through the slope front in the form of excavation. The highest excavated slope height is about 11m. The construction of National Road G317 and Wen-Ma Highway reduced the anti-slip section of the slope, forming the steep free face on the slope front, and damaging the strength of the slope. Therefore, anthropogenic activity is the secondary triggering factor of landslide reactivation.

The multi-source monitoring for the Tangjiawan landslide indicates that, the InSAR displacement measurements are, in general terms, coherent with the vegetation coverage and location of the studied landslide. In this study, the bare road is ideal for InSAR monitoring, which can be used to monitor the slopes in the vicinity of roads. Nevertheless, some discrepancy in the landslide monitoring were addressed by using SAR image interpretation and field checks, which suggest the need to select the monitoring period considering the road construction period, while the large excavation can contribute to the decoherence of the results. In situ monitoring provides a supplement for remote technique, which update the landslide deformation at the onsite and daily scales. However, difficult-to-access landslide areas are difficult or impossible to install more sophisticated monitoring equipment. The future work should be aim to enhance knowledge of landslide dynamics using both in situ and remote sensing data.

Conclusions

This study conducts a detailed investigation on deformation and mechanism of the recent reactivated landslide, which is located on a steep alpine slope, experienced a large-scale reactivation on 22 June, 2020. This event was triggered by a period of prolonged and intense precipitation. The joint analysis of satellite InSAR, UAV and in situ monitoring data, as a whole collected span a time period of four years, provided essential insights into the deformation and mechanism of the reactivated landslide. The landslide activity has been in the condition of creep since 2019, with the mean LOS velocity of -18~-5 mm/year. Once the countermeasures are implemented, the deformation rates of the slope are reduced based on the data measured from the GNSS stations, inclinometers and crack meters. The deformation rates are also closely associated with the precipitation. The reactivation of the landslide is attributed to the loose ancient landslide deposits, fragile geo-structure, large relief, precipitation and anthropogenic activity.

References

Casagli N, Intrieri E, Tofani V, Gigli G, Raspini F (2023) Landslide detection, monitoring and prediction with remote-sensing techniques. *Nature Reviews Earth & Environment* 4(1), 51-64.

He K, Tanyas H, Chang L, Hu X, Luo G, Lombardo L (2023a) Modelling InSAR-derived hillslope velocities with multivariate statistics: A first attempt to generate interpretable predictions. *Remote Sensing of Environment* 289, 113518.

He, K., Lombardo, L., Chang, L., Sadhasivam, N., Hu, X., Fang, Z., ... & Tanyas, H. (2023b). Investigating earthquake legacy effect on hillslope deformation using InSAR-derived time series. Earth Surface Processes and Landforms. 1-11.

Jaafari A, Najafi A, Rezaeian J, Sattarian A, Ghajar I (2015) Planning road networks in landslide-prone areas: A case study from the northern forests of Iran. *Land Use Policy* 47, 198-208.

Lollino P, Giordan D, Allasia P, Fazio NL, Perrotti M, Cafaro F (2020) Assessment of post-failure evolution of a large earthflow through field monitoring and numerical modelling. *Landslides* 17, 2013-2026.
Massey CI, Petley DN, McSaveney MJ (2013) Patterns of movement in reactivated landslides. *Engineering Geology* 159, 1-19.
Nappo N, Peduto D, Mavrouli O, van Westen CJ, Gullà G (2019) Slow-moving landslides interacting with the road network: Analysis of damage using ancillary data, in situ surveys and multi-source monitoring data. *Engineering geology* 260, 105244.
Tang H, Li C, Hu X, Su A, Wang L, Wu Y, ... Li Y (2015) Evolution characteristics of the Huangtupo landslide based on in situ tunneling and monitoring. *Landslides* 12, 511-521.
Tanyaş H, Görüm T, Kirschbaum D, Lombardo L (2022) Could road constructions be more hazardous than an earthquake in terms of mass movement? *Natural hazards* 112(1), 639-663.
Yan Y, Cui Y, Huang X, Zhou J, Zhang W, Yin S, ... Hu S (2022) Combining seismic signal dynamic inversion and numerical modeling improves landslide process reconstruction. *Earth Surface Dynamics* 10(6), 1233-1252.

How large is “large” for landslides? Introduction to destructive size scale

Marc Janeras[1], Pere Buxó[1], Jordi Marturià[1]

[1] Institut Cartogràfic i Geològic de Catalunya, ICGC, Barcelona, Spain

SUMMARY: A unique descriptor for landslide size is lacking when qualitatively assessing hazard. A new size scale is introduced based on the destructive potential, which is able to be applied to all kind of landslides and even in multi-hazard analysis.

Keywords: size, magnitude, destructive potential, scale, hazard

Introduction

According to the most recent version in use of the glossary for landslides (Corominas et al., 2015; Hantz et al., 2021), on the one hand, landslide *magnitude* is defined as the measure of the landslide size that may be quantitatively described by its volume or indirectly by its area, specifying in that case if the descriptor may refer to the scar, deposit or both. On the other hand, landslide *hazard* is defined as its condition with the potential for causing an undesirable consequence that expresses the probability of a particular threat occurring within a defined time period and area.

Many authors realized that magnitude is not an appropriate hazard descriptor. Even though it may be expected that the higher the landslide magnitude, the higher the potential for damage, this does not hold true in all cases (Corominas et al., 2014). The gravitational movement of the mass down the slope is determinant for the resulting damage potential. Additionally, the terms “large” and “small” do not fit homogeneously to the different types of landslide, which makes it difficult to find a common scale for magnitude in volume (Fell, 1994; McColl and Cook, 2023).

After a first approach that failed in the attempt to review the meaning of magnitude for landslides (Janeras et al., 2022a, 2022b), we have adopted a term in use for avalanches (Statham et al., 2018) to describe the global size of the mass movement, including both the amount of mass and a quantity of movement.

Destructive size scale

The sizing term that fits the best for hazard assessment together with the probability of occurrence is the destructive size of landslide, as a measure of the landslide severity. The proposed destructive size scale is presented in Table 1. We have defined the first five grades for destructive size ($S = 1$ to 5) because they where needed at Catalonia (Spain) scale to be applied to qualitative hazard assessment for land use planning, to the inventory of multiple-occurrence regional landslide events (MORLE) and to a territorial early warning system for landslides (TeLEWS) (Buxó et al., 2023; Hürlimann et al., 2023; Marturià et al., 2023). However, this scale is open by definition and higher grades ($S \geq 6$) are expected to be defined in the next future when using the scale under other geodynamical context where larger landslides occur. When destructive size S increases, both the maximum intensity and affected extension rise. Although, it is worth noting that destruction of conventional buildings and

infrastructures can be fully achieved for S =5, and the key variable turns into the extension of the area covered by destruction.

Table 1. Definition of the Destructive Size for landslides, being able to be applied to multi-hazard.

Size	Destructive potential
S1	It can hurt a person in open space. It can cause minor non-structural damage on buildings, and punctually to light vehicle. It constitutes an obstacle of easy withdrawal. Footprint on natural environment is practically imperceptible.
S2	People are guarded inside buildings, which may suffer minor structural damage. It may obstruct a road and severely impact a light vehicle. It leaves a small, short-lasting imprint on natural environment.
S3	People inside buildings are at risk, though they may have some protection as landslide can cause moderate structural damage or even it can destroy lightweight buildings. It can cause damage to infrastructure that limits its use until repair. It leaves a clear imprint on the natural environment.
S4	Buildings do not provide effective protection for occupants, as landslide can cause severe structural damage, also to several buildings and destroy some. It can cause damage and block infrastructure that prevents its use until repair. It leaves a lasting imprint on the physical environment.
S5	The survival of the people depends on fortuitous circumstances because landslide can destroy a built-up area. It can destroy or cause irreparable damage to infrastructure. It can transform the landscape with new terrain morphologies or destruction of forests.
≥S6	It can destroy towns, transforming valleys in large extent, blocking rivers, what could cause cascading effects or secondary phenomena as well significantly destructive.

Application to the main landslide types

The size scale so defined can be homogenously applied to all types of landslides, regardless their diverse features. And even more, it can be applied to multi-risk analysis, because it is based on the destructive potential independently of the phenomena. The scale is not defined by physical attributes of landslides, but on the contrary, according to a combination of landslide quantities on mass and movement, a size grade can be expected. Examples of hazard scenarios for rockfall and debris flow leading to each destructive size grade are presented in Table 2 and Table 3. It is worth highlighting that other combinations of the variables are also possible, and the included cases are only some representative cases. For slides (Table 4), the variety of cases is even wider, because different combinations of extension, sliding surface depth, and runout displacements can lead to similar destructive size value. Additionally, visual examples are presented in Figure 1 for every size and landslide type.

Table 2. Typical scenarios of rockfalls leading to each destructive size degree. Values of the main involved variables are given only as particular examples.

Total detached mass, M (kg)	Major block mass, m (kg)	Total height difference, H (m)	Maximum block velocity, v (m/s)	Corresponding destructive size
10^2	10^2	5	10	S1
3×10^3	10^3	10	15	S2
10^5	10^4	20	20	S3
3×10^6	10^5	50	25	S4
10^8	10^6	100	35	S5

Table 3. Typical scenarios of debris flows leading to each destructive size degree. Values of the main involved variables are given only as example.

Volume involved, V (m^3)	Runout length, L (m)	Maximum flow depth, h (m)	Maximum velocity, v (m/s)	Maximum deposit depth, g (m)	Deposit area, A (m^2)	Corresponding destructive size
3×10^1	30	1	1	0.5	200	S1
3×10^2	100	2	2	1	1,000	S2
3×10^3	300	3	4	2	5,000	S3
3×10^4	1,000	4	8	4	30,000	S4
3×10^5	3,000	5	16	8	200,000	S5

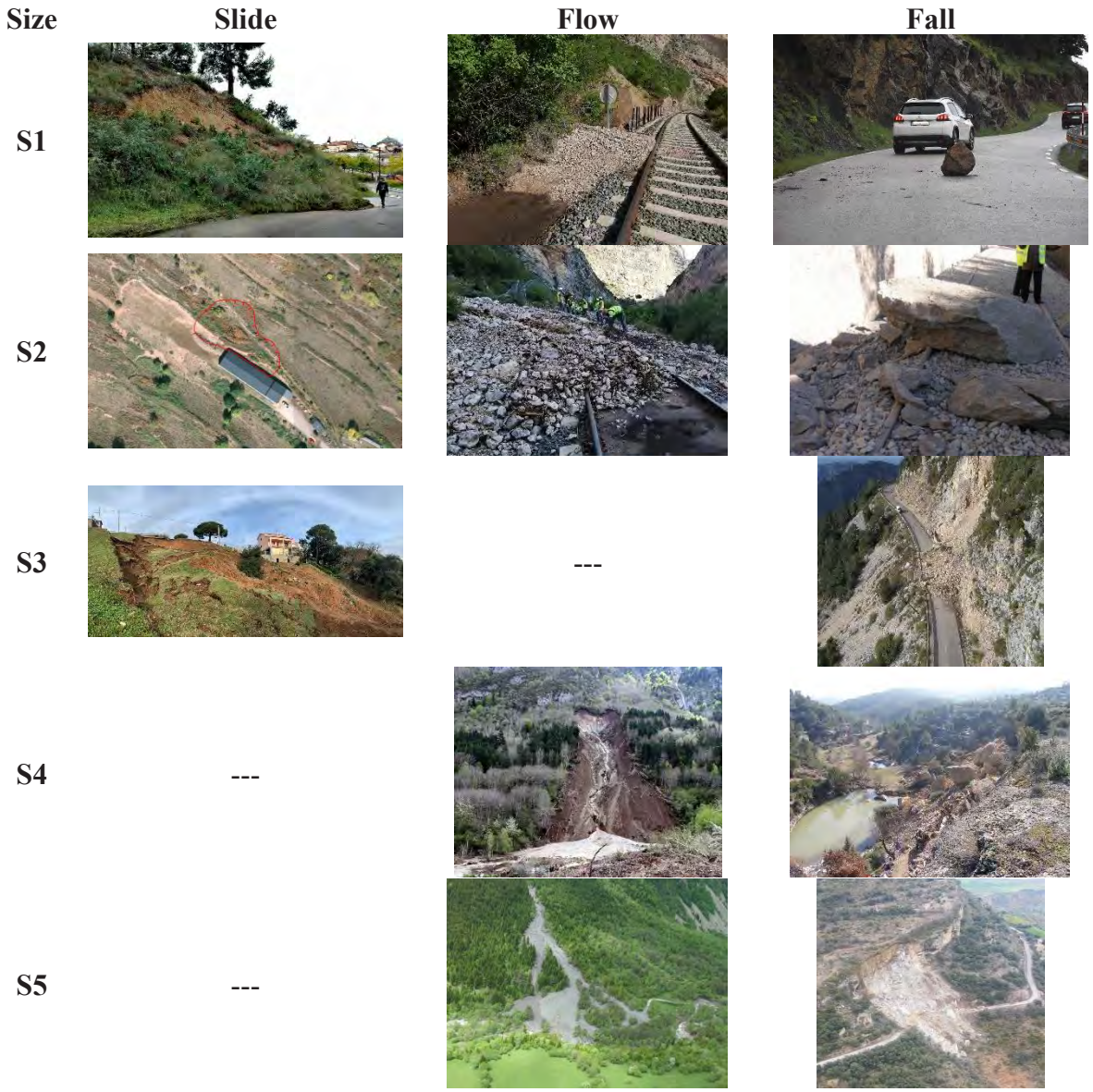

Figure 1. Visual examples of landslides causing damage representative of what could be expected for each destructive size grade.

Table 4. Typical scenarios of slides leading to each destructive size degree. Values of the main involved variables are given only as particular examples.

Extension area, A (m^2)	Maximum sliding depth, h (m)	Volume involved, V (m^3)	Runout length, L (m)	Corresponding destructive size
10^1	0.3	3×10^0	1	S1
10^2	1	5×10^1	2	S2
10^3	3	1×10^3	5	S3
10^4	10	2×10^0	10	S4
10^5	30	5×10^0	20	S5

Conclusion

A destructive size scale has been introduced for landslides to allow a size (small to large) categorization in a common basis for all types of landslides. This term also allows the proper meaning of size for qualitative hazard assessment when merged with probability of occurrence.

References

Buxó, P., Oller, P., Marturià, J., Fabregat, I., Xifre, D., 2023. Magnitude of regional episodes of landslides (ERML) in the Catalan Pyrenees, in: Proceedings of the 6th World Landslide Forum WLF-6. Florence, Italy.

Corominas, J., van Westen, C., Frattini, P., Cascini, L., Malet, J.P., Fotopoulou, S., Catani, F., Van Den Eeckhaut, M., Mavrouli, O., Agliardi, F., Pitilakis, K., Winter, M.G., Pastor, M., Ferlisi, S., Tofani, V., Hervás, J., Smith, J.T., 2014. Recommendations for the quantitative analysis of landslide risk. Bull. Eng. Geol. Environ. 73, 209–263. https://doi.org/10.1007/s10064-013-0538-8

Corominas, Jordi, Einstein, H., Davis, T., Strom, A., Zuccaro, G., Nadim, F., Verdel, T., 2015. Glossary of terms on landslide hazard and risk, in: Lollino, G., Giordan, D., Crosta, G.., Corominas, J., Azzam, R., Wasowski, J., Sciarra, N. (Eds.), Engineering Geology for Society and Territory - Landslide Processes. Springer International Publishing, pp. 1775–1779. https://doi.org/10.1007/978-3-319-09057-3_314

Fell, R., 1994. Landslide risk assessment and acceptable risk. Can. Geotech. J. 31, 261–272. https://doi.org/10.1139/t94-031

Hantz, D., Corominas, J., Crosta, G.B., Jaboyedoff, M., 2021. Definitions and concepts for quantitative rockfall hazard and risk analysis. Geosci. 11. https://doi.org/10.3390/geosciences11040158

Hürlimann, M., Berenguer, M., Tapia, L., Marturià, J., Buxó, P., Janeras, M., 2023. The Catalan Early Warning System for rainfall induced landslides. New online platform and experiences gathered during the testing phase, in: Proceedings of the 6th World Landslide Forum, WLF-6. Florence, Italy.

Janeras, M., Buxó, P., Marturià, J., 2022a. How big is «big» in rockfall? Test of a magnitude scale feasibility, in: 7th RocExs Interdisciplinary Rockfall Workshop. Sapporo, Japan, pp. 28–31.

Janeras, M., Buxó, P., Marturià, J., Barberà, M., Ripoll, J., 2022b. ¿Cuánto grande es "grande" en los movimientos de ladera?, in: X Simposio Nacional Sobre Taludes y Laderas Inestables.

Marturià, J., Buxó, P., Janeras, M., Ripoll, J., Barberà, M., 2023. Qualitative hazard assessment as first step for landslide consideration in land use planning, in: Proceedings of the 6th World Landslide Forum, WLF-6. Florence, Italy.

McColl, S.T., Cook, S.J., 2023. A universal size classification system for landslides. Landslides. https://doi.org/10.1007/s10346-023-02131-6

Statham, G., Haegeli, P., Greene, E., Birkeland, K., Israelson, C., Tremper, B., Stethem, C., McMahon, B., White, B., Kelly, J., 2018. A conceptual model of avalanche hazard. Nat. Hazards 90, 663–691. https://doi.org/10.1007/s11069-017-3070-5

Preliminary Investigation of displacement in Joshimath Town from the perspective of Deep-Seated Landslides

Shobhana Lakhera[1], Michel Jaboyedoff[1], Marc-Henri Derron[1], Leo Lettelier[1], Charlotte Wolf[1] Ajanta Goswami[2], Anil Kumar Maletha[3]

[1]Institute of Earth Science, University of Lausanne, Lausanne, Switzerland
[2]Department of Earth Science, Indian Institute of Technology Roorkee, India
[3]Megha Engineering and Infrastructures Limited, India

SUMMARY: Joshimath is a town in the Garhwal Himalayan Region of Uttarakhand India, located on unconsolidated and saturated, old landslide debris. It has been intermittently creeping past many decades, and since December 2022, has reported significant displacement. At present a total of 868 buildings developed cracks, with nearly 1000 people displaced. Thus, a comprehensive mapping of landslide scars was done using high-resolution DEM and it was observed that the sentinel-1 based InSAR-displacement was localized along certain mapped landslide scars. Moreover, the displacement activity along these reactivated scars increased after the 2021 debris-flow event.
The failure surfaces and displacement along the failure surfaces, for these reactivated landslides was modelled using a phython tool (Lettelier et al., 2023), based on the sloping base level (SLBL) method (Jaboyedoff et al., 2020). The depth of failure surface was modelled between 100m-250m; hence these landslides were identified as deep-seated landslides (DSL's). The displacement activity along the sliding surfaces showed characteristic patterns indicative of landslide-induced displacement and the location of active-landslide scars corresponded well with the cracks mapped on field. Furthermore, to analyse the impact of 2021 debris-flow event an analysis of Factor of Safety (FOS) was done under different scenarios and noticeable impact was observed.

Keywords: Landslides, Displacement, Sloping Base Level (SLBL), Deep-Seated landslides (DSL's), Factor of Safety (FOS).

Introduction

After the recent amplification of displacement since onset in October 2021, 81 ground cracks have been mapped in the Joshimath town of which the 46 are new linked to the event of 2 Jan 2023 and rest are old (GSI, 2023). The objective of this research was to understand the cause and factors that accentuated the displacement activity in Joshimath town and to analyse the displacement from the perspective of DSL's.

The township of Joshimath is situated on the banks of river Alaknanda within an elevation range of 1330m to 3200m and a north facing slope between 30˚ to 60˚. It is at a distance of only 7km from the hanging wall of Himalayan Main Central Thrust (MCT) (GSI, 2023). The lithology is characterized by the presence of thick overburden material composed of giant gneissic boulders embedded in loose sandy-silty matrix (GSI, 2023). According to a survey conducted by Garhwal scouts the thickness of the unconsolidated-overburden is estimated to vary from 40m to even more than 100m from the surface (GSI, 2023). Additionally, the occurrence of spring at different levels indicates the location of intersection between natural topography and flow lines of subsurface water. Thus, Joshimath township is situated, on saturated overburden material (GSI, 2023). Many recent incidences of water seepage are also indicative of presence of shallow saturated zones. Moreover, the water from natural springs and unplanned sewage is contributing to recharging the unconsolidated slope forming mass on which the Joshimath town

is situated, thus indicating the build-up of excess pore water pressure (GSI, 2023). Deep cutting and subsequent land sliding along local drainage channels is also quite evident and the town records incidences of slope failures even in dry seasons (Valdiya et al., 2014).

Methods and data

As Joshimath is located on old landslide debris and is prone to landslide activity, firstly a detailed landslide scar map was prepared using 2m digital elevation model (DEM), from MAXAR, google earth images, planet scope images and ancillary maps available online (Fig.1). Secondly, the InSAR based displacement for Joshimath was analysed using Sentinel-1 ascending pass, SAR images for the year 2020 and 2021(Fig.2). The displacement was found to be specifically concentrated along the overlapping landslide scars highlighted in shades of yellow in fig.1. The crack locations mapped from the 2023 report of the Geological survey of India and Sundriyal et al., 2023, when overlain with the mapped landslide scars, indicated that the cracks are mostly concentrated along scars shown yellow which also corresponds with the InSAR results (Fig.1 and Fig.2).

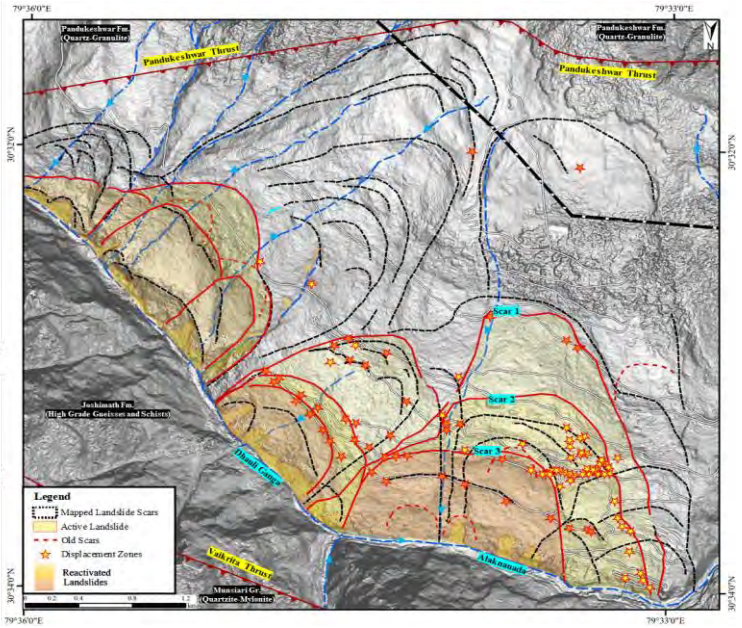

Figure .1 Landslide scar map with crack location

Furthermore, the InSAR analysis revealed that the Joshimath township is located on active landslides. As faint displacement activity of around 1 to -2cm was observed between the 28th of March 2020 and 9th of April 2020, this was even before the 2021 debris flow event (Fig.2). Additionally, after the 2021 event and successive heavy rain showers the displacement increased to around 5cm between the 30th Nov 2021 and 12th Dec 2021 (Fig.2). Also, the extent of displacement activity increased in the year 2021 with more overlapping and connected scars showing movements, w.r.t 2020, where it was comparatively more localised along the rim region (Fig.2). Hence the failure surface and landslide volume were modelled for the three active landslide scars i.e., scar1, scar2 and scar3. Also, the InSAR displacement along cross-section AA' was analysed using a python tool developed by Lettelier et al., in 2023 (Fig.3). The tool is based on the the sloping base level model (SLBL) proposed by Jaboyedoff et al., in 2020. SLBL is an iterative calculation that provides a landslide failure surface using a DEM and the landslide perimeter. The principle involves digitally excavating a grid DEM by replacing the elevation z_{ij} of the 'j' collum and the 'i' line with the average of its four nearest neighbours (z'_{ij}

$(z_{i+1,\,j} + z_{i-1,\,j} + z_{ij+1} + z_{ij-1})/4)$ if this value is lower than the actual elevation. To obtain a curved surface imitating a second-order surface, a constant positive value $\Delta z'$ can be subtracted, i.e. if $(z'_{ij}-\Delta z') < z_{ij}$ then $z_{ij} = z_{ij}-\Delta z'$ otherwise $z_{ij} = z_{ij}$. This operation is performed until the variation in z_{ij} is below a chosen threshold. The model also models the displacement along the failure surface, and provides a comparison between the modelled displacement and real line of site displacement (LOS) by projecting the LOS displacement vectors on the slope cross-section (i.e., AA'). These three landslide scars were considered for this analysis as they recorded the maximum InSAR displacements and the cracks were also localised along the three mentioned landslide scars. The failure surfaces modelled for the three landslide scars i.e., scar1, scar 2 and scar3 were named as - SLBL1, SLBL2 and SLBL3, respectively. The depth of these failure ranged between 100m to 250m and volume of the landslides varied between 100 to 300 million m^3. Thus, the three landslide scars i.e., scar1, scar2 and scar3 correspond to deep-seated landslides.

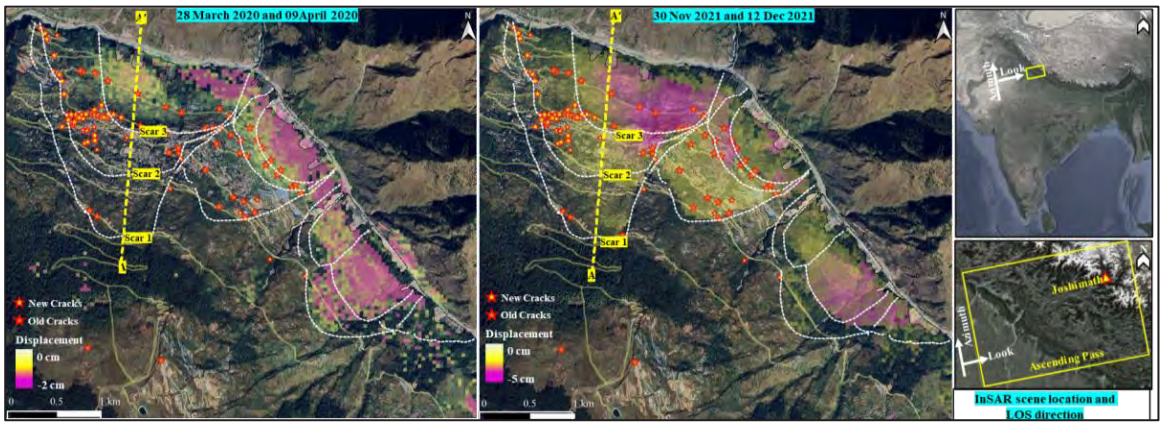

Figure.2 Sentinal-1 based InSAR displacement for specific dates of the year 2020 and 2021, along the reactivated landslides, and the cross-section (AA') considered for displacement analysis

The results of displacement analysis are shown in fig.3. The modelled and LOS projected real displacement along the cross-section AA' for the image pairs of 2020 and 2021 is presented. In 2020 the displacement seems localised along the SLBL3 and the magnitude of displacement vector decreases towards the boundary of SLBL3 and SLBL2 and becomes negligible towards the top portion of SLBL1. Whereas in the 2021 model the displacement magnitude varies along the three SLBL surfaces, with higher negative displacement along the SLBL3 and decreased displacement as we reach the boundary of SLBL3 and move up along SLBL2. A slight positive displacement is noticed as the boundary of SLBL2 is approached, along SLBL1. Hence, the changes in displacement magnitude along the boundary of SLBL surfaces are indicative of landslide induced displacement activity. Also, the model predicted displacement and the slope projected real LOS displacement are correlated well with a r^2 of ~0.7 for 2020 and 0.8 for 2021.

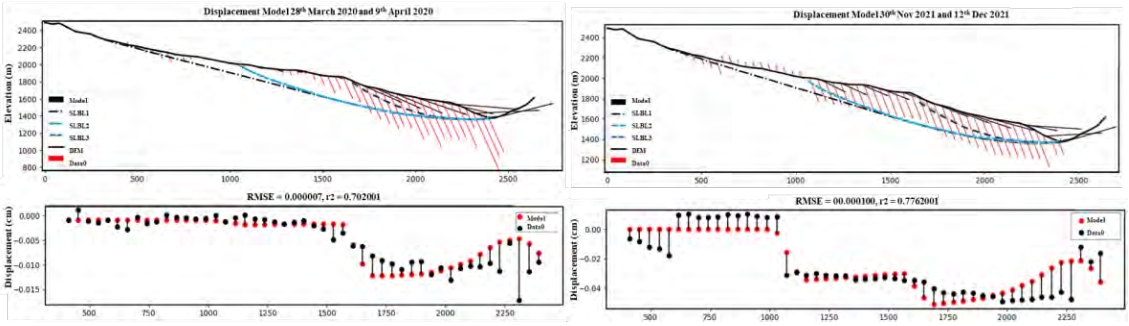

Figure 3: Model results for 2020 and 2021 image pair displacements along cross-section AA'

Lastly, the impact of toe cutting and subsequent slope failures on the factor of safety (FOS) was analysed for the sliding surface along cross-secting AA', using the Rockscience Slide2 software. This was done considering different scenarios, with input SLBL surfaces. The most important scenarios analysed were, hypothetical water table (WT) (S1), WT with toe cutting (S2) and WT with toe cutting with landsliding (S3). The parameter values considered are: unit weight = 20 KN/m3, strength type = Mohr-Coulomb, friction angle =30˚ and cohesion =10 Kpa (Sundriyal et al., 2023). The analysis highligted that toe cutting followed by landsliding can reduce the slope stabilty along the SLBL surfaces by as high as 6% . Furthermore the SLBL3 located at the rim region of Joshimath slope was affected the most by toe cutting and sliding activity and hence is most vulnerable (Tab.1).

Table 1. FOS results for scenarios considered using SLBL surfaces along cross-section AA'

	S1	S2	S3	% Decrease S1 & S2	% Decrease S1 & S3
SLBL1	0.91	0.90	0.89	**1.11**	**2.22**
SLBL2	0.80	0.79	0.78	**1.25**	**2.50**
SLBL3	0.67	0.64	0.63	**4.47**	**6.00**

Conclusion

The entire town of Joshimath is located on old landslide scars, that could be mapped using high resolution DEM and optical images. The InSAR analysis revealed that many of these overlapping scars were already active in the year 2020. Further the 2021 debris flow event followed by successive rainfall events, increased the movement along these active landslides and also reactivated other overlapping landslides. The crack locations on field, correspond well with the mapped and identified active landslides. Additionally, as per GSI, 2023 report many new cracks are curvilinear and follow contours thus indicating confined detachment planes or in other words landslide failure surfaces. The depth of the sliding surface for these active landslides was obtained around 250m, hence they were characterized as deep-seated landslides. Moreover, the thickness of loose formation in some areas in Joshimath town was determined between 40m to more than 100m (GSI, 2023). This is in line with the presence of DSL's. The InSAR based displacements along the SLBL surfaces for the landslide scars exhibited characteristic increase and decrease pattern, along the boundary of SLBL's. This is in order with the morphology of the three landslide scars mapped and discussed here. The model proposed by Lettelier et al., 2023 provides a quick and simple tool for efficiently analyzing displacements. Also, the modeled displacement gives a good correlation w.r.t the real projected displacement.

The impact of toe-cutting was quite evident on the FOS, as it reduced the FOS to as high as 7%, mainly along the SLBL3 (scar 3). Thus, further toe cutting and sliding at the rim region of these DSL's may cause increased displacement along the slip surfaces of the DSL's.

Reference

Bahuguna H, Kaistha MK, Singh B, Das S, Ahmad T & Rana H (2023) Preliminary Report on the Recent Event of Ground Subsidence at Joshimath, District Chamoli, Uttarakhand. *Technical Report GSI*. Government of India, Geological Survey of India.

Jaboyedoff M, Carrea D, Derron MH, Oppikofer T, Penna IM & Rudaz B (2020) A review of methods used to estimate initial landslide failure surface depths and volumes. Engineering Geology 267, 105478

Lettelier L (2023), SLBL-FSA. github.com, GitHub - LeoLetellier/SLBL-FSA: Failure Surface Analysis on landslides in cross-sections. Computes SLBL surfaces and simple displacement model. Compares with external displacement data in the LOS.

Sundriyal Y, (2023) Brief communication on the NW Himalayan towns; slipping towards potential disaster. *Nat. Hazards Earth Syst. Sci.*, 23, 1425–1431.

Valdiya KS, (2014) Damming rivers in the tectonically resurgent Uttarakhand Himalaya. *Current Science* 106, 1658-1668.

VIGIMONT project: towards landslide Early warning System

S. Bernardie[1], F. Liebault[2], S. Chave[3], A. Arnaud[4], Y. Thiery[1], N. Marçot[1], T. Lucas[1]

[1] BRGM, City, France
[2] IGE, Grenoble, France
[3] PREDICT, Montpellier, France
[4] LIEU, Aix-en-Provence, France

SUMMARY: The general objective of VIGIMONT is to develop a new service within two existing early warning platforms, by adding modules dedicated to real-time debris-flow and landslide dynamic vigilance for safety authorities in mountain areas. Indeed, with the deployment of meteorological radars, the occurrence of debris flows and landslides induced by meteorological events will be analysed, based on antecedent precipitations quantification and event rainfalls definition. It will permit to determine critical rainfall thresholds for events occurrences, allowing events detection and mapping. A multi-scale approach is proposed by considering both the regional and the local (municipality) scales, with the development of services for end-users acting at these two scales. Phenomena addressed here are focussed on some typologies of movements: it concerns shallow landslides, deep seated landslides and debris flows.

Keywords: Early warning system, Landslide susceptibility, debris flows

Introduction

Considering the current high number of landslides and the increase of events that might happen, there is a need to improve hazard assessment and risk mitigation. In many densely populated mountain regions, governmental agencies or the municipalities try to protect the habitants by different measures. Amongst these measures, territorial Early Warning Systems (**Te-EWS**) constitute one key challenge, as in mountainous areas, the living space is extremely limited. In particular, mountain regions have strongly benefited from recent advances in meteorological data acquisition for observation, process-understanding, and forecasting, with direct implications for prevention of natural hazards induced by heavy rainfall and snow episodes. Several EWSs have been developed at a regional scale (Gariano et al., 2015; Staley et al., 2017). Guzzetti et al., 2020, has analysed different Te-EWSs implemented in the world, through different features: the geographical location, the landslide and rainfall data considered, the threshold models used, the design of EWS considering the specialization, the operational framework, the advisory systems, the implementation, and the performance evaluation. They conclude that "operational forecasting of weather-induced landslide is possible and feasible today and it can contribute to mitigate landslide risk, reducing fatalities and economic losses". They also propose some recommendations for further development or improvement of EWSs, and indicate that still many areas with numerous fatal landslides are not covered by Te-EWSs. Most of the systems use information from rain gauge networks, meteorological models, weather radars, and satellite estimates, and their forecasting models are based on rainfall thresholds, distributed slope stability models, and soil water balance models. Besides, despite a lot of EWS developed around the world, it appears that there is a lack of exchanges on this issue. In France, few Te-EWS have been developed, despite a lot of landslide events leading to traffic interruption, village isolation, and casualties and deaths.

Objectives - The objective of the project is to improve existing EW platforms and services dedicated to hazards in mountain areas, by providing real-time dynamic vigilance maps for stakeholders and safety authorities. Both regional and local (municipality) scales will be addressed. At regional scale, focus will be put on designing innovative approaches for assessing debris-flow and landslide spatialized triggering thresholds, including propagation, in order to complement existing platforms dedicated to meteorological and flood events (RhyTMME, Wikipredict). At local scale, implementation of EWSs tailored to the needs and preparedness of local authorities and populations will be considered. The specific objectives addressed by the project are: 1) to analyze social acceptability of EWS 2) to define improved debris-flow and landslide rainfall thresholds; 3) to improve the spatiotemporal variability characterization of debris-flow and landslide triggering conditions; 4) concerning active deep seated landslide, it is planned to test the automatic production of ground motion Time Series using INSAR; 5) to integrate runout scenarios into EWS by coupling triggering thresholds with shallow landslide and debris-flow susceptibility and physical propagation models; 6) to develop an operational forecasting system for deep seated landslides based on INSAR measurements and on precipitation predictions; 7) to integrate real-time landslide and debris-flow warning maps in available EWS with the definition of warning levels and analysis of associated uncertainties.

Preliminary actions

A main drawback of landslide rainfall-based Te-EWS is their poor spatial prediction capacity: a threshold overcoming produces an alert for the entire area encompassing the events used for calibration, while the location of expected landslides is poorly constrained.
This is the main reason explaining why EWS only based on rainfall information generate many false alarms. To improve the spatial prediction of EWS, some authors proposed to combine rainfall fields to susceptibility maps. However, several issues have to be considered in defining the susceptibility maps. In particular there is a strong need for identification of the best geomorphic predictors and for their high-resolution mapping.

It is proposed here to indicate some preliminary results concerning landslide susceptibility map that has been computed in the south of France. For that, different steps are conducted:

Structuring a landslide database - the landslide inventory has been built based on several sources:
- National French database: it contains all the information available in France in the form of a shapefile point in a GIS. It includes the location of events, dates of occurrence, details (date, year, etc.) and other information such as surface area, volume, depth of rupture, etc. It has then been completed and improved by the work carried out as part of the AD-VITAM project specifically in Alpes-Maritimes department.
- an inventory carried out focusing on landslides triggered by the post-Alex storm. This inventory is based on the Ortho-Express-Tempête Alex (IGN, October 2020), focused on the Tinée, Roya and Vésubie valleys.
- a complementary inventory based on orthophotos from 2009, 2014 and 2020 with reference to intense rainfall events in 2009, 2014 and 2020. A procedure has therefore developped to identify landslide tracks on orthophotos so that they can be digitized.
Four types of landslide are defined within the area: shallow mudflow; medium mudflow; shallow earthslide; medium earthslide. This classification is inspired by international standards, based on material type, landslide depth and surface area (Hungr et al., 2014).

Strategy of landslide susceptibility mapping - The philosophy was guided by the need for project practitioners to easily understand the key factors. Therefore, the methodology for creating landslide susceptibility maps (LSM) was based on a straightforward and easy-to-implement approach. The quantitative method called weight of evidence (WoE) was selected (Bonham-Carter, 1996). The methodology is based on Baye's theorem (Bonham-Carter, 1996) and allows for a quick analysis of the influence of each variable class and obtaining failure probabilities based on the density of phenomena per class. Moreover, different updates can be easily carried out when new inventories or information become available at different time steps. Finally, the strategy employed to compute LSL was derived from Thiery et al. (2007) and involving a step-by-step selection of spatial variables best suited to compute the LSMs.

Results

After several simulations considering for each one a new added PV, it is found that the following 6 PV: slope classes, landforms, lithology, curvature, landuse and aspect, were sufficient to obtain results with satisfactory statistical tests.

The various PVs were all reclassified based on expert approach, with a separation between each class based on knowledge of the field, the inventory and their sensitivity:
- The lithology shows 36 classes, resulting from the assemblages of the BRGM lithological caissons;
- The slopes are classified by 5° intervals and thus comprise 10 different classes from 0-5° to 45° and more;
- The type of slope (General Curvature) is divided into three types: convex, straight and concave;
- Landforms are used to assess the type of slope and terrain. The algorithm calculates the altitude of a pixel, and compares it with that of surrounding pixels, in order to assign it a category. There are 10 different classes for the basic landform (Weiss, 2001) and 9 classes for the Iwahashi and Pike landform (Iwahashi and Pike, 2007);
- The exposure of the slopes was classified into 3 classes following the sensitivity analysis, with the first class running from north to east, the second from south-east to south-west and the third from west to north-west;
- Land cover (Corine Land Cover) has several levels of classification. Levels 1 and 2 were retained in order to carry out various sensitivity tests.

However, even if the statistical tests yield satisfactory results, certain limitations have been identified. For instance, areas known for producing numerous landslides were not identified in the moderate high, or very high susceptibility classes. This could pose challenges when studying temporality and triggering factors. Thus, two key issues need attention for the remainder of the project: (1) the landslide inventory, despite combining field analysis and aerial photograph analysis, was not subdivided into initiation (failure) and propagation areas; only centroids were used for landslide susceptibility calculations. This likely underestimates failure probabilities and, consequently, the derived susceptibility classes (Thiery et al., 2007). (2) The lithological map was a compilation of several 1:50,000 scale maps that varied in terms of spatial accuracy and nomenclature. Certain classes, particularly surficial formations, were significantly underestimated spatially, while field observations indicated that many landslides originate in these formations

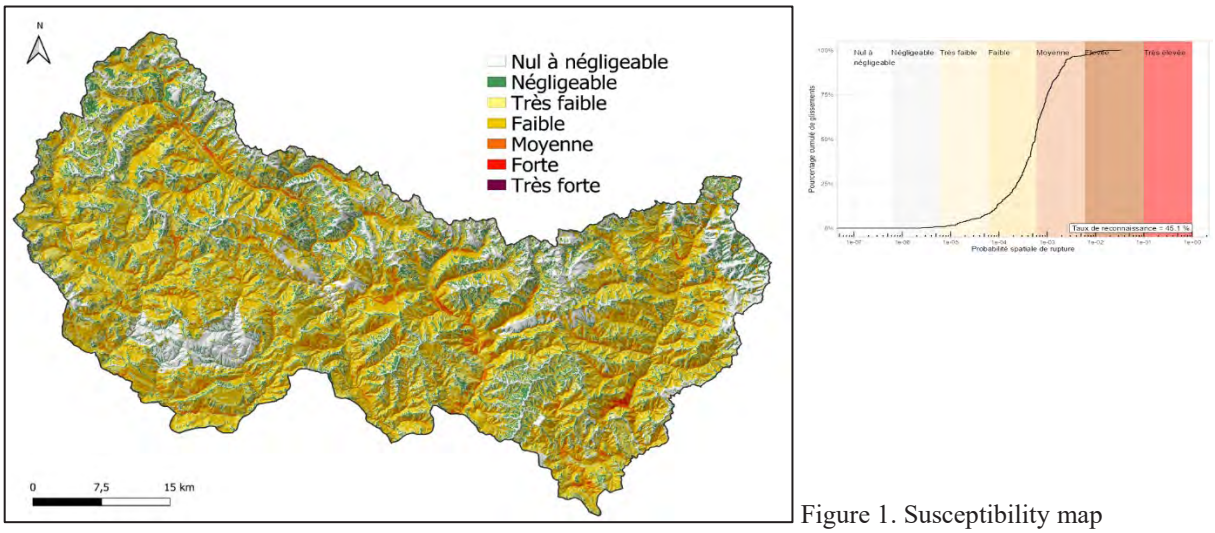

Figure 1. Susceptibility map

Acknowledgment

This work is financed by the ANR VIGIMONT project (VIGIlance MONTagne – Mountain Vigilance : Forecasting the risk of landslides and debris flows in mountainous areas. **ANR-22-CE04-0021**. **https://vigimont.fr/**

References

Bonham-Carter, G. F. (1994). Geographic Information System for Geoscientists: Modeling with GIS. Pergamon Press. Computer Methods in the Geosciences, Vol. 13, pp. 398.

Gariano, S.L. et al., 2015. Calibration and validation of rainfall thresholds for shallow landslide forecasting in Sicily, southern Italy. Geomorphology 228, 653–665. https://doi.org/10.1016/j.geomorph.2014.10.019

Guzzetti F. et al., Geographical landslide early warning systems, Earth-Science Reviews 200 (2020)

Hungr O., Leroueil S., & Picarelli L., (2013). The Varnes Classification of Landslide Types, an update. Landslides, 11(2), 167-194. https://doi.org/10.1007/s10346-013-0436-y

Interreg Alcotra. (2020). Analyse de la vulnérabilité des territoires alpins méditerranéens aux risques naturels (mouvements de terrain) (Progetto Interreg Alcotra n°1573 "AD-VITAM"). http://54.36.75.4/index.php/fr/

Iwahashi, J., & Pike, R. J. (2007). Automated classifications of topography from DEMs by an unsupervised nested-means algorithm and a three-part geometric signature. Geomorphology, 86(3-4), 409-440. https://doi.org/10.1016/j.geomorph.2006.09.012

Staley, D.M., et al., 2017. Prediction of spatially explicit rainfall intensity–duration thresholds for post-fire debris-flow generation in the western United States. Geomorphology 278, 149–162.

Thiery, Y., Malet, J., Sterlacchini, S., A, P., & Maquaire, O. (2007). Landslide Susceptibility Assessment by bivariate methods at large scales : application to a complex mountainous environment. Geomorphology, 92(1-2), 38-59. https://doi.org/10.1016/j.geomorph.2007.02.020

A French-language treatise on landslide to be published

Jaboyedoff M.[1], Locat J.[2], Merrien-Soukatchoff V.[3,1] and Michoud C.[4]

[1] Risk-group, Institute of Earth Sciences, University of Lausanne, Lausanne, Switzerland
[2] Laboratoire d'études sur les risques naturels (LERN), Université Laval, Québec, Canada
[3] GeF, EPN01, Cnam, 2, rue Conté, 75141 Paris cedex 03, France
[4] Terranum, Busigny, Switzerland

SUMMARY: In this article, a draft version of a treatise on landslides is presented, it will be published in French in the coming months. It is aimed at students and practitioners. It covers the theoretical bases needed to understand slope mass movements, then the different types of movement from initiation to propagation. Risk management and monitoring methods are also presented. Several specific contexts, such as the volcanic environment, earthquake-induced movements, etc., are presented in separate chapters. It is intended as a tool for quickly understanding and exploring a subject in greater depth.

Keywords: landslides, book, education, theory, practice.

Introduction

As in many languages, in the French-speaking world, there is a lack of recent treatises on landslides and gravitational slope movements. The primary aim of this treatise on slope mass-movements is to fill a gap in recent French-language scientific literature. Similarly in the English-speaking world, since the collective works SPECIAL REPORT 176 and 241 (Schuster and Krizek, 1978; Turner and Schuster, 1996), there has been no equivalent on this scale bringing together descriptions of the phenomena and practical aspects, except for rockfalls by the same publishers (Turner and Schuster, 2012). However, Clague and Stead (2012) published a book devoted more to a review of knowledge of the phenomena and Davies (2014) published a book in the same vein. The USGS has produced an introductory booklet on landslides (Highland and Bobrowsky, 2008), covering a broad spectrum. Only the work by Hoek and Bray (1973) dedicated to the stability of rock slopes has seen relatively frequent updates in 1977, 1981, 2004 (Wyllie and Mah, 2004) and 2018 (Wyllie, 2018).

Relatively few works have been published in French, including Antoine et al (2000). Flageollet (1989) was more widely available, which is like that of Záruba and Mencl (1969).

So, there is a lack of French-language works containing modern methods (especially remote sensing) and the associated vocabulary. One of the problems is that students and practitioners are often given English-language references. As a result, if young specialists in landslides are unfamiliar with French-language vocabulary, communication with local populations and authorities can become more complicated. Filling this gap was therefore the primary motivation.

The second aspect is to deal with the different types of landslides (Hungr et al., 2014), but also to address the particularities of landslides in various contexts such as coastal domains, cold environments, volcanic environments, as well as underwater areas, etc.

The third aspect, which is probably more prevalent in Europe, is the fact that students seem to be less and less well trained in mathematics and physics. In addition, the mobility from one program of study to another has increased, so that the tendency to mix courses of study does not help to maintain standards. Therefore, the basics relating to soil and rock mechanics, rheology or hydrogeology should also be briefly recalled in this book. This should enable novice readers to return to the basics, but also allow the more experienced to quickly access basics that may have been forgotten over time. We present the table of contents and the list of main authors (Table 1).

Table 1. Translated table of contents and lead authors (see table of content in French in annex).

N°	Chapter title	Main author	N°	Chapter title	Main author
0	Preamble		**Part 5: Post-rupture, Propagation and Deposition**		
Part 1: Introduction			**18**	Spread	J Locat
1	Description of landslides and other gravity movements	M Jaboyedoff	**19**	Earthflow	JP Malet
2	Socio-economic consequences and human causes	M Jaboyedoff	**20**	Debris flows and hyper-concentrated debris flows	A Remaître
Part 2: Theoretical foundations			**21**	Rockfalls	M Jaboyedoff
3	Basics of geology applied to slope movements	M Jaboyedoff	**22**	Massive landslides and rock avalanches	M Jaboyedoff
4	Fundamentals of rock mechanics	V Merrien-Soukatchoff	**Part 6: Hazard and risk management**		
5	Fundamentals of soil mechanics	A Ferrari	**23**	Risk management and risk communication principles	A Pedrazzini
6	Basics of rheology	G Chambon	**24**	Risk calculation	M Jaboyedoff
7	Water in soil and rock	M Jaboyedoff	**25**	Surveillance and prevention measures and work	C Cloutier
Part 3: Investigation and monitoring methods and tools			**Part 7: Environments and Special Effects**		
8	Field Survey	A Blais Stevens	**26**	Landslides in coastal environments	S Costa
9	Dating methods	M Jaboyedoff	**27**	Landslides in circumpolar environments	S Costa
10	GIS tools	D Turmel	**28**	Landslides in alpine environments	L Ravanel
11	Remote sensing applied to slope movements	MH Derron	**29**	Landslides in subtropical and equatorial environments	O Dewitte
12	Basics of geophysics	D Jongmans	**30**	Landslides in volcanic environments	I Manzella
13	Main geotechnical investigation methods	O Maquaire	**31**	Earthquake-induced gravity movements	M Gasc
14	Analogue and digital modelling of disruptions and post-breaks	MA Brideau	**32**	Mass movements in marine and lake environments	J Locat
Part 4: From movement initiation to rupture			**33**	Tsunamis induced by gravity movements	M Jaboyedoff
15	Progressive failure	J Locat	**34**	Summary and future prospects	
16	Soil instability	M Jaboyedoff			
17	Rock slope instability	M Jaboyedoff			

The back cover

We reproduce here below the back cover, which gives an initial idea of the principles that governed the writing of this treaty.

Landslides represent a major risk to infrastructure and human life, which needs to be managed. This underestimated hazard regularly causes many casualties in earthquakes, bad weather, thunderstorm, flash floods and cyclones. The variety of physical phenomena involved, from small landslides to gigantic rock avalanches, means that the field of study is vast. As a result, researchers, engineers, and authorities need to know how to use a wide range of theoretical concepts and technological tools to study, characterise and manage these slope instabilities.

In this context, this treatise on slope movements aims to answer the following questions: what are we studying, and why? What are the physical foundations and tools available? What are the new observation techniques and what have they contributed to our understanding of slope destabilisation processes? In detail, how do we characterise slope instability? And finally, how can we protect ourselves if the risk exists?

Organised into 34 clear chapters, written by French-speaking experts recognised in their scientific fields, the hierarchy and classification of the information and the wealth of illustrations make this treatise a French-language reference work that supports teaching and professional practice on landslides.

Table of contents and authors

The book divides the chapters into 7 parts (Table 1). The first part is devoted to the classification of ground movements and their socio-economic consequences (see Jaboyedoff et al., 2022). The second part provides the theoretical underpinnings needed to understand landslides, such as the basics of mechanics, hydrogeology, geology, etc., for the reasons given above.
The third part is devoted to monitoring investigation methods such as geophysics, remote sensing, etc., as well as an introduction to modelling. The fourth part is devoted to the initiation of slope failures, providing the basis for stability analysis. The fifth part is naturally dedicated to the post-rupture of the various types of movement. The sixth deals with risk management, and finally the seventh introduces the features of landslides occurring in specific environments.

All the authors are recognized in their field. Table 1 shows the titles and main authors of the chapters. These authors have often called on the services of colleagues; they are not cited here.

Conclusion

The purpose of this article is, firstly, to announce the arrival of such a book, and, secondly, to invite comments, as we are in the process of finalizing it, so that we can consider any comments from future readers. Last but not least it is a way to illustrate this original approach to other parts of the world.

A few short extracts are presented in this ISL 2024 which illustrate the philosophy of the book. As well as being a treatise, this book attempts to summarize recent advances. Nevertheless, the 800-odd pages will not be enough to cover every subject in details. The purpose of this book is to be of use to the slope mass movement community and to students intending to work in this field of research or practice. It seems that this is one of the first times, if not the first time, that the problems of landslides will be covered fairly comprehensively, from the physical basics to the human-related risk management.

References

Antoine P, Cojean R, Durville JL et al. (2000) Caractérisation et cartographie de l'aléa dû aux mouvements de terrain. Guide technique. *Laboratoire Central des Ponts et Chaussées*, Collection environnement, risques naturels,

Clague J.J., Stead D. (Eds.) (2012) Landslides Types, Mechanisms and Modeling*, Cambridge University Press*, 436 p.

Davies, T.R.H. (2014) Landslide hazards, risks, and disasters. Elsevier/Academic Press, Amsterdam; Boston.

Fell, R. & Hartford, D. 1997. Landslide risk management. *Landslide Risk Aassessment*, Cruden and Fell (eds), Balkema, Rotterdam, 51-110.

Flageollet, J. (1989) Les mouvements de terrain et leur prévention, Paris: Masson.
Highland, L.M., and Bobrowsky, P. (2008) The landslide handbook-A guide to understanding landslides: Reston, Virginia, *U.S. Geological Survey Circular 1325*, 129 p.
Hoek, E. and Bray, J. (1973) Rock Slope Engineering, Inst. Mining and Metall, London.
Hungr, O., Leroueil, S. & Picarelli, L. (2014) The Varnes classification of landslide types, an update. *Landslides*, 11, 167-194, doi: 10.1007/s10346-013-0436-y.
Jaboyedoff M., Locat J. and Michoud C., (2022) Beyond the classical socioeconomic impact of landslides. *Geohazard 8*, Quebec.
Schuster, R.L. and Krizek, R.J. (Eds.) (1978) Landslides, Analysis and Control, *Transportation Research Board, Special Report No. 176*, National Academy of Sciences.
Turner AK, Schuster LR (Eds.) (1996) Landslides, investigation and mitigation. *Transportation Research Board Special Report 247*. National Research Council, National Academy Press, Washington, DC, 673 p.
Turner, A.K. & Schuster, R.L. (2012) Rockfall: characterization and control. *Transport Research Board of the National academies*, Washington, D.C.
Wyllie, C. and Mah, W. (2004) Rock Slope Engineering Civil and Mining, *Taylor & Francis Group, London and New York*, 431 p.
Wyllie D. C., (2018) Rock Slope Engineering Civil Applications, 5th Edition, CRC Press, 620 p.
Záruba, Q. & Mencl, V. (1969) Landslides and their control. *Elsevier, Amsterdam*. 205 p.

Annex

N°	Titre du chapitre	Auteur principal
0	Préambule	
Part 1: Introduction		
1	Description des processus de glissements et autres mouvements de gravitaires	C Michoud
2	Conséquences socio-économiques	M Jaboyedoff
Part 2: Fondements théoriques		
	Géologie appliquée aux mouvements de versant	M Jaboyedoff
4	Bases de mécanique des roches	V Merrien-Soukatchoff
5	Bases de mécanique des sols	A Ferrari
6	Bases de rhéologie	G Chambon
7	L'eau dans les sols et les roches	M Jaboyedoff
Part 3: Méthodes et outils d'investigations et de surveillance		
8	Relevés de terrain	A Blais Stevens
9	Méthodes de datation	M Jaboyedoff
10	Outils SIG	D Turmel
11	Bases de télédétections	MH Derron
12	Bases de géophysique	D Jongmans
13	Principales méthodes d'investigations géotechniques	O Maquaire
14	Modélisations analogiques et numériques de rupture et post-rupture	MA Brideau
Part 4: De l'initiation des mouvements a la rupture		
15	Développement de la rupture	J Locat
16	Instabilités dans les sols	M Jaboyedoff
17	Instabilités en milieu rocheux	M Jaboyedoff

N°	Titre du chapitre	Auteur principal
Part 5: Post-rupture, propagation et dépôt		
		18
19	Coulées	JP Malet
20	Laves torrentielles et charriages hyper-concentrés	A Remaître
21	Chutes de pierre	M Jaboyedoff
22	Éboulements massifs et avalanches rocheuses	M Jaboyedoff
Part 6: Gestion de l'aléa et du risque		
23	Principes de gestion et de communication des risques	A Pedrazzini
24	Calculs de risques	M Jaboyedoff
25	Mesures et travaux de surveillance et prévention	C Cloutier
Part 7: Environnements et effets particuliers		
26	Mouvements de terrain en environnement côtier	S Costa
27	Mouvements de terrain dans les environnements circumpolaires	S Costa
28	Mouvements de terrain en milieu alpin	L Ravanel
29	Mouvements de terrain en milieux subtropicaux et équatoriaux	O Dewitte
30	Mouvements de terrain en milieux volcaniques	I Manzella
31	Mouvements gravitaires induits par des séismes	M Gasc
32	Mouvements de terrain en environnements subaquatiques marines et lacustres	J Locat
33	Tsunamis induits par des mouvements gravitaires	M Jaboyedoff
34	Synthèse et perspectives	

Data-driven scientific discovery framework inrheological constitutive model

Xu Han[1], Fiona C.Y.Kwok[1], Lu Jing[2], Gengchao Yang[3], Yuri Dumaresq Sobral[4]

[1] Department of Civil Engineering, The University of Hong Kong, Haking Wong Building, Pokfulam Road, Hong Kong, PR China

[2] Tsinghua Shenzhen International Graduate School, University Town of Shenzhen, Nanshan District, Shenzhen 518055, PR China

[3] School of Aeronautics and Astronautics, Sun Yat-sen University, Guangzhou 510275, PR China

[4] Departamento de Matemática, Universidade de Brasília, Campus Universitário Darcy Ribeiro, 70910-900 Brasília DF, Brazil

SUMMARY: Modelling of large-deformation geological hazards, such as landslides and debris flows, is of crucial significance to pre-disaster risk assessment and prevention efforts. However, the rheological constitutive model, as an essential part of the numerical simulation, still faces numerous challenges. Among them, the biggest one lies in searching suitable dimensionless numbers and establishing scaling laws. According to Buckingham π theory, we recognize that there may be a very large parameter space for dimensionless numbers. Traditional dimensional analysis relies on the subjective understanding of scientists, which presents a considerable probability of missing some important forms of non-dimensional numbers, especially in incomplete physical systems. This work innovatively constructed a data-driven framework to assist us to accelerate the discovery of new dimensionless numbers and scaling laws in rheological models. High-fidelity data of granular flow were generated by discrete element methods (DEM). Based on the extensive dataset, the proposed framework was verified by rediscovering well-known complete theories under certain physical conditions, demonstrating its potential to uncover new knowledge in the controversial realm. To some extent, this paper may provide novel insights into research for the rheology of granular materials.

Keywords: data-drive framework, artificial intelligence, rheological constitutive model, dimensionless learning

Introduction

Analysis of large-deformation geological hazards have always been a hot issue(Gariano & Guzzetti 2016, Legros 2002). When long-runout landslides and debris flows occur, the rheological properties of granular media directly determine the spatial scale of catastrophic hazards. Therefore, many researchers have been studying rheological constitutive laws in order to understand these natural disasters more clearly and to help with pre-disaster risk assessment and prevention. As early as about 25 years ago, Iverson (1997) successfully used three simple rheological models to elucidate various unique phenomena of debris flows, however, he also pointed out that factors (such as entrainment, pore-fluid pressures, segregation, etc.) are difficult to take into account in mathematical models. In fact, newly developed constitutive models solve these problems to a certain extent (Jing et al. 2017, Luna et al. 2012, Pudasaini & Krautblatter 2021, McArdell et al. 2007). Nevertheless, because granular flow always involves multi-scale, multi-phases and multi-physics coupling issues, its rheological research still faces many challenges.

To address these challenges, researchers have introduced dimensional analysis, using the equations of dimensionless numbers to represent physical laws in a more concise and compact form. This approach reduces the number of parameters while improving the generalizability and interpretability of physics (Butterfield 1999). For example, Jop et al. (2006) proposed the well-known μ(I)-rheology constitutive model to describe dense granular flow, and the law is dominated by the inertial number (a single dimensionless parameter) in an elegant way (Forterre & Pouliquen 2008). This is a typical successful application of dimensional analysis. However, we recognize that there may be a very large parameter space for dimensionless numbers according to Buckingham π theory (Buckingham 1914). Traditional dimensional analysis relies on the subjective understanding of scientists, which presents a considerable probability of missing some important forms of non-dimensional numbers, especially in incomplete physical systems. Moreover, the construction of scaling laws still encounters many difficulties due to the subjective guesswork of functional forms.

Nowadays, we are witnessing the ubiquity of big data, and artificial intelligence (AI) has already penetrated into various domains in our daily lives. In the field of geological disasters, using AI techniques for prevention and mitigation has become a developing trend (Dikshit et al. 2021, Ma & Mei 2021). However, most of AI technologies are predominantly applied as black-box models. In reality, we expect these models can provide us with some novel insights into physical knowledge. Fortunately, intelligent systems have been supported to have enormous potential in assisting scientific discovery (Blanco-González et al. 2023, Clark & Khosrowi 2022, Gomes 2023, Yao et al. 2022). Wang et al. (2023) have comprehensively reviewed and indicated that artificial intelligence can be utilized in observations, hypotheses and experiments (typical scientific discovery process) to augment and accelerate scientific discovery. It should be noted that our work starts from another perspective which attempts to use AI to empower dimensional analysis. Thanks to the robust computing power of computers, AI methods are naturally able to solve the two problems faced by traditional dimensional learning. On the one hand, machine learning combined with Buckingham π theory allows us to complete the search work in a large parameter space (Bakarji et al. 2022, Xie et al. 2022). On the other hand, explainable machine learning methods also give us opportunity to find the most appropriate form of function or governing equation based on data (Roscher et al. 2020). Thus, we are inspired to propose a data-driven version of dimensional analysis in this paper. The research structures of this article are shown in Fig.1.

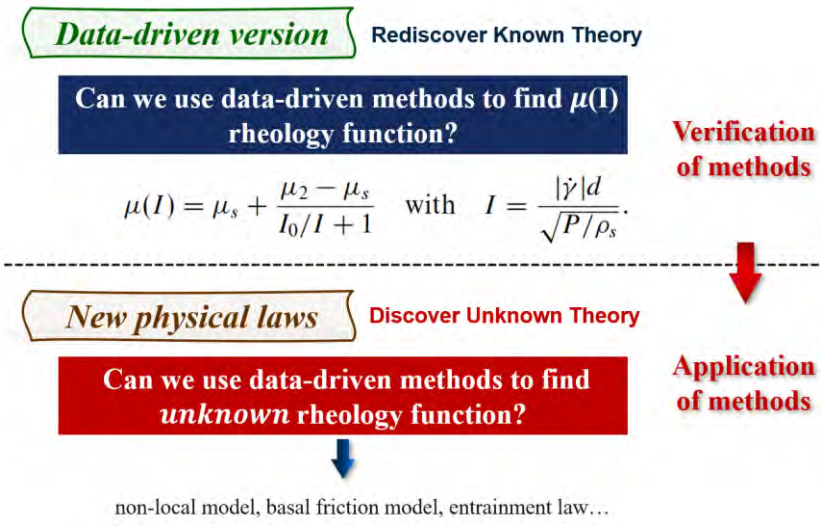

Figure 1. Research structures of this article

Conclusion

In conclusion, data always represents the rawest form of information without any modifications or alterations. In this study, we start from the data level to enhance the existing framework of dimensional analysis and utilize machine learning to supplement any potential points that humans may have overlooked. The main conclusions are as follows:

(1) High-fidelity data of granular flow, which serves as the engines for machine learning, were generated by discrete element methods (DEM).
(2) An innovative data-driven framework was constructed to accelerate the discovery of new dimensionless numbers and scaling laws in rheological models.
(3) Based on the extensive DEM dataset, the proposed framework was verified by rediscovering well-known complete theories under certain physical conditions, demonstrating its potential to uncover new knowledge in the controversial realm.

To some extent, this paper may provide novel insights into research for the rheology of granular materials.

References

Gariano, S. L. and Guzzetti, F. (2016) Landslides in a changing climate. *Earth-Science Reviews,* 162, 227-252.

Legros, F. (2002) The mobility of long-runout landslides. *Engineering Geology,* 63(3-4), 301-331.

Iverson, R. M. (1997) The physics of debris flows. *Reviews of Geophysics,* 35(3), 245-296.

Jing, L., Kwok, C. Y. and Leung, Y. F. (2017) Micromechanical Origin of Particle Size Segregation. *Physical Review Letters,* 118(11).

Luna, B. Q., Remaître, A., van Asch, T. W. J., Malet, J. P. and van Westen, C. J. (2012) Analysis of debris flow behavior with a one dimensional run-out model incorporating entrainment. *Engineering Geology,* 128, 63-75.

Pudasaini, S. P. and Krautblatter, M. (2021) The mechanics of landslide mobility with erosion. *Nature Communications,* 12(1).

McArdell, B. W., Bartelt, P. and Kowalski, J. (2007) Field observations of basal forces and fluid pore pressure in a debris flow. *Geophysical Research Letters,* 34(7).

Butterfield, R. (1999) Dimensional analysis for geotechnical engineers. *Geotechnique,* 49(3), 357-366.

Jop, P., Forterre, Y. and Pouliquen, O. (2006) A constitutive law for dense granular flows. *Nature,* 441(7094), 727-730.

Forterre, Y. and Pouliquen, O. (2008) Flows of dense granular media. *Annual Review of Fluid Mechanics,* 40, 1-24.

Buckingham, E. (1914) On Physically Similar Systems; Illustrations of the Use of Dimensional Equations. *Physical Review,* 4(4), 345-376.

Dikshit, A., Pradhan, B. and Alamri, A. M. (2021) Pathways and challenges of the application of artificial intelligence to geohazards modelling. *Gondwana Research,* 100, 290-301.

Ma, Z. J. and Mei, G. (2021) Deep learning for geological hazards analysis: Data, models, applications, and opportunities. *Earth-Science Reviews,* 223.

Blanco-González, A., Cabezón, A., Seco-González, A., Conde-Torres, D., Antelo-Riveiro, P., Piñeiro, A. and Garcia-Fandino, R. (2023) The Role of AI in Drug Discovery: Challenges, Opportunities, and Strategies. *Pharmaceuticals,* 16(6).

Clark, E. and Khosrowi, D. (2022) Decentring the discoverer: how AI helps us rethink scientific discovery. *Synthese,* 200(6).

Gomes, C. P. (2023) *AI for Scientific Discovery and a Sustainable Future,* translated by Lisbon, PORTUGAL: 2-2.

Yao, T. C., Wang, J., Wan, M., Xin, Z. K., Wang, Y. A., Cao, R. Q., Li, S. G. and Chi, X. B. (2022) VenusAI: An artificial intelligence platform for scientific discovery on supercomputers. *Journal of Systems Architecture,* 128.

Wang, H. C., Fu, T. F., Du, Y. Q., Gao, W. H., Huang, K. X., Liu, Z. M., Chandak, P., Liu, S. C., Van Katwyk, P., Deac, A., Anandkumar, A., Bergen, K., Gomes, C. P., Ho, S., Kohli, P., Lasenby, J., Leskovec, J., Liu, T. Y., Manrai, A., Marks, D., Ramsundar, B., Song, L., Sun, J. M., Tang, J., Velickovic, P., Welling, M., Zhang, L. F., Coley, C. W., Bengio, Y. and Zitnik, M. (2023) Scientific discovery in the age of artificial intelligence. *Nature,* 620(7972), 47-60.

Bakarji, J., Callaham, J., Brunton, S. L. and Kutz, J. N. (2022) Dimensionally consistent learning with Buckingham Pi. *Nature Computational Science,* 2(12), 834-844.

Xie, X. Y., Samaei, A., Guo, J. C., Liu, W. K. and Gan, Z. T. (2022) Data-driven discovery of dimensionless numbers and governing laws from scarce measurements. *Nature Communications,* 13(1).

Roscher, R., Bohn, B., Duarte, M. F. and Garcke, J. (2020) Explainable Machine Learning for Scientific Insights and Discoveries. *Ieee Access,* 8, 42200-42216.

Remote sensing assessment of road safety risk in mountainous areas on Laonong River Watershed, southern Taiwan

Rou-Fei Chen[1], Tzung-Ting Chen[1], Suet-Yee Au[1], Chris Kwei-Shr Li[2]

[1] National Taipei University of Technology, Materials and Mineral Resources Engineering, Taipei, Taiwan
[2] CECI Engineering Consultants, Inc. Center for Integration and Preparation of Disaster, Taipei, Taiwan

SUMMARY: Slope failures on mountainous roads in Taiwan are often caused by natural hazards, such as typhoons, earthquakes, landslides, debris flows, and inappropriate land use. These hazards can greatly impact the cost of constructing, operating, and maintaining linear infrastructure like highways and railways. In August 2021, Typhoon Lupit triggered a deep-seated landslide upstream of the Yusui Watershed, which brought a huge mass of debris flow that damaged the Mingbaklu Bridge in Southern Taiwan. The Southern Cross-Island Highway, which underwent repairs for over a decade, was again disrupted. This event highlights the importance of conducting rolling surveys and environmental monitoring of hydrogeological changes during road reconstruction projects to minimize road safety risks. In this study, the airborne LiDAR-derived DEM was used to determine the landslide characteristics and quantify changes in mass. InSAR monitoring was also used to identify potential deep-seated landslides. These complementary methods have their respective advantages and disadvantages in the context of the mountainous areas in the Laonong River Watershed.

Keywords: LiDAR-derived DEM, InSAR monitoring, deep-seated landslide, road safety risk, Laonong River Watershed.

Introduction

In Taiwan, the frequent occurrence of slope failure on mountainous roads is often attributed to natural disasters, such as typhoons, earthquakes, landslides, debris flow, and inappropriate land use. With the potential to significantly impact the cost of construction, operation, and maintenance of linear infrastructures (e.g. highway and railway), natural disasters have been continuously striking Taiwan, a young and active orogenic belt with 70% of its area covered by mountains. As 20% of Taiwan's linear infrastructure is over 500 m above sea level, with 11% of that exceeding 1,000 m, the fragility of the land mass, particularly under the attack of landslide, rockfall, debris flow, and flood, underscores the significance of roadside slope stabilization as a critical issue for the country.

Since its opening, the Southern Cross-Island Highway has played an important role in connecting southern and eastern cities in Taiwan. In recent years, it was struck by Typhoon Morakot, which caused a large-scale landslide upstream of the Putanpunas Watershed (on the right bank of the Laonong River), resulting in debris flow into the main channel and forming a nascent alluvial fan that blocked roads. A long-term road reconstruction and improvement project was initiated in 2009. Consequently, the Southern Cross-Island Highway had confidently been diverted to the left bank of the Lanong River, and the section at the confluence of tributary streams was spanned by an elevated bridge type in 2017. In August 2021, Typhoon Lupit triggered a landslide upstream of the Yusui Watershed (on the left bank of the Laonong River), causing an enormous mass of debris flow to cascade downstream and crash into Mingbaklu Bridge (see Fig. 1). Although the Directorate General of Highways cleared the route and built a temporary steel bridge for passage, this incident has highlighted the vulnerability of the road to damage during plum rain or torrential rain.

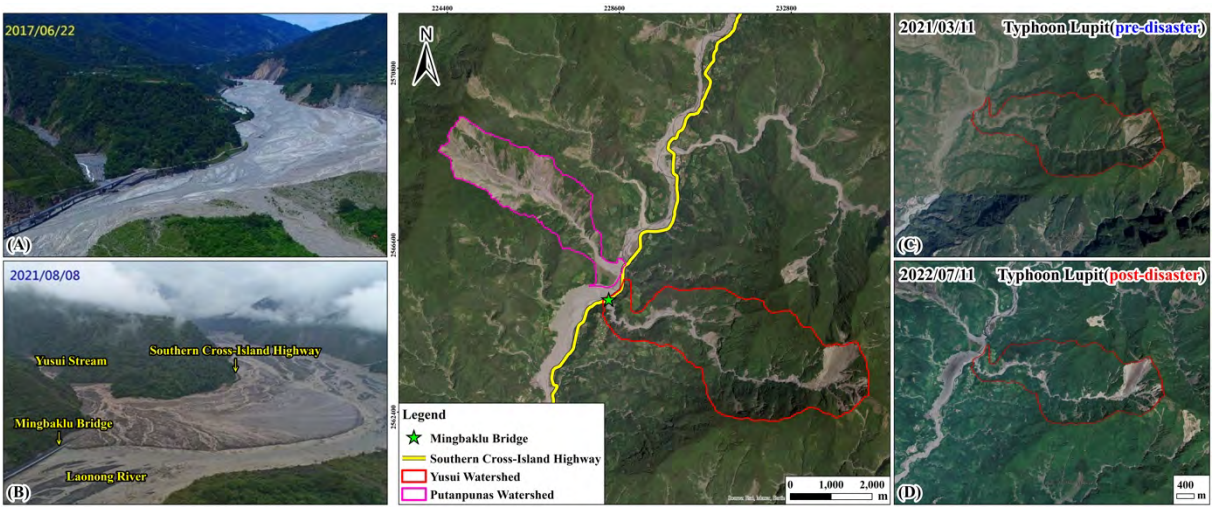

Figure 1. Location map of the study area along the Southern Cross-Island Highway: (A) and (B) Before and after the Mingbaklu Bridge was crushed by debris flow from the upstream Yusui Watershed; (C) and (D) Optical satellite images that show the pre- and post-disaster situation of Typhoon Lupit in 2021.

Multi-scale remote sensing data

This study has adopted the use of multi-scale remote sensing data, including those of LiDAR-derived DEM, radar, and optical satellites, to complement each other and overcome their respective advantages and disadvantages. For example, LiDAR can remove vegetation to obtain the actual ground surface for calculating the mass of landslides before and after Typhoon Lupit in the Yusui Watershed between 2016 and 2022; InSAR analysis can detect potential deep-seated landslides using ALOS-2/PALSAR2 satellite radar images collected between 2015 and 2022; and optical satellite images before and after the landslide event are necessary to measure changes in landslide mass and to better identify potential landslide and accumulation areas. In this study, a comprehensive analysis of the landslide activity characteristics, impact area, and potential disaster conditions of the middle and lower reaches of disaster-prone road sections was conducted (Chen et al., 2005; Lo et al., 2021). In addition, the ground surface activity obtained from InSAR analysis is used to monitor the surface deformation in the region (Zhang et al., 2012; Dong et al., 2019; Xu et al., 2021).

Yusui Watershed

The Yusui Watershed is located on the left bank of the Laonong River, covering an area of 615 ha with dimensions of 5,480 m in length and 1,555 m in width. It has an elevation of 2,134 m and a topographic elevation difference of 1,540 m, with an average slope of 30 degrees facing southeast. Utilizing the 2022 LiDAR data to interpret the geomorphological features within the Yusui Watershed, we generated first-order river catchments using the hydrological analysis module of ArcGIS. The stratum of this catchment is dominated by the Chaochou Formation (upper part) and the Pilushan Formation (lower part), separated by the Weijin River Fault. The topographic significance is notable because of the implicit catchment features and the uniformity of slope direction, as shown in Fig. 2A and B.

A comparison of the LiDAR-derived DEM before and after the 2021 landslide event reveals a collapse area of $3.6 \times 10^5 m^2$ with a mass of $1.2 \times 10^7 m^3$ and a maximum depth of 80 m. Moreover, there is accumulation over an area of $1.6 \times 10^5 m^2$ with a volume of $0.49 \times 10^7 m^3$. The results of 3D terrain interpretation and landslide volume calculation show that the landslide area has been continuously increasing over the past 6 years due to abundant rainfall brought by typhoons and torrential rains, causing a huge mass of debris to fall into the main river channel and pile up at its confluence with the Laonong River Watershed (see Fig. 2C and D).

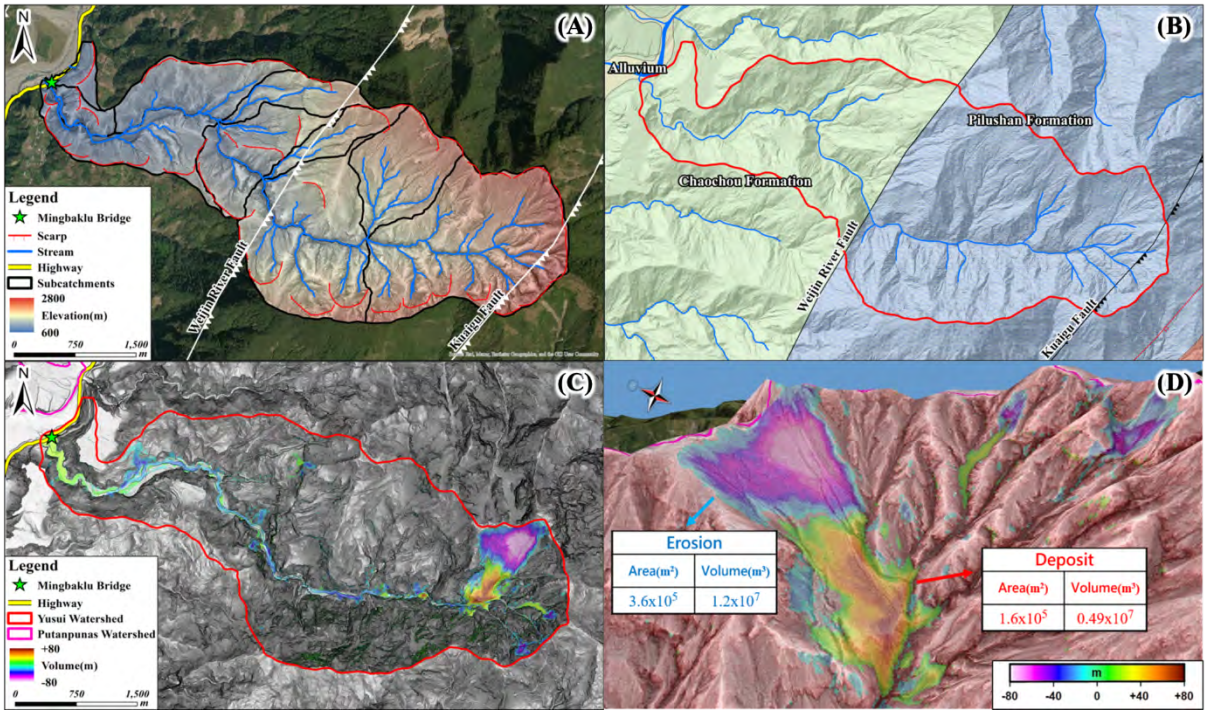

Figure 2. Geomorphological data in the Yusui Watershed: (A) Optical satellite imagery with hydrological features in the Yusui Watershed; (B) Geological map shows two stratigraphic and hydrological units separated by the fault system; (C) Deep-seated landslides are mostly identified based on their morphological signatures using airborne LiDAR; (D) Landslide mass is calculated based on results before and after the 2021 landslide event.

Through the analysis of long-term surface deformation, 66 ALOS-2/PALSAR images were collected and pre-processed for InSAR analysis to investigate the landslide activity in the Yusui Watershed. The results revealed three potential deep-seated landslides with a maximum displacement value of approximately -70 mm/yr. in the upper Yusui Watershed prior to Typhoon Lupit in 2021. Optical satellite imagery and LiDAR volume change confirm landslides at all three locations during the 2021 landslide event. The largest mass of landslides in the upper Yusui Watershed caused significant damage to the Mingbaklu Bridge due to debris flows (see Fig. 3).

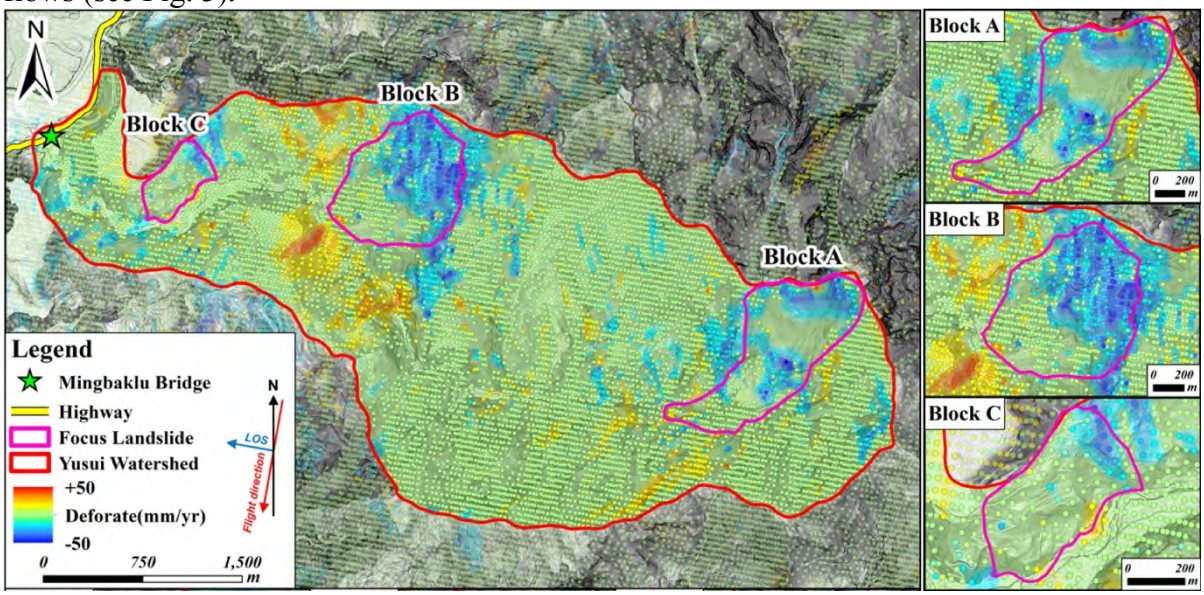

Figure 3. The surface displacement map of Yusui Watershed shows three potential deep-seated landslides according to InSAR results obtained from ALOS-2/PLASAR-2 satellite imagery data between 2015 and 2022.

Conclusion

This study utilizes advanced technology and remote sensing data sources, including airborne LiDAR-derived DEM and InSAR technology, to analyze hydrogeological features and surface deformation along the Southern Cross-Island Highway in Taiwan. By combining various sources, we can predict the mass of collapse and erosion before and after landslides occur. This data is crucial for assessing slope safety and understanding landslide-debris flow correlation at the catchment scale. The study reveals the following findings: (1) The landslide event in the Yusui Watershed that occurred in 2021 resulted in a collapse area of $3.6x10^5m^2$ with a mass of $1.2x10^7m^3$ and a maximum depth of 80 m. (2) The long-term surface displacement data before Typhoon Lupit reveal that the deep-seated landslides were mainly concentrated along the sub-catchment and identified three deep-seated landslides in the Yusui Watershed. (3) The multi-scale remote sensing data have identified five potential deep-seated landslides near the Southern Cross-Island Highway and Mingbaklu Bridge (See Fig. 4). Determining potential landslides that pertain to future studies of mountain roads can facilitate the interpretation and delimitation of landslide areas and to further improve the accuracy and reliability.

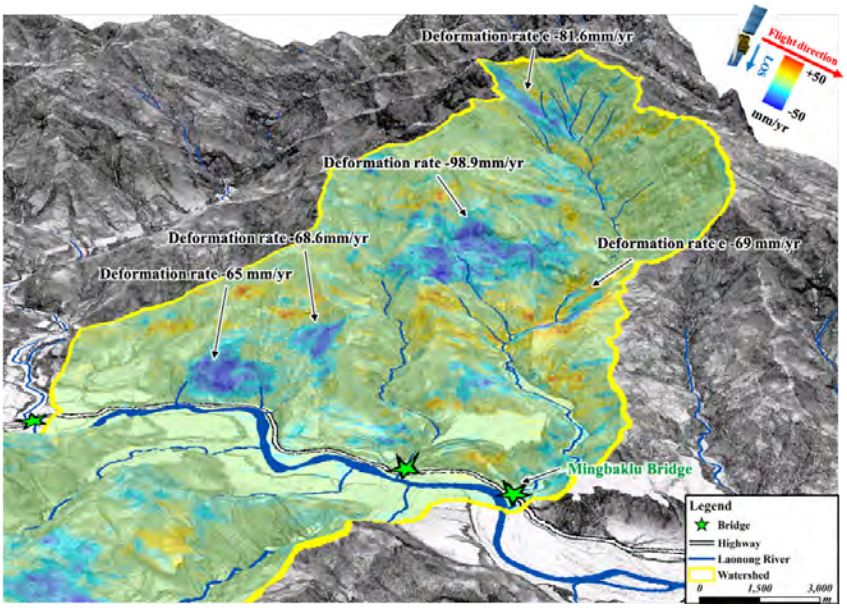

Figure 4. The surface displacement map shows five potential deep-seated landslides that may cause damage to the Southern Cross-Island Highway and Mingbaklu Bridge according to the InSAR results.

References

Chen RF, Lin CW, Chen YH, He TC & Fei LY (2015) Detecting and characterizing active thrust fault and deep-seated landslides in dense forest areas of southern Taiwan using airborne LiDAR DEM. *Remote Sensing* 7(11), 15443-15466.

Dong J, Zhang L, Liao M & Gong J (2019) Improved correction of seasonal tropospheric delay in InSAR observations for landslide deformation monitoring. *Remote Sensing of Environment* 233, 111370.

Lee CF, Huang WK, Chang YL, Chi SY & Liao WC (2018) Regional landslide susceptibility assessment using multi-stage remote sensing data along the coastal range highway in northeastern Taiwan. *Geomorphology* 300, 113-127.

Lo PC, Lo W, Wang TT & Hsieh YC (2021) Application of geological mapping using airborne-based LiDAR DEM to tunnel engineering: example of Dongao Tunnel in northeastern Taiwan. *Applied Sciences* 11(10), 4404.

Xu Q, Guo C, Dong X, Li W, Lu H, Fu H & Liu X (2021) Mapping and characterizing displacements of landslides with InSAR and airborne LiDAR technologies: a case study of danba county, southwest China. *Remote Sensing* 13(21), 4234.

Zhang L, Lu Z, Ding X, Jung HS, Feng G &Lee CW (2012) Mapping ground surface deformation using temporarily coherent point SAR interferometry: Application to Los Angeles Basin. *Remote Sensing of Environment* 117, 429-439.

Semi-automatic discontinuity detection using density in point cloud data

Antonin Chalé, Michel Jaboyedoff, and Marc-Henri Derron

Institute of Earth Sciences, University of Lausanne, Lausanne, Switzerland (antonin.chale@unil.ch)

Keyword: density map, point cloud (PC), structure from motion (SFM), Light Detection and Ranging (LiDAR)

Summary:

Studying geological discontinuities is essential for hazard analysis, especially concerning rock stability. Modern techniques like Structure-from-Motion (SFM) and Light Detection and Ranging (LiDAR) have revolutionized surveys by enabling the remote analysis of entire rock faces using high-density 3D point cloud (PC) data. However, detecting structural irregularities within PC data, particularly in complex geological formations, remains challenging. Traditional methods excel at fitting planar surfaces can't deal with more complex discontinuity shape.

To address these challenges, we developed an innovative discontinuity detection algorithm, emulating human visual perception. By employing multi-angle scanning, point cloud optimization techniques, and efficient multiprocessing, the algorithm creates density maps to identify discontinuities and determine their orientation. It's effective in detecting discontinuities on synthetic models and real LiDAR data, such as the yellow quarry in Ferreyres. While currently optimized for small point clouds, future enhancements could broaden its utility. This approach contributes to geological hazard analysis and enhances our understanding of complex rock formations.

Introduction:

Studying and characterizing discontinuities in geological formations is a fundamental step in hazard analysis, particularly for assessing the stability of rock walls. Parameters such as the frequency and orientation of discontinuity sets are crucial for evaluating the probability of rock volumes involved in potential movement, including sliding or toppling phenomena. The advancement of modern techniques, such as Structure-from-Motion (SFM) and Light Detection and Ranging (LiDAR) acquisition methods, has transformed these surveys, enabling remote analysis of entire rock face. However, detecting structural irregularities using PC data has posed challenges, particularly when dealing with complex geological structures. For instance, while the least square method (Riquelme et al., 2014) excels at fitting planar surfaces and has shown promising results, but doesn't work one curved or more complicated shape of discontinuities.

To address these limitations, we developed an innovative discontinuity detection algorithm. The approach aims to emulate human visual perception by discerning point alignments within the point cloud. To achieve this, we employ a multi-angle scanning technique, utilizing various viewpoints to comprehensively survey the point cloud. This method captures the full spectrum of visible planes representing discontinuities and faults, characterized by a concentration of points from specific viewpoints. The process incorporates sophisticated point cloud optimization techniques, including the implementation of octree data structures and multithreading calculation.

Our algorithm, depicted in Figure 1, encompasses three primary steps. To begin, we initiate the analysis by scanning the point cloud from various viewing angles. This scan serves as the foundation for generating density maps, which are presented in Figures 1.1, 2.2, and 3.2.

From these density maps, we visualize the discontinuities and determine their initial orientation. These discontinuities are also visible one real data as the case study of the yellow quarry in Ferreyres (figure 3) where we can see that the curve shape of some discontinuity are easy to visualize. In the following step, we conducted a secondary scan, this time focused on the density map, allowing the projection of density data into a 2D representation, as shown in Figure 1.2. this 2D projection allow us to constrain the discontinuity set by detecting a second vector orientation. In the case of the cube

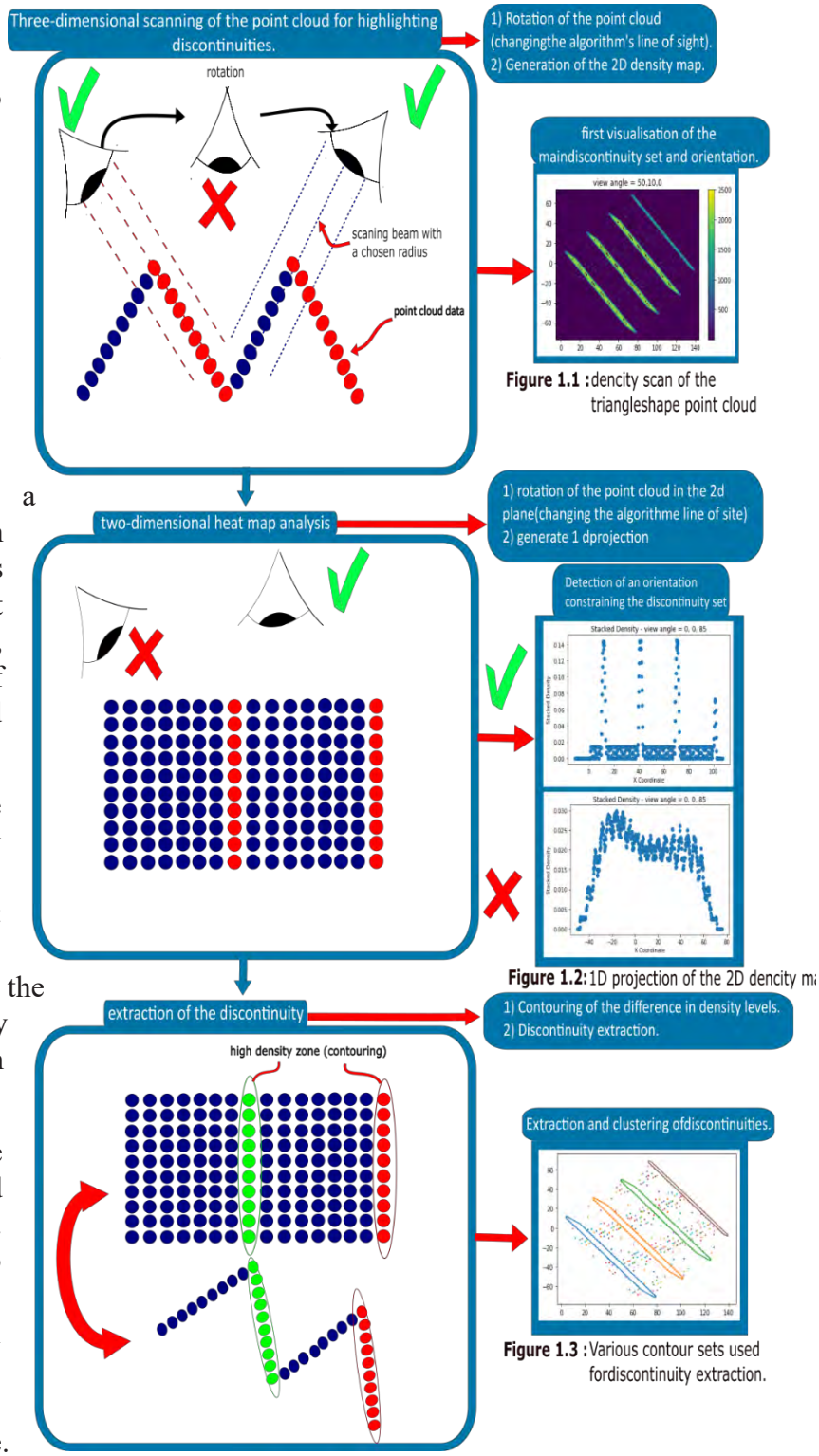

Figure 1: Discontinuity Detection Algorithm Schema: Describing the three main steps of the analysis.

model from the view angle 0.0.0 in the figure 2.1 and 2.2 there is 2 set of discontinuity clearly visible on the figure 2.3. These orientations are pivotal in identifying the discontinuity sets.

Leveraging these orientations and the density maps, we extract the set of points constituting the discontinuity using a straightforward contouring algorithm (figure 1.3).

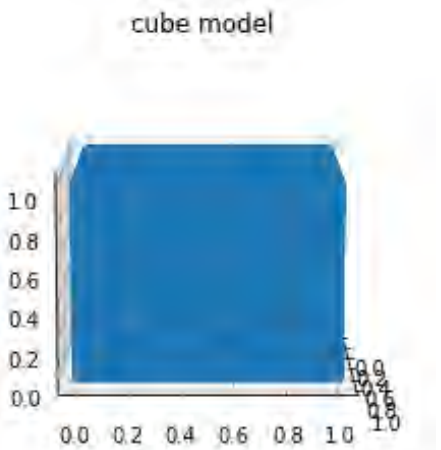

Figure 2.1

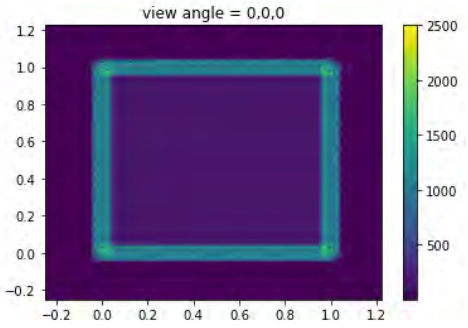

Figure 2.2

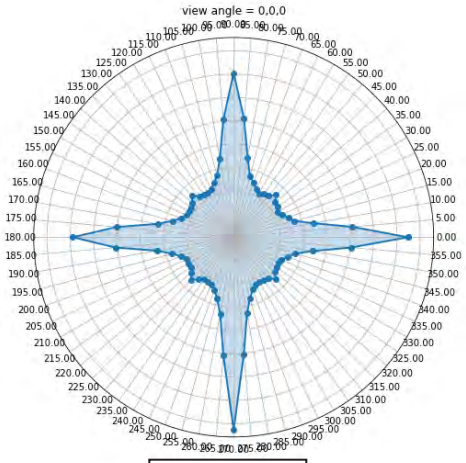

Figure 2.3

Figure 2: Demonstration of High-Density Point Detection. Figure 2.1 On the left is the initial model. Figure 2.2 In the middle is the density map generated from the (0,0,0) viewpoint. Figure 2.3 On the right is the maximum point density corresponding to various viewpoints on the density map.

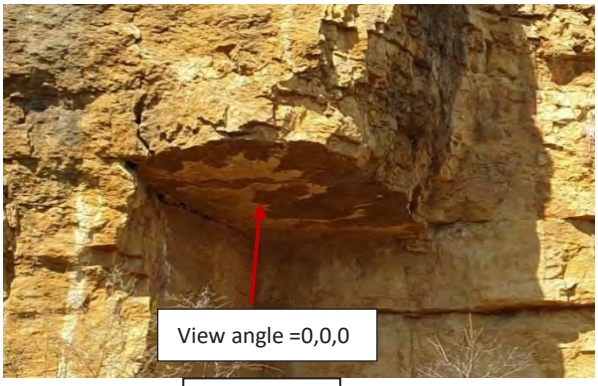

Figure 3.1

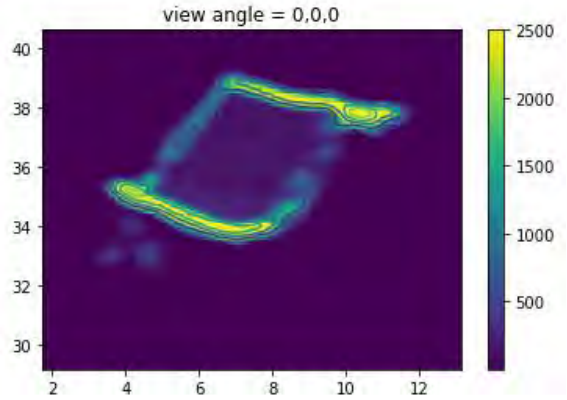

Figure 3.2

Figure 3 : figure 3.1 On the left, a picture of the real data scan of the yellow quarry in Ferreyres. Figure 3.2 On the right, a density map of the yellow quarry in Ferreyres, generated using a specific viewpoint (angle of the viewpoint = phi: 0, theta: 0, psi: 0 (looking from the bottom)). The color range indicates the point cloud density for this viewpoint.

Conclusion:

Our novel approach demonstrates its efficacy in the detection of discontinuities characterized by surface irregularities within PC data. It affords us the capability to quantitatively assess their presence, ascertain their orientation, and evaluate their spatial frequency in synthetic models. Additionally, when applied to authentic LiDAR data, our approach has yielded promising outcomes, as substantiated by our investigation of the yellow quarry in Ferreyres (Figure 3), where we effectively visualized complex discontinuity patterns.

It's important to note that the current algorithm is optimized for processing small point clouds. To further enhance scanning efficiency and extend its suitability for larger datasets, future improvements involve the utilization of gradient optimization techniques or the implementation of GPU multiprocessing. By incorporating point density as an additional dimension (PC density), our method opens up new possibilities for harnessing PC data.

References:

Adrián J. Riquelme, A. Abellán, R. Tomás, M. Jaboyedoff, (2014) " A new approach for semi-automatic rock mass joints recognition from 3D point clouds," Computers & Geosciences, Volume 68, 2014, Pages 38-52.

Matthew J. Lato, Malte Vöge, (2012) "Automated mapping of rock discontinuities in 3D lidar and photogrammetry models," International Journal of Rock Mechanics and Mining Sciences, Volume 54, 2012, Pages 150-158.

Two-dimensional Pseudostatic Analysis of Seismic Landslide Displacement

Meei-Ling Linr[1], Tien-Yi Zhou[1]

[1] Department of Civil Engineering, National Taiwan University, Taipei, Taiwan

SUMMARY: The Newmark's method has been developed by previous researchers for evaluating seismic landslide displacement with two-direction acceleration and often with planar sliding surface. A two-dimensional pseudostatic method is developed in this study, which considers the log-spiral sliding surface and vertical ground acceleration. A simple slope model was used to evaluate the effects of vertical acceleration on the location of sliding surface and critical acceleration. Finally, a field case triggered during Chi-Chi earthquake was adopted for further validation.

Keywords: seismic landslide displacement, vertical acceleration, sliding block method, log-spiral sliding surface

Introduction

Taiwan situates at the juncture of the Euroasian Continental Plate and Philippine Sea Plate, and thus, earthquakes occur frequently and often cause landslides. The Chi-Chi earthquake induced more than 30,000 landslide events in 1999. Newmark (1965) developed the sliding block method to evaluate displacement of a block caused by dynamic motion on a horizontal sliding surface, subsequently, the method was developed to consider sloping sliding plane, and curved sliding surface by further studies (Ling, 1997; Ingles, et al., 2006; Lin, 2010). However, the vertical ground acceleration could have significant effect on inducing seismic landslide, typically in the near field area (Hung, et al., 2000). A two-dimensional pseudostatic method is developed in this study, which considers the log-spiral sliding surface and vertical ground acceleration. A simple slope model was used to evaluate the effects of vertical acceleration on the location of sliding surface and critical acceleration. Finally, a field case triggered during Chi-Chi earthquake was adopted for further validation.

Materials

To consider the vertical acceleration, the two-dimensional sliding block analysis for planar sliding surface was developed by previous researchers (Huang et al., 2001, Ingles, et al., 2006) with simplified assumptions. Chen and Liu (1990) proposed that the log-spiral was the most likely sliding surface for simple homogeneous slope subjected to seismic load, and developed a limit equilibrium method to search for the sliding surface and critical acceleration. Huang and Lin (2003) adopted the limit equilibrium method and considered a simple slope with log-spiral sliding surface subjected to a horizontal ground acceleration. With the critical acceleration and sliding surface, the toe displacement of the log spiral sliding block was derived from the governing equation and resulting horizontal displacement of the block. We adopted the similar procedures to developed the two-dimensional log spiral sliding block analysis, and to compute the toe displacement as well as the crest displacement.

A simple slope model was constructed for evaluation of the effects of the vertical ground acceleration on the locations of the sliding surface and displacements of crest and toe of the sliding block. The material properties of the soil slope were: unit weight, γ= 20 kN/m^3, cohesion, c = 30 kPa, and friction angle, ϕ = 25 degree. The slope height was 50 m with a slope angle of 30 degree. The field case adopted situated in Tsao-Tuan Township, Nan-Tou County, in central Taiwan close to the epicenter of Chi-Chi earthquake. Fig.1 shows the locations of the case slope and the nearby TCU071 strong motion station. The slope profile was approximated as a simple slope with a slope height of 95.4 m, a slope aspect of 153 degree from north, and a slope angle of 25.8 degree. The material properties were: unit weight, γ= 19.6 kN/m^3, cohesion, c = 15.7 kPa, and friction angle, ϕ = 31.6 degree. The ground acceleration records of TCU071 during Chi-Chi earthquake, 1999, were used for analysis, and the ground accelerations in north-south direction and east-west direction were combined and resolved into the direction along the slope aspect as the acting horizontal acceleration.

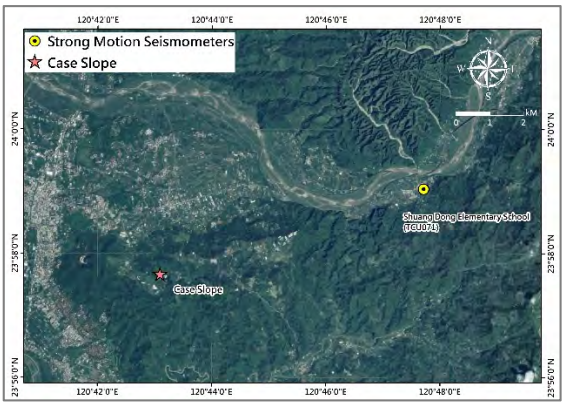

Figure 1. Locations of field case slope and strong motion station TCU071

Research Method

We referred the procedures of Huang and Lin (2003) utilizing the limit equilibrium method to derive the two-dimensional sliding block model considering vertical acceleration and log-spiral surface. The slope profile and definition of log-spiral of the analysis is illustrated in Fig. 2 along with the definitions of notations. The horizontal and vertical ground accelerations are denoted as the ground acceleration coefficients, k_h, and k_v, times the gravity acceleration, g, in the horizontal and vertical directions, respectively. The horizontal acceleration is taking outward direction as positive direction, and the vertical acceleration is taking downward direction as positive direction as shown in Fig. 2. By taking moment equilibrium with respect to the center of rotation of the log-spiral, the critical horizontal acceleration was derived as:

$$k_h = \frac{\frac{c}{\gamma H} f_c - \frac{(1+k_v)(f_1 - f_2 - f_3)}{\sin\theta_t \exp[(\theta_t - \theta_0)\tan\emptyset] - \sin\theta_0}}{\frac{f_4 - f_5 - f_6}{\sin\theta_t \exp[(\theta_t - \theta_0)\tan\emptyset] - \sin\theta_0}} \quad (1)$$

where: f_1 through f_6, and f_c were functions derived from taking moments of different wedges shown in Fig. 2 with respect to the rotation center. To find the minimum k_h, which suggests the critical acceleration, we take the derivative of Eq. 1 with respect to the rotation angles of θ_0, and θ_t, which define the log-spiral sliding surface. The solution provides a k_h- k_v correlation line for the critical condition, and as the ground acceleration exceeds the critical line, sliding occurs. By integrating the exceeding acceleration time record, the landslide displacement can be

computed. A correlation between the centroid displacement and toe displacement of the sliding block was also derived.

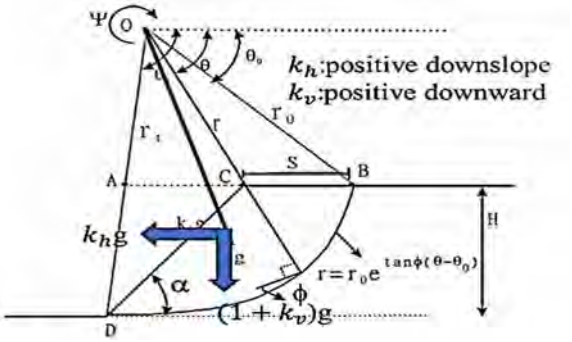

Figure 2. Slope profile and definitions of log-spiral and notations of the analysis

Results and Discussions

A simple harmonic wave with a horizontal acceleration amplitude of 0.5*g* was used for the parametric study of the simple slope, and vertical acceleration was set as 0, 1/4, 1/3, and 1/2 times the horizontal acceleration. Fig. 3(a) shows the resulting critical acceleration line, and as the vertical acceleration increases, the critical horizontal acceleration decreases. This suggests that the sliding occurs much faster with a larger vertical acceleration, and results in a larger landslide displacement. The changes of the vertical acceleration also lead to different sliding surfaces as shown in Fig. 3(b). The depth of the sliding surface decreases with increasing vertical acceleration, suggesting that shallow landslide is more likely to occur with vertical acceleration. This is consistent with actual field cases that a large number of shallow landslides triggered by earthquake were observed (Hung, et al., 2000).

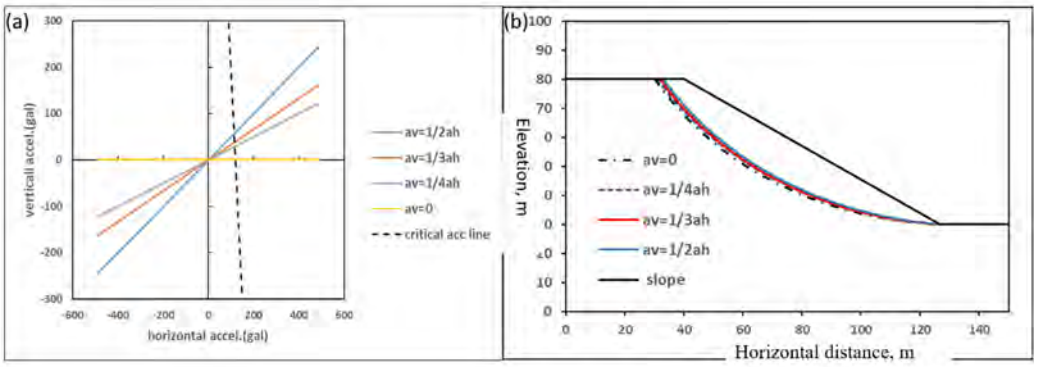

Figure 3. (a) the critical acceleration line; (b) the simple slope profile and sliding surfaces of different vertical accelerations

A field case triggered by Chi-Chi earthquake, 1999, was adopted for validation of the analysis, and Fig. 4(a) showed the simplified slope profile. The ground acceleration records of a nearby strong motion station TCU071 were used, which was 7.8 km from the slope site. The peak vertical acceleration was 0.416*g* and the peak horizontal acceleration was 0.562*g* in the dip direction. The sliding surface was determined as the sliding surface when the accelerations exceeded the critical acceleration line the first time as shown in Fig. 4(a). Fig. 4(b) shows the resulting critical acceleration line versus the ground acceleration time record, and by integrating the exceeding acceleration time record, the landslide displacement was 17.1 cm at the toe. Comparing to the analysis performed with horizontal acceleration only, the landslide

displacement at toe was 14.3 cm, which is smaller than the one with the vertical acceleration. Thus, the critical horizontal acceleration would be smaller with a larger toe displacement when the vertical acceleration is considered.

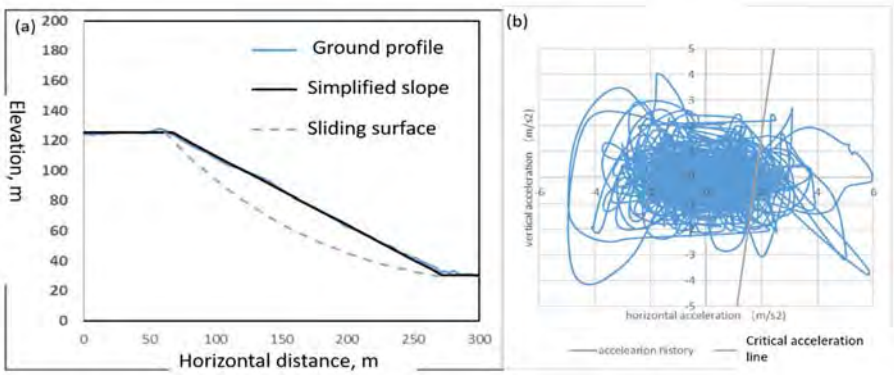

Figure 4. (a) the simplified slope profile and sliding surface; (b) the critical acceleration line versus the ground acceleration time record

Conclusion

The vertical ground acceleration could have significant effects on inducing seismic landslide, and the log-spiral sliding surface is more likely to occur. A two-dimensional sliding block model is developed in this study, which considers the log-spiral sliding surface and vertical ground acceleration. Results of a simple slope analysis suggested that the critical horizontal acceleration and the depth of the sliding surface decreased with increasing vertical acceleration. This suggests that the sliding occurs much faster with a vertical acceleration, and results in a larger landslide displacement, and a shallower landslide, which is consistent with field observation. The field case study showed that the critical horizontal acceleration was smaller and the toe displacement was larger when the vertical acceleration was considered. Thus, it is essential to take into account the vertical acceleration when analyzing the earthquake-induced landslide, especially in the near field condition.

References

Chen, WF, & Liu, XL (1990) *Limit analysis in soil mechanics* (No. 624.151 C4).

Chang CJ, Chen WF & Yao JT (1984) Seismic displacements in slopes by limit analysis. *Journal of Geotechnical Engineering* 110(7), 860-874.

Huang CC, Lee YH, Liu HP, Keefer DK & Jibson, RW (2001) Influence of surface-normal ground acceleration on the initiation of the Jih-Feng-Erh-Shan landslide during the 1999 Chi-Chi, Taiwan, earthquake. *Bulletin of the Seismological Society of America* 91(5), 953-958.

Huang JJ & Lin ML (2003) Application of sliding block method on earthquake induced landslide. *Journal of the Chinese Institute of Civil and Hydraulic Engineering* 15(4), 655-665.

Hung J J, Lin ML, Chen T C & Wang K L (2000) Disasters, characteristics, and case analysis of slope failures caused by Chi-Chi earthquake. *Sino-Geotechnics* 81, 17-32.

Ingles J, Darrozes J & Soula, JC (2006) Effects of the vertical component of ground shaking on earthquake-induced landslide displacements using generalized Newmark analysis. *Engineering geology* 86(2-3), 134-147.

Lin YJ (2010) *Analysis of seismic landslide behavior using numerical model*, MS thesis, Department of Civil Engineering, National Taiwan University.

Ling HI, Leshchinsky D & Mohri Y (1997) Soil slopes under combined horizontal and vertical seismic accelerations. *Earthquake engineering & structural dynamics* 26(12), 1231-1241.

Newmark N M (1965) Effects of earthquakes on dams and embankments. *Geotechnique* 15(2), 139-160.

Rock Avalanche Mobility: Influencing Parameters Analysis Based on Machine Learning

Ruoshen Lin[1], Michel Jaboyedoff[1], Alexander Strom[2]

[1] Institute of Earth Sciences, University of Lausanne, 1015 Lausanne, Switzerland
[2] Geodynamics Research Center Ltd., Moscow, Russia

SUMMARY: Rock avalanche is one of the most destructive and expensive geological hazards in mountainous regions. Understanding the dynamics and characteristics of rock avalanche movement plays a crucial role in assessing the potential hazards. However, the prediction for rock avalanche propagation is still challenging. Therefore, this paper proposes a new approach based on machine learning to analyse the controlling parameters on the mobility of rock avalanches. Input parameters including confinement type, headscarp height, mean slope angle of headscrap, length and width of the headscarp base, source volume, and maximal height drop are analyzed and discussed. The importance analysis of main parameters is proposed based on the SHapley Additive exPlanations model and the results showed the importance of each characteristic. The sensitivity analysis is conducted by controlling variable, which is to change one parameter manually while keeping the other parameters constant. Controlling parameters sensitivity analysis results showed that L-confined topography type, maximal height drop and source volume tend to increase the travel distance and total impacted area.

Keywords: Rock avalanche, Mobility, Machine learning, XGBoost model, Sensitivity analysis

Introduction

Rock avalanche characterized by high speed, long travel distance, large volumes and fragmenting rock, cause damage and many casualties. And it have the potential to reoccur at the same location after extended periods spanning thousands of years, as well as short intervals of days. Understanding the dynamics and characteristics of rock avalanche movement plays a crucial role in assessing the potential hazards posed by such event. The mobility of rock avalanche is commonly quantified by Fahrböschung (angle of reach), defined as the ratio of the fall height to the runout distance and travel distance (Scheidegger 1973, Corominas 1996). Existing studies have analysed the relationship between travel distance and failure volume (Nicoletti 1991, Mitchell 2020), but prediction for them are complicated because it also controlled by the other measurement of failed mass, properties of source zone, category of path confinement, and so on.

Traditional methods for influencing factor analysis include (1) theoretical methods; (2) statistical methods; and (3) numerical modelling (Zou 2017, Aaron 2019, Strom 2019). Theoretical models are based on mechanical principles and dynamic theories, which rely on precise modelling and parameter estimation. Empirical models are derived from observed data and real rock avalanche events, which utilize recorded data and establish statistical formulas to predict for future events (Locat 2006, Basharat 2015). Empirical models simplify the requirement for detailed physical modelling but rely heavily on sufficient and representative dataset for model calibration and validation. It is noted that some empirical models are widely used for the influencing factor analysis in the Wenchuan area (Zou 2017). Some advanced computational techniques are applied to numerical simulation models, such as finite element method or discrete element method, to predict the failure analysis of rock avalanche. By considering complex terrain conditions, rock mass properties, and boundary conditions,

numerous modelling can provide detailed information regarding speed, path, runout and depth. Compared with traditional methods, machine learning methods can extract complex nonlinear relationships from large-scale data, exhibiting superior performance in analysis. However, almost no researchers study on the application of machine learning models in influencing factor analysis of rock avalanches, which is still in its infancy(Aaron 2019).

Database and methods

1. Brief introduction to the database

Compilation of inventories is an indispensable first step for understanding these destructive geological phenomena in mountainous regions. As shown in Fig.1, the Central Asian database includes rock avalanches from the Pamir, the Tien Shan, and the Dzungaria mountainous systems located in Afghanistan, China, Kazakhstan, Kyrgyzstan, Tajikistan, and Uzbekistan. It is characterized as one of the "hotspots" for rock avalanches worldwide. This database was carried out through the remote sensing data based on free Google Earth, SAS Planet, and ArcGIS Earth space imagery that covers the entire Central Asia, and some high-resolution images, i.e. the old Soviet KFA-1000 stereoscopic and KFA-3000 images with a resolution of 5 ~ 8 and 3 m respectively, and Soviet 1:1000,000 ~ 1:25,000 topographic maps. This paper selects rock avalanches (412 cases) with a total of 8 parameters to establish the prediction model. Statistical results of the rock avalanche database based on total volume and travel distance are shown in Fig.1.

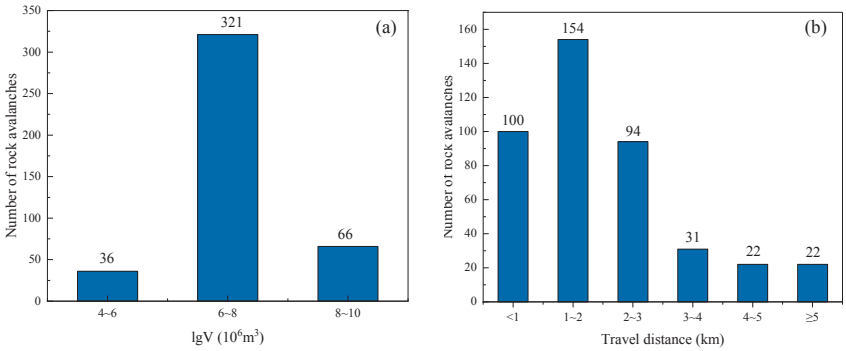

Figure.1 Statistical results of the rock avalanche database: (a) lgV (total volume); (b) travel distance

2. Methods

Principle of the XGBoost algorithm

The boosting algorithm includes traditional Gradient Boosted Decision Tree (GBDT) and XGBoost, which are decision tree models for regression and classification tasks (Chen and Guestrin 2016). The XGBoost is a famous improved algorithm of GBDT. Compared with GBDT, XGBoost adds regularization terms to the loss function, and XGBoost uses the second-order Taylor expansion of the loss function as the fitting of the loss function. Its principle is basically the same, but the speed and efficiency are further improved. XGBoost objective function consists of two parts, one is the Loss Function and the other is the Regularization Term. The goal of the objective function is to minimize the loss and control the complexity of the model. The regularization term consists of two parts, the sum of the squares of the weights of the leaf nodes of the tree (L_2 regularization) and the sum of the absolute values of the leaf nodes of the tree (L_1 regularization). The final prediction is obtained by summing the predicted values for each tree. Its functions are shown in formula (1) ~ (3). The XGBoost model with grid search optimization is used for predicting the distance of propagation L. Table 1 contains all the parameters we considered in our study.

$$\text{Loss function} = \sum_{i=1}^{n} L\,(yi, \hat{yi}) \tag{1}$$

$$\text{Regularization Term} = \gamma \cdot T + \frac{1}{2}\lambda \sum_{j=1}^{T} w_j^{\,2} \tag{2}$$

$$\hat{y}i = \sum_{k=1}^{K} f_k(x_i) \quad (3)$$

Where L is loss function, yi is the actual value, $\hat{y}i$ is the model's predicted value, T is the number of leaf nodes, w_j is the weight of the leaf node, γ and λ are the parameters of regularization, K is the number of trees, $f_k(x_i)$ is the predicted value of the K_{th} tree for the sample X_i.

Table 1 Parameters selected to describe events included in the dataset

Parameters	Description	Units	
Height	Headscarp height	km	
Length	Maximum length of headscarp	km	
Width	Maximum width of headscarp	km	
Source volume	80% of deposits' volume	10^6 m^3	
Travel distance (Lmax)	The horizontal distance from the headscarp crown to the deposits' tip	km	Quantitative
Total impacted area	Headscarp, the transition zone, and the depositional area	km^2	
Maximal height drop (Hmax)	The elevation difference between the headscarp crown and the lowermost point of the deposits	km	
Confinement	Topographic confinement	Unconfined Laterally confined Frontally confined	Qualitative

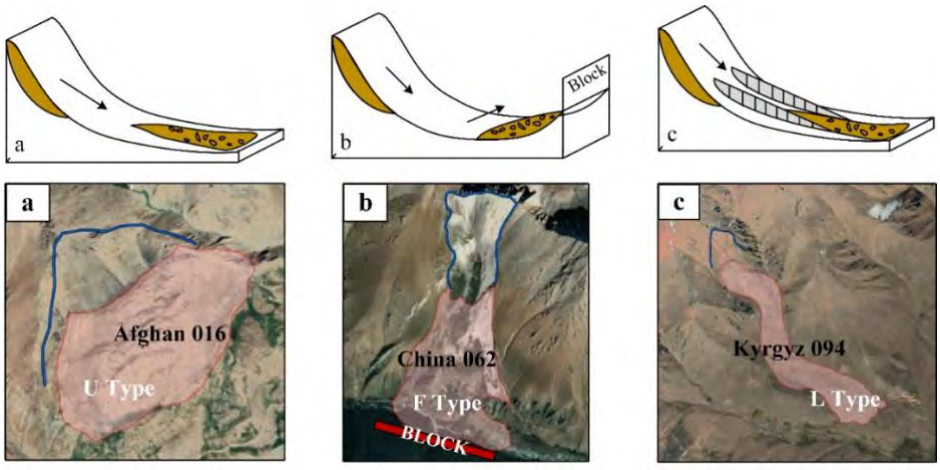

Figure.2 General models and examples of the different confinement categories: (a) the unconfined rock avalanches; (b) the frontally confined rock avalanches and (c) the laterally confined rock avalanches

H/L ratio ("Fahrböschung" or "angle of reach"), which is defined as the ratio of fall height H over runout distance L, has been commonly used to quantify the mobility of rock avalanches. Corresponding R^2 values for the angle of reach are significantly lower than the R^2 of runout based on the entire database. Runout seems to be preferable to characterize rock avalanche mobility and can be predicted for a given failed volume with much higher confidence. In addition, travel distance provides a more comprehensive measure of the overall distance covered. By prioritizing travel distance, we can assess the efficiency and effectiveness of the travel path without being limited by the specific angle at which the distance is covered.

Preliminary results

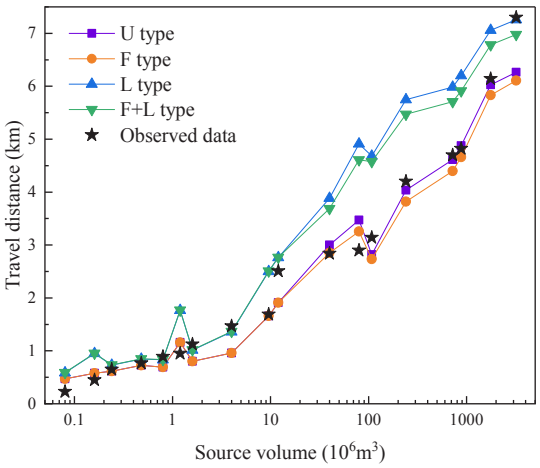

Figure.4 The result of sensitivity analysis of controlling parameter: sensitivity of confinement types

Conclusion

More than 400 catastrophic historical rock avalanches from the central Asian were used in our study. We propose a new approach based on machine learning for analysing the relative importance of the confinement categories, source volume and maximum height drop on the rock avalanche mobility. The results showed the importance of each characteristic and it revealed that failed volume has the most impact on propagation among the input parameters, except for height drop. Controlling parameters sensitivity analysis results showed that L-confined topography type, maximal height drop and source volume tend to increase the travel distance and total impacted area. Future work will explore the impact of terrain features along the path on the performance of the model, e.g. slope gradient, lithology, curvature, and landcover etc.

References

Aaron, J. and S. McDougall (2019). "Rock avalanche mobility: The role of path material." Engineering Geology 257.

Basharat, M. and J. Rohn (2015). "Effects of volume on travel distance of mass movements triggered by the 2005 Kashmir earthquake, in the Northeast Himalayas of Pakistan." Natural Hazards 77(1): 273-292.

Corominas, J. (1996). "The angle of reach as a mobility index for small and large landslides." Canadian Geotechnical Journal 33(2): 260-271.

Locat, P., R. Couture, S. Leroueil, J. Locat and M. Jaboyedoff (2006). "Fragmentation energy in rock avalanches." Canadian Geotechnical Journal 43(8): 830-851.

Mitchell, A., S. McDougall, N. Nolde, M. A. Brideau, J. Whittall and J. B. Aaron (2020). "Rock avalanche runout prediction using stochastic analysis of a regional dataset." Landslides 17(4): 777-792.

Nicoletti, P. G. and M. Sorrisovalvo (1991). "GEOMORPHIC CONTROLS OF THE SHAPE AND MOBILITY OF ROCK AVALANCHES." Geological Society of America Bulletin 103(10): 1365-1373.

Scheidegger, A. E. (1973). "On the prediction of the reach and velocity of catastrophic landslides." Rock mechanics 5(4): 231-236.

Schleier, M., R. L. Hermanns, J. C. Gosse, T. Oppikofer, J. Rohn and J. F. Tonnesen (2017). "Subaqueous rock-avalanche deposits exposed by post-glacial isostatic rebound, Innfjorddalen, Western Norway." Geomorphology 289: 117-133.

Strom, A. and K. Abdrakhmatov (2018). Rockslides and Rock Avalanches of Central Asia: Distribution, Morphology, and Internal Structure.

Strom, A., L. Li and H. Lan (2019). "Rock avalanche mobility: optimal characterization and the effects of confinement." Landslides 16(8): 1437-1452.

Zou, Z. X., C. R. Xiong, H. M. Tang, R. E. Criss, A. J. Su and X. Liu (2017). "Prediction of landslide runout based on influencing factor analysis." Environmental Earth Sciences 76(21).

Vulnerability Assessment of Landslide-vulnerable area for Hazard Levelbased Rainfalls

Chang-Ho Song[1], Ji-Sung Lee[1], *Ho-Hong Duy Nguyen*[1], *and* Yun-Tae Kim[1]

[1] [1]Department of Ocean Engineering, Geo-systems Engineering Laboratory, Pukyong National University, Busan 48513, Republic of Korea

SUMMARY: Reduce the risk of landslides, it is crucial to identify landslide-vulnerable areas and conduct quantitative vulnerability assessments. Hwangryeong Mountain in Busan has experienced numerous small and large landslides in the past and contains various factors that make it susceptible to landslides. Therefore, this study focuses on quantitatively assessing the vulnerability of landslide-vulnerable areas near Hwangryeong Mountain. Using rainfall initiation for different risk levels (None, Alert, Warning, Evacuation) based on domestic rainfall conditions, susceptibility was evaluated according to rainfall scenarios. Additionally, to assess vulnerability, the impact pressure of soil hitting buildings was calculated through numerical analysis of sediment movement. Building damage levels were evaluated using a soil hazard vulnerability curve. Furthermore, vulnerability indices for the study area were presented based on rainfall scenarios. This research enables proactive response to landslide occurrences based on rainfall forecasts and provides fundamental data for creating landslide vulnerability maps.

Keywords: Landslide, Debris flow, Hazard Level-based Rainfalls, Susceptibility, Vulnerability

Introduction

In South Korea, the high proportion of mountainous terrain, coupled with dense population settlements, has led to increased development in mountainous areas to address recent housing and transportation challenges. Moreover, the rapid climate change has caused an uptick in landslide damages, posing significant risks to both human lives and infrastructure. Particularly, since 2011, there have been ongoing studies on landslide occurrence locations, triggered by landslides in areas like Umyeon Mountain and Chuncheon.

Landslides are caused by a complex interplay of factors, including topographical characteristics, concentrated rainfall, geological conditions, and more. To reduce and prevent landslide damages, it is crucial to assess the likelihood of landslides based on factors like occurrence areas, triggering elements, and rainfall data. Systematic vulnerability assessments are needed for susceptible regions.

Landslide vulnerability assessments evaluate sensitive areas using numerical analysis of sediment movement to analyze the velocity, height, and impact pressure of soil on buildings, leading to building-specific vulnerability assessments. However, it is necessary to conduct quantitative vulnerability assessments for an entire watershed, as even if individual buildings are rated with high vulnerability, reinforcement efforts cannot be focused on each building's surroundings. Instead, reinforcement is needed along the landslide pathways in a watershed.

In this study conducted on-site investigations to analyze the physical properties of soil in landslide- vulnerable areas. Using historical rainfall data and landslide inventories, the study established rainfall initiation for different risk levels. Subsequently, using a physics-based model, the study assessed susceptibility hazard level-based rainfall initiation. The study also developed and applied a quantitative vulnerability assessment methodology.

Study area

Figure 1 represents the study area for this research. Hwangryeong Mountain in Busan has experienced several significant and minor landslides in the past, and it contains various factors that increase its susceptibility to landslides. The study area includes numerous valleys and has been exposed to sediment movement in the past. Additionally, there are traces of sediment deposition when cracks and rainfall occur. Therefore, this study focused on conducting a quantitative vulnerability assessment for landslide- vulnerable areas near Hwangryeong Mountain based on rainfall initiation for different risk levels.

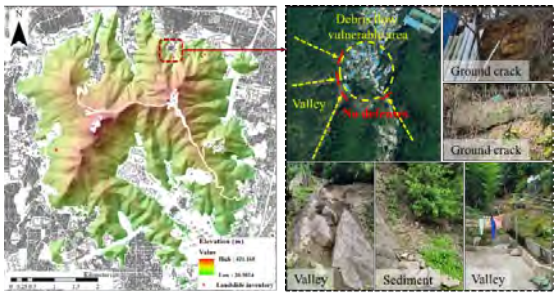

Figure 1. Study area

Methodology

The methodology of this study is shown in Figure 2. First, rainfall standards for each risk level are applied through the landslide occurrence DB and rainfall DB. In addition, field disturbance and undisturbed sample collection, field density testing, and ground depth investigation were conducted through field surveys in the study area. Based on this, geotechnical characteristics were established through indoor testing. Second, GIS-based infiltration analysis is performed based on hazard level-based rainfall, geotechnical characteristics, and topographic factors, and susceptibility is calculated through GIS-based stability analysis. Third, the landslide initiation area where landslide disasters occur is extracted by simultaneously considering the susceptibility and topographical characteristics obtained through GIS-based stability analysis (Song et al, 2021). Lastly, we performed debris flow analysis using DAN 3D, a debris flow analysis program, calculated the intensity of risk affecting the house according to hazard level-based rainfall, and performed a vulnerability assessment for each building according to the housing structure using the vulnerability curve according to the housing structure. We analyzed quantitative vulnerability.

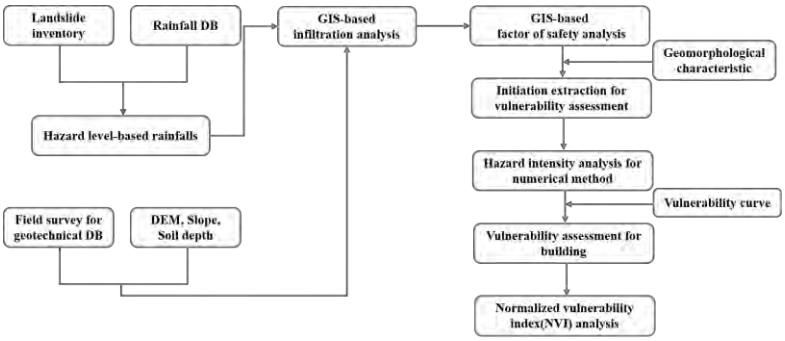

Figure 2. Methodology

Result and discussion

First, field surveys were conducted in the study area, followed by indoor experiments. The surveyed area is characterized by the distribution of weathered granitic, with geotechnical

properties estimated based on typical characteristics of residual soils. The physical properties of the soil, which were utilized for slope stability and numerical analysis, were determined from the results of both field and laboratary tests (Fig. 3). The geotechnical properties used for stability analysis were typical of weathered soil and included cohesion of 8.5 kPa, an internal friction angle of 31.8 degrees, and unit weight of 15.9 kN/m³. And based on the landslide inventory of the study area and a rainfall database, a total of four rainfall initiation, as presented in Table 1, were established for this study.

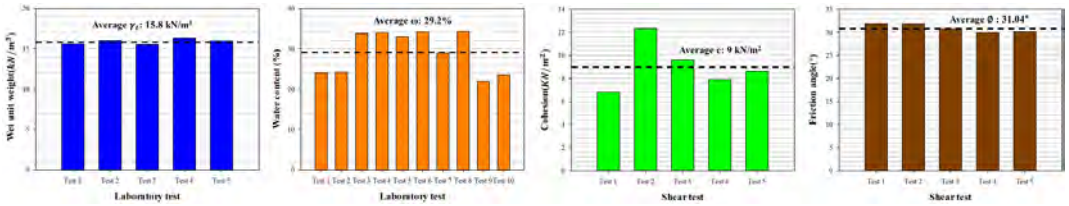

Figure 3. Soil properties in study area

Table 1. Hazard level-based rainfall

Class	Hour	Rainfall intensity *(mm/hr)*	Cumulative rainfall *(mm)*
None	24	4.3	103
Watch		5.0	144
Warning		8.2	196
Alarm		10.0	240

Geotechnical properties and the rainfall initiation for different hazard level-based rainfall were employed to conduct slope stability analysis. Based on the factor of safety obtained from slope stability analysis, susceptibility maps were created for different forecasting and alert scenarios(Figure. 4). It is evident that as the rainfall initiation increase, the landslide risk areas expand. Given the extensive nature of the risk areas identified, numerical analysis was performed using the debris flow initiation model proposed by Song et al. (2021) to extract areas where debris flow could potentially occur.

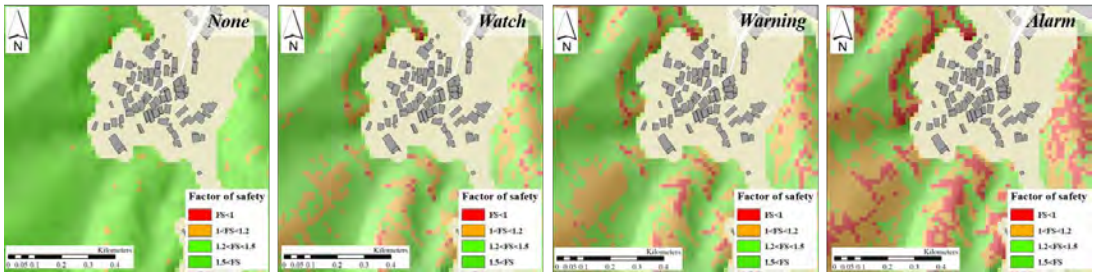

Figure 4. Susceptibility map for hazard level-based rainfall

Based on the extracted debris flow initiation points, debris flow simulations were performed using the DAN3D program. The DAN3D program offers five different rheological models. In this study, the Frictional model was used, which allows for inverse modeling using the data collected. The program's input parameters include the physical properties of the soil, pore pressure ratio, and yield strength. The values for the pore pressure ratio and yield strength were derived from debris flow analyses conducted in South Korea between 2011 and 2020 (Song et al., 2023). Using the DAN3D program, the Froude number, which is related to the velocitys and height of the debris flow, was analyzed, and the impact pressure on buildings was calculated. Subsequently, vulnerability levels for each building were assessed based on the impact pressure on buildings and the building structure type using vulnerability curves (Fig. 5).

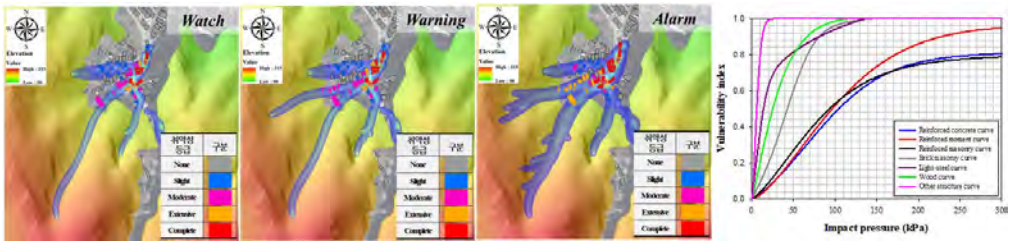

Figure 5. Vulnerability assessment results and vulnerability curve

Proposed NVI assessment methodology was applied in this study. Quantitative vulnerability assessment allows for the evaluation of vulnerability on a scale of 0 to 100 for an entire watershed (Fig. 6). The proposed formula calculates the vulnerability value for an entire watershed by summing the vulnerability values of all exposed buildings affected by debris flow. In the study area, NVI for hazard level-based rainfall was analyzed as None for no damage, Alert at 28.6, Warning at 32.8, and Evacuation at 47.7.

In this study, susceptibility analysis utilized a physical-based model. however, it is anticipated that integrating machine learning into the susceptibility analysis can significantly enhance the reliability of vulnerability assessments. Machine learning algorithms have the potential to unravel hidden insights and correlations within the data, providing a more nuanced comprehension of the underlying factors impacting the methodology. This, in turn, empowers practitioners to make well-informed, data-driven decisions. The predictive prowess of machine learning models further contributes to forecasting trends, mitigating risks, and optimizing resource allocation. By harnessing machine learning in the susceptibility analysis, the overall effectiveness of the methodology is poised to improve. This amalgamation of traditional physical-based models with machine learning not only strengthens the vulnerability assessment process but also fosters a more adaptive and insightful approach to addressing complex challenges in the realm of the study.

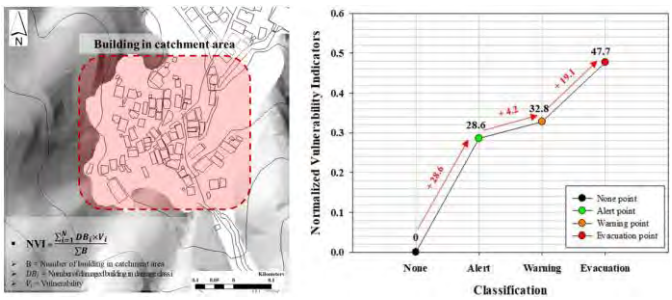

Figure 6. Proposed NVI(Normalized Vulnerability Index) example and NVI result

Acknowledgement

This work is supported by the Korea Evaluation Institute of Industrial Technology(KEIT) funded by the Ministry of Public Administration and Security grant (No. K_G012001951201).

References

Song CH, Lee JS & Kim YT (2021) Predicting the initiation area of a debris flow using geomorphological characteristics and a physically-based model. *Journal of the Korean Society of Hazard Mitigation* 21, 137–147.

Song CH, Lee JS, Nguyen HHD & Kim YT (2021) Development of physical vulnerability curve based on debris flow events considering entrainment and building. *Journal of the Korean Society of Hazard Mitigation* 23, 185–196.

Investigation of Seismic Signature Induced by Grain-bed Impact to Determine the Grain Size Distribution of Flow-type Landslides

Yihan Wang[1], Clarence Edward Choi[1]

[1] The Department of Civil Engineering, The University of Hong Kong, HKSAR, China

Summary
The grain size distribution plays a crucial role in the mechanical behavior of flow-type landslides, making it a key factor in understanding the underlying mechanisms. This study conducts a series of free fall tests using grains of varying size distributions. The objective is to employ signal processing and machine learning techniques to infer the size distribution of the granular flows. Furthermore, an analytical model has been developed to account for the influence of size distribution on the seismic signals generated by flow-type landslides. This discovery serves as a bridge between grain size distribution and the impact stresses on the bed caused by flow-type landslides. It provides valuable guidance to practitioners by utilizing seismic signals to uncover the characteristics of flow-type landslides.

Keywords: flow-type landslides, grain size distribution, seismic signal, impact stress, hazard monitoring

Introduction

Flow-type landslides are a common and destructive form of natural hazards that occur in hilly or mountainous regions *(Hungr et al. 2014)*. It represents an assembly of geomaterial driven downslope by gravity. Based on different forming mechanisms, the flow-type landslides contain the rock avalanche, debris flow, etc. The size distribution of geotechnical materials such as rocks, sands, and soils can vary due to complex forming processes, fragmentation, and wearing mechanisms. As a result, flow-type landslides can have different and complicated grain size distributions.

Studies have been conducted to investigate the impact of grain size on flow-type landslides. According to Bourrier et al. *(2009)*, the impact force of rock avalanches increases with the maximum diameter of the rocks. Zhou et al. *(2010)* have shown that the basal normal stress on the bed of debris flow can vary significantly with different grain size distributions. Song et al. *(2021)* have found that the grain size distribution significantly influences collision-driven erosion, as evident from the equation of the collisional stress. Powell et al. *(2002)* have reported that the bed load transportation rate can also vary significantly with different grain size distributions on the riverbed or seabed. Therefore, having a comprehensive understanding of grain size distribution is fundamental to fully comprehend the mechanisms of flow-type landslides.

Various methods have been employed to measure grain size distribution, including field sieving tests *(Chen et al., 2014)*, laser particle size analyzers *(Li et al., 2015)*, and image processing *(Chang et al., 2012)*. Sampling processes are required to obtain samples for grain size distribution measurement. Grain grading curves can be obtained from these measuring methods and effective diameters are often used to represent grain size distribution to simplify the representation. However, traditional methods can always ignore grains with larger sizes, and it is difficult to obtain the dynamic of grain size distribution with traditional methods.

The development of global and local seismic networks has led to the suggestion of warning perspectives based on modern seismic instrumentation. To complement predictions made hours

to days in advance, it would be useful to have an early warning system that accurately and robustly determines debris flow characteristics in real-time, and ideally far enough in advance so that loss of life can be prevented. The properties of flow-type landslides can significantly influence the characteristics of seismic signatures, such as the basal force of the bed, the force fluctuation *(Allstadt et al. 2020)*, the debris flow rate *(Kean et al. 2015)*, Energy dissipation *(Lin et al. 2022)*, etc. In this case, seismology can be a promising tool to reveal dynamic mechanisms of granular flows, including grain size distribution.

Methodology

Our study aims to investigate the grain impact mechanisms through free-fall impact tests. This investigation encompasses three distinct components:

1. Single-grain tests: These tests aim to elucidate the impact mechanism of individual grains.
2. Dual-grain tests: The objective is to comprehend the interaction between seismic waves generated by two different grains with varying sizes.
3. Multi-grain tests: These tests seek to uncover the seismic signature of grains with diverse size distributions. Each grain size distribution can be represented by a vector.

During the impact process, data of impact properties such as impact velocity, impact force, and elastic energy will be collected. Additionally, we will capture the seismic signals induced by the impact process. Ultimately, based on the relationship between impact properties and seismic signature, we intend to develop a seismic impact model that incorporates the grain size distribution.

Figure. 1 (a) and (b) illustrate the experimental arrangement of the newly-developed free fall test. The setup consists of a frame with a hopper affixed at the top, serving as the location for the grains. Directly beneath the frame is an inclined impact bed. The container used in the experiment has the capacity to accommodate various bed materials, such as sands, glass beads, and others. The inclined angle of the bed can be adjusted within the range of 0° to 30°.

(a) (b) (c)

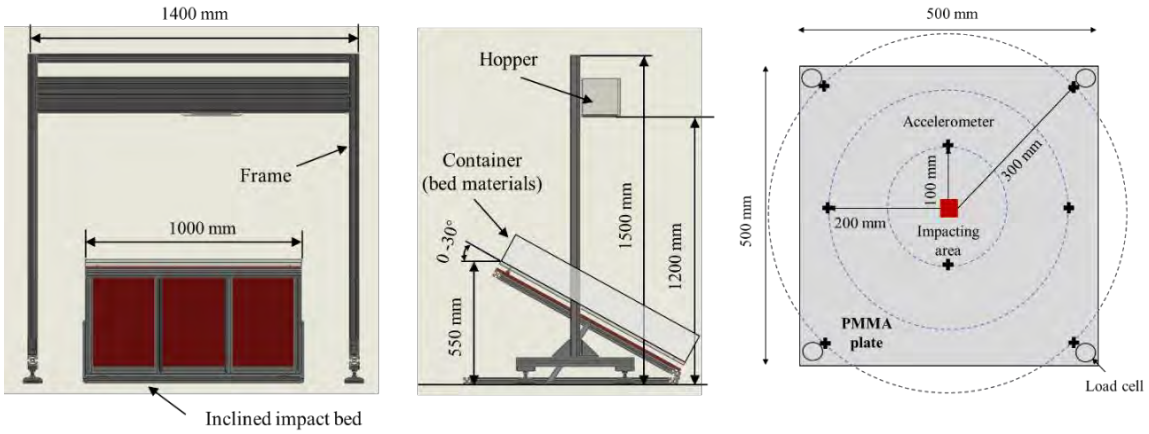

Figure 1. (a) Front view and (b) side view of the setup; (c) the plan view of instrumentation layout

Figure. 1 (c) presents the plan view of the instrumentation layout on the bed for reference. To assess the attenuating effect of elastic waves, multiple accelerometers are strategically placed at three distinct positions. One accelerometer is positioned directly beneath the impact area, another is located 100 mm from the center, and the third one is situated 200 mm from the center. Additionally, four load cells are fixed at the corners of the plate. The obtained elastic waves of the grain impacts are shown as **Figure. 2**.

In the experimental setup, glass beads ranging in diameter from 5 mm to 50 mm are utilized as samples for the free fall tests. Upon release from the hopper, the grains fall vertically and impact the beds. The sensors in place capture the seismic signals induced by these impacts. For the

single-grain impact tests, each diameter undergoes five repetitions to mitigate potential errors. In the case of dual-grain impact tests, grains of different diameters are randomly combined, and each group also undergoes five repetitions. For multi-grain tests, granular flows with same mass and different size distributions have been conducted free-fall tests.

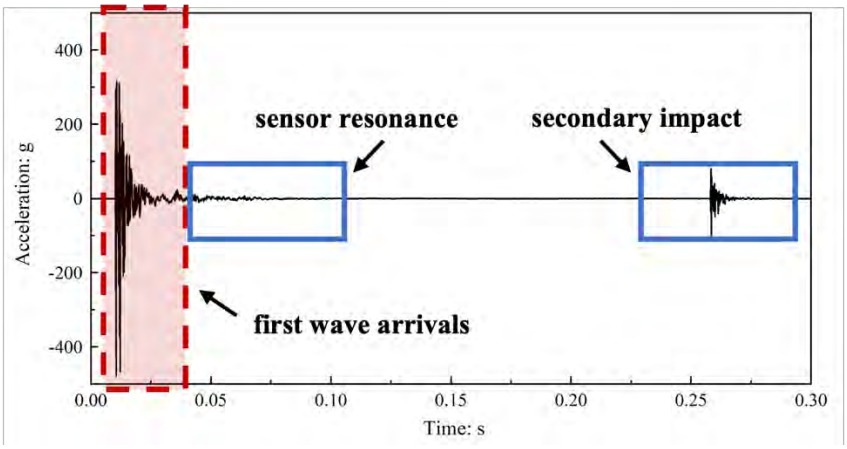

Figure 2. The elastic waves caused by the grain impacts

In order to link the seismic signal acquired with the characteristics of the granular flows, we will employ signal decomposition methods like the Fourier transform. By decomposing the signal, we can analyze the elastic energy and frequency components it contains. This analysis allows us to establish a connection between the signal generated by impacts and the distribution of grain sizes, with the help of Hertz theory and solid mechanics. Moreover, machine learning techniques can be utilized to exploit waveform features and accurately identify specific impact characteristics associated with various size distributions.

Conclusion

By conducting free fall tests and employing signal processing techniques, correlations between grain size distribution and grain bed impacts have been established. The analysis also involves examining the relationships between elastic energy and frequency components. Seismic signals, taking into account grain size distribution, provides insights into the underlying mechanisms of impacts from a granular perspective. Ultimately, an analytical model of seismic signals generated by flow-type landslides, incorporating the influence of grain size distribution, has been developed. It can be concluded that seismic signals contribute to a more comprehensive demonstration and explanation of the fundamental mechanisms underlying the granular flows.

References

Hungr, O., Leroueil, S. & Picarelli, L. (2014). The Varnes classification of landslide types, an update. Landslides, 11(2), 167-194.

Bourrier, F., Dorren, L., Nicot, F., Berger, F., & Darve, F. (2009). Toward objective rockfall trajectory simulation using a stochastic impact model. Geomorphology, 110(3-4), 68-79.

Zhou, G. G., & Ng, C. W. (2010). Dimensional analysis of natural debris flows. Canadian Geotechnical Journal, 47(7), 719-729.

Song, P., & Choi, C. E. (2021). Revealing the importance of capillary and collisional stresses on soil bed erosion induced by debris flows. Journal of Geophysical Research: Earth Surface, 126(5), e2020JF005930.

Powell, D. M., Reid, I., & Laronne, J. B. (2001). Evolution of bed load grain size distribution with increasing flow strength and the effect of flow duration on the caliber of bed load sediment yield in ephemeral gravel bed rivers. Water Resources Research, 37(5), 1463-1474.

Chen, H. X., Zhang, L. M., & Zhang, S. (2014). Evolution of debris flow properties and physical interactions in debris-flow mixtures in the Wenchuan earthquake zone. Engineering Geology, 182, 136-147.

Li, Y., Wang, B. L., Zhou, X. J., & Gou, W. C. (2015). Variation in grain size distribution in debris flow. Journal of Mountain Science, 12, 682-688.

Chang, F. J., & Chung, C. H. (2012). Estimation of riverbed grain-size distribution using image-processing techniques. Journal of Hydrology, 440, 102-112.
Allstadt, K. E., Farin, M., Iverson, R. M., Obryk, M. K., Kean, J. W., Tsai, V. C., et al. (2020). Measuring basal force fluctuations of debris flows using seismic recordings and empirical Green's functions. Journal of Geophysical Research: Earth Surface, 125, e2020JF005590.
Kean, J. W., J. A. Coe, V. Coviello, J. B. Smith, S. W. McCoy, and M. Arattano. (2015), Estimating rates of debris flow entrainment from ground vibrations, Geophys. Res. Lett., 42, 6365–6372.
Lin, Q., Wang, Y., Cheng, Q., Deng, K., Liu, S., & Li, K. (2022). Characteristics of the seismic signal generated by fragmental rockfalls: Insight from laboratory experiments. Journal of Geophysical Research: Solid Earth, 127, e2022JB025096.
Farin, M., Mangeney, A., Toussaint, R., Rosny, J. D., Shapiro, N., Dewez, T., & Berger, F. (2015) Characterization of rockfalls from seismic signal: Insights from laboratory experiments. Journal of Geophysical Research: Solid Earth 120(10), 7102-7137.

Mineralogy of Pelitic schist relating to Landslide and Weathering

Shintaro Yamasaki

Disaster Prevention Research Institute of Kyoto University, Kyoto, Japan

SUMMARY: The reasons behind the occurrence of landslides and gravitational slope deformations in pelitic schist include the development of schistose planes and the presence of thin layers of graphite along these planes. The graphite layer is low strength and work as solid lubricant. Furthermore, the graphite coexists with pyrite, both of which originate from seabed organic matter. Pyrite becomes a cause of weathering near the ground surface, involving oxidation and dissolution with sulfuric acid.

Keywords: pelitic schist, weathering, landslide, pyrite, graphite

Introduction

Landslides and deep-seated gravitational slope deformations (DGSDs) commonly occurs in pelitic schist in many countries (Figure 1). The pelitic schist, characterized by its easily cleaved structure known as "schistose plane," is prone to landslides and DGSDs along those planes. Consequently, dip-slopes often become high-risk areas for landslides. However, rockslides and their rupture surfaces develop at specific depth. The pelitic schist is a composite material with non-uniform components. The place of the rupture surface should depend on that material property. In this paper, I elucidate from a mineralogical perspective what constitutes these weak places in pelitic schist and how they relate to occurrence of landslides.
The pelitic schist in the Japanese islands originated from deep-sea sedimentary deposits. These sedimentary deposits, located within accretionary complexes, undergo recrystallization through high-pressure, low-temperature metamorphic processes. The mineral composition of pelitic schist includes phyllosilicates originating from clay minerals as well as organic-origin materials like graphite and iron sulfides. My presentation shows that those materials are responsible for the coloration of the rock and act as triggers for weathering and the formation of rupture surfaces.

Weathering by pyrite oxidation

Yamasaki and Chigira (2011) studied chemical weathering of pelitic schist and found that pyrite (a common constituent) has an important role in the weathering. They showed that pyrite is oxidized at oxidation fronts to form sulfuric acid, which in turn dissolves rock-forming minerals and weakens the surrounding rocks. The oxidation of pyrite occurs through the following chemical reactions,

$$FeS_2 \text{ (pyrite)} + 7/2O_2 + H_2O = Fe^{2+} + 2SO_4^{2-} + 2H^+ \quad (1),$$

$$Fe^{2+} + 1/4O_2 + H^+ = Fe^{3+} + 1/2H_2O \quad (2),$$

$$FeS_2 \text{ (pyrite)} + 14Fe^{3+} + 8H_2O = 15Fe^{2+} + 2SO_4^{2-} + 16H^+ \quad (3).$$

If pyrite is present enough, ferric ions can react again with pyrite. Conversely, when pyrite disappears, the precipitation of iron hydroxides begins. The dissolution of chlorite forms Al-vermiculite and iron ions. The oxidation of iron ions forms iron hydroxides that is responsible for the coloration of the yellowish weathered rock.

Figure 1. A reverse fault formed at the terminal of landslide in pelitic schist (Kanjo, Tokushima, Japan).

Pyrite is iron sulphide, and its sulphur component is abundant in seawater. Framboidal aggregates of pyrite (Figure 2) are common in argillaceous deposits and are genetically related to sulphur bacteria. Thus, pyrite and graphite are closely associated in the pelitic schist.
The pyrite oxidation and its caused dissolution of rock may develop landslide. In fact, Yamasaki and Chigira (2011) showed the occurrence of slips in the zone affected by sulfuric acid, just beneath of the oxidation front.

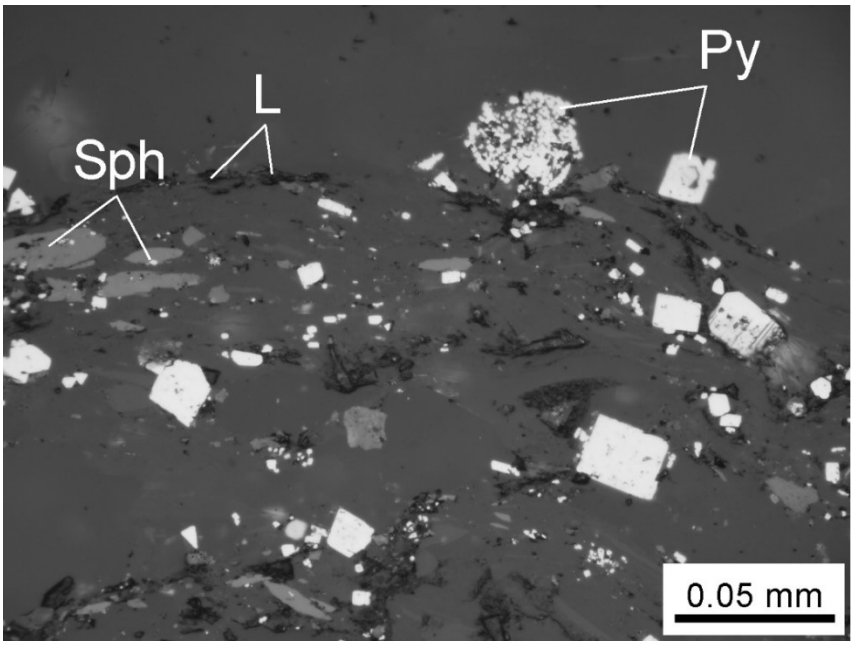

Figure 2. Polished section of pelitic schist observed under a reflected-light microscope. Py: framboidal pyrite and pyrite cubic crystals, L: low hardness minerals (graphite rich areas), Sph: sphene crystals.

Graphite-thin-layers as a weak strength factor

Among the constituent minerals of pelitic schist, graphite and pyrite exist independently, without bonding with other silicates. Layers rich in these minerals have lower strength compared to other parts. Graphite is a characteristic mineral of pelitic schist for coloration of the rock and is known to act as a solid lubricant in addition.

Yamasaki et al. (2016) found that pelitic schist commonly contains black, graphite-rich layers on a scale of millimeter to centimeter thickness that are typically weaker than neighboring layers. Microcracks were typically concentrated and developed within the dark-colored zones enriched in graphite (Figure 3). These microcracks are formed by shearing along graphite-rich -thin layers (Figure 4).

To investigate these mechanisms, Yamasaki et al. (2016) has performed high-precision direct shear tests, using a novel back-pressured shearbox, on artificial rock samples both with and without graphite layers placed between pre-cut shear surfaces. The tests used normal stresses up to 800 kPa (equivalent to 32 m isostatic depth of burial). Then they found that the coefficients of friction for samples with graphite layers embedded in the artificial rock samples (0.30, representing an angle of internal friction of 16.7°) were much lower than those without graphite layers on the pre-cut surface (0.85). The shear strength of the artificial rocks with embedded layers of graphite decreased abruptly with increasing areal extent of the graphite layer along the shear surface, from which it can be inferred that the continuity of a graphite layer in natural pelitic schist has a considerable effect on shear resistance.

From the results of our experiments it can be inferred that during shearing along schistosity of natural pelitic schist, graphite is smeared on the neighboring rock surfaces and dramatically reduces frictional resistance. Because the graphite in pelitic schist is derived from organic-rich sediment, one of the effects of metamorphism is to concentrate it in discrete horizons. If the schistosity of such graphite-rich layers is exposed downslope, shearing within the schistose layers is likely to initiate gravitational slope deformation and landslide.

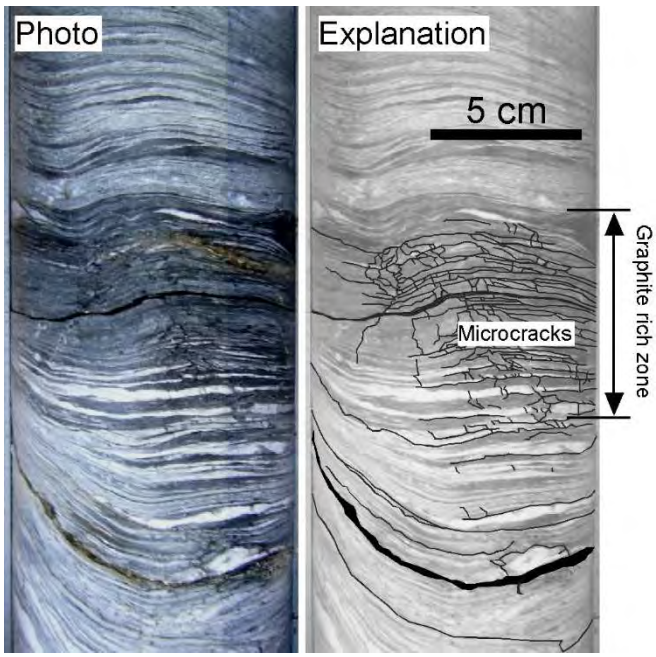

Figure 3. Microcracks are typically concentrated and developed within the dark-colored zones enriched in graphite. This core is a part of high-quality and virtually undisturbed core sample recovered from the depth of 42 m from ground surface.

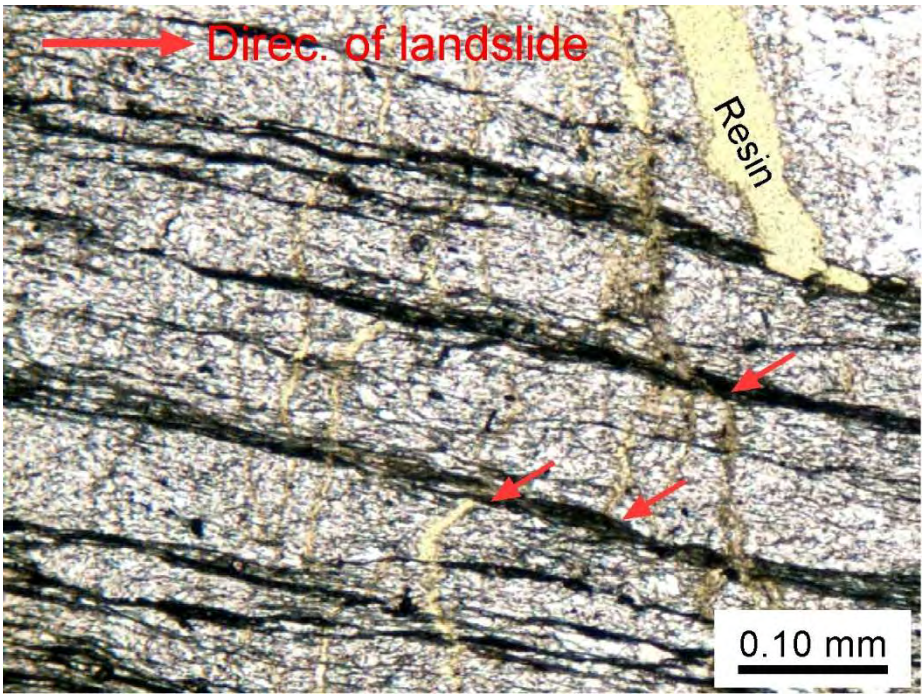

Figure 4. Micro-slips (red arrows) occurred along graphite-rich-opaque layers on a thin-section.

Conclusion

Pelitic schist derived from marine sediments contains two materials of material science and chemistry importance. One is pyrite, which reacts with oxygen on the surface to produce sulfuric acid. The other is graphite, which provides a slippery property to the rock. Sulfuric acid accelerates weathering, and graphite promotes gravitational deformation. Both contribute to the occurrence of landslides.

References

Yamasaki S & Chigira M (2011) Weathering mechanisms and their effects on landsliding in pelitic schist. *Earth Surface Processes and Landforms* 36(4), 481-494.

Yamasaki S, Chigira M & Petley, D (2016) The role of graphite layers in gravitational deformation of pelitic schist. *Engineering Geology* 208(24), 29-38.

A Finite Element model of the Montgonbert landslide calibrated on geophysical survey data

F. Prunier[1], A. Carrier[2], C. Ferey[1]

[1] GEOMAS, INSA, Lyon, France
[2] SAGE, Grenoble, France

SUMMARY: The road between Ugine and Mégève in the French Alps is a major traffic artery linking Savoie and Haute-Savoie. This road is subjected to several natural hazard like rockfall and landslides. In this work we focus on the Montgonbert landslide in the area of Ugine which affects the road and also the UGITECH metallurgy plant. We present a coupled hydro-mechanical model that aims to better understand the main mechanisms that affect the stability of this hillside. One of the main difficulties in using such kind of model is to propose a proper calibration of the mechanical and hydrogeological properties of the rock mass as well as a proper initial state in terms of stress field but also of the initial internal variables of the elasto-plastic model. Here, we present our observational approach to constraining our model using geophysical monitoring.

Keywords: landslide monitoring, hydro-mechanical model, observational approach, stability analysis

Introduction

The Montgonbert landslide overhangs the Arly Gorge road shortly after leaving Ugine. This road is an important communication route between the French departments of Savoie and Haute-Savoie. Because of the economic stakes involved, the region is investing to ensure the road's viability. As a result, the landslide is subject to extensive monitoring and surveillance. In this context, SAGE has developed extensive instrumentation to monitor the site. In this work, we are developing an approach that will enable us to enrich a coupled hydro-geomechanical model with data from this monitoring in order to gain a deeper understanding of the destabilizing mechanisms of this slope.

Instrumentation

For surface displacements, the landslide is tracked using topographic targets. However, some targets are lost due to landslide activity. Photogrammetric monitoring has also been set up (Carrier et al. 2023), with very good results. A few inclinometers have also been placed and used at the head of the landslide to obtain information at depth (see Figure 1). With regard to the site's hydrogeology, some piezometers have been installed at the head of the landslide. In addition, specific Electrical Resistive Tomography (ERT) instrumentation has been developed, providing good results for assessing the permeability of active ground. In fact, Carrier et al. were able to enhance standard ERT techniques with a Time Domain Induced Polarization (TDIP) measurement technique and specific inversion techniques to make this geophysical approach usable in a natural hazard context (see Figure 2).

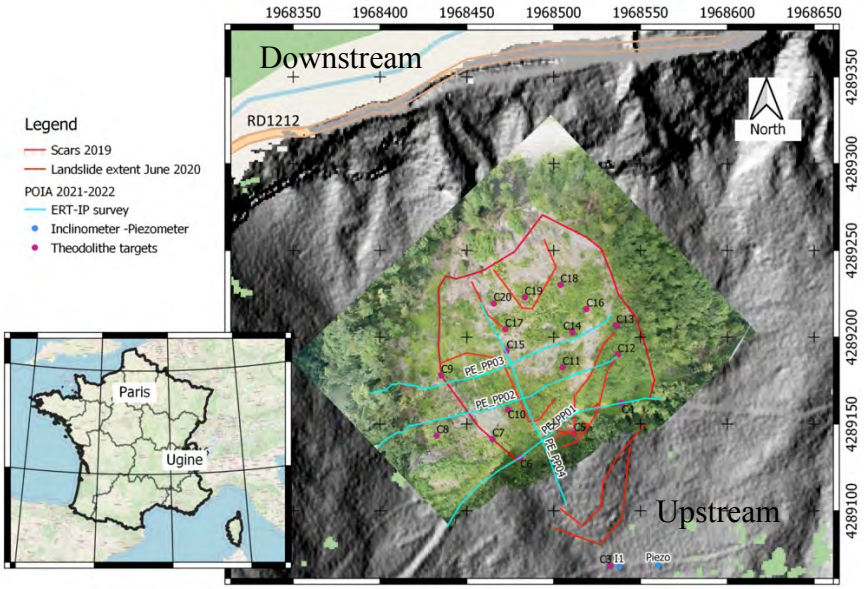

Figure 1: Location of the studied area. (Right panel) Map of the Montgombert Landslide. The spatial extent of the most active part of the landslide is represented by red lines. The location of the geophysical surveys (blue lines), inclinometers-piezometer (blue points) and theodolite targets (pink points) are also represented.

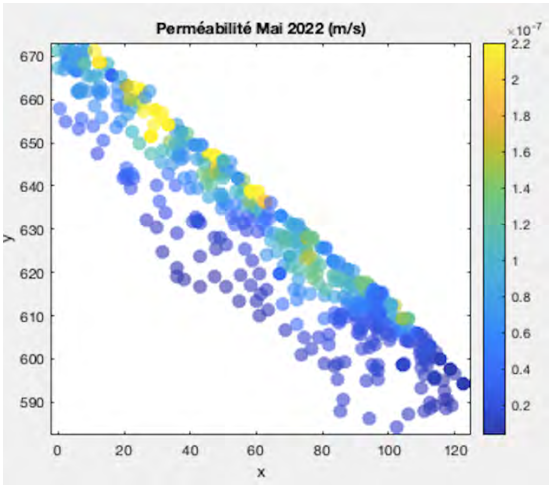

Figure 2: Results of ERT soil permeability assessment along a top-down section in the middle of the landslide

Geomechanical model

The model developed to describe this landslide is rather standard in an academic research context. However, this type of approach is not widely used in practice. On the one hand, the model solves the momentum balance equations in an elasto-plastic framework. On the other, it solves the equations for stationary water flow in porous media, using Darcy's law extended to unsaturated soils. For the problem under consideration, a weak coupling between the solid and the fluid phases using the effective stress principle of (Terzaghi 1936) is sufficient.
The elasto-plastic model used in the simulations is chosen as simple as possible to be able to describe bifurcation problems well known in soils like liquefaction phenomena encountered along undrained loading paths or along an unloading path of the mean stress at constant shear stress. This last loading path can be typical of a rise of a water table due to weather changes (Lignon et al. 2009, Daouadji et al. 2010). The model used is inspired from the Plasol model (Barnichon 1998) and allows simulate the response of dense and loose soils as shown in Figure 3:

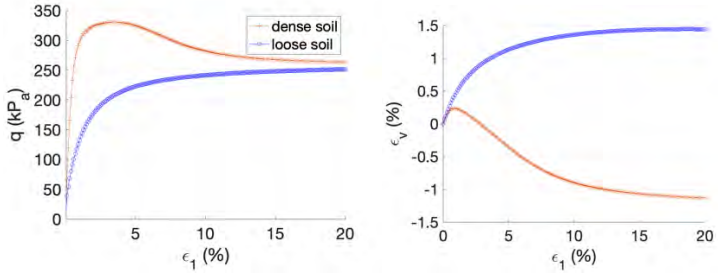

Figure 3. Example of the response of the model along a drained triaxial loading path

For the flow model, the Darcy's law is used. The permeability tensor can be also defined as cross anisotropic. For a sake of simplicity, the permeability tensor is supposed to evolves with the suction in the unsaturated domain using a sigmoïd shape function *P*:

$$\boldsymbol{k} = \frac{1}{\left(1+\left(\gamma\varepsilon_{eq}^{p}\right)^{\delta}\right)^{(1-1/\delta)}}\boldsymbol{k_{sat}} \quad (1)$$

with $\boldsymbol{k_{sat}}$ the tensor of permeability at saturation.

Modelling approach

Even if the model used can be seen as rather simple, it is easy to understand that in a context of natural hazard the identification procedure of the parameters of the model as well as the identification of an initial state of the hillside remains a challenge. We present in the poster attached to this summary the results obtained following the procedure describe bellow on this real case study:

1. find a first set of the permeability tensor for every geological units by back analysis of the geological et geophysical survey
2. initialization of the stress field with a gravity loading by blocking the horizontal displacement along the slope and then relaxing this horizontal locking in several sub step from the top of the slope.
3. identification of the failure parameters of the rock mass using an auxiliary model based on a limit analysis theory.
4. test several sets of unidentified parameters such as elastic parameters and dilatancy angle on the model prediction to qualitatively reproduce observed motions of the landslide over a time series of seasonal events.

The Figure 4 illustrate the results of the 3rd and 4th phase of this procedure. The results are then also analyzed in terms of stability of the hillside using the second order work criterion (Hill 1958). This criterion allows to detect unstable zones along the simulation of a weather loading and to provide a scalar indicator of the stability of the all mass when computing its integral over the volume (Prunier et al. 2016, Prunier and Branque 2019). When this criterion is negative or zero an unstable state is detected, a loss of uniqueness of the mathematical solution of the problem is also detected. Hence the stability of the numerical solution is also very sensitive to small numerical errors.

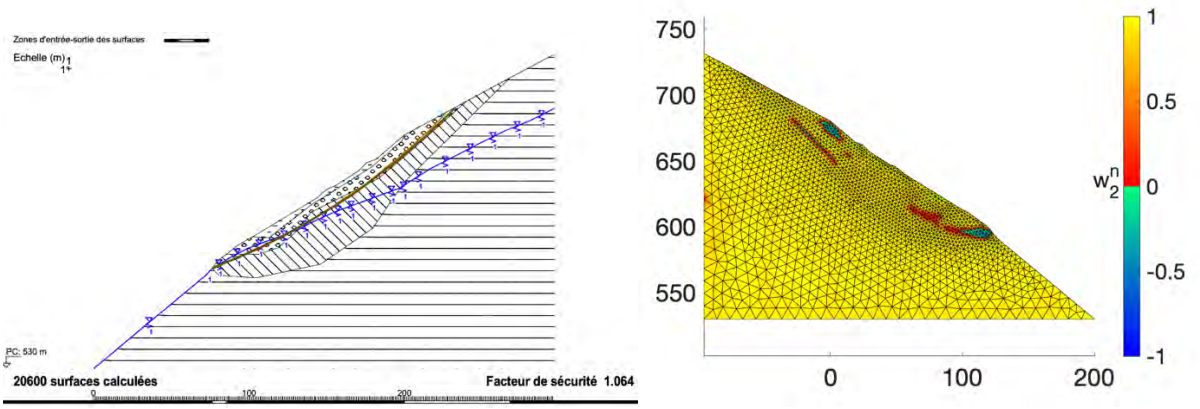

Figure 4: On the left, assessment of the strength parameters of the model using the Bishop limit equilibrium model using pore pressures coming from the flow simulation. On the right, results in term of second order work criterion coming from the finite element simulation: negative values indicate unstable zones

Conclusions

In view of our last remarks on the stability analysis of the problem under consideration, we must remain humble in our attempt to calibrate and optimize our models with inversion methods. Nevertheless, it seems complicated to propose alternative methods. That's why we still like to show our results on this real case study and open a discussion on the possible benefits of integrating an artificial intelligence model into our deterministic model to solve this complex inverse analysis problem.

References

Barnichon J.D., (1998) Finite element modelling in structural and petroleum geology, Ph.D. Thesis, University of Liège.

Carrier A., Meric O., Bottelin P. (2023) Caracterizing landslide dynamics from time-lapse time domain induced polarization and ground based imaging, case study of the MontGombert landslide. *Landslides,* https://doi.org/10.1007/s10346-023-02137-0

Daouadji A, Darve F, Gali HAI, Hicher PY, Laouafa F, Lignon S, Nicot F, Nova R, Pinheiro M, Prunier F, Sibille L, Wan R. (2010) Diffuse failure in geomaterials: experiments, theory and modelling. *International Journal for Numerical and Analytical Methods in Geomechanics*; DOI: 10.1002/nag.975.

Lignon S, Laouafa F, Prunier F, Khoa HDV, Darve F. (2009) Hydro-mechanical modelling of landslides with a material instability criterion. *Geotechnique* **59**(6):513–624

Prunier, F., Chomette, B., Brun, M., & Darve, F. (2016). Designing geotechnical structures with a proper stability criterion as a safety factor. *Computers and Geotechnics*, 71, 98–114. doi:10.1016/j.compgeo.2015.09.007

Prunier F., Branque D. (2019) On the definition of a safety factor using the finite element method in geomechanics, from the static to the dynamic regime, *European Journal of Environmental and Civil Engineering*, https://doi.org/10.1080/19648189.2019.1650119, 2019.

Hill R. (1958) A general theory of uniqueness and stability in elastic-plastic solids, *Journal of the Mechanics and Physics of Solids*, **6**, 239-249.

Terzaghi, K. (1936). The shearing resistance of saturated soils and the angle between the planes of shear. In 1st *international conference for soil mechanics and foundation engineering* (Vol. 1, pp. 54–56). Cambridge.

Van Eekelen H.A.M. (1980) Isotropic yield surfaces in three dimensions for use in soil mechanics, *International Journal For Numerical And Analytical Methods In Geomechanics*, **4**, 89-101.

Applicability of different seismic landslide risk assessment methods: a case study of Maduo Ms 7.4 earthquake

Xiaoli Chen[1]

[1] Institute of Geology, China Earthquake Administration, Beijing, 100029, China

SUMMARY: The following guidelines briefly illustrate the design of extended abstracts for the XIVth International Symposium on Landslides, July 8th-12th, 2024, Chambéry, France. Participants are encouraged to submit at most four DIN A4 pages according to these abstract guidelines.

Keywords: Maduo earthquake, earthquake-induced landslides, hazard analysis,Newmark model, discrimination analysis method

Overall view

Seismic landslide is a kind of natural disaster in which the slope is unstable and slips under the action of earthquake. Unlike landslides triggered by factors such as rainfall, strong earthquakes in mountainous areas tend to trigger a large number of landslides over a wide area, which can cause more casualties and economic property losses than the earthquake itself in many cases. Moreover, the occurrence of earthquake-induced landslides is characterized by abruptness and concealment, so it is difficult to spot monitoring and prevention. In order to reduce the loss of earthquake-induced landslide disaster, scientists have developed a variety of prediction and evaluation methods for earthquake land-slide hazard based on different theories and models through long-term research. The Ms7. 4 earth-quake, which occurred at 2: 04 a.m. on 22 May 2021 in Maduo, Qinghai (34.59°N, 98.34E), provided an opportunity to test the validity of the different models. On the one hand, based on the simplified Newmark displacement model, the susceptibility of seismic landslide in Maduo earthquake area is calculated. Furthermore, the seismic landslide risk is evaluated by combining with the seismic intensity distribution map after Maduo earthquake. On the other hand, based on the discrimination analysis method, the empirical model obtained from the Niigata earthquake in Japan is used to predict the earthquake landslide in Maduo earthquake area. This study will use representative physical and empirical models to predict landslides in the Maduo earthquake research area, and compare the predicted results. Based on this, the applicability of these two types of methods will be further explored.

Result

Based on the rapid assessment of earthquake-induced landslide risk by simplified Newmark displacement model, the potential high-risk areas are mainly concentrated in the intensity area of VI, IX and X which are greatly affected by the intensity of ground motion (Fig.1). On the whole, with the weakening of the impact of ground motion, the landslide risk decreases gradually, this is in good agreement with the actual situation. As an empirical model, discrimination analysis method is relatively dependent on a specific environment. When it is used out of its own environment, it is necessary to verify the universality of empirical formula, re-understand the relationship between various impact factors, and adjust the weight of each factor. The difference between the two methods in the prediction results is mainly in the seismic intensity VI region. In the areas with intensity VII and above, the risk zoning obtained by the two methods is generally consistent. Due to the differences in the research models adopted by the two methods, there are some differences in the distribution of seismic landslide hazard areas with different risk levels in the prediction results, especially in the VI intensity region. Intensity VI region is wide with more mountainous areas, and steep slopes are distributed in most of the areas. As a result, the discriminant analysis results in this area are more influenced by slope and curvature value, so there are more highly dangerous areas in the prediction results (Fig.2).

However, the simplified Newmark method is greatly affected by the ground motion. Because this region is far away from the epicenter and the impact of ground motion is weak, so the main prediction results of this region show more low riskareas. However,in the intensity VlI and above areas, the risk zoning of the two methods was generally consistent, and the prediction effect was good.

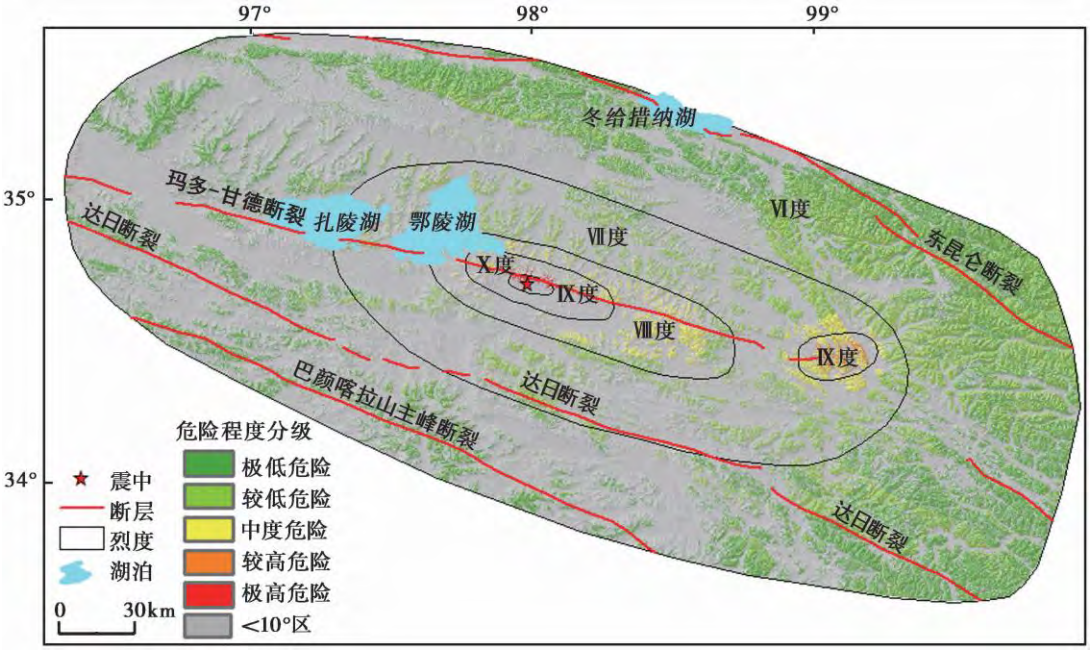

Fig.1 Evaluation of coseismic landslide hazardous zones on Newmark analysis

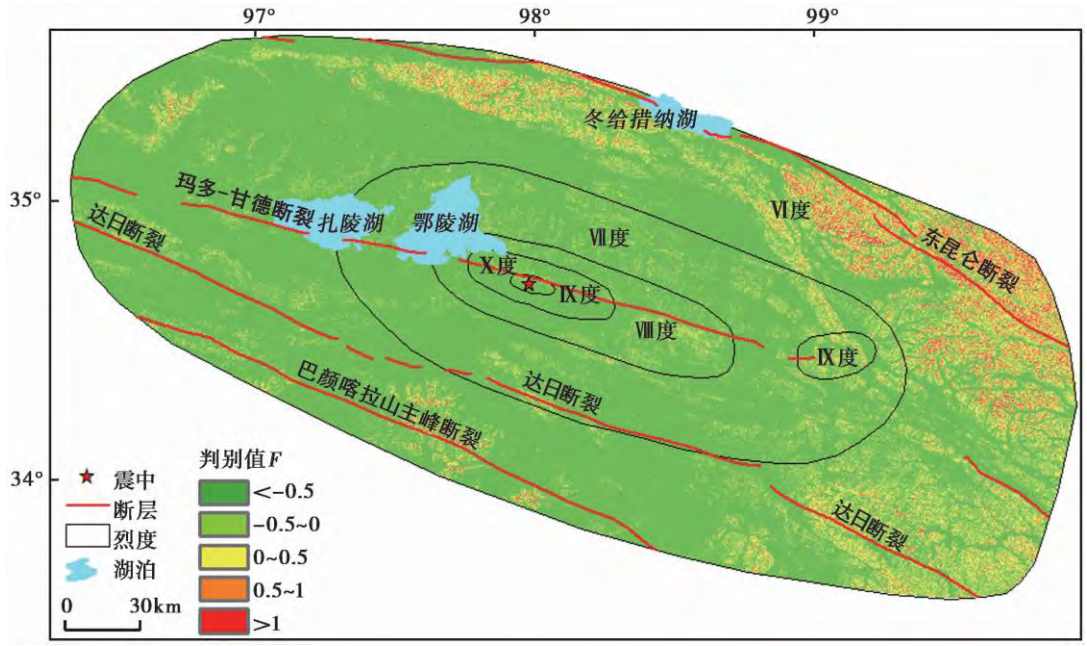

Fig.2 Evaluation map of seismic landslide based on discriminant analysis method

Discussion

It can be seen from the prediction results that these two methods reflect their effectiveness to some extent. However, due to the different factors and fewer constraints, there are some

differences in the results. In the seismic landslide risk assessment based on the discriminant analysis method, objective and complete landslide samples need to be fully analyzed, which is also a problem faced by the prediction method based on empirical model. As a physical model, Newmark model does not depend on the specific environment, althoughit has the problem in accuracy of input parameters, it is more objective and reasonable in the calculation results. In this paper, a simple evaluation and analysis of the Maduo earthquake was conducted based on the Newmark model method, which only considered the impact of slope itself and ground motion, but did not take into account hydrological factors, human activities, geomorphic factors and other conditions. Meanwhile, the Newmark evaluation method needs to obtain relatively clear rock-soil physico-mechanical properties and ground motion parameters, but it is difficult to obtain accurate data of each slope in practice, so there are still defects and deficiencies in regional risk assessment using this model. Compared with other traditional prediction methods based on statistical analysis, the physical meaning of this method is clearer, and it has irreplaceable advantages in combination with ground motion parameters. As a qualitative method, the discriminant analysis method uses the empirical formula derived from other earthquake cases to predict landslides. Engineering geological conditions are different in different earthquake regions, so the controlling factors of earthquake-induced landslide are not the same and the influence weight of each factor is different to some extent. Both qualitative and quantitative methods have their own advantages and disadvantages in the study of regional seismic landslide hazard prediction. It would take a long time to achieve accurate prediction of earthquake landslides.

References

CHEN Xiao-li,SHAN Xin-jian,ZHANG Ling,et al.2019.Quick assessment of earthquake-triggered landslide hazards:A case study of the 2017 Ms7.0 Jiuzhaogou earthquake [J].Earth Science Frontier, 26(2)：312-320 in Chinese).

CHEN Xiao-li,YUAN Ren-mao,YU Lu.2013.Applying the Newmark's model to the assessment of earthquake triggered landslides during the Lushan earthquake J]. Seismology and Geology,35(3)：661-670(in Chinese).

A cross-continent exposition on geohazard risk management strategies

Karlee D. Isfeld[1], James M. Strout[2]

[1] BGC, Calgary, Canada
[2] NGI, Oslo, Norway

SUMMARY: This research explores the similarities and differences of contributing factors for managing and mitigating geohazard risk between regions around the world. It discusses how to manage and communicate geohazards involving engineers, citizens, risk analyzers, and decision makers more effectively and efficiently. This is done through reviewing the history of natural disasters alongside the connection between governmental policy, industry guidelines, and community initiatives for Norway, Canada, and Guatemala.

Keywords: Geohazards, risk management, policy development, case studies, exposition

Introduction

Geohazards, such as landslides, floods, and avalanches, are among the main contributors to worldwide disaster consequences and economic losses due to geohazards are increasing (UNDRR, 2022). The funding available for geohazard risk reduction is limited and competes with other essential activities such as societal development, public health, and environmental protection. The process of allocating resources necessitates a balance between engineering considerations and policy implementation, and raises essential questions: Who is responsible for allocating funds to geohazards and setting priorities? Do citizens have the opportunity to learn about geohazards and express their concern or comfort levels? Are policies, guidelines, institutions, and initiatives approached differently across nations and regions?

These questions are explored through an in-depth look at the timeline of major disasters alongside the development, or absence of, the policies, guidelines and community initiatives for Norway, Canada, and Guatemala. Isfeld (2022) identified strengths and gaps in the systems related to geohazard risk management by displaying the contrast of each of these nations and highlights are provided in this extended abstract. Case studies are presented for each country to emphasize the complexity of implementing geohazard management strategies.

Projects such as SafeLand: Living with landslide risk in Europe: Assessment, effects of global change, and risk management strategies; Work Package 5.2 (Pelling and Demeritt, 2011) and the multi-hAzard monitoring and earLy wARning system (ALARM) (Brenot et al., 2022) previously looked at cross-jurisdictional geohazard risk management. The current study brings a unique perspective to reviewing similarities and differences in geohazard risk management strategies by calling on first-hand accounts and research from three specific countries with different cultures, land mass, population, and governance structures.

Geohazard management state-of-practice

Geohazard risk management is the act of assessing and mitigating the risk of geohazards regarding society, individuals, and the environment. It includes the components of risk assessment, monitoring, and reduction. Quantifying geohazard risk means classifying the

probability of an event, which is the hazard, and identifying the degree to which elements are exposed and their capacity and preparedness to react to and recover from a disaster, also known as the vulnerability. Managing and mitigating this risk requires evaluating multiple risk scenarios, identifying the uncertainty of these estimates, and comparing risks to prioritize funding and resource allocation.

The exposition focuses on the geohazard management techniques of three nations – Norway, Canada, and Guatemala. The countries were chosen, in part, due to the authors connection to and familiarity with them, but also since all three face many compounding geohazards that have caused economic destruction and death to citizens (Guha-Sapir, 2021). In Norway, floods, avalanches, rock falls and quick clay landslides contribute to the most economic and life loss (DSB, 2019). In Canada, earthquakes, floods, and debris flows are among the most destructive (Sassa et al., 2013). The main culprits in Guatemala are hurricanes, earthquakes, extreme weather, and subsequent landslides along ravines (Faber, 2016). These hazards are forecasted to increase in severity and frequency with the rapidly changing climate (UNDRR, 2022).

This study is not intended to be a direct comparison of these three countries. They all have different mixtures of population density, land size, climate, economics, development, and culture. It would be unfair to assume each of these countries should or could manage geohazards in the same manner – Norway being small in population, Canada being the second largest country in land mass of the world, and Guatemala being a developing nation. It is an opportunity to showcase how different societies address geohazard risk management and identify strengths and gaps of each countries' techniques through a comparative study on policy, guidelines and community initiatives.

Case Studies

The case studies presented reflect the geohazard risk management techniques and strategies of the three countries in the context of policy, guidelines, and community initiatives. The Norwegian case study site was evaluated by the Norwegian Public Roads Administration and focused on using the policies and guidelines set by the government institutions for the analysis. The Canadian case study was evaluated by a consulting company which used evaluation techniques reflective of those set in the national guidelines. Reference thresholds were used from nearby jurisdictions since there is no national policy for geohazard risk thresholds. Lastly the Guatemalan case study site was evaluated by an external organization in cooperation with government institutions resulting in education of citizens to perform risk evaluations and implement simple, cost-effective mitigation strategies.

Figure 1. Case study areas: Trollstigen (Norway), Cold Spring Creek (Canada) and Guatemala City (Guatemala). *Photos by J. Strout, RDEK provided to BGC and E. Faber.*

The Norwegian study area is a stretch of road climbing a mountain pass, named Trollstigen in Norwegian. This case study gives detail of the many steps, policies, thorough risk analysis and

citizen engagement that the Norwegian approach to geohazard risk management possesses. However, it also highlights the difficulty local authorities have to allocate funding to geohazards, even when presented with an adverse risk analysis.

The Canadian study area is in the Rocky Mountains of south-western Canada at the Cold Spring Creek fan in the Fairmont Hot Springs community. The Canadian case study will reveal the decentralized decision-making process for risk management that is currently state-of-practice in Canada. The case study follows the risk evaluation and mitigation options presented with reference to surrounding communities to suggest thresholds and suitable mitigation.

The Guatemala study area is in the informal settlements on the margins of the capital, Guatemala City, where even though geohazard risks are threatening homes, the benefits and opportunities being near the city outweigh the risks. The Guatemalan case study is a story of motivated, knowledgeable citizens living in unfavorable conditions. Here the policy restricting building near ravines holds little weight, and due to the lack of governing authority, is rarely enforced.

Discussion

In Norway, there is strong national governance of building codes and land use plans with supplementary guidelines to ensure each new development is being evaluated properly. Consistent, focused effort from governmental organizations like NVE and NPRA have enabled hazard maps, susceptibility maps and warning systems to be developed and openly accessible. Education and online tools have enabled a sense of ownership of hazard recording for civilians, resulting in a more thorough database and prepared communities. Norway's funding allocation for geohazard risks is at a county level and is pooled with all other risks the county may face (Det Kongelige Samferdselsdepartement, 2021). The benefit of this is all risks are evaluated against each other. The drawback is efforts in assessing the hazards may result in more knowledge about the unacceptable risk, however without having the funds to mitigate the risk. This is seen in the case of Trollstigen.

There is much effort put into geohazard risk management in Canada, however it is often isolated to certain municipalities or jurisdictions who set their own management strategies and risk thresholds based on the hazards they face and recommendations from consultants. This can be positive when the thresholds are suited to their unique circumstances. However not having a nation-wide policy on risk management for land use plans, building codes, or risk thresholds leaves much of the decisions up to interpretation and the municipalities with less resources are left without policy to lean on. The awareness of the importance of knowledge transfer in risk reduction, not only from governmental organizations and consultants, but also to civilians, has gained traction in the 2000s in Canada. In recent years, programs have been initiated to set guidelines for practitioners and decision makers (Porter and Morgenstern, 2013) and engage locals in understanding what geohazards are present in the area they live (Reynolds, 2022).

Guatemala's risk management is lacking in terms of enforced land use plans and sound construction practices. However, significant effort has been made to reduce geohazard risk and create resilient communities through community engagement and thoughtful, impactful institutions. Education of community members has been a leading contributor to reducing the risk to geohazards (LaPorte, 2018). A decentralized management institution, CONRED, enables each municipality and jurisdiction to consult with and be educated by CONRED

representatives, who then collaborate, share knowledge and resources among the committee (OCHA, 2022).

There needs to be a shift in the narrative from the notion that risk reduction is solely an expensive way to decrease risk of a hazard that may not happen. Investing in strengthening social safety nets, increasing collaboration and networking, increasing awareness of the risk, and creating community involvement and ownership need to be seen as valuable gains from proactive risk reduction.

Key future studies could extend this research into more countries, review the funding and insurance schemes for geohazards in each country, and study the compatibility and feasibility of implementing the practices of the United Nations Global Risk Assessment Framework methodology.

Conclusion

This research studies connection between governmental policy, industry guidelines, and community initiatives for managing and mitigating geohazard risk implemented in Canada, Norway and Guatemala. It utilizes the differences of these three nations to emphasize the strengths and gaps within their geohazard risk management systems.

The climate is changing, and more disasters are being recorded every year (UNDRR, 2022). Developing state-of-art strategies and proactive risk reduction and adaptation, involving citizens, engineers, risk analyzers and decision makers, need to be the focus for effective geohazard risk management.

References

UNDRR (2022) Global Assessment Report on Disaster Risk Reduction 2022: Our World at Risk: Transforming Governance for a Resilient Future. Geneva.

Isfeld, K. (2022) A cross-continent exposition of geohazard risk management strategies. NTNU. Trondheim.

Pelling, M., Demeritt, D. (2011) Deliverable 5.5 Five scoping studies of the policy issues, political culture and stakeholder views in the selected case study sites – description of methodology and comparative synthesis report. SafeLand Living with landslide risk in Europe: Assessment, effects of global change, and risk management strategies. Work Package 5.2 – Stakeholder process for choosing an appropriate set of mitigation and prevention measures.

Brenot, H. et al. (2022) Decrease of anthropogenic emission from aviation and detection of natural hazards with potential application in geosciences using satellite sensors, ground-based networks and model forecasts in the context of the SACS/ALARM early warning system. EGU General Assembly Conference Abstracts. Vienna.

Guha-Sapir, D. (2021) Our World in Data based on EM-DAT, CRED / UC Louvain. Published online: OurWorldInData.org, https://ourworldindata.org/natural-disasters [Accessed 2023].

Direktoratet for samfunnssikkerhet og beredskap (2019) Analyses of Crisis Scenarios (2019). Protection, N. D. F. C. (ed.). DSB Skien, Norway. (In Norwegian)

Sassa, K., Badaoui, R., Briceño, S., McSaveney, M. & He, B. (2013) Landslides: Global Risk Preparedness.

Faber, E. J. (2016) Development of a landslide risk rating system for small-scale landslides affecting settlements in Guatemala City. Master of Science Geological Engineering, Colorado School of Mines.

Det Kongelige Samferdselsdepartement (2021) Nasjonal transportplan 2022-2033. In: Transport, M. O. (ed.). (In Norwegian).

Porter, M. & Morgenstern, N. (2013) Landslide risk evaluation, Canadian technical guidelines and best practices related to landslides: a national initiative for loss reduction.

Reynolds, R (2022) The Canadian Hazards Emergency Response & Preparedness Research Initiative. School of Community and Regional Planning at University of British Columbia. Published online: https://resiliencemapping.ca/cherp [Accessed 2023].

OCHA. February (2022) RE: United Nations National Disaster Response. Personal Communication.

Rotenfels: analysis of the rockfall hazard on the highest rock face north of the Alps

Steve Gruslin[1], Tiffany Hennebaut[1], Anaïs Endrès[2]

[1] GEOCONSEILS, Contern, Luxembourg
[2] Ecole Nationale Supérieure de Géologie, Nancy, France

SUMMARY: This article describes the methodology used to analyse the geological hazards affecting the highest rock face north of the Alps and presents the results obtained with a view to protecting the road and railway below from the risk of rockfall.

Keywords: Rockfall, trajectometry, risk analysis, securing infrastructures, natural area

Situation

The Rotenfels rock face, the highest north of the Alps (over 200 m high), presents a particular risk of falling and scattered boulders. In recent years, numerous blocks have fallen onto the road and railway below. None risk analysis had been carry out in the past, neither historical monitoring or systematic recording of the number and location of boulders have never been done, so historical statistical data is virtually non-existent.

Figure 1. Two views of Rotenfels, with the road and railway line to be protected clearly visible

Protection against geological hazards is complicated by the fact that the site is a protected natural area, particularly due to the presence of falcons. It is therefore impossible to secure the rock face directly, and boulder barriers are the only possible solution. Boulder barriers already exist in various places, but they are currently insufficient to protect the road and railway effectively. In addition, as we have no statistical data on the history of boulder falls (size, number, point of arrival, etc.), several assumptions have had to be made.

The study we carried out had several objectives: identify the geological risks that could affect the road and railway, determine, where there is no fence, the rebound energies and heights that the fences to be installed will have to withstand, and, where there are already fences, to establish whether the current fences are suitable and which part requires additional fences, which will be designed in an upcoming study. The safety measures to be implemented were determined by means of an in-situ characterisation of the rock, a risk analysis and trajectometric studies. This article presents the methodology adopted, the calculations made, and the results obtained.

Geological situation

Rotenfels lies in the north-east of the Saar-Nahe basin, within a Quartzporphyry (Rhyolite) complex in the Bad-Kreuznach region. The Rotenfels rock face in the Nahe valley at Bad Münster am Stein-Ebernburg is up to 200m high, making it the highest rock face north of the Alps. This domed volcanic edifice was formed by highly viscous rhyolitic magma around 280 million years ago. It consists of rhyolite, a glass-rich effusive magmatic rock with a light colour. The rock is grey to pinkish or red. The rhyolite here contains up to 20-30% quartz phenocrysts, orthoclase, plagioclase, and biotite. Andesite enclaves can also be found in several places.

Methodology

Based on field observations, the entire site was divided into 19 zones with similar characteristics in terms of topography, wall height, rock aspect, ground occupation at the foot of the wall, etc. Due to the protected area restitution, the fields observations must have been made from the bottom and the top of the slope, no rope descent were possible. For each of the zones thus defined, except few zones that were not accessible, the rock was characterised by a series of in situ measurements including stereographic measurements, a survey of the instabilities affecting the wall, Rockschmidt hammer measurements and a classification of the rock mass according to several internationally recognised systems (Q, RMR, GSI). All the measurements taken in the field were used for our risk analysis, enabling us to define the areas from which the blocks could have originated and the dimensions of the unstable boulders to be expected. All these observations have been summarized in a table, the size of the critical blocks (plurimetric), and the blocks found on the ground (around 0.1m^3), have been added to estimate a volume of block (between 0.1m^3 and 1m^3) that should be modelised in the trajectory modelisation. Small stones (<0.1m^3) have also been modelised, according to the volume of scree cone found on site. The distribution of blocks' volume has been determined following a logarithmic normal distribution or normal distribution. The distribution has been changed in function of the zone classification: the most fractured areas present more 0.1m^3 blocks, and the more massive areas 0.2m^3 blocks.

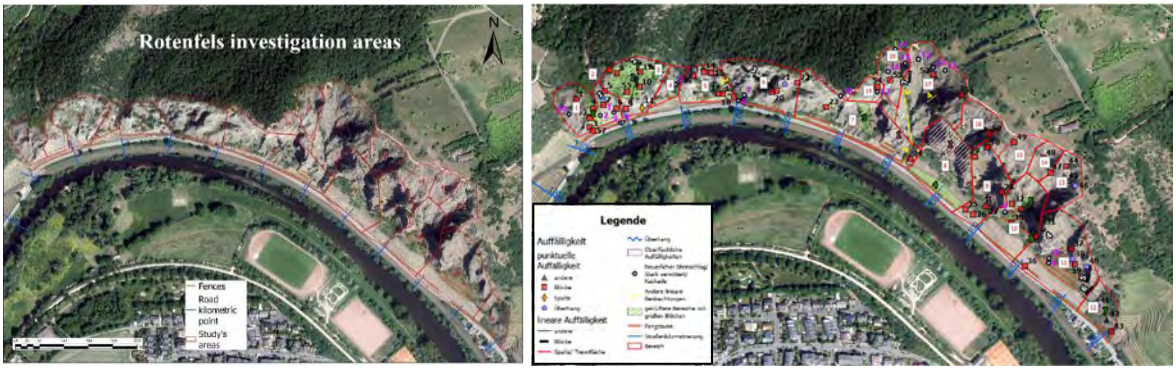

Figure 2. Zoning of the site studied into 19 zones (left) and the diverse observations made on site (right)

Trajectometric studies and Rocfall simulations

Three main types of blocks have been defined. The volume of the block was defined by field assessment, i.e.: the critical volume of the block verified for each zone, the orientation of the various joints and their persistence, and the volume of the block found on the ground or at the foot of the slope for each zone. These observations enable us to estimate two main scales of boulder, with a volume of around 0.1 – 0.2m^3, and a volume of around 1m^3. The small rocks (from 0.0005m3 to 0.1m3) have also been modelised by the interpretation of scree cone volume. They have been modelised in the 3D model along weathered areas mostly located on the crest.

To a lesser extent, boulders with a volume of 5m^3 were also modelled to consider the collapse of the largest element. This volume of 5m^3 is an average volume given the fragmentation of the block along the fall and the rebound. Some exceptional boulders, close to the foot of the cliff, have been modelled with a volume of 10m^3. But these events remain exceptional, and therefore haven't been used to estimate the energy and rebound to be taken up by the barriers. The 2D simulation with large boulders have been made only for critical cut or where large block where suspected on site. For the 3D simulation, all observations collected in the field were uploaded to the 3D model (weathered areas, critical blocks, scree cone, angle slope …), the seeders have been modelised with lines or punctual points.

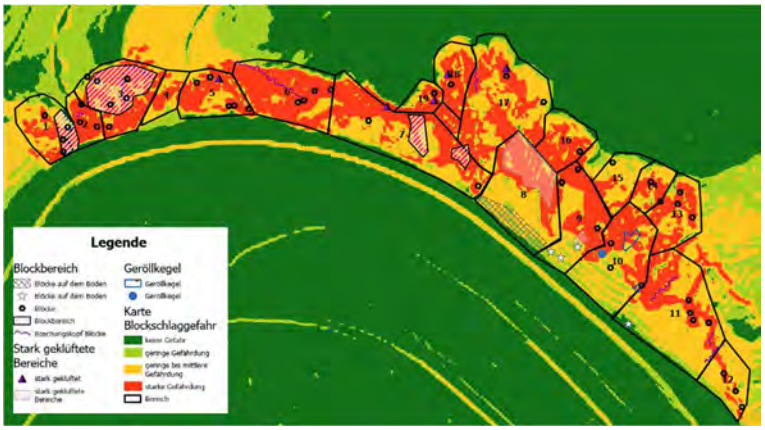

Figure 3: map used for the 3D model

The punctual points were assimilated as 1 linear meter, and by linear meter between 2 to 5 block and 45 stones per linear meter were modelised each time in the 3D model, according to the steep of the slope and the observation made on site.

Table 1 : Number of blocks per type

Blocks and rocks size	**Occurrence per linear meter in function of blocks**
0,1 m^3	5
0,2 m^3	2-3 depending on the weathering of blocks
0,3 to 1 m^3	3
0,1 to 0,0005 m^3 (stones, very weathered areas in the crest of the slopes)	45 / lm

The parameters used in the simulations are based on the Schmidt hammer when measurement have been possible (Rayudu, 1997), or from the Rocfall library for a granite material. For the 3D modelling, the contour lines acquired by Lidar were imported. The software then creates a surface by triangulating these lines. This 3D representation is used to model the propagation of the blocks in space. The 3D model also allows to represente the ended point of each modelised block Figure 4, the simulations shows that the ended point could reach the highway and the train tracks. Thanks to this simulation we have been able to converge the models results with the observation made on site. Indeed, the models showed a lot of end points where most of the falling blocks and scree cone have been referenced. The rocks falling from the model also follow the preferential path of hydraulic surface flows.

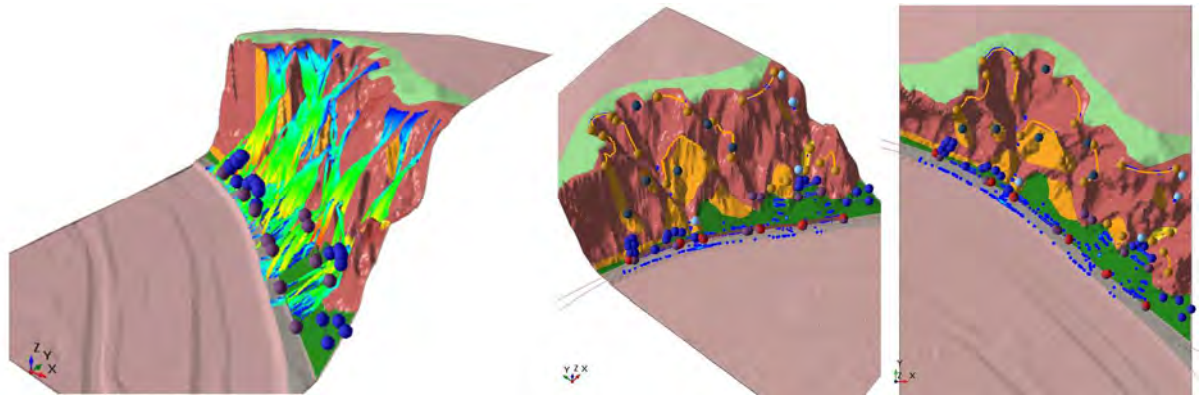

Figure 4: some rockfalls simulation in areas 7 to 10 (left), and the ended distance they reached (right)

With these simulations, we were able to estimate the propagation hazard, which will draw the areas to be treated as a priority.

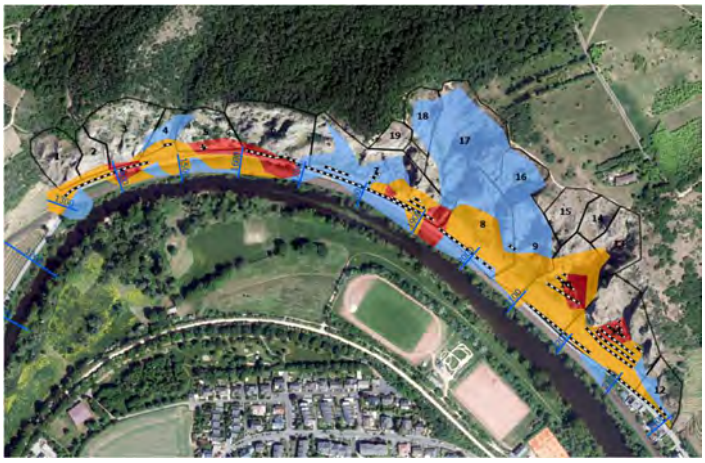

Figure 5: propagation hazard

Thanks to the 3D refined model, we were also able to precise the most critical areas where the fences should be installed or renew, in order to protect the most mainly risky part of the road and train track. These results are limited to blocks with a 95% probability of occurrence, which mean that the more extreme results are considered exceptional events with an acceptable occurrence rate for users.

Conclusions

All the calculations have shown that the risk is very real for road and rail. The methodology put in place, enabling the acquisition of the field data needed for the trajectometric calculations, made it possible to determine the input data (energy and height of rebound) needed to dimension, in a second phase, the safety measures to be implemented to protect the road and the railway line.

References

Landsamt für Geologie und Bergbau Rheinland-Pfalz (2005) Geologie von Rheinland-Pfalz, E. Schweizerbart'sche Verlagsbuchhandlung (Nägele u. Obermillen), Stuttgart.

Rayudu DNP (1997) Computer simulations of rockfalls – Application to rockfalls at fox glacier, West Coast, New Zealand, *Thesis,* Lincoln University.

Sari M (2018) Investigating relationships between engineering properties of various rock types. *Global Journal* of earth sciences and engineering 5, 1-25.

A New Natural Hazard Management Policy For The French Railway Network As Applied To Rock Slope Stabilisation

A. McCallum[1], F. Chirouze[2], A. Lelièvre[1], A. Frison[3]

[1] SNCF RESAU, DGII DT GC VA PGRN, La Plaine St Denis, France
[2] SCNF RESEAU, DGII DZI SE PRI MONTPELLIER, Montpellier, France
[3] SCNF RESEAU, DGII DZI SE PRI CHAMBERY, Chambéry, France

SUMMARY: SNCF RESEAU has adopted a new natural hazard management policy to help maintain safety levels along the railway network based on *quantitative risk assessment* combined with the concept of *risk acceptability*. The systematic quantification of derailment risk related to rockfall, landslide, mudflow, flooding, or riverbank erosion events allows SNCF RESEAU to determine precisely the reinforcement works needed on each site to reach the acceptable threshold. It also makes it possible to prioritise these works and to propose regional multi-year investment plans adapted to the degree of risk of each studied site.

Keywords: risk management, natural hazards, risk acceptability, railway network, rockfalls

Introduction

Efforts to reduce the risk related to natural hazards to the lowest possible level are unattainable due to unbearable costs placed upon the infrastructure manager. As a result, certain required stabilisation works must be abandoned or postponed, resulting in degraded network quality which can last for many years.

To solve these complex situations, SNCF RESEAU has developed a risk management policy based on *quantitative risk assessment* combined with the concept of *risk acceptability*. In other words, we accept that a critical event (i.e., collision or derailment) may occur at a specific risk threshold, which greatly impacts our natural hazard management policy. This threshold stems from French regulatory texts on the level of acceptability of natural risks, for example prevention plans of foreseeable natural hazards (see Code de l'environnement 2019) and is expressed as the occurrence of an event on the scale of human life (i.e., one in 100 years).

Risk management methodology

Our risk management methodology relies on the quantification of the risk of collision/derailment (also known as the *quantitative risk assessment* method or QRA, *as seen in Farvacque et al., 2019 and 2021*). First a risk analysis is conducted which helps both understanding of the mechanisms involved in the initiating events (landslips, rockfalls, flooding, riverbank erosion, etc.) and estimating to what extent the earthwork asset will be able to withstand these events without a critical event occurring (i.e., collision or derailment). This analysis relies on field study combined with archived data including records of previous events, stabilisation works, and reports. Modelling techniques can also be used to support risk analyses, particularly for flooding and rockfall hazards.

The risk of collision/derailment R_{OTH} is expressed as the annual probability of occurrence of such critical event and relies on the characterisation of three parameters:

$$R_{OTH} = O * P * A \quad (1)$$

The probability of occurrence (O) is the probability of an initiating event (e.g., landslip) to take place within a specific time frame. The probability of propagation (P) is the probability, once the initiating event has occurred, that obstruction or lack of rail support (e.g., riverbank erosion) takes place. The probability of arrival (A) is the probability that the train hits the obstacle/reaches the unstable or unsupported rail section.

Then, if the resulting risk of collision/derailment is above the acceptable threshold (defined as 1% per year), risk reduction measures must be taken within a given timeframe to reach the acceptable level, not necessarily the null level. The higher the degree of risk, the shorter the timeframe for response. This methodology is now regularly applied to assess the need of stabilisation works and their completion time; “au juste besoin”.

The ultimate objective of this new methodology is to ensure the reinforcement of a maximum number of assets at the right level of need within appropriate time frames, while assuring railway safety (see Fig. 1).

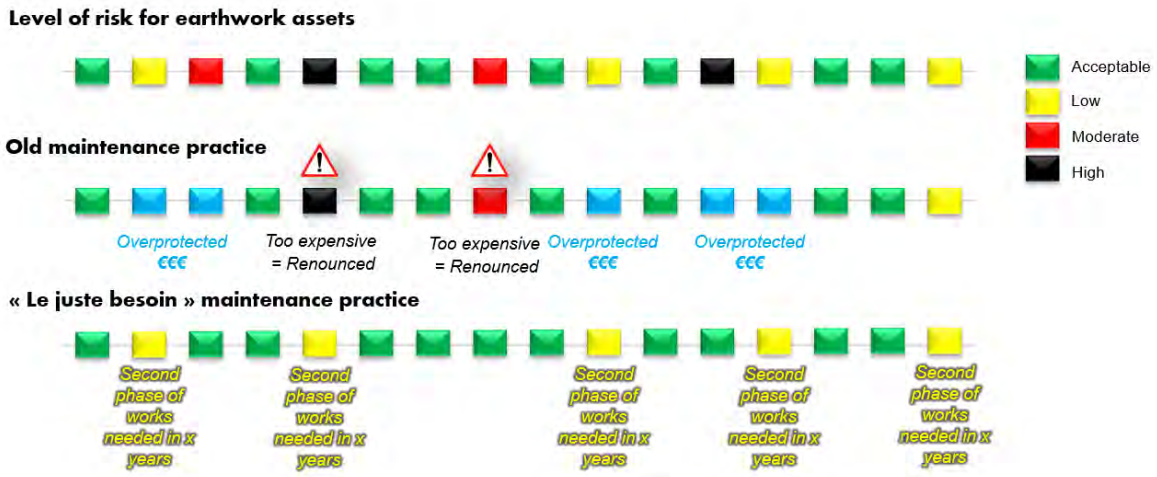

Figure 1. Managing and planning rail safety maintenance using the new natural hazard management policy

Application to rock slope stabilisation

This policy was first implemented during the study of a 5-km-long line section located along the railway line going from Miramas to L'Estaque, west of Marseille, in 2019. There, several rock walls carved into folded limestone beds had suffered repeated rockfalls with significant consequences for rail traffic safety and flow over the past ten years. The corresponding reinforcement works would have mitigated rockfall hazards at three of the twelve identified earthworks with a provisional cost estimate of €12,000,000.

Quantifying the risk of collision/derailment related to the rockfall hazard along the line section allowed SNCF RESEAU to determine the exact reinforcement works needed on each site to reach the acceptable threshold. It was also possible to propose a multi-year investment plan adapted to the level of risk based upon the prioritisation of stabilisation works. The works aiming to secure the line section could finally be implemented on five earthworks for an amount

totalling €3,000,000. This brought the degree of risk below the acceptable threshold and helped raise the performance of that line section.

The policy has since been rolled out network wide. Here we describe a further three rockfall-prone study sites illustrating the wide-reaching benefits of the policy.

The first study site is located along the railway line going from Béziers to Neussargues, Southwest of Millau. This site exposes a 90m-high vegetated, rocky hillslope where 5 to 30m-high limestone and dolomite beds are visible. These highly fractured outcrops show rock masses reaching up to 200m^3. A private study, first carried out in 2009 then reassessed in 2013, recommended the installation of several flexible rockfall barriers in the following five years based upon visible hazards. However, these works could not be financed within this timeframe.

A detailed analysis of rocks fallen on the hillslope and in the vicinity of the railway made it possible to characterise the distribution of associated rockfall volumes. Two rock groups could be identified: blocks from 1 to 5 m^3 represent 90% of observed fallen rocks while blocks from 5 to 20m^3 represent only 10% of the observed blocks. Given the lack of recent fall or activity in the past twenty years (fallen blocks are covered with moss or embedded in the soil), the probability of occurrence (*O*) for common and rare rockfalls was then lowered from the 2013 reassessment. Combined with the probability of propagation (*P*) estimated in the private 2009 study for these two groups (using rockfall propagation simulations), the degree of risk for rare events ended being beneath the acceptable threshold and the time frame to implement flexible rockfall barriers for common events in order to reach the acceptable threshold has been extended up to twelve years.

The second study site is located along the railway line going from Culoz to Modane, Southeast of St Jean de Maurienne. This site exposes a 50m-high, subvertical limestone rock wall topped by a 140m-high cliff. Both are highly fractured outcrops showing rock masses of up to 10m^3. Fifteen rockfall events have been recorded over the past 60 years, attesting to a relatively active site. Since 1983, the site has already been equipped with passive rockfall netting, bolting and local rock meshes confining some of the bigger rock masses, as well as a vertical detection system. Two private studies carried out in 1996 and 2005 recommended adding horizontal detection to the existing detection system, a rockfall barrier, and rock bolts. The resulting response cost to fully secure the site was estimated near €1,500,000.

Combining detailed mapping of rock masses using UAV, in-situ rockfall hazard identification, and 3D-modelling of rockfall trajectories, we were able to better constrain rock hazard, i.e., volumes considered as a risk for rail traffic, and to reassess the probability of occurrence (*O*) for each of those rock groups. In-depth analysis of rockfall propagation simulations helped us characterise the associated probabilities of propagation (*P*). The corresponding calculated degrees of risk confirmed the need for stabilisation works for only one of the four sections of the site investigated in the previous studies. Moreover, comparison with the acceptable risk threshold made it possible to determine the characteristics (maximum energy and height) of the required flexible rockfall barrier to guarantee an acceptable level of risk. The barrier must intercept 72% of the propagating simulated blocks, not all of them. In the end, the risk is made acceptable with the sole implementation of two flexible rockfall barriers (>2200 kJ at SEL and >100kJ at MEL) for a total cost of less than €200,000.

The third study site is located along the railway line from Lyon to Genève, 30km West of Culoz. The site exposes a poorly vegetated scree slope at the base of a 40 to 200m-high, subvertical

limestone rock cliff. Large rockfalls and rockslides involving volumes of 5 to 300m^3 have been recorded over the past 100 years. The site is equipped with a vertical detection system; undetected rock masses falling on the tracks is considered the predominant risk. The rockfall study carried out in 2009 helped characterise rockfall hazard and suggested installation of a 600m-long rockfall protection embankment topped with a detection system, as well as flexible rockfall barriers over a 400m-long section to manage the risk.

A recent in-situ rockfall hazard identification showed that most of the fallen rock masses are smaller than 5m^3 despite larger volumes identified on the outcrops, implying fragmentation process at the moment of impact. 2D and 3D rockfall simulations of the two rock groups helped locate the preferential paths, identify sections at risk, and quantify the corresponding probability of reaching certain track sections (P). The reassessment of parameters O and P, and the consideration of the existing detection system reducing parameter A, shows that the risk R_{OTH} is below the acceptable threshold. The proposed protection infrastructures could therefore be abandoned, saving more than €1,350,000 to be allocated to other sites.

Conclusion

The risk management methodology recently implemented at SNCF RESEAU is an essential tool for managing and planning rail safety maintenance at the scale of individual sites but also of entire line sections. The methodology, described here for rockfall hazard, makes it possible to standardise the quantification of the risk of collision/derailment towards the variety of natural hazards (landslips, floods, riverbank erosion, etc.) affecting the railway network. The acceptable risk is therefore standardised at the scale of our entire network regardless of the hazard and enables optimisation and priorisation of stabilisation works on a national scale; reducing the degree of risk to the network as a whole and increasing safety levels nationwide.

References

Code de l'environnement (2019) Partie réglementaire (Articles R121-1 à R714-2) - Titre VI : Prévention des risques naturels (Articles R561-1 à R566-18) - Chapitre II : Plans de prévention des risques naturels prévisibles (Articles R562-1 à R562-20).

Farvacque M. et al. (2019) Quantitative risk assessment in a rockfall-prone area: the case study of the Crolles municipality (Massif de la Chartreuse, French Alps), Géomorphologie : relief, processus, environnement, vol. 25 – n° 1 (7-19).

Farvacque M. et al. (2021) Quantitative rockfall risk analysis for railway using 2D block propagation simulations, 5th RSS Rock Slope Stability Symposium, Chambéry 2021 (pp.71).

Failure Surface Reconstruction of The Frank Landslide, Alberta, Using Spline Interpolation Method

Jaspreet Singh[1], Sergio A. Sepúlveda[1]

[1] Simon Fraser University, Department of Earth Sciences, Burnaby, B.C., Canada

SUMMARY: Landslide natural hazards are frequently encountered in hilly terrains. In rock slides, the slope failure surface might be governed by different discontinuity sets, leading to a complex failure. Sometimes, it becomes difficult to determine the failure surface/depth even after the failure due to debris cover. Borehole or geophysical methods are commonly used for logging to determine the location of the main failure surface. Alternatively, spline curves can be used to obtain reliable approximation of failure surface profiles based on surface geomorphic features using simple 1D approximations. This study presents a new approach based on existing spline interpolation techniques to automatically estimate the failure surface depth of the Frank landslide, Alberta, Canada using input gridded DEM data.

Keywords: Landslide, failure surface, debris, remote sensing, DEM

Introduction

A landslide is a complex phenomenon that includes the failure of natural material under the influence of gravitational forces along a weak surface (e.g. Hutchinson, 1983; Sepúlveda et al., 2023; Singh et al., 2023). This weak surface is defined as a failure surface. The failure surface can be planar, circular, parabolic, or complex, depending on the nature of the material involved. The landslide failure surface controls the propagation of the slide and the volume of the material involved (Singh & Sepulveda, 2023). The landslide volume, defined by the failure surface, is an important parameter that controls the runoff distance of failed mass and, thus, the potential damages related to this phenomenon. In this study, we selected the famous Frank landslide (year 1903), Alberta (Fig. 1), to validate our methodology based on spline interpolation to estimate the failure surface depth using high-resolution remote sensing LiDAR data originally acquired by Dr. Matthieu Sturzenegger.

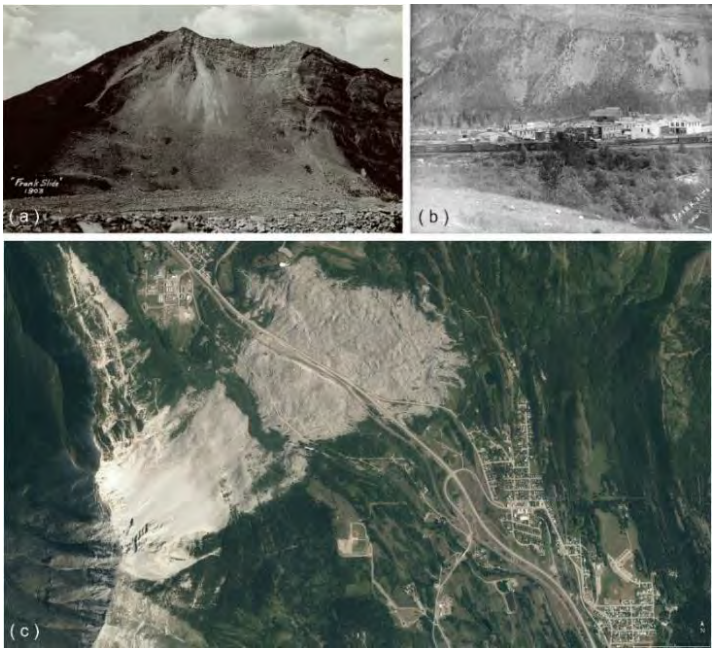

Figure 1. (a) Old photo of the Frank Landslide (Glenbow Archives) (b) Archive photograph of the Turtle Mountain before the landslide (Glenbow Archives) (c) Google Earth imagery showing the scarp

Spline interpolation method

Mathematically, a cubic spline is described as a function defined piecewise by a cubic polynomial having continuous first and second derivatives along each section (Guéziec 1996). Splines are lines or surfaces that are commonly used in 3D geological models. Splines can be used to obtain reliable estimates of failure surface profiles based on geomorphic features using simple 1D approximations (Jaboyedoff & Derron, 2015). A cubic spline curve is computed using two endpoints marking the boundary conditions and their first and second derivatives (Eq. 1).

$$S_i(x) = a_i + b_i(\mathrm{x} - x_i) + c_i\,(\mathrm{x} - x_i)^2 + + d_i\,(\mathrm{x} - x_i)^3 \qquad (1)$$

Where $S_i(x)$ is the cubic spline function for the i^{th} segment, passing through x_i. a_i, b_i, c_i and d_i are constants. This work is based on the development of existing methodology proposed by Prajapati & Jaboyedoff (2022), where the user manually feed the slope angles of left and right flanks for interpolation. The algorithm developed in Python in this study automatically considers the slope of the extreme boundary (such as right flank, left flanks, toe and crown region) based on the input DEM gridded data to interpolate the failure surface.

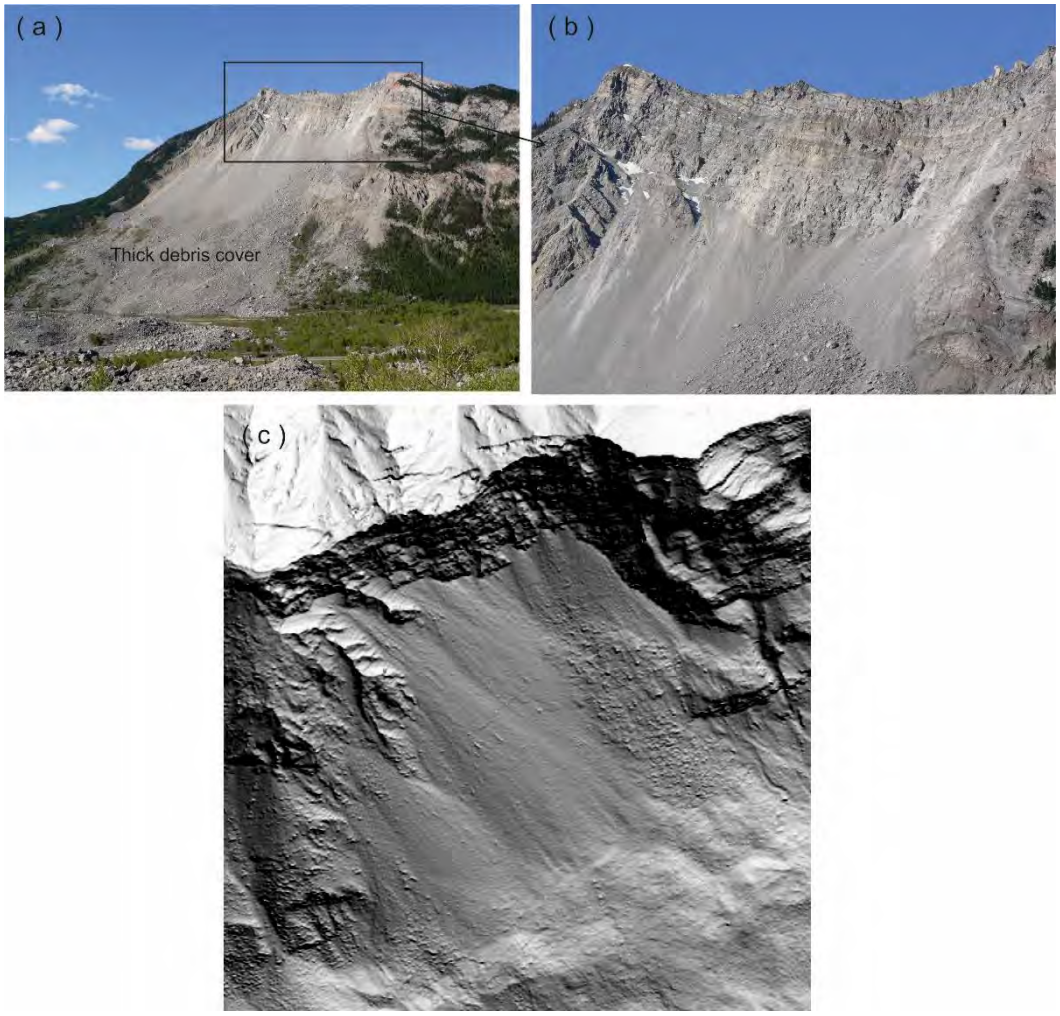

Figure 2. (a) Full view of the scarp of the Frank landslide showing deposited debris in the central region (Photo taken by Dr. D Donati) (b) Crown portion with visible failure surface (c) Hillshade of the affected region, showing visible failure scarp in the crown and left flank region.

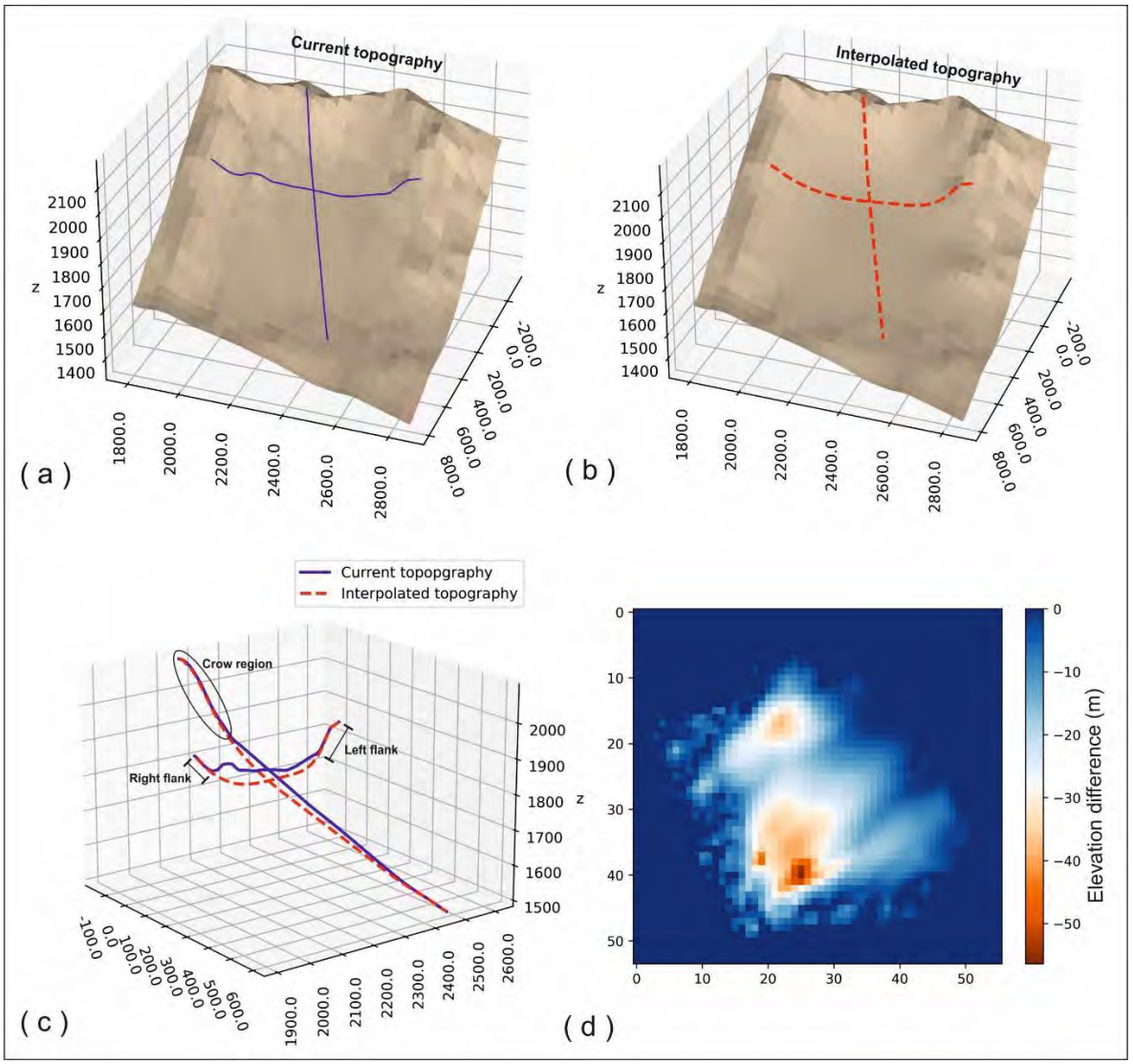

Figure 3. (a) Current 3D topography of the Frank slide (b) Interpolated 3D failure surface (c) 2D profiles marked along and across the slope (d) Comparison between current and interpolated topography

Landslide failure surface and depth estimation

A case study was conducted to demonstrate the applicability of new algorithm developed in Python for failure surface and depth estimation. It can be seen in the field photographs (Fig. 2a,b) and hillshade (Fig. 2c) that the failure surface of Frank Landslide is not fully visible, it is covered by the failed debris material. The thickness of the debris cover is increasing down the slope. The exposure of the failure surface can only be seen in the crown and flank region (Fig. 2). To estimate the failure depth, first, the DEM of the affected region was generated using available LiDAR data. The most important part, boundary of the landslide was marked from the hillshade to run the interpolation just in the designated region. The developed cubic spline method algorithm in Python was used on the input gridded data (DEM) for interpolation to reconstruct its failure surface and depth estimation. The results of the interpolation are displayed in Fig 3b, c. 2D profiles along and across the slope are plotted in Fig. 3c. The Blue line marks the existing topography, and red indicates the reconstructed one. The overlapping of the red and blue lines in crown regions marks that the reconstructed topography followed the slope of the crown region where the failure surface was visible. A similar pattern can be seen in the section across the slope profile, where the interpolation follows the slope of the flanks (Fig. 3c). The algorithm automatically reconstructed the 3D failure surface by following the slope of the

boundary constraints (crown, toe, right flank and left flank) interpolated towards the centre of the slide without any manual intervention. The iterations were interrupted when the change in the subsequent iteration was less than a given threshold limit. Fig. 3a and Fig. 3b show the current 3D topography and interpolated failure surface of the landslide after removal of the debris, respectively. The comparison of the current and interpolated topography is shown in Fig. 3d. The figure shows the elevation difference between interpolated topography minus current topography for each cell. It was found that on an average the estimated failure surface is 13m below the current debris cover, with the maximum depth of 50m in the lower regions. The thick debris cover in the lower region of the slope can also seen in Fig. 1a. Computing the volume, it was found that approx. 7 Mm^3 of debris is still resting over the failure surface. It is not the final volume of the slide, as lot of material has been displaced during the initial rock avalanche and later due to erosional activities. But the figure lies close to the volume computed by Jaboyedoff et al. (2009) using SLBL which was approx. 10 to13.5 Mm^3.

Concluding remarks

Landslides are an alarming risk of loss of infrastructure and lives. To understand the hazards associated with them, it's important to study the failure surface, depth and the volume involved. In most cases, the failure surface is not visible even after failure due to buried underneath the failed debris. Geophysical or borehole drilling is commonly adopted for subsurface mapping and failure surface depth estimation, which is economically expensive. This study discussed a new methodology based on spline interpolation algorithm developed in Python to estimate the depth and failure surface of a landslide. The algorithm automatically considers the slope of the failure boundary, such as crown, toe and flanks, based on input DEM to interpolate the failure surface. The method provides a good approximation of the failure depth where other means are inaccessible and can be further refined using the additional available data.

Acknowledgements

This work is funded by the FRBC Endowed Research Chair at Simon Fraser University. LiDAR data was originally taken and processed by Dr. M. Sturzenegger.

References

Guéziec A (1996) Spline curves and surfaces for data modeling. In: Marcus LF, Corti M, Loy A, Naylor GJP, Slice DE (eds) Advances in Morphometrics. *NATO ASI Series (Series A: Life Sciences Springer, Boston, MA)*.

Hutchinson JN (1983) Methods of locating slip surfaces in landslides. *Bull. Assoc. Eng. Geol.* 20, 35–252.

Jaboyedoff M, Couture R, Locat P (2009) Structural analysis of Turtle Mountain (Alberta) using digital elevation model: Toward a progressive failure. *Geomorphology (Amst)* 103,5–16.

Jaboyedoff M, Derron M-H (2013) A method for quantifying the probability of the depth of a landslide failure surface and of quaternary valley infilling. *In: GéoMontréal 2013, the 66th Canadian Geotechnical Conference*.

Prajapati G, Jaboyedoff M (2022) Method to estimate the initial landslide failure surface and volumes using grid points and spline curves in MATLAB. *Landslides* 19, 2997–3008.

Sepúlveda SA, Ward BC, Cosman SB & Jacobs R (2023) Preliminary investigations of ground failures triggered during the mid-November 2021 atmospheric river event along the Southwestern British Columbia highway corridors. *Canadian Geotechnical Journal* 60, 580-586.

Singh J, Sepúlveda SA (2023). Landslide failure surface and volume estimation using a sloping local base level (SLBL) method: a case study. *Indian Geotechnical Conference*, Roorkee, December 2023.

Built infrastructure and small mass movements in western Switzerland– What can be expected in the future ?

C. Amalia Gutierrez[1,2], Michel Jaboyedoff[1], Christian Gerber[2], Marc-Henri Derron[1]

[1] Risk Group - Institute of Earth Sciences - University of Lausanne, Switzerland
[2] Unité des Dangers Naturels, Direction Générale de l'Environnement, Canton de Vaud, Lausanne, Switzerland

SUMMARY: Analysis of an inventory of mass movement events related to roads, railways and related infrastructure was carried out in the canton of Vaud, in Switzerland. The majority of events are concentrated around the main cities and roads in pre-alpine and alpine regions. General analysis of the inventory revealed the trend of events over time and a more in-depth analysis of a second inventory, compiled by the authors, aims to estimate the costs in preventive measures, damages, and repairs of small events, over time. A simple model was used to extrapolate the given costs in a year into the future, which are expected to increase given current conditions.

Keywords: Transport infrastructure, cost prediction, landslides, climate change

Introduction

The canton of Vaud, located in western Switzerland, witnesses a great variety of relief – from plains to steep alpine mountains– various climatic conditions, when combined with the geology and topography, results in a wide range of susceptibilities to landslides and other mass movements. The highest are found in the Alps, additionally to being the first natural barrier of over 3000 meters for winds coming from the Atlantic, is subject to a growing number of very localized storm cells. This explains that the main hazards in this area are either liked to snow (avalanches) or to high precipitation events (floods, debris flows, and landslides).

Additionally, a dense network of roads and railways is exposed to the effects of all kinds of instabilities, especially in mountainous areas, which can represent significant costs for authorities. In turn, changes in the weather patterns such as increase of precipitation during single events can further accelerate natural processes of degradation impacting the built infrastructure, such as roads, bridges, walls, and protective nets.

Methods and data

In order to get a better overview of the costs and impacts of instabilities affecting transport networks, pre-existing inventories of events in the region were used, mainly from the cantonal inventory which includes data collected by Voumard et al., (2018), as well as manually collected data on more recent events (last 5 to 10 years). Sources for these events include newspaper articles, official statements, field inspections and reports from firsthand witnesses, as well as cantonal and municipal documents (freely available on the web) from which repair and/or cleanup costs could sometimes be ascertained. A general statistical and spatial analysis of this first inventory was carried out. The classification of mass movements and their acronyms, defined in the cantonal inventory are used here: shallow landslides (GSS), rockfalls (CPB), deep-seated landslides (GPP), debris flows (LTO) and rockslide (EBO).

Then, a second inventory was compiled, including only events for which the precise date, location and damages or repair, as well as costs of either preventive measures or post-event reparation and cleanup, were known. This was used for the analysis and modelling carried out at a later stage. The following data were compiled: site location, event date, event coordinates, type of damage, type of infrastructure, repair type, meteorological conditions, geometrical dimensions, temporality, costs of works, duration of interruption, presence in the cantonal inventory and presence of cluster of events or not.

Analysis of the inventories

The initial cantonal inventory was downsized from an initial 4366 events dating from 1740, to 735 events corresponding to mass movements along roads and railways since 1970. From these, 56% correspond to shallow landslides, 20% to rockfalls, 12% to debris flows. Only 10% are deep-seated landslides. For a great number of events, the date and year are unknown, and a clear bias in documentation over the years can be seen. Small events in rural, mountain or forest areas, are grossly underrepresented, independently from their impact on infrastructures. Two peaks in the number of reported events in 2001 and 2007 can be highlighted. Spatial distribution of events shows high concentrations on primary and secondary axis in the cities of Lausanne and Montreux as well as on the cantonal routes 705 and 706, going from the Rhone valley into the Alps. These axes are important for the transport of merchandise and for tourism. For RC705 alone, approximately 13 million Swiss francs have been invested since 2004 for rockfall protection, and damage control.

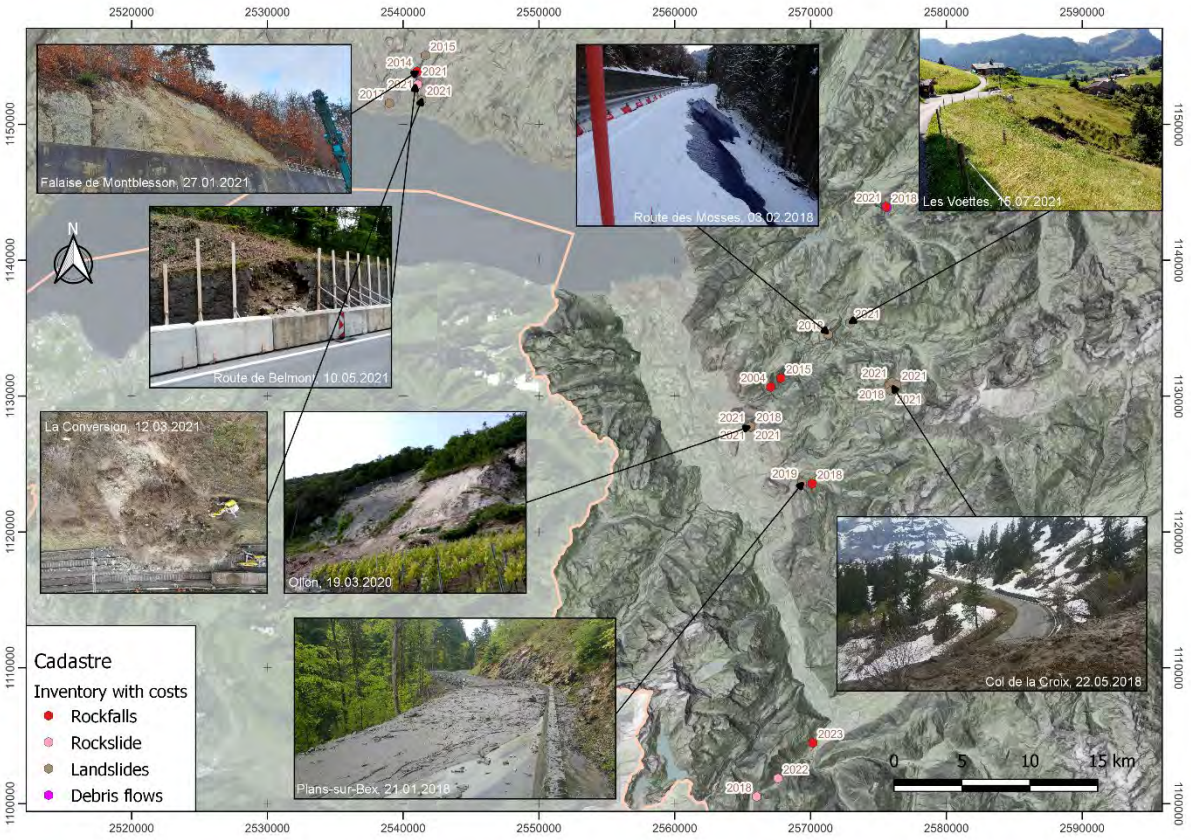

Figure 1: Illustration of the main events of the compiled inventory

Events such as those of La Conversion (2021), Châtillens Ecublens-Rue (2013), Col de la Croix (2021), L'Etivaz (2018), La Forclaz (2018, 2022), Col des Mosses (2015), route d'Oron (2014, 2021), Ollon (2021), and Belmont-sur-Lausanne (2021) were used in this inventory (Figure 1) and studied in detail. The second inventory was subdivided into two different sub-inventories: (a) one based on the available documentation, with all the associated costs excluding the 13M CHF for RC 705/706, and (b) one based on relevant events, where costs are incomplete and biased due to the invested costs for RC 705/706 (Table 1).

Table 1. Summary of costs for sub-inventories (a) and (b)

Sub-inventory costs	Sub-inventory (a)	Sub-inventory (b)
Maximum value	2'173'000 CHF	10'000'000 CHF
Minimum value	6'400 CHF	6'400 CHF
Mean value	110'783 CHF	247'284 CHF
Median value	94'317 CHF	370'850 CHF
Average value	277'811 CHF	1'009'962 CHF

For sub-inventory (a), the most common types of events are roads impacted by landslides and rockfalls. Consequently, the most common type of reparations are road rehabilitation, cleaning, and anchoring using wood boxes. Regarding the costs, 42% of the listed costs where invested post-event, while only 2% where invested pre-event, and for the rest the temporality is unkown. Between 2016 and 2022, the highest amount was invested in 2021 with a total of 6'879'350.00 CHF, while the greatest number of events for this sub-inventory were counted in 2021 and 2022.

Calculation and modelling of costs

Given the limited amount of available data regarding costs of different types of events in recent years, it was not possible to fit a distribution for each event class, and only three classes with enough entries (>5) were considered in this study: 'shallow landslides', 'rockfalls', and 'other'. A simple triangular distribution (Kotz & Van Dorp, 2004; Haimes, 2015) was used to approximate the probability distribution (PDF) of costs for each class, using min, max and median as parameters a, b, and c, respectively (Figure 2, left). Once the distributions of the three classes were obtained, a randomized simulation of these distributions was carried out.

Here 1000 simulations for 12 events, divided into 3 classes, using an inverse Poisson distribution, were carried out, and the individual costs were summed to obtain the probability of exceedance of total cost of events per year. The result was a 90% of probability of exceedance for approximately 2 million CHF, and 10% to exceed 6 million CHF in damages and repair costs for 2024 (Figure 2, right).

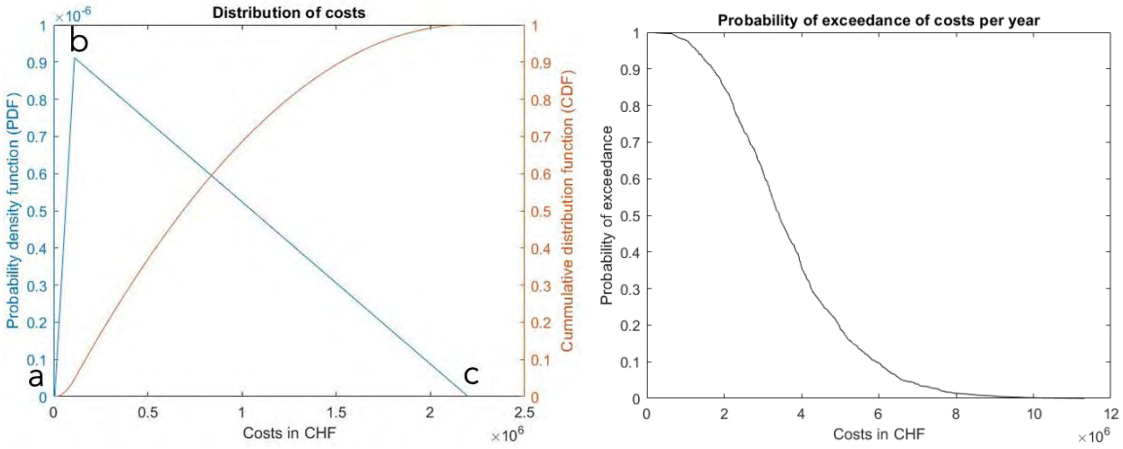

Figure 2: Approximation of the "other" class distribution using a triangular distribution (left) and modelling of the probability of exceedance in total costs over a given year (right)

Using the complete cantonal inventory to enlarge our dataset, a polynomial distribution could be fitted to the cumulative sum of events, divided by movement class, over the years.. Although only the 'Shallow landslide' and 'Rockfall' classes contain enough data to be used, the next steps aim to integrate the obtained trend to the randomized model, to better estimate the future progression of events and simulate more accurately the probability of exceedance of total costs per year.

Conclusions

Preliminary results in this work show that using a simple triangular distribution to model the distribution of costs for each class of events, and a randomized inverse Poisson distribution of the number of events and associated costs over time, it is possible to adequately model future trend of mass movements related to transport infrastructures and predict the expected costs in damages over a given year. Nonetheless, the inventory used here is limited, and current plans include expanding the inventory and refining the model. Other plans involve running simulations for the past years and integrating inflation correction. In any case, it is clear that if the current trends regarding changes in weather patterns and degradation of infrastructure without maintenance persist; the number of events causing damages and their associated costs will also increase over time.

References

Haimes, Y.Y. (2015) Risk Modeling, Assessment, and Management, 4th ed.;Wiley: Hoboken, NJ, USA; 720p.

Kotz, S. and Van Dorp, J.R., (2004). *Beyond beta: other continuous families of distributions with bounded support and applications*. World Scientific.

Voumard, J., Derron, M.H. and Jaboyedoff, M., (2018) Natural hazard events affecting transportation networks in Switzerland from 2012 to 2016. *Natural Hazards and Earth System Sciences*, *18*(8), pp.2093-2109.

Study on the Identification, Failure Mode, and Spatial Distribution of Bank Collapses after the First Storage Cycle in the Head Section of Baihetan Reservoir in Jinsha River, China

Chuangchuang Yao [1,2,3], Xin Yao [1,2,3,*], Renjiang Li [4], Kaiyu Ren [1,2,3], Shu Jiang [4], Ximing Chen [1,2,3], Li Ma [4]

1 Institute of Geomechanics, Chinese Academy of Geological Sciences, Beijing 100081, China
2 Key Laboratory of Active Tectonics and Geological Safety, Ministry of Natural Resources, Beijing 100081, China
3 Research Center of Neotectonism and Crustal Stability, China Geological Survey, Beijing 100081, China
4 Relocation & Resettlement Office, China Three Gorges Corporation, Chengdu, 610017, China

SUMMARY: After the first impoundment of Baihetan Reservoir in April 2021, the water level in front of the dam rose about 280 m. The mechanical properties and effects of the bank slopes in the reservoir area changed significantly, inducing many bank collapses. This paper systematically interpreted the bank collapse of the head section of the reservoir using UAV photogrammetry and ground surveys after the first water storage cycle. The following achievements were reached: (1) There were 276 bank collapses, and the total area of collapsed banks were 1.1 km^2, and the area of the single unit was range from 117 to 88,383 m^2. (2) According to the combination of lithology and movement mode, the bank failure mode is divided into six types, which are surface erosion type of weathered deposit, surface collapse type of weathered deposit, surface slide type of weathered deposit, bedding slip type of clastic rock, toppling type of clastic rock, and cavity corrosion type of carbonate rock. (3) In the reservoir area, 85% of the collapsed banks developed in weathered deposits, 15% in the clastic rock and carbonate rock. (4) Five collapsed banks posing severe threats to roads and residential buildings were identified based on the above pattern, improving the ability to prevent and control disasters in the reservoir area.

Keywords: Baihetan Reservoir、Bank collapse、Bank collapse identification、Bank Failure mode、Distribution laws

1 Introduction

Reservoir impoundment induces numerous bank collapse geohazards (Wang et al., 1996; Wang et al., 1997; Shu et al., 2012), which lead to bank retreat, siltation of the river channel, and restriction of ship navigation, seriously threatening the safety of people's lives and properties. The deformation and damage of bank slopes caused by reservoir impoundment mainly include landslides, avalanches, debris flows, ground cracks, ground subsidence, and bank collapse (Tang et al., 2019). Among them, bank collapse is a type of geohazard that develops more widely in the initial stage of water impoundment, and its severity is reflected in reservoir bank reconstruction. Therefore, strengthening the systematic investigation, type division, and law analysis of bank collapses during reservoir impoundment is a crucial basis for predicting the extension of bank failures into landslide occurrence and mitigating such geological hazards. For the impact area of bank collapse caused by impoundment, high-resolution images generated by UAV aerial photography were used for interpretation and combined with the investigated stratigraphic lithology and bank slope structure, the bank collapse types and spatial development laws in the reservoir area were summarized.

2 Study area

The area has extensive background geohazards due to steep bank slopes, significant vertical height differences, and strong tectonic activities (Liu et al., 2021; Li et al., 2023). Baihetan Hydroelectric Power Station, located downstream on the Jinsha River, is the world's third largest power station after China's Three Gorges Hydroelectric Power Station and Brazil-Paraguay's Itaipu Hydroelectric Power Station, belongs to an alpine canyon geomorphology (Fig. 1a, b). Annual precipitation reaches 500-800 mm, with the rainy season (May-October) concentrating 86% of the rainfall (Fig. 1c). Baihetan Reservoir was impounded in April 2021 with an initial level of 630 meters. In October 2021, the water location height reached 816 meters and fluctuated, rising to a maximum level of 825 meters in late October 2022. The maximum water level of the reservoir in front of the dam was raised by about 280 m, and the water level varied by 60 m during the design operation.

The UAV survey can obtain accurate DOM and DSM of the bank slopes during the bank collapse. Based on the field survey and geological map, the study area's stratigraphic lithology, fault properties, and bank slope structure were determined and updated.

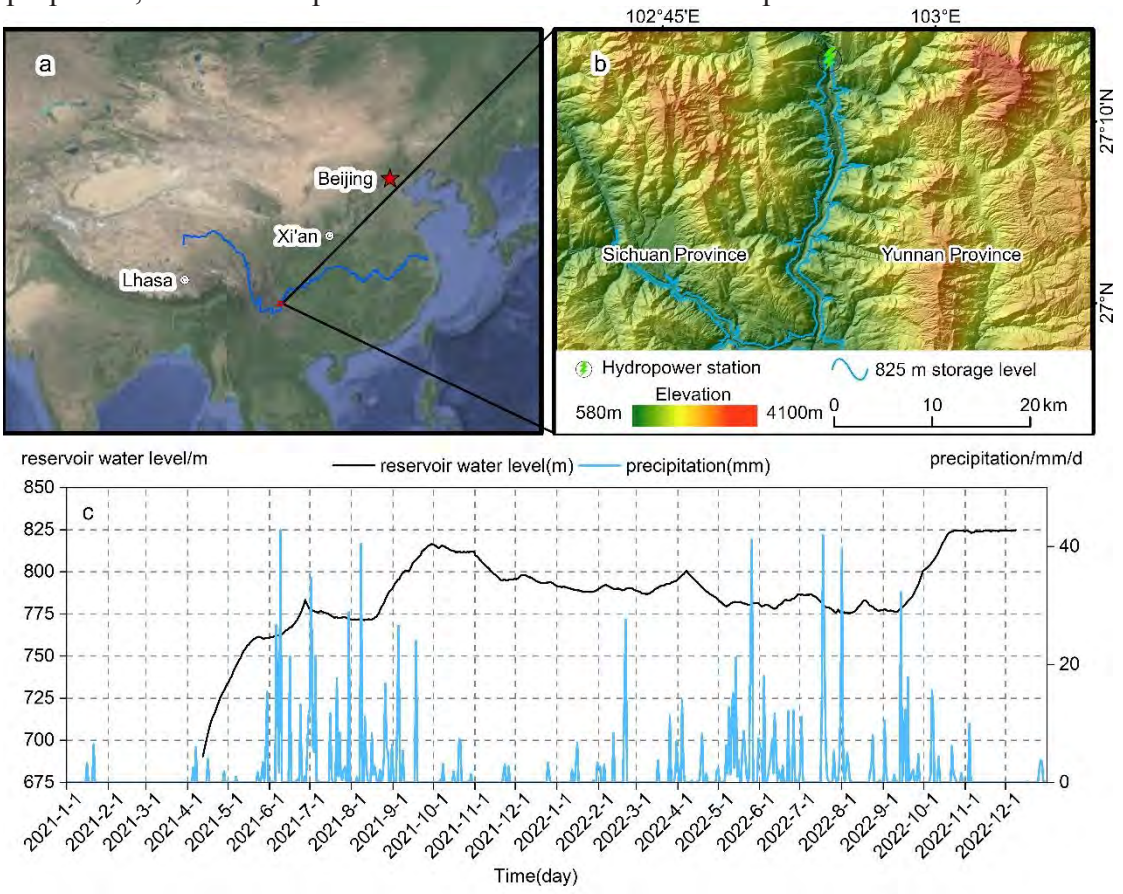

Fig.1 a、b The location of study area. c Relationships among precipitation and water level fluctuations (The rainfall data and water level data are from the actual measurements of Baihetan Hydropower Station)

3 Results and Discussion

The storage of water in Baihetan Reservoir has led to changes in the geological environment, and both sides of the reservoir have experienced different degrees of deterioration and instability. The main results are as follows:

(1) In the head section of Baihetan Reservoir, there are 276 collapsed banks on the left and right sides of the 30-kilometer-long reservoir, with a development density of 4.6 collapsed banks/km. 85% of the collapsed banks were developed in weathered deposits and 15% in clastic and carbonate rock types. The loosely structured overburden developed at the mouth of the

branch gully, and 46% of the collapsed bank developed here. The branch gully is a place where the collapsed bank develops intensively.

Table 1 The types and characteristics of bank collapse in the study area

Material		Characteristics	Type	Code
Soil: weathered deposit		Erosion of weathered deposit	Surface erosion type	A
		The profile pattern shows two sections, steep at the top and slow at the bottom	Surface collapse type	B
		Surface develops tension cracks	Surface slide type	C
Rock	Clastic rock	Exposure of smooth rock layer faces	Bedding slip type	D
		Rock toppling	Toppling type	E
	Carbonate rock	cavity development	Cavity corrosion type	F

(2) Through the field investigation of 276 collapsed banks along the reservoir, six types of collapsed bank patterns were summarized in Table 1. They are the surface erosion type of weathered deposit, surface collapse type of weathered deposit, surface slip type of weathered deposit, bedding slip type of clastic rock type, toppling type of clastic rock type, and cavity corrosion type of carbonate rock type, respectively.

(3) Different types of bank collapse have different characteristics. Weathered deposits of the surface erosion type undergo denudation under the influence of reservoir water. Surface collapse banks have a vertical profile pattern. Tensile cracks appear at the top and waist of the surface slip type. The bedding slip-type profile shows a jagged shape. Toppling-type bank failures undergo toppling deformation along the discontinuity surface. The cavity corrosion type deformation occurs along the dissolution concave cavity.

(4) 94% of the collapsed banks in the reservoir area are larger than 500 m², 81% are larger than 1,000 m², and 7% are larger than 10,000 m^2. The slope of 26% of the collapsed bank increased by 5 to 20° after impoundment, while the other slopes remained essentially constant. A collapsed bank with a width, height, and length greater than 200m and an area greater than 6,000 m^2 will be a hazard to roads and residential building facilities.

4 Conclusion

In this paper, the deformation pattern and developmental law of the collapsed bank in the head section of the reservoir after the first impoundment were obtained by analyzing and interpreting the remote sensing data from the UAV aerial flights in the reservoir area (Fig. 2). In the head section of Baihetan Reservoir, there were 276 bank collapses, and the geohazards development density was 4.6/km. 85 percent of the collapsed banks were developed in weathered deposits and 15 percent in clastic and carbonate rock types. According to the combination of lithology and movement mode, the bank failure mode is divided into six types. The understanding of these laws improves the ability to prevent and control disasters in the reservoir area.

References

A.P. Shu, F.H. Li, K. Yang, 2012. Bank-collapse disasters in the wide valley desert reach of the upper Yellow River. Procedia Environmental Sciences 13, 2451–2457. https://doi.org/10.1016/j.proenv.2012.01.234

Shitian Wang, Hanchao Liu, Zhuoyuan Zhang, et al. 1997. Water-rock interactions in large waters and their environmental effects [J]. Journal of Geological Hazards and Environment Preservation, 1,70-90. (in Chinese)

Sijing Wang, Fengshan Ma, Yonglian Du. 1996. On the rock-water interaction in reservoir areas and its geoenvironmental effect. Journal of Engineering Geology, 4(3): 1-9. (in Chinese)

Huiming Tang, Janusz Wasowski, C. Hsein Juang, 2019. Geohazards in the three Gorges Reservoir Area, China – Lessons learned from decades of research. Engineering Geology 261, 105267. https://doi.org/10.1016/j.enggeo.2019.105267

Xiaojie Liu, Chaoying Zhao, Qin Zhang, Zhong Lu, Zhenhong Li, Chengsheng Yang, Wu Zhu, Jing Liu-Zeng, Liquan Chen, Chuanjin Liu, 2021. Integration of Sentinel-1 and ALOS/PALSAR-2 SAR datasets for mapping active landslides along the Jinsha River corridor, China. Engineering Geology 284, 106033. https://doi.org/10.1016/j.enggeo.2021.106033

Lingjing Li, 2023. InSAR-based method for monitoring the long-time evolutions and spatial-temporal distributions of unstable slopes with the impact of water-level fluctuation: A case study in the Xiluodu reservoir. Remote Sensing of Environment. 295.https://doi.org/10.1016/j.rse.2023.113686.

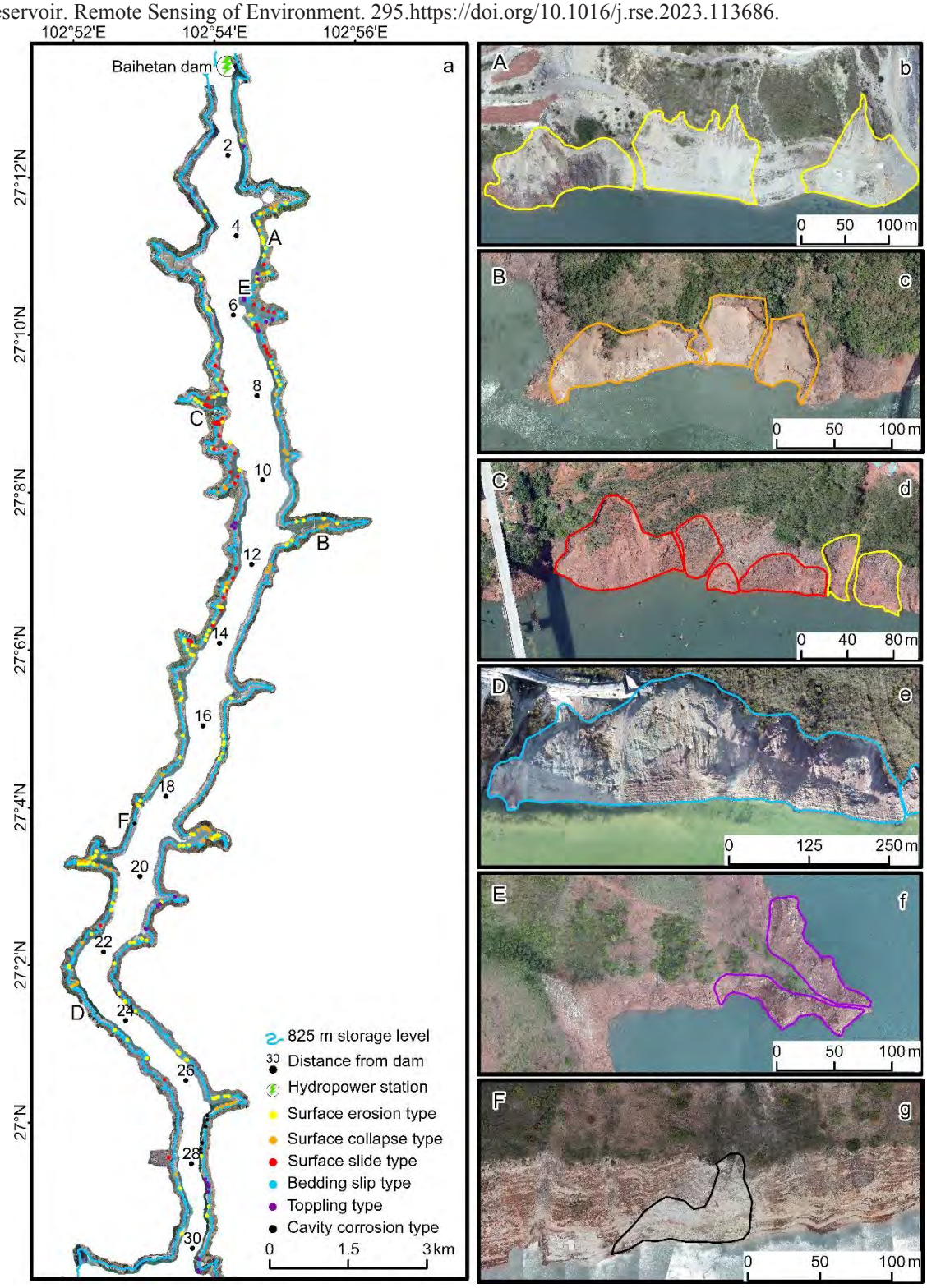

Fig. 2 The head section of the bank collapse interpretation

Estimating landslide volume from InSAR-derived deformation rates

Sergey Samsonov[1] and Andrée Blais-Stevens[2]

[1] Canada Centre for Mapping and Earth Observation, Natural Resources Canada, 580 Booth St, Ottawa, K1A0E4, Ontario, Canada
[2] Geological Survey of Canada, Natural Resources Canada, 601 Booth St, Ottawa, K1A0E8, Ontario, Canada

SUMMARY: Large slow-moving deep-seated landslides are observed in two different regions of northern Canada with advanced Differential Synthetic Aperture Radar (DInSAR). Two-dimensional vertical and horizontal east-west deformation rates and time series are computed from ascending and descending Sentinel-1 imagery acquired during 2017- 2022. The landslides' east-west deformation rate is significantly larger than the vertical deformation rate, so it is better suited for landslide characterization. The deformation rates remain nearly constant during the entire period, suggesting substantial landslide thickness. Two large landslides in Alberta and the largest landslide in the Northwest Territories are studied in detail to demonstrate various advanced value-added products that can be produced from DInSAR results. The Surface-Parallel Flow (SPF) and Aspect-Parallel Flow (APF) constrained three-dimensional deformation rates are computed, and the landslide thickness is estimated. The described techniques allow for mapping slow-moving deep-seated landslides in harsh conditions in areas affected by seasonal land cover changes, as in northern Canada. The decomposition of landslide motion into two or three components in certain conditions allows us to derive landslide thickness and volume and improve the estimation of a potential hazard posed by landslides.

Keywords: Differential Interferometric Synthetic Aperture Radar (DInSAR), Canada

Introduction

Northern Canada is a vast territory and an excellent candidate for applying remote sensing methods for detecting and monitoring landslides. Recent systematic analysis of DInSAR over Canada revealed several previously known and unknown areas with the largest in Canada, slow-moving deep-seated landslides. Here, we compute from DInSAR measurements various derived products and use them for studying these large landslides in detail. The methods presented here are tested in two areas to show their versatility.

Data and Results

Six sets of Sentinel-1 Synthetic Aperture Radar (SAR) data in Single Look Complex (SLC) format were acquired and processed. In Alberta, we used two ascending sets from tracks 020 and 049, and one descending set (consisting of two concatenated frames) from track 042. In the Northwest Territories, we used two ascending sets from tracks 079 and 108, and one descending set from track 116. Each Sentinel-1 set was processed independently with the GAMMA software (Wegmuller and Werner, 1997) on a High-Performance Computer (HPC) Linux cluster operated by the Canadian Government (Dudley and Samsonov, 2020). The fully automated processing strategy is described in Samsonov and Feng (2023) and was executed using the MSBAS version 10 software for calculating the two- and three-dimensional (2D and 3D) deformation rates and time series. For several large landslides, the 3D deformation rates were used to estimate the landslides' volume assuming the law of mass conservation (Booth et al., 2013; Hu et al., 2018.

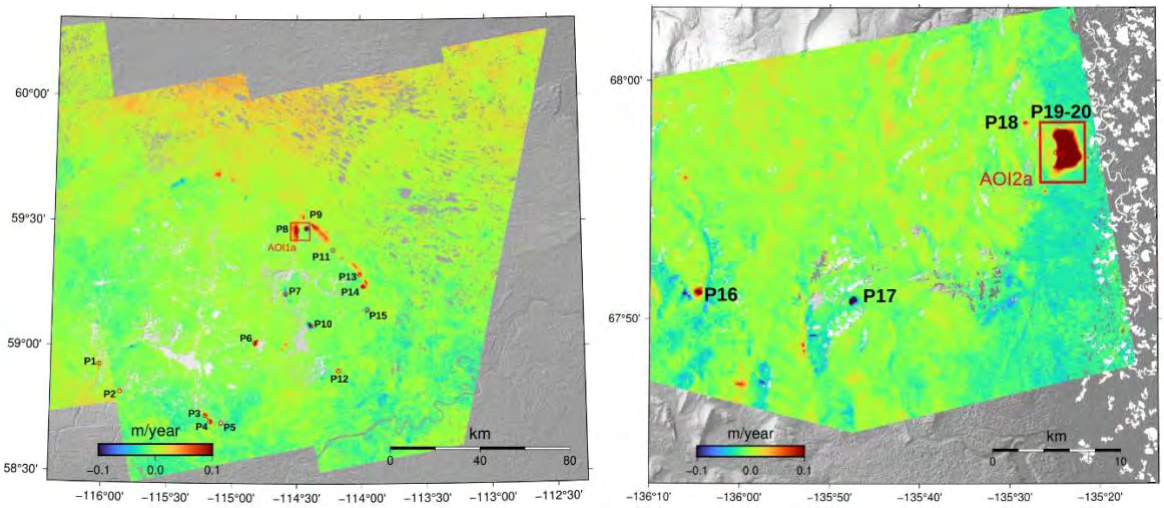

Figure1: Horizontal east-west deformation rate maps computed from 2017-2022 Sentinel-1 data. For sites P1-P20 3D time series were studied in detail. For landslides in AOI1a and AOI2a volume was estimated.

Conclusions

Using freely available SAR data, we mapped two regions in northern Canada where several large slow-moving deep-seated landslides were observed (Figure 1). These landslides are located in remote areas, yet their impact can be substantial. For example, several oil and gas wells and transportation corridors are located near some of the landslides in Alberta. It is, however, unknown if these wells are currently active. In both areas, landslides move towards moderate-size rivers that can be blocked in the case of landslide failure. Among several time series techniques demonstrated here, 2D decomposition offers the most benefits as it is very robust. We observed that the east-west deformation component is most sensitive to the landslide motion, while the 3D deformation rates computed assuming the Aspect-Parallel Flow (APF) constrain can be used for estimating landslide thickness.

References

Booth, A.M., Lamb, M.P., Avouac, J.P., Delacourt, C., 2013. Landslide velocity, thickness, and rheology from remote sensing: La Clapi`ere landslide, France. Geophysical Research Letters 40, 4299–4304. doi:10.1002/grl.50828.

Dudley, J.P., Samsonov, S.V., 2020. The Government of Canada automated processing system for change detection and ground deformation analysis from RADARSAT-2 and RADARSAT Constellation Mission Synthetic Aperture Radar data: description and user guide. Technical Report. Geomatics Canada Open File 63. doi:10.4095/327790.

Hu, X., Lu, Z., Pierson, T., Kramer, R., George, D., 2018. Combining InSAR and GPS to determine transient movement and thickness of a seasonally active low-gradient translational landslide. Geophys. Res. Lett. 45, 1453–1462. doi:10.1002/2017GL076623.

Samsonov, S.V., Feng, W., 2023. Deformation retrievals for North America and Eurasia from Sentinel-1 DInSAR: Big data approach, processing methodology and challenges. Canadian Journal of Remote Sensing 49. doi:10.1080/07038992.2023.2247095

Wegmuller, U., Werner, C., 1997. GAMMA SAR processor and interferometry software, in: The 3rd ERS symposium on space at the service of our environment, Florence, Italy, pp. 1687–1692.

Risk Assessment of Landslides Considering Spatial Variation of Soil Parameters

Himanshu Rana[1], G L Sivakumar Babu[2]

[1] Faculty of Geo-Information Science and Earth Observation (ITC), University of Twente, Netherlands
[2]Civil Engineering Department, Indian Institute of Science, India

SUMMARY: This paper presents a methodology for probabilistic assessment of landslide risk considering spatial variability of soil parameters. The study utilized Monte Carlo simulation method and random field theory. Monte Carlo simulation method is used to determine the failure probability of the slope. Random field theory is utilized to generate random field for soil parameters using local averaging simulation. An example application is demonstrated to validate the proposed methodology. The results of the example application suggest that the spatial variation of soil parameter significantly affects the landslide risk. The determined posterior distribution can be used for design of slope and planning of remedial measures against slope failure.

Keywords: Landslide risk, Spatial variation, Monte Carlo simulation

Introduction

Landslides is a major natural catastrophe leading to damage to environment, topography, livestock, and infrastructure globally. This damage can be reduced by efficient landslide analysis in terms of risk associated with slope failures. The landslide risk assessment provides information regarding the potential damage different elements will experience i.e., consequences of landslides. Landslide analysis is widely conducted using deterministic as well as probabilistic techniques. The deterministic technique for landslide analysis considers one set of input parameters and provides conservative results (Rana & Sivakumar Babu, 2022c, 2023). On the other hand, probabilistic analysis takes into account multiple sets of input parameters with different likelihoods to estimate the probability of failure of the geosystem. Several researchers have previously used probabilistic techniques to analyze slope systems (Cho, 2010; Griffiths et al., 2009; Rana et al., 2023; Rana & Sivakumar Babu, 2022b, 2022a).

Assessment of the probability of failure using random field theory requires repeated simulations of slope for multiple realizations of random field elements, which requires extensive computational resources (Cho, 2007; Li et al., 2016; Wang et al., 2019). To handle this issue, many researchers have used metamodel or surrogate model-based approach to improve the efficiency of slope reliability analysis (Xu et al., 2013; Zhao & Yin, 2009). However, the use of the convolution neural network (CNN) algorithm is rarely reported in previous studies focused on the reliability analysis of slope systems consisting of spatially variable soil properties.

This study presents a methodology to estimate the probability of failure of a slope system considering spatially variable soil parameters. This probability of failure is further used to estimate the consequences i.e., risk associated with slope failure. The finite difference method is used to simulate the slope and evaluate the safety factor and area of failed slope material. The

spatially variable soil parameters are considered by using random field theory. Several realizations of random field elements are generated using the mid-point method for each spatially variable parameter. The relationship between spatially variable soil parameters and the corresponding safety factor and area of failed slope material is established using the CNN algorithm. The probability of failure of the slope system is estimated using the Monte Carlo Simulation (MCS) method. The proposed methodology is validated by applying an example slope system. The results of the study suggest that the proposed method is effective in estimating practical values of the probability of slope failure and risk associated with it.

Methodology

The MCS method is incorporated in this study for risk analysis of slope system. The relationship between spatially variable soil parameters; and safety factor and area of failed slope material is vital for risk analysis. This relationship is mapped using the CNN algorithm instead of the Finite difference method simulation to make it less arduous. The proposed methodology can be described in the following steps

1. Collect the slope details, i.e., soil properties, statistics of soil parameters, geometric information, boundary condition, and topographic information, and simulate the slope using finite difference method.
2. Generate samples of random field using the mid-point method for spatially variable soil parameters considering the statistics of these parameters gathered in step 1.
3. Determine the safety factor and area of failed slope material for each sample of random field using the finite difference method and prepare data for training of the CNN model.
4. Divide the obtained data into training and validation set. The training data involve 80% of the generated samples of spatially variable soil parameters and the corresponding value of safety factor and area of failed slope material. The validation data consist of the remaining 20% of the generated data.
5. Train the CNN model using the previously obtained training dataset and validate the model using the remaining data set.
6. Replace the finite difference method simulation with the trained CNN model to predict values of safety factor. The probability of failure is calculated by using the MCS method.
7. The risk (R) due to slope failure is calculated using the following relationship

$$R = \frac{1}{N_{mc}} \sum_{i=1}^{N_{mc}} I(FOS_i < 1) \times C_f \quad (1)$$

where C_f is area of failed slope material. I represents indicator function for factor of safety smaller than one. N_{mc} indicates the number of MCS samples.

Results

Example application

The proposed methodology was applied to a slope taken from (Le et al., 2015). The geometry of the slope is shown in Fig. 1. The geotechnical properties of the slope material are adopted from (Le et al., 2015). The slope was simulated using finite difference method software FLAC 2D. The slope was simulated in two stages. The first stage involved simulation of unsaturated slope material under rainfall intensity of 5×10^{-7} m/s for 10 days. The second stage consisted of the period of seepage after the precipitation for 365 days. The variation of safety factor values with time was observed. To validate the simulated slope, the calculated values of safety factor

using FLAC 2D were compared with the values of safety factor obtained by (Le et al., 2015). The results of the comparison show that the obtained variation of safety factor values with time was consistent with the variation of safety factor obtained by previous study (Fig. 2). Hence, the simulated model can be used for further analysis.

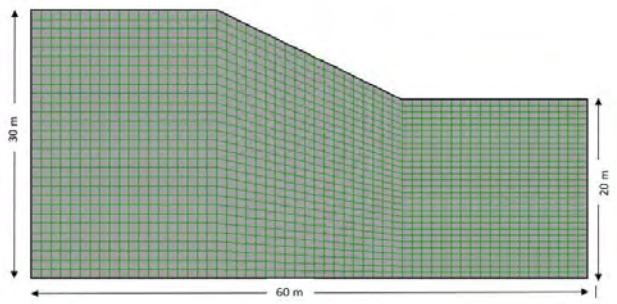

Figure 1. Geometry of the considered slope.

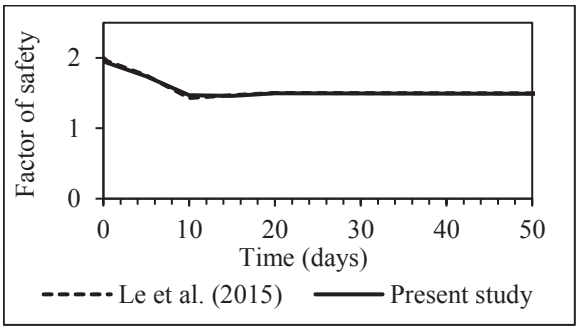

Figure 2. Comparison of values of safety factor calculated in this study and Le et al. (2015).

100 samples of random field elements were generated, and values of safety factor were estimated for each sample using FLAC 2D software. The developed data is used to train the CNN model. The accuracy of the trained CNN model was determined by comparing the predicted values of safety factor by CNN and calculated values of safety factor for the validation dataset. This comparison shows that the trained CNN model can substitute the simulated model for probabilistic analysis as the predicted values of safety factor by the CNN model were consistent with the calculated values of safety factor by the numerical or simulated model.

The Monte Carlo simulation model was utilized to estimate the probability of slope failure by considering the trained CNN model. The variation of probability of slope failure and coefficient of variation (COV) of the probability of slope failure with the number of simulations is plotted in Fig. 3. It was observed from Fig. 3 that 5000 samples of Monte Carlo simulation are sufficient as it leads to COV of the probability of slope failure less than 10%. The 5000 samples of Monte Carlo simulation took less than one minute to run on MATLAB 2022 using 8GB RAM system. The obtained value of the probability of slope failure is 0.04, which is consistent with (Wang et al., 2019). The variation of estimated risk and COV of landslide risk is plotted in Fig. 4. As evident from Fig. 4, the landslide risk decreases rapidly till 1000 samples. After 2000 samples, the risk becomes almost constant. The COV of risk also becomes constant after 2000 samples. The mean value of risk is 2.2, which closely matches with (Wang et al., 2019). Hence, the proposed methodology is efficient in the estimation of the landslide risk considering spatially varying soil properties. The results of the example can be used for the reliability-based slope design.

Conclusion

This paper presents a methodology for estimating the probability of slope failure and the consequences of slope failure in terms of landslide risk under rainfall conditions considering the spatial variability of soil parameters. The slope under rainfall infiltration was simulated using FLAC 2D. The spatial variable property of soil parameters was considered using discretized random field elements using the mid-point method. The relationship between spatially variable soil parameters and the corresponding safety factor and area of failed slope material was mapped using the CNN model. The probability of slope failure and associated risk was estimated using the Monte Carlo Simulation. The proposed methodology was applied for

an example of slope under rainfall infiltration. The results of the example application suggest that the proposed methodology efficiently estimates the probability of slope failure and the associated consequences.

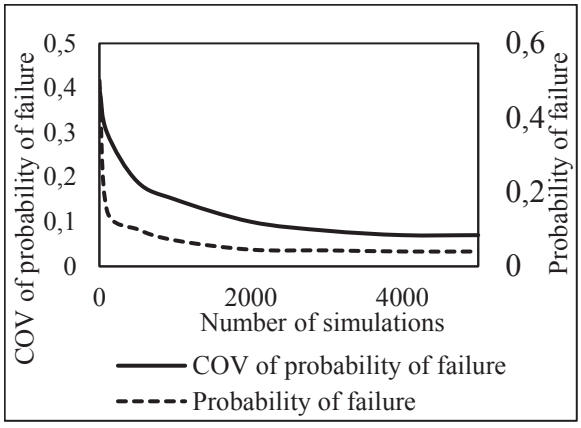

Figure 3. Variation of probability of slope failure and COV of probability of slope failure with number of simulations.

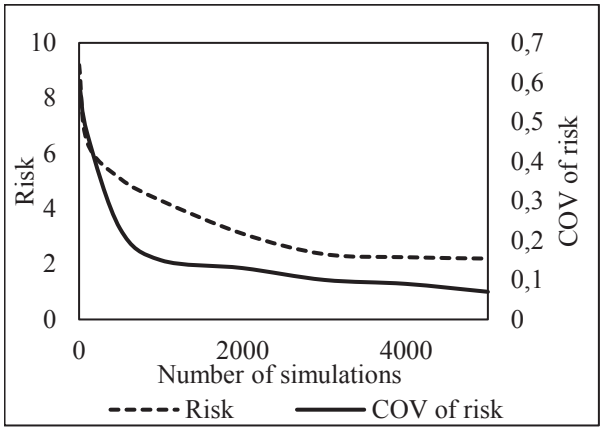

Figure 4. Variation of landslide risk and COV of landslide risk with number of simulations.

References

Cho, S. E. (2007). Effects of spatial variability of soil properties on slope stability. *Engineering Geology*, *92*(3–4), 97–109. https://doi.org/10.1016/j.enggeo.2007.03.006

Cho, S. E. (2010). Probabilistic Assessment of Slope Stability That Considers the Spatial Variability of Soil Properties. *Journal of Geotechnical and Geoenvironmental Engineering*, *136*(7), 975–984. https://doi.org/10.1061/(asce)gt.1943-5606.0000309

Griffiths, D. V., Huang, J., & Fenton, G. A. (2009). Influence of Spatial Variability on Slope Reliability Using 2-D Random Fields. *Journal of Geotechnical and Geoenvironmental Engineering*, *135*(10), 1367–1378. https://doi.org/10.1061/(asce)gt.1943-5606.0000099

Le, T. M. H., Gallipoli, D., Sanchez, M., & Wheeler, S. (2015). Stability and failure mass of unsaturated heterogeneous slopes. *Canadian Geotechnical Journal*, *52*(11).

Li, S., Zhao, H., Ru, Z., & Sun, Q. (2016). Probabilistic back analysis based on Bayesian and multi-output support vector machine for a high cut rock slope. *Engineering Geology*, *203*, 178–190. https://doi.org/10.1016/j.enggeo.2015.11.004

Rana, H., Pandit, B., & Sivakumar Babu, G. L. (2023). Estimation of Uncertainties in Soil Using MCMC Simulation and Effect of Model Uncertainty. *Geotechnical and Geological Engineering*, *41*(8), 4415–4429. https://doi.org/10.1007/s10706-023-02523-4

Rana, H., & Sivakumar Babu, G. L. (2022a). Evaluating Soil Parameters Considering Probabilistic Back Analysis for Slope Failures. *Geo-Congress 2022*, 360–369. https://doi.org/10.1061/9780784484043.035

Rana, H., & Sivakumar Babu, G. L. (2022b). Probabilistic back analysis for rainfall-induced slope failure using MLS-SVR and Bayesian analysis Bayesian analysis. *Georisk: Assessment and Management of Risk for Engineered Systems and Geohazards*, *0*(0), 1–14. https://doi.org/10.1080/17499518.2022.2084555

Rana, H., & Sivakumar Babu, G. L. (2022c). Regional back analysis of landslide events using TRIGRS model and rainfall threshold: An approach to estimate landslide hazard for Kodagu, India. *Bulletin of Engineering Geology and the Environment*, *81*(4). https://doi.org/10.1007/s10064-022-02660-9

Rana & Sivakumar Babu. (2023). Probabilistic Assessment of Landslide Risk Considering Spatial Variation of Soil Parameters. *Geo-Risk 2023*, 75–84.

Wang, L., Wu, C., Li, Y., Liu, H., Zhang, W., & Chen, X. (2019). Probabilistic Risk Assessment of unsaturated Slope Failure Considering Spatial Variability of Hydraulic Parameters. *KSCE Journal of Civil Engineering*, *23*(12), 5032–5040. https://doi.org/10.1007/s12205-019-0884-6

Xu, F., Huang, B. Q., & Wang, K. (2013). Study and application of slope displacement back analysis based on SVM-CTS. *Applied Mechanics and Materials*, *353–354*, 163–166. https://doi.org/10.4028/www.scientific.net/AMM.353-356.163

Zhao, H. bo, & Yin, S. (2009). Geomechanical parameters identification by particle swarm optimization and support vector machine. *Applied Mathematical Modelling*, *33*(10), 3997–4012. https://doi.org/10.1016/j.apm.2009.01.011

Hydrogeological simulations of a deep-seated landslide: implications for hazard mitigation

Joshua Ducasse[1], Catherine Bertrand[1], Olivier Maillard[1], Delphine Charpentier[1], Jean-Pierre Sizun[1], Myriam Lajaunie[2], Joachim Rimpôt[3], Céleste Broucke, Jean-Philippe Malet[3,5]

[1] University of Franche-Comté, CNRS, UMR 6249, Laboratoire Chrono-Environnement, Besançon, France
[2] Service Hydrographique et Océanographique de la Marine (SHOM), Brest, France
[3] Institut Terre et Environnement de Strasbourg (ITES), CNRS UMR 7063, University of Strasbourg, Strasbourg, France
[4] Institut de Physique du Globe de Paris (IPGP), CNRS UMR 7154, Université Paris Cité, Paris, France
[5] École et Observatoire des Sciences de la Terre (EOST), CNRS UAR 830, University of Strasbourg, Strasbourg, France

SUMMARY: Following a rockslide triggered in 2018, a slow-moving landslide has been reactivated affecting the Viella municipality (Hautes-Pyrénées, Southwest France). The slope is now sliding inexorably down to the valley; several landslide kinematic sub-units lcharacterized by several ground motion have damaged infrastructures and buildings. In the months following this reactivation, surface velocities of up to one centimeter per day were observed, endangering some buildings and necessitating the implementation of mitigation measures. To assess the water circulation and storage in the slope, a three-dimensional geological model was built as a prerequisite of 3D hydrogeological simulations carried out with GeoModeller. The geological model allows for improving the knowledge of the slope internal structures, the position of the bedrock and of the sliding surfaces. Three-dimensional finite element water flow simulations obtained with the FEFLOW (©DHI) model provide an understanding of the functioning of the landslide aquifer. The integrative approach allows proposing a robust hydrogeological model and the establishment of a piezometric map of the site at equilibrium. In the landslide, the piezometry is between 780m and 970m in elevation, and the direction of the groundwater flow is about 340° North. The hydraulic conductivities determined by the model are between 10^{-4} and 10^{-5} $m.s^{-1}$ in the shallow sub-surface (colluvium), up to 10^{-7} $m.s^{-1}$ in depth (Devonian's shales). From the calibrated hydrogeological model, various simulations were carried out in order to estimate the impacts of mitigation works on the water storage and circulation. It further helped to simulate the piezometric response of the slope to an extreme flood event at the toe of the landslide. Model simulations showed that the "sealing" or "waterproofing" of a 650m section in the lower part of the Bayet-Badoueil stream would lower the piezometric height under the village up to a maximum of 30 m and reduce the hydraulic load uphill. A decrease of the water table height of 5 m seems achievable and would be sufficient to significantly reduce the sliding motion with the boundary conditions set (zero flux) in these simulations.

Keywords: Slow-moving landslide, Numerical modelling, Hydrogeological model, Drainage scenario

Introduction

Large landslides have a potentially dramatic socio-economic impact. They are a major threat to human life, buildings, infrastructure and the natural environment in most mountainous and hilly regions of the world (Petley, 2012). The mechanisms controlling their dynamics and their triggering are numerous and complex, which lead to a high degree of uncertainty in

behaviour forecasts both spatially (volume involved, location) and temporally (occurrence, dynamics).
The hydromechanical processes that control the reactivation of large landslides are influenced by the evolution of the terrain deformation in space and time and the water circulation and storage in highly heterogeneous material. In the case of an aquifer located on unstable slopes, it is essential to understand its behaviour in order to propose mitigation solutions such as groundwater drainage.

Spatial and temporal variations of water storage in the subsoil are controlled by the structure, internal geometry and petrophysical properties of the aquifer (Maréchal 1998; Cappa et al. 2004; Bogaard et al. 2007, Vallet et al. 2015a). The main hydrogeological methods to infer these properties are single- and cross-borehole hydraulic tests and tracer tests. These classical methods are not always appropriate and their applications are limited, especially if the groundwater-bearing fracture is not close to the borehole (Ellefsen et al., 2002). Recent studies based on indirect, non-intrusive methods, such as hydro-geophysical methods allow identifying water stocks and variations (Perrone et al. 2014; Gance et al. 2016). These methods can also be used to characterize the geometry of the aquifer and identify preferential flow paths (Kukemilks and Wagner, 2021). However, due to the high heterogeneity of landslide media systems, the hydrogeological behaviour can be very complex, and prone to multiple interpretations and /or conceptualizations. Modelling can be used to test several hydrogeological conceptual models (De Filippis et al., 2017) but also for predicting the hydrogeological system behaviour for several water recharge conditions (Pétronici et al., 2019).
The aim of this work is to develop a numerical hydrogeological model of a landslide aquifer by combining geological and geophysical information. The model supports the test of hypotheses on the aquifer functioning and on inferring the impacts of drainage scenarios on the groundwater levels.

I Study site: the Viella landslide (Hautes-Pyrenees).

The municipality of Viella is located on the Hautes-Pyrénées (65) in the Occitanie region (Southwest France). The Viella landslide has experienced a rare combination of triggering factors, with an extreme flood event (2017) which steepened the lower part of a paleo-landslide, followed some months later by a rockslide (March 2018) that loaded the upper part of the paleo-landslide changing the water circulation in the slope. These factors altered the equilibrium line and the groundwater dynamics modifying the stress regime of the slope. The Viella landslide consists of several nested sliding units of varying surface displacement rates (Fig. 1a). The Bayet stream flows over the landslide and divides it into two lobes. The lithological bedrock outcrops above 1000 m a.s.l. to the south of Viella. It is composed of sandy shale and grey-black clay shale (pelites) with limestone facies from the Devonian. The rockslide of February 2018 consists of shales and pelite screes. The landslide material is composed of glacial moraines on which colluvium and highly weathered screes from the successive dismantling of the overlying reliefs have accumulated. The landslide thickness exceeds 71 m in its central part, close to the center of the village. These formations, with their permeability and porosity, support several aquifers: a) the colluvial aquifer, which is located in the morainic and colluvial formations that form the slopes around the village; b) the scree aquifer is located in the Devonian limestone and shale formations as far as the Couret crest, c) the substratum aquifer of the shales and/or Devonian limestones that form the relief of the mountain of Herrère and, finally, 5) the aquifer of the small valley of Badouiel, located in shale debris from the numerous landslides that have occurred in the area.

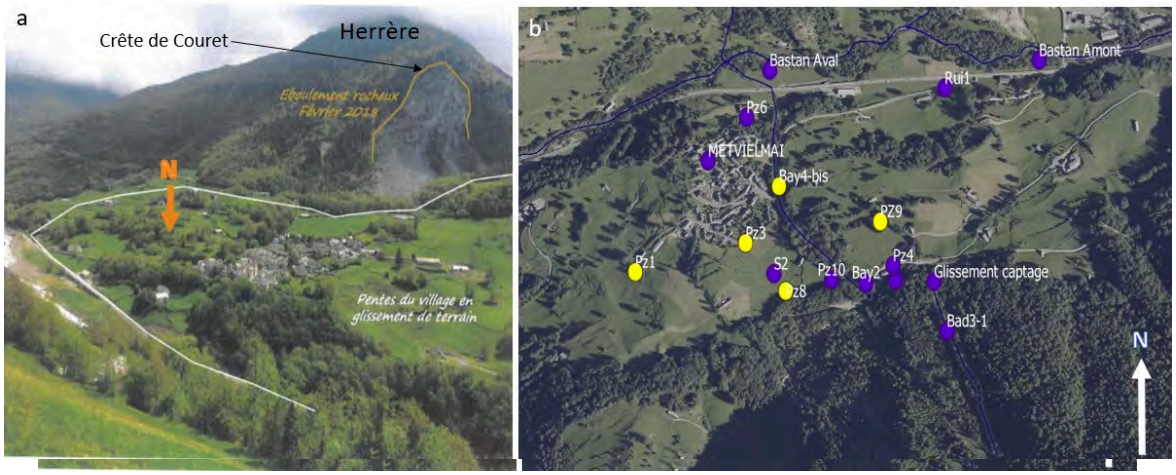

Figure 1: a - View of the Viella landslide (Hautes-Pyrénées); (b) - Location of the hydrogeological sensors, consisting of borehole piezometers with high-frequency groundwater level measurements, electrical conductivity, and water temperature (yellow points), along with the tracing of fluorescein (blue points)

In 2019, the implementation of 16 boreholes of 20 m depth, along with the installation of 7 inclinometers and 9 piezometers, allowed for an investigation of the first 20 m of the moving mass. A network of sensors continuously measuring water level, electrical conductivity, and water temperature (yellow points in fig 1b) was deployed to gather information about the hydrodynamic behavior of the colluvial aquifer and to establish hydraulic connections between surface water (the Bayet/Badouiel streams) and groundwater (the screes aquifer, the colluvial aquifer). Hydrochemistry analyses were conducted at all monitoring points (Fig. 1b) to identify the origin of the water masses. A first hydrogeological conceptual model of the colluvial aquifer was proposed based on the hydrochemistry and hydrodynamic data Additionally, an artificial tracing was conducted in June 2020 to identify hydraulic connections and the water flow velocities between the surface waters and the groundwater (tracing results showed as blue points in fig 1b). In July 2020, a dense 3D tomography of electrical resistivity and seismic acquisitions were carried out to create several 3D geophysical models in order to image the deep structure of the landslide, from -20m to – 120 m (Fig. 2a). This model highlights highly conductive and highly resistant zones within the unstable mass, thereby indicating the presence of several discontinuities and preferential fluid flow pathways (Fig. 2b).

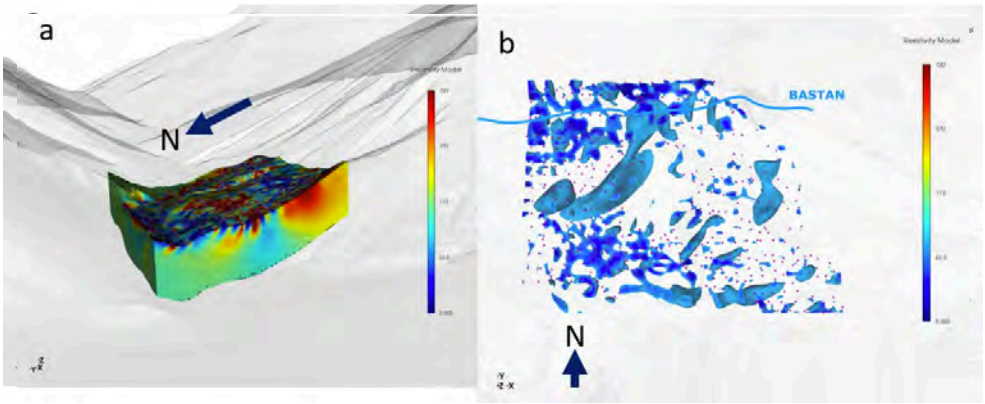

Figure 2: (a) - 3D structure of the landslide with a cube of electrical resistivity values inferred from dense and distributed measurements; (b) - Conductive anomalies seen from above (threshold: resistivity < 120 Ohm.m; small-size anomalies near the surface, large-volume conductive anomalies at depths of 150 to 200 m) colluvium.

II 3D geological modeling

A 3D geological model was constructed by integrating the in-situ geological observations (Fig. 3a), the borehole information, and the 3D electrical resistivity and seismic models. The

data integration and modelling were realized with the 3D GeoModeller software (©BRGM-Intrepid Geophysics). The software enables the interpolation of complex geology using geostatistical methods allowing the creation of a robust 3D geometric model (Fig. 3b) based on a Digital Elevation Model (DEM), as well as stratigraphic and structural information (dip, orientation, interface) and field observations (boreholes, cross-sections)

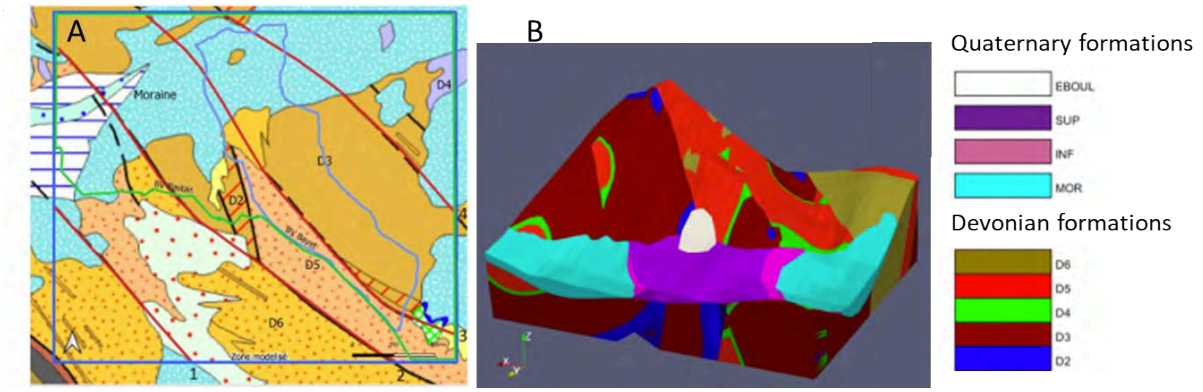

Figure 3 : A- : Location of the material superficial formation on top of the geological map at 1:25.000 scale (©Infoterre -BRGM-) Devonian formations D2 massive limestone (aquifer), D3 Black schist with limestone interlayers (aquifer), D4 detrital calcareous schists (aquifer) D5 black clay pelites((aquitard), D6 Quartzites (aquitard). Quaternary formations: MOR: moraines INF colluvium and scree below the rupture surface SUP: colluvium and scree above the rupture surface, the fracture surface to be represented as the interface between these two units; EBOUL; screes of 2018 landslide. B-: Geological 3D model: Full view of the modeled site.

The geological model provides a 3D reconstruction of the Devonian sedimentary sequence (Fig. 2b). Faults at unconformities cut this sequence. Overlying these formations are the glacial moraines of the Bastan Valley (represented in light blue). The mauve and purple layers are the colluvium and altered scree resulting from ancient landslides that have affected the area. The white mass represents the landslide that occurred in 2018. The volume of moving ground is represented by the purple layer. This area represents a volume of ca. 13 million m^3 (13,593,000 m^3). The 2018 landslide zone is shown in white. The volume calculated by this model is 201,360 m^3.
The model provides a 3D morphological representation of the rupture surface and its location. The simulated rupture surface extends from the 2018 scree to the Bastan, i.e., around 550 m long and 800 m wide. The rupture surface's depth varies from a few meters below the Bayet to a depth of up to 55 m beneath the village before leveling off towards the Bastan River without reaching the moraines at the base of the valley. Structural analysis reveals that rupture interacts with various geological formations within the colluvium.

III 3D hydrogeological modelling

The 3D geological model used a geometric base layer for the hydrogeological modelling carried out with Feeflow (DHI-WASY, 2009). The elevation of the domain ranges from 740 m (western outlet of Bastan) to 1951 m at the summit of Herrère ridge, which forms the northern and southern boundaries of the sector. To the North, an extension has been added beyond the boundaries of the geological model to avoid edge effects in the area. The lateral extent of the study area is bounded by two sub-vertical faults on the east and west sides. The steady-state model for an unconfined aquifer was constructed using a layered destructured approach, with variable-sized mesh volumes and higher resolution within the first 100 m of depth. Resolution is also increased within the geophysical model area to achieve mesh volumes smaller than 10 m^3. A final refinement is performed near significant features such as rivers and wells to attain mesh volumes smaller than 1 m^3. In this type of model, material

properties are defined for elemental selections. In our approach, we chose to use the geological model to provide the geometry of the elemental selections for formations D2, D3, D4, D5, and to use three threshold values of the electrical resistivity model to define the elemental selections included within the scope of the electrical modeling. The chosen thresholds are - resistivity less than 100 ohm.m^{-1} - resistivity ranging from 100 to 300 ohm.m^{-1} - resistivity greater than 300 ohm/m. Finally, the model includes 7 types of materials, with moraine and colluvial formations integrated into the resistivity model discretization.
The model boundary conditions consist of three components. The first component is a first-order boundary condition, known as the Dirichlet type. It is localized at the model's boundary on both sides of the Bastan, covering an approximately ten-meter-wide area that extends through the entire thickness of the model. The second component is a third-order mixed condition, following the Cauchy type, which combines prescribed hydraulic head and flux. This condition is specifically employed for characterizing rivers. The third component is a no-flow condition is applied by default to the remaining edges of the domain.
The water baseline recharge amounts are estimated using meteorological observations from the Luz-Saint-Sauveur measurement point at 2 km with effective rainfall calculated using the OUDIN method (Oudin et al., 2005) for a 30 mm rainfall event. The parameters (permeability k and specific storage Ss coefficients) and boundary conditions are initially tuned according to natural conditions
A semi-automatic calibration is performed with PEST (automated software for model calibration and uncertainty calculation for numerical models) using the piezometric data from the 9 piezometers in the sector. It enables a large number of iterations by varying parameter sets to make the model converge. The parameter set calibrated (Fig. 4b) is used to simulate the groundwater regime in a steady state, averaged over one hydrological year.

a

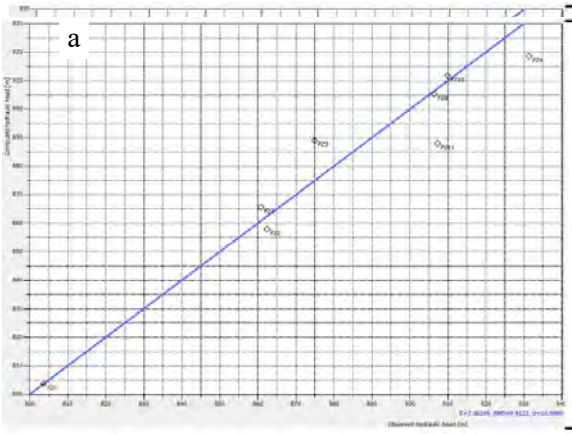

b

Paramètres (sélection élémentaire)	Valeurs calibrées du modèle en régime permanent
Matériaux	
Kx(D2) [m/j]	2.3*-5
Kx(D3) [m/j]	4.5*-5
Kx(D4) [m/j]	7.5*-5
Kx(D5) [m/j]	1.3*-7
Kx(res<100) [m/j]	1.2*-4
Kx(100<res<300) [m/j]	4.4*-5
Kx(res>300) [m/j]	7.5*-5
Conditions limites	
In-flow(Bastant) [j^{-1}]	1.13
In-flow(Badoueil) [j^{-1}]	1.46
In-flow(Bayet) [j^{-1}]	1.27
Out-flow(Bastant) [j^{-1}]	2.05
Out-flow(Badoueil) [j^{-1}]	7.31
Out-flow(Bayet) [j^{-1}]	1.14
Recharge	
Rr [mm.j^{-1}]	2.5

Figure 4: a - Comparison of observed water levels (x-axis) with the water level calculated by the steady-state model (y-axis). b - Optimized parameter values of the steady-state calibrated model.

In the final steady-state model calibration curve (Fig. 4a). The y-axis represents simulated piezometric levels, while the x-axis indicates the observed groundwater table elevation. The blue reference line signifies a perfect match between simulated and observed values.
The optimized hydraulic conductivities determined during calibration are, in both models, on the order of 1e-5 m.s^{-1} for the Devonian aquifer formations D2, D3, and D4, and 1e-7 m.s^{-1} for the shale mudstones (D5). The input/output transfer rates of the three rivers have been optimized in the steady-state model without field measurement.
The calibrated model is used to simulate two scenarios:
Scenario #1: Bayet waterproofing simulated in steady-state flow at equilibrium. In this scenario, waterproofing of the Bayet results in a significant reduction in piezometric height at the base of the landslide, of approximately 10 m. Some piezometers, such as PZ1 and PZ2

located to the west of the landslide, record a 10-meter drop in the water level. In the centre of the landslide (PZ10), the potential reduction in the water table height reaches approximately 20 m. Finally, complete waterproofing of the Bayet could lead to a reduction of about 30 m at the piezometer at the foot of the landslide (I8).
Scenario #2: Badoueil waterproofing simulated in steady-state flow at equilibrium. In this scenario, total waterproofing of the Badoueil results in a very significant decrease in piezometric height. All piezometers record a decrease of more than 30 meters, except for PZ6, which also experiences a drop in water level, unlike the previous scenario.

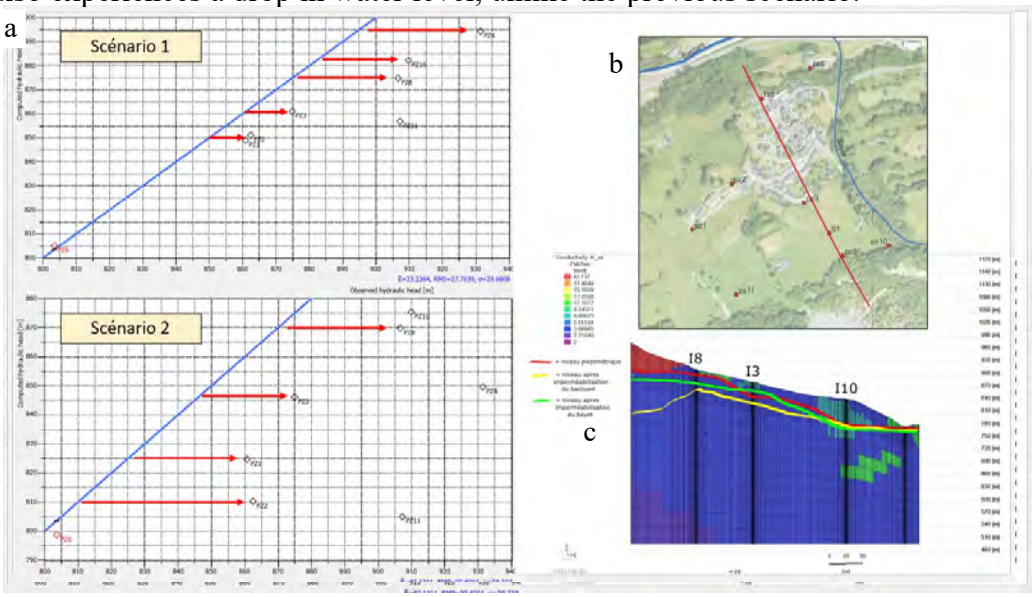

Figure 5: a - Comparison of simulated water levels (y-axis) in scenarios 1 and 2 with the water level calculated by the steady-state model (x-axis). b - Location of the I8-I3-I10 cross-section on orthophotography. c - Representation of the piezometric level in steady-state and in the two scenarios on the I8-I3-I10 cross-section overlying the calibrated hydraulic conductivity of the steady-state model.

It has been possible to test other remedial solutions using pumping systems. In their study, Tacher et al (2005) showed that the displacement intensity of the unstable slope under investigation was significantly reduced by pumping, which was simulated by means of hydrodynamic numerical flow simulations.

Conclusion

The results of this study are promising, and open the door for the using calibrated/validated hydrogeological model to simulate mitigation solutions. However, these models must be based on conceptual hydrogeological model that result from the analysis of multidisciplinary informationdata (geology, geochemistry, geophysics). They have to be calibrated and validated by means of multi-sensor data (variation of the piezometric level in response to external water inflows, origin of the water masses, and their transit). This approach requires the upstream construction of a 3D geological model, based on complementary geological and geophysical approaches (Loke et al., 2022), which will serve as a mesh for the hydrogeological simulations. Indeed, geometric modelling actively contributes to improving both geological and hydrogeological knowledge by clarifying the relative positions of formations in relation to each other and by highlighting the presence or absence of - potential hydraulic - connections between aquifer levels. The analysis of a large landslide by means of finite element modelling is a very efficient method for studying aspects of natural slope movements (François et al, 2007)
In this study, in order to understand the main causes and mechanisms of the phenomenon and to predict the behaviour of this slope under critical future conditions, it is planned to combine the hydrogeological simulations to a geomechanical model. The numerical simulation of such

problems is particularly convenient for clarifying complex mechanisms governing the movements and slope stability conditions.

References

Bertrand C, Vallet A. & Mudry J. (2015) Hydrochemical approach of mechanical degradation of the Séchilienne unstable slope. G Lollino et al. (Eds). *Engineering Geology for Society and Territory*, *Vol 2*, DOI: 10.1007/978-3-319-09057-3_383, © *Springer International Publishing Switzerland 2015*

Bogaard T., Guglielmi Y., Marc V., Emblanch C., Bertrand C. & Mudry J. (2007) Hydrogeochemistry in landslide research: a review. *Bulletin de la Societe Geologique de France 178*, *113–126*. doi:10.2113/gssgfbull.178.2.113

Cappa F., Guglielmi Y., Merrien-Soukatchoff V., Mudry J., Bertrand C. & Charmoille A. (2004) Hydromechanical modeling of a large moving rock slope inferred from slope levelling coupled to spring long-term hydromechanical monitoring: example of the La Clapière landslide (Southern Alps, France). *J. of Hydrology, 291, 67-90*

De Filippis G., Foglia L., Giudici M., Mehl S. & Margiotta S. (2017) Effects of different boundary conditions on the simulation of groundwater flow in a multi-layered coastal aquifer system (Taranto Gulf, southern Italy) *Hydrogeology Journal; Heidelberg Vol. 25, N° 7, 2123-2138*. DOI:10.1007/s10040-017-1589-x

DHI-WASY (2009). FEFLOW 5.4. Finite Element Subsurface Flow & Transport Simulation System. *User's Manual. 208 pp*. Berlin, Germany.

François B., Tacher L., Bonnard Ch., Laloui L., & Triguero V. (2007) Numerical modelling of the hydrogeological and geomechanical behaviour of a large slope movement: The Triesenberg landslide (Liechtenstein), *Can. Geotech. J. 44: 840–857*

Gance J., Malet J.-P., Supper R., Sailhac P., Ottowitz D. & Jochum B. (2016). Permanent electrical resistivity measurements for monitoring water circulation in clayey landslides. *Journal of Applied Geophysics, 32p*. doi: 10.1016/j.jappgeo.2016.01.011

K.J. Ellefsen *et al.* (2002) Crosswell seismic investigation of hydraulically conductive, fractured bedrock near mirror lake, New Hampshire*, J. Appl. Geophys.*

Kukemilks K, Wagner J-F (2021) Detection of Preferential Water Flow by Electrical Resistivity Tomography and Self-Potential Method. *Applied Sciences*. *11(9) :4224*.

Loke M. H., Wilkinson P. B., Kuras O., Meldrum P. I., Rucker D. F., The use of a semi-structured finite-element mesh in 3-D resistivity inversion, *Geophysical Prospecting*, 10.1111/1365-2478.13260, 70, 9, (1580-1601), (2022).

Maréchal J.C. (1998) Les circulation d'eau dans les massifs cristallins alpins et leurs relations avec les ouvrages souterrains. PhD thésis, *Ecole Polytechnique Fédérale de Lausanne, Lausanne, Suisse, 295 p*.

Oudin L., Hervieu F., Michel C., Perrin C., Andreassian V., Anctil F. & Loumagne C. (2005). Which potential evapotranspiration input for a lumped rainfall-runoff model? Part 2-Towards a simple and efficient potential evapotranspiration model for rainfall-runoff modeling. *Journal of Hydrology, 303, 290-306.*

Perrone A., Lapenna V. & Piscitelli, S. (2014) Electrical resistivity tomography technique for landslide investigation: a review. *Earth Sci. Rev. 135, 65–82.*

Petley D. (2012). Global patterns of loss of life from landslides. *Geology 40, 927–930*. doi:10.1130/G33217.1

Rice JR (2001) New perspectives in crack and fault dynamics. Mechanics for a New Millennium. Proceedings of the 20th International Congress of Theoretical and Applied Mechanics. H. Aref and J. W. Phillips (eds.). Chicago. *Kluwer Academic Publishers, pp. 1-23.*

Tacher, L., Bonnard, Ch., Laloui, L. & Parriaux, A. (2005). Modelling the behaviour of a large landslide with respect to hydrogeological and geomechanical parameter heterogeneity. *Landslides Journal, 2(1): 3–14*.

Mechanism of Deep-seated Toppling Deformation Revealed by Multi-SAR Observations: A Case Study in the Xiluodu Reservoir, Jinsha River

Kaiyu Ren[1,2], Xin Yao[1,2], Chuanchuang Yao[1,2]

[1] Institute of Geomechanics, Chinese Academy of Geological Sciences, Beijing, China
[2] Key Laboratory of Active Tectonics and Geological Safety, Ministry of Natural Resources, Beijing, China

SUMMARY: Reservoir filling in large hydropower stations triggers or accelerates deep-seated toppling deformations (DSTDs). It is of great significance to study the mechanism of DSTDs for the prediction of affected areas before filling. Taking Yanwan (YW) DSTDs in Xiluodu Reservoir as a sample, we collected 20 scenes of ALOS/PARSAR-2 images and used the small baseline subset interferometry synthetic aperture radar (SBAS-InSAR) and time-series offset tracking (TSOT) methods to analyze the spatiotemporal evolution of YW DSTDs from 2017 to 2023, which was validated with GNSS data. Our results show that the maximum deformation rate of YW DSTDs during the study period was around 1.5 m/y in the line-of-sight (LOS) direction. The displacements measured by the TSOT method had a consistent trend with the displacements monitored by GNSS. The soft-hard-interbedded structure provides favorable lithology conditions for toppling. The incision of the Jinsha River and the development of gullies lead to the topographic condition of exposure on three sides, shaping a convex slope similar to a triangular cone, which provides advantageous topographic conditions for toppling. Combined with field investigation, a deformation model of the "cantilever beam and retaining wall" of YW DSTDs was proposed.

Keywords: Deep-seated toppling deformations; Reservoir filling; Time-series offset tracking;

Introduction

Toppling is one of the basic types of slope movement (Varnes 1978; Hunger et al. 2014). In hard and thickly layered strata, topping is generally small and shallow, reaching depths between 20 and 60 m. Slow, ductile toppling typically creates deep-seated slope deformations in mountains and impacts at depths generally greater than 100 m and up to 250-300 m. In this study, the term "deep-seated toppling deformations" (DSTDs) is used to describe slope toppling motions with a maximum depth greater than (or close to)100 m and an average depth greater than 50 m.

Space-borne synthetic aperture radar (SAR) is an effective tool for monitoring the movement of landslides (Li et al. 2019), and its advantages of noncontact and traceable historical deformation are helpful for studying the evolution process of landslides. Phase-based differential interferometry SAR (DInSAR) methods are suitable for measuring slow-moving landslides with deformation rates ranging from several mm/y to a few tens of cm/y. Amplitude-based offset tracking is better for detecting landslides in active deformation processes with rates ranging from several tens of centimeters to several meters per year (Li et al. 2019).

Taking the YW DSTDs in Xiluodu Reservoir as a sample, this paper reveals the mechanism of toppling deformation and the correlation between DSTDs and reservoir water filling-drawdown. Moreover, the line-of-sight (LOS) spatiotemporal deformation is measured by SBAS-InSAR and the time-series offset tracking (TSOT) method, which is validated with GNSS data.

Geology

The geological section of the YW DSTDs was drawn according to the field investigation (Fig. 1), with a syncline and an anticline developed. The dip angles of the rock mass gradually transition from 79° to 35° along Xinchang Gully .

Spatiotemporal deformation mapped by TSOT

Fig. 2 illustrates the time-series displacements measured by TSOT between July 2017 and June 2020. From July 2017 to July 2018, the slope showed weak signs of deformation. From July 2018 to July 2019, the deformation in the middle and lower parts of the slope increased significantly. By June 2020, the deformation increased continuously and gradually expanded upwards, forming a basically symmetrical feature along the ridgeline. During the observation period, the maximum cumulative displacement of the slope reached 4.5 m, and the mean deformation rate was about 1.5 m/y. The deformation was concentrated in the middle and lower parts of the slope and gradually decreased towards the surrounding area.

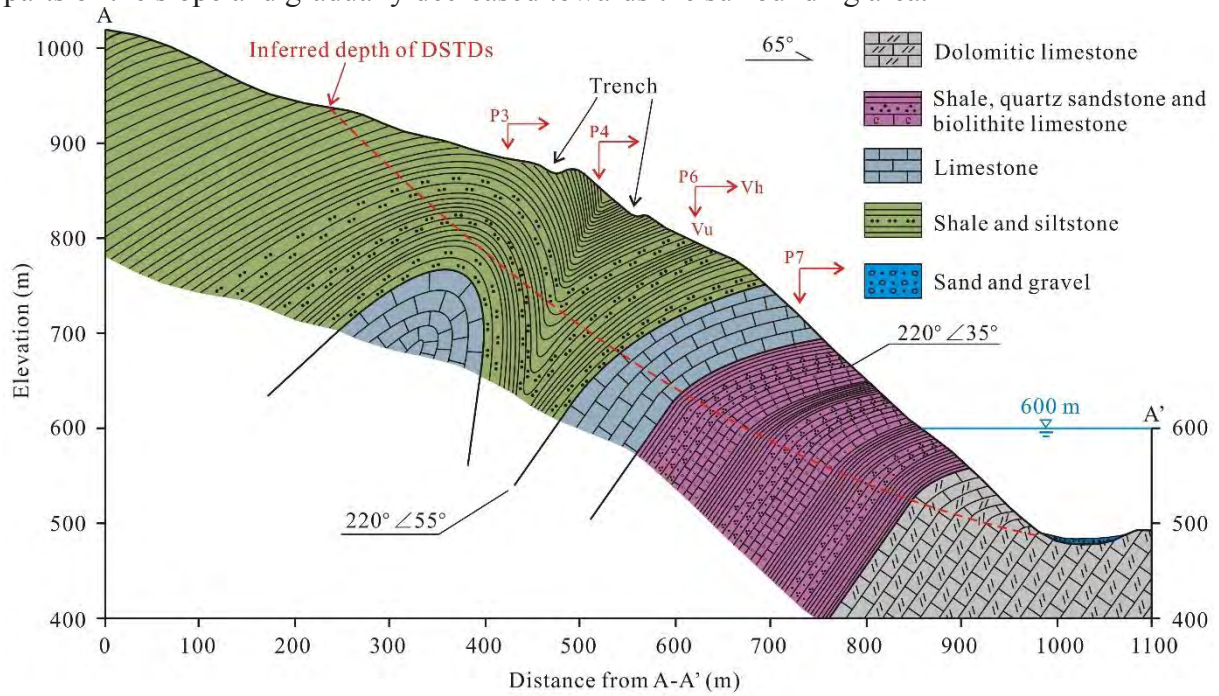

Fig. 1 Geological section (arrows represent the horizontal rates (Vh) and the vertical rates (Vu) of each GNSS, and the size of the arrows indicates the deformation magnitude).

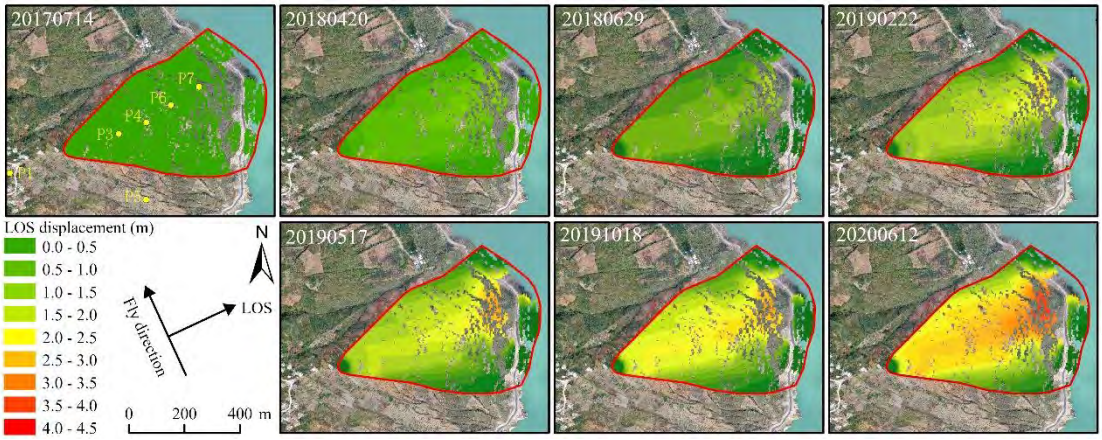

Fig. 2 Time-series deformation measured by offset tracking in the range direction

Taking P7 as an example, the black line in Fig. 3a is the fitted line of the displacement trend. In several filling-drawdown cycles, the deformation rates of the four stages from fast to slow were in the order of rapid drawdown of water level period, high water level period, low water level period and rapid rise of water level period (Fig. 3b). Obviously, compared with the static period of high and low water levels, the dynamic period of rapid rise and drawdown of the water level has a greater impact on the deformation rate. In other words, it can be considered that the effect of float weight and seepage pressure caused by the rise and drawdown of the

water level have a greater impact on the deformation rate than the softening effect of reservoir filling on the rock mass.

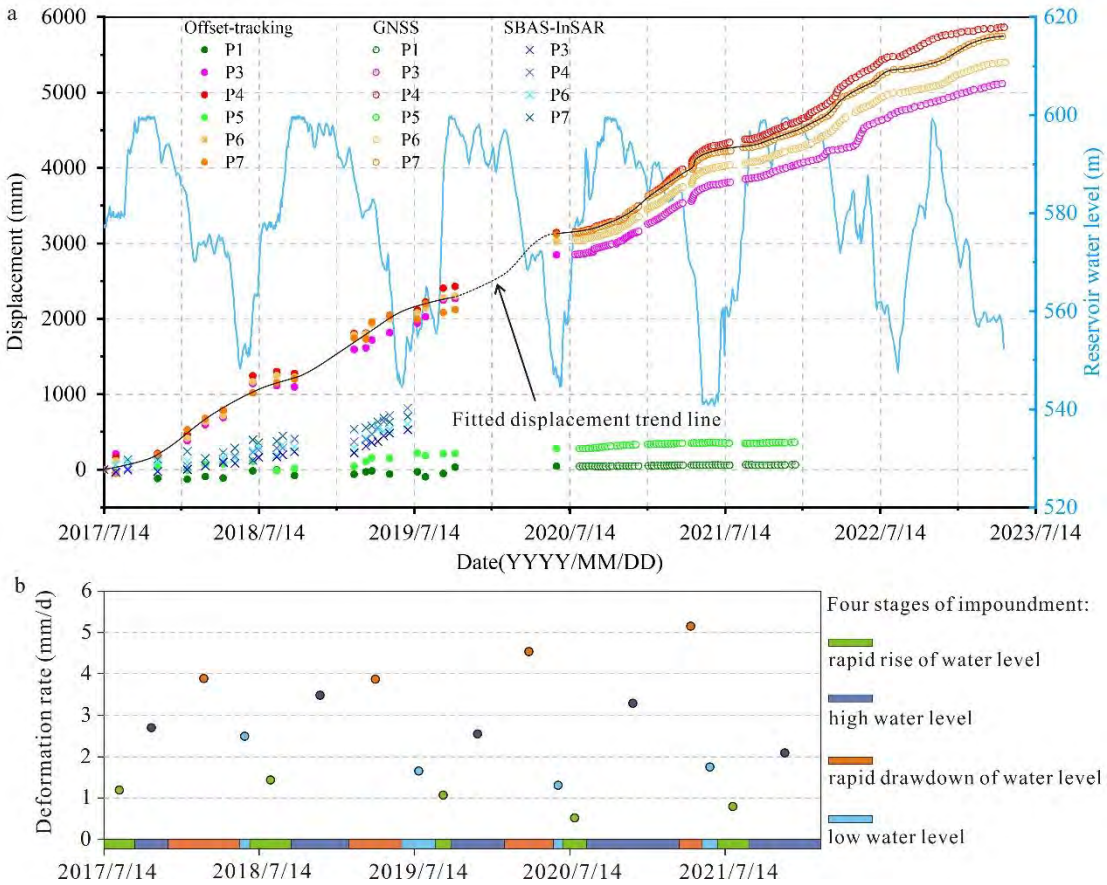

Fig. 3 (a) Time-series displacements of offset tracking, SBAS-InSAR and GNSS in the LOS direction. (b) The deformation rates of the four stages of reservoir filling

From the viewpoint of the deformation within a filling-drawdown cycle, the cumulative displacements of P7 in five cycles were 1001 mm, 920 mm, 1128 mm, 1064 mm, and 1077 mm successively, fluctuating around 1000 mm. Compared to the law of displacement variation presented by GNSS data, it could be considered that the displacements measured by offset tracking were basically consistent with those of GNSS. In contrast, the LOS accumulative displacement measured by SBAS-InSAR from July 2017 to June 2019 was only 706 mm, which was far less than the result of offset tracking.

“Cantilever beam and retaining wall” model

We speculated that the Qiaojia Formation limestone blocks the expansion of the topping deformation to the inside of Xinchang Gully. The Qiaojia Formation limestone, as a hard rock, plays the role of a "retaining wall" in slope stability (Fig. 1). This "retaining wall" model is similar to that proposed by Huang (2007) in their study of the Xikou landslide and Toushai landslide (Fig. 4a). The hard rock strata in the middle of the slope all play a role in bearing the pushing force transmitted by the deformation of the upper rock mass, and the weak rock mass will be pushed forward, which is proven by the bulging deformation observed at the foot of the slope (Fig. 4a).

The Qiaojia Formation limestone is also similar to the "cantilever beam" proposed by Gu and Huang (2016) in the study of the Gongjiafang landslide (Fig. 4b). However, in this model, the landslide is initiated with toe collapse connected with water fluctuation, and the "cantilever beam" is formed after the failure of the slope toe. Then, a composite shear and flexural failure mode is revealed.

The deformation mode of YW DSTDs belongs to the composite model of the above two. After filling, the softening effect of the rock mass at the toe leads to a significant reduction in the

supporting force. The Qiaojia Formation limestone, as a hard rock, acts as a "cantilever beam", resisting the pushing force transmitted by the upper rock mass, and the rock mass below the road acts as a "retaining wall", blocking the expansion of the topping deformation to the inside of Xinchang Gully. Thus, the bottom boundary of the deformation is determined (Fig. 4c).

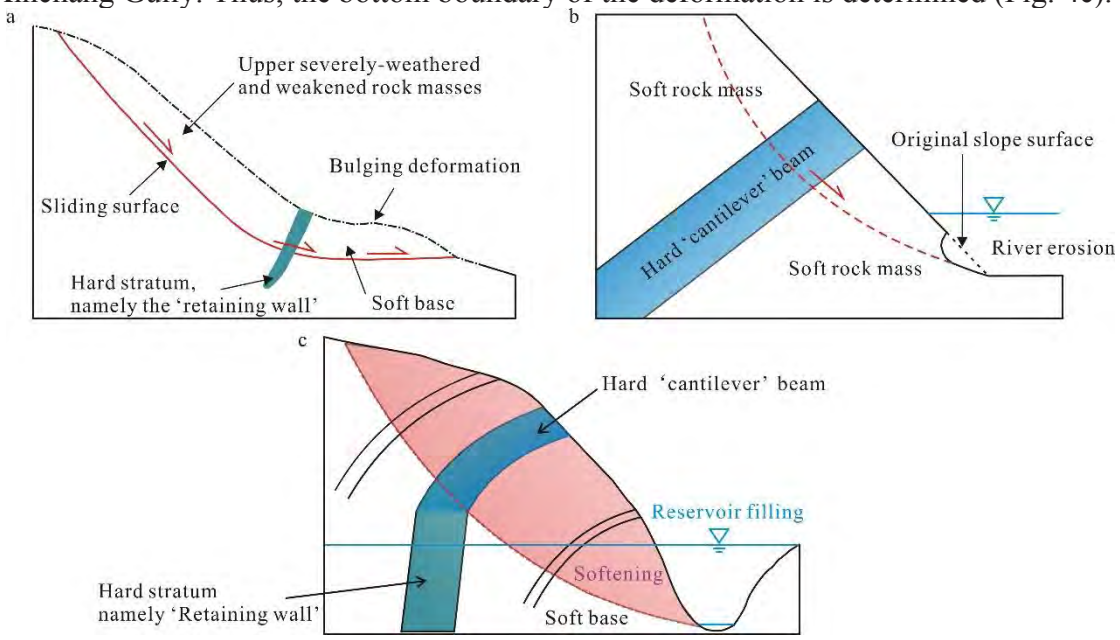

Fig. 4 (a) "Retaining wall" model modified from Huang (2007). (b) "Cantilever beam" model modified from Gu and Huang (2016). (c) "Cantilever beam and retaining wall" model of the YW DSTD.

Conclusion

(1) The maximum deformation rate of the YW DSTDs during the observation period was about 1.5 m/y. After filling, the YW DSTDs showed a fluctuating deformation trend, and the deformation rates of the four filling stages were successively from fast to slow: rapid drawdown of water level period, high water level period, low water level period and rapid rise of water level period.

(2) The soft-hard-interbedded structure provides favorable lithology conditions for toppling. The incision of the Jinsha River and the development of gullies lead to the topographic condition of exposure on three sides, increasing the contact area with the reservoir water, and shaping a convex slope similar to a triangular cone, which provides advantageous topographic conditions for toppling. Reservoir filling triggered YW DSTDs.

(3) YW DSTDs belong to the composite deformation mode of the "cantilever beam and retaining wall". The Qiaojia Formation limestone, as a hard rock, acts as a "cantilever beam", resisting the pushing force transmitted by the upper rock mass, and the rock mass below the road acts as a "retaining wall", blocking the expansion of the topping deformation to the inside of Xinchang Gully. Thus, the bottom boundary of the deformation is determined.

Reference

Gu DM, Huang D (2016) A complex rock topple-rock slide failure of an anaclinal rock slope in the Wu Gorge, Yangtze River, China. *Eng Geol* 208:165–180.

Huang RQ (2007) Large-scale landslides and their sliding mechanisms in China since the 20th century. Chinese *Journal of Rock Mechanics and Engineering* 26 (3): 433-454. (in Chinese)

Hungr O, Leroueil S, Picarelli L (2014) The Varnes classification of landslide types, an update. Landslides 11 (2):167–194.

Li M, Zhang L, Shi X, Liao M, Yang M (2019) Monitoring active motion of the Guobu landslide near the Laxiwa Hydropower Station in China by time-series point-like targets offset tracking. *Remote Sens. Environ.* 221, 80–93.

Varnes DJ (1978) Slope movement types and processes. In: Schuster RL, Krizek RJ (eds) Landslides, analysis and control, special report 176: transportation research board. National Academy of Sciences, Washington, DC., pp 11–33

Fundamental aspects of structural transformations of the geological environment in preparation of a landslide block – XIVth ISL, Chambéry 2024

G. P. Postoev[1], A.I. Kazeev[1], M.M. Kuchukov[1], N.A. Orlova[1]

[1] Sergeev Institute of environmental geoscience, Moscow, Russia

In the geological environment in the gravitational field of the Earth in each point of the soil body arises, in accordance with the Coulomb-Mohr law, a steady-state pressure, which depends on the weight of the strata above and the strength of the soil at the point. I.e. the law of preservation of stability of the stress-strain state (SSS) with the allowance of its evolutionary changes (e.g. pressure decrease in points) in separate areas of the field (Postoev et al., 2020). Local force impact of geodynamic process (e.g. landslide development) can cause an intensive process of stress unloading at the impact site and, in this connection, create a threat to the stability of the initial state in the form of revolutionary propagation in the geological environment of local changes in the SSS. In this case, the law of protection of the initial stress-strain state and the established regime of its formation in the points of the geological environment begins to operate.

Keywords: stress-strain state, dissipative geological structures (DGS), landslide, stress-strain state (SSS)

Introduction

Protection of the SSS is carried out by local transformation with the formation of new dissipative geological structures (DGS) at the boundary with the source of danger (Postoev et al., 2020; Prigogine & Nicolis, 1977). At the same time, the formation of DGS parameters and the restructuring of the SSS happen in such a way that the DGS independently interacts with the source of threat (e.g., landslide zone). The DGS in the soil body of the landslide scarp (above the boundary of the landslide source) reacts to the displacements of the landslide slope and when the limit state of the scarp is reached, it starts the rotational movement (rotation) with the development of soil mowing deformations in the narrow zone of the DGS boundary shell. Thus, a natural mechanism is triggered, which allows the separation of the DGS in the form of a landslide block when the interaction between the DGS and the external threat exceeds a critical level. I.e. with the formation of DGS the boundaries of massifs prepared for displacement and their possible separation from the main part of the geological environment are manifested. To date, the mechanism of DGS formation in the area of external impact on the geological environment has been revealed. The regularities determining the scale and degree of catastrophic manifestation of destructive deformations in the form of landslide blocks, failures above the underground cavity, ground base protrusion (under the load from the foundation) have been determined (Postoev et al., 2020). Common to various types of local force impacts is the transformation of the SSS of the geological environment as the action of the natural protective mechanism to create appropriate large structures of DGS, designed to interact with the force perturbation. The geological criterion of 0.009 (geological constant) regulating the processes of SSS changes in the local area is identified. The equations of limiting equilibrium of DGS were obtained, the mechanism of their formation (mostly on landslide problem) and separation with destructive deformation in the form of large volumes of soil were studied.

Most of the established regularities of origin and development of DGS were initially detected in the study of landslide processes.

Initial condition of the original bedrock massif

The stress-strain state in the soils of the bedrock massif is formed under conditions of gravitational compression according to the Coulomb-Mohr law. In accordance with this, the pressure in the *i*-th point of the massif is established (Postoev et al., 2020):

$$p_i = (\gamma Z_i - \sigma_{str,i}) \cdot tg^2(45 - \varphi_i/2), \quad (1)$$

where p_i - stabilised pressure in a point of the massif, equal in all directions; γ - average value of specific weight of soils overlying the point under consideration; Z_i - depth of occurrence of the point; $\sigma_{str,i}$ and φ_i - strength of structural bonds and angle of internal friction of the soil in the point at the depth of Z_i.

The Coulomb-Mohr law also means that because the soil has the strength of structural bonds $\sigma_{str,i}$ and friction resistance at contacts between particles and aggregates (parameter φ_i), the stabilised (steady-state) pressure p_i at the point according to (1) is always less than the value of vertical pressure - γZ_i (in contrast to Pascal's law for the atmosphere and hydrosphere). Stability at a point is ensured as long as the stress equilibrium of the point with the surrounding soil at the horizon Z_i is maintained. That is, the pressure p_i at the i-th point meets the mobilised pressure (reactive value) equal to it at the neighbouring point at the given horizon.

A local force perturbation, for example, in the form of a slope (slope formation) can cause a decrease in vertical pressure (from the weight of overlying soil masses) at its base and, accordingly, a decrease in pressure p_i at points (stress unloading), both in the soils composing the slope and in the adjacent bedrock (slope influence), above the slope edge. At the same time, there may be a gradual subsidence of the day surface of the bedrock massif in the form of a tilt to the slope edge. But at each point, the steady state is maintained because the pressure p_i (as indicated above) mobilises an equal reactive pressure at the neighbouring point. The rock massif can experience up to the limit deformations while retaining its overall stability.

Formation of dissipative geological structures in a landslide area

Let us consider the formation of DGS in the bedrock of the landslide scarp at the landslide development site in the form of displacement of previously separated blocks. The main parameter determining the boundaries of the force impact of the landslide centre is the depth in the bedrock to the landslide base (lower boundary of landslide displacement development at the site) Z_a (Fig. 1). It has been established that DGS in the bedrock above the landslide origin arises when there is a threat of landslide process development, in particular, when the slope height of the bedrock massif above the landslide scarp, as a result of landslide process development on the slope, reaches a critical value H_{cr} (see Fig. 1).

The equation of limit state of the DGS, which is prepared for separation in the form of a landslide block, is obtained:

$$\gamma Z_a - \sigma_{str,a} = \gamma (Z_a - H_{cr}) \cdot \pi/2, \quad (2)$$

where Z_a - depth to the base of block sliding; γ - average value of specific weight of soil to the depth of Z_a; $\sigma_{str,a}$ - structural strength of soil in DGS at the depth of Z_a; H_{cr} - critical value of DGS slope height.

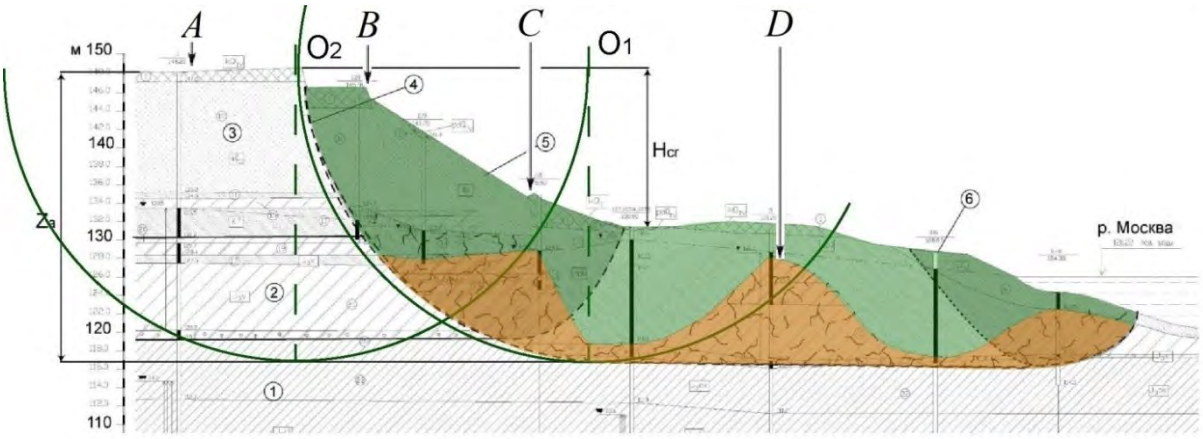

Figure. 1. Schematic engineering-geological section along the central site during the formation and separation of the DGS block at the landslide area of Khoroshevo (Moscow) in 2007. 1 and 2 - clays of Volga and Oxford stages of Jurassic system, respectively; 3 - sands of Quaternary sediments; 4 - circular sliding surface in the DGS shell; 5 - separated DGS block; 6 - borehole. The boundaries of DGS-blocks are shown as arcs of a circle with radius Z_a by green lines. *A, B, C, D* - indicators of DGS manifestation.

Regularities of dissipative geological structure functioning

- The parameters of the DGS, its boundary shell and the pressure values in the soils within their boundaries are set according to Z_a and the geological criterion of 0.009:

$$p_a/\sigma_a = h/Z_a = 0.009, \quad (3)$$

where p_a and σ_a are the pressure values at the point, respectively, in the soils of the DGS and its shell at the depth Z_a (the base of landslide displacement development); h is the thickness of the DGS shell.

-In accordance with (3), the geological criterion is numerically equal to the ratio of the shell thickness to the radius of its curvature. Upon reaching the limit state according to (2), further functioning of the DGS prepared for separation takes place in the form of its rotation (see Fig. 1, around the centre O_1) along the shell with radius Z_a. At the same time, the soils in the shell are deformed in the mowing mode.

-The separation of the DGS block and its displacement on the resulting shear (sliding) surface occurs when the angle α_i of DGS rotation reaches the critical value α_{cr}:

$$\alpha_i = \alpha_{cr} = h/Z_a = 0.009 \text{ radian}. \quad (4)$$

When $\alpha_i = \alpha_{cr}$ the deformation Δ_{cr} of the soil in the shell will be:

$$\Delta_{cr} = h = 0.009 Z_a. \quad (5)$$

-Thereafter there is a destruction of soils in the shell, with breaking of structural bonds, and transition from deformation in the mode of mowing to shear with displacement of DGS along the formed circular sliding surface with radius Z_a (along the central shaft, see Fig.1).

-The occurrence of high pressure in the shell soils, according to (3), prevents the steady filtration of groundwater. In connection with this, in the area of the central section of the site, the filtered water can be pressurised and reoriented towards the lateral boundaries of the DGS block (see Fig. 1, indicator A).

-Groundwater within the DGS is in a closed volume and changes in its level are not consistent with the hydrogeological conditions of the area outside the DGS boundaries (indicator B, see Fig. 1)

-Detachment and displacement of the DGS block takes place on a circular sliding surface with radius Z_a (indicator D, see Fig. 1), not taking at this stage the whole landslide massif on the site.

-The participation of the neighbouring DGS (with the centre O_2, see Fig. 1) in the preparation of the landslide block is manifested in the formation of a crack (indicator C, see Fig. 1) and a shear surface inside the DGS-block (downward arc from the point O_1, see Fig. 1).

The main fundamental aspects of the natural technology to protect the initial stress-strain state of the geological environment are also confirmed when analysing the mechanism of DGS formation during the preparation of a failure above the underground cavity and in the soil basement under the foundation of a building (Postoev et al., 2020).

Conclusion

In the geological environment, in the rock and soil massifs, the initial stress-strain state (SSS) is formed in the gravitational field of the Earth, in accordance with the laws of physics. Local manifestation of geodynamic process (for example, in the form of landslide origin) can be represented as an external impact on the geological environment, threatening a fundamental change in its initial SSS. In the preparation and formation of a new landslide block the fundamental aspects of the natural technology of protection of the initial state of the geological environment are manifested. It includes formation and functioning of dissipative geological structure (DGS), its boundary shell, construction of SSS change regime in new structures in accordance with geological criterion 0.009 and conditions of interaction with landslide source. Separation of DGS in the form of landslide block for the geological environment (bedrock massif) is presented as elimination of landslide threat and providing the initial SSS.

References

Postoev G.P., Kuchukov M.M., Kazeev A.I. (2020) Physical laws of pressure distribution in the geological environment. *Geoecology. Engineering geology, hydrogeology, geocryology* № 6. pp. 22-31.

Prigogine I., Nicolis G. (1977) Self-Organisation in Non-Equilibrium Systems: From Dissipative Structures to Order Through Fluctuations. New York: *J. Wiley & Sons*.

Quantification of erosion by cosmogenic nuclides and rockfall inventories: contribution to the estimation of rockfall hazard in the Mont-Blanc massif

Courtial-Manent L.[1,2], Mugnier J.-L.[1], Ravanel, L.[2], Buoncristiani J.-F.[3]

[1] ISTerre, USMB, Chambéry, France
[2] EDyTEM, USMB, Chambéry, France
[3]Biogéosciences, Université de Bourgogne, France

SUMMARY: Long-term erosion in high-altitude rock walls is controlled by rockfall distribution, and the maximum volume is an important parameter in estimating rockfall hazard. We wondered whether long-term rock wall erosion, which can be estimated with cosmogenic nuclides methods, could constrain the value of this maximum volume. We formulated the analytical link between maximum volume and long-term erosion rate in a power law and used it for the upper part of the Mer de Glace basin (Mont-Blanc massif). In this area, we compared rockfall volume distribution obtained by Terrestrial Laser Scanning and direct observations with the erosion rate derived from ^{10}Be concentrations of supraglacial clasts. The ^{10}Be concentrations are rather homogeneous ($2.7 \pm 1.3\ 10^4$ at.g^{-1}) and are related to an average erosion rate of 1.2 ± 0.4 mm/yr. The inventories indicate that the power law is applicable between 1 and 20,000 m^3, with a *b* parameter between 0.66 and 0.54. The erosion rates estimated from the inventories are 6.9 and 5.2 mm/yr, with a maximum observed volume of 20,000 m^3. These inventory-related erosion rates are clearly superior to those obtained using the cosmogenic nuclides approach. This comparison does not reveal any past rockfall of greater volume than those observed recently, but it does suggest that the number of rockfalls has increased, and that the rate of erosion has at least quadrupled between the pre-1940 period and the 2003-2015 period. This increase could be linked to the degradation of permafrost at high altitude.

Keywords: rockfalls, erosion, permafrost, LiDAR, cosmogenic nuclides, Mont-Blanc massif

Introduction

The study of past rockfalls provides one of the major bases for estimating rockfall hazards. However, intrinsic difficulties are encountered: the maximum possible volume of a rockfall event to be considered in the hazard assessment could be higher than the greatest observed volume (Mavrouli and Corominas, 2020) due to the small number of large events, in registrable times. The question arises as to which area and for which period a catalog is representative, and is there a derive over time concerning the rockfall productivity?

In this paper, we propose the basis for a method that could enable an assessment of the maximum possible rockfall volume and the estimation of cumulative rockfall volumes. This cumulative volume corresponds to the long-term erosion, which is estimated using methods based on the concentration of cosmogenic nuclides in sediments, at the catchment scale (Dunai, 2010). This approach has been adapted to the case of the rock walls of glaciated basins (Ward and Anderson, 2011; Sarr et al., 2019; Scherler, & Egholm, 2020; Orr et al., 2021).

We both review the methods for analyzing rockfall inventories and estimating erosion rates by measuring cosmogenic nuclides in transported clasts. These two approaches are then applied to the upper part of the Mer de Glace basin (Mont-Blanc massif, MBM) (Figure 1) where

numerous rockfalls are observed (Ravanel et al., 2010, 2011, 2017), possibly linked to the degradation of permafrost at high altitude (Magnin et al., 2017).

Power law and rockfall erosion rate

Any observed distribution of rockfall volumes V must be regarded as an estimate of the mean value of a random variable and can be approached by a power law (Graber and Santi, 2022), where a and b are respectively the number of rockfalls greater than 1 m^3 and the exponent parameter:

$$fs(V) = aV^{-b} \qquad \text{(eq. 1)}$$

The total eroded volume Vt_p, due to rockfalls can be calculated from a numerical integration till the maximum volume Vmp and is then (Hantz et al., 2003):

$$Vt_p = \int_{V_{mp}}^{0} aV^{-b}\, dv = \frac{a}{(1-b)}\left(V_{mp}{}^{(1-b)}\right) \text{ (eq. 2)}$$

By replacing a by $\bar{a}$ (the number of rockfalls greater than 1 m^3 produced per year and for a unit surface) and Vt_p by $S * \varepsilon_{pl}$ (the product of the rock wall surface by the erosion rate) and with certain mathematical reorganization:

$$V_{mp} = \left(\frac{1-b}{\bar{a}} . \varepsilon_{pl}\right)^{\frac{1}{1-b}} \qquad \text{(eq. 3)}$$

This equation shows that V_{mp} is a power function of ε_{pl} and is expressed as a straight line in a log-log diagram (Figure 2).

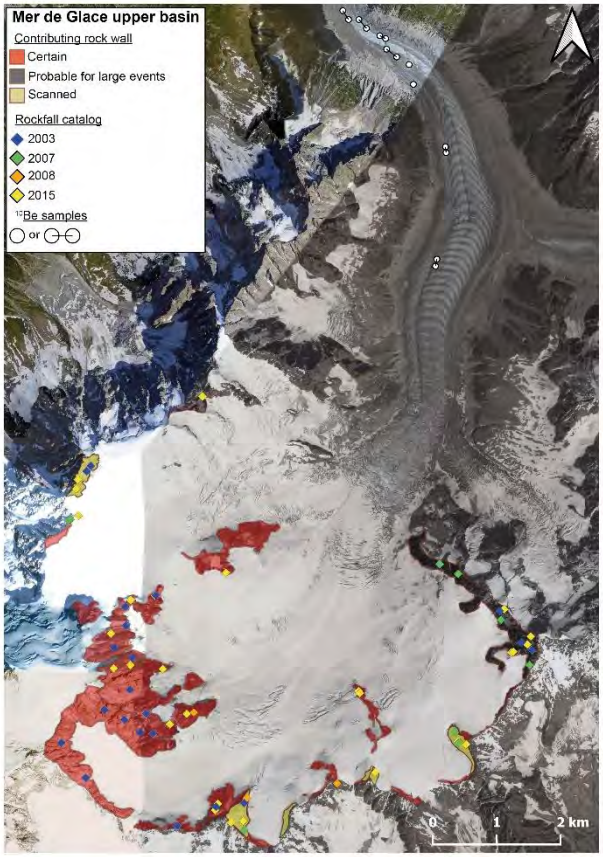

Figure 1. The Mer de Glace glacier, with location of the study area, ^{10}Be samples, contributing rock walls to the supraglacial load of the central part of the Mer de Glace, and rockfalls inventoried (Ravanel et al., 2010, 2017).

Rockfalls and ^{10}Be concentrations

The basic assumption used to study the erosion is that the ^{10}Be concentration of sedimentary clasts from the catchment is equal to the average ^{10}Be concentration of the catchment surface, itself depending on the average atom production rate of the catchments (P_m), the attenuation length of cosmic particles (Λ_n), and the average erosion rate of the catchment (ε_c) (Dunai, 2010). The concentration measured in the clasts (C_0), is then equal to:

$$C_0 = \frac{P_m \Lambda_n}{\varepsilon_c} \qquad \text{(eq. 4)}$$

We used the same analytical protocol as Courtial-Manent et al. (2022) to measure the ^{10}Be concentration of the samples.

Application to the rock walls of the upper basin of the Mer de Glace

Each of the ^{10}Be samples was composed of an amalgam of small clasts (sand or gravel) collected over around 2,500 m^2 of the glacier surface. The 8 amalgams were sampled on different transported moraines at different altitudes so that the sampled clasts would represent as many

initial rockfalls as possible. The concentration of the 8 samples measured ranged from 1.2 ± 0.2 to 6.7 ± 0.4 10^4 at.g^{-1}, with an average of 2.7± 0.35 10^4 at.g^{-1}.

The rock walls in the upper part of the basin that contribute to feed the central downslope part of the Mer de Glace were determined (Figure 1) taking into account the topography of transported moraines and the ice flow lines estimated from glacier velocity field derived from interferometric analysis between satellite images (Millan et al., 2022). The average cosmogenic nuclide production rate of these upslope rock walls was estimated using the method presented by Sarr et al. (2018) with a value of 46 ±18 at.g^{-1}.yr^{-1}. This leads to a long-term erosion rate of 1.2 ± 0.4 mm/yr. Given the productivity of the walls considered, the glacier's flow velocity and its melting (Sarr et al., 2019), this erosion rate considers the initial ^{10}Be concentrations of several thousand rockfalls greater than 1 m^3 that occurred before 1960.

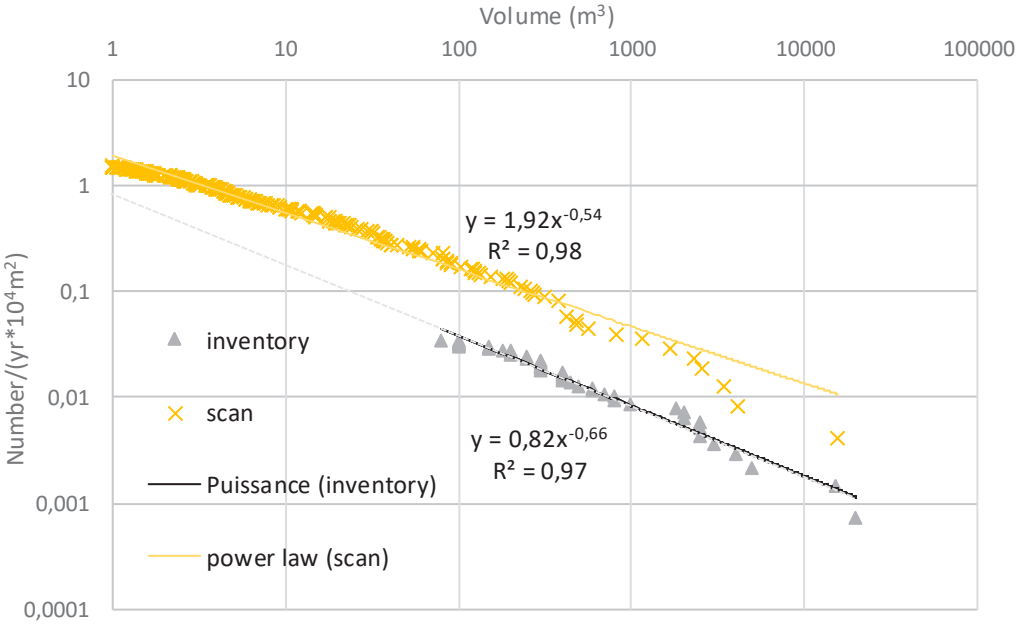

Figure 2. Cumulative frequency of rockfalls estimated by scan comparison and direct observations for the upper part of the Mer de Glace basin.

The rockfalls affecting the rock walls in this upper part of the basin (Figure 3) have been inventoried in previous catalogs (Rabatel et al., 2008; Ravanel et al., 2010; 2011; 2017). The largest rockfall over the period considered is 20,000 m^3, and the cumulative volume curves follow power laws over the ranges 1 to ~5,000 m^3 and 100 to 20,000 m^3, respectively for the results from LiDAR and the direct observation catalogs (Figure 3). The *b*-values of the two cumulative curves are fairly close (0.54 ± 0.03 and 0.66 ± 0.09) but the values of ā are respectively 1.92 10^{-4} number.yr^{-1}.m^{-2} and 0.82 10^{-4} number.yr^{-1}.m^{-2}. As the LiDAR DEMs cover only 6 rock walls, constituting only part of the rock wall of the upper Mer de Glace area (0.3 km^2 scanned rock walls out of a total of 8.3 km^2), we considered the direct observation catalog to be more representative of the basin as a whole. Erosion rates were calculated in two different ways: by summing observed events or by using equation (2) and parameters from the direct observation catalog. The results obtained are 5.2 and 6.9 mm/yr respectively.

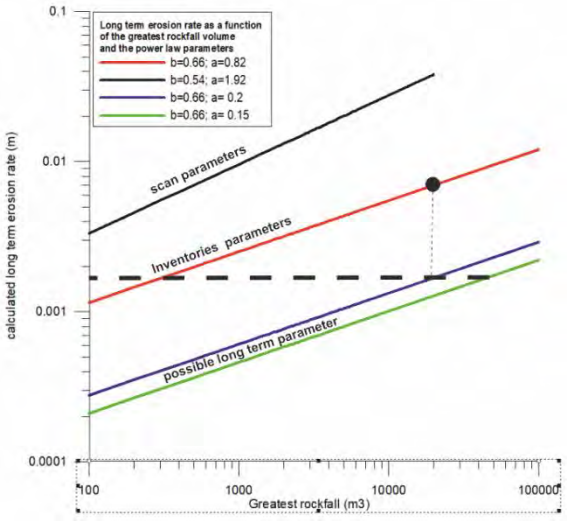

Figure 3. Relationships between maximum rockfall volume, erosion rate and parameter of the rockfall distribution power law (ā and b), calculated using equation (2). The black dot refers to the greatest observed rockfall (20,000 m^3); the horizontal dashed line to the long-term erosion rate estimated from ^{10}Be.

Discussion

An analytical calculation is proposed to estimate the erosion rate from the $\bar{a}$ and b parameters of a power law volumes distribution and the maximum rockfall volume. Regardless of the method used to estimate inventory-related erosion rates (mathematical integration or summation), these are in excess of 5 mm/year and therefore, superior to those obtained using the ^{10}Be cosmogenic nuclide method ($\varepsilon_c = 1.2 \pm 0.4$ mm/yr). This comparison does not allow to reveal any past rockfall of greater volume than those observed recently, but it suggests that the number of rockfalls has increased. In case the greatest rockfall volume during the pre-1960 period was the same as the one during the 2003-2015 period (20,000 m^3), the rockfall productivity of rock walls ($\bar{a}$) was four times lower in the pre-1960 period than in the 2003-2015 period. If the greatest rockfall volume during the pre-1960 period was > 20,000 m^3, the rockfall productivity of rock walls ($\bar{a}$) was at least four times lower in the pre-1960 period than in the 2003-2015 period.

References

Courtial-Manent L. J-L. Mugnier, S. Zerathe, J. Carcaillet, R. Vassallo, L. Ravanel, L. Tavernier, J-F. Buoncristiani (2022) Late Holocene initiation of a deep rock slope failure in an Alpine valley revealed by 10Be surface exposure dating (Chamonix, France). Quaternary International 652, 52-62.

Dunai, T. J., 2010. Cosmogenic nuclides, Principles, Concepts and Applications in the Earth Surface Sciences. Cambridge University Press.

Graber A., and Santi, P., 2022. Power law models for rockfall frequency-magnitude distributions: review and identification of factors that influence the scaling exponent. Geomorphology 418. 108463

Magnin, F., Josnin, J.-Y., Ravanel, L. et al.., 2017. Modelling rock wall permafrost degradation in the Mont Blanc massif from the LIA to the end of the 21st century. The Cryosphere 11, 1813–1834.

Mavrouli, O.; Corominas, J. Evaluation of Maximum Rockfall Dimensions Based on Probabilistic Assessment of the Penetration of the Sliding Planes into the Slope. Rock Mech. Rock Eng. 2020, 53, 2301–2312.

Millan, R., Mouginot, J., Rabatel, A., Morlighem, M., 2022. Ice velocity and thickness of the world's glaciers. Nat. Geosci. 15, 124–129. https://doi.org/10.1038/s41561-021-00885-z

Orr, E. N., Owen, L. A., Saha, S., Hammer, S. J., & Caffee, M. W. (2021). Rockwall slope erosion in the northwestern Himalaya. Journal of Geophysical Research: Earth Surface, 126, e2020JF005619. https://doi.org/10.1029/2020JF005619

Ravanel L, Allignol F, Deline P, Gruber S, Ravello M. 2010. Rock falls in the Mont Blanc massif in 2007 and 2008. Landslides 7: 493–501 https://doi.org/10.1007/s10346-010-0206-z

Ravanel L, Deline P, Jaillet S. 2011b. Quantification des éboulements/écroulements dans les parois à permafrost de haute montagne: quatre années de relevés laser terrestres dans le massif du Mont-Blanc. Revue Française de Photogrammétrie et de Télédétection 192: 58–65.

Ravanel L, Magnin F, Deline, P., 2017. Impacts of the 2003 and 2015 summer heat waves on permafrost-affected rockwalls in the Mont Blanc massif. Science of the Total Environment 609: 132–143 https://doi.org/10.1016/j.scitotenv.2017.07.055.

Sarr A-C., Mugnier, J.L., Abrahami, R., Carcaillet, J, Ravanel, L. (2019) Sidewall erosion: insights from in situ-produced 10Be concentrations measured on supraglacial clasts (Mont Blanc massif, France). Earth Surface Processes and Landforms. 44, 1930-1944. DOI: 10.1002/esp.4620

Scherler, D., & Egholm, D. L. (2020). Production and transport of supraglacial debris: Insights from cosmogenic 10Be and numerical modeling, Chhota Shigri Glacier, Indian Himalaya. Journal of Geophysical Research: Earth Surface, 125, e2020JF005586. https://doi.org/b10.1029/2020JF005586

Utilizing technology for safeguarding against rockfalls: La Rochaille case study

Alberto Grimod[1], Elena Metz[2], Paolo Gandolfi[1], Luca Gobbin[1]

[1] France Maccaferri, 8 Rue Pierre Mechain, 26000, Valence, France
[2] Géolithe, 181 Rue des Bécasses, 38920, Crolles, France

SUMMARY: The securing of the departmental road RD 900 at the Rochaille passage is a complex yet vital challenge. The presented project, aimed at protecting travelers, local residents, and sustaining economic and touristic activity, serves as a showcase for modern engineering and technological innovation. The combination of advanced protective structures, sophisticated detection systems, and meticulous planning represents a significant step in ensuring safety on this strategically important road connecting France and Italy. As the work continues, Rochaille emerges as an exemplar of how technology can address complex issues, save lives, all while preserving the natural beauty of the Alpes-de-Haute-Provence

Keywords: alerting system, rockfall barriers, rockfall, alarm, satellite.

Introduction and location

In the heart of Alpes-de-Haute-Provence, the RD 900 departmental road, connecting the Durance Valley (FRA) to Italy via the Larche Pass (colle della Maddalena in Italy), traverses a majestic yet unpredictable territory. A segment of this road, known as "La Rochaille," near the village of Meyronnes, faces exceptional natural challenges. La Rochaille is a place where the raw beauty of nature clashes with its devastating force, with impressive rockfalls, mudslides, and threatening avalanches posing significant dangers to this part of the road.

The RD 900 is not just a passage road; it serves as a vital link between France and Italy, connecting the town of Barcelonnette in France to Cuneo in Italy. This road facilitates international road transport and promotes Alpine tourism. It is of paramount economic importance to the local area, generating business opportunities and attracting visitors from around the world. For the residents of the villages of Meyronnes and Larche, located in the Val d'Oronaye commune, this road represents their connection to the rest of the Ubaye Valley.

The history of La Rochaille is marked by exceptional events, including several major rockfalls and two fatal accidents caused by falling rocks in 1959 and 1987, events that have left a lasting impact on people's memories. In response to these tragedies, in 1994, the Alpes-de-Haute-Provence department took measures by installing 300 meters of rockfall protection netting along a section of the road. However, despite these initial precautions, rockfalls continue to occur at an alarming rate, and the threat of falling rocks and debris remains ever-present.

This paper is dedicated to elucidating the pivotal role of IoT technology in addressing critical challenges faced by road owners, specifically in the context of rockfall mitigation on the Rochaille passage. Instead of focusing on presenting probabilistic hazard analyses, given that current assessments rely on outdated studies from CETE, our objective is to demonstrate how alerting systems can effectively resolve crucial issues. These systems aim to augment the efficiency of rockfall passive measures, working in tandem with advanced IoT sensor systems. The latter are deployed to replace the outdated infrastructure and, concurrently, reduce the necessity for installing numerous rockfall fences. Furthermore, this paper aims to shed light on the transformative impact of these technological interventions in enhancing road safety.

Geological and Topographic Characteristics

La Rochaille is a place of wild beauty but also unique geological complexity. The road runs through an environment at an altitude of 1400 meters, at the base of a steep 1000-meter drop, dominated by the majestic "Tête de l'homme." The geological layers of this region belong to the Helminthoid flysch, part of the Parpaillon nappe. The topography is characterized by highly folded and fractured rocky cliffs, crisscrossed by large North-South-oriented corridors. In the heart of La Rochaille lies an active rockslide, a mountain of rock spanning over 400 meters in elevation and 300 meters from the road. This geological configuration led authorities to install a rockfall detection system in 2001, following a major event that destroyed existing rockfall protection netting. The system involved sending alerts through a pendulum system that detected ground movement along the slope. A data acquisition center along the road allowed for activating lights and warning signs in case of rockfalls. A previously mentioned, unfortunately, this system was obsolete, inefficient and not active any more due to high maintained costs.

Security Plan and Design Studies:

In 2018, the Alpes-de-Haute-Provence department (CD-04) launched an ambitious effort to secure RD 900. The security plan includes the creation of civil engineering rockfall galleries along the main corridors and the installation of various measures, including rockfall protection netting, deflector screens, and active protection (reinforcement or rock removal) on the slopes between the corridors. This complex task was entrusted to Géolithe, a French engineering firm specializing in rockfall protection designs recognized worldwide.

The first phase of the work began in March 2021 and focuses on securing slope areas. This crucial phase is being carried out by the company EPC France. To date, seven sectors have been secured, covering approximately 830 meters of road. Simultaneously, the design studies for the rockfall galleries, conducted by Géolithe, are preparing for the second phase of the work, scheduled for 2024, which includes the construction of several "hood" rockfall galleries. The entire operation, including slope securing (phase 1) and the construction of rockfall galleries (phase 2), is estimated to cost €40 million inclusive of VAT, with funding coming from the department (52%), the region (24%), and the French state (24%).

Traditional passive measures, such as parallel barriers lines, prove insufficient, particularly in handling major events like significant rockfalls. The vulnerability of such measures necessitates additional interventions to ensure comprehensive protection along the Rochaille passage.

In pursuit of heightened safety and cost-effectiveness, the implementation of an advanced monitoring system has become imperative. Introducing an alerting system, rooted in sensors directly integrated into the rockfall barriers, emerges as a holistic solution. This not only addresses immediate safety concerns but also establishes a systematic approach for impact monitoring.

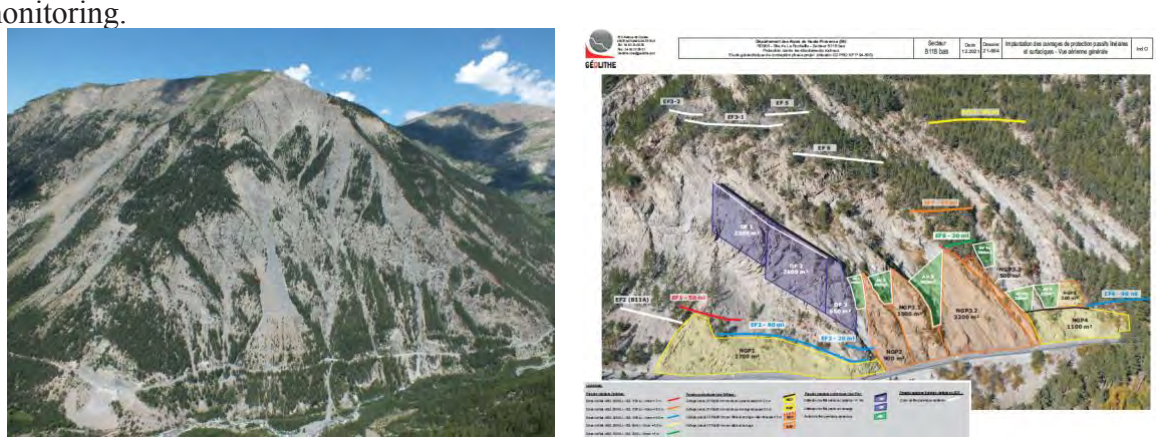

Figure 1: LEFT: Front view of the RD 900 at La Rochaille passage. RIGHT: Front view of the designed rockfall protection structures.

Design of Protection Structures:

In 2019 and 2020, Géolithe conducted the design studies for rockfall protection measures. The complexity of the area required extensive surveys, including by helicopter, on foot, rappelling, and the use of drones. The diagnostics relied on a Digital Terrain Model (DTM) derived from georeferenced photogrammetric surveys of the entire slope. Each sector received specific design, taking into account geological phenomena, slope morphology, and site-specific constraints. The ultimate goal is to minimize rockfall risks to the road.

Some sections of La Rochaille have relatively simple morphology, with rocky bars upstream of a forested slope, flanked by two corridors and a steep slope at the base. Here, attenuator barriers have been installed at the lower part of the slope, along with individual treatments with steel bolts as well as with rock scaling. The aim is to minimize maintenance interventions on rocky bars due to their difficult access and continuous activity.

Figure 3: Attenuator barrier (left). Installation of RB 3000 WGC rockfall barrier without anchors at the base of the posts (right).

Some areas required the use of high-energy capacity rockfall barriers. These barriers, distributed across five sectors, have capacities of 750kJ (200 m), 1000kJ (180 m), 1500kJ (60 m), 2000kJ (70 m), 3000kJ (375 m), and 5000kJ (576 m), with varying heights ranging from 3m to 7m. These protection structures, full-scale tested, meet the strictest European standards allowing for CE certification. Rockfall protection kits are guaranteed as they are tested in real-scale conditions following the testing protocol defined by EAD 340059-00-0106. All structures are characterized by their significant residual height (Category A), limited dynamic deformation, and absence of lateral opening between the post and the netting, resulting in exceptional performance in terms of residual height and elongation.

Recognizing the constraints inherent in passive measures, the governing authority acknowledges the imperative for an active monitoring system. This system should possess the capability to promptly identify potential rockfall risks, facilitating timely road closures when necessary. The shortcomings of the current monitoring system, deemed obsolete and unsustainable, propel the road owner toward transitioning to a more advanced and effective system.

The introduction of the technology

In conjunction with certified protective rockfall barriers, the project stakeholders and designers have integrated technological innovations to fortify safety in a highly technical manner. A salient progression entails the development of an intelligent alerting system intricately designed to discern critical occurrences, including impacts and rockfall fence deformations. This system facilitates instantaneous responses to potential hazards.

The “La Rochaille” construction site attains a commendable milestone by pioneering the adoption of this innovative technology in France. This state-of-the-art system has been deployed on both newly implemented EAD 340059-00-0106 (ETAG 027) rockfall barriers and those in existence since 2009 (pre-ETAG 027). In the event of an impact, a hierarchical alert

system is triggered, enabling prompt and tailored responses to impending threats. This technological innovation is poised to substantially diminish response times, thereby enhancing safety standards on the RD 900 road in the sector of “La Rochaille”.
The system's calibration by specialized technicians focuses on detecting potential impacts based on the positioning of rockfall barriers on the slope, either at the Maximum Energy Level (MEL) and/or the Service Energy Level (SEL). The alerting units, seamlessly integrated into passive protective structures, establish communication via radio to two data acquisition hubs. Upon impact, these units activate alert signals directly on the road (lights, traffic road signs, and sirens), concurrently dispatching notifications to personnel responsible for road management, maintenance, and safety via a dedicated smartphone application. Given the site's geographical location and the constraints of the phone network, the acquisition hubs communicate with a central server via satellite.

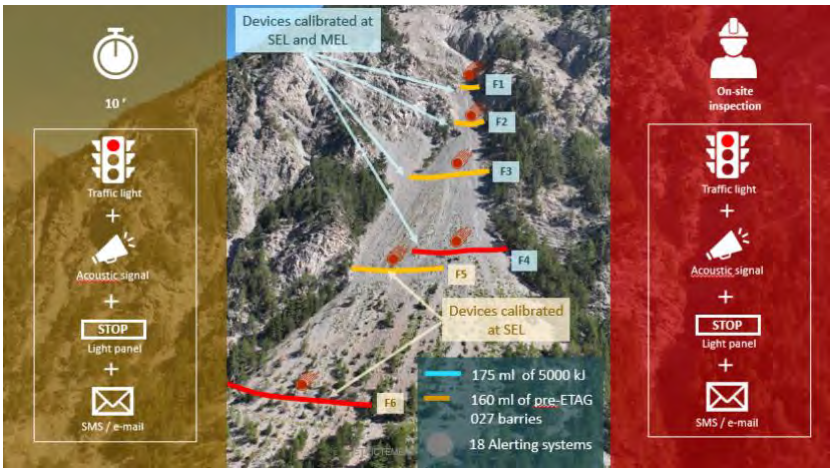

Figure 5: general front view of the installed alerting systems

Figure 6: Alerting system installed on 5000 kJ barrier (left). Connection of the alerting system with sign and light on the road (right).

Conclusion

Securing the passage of La Rochaille is a complex but vital challenge. This project, aimed at protecting travellers, local residents, and maintaining economic and tourist activities, is a testament to modern engineering and technological innovation. The combination of advanced rockfall mitigation structures, sophisticated detection devices, and meticulous planning marks a significant milestone in ensuring safety on this strategic road connecting France and Italy. As work continues, La Rochaille stands as an example of how IoT technology can solve complex problems and save lives while preserving the natural beauty of the Alpes-de-Haute-Provence.
The new IoT sensors not only offer a solution to the inadequacies of passive measures but also enable the Authority to monitor and track impacts on its structures. The technological innovation brought by these devices is crucial for both immediate safety concerns and long-term infrastructure management.

Hydrological field monitoring and geotechnical characterisation of terraced slope prone-to-landslide: the case study of Cinque Terre (Italy)

Matteo Fiorucci[1], Giacomo Pepe[2], Gian Marco Marmoni[3], Diego Di Martire[4], Luigi Guerriero[4], Giuseppe Bausilio[4], Enza Vitale[4], Emanuele Raso[5], Luca Raimondi[2], Andrea Cevasco[2], Domenico Calcaterra[4], Gabriele Scarascia Mugnozza[3]

[1] Department of Civil and Mechanical Engineering, Univerity of Cassino and Southern Lazio, Via G. Di Biasio 43, 03043 Cassino (FR), Italy
[2] Department of Earth, Environment and Life Sciences (DISTAV), University of Genova, Corso Europa 26, 16132 Genova, Italy
[3] Earth Sciences Department and CERI Research Centre on Geological Risks, Sapienza University of Rome, P.le Aldo Moro 5, Rome, 00185, Italy
[4] Department of Earth, Environmental and Resource Sciences (DiSTAR), Federico II University of Naples, Complesso Universitario di Monte Sant'Angelo, Via Cinthia 21, 80126 Napoli, Italy
[5] Cinque Terre National Park, Via Discovolo snc, Manarola, 19017 Riomaggiore, La Spezia, Italy

SUMMARY: Shallow landslides triggered by strong rainfall represent a widespread geological hazard impacting natural and anthropic environments. The study of geological and hydrological features of soil represents an essential task in understanding the slope behaviour when struck by heavy rainfall, significantly when the presence of man-made terraces modifies the regularity of the relief. To address this purpose, a multi-sensor monitoring system has been operating in the Monterosso al Mare catchment (Liguria region, Italy) since 2018, acquiring both hydrological parameters and weather conditions. The data acquired in this way were interpreted based on the engineering geological model obtained starting from the field investigations to point out the hydro-mechanical characterisation of terraced soils and to evaluate their hydrological behaviour. The first results suggest how the coarse-grained grain size distribution favours the infiltration of meteoric water, inducing sharp changes in soil moisture and pore water pressure and highlighting seasonal trends. The preliminary outcomes provide valuable insights into the evolution of hydrological factors in the slope, laying the groundwork for a better understanding of the time-dependent processes that guide water circulation in terraced systems and the triggering conditions to landsliding.

Keywords: terraced slope, multi-parametric soil monitoring, soil hydrological behaviour, rainfall-induced landslides, Cinque Terre National Park

Introduction

Shallow landslides due to heavy rainfall, like slides and flows, represent a common geological hazard that frequently interferes with the anthropic component of the environment (Marc et al., 2018). In recent years, the frequency of strong rainfall events has increased due to global climate changes amplifying their impact on the environment (Kirschbaum et al., 2012; Gariano et al., 2020). Failure initiation can be correlated to a wide range of destabilising factors, among which the most notable are soil saturation due to the perched water table, slope-parallel or upward groundwater seepage, matrix suction dissipation during rainwater infiltration and groundwater seepage mechanisms from fissures of the underlying bedrock (Crosta, 1998; Guadagno et al., 2005; Bordoni et al., 2015; Bogaard et al., 2016).
Terraced slopes are one of the most widespread man-made landscapes, especially in regions where rural activities have played an important economic role (Tarolli et al., 2014). Today,

these landscapes represent cultural heritage because of their historical and environmental value, increasing tourism and social and economic development (Brandolini, 2017; Varotto et al., 2019). Terraces enable agriculture in steep terrains, and slope gradient reduction is obtained by cutting naturally steep slopes to produce a step-like profile. The slope topography adjustment leads to a mitigation of both runoff and soil erosion processes, which is accompanied by increased infiltration. This increases soil moisture content (Stanchi et al., 2012). However, in the case of intense rainfall, the progressive saturation of soils and the development of critical regimes of pore-water pressures can negatively affect slope stability (Camera et al., 2012, 2014; Preti et al., 2018). The occurrence of mass movements along agricultural terraced slopes can have serious consequences in terms of economic loss also in terms of risk scenarios for infrastructures, settlements, and people (Agnoletti et al., 2019; Giordan et al., 2020). To effectively address the complex hydrological dynamics occurring in terraced slopes, it is essential to investigate the soil's hydromechanical and geotechnical features and acquire the longest possible monitoring data series. The following presents the outcomes of more than two years of continuous monitoring of the soil hydrological parameters in a terraced slope, susceptible to shallow landsliding, in the Cinque Terre National Park (northwestern Italy).

Materials and Methods

A multi-sensors monitoring system devoted to recording both meteorological forcings and hydraulic parameters of the soil has been operating since 2018 on a portion of a terraced slope located within the Pastanelli-Morione stream catchment in Monterosso al Mare (Cinque Terre, Liguria region, Italy). The Cinque Terre are well-known worldwide and represents a well-known example of a man-made area of century-old agricultural terraces retained by dry stone walls. This field study site was chosen because, in the past, it experienced several landslide events like the 25th of October 2011 flash flood when 260 shallow landslides, approximately, were triggered by extreme rainfall as debris slides, many of which evolved into debris flow and debris avalanches. The installed multi-sensors monitoring system consists of i) a fully equipped weather station, ii) soil temperature sensors, iii) soil moisture sensors, and iv) soil water potential sensors. The sensors were installed at different depths to reconstruct a vertical profile of soil hydrological conditions. Before the installation of the monitoring system, a combination of in-situ and laboratory geotechnical and geophysical investigations were carried out to define an engineering geological model across the monitoring site and to characterise the main textural, physical, and mechanical soil features. Three dynamic probing tests (DP) were performed to detect the bedrock's depth. The DP tests were performed along an alignment oriented toward the slope dip. A seismic refraction survey, consisting of one tomographic profile, was also carried out through 12 geophones and developed along the same route as the DP test. Five *in-situ* soil density determinations were also carried out using the sand cone method, sampling the soil for laboratory geotechnical determinations.

Results and main observations

The engineering geological model of the slope is based on the results of both *in-situ* surveys and laboratory determinations. The results of the DP tests highlighted that the soil cover has reduced thicknesses along the monitored section of the slope. The bedrock was detected approximately between 1.0 and 1.7 m depth. From the outcomes of the in-situ soil density measurements, the investigated soils show a natural unit weight of 14.6 ± 1.05 kN/m^3. The grain size distribution, conducted on three different samples, highlighted a sand fraction ranging from 24,7% to 28,5%, whereas gravel content ranged from 50% to 60.2%. Laboratory determination of plasticity characteristics of soil samples showed a range of 27–30% and 35–41% for plastic

limit (w_P) and liquid limit (w_L), respectively, while the Plasticity Index (PI) varies between 8% and 13%. Based on the unified soil classification system (USCS), the fine-grained soil fraction is classified as inorganic silts with low to medium plasticity (ML) and organic silts and clays of low plasticity (OL).
The availability of more than two years of monitoring data allowed to analyse the variation of the soil hydraulic parameters during the different seasonal cycles. The most intense rainfall event recorded 225 mm of rain in three days, with a peak of 159 mm in a single day. Regarding hydraulic monitoring, data recorded by tensiometers showed very high matric suction values (i.e., negative soil water pressure) under hot and dry summer conditions (drought periods). These values, reaching up to −900 hPa at the deepest sensor (T1, see Figure 1), became approximately equal to zero immediately after the first autumn rains and remained primarily unchanged until the following summer (wetting periods). Furthermore, soil moisture showed a clear relationship with rainfall peaks. However, the deepest sensor (i.e., W1, see Figure 1) recorded lower values (0.05 to 0.15) than the others (0.10 to 0.3). Regarding the spatial distribution of the sensors (Fig. 3), it is observed that those positioned downstream in the terrace (e.g., W5 and W3, see Figure 1) generally recorded higher soil moisture than the sensor positioned upstream in the terrace at the same depth (e.g., W2–W4 and W1, see Figure 1).

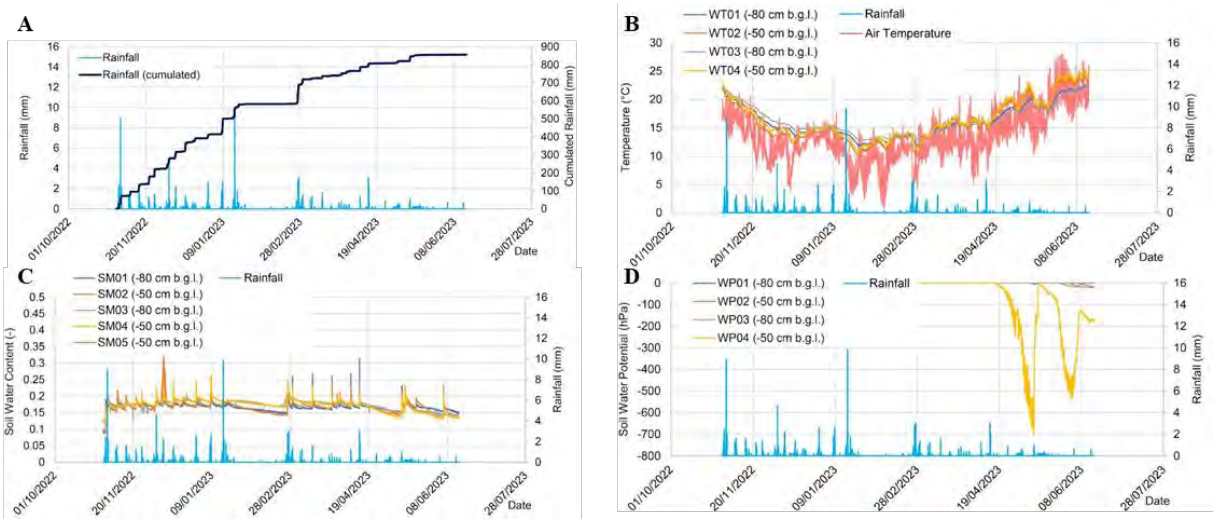

Figure 1: Multi-parametric data acquired from 2018 to 2020: (A) rainfall air and soil temperature, (B) air and soil temperature, (C) soil moisture (W) and (D) pore water pressure data (T).

Thanks to the availability of monitored data, it was possible to investigate the soil hydraulic behaviour through the reconstruction of the Soil Water Retention Curves (SWRCs), obtained by crossing point-by-point the matric suction values and soil moisture conditions. The curve's trend offers an overview of the hydrological properties of the soil and proceeding to their fitting, according to the van Genuchten equation (1980), it is possible to obtain the volumetric water content parameters in saturation and residual conditions (θ_s e θ_r), and the empirical parameters dependent on the pore-air pressure (α) and on the pore size distribution (n). The parameters thus obtained allow us to proceed with stability analysis of the surface beds, which is also possible continuously thanks to site monitoring data, which returns values of the safety factor according to the approach of Lu and Godt (2008).
The developed geotechnical framework undoubtedly affects the soil's hydrogeological behaviour, suggesting that saturation may be rapid in case of rainfall. Hydrological monitoring data from continuous time series confirmed this in the field, showing fast changes in pore water pressure and a peculiar behaviour resulting from terraces and coarse grain size distribution. At this aim, the study of SRWCs from field data suggested that soil saturation is almost contextual

to rainfall episodes, both on the small (seasonal) and on the large (daily) time window. As regards the hydraulic conditions of the soil along the investigated section (i.e., considering both the geometry of the slope and of the terrace bench itself with an average inclination of 27°), it is possible to notice that, in the downslope portion of the terrace, higher soil moisture values are recorded than those acquired in the upslope portion (i.e., at the same depth b.g.l.). At the investigated terraced site, the hydrological evidence coming from field monitoring may be explained through a wetting front infiltration scheme, already proposed by Schilirò et al. (2019), according to which the infiltrating water tends to accumulate on the lower edge of the terrace. Following this scheme, a reduction of the matric suction values occurs in the shallower soil layer during rainfall, and, if rain continues, positive pore water pressure can also develop.

References

Agnoletti M, Errico A, Santoro A, Dani A & Preti, F (2019) Terraced Landscapes and Hydrogeological Risk. Effects of Land Abandonment in Cinque Terre (Italy) during Severe Rainfall Events. *Sustainability* 11, 235.

Bogaard TA & Greco R (2016) Landslide hydrology: from hydrology to pore pressure. *Wires Water* 3, 439–459.

Bordoni M, Meisina C, Valentino R, Lu N, Bittelli M & Chersich S (2015) Hydrological factors affecting rainfall-induced shallow landslides: from the field monitoring to a simplified slope stability analysis. *Eng. Geol*. 193, 19-37.

Brandolini P (2017) The outstanding terraced landscape of the Cinque Terre coastal slopes (eastern Liguria). *Landforms and landscapes of Italy*. M. Soldati and M. Marchetti (eds,), (Cham, Switzerland, Springer International), pp. 235–244.

Camera C, Apuani T & Masetti M (2014) Mechanisms of failure on terraced slopes: the Valtellina case (northern Italy). *Landslides* 11, 43–54.

Camera C, Masetti M & Apuani T (2012) Rainfall, infiltration, and groundwater flow in a terraced slope of Valtellina (Northern Italy): field data and modelling. *Environ. Earth Sci*. 65(4), 1191-1202.

Crosta G (1998) Regionalization of rainfall thresholds: an aid to landslide hazard evaluation. *Env. Geol*. 35(2-3), 131-145.

Gariano SL, Melillo M, Peruccacci S & Brunetti MT (2020) How much does the rainfall temporal resolution affect rainfall thresholds for landslide triggering? *Nat Hazards* 100, 655–670.

Giordan D, Cignetti M, Godone D, Peruccacci S, Raso E, Pepe G, Calcaterra D, Cevasco A, Firpo M, Scarpellini P & Gnone MA (2020) New Procedure for an Effective Management of Geo-Hydrological Risks across the "Sentiero Verde-Azzurro" Trail, Cinque Terre National Park, Liguria (North-Western Italy). *Sustainability* 12(2), 561-578.

Guadagno FM, Forte R, Revellino P, Fiorillo F & Focareta M (2005) Some aspects of the initiation of debris avalanches in the Campania Region: the role of morphological slope discontinuities and the development of failure. *Geomorphology* 66, 237–254.

Kirschbaum D, Adler R, Adler D, Peters-Lidard C & Huffman G (2012) Global distribution of extreme precipitation and high impact landslides in 2010 relative to previous years. *J Hydrometeorol* 13, 1536–1551.

Lu N & Godt J (2008) Infinite slope stability under steady unsaturated seepage conditions. *Water Resour. Res.* 44, W11404. DOI: 10.1029/2008W R006976

Marc O, Stumpf A, Malet JP, Gosset M, Uchida T & Hao CS (2018) Initial insights from a global database of rainfall-induced landslide inventories: the weak influence of slope and strong influence of total storm rainfall. *Earth Surf Dyn* 6, 903–922.

Preti F, Guastini E, Penna D, Dani A, Cassiani G, Boaga J, Deiana R, Romano N, Nasta P, Palladino M, Errico A, Giambastiani Y, Trucchi P & Tarolli P (2018) Conceptualization of water flow pathways in agricultural terraced landscapes. *Land Degr. Dev*. 29(3), 651-662.

Schilirò L, Poueme Djueyep G, Esposito C & Scarascia Mugnozza, G (2019) The role of initial soil conditions in shallow landslide triggering: insights from physically based approaches. *Geofluids* 2019, 2453786.

Stanchi S, Freppaz M, Agnelli A, Reinsch T & Zanini E (2012) Properties, best management practices and conservation of terraced soils in Southern Europe (from Mediterranean areas to the Alps): A review. *Quat. Int*. 265, 90–100.

Tarolli P, Preti F & Romano N (2014) Terraced landscapes: from an old best practice to a potential hazard for soil degradation due to land abandonment. *Anthropocene* 6, 10–25.

van Genuchten M, Th. (1980) A closed-form equation for predicting the hydraulic conductivity of unsaturated soils. Soil Sci. Soc. Am. J. 44, 892-898. DOI: 10.2136/sssaj1980.03615995004400050002x

Varotto M. Bonardi L and Tarolli P (2019) World terraced landscapes: History, environment, quality of life, environmental history. Cham, Switzerland: Springer Nature Switzerland AG DOI: 10.1007/978-3-319-96815-5.

Understanding the way water is a destabilizing factor: an update

JC. Gress[1], RM. Faure[2]

[1] Soil treatment techniques Professor. 1983-2012. Ecole Nationale des Travaux Publics de l'Etat. Vaulx en Velin. France
[2] Soil Mechanics Professor. 1985-2022. Ecole Nationale des Travaux Publics de l'Etat. Vaulx en Velin. France.

SUMMARY: During the past fifty years, many improvements have been made in understanding the way water contributes as a destabilizing factor to generate landslides. We will present hereafter creep results due to Bishop, and propose relations explaining the way creep leads to failure.

Keywords: lanslides, creep, failure.

Introduction

Slope movement can generally be divided into six basic categories: rockfalls, surficial slope stability, gross slope stability, landslides, debris flows and creep. Water is involved in all of them, except rockfalls for which vibrations or thermal expansion can be the major instability vector. For debris flows, soil with entrained air and water moves readily as a fluid on low slopes. For both other cases, it is the shearing effort along the shearing surface compared to the shearing resistance that control the rate at a preliminary step of creep, maybe followed by a second step leading to failure. For surficial slope stability, gross slope stability and landslides, creep can be divided into a primary or transient stage and a secondary or steady state before a tertiary that can lead to failure of the slope. These three stages are illustrated on fig N°1. The primary phase is short and very often ignored. The second one produces a relatively constant rate of strain, and could continue for a considerable number of years in some cases. On the contrary, the tertiary phase can be, in some cases very quickly reached and then the strain rate accelerates towards failure.

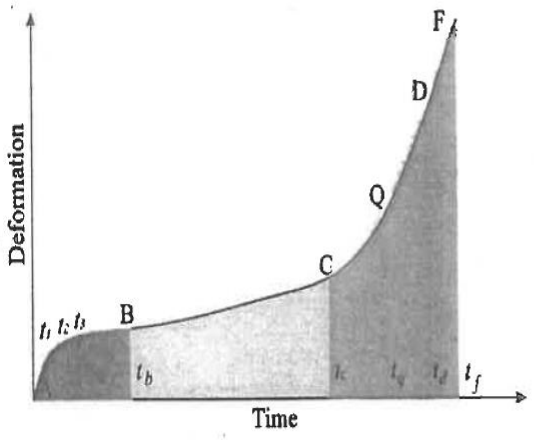

Deformation stage of landslide with creep characteristics.
Note: AB, primary creep; BF, unstable creep; BC, secondary creep; CF, tertiary creep; CQ, initial accelerated sub-phase; QD, medium accelerated sub-phase; DF, critical failure sub-phase.

. Figure N°1. Three stages of creep towardsfailure according to Shuo Zhang et al.

In order to understand the secondary stage,are detailed hereunder BISHOP's creep laboratory results on Hendon clay . Will be proposed our analysis on the way creep is leading to failure.
BISHOP has conducted drained triaxial tests on HENDON highly overconsolidated plastic clays (PI = 29.
Wl = 76 ; %2μ = 58). These tests were conducted at controlled constant loads Strains were followed with increasing time, for different constant D ratios, D being the applied deviator value divided by the deviator value at failure. BISHOP gradually increased this ratio for each sequence. Results are displayed on figure N°2 for $\sigma'_3 = 138$ kpa, axial strain ε being followed in % as a function of decimal logarithm of time, t in days. On a parallel classic drained triaxial test, he measured $\varepsilon f = 3.7\%$ and $(\sigma_1-\sigma 3)f = 227$ kpa.

Bishop laboratory creep tests. (1966).

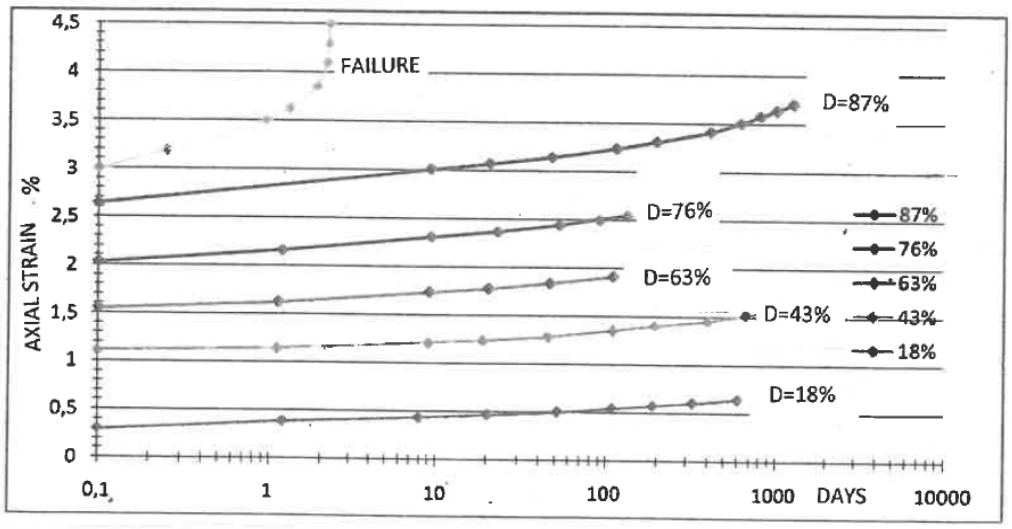

FigureN°2. BISHOP creep drained triaxial tests. redrawn by Mauro Cacucci

Suggested approach for the evolution of ε and log(dε/dt) with logt.

Looking at the curves on figure N°2, it appears that they have the shape of hyperboles. Then we search the possibility to represent these curves by a relationship the type of:

$$\varepsilon = (a \log t - b)/(\log t - c) \quad (1)$$

the values of a, b, and c are summarized in table N°1, D being equal to the effective deviator stress divided by the deviator stress at failure:

D	0.18	0.43	0.63	0.76	0.87	at failure
a	-0.219	0.909	1.158	1.102	1.882	2.585
b	-2.90	-5.52	8.66	16.66	-16.61	-2.76
c	-8.26	-4.79	5.33	-7.75	-6.00	-0.78

Table N°1. Values of a,b and c for different D values.

When we represent the variations of a, b and c as a function of D, we notice that they are not as regular we could expect for values for D between 0.18 and 0.87. This is probably due to samples heterogeneities.

When leading to failure, the curve is totally different.
We can derive relationship (1) and we obtain:

$$d\varepsilon/dt = A / (t \times (B - \log t)^2) \quad (2)$$

Values of A and B are summarized in table N°2:

D	0.18	0.43	0.63	0.76	0.87
A	4.7	1.17	2.49	8.12	5.31
B	8.26	4.79	5.33	7.75	6.00

Table N°2. Values of A and B for different D values.

Values are also not as regular as we could expect. What is very interesting, is to look at figure N°3 representing the different curves log(dε/dt) as a function of logt. The curves corresponding to values of D between 0.18 and 0.87 are quite straight parallel lines, their slopes(-α) being summarized in table N°3:

D	0.18	0.43	0.63	0.76	0.87
α	0.878	0.739	0.813	0.877	0.813

TableN°3. Values of α for different D values.

We observe a quite constant α value for D varying from 0.18 to 0.87 and we can write:

$$d\varepsilon/dt = (d\varepsilon/dt)_{0.1x}\, e^{(-\alpha \times LN10)} x\, t^{(-\alpha)} \quad (3)$$

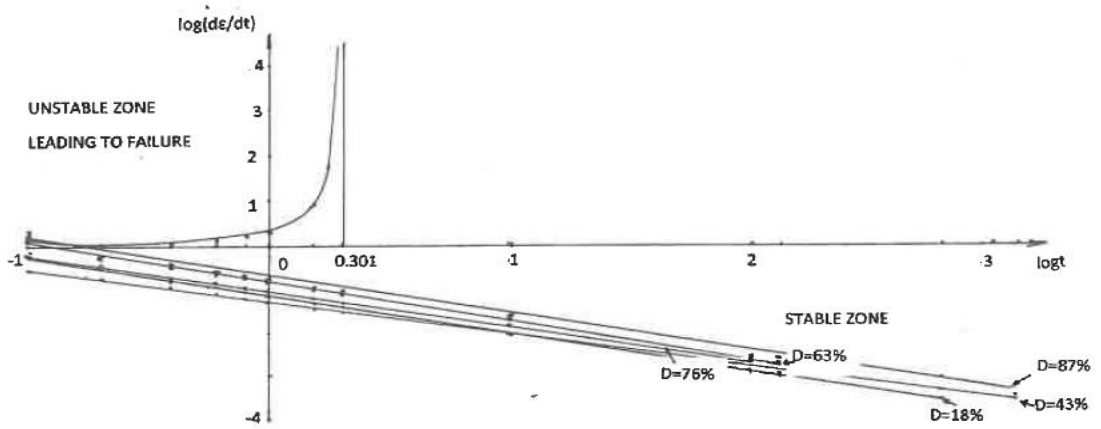

Figure N°3. log(dε/dt) as a function of logt.

For the curve leading to failure, its shape is that of an hyperbola; its equation can be written:

$$d\varepsilon/dt = 0.218/(tx\,(0.301 - \log t)^2) \quad (4)$$

It has the form of equation (2), but A and B are very different and much lower. When we look at the variation of $(d\varepsilon/dt)_{0.1}$ with D, in table N°4, we notice that up to failure it is not possible to anticipate failure with the survey of this parameter.

D	0.18	0.43	0.63	0.76	0.87	1
$(d\varepsilon/dt)_{0.1}$	0.548	0.348	0.621	1.06	1.082	1.287

Figure N°4.

Conclusions after the analysis of the secondary BISHOP creep phase.
Up to a value of D equal to 0.87, the variation of dε/dt, as a function of logt, is quite linear. On the contrary, when near failure, it becomes hyperbolic, being aware that at the start of this type of behavior, the value of $(d\varepsilon/dt)_{O.1}$ does not warn of this change. The only parameters being a possible warning are the values of D and of ε compared to εf. For the variation of dε/dt as a function of logt, it is when it takes an hyperbolic trend, that we are moving towards failure

Classical approach of phase 3.

Here the stability analysis is made comparing the effects of the driving forces to the resisting forces on a given slip surface. It leads to a factor of safety F. When F is greater than 1.5, we consider that the slope is in a safe state. We must consider that F is the inverse of D, 0.66 being the inverse of 1.5. This means that though we can be in an apparent security with F equal to 1.587, creep is still possible for D equal to 63% failure occuring at $10^{5.33}$days. Before, failure slope is creeping. For long creeping slopes, we must be aware that movements are not uniform, and the differential movements at the limit of two compartments will fracture buildings located in this zone.

Possible techniques to stabilize slopes.

Two situations can be met. In the first one, heave due to cut unloading and increase of watercontent in the shearing zone due for example to different electrochemical potential s of two layers in contact, or viscous behaviour of plastic clays can soften soil material leading to creep and perhaps to failure. A possible stabilizing technique is then a set of inclined nails. The second one is due to the increase of pore pressure diminishing the effective stress level. Then, we will generally try to drain the aquifer at the origin of the pore pressure increase.

Conclusions.
Bishop creep tests analysis allows to understand the way creep is either in a quite stable zone, difficulties being sometimes due to differential behaviours due to heterogeneities, or either in the upper unstable zone leading to failure. The best parameters to anticipate the risk are either D values or ε values compared to εf at failure. Looking at the variation of log(dε/dt) as a function of logt, we must wait sufficiently in order to check whether it is a linear function corresponding to the stable zone, or if it is hyperbolic, then leading to failure. The hyperbolic function will then give the time to failure (10^B days).

References.

BISHOP A.W. LOWENBURY H.T. (1966) Creep caracteristics of two undisturbed clays. IMPERIAL COLLEGE. UNIVERSITY OF LONDON. UNITED KINGDOM.
CACUCCI M. (2010) Formulations analytiques du fluage triaxial. Projet de fin d'études. ECOLE DES PONTS. PARIS TECH FRANCE.
GRESS J.C. (2024) Instabilités éventuellement induites par des dragages en Seine sur le versant de Villequier. 76. Port autonome de Rouen. ACE GEOTECHNIQUE. FONTAINES 71150 FRANCE.
ZHANG S. et al. (2022) A new forecasting method for failure time of creep lanslide based on nonlinear creep behavior and new prewarning criterion. College of Geosciences and Engineering. ZHENGZHOU. CHINA.

Electrical Resistivity Investigation on a Tropical Slope Prone to Translational Earth Slides in Guarujá-SP, Brazil

Cleber de Jesus Santos[1], Jefferson de Lima Picanço[1], Otavio Coaracy Brasil Gandolfo[2], Malena D'Elia Otero[1], Alessandra Cristina Corsi[2], Eduardo Soares de Macedo[2], Ana Elisa Silva de Abreu[1]

[1] University of Campinas, Institute of Geosciences, Campinas, Brazil
[2] Institute for Technological Research (IPT), São Paulo, Brazil

SUMMARY: The frequent occurrence of landslides in mountainous areas has sparked discussions about the need to seek more detailed ways of monitoring hydrological processes. In this context, geophysics emerges as a promising alternative approach to address these challenges, owing to its convenience in data collection, resolution capabilities, favourable cost-benefit ratio, and the use of non-invasive methods. The aim of this research was to analyse, based on electrical resistivity tomography, the hydrological processes in regoliths of a slope prone to slides in the municipality of Guarujá-SP, Brazil, in different climatological scenarios (dry/rainy season). The investigations revealed that the regolith profile in the studies slope is about 6 meters thick. The first two meters can be interpreted as a colluvial soil. The water table was not identified up to the maximum investigation depth (10 meters), but the studied slope shows a vertically-oriented low-resistivity anomaly at mid-height, which can be identified even in the dry season.

Keywords: Landslides, Electrical Resistivity Tomography (ERT), Geotechnical Investigation, Hydrology.

Introduction

The geotechnical challenge in assessing areas with landslides involves both the geological complexity due to layer movement and mixing, as well as operational limitations related to the depth of investigation and access to the entire area due to topographical irregularities. In this context, geotechnical engineering has gradually explored indirect methods, such as geophysics, to address these challenges, due to their convenience in data collection, resolution capabilities, and cost-effectiveness.

Geophysics proved effective in these cases due to its ability to investigate regolith with satisfactory spatial and temporal resolution throughout its extent. In this way, geophysical techniques enable the assessment of landslide-triggering mechanisms and, consequently, the implementation of preventive interventions to minimize the negative socio-environmental impacts resulting from this process (Petley, 2012; Crawford and Bryson, 2018).

The idea of conducting electrical profiling on the slope's surface in the study area aimed at detailing the geological materials, assess the moisture distribution and its temporal variations, and detect potential preferential domains of infiltration water percolation, as well as the presence of intact rock. The literature on the use of geophysical methods in slope evaluation in Brazil is still limited. Therefore, this study aims to contribute to the discussions on the use of Electrical Resistivity Tomography to assess mass movements in Brazil

The study area

The study area is located on the forested slope in the city of Guarujá-SP, Brazil (coordinates 23° 55' 40"S and 46° 12' 31"W, DATUM – SAD69/Zone 23), a prominent region in the Baixada Santista known for its tourism activities.
The substrate of the study area is characterized by kinzigite gneiss. Typically, these lithotypes are covered by thick regoliths, predominantly clayey, and more micaceous in nature. Otero et al. (2024) present a geotechnical characterization of these soils.

Methods

Electrical resistivity (ER) data were acquired using the Rho/IP system, consisting of a Syscal R2 resistivity meter acting as the receiver, with 10 channels, operating in conjunction with a current transmitter connected to a 250 W DC/DC converter and a 12 V battery (Figure 1). The data were acquired semi-automatically using the dipole-dipole array with 3m electrode spacing. The spacing could not be larger due to operational limitations. The resistivity data processing was carried out using the Res2Dinv software, which included preprocessing, inversion, and 2D modeling stages.

Figure 1. a) Rho/IP System used in electrical propagation, 1 (receiver), 2 (transmitter), 3 (DC/DC converter), 4 (battery). b) Data acquisition along Line 4

The sampling grid established for the research consists of 4 lines. Two of them are located at the top of the slope (L1 and L2), one is located within the displaced mass (L3) and one is located at the toe of the slope (L4), as illustrated in Figure 2. The number of lines was based on the size of the study area, following representativeness criteria. Their positioning on the slope adequately adhered to spatial distribution criteria, allowing for investigation of the slope's top, colluvial mass, and base.

Figure 2 – On the left, we have the planimetric map of the study area, highlighting the geophysical acquisition lines and landslide scars. On the right, we have the actual image of the slope obtained from Google Earth.

The first campaign was performed at the end of the dry season (September 2022) to establish a baseline for monitoring moisture distribution over time and space, while the second campaign was carried out at the beginning of the rainy climatic period (December 2023). And finally, we carried out the third campaign to collect data regarding the end of the rainy season (March 2023).

Results

Only the results for L3 are presented in this paper. The section exhibited significant variations in resistivity values, which can be attributed to the natural complexity of the local soils. The substantial textural variability, the presence of rock fragments, and soil movement caused by gravity contribute to the considerable variability in the data. The resistivity patterns indicated the rocky outcrop with the lowest value in the area, at a depth of 6 meters, a feature directly influenced by topographic control. Within the first 2 meters, we observed a distinct pattern with well-defined contours, suggesting the occurrence of differential movements between the substrate horizons. The electrical resistivity patterns at greater depths indicate the delineation of intact rock.
The surveys were able to investigate the subsurface to a maximum depth of approximately 10 meters but couldn't identify the static water level. Direct investigations at the crest (6 meters depth) and around stake 48 (2 meters depth) did not identify standing water. A sounding at the slope toe (around stake 0) identified standing water at 2.5 meters depth. The section features a vertically-oriented low-resistivity anomaly at mid-height (Figures 3 and 4), which can be identified even in the dry season. No direct investigation has been performed in this area so far.

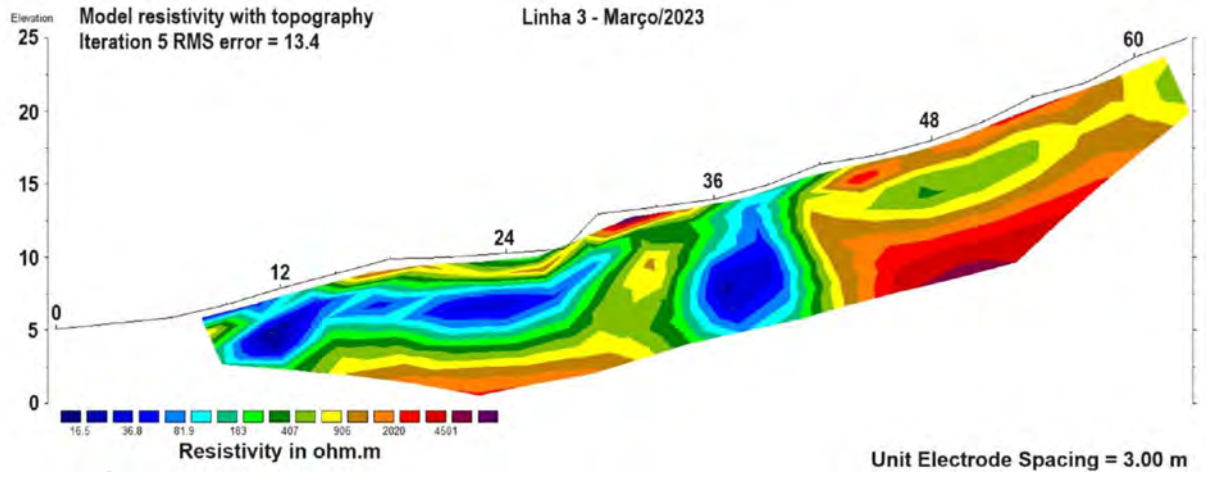

Figure 3. Resistivity of the slope interpreted for the end of the rainy season (March 2023)

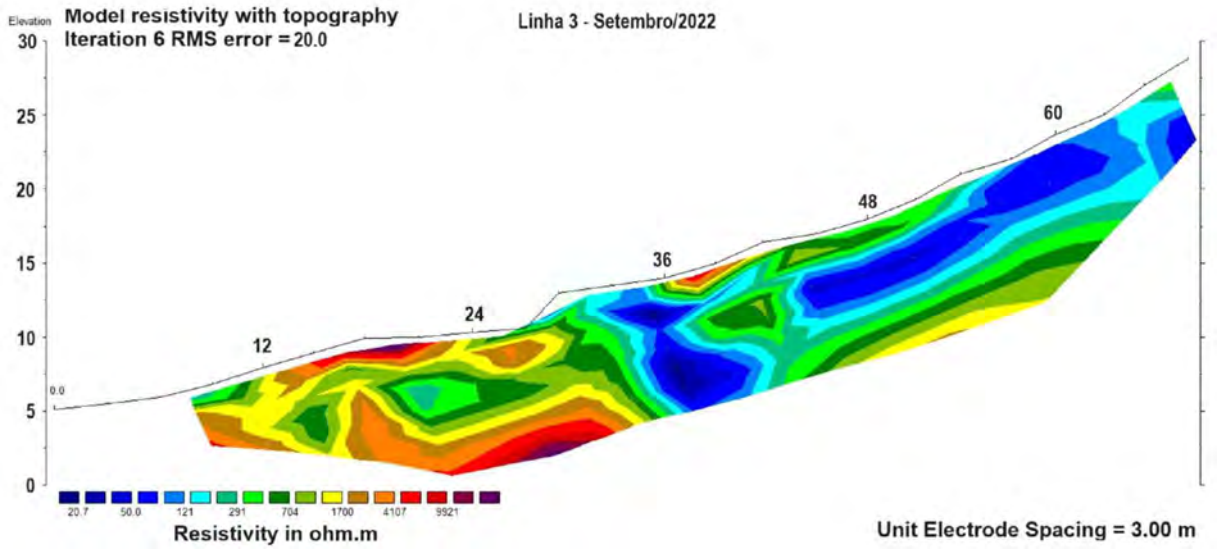

Figure 4 Resistivity of the slope interpreted for the end of the dry season (September 2022)

Conclusion

The results obtained in this study demonstrate that the proposed methodological approach constitutes a powerful assessment tool for hillside areas, providing an accurate view of the regolith in the landslide-affected area and thus offering a basis for establishing points for direct investigations.

Acknowledgements

The authors would like to thank the São Paulo Research Foundation (FAPESP), Grant # 2017/50343-2, the National Council for Technological Development (CNPq), Grant # 405565/2021-6 and the Coordination of Superior Level Staff Improvement (CAPES) for financial support.

References

Crawford, M. M. e Bryson, L. S. (2018) Assessment of active landslides using field electrical measurements. Engineering Geology, v. 233, n. June 2017, pp. 146–159.

Otero MD, Abreu AES, Corsi AC, Macedo ES, Almeida RZH, Picanço JL, Santos CJ, Gandolfo OCB & Araujo GRMB (2024) Field instrumentation for translational earth slide early detection in a tropical mountainous area. 14th *International Symposium on Landslides*, Chámbery, France, 4p (submitted)

Petley, D. (2012) Global patterns of loss of life from landslides. Geology, v. 40, n. 10, pp. 927–930.

Field instrumentation for translational earth slide early detection in a tropical mountainous area

Malena D'Elia Otero[1], Ana Elisa Silva de Abreu[1], Alessandra Cristina Corsi[2], Eduardo Soares de Macedo[2], Rynaldo Zanotele Hemerly de Almeida[2], Jefferson de Lima Picanço[1], Cleber de Jesus Santos[1], Otavio Coaracy Brasil Gandolfo[2], Gabriel R. M. B. de Araújo[3]

[1] University of Campinas, Institute of Geosciences, Campinas, Brazil
[2] Institute for Technological Research (IPT), São Paulo, Brazil
[3] University of São Paulo, São Paulo, Brazil

SUMMARY:
The rainfall water infiltration phenomena in the unsaturated zone in tropical regions and their ability to trigger translational earth slides are still not totally clear. Therefore, the purpose of this research is to monitor a slope prone area to this kind of slide, in the tropical region of Southeast Brazil by installing soil moisture sensors, tensiometers and piezometers together with inclinometers and inertial measurement units (IMUs) and to monitor the slope behaviour to better understand translational earth slides triggering and evolution mechanisms. This paper presents the characteristics of the monitored slope area and the monitoring clusters, as well as the results available until September 2023. During the dry season there is no standing water in the piezometers, but the inclinometers reveal that the soil is moving, even in the dry season. With the continuation of the monitoring we hope to reach a better understanding of the influence of infiltration water in slope movements and to test the hypothesis that this group of geotechnical instruments is capable of detecting pre-failure signals that are of use for establishing early warning thresholds based on other variables alongside rainfall thresholds.

Keywords: monitoring, early warning, infiltration, triggering mechanism

Introduction

Translational earth slides are one of the most common hazards in Southeast Brazil. This kind of landslide is triggered by rainfall and causes many losses and damages every year, especially in low-income settlements. Many civil defenses base their alert systems on rainfall thresholds as presented by Calvello et al. (2014), Mendes & Filho (2015), among others. However, the phenomena of rainfall water infiltration in the unsaturated zone in tropical regions and the details of its ability to trigger landslides, pointed out by Wolle & Carvalho (1987), still remains not totally clear. Understanding landslide triggering and evolution is crucial for developing more accurate prediction failure models (Petley et al. 2002, Petley 2004, Federico et al. 2012). The purpose of this research is to present and discuss a slope monitoring program in the tropical region of Southeast Brazil through the installation of soil moisture sensors, tensiometers and piezometers together with inclinometers and inertial measurement units (IMUs), aiming at understanding the influence of infiltration water in slope movements and testing the hypothesis that those sensors are capable of detecting translational earth slides pre-failure signals and of contributing to our understanding of triggering and evolution mechanisms.

Study Area

The study area is located in Guarujá city in São Paulo State and it was chosen because in March 2020, during the rainfall season, the region was severely affected by landslides (mostly,

translational earth slides) (Figure 1). According to the Landslide Susceptibility Map issued by the Institute for Technological Research – IPT (2015), the susceptibility of the study area to landslides is high.
The monitored slope area is located in the Paragnaissic Unit of the Costeiro Complex of Mantiqueira Province (Perrota et al. 2006), which is composed by kinzigite gneiss.
The weather in Guarujá is considered tropical, according to Köppen-Geiger classification, with annual average temperature of 22ºC and annual rainfall of approximately 1900mm. Therefore, chemical weathering is strong, resulting in heterogeneous and thick soil horizons.

Geological Investigations and Geological Setting

Figure 1 presents the location of the geological surveys performed in the study area. Geological and geotechnical surveys included: four geophysical surveys lines (L1, L2, L3, L4) (electrical resistivity, seismic refraction and MASW), four auger drills with disturbed samples collection (AD1, AD2, AD3, AD4), two percussion drills with SPT tests (PD1, PD2) and undisturbed samples collection (US). Disturbed samples were used to determine soil characteristics properties and undisturbed samples were used for water retention curve determination (Richard chamber method), permeability at saturation and triaxial tests.
Soil horizons in the studied slope were divided into colluvial soil and gneiss residual soil. Table 1 presents a summary of the characteristics of both soil types. The results of the geophysical investigation are presented in Santos et al. (2024).

Table 1 Summary of the characteristics of the colluvial soil and of the gneiss residual soil

	Thickness	Percentage of particle size			Permeability
		Clay	Silt	Sand	
Colluvial soil	Aprox. 2m	31-48%	16-24%	36-44%	1 x 10^{-5} m/s
Residual soil	Aprox. 2m	4-15%	3-26%	48-64%	1 x 10^{-6} m/s

Geotechnical Instrumentation

The instrumentation proposed in this work is organized in two clusters: one located at the crest of the earth slide that happened in 2020 (CL-01) and the other at the top of the slope (CL-02). Each cluster will be composed of one 2m long soil moisture probe (Sentek TDR probe), three tensiometers (0.60m, 1.20m and 1.80m long), three inertial measurement units (IMU) embedded into the soil at the same depth as the tensiometers, one piezometer (PZ) and one inclinometer (INC) (Figure 2). PZ-01 and INC-01, located at CL-01, are 4m long, whereas PZ-02 and INC-02 are 8m long. A raingauge (PV) will be installed near the slope.

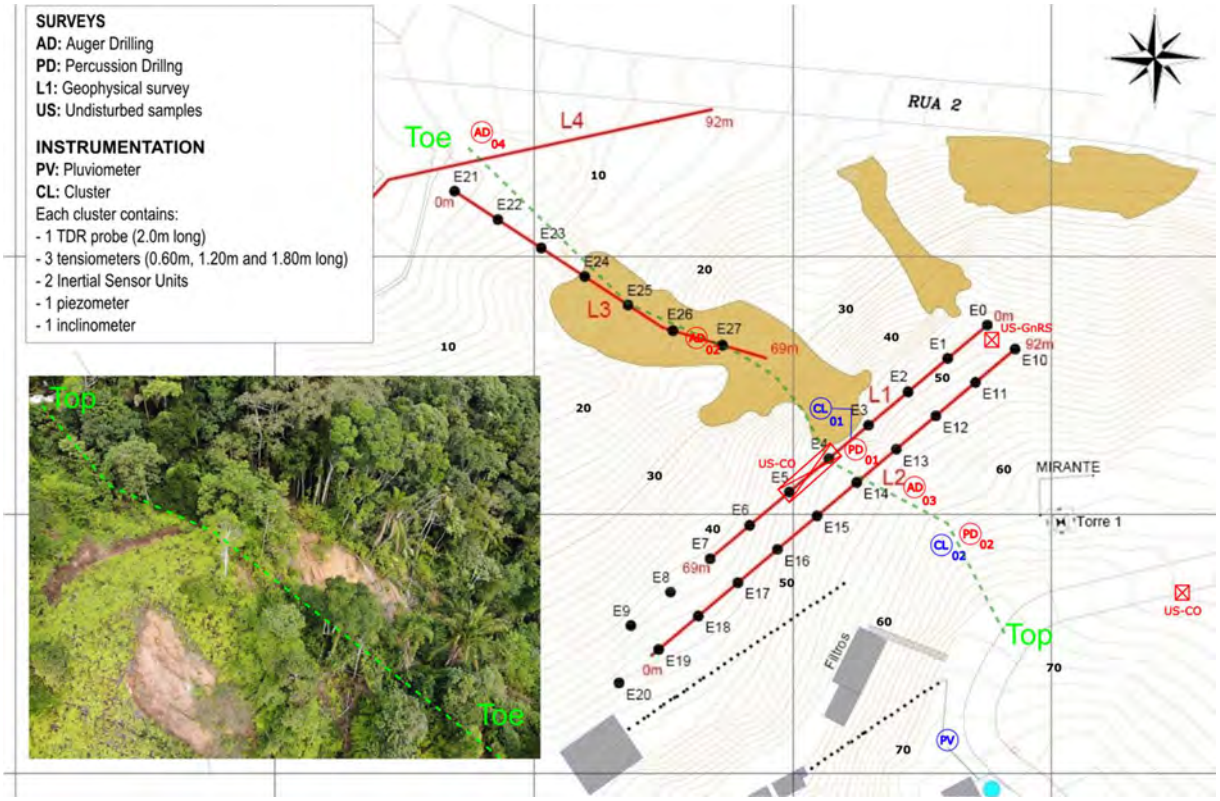

Figure 1: Geological surveys and field instrumentation. Polygons in light brown refer to the scars of the slides that occurred in 2020 (triggering area and deposition area are not separated). Cross view of the slope shown in the picture on the left is indicated in the map in green dashed line.

Figure 2 Piezometers and inclinometers installed in Cluster 1 (left) and in Cluster 2 (right).

Instrumentation Preliminary Results and Further Works

Up to September 2023, only the piezometers (PZ) and the inclinometers (INC) were already in place. Their monitoring data started to be collected monthly since July 2023. No water table level was measured in either piezometer in the first three months. This was expected since the dry season in Southeast Brazil runs from the beginning of April until the end of September, whilst the rainy season goes from beginning of October until the end of March.

Regarding inclinometers, data from INC-02, located at the top of the slope, suggests that movement is happening, regardless of the absence of standing water in this part of the slope

during the dry season. The sliding surface is located at the contact between gneiss residual soil and colluvial soil.
Future works include installing the other instrumentation devices namely soil moisture probes, tensiometers and Inertial Measurement Units (IMUs), monitoring the slope and modelling its behaviour. These IMUs are low-cost sensors developed by IPT specially for slope monitoring, as presented by Corsi et al. (2024).

Conclusion

It is expected that the complete monitoring setup and the analysis of the data acquired with this setup will give information about the mechanics of the slope behaviour and the influence of the saturation front in the movement development.
In the long run, we hope to test the hypothesis that this group of geotechnical instruments is capable of detecting pre-failure signals that are of use for establishing early warning thresholds based on other variables alongside rainfall thresholds.

Acknowledgements

The authors would like to thank the São Paulo Research Foundation (FAPESP), Grant # 2017/50343-2, the National Council for Technological Development (CNPq), Grant # 405565/2021-6 and the Coordination of Superior Level Staff Improvement (CAPES) for financial support.

References

Calvello M, D'Orsi RN, Piciullo L, Paes N, Magalhães M & Lacerda WA (2014) The Rio de Janeiro early warning system for rainfall-induced landslides: analysis of performance for the years 2010-2013. *International Journal of Disaster Risk Reduction*, 12, 3-15

Corsi AC, Macedo ES, Abreu AES, Otero MDE & Araujo GRMB (2024) Development of Low-Cost Sensor System for Translational Earth Slide Early Warning System. 14th *International Symposium on Landslides*, Chámbery, France, 4p (submitted)

Federico A, Popescu M & Murianni A (2012) Temporal prediction of landslide occurrence: a possibility or a challenge? *Italian Journal of Engineering Geology and Environment*. 1, 41-60.

Institute for Technological Research – IPT (2015) *Carta de suscetibilidade a movimentos gravitacionais de massa e inundações – Município de Guarujá, escala 1:25* 000 (in Portuguese).

Mendes MM & Filho MV (2015) Real-time monitoring of climatic and geotechnical variables during landslides on the slope of Serra do Mar and Serra da Mantiqueira (São Paulo State, Brazil). *Engineering*, 7, 140-159.

Perrotta MM, Salvador ED, Lopes RC, D'Agostino LZ, Peruffo N, Gomes SD, Sachs LLB, Meira VT & Lacerda Filho JV (2006) *Mapa geológico do Estado de São Paulo, escala 1: 750 000.* Programa Levantamento Geológicos Básicos do Brasil, Serviço Geológico Brasileiro, São Paulo (in Portuguese).

Petley DN, Bulmer MH, Murphy W (2002) Patterns of movement in rotational and translational landslides. *Geology*, 30, 719-722.

Petley DN (2004) The evolution of slope failures: mechanism of rupture propagation. *Natural Hazards and Earth System Science*, 4, 147-152.

Santos CJ, Picanço JL, Gandolfo OCB, Corsi AC, Macedo ES, Otero MD & Abreu AES (2024) Electrical Resistivity Investigation on a Tropical Slope Prone to Translational Earth Slides in Guarujá-SP, Brazil. 14th *International Symposium on Landslides*, Chámbery, France, 4p (submitted)

Effect of temperature on seismic interferometry measurementsfor landslide monitoring

Rey E.[1,2], Royer A.[1], Guillemot A.[1,2], André L.[1]

[1] GEOLITHE, Crolles, France
[2] ISTerre, Grenoble University, France

SUMMARY: As an innovant method for landslide monitoring, seismic interferometry is an innovant method used since a few years to monitor landslides. The relative variation of seismic wave velocity (dV/V) within time generally show reversible variations that are impacted by environmental forcings. In the present work, we analyse more than two years of seismic data measured on a morainic landslide located in Valloire (Savoie, France). The relative variation of seismic wave velocity (dV/V) appears well correlated with on-site temperature, at both daily and seasonal time scales. We precisely describe and quantify these correlations, towards in a second time correcting reversible temperature effects on dV/V and distinguish them from other processes precursor to failure.

Keywords: seismic interferometry, dV/V, temperature, landslide, monitoring

Introduction

Since a ten of years, seismic interferometry is used to monitor several natural objects at depth, such as landslides (Le Breton et al., 2021; Larose et al., 2022). Since a sharp decrease of about 7 % in relative seismic velocity have been measured on the Pont-Bourquin clay landslide (Switzerland) a few days before a significative reactivation of the instable slope (Mainsant et al. 2012), the relative variation of seismic wave velocity (dV/V) is used to indicate the hydro-mechanical state of the subsurface, and provides a good precursory signal before a failure.

Integrating this seismic noise-based method to an early warning system needs to better understand environmental forcings (temperature, rainfall, frost) influencing the estimated relative seismic velocity changes (dV/V).

Data collection and analysis

Flowing in the valley of Beaujournal, the Rieu Benoit regularly provides debris-flows, threatening the hamlet of Les Verneys (Valloire, Savoie, Western French Alps). During winter 2011-2012, a landslide appeared on the left bank of the torrent, potentially involving up to 225 000 m^3 of unstable material on a 35 to 40° slope constituted of glacial clayey tills laying on a substratum made of Flysh. The summit scar is located about 110 meter above the torrent and the total dimensions of the unstable slope are around 100 meter wide and 160 m long.

This landslide was recently monitored during 2.5 years (2020-2022) with a multi-method instrumentation, including RFID tags, time-lapse cameras, a meteorological station and seismometers that allow a monitoring of the ground rigidity through ambient noise seismic interferometry (dV/V). This instrumentation has been undertaken within the FEDER/POIA project SIMOTER-1&2, aiming at studying debris flows in connection with the reactivation of a landslide and threatening infrastructures downstream.

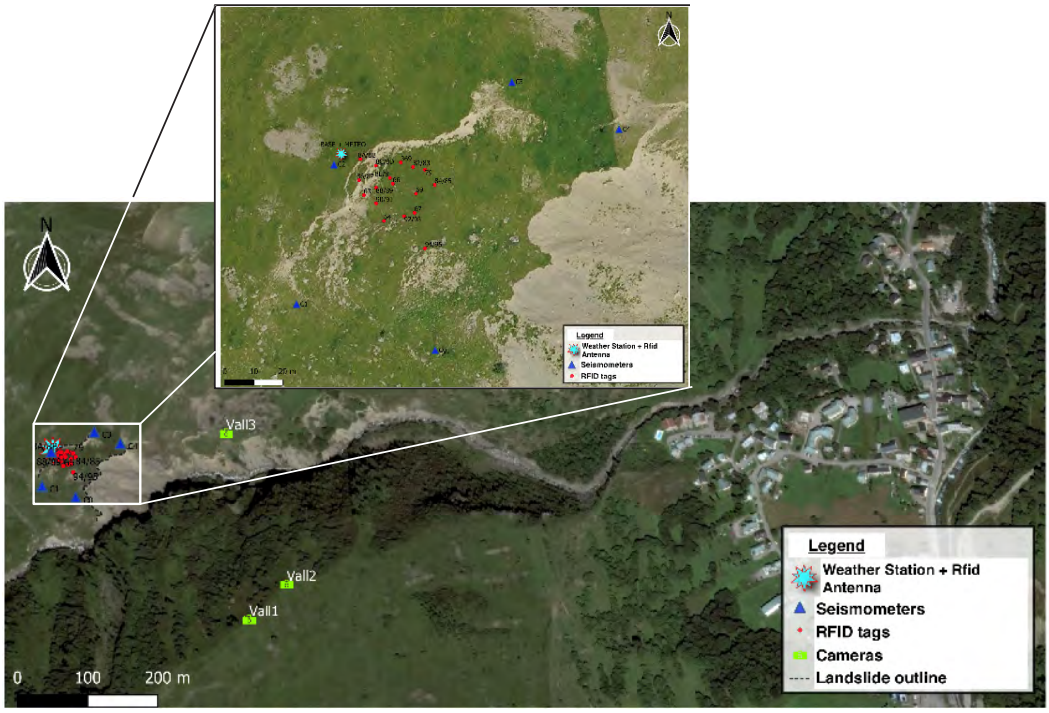

Figure 1. Instrumentation of the monitored landslide, located about 700m upstream of the hamlet Les Verneys, Valloire (73).

As shown in Figure 1, five seismometers (represented by blue triangles) have been set around the unstable area. Real time processing of the continuous recorded signals provided a daily dV/V estimation for different frequency ranges, as variations of the elastic properties of the medium at different depths. This instrumentation was completed by surface displacement monitoring, such as RFID measurements and time-lapse photographies (Laigle et al., 2019, Jongmans et al., 2022).

Although the landslide didn't reactivate during the monitored period, the dV/V times series show significant variations with several time scales, from daily to seasonal periodicity. The seasonal maximal amplitude of dV/V is about +/- 3 %.

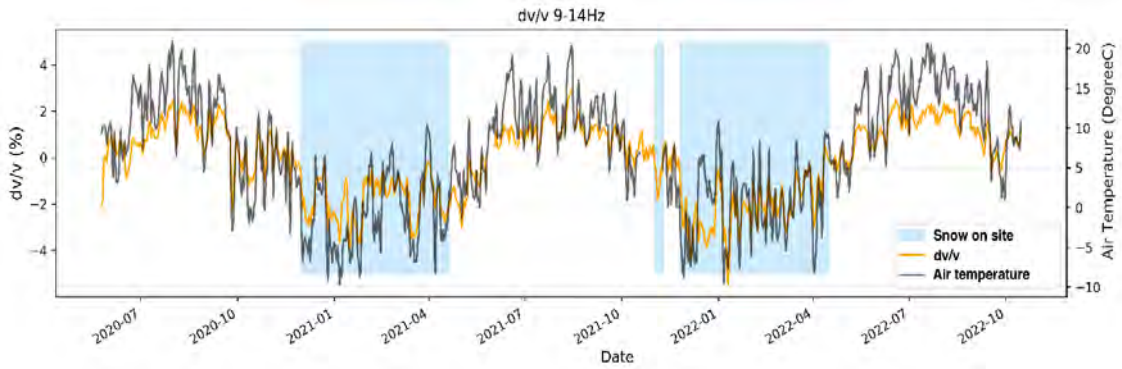

Figure 2. Daily relative changes in seismic velocity dV/V (over 9-14 Hz range) and observed air temperature during the whole monitored period on the Combe de Beaujournal landslide.

Results

Statistical methods have been used to study the correlations between in-situ environmental parameters and relative velocity changes.

Since there is no water table in this steep and permeable slope, the effect of hydrologic forcing on dV/V is negligible. However a high correlation between dV/V and temperature is obtained, as shown on Figure 2 and Figure 3, at different temporal periodicity from day to year.

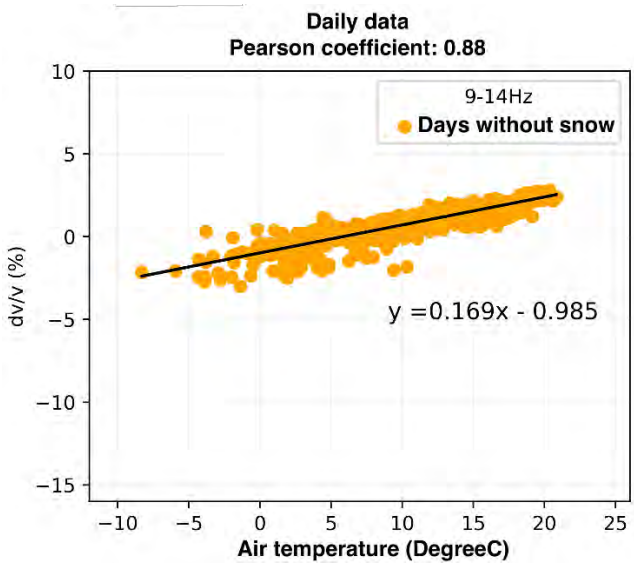

Figure 3. Correlation between daily dV/V and air temperature time series.

More precisely, cross-correlations between these two curves (integrating moving windows +/- 1 month) point out a time delay lower than one day (Figure 4). This very short response is especially valuable when there is no snow on the ground.

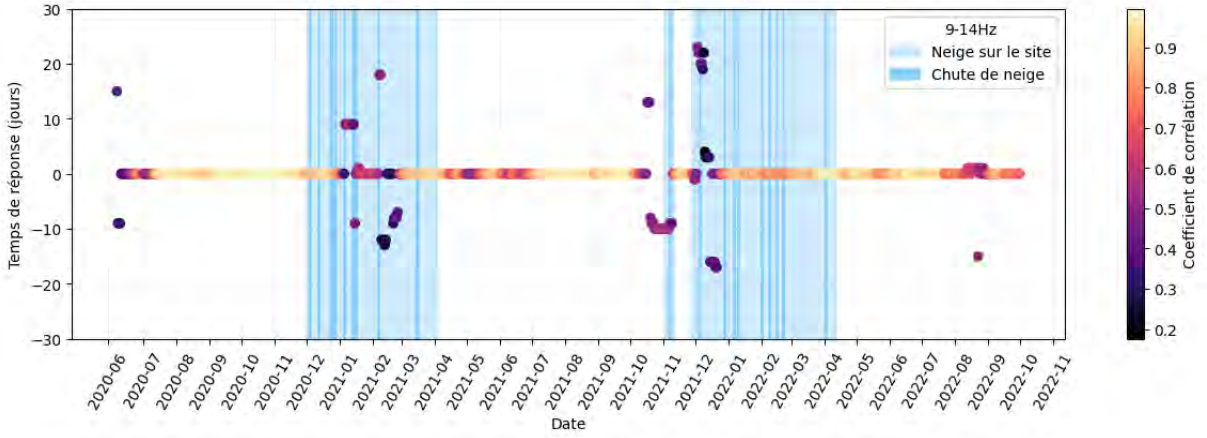

Figure 4. Delay response between dV/V and temperature is less than 1 day, with loss of coherence in presence of snow mantle.

We then analyzed hourly time series of both dV/V and temperature. Figure 5 shows the hourly evolution of temperature and dV/V averaged on a period in summer 2021. These variations are also correlated at daily scale, and reveal a time delay of 5-6 hours between temperature and dV/V time series. First, such a short delay is not consistent with the usual diffusion velocity of the thermal wave in the ground. Second, physically we expected to observe an anticorrelation between the two parameters, an increase of the ground temperature being supposed to cause a

decrease of dV/V due to the associated loss of rigidity. The observed increase of dV/V can be interpreted as an thermo-elastic effect of the medium, inducing an increase dV/V due to additional thermal-induced stresses over the surface layer, as already observed for dF/F rock columns (Guillemot et al. 2012).

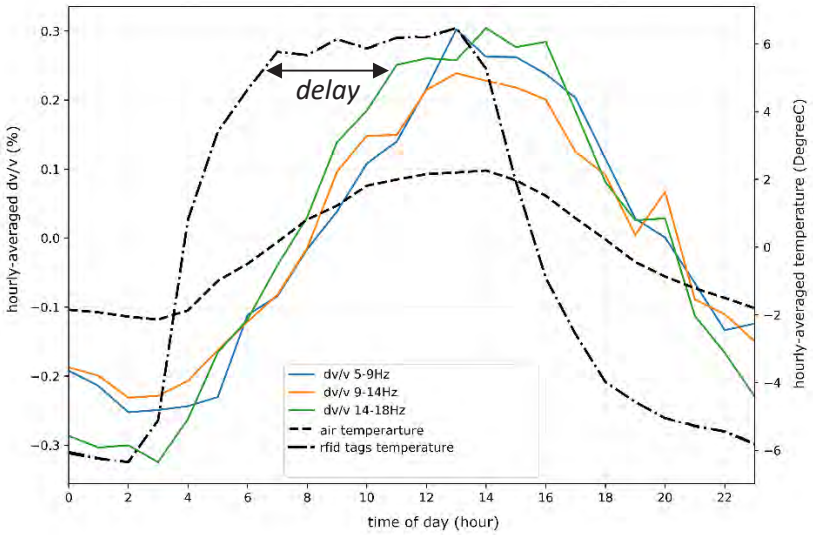

Figure 5. Hourly-averaged results of both dV/V and temperature (black curves), showing the delayed response of dV/V to temperature at daily scale.

Conclusions

Over the whole data period, the very high and stable correlation between dV/V results and observed temperature allows us to correct the initial results from the expected temperature reversible effect, using our statistical analysis. After this correction, it is possible to highlight other effects on subsurface, such irreversible processes affecting landslides. Moreover, thermal forcing seems to have a stabilisation effect on slopes due to an increase of the ground stiffness. But cyclic thermal variations may generate damage and cracks on slope instabilities, that could be detected by unusual dV/V values. Our study paves the way to investigate more in details thermal-induced processes on landslides.

References

Mainsant G, Larose E, Brönnimann C, Jongmans D, Michoud C & Jaboyedoff M(2012). Ambient seismic noise 505 monitoring of a clay landslide: Toward failure prediction. *J. Geophys. Res.* 117, F01030. 506 https://doi.org/10.1029/2011JF002159

LeBreton M, Bontemps N, Guillemot A, Baillet L & Larose E (2021): Landslide Monitoring Using Seismic Ambient Noise In-terferometry: Challenges and Applications, *Earth Science Review* 216, 103518

Larose E, Royer A, Guillemot A, LeBreton M, L. Baillet, E. Rey (2022). SOILSTAB: A seismic noise-based solution for near real-time monitoring of soil rigidity in the context of slow moving landslides (and beyond). *Journées Aléas Gravitaires,* Montpellier 2022.

Guillemot A, Baillet L, Larose L, Bottelin P (2022). Changes in resonance frequency of rock columns due to thermoelastic effects on a daily scale: observations, modelling and insights to improve monitoring systems. *Geophys. J. Int.* 231, 894-906.

Jongmans D., Laigle D., Rey E. (2022). Méthodologie de surveillance des mouvements de terrain adaptée aux territoires de montagne et préconisations. *Livrable L1 du projet POIA-FEDER SIMOTER 1 & 2.*

Laigle D., Jongmans D., Liebault F., Baillet L., Rey E., Fontaine F., Borgniet L., Bonnefoy-Demongeot M., Ousset F. (2019). Implementation of an integrated management strategy to deal with landslide triggered debris-flows : the Valloire case study (Savoie, France). *7th Int. Conf. on Debris-Flow Hazard Mitigation, June 10-13 2019, Golden, Colorado.*

Detection And Mapping Of Actively Deforming Areas Using Psinsar For Landslide Monitoring In Himachal Pradesh, India

Aarathi Shylu[1] , Reet Kamal Tiwari[2], Naveen James[2] Aravind K Suresh[1]

[1] Research scholar, Department of Civil Engineering, Indian Institute of Technology Ropar, Rupnagar, Punjab, India-140001
[2]Assistant Professor, Department of Civil Engineering, Indian Institute of Technology Ropar, Rupnagar, Punjab, India-140001

SUMMARY: Rainfall triggered landslides and slope failure events in Himachal Pradesh show a seasonal recurring nature. Every monsoon season passes with serious threats to life and loss of property throughout Himachal Pradesh, India. This study aims to identify and map actively deforming areas incorporating PSInSAR time series analysis of SENTINEL I SAR (both ascending and descending tracks) images during the time period of 2020 to 2023. SNAP and STAMPS are the software used for processing and analysis of interferograms. Slow moving masses, suspected to be potential landslides can be identified by clubbing the PSInSAR results to slope characteristics. The sensitivity of deformation measurement to slope direction is also considered. Actively deforming area is delineated from the velocity map by thresholding and clustering. A database of landslide history in the study area is also created to aid validation.

Keywords: landslide mapping, PSInSAR, Deformation Monitoring

Introduction

Continuous geodetic measurements in landslide prone regions are necessary to avoid disasters and better understand the spatiotemporal and kinematic evolution of landslides (Aslan et al 2020).With the increase in popularity of remote sensing based methods for monitoring and early warning of landslides, availability of data and different processing software increased. Different methodologies based on InSAR-derived displacements combined with in-situ observations have been in use in landslide activity assessment of different scales (Casini, 2010). Variety of thematic data such as topographic, geological, land use, ground deformation maps etc are used for the above. Combined use of InSAR-derived deformation maps and DEM gradient maps is also an effective and systematic way of detecting potential active slow-moving landslide candidates by setting a threshold of topographic slopes based on in-situ geological investigations (Zhao et al, 2012). Deformation Areas (ADA) are slow moving land masses or spatially aggregated moving points which can be considered as a potential landslide. The current study investigates spatial patterns and boundaries of ADA in Himachal Region. The combined use of DEM based parameters (slope and aspect) and PSI derived ground velocity is incorporated.

Study area

Himachal Pradesh is a predominantly mountainous state of India situated in western Himalayas. It covers an area of 55,673 km^2. The current study area is taken as the entire state. Later stage of work expected to focus on smaller regions within the state with prominent movements. The climate varies from hot and humid subtropical in the southern tracts, with

more elevation, cold, alpine, and glacial in the northern and eastern mountain ranges. Climatic variations, soil type, nature of slopes and unscientific anthropogenic activities like slope cutting in Himachal Pradesh caused an increase in the number of landslides. Monsoon season every year witnessess peak of landslides triggered by rainfall. The monsoon of 2023 was devastating with the highest rainfall in 70 years resulting in multiple slope failures of different scales.

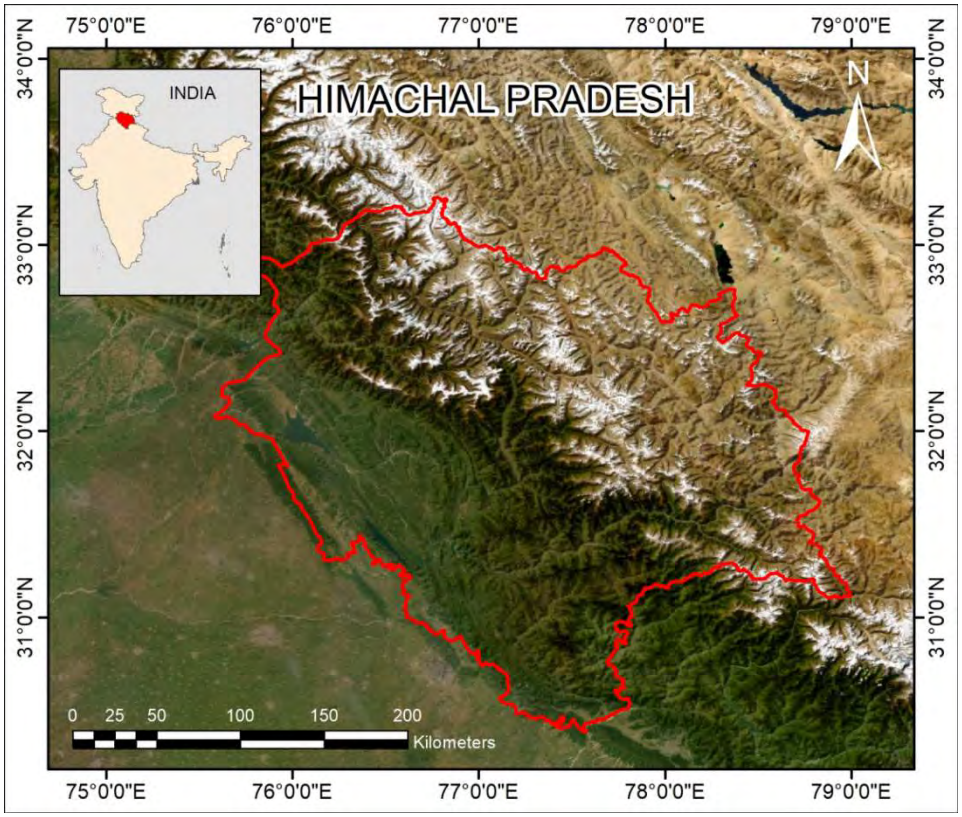

Figure 1: Map showing the study area

PSInSAR

Three sets of SAR images obtained from Alaska Satellite Facility Vertex belonging to the years 2020-21, 2021-22, and 2022-23 respectively were used for this study. The compatibility of the images in terms of the baseline requirements (perpendicular and temporal) was checked using the inbuilt baseline tool. All the images are subsetted for computational ease. Precise orbit file is applied and then the images are stacked or co-registered. The interferograms are generated with the assigned master in the stack. The interferograms are later exported to stamps and PSInSAR is performed in STAMPS. After internal processing steps in stamps such as selection of presistent scatters, phase noise estimation, 3D unwrapping, and phase correction finally giving Time series mean LOS velocity. Velocities from ascending and descending passes are combined for final results. Now the Mean LOS velocity is converted to Slope velocity ie the component in the direction of slope is derived from LOS velocity using the formula given by Notti et al (2012).

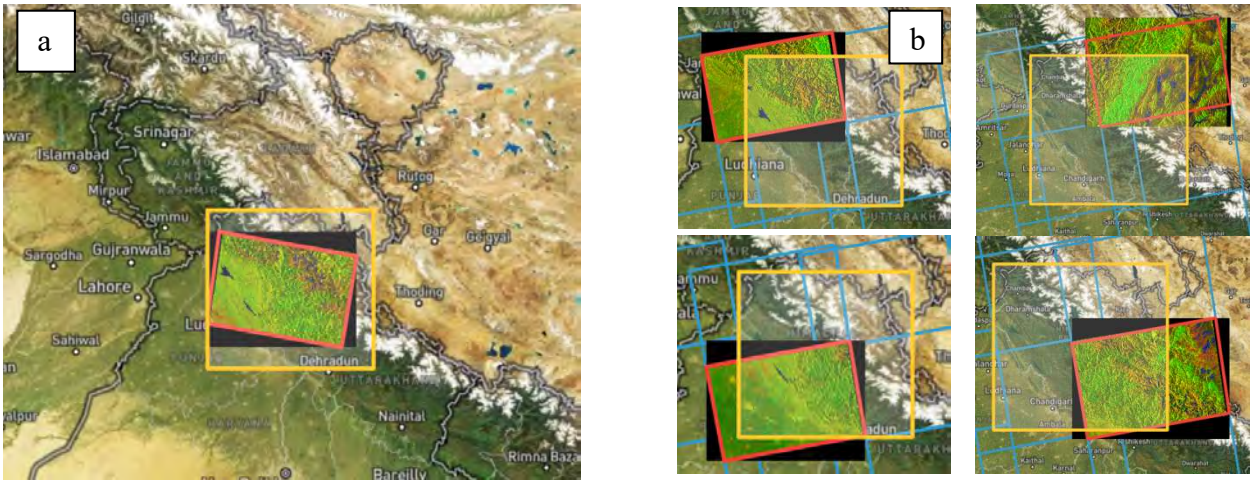

Figure 2: (a) Decending and (b) Ascending tracks and extends chosen for InSAR analysis

Detection of Active Deformation Area

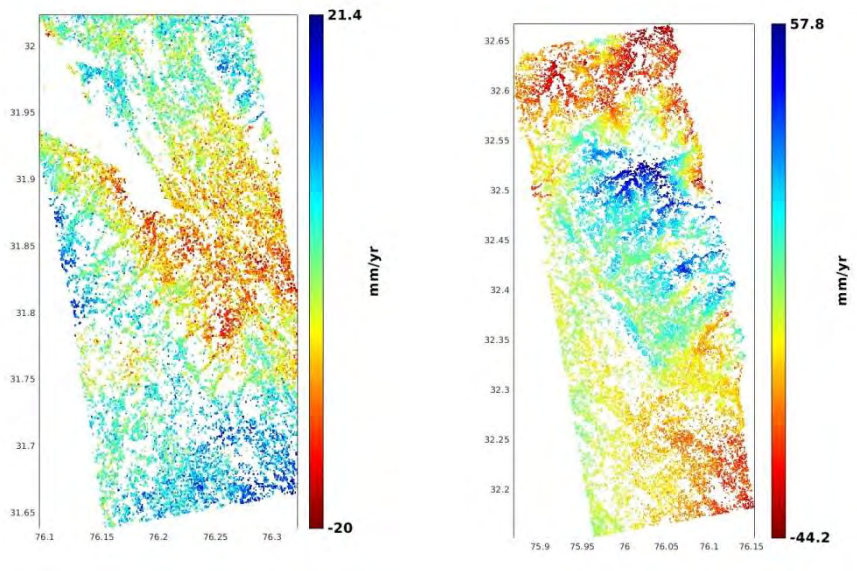

Figure 3 : PSInSAR results showing LOS velocity for different scenes within study area

Thresholding for active deformation area identification is done with standard deviation (sigma) of the mean PS velocity this is an indication of noise present in the deformation map. The thresholds may vary from study area to area and has to be identified with multiple trials. Some studies used a threshold of twice the multiple of standard deviation. The cluster is considered moving if velocity is greater than twice the standard deviation and stable vice versa. The velocity map is clustered using suitable clustering algorithm so that areas with similar behaviour can be identified and grouped into a single unit. Then the units are classified as either stable or moving. The area of influence of clusters is decided prior. With the deformation map, slope and aspect information of the terrain, intuitive direction of ground movement can be identified and colour coded. The directional sensitivity of deformation can be verified at this stage of study.

Validation with Landslide Inventory

Landslide inventory of previous landslide events within the area is prepared using information from various sources like newspaper article, trusted social media handles, previous inventories etc. The past events will be super imposed over the ADA map to validate the credibility of the results obtained.

Conclusion

This study identified actively deforming area within Himachal Pradesh, India, using PSInSAR approach. Applicability of Sentinel 1 images in Himalayan terrain is verified in terms of slope parameters such as slope and aspect. The study considers current limitation of PSInSAR techniques and tries to eliminate chances of wrong estimations. By converting the line of sight velocities to slope velocity the displacements are more realistic. The actively deforming areas identified in this study can be further subjected to site-specific continuous monitoring within the study area thus aiding in mitigation.

Acknowledgements

The authors extend their gratitude towards the lab equipment and software present at Indian Institute of Technology Ropar that was utilized to efficiently complete the data collection and processing.

References

Aslan, G., Foumelis, M., Raucoules, D., De Michele, M., Bernardie, S. and Cakir, Z., 2020. Landslide mapping and monitoring using persistent scatterer interferometry (PSI) technique in the French Alps. *Remote Sensing*, *12*(8), p.1305.

Cascini, L., Fornaro, G. and Peduto, D., 2010. Advanced low-and full-resolution DInSAR map generation for slow-moving landslide analysis at different scales. *Engineering Geology*, *112*(1-4), pp.29-42.

Zhao, C., Lu, Z., Zhang, Q. and de La Fuente, J., 2012. Large-area landslide detection and monitoring with ALOS/PALSAR imagery data over Northern California and Southern Oregon, USA. *Remote sensing of environment*, *124*, pp.348-359

Notti, D., Herrera, G., Bianchini, S., Meisina, C., García-Davalillo, J.C. and Zucca, F., 2014. A methodology for improving landslide PSI data analysis. *International Journal of Remote Sensing*, *35*(6), pp.2186-2214.

Analysis of Slope Stability and Mitigation Provision of Slope Failure at Kullu, India: Case Study

Sachchidanand Kushwaha[1], Veena U[2], Manoj Kannan[3], Ankit Tyagi[4], Naveen James[5], Reet Kamal Tiwari[6]

[1,2,3,4] Research scholars, Department of Civil Engineering, Indian Institute of Technology Ropar, Rupnagar, Punjab, India
[5,6]Assistant Professor, Department of Civil Engineering, Indian Institute of Technology Ropar, Rupnagar, Punjab, India

SUMMARY: Landslides have become one of the most disastrous nature-induced events, causing human and economic losses worldwide. The study reveals a landslide-prone slope in India's Kullu region experienced initial mass movement due to seepage of rainfall and drainage water, resulting in a displaced retaining wall. Field surveys, field testing, and laboratory tests were conducted to characterize soil and slope profile. Seepage and Slope stability analysis assessed the factor of safety (FOS) using numerical software slope/w and seep/w of the Geo-slope 2016 version. Micropile installation is considered as an effective remedial measure to safeguard the slope and the village located uphill. A comparative numerical analysis assessing potential benefits of micropile is discussed.

Keywords: slope stability, landslide mitigation, micropile,

Introduction

The most used definition and understanding of landslide can be interpreted as a movement of mass of rock, earth or debris down the slope, causing severe damage along the slope and at the toe (Cruden, 1991). India is among the top four countries with the highest landslide risk, where every year, the estimated loss of life per 100 km^2 is greater than one (Froude and Petley, 2018). North-west Himalayas are one of the major regions susceptible to landslides (Tyagi et al., 2022).

Slope stability analysis (SSA) is an effective way to evaluate the safe and cost-effective design of natural and man-made slopes which undergoes deformation due to reduced shear strength due to increased water content due to rainfall. For a slope to be considered stable, the forces operating against it must be significantly higher than the forces driving it to fail. The placement of micropiles has been an approach used to enhance the stability of slopes. Micropiles are replacement piles that are typically reinforced and have a small diameter, typically less than 300 mm (Bruce et al., 1997). Since they perform effectively and are easy to create, micropiles are frequently employed to strengthen slopes to prevent the mass of the slope from descending below the potential slip surface.

The following objectives were considered as the work was done: 1) Geotechnical characterization of the site's soil; 2) Analysis of slope stability and seepage to determine the factor of safety under heavy rain; 3) Comparison of the FOS analysis following the installation of the micropile and the provision of appropriate installation procedure instructions.

Study area

The slope under study observed a mass movement in terms of displaced retaining wall of 100 m stretch at the toe adjacent to National Highway (NH) and damages to several houses present

uphill. The gravity retaining wall was found to be failing in sliding and overturning due to excess seepage. The slope is located at 31.9660° N, 77.1218° E in Deodhar village of Kullu region of Himachal Pradesh on the banks of beas river. The valleys in the region ranges from 1000-45000 m above mean sea level. The district receives moderate rainfall, most of which is received during July to December and august is the wettest month with average maximum and minimum of 1305.8 mm and 976.80 mm respectively.

(a) (b) (c)

Figure 1: (a) Study area and slope profiles; (b) Failed retaining wall; (c) Exposed foundation of a house uphill

Field and laboratory investigation

Laser scanning, Unmanned Air Vehicle (UAV) photogrammetry and Differential Global Positioning System (DGPS) survey were used to obtain a 1 m resolution Digital Elevation Model (DEM). To comprehend the geotechnical and geological understanding of the slope, Standard Penetration Tests (SPT) were performed at 15 borehole locations. Due to excess seepage and steep terrain only four locations were mechanically drilled and rest manually. The shear strength properties of the soil samples were evaluated by performing a series of unconfined compressive strength (UCS) and unconsolidated undrained (UU) triaxial tests. Based on index property results the soil is low plastic silt with a minor clay fraction, mixed with large boulders. Undrained cohesion values obtained from UU test for saturated samples obtained was 11-20 kPa and from UCS test for undisturbed sample with natural water content obtained was 15-50 kPa for saturated samples. UCS for rock samples obtained was in a range of 18.23-25.36 MPa.

Table 1 Material Properties

Parameters	Value for soil (a range for 9 slopes)	Value (for subgrade)
Unit Weight, γ (kN/m^3)	14.58-16.67	18.6
Saturated water content	0.6-0.8	0.4-0.6
Natural water content	20-32	18-25
Cohesion, c' (kPa)	11-50	90
Angle of friction, φ' (º)	0	50

The direct shear test results show that the soil has a friction angle of 28 degrees at one borehole, but in most boreholes, the friction angle came out near zero, so the stability analysis was done considering the friction angle to be 0.

Slope Stability Analysis

Current stability analysis methods mainly rely on the concept of limiting equilibrium, which analyses the stability of a slope in terms of the driving and resisting forces acting both within

and upon it. The entire stretch was split up into nine 2D slope profiles (see Figure 1), and stability analysis was carried out for each slope profile using Mohr-coulomb model with respective soil properties obtained. SSA were done for in-situ condition and under rainfall condition for each slope. However, this writeup discuss the analytical results of the most critical one i.e. slope 2 (see Figure 1). An examination of slope stability is shown in Figure 2, along with a stress deformation analysis that uses finite element analysis to indicate the displacement of the soil mass. The unit weight, cohesion and internal friction angle for the soil were taken as 17 kN/m^3, 22 kPa and zero degrees respectively; and for the subgrade 18.6 kN/m^3, 50 kPa and 50 degrees respectively. The rock layer was considered a high strength material of 25 kN/m^3.

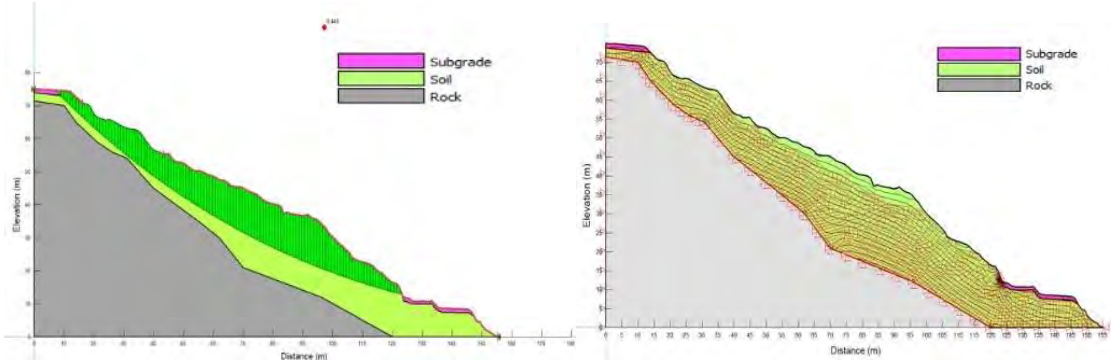

Figure 2 SSA and deformation analysis

The factor of safety obtained for in-situ conditions ranged between 0.748 to 0.845 and with transient seepage by imposing a rainfall of 250 mm/day (as per the Indian Meteorological Department for the region) were found to be in the range of 0.333 to 0.408. The results shown in the deformation analysis clearly depicts the damage caused to the retaining wall at the toe (see Figure 2b).

Remedial measures

From the remedial measures available in literature (Holtz and Schuster, 1996), use of micropile was found to be more suitable as mean to stabilize the slope. Stabilization schemes using micropiles aim to determine resistance and number of micropiles needed to stabilize a slope. Micropiles must provide the necessary force to increase the slope's factor of safety, determined using SSA programs.

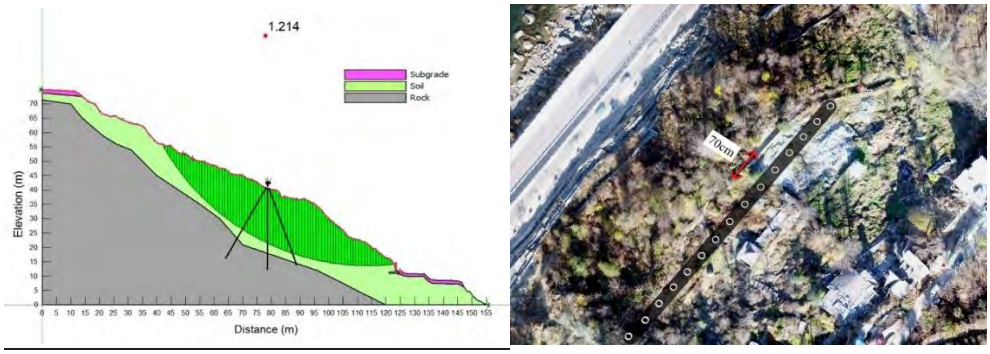

Figure 3 SSA after micropile installation and top view of placement of micropile

SSA were repeated for each slope with the provision of micropile in mid of the slope (Figure 3). The FOS for slope 2 obtained after micropile provision was found to be increasing to 1.214 from 0.369 as obtained under rainfall condition. The improved FOS with micropile hence

indicates the use of micropile as viable option for remedial measure. The study used guidelines from Federal Highway Administration (FHWA) for micropile to calculate displacement, bending moment, and shear force at points, considering pile head slope compatibility at slip surface. Micropile installation increased FOS. The installation of micropile interestingly shown a subsequent increment in FOS. We recommended providing a series of CASE-1 type micropiles at the mid-slope section with length of 28 m at 70 cm spacing (Figure 3b) and suitable cross section (Figure 4) to arrest the slope movement.

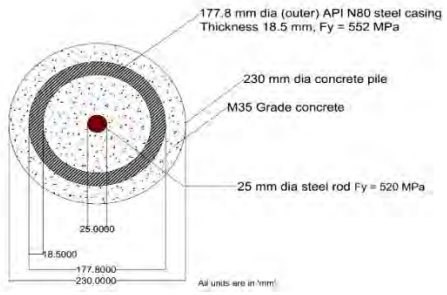

Figure 4 Cross sectional design of micropile

Conclusion

A strategy has been put forth to protect the slope at the Kullu site that was in danger of failing. The investigation included a field survey, field testing, laboratory testing, and an assessment of slope stability. Based on laboratory analysis, the soil consists mainly of sandy clay. The depth and area of the soil that is susceptible to failure were revealed by the slope stability assessments utilizing the soil data. Following the recommendations provided in FHWA report, the design of the micropile was carried out as a corrective solution to protect the slope. The examination of slope stability while keeping the micropiles in the middle of the slopes demonstrates the adequate improved safety factor. The NHAI (National Highway Authority of India) was given the suggested micropile placement method and design procedure for further action.

Acknowledgements

This work was supported by National Highway Authority of India (NHAI) with grant NHAI/PD/PIU-Mandi/T-K/06/06-B/2952. The authors extend their gratitude towards the lab equipment and software present at Indian Institute of Technology Ropar that was utilized by to efficiently complete the SSA, laboratory testing, and field testing.

References

BRUCE, D., DIMILLIO, A. & JURAN, I. 1997. Micropiles: the state of practice part 1: characteristics, definitions and classifications. *Proceedings of the Institution of Civil Engineers-Ground Improvement,* 1**,** 25-35.

CRUDEN, D. 1991. A simple definition of a landslide. *Bulletin of Engineering Geology & the Environment,* 43.

FHWA, N. 2005. Micro-Pile Design and Construction Reference Manual, US Department of Transportation, McLean, Va. Publication No. FHWA NHI-05-039.

FROUDE, M. J. & PETLEY, D. N. 2018. Global fatal landslide occurrence from 2004 to 2016. *Natural Hazards and Earth System Sciences,* 18**,** 2161-2181.

HOLTZ, R. D. & SCHUSTER, R. 1996. Stabilization of soil slopes. *Landslides Investigation and Mitigation, Eds. Turner AK and Schuster, RL, Special Report,* 247.

TYAGI, A., TIWARI, R. K. & JAMES, N. 2022. A review on spatial, temporal and magnitude prediction of landslide hazard. *Journal of Asian Earth Sciences: X,* 7**,** 100099.

Multiple landslides in a natural touristic area (Mullerthal, Luxembourg)

Steve Gruslin[1], Tiffany Hennebaut[1], Mattia Tirone[1]

[1] GEOCONSEILS, Contern, Luxembourg

SUMMARY: The touristic region of Mullerthal located in Luxembourg is a protected natural area at particular risk of landslides. The purpose of this article is to explain the main causes of some of these landslides and the solutions being implemented to remedy them.

Keywords: touristic region, protected natural area, complex geology, Luxembourg

Introduction

Situated in the east of the Grand Duchy of Luxembourg, the touristic region of Mullerthal, also known as "Luxembourg's Little Switzerland", is an area at particular risk of landslides. In recent years, the combination of complex geology, steep topography, and heavy rainfall, has led to numerous landslides, causing extensive damage, and blocking roads for months at a time. The area is also designated as a nature protection area (Natura 2000 and drinking water catchment areas), which limits the options for securing the sites and means that innovative solutions had to be found. This article presents the causes of some of these landslides and the solutions being implemented to remedy them. The document offers five instances, four of which are situated on the CR364 route and one on the CR356 route (see Figure 1).

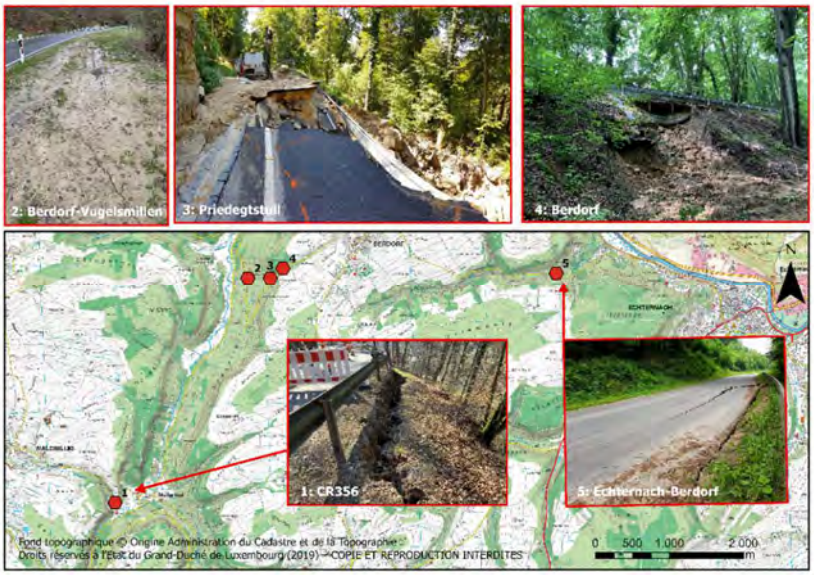

Figure 1. Location of the landslides

Geological situation

In the projects area, complex geological formations from Triassic and Jurassic are found, as shown on Figure 2. Li2, more commonly known as "Luxembourg Sandstone", is composed of calcareous sandstones of whitish color alternating with sandstones, of which the calcareous

cement is less present or totally absent, of yellowish color. Li1 (called "Elvange Marls"), is made up of alternating dark gray marls and partially sandy limestone beds. The ko2 ("Rhaetian: Argile de Levallois – Levallois Clay") are clays and red clayey marls whose presence strongly influences the risk of landslides (by acting as a soap layer). The ko1 ("Rhaetian: Mortinsart Sandstone"), meanwhile, is composed of sandstone, conglomerates and black laminated argilites. Finally, km3 (named “Keuper with compact marnolites”) is made up of motley marl with thin dolomitic beds that may contain gypsum.

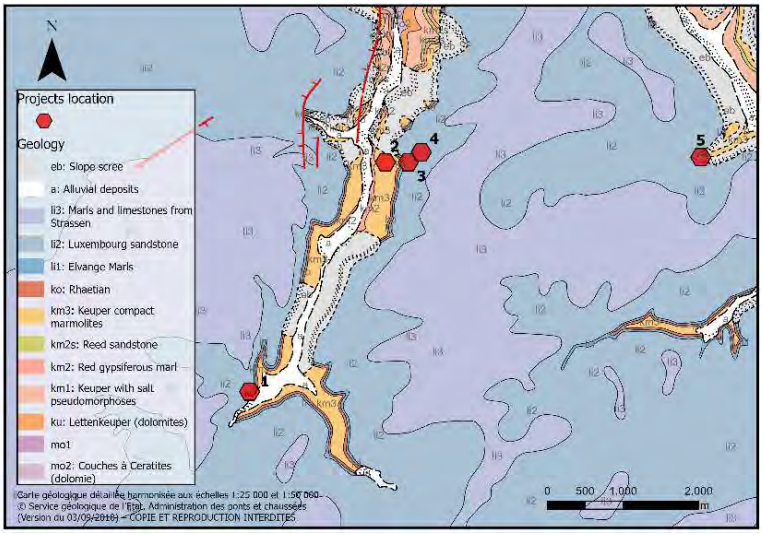

Figure 2. Location of the zones on the geological map

CR364

The first landslide occurred on the road CR364 between Echternach and Berdorf. During the investigations, stony-gravelly backfills up to 3 m thick were found underneath the road. Below is slope scree consisting of sand and gravel with partially altered layers of the Upper Triassic (Rhaetian) then finally the layers of the Middle Keuper. Rhaetian layers have a high consistency in the dry state but are very sensitive to water. They soften very quickly on contact with water, thus playing the role of a "soap layer" which, in combination with the inclination of the layer, can constitute a potential sliding surface for overlying materials that are not very cohesive. The water masses resulting from the heavy rains coming from the hill above the site reached the road, ran off on the embankment and caused significant erosion on the surface. The water which penetrated under the road quickly crossed the permeable layers (backfills and scree) and mobilised the sliding surface constituted by the Rhaetian layers, so that all the embankments and scree slipped, which has led to the appearance of cracks in the roadway. It was estimated by drillings that about 10,000 m^3 of underground materials had slipped.

The slope damaged by the landslide was replaced by a reinforced earth wall between 3 and 9 m high constructed with *in situ* soil and polymeric geogrids. Extensive geotechnical studies and calculations have shown that landslides can reoccur in affected areas if only limited near-surface stabilisation measures are taken. To avoid long-term instabilities, it was necessary to excavate the entire slip body over the entire width of the roadway down to the layers of the Rhaetian formation where the slip surface developed. The excavated material (stones, boulders, sand, and gravel) was processed on site to produce a 0/45 mm backfill material. This enabled approximately 70% of the required backfill material to be reused as backfill for the earth wall.

The reinforcement comprises a galvanized steel grid, an anti-erosion-mat, and horizontally laid polymer geogrids, all connected together (Figure 3).

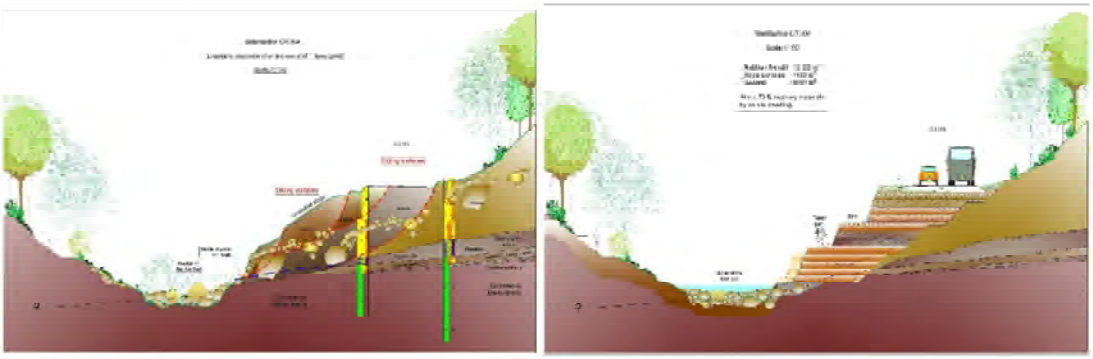

Figure 3. Interpretation of the situation (left) and principle of stabilisation with an earth retaining system (right)

The second landslide, also secured by reinforced earth, is located at the so-called "Priedegtstull". The geological situation differs from that of the first zone, with slope scree up to 7 m thick, followed by the Luxembourg sandstone, first altered then intact. In this area, the heavy rainfall also considerably eroded the road embankment. The water seeped into the embankment and destabilised it, causing landslides in several places (Figure 4).

Figure 4. Situation before and after stabilisation

The third place is located near the village of Berdorf. There are backfills and slope scree (6,4 m thick) overlying the Luxembourg Sandstone. The embankments and scree have slipped due to the large amounts of water that have infiltrated them. Piles were used to secure the road.

The fourth landslide affected the road between Berdorf and Vugelsmillen. This is an old, backfilled landslide area. The landslide occurred here because of water seeping into backfills to 12 m thick, overlying Rhaetian sandstone or km3 marl, depending on the location. The investigations carried out suggest the presence of a fault bringing the Rhaetian sandstones and the Middle Keuper marls into contact at the same altitude and over a very short distance. This fault undoubtedly affects the movement of underground water. An earth retaining system has also been proposed as a solution.

CR356

The landslide took place on the downstream side slope of road CR356, between the villages of Mullerthal and Waldbillig. The area is characterised by slope scree of up to 50° mainly

overlying Luxembourg sandstone and, in the lower part of the project, the Li1 marl formation. The visual observation of a strike-slip fault and several normal faults clarifies the varying level at which the rock top has been encountered here, as well as the presence of the marl at heights where the overlying sandstone remains in other areas. The entire zone is designated as a protected zone on account of its water sources.

Multiple stabilisations were used in this project. The safety factor of the downstream slopes was calculated using the limit equilibrium method. A series of micropiles were installed at alternating batter angles, along with a reinforced concrete cap wall, to stabilise the CR356. Additionally, a shotcrete wall with self-drilling anchors was implemented to stabilise the bottom of the slope. A substantial amount of 1000 m³ was utilised to stabilise the slope during shotcreting, in accordance with a predetermined work phase. Additionally, sub-horizontal drains were designed to improve slope drainage. To comply with the standards for natural slopes and the existing masonry wall along the road, a steel mesh and soil nail were designed to increase the safety factor. Furthermore, some naturalistic engineering measures (wooden mesh, palisades combined with the planting of local pioneer species) were provided to stabilise the first metre of the steep slopes by improving soil cohesion. Figure 5 shows the safety work in progress.

Figure 5. Situation during stabilisation works

Conclusions

The roads and the steep slopes of the embankments present in the Mullerthal require special attention due to their very specific geological and topographical characteristics and the resulting requirements for stability and drainage conditions. Several examples were provided to demonstrate how landslides can be economically and safely remedied using both conventional and innovative methods, such as earth retaining systems and biological engineering, while ensuring environmental constraints are respected and future stability is guaranteed.

References

© Service géologique de l'Etat, Administration des ponts et chaussées – Carte géologique détaillée harmonisée aux échelles 1:25000 et 1:50000. Version 03 sept. 2018.

Gruslin, Steve, & Nola, Domenico. (2021). Slope protection with an earth retaining system: respectful of natural resources and the landscape. *European Geologist, 51*. http://doi.org/10.5281/zenodo.4954439

Gruslin, Steve, & Nola, Domenico. (2021). Slope protection respectful of natural resources and landscape thanks to earth retaining system *Proceedings of the 3rd European Regional Conference of IAEG, Athens, Greece, 6-10 october 2021*

Quantifying Landslide Activity Using Unmanned Aerial Vehicle And Terrestrial Laser Scanner: A Case Study Of Soldha Landslide In Kangra, Himachal Pradesh, India

Aravind K Suresh[1], Reet Kamal Tiwari[2], Naveen James[2], Aarathi Shylu[1]

[1]Research scholar, Department of Civil Engineering, Indian Institute of Technology Ropar, Rupnagar, Punjab, India-140001
[2]Assistant Professor, Department of Civil Engineering, Indian Institute of Technology Ropar, Rupnagar, Punjab, India-140001

SUMMARY: Landslide is one of the major disasters affecting mountainous regions all over the globe and has devastating consequences, including loss of life. Considering the global scenario, the Indian Himalayan region is highly susceptible to a landslide. Most of the landslides in this region are triggered. Considering the hazardous nature, it is essential to study landslides, which involve the change detection of landslide magnitude, mapping, monitoring, and further early warning. Over the period, there have been various techniques adopted for landslide studies. Among them, remote sensing is a powerful tool for landslide investigations. Over the years, innovations in remote sensing methods have helped researchers reduce the cost and time required for disaster studies. This study aims to model the topography post and pre-landslide event in Soldha village in the Kangra District of Himachal Pradesh, India. Unmanned Aerial Vehicle (UAV) integrated with Terrestrial Laser Scanner (TLS) and DGPS surveys were used to develop the pre and post-digital elevation model (DEM) for the study area. Structure from motion (SfM) algorithm was used to generate DEM. The volume of landslides and the areas of erosion and deposition were identified after the analysis. The results will be used for the mitigation and risk reduction of the area.

Keywords: landslide mapping, UAV, terrestrial laser scanner

Introduction

Landslide is one of the important geological hazards, causing damage to the social and natural environment. Researchers around the globe have been mainly dealing with the recognition, measurement, and forecasting of landslides (Scaioni et al. 2014). Various tools are available for studying landslides. Among them, remote sensing techniques have made an important contribution to landslide studies. Integrating remote sensing techniques with sensor networks and geotechnical measurements is a powerful tool for analysing landslides and their risk reduction (Qiao et al. 2013). The use of unmanned aerial vehicles (UAV), terrestrial laser scanner (TLS), and interferometric synthetic aperture radar (InSAR) have increased over the past decade (Mao et al. 2021). Among them, UAV and TLS are commonly used for fine three-dimensional (3D) mapping (Guisado-Pintado et al. 2019). Although multisource surveying techniques provide enough data, they are subjected to certain problems individually. Thick vegetation cover and weather conditions is a challenge in the case of UAV. Inaccessibility to the area and the presence of large trees are challenges in case of TLS (Mao et al. 2021). A fusion of both UAV and TLS data is helpful in this case since the gap in one data is covered by the other. Ground control points (GCP) collected from DGPS survey can be used for registering both TLS and UAV data and further improve the result's accuracy.

The landslide at Soldha village of Kangra, Himachal Pradesh, India was studied. UAV, TLS, and DGPS surveys were conducted to map the landslide topography. The survey was conducted pre and post-landslide event which happened on 20th August 2023. For the pre event survey data was collected using all three methods, while post-survey UAV data was collected. Structure from motion (SfM) algorithm was used for generation of 3D slope from 2D aerial photo. The goal of this study is: 1) Model the terrain before and after the event using a multiple survey methods; 2) Compute the volume of landslide and identify the areas of erosion and deposition.

Study area

Soldha landslide zone is one of the prominent site in Kangra district, Himachal Pradesh that witnessed large-scale mass movement in October 2013 and August 2023 (Figure 1). In 2013 5.6 ha of agricultural land and 23 ha of forest cover were destructed following the landslide (Mahajan et al. 2022). On 20 August 2023, the slope failed causing damage to house and agricultural land.

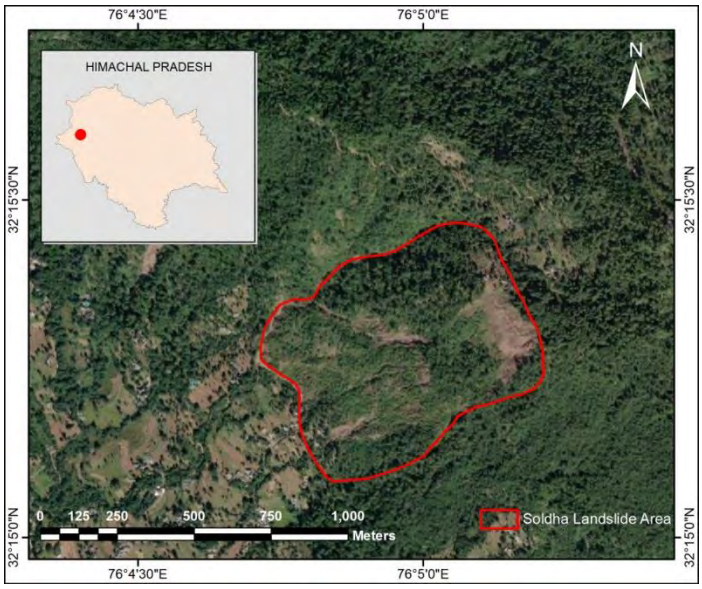

Figure 1: Map showing the study area

Field Survey

A field survey was carried out before (23rd June 2023) and after the event (1st September 2023). Before the landslide, a major area was covered in sparse and thick vegetation. The UAV survey was carried out at an altitude of 80m and 80% overlap in both front and side directions. A total of 749 two-dimensional aerial images were captured. Eleven full dome scans were done using TLS across the study area. DGPS survey was carried out to collect data from areas, that are not obtained in TLS and areas covered in thick vegetation. GCPs were collected for georeferencing both TLS and UAV data. In the post-event, vegetation cover was destroyed in a landslide. Moreover, the slope was much more difficult to do TLS and DGPS surveys. But ground visibility was high from the UAV. Hence, a UAV survey was done post-event. A total of 748 2D aerial images were collected.

Landslide Topography and Volume

For processing of UAV data, PIX4D software was used. Structure from motion (SfM) algorithm is used for the generation of 3D models from 2D photographs. GCPs were provided in the initial

processing of the pre-event data for the georeferencing. Point cloud and DSM were generated. TLS data was processed using Trimble Business Center (TBC) software (Figure 2). The scans were registered with each other and then GCPs were used to georeference the data. Both UAV and TLS were georeferenced to the same coordinate system: WGS84-UTM Zone 43N, with EGM96 geoid.

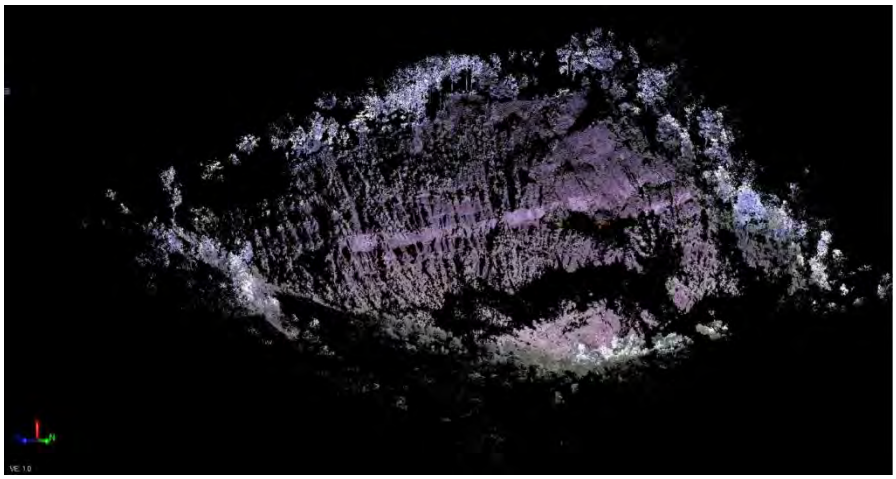

Figure 2: One of the TLS scans taken near the previously failed slope

The point cloud obtained from UAV data and TLS, along with the DGPS data was imported in TBC and merged. Point cloud classification was done to remove the thick vegetation and other structures, leaving only the ground. Further, pair-wise registration between the point clouds was done to increase the accuracy. The merged point cloud was converted into DTM in ArcGIS software. Accuracy assessment of the resulting DTM was done using the GCPs collected. For the post-event UAV data, processing was done in PIX4D. For georeferencing, coordinates from the pre-event point cloud were taken. Sparse vegetation was removed after classifying the point cloud in TBC. DTM for the post-event survey was obtained using ArcGIS. Figure 3 shows the post and pre-event ortho-mosaic image of the study.

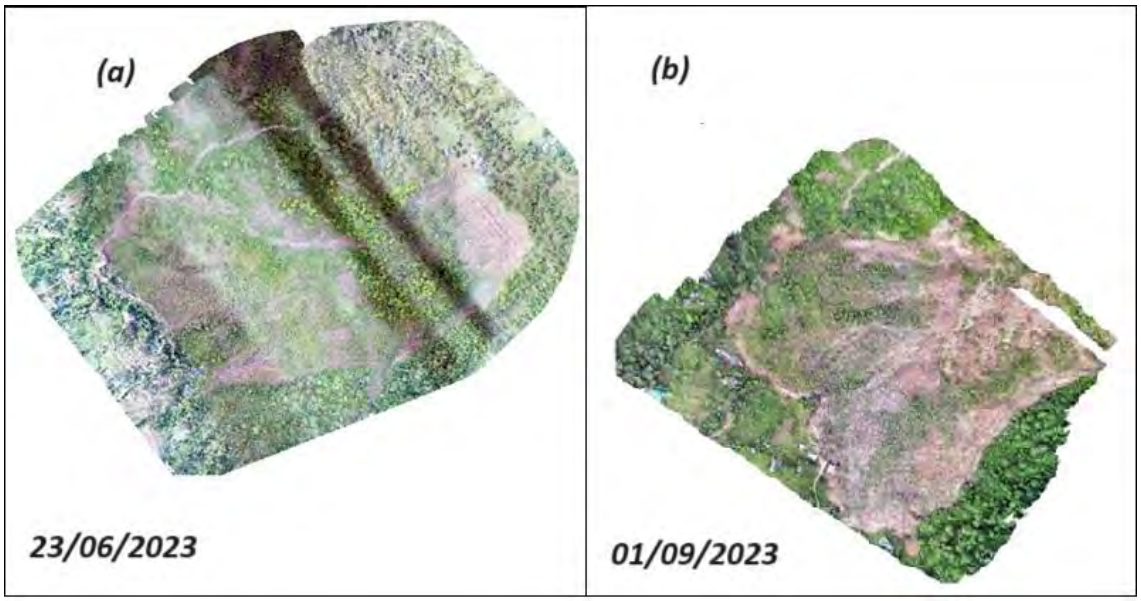

Figure 3: (a)Pre event and (b)post event ortho-mosaic image of the study area

Both the DTMs were further analysed to identify the regions of erosion and deposition. The volume of landslide was calculated from both DTM. Slope profiles from the model were extracted, which could be used for slope stability analysis.

Conclusion

DTM for the Soldha landslide region was generated using multiple survey methods. UAV, TLS and DGPS survey were used. SfM algorithm was used for obtaining 3D point cloud from 2D aerial photographs. Based on the generated DEM for post and pre event, the volume of landslide was computed. The regions of erosion and deposition were identified. Further slope profiles were generated from the model, which can be used for slope stability analysis. The information collected could be used for understanding landslide behavior, mitigation, and decisions in landslide risk reduction.
SfM algorithm generates the DSM, and the tree cover needs to be removed for the generation of DTM. Majority of the slopes in Himalayan region is covered by forest or thick vegetation and this makes the generation of DTM a challenging task. A canopy height model (CHM) for any region could be used for obtaining DTM from a DSM. For site specific studies, an integration of DGPS, TLS and UAV survey can provide the elevation information under the canopy. Machine learning models can be introduced to terrain modeling studies by modeling the canopy height information from similar sites and using it to generate the DTM.

Acknowledgements

The authors extend their gratitude towards the lab equipment and software present at Indian Institute of Technology Ropar that was utilized to efficiently complete the field survey and data processing.

References

Scaioni, M., Longoni, L., Melillo, V. and Papini, M., 2014. Remote sensing for landslide investigations: An overview of recent achievements and perspectives. *Remote Sensing*, *6*(10), pp.9600-9652.

Qiao, G., Lu, P., Scaioni, M., Xu, S., Tong, X., Feng, T., Wu, H., Chen, W., Tian, Y., Wang, W. and Li, R., 2013. Landslide investigation with remote sensing and sensor network: From susceptibility mapping and scaled-down simulation towards in situ sensor network design. *Remote Sensing*, *5*(9), pp.4319-4346.

Mao, Z., Hu, S., Wang, N. and Long, Y., 2021. Precision evaluation and fusion of topographic data based on UAVs and TLS surveys of a loess landslide. *Frontiers in Earth Science*, *9*, p.801293.

Guisado-Pintado, E., Jackson, D.W. and Rogers, D., 2019. 3D mapping efficacy of a drone and terrestrial laser scanner over a temperate beach-dune zone. *Geomorphology*, *328*, pp.157-172.

Mahajan, A.K., Sharma, S., Patial, S., Sharma, H., Pandey, D.D. and Negi, S., 2022. A brief address of the causal factors, mechanisms, and the effects of a major landslide in Kangra valley, North-Western Himalaya, India. *Arabian Journal of Geosciences*, *15*(9), p.925.

Landslide analysis improvements through LIDAR– Example of the landslides of Villequier, Normandy, France

BOUTET Claire[1]

[1] Hydrogéotechnique, Rouen, FRANCE

SUMMARY: New high-resolution topographic data, coming from the national LIDAR campaign, give us today a better understanding of the past landslides through the precise topographic analysis. The example of the landslides of Villequier in France quickly shows the possible advancements brought by this technology.

Keywords: landslide, topography, LIDAR

Introduction

The Villequier's hillside in Normandy, France is known for its slope instabilities. Several landslides have already happened in the past. The most known is the landslide of the Roquette which destroyed two households by moving 400 000 m^3 of soils in 1969. It is important to understand the geology and the local topography to master the stability of the present hillside.

Presentation of the site

Villequier is a Norman city, bordered by the river "la Seine", located in a sedimentary basin. The regional geologic documents detail the presence of an anticline eroded to the side by the Seine river. That's why this area presents the distinctive feature of a visible continuous section from the Kimmeridgian to the Cretaceous as shown on figure 1:

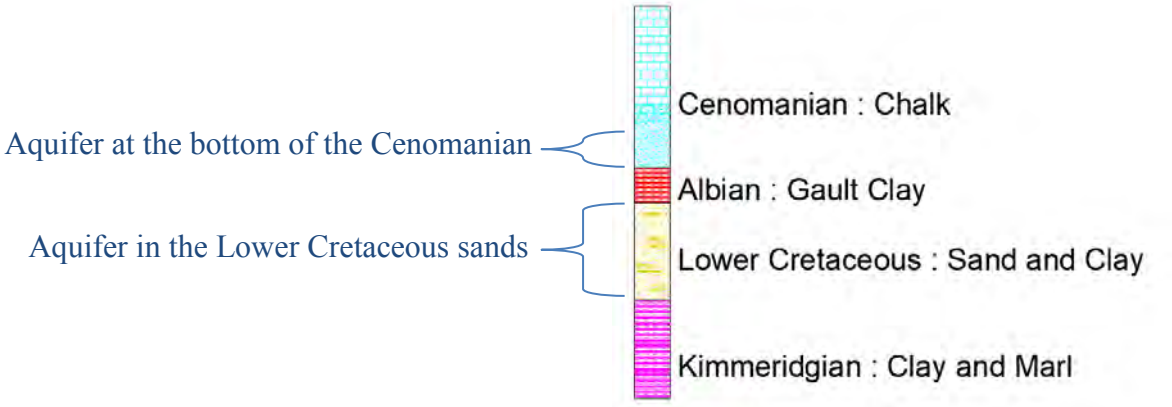

Figure 1. Stratigraphy of Villequier

The site of Villequier has been studied several times following the landslide of the Roquette, but there is still a lack of data to understand the past landslides. The main reason being that investigations are delicate to do: the area presents collapses and the vegetation is very dense and chaotic. The bringing of a mobile drill rig or the production of geophysical and topographic profiles are near impossible considering the state of a large portion of the hillside. In these "hard access" situations, LIDAR brings very useful information and let us compile data that were missing in the past for the hillside comprehension.

LIght Detection And Ranging (LIDAR)

The National Institute of Geographic and Forest Information (l'Institut National de l'Information Géographique et Forestière), or IGN, undertakes in France the LIDAR HD national project in which it performs the acquisition, processing and diffusion of LIDAR Hight Density (HD) scatter points on the entire metropolitan and overseas (DROM, French Guyana excluded) territory. This work has started in 2021 and should end in 2025. The first data are already available in free access in France. This is a powerful tool available to all geotechnical engineers which can enhance our work methods.

Before all, let us quickly see what is LIDAR and its precise outcomes. The LIDAR technology is a telemetry technique (distance measurement) harnessing the properties of light. A scan emits toward the ground some high frequency infrared laser pulses then records the precise time interval between the emission and reception of these pulses to calculate the positions of the impacted points. Subsequently, the acquired data are processed to generate Digital Elevation Models (DEM) (Modèle Numérique de Terrain, or MNT in French). This results in a high-precision meshed DEM with a very high topographic and geometric resolution: 1m for the x and y axis and 0.2m for the z axis (altimetry).

For the Villequier's hillside, the DEM is now available, providing the actual topography of the hillside, without vegetation nor buildings, as shown on figure 2.

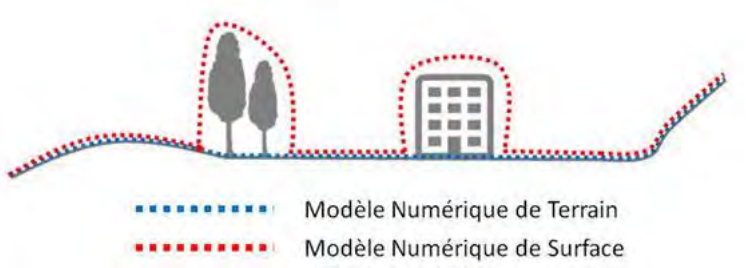

Figure 2. Theoretical diagram of the DEM (geoservices.ign.fr)

Performed Analysis

An analysis of these data lead to the understanding and localisation of the past landslides. Here is our approach:

1. Download the freely available online data of IGN
2. Insert these data in a cartography software (QGIS® in our work)
3. Analyse the topographic curves by superposing layers composed of the geological map, the archive plans, the historical aerial photos, etc
4. Look for abnormal or hazardous areas
5. Create profiles of these zones for a better visualisation ("Profile Tool" module in QGIS) as shown on figure 3

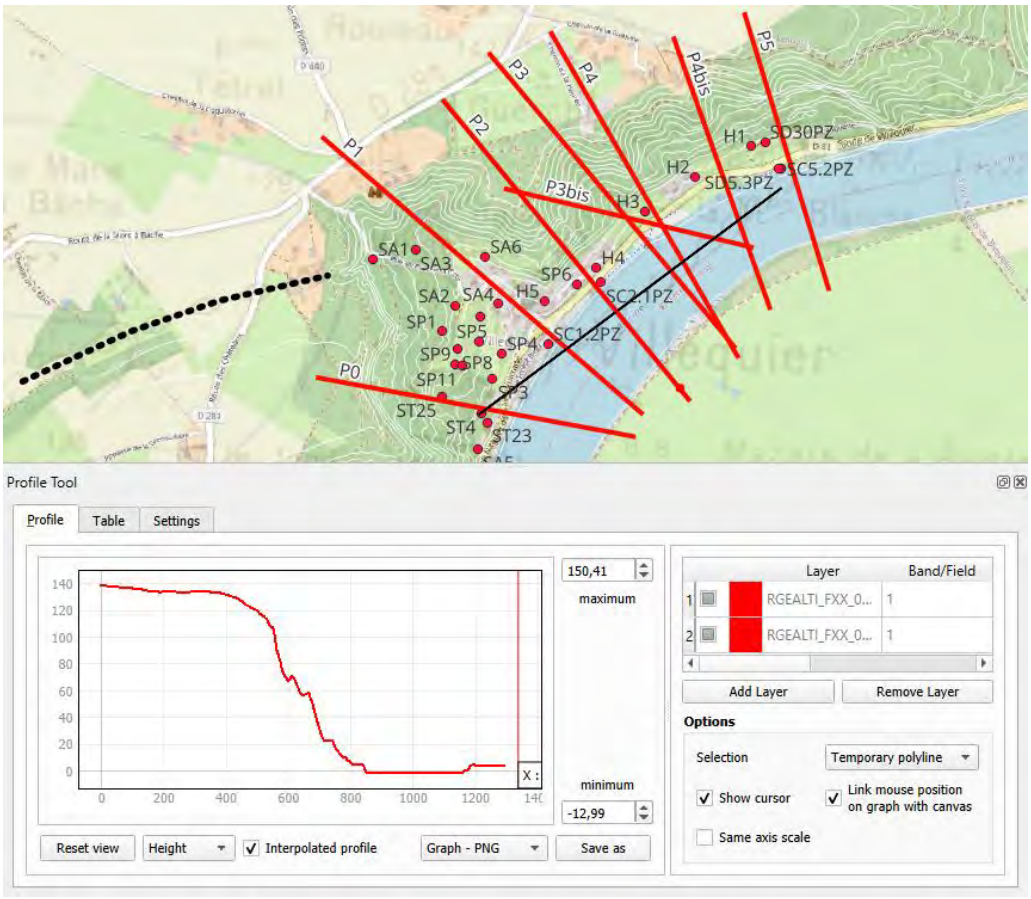

Figure 3. Screenshot of the analysis and creation of profiles in QGIS

The profiles then are easily exported in .dxf format. We add the available boreholes and the known information of regional geology.

Results

We can see on this interpreted profile (figure 4) two circles in the topography which correspond to two past landslides.

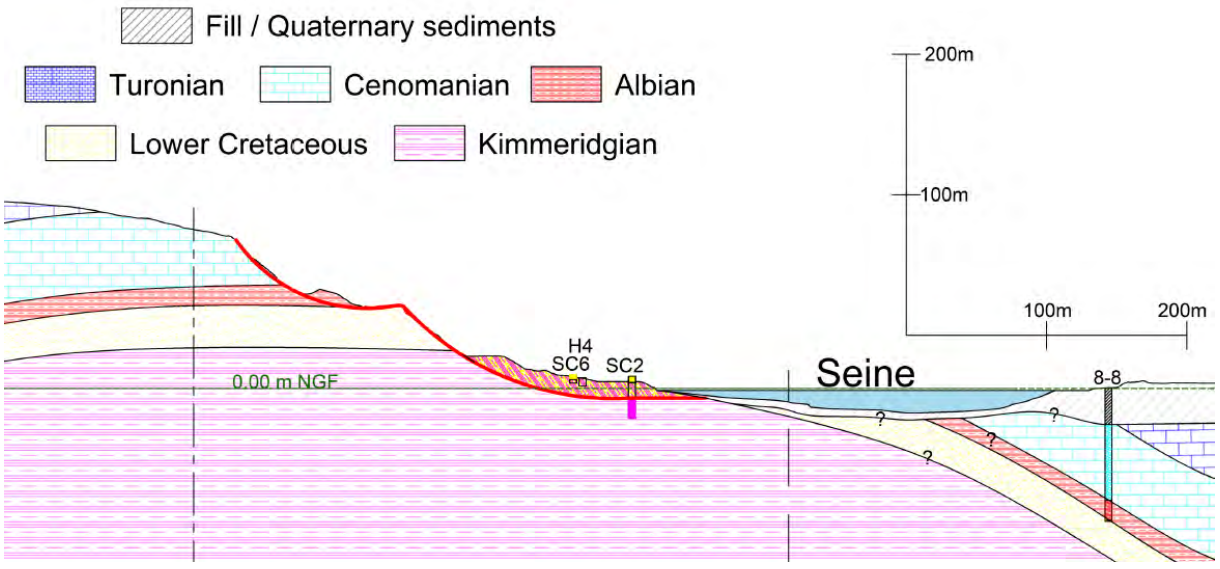

Figure 4. Interpreted profile obtained from the LIDAR and available data

By extending the visible portion of the circle on the topography, we obtain the complete rupture surface and the entire sliding area. Some boreholes at the base of the slope confirmed the presence of remolded soils throughout this height, thereby validating the delineation of the surface rupture.

By applying this principle on all observable arcs on the hillside, we can go back to a large portion of the past landslides that are presently completely hidden by the vegetation.

In Villequier, this analysis, performed on multiple profiles, reveal various types of landslides:

- Sliding surface on Gault clays
- Instabilities in Lower Cretaceous sands
- Instabilities in the Kimmeridgian, due to erosion at the foot of the circle by the Seine.

Once this understanding work and the exact localisation of the past landslides done, it is possible to realise a classic slope stability analysis to conclude on the current and future stability of the site. Having archived LIDAR data from before the landslides would additionally facilitate the retroanalysis-based calibration of in-situ soil parameters. Without these data, we depend on the in-situ boreholes and laboratory soil testing to acquire the inherent parameters of the soil.

Analysis Limitations

While LIDAR ensures precise topographical alignment, digitally modeling the complexity of the entire Villequier hillslide remains challenging. The crucial missing element significantly affecting the hillside stability is water. A site visit quickly reveals the presence of numerous water sources throughout the entire hillside, linked to two main aquifers at the base of the Cenomanian and within the Lower Cretaceous sands. With the numerous past landslides and the mixing of the different geologic layers in the landslide, a lot of water pockets and flows are created in the more permeable sandy lenses. The water sources are thus unpredictable and untraceable precisely due to the chaotic nature of the landslides.
The modelling of the whole region needs simplifications. We should then stay critical on the obtained results and associate them to a local knowledge of the site and its history.

Conclusion

The French LIDAR program is a potent tool to use when studying landslides. It enables to understand the morphology of complete hillside with precision, to deduce the geometry and the depth of the past instabilities and to then analyse the present and future stability.

Impact Of Site Effects On Landslides Reactivation

Céline Bourdeau[1]

[1] celine.bourdeau-lombardi@univ-eiffel.fr, Université Gustave Eiffel, Paris, France

SUMMARY: Moderate to strong earthquakes are likely to trigger landslides in mountainous regions. There can be first-time generation landslides or reactivation of existing landslides. Associated losses may overcome those produced by the ground-shaking itself. Despite the dramatic impact such landslides may have on local communities, mechanisms by which seismic waves interact with slopes in general and existing landslides in particular continue to raise questions. The lack of instrumentation on existing landslides prevents from developing a clear understanding of ground-motions impact on the seismic response of slopes. To shed light on earthquake-induced landslides reactivation, this paper investigates the case of a simple rotational landslide using 2D numerical simulations accurately reproducing the propagation of seismic waves inside the slope. Correlation between ground-motion amplifications (lithological and topographic site effects) and earthquake-induced displacements is investigated considering several possible landslide positions along the hill slope as observed in landslide inventories. The results show that the seismic response of the landslide is influenced by an intricate interplay involving predisposing factors and amplifications in ground-motion.

Keywords: landslides, earthquakes, numerical modeling, slope scale.

Introduction

The worldwide availability of landslide inventories (Tanyas et al., 2017) has made possible the setup of correlations between the main characteristics of earthquake-induced landslides (e.g. landslide-affected area and volume) and earthquakes (e.g. distance to the fault, Peak-Ground-Acceleration PGA). Yet, understanding how seismic waves contribute to landslides initiation or reactivation continues to raise questions. In particular the relative importance of predisposing local geological and topographic settings on the one hand, the frequency content of the seismic signal and ground-motion amplifications on the other hand is still poorly investigated. Rault et al. (2019) who performed statistical analyses on landslides distributions and seismic parameters (e.g. PGA, Peak-Ground-Velocity PGV) derived from USGS Shakemaps (Wald et al., 2022) for three large earthquakes (Northridge (1994), Chi-Chi, (1999) and Wenchuan (2008)) observed a landslide clustering either at ridge crests or at slope toes within the epicentral areas of the earthquakes. They attributed this pattern to a combination of seismic mechanisms (in particular topographic site effects at ridge crests) and geological settings of involved materials highlighting that some geological features (e.g. stratigraphy and bedding of rock materials) favour landsliding independent on the level of seismic shaking. They concluded that ground-motion amplifications only have a secondary effect on landslides clustering in such materials. One of the main limitations of such a work is related to the use of simple, often too poorly constrained, seismic shaking proxies (e.g. PGA) derived from Shakemaps.

To go beyond the use of Shakemaps, Dunham et al. (2022) proposed to study earthquake-induced landslides distributions at regional scale in more details using ground-motion simulations. Performing low-frequency 3D simulations on the 2015 Mw = 7.8 Gorkha earthquake using Roback et al. (2018) landslides catalogue, they showed that initiation of the

largest co-seismic landslides corresponds to topographic features characterized by steep slopes, high elevations and high topographic amplifications expressed by simple seismic metrics assessed by numerical simulations (e.g. PGV). Yet, the authors acknowledge that the use of low-frequency seismic wavefield numerical simulations driven by the large size and extent of the modelled region hinders from deriving any conclusion on processes governing small scale landslides initiation. Using the same dataset, Dahal et al. (2023) introduced seismic parameters derived from 3D numerical simulations able to capture not only peak values of ground-motions but also a more comprehensive summary of wave propagation. They showed that displacement-related seismic parameters are the best candidates to explain landslides distributions in such materials at large scale.

Focusing on regional scale analyses, these previous works consider only large-scale topographic features and rough estimates of geology. In this paper, we focus on earthquake-induced reactivation of moderate-size landslides. Reactivation of existing landslides by earthquakes is common in seismic-prone mountainous areas such as Haiti (Zhao et al., 2022). According to Martino et al. (2021), lithological contrasts as well as topographic features are likely to modify ground-motions inside the slopes producing amplified and de-amplified zones that may have an impact on the seismic response of slopes. In this work, we investigate the relative importance of predisposing factors associated to local relief, soil parameters and landslide position along the hillslope on the one hand and ground-motion amplifications on the other hand. Our aim is to demonstrate that landslide reactivation by seismic shaking results from a complex interplay between static and dynamic processes.

Data and method

We consider a 100 m high hillslope (Fig. 1) with a mean slope angle of 20° hosting a homogeneous rotational landslide made of cohesive soils (shear-wave velocity Vs = 242 m/s, cohesion = 140 kPa and friction angle = 21°). The landslide has a total length of 150 m and a depth of 22 m. The landslide-bedrock impedance contrast is strong (equal to 4) suggesting that significant ground-motion amplifications are likely to develop in the landslide due to the trapping of seismic waves. To investigate the impact of landslide position along the hillslope on the seismic response of the slope, we adopt the relative position index r = L/S proposed by Zhao et al. (2022) where L represents the distance from the landslide headscarp to the valley bottom and S the distance between the ridge crest and the valley bottom. Three landslide positions representing different landslide configurations as observed in landslide inventories are here considered (Fig. 1): “top landslide” below the crest (r = 1), “middle landslide” in the middle part of the slope (r = 0.8) and “bottom landslide” above the toe (r = 0.7).

To assess ground-motion amplifications in the slope, we performed elastic numerical simulations using the 2D finite difference code FLAC (ITASCA) adopting a mesh resolution able to propagate seismic waves till a frequency of 20 Hz (Kuhlemeyer and Lysmer, 1973). In addition, we performed visco-plastic numerical simulations using the horizontal component of a seismic recording (1990 Mw = 6.2 Griva earthquake characterized by a PGA = 0.99 m/s², significant duration = 7.23 s and mean period = 0.58 s) from the European Strong Motion Database (Ambraseys et al., 2004) and the Mohr-Coulomb failure criterion to investigate progressive failure of the slope resulting from seismically-induced shear stresses overpassing material strength. This seismic signal is applied as an SV-plane wave propagating vertically from the bottom boundary of the model.

Results

Figure 1 shows ground-motion amplifications (along the whole hillslope as illustrated by transfer function in Fig. 1a, c, e and zoomed in the landslide area as depicted by amplification curves as a function of frequency in Fig.1b, d, f). These plots show that ground-motion amplifications are not only controlled by the impedance contrast but also depend on landslide position along the slope as a result of wave focusing below the hillslope crest (e.g. topographic site effects). Figure 2 illustrates permanent earthquake-induced displacements in the slope for the three landslide positions. Independent on landslide volume and material strength properties, the static Factor of Safety (FoS) of the slope characterizing first-order susceptibility to landslide (ie. before the earthquake occurrence) depends on landslide position along the hillslope : FoS is equal to 1.9 for "top landslide", 1.5 for "middle landslide" and 1.7 for "bottom landslide". This parameter describing slope stability in static conditions is influenced only by the local relief being slightly steeper and more convex in the middle and at the toe of the slope.
Comparing results for the "middle" and "bottom" landslides which are characterized by similar ground-motion amplifications (Fig. 1d, f), we observe that the seismic response of the slope (Fig. 2b, c) is governed by predisposing factors : earthquake-induced displacements are larger when FoS (ie. a static parameter) is smaller. In this case, FoS has a first-order control on the seismic response of the slope. Comparing results for the "middle" and "top" landslides, we observe that earthquake-induced displacements are similar in both cases (Fig. 2a, b) while the initial proneness to landslide is larger for the "middle" landslide than for the "top" landslide. This increased initial susceptibility to failure for the "middle" landslide allows for the triggering of relatively large earthquake-induced displacements even in the presence of relatively smaller ground-motion amplifications compared to the ones modeled in the "top" landslide (Fig. 1b, d). Again for this case, FoS seems to play a first-order control on the seismic response of the slope. Finally, comparing results for the "top" and "bottom" landslides, we observe that FoS values play a negligible role on earthquake-induced displacements in the slope (Fig. 2a, c). Indeed, the larger ground-motion amplifications that develop in the "top" landslide as a combination of lithological and topographic site effects (Fig. 1b) are responsible for much larger permanent displacements in the slope than in the "bottom" landslide although the latter is statically less stable. This study shows that the seismic response of existing landslides is complex, moduated by initial proneness to landslide (controlled by material strength properties and local relief – slope angle and curvature -) and ground-motion amplifications as hypothesized by Rault et al. (2019) using rough estimates of topography and geology at large scale. This calls for future research considering various hillslope geometries, landslide materials and dimensions, and seismic scenarios to increase the understanding of landslides reactivation at local scale.

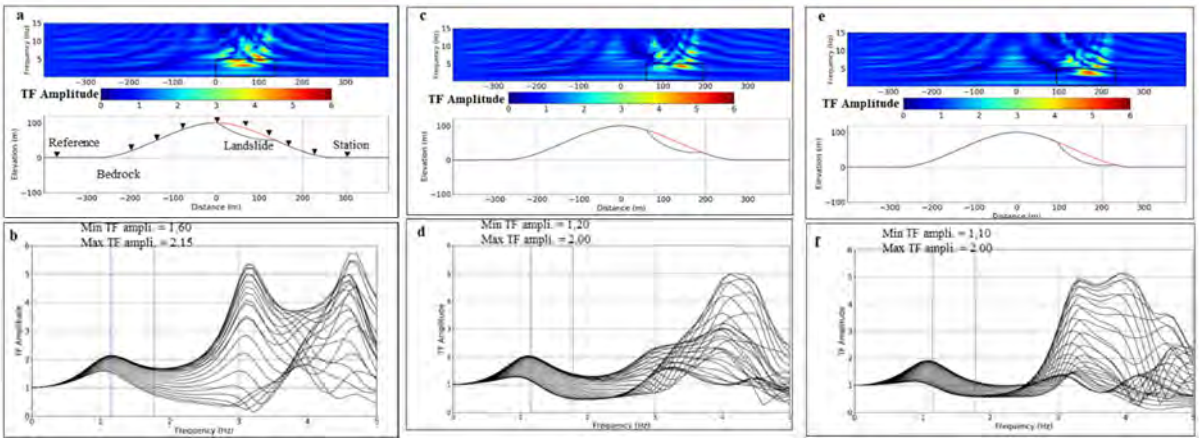

Figure 1. Ground-motion amplification functions. (a,b) "top landslide" (c,d) "middle landslide" and (e,f) "bottom landslide". (a,c,e) depict transfer functions (TF) amplitude for the whole models obtained dividing Fourier amplitude spectra of each station by Fourier amplitude spectrum of the reference site. (b,d,f) show amplification curves as a function of frequency for stations located on top of the landslides only (shown by the rectangles).

The vertical lines in (b,d,f) highlight the frequency band containing most of the energy of the seismic signal used to compute earthquake-induced displacements (Fig. 2).

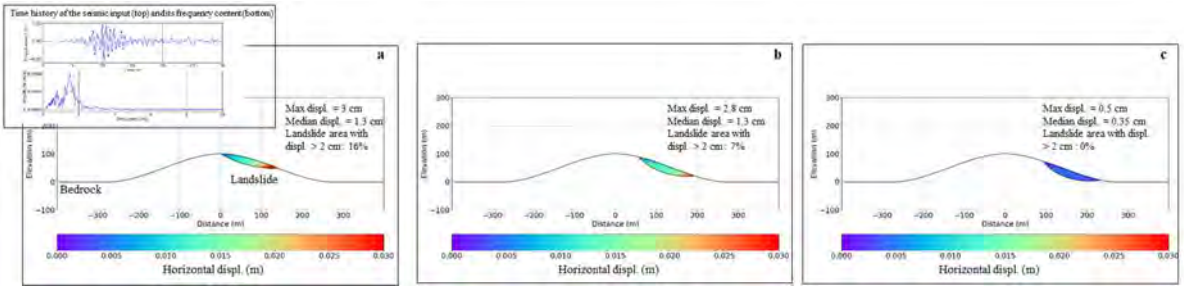

Figure 2. Earthquake-induced displacements. (a) "top landslide" (b) "middle landslide" and (c) "bottom landslide". Inset shows the seismic input signal used in the numerical simulations along with its frequency content.

Conclusion

Earthquake-induced reactivation of landslides in soils is a complex phenomenon controlled by an intricate interplay involving predisposing factors and amplifications in ground-motion. Such a behaviour cannot be captured by regional scale analyses. To further shed light on the most relevant parameters controlling the seismic response of landslides and overcome the main limitations of the present study (limited range of landslide and hillslope geometries; 3D effects are neglected; use of only one seismic signal; the polarization of incoming waves is not taken into account), additional numerical simulations will be performed.

References

Ambraseys N. N. et al. (2004). Dissemination of European Strong-Motion Data. *Engineering and Physical Sciences Research Council of the United Kingdom*, vol. 2, CD ROM collection.

Dahal A., Cruz D.A.C., Tanyas H. et al. (2023). From ground motion simulations to landslide occurrence prediction, *Geomorphology*, https://doi.org/10.1016/j.geomorph.2023.108898.

Dunham A. M., Kiser E., Kargel J. S., Haritashya U. K., Watson C. S., Shugar D. H., et al. (2022). Topographic control on ground motions and landslides from the 2015 Gorkha earthquake. *Geophysical Research Letters*, 49, e2022GL098582. https://doi.org/10.1029/2022GL098582.

Fan, X., Scaringi, G., Korup, O., West, A.J., van Westen, C.J., Tanyas, H., Zhang, L. (2019). Earthquake-induced chains of geologic hazards: patterns, mechanisms, and impacts. *Rev. Geophys.* 57 (2), 421–503. https://doi.org/10.1029/2018RG000626.

Kuhlemeyer, R.L., Lysmer, J., (1973). Finite element method accuracy for wave propagation problems. *J. Soil Mech. Found. Eng. Div*. ASCE 99 (SM5), 421–427 (1973).

Martino S., Bourdeau C., Delgado J. and Lenti L. (2021). Earthquake-Triggered Landslides and Slope-Seismic Waves Interaction Inferring Induced Displacements. 10.1007/978-3-030-60319-9_4.

Rault C., Robert A., Marc O., Hovius N. and Meunier P. (2019). Seismic and geologic controls on spatial clustering of landslides in three large earthquakes. *Earth Surface Dynamics*, 7(3), 829–839. https://doi.org/10.5194/esurf-7-829-2019.

Roback K., Clark M. K., West A. J., Zekkos D., Li G., Gallen S. F., Chamlagain D. and Godt J. W. (2018) The size, distribution, and mobility of landslides caused by the 2015 Mw7.8 Gorkha earthquake, Nepal. *Geomorphology* 301, 121–138.

Tanyas H., van Westen C. J., Allstadt K. E., Nowicki Jessee M.A., Görüm T., Jibson R.W., Godt J.W., Sato H.P., Schmitt R.G., Mars O. and Hovius N. (2017). Presentation and analysis of a worldwide database of earthquake-induced landslide inventories. *Journal of Geophysical Research: Earth Surface*, 122, 1991–2015. https://doi.org/10.1002/ 2017JF004236.

Wald D. J., Worden C. B., Thompson E. M. and Hearne M. (2022). Shakemap operations, policies, and procedures. *Earthquake Spectra* 38(1), 756–777.

Zhao B., Wang Y., Li,W., Lu H., and Li Z. (2022). Evaluation of factors controlling the spatial and size distributions of landslides, 2021 Nippes earthquake, Haiti, *Geomorphology*, 415, 1–16, https://doi.org/10.1016/j.geomorph.2022.108419, 2022.

Rock slides induced by atmospheric rivers in deglaciated valleys: Three case studies from Patagonia and British Columbia

Sergio A. Sepúlveda[1], Nicolás Jaimes[1], Jaspreet Singh[1], Paul Duhart[2], Brent C.Ward[1]

[1] Simon Fraser University, Department of Earth Sciences, Burnaby, B.C., Canada
[2] Servicio Nacional de Geología y Minería, Puerto Varas, Chile

SUMMARY: Rainfall-induced, large-volume rock slides are a less common landslide type during rainstorms. However, recent atmospheric river events at high latitudes, such as British Columbia in Canada or Patagonia in South America, have shown that large rock collapses can also be triggered and result in large debris flows with catastrophic consequences. Three case studies are revised, with analysis of their failure mechanisms, volume estimates, conditioning geological and geotechnical factors, and challenges to be addressed to advance in the inclusion of these types of slope failures in hazard assessments in the context of climate change.

Keywords: rock slope failure, atmospheric rivers, rainfall-induced landslides, deglaciation

Introduction

Landslides are a very common consequence of heavy rainfall in mountain areas. While debris flows, rock falls and shallow soil slides are the most common slope failure types usually observed during large storms, large rock slides can impose a significant risk to infrastructure and communities downslope. The collapse of large volumes (10^5 – 10^6 m^3) of fragmented rock with a significant amount of water, and sometimes snow and ice, may result in long runout debris flows that can impact transport infrastructure, pipelines or human settlements, even far away from the original landslide. In this paper, we revise research in progress on two case studies in the Patagonian Andes, the fatal Villa Santa Lucia landslide in December 2017 and the Termas del Amarillo landslide in May 2020, and one example in the Fraser Valley of British Columbia, the Highway 7- Seabird island landslide triggered in November 2021 (see Fig. 1). All these case studies are rock slides induced by atmospheric river events, which derived in large debris flows with significant consequences to life or infrastructure.

Case Studies in Patagonia: 2017 Santa Lucia and 2020 Termas del Amarillo landslides

On 16 December 2017, a massive, ca. 2 Mm^3 debris flow impacted the village of Santa Lucía in Chilean Patagonia, causing 22 fatalities and burying half of the town and several kilometres of the Austral Highway 7 (Duhart et al. 2019). The main landslide originated in a ca. 9 Mm3 rock avalanche (Singh et al. 2023) in the headers of Rio Burritos Valley that derived into a debris flow (Fig. 2), in a paraglacial environment with a recent glacial retreat (Palma et al. 2023). A second lateral failure contributed with a few more Mm3 of rock and debris to the avalanche. The landslide is a reactivation of an older rock slide, and has been shown through numerical modelling that deglaciation can be considered a key preparatory factor (Palma et al. 2023). The landslide was triggered during a Summer atmospheric river that lasted 2 days, with 122.8 mm in the 24 hours prior to the slide and a high 0°C isotherm over the mountain tops. Numerical modelling in 3DEC shows increasing displacements with higher saturation, confirming the role of high-rate water infiltration as a main trigger for rock slope failure (Palma et al. 2023).

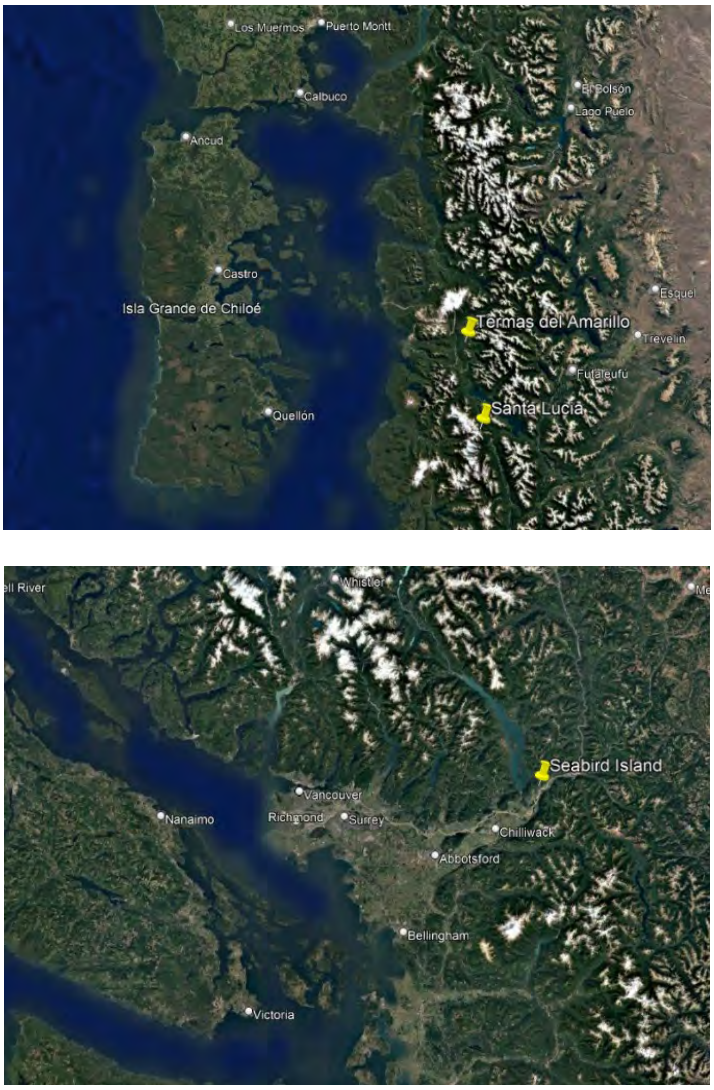

Figure 1. Top: Location of Termas del Amarillo and Santa Lucia landslides in northern Chilean Patagonia. Bottom: Location of Seabird Island landslide in southwest B.C. Source: Google Earth

Based on detailed structural analysis using the Structure from Motion (SfM) photogrammetry technique, four prominent discontinuity sets were identified in the rock mass. These include the bedding plane and three major joint sets that might be of shear or tensional origin. Coltop3D point cloud analysis shows that more than 90% of the main scarp surface belongs to the bedding and two joint sets within ranges of ± 20° around their mean values, suggesting they were involved in the 2017 rockslide. Two discontinuity sets are present in the right and left flanks, respectively, providing a lateral release surface. The third set can be found in the central portion and provides a surface for planar failure following the daylighting conditions. The kinematic analysis shows multiple potential failure modes, including three wedges and the planar sliding aforementioned. One wedge provides feasible failure conditions for kinematic release within the wider range, controlling the primary failure. Further, the dip angle of the set favourable for planar sliding is high and variable, acting as a secondary failure when meeting the daylighting conditions. The failure surface of the scar is thus composite, a result of the direct involvement of three different discontinuity sets.

Meanwhile, on 14-16 May 2020, a new atmospheric river caused another rock slide-debris flow event in the area of Termas del Amarillo, 40 km north of the Santa Lucia landslide (Fig. 2). Regional rainfall records vary from 73 to 267 mm, depending on latitude and orographic effect.

Figure 2. Left: Panoramic view of the 2017 Santa Lucia rock slide and debris flow deposits. Right: 2020 Termas del Amarillo landslide

The rock and soil cover slide of about 300 metres high derived into a massive debris flow that inundated the valley, destroying the local road and the nearby Termas del Amarillo hot springs 2.5 km downstream, killing one person. This landslide is currently under investigation by the authors.

Case study in British Columbia: The 2021 Seabird Island landslide

An unusually intense atmospheric river affected the southern coastal region of British Columbia, western Canada, in mid-November 2021, causing extensive flooding and landslides, with significant disruption to roads, railways, farms, and local communities. Up to over 200 mm in less than 72 hours were measured across the Fraser Lower Mainland, east of Vancouver. While most slope failures corresponded to shallow soil slides, debris flows, and riverbank erosion, one major rock slide at the Seabird Island area in the Fraser Valley was also identified (Sepúlveda et al. 2023). The rock slide on a steep, forested slope derived into a large debris flow blocking Highway 7, trapping hundreds of people along the river's north shore. Initial volumes were estimated between 0.5 and 0.9 Mm^3 (Sepúlveda et al. 2023).

The initiation area for the rock slide (Fig. 3), developed at 610 meters above sea level, has a triangular shape with an area of 35,000 square metres and a maximum width of 180 metres. At 490 m a.s.l, the landslide splits into two branches and then three until reaching the main debris flow path at 300 m a.s.l. The runout distance from the source area to the debris flow lobe, which blocked the highway, is 1200 metres. The total surface covered by the scarp and the deposits is ca. 100,000 square metres. The rock slide can be categorised as a translational landslide in highly to moderately weathered granitic rock, with the failure surfaces controlled by jointing.

The failure surface on the more competent bedrock is exposed along the scarp and left flank of the landslide, while it is primarily covered by debris and fallen trees. The top highly weathered granitic remnants in the slope have a variable thickness ranging from 3 to 6 m with extensive fracturing. A set of southwest-dipping persistent joints is noticeable in the left flank region, indicating a kinematically favourable orientation for planar sliding. These persistent joints were extracted from photogrammetric analysis with a dip and dip direction of 32/203. Further analysis to understand the failure mechanism with the role of water is ongoing by the authors.

Figure 3. Left: Seabird Island landslide, view of the left flank and scarp area. Right: 3D model of the rock slide, produced with SfM photogrammetry from drone flights photographs.

Concluding Remarks

Atmospheric rivers that bring warm moisture from tropical regions to mid-latitudes in the Pacific coast in both hemispheres are a main source of intense rainfall in coastal mountain regions that can trigger major landslides, including less common, but large volume rock slope failures as observed in the examples presented in Canada and Chile. The rock slides, generated in steep slopes of formerly glaciated valleys, tend to derive into rock avalanches and debris flows of significant volume, posing a risk to population and infrastructure. The frequency and intensity of these storms may be augmented by climate change, increasing the risk. Detailed engineering geological analysis and modelling of these failures are necessary to better understanding of the failure mechanisms of these rock slope instabilities, combining structural and geotechnical analyses with long-term deglaciation and short-term rainfall effects.

References

Duhart P, Sepúlveda V, Garrido N, Mella M, Quiroz D, Fernández J, Moreno H, Hermosilla G (2019). The Santa Lucía landslide disaster, Chaitén-Chile: origin and effects. *Proceedings, 7th International Conference on Debris-Flow Hazards Mitigation*, Golden, Colorado.

Palma S, Ochoa-Cornejo F, Sepúlveda SA, Lara M, Burgos K, Duhart P (2023). Rock slides in paraglacial environments: three dimensional modelling of the Santa Lucia landslide in Chilean Patagonia. Submitted.

Sepúlveda SA, Ward BC, Cosman SB & Jacobs R (2023) Preliminary investigations of ground failures triggered during the mid-November 2021 atmospheric river event along the Southwestern British Columbia highway corridors. *Canadian Geotechnical Journal* 60, 580-586.

Sernageomin (2020) Remoción en masa en valle Los Turbios-Termal El Amarillo, provincial de Palena, región de Los Lagos. Informe Técnico INF.LOS LAGOS-04-2020. *Servicio Nacional de Geología y Minería.*

Singh, J, Sepúlveda, SA (2023). Landslide failure surface and volume estimation using a sloping local base level (SLBL) method: a case study. *Indian Geotechnical Conference*, Roorkee, December 2023.

.

Probabilistic slope stability analysis applied to a mine site in France

R. Milane[1], S. Bretelle[1]

[1] Antea Group, Antony, France

SUMMARY:
Recent developments in slope stability analysis have shown the importance of implementing probabilistic analysis to determine the most critical parameters in slope design. After a summary of the key elements of probabilistic analysis, this paper will present a practical application of probabilistic analysis at a mine site in France. The selection of the geotechnical design parameters will be described, using site specific data and literature distribution. Then the selection of permanent slope (both for mining pits and waste dumps) will be described, using a combination of deterministic and probabilistic methods. Client defined design criteria will be applied, in terms of required minimum factor of safety or maximum probability of exceedance. The project will also be used to emphasise the required additional investigation, and to confirm the most critical parameters.
Keywords: slope stability, probabilistic approach, coefficient of variation

Introduction

Stability analyses are generally carried out using several deterministic methods which can be grouped into categories: limit equilibrium, numerical methods (finite element, finite difference or discrete element methods), artificial neural network method, limit analysis method or vector sum method (Ullah et al., 2020).

With the huge number of structures being built all over the world, the consequence of any slope failure can have a considerable human and material toll. To limit these risks, the European Standards defined several partial factors to be applied in slope stability verifications. The safety factor is often overestimated, as it ignores the uncertainties of the various parameters; more precisely, the safety factor does not consider the well-known variability of the soil shear strength.

With the progress of the numerical tools used in geotechnical engineering, the uncertainties in slope stability calculations no longer concern the accuracy of the calculations themselves or mistakes in design. It is rather related to geological anomalies, inherent spatial variability of soil properties, scarcity of representative data, changing environmental conditions, unexpected failure mechanisms, simplifications and approximations adopted in geotechnical models (El-Ramly et al. 2002). According to Frank (2004), the soil failure strongly depends on the distribution of the values of soil strength parameters.

To reduce the uncertainties related to the slope analyses, probabilistic calculation methods were developed and are now available in commercial software to help the assessment of the probability of failure.

Recent developments in slope stability analysis (El-Ramly, 2002) have shown the importance of implementing probabilistic methods that enable the uncertainties of ground parameters to be quantified by calculating failure probabilities.

Probabilistic approach

Probabilistic methods were first introduced in slope stability analysis in the 1970s (El-Ramly, 2002) by Alonso (1976), Tang et al. (1976) and Harr (1977). They were then developed by several authors (Selmi et al.,2006; Obregon and Mitri, 2019; Abdulai and Sharifwadeh, 2021). A few years later, these methods were gradually implemented in many commonly used software in geotechnical engineering.
SLOPE/W (v 2021.3), the software used in the framework of the present study, computes the probability of failure, defined as the probability of the safety factor being less than one, using a Monte-Carlo approach that produces a range of possible values for an uncertain factor rather than a single average value.

Case study – Project presentation

The present paper presents the study carried out for a mine project in France covering an area of around 1.25 km2. The aim of the project is to study the stability of the slopes obtained when deepening the pits. For reasons of confidentiality, the location of the project and the study area concerned by this paper will not be shown.
It should be noted that deterministic calculations were performed on the different slopes of the cross section presented in Figure 1. This paper focus on the slope located in the highly weathered granite layer presented in orange in Figure 1, using a probabilistic approach.

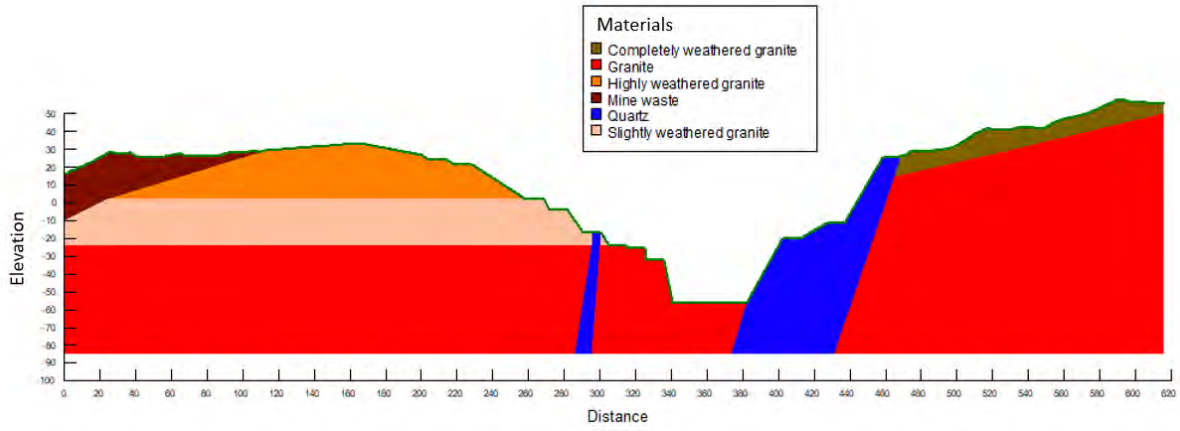

Figure 1. Cross-section A-A' as modelled in SLOPE/W

Definition of the probabilistic parameters

In order to define the geotechnical parameters required for stability studies, laboratory tests were carried out on samples extracted from the site. The shear strength parameters used in the calculations are based on the laboratory tests and Antea Group's previous experience on similar projects. In the following, we will only present the study based on the statistical distribution of shear strength parameters in the highly weathered granite. This material is described as a mixture of gravel size particles, sand silt and clay matrix. The rock structure is visible, but the behavior is similar to a frictional material with cohesion. Between 2016 and 2021, 7 direct shear tests were conducted on samples extracted from the site. Statistical analysis of these shear tests yielded the following values:

- Cohesion: Mean = 5 kPa, SD = 2
- Friction angle: Mean = 35°, SD = 3,5.

The coefficient of variation (COV) which is defined as the ratio of the standard deviation to the mean was calculated according to the previous results. It was shown that the calculated values from the test results were close to the litterature COV (Duncan, 2005) for this type of material (40% for the cohesion and 10% for the angle of friction), which reflects the dispersion of data points around the mean. This is an input parameter for probabilistic analysis software, and it shows the level of uncertainty associated with the available data.
In order to show the influence of the COV on the slope stability analyses, three cases were calculated as presented in Table 1. It should be noted that the ranges were adapted in order to keep realistic values of the cohesion and friction angle (for example, cohesion is positive and friction angle lower than 35°). All calculations were undertaken with the same mean values.

Table 1. Probabilistic parameters

	Cohesion				**Friction angle**			
	Mean	**SD**	**COV**	**Range**	**Mean**	**SD**	**COV**	**Range**
Case 1	5	2	40%	[0 kPa; 15 kPa]	35	3,5	10%	[25°; 35°]
Case 2	**5**	**1**	**20%**	[0 kPa; 10 kPa]	35	3,5	10%	[25°; 35°]
Case 3	5	2	40%	[0 kPa; 15 kPa]	**35**	**1,7**	**5%**	[26,5°; 35°]

Application of the probabilistic method

As said earlier, the calculations were carried out using the software SLOPE/W edited by Geostudio, that uses Monte Carlo simulation. In this work, 2000 Monte-Carlo samples were used. The slice method used to obtain the values of safety factors was Morgenstern-Price method (Morgenstern and Price, 1965). Variability in permeability and water table height has not been considered, given the limited information available at this stage of the study.
The client developed protocols to cover the technical requirements for the different parts of their mine sites. An overall slope stability requires a deterministic safety factor between 1.3 and 1.5 and a probability of failure lower than 5% for an area with high consequence of failure, for instance an active mining pit.

Results

Deterministic calculations developed based on Morgenstern-Price method (Morgenstern and Price, 1965) showed a safety factor of 1.36. The probabilistic analysis resulted in the values, summarized in Table 2. The FS min is the minimum factor of safety obtained in all the simulations (with all the parameters taken at their minimum).
As defined earlier, the probability of failure is calculated as follows:

$$PF = \frac{Number\ of\ Monte - Carlo\ simulations\ where\ FS < 1}{Total\ number\ of\ simulations} \quad (1)$$

Table 2. Results of the probabilistic analysis

	COV (cohesion)	**COV (Friction angle)**	**PF (%)**	**FS min**
Deterministic analysis (c = 5 kPa, φ = 35°)	-	-	-	**1.36**
Case 1	40%	10%	2.2	0.86
Case 2	20%	10%	1.05	0.92
Case 3	40%	5%	0.1	0.99

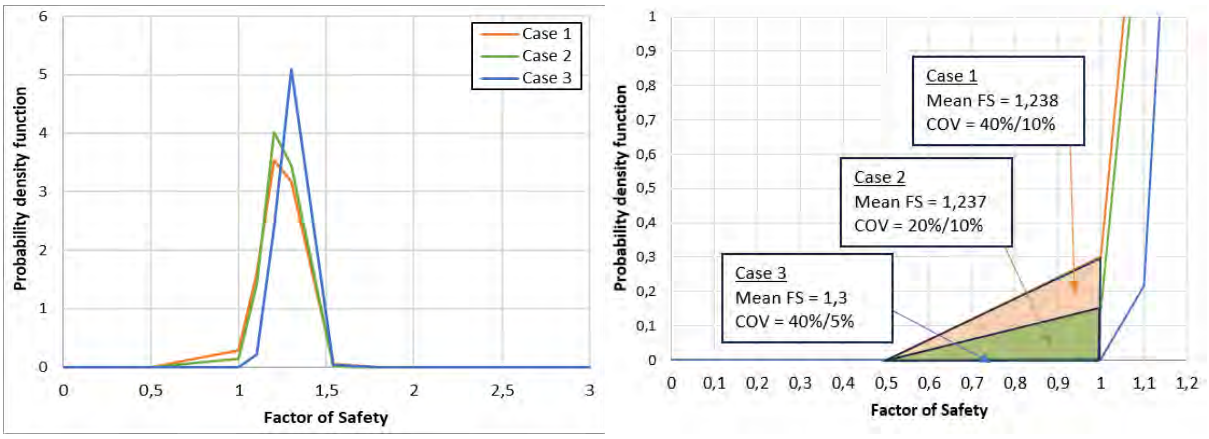

Figure 2. Normal distribution of the safety factor

The deterministic calculation shows a "safe" slope for temporary conditions. However, the probabilistic analysis shows that the failure is possible (with a probability of failure of 0.1% to 2.2%). As shown in the previous graphs, the coefficient of variation plays a major role in determining the probability of rupture. When reducing the COV of a parameter, the PF reduces. For this specific case, the cohesion, despite a large COV, has little influence on the resulting PF. This can be explained by the small range of values investigated. With a larger number of tests, resulting in a better-defined set of representative parameters, a lower COV would be expected (or a narrower distribution of shear strength).

Conclusions

It can be seen from the previous study that the probabilistic analysis in slope stability calculations allows to cover more precisely the uncertainties in soil parameters unlike deterministic calculations. The probability of failure can be easily calculated in some geotechnical software using some parameters such as the COV, the mean and the standard deviation. The calculations showed that the probability of failure is directly related to the COV and that it can be decreased by decreasing the COV.

References

Abdulai M and Sharifzadeh M (2021) Probability methods for stability design of open pit rock slopes: an overview. *Geosciences*, *11*(8), 319

Alonso, EE (1976) Risk analysis of slopes and its application to slopes in Canadian sensitive clays. G*éotechnique*, 26(3), pp 453–472.

Duncan J., Wright S. (2005). Soil Strength and Slope Stability. JohnWiley & Sons Inc, pp. 293.

El-Ramly H, Morgenstern NR & Cruden DM (2002) Probabilistic slope stability analysis for practice. *Canadian Geotechnical Journal,* 39(3), pp 665-683.

Frank R (2004) *Designers' guide to EN 1997-1 Eurocode 7: Geotechnical design-General rules* (Vol. 17). Thomas Telford.

Harr ME (1977) Mechanics of particulate media — a probabilistic approach. McGraw-Hill, New York, 543 pp.

Morgenstern N. R and Price V. E (1965) The analysis of the stability of general slip surfaces. *Geotechnique*, 15(1), 79–93

Obregon C and Mitri H (2019) Probabilistic approach for open pit bench slope stability analysis–A mine case study. *International Journal of Mining Science and Technology*, *29*(4), 629-640.

Selmi M, Ltifi M and Bel Hadj Ali N (2006) Application de la méthode de Monte Carlo dans l'analyse de la stabilité des pentes. *Journées Nationales de Géotechnique et de Géologie de l'Ingénieur (JNGG 2006)*, 27-29.

Tang WH, Yucemen MS and Ang AHS (1976) Probability-based short-term design of slopes. *Canadian Geotechnical Journal*, 13(3), pp 201–215.

Ullah S, Khanb MU & Rehmana GA (2020) A brief review of the slope stability analysis methods. *Geological Behavior (GBR),* 4(2), pp 73-77.

RIDIM: Unveiling Rock Instabilities through Hierarchical Segmentation of 3D Point Clouds

Le Moigne Benoit[1], Rault Claire[1], Guiotte Florent[3], Dewez JB Thomas[2]

[1] BRGM, La Réunion, France
[2] BRGM, Orléans, France
[3] Université Rennes 2 – UMR 6554 LETG, France

SUMMARY: RIDIM (Rock Instability Detection and Inventory from a point Cloud Method) (Guiotte et al., 2023) has been developed to map out sections of large, towering rock cliffs that are prone to failure. This method leverages a hierarchical segmentation approach, analysing 3D point clouds using watershed tree method. RIDIM was devised and validated on a lava cliff in Reunion Island. The results not only enable the identification and mapping of unstable blocks but also facilitate discussions regarding the necessary preventive measures to mitigate risks posed by rockfalls along the studied cliff.

Keywords: rockfall, 3D point clouds, hierarchic segmentation, impact energy.

Introduction

Rockfalls pose significant financial and safety risks to both people and infrastructure, necessitating proactive prevention strategies. Conducting expert analyses is crucial for understanding the potential changes in rocky terrains and for evaluating the risks associated with rockfalls. Such analyses involve identifying areas susceptible to rockfalls, establishing stability criteria informed by the lithology of the cliff faces, assessing the likelihood of instability over time, pinpointing areas where rockfalls are likely to extend, and calculating the kinetic energy that could be released by falling rocks.

A rock mass, typically stable, may have its equilibrium disturbed by exacerbating factors. The likelihood of block falls within this mass is closely associated with its shape and intrinsic discontinuities.(Hudson and Priest, 1983).

Traditional rock face stability assessments, conducted through expert analysis, suffer from subjectivity and low spatial resolution. 3D scanning imagery for rocky cliffs emerges as a promising alternative, offering higher spatial resolution and broader coverage (Abellán et al., 2014; Battulwar et al., 2021). Despite progress in automatic or semi-automatic approaches for discontinuity identification within 3D point clouds or ortho-rectified image analysis, these methods demonstrate lower efficiency for highly discontinuous or lower quality rocks such as volcanic formations, and their effectiveness is contingent on the quality and resolution of the reconstruct topographic images. These formations, especially in tropical contexts, exhibit significant anisotropy from thermal cooling fractures and rapid weathering, deteriorating their geomechanical properties.

Hierarchical segmentation algorithms facilitate object delineation and classification in 2D raster images add parent-child topological relationship (Beucher, 1994; Perret et al., 2019). Various approaches and techniques for hierarchical segmentation have been developed (Nguyen and Le, 2013; Richter et al., 2013), among which watershed segmentation (ws) stands out adapts well to rough rock surfaces. Ws effectively identifies regional boundaries, groups neighbouring regions, and enables multi-scale analysis by construction, making it a robust choice for identifying overhanging blocks on volcanic cliffs.

This study aims at applying hierarchical watershed segmentation to a volcanic cliff to outline overhanging blocks and describe their shape, hence supplying metrics to propose suitable safety measures.**Study site**

The interior of Réunion Island is served by mountain roads that are very prone to rockfalls. The RN5 is the only road leading to the Cilaos, home to about 5,700 residents, and is a major tourist destination on the island. Almost 25km of this road, bordered by 200m high rock cliffs, are highly susceptible to rockfalls. The Aloès cliff, stands over 200 m high and spans more than 200 m in length. This cliff exhibits a morphology characteristic of the cliffs that line the RN5

The Aloès Cliff comprises layers of massive olivine basalts, ranging from metric to plurimetric in scale, with variable vesicularity, interlayered with scoriaceous layers. The basaltic flows are intersected by numerous vertical joints outlining flow prisms formed during cooling, with scoriaceous levels averaging over 50 cm thick. The rock displays multiple levels of alteration and numerous fractures. Given its geological nature, the cliff is subjected to differential erosion and weathering of geological formations, resulting in phenomena such as exfoliation joints, opening of pre-existing fractures, creation of new fractures, undercutting, and others (Collins and Stock, 2016). The basaltic flow flew parallel to the outcrop face, without any downstream-tilt component towards the void.

Data and methods

The 3D point cloud for this study was produced using UAV-based Structure-from-Motion (SfM) photogrammetry. Images were captured with a ZenMuse X5s camera mounted on a DJI drone, maintaining a flight distance of approximately 40 meters from the cliff. This distance was strategically chosen to optimize the Field of View (FOV) of the drone's camera, achieve the desired image resolution, and obtain the optimal angles of incidence. A total of 249 photographs were taken, incorporating both orthogonal and oblique angles to comprehensively image the cliff, yielding a point cloud with an average density exceeding 300 points/m².

Vegetation was removed from the point cloud in Cloud Compare by leveraging the geometric characteristics of the points: sphericity, planarity, and connectivity.

The estimation of block overhang utilized a saliency criterion, achieved by subtracting the vegetation-filtered point cloud from a smoothed point cloud adjusted to align with local minima perpendicular to the cliff's main orientation.

Segmentation was carried out on the inverse raster of 'saliency' using the watershed hierarchical method. In this technique, areas in overhang are depicted as depressions (watersheds), with the watershed boundaries defining their contours. The regions are organized hierarchically by area, meaning the tree's lowest level represents the initial segmentation of the 'saliency' raster along watershed boundaries. Each level of the tree indicates a stage of adjacent region fusion, with regions at each level characterized by an area within a specific range of saliency. The apex of the tree symbolizes a unified region covering the entire cliff face. Following segmentation, several statistical and morpho-mathematical parameters were analyzed to describe the tree's elements, including area, perimeter, and compactness.

Results

Some of the watersheds delineated by the morpho-matematical analysis contour actual overhanging blocks. To extract those contours from the watershed-tree, shape descriptors metrics need to be thresholded.

To determine the thresholds, we cross-reference the matrix of manually mapped rocky overhangs with that of automatically mapped overhangs, enabling us to assess the percentage

of overlap. The mapping is also visually evaluated by overlaying the overhang map onto orthophotographs. It is observed that with the selected criteria described in Table 6, 86% of the pixels identified on the orthophotos as belonging to overhangs are mapped. The unidentified 14% consist of areas where there are no points on the 3D point cloud, pixels located on the periphery of an overhang, or areas where the saliency is not sufficient. Only 4% of pixels manually identified as overhangs but in fact belonging to vegetation patches.

Due to their geological nature, blocks from basaltic flows are fractured along their cooling fractures. A strong assumption is made to retain rock blocks with a W/H ratio ≤ 1, where W represents the width of the block and H, its height. Therefore, polygons with a width 1.1 times greater than their depth are disregarded. This filtering might result in the exclusion of contiguous blocks, which with this method emerge as a single block, consequently possessing a W/H ratio >1.

The median volume of blocks, estimated from "saliency" with a volume smaller than 10 m^3 is 0.045 m^3. This implies that 50% of the blocks delineated by the method correspond to blocks of less than 50 liters (approximately 120 kg).

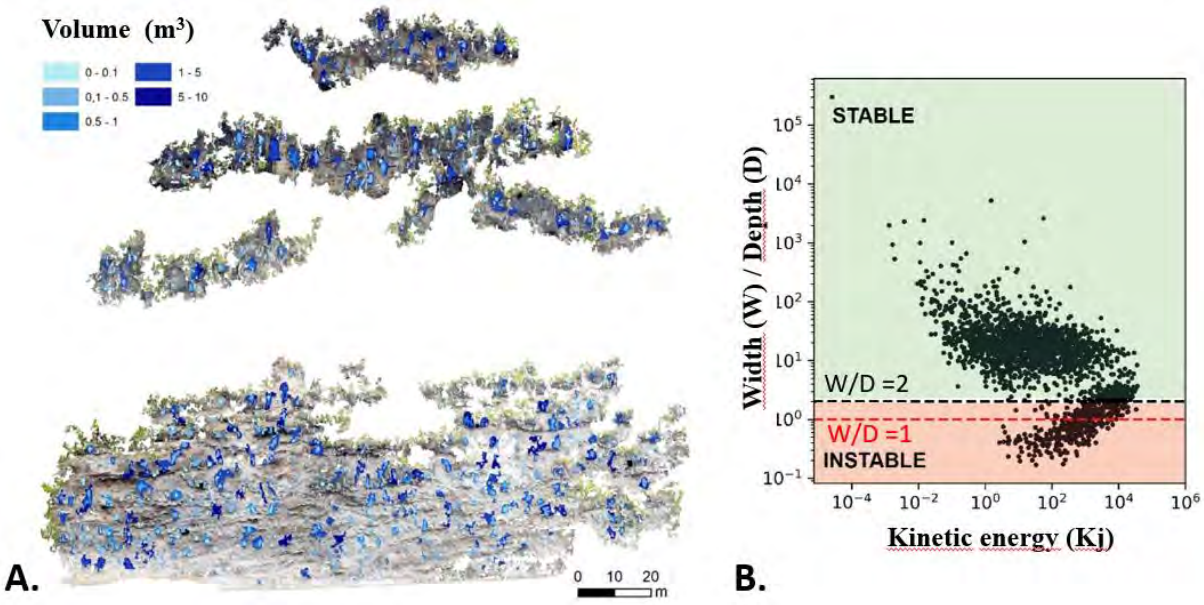

Figure 1. A. Volume of the delineated blocks determined through watershed hierarchical segmentation on the Aloès Cliff. B. Stability and kinetic energy of the delineated blocks.

Discussions

The stability of a rocky massif becomes compromised when the forces of traction, flexion, and shear, caused by geometric imbalance, exceed the resistance of the material. It is posited that in basalts, rocky blocks are primarily fractured by cooling fractures with pseudo hexagonal geometry and perpendicular to the flow surfaces (Aydin and DeGraff, 1988; Goehring and Morris, 2008). It was thus deduced that the width of the blocks visible in the outcrop could serve as a proxy for their depth. In scenarios where the dip direction is nearly coplanar with the wall direction, the bases of blocks are considered perpendicular to the wall. Hence, it is inferred that when the overhang depth (D) exceeds half the width (W), the center of gravity shifts beyond the overhang line rendering the block unstable (González De Vallejo et al., 2020). The identified unstable blocks (W/D < 2) constitute approximately 15% of mapped blocks, with volumes spanning from 10^{-3} to 10 m^3.

Given their respective elevations compared to the elevation above the road, block energy upon impact can be estimated. The kinetic energy of mapped unstable blocks ranges from 2 kJ to 10^4kJ. Half of these blocks exhibit kinetic energy beyond 594 kJ, and 95% possess energy under 6500 kJ. Such indications offer insights for selecting the appropriate rockfall protection system.

Conclusions and follow up

Employing watershed hierarchical segmentation on pre-processed 3D point clouds significantly enhances the ability to detect, isolate, and classify block sizes in densely fractured lava flow cliffs. The innovative RIDIM methodology provides a swift and systematic way to identify blocks at risk of dislodging across extensive rock cliff faces (Guiotte et al., 2023). Given its effectiveness, it is recommended that the RIDIM technique be further explored and adapted for various lithologies, offering a comprehensive, efficient, and straightforward solution for rockfall monitoring and the implementation of safety measures along cliff landscapes.

References

Abellán, A., Oppikofer, T., Jaboyedoff, M., Rosser, N.J., Lim, M., Lato, M.J., 2014. Terrestrial laser scanning of rock slope instabilities: STATE-OF-SCIENCE (TERRESTRIAL LiDAR VS. ROCK SLOPE INSTABILITIES). Earth Surf. Process. Landforms 39, 80–97. https://doi.org/10.1002/esp.3493

Asroun, A., Durville, J.-L., 2005. Stabilité des massifs rocheux fissurés. Rev. Fr. Geotech. 5–9. https://doi.org/10.1051/geotech/2005112005

Aydin, A., DeGraff, J.M., 1988. Evolution of Polygonal Fracture Patterns in Lava Flows. Science 239, 471–476. https://doi.org/10.1126/science.239.4839.471

Battulwar, R., Zare-Naghadehi, M., Emami, E., Sattarvand, J., 2021. A state-of-the-art review of automated extraction of rock mass discontinuity characteristics using three-dimensional surface models. Journal of Rock Mechanics and Geotechnical Engineering 13, 920–936. https://doi.org/10.1016/j.jrmge.2021.01.008

Beucher, S., 1994. Watershed, Hierarchical Segmentation and Waterfall Algorithm, in: Serra, J., Soille, P. (Eds.), Mathematical Morphology and Its Applications to Image Processing, Computational Imaging and Vision. Springer Netherlands, Dordrecht, pp. 69–76. https://doi.org/10.1007/978-94-011-1040-2_10

Collectif GT MEZAP, G.M., 2021. Guide technique MEZAP. Caractérisation de l'aléa rocheux dans le cadre d'un Plan de Prévention des Risques Naturels (PPRn) ou d'un Porter a connaissance (PAC), Collection Scientifique et Techniques. BRGM.

Collins, B.D., Stock, G.M., 2016. Rockfall triggering by cyclic thermal stressing of exfoliation fractures. Nature Geosci 9, 395–400. https://doi.org/10.1038/ngeo2686

Goehring, L., Morris, S.W., 2008. Scaling of columnar joints in basalt. J. Geophys. Res. 113, B10203. https://doi.org/10.1029/2007JB005018

González De Vallejo, L.I., Hernández-Gutiérrez, L.E., Miranda, A., Ferrer, M., 2020. Rockfall Hazard Assessment in Volcanic Regions Based on ISVS and IRVS Geomechanical Indices. Geosciences 10, 220. https://doi.org/10.3390/geosciences10060220

Guiotte, F., Rault, C., Dewez, J.T., Le Moigne, B., 2023. Procédé de caractérisation d'un risque de chutes de blocs.

Hudson, J.A., Priest, S.D., 1983. Discontinuity frequency in rock masses. International Journal of Rock Mechanics and Mining Sciences & Geomechanics Abstracts 20, 73–89. https://doi.org/10.1016/0148-9062(83)90329-7

Perret, B., Chierchia, G., Cousty, J., F. Guimarães, S.J., Kenmochi, Y., Najman, L., 2019. Higra: Hierarchical Graph Analysis. SoftwareX 10, 100335. https://doi.org/10.1016/j.softx.2019.100335

Estimating the evolution of shear strength of natural clays in high mobile mass movements

Sueng-Won Jeong[1], Jacques Locat[2], Serge Leroueil[3]

[1] Korea Institute of Geoscience and Mineral Resources, Daejeon, Republic of Korea
[2] Laval University, Quebec, Canada

SUMMARY: The determination of shear strength of clayey soils during a landslide is crucial for estimating the slope stability and post-failure dynamics. In order to examine the change in shear strength at three different stages of intact, remoulded and immerse conditions, vane measuring system can be used. The vane test was conducted in the stage of non-destructive soil condition; after a measurement of intact shear strength, a soil sample was fully rotated manually by vane blade itself and the remoulded shear strength was measured; in order to mimic the water infiltration condition during a landslide, the sample was filled with water in a fully saturated state, and then the shear strength was measured through shear rotation. As result, the shear strength measured at each stage tended to gradually decrease. These results can explain how shear strength changes when a landslide occurs. As bonus, the tomographic intensity value obtained from Cat-scan image was determined at the rotated portion before and after the vane blade was rotated.

Keywords: Shear strength, vane test, reduction in shear strength, Cat-scan image, tomographic intensity

Introduction

For landslides, it is important to determine the shear strength of slope materials. The failure and post-failure characteristics of a large landslide can be inferred from changes in the shear strength of the ground. The movement velocity and processes of a landslide can vary depending on the degree of fragmentation of soil particles and the degree of mixing with the surrounding fluid. Grounds containing large amounts of natural clay particle may be related to the degree of remolding rather than the degree of fracture, and slippage along the shear plane may be related to the resistance of the fluidized soil condition. In this study, we aim to experimentally observe changes in shear strength when a landslide occurs in natural clay ground. A sudden reduction in undrained shear strength is directly related to the increase in water content. This can be explained by stress-strain relationship with strain-softening behavior (Fig. 1). The water content may not change until the soil sample had experienced a fully remolded stage. The last stage, the evolution of yield stress, is caused by the soil-water interaction. It is assumed that shear strength with intact and remolded condition, residual, and yield stress with viscoplastic behavior tend to gradually decrease in that order. If this hypothesis is correct, through entire landslide evolution process, the water infiltration into the ground during shearing helps to reduce the soil resistance along the shear plane. As a consequence, it may yield a fast-moving landslide, such as debris flow.

Materials and Methods

A series of vane tests were conducted on clay samples to examine the evolution of shear strength during shearing. The soil samples can be classified as natural silty clay. The following conditions are considered: (a) intact and remolded condition; (b) immersion in water (i.e., submerged condition); (c) continuous measurement of remoulded shear strength under fully saturated condition (Fig. 2). The vane blade has a diameter and a height of 16×32 mm, 20×40 mm and 25.4×50.8 mm (Fig. 3).

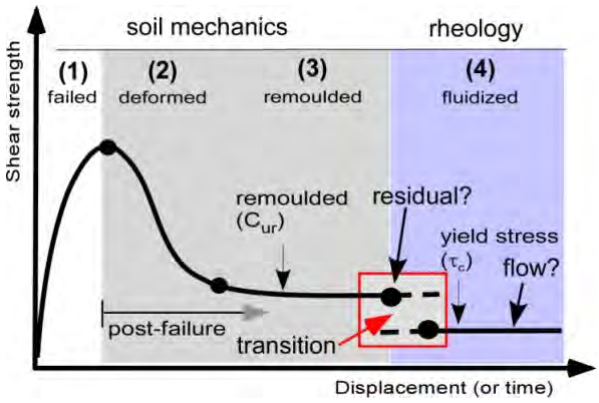

Figure 1. Shear strength with shear displacement (or time) in the failure and post-failure stage

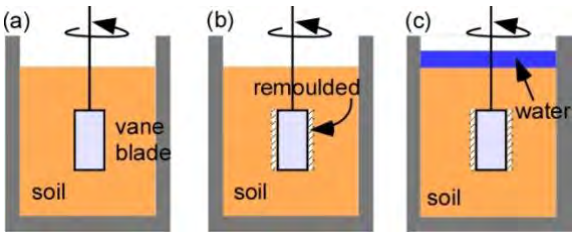

Figure 2. Test procedure for examining the evolution of shear strength during shearing in the stage of intact, remolded and immerse condition

Results

Undisturbed soil sample was selected for determining the shear strength (Fig. 3). Water infiltration into soil ground may affect the evolution of shear strength during shearing (Fig. 4). It may explain the strength evolution in high mobile mass movement (Jeong, 2006). The final goal of this study is to examine the evolution of shear strength due to water infiltration into ground and the structural change before and after shear banding formation. Although not covered in this study, lubrication through hydroplaning could be the key to explaining the high mobile mass movements (Mohrig et al., 1999; Ilstad et al., 2004). Although the biggest difference in strength was observed between intact and remoulded condition, a continuous decrease in shear stress with increasing water content when the soil sample filled with ambient fluid is clear (Fig. 4).

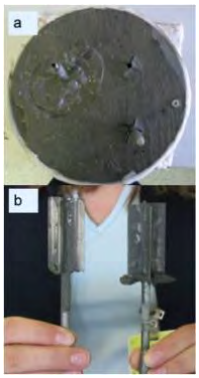

Figure 3. Soil sample used and vane blade

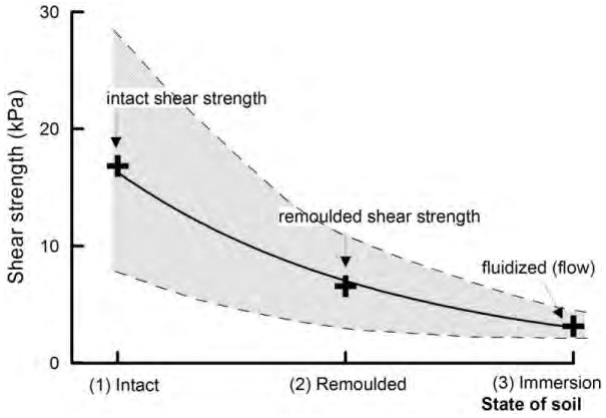

Figure 4. Vane test results

CAT-scan (computer axial tomography) represents a complete non-destructive imaging technique (Duliu 1999). It is often used for examining the internal structure of soil and rock

mass (Fig. 5). CAT-scan imaging technique was used with vane tester. Cat-scan image data are associated with the soil density; each image pixel is known as a Hounsfield Unit (HU) value (Brown et al. 2008). CTN can be converted from HU value (Fig. 6). Even though the HU and CTN value obtained from CAT-scan images remain unclear, but the soil density with and without vane blade is quite clear (Fig. 7). The large difference is found between void (e.g. Fig. 7f). The biggest difference was where the vane had passed, and the smallest value was observed in the empty space.

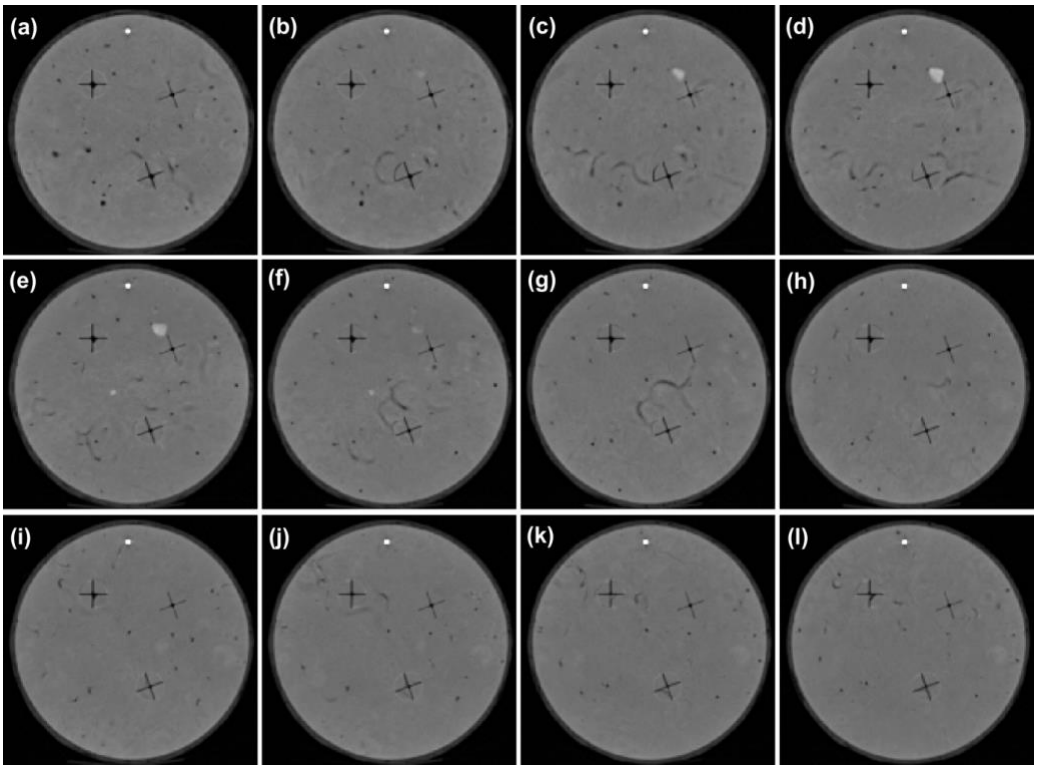

Figure 5. Cat-Scan image during vane tests

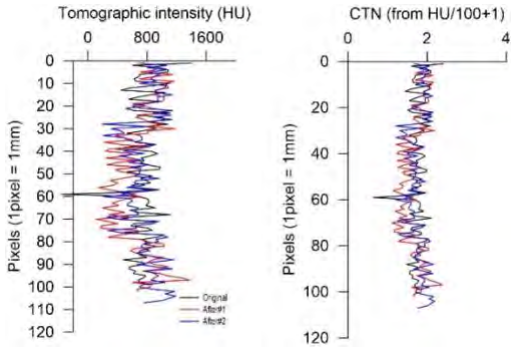

Figure 6. HU and CTN value

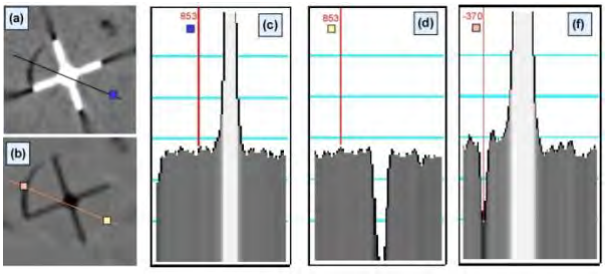

Figure 7. Measurement of sediment density during tests: with and without vane blade

A laboratory vane apparatus may be nothing more than a tool. Since testing devices that can properly examine the entire process of developing shear stress are relatively rare and difficult to verify; it can be used in a variety of test conditions. In particular, shear strength determination is very important in the development of various types of landslides from the onset stage to post-dynamics, e.g., flow type, stages. It is difficult to measure them continuously, so taking this into consideration, it is judged that it can be a good test method in examining the strength evolution of landslides.

Acknowledgements

Financial Support: KIGAM Research Project (23-3412-1; 24-3412-1). The authors would like to thank the Natural Sciences and Engineering Research Council Canada via the Continental Slope Stability (COSTA) Canada project.

References

Brown S, Baileya DL, Willowson K & Baldock C (2008) Investigation of the relationship between linear attenuation coefficients and CT Hounsfield units using radionuclides for SPECT. *Applied Radiation and Isotopes* 66, 1206-1212.

Duliu OG (1999) Computer axial tomography in geosciences: an overview. *Earth-Science Reviews* 48, 265-281.

Ilstad T, Elverhøi A, Issler D & Marr JG (2004) Subaqueous debris flow behavior and its dependence on the sand/clay ratio: a laboratory study using particle tracking. *Marine Geology* 213, 415-438.

Jeong (2006) Influence of pysico-chemical characteristics of fine-grained sediments on their rheological behavior. Laval University.

Mohrig D, Elverhøi A & Parker G (1999) Experiments on the relative mobility of muddy subaqueous and subaerial debris flows, and their capacity to remobilize antecedent deposits. *Marine Geology* 154, 117-127.

Regional scale landslide forecasting using data driven approaches: A case study from Western Ghats, India

Minu Treesa Abraham[1,2], Neelima Satyam[3]

[1] Methods for Model-based Development in Computational Engineering, RWTH Aachen University, Aachen, Germany
[2]Norwegian Geotechnical Institute, Oslo, Norway
[3] Department of Civil Engineering, Indian Institute of Technology Indore, Indore, India

SUMMARY: Forecasting landslides is a critical aspect in disaster risk reduction. With the increase in extreme climate events and urbanisation of hilly regions, developing a forecasting framework for Landslide Early Warning System (LEWS) has become the need of the hour. Even though the triggering mechanism of rainfall induced landslides depends upon the hydrological processes and the subsurface properties, challenges in precise data collection often limits the use of physics-based landslide forecasting in regional scale. This study proposes a data-driven approach, integrating rainfall thresholds and landslide susceptibility maps (LSMs). The method is tested for a study area in the Western Ghats of India (Idukki) and was compared with two well established process-based approaches. The results indicate that the proposed data driven approach outperforms the conventional process-based approaches and can be used for regional forecasting of rainfall induced landslides.

Keywords: landslides, random forest, machine learning, forecasting, rainfall thresholds

Introduction

Landslides result in severe socio-economic setbacks in hilly regions across the world. Forecasting the hazard and taking necessary precautions before the occurrence of landslides are one among the most effective risk reduction strategies. Attempts for developing Landslide Early Warning Systems (LEWS) is a concern for both scientific community and the policy makers, to reduce the aftereffects of landslide hazards (Leonarduzzi *et al.*, 2017). The forecasting framework is a critical part of LEWS, and it depends upon many factors such the scale, landslide typology and the end-user compatibility. The scale depends upon the area under consideration and can vary from slope scales to global scales. While precise process-based forecasting and real-time field monitoring is feasible at slope and local scales (Baum *et al.*, 2008) empirical or statistical methods are a viable solution when the area under consideration is large, over a few hundreds of square kilometers (Baum and Godt, 2010). This study considers a case from the Western Ghats of India (Idukki), where landslides a spatio-temporal landslide forecasting framework is developed using data-driven approaches. The proposed method includes a rainfall threshold based temporal forecast, and a machine learning based spatial forecast of landslides in the study region, integrated together using a matrix-based approach. The method is then compared with two process-based approaches, the Transient Rainfall Infiltration and Grid-Based Regional Slope-Stability (TRIGRS) model, and the SHALSTAB model, to find the best suited forecasting method for the region.

Methodology

The methodology involves developing a spatio-temporal forecasting framework for the study area, using rainfall thresholds and landslide susceptibility mapping (LSM). The rainfall thresholds are developed using an automatic algorithm-based approach Calculation of

Thresholds for Rainfall-induced Landslides -Tool (CTRL-T) (Melillo *et al.*, 2015). The historical rainfall and landslide data for the Idukki from 2010 to 2018. The multiple levels of exceedance defined using the algorithm is used to define the severity of rainfall event, and it is then used along with the antecedent soil moisture conditions to define conditional probabilistic thresholds using Bayes theorem (Abraham *et al.*, 2021). The probability of occurrence of landslides subject to the rainfall severity and antecedent soil wetness was used to create different levels of temporal forecast as shown in Figure 1. Similarly, the LSMs were developed using random forest (RF) algorithm using the landslide inventory of a major hazard event happened in 2018. The probability of occurrence of landslides predicted by RF was used to define 5 levels of warning for spatial probability. Both spatial and temporal probabilities were then compared to define a new level of warning for the spatio-temporal forecasting framework, named as RF model, as shown in Figure 1.

Temporal Probability	Spatial Probability				
	Very low	Low	Medium	High	Very high
Very low	Green	Green	Green	Yellow	Yellow
Low	Green	Green	Yellow	Yellow	Orange
High	Green	Yellow	Yellow	Orange	Orange
Very high	Green	Yellow	Orange	Red	Red

Figure 1. Proposed matrix-based approach to combine spatial and temporal probabilities of occurrence of landslides for RF model.

The colors used in the matrix (Figure 1) are according to the warning levels currently used in the country, where green means no action needed, yellow means watch and stay updated, orange means be prepared and red means take action. For quantitative comparison, the green and yellow alerts are considered to be negative predictions (no landslides expected) and orange and red are considered to be positive predictions (landslides are expected). The predictions made by the proposed data-driven model are then compared with two process-based models, TRIGRS and SHALSTAB, to find the best suited model. The quantitative comparison is carried out using a confusion matrix, considering orange and red alert pixels are landslide predictions, and green and yellow as non-landslide predictions. The efficiency values are then calculated for each model, which is defined as the ratio of pixels with correct predictions to the total number of pixels.

Results and discussion

Figure 2 shows the mutual agreement of the process-based models considered, and the RF model. The outer circle represents the percentage of pixels covered by each color by the RF model, and the inner circle represents the share of each alert predicted by the process-based model, within each alert class of the RF model. The labelled values with a prefix 'LS' indicate the percentage of landslide pixels in each category, which is defined by the combination of alerts made by the RF model and the process-based model. The mutual agreement between the data-driven model proposed in this study and the process-based models were accessed by comparing the percentage of pixels predicted for each alert, and the percentage of landslides in each case (Figure 2). It was found that 13.98 % of the study area is assigned green alert by both TRIGRS and RF models, and 21.56 % for SHALSTAB and RF. The landslides pixels in these green alert regions are only 0.23 % and 0.28 % respectively. Similarly, 14.43 % of the total area is classified into red by both TRIGRS and RF, where 62 % of the landslide pixels are present. In the case of SHALSTAB and RF, these numbers are 16.58 % and 69 % respectively. Among the 3.73 % of landslide pixels missed by RF model, 1.91 % and 2.28 % have happened in areas classified as red or orange by TRIGRS and SHALSTAB, respectively. The efficiency values are 81.21 % for RF, 72.15 % and 70.10 % for TRIGRS and SHALSTAB respectively. From the analysis, it was found that RF performs better than the process-based models, and therefore

different alert maps were prepared for the study area based on the four temporal probability classes as shown in Figure 3.

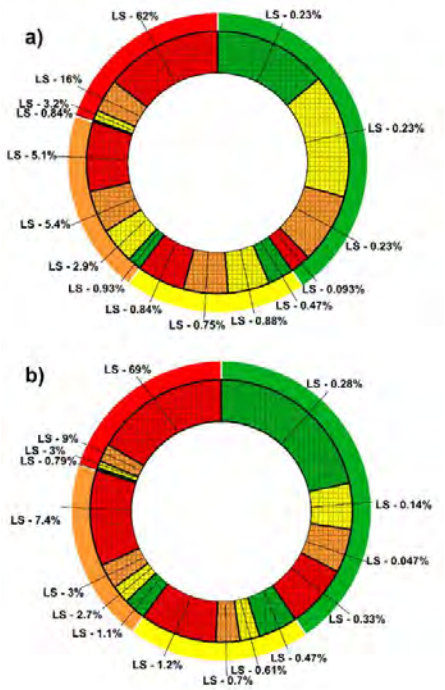

Figure 2. The mutual agreement between the proposed model (RF with 12.5 m DEM) with the process-based models of same resolution. a) comparison between RF and TRIGRS and b) comparison between RF and SHALSTAB (Modified after (Abraham et al., 2023))

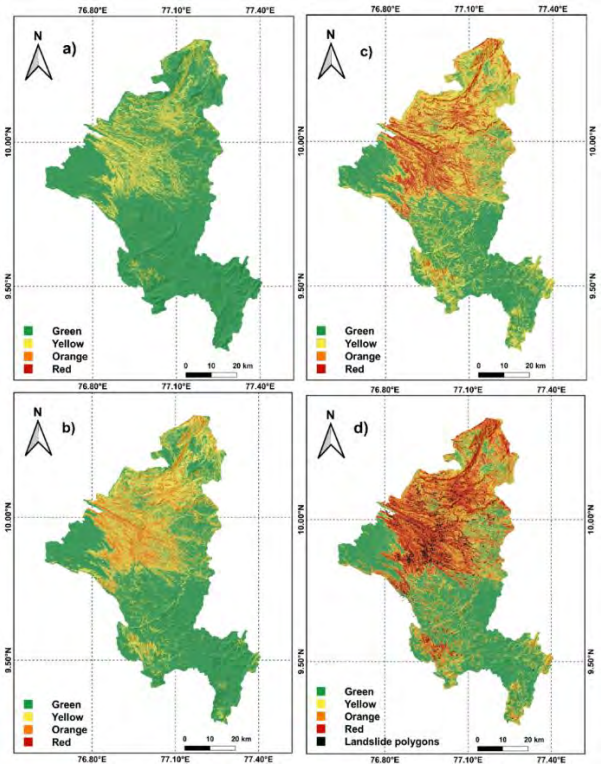

Figure 3. Proposed spatio-temporal landslide forecasting model for the study area (Idukki) for different temporal probability classes. a) very-low, b) low, c) high, and d) very-high, overlaid with landslide polygons (Abraham *et al.*, 2023).

Conclusions

A quantitative comparison of the performance of three different models, two process-based and one data-driven, in forecasting landslides for a 4358 km^2 area was conducted. The temporal features of the data-driven approach were taken into account by combining the spatial LSM with the probabilistic rainfall thresholds established for the research area, whereas process-based approaches take into account both geographical and temporal aspects as input data.

All the three models were derived in two different spatial resolutions, 12.5 m and 30 m. The results indicate that RF model performs better, using the 12.5 m DEM. The highest efficiency obtained was for RF model using 12.5 m DEM, and the value was 0.81. The performance of the RF model was shown to be dependent on the DEM resolution, whereas the performance of the TRIGRS and SHALSTAB models was found to be less dependent on DEM resolution. The outcomes also demonstrate that the performances of process-based approaches are comparable to those of data-driven models, and they may be successfully employed for regional scale forecasting with more exact data gathering and finer property zoning. The findings can be incorporated into regional planning and development to reduce the risk due to landslides.

References

Abraham M T, Satyam N, Rosi A, Pradhan B and Segoni S (2021) Usage of antecedent soil moisture for improving the performance of rainfall thresholds for landslide early warning, *Catena*, 200(January), p. 105147.

Abraham M T, Vaddapally M, Satyam N and Pradhan B (2023) Spatio-temporal landslide forecasting using process-based and data-driven approaches: A case study from Western Ghats, India, *CATENA*, 223, p. 106948.

Baum R L and Godt J W (2010) Early warning of rainfall-induced shallow landslides and debris flows in the USA, *Landslides*, 7(3), pp. 259–272.

Baum R L, Savage W Z and Godt J W (2008) *TRIGRS — A Fortran Program for Transient Rainfall Infiltration and Grid-Based Regional Slope Stability Analysis*.

Leonarduzzi E, Molnar P and McArdell B W (2017) Predictive performance of rainfall thresholds for shallow landslides in Switzerland from gridded daily data, *Water Resources Research*, 53(8), pp. 6612–6625.

Melillo M, Brunetti M T, Peruccacci S, Gariano S L and Guzzetti F (2015) An algorithm for the objective reconstruction of rainfall events responsible for landslides, *Landslides*, 12(2), pp. 311–320.

Physical and rheological studies of debris flow in Western Himalayas (India) using Latin hypercube sampling

Nikhil Kumar Pandey[1], Neelima Satyam[1], Jatin Pardhi[1], Badal Ranjit Singh[1]

[1]Department of Civil Engineering, Indian Institute of Technology Indore, Simrol, Indore, India 453553

SUMMARY: Debris flows represent significant geological hazards in the Western Himalayas, posing multifaceted challenges with profound social and environmental implications. Accurate modeling and prediction of their behavior necessitate a thorough understanding of their rheological characteristics. In this study, we conducted laboratory tests using an inclined plane and rheometer setups to determine key rheological parameters like yield stress and viscosity. Employing an optimized sampling approach, we manipulated solid volume concentration and water content in reconstituted soil samples, testing 25 distinct compositions through Latin hypercube sampling. Utilizing a machine learning regressor, we evaluated the feature importance of debris flow constituents in rheology and findings underscored the significant influence of water content and silt concentration on debris flow rheology. We developed regression models for rheological parameters, achieving robust model fitting with an r^2=0.90 for yield stress and r^2=0.94 for viscosity. Silt content predominantly influenced yield stress, followed by sand, while water content had the most substantial impact on viscosity compared to solid concentration. Additionally, the distribution of grain sizes affected flow behavior, with finer particles exhibiting higher viscosity and shear stress. These insights advance our understanding of debris flow rheology and contribute to broader discussions on the feature importance of constituent particles.

Keywords: debris flow, rheometer, Western Himalayas, solid volume concentration, XGBoost

1. Introduction

Debris flows represent a serious threat to areas far from their point of origin because of their quick and broad movement. These abrupt and quick occurrences can travel across long distances, affecting foothill plains and wreaking disasters on towns, transportation systems, and industrial infrastructure. The states of Himachal Pradesh and Uttarakhand, which are mostly located in the Western Himalayan region, are particularly susceptible to such events (Fig. 1). Western Himalayas in India have been facing geohazards like landslides, debris flow, avalanches, etc because of increase in the rate of torrential rainfall, co-seismic activities, and human interferences (Bookhagen & Burbank, 2010; Dash et al., 2021; Pandey et al., 2024). As they spread, debris flows become slower and eventually stop, indicating that a minimum yield stress ($\boldsymbol{\tau}_c$) is necessary to keep the flow going. Natural flows like mud, concentrated debris, and earth flows can be conceptualized as the movement of slopes in which the collapsed material travels as a viscous fluid. The debris flows are highly influenced by rheological parameters like yield stress, viscosity, etc as observed by previous researchers (Jeong, 2010; Khan et al., 2022; Kostynick et al., 2022). But a majority of the work has been done considering debris samples from the time of event perspective i.e., employing only fixed or very thin range of solid volume concentration of debris material in experiments hence creating a bias towards sampling (Abraham et al., 2023; Ray et al., 2022). The debris material was reconstituted to create 25 samples using Latin hypercube sampling which is an optimized sampling approach (Fig. 1b).

This optimized sampling approach helped reduce biases in the proportion of different constituents (clay, silt, sand, etc) in debris material as shown in Fig. 1c. This work later delves into study the rheological properties of debris flow in the Western Himalayas and to determine the feature importance (influence) of constituent particles (gravel, sand, silt, and clay) using numerical analysis (XGBoost regressor).

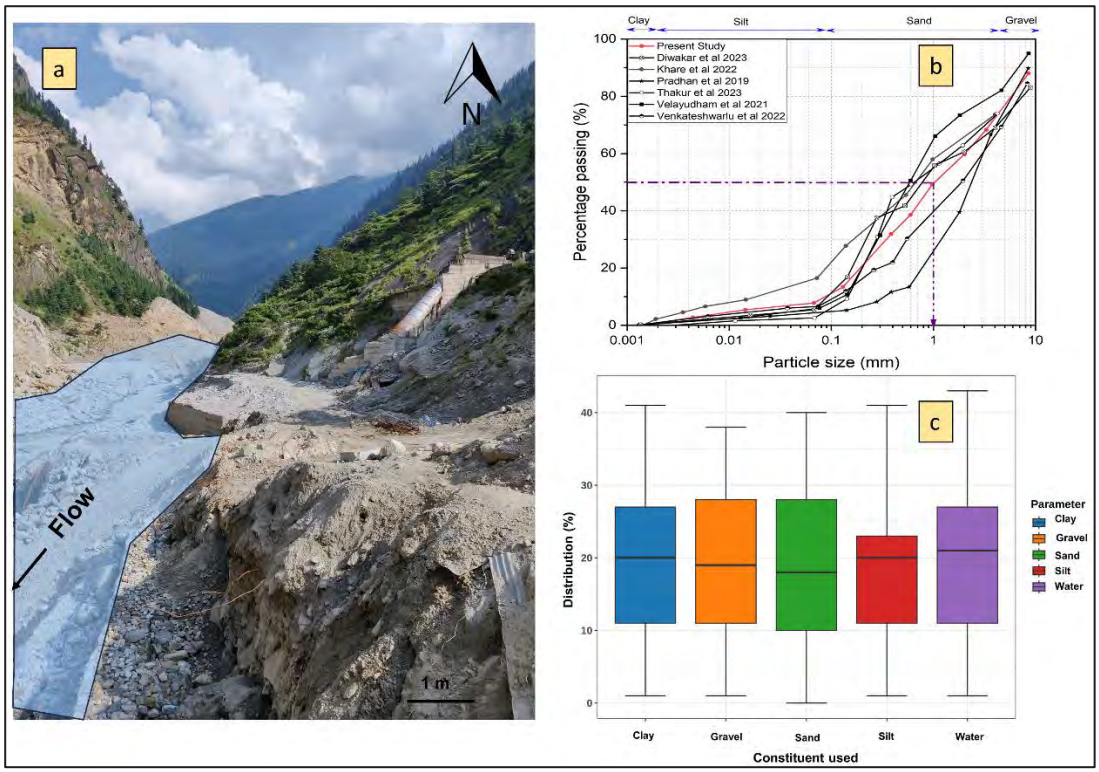

Figure 1. Description of debris sample collected for study where a) shows change in morphology of landform after a debris flow in Western Himalaya b) grain size distribution of reconstituted soil sample using earlier debris flow database c) composition of samples prepared for rheological testing as per Latin Hypercube sampling

2. Methodology

The samples were mixed using a homogenizer (Fig. 2a), at 60-120 revolutions/minute by taking 200-400 ml mixtures for further analysis. The mixtures were then separated based on solid volume concentration (Pierson & Costa, 1987) as shown in Fig. 2b. The samples underwent a rheometric test (Fig. 2d) and those having very high mobility were tested using an inclined plane setup to observe the flow of material at $i = 35°$ to $i = 40°$ where $'i'$ is inclination angle (Fig. 2c). This study utilized the XGBoost regressor to evaluate the significance of rheological parameters, such as yield stress and viscosity (Chen et al., 2019). The model incorporated a dataset comprising diverse constituent compositions (gravel, sand, silt, clay) and volumetric water content to enhance its robustness. Due to the limited dataset derived from 25 experiments, this expansion aimed to bolster the model's reliability. The dataset was partitioned into a 70:30 ratio for training and testing, ensuring comprehensive evaluation. SHAP (SHapley Additive exPlanations) values were used, which measure the impact of each feature on the predictions.

3. Results and conclusions

A strong correlation was observed for yield stress (r^2= 0.90) and viscosity (r^2 = 0.94), with reliable results indicated by root mean square error (RMSE) values between 4.79 and 151.44 (Fig. 3a & 3c). However, deviations in accuracy were noted at higher concentrations of

constituent particles, reflected in the mean absolute error (MAE). The XGBoost model effectively predicted rheological parameters, with SHAP values used to visualize the importance of independent variables like constituent particles and water content. Feature importance was ranked using a violin plot (Fig. 3), highlighting constituents and water content.

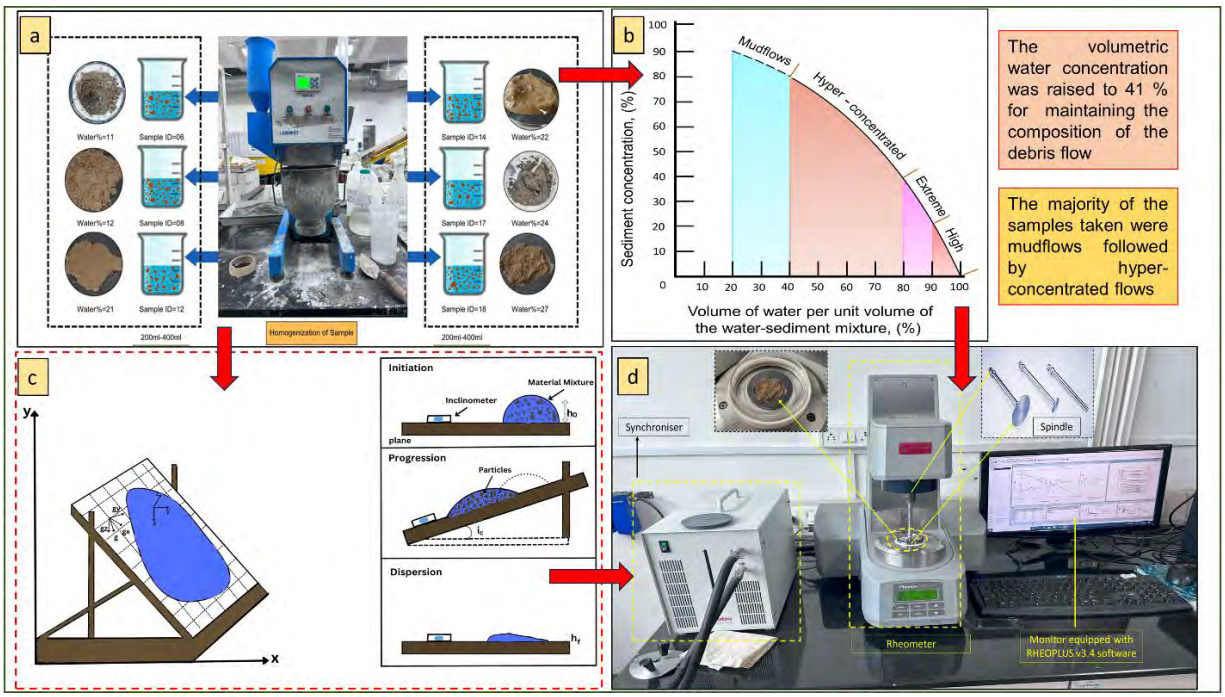

Figure 2. Methodology used in study a) homogenizer b) variation of solid volume concentration with the volume of water c) inclined plane experimental setup d) rheometer setup

3.1 Feature importance in yield stress

Observing prevalent values, silt particles exhibited a wide range of feature values impacting yield stress, increasing as their fraction rises (Fig. 3b). Conversely, sand and gravel particles displayed diverse influences, with sandy particles positively affecting yield stress, while gravel had a decreasing impact with higher volumetric content. Clay and water content showed minimal influence, highlighting the significant contribution of silt particles to overall debris flow strength and resistance. Their finer nature and higher surface area-to-volume ratio promote cohesive connections, increasing internal friction and flow resistance.

3.2 Feature importance in viscosity

Volumetric water content exhibited the greatest impact on viscosity, with higher values correlating with lower SHAP values (Fig. 3d). This suggests a strong influence of water content, particularly at lower values (1% - 13%), diminishing as content increases. Sandy and silty particles also played significant roles in viscosity, with sand maintaining consistent influence across its content range and silt increasing in influence with higher content. The increased interparticle connections and overall cohesiveness associated with finer constituents contribute to greater resistance to shear deformation, necessitating higher water content to initiate flow against this resistance.

It can be concluded that an increase in water content reduced shear stress and viscosity, indicating its pivotal role in debris flow dynamics. Clay, silt, and gravel notably affected rheological behavior, with silt having a pronounced impact on yield stress and water content on

viscosity. Sandy particles also played a significant role in determining rheological characteristics.

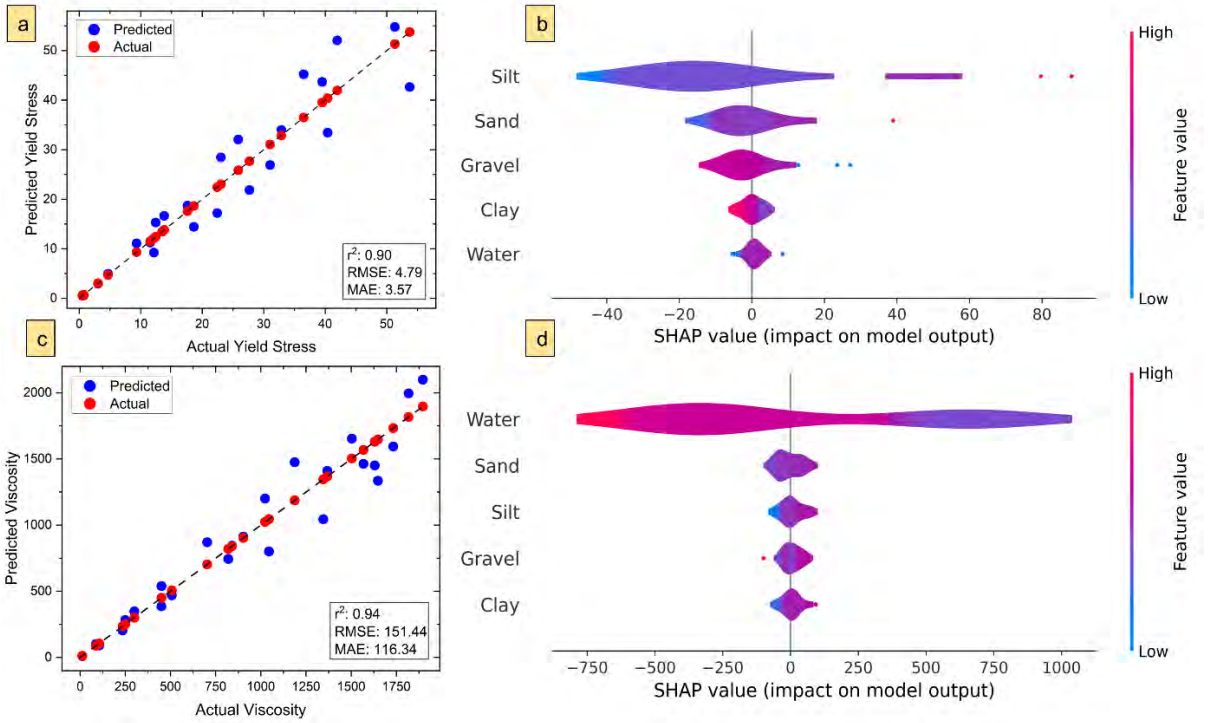

Figure 3. Prediction results for showing a) validation of fit between test and model fitting of yield stress (Pa) b) feature importance in yield stress c) validation of fit for viscosity (Pa-s) d) feature importance in viscosity

References

Abraham, M. T., Satyam, N., & Pradhan, B. (2023). A novel approach for quantifying similarities between different debris flow sites using field investigations and numerical modelling. *Terra Nova*. https://doi.org/10.1111/ter.12679

Bookhagen, B., & Burbank, D. W. (2010). Toward a complete Himalayan hydrological budget: Spatiotemporal distribution of snowmelt and rainfall and their impact on river discharge. *Journal of Geophysical Research: Earth Surface*, *115*(3). https://doi.org/10.1029/2009JF001426

Chen, M., Liu, Q., Chen, S., Liu, Y., Zhang, C. H., & Liu, R. (2019). XGBoost Based Algorithm Interpretation and Application on Post-Fault Transient Stability Status Prediction of Power System. IEEE Access, 7, 13149–13158. https://doi.org/10.1109/ACCESS.2019.2893448

Dash, R. K., Kanungo, D. P., & Malet, J. P. (2021). Runout modelling and hazard assessment of Tangni debris flow in Garhwal Himalayas, India. *Environmental Earth Sciences*, *80*(9). https://doi.org/10.1007/s12665-021-09637-z

Jeong, S. W. (2010). Grain size dependent rheology on the mobility of debris flows. *Geosciences Journal*, *14*(4), 359–369. https://doi.org/10.1007/s12303-010-0036-y

Khan, M. A., Mustafa, Z., Sati, I., Harahap, H., Balogun, A.-L. B., Ibrahim, M. B., & Ahmad, A. (2022). Effect Of Solid Volume Fraction and Particle Size on Rheology of. In *Journal of Engineering Science and Technology* (Vol. 17, Issue 6).

Kostynick, R., Matinpour, H., Pradeep, S., Haber, S., Sauret, A., Meiburg, E., Dunne, T., Arratia, P., & Jerolmack, D. (2022). Rheology of debris flow materials is controlled by the distance from jamming. *Proceedings of the National Academy of Sciences*, *119*(44). https://doi.org/10.1073/pnas.2209109119

Pandey, N.K., Satyam, N., & Gupta, K. (2024). Landslide-induced debris flows and its investigation using r. avaflow: A case study from Kotrupi, India. *Journal of Earth System Sciences*. Springer

Pierson, T. C., & Costa, J. E. (1987). A rhéologie classification of subaerial sediment-water flows. *GSA Reviews in Engineering Geology*, *7*, 1–12. https://doi.org/10.1130/REG7-p1

Ray, A., Verma, H., Bharati, A. K., Rai, R., Koner, R., & Singh, T. N. (2022). Numerical modelling of rheological properties of landslide debris. *Natural Hazards*, *110*(3), 2303–2327. https://doi.org/10.1007/s11069-021-05038-4

Characterization of rockfall events in Tramuntana range (Mallorca)

Joan M Rius[1], Raül Aguiló[1]

[1] Consell de Mallorca, Palma, Spain

SUMMARY: Rockfalls are one of the main geological events that cause both economic losses and human lives. the characterization of such events is important since the great variability in their magnitude implies different possible protection measures. Thus, the competent administration for roads on the island of Mallorca, the Consell de Mallorca, and given the special dynamics of rockfalls that occur on the roads of the Serra de Tramuntana, its main mountain range, a double task of protection against rock falls for more than 10 years has been undertaken. On the one hand, corrective actions have been carried out in very active areas, cleaning up and installing additional elements such as dynamic barriers, to protect the roads. On the other hand, other tasks have been carried out to collect data related to rockfall events. Data collected in a database have been useful to achieve the rockfall characterization. Therefore, in this communication, the different tasks carried out to set up and update the Tramuntana rockfall database are presented. Furthermore, the design of protection barriers by means of rockfall simulation models, using available data from the database, has been performed. Most of the designed barriers are currently operating on the roads.

Keywords: rockfall, database, geomechanical characterization, Tramuntana range

Introduction

Rock falls on mountain roads are one of the main threats to their safety as well as to their users. These are rock masses of one or several blocks of rock that, once detached from a cliff, run down a slope at a certain speed until they stop or until some element stops them. One of the main characteristics of landslides is the great variability in their magnitude which, in any case, can cause significant material damage and loss of human life. To prevent these effects, different methods of protection against rockfalls can be applied: static and dynamic barriers located along the slopes or other type of elements like wire meshes fixed on the rock blocks.

Consequently, there are a significant series of parameters to take into account for the design and installation of this type of protection methods. Some related to the geology and geomorphology of the area: type of rock mass material, rock fractures and discontinuities, geomechanical characteristics, slopes and typology of the ground or affected slopes. There are others closely related to both anthropic and climatic aspects, etc. Thus, a more detailed characterization of the rock falls will result in a more accurate design. This one is usually achieved by means of rockfall simulation models.

The competent administration for roads on the island of Mallorca, the Consell de Mallorca, (CIM), given the special dynamics of rock falls that affect the roads of the Serra de Tramuntana mountain range (figure 1), has been carrying out protection tasks against rock falls during the last decades. Moreover, since 2010 exhaustive data on most events have been collected. In this communication, the methodology to set up the Tramuntana rockfall database and the characterization parameter assessment for the design of protection barriers are presented.

Figure 1.- Location of rockfall events on Serra de Tramuntana roads and a 2020 rockfall event.

Rockfall and climate in Tramuntana Range

The Tramuntana range runs parallel to the north coast of the island of Mallorca in a SW to NE direction, constituting an abrupt area. Regarding geology, it is formed by superimposed folds of dolomites, marls and limestone rocks from the Jurassic and Cretaceous ages, which slide over materials from the Trias, along with levels of conglomerates, detrital limestone, marls and clays from the Miocene. Its geological structure is very complex, with abundant longitudinal and transverse faults and various thrusts. The materials are of different typologies, the most common being Liassic limestone as the most competent materials and Keuper shale and gypsum as the weak ones. In areas of competent materials, different escarpments and cliffs have been formed. The weathering and alteration of these rock fronts causes frequent rock falls. The volumes involved can reach up to thousands of cubic meters, as is the case of the Son Cocó rock avalanche in 2008 with an involved volume of about 300,000 m^3.

In the area of Tramuntana there are various small towns, villages and scattered country houses. An extensive communications network with roads and paths crosses its different valleys. These facilities are systematically affected by different geological events, the most usual of which is the detachment of rock masses. The main roads of the Serra de Tramuntana, owned by the CIM, form a road communication network of about 600 km, most of which belong to the second and third order network of the island, but in some cases, they are the only way to reach to inhabited areas and villages.

The climate is typically Mediterranean, with very wet periods and also significant droughts. Local episodes of high precipitation intensities also happen in these humid periods. One of the main triggering factor for slope instabilities is rainwater. Its infiltration through cracks and fractures causes a double effect: on the one hand, it increases the pressures in them, causing an increase in the magnitude of the cracks and their opening, resulting in the destabilization of rock masses and blocks. On the other hand, the humidity in these cracks, the alteration of their surfaces and their filling with superficial granular material, implies the development of vegetation that with its roots also causes the increase in the magnitude of the cracks and their opening with the same effect on rock masses and blocks. This causes an increase of rockfall events. Thus, this climatology is closely related to the general activity of slope movements and rock falls that occur in the Serra de Tramuntana (Mateos et al., 2012).

Rockfall data base

The work of collecting data on all types of geological events and recording them has been carried out for many years with regard to the Serra de Tramuntana of Mallorca. In fact, there is knowledge of case histories since more than 500 years ago. In any case, the first analysis of slope movements with geomechanical characterization and hazard analysis dates back to the beginning of the 21st century (Mateos, 2001). Subsequently, these types of records have been updated including analysis with remote techniques and simulations (García Moreno, 2017). Currently, these records that cover the entire range are updated by the IGME within the framework of the European RiskCoast project and a current version is available from 2022.

The methodology currently used by the CIM to characterize rockfalls is based on recording data just after an event to obtain the most recent information possible. Thus, there is a current record of almost 330 events from 2005 to the end of 2023 (table 1). However, it should be noted that, until 2010, there was practically no information from the maintenance personnel other than that stones had been found on the road. And until 2014, although inspection of important events improved, there were still some events with almost no information. Since 2015, much more data has been recorded for almost every event, as can be seen in columns 4 and 5 of table 1, which represents a summary of the events recorded and classified based on their volumes involved. Therefore, it should be noted that table 1 is an inventory of events that, until 2014, does not show a complete record of the occurred events. On the other hand, since 2015, it shows an almost complete record of practically all the events that have happened affecting the roads or in their surroundings. The reason for the latter is that those events that, although they do not reach the roads but affect their surroundings, are also recorded. To this end, systematic field inspections are carried out to detect these nearby events.

Table 1. Rockfall volume data from the event log

Rockfall	2005 - 2009	2010 – 2014	2015-2019	2020 – 2023	Total
Num. events	107	45	88	86	326
Unknown Vol.	98	21	-	-	119
V < 1 m^3	4	3	18	26	51
1 < V < 5 m^3	4	13	55	48	120
5 < V < 10 m^3	-	2	8	4	14
10 < V < 100 m^3	-	3	6	7	16
V > 100 m^3	1	3	1	1	6

Rockfall Characterization and modeling

With all the available information, it has been possible to proceed with rockfall modeling tasks, (volumes of blocks on the fronts susceptible to mobilization, characteristics of the source areas and runout information along the slopes, etc.). Specifically, this characterization has been carried out based on some of the events included in the database. Thus, about 10% of the events have extensive information and, some of them have been useful to perform rockfall simulation tasks (figure 2a). Some examples of rockfall events are presented in table 2 with some of their most significant data.

One main characteristic that has been detected is the high fragmentation of the rock blocs during the runout trajectories. A study of the fragmentation of rock blocs has been carried out (Rius, Aguiló, 2022). With the data on the number of blocks and the volume of each block, a correlation between block frequency and its volume can be obtained (figure 2b).

Table 2. Selected rockfall events for modeling purposes

Event	Date	Mechanism	Volume (m3)	Runout (m)	H/L	# total blocks	Máx. Block Vol. (m3)	Vol. Road (m3)
Estellencs	15/1/2010	Planar	500	100	0,50	599	30,6	107
Son Poc	6/3/2013	Toppling	4000	440	0,50	1000	100	0
Formentor	30/1/2017	Wedge	25	55	1,09	34	6	23
Sa Llova	11/9/2019	Wedge	9	40	0,50	120	2,8	5,6
Alaró	18/11/2021	Toppling	36	10	0,70	82	7,3	1

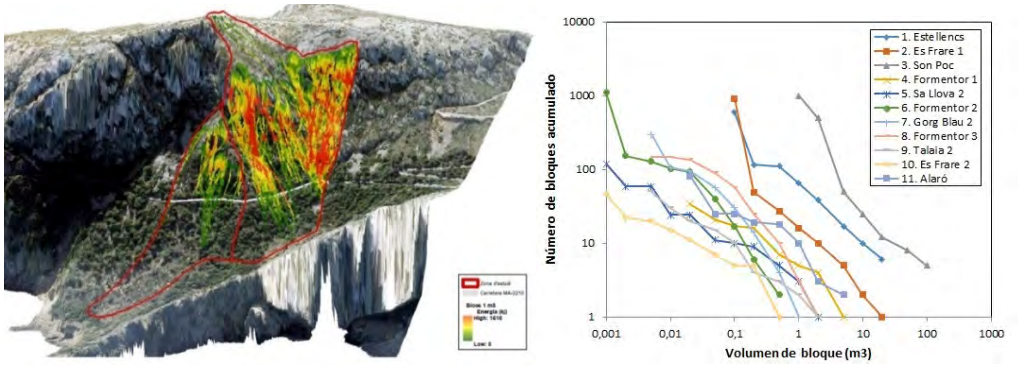

Figure 2.- a) Formentor event rockfall simulation and, b) Distribution of blocks by volume in some events

With such correlation, the fractal fragmentation model developed by Ruiz Carulla et al (2017) could be applied. Thus, it has been noted that it follows an exponential law between the accumulated relative frequency of blocks and its size. Moreover, collaborations have been carried out with the Polytechnic University of Catalonia (UPC), within the framework of the European projects, RockRisk and RockModels, to characterize some events in the Serra. The main objective has been the characterization of the process of block fragmentation in rock falls for a better definition of the parameters for its modeling. Thus, a task is also being carried out to model landslides with the RockGis code (Matas, 2020) and improve the sizing of the necessary protections on roads affected by landslides.

The main conclusion of the performed tasks, is that a more realistic approach to the event can be achieved, with block fragments that stop along the runout, creating some block deposits. The affected area is also expanded compared to a single block that follows a single trajectory, representing a better approximation for the design of protection barriers.

References

García-Moreno, I, 2017. Actividad de los movimientos de ladera de la Serra de Tramuntana (Mallorca). Aplicación de técnicas remotas (DInSAR) y simulación de desprendimientos rocosos. Tesis Doctoral. UIB, 289 p.

Matas, G., 2020. Modelling fragmentation in rockfalls. Tesis Doctoral. Universitat Politécnica de Catalunya, BarcelonaTech., 171 p.

Mateos, R.M, 2001. Los movimientos de ladera en la Serra de Tramuntana (Mallorca). Caracterización geomecánica y análisis de la peligrosidad. Tesis Doctoral. Universidad Complutense de Madrid, 299 p.

Mateos, R.M., García-Moreno, I. & Azañón, J.M., 2012. Freeze-thaw cycles and rainfall as triggering factors of mass movements in a warm Med region: The case of the Tramuntana (Majorca). *Landslides*, 9, pp.417–432.

Rius, J.M. y Aguiló, R., 2022. Caracterización de los desprendimientos rocosos en las carreteras de la Serra de Tramuntana de Mallorca. X Simposio Nacional sobre Taludes y Laderas Inestables, Granada. M. Hürlimann y N. Pinyol (Eds.). CIMNE, Barcelona.

Ruiz-Carulla, R., Corominas, J., Mavrouli, O., 2017. A fractal fragmentation model for rockfalls. *Landslides*, 14, pp.875-889.

Hybrid design approach for anchored wire mesh on soil nailing applications

Alberto Grimod[1], Gobbin Luca[2]

[1] France Maccaferri, 8 Rue Pierre Mechain, 26000, Valence, France
[2] Officine Maccaferri, Via J.F. Kennedy n.10, 40069, Zola Predosa Italy

SUMMARY: In this paper, the authors propose an advanced "hybrid" design method that combines Ultimate Limit State (ULS) analysis for the unstable slope with Serviceability Limit State (SLS) analysis for the steel wire mesh used as a flexible structural facing on soil nailing applications. This approach allows designers to estimate how soil displacement affects the slope's factor of safety, demonstrating the mesh's ability to reduce soil displacement while considering both its strength and stiffness.

Keywords: Steel wire mesh, soil nailing, hybrid design approach, structural flexible facing.

Introduction

Soil nailing aims to enhance soil stability under unfavourable conditions by inserting reinforcing bars into the soil, generating friction forces that improve stability during soil displacement (Schlosser F. et al., 2002; Soulas R., 1991; BS 8006-2; Byrne, R.J et al., 1998). To protect the soil reinforced by nails, a facing, either flexible (e.g., steel wire mesh) or rigid (e.g., shotcrete), is used to prevent erosion and provide an aesthetic function (Giacchetti et al., 2011).

Designing slope stabilization measures involves various factors: slope geometry, geotechnical properties, stabilizing element type and position, soil displacement profile, water table, and load amplitudes (especially environmental loads) (Koutsourais M., 2018). Anchored wire mesh on unstable slopes relies on complex interactions, with stabilizing reactions activated only during soil displacement, making it a passive intervention.

Figure 1 Example of wide punch displacement of flexible structural facing loaded by the soil. The cables reduced the mesh displacement.

Methodology

Standard design methods are often force-based and oversimplified, not considering all relevant factors or deformation characteristics. They focus solely on the ULS condition, neglecting slope

displacement (SLS), which is often the key concern. Accurate numerical approaches exist but are demanding in terms of expertise and computational resources.
Simplified methods are needed to consider soil and mesh deformation properties, improving safe design procedures. A recent study outlines three design approaches: Limit State Methods, Hybrid Methods, and Displacement Methods.
Limit State Methods assume rigid-perfectly plastic behaviour for soil and structures, estimating the maximum load transfer without considering soil-structure displacement. ULS methods fall into this category.
Hybrid Methods introduce a soil-structure interaction model that accounts for the evolution of stabilizing forces during relative soil-mesh displacement. This approach combines ULS analysis for slope stability with SLS analysis for the structure. It quantifies the performance of the stabilizing intervention based on slope displacement.
Displacement Methods use the "Characteristic Function" concept and integrate the motion equation of unstable soil masses over time, allowing for long-term behaviour evaluation.
This paper focuses exclusively on "Hybrid Methods" and introduces the crucial concept of the characteristic curve for improved slope stabilization design.

Hybrid method

In the following section, attention will be uniquely focused on the case of homogeneous unstable layers of thickness (s) on a slope with inclination (α) and total height (H) (Figure 2). In this case, several different failure surfaces are possible, each one identified by the position of its emerging point. But thanks to the similarity of the geometries, the displacement pattern of each mechanism can be ideally described as in Figure 3a, where a simplified two-wedge model composed by the unstable layer and a triangular base wedge, is considered. The whole displacement field is fully described by the value of the rigid downward displacement U of the unstable layer and by the corresponding horizontal displacement U_H of the base wedge. In particular, the normal component U_N, with respect to the slope profile, of the wedge displacement is responsible for the normal interaction with the mesh and the increase in the stabilizing pressure q along the “active” length L_a denoting the size of the base wedge (Figure 3b). Note that the tangential interaction is disregarded for the sake of simplicity.

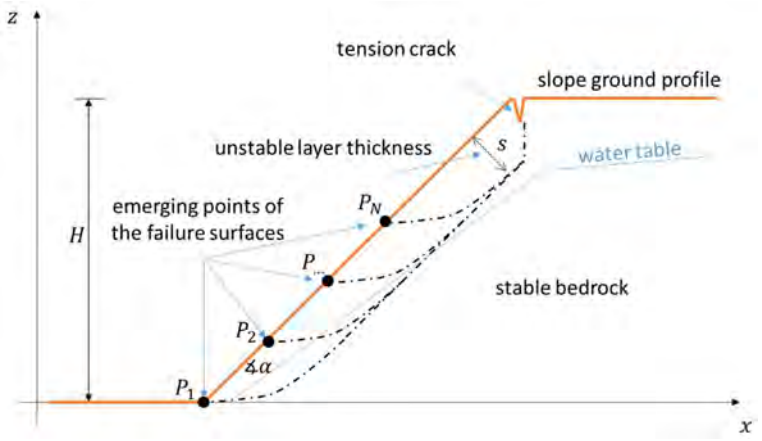

Figure 2: Schematic view of an unstable layer on a sloping ground.

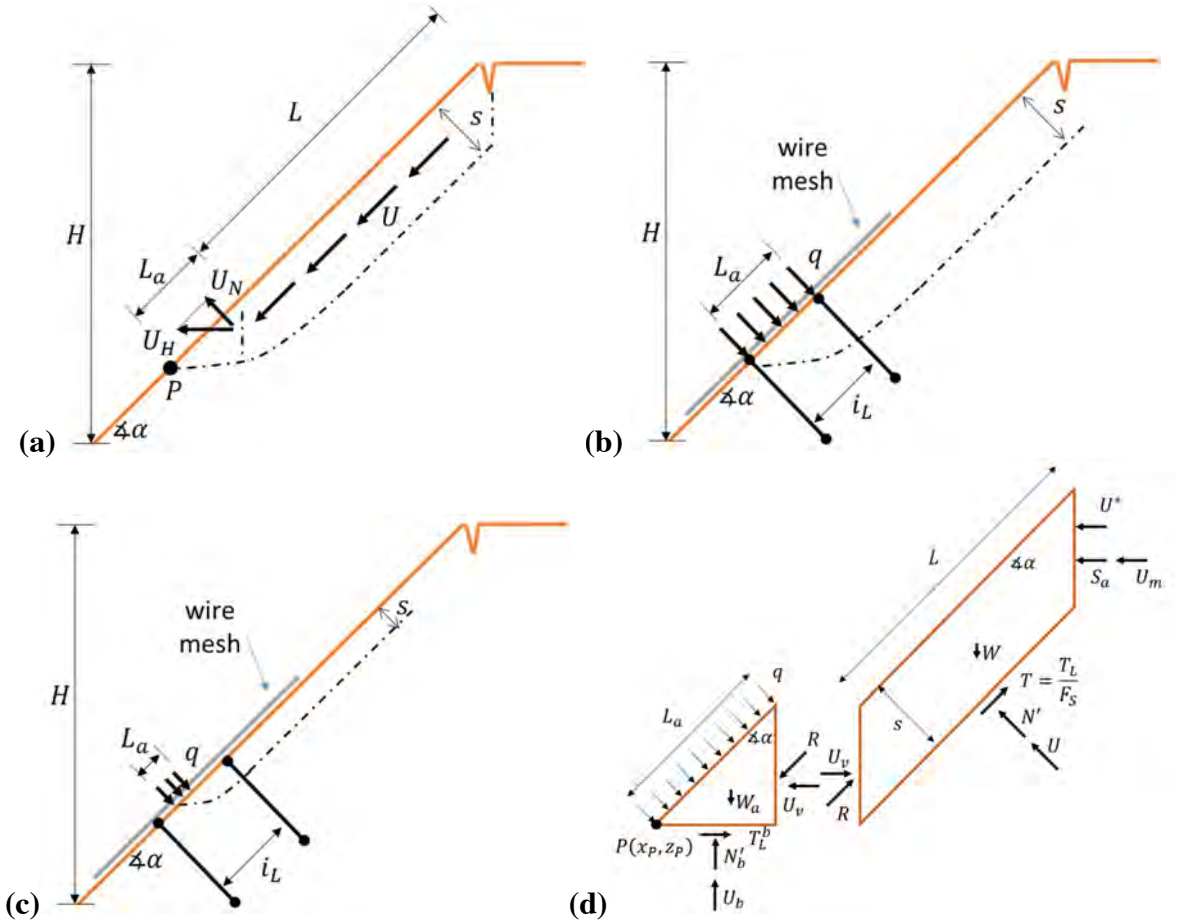

Figure 3: (a) displacement pattern of the chosen failure mechanism; (b) activation of the stabilizing pressure q at the soil-mesh interface; (c) partial mobilization of the mesh between two anchors; (d) equilibrium of the two blocks.

It is worth noting that the ratio between the thickness s and the longitunial anchor spacing i_L directly affects the efficiency of the stabilizing system, thanks to the assumed simplified displacement pattern. The correct dimensioning of anchor spacing implies in fact the full mobilization of the mesh (Figure 3c), while an over dimensioning of i_L implies only a partial mobilization of the wire mesh, with a significant reduction of the system efficiency in limiting slope displacement.

For each considered failure mechanism along the slope, each one identified by means of its emerging point P, it is then possible to solve the equilibrium equations of the two wedges (i.e. the soil layer and the base wedge, schematically shown in Figure 3d) under the hypothesis that the base wedge reaches a passive failure condition (i.e. its internal state of stress is governed by a passive earth pressure coefficient). The value of the supporting action R provided by the wedge to the unstable layer can then be directly related to the pressure q arising at the soil-mesh interface along the active length L_a, which is on its turn determined by the wedge displacement itself.

The global safety factor F_S for the unstable layer, defined as a reduction factor for the soil shear strength at the base of the unstable soil layer, is then actually dependent on the slope displacement, through the pressure q and, hence, through the characteristic curve. From a design point of view, this procedure allows the designer not only to verify the structural safety for the required value of the F_S (i.e. a design value $F_{S,d}$), but also the working ration of the mesh along the slope.

Conclusion

In this paper, an innovative simplified design approach for anchored wire mesh on unstable soil slopes has been presented. The procedure has been developed within the framework of the so called "hybrid methods" developed for performing slope stability analyses by accounting for the presence of stabilizing structures. In particular, the key concept is represented by the "characteristic curve" of the system representing the relationship between the stabilizing action of the mesh and the slope movement. This is particularly important for a hybrid method since it allows a direct relation between the desired degree of safety of the slope, F_S, and the corresponding slope displacements, i.e. performance of the stabilizing system. Some example numerical analyses, quickly performed on standard laptops, shows the efficiency of the method in evaluating the slope displacement profile corresponding to the chosen value of the F_S of the slope, and proves the capability of the method to capture the main geometrical parameters affecting the problem.

From a design perspective, the proposed "hybrid method" is particularly suitable to perform extended parametrical analyses to rapidly optimize stabilizing systems both in terms of geometrical (e.g. number of anchors) and mechanical (e.g. type of wire mesh) properties.

References

BS 8006-2, 2011. Code of practice for Strengthened/ reinforced soils and other fills – Part 2: Soil Nailing design.

Byrne R.J, Cotton D., Porterfield J., Wolshlag C., e Ueblacker G.,(1998). "Manual for design & construction monitoring of soil nail walls" U.S. Department of transportation – Federal Highway Administration. FHWA A-SA-96-06R – Washington D.C

Giacchetti G., Grimod A., Cheer D. (2011). Soil Nailing with flexible structural facing: design and experience. World Landslide Forum, Rome 2011

Koutsourais M., Deana M. (2018). Design of pinned drapery systems for rockfall protection. HGS 2018.

Schlosser F., (Chairman) (2002). "Additif 2002 aux recommandations clouterre 1991 pour la conception, le calcul, l'exécution et le controle des soustènements realises par cluage des soil", Presses Ponts et chaussées.

Soulas R., (Chairman) (1991). "Recommandations clouterre 1991 pour la conception, le calcul, l'exécution et le controle des soustènements realises par cluage des soil", Presses Ponts et chaussées.

Soilstab and Evorisk: a Web-Service and Web-Platform for Landslide and Rockfall Hazards Using Ambient Seismic Noise Methods

Alexandra Royer[1], Antoine Guillemot[1], Mathieu Le Breton[1], Eric Larose[2], Laurent Baillet[2], Fabrice Guyoton[1], Raphael Mayoraz[3]

[1] Géolithe & Géolithe Innov, Crolles, France
[2] Université Grenoble Alpes & CNRS, ISterre, Grenoble, France
[3] SFCEP, Canton du Valais, Suisse

SUMMARY: For several years, the seismic ambient noise interferometry method has been applied to estimate relative variations in seismic surface wave velocity in depth (dV/V). This technique has led to the detection of a decrease in wave velocity several days before the rupture of a clay landslide, suggesting the value of this new precursor signal in landslide monitoring. Also, the relative variation over time of the natural resonance frequencies of rock instabilities, dF/F, depends on the elastic properties and the geometry of the vibrating structure, which makes it possible to monitor its mechanical state, and to deduce precursor signals to significant failure. To make these technologies operational, we have built the web-service Soilstab, which allows for the processing of an existing data set with the seismological methods described previously. This service is associated with Evorisk, a web-platform that displays the time series (updated daily or over a fixed period) of the results (dV/V and/or dF/F). This platform can integrate other available observations, such as environmental data (temperature, rainfall, snow depth) or displacement measurements (from photogrammetry, GNSS sensors, extensometers, etc.). Correlating these observations permits us to better understand and quantify the effect of environmental forcings on the dynamics of landslides and rock instabilities.

Keywords: web-service, web-platform, landslide, rockfall hazards, ambient seismic noise

Introduction

Landslide monitoring is essential to a better understanding of their dynamics and to the reduction of human casualties by detecting precursors before failures. In general, observations on the surface must be supplemented by subsurface observations. Ten years ago, the seismic ambient noise interferometry method has been applied to monitor the relative variations in surface seismic wave velocity in depth (dV/V). As seismic wave velocities are directly related to the stiffness of the material, any reduction in seismic velocity can be associated with a loss of stiffness with high probability (due to clay liquefaction or strong fracturation for example). This technique has led to the detection of a decrease in wave velocity several days before the rupture of a clay landslide (Mainsant et al, 2012), opening the way to a new precursor signal that could be used for alerts or early warning systems. Since then, several landslides have been monitored to this end (Le Breton et al, 2021).
In addition, by analyzing the spectral content of seismic data, the natural resonance frequencies of rock instabilities (rocks columns, rock glaciers) can be tracked (Colombero et al, 2021). Their relative variation (dF/F) over time depends on the elastic properties and the geometry of the vibrating structure, which makes it possible to monitor its mechanical state, and to deduce precursor signals to significant failure.

Web-service Soilstab

We have built a web-service, Soilstab, which allows for the processing of an existing dataset with the seismological methods described previously, resulting in temporal evolution of dV/V (Figure 1) or dF/F (Figure 2). We propose a custom configuration of the data processing by our

experts, adapted to the site, which makes the web-service Soilstab suitable for non-expert seismologists. Web-service Soilstab includes:

- a 24/7 automatic monitoring from data reception/transmission to processing.
- a warning system with the generation of alerts when results cross a threshold.
- a visualization of the data on the web-platform Evorisk, easily accessible.

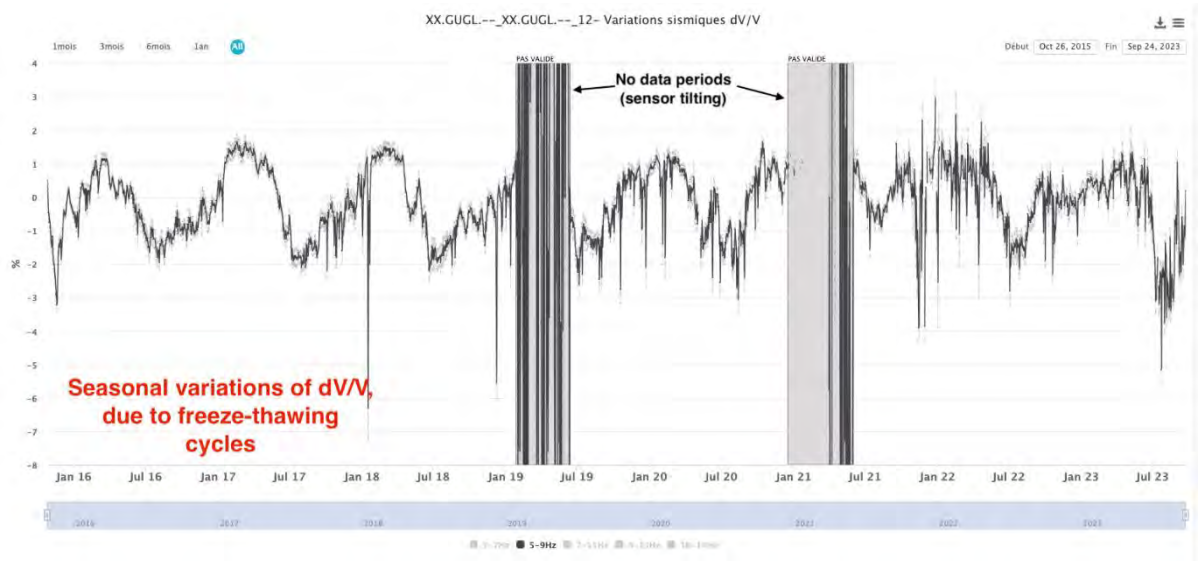

Figure 1. Application of Soilstab to permafrost monitoring: dV/V results on Gugla rock glacier (Canton of Valais, Switzerland).

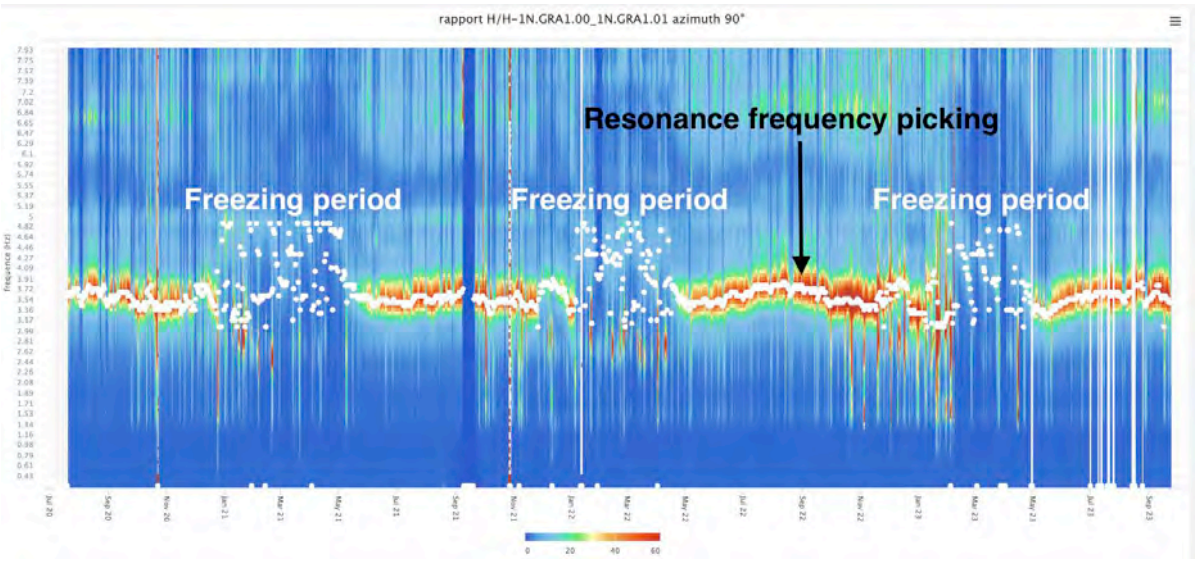

Figure 2. Application of Soilstab to rock column monitoring: dF/F results on Mont Granier (Isère, France).

Web-platform Evorisk

The Web-service Soilstab is associated with Evorisk, a web-platform that displays the temporal evolution (updated daily or over a fixed period) of the results (dV/V and/or dF/F). The platform also integrates other available observations such as environmental measurements (temperature,

rainfall, snow depth, etc.) or surface observations (by photogrammetry, GNSS/GPS-based displacement measurements, extensometers). Correlating all these observations is thus made easier to better understand and quantify the effect of environmental forcings (temperature, precipitation) on the dynamics of landslides and rock instabilities.
The case of the Combe de Beaujournal at Valloire (Savoie, France), illustrates an example of multi-method measurements. As part of the instrumentation, a meteorological station, an array of 6 seismometers, a system for measuring surface displacements (based on RFID) and cameras were installed. The Evorisk platform makes it possible to combine all these measurements data in one place, and thus help to highlight similar behaviors between time series, such as variations in dV/V and temperature over time (Figure 3).

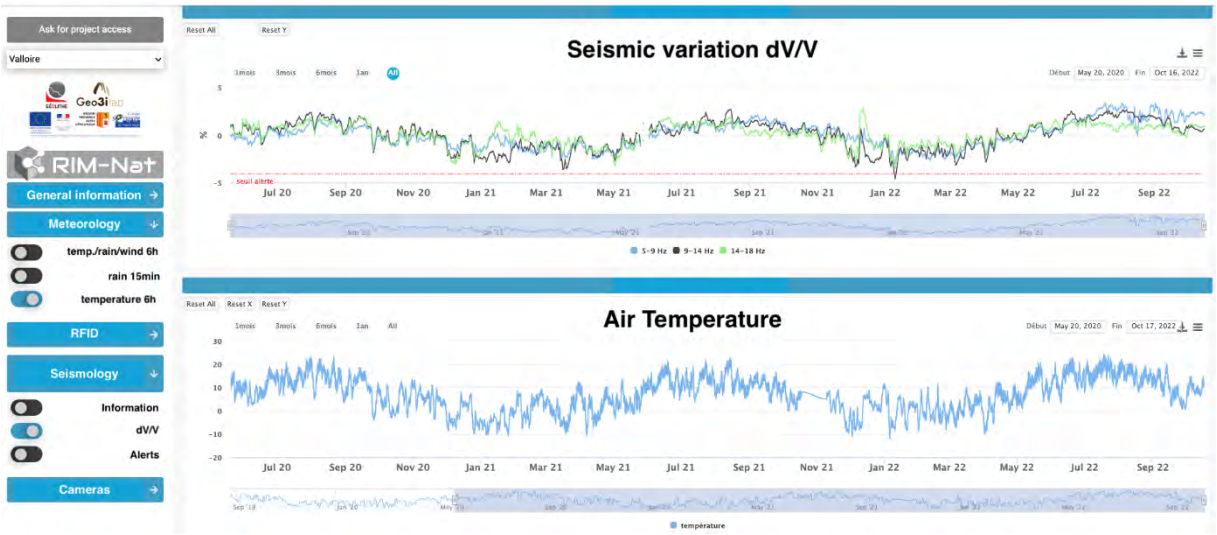

Figure 3. Example of visualization on the web-platform Evorisk: case of Combe de Beaujournal site (Savoie, France)

Conclusion

The web-service Soilstab makes the data processing of ambient seismic noise accessible to non-seismologists. The web-platform Evorisk offers the possibility to visualize and correlate several observations from an instrumented site. Combining the two aims at better understanding and quantifying the effect of environmental forcings (temperature, rain, frost) on the subsurface, towards predicting the dynamics of landslides and rock instabilities.
From Evorisk's home page, https://evorisk.fr, direct access to the web-service Soilstab can be found on the lateral menu.

References

Mainsant G, Larose E, Brönnimann C, Jongmans D, Michoud, C & Jaboyedoff M (2012). Ambient seismic noise monitoring of a clay landslide: Toward failure prediction. Journal of Geophysical Research (Earth Surface). 117. 1030-. 10.1029/2011JF002159.

Le Breton M, Bontemps N, Guillemot A, Baillet L, Larose E (2021) Landslide Monitoring Using Seismic Ambient Noise Interferometry: Challenges and Applications. Earth Science Reviews, 216, 103518.

Colombero C., Jongmans D., Fiolleau S., Valentin J., Baillet L., & Bièvre G. (2021). Seismic noise parameters as indicators of reversible modifications in slope stability: a review. Surveys in Geophysics, 42(2), 339-375.

Cross-Plot Analysis Using Electrical Resistivity and Seismic Velocity for the Assessment of Slope Creep Vulnerability

Taeho Bong[1], Sangjun Im[2], Jungil Seo[3], Dongyeob Kim[4], Joon Heo[5]

[1] Department of Forest Science, Chungbuk National University, Cheongju, Republic of Korea
[2] Research Institute of Agriculture and Life Sciences, Seoul National University, Seoul, Republic of Korea
[3] Department of Forest Science, Kongju National University, Yesan, Republic of Korea
[4] Department of Forest Resources, Daegu University, Gyeongsan, Republic of Korea
[5] Rural Research Institute, Korea Rural Community Corporation, Ansan, Republic of Korea

SUMMARY: Slope creep is a type of mass movement and is considered one of the slowest forms of landslides. Slope creep is influenced not only by rainfall and groundwater but also by the presence of expansive soils such as clay and the existence of anomalous or saturated zones within the ground. The aim of this study is to assess slopes susceptible to creep using electrical resistivity survey and seismic survey, which are geophysical methods. The geophysical survey results were collected from 28 slope sites, and the data set is categorized into two groups based on the degree of vulnerability of slope creep. Cross-plot analysis was implemented to integrate both electrical resistivity and seismic velocity, and the resulting points were divided into four quadrants based on the ranges of electrical resistivity and seismic velocity. The classification criteria of four quadrants for distinguishing the two slope groups were determined using t-tests. As a result, when the resulting points were divided into four quadrants based on electrical resistivity of 400 Ω·m and seismic velocity of 600 m/s, it was found that the ratio of Q4 (low resistivity, high velocity) effectively distinguishes the two slope groups with a *p*-value of 0.001.

Keywords: slope creep, electrical resistivity, seismic velocity, cross-plot analysis

Introduction

Slope creep is a type of mass movement characterized by the gradual and slow downward movement of rock and soil along a slope. One of the causes of slope creep is the expansion of materials such as clay, which are soils susceptible to swelling and shrinking when exposed to water. Additionally, the presence of anomalous or saturated zones within the ground can also affect soil creep. However, it is not easy to find out if those vulnerable zones exist in soil slopes. Recently, electrical resistivity survey and seismic survey have been widely used to determine the spatial and temporal variability of soil properties. These methods are primarily used to investigate the subsurface conditions of the slope in two or three dimensions and determine the location of critical failure surface. In particular, the electrical resistivity tomography (ERT) is a highly effective method in landslide research (Zainal et al., 2021), such as predicting the location of critical failure surface in a soil slope, evaluating slope deformations, and identifying saturated zones (Pasierb, 2015; Bellanova et. al., 2018; Nordiana et. al., 2018). Seismic surveys measure the propagation of seismic waves through earth materials, and can be used to determine the internal structure of materials in a slope (Hack, 2000). However, geophysical surveys have limitations in comprehensively understanding the physical characteristics of the subsurface through a single method because each geophysical method is influenced by the specific physical properties of subsurface materials. Therefore, geophysical surveys are often conducted in conjunction with geotechnical surveys or a combination of various geophysical methods. The electrical resistivity survey and seismic survey have different investigation purposes and

provide different physical properties of soil, making them complementary to each other. Therefore, considering both geophysical methods simultaneously can provide better insights into slope vulnerability assessment than analyzing one or two methods separately. The cross-plot analysis was introduced based on the integration of electrical resistivity and seismic velocity in order to enhance the subsurface resolution besides the provided comprehensive subsurface images. Zakaria et al. (2021) applied cross-plot analysis to determine the weak zones suspected to be landslides with sliding, and calculated the volume of mass sliding. However, little research has been conducted on landslides using cross-plot analysis that integrates geophysical methods. In particular, the analysis of threshold values of electrical resistivity and seismic velocity in a cross-plot to assess slope creep vulnerability has not yet been conducted.

In this study, field surveys and geotechnical laboratory tests were conducted to verify the physical and environment characteristics of slopes vulnerable to creep. Additionally, electrical resistivity surveys and seismic wave surveys were conducted to investigate the 2-dimensional spatial distribution of subsurface physical properties and identify vulnerable zones. A database for a total of 28 slope sites was constructed for slope creep vulnerability assessment. The dataset is divided into two groups: susceptible and non-susceptible slopes to creep, based on the field survey results. To assess the vulnerability of slope creep using the geophysical survey results, the two geophysical survey results were matched to the same locations, and the cross-plot analysis was implemented to integrate both electrical resistivity and seismic velocity. The resulting points have been divided into four quadrants based on the threshold values of electrical resistivity and seismic velocity, and classification criteria for distinguishing the two slope groups were determined using *p*-value from a t-test.

Materials and Methods

In this study, field surveys, geotechnical laboratory tests, and geophysical survey were conducted to verify the physical and environment characteristics of slopes vulnerable to creep. The schematic view of creep vulnerability assessment through cross-plot analysis is shown in Figure 1.

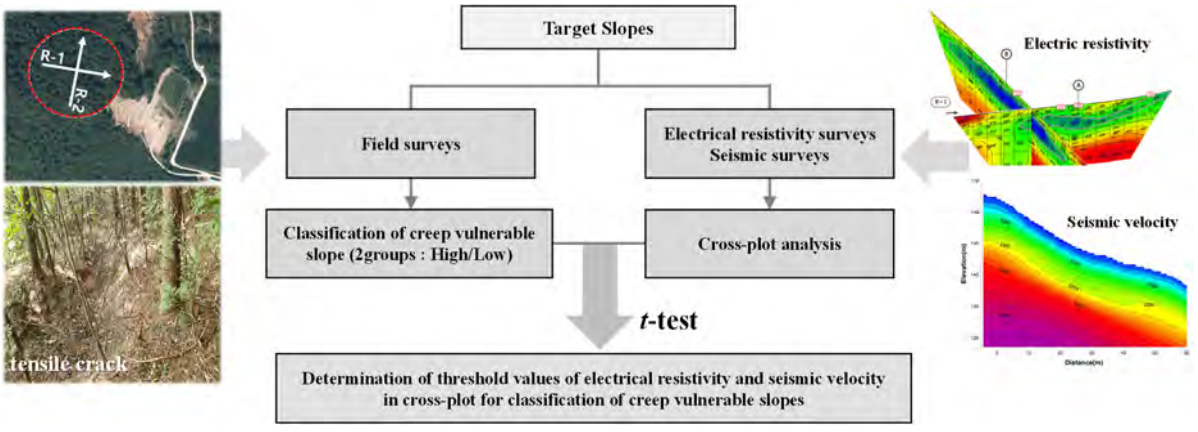

Figure 1. Flow chart of cross-plot analysis for the assessment of slope creep vulnerability

In the field surveys, various factors known to affect slope creep, such as soil types, physical and hydraulic properties of soils, gradient, topography, geological characteristics, and forest vegetation, were investigated, and traces of slope creep, such as tension cracks or tilted trees, were also observed. From the results of the field survey, the 28 slopes were divided into two groups: a group with a high creep vulnerability (10 slopes) and a group with a low creep

vulnerability (18 slopes). Then, cross-plot analysis utilizing geophysical survey results was performed to quantitatively assess vulnerability of slope creep.

Electrical resistivity survey measures the ability of electrical current to flow through the subsurface materials, and seismic survey is based on the measuring of an elastic wave traveling through the subsurface materials. These surveys reflect many physical properties such as soil types, soil density, porosity, saturation state, groundwater, strength, and other properties of subsurface materials, but they are not directly related to engineering properties (Hayashi & Konishi, 2010). Therefore, these survey results complement each other, and it is important to integrate and interpret these results collectively for a more accurate evaluation of subsurface structures. Cross-plot analysis is a method that considers the correlation between electrical resistivity and seismic velocity, and four quadrants used to divide the parameters based on Hayashi & Konishi (2010). Figure 2 shows the process of conducting cross-plot analysis using two geophysical surveys, and the schematic relationship between electrical resistivity and seismic velocity data.

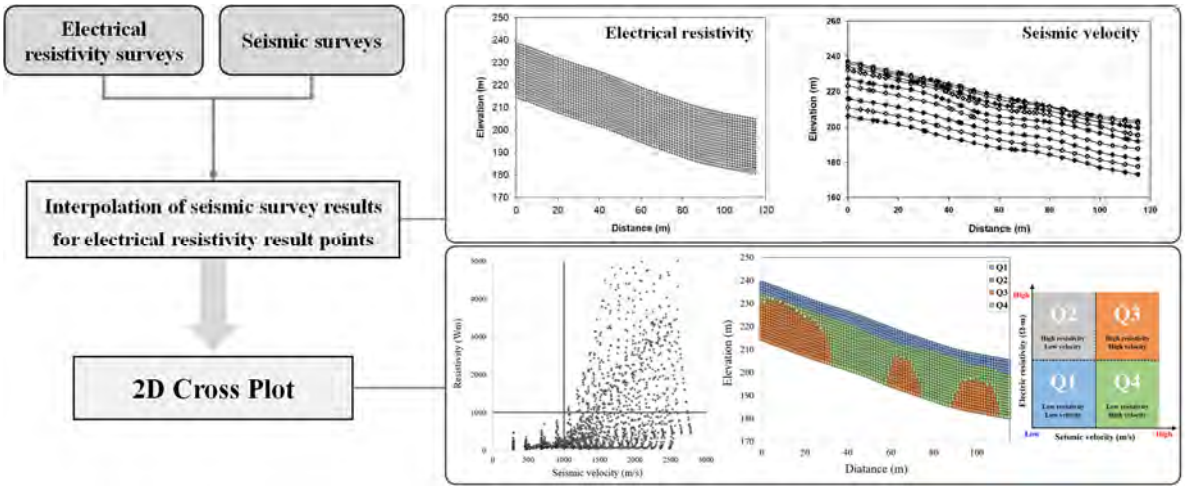

Figure 2. Process and schematic diagram of cross-plot analysis.

The four quadrants of cross-plot analysis (Q1: low resistivity, low velocity, Q2: high resistivity, low velocity, Q3: high resistivity, high velocity, Q4: low resistivity, high velocity) are determined by threshold values of electrical resistivity and seismic velocity, and the selection of threshold values can result in different interpretations of vulnerable areas. In this study, in order to determine threshold values that can most effectively classify the two slope groups for slope creep vulnerability, the proportions of each quadrant for various combinations of threshold values were calculated. Finally, the threshold values of electrical resistivity and seismic velocity were statistically determined based on the t-test results.

Results and Discussion

The threshold value range for electrical resistivity was set from 200 Ω·m to 1,400 Ω·m, and for seismic wave surveys, it was set from 500 m/s to 1,500m/s. Based on the combinations of these threshold values, the proportions of geophysical survey points, evenly distributed spatially on the slope, for each quadrant were calculated. From the t-test, the distribution of *p*-values for each quadrant based on different threshold criteria are summarized in Table 1.

As a result, when the resulting points were divided into four quadrants based on electrical resistivity of 400 Ω·m and seismic velocity of 600 m/s, the ratio of Q4 was found to be the most

statistically significant with a *p*-value of 0.001 to distinguish the two groups regarding slope creep vulnerability.

Table 1. t-test results for each quadrant according to the threshold values

Quadrant	Threshold value		*p*-value	Rank
	Velocity	Resistivity		
Q1	1,500	400	0.024	3
Q2	1,100	400	0.186	4
Q3	500	400	0.004	2
Q4	600	400	0.001	1

Conclusions

This study aims to quantitatively evaluate the vulnerability of slope creep using geophysical methods. Cross-plot analysis was implemented to integrate both electrical resistivity and seismic velocity, and the threshold values for assessing slope creep vulnerability were statistically determined as electrical resistivity (400 Ω·m) and seismic velocity (600 m/s). The proportion of results points belonging to the third quadrant was found to average 52.3% for slope with high creep vulnerability and 18.5% for slope with low creep vulnerability, indicating that a higher proportion in the third quadrant is associated with vulnerability to slope creep.

Acknowledgement

This work was supported by the National Research Foundation of Korea (NRF) grant funded by the Korea government (MSIT) (No. 2022R1A2C4002583).

References

Zainal M, Munir B & Marwan (2021) The electrical resistivity tomography technique for landslide characterization in Blangkejeren Aceh. *Proceedings of the 10th International Conference on Physics and Its Applications.* Journal of Physics Conference Series 1825(1):012022.

Pasierb B (2015) Numerical Evaluation 2D electrical resistivity tomography for investigations of subsoil. *Technical transactions environmental engineering* 2-S, pp. 101-113.

Bellanova J, Calamita G, Giocoli A, Luongo R, Macchiato M, Perrone A & Piscitelli S (2018) Electrical resistivity imaging for the characterization of the Montaguto landslide (southern Italy). *Engineering Geology* 243, pp. 272-281.

Nordiana MM, Azwin IN, Nawawi MNM & Khalil AE (2018) Slope failures evaluation and landslides investigation using 2-D resistivity method. *NRIAG Journal of Astronomy and Geophysics* 7, pp. 84-89.

Hack R (2000) Geophysics for slope stability. *Surveys in Geophysics* 21, pp. 423-448.

Zakaria MT, Mohd Muztaza N, Zabidi H, Salleh AN, Mahmud N, Samsudin N, Rosli FN, Olugbenga AT & Jia TY (2021) 2-D Cross-Plot Model Analysis Using Integrated Geophysical Methods for Landslides Assessment. *Applied Sciences* 11: 747.

Hayashi K & Konishi C (2010) Joint use of a surface-wave method and a resistivity method for safety assessment of levee systems. *Proceedings of the GeoFlorida 2010: Advances in Analysis, Modeling and Design*, Florida. ASCE. pp. 1340-1349.

An Analysis of Landslide Vulnerability Considering Changes in the Ratio of Saturated Infiltration Depth of Soil Layers at Different Rainfall Intensity Levels

Man-Il Kim[1], Seungyoub Yi[2], Jawhwan Kwak[3], Namgyun Kim[1]

[1] National Forestry Cooperative Federation, Daejeon, Republic of Korea
[2] Protec Engineering, Goyang, Republic of Korea
[3] Korea Slope Safety Association, Sejong, Republic of Korea

SUMMARY: In this study, we analyzed the landslide vulnerability of the research area using an infinite slope stability analysis model that considers the saturated infiltration depth ratios of the soil layers at different rainfall intensity levels. To that end, we identified the geotechnical properties of the research area, including cohesion (30.84 kPa), unit weight (1.46 t/m^3), specific gravity (2.65), effective soil depth (0.41 m), and internal friction angle (27.15°). Based on the probable rainfall, we analyzed landslide vulnerability for different rainfall intensity levels over different rainfall return periods: 57.8 mm/h over 10 years, 78.5 mm/h over 50 years, 87.3 mm/h over 100 years, and 107.5 mm/h over 500 years. Using our analysis model, which considers the ratios of saturated infiltration depth at different rainfall intensity levels, we identified four classes ranging from 0.0 to 1.3 based on changes in the ratios of saturated infiltration depth of the soil layers. The percentage of the 1st class areas (most vulnerable to landslides) increased with rainfall intensity, and the percentage of 4th class areas (least vulnerable to landslides) declined as rainfall intensity increased. The findings indicate the direct effect of changes in ratios of saturated infiltration depth of soil layers at different rainfall intensity levels on landslide vulnerability.

Keywords: Rainfall Return Period, Rainfall Intensity, Ratio of Saturated Infiltration Depth, Landslide Vulnerability

Introduction

The internal factors that affect landslides are geological features, topography, ground (soil), and forest covers, whereas the external factors are rainfall and earthquakes. These factors must be considered in a landslide vulnerability assessment. Many researchers have previously analyzed the mechanisms of landslides and debris flow and used the findings to assess landslide / debris flow vulnerability and risks (Ko et al., 2014; Paola et al., 2015). Researchers have also predicted the areas to be affected by landslides by analyzing correlations among the factors. In addition to analyses based on correlations between rainfall events and landslide factors, other studies considered the factors affecting rainfall infiltration along with an infinite slope stability analysis model based on the limit equilibrium theory, which is one of the methods used to assess landslide vulnerability (Cha et al. 2011, Santoso et al. 2011, Ali et al. 2014).

It is widely understood that a landslide occurs when the pore water pressure increases within a soil layer because of a rainfall-induced increase in groundwater levels within unsaturated soil. However, in case of intense rainfall in a short period of time, the predominant cause of landslides is the weakening of the shear strength in the soil layer caused by an expansion of the wetting front caused by rainfall infiltration into the soil layer rather than a rise in groundwater levels. In Korea, most soil layers are thin (2 m or thinner). As such, landslide slopes are distributed in alignment with the behavior range of the wetting fronts within the soil layer caused by rainfall infiltration. For this reason, with regard to rainfall infiltration into an

unsaturated soil layer, the behavior range of the wetting front has the same meaning as the depth of saturated infiltration at which the soil layer becomes saturated. As such, in this study, we analyzed landslide vulnerability considering the ratios of saturated infiltration depth based on the wetting front behaviors within soil layers at different rainfall intensity levels for different rainfall return periods. Afterward, we used the findings to propose a landslide risk classification.

Method

The research area is 1,061 km^2–wide, of which 640 km^2 is covered by forests. The landslide hazard map provided by the Korea Forest Service (KFS) classifies 9.3% of the forest area as high-risk areas (1st grade) and 25.6% as risk areas (2nd grade). Between 2001 and 2018, the research area recorded a low landslide area at 0.49 km^2. Major landslide incidents in this area include the landslide caused by Typhoon "Chaba" in 2016, a ground subsidence caused by heavy rain in 2017, and a debris runout caused by Typhoon "Soulik" in 2018.

To assess landslide vulnerability based on space lattices, an infinite slope stability analysis model uses geological, topographic, and rainfall features. For the topographical factors, we derived slopes from the numerical topographic map provided by the National Geographic Information Institute and the soil layer depth information from the Forest Soil Map provided by the KFS. For the soil properties, we calculated the specific gravity, unit weight, cohesion, and internal friction angle of the soil through an on-site survey. We considered rainfall intensity levels for rainfall return periods of 10, 50, 100, and 500 years, using the Korea Probability Rainfall Information provided by the Ministry of Land, Infrastructure and Transport (MOLIT). We applied this data to our infinite slope stability analysis model to analyze the landslide vulnerability of the research area based on space lattices in the form of safety ranges. To elaborate on the safety criteria used in this study, we applied the construction slope design standard of the MOLIT, where the reference safety level during the rainy season is 1.3. Based on the safety levels identified for each lattice, areas with a safety level of 1.3 or higher were considered safe and excluded from the analysis as "null." We classified the areas with safety levels of 1.3 or lower into four risk classes (Figure 1).

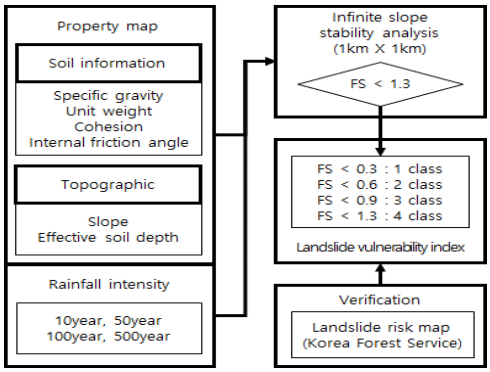

Figure 1. A flowchart of landslide vulnerability analysis at different rainfall intensity levels for different rainfall return periods

Calculation of Saturated Infiltration Depth Ratio of the Soil Layers at Different Rainfall Intensity

In this study, we used Equation (1), proposed by Chae et al. (2015), to apply a concept of saturated infiltration depth ratio that considers changes in the wetting front of the soil layer and calculates changes in safety levels under different rainfall conditions. We chose this method because the depth of the wetting front (Dwf) within the soil layer slope under different rainfall

conditions serves as a key variable with a significant impact on changes in safety levels, and the depth of the wetting front changes with rainfall intensity levels.

$$FS = \frac{C+cos\theta(1-H(t)r)tan\phi}{sin} \quad (1)$$

$$H(t) = \frac{Dwf}{D} \quad (2)$$

where, C is the cohesion ratio against the soil layer weight (dimensionless), θ is the slope angle, ϕ is the internal friction angle of the soil, $H(t)$ is the ratio of saturated infiltration depth of the soil layer over time, Dwf is the wetting front depth, and D is the soil layer.

Landslide Vulnerability Analysis at Different Soil Layer Saturated Infiltration Depth Ratios

Table 1 represents our findings on the landslide risk areas within the research area and safety classification at different rainfall intensity levels. The average area with landslide risk (safety level 1.3 or lower) is 410 km^2, which takes up around 64% of the total mountainous areas within the research area (640 km^2). The landslide risk area was the lowest at 402 km^2 at 10-year rainfall intensity and the highest at 415 km^{2}at 500-year intensity. However, the difference between them was only 13 km^2, which suggests that rainfall return periods do not significantly affect differences in landslide risk areas.

Table 1. Distribution of the percentages of landslide risk areas according to the safety classification calculated using the ratio of saturated infiltration depth of the soil layer for different rainfall return periods

Rainfall return period \ Landslide vulnerability index		1st Class (0.0<FS<0.3)	2nd Class (0.3<FS<0.6)	3rd Class (0.6<FS<0.9)	4th Class (0.9<FS<1.3)
Landslide risk area (km^2) (Percentage of landslide risk area per mountain area [%])	10-year (57.8 mm/h)	157 (24.5)	99 (15.5)	92 (14.4)	54 (8.4)
	50-year (78.5 mm/h)	261 (40.8)	82 (12.8)	49 (7.7)	20 (3.1)
	100-year (87.3 mm/h)	283 (44.2)	76 (11.9)	40 (6.3)	14 (2.2)
	500-year (107.5 mm/h)	325 (50.8)	60 (9.4)	24 (3.8)	6 (0.9)

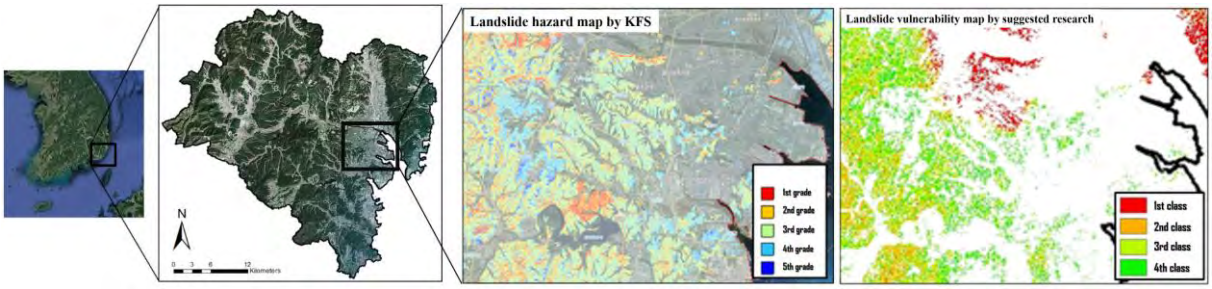

Figure 2. Comparison of the KFS landslide hazard map for the research area and the landslide vulnerability map based on the safety classification using the saturated infiltration depth ratio of the soil layer for different rainfall return periods

As shown in Table 1, the 1st class areas take up 157 km^2 at the 10-year rainfall intensity level, accounting for around 39% of the total area. However, the 1st class areas increase as the rainfall intensity rises; at the 500-year intensity level, the 1st class areas took up 78% of the total area at 325 km^2. On the contrary, at the 10-year rainfall intensity, the 4th class areas took up 54 km^2, whereas the total area of the 4th class areas was 6 km^2 at the 500-year intensity level. In particular, the 4th class areas relatively declined with the rainfall intensity level. These findings indicate that the results of the infinite slope stability analysis considering the ratios of saturated

infiltration depth of the soil layer were reasonably applied, as the safety levels decline as the rainfall intensity increases.
According to the KFS' landslide risk map for the research area (Figure 2), the high-risk areas (1st class) take up 9.3% of the total area, whereas the percentage of the risk areas (2nd class) is 25.6% (around 35% of the mountainous areas), which is similar to the percentage of landslide risk areas at the 10-year rainfall intensity level identified in this study (around 40%).

Conclusion

In this study, we analyzed landslide vulnerability based on safety levels using an infinite slope stability analysis model that considers the ratios of saturated infiltration depth in soil layers at different rainfall intensity levels. Around 64% of the mountainous areas in the research area were identified as highly vulnerable areas with a safety level of 1.3 or lower. The landslide risk areas increased along with the rainfall intensity. However, when we compared landslide risk areas at rainfall intensity levels for four different rainfall return periods, the difference was around 13 km^2, which does not represent a highly significant growth. This finding seems to be attributable to the fact that, when analyzing slope stability, the ground strength properties (cohesion, internal friction angle, etc.) have a greater impact than rainfall within the soil layers. In addition, our landslide risk classification based on the calculated safety levels showed that the risk areas increase as the rainfall intensity rises. We compared our findings with the KFS' landslide risk levels and obtained significant results indicating landslide vulnerability in 35%–40% of the mountainous areas. The findings suggest that useful landslide risk information can be derived from changes in landslide safety levels by considering the strength factors affecting soil layer stability along with the ratios of saturated infiltration depth in soil layers at different rainfall intensity levels during different rainfall return periods.

Acknowledgement

This research was supported by a grant(2022-MOIS61-001) of Development Risk Prediction Technology of Storm and Flood For Climate Change based on Artificial Intelligence funded by Ministry of Interior and Safety(MOIS, Korea).

References

Ali A, Huang J, Lyamin AV, Sloan SW, Griffiths DV, Cassidy MJ & Li JH (2014) Simplified quantitative risk assessment of rainfall-induced landslides modelled by infinite slopes, *Engineering Geology*, 179(4), 102-116.

Cha KS & Kim TH (2011) Evaluation of slope stability with topography and slope stability analysis method, *Journal of Civil Engineering*, 15(2), 251-256.

Chae BG, Lee JH, Park HJ & Choi JH (2015) A method for predicting the factor of safety of an infinite slope based on the depth ratio of the wetting front induced by rainfall infiltration, *Natural Hazards and Earth System Sciences*, 15, 1835-1849.

Ko SM, Lee SW, Yune CY & Kim GH (2014) Topographic analysis of Landslides in Umyeonsan, *Journal of the Korean Society of Surveying, Geodesy, Photogrammetry and Cartography*, 32(1), 55-62.

Paola P, Patrick B, Dennis MS, Jeffrey DS, Ramon A, Collin AB, Christopher C, Stephen BD, Nancy FG, Sara AK, Dimitri L, Harish S, Keelin S, David GT, Thad W & Joseph MW (2015) Analyzing high resolution topography for advancing the understanding of mass and energy transfer through landscapes: A review, *Earth-Science Reviews*, 148, 174-193.

Santoso AM, Phoon KK & Quek ST (2011) Effects of soil spatial variability on rainfall-induced landslides, *Computers & Structures*, 89(11-12), 893-900.

The optimal empirical relationships characterizing rock avalanche mobility

Alexander Strom[1]

[1] JSC "Hydroproject Institute", Moscow, Russia

SUMMARY: The most traditional way to characterize the abnormal mobility of rock avalanches quantitatively is the relationship between angle of reach (H/L) and debris volume (V). However, such regressions have rather low correlation (determination – R^2) coefficients, much lower than those of the regressions of just runout (L) on V. The highest R^2 values were derived for the regressions of the runout (L) and of rock avalanches' area, either total (source zone + transit zone + deposition zone = A_{total}), or just of the deposits (A_{dep}) on the $V \times H$ product. The latter is proportional to the potential energy released during rock avalanche motion. The strict meaning of height drop (H) that can be used in such analysis is discussed. Considering high R^2 values of the corresponding regressions, the $V \times H$ product appears to be an optimal input variable to predict the runout (L) or the area (A) of the anticipated rock avalanches.

Keywords: rock avalanche, potential energy, volume, height drop, runout

Introduction

The abnormal mobility of rock avalanches and its dependence from rock slope failure volume is the well-known phenomenon identified first by Albert Heim (1932). Numerous studies where devoted to find empirical relationships allowing to characterize such dependence and to predict the dimensions of the endangered zone that might be affected in case of rock avalanche formation (Sheidegger, 1973; Howard, 1973; Hsü, 1975; Davies,1982; Li, 1983; Shaller 1991; Nicoletti, Sorriso-Valvo, 1991; Corominas, 1996; Kilburn, Sørensen, 1998; Legros, 2002; 2006; Hungr, 2006; Iverson 2006; Griswold, Iverson, 2008; Strom, Abdrakhmatov, 2018; Strom et al. 2019; Wen, Guan, 2022). In most of these studies the relationships between failure volume (V) and the angle of reach (fahrboschung) defined as height drop to runout ratio (H/L) were analysed. The H/L ratio has been considered as a variable, characterising rock avalanche mobility. The height drop is defined as elevation difference between headscarp crown and the deposit's tip (H_1 or H_2 in Fig. 1; hereafter marked as H_{tip}); the runout – as a horizontal projection of the distance between these points measured along the central line of the travel path (L_1 or L_2 in Fig. 1) (Li et al., 2022); volume is an independent input variable.

In 2002 F. Legros demonstrated that the regression of just L on V has much higher correlation coefficient than that of H_{tip}/L on V and, thus, such relationships have much higher predictive reliability if failure volume is known beforehand. This conclusion was confirmed in (Strom, Abdrakhmatov, 2018; Strom et al., 2019) based in the analysis of the Central Asian rockslide and rock avalanche database that includes 500 cases for which the required quantitative parameters have been measured. The latter analysis was performed separately for unconfined, laterally confined and frontally confined rock avalanches and determination coefficients R^2 of $L \div V$ regressions appeared to be about two timed larger than those of the $H_{tip}/L \div V$ regressions. But is volume really the best input parameter to predict dimensions of the zone that might be affected by rock avalanche?

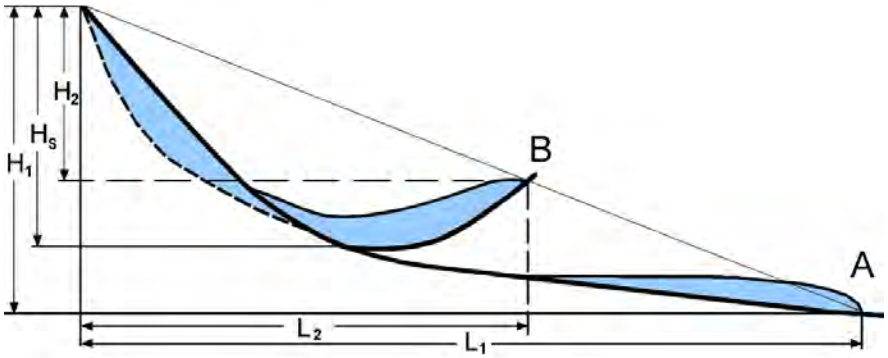

Figure 1. The schematic profiles of rock avalanches. A – unconfined and laterally confined; B – frontally confined. $L_{1,2}$ - runout; $H_{1,2}$ - height drop (H_{tip}); H_s - source zone height

Effect of the potential energy on rock avalanche mobility

Value of the correlation coefficient or of the more commonly used determination coefficient (R^2) should be considered as a good indicator of the physical meaning of the regressions in question. Thus, regressions with higher R^2 value allow better prediction of the required parameters, in our case of those characterizing size of the rock avalanche affected zone. It was found (Strom, Abdrakhmatov, 2018; Strom et al., 2019) that regressions of the A_{total} on the product of $V \times H_{max}$, where A_{total} is the total affected area (headscarp + transition zone + depositional zone measured in plan view), V – is volume, H_{max} (maximal height drop) is equal to H_1 in Fig. 1-A and to H_s in Fig. 1-B, have the highest R^2 values exceeding 0.92. High R^2 values were derived also for the regressions of A_{dep} (area just of rock avalanche deposits; R^2 >0.9) and of L (runout; R^2 >0.8) on the $V \times H_{max}$, except the regression of L on $V \times H_{max}$ for laterally confined rock avalanches that appeared to be unexpectedly low (R^2 ~0.05). All there regressions were derived separately for rock avalanches that moved in unconfined, laterally confined and frontally confined conditions.

So good correlations have logical physical explanation since the $V \times H$ product is proportional to the potential energy (E_{pot}) of the rock mass involved into slope failure, which is the main, if not the only source of energy released during rock avalanche motion. Additional kinetic energy (E_{kin}) that can be supplied for it by seismic shaking is negligible (Strom, Abdrakhmatov, 2018). It can be demonstrated easily by comparison of the potential energy of the unit mass (m) resting on a slope 100 m high or higher ($E_{pot}=m \times g \times H;\ H \geq 100\ m$) with the kinetic energy that can be supplied to the same unit mass ($E_{kin}=m \times v^2/2$), considering the typical mass velocities (v) caused by the strong motion of large earthquakes that are of the order of 1-3 m/sec (Aptikaev, 2012). For the unit mass (m=1) E_{pot} is of the order of 10^3-10^4, while E_{kin} – of the order of 10^{-1}-10^1. It is also quite unlikely that large rock mass can be "pushed" by sudden release of the tectonic or gravitational stress, because high stress level that really exist in the Earth crust below regional erosional level cannot retain within the upper parts of the mountain ridges subjected to the millennia-long erosion and unloading.

The mechanical process evolving during rock avalanche motion, as well as during motion of a landslide of any type, can be described, in general, as transformation of the potential energy of a rock/soil mass located at high position on a slope ($E_{pot}=V \times \rho \times g \times H$) into kinetic energy of moving mass (E_{kin}). Here V is failure volume, ρ – rock mass density, g – gravity acceleration. The exact definition of H will be described later. Though volume (V) that can be measured, and, the more so, predicted with rather low accuracy, it ranges for more than 6 orders of magnitude within the entire Central Asian database – from ca.10^5 m^3 to 10^{10} m^3. Such variability makes

the low accuracy of its estimate acceptable. The parameters that can be ascribed as *'H' (H_{tip}, H_{max}, H_s)* vary for less than 2 orders of magnitude only – from few hundred meters to more than three kilometres. Rock mass density (ρ) for the most widespread types of rocks vary within quite narrow range and, therefore, along with the gravity acceleration (g) can be considered as constant values. Due to the approximate constancy of 'ρ' and 'g', the equation ($E_{pot}=V\times\rho\times g\times H$) can be simplified to the statement that the potential energy is proportional to the $V\times H$ product ($E_{pot}\div V\times H$).

Considering high R^2 values of the corresponding regressions, the $V\times H_{max}$ product appears to be an optimal predicated variable to estimate such parameters as runout (L) or the affected area (A) of the anticipated rock avalanches.

Preferable meaning of the height drop

As it was shown above, while volume (V) can be defined univocally regardless of its assessment accuracy, the height drop (H) can have different meanings. For the events that had occurred already it can be considered either as H_{tip}, or as H_{max} that differ significantly depending on the confinement conditions (see Fig. 1). Besides, H_{tip} cannot be predicted before the rock avalanche occurrence – we know neither how far could it spread in plan view, nor how low it could move downslope or down the valley in unconfined or laterally confined conditions, nor how high it could climb upslope in case of frontal confinement. The same is for the H_{max}, of the unconfined and laterally confined events. Thus, for the predictive purpose it is better to use the source slope height (H_s in Fig. 1) that can be defined as the elevation difference between the real or anticipated headscarp crown and the foot of the steep slope and can be estimated prior to the slope failure regardless of the confinement conditions.

Some researchers analyzed vertical descent of the center of mass (e.g., Adushkin, 2006), but it's both initial and final positions are difficult to measure unlike the altitude of the anticipated headscarp crown and of the slope base, and, thus, use of the center of mass descent could introduce significant additional error.

It was found that all regressions of L, or A_{total}, or A_{dep} on $V\times H_s$ product have high determination coefficients R^2 without any exceptions ($R^2 > 0.9$ for A_{total}, $R^2 > 0.88$ for A_{dep}, and $R^2 > 0.73$ for L) that means that they can be really used to predict the dimensions of the zones that might be affected by the assumed rock avalanches and, thus can provide valuable information on the exposure required for risk assessment (Corominas et al., 2014).

Conclusions

Analysis of the Central Asian rockslide / rock avalanche database (Strom, Abdrakhmatov, 2018) performed separately for rock avalanches in different confinement conditions (332 frontally confined, 92 laterally confined and 76 unconfined cases) revealed that parameters characterizing their mobility, such as runout (L), total affected area (A_{total}), and area of the deposits (A_{dep}) correlate in the best way with the product of $V\times H_{max}$ or of $V\times H_s$. Both products are somehow proportional to the potential energy released during rock avalanche motion. Such regressions have highest R^2 values and reflect physically meaningful relationships between the required parameters that can be used for rock avalanche hazard and risk assessment and those that can be predicted with reasonable accuracy prior to the catastrophic rock slope failure.

It should be pointed out that, to my knowledge, correlations of rock avalanche runout (L) and area (A) with $V \times H$ product have not been used before, despite its obviousness and physical sense.

References

Adushkin VV (2006) Mobility of rock avalanches triggered by underground nuclear explosions. In: Evans SG, Scarascia Mugnozza G, Strom A, Hermanns RL (eds) *Landslides from massive rock slope failure.* NATO science series: IV: earth and environmental sciences. 49. Springer, New York, pp 267–284.

Aptikaev FF (2012) *Instrumental seismic intensity scale*. Moscow, 175 p. (in Russian). ISBN: 978-5-906235-02-2

Corominas J (1996) The angle of reach as a mobility index for small and large landslides. *Canadian Geotechnical Journal* 33, 260–271.

Corominas J, van Westen C, Frattini P, Cascini L, Malet J-P, Fotopoulou S, Catani F, Van Den Eeckhaut M, Mavrouli O, Agliardi F, Pitilakis K, Winter MG, Pastor M, Ferlisi S, Tofani V, Hervás J, Smith JT (2014) Recommendations for the quantitative analysis of landslide risk. *Bull. Eng. Geol. Environ.* 73, 209–263.

Davies TR (1982) Spreading of rock avalanche debris by mechanical fluidization. *Rock Mechanics,* 15, 9–24.

Griswold JP, Iverson RM (2008) Mobility statistics and automated hazard mapping for debris flows and rock avalanches (ver. 1.1, April 2014): *U.S. Geol. Survey Scientific Investigations Report 2007–5276*, 1–59.

Heim A (1932) *Bergsturz und Menschenleben*. Fretz and Wasmuth, Zurich.

Howard K (1973) Avalanche mode of motion: implications from lunar examples. *Science, New Series,* 180, 1052–1055.

Hsü KJ (1975) Catastrophic debris streams (sturzstroms) generated by rock falls. *Geol. Soc. Am. Bull*. 86,129–140.

Hungr O (2006) Rock avalanche occurrence, process and modelling. In: Evans SG, Scarascia Mugnozza G, Strom A, Hermanns RL (eds) *Landslides from massive rock slope failure. NATO science series*: IV: earth and environmental sciences, 49. Springer, New York, 243–266.

Iverson RM (2006) Forecasting runout of rock and debris avalanches. In: Evans SG, Scarascia Mugnozza G, Strom A, Hermanns RL (eds) *Landslides from massive rock slope failure. NATO science series*: IV: earth and environmental sciences, 49. Springer, New York, 197–209.

Kilburn CRJ, Sørensen S-A (1998) Runout length of sturzstroms: the control of initial conditions and of fragment dynamics. *J Geophys Res* 103B, 17877–17884.

Legros F (2002) The mobility of long-runout landslides. *Engineering Geology* 63, 301–331.

Legros F (2006) Landslide mobility and the role of water. In: Evans SG, Scarascia Mugnozza G, Strom A, Hermanns RL (eds) *Landslides from massive rock slope failure. NATO science series*: IV: earth and environmental sciences, 49. Springer, New York, 233–242.

Li L, Lan H, Strom A, Macciotta R (2022) Landslide length, width, and aspect ratio: path-dependent measurement and a revisit of nomenclature. *Landslides*, 19, 3009–3029, https://doi.org/10.1007/s10346-022-01935-2.

Li T (1983) A mathematical model for predicting the extent of a major rockfall. *Z. Geomorphol.* 27, 473–482.

Nicoletti PG, Sorriso-Valvo M (1991) Geomorphic controls of the shape and mobilily of rock avalanches. *Geol. Soc. Am. Bull.* 103, 1365–1373.

Shaller PJ (1991) *Analysis and implications of large Martian and terrestrial landslides*. Ph.D. Thesis. California Institute of Technology.

Sheidegger AE (1973) On the prediction of the reach and velocity of catastrophic landslides. *Rock Mechanics,* 5, 231–236.

Strom AL (2022) Prediction of the dimensions of rock avalanches' affected areas based on the empirical relationships. *Georisk*, XVI, No 2, 8–20 (in Russian), https://doi.org/10.25296/1997-8669-2022-16-2-8-20.

Strom A, Abdrakhmatov K (2018) *Rockslides and rock avalanches of Central Asia: distribution, morphology, and internal structure*. Elsevier. ISBN: 978-0-12-803204-6

Strom A, Li L, Lan H (2019) Rock avalanche mobility: optimal characterization and the effects of confinement. *Landslides*, 16, 1437−1452.

Wen B, Guan L (2022) A re-examination of the factors controlling mobility of large rock avalanches. *Bull. Eng. Geol. Environ.,* 81, 356 https://doi.org/10.1007/s10064-022-02851-4.

Field Monitoring of the Unsaturated Characteristics in a Mine Waste-Dump Slope during Rainfall

Song, Young-Suk[1], Park, Joon-Young[1]

[1] Korea Institute of Geoscience and Mineral Resources, Daejeon, South Korea

SUMMARY: Field measurement units and a system were constructed and installed in a waste-dump slope at the Imgi mine to investigate and analyze the variations in the unsaturated characteristics of the soil. The rainfall, matric suction, and volumetric water content were continuously measured from the units at the instrumented site and analyzed with the soil water characteristic curve (SWCC) estimated from laboratory experiments. The variations in matric suction and volumetric water content were primarily affected by the rainfall intensity. At the surface of the slope, the largest increase and decrease in matric suction and volumetric water content, respectively, were observed during the wetting and drying processes. The matric suction and volumetric water content measured from the instrumented area were compared with the SWCCs obtained from the laboratory test, and the measured data were collected between the drying and wetting paths. The drying and wetting paths obtained from the laboratory test are regarded as primary drying and wetting curves, respectively. Therefore, the measured data can be defined as scanning curves, which are located between the primary drying and wetting curves.

Keywords: field monitoring, waste-dump slope, matric suction, volumetric water content, soil water characteristic curve

Introduction

To investigate the variations in the unsaturated features of a waste-dump slope at the Imgi mine in Busan, South Korea, resulting from rainfall, field measurement units and a system for the unsaturated soil of the slope were designed and installed at the site. The unsaturated characteristics of a mine waste-dump slope were thoroughly analyzed based on monitoring data, including the amount of rainfall, matric suction and volumetric water content. Additionally, the relationships between the SWCC estimated from laboratory experiments and the observed data were investigated.

Field Instrumentation

The mine waste-dump slope was located in Imgi-ri, Busan, South Korea. Since the mine was abandoned, there has been no specific plan for preventing environmental damage by the mine; thus, the surface of the mine waste-dump slope was lost by erosion and seepage erosion. In this area, rainfall infiltration and unsaturated soil movement were measured during rainfall events using a field instrumentation system. Figure 1 shows the instrumented slope used to monitor the unsaturated soil features. The tensiometer and TDR were installed in the middle of the slope to measure the changes in matric suction and volumetric water content during rainfall. In particular, tensiometers and the TDR were placed at depths of 0.5, 1.0, and 1.5 m to observe the behavior of the wet front and the variations in matric suction and volumetric water content

according to depth during rainfall. A tipping-bucket rain gauge was installed to measure the rainfall amount at the site. A data acquisition system (DAS) and solar system were used to collect and transmit the field monitoring data.

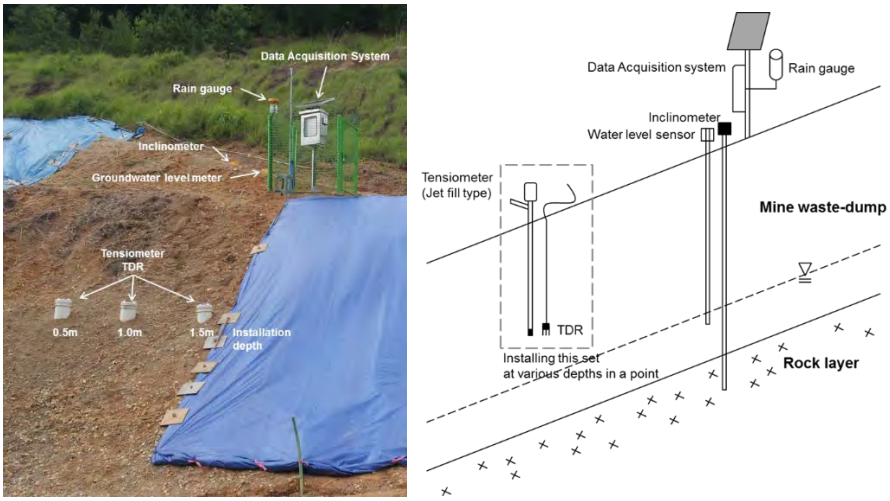

Figure 1. Schematic diagram of the installation of the measuring devices

Engineering properties of mine tailings

Several laboratory tests, including unit weight and grain size analysis, were performed to determine the engineering properties of the mine waste tailings at the Imgi mine. According to the Unified Soil Classification System, the sample was silty sand (SM), and the field dry unit weight was 1.594 t/m^3. Figure 2 displays the grain size distribution curve of the mine tailings.

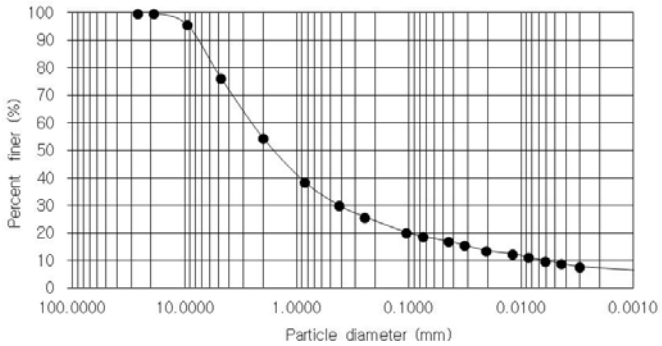

Figure 2. Grain size distribution curve of the mine tailings

The SWCCs of unsaturated mine waste tailings were estimated by an automated SWCC apparatus (Song et al. 2012). The parameters α, n, and m in the model proposed by van Genuchten (1980) were calculated based on a nonlinear least squares analysis between matric suction and volumetric water content. The SWCC for mine waste dump slope tailings in the drying and wetting paths was estimated based on the parameters in Table 1 (Song et al., 2014).

Table 1. Best curve-fitting parameters of the SWCC from the van Genuchten model (Song et al., 2014)

Path	α (kPa^{-1})	n	m	R^2
Drying	0.180	1.811	0.448	0.994
Wetting	0.787	1.670	0.401	0.998

Measurement results and analysis of unsaturated characteristics

Figure 3 represents the variation in volumetric water content at different depths according to rainfall intensity. The volumetric water content was strongly influenced by the rainfall intensity. The volumetric water content increased as a result of rainfall infiltration during the wetting period and decreased during the drying period. For rainfall, the volumetric water content was the highest at the surface and decreased with depth. However, for the drying period, the highest volumetric water content was observed at a depth of 1.0 m, while the volumetric water content was the lowest at a depth of 0.5 m. The primary reason that the lowest volumetric water content was measured at a depth of 0.5 m appeared to be that evaporation at the surface can result in a decrease in volumetric water content (Rahardjo et al. 2013). In other words, the variation range in volumetric water content was the largest between the surface and a depth of 0.5 m for both the drying and wetting periods, and the amount of variation was approximately 10%. The variations in matric suction measured by the tensiometers at different depths are shown in Figure 4. The matric suction was also affected by the rainfall intensity. The pattern of variation in matric suction was the same as that of the volumetric water content. The maximum amount of variation in matric suction for the drying and wetting periods was approximately 40 kPa.

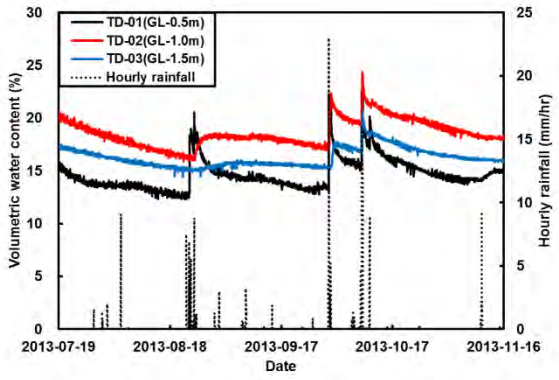

Figure 3. Variation in volumetric water content at different depths according to rainfall intensity

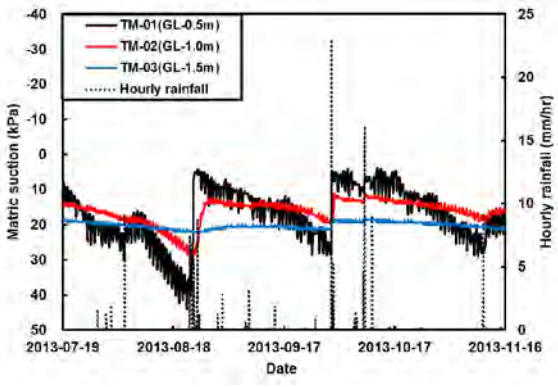

Figure 4. Variation in matric suction at different depths according to rainfall intensity

In general, the stress state of unsaturated soil can be simply predicted based on the estimated SWCC. The estimated SWCC, the measured matric suction, and the observed volumetric water content at different depths are plotted together in Figure 5. All the measured matric suction and volumetric water content data are located below the drying path of the estimated SWCC. In particular, the measured data are located between the drying and wetting paths of the estimated SWCC. The drying and wetting paths obtained from laboratory tests are regarded as primary drying and wetting curves, respectively, as proposed by Feng and Fredlund (1999) and Muraleetharan et al. (2009). As shown in the figure, the measured values at a depth of 0.5 m in the field, which can be regarded as a scanning curve between primary curves, seem to coincide with the primary wetting curve obtained from the laboratory. The results show that the characteristics of unsaturated soil near the ground surface are strongly associated with the primary wetting curve. Therefore, the relationship between matric suction and volumetric water content measured near the ground surface might be similar to the primary wetting curve of the estimated SWCC in the laboratory.

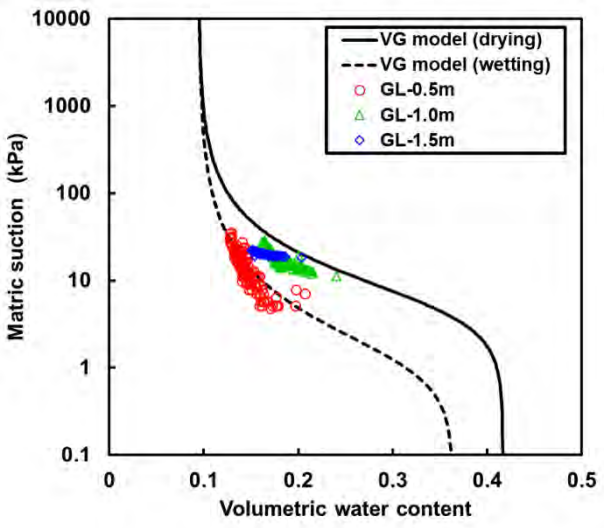

Figure 5. Relationship between matric suction and volumetric water content

Conclusions

To analyze the variations in the unsaturated features of a waste-dump slope at the Imgi mine according to rainfall infiltration, a field measurement system for the unsaturated soil of the slope was installed at the site. During rainfall, the variations in matric suction and volumetric water content were influenced by rainfall intensity. All of the matric suction and volumetric water content values measured in the field were located below the drying path of the SWCC estimated from the laboratory test. In particular, the measured values were located between the drying and wetting paths of the estimated SWCC. The measured data with a nonlinear relationship between matric suction and volumetric water content can be defined as scanning curves, which are located between the primary drying and wetting curves. In particular, the characteristics of unsaturated soil near the ground surface are strongly associated with the primary wetting curve.

Acknowledgment

This research was supported by Basic Research Project of Korea Institute of Geoscience and Mineral Resources (KIGAM) funded by the Ministry of Science and ICT of Korea.

References

Rahardjo H, Satyanaga A & Leong E (2013) Effects of flux boundary conditions on pore-water pressure distribution in slope. *Engineering Geology* 165, 133-142.

Feng M & Fredlund DG (1999) Hysteretic influence associated with thermal conductivity sensor measurements. *Proceedings of Theory to the Practice of Unsaturated Soil Mechanics, in association with 52nd Canadian Geotechnical Conference and the Unsaturated Soil Group*, Regina, Canada, pp. 14:2:14-14:2:20

Song YS, Hwang WK, Jung SJ & Kim TH (2012) A comparative study of suction stress between sand and silt under unsaturated conditions. *Engineering Geology* 124, 90-97.

Song YS, Kim KS, Jeong SW & Lee CO (2014) Estimation on unsaturated characteristic curves of tailings obtained from waste dump of Imgi mine in Busan, *Journal of the Korean Geotechnical Society* 30(3), 47-58. (in Korean with English Abstract)

Muraleetharan KK, Liu C, Wei C, Kibbey TCG & Chen L (2009) An elastoplatic framework for coupling hydraulic and mechanical behavior of unsaturated soils. *International Journal of Plasticity* 25, 473-490.

Rock Avalanche Risk Assessment at Mount Currie, British Columbia, Canada

Marc-André. Brideau[1], Matthieu Sturzenegger[1], Jordan Aaron[3], Sarah Kimball[1], Kris Holm[1]

[1] BGC Engineering Inc., Canada
[2] ETH Zürich, Switzerland

SUMMARY: Mount Currie is located near the village of Pemberton in southwestern British Columbia, Canada. A geohazard assessment based on landslide activity level, kinematics, and volume estimate identified four main potential rock avalanche sources. Numerical models estimated potential rock avalanche travel distance and the extent of associated landslide dam flooding. A risk assessment identified and characterized elements potentially exposed to the geohazard scenarios. These included people, buildings, critical facilities, business activities, power and communication lines. While there is considerable uncertainty in the risk estimates, the results indicate that rock avalanche hazards from Mount Currie pose risks that likely exceed individual and group tolerance criteria adopted by other jurisdictions in Western Canada.

Keywords: Rock avalanche, runout modelling, landslide dammed lake, risk assessment

Introduction

Following a series of larger than usual rock fall events from Mount Currie in 2015 and 2016, a rock avalanche risk assessment was commissioned by Squamish Lillooet Regional District (SLRD) (BGC, 2018). Mount Currie is located immediately south of the village of Pemberton and the hamlet of Mount Currie in southwestern British Columbia (Figure 1). The mountain range is delimited to the north by the Lillooet River Valley, to the west and northwest by Green River Valley, and to the southeast by Gravell Creek. Mount Currie's rugged topography and geology contribute to the occurrence of a range of landslide types.

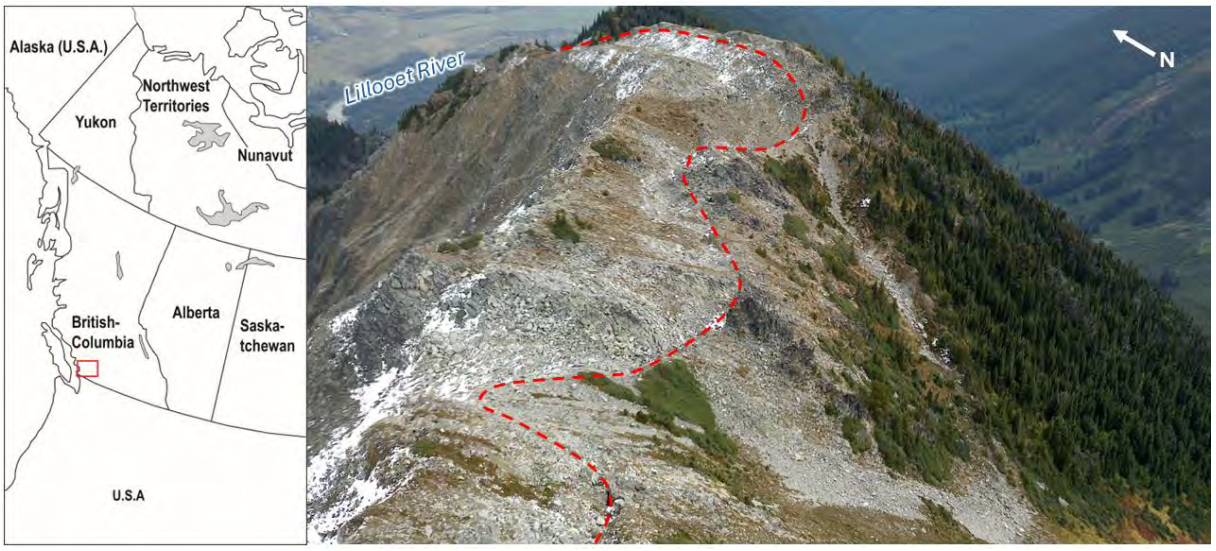

Figure 1. Location map and overview of potential rock avalanche source 1. Dashed red line highlights main down dropped block.

The main rock type in the study area is a fine- to medium-grained diorite. The diorite has a well-developed foliation which dips steeply into the slope. Volcanic rocks are present at the eastern end of Mount Currie ridge. Two northwest-southeast trending faults have been previously mapped along Mount Currie ridge.

Hazard Assessment

Review of previous studies (Evans, 1987; Bovis and Evans, 1995), historical aerial photographs, and newly acquired lidar data along with fieldwork informed geomorphic mapping of the study area. The mapping identified various geohazards, their locations, magnitude, runout extents, and factors contributing to slope instability. The geohazards identified include snow avalanches, rock falls, debris flows, debris slides, rock avalanches, landslide damming and associated flooding. Although no direct evidence of previous rock avalanche events was found on the floodplain or through seismic surveys, structural mapping and rock slope activity on Mount Currie suggested that rock avalanches and their associated secondary hazards (landslide dam and flooding) should be considered a risk to infrastructure and people north of the Green River (Figure 2).

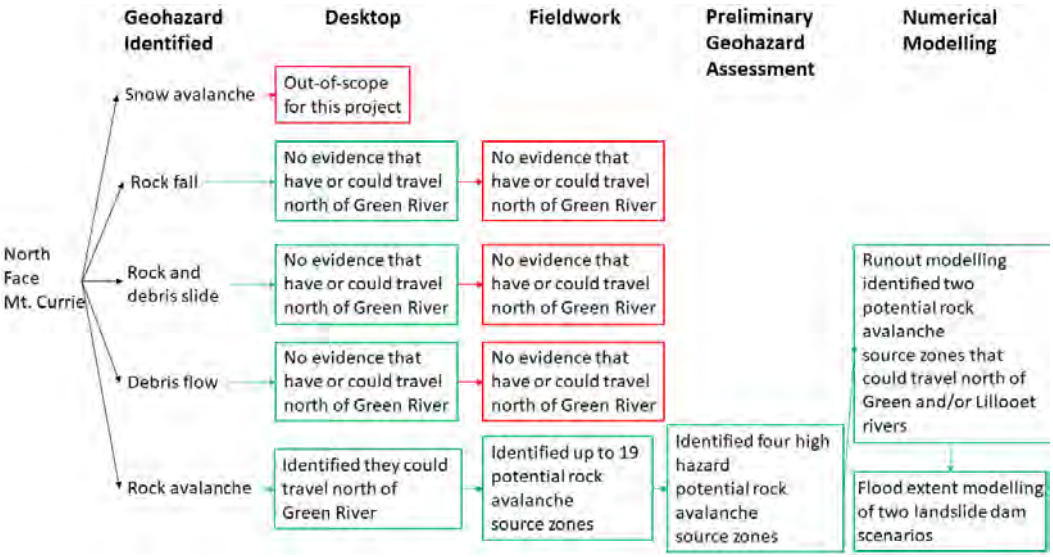

Figure2. Summary diagram outlining which geohazard scenarios were identified and which were analysed in each step of the geohazard analysis.

Thirty-one past rock avalanche events were mapped in a regional inventory completed within a 4,900 km^2 area centered on Mount Currie. The number of rock avalanche events were normalized by time (the last 10,000 years – post-deglaciation rock avalanches have well-defined deposit) and space (only areas with slope gradient greater than 20° from the inventory area). The estimate of the rock avalanche frequency during the last 10,000 years for the inventory area is one rock avalanche per 105 km^2 (i.e., 9.5 * 10^{-7} rock avalanche per year per km^2). This regional estimate of rock avalanche frequency was augmented with structural data, landslide activity, and permafrost observations to arrive at rock avalanche frequency estimate specific to Mount Currie, using the methodology in Oppikofer et al. (2018). This estimated mean rock avalanche frequency compares favourably to the estimate obtained by applying the Norwegian hazard and risk assessment methodology (Hermanns et al. 2012) to the project area.

Potential rock avalanches initiating from Mount Currie are expected to travel at over 100 km/hr and involve volumes up to approximately 8 million m^3 of material. The 3D dynamic runout

model DAN3D (McDougall and Hungr, 2004) was used to estimate potential rock avalanche impact areas. Additionally, potential splash zones (liquefied and displaced floodplain material that can often surround rock avalanche deposits) were estimated based on published values (Figure 3). The hydrodynamic modelling software package *TELEMAC* (Hervouet and Bates 2000) was then used to model the flooding associated with potential landslide blocking of the Green and Lillooet rivers. The numerical models showed that two of the four potential rock avalanche sources have the potential to affect areas on the north side of Green River.

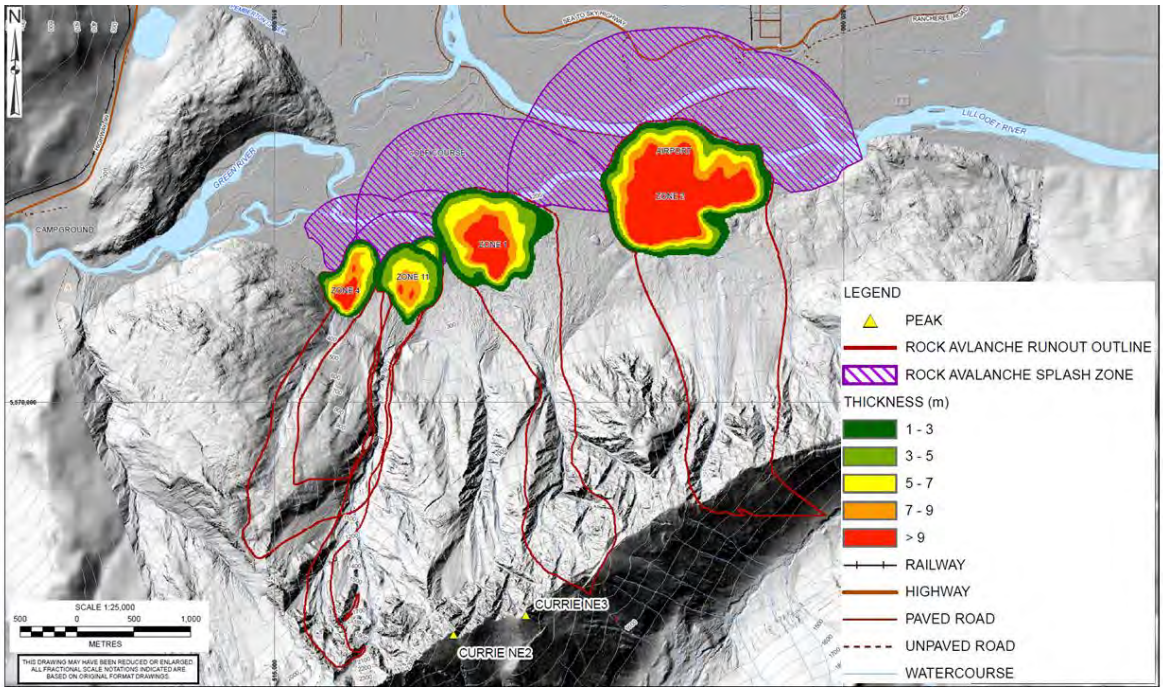

Figure 3. Modelled rock avalanche deposit and estimated splash zone for four scenarios.

Risk Assessment

Risk is a measure of the probability and severity of an adverse effect to health, property or the environment, and is estimated by the product of hazard probability (or likelihood) and consequences (vanDine, 2012). The identified elements exposed to rock avalanche (and associated secondary hazards) north of the Green River included people, buildings, critical facilities, business activities, power and communication lines. Risk was assessed for direct impact of a rock avalanche. Assessment of landslide dam flood scenarios on Green and Lillooet rivers included identification of exposed critical infrastructure, dwellings with higher life safety vulnerability, and estimation of building damage costs.

The rock avalanche risk was calculated for an individual person and for groups of people and compared to risk tolerance criteria developed for other jurisdictions in Western Canada. Occupants in up to 15 parcels could be exposed to risks that exceed individual risk tolerance criteria. For the group risk, depending on the rock avalanche scenario and a climate sensitivity analysis, the results indicated the risk could range from tolerable to unacceptable.

For the landslide dam flooding hazard, the water depth is expected to increase over minutes to hours allowing for people to respond to the hazard. This response is difficult to quantify as it varies in different sections of the valley (due to different road networks providing exit routes) and it varies in time (whether the flooding occurs during the day or night, summer or winter).

Furthermore, the timing and location of a breach of a landslide dam are difficult to quantify. Approximately 160 buildings were identified as being potentially impacted by flooding associated with one of the rock avalanche scenarios.

Preliminary economic loss estimates were provided in association with direct impact and flooding for building damage (between $1.6 million and $16 million depending on the rock avalanche scenario) and business activity (between $2 million and $31.5 million depending on the rock avalanche scenario). Critical infrastructure and lifelines potentially affected by rock avalanche direct impact or flooding include the wastewater treatment plan and various water and sewer infrastructure (i.e. mains and lift stations), search & rescue base, and wildfire response base.

Conclusions and Recommendations

Mount Currie's geomorphology and geology lends itself to landsliding and particularly rock avalanches that can travel and impact developed areas. Numerical modelling results suggest that two rock avalanche scenarios have the potential to affect areas on the north side of Green River. A splash zone was also considered in front of the modelled main rock avalanche deposits. Although there is considerable uncertainty in the risk estimates, the results of the study indicate that rock avalanche hazards from Mount Currie pose risks that likely exceed individual and group tolerance criteria adopted by other jurisdictions in Western Canada. Given the uncertainties and potential risks, additional investigation, analysis, and implementation of a monitoring system likely represents the most practical and cost-effective approach to risk management.

Acknowledgements

This project benefited immensely from contributions by our colleague and friend Matthias Jakob who passed away in October 2022. The consulting report from which this extended abstract is based on can be found at https://www.slrd.bc.ca/emergency-program/hazard-reports-information/local-hazard-reports/mount-currie-landslide-hazard.

References

Australian Geomechanics Society (AGS) (2007) Guideline for landslide susceptibility, hazard and risk zoning for land use management. *Australian Geomechanics* 42 (1): 13-36.

BGC Engineering (BGC) (2018) Mount Currie Landslide Risk Assessment. submitted to the Squamish-Lillooet Regional District.

Bovis, M.J. and Evans, S.G (1995) Rock slope movements along the Mount Currie "fault scarp", southern Coast Mountains, British Columbia. *Canadian Journal of Earth Sciences* 32: 2015 – 2020.

Evans, S.G (1987) Surface displacement and massive toppling on the northeast ridge of Mount Currie, British Columbia. *In: Current Research, Part A. Geological Survey of Canada, Paper 87-1A*: 181 – 189.

Hermanns, R.L., Oppikofer, T., Anda, E., Blikra, L.H., Bohme, M., Bunkholt, G., Crosta, G.B., Dahle, H., Devoli, G., Fischer, L., Jaboyedoff, M., Loew Simon, Saetre, S., Yugsi Molina, F (2012) Recommended hazard and risk classification system for large unstable rock slopes in Norway. Prepared by Norges geologiske undersokelse, Report Number 2012.029.

Hervouet, J.M., Bates, P., (2000) The TELEMAC modelling system, Special Issue. *Hydrological Process.* 14 (13), 2207–2363.

McDougall, S., Hungr, O (2004) A model for the analysis of rapid landslide motion across three-dimensional terrain. *Canadian Geotechnical Journal* 41: 1084-1097.

Oppikofer, T., Hermanns, R., Jaboyedoff, M., Brideau, M.-A., Jakob, M., Sturzenegger, M (2018) Comparison between three rock slope hazard assessment methodologies using a case study from Norway. *Proceedings of the Geohazards 7 Conference*. Canmore, Canada. Paper 205, 8 p.

VanDine, D (2012) Risk management - Canadian technical guidelines and best practices related to landslides: a national initiative for loss reduction. *Geological Survey of Canada, Open File 6996.*

Online geographical early warning system for gravitational hazard

Héloïse Cadet[1], David Rouquet[2], Anne Lescurier[3]

[1] SAGE ingénierie, Grenoble, France
[2] Tétras Libre, Grenoble, France
[3] Département Savoie, Chambéry, France

SUMMARY: We developed an experimental early-warning system called SIGALE (System of Information Geographic for grAvitational hazard vigiLancE assessment) to manage gravitational hazard occurrence. A landslides and rockfalls database has been consciously built for the Savoie area (French Alps), feeding Artificial Intelligence algorithms used to predict forthcoming events. This experimental geographical early-warning system is easily accessible via an experimental web-service and represents a decision-support tool for stakeholders.

Keywords: geographical early-warning system, web-service, landslide, rockfall

Introduction

Over the last decades, gravitational hazards caused significant economic losses and fatalities in mountainous areas. Thus, there is a need to enhance the protection of the stakes. early-warning systems are one of the possible approaches for such issue.
SIGALE project aims at developing an experimental early-warning system of gravitational hazard (landslide and rockfall) potentially affecting the road infrastructure network of the Savoie department (Alps, France). This network represents about 3, 300 km, managed by the CD73 (Savoie department) and the DIR-CE (Direction Interdépartementale des Routes Centre-Est). The terminology used further in this article, is based on Guzzetti et al. (2020). We propose a new approach based on machine learning to predict a vigilance level. The vigilance level is a combination of a susceptibility model and a trigger model. The vigilance level is defined separately for both landslide and rockfall hazards.

Landslide vigilance level

We built the susceptibility and trigger models based on a landslide event database (LDB) of 863 landslide occurrences along the road dating back from 2008 to 2020.
Landslide susceptibility model
The landslide susceptibility model is based on three parameters: i) the slope computed on topographical data with 20 m resolution, ii) the landcover from the Corine Land Cover and iii) a simplified lithology based on geological map of BRGM (French geological institute). Other parameters (aspect, slopes over other resolutions) have been tested and rejected because of their lower capacity to explain the landslide occurrence. The statistically-based landslide susceptibility assessment methodology has been inspired by Wilde et al. 2018. A landslide susceptibility index (LSI) has been computed for each point t on the road (1st version in Cadet et al. 2022):

$$LSI\ (t) = \sum_{j=1}^{3} \omega_j x_{ij} \quad (1)$$

- j: controlling parameter: slope (j=1), Corine land cover (j=2) or lithology (j=3)
- wj: weight of the parameter j
- xij: weight of category i depending on location t and parameter j

In order to equilibrate the unbalanced dataset, we defined an artificial database (ADB) composed of the 863 events and of a thousand road points randomly selected over the 37 076 points defined along the road every 100 m. The 37 076 points are called the non-event database (NEDB). The ADB is used to compute correlation coefficients of the three controlling parameters to characterize event versus non-event. The w_j weights are the normalized correlation coefficients (i.e. the sum of the weights equals 1).
The histograms of the three controlling parameters are computed for both event database LDB and non-event database NEDB. For each category the histogram values ratio of the LDB over the NEDB is computed. The x_{ij} weight of category i comes from the normalisation of those ratios: $\sum_{i=1}^{n(j)} x_{ij} = 1$, with n(j=1)=6; n(j=2)=14, n(j=3)=10.
The area under the curve (AUC) of the Roc-curve (Figure 1) is 87%, higher than the first version (Cadet et al. 2022) and higher than ELSUS2 with 68% for mountainous area (Wilde et al 2018). 5,028 homogenous (in term of landslide susceptibility) sectors were defined by gathering road points with close LSI. The LSI by sector is the median value of the LSI of the points included into the sector. Finally, LSI by sector is normalised from 0 to 1 and four levels are defined:

- Low: LSI < 0.16 (it corresponds to the quantile 0.1)
- Moderate: 0.16 < LSI < 0.27 (quantiles 0.1 and 0.25)
- High: 0.27 < LSI < 0.6 (quantiles 0.25 and 0.5)
- Very high: LSI > 0.6

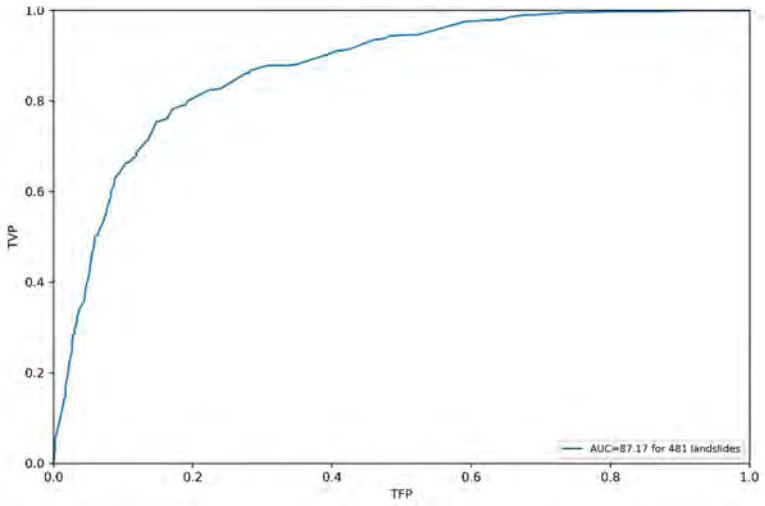

Figure 1. Roc curve for the LSI based on the LDB, applied to the ADB. The area under the curve (AUC) is 87%.

Landslide trigger model

The database covers 13 years (4,745 days) over 5,028 homogenous sectors covering the 3,300 km long Savoie road infrastructure. Thus, the 863 events are spread over 24 millions of spatio-temporal sectors. This represents a highly unbalanced dataset, non-events being 27 645 times more numerous than events. We reduced the dataset unbalance by choosing to work only on the event geographical points: non-events were thus reduced to 4 millions (4 745 days over 863 points). Then, specific machine learning approaches have been deployed to manage this unbalanced issue.
For each of the 4 millions spatio-temporal data, cumulative rainfalls were defined for the previous 1 to 45 days from daily rains extracted from ANTILOPE data (Météo-France). Random forests and gradient boosted trees were used for our supervised learning problem. To manage the unbalanced issue, we introduce cross-validation, under and over samplings, as well as loadings of the categories (event versus non-event). Hyperparameters and inputs features were selected according to numerous metrics observed for each model. Finally, the selected trigger model features are three cumulative rainfalls of short, medium and long durations. The

test set (based on under sampling no-events) shows the metrics: recall of 82%, precision of 54%, accuracy of 60% and f-beta score (with beta=1.8) of 73%. It means that 82% of the events are detected but 46% of the detection are false. It is a good result regarding our extremely unbalanced dataset issue.

Rockfall vigilance level

The rockfall database (RDB) is composed of 481 rockfalls from 2008 to 2020.
Rockfall susceptibility model
The rockfall susceptibility model is based on statistical results of propagation using Flow-R (Hortaon et al., 2013). Parametrizations of Flow-R were tested in order to obtain an acceptable trade-off between i) the number of rockfall events included into the runout and ii) the number of meters along the road concerning by the run-out. Finally, the rock susceptibility index is defined as the normalization of the maximum of the susceptibility sum (defined by flow-R) over continuous pixels on the road. 2 250 sectors are defined with a susceptibility index from 0 to 1.
Rockfall trigger model
The trigger models have been trained on the event database with the same issue of unbalanced data as for landslide. Similar techniques were applied. The freezing potential (FP) is introduced as a proxy of air temperature.

$$FP=\sum -T; \quad with\ 0\leq FP\leq 1000 \quad (2)$$

With T: maximal and minimal daily air temperature in °C from nearby meteorologic station
A total thaw is defined by FP(day)=0 and FP(day-1)>0. A partial thaw is defined by d(FP)/dt=0. The selected input features are three cumulative rain over the previous: 1, 20 and 45 days, the number of total thaws over 30 days (ThawTotalFP30) and the number of partial thaws over 30 days (ThawFP30). The test set (based on under sampling no-events) shows the metrics: recall of 80%, precision of 56%, accuracy of 57% and f-beta score (with beta=1.8) of 73%.

SIGALE early warning system online interface

An experimental web-service has been developed to visualize and to analyse the vigilance levels. The AROME weather forecast from Météo-France is used to compute the input features. Using these data, the forecast deadline is one day.
The vigilance level is then computed on a daily basis for all sectors (5,028 for the landslide vigilance, 2,250 for the rockfall vigilance). A visualizing period up to 14 days is possible on the graphical interface in order to observe the evolution of the vigilance level (Figure 2, left panel). A weighted mean is computed for four different levels of zoom: the department, 10 geographical zones ((Figure 2, right panel), clusters of sectors and sectors.

Conclusion

The SIGALE project has allowed to build an online, experimental geographical early-warning system along the Savoie's roads. It takes into account both landslide and rockfall hazards. Artificial intelligence was used with expertise, which allowed us to overcome the issue raised by a highly unbalanced dataset, characterized by rare events. Our efforts are now focused towards the improvement and automatization of the prediction routines, notably the augmentation of the forecast deadline. We also focus on upgrading the web service to make SIGALE more user friendly, intuitive and facilitate its use as a risk mitigation operative tool.

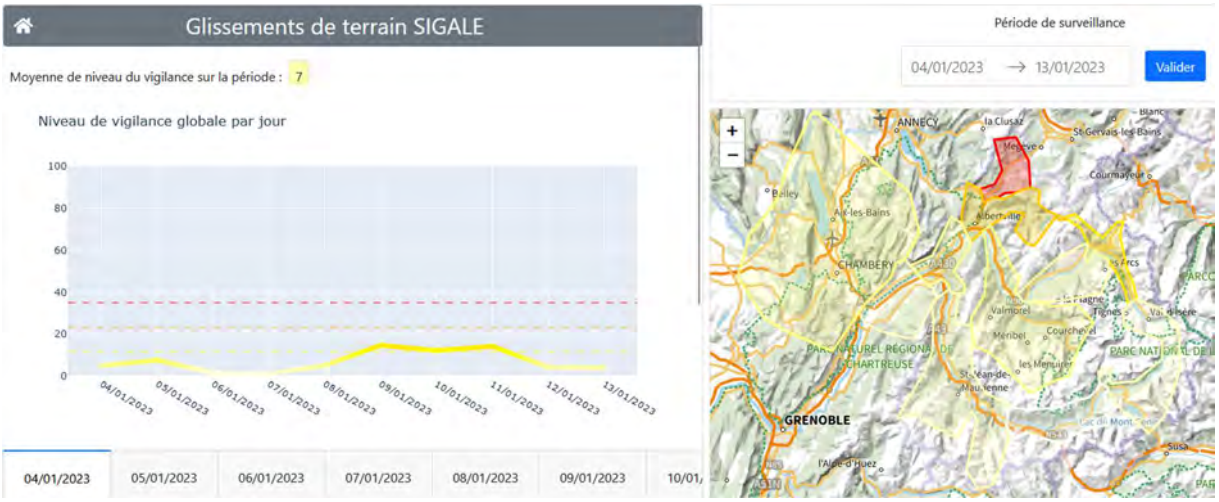

Figure 2: Screen print of SIGALE web-service, for the period from the 4th of January 2023 to the 14th

It shows the average vigilance level of the whole department over time (left panel). Thresholds XXX are shown with orange and red dashed lines. The right panel shows the map of vigilance levels for different coloured geographical zones, defined in collaboration with the department managers, from yellow to red.

Acknowledgement

Research partially supported by grants from AURA region (Auvergne Rhone Alpes, France), by the CD73 (Savoie department) and the DIR-CE (Direction Interdépartementale des Routes Centre-Est).

References

Guzzetti F, Gariano SL, Peruccacci S, Brunetti MT, Marchesini I, Rossi M, et al. (2020) Geographical landslide early warning systems. *Earth-Science Rev. 200, 102973.doi:10.1016/j.earscirev.2019.102973*

Wilde M, Gunther A, Reichenbach P, Malet JP & Hervas J (2018) Pan-European landslide susceptibility mapping: ELSUS Version 2, *JOURNAL OF MAPS, ISSN 1744-5647, 14 (2), p. 97-104, JRC105147*

Cadet H, Rouquet D & Lescurier A (2022) Gravitational hazard (landslide and rockfall) susceptibility indexes for the Savoie Departement infrastructure ; *Conférence: JAG-2022 ; DOI: 10.13140/RG.2.2.24454.45125*

Wagner Cipriano (2018) https://github.com/wcipriano/pretty-print-confusion-matrix/blob/master/confusion_matrix_pretty_print.py

Horton P, Jaboyedoff M, Rudaz B & Zimmermann M (2013) Flow-R, a model for susceptibility mapping of debris flows and other gravitational hazards at a regional scale. *Natural Hazards Earth System Sciences, 13, 869-885, doi:10.5194/nhess-13-869-2013*

The Role of Rainfall Pattern on Rainfall-Induced Slope Failure: New Insights from Cataclysmic Sau Mau Ping Failure

Levinna Natalia[1], Jun Yang[1]

[1] Department of Civil Engineering, The University of Hong Kong, Hong Kong, China

SUMMARY: Rainfall thresholds in terms of intensity, duration, and frequency have been a valuable means to facilitate the design process and prevent failure occurrences which might lead to devastating consequences. However, some of the past destructive failures are found to be triggered by rainfalls whose intensity is lower than these rainfall thresholds. Examples include the two deadly landslides in Sau Mau Ping, Hong Kong, in June 1972 and August 1976, which caused 165 casualties. What is interesting from these two events is that the slopes that were able to withstand the previous 1972 rainfall failed in the 1976 rainfall, which had a maximum rainfall intensity of only half of the former. We conducted an extensive review of the case histories and numerical analyses using a combination of seepage and stability modelling. The possible contributions of the rainfall characteristics, specifically the rainfall antecedent temporal pattern, to explain these failure phenomena are discussed in this paper.

Keywords: landslide, case history, rainfall pattern, antecedent rainfall, rainfall thresholds

Introduction

Rainfall-induced slope failures are among the most devastating disasters affecting man-made and natural slopes. Previous studies highlighted the intricate relationships between the controlling factors of slope instability (Natalia and Yang, 2022; Yang et al., 2022). Moreover, depending on the initial state (i.e., density and initial stress), particle shape, and fines content, slopes might fail due to flow liquefaction, which causes the soil to lose its strength and fail in a liquefied manner and might amplify the danger (Yang 2002; Yang and Wei, 2012).

Threshold conditions such as rainfall intensity, duration, and frequency have been attempted to be developed in previous studies, especially for practical reasons. Lumb (1975) and Brand et al. (1984) attributed localized short-duration storms with intensity higher than 70mm/hr to trigger landslides in Hong Kong. Nevertheless, in some past events, devastating landslides have been recorded to occur after rainfall, having an intensity far lesser than these threshold values, one of which is the Sau Mau Ping's 1976 slope failure. The areas that were previously able to sustain far higher rainfall intensity in 1972 were found to fail in 1976, with rainfall intensity lesser than the previous event. Recent studies evaluated the potential contribution of rainfall patterns and found that long-duration intermediate-intensity rainfalls promote landslide activity relative to high-intensity rainfalls with the same total rainfall and duration (Rahimi et al. 2011, Fan et al. 2020). Nevertheless, none of these conclusions are supported by an *actual* physical failure. In this study, Sau Mau Ping failure will be revisited, and the possible contribution of antecedent rainfall patterns in triggering such events will be evaluated.

Case history

Due to the rapid increase in land demand, a hurried land formation was done in Hong Kong in the 1970s using the end-tipping method, layering 100-300mm thick soil parallel to the slope

surface (Binnie & Partners, 1976). One of these areas is Sau Mau Ping, which experienced a catastrophic failure on June 18, 1972, and engulfed a resettlement area consisting of temporary huts (Fig. 1(a)). The failure was preceded by a series of extreme rainfall with a maximum rainfall intensity of 98.7mm/hr, causing 71 fatalities and injuring 60 others (Yang et al., 1972). Four years after the deadly landslides, on August 25, 1976, another disastrous failure happened 200m from the 1972 failure area (Fig. 1(b)). What is intriguing is that the failed slopes were examined right after the previous failure and were considered reasonably safe, with some remedial works conducted following the examination. Additionally, the maximum rainfall preceding the 1976 failure was around 51.5mm/hr, nearly half of the former failure event.

Numerical analysis

Numerical means are adopted in this study to obtain the transient seepage and the resulting slope stability. Richards equation [Eq. (1)] is used in the SEEP/W to evaluate the transient and two-dimensional seepage analysis:

$$\frac{\partial}{\partial x}\left(k_x \frac{\partial H}{\partial x}\right) + \frac{\partial}{\partial y}\left(k_y \frac{\partial H}{\partial y}\right) + Q = m_w \gamma_w \frac{\partial H}{\partial t} \tag{1}$$

where H, k_x, k_y, Q, m_w, and γ_w are total head, coefficient of permeability in x-direction, coefficient of permeability in x-direction, applied boundary flux, the slope of storage curve, and the unit weight of water. The simulation results are then used as an input for the stability analysis in SLOPE/W, which utilize the unsaturated strength as defined in Eq. (2):

$$\tau = c' + (\sigma - u_a)\tan\phi' + (u_a - u_w)\left[\left(\frac{\theta_w - \theta_r}{\theta_s - \theta_r}\right)\tan\phi'\right] \tag{2}$$

where τ, c', $(\sigma - u_a)$, ϕ', and $(u_a - u_w)$ are the shear strength of unsaturated soil, effective cohesion of soil, net normal stress, effective friction angle, and suction of the soil, respectively. Additionally, θ is the volumetric water content and the subscripts w, r, and s indicate the current, residual, and saturated conditions, respectively.

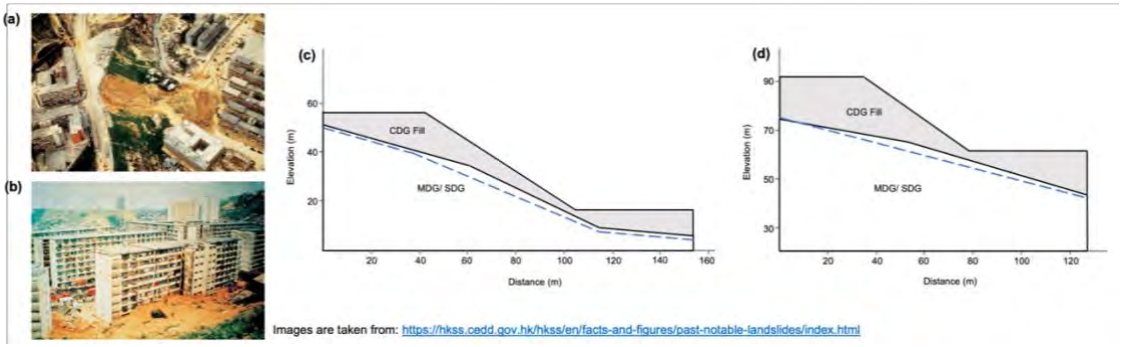

Figure 1. Slope geometry for numerical analysis: (a) SMP72 and (b) SMP6

Two-dimensional seepage analyses were carried out using the slope geometry illustrated in Fig. 1(c) and 1(d) for the slopes failed in 1972, SMP72, and the main slip in 1976, SMP6, respectively. The input parameter used in the modelling is summarized in Table 1. Fig. 2(a) and 2(b) exhibit the rainfall events leading to the landslides in 1972 and 1976, respectively, which we will refer to as 'incident rainfall'. The 'incident rainfall' is selected such that the cumulative intensity prior to the failure is around 470mm (the shaded grey area in Fig. 2(c) and (d)). Two types of cases will be evaluated: Main Analysis (MA) and With Previous rainfall (WP) cases. In MA test cases, the initial seepage is assumed to be hydrostatic with a maximum suction value of 10kPa. In the WP cases, the 19-day antecedent rainfall, referred to as 'previous rainfall' (Fig.

2(c) and (d)), will first be applied to generate the field's initial condition and then followed by the 'incident rainfall'.

Table 1. Summary of the input parameters used in the modeling.

Input parameters		CDG Fill	MDG/SDG
SWCC (Fredlund and Xing 1994)	θ_S, a_f, n_f, m_f	0.37, 1.70, 2.10, 0.30	0.08, 0.20, 5.00, 0.45
Permeability (m/s)	k_{sat}	2.68 x 10^{-6}	2 x 10^{-8}
Unit weight (kN/m^3)	γ_{sat}	18.00	18.00
Friction angle	ϕ'	34° - 36.8°	45°
Cohesion (kPa)	c'	0 – 2	10

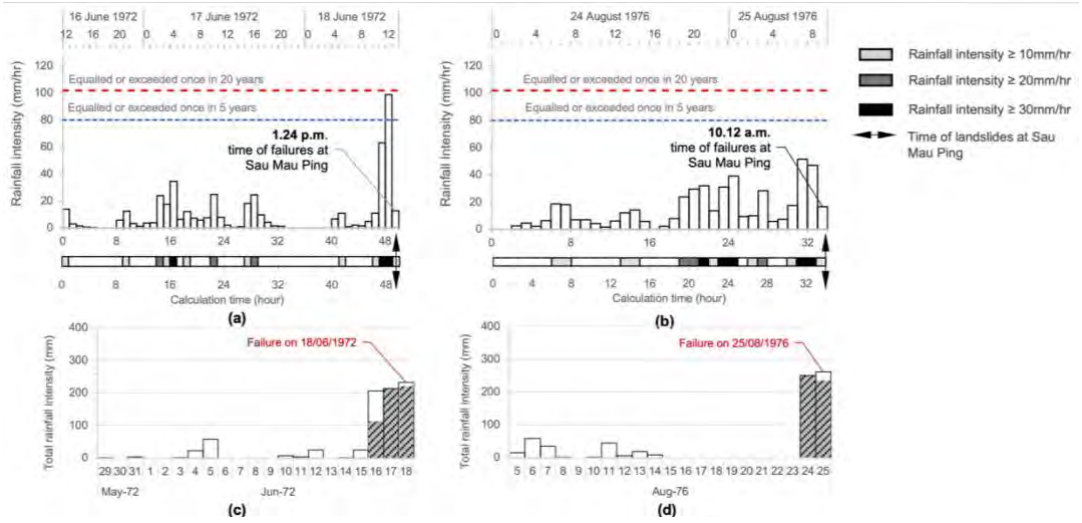

Figure 2. Rainfall intensity recorded in Sau Mau Ping area prior to failure.

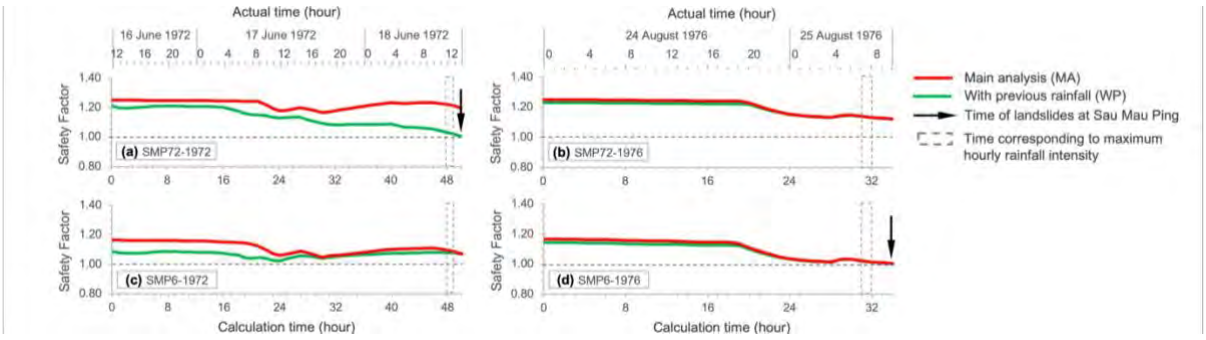

Figure 3. Numerical results: SMP72 under **(a)** 1972 and **(b)** 1976, SMP6 under **(c)** 1972 and **(d)** 1976 rainfall

Results and Discussions

Fig. 3 summarizes the numerical analysis results. The red lines (MA cases) generally give higher initial FOS than the green lines (WP cases), especially for slopes under the 1972 rainfall (Fig. 3(a) and (c)). The 'previous rainfall' of 1972 incidents has higher intensity and is closer to the 'incident rainfall' than the 1976 event, causing the slope strength to be significantly reduced prior to the 'incident rainfall.' The SMP72 slope failure in 1972 was caused by a combination of unfavourable seepage conditions and extreme rainfall events, as shown in Fig. 3(a), which caused the slope to fail at a calculation time of 50hr with FOS equal to 1.004. The influence of 'previous rainfall' of 1976 events, which consisted of 9-day no-rain periods, on the FOS is less significant (see Fig. 3(b) and (d)) as the green and red lines almost overlapped.

The FOS of both SMP72 and SMP6 under the 1972 rainfall seems to be more fluctuate compared to the 1976 rainfall. The decrease and increase of FOS throughout the calculation time of 20hr – 50hr is comparable to the 1972 'incident rainfall' pattern shown in Fig. 2. The FOS decreases and increases following the rainfall and no-rainfall periods, respectively. On the other hand, slopes under the 1976 rainfall event experienced a continuous decrease in FOS after a calculation time of 20hr. The compact and relatively uniform rainfall intensity in 1976 gave a continuous water supply to the slope without allowing any suction and strength to be regained. This explains the failure of the slope (SMP6), which previously sustained extreme rainfall with a doubled maximum rainfall intensity. The time of failure for the WP case of both SMP72 under 1972 and SMP6 under 1976 rainfall agrees with the forensic report (Vail, 1984).

Conclusion

Rainfall-induced slope failure can cause a substantial hazard to our natural and built environment. This study found that the long-duration and relatively uniform antecedent rainfall pattern can pose a greater danger than the delayed high-intensity rainfall pattern, explaining why the slope that previously sustained extreme rainfall events failed in 1976. Additionally, the antecedent conditions from preceding rainstorms might also exacerbate the instability by lowering the slope's initial safety and causing critical seepage conditions, which might be the case of the 1972 failures. Due to the intricate nature of the triggering factors, it might not be sufficient to use only the rainfall intensity and duration to predict slope instability.

Acknowledgement

The financial support provided by the Research Grants Council of Hong Kong through the GRF Grant No. 17207923 and the HKPF scheme is gratefully acknowledged.

References

Binnie & Partners (1976) *Report on the slope failures at Sau Mau Ping 25th August 1976 Vol. 1-3.*

Brand EW, Premchitt J & Phillipson HB (1984) Relationship between rainfall and landslides in Hong Kong. *In Proceedings of the 4th international symposium on landslides.* Toronto, Canada.

Cascini L, Cuomo S, Pastor M & Sorbino G (2010) Modeling of Rainfall-Induced Shallow Landslides of the Flow-Type. *Journal of Geotechnical and Geoenvironmental Engineering* 1361, 85–98.

Fan L, Lehmann P, Zheng C, Or D (2020) Rainfall Intensity Temporal Patterns Affect Shallow Landslide Triggering and Hazard Evolution. *Geophysical Research Letter* 47.

Lumb, P (1975) Slope failures in Hong Kong. *Quarterly Journal of Engineering Geology* 8(1), 31–65.

Natalia L & Yang J (2022) Investigation of rainfall-induced slope failures from an integrated perspective. *Proceedings of the 8th Canadian Conference on Geotechnique and Natural Hazards: Innovative geoscience for tomorrow.* C. Cloutier, D. Turmel, P. Maghoul and A. Locat (eds.), 457–463.

Rahimi A, Rahardjo H & Leong EC (2011) Effect of Antecedent Rainfall Patterns on Rainfall-Induced Slope Failure. *Journal of Geotechnical and Geoenvironmental Engineering* 1375, 483–491.

Vail AJ (1984) Two Landslides in Hong Kong. *In: Proceedings of 4th international symposium on landslides.* Toronto, Canada.

Yang J (2002) Non-uniqueness of flow liquefaction line for loose sand. *Géotechnique* 54: 66–68

Yang J, Liang LB & Chen, Y (2022) Instability and liquefaction flow slide of granular soils: the role of initial shear stress. *Acta Geotechnica* 171, 65–79.

Yang TL, Mackey S & Cumine E (1972) *Interim report of the commission of inquiry into the rainstorm disasters 1972.*

Yang, SY, Jan CD & Wang JS (2018) Landslides triggered by Typhoon Morakot in Taiwan. *Environmental Risks*, 13–43.

Yang J & Wei LM (2012) Collapse of loose sand with the addition of fines: the role of particle shape. *Géotechnique* (62), 1111–1125

Zhang L, Li J, Li X, Zhang J & Zhu H (2016) *Rainfall-Induced Soil Slope Failure Stability Analysis and Probabilistic Assessment*. Boca Raton: CRC Press.

Time-domain Induced Polarisation measurements as a complementary tool to classical Direct Current measurements for the study of landslides Time-lapse case study of the Montgombert Landslide (Savoie, France)

A. Carrier[1,2], O. Meric[1,2], P. Bottelin[1,2]

[1] SAGE Ingénierie, Gières, France
[2] ADRGT, Gières, France

SUMMARY: Landslides dynamic is related to the spatial distribution of pore pressure, hydraulic conductivity, and clay content. Fully saturated clay-free materials and clays are both able to conduct the electrical current efficiently. Therefore, standard direct current methods fail at distinguish between them. This study presents a case study for which induced polarization has proven to be an efficient tool to identity impermeable/permeable materials the landslide. The addition of the mean relaxation time variable, thanks to an acquisition performed on long enough duration time, enables to get a complementary useful information to discriminate the different materials. Time-lapse acquisitions provide information about the evolution of the hydrological state of the soils.

Keywords: Geophysics, electrical methods, induced polarization, clustering

Introduction

Landslides represent a major issue for infrastructures in mountainous environments (Mallet et al., 2007). Landslide monitoring, identification, and quantification of the unstable volumes as well as the understanding of the triggering processes are major human, political and economic stakes.
Landslide activity is significantly enhanced by heavy rains and rapid snow melt during spring, underlying the importance of water saturation and pore water pressure in landslides triggering (Mallet et al., 2005). Moreover, the spatial distribution of permeable versus impermeable areas within the landslide body is a key factor to understand the dynamics of the fluids circulations and the landslide evolution through time.
Up to now, geophysical methods, and especially electrical direct current methods, are widespread tools for landslide characterization (Gance et al., 2016; Helmann et al., 2017; Holmes et al., 2020). However, very few studies focused on the precise determination of permeable and impermeable areas (Marescot et al., 2008; Revil et al., 2020; Orozco et al., 2022). To do so, Induced Polarization (IP) methods appear to be promising tools. From a petrophysical model and laboratory data, Revil et al., 2020 ,estimated the water content and the permeability in a clayey landslide in the French Alps. Orozco et al., 2022, determined the hydrological properties of materials within a landslide from IP measurements in time and frequency domains. In particular, he underlined the importance of considering the spectral content of the IP data, previously suggested by Gazoty et al., 2012, Doetsch et al., 2015 and Martin et al., 2020.
Our study proposes the realization of three time lapse Time Domain IP (TDIP) surveys as a complementary information to standard direct current measurements on a landslide affecting a major road in the French Alps (Montgombert, Savoie, France). This study underlines the relevance of the complementary information brought by the TDIP surveys for landslide characterization and dynamics understanding

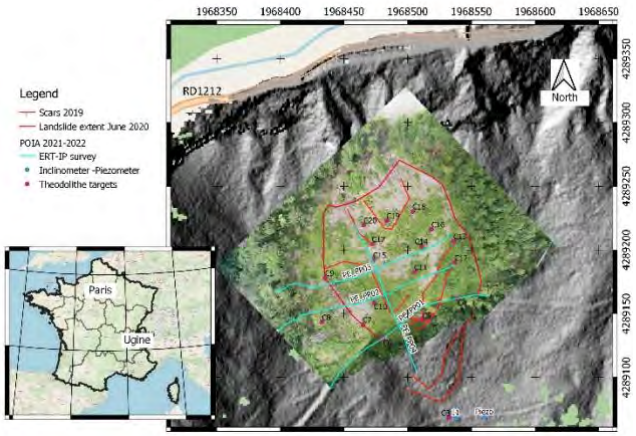

Figure 1. Localisation of the site.

Methodology

TDIP data are acquired in the framework of the MIROIR POIA Feder project. TDIP data are acquired with double cable (one cable for the injection and one cable for the potential measurements) and multiple gradient protocol (Dahlin et al., 2003; Zou et al., 2020). Three campaigns have been realized in April 2021, September 2021 and May 2022. In April 2021 a ABEM SAS 4000 have been used, for the further campaigns a ABEM LS2 have been used in 100% duty cycle with optimized protocols on 8 channels in order to save time and get better quality data. Quality control can be performed on decay curves and full waveforms (Martin et al., 2020). Negative apparent chargeabilities and non-exponential decays are systematically removed.
The resulting data sets are inverted thanks to the freely available BERT and PyGIMLI tools (Rucker et al., 2017; Martin et al., 2020). In order to get as many information as possible from the data and to improve the interpretation of the results, the mean relaxation time is extracted through a Debye Decomposition (Nordsiek & Weller, 2008, Tarasov & Titov, 2007; Martin et al., 2021). Groups with similar parameter variations through time are extracted thanks to unsupervised classification. It enables to help the readability and the interpretation of the results.

Results of the time-lapse TDIP on the Montgombert Landslide

The landslide is perched 100 m above an essential road connecting some major ski resorts and cities to bigger cities in the area. The Montgombert landslide results from the general toppling failure of the micaschists and their transformation into clayey micaschists rockslides. The comparison of the resistivity, chargeability and mean relaxation time models obtained at the end of the summer and the beginning of the spring enable to identify fluid accumulation areas (fig 2). For this case study, the most important and significant variations are obtained on the variables linked to the TDIP measurements (normalized chargeability and mean relaxation time). These areas are in agreement with the surface deformation obtained by the Tracing Surface Motion method (Desrues et al., 2022) based on the comparison of optical images taken at the same times. This underlines the relevance of the method for landslides studies.

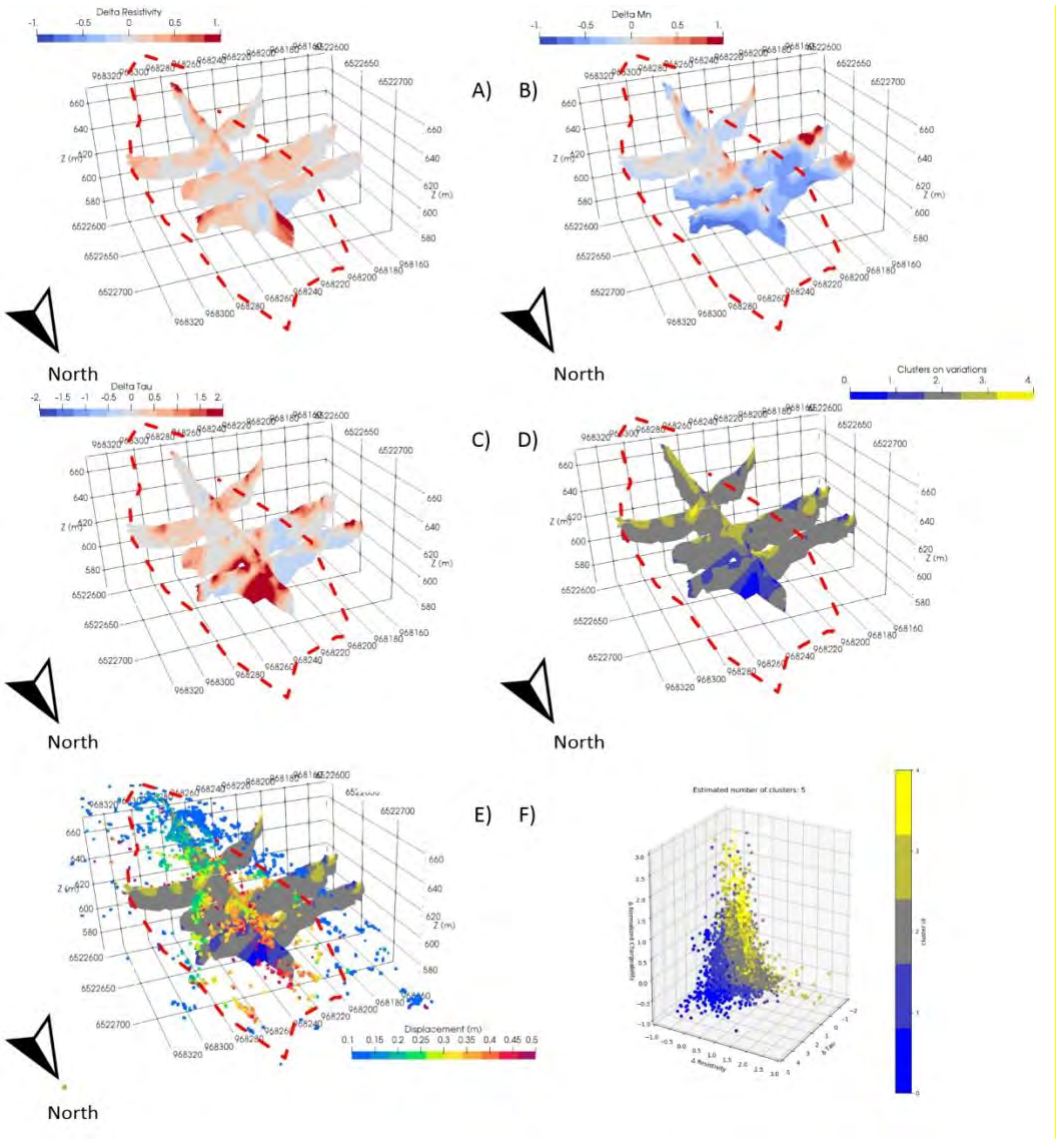

Figure 2. Relative resistivity (A), normalized chargeability (B), mean relaxation time (C) variations between September 2021 and May 2022. The results of the clustering applied on relative variations and its confrontation to surface displacements is presented on pannels D, E and F. (Carrier et al 2023, Landslides)

Conclusion

Our study underlines the relevance of the use of the Time Domain Induced Polarization on landslide characterization as a complementary tool to classical direct current measurements and geotechnical data. The method enables to identify hydrological units and fluid accumulations through time. The time-lapse approach appears to be decisive for the understanding the fluids circulations and the landslide dynamics. Time lapse TDIP enables to evaluate potentially unstable volumes and brings useful information to help the design of security systems. For the Montgombert landslide the method has enabled to identify and quantify volumes where fluids accumulate and therefore the potential unstable volumes to consider to design safety works.
We suggest that the performance could be further improved by the improvement of the data processing methodology, the use of complementary geophysical data and even the use of

laboratory data to build an appropriate petrophysical model and help the interpretation of the results.

References

Carrier, A., Meric, O., & Bottelin, P. (2023). Caracterizing landslide dynamics from time-lapse time domain induced polarization and ground-based imaging, case study of the MontGombert landslide (French, Alps). Landslides, 1-17..

Dahlin, T., Leroux, V., & Nissen, J. (2002). Measuring techniques in induced polarisation imaging. Journal of Applied Geophysics, 50(3), 279-298.

Desrues, M., Malet, J. P., Brenguier, O., Carrier, A., Mathy, A., & Lorier, L. (2021). Landslide kinematics inferred from in situ measurements: the Cliets rock-slide (Savoie, French Alps). Landslides, 1-16.

Doetsch, J., Ingeman-Nielsen, T., Christiansen, A. V., Fiandaca, G., Auken, E., & Elberling, B. (2015). Direct current (DC) resistivity and induced polarization (IP) monitoring of active layer dynamics at high temporal resolution. Cold Regions Science and Technology, 119, 16-28.

Gance, J., Malet, J. P., Supper, R., Sailhac, P., Ottowitz, D., & Jochum, B. (2016). Permanent electrical resistivity measurements for monitoring water circulation in clayey landslides. Journal of Applied Geophysics, 126, 98-115.

Gazoty, A., Fiandaca, G., Pedersen, J., Auken, E., & Christiansen, A. V. (2012). Mapping of landfills using time-domain spectral induced polarization data: the Eskelund case study. Near Surface Geophysics, 10(6), 575-586.

Hellman, K., Ronczka, M., Günther, T., Wennermark, M., Rücker, C., & Dahlin, T. (2017). Structurally coupled inversion of ERT and refraction seismic data combined with cluster-based model integration. Journal of Applied Geophysics, 143, 169-181.

Holmes, J., Chambers, J., Meldrum, P., Wilkinson, P., Boyd, J., Williamson, P., Donohue, S. (2020). Four-dimensional electrical resistivity tomography for continuous, near-real-time monitoring of a landslide affecting transport infrastructure in British Columbia, Canada. Near Surface Geophysics, 18(4), 337-351.

Malet, J. P., Durand, Y., Remaître, A., Maquaire, O., Etchevers, P., Guyomarc'h, G., ... & Van Beek, L. P. H. (2007). Assessing the influence of climate change on the activity of landslides in the Ubaye Valley. In Proceedings of the International Conference on Landslides and Climate Change–Challenges and Solutions, edited by: McInnes, R., Jakeways, J., Fairbank, H., and Mathie, E., Taylor & Francis, London (pp. 195-205).

Malet, J. P., Laigle, D., Remaître, A., & Maquaire, O. (2005). Triggering conditions and mobility of debris flows associated to complex earthflows. Geomorphology, 66(1-4), 215-235.

Marescot, L., Monnet, R., & Chapellier, D. (2008). Resistivity and induced polarization surveys for slope instability studies in the Swiss Alps. Engineering Geology, 98(1-2), 18-28.

Martin, T., Günther, T., Orozco, A. F., & Dahlin, T. (2020). Evaluation of spectral induced polarization field measurements in time and frequency domain. Journal of Applied Geophysics, 180, 104141.

Martin, T., Titov, K., Tarasov, A., & Weller, A. (2021). Spectral induced polarization: frequency domain versus time domain laboratory data. Geophysical Journal International, 225(3), 1982-2000.

Nordsiek, S., & Weller, A. (2008). A new approach to fitting induced-polarization spectra. Geophysics, 73(6), F235-F245.

Orozco, A. F., Steiner, M., Katona, T., Roser, N., Moser, C., Stumvoll, M. J., & Glade, T. (2022). Application of induced polarization imaging across different scales to understand surface and groundwater flow at the Hofermuehle landslide. CATENA, 219, 106612.

Revil, A., Ahmed, A. S., Coperey, A., Ravanel, L., Sharma, R., & Panwar, N. (2020). Induced polarization as a tool to characterize shallow landslides. Journal of Hydrology, 589, 125369.

Rücker, C., Günther, T., & Wagner, F. M. (2017). pyGIMLi: An open-source library for modelling and inversion in geophysics. Computers & Geosciences, 109, 106-123.

Tarasov, A., & Titov, K. (2007). Relaxation time distribution from time domain induced polarization measurements. Geophysical Journal International, 170(1), 31-43.

Zhou, B., Bouzidi, Y., Ullah, S., & Asim, M. (2020). A full-range gradient survey for 2D electrical resistivity tomography. Near Surface Geophysics, 18(6), 609-626.

Research on the Accuracy of Potential Landslide Identification Based on Airborne Radar

Yifan Tian[1], Lichao Wang[1], Liang Chen[1], Zhen Feng[1]

[1] China Institute of Geological Environment Monitoring, Beijing, China

SUMMARY: Airborne Lidar can be used to obtain high-precision terrain and image data in areas that are difficult to reach by humans, so as to identify slope deformation areas, boundary conditions and deformation markers, thereby improving the level of landslide identification and geological disaster investigation. In this study, the detection accuracy of airborne LiDAR was compared by changing the flight altitude and sampling frequency to identify landslide feature such as tension cracks and scarps.
Keywords: airborne LiDAR, potential landslide, identification accuracy, flight altitude, sampling frequency

0.Introduction

In previous investigations of landslide disasters, due to the limitation of the accuracy of topographic map and remote sensing data, some inaccessible areas such as high mountains and steep slopes were often ignored or speculated, and the actual situation of disaster development was not clear. Currently, remote sensing technology provides efficient and simplified solutions for identifying and understanding the evolution process of landslides [1]. Landslide identification not only includes drawing the range of landslides that have occurred, but also observing the deformation of unstable slopes [2].

Remote sensing technology has limited effectiveness in identifying landslide features in areas with vegetation cover or shadows [3]. Airborne LiDAR (Light Detection Ranging) not only can reconstruct high-precision terrain data, but also has the advantage of strong penetration ability and stronger ability to identify small deformations [4]. The study aimed to explore the technical parameters of landslide feature identification using airborne LiDAR under different flight heights and sampling frequencies in the loess region of China. It also proposed a comprehensive method for identifying loess landslide hazards. The research findings are of great significance for guiding high-precision geological disaster investigations and hazard identification in loess regions.

1.Study area

This study selected a county in Gannan, China. The study area is located at the junction of the Gannan Plateau, the central Loess Plateau, and the mountainous area of Longnan. Due to significant elevation differences and intense weathering and erosion, the surface soil and rock structure is loose, and many slopes are in a state of limit equilibrium or instability. The loess deposits mainly cover the terraces of the Tao River and its tributaries, with a thickness generally ranging from 8 to 15 m and locally reaching 20 m. When conducting airborne LiDAR laser scanning, it is less affected by vegetation interference and has more effective

ground points. This leads to a higher ability to identify micro-landforms and concealed cracks related to landslides.

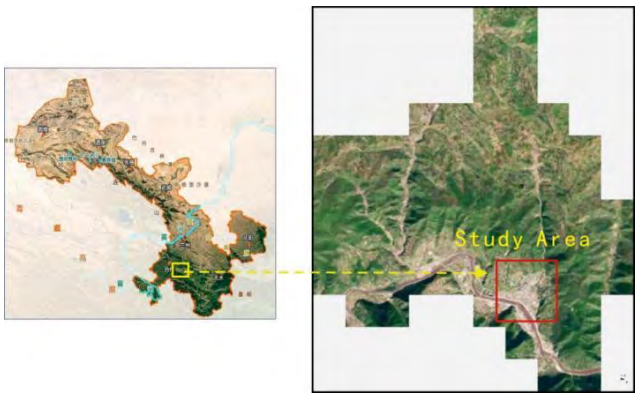

Figure.1 Study area

2.Data and methods

2.1 Research methods

This study identified typical landslide disasters in loess areas using drone orthophotos and airborne LiDAR technology. The interpretation of airborne LiDAR mainly includes:

1. The geographic location, extent, geometric shape, and deformation signs of landslides.
2. Landslide microtopography, such as tension cracks and scarps.
3. The types and areas of buildings in the study area.

By combining orthorectified remote sensing images to obtain geological disaster feature elements and using airborne LiDAR scanning to generate high-precision digital elevation model (DEM), digital surface model (DSM) and digital orthophoto map (DOM), a three-dimensional interpretation scene of geological disasters is constructed.

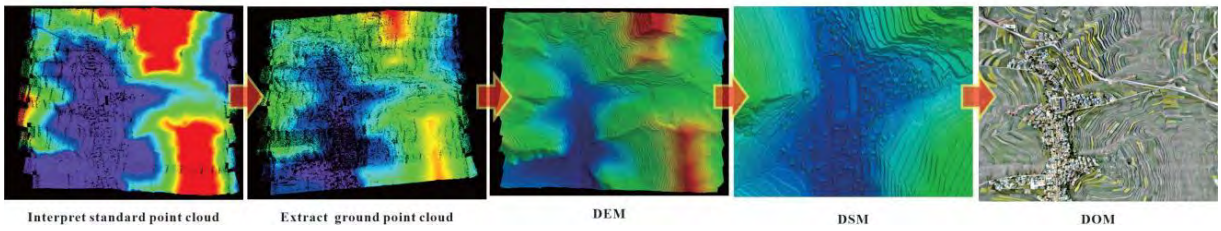

Figure.2 Data processing

The parameter settings for flight height and sampling point cloud density are shown in Table 1, and the testing error is controlled at 20 cm.

Table. 1 Aerial survey plan design

Flight altitude/m	Flight speed /m/s	Number of checkpoints	Number of collected point clouds /m^2	Error in plane /cm	Error in elevation /cm
50	14	5	35	20	20
100	14	4	30	20	20
150	14	3	25	20	20

2.4 The Sign of Landslide Interpretation

Before conducting remote sensing interpretation work, it is necessary to establish remote sensing interpretation indicators suitable for the working area, such as backscarp, tension crack, scarp and sliding mass. The collected landslide deformation characteristics are shown in Figure 3.

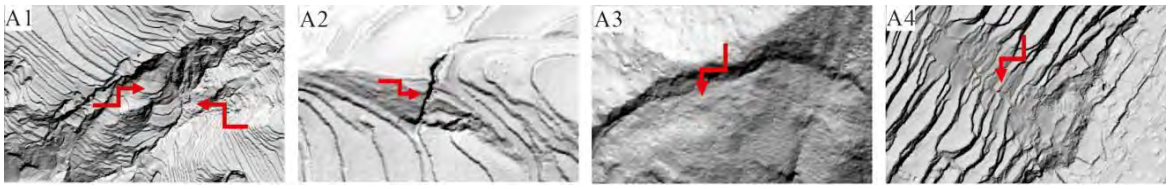

Figure.3 Characteristics of landslide deformation
(A1:Backscarp;A2:BackscarpTension crack;A3:Scarp;A4:Sliding mass)

3. Results and discussion

3.1 Comparative analysis of landslide elements identification

Based on the classification and statistical analysis of the geometric features of identified landslide cracks and scarps (Table.2,Table.3), the identified feature lengths are mainly concentrated below 10 m. As the flight altitude decreases, the number of cracks below 5 m and scarps below 10 m in length slightly increases. The identification width of cracks is mainly concentrated in the range of 0.3~1.0 m, while the height of scarps is mainly below 3 m. The results indicate that as the flight altitude decreases, the accuracy of the measured data significantly improves, and the interpretation of cracks or scarps become clearer. For small scale features, the effect of flight altitude becomes more obvious.

Table. 2 Comparison and Analysis of Crack Identification under Different Flight Conditions Statistical

Identification length	Flight altitude			Identification width	Flight altitude		
	150 m	100 m	50 m		50 m	100 m	150 m
＜2 m	19	26	29	＜0.3 m	0	9	12
2-5 m	66	68	68	0.3-0.5 m	99	99	99
5-10 m	45	45	45	0.5-1.0 m	47	47	47
10-20 m	15	15	15	1.0-1.5 m	5	5	5
＞20 m	7	7	7	＞1.5 m	1	1	1
Summation	152	161	164	Summation	152	161	164

Table. 3 Comparison and Analysis of Scarp Identification under Different Flight Conditions Statistical

Identification length	Flight altitude			Identification height	Flight altitude		
	50 m	100 m	150 m		50 m	100 m	150 m
＜10 m	40	38	34	＜0.5 m	13	17	19
10-20 m	12	12	12	0.5-1.0 m	28	28	28
20-50 m	12	12	12	1.0-3.0 m	16	16	16
50-100 m	5	5	5	3.0-5.0 m	3	3	3
＞100 m	3	3	3	5.0-10 m	3	3	3
Summation	72	70	66	＞10 m	3	3	3
				Summation	66	70	72

3.2 Effect of point cloud density on identification results

In the past few years, the project team has conducted airborne LiDAR surveys of loess landslides in multiple work areas. Based on previous aerial survey results, point cloud density directly determines the quality of LiDAR measurement results. Under low altitude flight conditions, the higher the density of point clouds, the more detailed the investigation results (Figure.4a), which is beneficial for identifying loess landslides and their accompanying deformation cracks or scarps. When the flight altitude is lower than 150 m, the recognition quantity of cracks does not increase significantly, but the recognition accuracy has been improved to a certain extent (Figure.4b).

3.3 Comparison of identification effects

Comparing the mountain shadow maps generated from Lidar results and orthophoto images

(Figure.5), remote sensing images have richer texture features. However, mountain shadow maps can better reflect the changes in overall slope, and use the changes in surface roughness to identify some landslide deformation features.

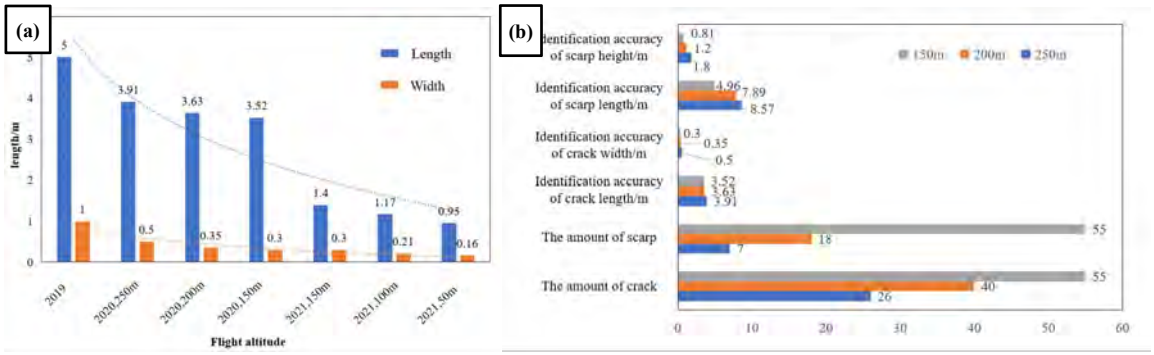

Figure.4 Statistical analysis of airborne LiDAR identification accuracy

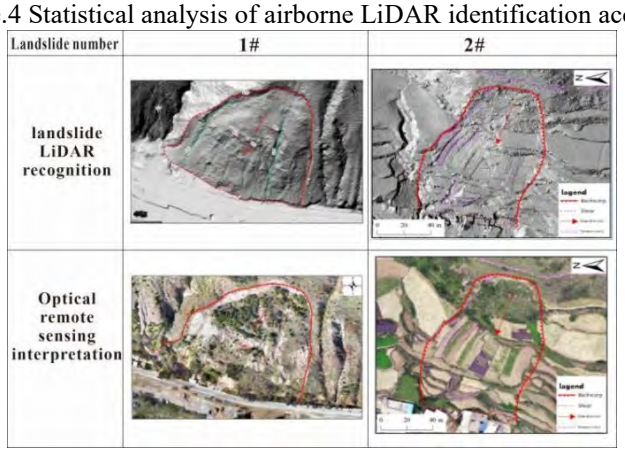

Figure.5 Comparison of landslide identification

4. conclusion

Based on the accuracy results of landslide feature recognition using airborne radar, the following conclusions are drawn:

1. Higher point cloud density is more favorable for interpreting and identifying loess landslides.

2. Lower flight altitudes result in higher point cloud density. Considering the cost-effectiveness and practicality of airborne LiDAR, a flight altitude setting of 150 m to 200 m is more suitable.

3. Compared with orthophoto recognition, mountain shadow maps obtained by airborne LiDAR can more clearly identify landslide boundaries.

Reference

Xu Q, Li WL, Ju YZ, Dong XJ & Peng DL (2020) Multitemporal UAV-based photogrammetry for landslide detection and monitoring in a large area: a case study in the Heifangtai terrace in the Loess Plateau of China. *Journal of mountain science* 17(8), 1826-1839.

Görüm T (2019). Landslide recognition and mapping in a mixed forest environment from airborne LiDAR data. *Engineering Geology* 258, 105155.

Razak KA, Santangelo M, Van Westen CJ, Straatsma MW & De Jong SM (2013) Generating an optimal DTM from airborne laser scanning data for landslide mapping in a tropical forest environment. *Geomorphology* 190, 112-125.

Görüm T (2019) Landslide recognition and mapping in a mixed forest environment from airborne LiDAR data. *Engineering Geology* 258, 105155.

INDEX

M

N

O

P

R

S

T

U

V

W

X

Y

Z

14TH

INTERNATIONAL SYMPOSIUM ON LANDSLIDES

03/2025 - ISBN 978-2-9585706-1-3